POLYMER COMPOSITES IN THE AEROSPACE INDUSTRY

SECOND EDITION

Edited by
P. E. IRVING
C. SOUTIS

ELSEVIER

Related titles

Njuguna, *Lightweight Composite Materials in Transport*, 2016, $330, 470pp
(ISBN 9781782423256)

Rana, *Advanced Composite Materials for Aerospace Structures,* 2016, $260, 490pp
(ISBN 9780081009390)

Yuan, *SHM in Aerospace Structures,* 2016, $285, 496pp
(ISBN 9780081001486)

Summerscales, *Marine Application of AFRC*, 2015, $265, 360pp
(ISBN 9781782422501)

Giurgiutiu, *SHM of Aerospace Composites,* 2015, $140, 470pp
(ISBN 9780124096059)

Woodhead Publishing Series in Composites Science and Engineering

Polymer Composites in the Aerospace Industry

Second Edition

Edited by

Philip Irving
School of Aerospace, Transport and Manufacture, University of Cranfield, Cranfield, United Kingdom

Constantinos Soutis
School of Mechanical, Aerospace and Civil Engineering and the Aerospace Research Institute, University of Manchester, Manchester, United Kingdom

WP
WOODHEAD
PUBLISHING

An imprint of Elsevier

ELSEVIER

Working together
to grow libraries in
developing countries

ELSEVIER • Book Aid International

www.elsevier.com • www.bookaid.org

Contributors

E. Archer   Ulster University, Newtownabbey, Ulster, United Kingdom

R.H. Bossi   The Boeing Company (retired), Seattle, WA, United States

Andreas J. Brunner   Empa, Swiss Federal Laboratories for Materials Science and Technology, Dübendorf, Switzerland

Richard Butler   Materials and Structures Research Centre, Department of Mechanical Engineering, University of Bath, Bath, United Kingdom

W.J. Cantwell   Department of Aerospace Engineering, Khalifa University of Science and Technology (KUST), Abu Dhabi, United Arab Emirates

M. David   ARC Training Centre for Automated Manufacture of Advanced Composites, School of Mechanical and Manufacturing Engineering, UNSW, Sydney, NSW, Australia

Glyn Davies   Imperial College, London, United Kingdom

J.P. Foreman   University of Sheffield, Sheffield, United Kingdom

G.E. Georgeson   The Boeing Company, Seattle, WA, United States

Victor Giurgiutiu   University of South Carolina, Columbia, SC, United States

Philip Irving   School of Aerospace, Transport and Manufacture, University of Cranfield, Cranfield, United Kingdom

Dmitry S. Ivanov   Bristol Composites Institute ACCIS (Advanced Composite Collaboration for Innovation and Science), University of Bristol, Bristol, United Kingdom

A.F. Johnson   Composites Consultant, Stuttgart, Germany

F.R. Jones   University of Sheffield, Sheffield, United Kingdom

M.W. Joosten   Deakin University, Geelong, VIC, Australia

C. Kassapoglou   Delft University of Technology, Delft, The Netherlands

G.S. Langdon   Blast and Impact Survivability Research Unit, Department of Mechanical Engineering, University of Cape Town, Rondebosch, Western Cape, South Africa

Stepan V. Lomov   Department of Materials Engineering, KU Leuven, Leuven, Belgium

C.T. McCarthy   University of Limerick, Limerick, Ireland

M.A. McCarthy   University of Limerick, Limerick, Ireland

A. McIlhagger   Ulster University, Newtownabbey, Ulster, United Kingdom

R. McIlhagger   Ulster University, Newtownabbey, Ulster, United Kingdom

A. Murphy   School of Mechanical & Aerospace Engineering, Queen's University Belfast, Belfast, United Kingdom

Mark W.D. Nielsen   Materials and Structures Research Centre, Department of Mechanical Engineering, University of Bath, Bath, United Kingdom

Andrew T. Rhead   Materials and Structures Research Centre, Department of Mechanical Engineering, University of Bath, Bath, United Kingdom

Constantinos Soutis   School of Mechanical, Aerospace and Civil Engineering and the Aerospace Research Institute, University of Manchester, Manchester, United Kingdom

Ramesh Talreja   Department of Aerospace Engineering, Department of Materials Science and Engineering, Texas A&M University, College Station, TX, United States

R.S. Thomson   Advanced Composite Structures Australia, Port Melbourne, VIC, Australia

M. Waimer   German Aerospace Center (DLR), Stuttgart, Germany

S. Waite   Senior Expert − Materials, Certification Directorate, EASA, Cologne, Germany

Zhangming Wu   School of Mechanical Engineering & Mechanics, Ningbo University, China; School of Engineering, Cardiff University, Cardiff, United Kingdom

Preface

Polymer composites are increasingly used in aerospace applications because of their excellent strength and durability compared to weight. The revised edition of this book summarizes the latest research and developments on the design, manufacture, and performance of composite components for aerospace structures. It provides detailed discussion on the design, modeling, and analysis of conventional and advanced polymer composites with an in-depth understanding of mechanical properties and long-term performance, such as strength, stiffness, impact, blast resistance, and fatigue. The book features additional chapters on aircraft-specific topics such as lightning strike protection, damage tolerance, and airworthiness.

Part one includes chapters on the modeling, structure, and behavior of 2D and 3D woven composites; the manufacture processes used for composite materials and components; buckling and compressive strength of laminates; and manufacturing defects in composite materials. Part two discusses aspects of composite performance in aerospace structural design, including chapters on modeling stiffness and strength of structural elements; fatigue under uniaxial and multiaxial loads; fracture mechanics; impact strength; crashworthiness; design and failure analysis of bolted joints; response of aerospace composite to temperatures and humidity; blast response; repair; nondestructive evaluation of damage; structural health monitoring (SHM); airworthiness; and certification.

There is general acceptance that the current practice of designing a damage-tolerant structure is to take advantage of composite material heterogeneity and to configure the material such that it will withstand certain types of damage and will naturally arrest its propagation. Yet, this is a passive approach and for this reason it is subject to its own limitations. On the other hand, the development of SHM techniques for composites is an emerging technology, which seemingly can provide the means to enhance reliability and safety by ensuring early detection and monitoring of damage. Predictive capabilities enabling estimations of residual stiffness and strength of a composite structure with a known state of damage are also emerging. It is envisioned that new strategies for designing damage-resistant and -tolerant composite structures may become available, if we first develop and then synergistically combine new capabilities enabling in-service damage detection and characterization, health monitoring, and structural prognosis. The assurance of structural reliability of aircraft systems will greatly enhance confidence in their safety, reduce the probability of premature failures, and diminish the costs of operation and maintenance. The threads running through these

chapters can be drawn together, leading to an understanding of the structural behavior and integrity of modern composite structures.

Polymer Composites in the Aerospace Industry, Second Edition is an essential reference resource for engineers, scientists, and designers working in the development of composite materials in aerospace applications.

Part One

Design and manufacture of composite components for aerospace structures

Aerospace engineering requirements in building with composites

1

Constantinos Soutis
School of Mechanical, Aerospace and Civil Engineering and the Aerospace Research Institute, University of Manchester, Manchester, United kingdom

1.1 Introduction

Composite materials have gained popularity (despite their generally high cost) in high-performance products that need to be lightweight, yet strong enough to take high loads such as aerospace structures (tails, wings, and fuselages), wind turbine blades, boat construction, bicycle frames, and racing car bodies. Other uses include storage tanks and fishing rods. Natural composites (wood and fabrics) have found applications in aircraft from the first flight of the Wright Brothers' Flyer 1, in North Carolina on December 17th, 1903, to the plethora of uses now enjoyed by man-made (engineered) composite materials on both military and civil aircraft, in addition to more exotic applications on unmanned aerial vehicles (UAVs), space launchers, satellites, and solar sails. Their adoption as a major contribution to aircraft structures followed on from the discovery of carbon fiber at the Royal Aircraft Establishment at Farnborough, UK, in 1964. However, not until the late 1960s did these new composites start to be applied, on a demonstration basis, to military aircraft. Examples of such demonstrators were trim tabs, spoilers, rudders, and doors. With increasing application and experience of their use came improved fibers and matrix materials (thermosets and thermoplastics) resulting in CFRP composites with improved mechanical properties, allowing them to displace the more conventional materials, aluminum and titanium alloys, for primary structures. In the following sections, the properties and structure of carbon fibers are discussed together with thermoplastic and thermoset resins and the significance of the interface between the fiber and the matrix (resin) that affect performance.

1.1.1 Carbon fiber types and properties

High strength, high modulus carbon fibers are about $5-6$ μm in diameter and consist of small crystallites of "turbostratic" graphite, one of the allotropic forms of carbon. The graphite structure consists of hexagonal layers, in which the bonding is covalent and strong (~ 525 kJ/mol) and there are weak Van der Waals forces (<10 kJ/mol) between the layers [1,2]. This means that the basic crystal units are highly anisotropic; the in-plane Young's modulus parallel to the α-axis is approximately 1000 GPa and

Young's modulus parallel to the c-axis normal to the basal planes is only 30 GPa. Alignment of the basal plane parallel to the fiber axis gives stiff fibers, which, because of the relatively low density of around 2 Mg/m^3, have extremely high values of specific stiffness ($\sim$200 GPa/(Mg/m^3)). Imperfections in alignment, introduced during the manufacturing process result in complex-shaped voids elongated parallel to the fiber axis. These act as stress raisers and points of weakness, leading to a reduction in strength properties. Other sources of weakness, which are often associated with the manufacturing method, include surface pits and macro-crystallites. The arrangement of the layer planes in the cross-section of the fiber is also important since it affects the transverse and shear properties of the fiber. Thus, for example, the normal polyacrylonitrile-based (PAN-based) Type I carbon fibers have a thin skin of circumferential layer planes and a core with random crystallites. In contrast, some mesophase pitch-based fibers exhibit radially oriented layer structures. These different structures result in some significant differences in the properties of the fibers, and of course, those of the composites.

Refinements in fiber process technology over the past 20 years have led to considerable improvements in tensile strength ($\sim$4.5 GPa) and in strain to fracture (more than 2%) for PAN-based fibers. These can now be supplied in three basic forms, high modulus (HM, $\sim$380 GPa), intermediate modulus (IM, $\sim$290 GPa), and high tensile strength (HS, $\sim$4.5 GPa with a modulus of around 230 GPa). The more recent developments of the high strength fibers have led to what is known as high strain fibers, which have strain values of 2% before fracture. The tensile stress-strain response is elastic up to failure, and a large amount of energy is released when the fibers break in a brittle manner. The selection of the appropriate fiber depends very much on the application. For military aircraft, both high modulus and high strength are desirable. Satellite applications, in contrast, benefit from the use of high fiber modulus, improving stability and stiffness for reflector dishes, antennas, and their supporting structures.

Rovings are the basic forms in which fibers are supplied, a roving being a number of strands or bundles of filaments wound into a package or creel, the length of the roving being up to several kilometers, depending on the package size. Rovings or tows can be woven into fabrics, and a range of fabric constructions are available commercially, such as plain weave, twills, and various satin weave styles, woven with a choice of roving or tow size depending on the weight or areal density of fabric required. Fabrics can be woven with different kinds of fiber, for example, the carbon in the weft and glass in the warp direction, and this increases the range of properties available to the designer. One advantage of fabrics for reinforcing purposes is their ability to drape or conform to curved surfaces without wrinkling. It is now possible, with certain types of knitting machines, to produce fiber performs tailored to the shape of the eventual component. However, generally speaking, the more highly convoluted each filament becomes, as at crossover points in woven fabrics, or as loops in knitted fabrics, the lower its reinforcing ability.

1.1.2 Fiber-matrix interface

The fibers are surface treated during manufacture to prepare adhesion with the polymer matrix, whether thermosetting (epoxy, polyester, phenolic, polyimide resins) or

thermoplastic (polypropylene, Nylon 6.6, PMMA, PEEK). The fiber surface is roughened by chemical etching and then coated with an appropriate size to aid bonding to the specified matrix. Whereas composite tensile strength, primarily, is a function of fiber properties, the ability of the matrix to both support the fibers (required for good compression strength) and provide out-of-plane strength is, in many situations, equally important. The aim of the material supplier is to provide a system with a balanced set of properties. While improvements in fiber and matrix properties can lead to the improved lamina or laminate properties, the all-important field of the fiber-matrix interface must not be neglected.

The load acting on the matrix has to be transferred to the reinforcement via the **interface**. Hence, fibers must be strongly bonded to the matrix if their high strength and stiffness are to be imparted to the composite. The fracture behavior is also dependent on the strength of the interface. A weak interface results in a low stiffness and strength but high resistance to fracture, whereas a strong interface produces high stiffness and strength but often a low resistance to fracture, i.e., brittle behavior. Conflict therefore exists, and the designer must select the material most nearly meeting his requirements. Other properties of a composite, such as resistance to creep, fatigue, and environmental degradation, are also affected by the characteristics of the interface. In these cases, the relationship between properties and interface characteristics are generally complex, and analytical/numerical models supported by extensive experimental evidence are required [3].

1.1.3   Resin materials

Thermoplastic materials are becoming more available; however, the more conventional matrix materials currently used are thermosetting epoxies. The matrix material is the Achilles' heel of the composite system and limits the fiber from exhibiting its full potential in terms of laminate properties. The matrix performs a number of functions some of which are stabilizing the fiber in compression (providing lateral support), translating the fiber properties into the laminate, minimizing damage due to impact by exhibiting plastic deformation, and providing out-of-plane properties to the laminate. Matrix dominated properties (interlaminar strength, compressive strength) are reduced when the glass transition temperature is exceeded, whereas, with a dry laminate this is close to the cure temperature, the inevitable moisture absorption reduces this temperature, and hence, limits the application of very high-temperature-cure thermoset epoxy composites to less than $120°C$.

Conventional epoxy aerospace resins are designed to cure at $120-135°C$ or $180°C$, usually, in an autoclave or closed cavity tool at pressures up to 8 bar, occasionally with a postcure at a higher temperature. Systems intended for high-temperature applications maybe undergo curing at temperatures up to $350°C$. The resins must have a room temperature life beyond the time it takes to lay-up a part and have time/temperature/viscosity suitable for handling. The resultant resin characteristics are normally a compromise between certain desirable characteristics. For example, improved damage tolerance performance usually causes a reduction in hot-wet compression

properties, and if this attained by an increased thermoplastic content, then the resin viscosity can increase significantly. Increased viscosity is especially not desired for a resin transfer molding (RTM) resin where a viscosity of 50 cPs or less is often required, but toughness may also be imparted by the fabric structure, such as a stitched noncrimped fabric (NCF).

The first generation of composites introduced to aircraft construction in the 1960s and 1970s employed brittle epoxy resin systems leading to laminated structures with a poor tolerance to the low-energy impact caused by runway debris thrown up by aircraft wheels or the impacts occurring during manufacture and subsequent servicing operation. Although the newer toughened epoxy systems provide improvements in this respect, they are still not as damaged tolerant as thermoplastic materials. A measure of damage tolerance is the laminate compression after impact (CAI) and the laminate open-hole compressive (OHC) strengths. The ideal solution is to provide a composite exhibiting equal OHC and CAI strengths, and although the thermoplastics are tougher, they have not capitalized on this by yielding higher notched compression properties than the thermoset epoxy composites. Polyetheretherketone (PEEK) is a relatively costly thermoplastic with good mechanical properties. Carbon fiber-reinforced PEEK is a competitor with carbon fiber/epoxies and Al−Cu and Al−Li alloys in the aircraft industry. On impact at relatively low energies (5−10 J) carbon fiber-PEEK laminates show only an indentation on the impact site, whereas in carbon fiber-epoxy systems, ultrasonic C-scans show that delamination extends a considerable distance affecting more dramatically the residual strength and stiffness properties of the composite. Another important advantage of carbon fiber-PEEK composites is that they possess unlimited shelf-life at ambient temperature; the fabricator does not have to be concerned with proportioning and mixing resins, hardeners, and accelerators as with thermosets; and the reversible thermal behavior of thermoplastics means that components can be fabricated more quickly because the lengthy cure schedules for thermosets, sometimes extending over several hours, are eliminated.

It can be seen that in the effort to improve the through-the-thickness strength properties and impact resistance the composites industry has moved away from brittle resins and progressed to thermoplastic resins, toughened epoxies, through damage-tolerant methodology, Z-fiber (carbon, steel or titanium pins driven through the z-direction to improve the through-thickness properties), stitched fabrics, stitched performs, and the focus is now on affordability. The current phase is being directed toward affordable processing methods, such as nonautoclave processing, nonthermal electron beam curing by radiation, and cost-effective fabrication [4,5]. NASA Langley in the USA claims a 100% improvement in damage tolerance performance with stitched fabrics relative to conventional materials (ref. Advanced Composites Technology (ACT), a program where noncrimped fabric (NCF) laminates are processed by resin film infusion (RFI)). It is essential that if composites were to become affordable, they must change their basic processes to get away from pre-preg material technology, which currently results in an expensive solution, and hence, product. However, autoclaved continuous fiber composites will still dominate for the high levels of structural efficiency required.

1.2 Analysis and design

Aircraft design from the 1940s has been based primarily on the use of aluminum alloys, and as such, an enormous amount of data and experience exists to facilitate the design process. With the introduction of laminated composites that exhibit anisotropic properties, the methodology of design had to be reviewed, and in many cases, replaced. It is accepted that designs in composites should not merely replace the metallic alloy but should take advantage of exceptional composite properties if the most efficient designs are to evolve. Of course, the design should account for through-thickness effects that are not encountered in the analysis of isotropic materials. For instance, in a laminated structure, since the layers (laminae) are elastically connected through their faces, shear stresses are developed on the faces of each lamina. The transverse stresses (σ_z, τ_{xz}, τ_{yz}), thus produced can be quite large near a free boundary (free edge, cut-out, an open hole) and may influence the failure of the laminate [6].

The laminate stacking sequence can significantly influence the magnitude of the interlaminar normal and shear stresses, and thus, the stacking sequence of plies can be important to a designer. It has been reported that the fatigue strength of a ($\pm15/\pm45$)$_s$ Boron fiber/epoxy laminate is about 175 MPa lower than a ($\pm45/\pm15$)$_s$ laminate of the same system. The interlaminar normal stress σ_{zz}, changes from tension to compression by changing the stacking sequence, and thus, accounts for the difference in strengths. In this case, progressive delamination is the failure mode in fatigue. Approximate analytical methods and numerical approaches, such as finite difference and finite element (FE) techniques [7] can be used to analyze the interlaminar stress distributions near free edges, open holes, bolted joints, and help to identify the optimum fiber orientation and laminate stacking sequence for the given loading and kinematic boundary conditions. Generally, the determination of local stress distribution in a bolted joint is a three-dimensional problem due to bending effects and clamping of the fastener. The stress state in the vicinity of a bolted hole depends on many complex factors, such as friction properties of the members, contact problem, geometry, and stiffness of the joined members, joint configuration, clamping force, and loading conditions. To precisely include all these factors in stress analysis of a joint based on conventional analytical methods is extremely cumbersome [8−11]. Fig. 1.1 illustrates a finite element model used to analyze a single bolt fastener in a double-lap joint and simulate the clamping force in the joint [10].

The lay-up geometry of a composite strongly affects not only crack initiation but also crack propagation, with the result that some laminates appear highly notch sensitive, whereas others are insensitive to the presence of stress concentrators [12−14], especially in 3D woven fiber architectures [15]. The selection of fibers and resins, how they are combined in the lay-up, and the quality of the manufactured composite must all be carefully controlled if optimum toughness is to be achieved. Furthermore, materials requirements for the highest tensile and shear strengths of laminates are often incompatible with requirements for highest toughness. Compared with a fracture in metals, research into the fracture behavior of composites is in its infancy. Much of
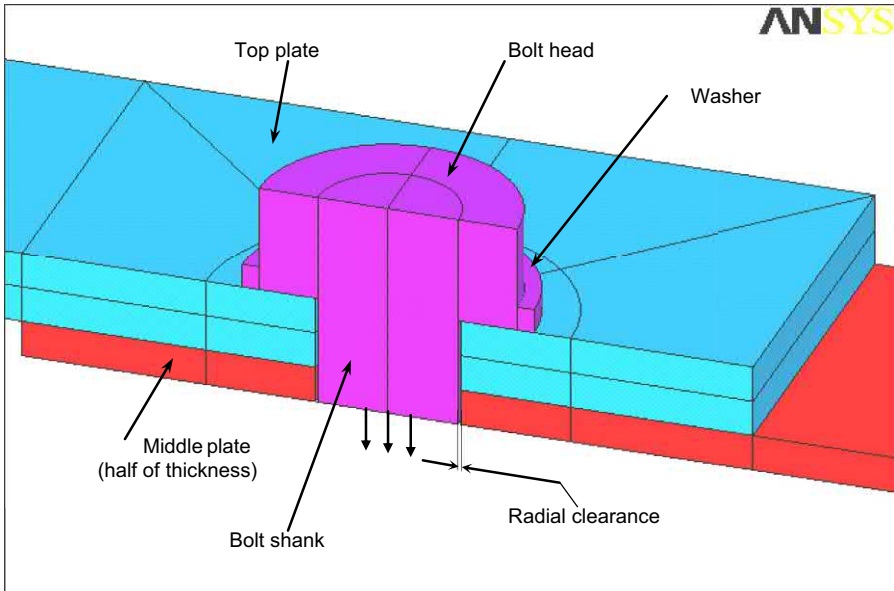
Figure 1.1 A finite element solid bolt model, where the clamping force is represented by a negative displacement at the bottom surface of the bolt shank [10].

the necessary theoretical framework is not yet fully developed, and there is no simple recipe for predicting the toughness of all composites. However, we are not able to design the structure of any composite with certainty to produce the optimum combination of strength and toughness.

In metallic and plastic materials, even relatively brittle ones, energy is dissipated in nonelastic deformation mechanisms in the region of the crack tip. This energy is lost in moving dislocations in metal and viscoelastic flow or craze formation in a polymer. In composites stressed parallel to the fiber axis, the fibers interfere with crack growth, but their effectiveness depends on how strongly they are bonded to the matrix (resin). For example, if the fiber/matrix bond is strong, the crack may run through both fibers and matrix without deviation, in which case, the composite toughness would be low and approximately equal to the sum of the separate component toughness. On the other hand, if the bond is weak, the crack path becomes very complex, and many separate damage mechanisms may then contribute to the overall fracture work of the composite. For example, a brittle polymer or epoxy resin with a fracture energy $G \cong 0.1$ KJm^{-2} and brittle glass fibers with $G \cong 0.01$ KJm^{-2} can be combined together in composites, some of which have fracture energies of up to 100 kJm^{-2}. For an explanation of such a large effect, we must look beyond simple addition [16,17].

If the crack is oriented parallel to the fibers and is subjected either to tensile stresses perpendicular to the fibers or shear stresses parallel to them, the fibers have little influence on crack propagation. In these circumstances, a weak fiber-matrix bond can cause the crack to propagate rapidly along the fiber/matrix interface. If the interface bond is

stronger than stresses required to fail the matrix in either shear or direct stress, crack growth is largely a function of matrix strength and toughness.

Fracture in composite materials seldom occurs catastrophically without warning but tends to be progressive, with substantial damage widely dispersed through the material. Tensile loading can produce matrix cracking, fiber bridging, fiber pull-out, fiber/matrix debonding, and fiber rupture, which provide extra toughness and delay failure [16]. The fracture behavior of the composite can be reasonably well explained in terms of some summation of the contributions from these mechanisms, but as said earlier, it is not yet possible to design a laminated composite to have a given toughness.

Another important modeling issue is the fatigue life of the composite. In contrast to homogeneous metallic materials, in which fatigue failure generally occurs by the initiation and propagation of a single crack, the fatigue process in composite materials is very complex and involves several damage modes, including fiber/matrix de-bonding, matrix cracking, delamination, and fiber fracture (tensile or compressive failure in the form of fiber microbuckling or kinking); Fig. 1.2 shows a typical fiber microbuckling failure observed in currently used carbon fiber/epoxy systems [18,19]. By a combination of these processes, widespread damage develops throughout the bulk of the composite and leads to a permanent degradation in mechanical properties, notably, laminate stiffness and residual strength [20,21]. Despite these complexities, the in-plane fatigue strength of both glass and carbon fiber laminates is significantly superior to most metallic alloys, to such an extent that in-plane fatigue durability is no longer a design issue. As in the static loading case, it is the out-of-plane fatigue properties which can limit design strains, and this is where 3D textile composites may be found attractive [22,23].

Although these complexities (free edge effects, impact damage, joints, fatigue life prediction) lengthen the design process, they are more than compensated for by the mass savings and improvements in aerodynamic efficiency that result. The finite element analysis is also a crucial component, and the biggest time-saving strides have been in the user-friendly developments in creating the data and interpreting the results using modern, sophisticated graphical user interfaces. The key is using parametric software to generate geometry and meshes.It used to take Boeing (Phantom Works) in St Louis, USA, more than 6 months to perform the initial FE element
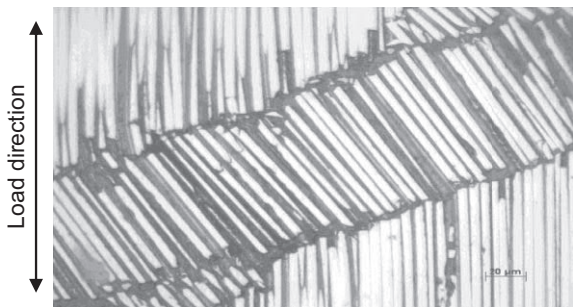
Figure 1.2 Fiber kinking induced by fiber instability or fiber microbuckling observed in a carbon fiber/epoxy laminate; fiber diameter is about 6 m [18].

stiffness and strength analysis for a complete aircraft; now, this takes less than 3 weeks with a handful of engineers, and composites have become more attractive and economically viable.

The majority of aircraft control-lift surfaces produced has a single degree of curvature due to the limitation of metal fabrication techniques. Improvements in aerodynamic efficiency can be obtained by moving to double curvature allowing, for example, the production of variable camber, twisted wings. Composites and modern mold tools allow the shape to be tailored to meet the required performance targets at various points in the flying envelope. A further benefit is the ability to tailor the aeroelasticity of the surface to improve the aerodynamic performance further. This tailoring can involve adopting laminate configurations that allow the cross-coupling of flexure and torsion, such that, wing twist can result from bending and vice-versa. Finite element analysis allows this process of aeroelastic tailoring, along with strength and dynamic stiffness (flutter) requirements to be performed automatically with a minimum of postanalysis engineering yielding a minimum mass solution.

Early composite designs were replicas of those, which employed metallic materials, and as a result, the high material cost and man-hour-intensive laminate production jeopardized their acceptance. This was compounded by the increase in assembly costs due to initial difficulties of machining and hole production. The cost is directly proportional to the number of parts in the assembly and, as a consequence, designs and manufacture techniques had to be modified to integrate parts, thereby reducing the number of associated fasteners. A number of avenues are available for reducing the parts count, such as the use of integrally stiffened structures, co-curing or co-bonding of substructures onto lift surfaces like the wings and stabilizers, and the use of honeycomb sandwich panels. Hand lay-up techniques and conventional assembly results in manufacturing costs 60% higher than the datum and only with the progressive introduction of automated lay-up and advanced assembly techniques, composites compete with their metallic counterparts. Also, the introduction of virtual reality and virtual manufacturing will play an enormous role in further reducing the overall cost. The use of virtual reality models in engineering prior to manufacturing to identify potential problems is relatively new but has already demonstrated great potential. Bell Textron in the USA made significant use of IT during the product definition phase (for the V22 Osprey Tilt-rotor, Fig. 1.3) to ensure "right first-time" approach. Other manufacturing tools that can reduce production cost and make composites more attractive are Virtual Fabrication (creating parts from raw materials), Virtual Assembly (creation of assembly from parts), Virtual Factory (evaluation of the shop floor). Virtual manufacturing validates the product definition and optimizes the product cost; it reduces rework and improves learning, making Industry 4.0 possible, and the smart factory for composites a reality. Industry 4.0 is a name given to the current trend of automation and data exchange in manufacturing technologies, commonly referred to as the fourth industrial revolution. It includes cyber-physical systems—physical assets connected to digital twins—the Industrial Internet of Things (IIoT), cloud computing and cognitive computing, data analytics, 3D printing, and artificial intelligence. With Industry 4.0, the physical world is merging with the virtual world. PLM Software from Siemens is an example of how this can work [24]. The software is used to virtually develop

Figure 1.3 V22-Osprey Tilt-rotor plane.
Photo by C. Soutis.

and extensively test products even before a single screw is turned in real life. With this technology, products reach the market as much as 50% faster, with at least the same level of quality achieved without PLM. This is possible thanks to simulation with a **digital twin**—a virtual image of the product into which different designs of its individual components can be inserted and tested along the entire development chain. This approach was used to simulate the landing of the Mars Curiosity Rover in 2012. The landing was tested 8000 times using Siemens PLM software.

Information technology, telecommunications, and manufacturing are merging, as the means of production becomes increasingly autonomous. However, it is impossible to say what **smart factories** will exactly look like in the future. The smart factory, sometimes referred to as "the factory of the future" is the keystone of the fourth industrial revolution. Indeed, it is often represented as the aggregate of all the Industry 4.0 technologies, the IIoT, and systems. One possible scenario in the factory of the future, whereby connecting equipment up to the cloud environment, the machines will organize themselves to a great extent, delivery chains will automatically assemble themselves, and orders will transform directly into production information and flow into the production process. Still, people will remain essential in an Industry 4.0 world—as the creative leaders and thinkers who will use their intelligence to conceive of all the processes and procedures in advance and who will write the right software to convey that information to machines. Then the challenge arises of how to improve and optimize human-machine interaction and whether this can also be achieved by big data analytics.

1.3 Manufacturing techniques

The largest proportion of carbon fiber composites used in primary class-one structures is fabricated by placing layer upon layer of unidirectional (UD) material to the

designer's requirement in terms of ply profile and fiber orientation. On less critical items, woven fabrics very often replace the prime unidirectional form. A number of techniques have been developed for the accurate placement of the material, ranging from labor-intensive hand lay-up techniques to those requiring high capital investment in automatic tape layers (ATLs). Tape-laying machines operating under numerical control are currently limited in production applications to flat lay-up or gently curved panels, and significant effort is being directed by machine manufacturers at overcoming these problems associated with laying on more complex contoured surfaces. The width of UD tape applied varies considerably from about 150 mm down to a single tow for curved structures. The need for individual tows or a single wideband should always be a compromise between surface geometry and the manufacturing throughput. Simple geometries over large surface areas are typically approached by industry with ~ 150 mm ($\sim 6'$) wide tapes. While this solution may adequately handle the overall simple geometry, localized pad-ups and occlusions may still demand hand lay-up or pre-kitted plies and hand trimming on the part surface. Complex ATL systems with "flying knife" technology may trim to a perfect edge of ply, but the scrap generated needs to be removed by hand. This precision capability adds to machinery complexity, which increases cost and manufacturing time.

In general, the cost of ATL machinery is high, and deposition rates low. In 1988, the first Cincinnati tape layer was installed in the Phantom Works, and in 1995, a 7-axis Ingersol fiber placement machine was installed. This gave the capability to steer fibers within an envelope of 40 ft $\times$ 20 ft with a 32-tow capability. An over-wing panel had been manufactured which was able to steer around cut-outs. Collaboration with DASA on global optimization software was completed at the end of 1998. This software is claimed to have produced a 13% weight saving. Other applications include an engine cowling door, ducting with a complex structure, FA18 E/F, and T45 horizontal stabilizer skins. Its capacity was extended to take a 6-inch wide tape, and Boeing 777 has been converted from hand lay-up to fiber placed (back to back then split) spars with a saving of $5000 per set. Bell Textron has a 10-axis Ingersol, contoured, automatic tape laying machine for the B609 skin lay-up, which is placing a six in wide T300 tape onto an inner mold line Invar tool with preinstalled hat stringers. Fiber placement and filament winding technologies are also being used to manufacture components for the V22 [4].

Once the component is laid-up on the mold enclosed in a flexible bag tailored approximately to the desired shape and the assembly is enclosed usually in an autoclave, a pressure vessel designed to contain a gas at pressures generally up to 1.5 MPa and fitted with a means of raising the internal temperature to that required to cure the resin. The flexible bag is first evacuated, thereby removing trapped air and organic vapors from the composite, after which the chamber is pressurized to provide additional consolidation during cure. The process produces structures of low porosity of less than 1% and high mechanical integrity. Large autoclaves have been installed in the aircraft industry capable of accommodating complete wing or tail sections.

Alternatively, low-cost nonautoclave processing methods, such as the vacuum molding (VM), resin transfer molding (RTM), vacuum-assisted RTM (VARTM),

and resin film infusion (RFI), can be used. The vacuum molding process makes use of atmospheric pressure to consolidate the material while curing, thereby obviating the need for an autoclave or a hydraulic press. The laminate in the form of preimpregnated fibers or fabric is placed on a single mold surface and is overlaid by a flexible membrane, which is sealed around the edges of the mold by a suitable clamping arrangement. The space between the mold and the membrane is then evacuated, and the vacuum is maintained until the resin has cured. Quite large, thin shell moldings can be made in this way at a low cost. The majority of systems suitable for vacuum only processing are cured at $60-120°C$ and then postcured typically at $180°C$ to fully develop properties. In 1991, the evaluation of this method started at the Phantom Works using the resin system LTM10 (low-temperature molding), and they created a small allowables database for their X36 fighter research aircraft study. In 1996, McDonnel Douglas characterized LTM45 EL for the Joint Strike Force (JSF) prototype and generated design allowable data. In 1998, Boeing also produced LTM45 EL data. LTM10 applications demonstrated for complex parts with a $140°F$ cure under vacuum include a serpent inlet duct. A box using LTM10 was shown at the 1998 Farnborough Air show. A research program at NASA Langley invested effort at the development of $180°C$ material properties using low-temperature curing resins. The main advantages of LTM systems are the potential to use autoclave free cures, the use of cheaper tooling and reduced spring-back of parts.

RTM and RFI are the predominant curing processes among the several variations being developed today. In traditional preimpregnated (prepreg) technology, the resin has already infiltrated the fibers and processing mainly removes air and volatiles, consolidates and cures. RTM, in its simplest form, involves a fabric preform being placed in an enclosed cavity and resin forced into the mold to fill the gaps under pressure and cure. The RFI method utilizes precast resin tiles with thickness ranging from 0.125 to 0.25 in. This approach reduces the number of consumables used but is very process sensitive relying on the resin being of sufficiently low permeability to fully impregnate the fabric before cure advances too far. The use of an autoclave or press to apply pressure varies. The RFI process is being applied within the Advanced Composites Technology (ACT) Program in conjunction with traditional autoclave processing. Heat is the energy source to activate the resin cure, but some resin systems can be activated by radiation. It is claimed that thermal oven processing could save 90% of autoclave processing time and energy, and hence, 50% cost. There is also a radiation curing process developed jointly by NASA and Advanced Composites Group (ACG) and of innovative electron beam cured structures being developed by Foster-Miller, Lockheed Martin, and Oakridge National Laboratories in the USA [4].

The Vacuum Assisted RTM (VARTM) is a liquid resin infusion process and is currently considered by the aircraft industry to be the favored low-cost manufacturing process for the future. It is an autoclave-free process that has been identified as reducing the cost of component processing. It is reported that dimensional tolerance and mass measurements are comparable with stitched RFI autoclave panels. A conventional blade stiffened test panel (3 ft × 2 ft with a 4′ high blades 0.5′ thick) was manufactured recently at NASA by using the VARTM method achieving a reasonable quality.

Further cost reduction when manufacturing with composites will be achieved by reducing the assembly cost, by moving away from fastening (drilling of thousands of holes followed by fastener insertion and sealing) toward bonding and to assembly with less or no expensive jigging. Bell Textron, among others, built and developed several structures (for the V22 and B609) where they applied state-of-the-art composites technology/processes to achieve a unitized approach to manufacturing and assembly. There are, of course, significant certification challenges with an adhesively bonded joint without fasteners for a primary aircraft structure application that needs to be addressed.

The airliner Boeing 787 and the Airbus A350 XWB (Extra Wide Body) where the fuselage, wing box, and wings are mostly made of CFRP composites still require assembly with thousands of mechanical fasteners, since it is the easiest and least expensive way to meet current certification requirements, which mandate proof that each and every adhesively bonded joint will not separate and cause structural failure should it reach its critical design load. Many in the industry argue that the full cost and weight savings of composites cannot be realized until bonded joints can be certified without fasteners.

In 2018, research effort by the aircraft industry in USA and EU offered the hope of building reliability into the bonding process and of gauging final bond strength via a coordinated certification system that includes design, process control, and quality assurance.

1.4 Applications in aircraft construction

In the pioneering days of flight aircraft structures were composite being fabricated largely of wood (natural composite), wire, and fabric. Aluminum alloys took over in the 1930s and have dominated the industry until recent time. Wooden structures did, however, persist until World War II and the de Havilland Mosquito aircraft (DH98) constructed of a plywood-balsa-plywood sandwich laminate probably represents the high point of engineering design with wood. The DH91 Albatross airliner in 1937 was molded as a ply-balsa-ply sandwich construction, and the Spitfire fuselage in 1940 was designed and built of Gordon Aerolite material that was a phenolic resin incorporating untwisted flax fibers that could be regarded as the precursor of modern fiber-reinforced plastics.

Current civil aircraft applications have concentrated on replacing the secondary structure with fibrous composites where the reinforcement media have either been carbon, glass, Kevlar, or hybrids of these. The matrix material, a thermosetting epoxy system is either a 125 or 180°C curing system with the latter becoming dominant because of its greater tolerance to environmental degradation. Typical examples of the extensive application of composites in this manner are the Boeing 757, 767, and 777 and from Europe the Airbus A310, A320, A330, and A340 airliners. The A310 carries a vertical stabilizer (8.3 m high by 7.8 m wide at the base) a primary aerodynamic and structural member fabricated in its entirety from carbon composite

(now £10−20/kg for large tow HS fiber) with a total weight saving of almost 400 kg when compared with the Al alloy unit previously used. In addition, the CFRP fin box comprises only 95 parts excluding fasteners, compared with 2076 parts in the metal unit, thus making it easier to produce. The A320 has extended the use of composites to the horizontal stabilizer in addition to the plethora of panels and secondary control surfaces, leading to a weight saving of 800 kg over Al alloy skin construction. As an indication of the benefit of such weight saving, it has been estimated that 1 kg weight reduction saves over 2900 L of fuel per year. From nose to tail, Airbus continues to utilize advanced composites in its A320neo narrow-body airliner launched in 2010 and introduced by Lufthansa on 25 January 2016 with improved fuel efficiency and much-reduced noise and emissions.

Larger amounts of FRPs are used in the bigger A330, A340 models, and of course, in the A380 superjumbo airliner built by the European Airbus consortium. The wing trailing edge panels are made of glass and carbon fiber-reinforced plastics using a new resin film infusion method (RFI), in which resin film, interleaved between glass and carbon fabric layers, when the laminate is laid up, melts when the heat is applied. Melted low-viscosity resin migrates easily through the thickness of the laminate, where it cures to form the final component. A hybrid aluminum/glass-reinforced plastic system (GLARE) is used for the A380 fuselage crown, Fig. 1.4, which results in reduced weight, increased damage tolerance, and improved fatigue life.


Figure 1.4 A380 all-composite tail assembly (empennage) with Glare fuselage crown. Photo by C. Soutis, Farnborough Air Show, July 2018.

The application of CFRP reached new proportions with the A350 XWB, which boasts the application of composites throughout the structure with an amount of 52% by weight. Most of the wing is carbon fiber (CF) made, including the upper and lower covers, measuring 32 m long by 6 m wide, making them among the largest single aviation parts ever made from CF. According to Airbus, the A350 requires 50% fewer structure maintenance tasks, while the threshold for airframe checks is 12 years compared to 8 years for the A380.

Similarly, the new Boeing 787 Dreamliner structure, including the fuselage, wings, tail, doors, and the interior is made of over 50% by weight composite materials (80% by volume). The all-composite fuselage made it the first composite airliner in production (its first flight was before the A350). Each fuselage barrel is manufactured in one piece (about 45 ft long) eliminating the need of more than 50,000 fasteners used in conventional aircraft building. However, major assembly issues with the composite fuselage sections were encountered that caused long delays in delivering the aircraft to the customer and there were problems with what was coming out of the autoclave, which is certainly a costly experience. Other technical issues that had to be resolved were on safety with electromagnetic hazards like lightning strikes, since the polymer material does not conduct away electric energy. Another major worry, but mostly for the operator, will be damage detection, which as it was said earlier occurs mainly internally and becomes difficult to detect. Soutis and coworkers [25–29] have demonstrated the possibility of using a linear array of piezoelectric transducers for the detection of delaminations and other modes of damage in composite plates. In order to detect low-velocity impact damage in multidirectional laminates they employed the fundamental antisymmetric A_0 Lamb mode at frequencies of 15–20 kHz; Fig. 1.5 illustrates an ultrasonic C-scan image of the undamaged and damaged configuration together with time of flight method used to detect the location of damage; its location was calculated with an error of just 2.3% from the actual position [27]. Electromagnetic sensors have also been developed and applied successfully to nondestructively detect impact-induced delaminations [30]. Some success, but further research and development in damage detection is required, especially on monitoring bonded repair [31,32] and structural health monitoring of repaired configurations [33–35]. Fig. 1.6 illustrates the test set up for bending fatigue of a patch repaired
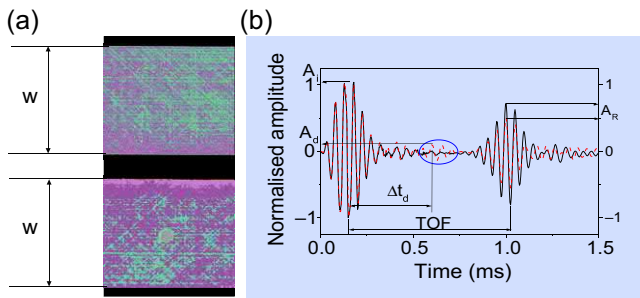
Figure 1.5 (a) An ultrasonic C-scan image (across the width, W) of undamaged and 2 J impact damaged laminate and (b) response of pristine and damaged composite plate [29].
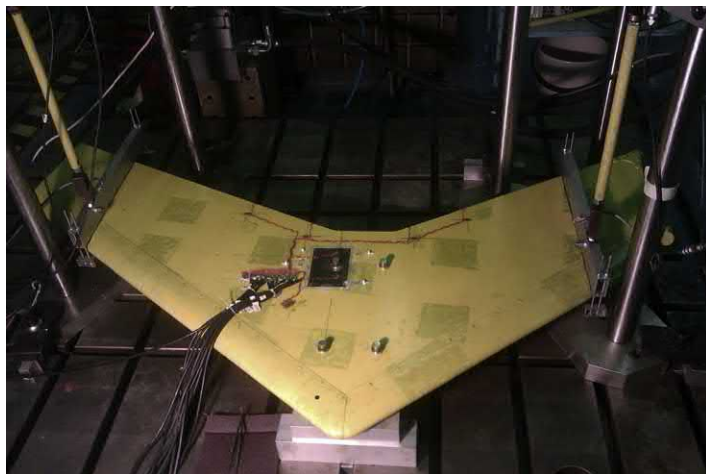
Figure 1.6 A composite bonded patch repair of a helicopter stabilizer with PZT transducers for Lamb wave SHM monitoring [36].

helicopter stabilizer, where PZT transducers were employed for Lamb waves monitoring [36]. In that study, composite bonded patch repairs have been performed and successfully monitored, but for them to be certified by the Aviation Authorities a robust real-time damage monitoring system will be required, where signals are not affected by the service environment.

Composites have been used in Bell helicopters (Dallas Fort Worth, USA) since the 1980s following their advanced composites airframe program (ACAP) when they were able to achieve a 20% reduction in weight on metallic airframes. All blades on their newer vehicles (412, 407, 427, 214, 609, OH58D, V22) are all composite. The V22 Osprey tilt-rotor has a composite fuselage stiffened skin and an all-composite wing, chosen for its stiffness critical design, which was only possible in composites at low enough weight. The skins of the V22 wing are I-stiffened with cobonded spars and bolted on ribs (the civil 609 version will use bonded ribs). It should be noted that buckling can generate severe stresses in the bond line between skin and stiffeners. Early demonstrators (from the 1960s onwards) did not meet expectations until composites were available. The pylon support spindle is currently filament wound, but it is planned to have fiber replace this part. Over 60% of the whole vehicle weight is carbon composite, plus a further 12% in GRP. The V22 uses tape laying, hand lay-up, and filament winding for most of the composite construction but is moving to fiber placement for the 609 civil version [4]. Mechanical fastening features heavily in the composite structure, some 3000 each side of the wing, is introduced by manual drilling with templates, but they are looking toward the use of automated drilling and probably involving water jet cutting.

Other examples where composites are extensively applied are the new military cargo Airbus A400M and the tail of the C17 (USA). A 62 ft C-17 tail demonstrator has been successfully completed yielding 4300 fewer parts (including fasteners),

weight reduced by 20% (260 kg) and cost by 50% compared with the existing metal tail. The A400M is a long-range military transport aircraft, has a much larger payload (37,000 kg) than the C-160 Transall and C-130, and the design makes extensive use of composite materials, Fig. 1.7. The first A400M aircraft was officially rolled out in June 2008, and the long-awaited maiden flight took place on 11 December 2009.

Without exception all agile fighter aircraft currently being designed or built in the USA and Europe (e.g., JSF/F-35 and the European Typhoon, Fig. 1.8) contain about 40% of composites in the structural mass, covering some 70% of the surface area of the aircraft. The essential agility of the a/c would be lost if this amount of composite material was not used because of the consequential mass increase.

Many of the materials, processes, and manufacturing methods discussed earlier in the chapter have been implemented in their construction. Another interesting and relatively new field of development in the military aircraft sphere is that of "stealth," a concept that requires the designer to achieve the smallest possible radar cross-section (RCS), to reduce the chances of early detection by defending radar sets. The essential compound curvature of the airframe with a constant change of radius is much easier to form in composites than in metal while radar-absorbent material (RAM) can be effectively produced in composites [37].

Figure 1.7 Composite tail of the A400M long-range aircraft.
Photo by C Soutis.

Figure 1.8 The Typhoon jet fighter**,** Eurofighter.
Photo by C. Soutis.

1.5 Conclusion

The application of carbon fiber has developed from small-scale technology demonstrators in the 1970s to large structures today. From being a very expensive exotic material when first developed relatively a few years ago, the price of carbon fiber has dropped to about £10/kg, which has increased applications such that the aerospace market accounts for only 20% of all production [38,39]. The main advantages provided by CFRP include mass and part reduction, complex shape manufacture, reduced scrap, improved fatigue life, design optimization, and generally improved corrosion resistance. The main challenges restricting their use are material and processing costs, damage tolerance, repair and inspection, dimensional tolerance, and conservatism associated with uncertainties about relatively new and sometimes variable materials. Claims of 100% improvement in damage tolerance performance with stitched fabrics (3D woven fabrics) relative to conventional pre-preg materials are made; however, autoclaved continuous fiber composites will still dominate for the high levels of structural efficiency required in primary aircraft structures.

Carbon fiber composites are here to stay in terms of future aircraft construction since significant weight savings can be achieved. For secondary structures, weight savings approaching 40% are feasible by using composites instead of light metal alloys, while for primary structures, such as wings and fuselages 20% is more realistic. These figures can always improve, but innovation is the key to making composites more affordable. Some recent progress on composites failure analysis and design, where modern finite elements techniques have been employed to simulate blast behavior of fiber metal laminates [39] and model resin cracking and delamination developed during an impact event or a bolted joint are reported in Refs. [40,41].

The reader will be informed in the following chapters of the publication of the latest developments on new materials, 2D and 3D woven architectures, fabrication techniques, environmental effects (temperature and humidity), fracture and fatigue, design and analysis of impact, crash (at laminate and component level) and blast energy absorption, joints, in addition to repair, nondestructive evaluation and real-time structural health monitoring.

References

[1] A. Kelly (Ed.), Concise Encyclopaedia of Composite Materials, Pergamon, 1994.
[2] D. Hull, An Introduction to Composite Materials, Cambridge University Press, 1987.
[3] E. McCarthy, C. Soutis, Determination of interfacial shear strength in continuous fibre composites by multi-fibre fragmentation: a review, To Appear in Compos. Part A: Appl. Sci. Manuf. JCOMA-18−1453 118 (March 2019) 281−292.
[4] Report for the International Technology Service, Aerospace Composite Structures in the USA, Overseas Missions Unit) of the DTI, UK, 1999.
[5] C. Soutis, Fibre reinforced composites in aircraft construction, Prog. Aerosp. Sci. 41 (2) (2005) 143−151.
[6] F.Z. Hu, C. Soutis, E.C. Edge, Interlaminar stresses in composite laminates with a circular hole, Compos. Struct. 37 (2) (1997) 223−232.
[7] F.L. Matthews, G.A.O. Davies, D. Hitchings, C. Soutis, Finite Element Modelling of Composite Materials and Structures, Woodhead Publishing Ltd., 2000.
[8] N. Andreasson, C.P. Mackinlay, C. Soutis, Experimental and numerical failure analysis of bolted joints in CFRP woven laminates, RAeS Aeronaut. J. 102 (1018) (1998) 445−450.
[9] P. Berbinau, C. Soutis, A new approach for solving mixed boundary value problems along holes in orthotropic plates, Int. J. Solids Struct. 38 (1) (2001) 143−159.
[10] R.H. Oskouei, M. Keikhosravy, C. Soutis, Estimating clamping pressure distribution and stiffness in aircraft bolted joints by finite element analysis, J. Aerosp. Eng. Part G, Proc. Inst. Mech. Eng. 223 (2009) 863−871.
[11] A. Atas, C. Soutis, Strength prediction of bolted joints in CFRP composite laminates using cohesive zone elements, Compos. B Eng. 58 (2014) 25−34.
[12] C. Soutis, S.M. Spearing, Compressive response of notched woven fabric face-sheet honeycomb sandwich panels, J Polym. Rubbers Compos. 31 (9) (2002) 392−397.
[13] C. Soutis, J. Lee, Measuring the notched compressive strength of composite laminates: specimen size effects, Compos. Sci. Technol. 68 (12) (2008) 2359−2366.
[14] C. Soutis, Modelling the open hole compressive strength of composite laminates tested in hot-wet conditions, Plast. Rubber Compos. 38 (2/3/4) (2009) 55−60.
[15] M.N. Saleh, A. Yudhanto, P. Potluri, G. Lubineau, C. Soutis, Characterising the loading direction sensitivity of 3D woven composites: effect of z-binder architecture, Compos. Part A Appl. Sci. Eng. 90 (1) (2016) 577−588.
[16] C. Soutis, P.T. Curtis, A method for predicting the fracture toughness of CFRP laminates failing by fibre microbuckling, Compos. Part A. 31 (7) (2000) 733−740.
[17] F. Edgren, C. Soutis, L.E. Asp, Damage tolerance analysis of NCF composite sandwich panels, Compos. Sci. Technol. 68 (13) (2008) 2635−2645.
[18] J. Lee, C. Soutis, A study on the compressive strength of thick carbon fibre/epoxy laminates, Compos. Sci. Technol. 67 (10) (2007) 2015−2026.

[19] C. Soutis, J. Lee, Scaling effects in notched carbon fibre/epoxy composites loaded in compression, J. Mater. Sci. 43 (20) (2008) 6593−6598.

[20] M. Kashtalyan, C. Soutis, Stiffness and fracture analysis of laminated composites with off-axis ply matrix cracking, Compos. A 38 (4) (2007) 1262−1269.

[21] M. Kashtalyan, C. Soutis, Mechanisms of internal damage and their effect on the behaviour and properties of cross-ply laminates, Int. Appl. Mech. 38 (2002) 641−657.

[22] B. Yu, R. Blanc, C. Soutis, P.J. Withers, Evolution of damage during the fatigue of 3D woven glass fibre reinforced composites subjected to tension-tension loading observed by time-lapse X-ray tomography, Compos. Appl. Sci. Manuf. 82 (2016) 279−290.

[23] C. Soutis, X. Chen, Guest Editors, '3D textile composites and their applications', Appl. Compos. Mater. 25 (4) (2018). ISSN 0929-189X.

[24] https://www.siemens.com/innovation/en/home/pictures-of-the-future/industry-and-auto-mation/digtial-factory-trends-industrie-4-0.html.

[25] S.H. Diaz Valdes, C. Soutis, Health monitoring of composites using lamb waves generated by piezo-electric devices, Plast. Rubber Compos. 29 (9) (2000) 496−502.

[26] S.H. Diaz Valdes, C. Soutis, Real-time non-destructive evaluation of fibre composite laminates using low-frequency lamb waves, J. Acc. Soc. Am. 111 (5) (2002) 2026−2033.

[27] K. Diamanti, J.M. Hodgkinson, C. Soutis, Detection of low-velocity impact damage in composite plates using lamb waves, Struct. Health Monit. J. 3 (1) (2004) 33−41.

[28] K. Diamanti, C. Soutis, J.M. Hodgkinson, Lamb waves for the non-destructive inspection of monolithic and sandwich composite beams, Compos. A 36 (2) (2005) 189−195.

[29] K. Diamanti, C. Soutis, J.M. Hodgkinson, Piezoelectric transducer arrangement for the inspection of large composite structures, Compos. A 38 (4) (2007) 1121−1130.

[30] Z. Li, A. Haigh, M.N. Saleh, C. Soutis, A. Gibson, R. Sloan, Detection of impact damage in carbon fibre composites using an electromagnetic sensor, Res. Nondestruct. Eval. 29 (3) (2018) 123−142.

[31] C. Soutis, D.-M. Duan, P. Goutas, Compressive behaviour of CFRP laminates repaired with adhesively bonded external patches, Compos. Struct. 45 (4) (1999) 289−301.

[32] F.Z. Hu, C. Soutis, Strength prediction of patch repaired CFRP laminates loaded in Compression, J. Compos. Sci. Technol. 60 (7) (2000) 1103−1114.

[33] K. Diamanti, C. Soutis, J.M. Hodgkinson, Non-destructive inspection of sandwich and repaired composite laminated structures, Compos. Sci. Technol. 65 (13) (2005) 2059−2067.

[34] S. Pavlopoulou, K. Worden, C. Soutis, Novelty detection and dimension reduction via guided ultrasonic waves: damage monitoring of scarf repairs in composite laminates, J Intell.Mater. Syst. Struct. 27 (4) (2016) 549−566.

[35] C. Soutis, J.-B. Ihn, Design, analysis and structural health monitoring of bonded composite repair and substructure, in: C. Boller, F.-K. Chang, Y. Fujino (Eds.), Encyclopaedia of Structural Health Monitoring, J. Wiley & Sons Ltd., 2009, pp. 1923−1940. ISBN: 978-0-470-05822-0.

[36] S. Pavlopoulou, S.A. Grammatikos, E.Z. Kordatos, K. Worden, A.S. Paipetis, T.E. Matikas, C. Soutis, Continuous debonding monitoring of a patch repaired helicopter stabilizer: damage assessment and analysis, Compos. Struct. 127 (2015) 231−244.

[37] Z. Li, A. Haigh, C. Soutis, A. Gibson, X-band microwave characterisation and analysis of carbon fibre-reinforced polymer composites, Compos. Struct. 208 (2019) 224−232.

[38] C. Soutis, Carbon fibre reinforced plastics in aircraft structures, Mater. Sci. Eng. A 412 (1−2) (2005) 171−176.

[39] C. Soutis, Composite material systems and structures, in: R. Kasunic (Ed.), McGraw-Hill 2009 Yearbook of Science and Technology, 2009, pp. 58−61. ArticleID-YB090146, ISBN 978-007-160562-5.

[40] Y. Shi, C. Soutis, A finite element analysis of impact damage in composite laminates, The Aeronaut. J. 116 (1186) (2012) 1331−1346.

[41] A. Ataş, C. Soutis, Subcritical damage mechanisms of bolted joints in CFRP composite laminates, Compos. B Eng. 54 (2013) 20−27.

Further reading

[1] G. Mohamed, C. Soutis, A. Hodzic, Multi-material Arbitrary-Lagrangian-Eulerian formulation for blast-induced fluid-structure interaction in fibre metal laminates, AIAA J. Am. Inst. Aeronaut. Astronaut. Struct. Mech. Mater. 50 (9) (2012) 1826−1833.

Modeling of 2D and 3D woven composites

2

Dmitry S. Ivanov [1], Stepan V. Lomov [2]

[1]Bristol Composites Institute ACCIS (Advanced Composite Collaboration for Innovation and Science), University of Bristol, Bristol, United Kingdom; [2]Department of Materials Engineering, KU Leuven, Leuven, Belgium

2.1 Introduction

Textile, and more narrowly, woven composites are an important class of high-performance composite materials, used in aerospace. In the production of composite parts, the use of textile reinforcements brings benefits in handability of the fabrics and easier applicability of closed-mold processes. In performance, due to the interlacing of yarns in textile, damage tolerance is improved in comparison with unidirectional cross-ply laminates, even if stiffness and strength are to a certain extent compromised because of yarn crimp, inherent for textile reinforcements. For the general introduction in the field of textile reinforcements and textile composites, as well as modeling of a dry textile behavior during forming, the reader is referred to the classical works [1−3], books [4−7], on-line encyclopedia [8,9], and proceedings of conference series on textile composites (the latest was TexComp-13, Milan, 2018 [10]), which can serve as a starting point for studying the current literature.

Modeling of textile composites may be seen as an integrated simulation process that involves two integration paths. On the one hand, the behavior of a composite (be it in processing or in performance) is determined by its reinforcement fibrous architecture. This dictates the necessity to develop a scale integration of the models: from microscale, representing the local behavior of dry or impregnated fibrous yarns and plies, through mesoscale, corresponding to a unit cell (representative volume element, RVE) of textile reinforcement up to macroscale analysis of a composite part. On the other hand, processing of a composite (involving reinforcement deformation in draping, its impregnation, and the material consolidation) defines the final reinforcement architecture, as well as its defects (voids, fiber misplacement). Hence, the performance models on all the scale levels should be integrated with process models. Fig. 2.1 illustrates this integration of models.

This chapter is dedicated to meso-level modeling of internal architecture, mechanical behavior, and damage of 2D and 3D woven composites, focusing on meso-level models of a textile reinforcement unit cell. The chapter is intended to represent personal views and approach of the authors in the context of the state-of-the-art rather than a review of the current literature and the history of the subject; therefore the reference list is by no means exhaustive.
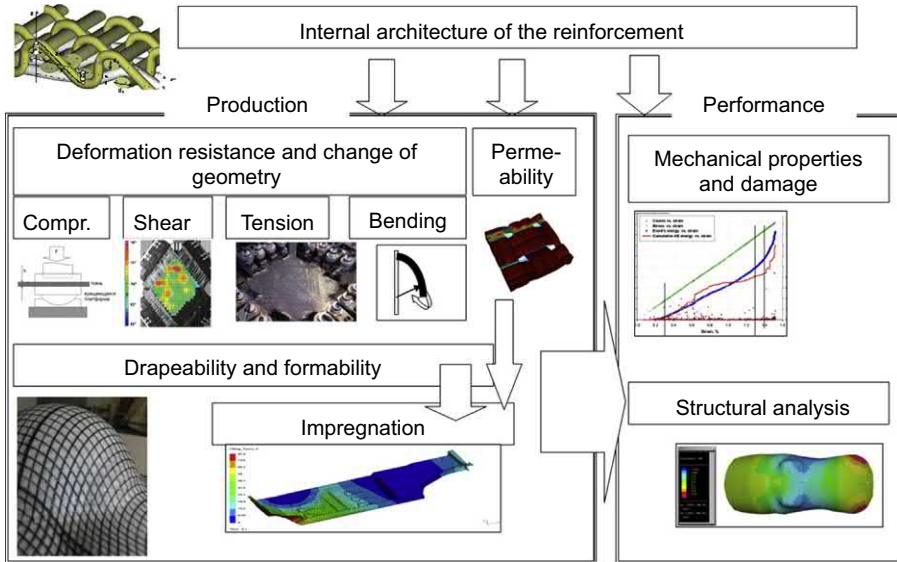
Figure 2.1 Integration of textile composite models.

For adequately representing property-structure dependencies between the reinforcement woven architecture and mechanical behavior of the composite, it is necessary first to introduce a generic way for a description of the internal geometry of a woven unit cell. The geometrical models and algorithms of weave coding are general enough to cover all 2D and 3D weaves used as composite reinforcements. Then two types of mechanical models of a woven composite are presented. Calculation of the composite stiffness can be based, of course, on a finite element (FE) model of the unit cell and rigorous asymptotic homogenization theory. However, less rigorous homogenization, employing representation of the unit cell with an assembly of Eshelby inclusions, which are subject to Mori-Tanaka homogenization scheme, give quite adequate predictions of the full stiffness matrix of the composite even for complex weaves, accounting for peculiarities of the architecture better than simple iso-strain orientation averaging. When details of the stress-strain distribution in the composite, damage behavior, and ultimate strength of the composite is the simulation goal, a full representation of the geometry and use of finite elements becomes indispensable. The chapter explores both approaches—inclusion and meso-FE models.

2.2 Architecture of a woven unit cell

2.2.1 2D and 3D weave topology and geometry

The mathematical description of the weave topology is the first necessary step in modeling the architecture of the unit cell. The matrix weave coding for 3D fabrics,

described here, was proposed in Refs. [11,12], and is implemented in the software *WiseTex* [13] with GUI for definition and editing the weave (the images in this chapter are produced using this software). Note that this approach differs from the approach used in Refs. [14−16], who aim at technological issues, such as, for example, the shedding lifting plan for a loom. In Ref. [17] the specific matrix coding is applied to produce 3D images of a fabric, and their approach is closer to the one described here.

Consider a warp-interlaced 3D weave (rather "multilayered" weave) − Fig. 2.2. The topological coding of a multilayered weave is based on the warp yarns paths. The i-th warp path is coded by a sequence of *intersection levels* w_{ij}—denoting either the index number of the weft layer situated above the warp yarn in its intersection with the j_k -th weft row, or 0, if the warp yarn lies on the face of the fabric. Let a fabric have L weft layers. Then warp in intersections with the weft can occupy $L+1$ levels, level 0 corresponding to the face of the fabric, level L—to the back of the fabric. Each warp can be now coded as a sequence of level codes, and the entire weave—as a matrix, as shown in Fig. 2.2. The matrix coding of a one-layer weave also represents a checker-board pattern, if level 0 were identified with a black square, level 1—with a white square Fig. 2.2(b). In the pattern shown in Fig. 2.2(a), all the warps are situated side by side. It is very often in composite reinforcements that warps are also layered,
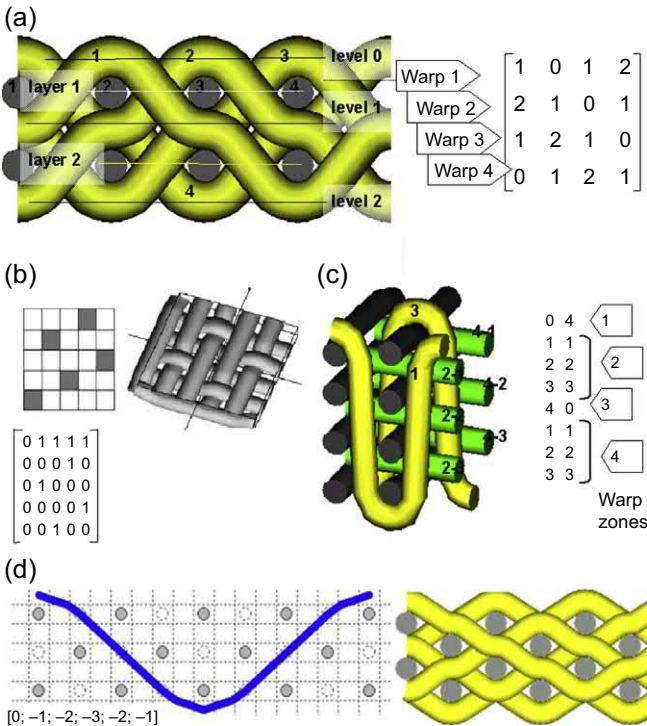
Figure 2.2 Matrix coding of a multilayered weave: (a) building the matrix; (b) warp in zones; (c) angle interlock; (d) "missing weft" algorithm.

as shown in Fig. 2.2(c). Paths of the warps, in this case, can also be coded as a sequence of level codes. For representing their layered positioning, a notion of *warp zones* is introduced. A warp zone is a set of warp yarns layered one over another. The yarns going through the thickness of a fabric are called Z-yarns.

Once a weave coding is defined, an analysis of the weave matrix allows answering questions about mutual positions of the yarns. Consider a warp yarn between two intersections with weft. Which weft yarns is it interacting with in these intersections? What is its position vis-à-vis these yarns? An answer to these questions is evident for one-layer weave, but for multilayered weaves, it needs analysis of the weave code. Knowing these answers allows, on the one hand, the definition of interactions between warp and weft, which is needed for building a geometrical model of the unit cell based on mechanics of these interactions, and on the other hand, the definition of contacts between the yarn needed for the creation of meso-level finite element models.

Consider a warp yarn first, e.g., the first warp yarn in Fig. 2.2(a), up. Its level codes are $\{w_i\} = \{0,2,4,2\}$. The yarn can be subdivided into *crimp intervals*, which constitute a part of the yarn between two intersections. At the first crimp interval, the yarn is supported (interacts with at the ends of the interval) with weft yarns in the layers $l_1^1 = 1$ and $l_1^2 = 2$ (the subscript gives the number of the crimp interval, the superscript identifies one of its ends). The yarn is situated above its supporting weft at the left end of the crimp interval and below the supporting weft at the right end.

The intersection codes and parameters of crimp intervals of warp are used to construct the same description for weft yarn. Consider a weft yarn i at layer l. First, looking up the lists of crimp interval parameters, find the first warp which has in its lists $l_i^1 = l$ or $l_i^2 = l$ (i.e., supported by the weft yarn i at layer l). This would be the left end of the first crimp interval on the weft yarn. The support warp number is thus found, and the position sign of the weft would be inverse to the position sign of the warp. Then find the next warp yarn supported by the weft (l,i). This would be the right end of the first crimp interval on the weft yarn and the left end of the second crimp interval. Continue until all the crimp intervals would be defined. Note that in multilayered structures the number of crimp intervals on a weft yarn can be smaller than the total number of the warp zones. For example, the first weft yarn in the first layer of the weave Fig. 2.2(a), up (eight warp zones) has only five crimp intervals, as it does not intersect with three of the Z-yarns.

The matrix coding is further developed to represent weaves, which do not have necessarily the same number/placement of the weft yarns in the weft rows/layers (d). The topology on Fig. 2.2(d) can be in principle described by the coding explained above (with a shift of weft layers when the geometry is built), but this will not lead to an adequate reconstruction of the yarn shapes. The simple solution to represent such weaves is to skip weft yarns in certain positions—a "missing weft" algorithm [18]. This is done by introducing Boolean values WE_{li}, which are **true** if the weft yarn is present in the position (l,i) and **false** if not. When processing the weave topology, the weft yarns with $WE_{li} = $ **false** are considered as not present. The coding based on the intersection levels can be further developed for more complex yarn paths. First, a modification of the matrix coding is needed to take into account the eventual

"missing" wefts. To describe cases where a warp yarn goes through space where a weft yarn has been removed, negative values for the matrix coding have been introduced (Fig. 2.2(d)). Consider a missing weft on the first weft layer number L: if a warp goes through this empty space, the corresponding value of the matrix coding will be equal to -L. In this case, the matrix coding value does not correspond directly to the supporting weft layer but indicates the position of the warp yarn in the weft network. Then a modified algorithm of the definition of supporting wefts is used to decide which of the above or below weft yarn is considered as supportive.

Once crimp intervals are defined, the spatial positions of the interval ends should be defined. These positions depend on yarn cross-section dimensions and yarn crimp heights. These parameters of the yarn geometry can be either measured on the actual composite or calculated using textile mechanics models for relaxed fabric and the fabric compressed and deformed during composite production. The reader is referred to Refs. [13,19] for a description of these models. With the interval ends defined, the full yarn paths are reconstructed by connecting the interval ends with curves satisfying the contact conditions of the supporting yarns in the interval and the least elastic energy requirements between the supports. The result is the full geometrical model of the fabric unit cell, which defines the yarn volumes and direction of the fibers inside the yarns.

2.2.2 Geometrical model: yarn volumes

The geometrical description of the fabric unit cell, outlined in the previous section, is constructed using the specific textile information, such as weave codes, ends/picks spacing, and retains this information. For further transformation into input data for micromechanical models and finite element models of the unit cell, the geometrical description is transformed into yarn volume definition. The format of the latter is unified for different textile structures (woven, braided, knitted), which are character-ized by certain spatial arrangement of yarns in periodically repeating unit cells. The yarn volume description loses the particularities of the specific textile. It "forgets" that the unit cell represents a certain weave or knitted pattern. However, it contains all the information necessary to reconstruct the volumes of the yarn, local fiber volume fraction, and fiber direction inside them. The gain is generality and the unification of the data format.

The yarn volume description data is shown in Fig. 2.3. The midline of the yarn is given by an array of the spatial positions of the centers of the yarn cross-sections O: $r(s)$, where s is the coordinate along the midline, r is the radius-vector of the point O. Let $t(s)$ be the tangent to the midline at point O. The cross-section of the yarn, normal to t, is defined by its dimensions $d_1(s)$ and $d_2(s)$ along axes $a_1(s)$ and $a_2(s)$. These axes are "glued" with the cross-section and rotate around t(s); if the yarn is twisted along its path Because of this rotation the system $[a_1,a_2,t]$ may differ from the natural coordinate system along the spatial path $[n,b,t]$ (t = dr/ds, n = dt/ds, b = t × n). The shape of the cross-section can be assumed to be elliptical, lenticular, etc. The shape type does not change along the yarn, but dimensions d_1 and d_2 can change because of varying compression of the yarn in the contact zones and between
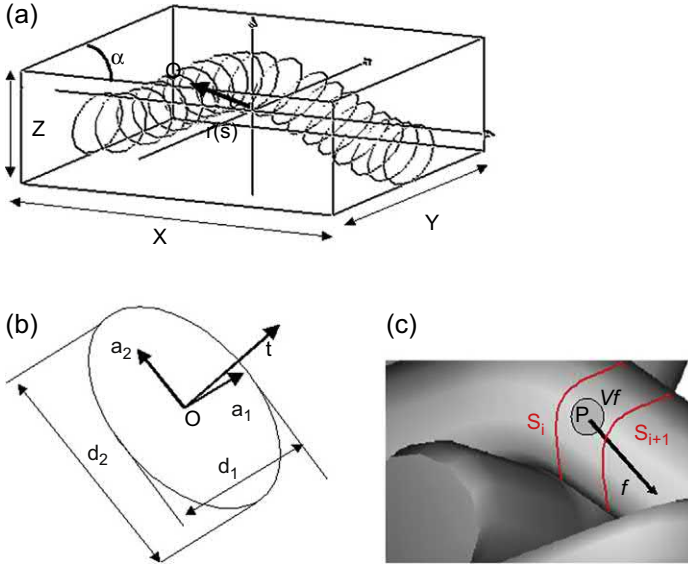
Figure 2.3 Geometry of yarn volumes: (a) a set of cross-sections defining the yarn volume; (b) the parameters of a cross-section; (c) fiber parameters near a point P in a yarn.

them. The reader is referred to Ref. [20] for more details of the yarn geometry description.

Based on the yarn volume description, the fibrous structure of the yarn, or, more generally, the fibrous structure of the unit cell is described as follows. Consider a point P and the fibers in the vicinity of this point. The fibrous assembly can be characterized by physical and mechanical parameters of the fibers near the point (which are not necessarily the same in all points of the fabric), fiber volume fraction V_f and direction f of them. If the point does not lie inside a yarn, then $V_f = 0$ and **f** is not defined. For a point inside a yarn, fibrous properties are easily calculated, providing that the fibrous structure of the yarn/ply in the virgin state is known and its dependency of local compression of the yarn/ply, bending and twisting of the yarn are given. Searching the cross-sections of the yarns, cross-sections $S_i = S_{(si)}$ and $S_{i+1} = S_{(si+1)}$ (s is a co-ordinate along the yarn midline) containing between their planes the point P, are found (binary search in the unit cell volume is employed to speed up the calculations). Then, using interpolation by s, the cross-section $S_{(s)}$, which plane contains the point P, is built. By using the dimensions of the cross-section S, for a given shape of it, point P is identified as lying inside or outside the yarn. In the former case, with the position of the point P inside the yarn known, using the model of the yarn microstructure, the parameters of the fibrous assembly in the vicinity of the point P are calculated.

2.2.3 Transformation of the geometry into FE model

Geometrically, woven reinforcement is a very complex object. During weaving, yarns are interlaced, stretched, and compacted. Yarns, being compliant transversely, are

diversely shaped due to interactions with mold and with each other. An ideal meso-scale model must capture the main geometric features of the textile architecture without running into excessive nuances of its highly uncertain geometry.

In this paragraph, we select the most important criteria of correspondence of a model to reality. Then, we overview both the peculiarities of textile reinforcement, which must be accounted for in an ideal damage model and the requirements to the solid models asserted by various finite element (FE) approaches. Mesoscale 3D FE models available in the literature are classified according to the selected geometric features. Models of 2D braided composites are included in the overview to give a wider perspective. In many aspects, challenges for modeling 2D braided and 2D woven yarn architectures are exactly the same.

2.2.3.1 Geometrical challenges

Interyarn fiber and yarn volume fractions. Within the mesoscale modeling para-digm, yarns are considered as a continuous solid medium with effective properties, which are primarily governed by the fiber volume fraction (FVF). The correct overall FVF (o-FVF) is an obligatory feature of any acceptable model as it has to match the fabric areal density, resin content, and specific composite weight. The o-FVF is deter-mined as the product of the yarn volume fraction (YVF) and the local intrayarn FVF (iy-FVF). The latter depends on the yarn compressibility, the pressure used for preform consolidation, and even the matrix viscosity.

As will be shown below, it is difficult to match the correct iy-FVF using a simple representation of yarn geometry. In general practice, certain freedom for an interplay of o-FVF and iy-FVF is deemed acceptable: yarn volume is generally taken lower to allow for simpler yarn cross-section shapes, and the iy-FVF is then increased to compensate discrepancy in the o-FVF. There is a natural constraint to this approach: yarns have a fiber packing limit.

Experimental studies of various textile composites show that the maximum possible values of iy-FVF are in a relatively narrow band. Summarizing various observations across literature (e.g., Refs. [21−23]) it can be stated that (1) actual iy-FVF can hardly exceed 75% and in most cases it is lower, (2) the o-FVF for some typical textile composites is rather high (above 50%) and can exceed 60%. That gives the YFV of 70%−80% and higher, which is not easy to achieve in a model.

Composite thickness and ply nesting. Actual composite thickness is another "must-comply" requirement, not only because it directly relates to the o-VFF, but also because it delimits the span of the yarn walk from one unit cell surface to the other one. Consequently, it governs the out-of-plane yarn crimp. The geometry of interply boundaries is stochastic due to noncontrolled positioning and nesting of the plies. In an extreme case of very open architecture, the maximum local one-ply thickness of may exceed 100% of the average ply thickness and minimum local ply thickness will be zero [24]. The nested plies exhibit at least 5%−10% higher compaction than the single-ply 2D preforms [23]. Hence, a conventional model with a flat ply surface has at least 10% higher iy-FVF than in reality and underestimates yarn crimp.

In contrast to 2D woven and braided fabrics, yarns of various layers in 3D fabrics are stacked regularly. Hence, nesting in 3D weaves appears to be less pronounced except for the cases of unbalanced fabric patterns [25].

Yarn spacing overlap and side crimp. Comparing the compressibility limits of single-ply twill fabric, and yarns extracted from this fabric leads to an important insight into fabric topology [23]. Conventional geometrical models of fabrics imply that yarn width is smaller than the interyarn distance. It means that for balanced and sparse fabrics, the yarn thickness constitutes half of the ply thickness. However, in the case of dense fabric, the yarn width exceeds the interyarn distance and overlaps the neighboring yarns of the same direction. In other words, the weft yarns are squeezed between two parallel warp yarns and vice versa. Disregarding the yarn overlap may result in underestimating yarn volume and overestimating iy-FVF: 30% for a sheared fabric and above 10% error for a simple orthogonal configuration. Another consequence of the yarn overlap is the side crimp of the yarns.

Local fiber volume fractions. Fibers are distributed non-uniformly within the yarns. Experimental measurements show that the distribution of fibers in yarn can vary and be up to 15% lower at the yarn edges than in the middle zone [26−28]. In contrast, the local FVF in the overlap configurations may be up to 30% higher at the edges. Introduction of the local FVF variation within given iy-VFV constraints reduces o-FVF. This is why accounting for FVF variation is often treated as an unnecessary luxury. On the other hand, the introduction of FVF variation may be useful for FEA to smooth down artificial stress concentration imposed by the edges (see below).

2.2.3.2   Overview of 3D meso-FE models

Table 2.1 aims to give a flavor of typical models created during the past 20 years. The selection of the discussed models is restricted by full 3D FE models of unit cells, where the yarn paths are continuous and smooth (voxel models are discussed below separately). The list does not include (semi-) analytical, orientation averaging, inclusion, discrete mosaic models as far as they are founded on completely different modeling principles.

To classify geometric features, we select two thresholds for FVF. The values above 75% of iy-FVF are called high or excessive. Models with such iy-FVF do not necessarily exaggerate the actual fiber packing. The 75% boundary shows the models created at their geometrical limits. Likewise, moderate and low iy-FVF does not mean a better quality or a higher precision of the models. Relatively low o-FVF of considered sparse architectures (in the range of 22%−46%) does not push these models against the iy-FVF roof. The category of particular interest is populated by the models for dense architectures, where the o-FVF is high, and iy-FVF is still within the realistic limits. The threshold for o-FVF was selected as 50%, though woven fabrics can be much denser (up to 60%) and 3D woven triaxial systems may have a lower o-FVF limit ($\sim$45%).

The other factors that indirectly influence yarn crimp and o-FVF are nestings, ply waviness, side interaction of yarns, and yarn overlap. If they are not in a model, it may mean that either these peculiarities have not been observed in the studied materials or

Table 2.1 Summary of mesoscale 3D FE composite models.

Parameter	References
iy- FVF and o-FVF	High/excessive iy-FVF (>75%) [24,37] = [38] = [39][a] (for graphite and carbon), [40−44] = [24,45,46] = [47] (lenticular cross-sections), [48−50] = [51−53] Moderate/low iy-FVF (<=75%)[b] [37] (glass), [21,54−60], [61] = [62−65] (twill), [66−68] = [69−79] o-FVF >= 50% and iy-FVF <=75% [21,46] = [80] = [81] (flattened cross-sections), [74] (o-FVF = 49%), [52] (through binder yarns 89% iy-FVF), [82−84]
Nesting and ply waviness	Flat laminate [85,86] (modeling top ply of a laminate), [82] (modeling three-ply laminate), [83] (modeling four-ply laminate), [87] (CT reconstruction of 8-ply laminate and modeling 2 nested plies) Curved laminate [85,86] (modeling three-ply laminate on cylindrical tool)
FVF variation across yarn	Employed [28,44]
Edges	Sharp edges [21,31,37,38,40,41,54,58,59,61,62,67,68,71−73,88−90] Blunt edges [50,52,82] Elliptical edges [57,59,63], [91,91] Rectangular or trapezoid with sharp corners [64,66,71,74] Complex shapes (result of premodeling) [48,49,85]
Interyarn/interply matrix layer	Inserted [24,42,44], [24,57,59,63,65] [31,48,68,88] [48,73,79,90,92], [52,76,91,93] Direct interyarn contact [21,37] = [38] = [39,40,46] = [47], [45,51,55,56,58], [54,64,66,67,72,74,82], [77,78,83,94]

[a]"="Denotes the fact that the same or similar geometrical model has been employed.
[b]o-FVF is in the range of (22%−46%) if sometimes specified.

they have not been taken into account. The overview aims at giving an overall picture, rather than demanding all the models to have the same level of geometric refinement.

Some published models are not intended for the description of actual fibrous geometry, but rather discuss general concepts and modeling principles, such as boundary conditions [29−32], peculiarities of stress distribution [33,34], material model [35] or a finite element approach [36]. These models are not included in the table. Table 2.1 summarizes other known models that are targeted at the prediction of mechanical properties and where iy-FVF or o-FVF is specified.

The presented summary illustrates the actual complexity of the problem. Despite vast efforts from the research community, a realistic description of the fabric remains a challenge in many practically relevant cases. The vast majority of mesoscale models of 2D woven or braided composites in the past and till date consider composite plies to

be limited by two straight parallel ply boundaries. This approach dramatically constrains the space available for yarns or leads to unrealistic matrix pockets, compromises the actual YVF, and resolves in either excessive iy-FVF or unrealistically low o-FVF. Considerate progress has been made in the recent years to generate realistic geometries with full considerations of nonorthogonal reinforcement [59,60] and modeling multiaxial reinforcement with three or more interlacing yarns [24,43,71]. Promising modeling of nested architectures has been demonstrated by Iarve et al. [86], Pickett et al. [85], Grail et al. [83] followed by the exploiting this modeling approach by Doitrand et al. [77,94], Wehrkamp-Richter et al. [82], Sevenois et al. [87]. In Refs. [21,74], the composite architectures were made through the detailed reconstruction of the actual geometry. In Ref. [50], it has been achieved through employing a particular flattened cross-section shape. In [6] contact compaction modeling served as a basis for mechanical model construction. In Ref. [82], a sophisticated yarn surface matching algorithm was developed. In Ref. [87], the reconstructed architecture of nested laminates is compared with the modeling approach, where neighboring plies are shifted and brought together.

Some features of textile architecture remain to be tough challenges for modeling:

(1) Apart from the cases when the deformation of reinforcement is modeled in direct consolidation/forming simulations, the side interaction of yarns and yarn overlap have rarely been approached and examined in the textile architectures. However, it is essential both for preform density, laminate thickness, and yarn crimp. Lomov et al. [95] and Wendling et al. [96] suggested analytical algorithms enabling the inclusion of this feature in the model.

(2) Manufacturing induced features have massive implications on mechanical properties and structural performance of textile composites. At present, only a few of the published models demonstrate the ability to take these features into account. While preform shearing resultant from forming and draping is paid attention to in Refs. [59,97], geometrical distortions of unit cells related to corner features, gradients in consolidation pressure, irregularities of yarn spacing present substantial difficulties from the modeling point of view. One of the essential issues in modeling these geometries come from the fact that their characteristic scale is significantly larger than the unit cell size. El Said et al. [98,99] demonstrated mechanical modeling of composite with 3D reinforcement formed over a complex tool through direct stimulation of compaction and forming processes.

(3) Recent progress with modeling nesting in textile laminate is a significant step forward but does not address nesting of plies oriented at an angle to each other. This is a fundamental challenge not only from the geometrical point of view but also because the conventional multiscale framework for modeling materials is based on periodic boundary conditions. The periodicity assumption fails to address non-matching unit cell patterns in the interacting plies which have their individual geometrical configurations.

2.2.3.3 Paths forward

As the history of research shows, reconstruction of the internal geometry demands complex solid modeling of yarn volumes. Perhaps, the most promising concept is direct mesoscale modeling of fabrics. Miao et al. [100] have employed the digital

element method, where yarns are modeled as chains of truss elements. The output example of such an approach is shown in Ref. [101] for the case of 3D woven composite. A similar concept has been employed by Mahadik and Hallett [102], Green et al. [103], El Said et al. [98,99], Joglekar and Pankow [104], Tsukrov et al. [48] for modeling 3D woven fabrics and Thompson et al. [105] for 2D textile laminate. Iarve [86] has also applied this approach to get braided geometry and handle the problem of nesting. Pickett et al. [85] have reconstructed a fragment of three-ply triaxial braided composites by (1) modeling braiding process with 1D beam elements, (2) inflating yarns along with solving contact problem. Stig and Hallström [49] employed a similar strategy to reproduce the yarn geometry of a fragment of a 3D woven composite. Solid modeling of yarns volumes under compaction as preprocessor for the mechanical volume has been suggested by Grail et al. [83] and demonstrated for the case of nested laminate. Nilakantan et al. [106] suggested an iterative algorithm of unit cell based on the thermal growth of yarn volumes.

Robitaille et al. [107] started 3D modeling of yarn volumes considering the 2D geometries of the yarn volume projections on unit cell faces. Then tow surfaces are constructed based on predefined yarn midlines and interaction of yarns with unit cell boundaries, as well as with each other. Hivet et al. [108,109] have introduced a so-called model for the non-intersecting yarn volumes with a variable nonsymmetrical cross-sectional shape of the yarn. Wendling et al. [96] developed an algorithm for modeling 3D interlock fabrics based on detailed considerations of various yarn interaction modes. Isart et al. [110,111] suggested an analytical approach to high fidelity reconstruction of orthogonal interlock woven composites based on examination of composite cross-sections. Another modeling philosophy is based on a direct conversion of micro-CT measurements into a voxel model of representative elements. Good examples of such an approach have been presented by Straumit et al. [112−114], Vanaerschot et al. [115−118], Sevenois et al. [87], Rinaldi et al. [119]. This approach, although requiring high-resolution measurements of the architecture and numerical algorithms to track fiber orientation, allows releasing assumptions associated with geometrical or mechanical modeling of textile reinforcement.

2.2.3.4   Specifics of finite element modeling of textile composites

In traditional finite element models, the tractions and displacement are continuous across the yarn-yarn and yarn-matrix interface boundaries. The elements cannot be shared between different materials, but the nodes on the interfaces belong to the elements of both the phases. The mesh continuity demands an ideal geometrical match between the volumes of matrix and yarns. Adjacent yarns can either contact each other directly or be separated by a thin layer of matrix—Table 2.1. In reality, the thickness of the matrix layer does not exceed the interfiber distance, i.e., just a few micrometers. Obviously, the need for quality meshing forces to make the layer

much thicker—comparable to the yarn thickness. There are two reasons for using this feature in a model:

(1) It is easier to generate and mesh the volumes of yarns independently. The inter-yarn matrix layer connects these volumes.
(2) The matrix layer guarantees that there is no interface where three different materials meet, i.e., two yarns and matrix. It has been shown by Sihn et al. [33,34] that such contact leads to stress singularity.

Inserting a matrix layer leads to a number of problems. Its finite thickness impacts the YVF and, consequently, raises the iy-FVF. On the other hand, a very thin layer inevitably leads to highly distorted elements and poor quality of stress approximation in that region.

Another problem associated with the interfaces is the shape of yarn edges. In most cases, the yarn cross-section contours look seemingly sharp. Lenticular-like yarn cross-section edges are typical for 2D woven architectures due to yarn spreading under compacting pressure. The razor blade tips create a substantial stress concentration both in the matrix and the yarn volumes. Moreover, the neighboring edges of contacting warp and weft yarns create a scissoring effect, which is particularly pronounced in the matrix at off-axis loadings. In reality, there is no physical edge: dispersed fibers are held together by the matrix spreading continuously from the volume within the yarn to the matrix pocket volume. Hence, the stress concentration caused by introducing a yarn-matrix boundary is rather artificial. This statement is supported by the experimental observations indicating that damage hardly ever initiates at the yarn edges.

In general, these variations of the geometry may have a distinct effect on the local stress. It means that at a certain level of geometry refinement the model becomes unstable in the sense of a system (geometrical input)-(mechanical output). This understanding poses the question of how sophisticated should a model be.

Various numerical schemes are used to resolve the problem of matrix pocket meshing. For instance, within the Domain Superposition Technique (DST) [36,120−125] yarn and matrix meshes share the same space. Independent meshes interact through the integration points of the elements. The yarn stiffness is reduced to account for the combined action of these volumes. Hence, the matrix can mesh with regular elements. The extended finite element formulation (X-FEM) [70] deals with the problem by enriching the shape function of an element with additional degrees of freedom, allowing the strain discontinuity. Thus, a rough mesh can contain a complex yarn-matrix boundary crossing the element in arbitrary locations. In Ref. [85] the yarn volumes mesh independently and the elements are connected through the numerical meshless method: Smooth Particle Hydrodynamics (SPH).The Independent Mesh Method (IMM) [86] combines rough mesh within the yarns with local voxel-type refinement in the vicinity of the interface.

The voxel meshing follows the route of a very fine discretization of the unit cell and offers a highly attractive feature of a versatile, robust, and universal mesh tool. A significant volume of mesoscale models is following the voxel meshing route to generate

geometrically complex architectures, where yarn geometry is created in prior compaction or geometrical modeling [84,98,99,103,110,126,127]. In many cases, voxel treatment allows generating a correct balance of iy-FVF and o-FVF (e.g., Ref. [103]— 58.5% o-FVF, 70% iy-VF for 3D woven fabric). On the other hand, a rough stepwise representation of yarn surfaces results in spurious stress concentration and numerical noise. This creates a challenge for mesh-independent stress analysis and damage modeling. A promising solution to this problem was suggested by Fang et al. [127] where stress is smoothed in a postprocessing operation by locally averaging the stress field. The paper also showed the importance of such postprocessing operation to predict damage pattern correctly.

2.3   Stiffness modeling: method of inclusions

2.3.1   Analytical approaches to stiffness calculations

Due to the inherent symmetry of as-produced textile fabrics, woven composite plates are orthotropic. Their stiffness can be represented by engineering constants: Young modules E_{ii}, shear modules G_{ij} and Poisson coefficients ν_{ij}, $i,j = 1.3$. If the reinforcement is deformed during the production of the composite, or if the preform is net-shaped, or for some knitted performs, then the assumption of orthotropy does not necessarily apply, and the full stiffness matrix has to be introduced.

The stiffness of woven reinforcements made of yarns, which are straight in-plane, can be calculated, as a first rough approximation, using the Classical Laminate Theory (CLT), which considers an equivalent cross-ply laminate with ply directions corresponding to the principal directions of the yarns in the textile composite, the thickness and fiber volume fraction are the same as in the textile composite, and the thickness of the plies is proportional to the amount of the fibers with the corresponding direction. Such a calculation provides an overestimation of the woven composite stiffness because yarn crimp causes deviation of the fiber directions from the cross-ply laminate model. For the engineering constants in fiber directions, the CLT-calculated modules can be corrected using empirical knock-down factors, which would account for crimp. With low out-of-plane inclination angles, such a calculation gives acceptable results, especially for modules in the fiber direction.

More elaborate approaches have to be used to account for the crimp. Calculation of the homogenized stiffness must take into account the fact that the fibers are organized into impregnated yarns; hence, the homogenization calculation should be two-step: first, homogenize the stiffness of the impregnated yarns, second, homogenize the stiffness of the unit cell, taking into account their orientation.

Impregnated yarns are considered as UD reinforced composites (twist of the yarns used in composite reinforcement is normally negligible) with the given fiber volume fraction V_f^y; this value is determined by the dimensions of the cross-section of the yarn (which can differ from point to point in the unit cell, but most often assumed

to be constant) and the number of fibers inside the yarn, given by the fiber count or yarn linear density:

$$V_f^y = \frac{T_y}{A_y \cdot \rho_f} = \frac{N_f A_f}{A_y}$$

where T is linear density, A—cross-section area, ρ—density, N_f—number of fibers in the yarn, subscript "f" means "fiber," "y"—"yarn." With the fiber volume fraction V_f^y given, homogenized stiffness of the impregnated yarn can be calculated using one or another set of micromechanical formulae for UD plies, for example, Chamis formulae [128]:

$$E_{11}^y = V_f^y E_{11}^f + \left(1 - V_f^y\right) E_m; \ E_{22}^y = E_{33}^y = \frac{E_m}{1 - \sqrt{V_f^y}\left(1 - \dfrac{E_m}{E_{22}^f}\right)}$$

$$G_{12}^y = G_{13}^y = \frac{G_m}{1 - \sqrt{V_f^y}\left(1 - \dfrac{G_m}{G_{12}^f}\right)}; \ G_{23}^y = \frac{G_m}{1 - \sqrt{V_f^y}\left(1 - \dfrac{G_m}{G_{23}^f}\right)}$$

$$\nu_{12}^y = \nu_{13}^y = V_f^y \nu_{12}^f + \left(1 - V_f^y\right)\nu_m; \ \nu_{23}^y = \frac{E_{22}^y}{2G_{23}^y} - 1$$

where E is the Young modulus, G—shear modulus, ν − Poisson coefficient; sub- or superscript "f" means "fiber," "y" − "yarn," "m" − matrix; axis one of the Cartesian coordinate system *123* is aligned with the fiber direction.

Another alternative, the closed-form expressions for Mori-Tanaka homogenization can be found in Ref. [129].

Once the homogenization of the impregnated yarns is performed, the homogenized stiffness of the textile composite can be calculated using different methods. The simplest one, *orientation averaging (OA)* (also called *fabric geometry model*) [130] uses the iso-strain assumption for the unit cell of the textile composite. Based on the geometry of the reinforcements, N groups of segments of the yarns are defined inside the unit cell, so that inside a group i the orientation of the fibers (or centerline of the yarn) is approximated by the coordinate system CS_i, aligned with the fibers. V_y^i is the volume fraction of the impregnated yarn segments belonging to the group i. In the geometrical model described in the previous section, the segments represent the yarn volumes between the subsequent yarn cross-sections. The homogenized stiffness of the composite is then calculated as

$$\mathbf{C}^{eff}[GCS] = \mathbf{C}^m[GCS] \cdot (1 - V_y) + \sum_{i=1}^{N} \mathbf{C}_i^y[CS_i \rightarrow GCS] \cdot V_y^i; \quad V_y = \sum_{i=1}^{N} V_y^i$$

$$(2.1)$$

where $\mathbf{C}^{eff}$ is averaged stiffness matrix of the composite, $\mathbf{C}^m -$ stiffness of the matrix, $\mathbf{C}^y -$ homogenized stiffness of the impregnated yarns; V_y is the total volume fraction of the impregnated yarns. All the stiffness matrices are written in or transformed into the global coordinate system (GCS).

With all the simplicity of the OA method, it produces reasonable predictions for the fiber-dominated properties and low crimp when deviations from the iso-strain assumption play a minor role. For off-axis properties, or for cases when transverse parts of the reinforcement (for example, weft yarns for warp direction loading) play an important role, or in the presence of high-crimp yarns (for example, 3D reinforcements with significant fraction of binder) the iso-strain assumption is not valid anymore, and quality of the OA predictions is decreased. There are approaches which combine iso-strain and iso-stress formulations [3], but these approaches leave open the choice of the combination rules open, which makes their predictive abilities limited.

This chapter describes the method of the stiffness homogenization for textile composites based on Eshelby solution of the elastic problem for an ellipsoidal inclusion and Mori-Tanaka homogenization scheme. The approach was proposed by Huysmans et al. [131−134] and is successfully applied to very different textile composites, woven [135], braided [136], and knitted [131,132]. In short, the approach is called *method of inclusions* (MoI). It was extended to the modeling of visco-elastic behavior [137].

2.3.2 Method of inclusions and Mori-Tanaka homogenization

MoI homogenization of a heterogeneous medium, which should have a homogeneous matrix with a second (discontinuous) phase, or more phases of reinforcement embedded in it, is done via the following steps:

1. Build a geometrical model of the RVE of the reinforcement
2. Subdivide the reinforcement into elements, which somehow could be represented as ellipsoids.
3. Consider the assembly of the ellipsoidal inclusions in the matrix
4. Using properties of the reinforcement, assign stiffness tensors to the inclusions (micro-homogenization may be performed on this step)
5. Apply the Mori-Tanaka/Eshelby theory to calculate the equivalent stiffness of the RVE

The application of MoI is straightforward if the reinforcing particles/fibers are short, slender, straight, and can be effectively approximated as ellipsoids. For textile composites, with well-organized structure (vs. randomness in short fiber composites) and consist of crimped yarns (vs. straight, short fibers), a mechanically equivalent assembly of inclusions should be constructed first. This is based on the segmentation of the yarn geometry described in Section 2.

First, elastic properties of each impregnated yarn segment are calculated using homogenization formulae (for example, Chamis' above) for the unidirectional array of fibers, using local fiber volume fraction at the segment, properties of the fibers and elastic properties of the matrix. The result is the stiffness matrix $\mathbf{C}_i^y$, expressed

in the local *123* coordinate system. Then each yarn segment is represented by an ellipsoidal inclusion with the axis

$$a_1 = \alpha d_1; a_2 = \alpha d_2; a_3 = \lambda \sqrt{a_1 a_2}$$

where α is the volume correction coefficient, and the elongation λ depending on the curvature of the yarn segment:

$$\lambda = 3.14 \frac{R}{\sqrt{d_1 d_2}}$$

where R is the radius of curvature of the yarn path in the segment (Fig. 2.4). The volume correction factor α ensures that the volume of the inclusion is equal to the volume of the yarn segment. The stiffness of the inclusion in the local coordinate
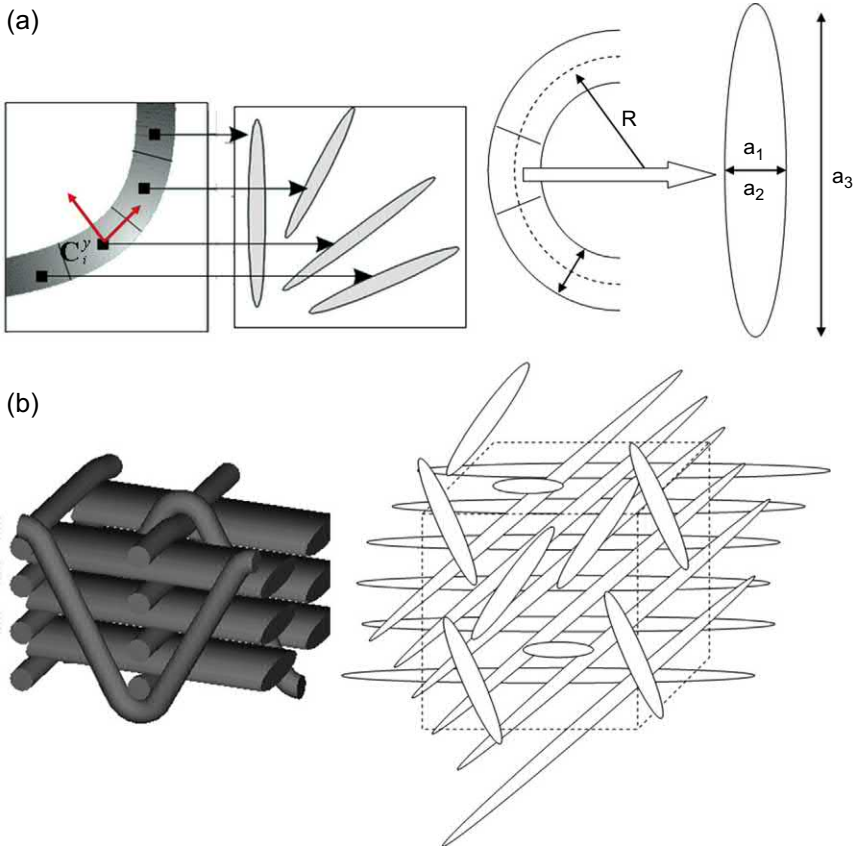
Figure 2.4 Equivalent ellipsoidal inclusions for yarn segments: (a) a scheme of the inclusion parameters; (b) an inclusion set for 3D woven unit cell.

system CS_i is equal to $\mathbf{C}_i^y$. Note that the spatial location of the inclusions is irrelevant for the Mori-Tanaka homogenization; the only important geometrical factors are orientation and elongation of the inclusions.

Fig. 2.4(b) illustrates the inclusion assembly for a very rough segmentation of yarns in a 3D woven reinforcement.

Once the inclusion assembly has been constructed, the homogenized stiffness matrix of the composite is calculated as follows. First, calculate Eshelby tensors Si for the inclusions [138,139] in local coordinates CS_i. Transform the result in the global coordinate system GCS. Then calculate the strain concentration tensors for all the inclusions:

$$\mathbf{A}_i = \mathbf{A}_i^m \left(c_m \mathbf{I} + \sum_i c_j \mathbf{A}_j^m \right)^{-1} \tag{2.2}$$

where $\mathbf{I}$ is the unit tensor, c_i are relative volumes of the inclusions, c_m is the relative volume of the matrix:

$$c_m + \sum_i c_j = 1 \tag{2.3}$$

and $\mathbf{A}_i^m$ are calculated as:

$$\mathbf{A}_i^m = \left[\mathbf{I} + \mathbf{S}_i \mathbf{C}_m^{-1} (\mathbf{C}_i - \mathbf{C}_m) \right]^{-1} \tag{2.4}$$

The homogenized stiffness matrix $\mathbf{C}_{eff}$ of the composite is then calculated as

$$\mathbf{C}_{eff} = \mathbf{C}_m + \sum_i c_i (\mathbf{C}_i - \mathbf{C}_m) \mathbf{A}_i \tag{2.5}$$

For the iso-strain assumption $\mathbf{S}_i = 0$ (strain in inclusions equal the far-field strain), $\mathbf{A}_i = \mathbf{I}$, and formulae (2−5) are reduced to Eq. (2.1).

2.3.3 Example: 3D angle interlock composites

This case study [18] considers carbon/epoxy ply-to-ply interlock woven composites, with the textile structure illustrated in Fig. 2.5. The full weave pattern is defined in several warp and weft plans by shifting the position of warp interlacing yarns. The aim of the parametric study is to establish dependency of the mechanical properties of the composite (presented below as normalized values) on the fiber volume fraction and spacing of the weft. As the warp spacing is fixed by the dimensions of the reed during the weaving process, this parameter is not investigated.

The geometrical model is built using the "missing weft" approach described in Section 2. Fig. 2.5(a) illustrates the placement of the supporting wefts for a given
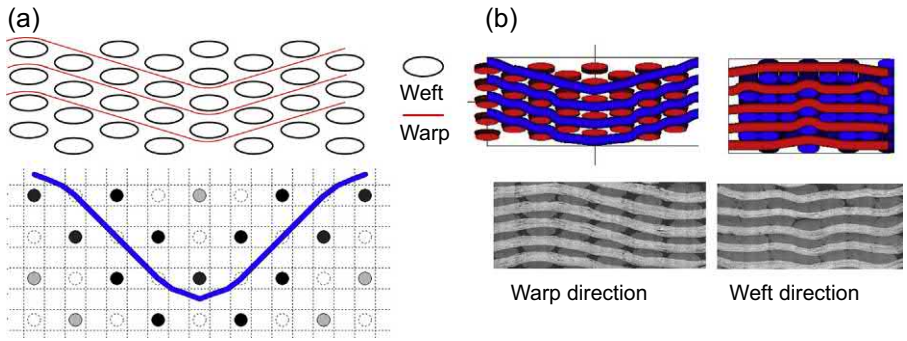
Figure 2.5 Angle interlock fabric: (a) warp plan for the ply-to-ply interlock fabric and definition of the interlacing sites; (b) cross-sections calculated (above) and observed (below).

Table 2.2 Parameters of the angle interlock fabric.

	Warp crimp (%)	Well crimp (%)	Average interlock angle (degrees)
Measured	1.44	1.49	9.2
Calculated	1.5	1.5	8.0

warp yarn. Fig. 2.5(a) and Table 2.2 compare geometry calculated by *WiseTex* with experimentally measured shapes of the yarn.

WiseTex models of this interlock fabric have been created with the evolution of the pick spacing. For representing the real materials, fiber volume fraction has to remain constant in the composite models and equal to 58%. Compression was then applied to maintain the fiber volume fraction at the level of 58%. This means that the thickness of *WiseTex* models and samples decreases with pick spacing. The average interlock angle decreases, and the warp/weft ratio in the unit cell increases in the warp direction but decreases in the weft direction. The undulations in the warp path imposed by the tightened weft network for low pick spacing are attenuated when the fabric becomes looser. The effect of these changes in the geometry on the elastic mechanical properties is discussed below.

The evolution of modulus in the **warp direction** is shown in Fig. 2.6(a). We notice first a strong increase of the modulus. This can be explained by both the increase of warp ratio in the unit cell and by the decreasing interlock angle. The orientation of warp yarns becomes closer to the x-axis, increasing mechanical properties in this direction. Fig. 2.6(b) shows the evolution of the modulus in **weft direction**. We notice a drop of the modulus with the increase of the pick spacing. Only the drop of the weft ratio in the unit cell is responsible for this. Indeed, an increase of the pick spacing has no effect on crimp or orientation of the weft yarns. The results of homogenization in the **thickness direction** shows that modulus in the thickness direction remains constant when pick spacing is increased. However, the modulus in Z direction should decrease because of the decrease of interlock angle caused by the rise of the pick
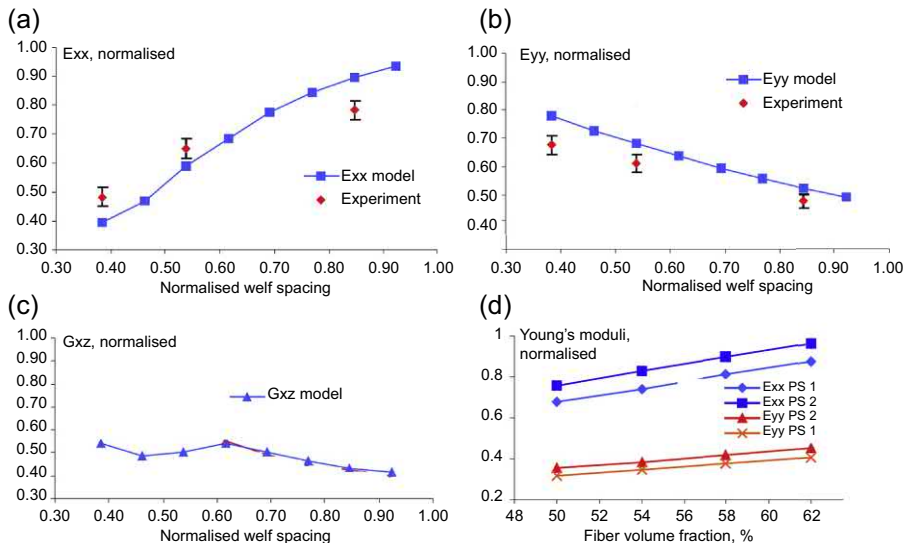
Figure 2.6 Dependencies of mechanical properties of angle interlock reinforced composite on parameters of the reinforcement (normalized values): (a) Young's modulus in the warp direction, Vf = 58%; (b) Young's modulus in the weft direction, Vf = 58%; (c) shear modulus, Vf = 58%; (d) Young's moduli versus fiber volume fraction, PS1 and PS2 refer to two values of the pick spacing.

spacing, which means fewer fibers in the thickness direction. Indeed, compression was used to maintain constant fiber volume fraction of the unit cells, compression that has increased intrayarns fiber volume fraction, and transverse properties of yarns. This means that the decrease of E_{zz} that should be observed is balanced by this increase of transverse properties of yarns, introduced by compression of the fabric. Shear modulus is influenced by the orientation of fibers in xz plane, which means interlock angle. That what is shown in Fig. 2.6(c) with the first model where warp yarns are straight in the interlock direction. The increase of pick spacing, which causes a diminution of interlock angle, for effect, has an important drop of G_{xz} modulus. The introduction of a crimp in the interlock angle direction with the second model causes a strong decrease of G_{xz} for lower pick spacing. Then the decrease of G_{xz} that should occur is balanced by the progressive elimination of local undulations in the interlock direction while increasing pick spacing. No experimental characterization of this behavior has been achieved for validation, but this result shows the importance of yarn crimp in the three main directions. Finally, Fig. 2.6(d) shows a linear dependence of the modulus with fiber volume fraction, and this is for the two different pick spacings.

All these mechanical results demonstrate the ability of 3D woven fabrics to be adjusted to requirements and cover a wide range of mechanical properties by modifying weaving or manufacturing parameters, such as spacing between yarns or fiber

volume fraction of the composite. Databases of materials can be built, in order to help design or selection of these 3D textile reinforced composites.

2.4 Stress and strength modeling: FE analysis

2.4.1 Stress modeling

The previous investigations [30,31] have clearly illustrated the dependence of the mesoscale stresses on (a) the number of plies in laminate, (b) the distance between a ply and composite surface, (c) the position of plies relatively to each other. Hence, the interaction of plies has a dramatic effect on intrayarn crack initiation, inter-ply delamination, longitudinal splitting, and stress in fibers. For instance, consider two material configurations of a carbon-epoxy twill composite differing in a position of the plies relative to each other. The shift between the plies is of an order of just a few millimeters. However, it appears that there is a strong contrast in stress states. Failure criteria predict 1.7 times difference between the load levels at damage initiation, 2.5 times difference in delamination occurrence and 1.3 times difference between the expected strengths. These studies also show that the crack onset must be different in outer and inner plies, and 1-ply composite behaves differently than a thick laminate. In other words, one ply of the composite is representative neither in the sense of stress distribution nor in regards to the damage pattern. For avoiding the modeling of the full laminate stack, a multiscale concept based on laminate decomposition has been proposed [31]. It allows construction of boundary conditions for one ply in a laminate explicitly taking into account the position within a laminate, number of plies, and inter-ply configuration. This concept appears to be convenient for modeling delamination as a process of transformation of multiply laminate into noninteracting single-ply composites [140].

2.4.2 Specifics of damage accumulation in textile composites

The primary purpose of the mesodamage modeling is to describe failure as processes occurring at the yarn scale. Compared to unidirectional laminated composites, damage accumulation in textile composite has a number of specific features: (1) the early initiation of intrayarn cracking (0.1%−0.3% of applied deformation), (2) the concurrent accumulation of crack density and incremental crack length growth [9,141].

To simulate intrayarn cracking the vast majority of the known models employ local damage mechanics, where yarn properties at any point evolve as a function of local stress, strain or energy. There are two major problems associated with this approach: (1) a local model is sensitive to the peculiarities of textile geometry, such as edges, shape of interyarn matrix volume, multimaterial contacts, (2) approximation of intrayarn cracks by locally damaged material has no physical ground. The second problem relates to the scale resolution. Few (2−3) discrete cracks per yarn width cannot be simulated by a model lacking information on the crack geometry and not distinguishing damage initiation and propagation. In particular, the presence of intrayarn shear

stress forces the damage zone to extend across the fiber direction [142]. As a result, the damage pattern has an unrealistic geometry. There are very few attempts to model crack geometry explicitly, e.g., by Doitrand et al. [94] for intrayarns cracks and inter-yarn debonds. This is a promising approach and may highlight many important features of yarn interaction yet computationally efficient and robust estimates of stiffness degradation offered by continuous damage mechanics are also attractive.

To avoid the problems of unphysical damage patterns, the size of a damaged zone can be selected with respect to typical features of textile architecture. We suggest defragmenting the yarn along its midline into short segments where the fiber orientation can be assumed constant Fig. 2.7.

In agreement with available experimental observations, it is stated that cracks propagate step-wise. They instantly cross straight intervals of yarn and may stop at the location where yarn changes its orientation. The dominant damage mechanism within segments is crack density accumulation. It makes a segment analogous to a ply in a flat laminated composite. Hence, a damage evolution law tuned and validated for the flat laminated composites can be used.

This concept offers not only an exemption from the fundamental problems of local damage mechanics, but it also gives a few extra advantages. First of all, a different degree of stiffness degradation along the yarn midline has a clear physical interpretation: it reflects variation in the crack density along the yarn and hence reflects the incremental crack length growth. Secondly, it naturally diminishes the sensitivity of a model to local stress concentration. In the authors' opinion, the segment is the smallest entity where the damage mechanics paradigm may be employed without compromising a physical sense of the mesoscale simulations.

2.4.3 Local stiffness degradation and damage evolution law

We consider damage as a measure of property degradation. The complexity of textile architectures does not allow making a flawless choice of degradation scheme. Analytical and numerical models developed for the flat laminates clearly show that at a given crack density ply degradation depends on the stiffness of constraining plies, the thickness of a cracked ply, and the ply position in a laminate. The situation with the textile composite is more complicated. The degradation of a particular segment may also depend on interply nesting configuration, segment location and crack length.
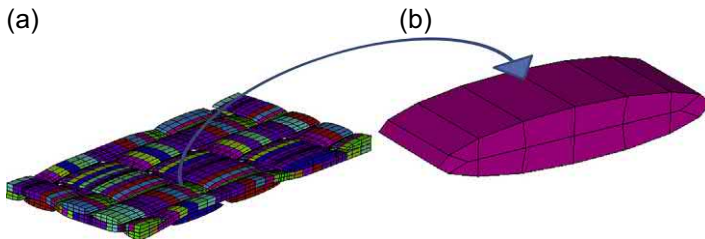
Figure 2.7 (a) Example of twill reinforcement. Different colors represent the segments; (b) Meshed segment of a yarn.

The implementation of a sophisticated multiparametric damage model does not make sense unless all these peculiarities are taken into account. Currently, the error introduced by the simplifications of actual reinforcement geometry exceeds all possible benefits of employing a complex damage model.

To capture the stiffness evolution, it seems reasonable to follow the physically founded and very simple idea of Zinoviev [143], who suggested that the effective transverse and shear stresses in the damaged ply do not exceed the level at which cracks initiate. The model of Zinoviev proved to be one of the five most successful models of the World-Wide Failure Exercise I [144]. Another successful degradation model of WWFE, the model of Puck [145], employs a similar postcracking assumption. It requires reducing the elastic constants in a way which keeps the failure initiation index at a constant level. Upon active loading, both the models exhibit a stress-strain response resembling the curve of ideal plasticity. Both the damage models do not require any material constants other than those needed for the failure initiation prediction.

Zinoviev's model is formulated as an elaborated conditional algorithm distinguishing various possible situations in loading and unloading. In overcoming the difficulties of implementing this algorithm in multisegment textile architectures, we marry this concept with damage evolution laws offered by continuous damage mechanics. A single damage evolution law can then be obtained.

Following the considerations of Murakami and Ohno [146], the damage is introduced as a second rank tensor. For a case of an open crack (transverse stress is tensile), energy equivalence of cracked and homogenous damaged media imposes the following reduction of the elastic constants:

$$
\begin{aligned}
E_2 &= E_2^0(1 - d_2)^2 & v_{21} &= v_{21}^0(1 - d_2) \\
v_{23} &= v_{23}^0(1 - d_2) & G_{12} &= G_{12}^0(1 - d_{12})
\end{aligned}
\tag{2.6}
$$

where E, G are Young's and shear moduli, and d_2, d_{12} degradation of the elastic constants, index "0" corresponds to intact material, coordinate "1" denotes the fiber direction, 1-3 is the plane of the crack defined by means of the Mohr-Hashin-Puck failure initiation criteria [147]. Without contradicting available experimental data, it is postulated that all the cracks in a segment have the same orientation [148]. All the other elastic constants remain unaffected by cracking. The symmetry of the stress tensor in the damaged media leads, as described by Zako et al. [57], to the following relation between degradation of the Young's and shear moduli:

$$
d_2 = \frac{2\left(1 - \sqrt{1 - d_{12}}\right)}{\left(2 - \sqrt{1 - d_{12}}\right)}
\tag{2.7}
$$

The damage factors d_2 and d_{12} are nearly proportional at small values, and the transverse degradation is slightly higher at the advanced damage levels. Following the continuum damage models [149], we employ the energy release rate Y_{12} as a factor

driving damage accumulation. It is introduced as the derivative of the elastic energy of the damaged material Ψ with respect to the degradation parameter:

$$Y_{12} = \sqrt{\underset{\tau \leq t}{Sup}(Z_{12})} \quad Z_{12} = -\frac{\partial}{\partial d_{12}}\Psi \tag{2.8}$$

where operator $\underset{\tau \leq t}{Sup}(\dots)$ denotes the maximum over the time period t and reflects the fact that the damage state is non-healing. The square root is used for convenience, to make it proportional to strain. The elastic energy may be written as a function of the damage parameters d_2, d_{12}, the elastic stiffness matrix of intact material C^0, and the strains averaged over the segment volume ε. This allows differentiation of the expression explicitly, which results in the following definition:

$$Z_{12} = \frac{\partial d_2}{\partial d_{12}}\varepsilon_{22}\left(\varepsilon_{22}C_{22}^0(1-d_2) + \varepsilon_{11}C_{12}^0 + \varepsilon_{33}C_{23}^0\right) + \frac{1}{2}\left(G_{12}^0\gamma_{12}^2 + G_{23}^0\gamma_{23}^2\right) \tag{2.9}$$

In the case of a closed crack (transverse compression), the normal stress traction is assumed to be continuous across the crack face. Hence, the degradation factor $d_2 = 0$ and $\frac{\partial d_2}{\partial d_{12}} = 0$. Zinoviev's and Puck's assumptions are in good correspondence with the following damage evolution law:

$$d_{12} = 1 - \frac{Y_{12}^i}{Y_{12}} \tag{2.10}$$

where index i reflects the value of a variable at the moment of failure onset and $Y_{12} \geq Y_{12}^i$. Eq. (2.10) matches the shear diagram assumed in Ref. [143]— Fig. 2.8(a), as it is reduced to $d_{12} = 1 - \frac{\gamma_{12}^i}{\gamma_{12}}$ in pure shear. The stress-strain responses in other loading situations are obtained from the solution of Eqs. (2.8) and (2.10) relative to d_{12}. Fig. 2.8(b) shows predicted response in uniaxial transverse tension. Right after the damage onset, the stress drops and before settling down at a value of about 80%—90% of transverse strength.
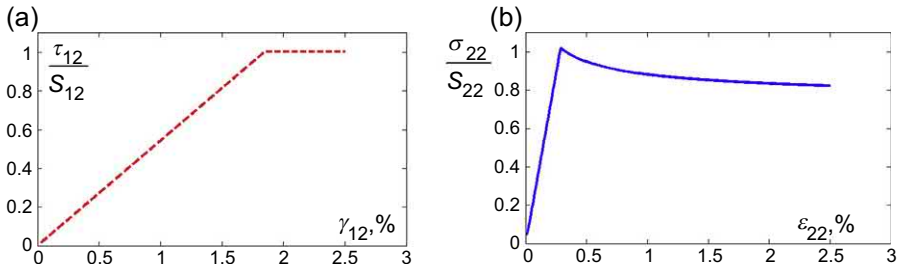
Figure 2.8 Stress-strain diagrams of an elementary unidirectional fiber bundle in (a) pure shear (input), (b) pure transverse tension (as follows from the damage evolution law). S_{12}, S_{22} are shear and transverse strengths, σ_{12}, σ_{22} are the correspondent stresses.

Such a law has an analogy with classical fracture mechanics, where the energy released through crack propagation is linked to the crack length. The meaning of (2.10) is that the stiffness reduction is proportional to the energy, which can be released through damage accumulation.

As far as the numerical implementation is concerned, it is required to (a) calculate the damage parameters at a given strain state, (b) redefine the elastic constants according to (2.1). An iteration procedure is needed to ensure convergence and satisfaction of (2.8) and (2.10) at the same time. The procedure is found to be insensitive to load step size and defragmentation of yarns into segments.

2.4.4   An example of failure modeling

Uniaxial tensile tests have been performed for 4-ply and 1-ply composites based on glass plain-weave reinforcement Table 2.3. The composites are produced by resin infusion molding using Dow Derakane 8084 Epoxy-Vinyl Ester resin. The weave architecture is slightly unbalanced exhibiting different crimp in warp and weft directions. The lay-up of 4-ply composite has been balanced.

The thicknesses of a single ply in 4-ply and 1-ply composites are essentially different. Due to the nesting, they differ by factor 1.2, although the same production parameters have been used for both the materials. As a result, the crimp of the 1-ply composite is higher and the total fiber volume fraction is 6% lower. The dimensions of the fabric unit cell are 10.3 × 12.5 mm in the plane of the textile.

The tensile tests have been accompanied by acoustic emission (AE) registration, full-field surface strain-mapping (SM), progressive crack imaging at different load levels, and micrographic inspection of the cross-sections of samples. The results of testing have been reported in Refs. [150,151].

The geometrical model of the reinforcements has been created by WiseTex and processed by the MeshTex program to get rid of interpenetrations, insert interyarn matrix, and mesh matrix/yarns. The correct iy-FVF of the one-ply composite has been achieved using relatively simple cross-section shapes. Nesting has not been modeled.

Table 2.3 Principal parameters of the 2D preforms and composites.

Parameter	Four-ply laminate	One-ply composite
Ply orientation	0°/90°/90°/0°[a]	90°
Composite thickness, mm	2.45 ± 0.08[b]	0.73
Average ply thickness, mm	0.61	0.73
Total areal density of preform, g/m^2	3260	815
Total fiber volume fraction in composite, %	52.4	44.0
Crimp of warp/weft, %	0.1/0.2	02/0.3

[a]0° or 90° corresponds to the angle between the warp and loading directions.
[b]"±"designates standard deviation.

Hence, to achieve the realistic iy-FVF of the multiply composite, the YVF has been artificially increased in a simple procedure. After the meshing is complete, the first row of matrix elements enveloping yarns has been attributed to the corresponding yarn. This procedure violates the smoothness of the yarn surface. However, since damage evolution is governed by the average stress within the yarn, it does not affect the results. The periodic boundary conditions have been used in-plane, and the novel laminate conditions [30] have been used for modeling the interaction of the plies. Failure initiation and the orientations of crack planes have been predicted by the criterion of Puck [145]. Intraply cracking has been simulated by the model described above, the plasticity of the matrix can be ignored when testing orthogonal fabric along yarns, the delamination has been modeled as a gradual reduction of the plies in the laminate, matrix in the resin-rich zones is assumed to be elastic, and fiber failure has been considered as a single failure event leading to the catastrophic fiber rupture and a disintegration of the composite.

The simulation of the one-ply composite shows that the post-critical assumptions and the simple modeling procedure work fairly well Fig. 2.9. Hence, this approach can be used further for the simulation of the 4-ply laminate. A slight stiffening response of the material at the end of the test is probably caused by straightening of the yarns in the loading direction, which has not been accounted for in the model.

Modeling of the four-ply laminate has a number of specific problems. The mismatch of the unit cell dimensions does not allow modeling of the $(0°/90°)_s$ composite configuration explicitly. Strictly speaking, the periodic building block of such a laminate does not exist. The in-phase and the out-of-phase configurations of the unbalanced $(0°)_4$ laminate are considered separately to simplify the analysis. The crimp of warp and weft yarns is different. Hence, there is a strong contrast in the stress-strain curves of the unbalanced laminate loaded in the orthogonal directions Fig. 2.10. By disregarding the interaction between the 0° and 90° plies, it can be
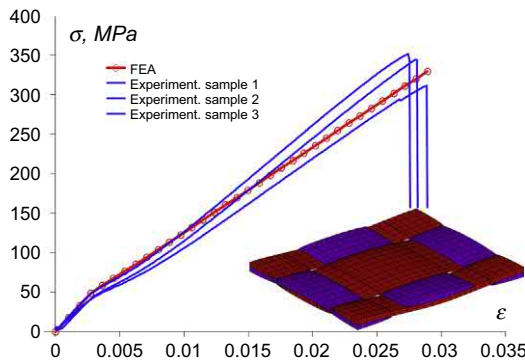
Figure 2.9 Tensile test for one-ply composite: "Experiment" experiments (3 representative samples) and "FEA" the simulation results. The model has the following features:
O-FVF = 44%, iy-FVF = 74.5%, interyarn matrix layer is 20 microns. The transverse strength is assumed to be 40 MPa, the longitudinal strength is 1280 MPa at 60% FVF. The local stress is used to predict the failure.
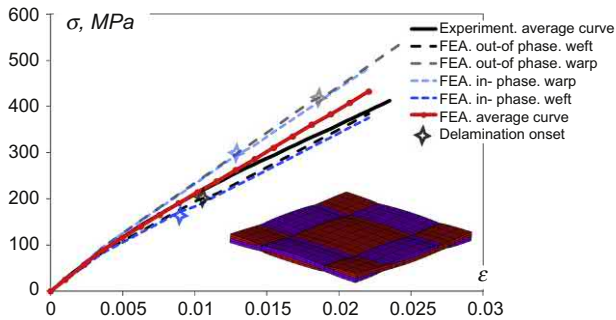
Figure 2.10 Tensile test for four-ply composite: "Experiment" experiments (average curve) and the simulation (FEA). "In-phase" and "Out-of phase" denote the interply configurations. "Warp" and "Weft" are the directions of tensile test. The model has the following features: O-FVF = 52.4%, iy-FVF is in the range of 60.1%−75.1%, direct contact of the yarns (no interyarn matrix). The transverse strength is assumed to be 40 MPa, and the longitudinal strength is 1280 MPa at 60% FVF. The local stress is used to predict the failure. The average curve FEA is built by averaging all the four simulations.

assumed that an average curve gives a rough representation of the behavior of the balanced composite. Indeed, it appears to be in good correspondence with experiments until 1.5% of the applied deformation Fig. 2.10. At this stage, active delamination is observed experimentally.

In order to account for the influence of delamination, the transformation of the 4-ply laminate to 3-ply and 1-ply composite is considered. The occurrence of this event is governed by the criterion for cracking of brittle matrix in the interply space. However, as can be seen, this event does not cause a significant drop in average laminate stress. Hence, elaborated modeling is required to describe the spreading of the delaminated zone.

The concurrent experimental-modeling study shows several important effects:

(1) One-ply composite and multiply laminate behave substantially different. The model of intra-yarn cracking has to be verified in the one-ply case;
(2) Delamination plays a significant role in the textile composite performance and stiffness degradation;

When modeling textile composites, it is important to find a proper balance between the finest details of all three: geometrical model, finite element approach, and damage mechanics. As has been discussed above, some details may appear to be not only excessive but even harmful for the analysis. The refinement of geometry affects the robustness of stress/damage calculations and makes the analysis sensitive to irrelevant features. There is a certain controversy about the textile geometry actualities. For instance, precise replication of the yarn cross-section shape is needed as it guarantees the correct YVF and iy-FVF. Yet, it promotes artificial stress concentration at the

sharp yarn edges. By doing a segment-wise damage analysis, we disregard the local instabilities of the stress field and tolerate a coarse mesh, which is just fine enough to respect the YVF. We also choose the minimum damaged zone to be courser than the resolution of the stress field, avoiding issues with the non-physicality of local damage mechanics. Hence, from the viewpoint of the discussed problems, course geometry and stress resolution appear to be effective if chosen in the correct way.

All of these issues illustrate the fact that in the wide field of available modeling options, there is a narrow path to the effective analysis. We believe that the chosen modeling paradigm allows capturing the essential features of the composite deformations.

2.5 Conclusions

Modeling of textile, and in particular, woven composites is an established, mature field, which has passed a long way of increasing model complexity from early models referring to the Classical Laminate Theory, adapted to account for knock-down factors due to fiber crimp, to advanced models of today, based on meso-level (woven unit cell) FE analysis. Several specialized commercials and open-source numerical tools for simulation of textile unit cells are now available.

Predictions of 2D and 3D woven composite stiffness properties have the adequacy level necessary for their use in practical design optimizations. Meso-level predictors for composite stiffness are integrated with macro-level FE tools for structural analysis.

The strength and damage models are rather in the research phase of development. Empirical damage models for woven plies are available and are implemented in commercial FE packages. However, damage and strength models on the meso-level, which would allow predictions of the ply model parameters based on the internal architecture of the composite and matrix/fiber properties, are just attaining the level of adequacy needed for their use in engineering design practice. One of the main stumbling block is consistent geometrical models of 2D and 3D woven unit cells. Available geometrical modeling tools just started to approach automated creation of the internal geometry, which is free from yarn volumes interpenetrations, suitable for quality meshing and preserving the realistic fiber volume fraction inside the yarns. Computational requirements for such modeling are very high; however, the predictive capabilities are still limited. Along with technical questions on geometry generations, there are still pending fundamental questions on multiscale modeling of nonperiodic interaction of plies of nonmatching orientations, modeling processing features at larger structural scales, and computationally efficient modeling of damage at higher structural levels. Solutions to these challenges begin to appear. There is a clear perspective that an adequate automated FE tool for meso-level analysis of woven composites will emerge in the near future.

References

[1] T.-W. Chou, F.K. Ko (Eds.), Textile Structural Composites, Elsevier, Amsterdam, 1989, p. 387.

[2] N.K. Naik, Woven Fabric Composites, Technomic, Lancaster-Basel, 1994, p. 192.

[3] A.E. Bogdanovich, C.M. Pastore, Mechanics of Textile and Laminated Composites, Chapman and Hall, London, 1996.

[4] A.C. Long (Ed.), Design and Manufacture of Textile Composites, Woodhead Publishing Ltd, Cambridge, 2005.

[5] A. Long (Ed.), Composite Forming Technologies, Woodhead Publishing, Cambridge, 2007.

[6] P. Boisse (Ed.), Composite Reinforcements for Optimum Performance, Woodhead Publishing, Oxford, 2011.

[7] W. Composites, M.H. Aliabadi, in: Computational and Experimental Methods in Structures, vol. 6, World Scientific Publishing, London, 2015.

[8] S.V. Lomov, I. Verpoest, Textile composite materials: polymer matrix composites, in: R. Blockley, W. Shyy (Eds.), Encyclopedia of Aerospace Engineering, John Wiley & Sons, Ltd., Chichester, 2010, pp. 2159−2176.

[9] L. Gorbatikh, S.V. Lomov, 2.15 damage in architectured composites, in: P.W.R. Beaumont, C.H. Zweben (Eds.), Comprehensive Composite Materials II, vol. 2, Academic Press, Oxford, 2018, pp. 291−306.

[10] V. Carvelli (Ed.), 13th International Conference on Textile Composites (TEXCOMP-13), 17−19 September 2018, Milan, Italy, vol. 406, 2018. IOP Conference Series: Materials Science and Engineering.

[11] S.V. Lomov, A.V. Gusakov, Coding of carcasse-layered weaves, Technol. Tekst. Promyshlennosty (4) (1993) 40−45.

[12] S.V. Lomov, A.V. Gusakov, Modellirung von drei-dimensionalen gewebe Strukturen, Technische Textilen 38 (1995) 20−21.

[13] I. Verpoest, S.V. Lomov, Virtual textile composites software Wisetex: integration with micro-mechanical, permeability and structural analysis, Compos. Sci. Technol. 65 (15−16) (2005) 2563−2574.

[14] X. Chen, P. Potiyaraj, CAD/CAM of orthogonal and angle-interlock woven structures for industrial applications, Text. Res. J. 69 (9) (1999) 648−655.

[15] X. Chen, P. Potiyaraj, CAD/CAM for complex woven fabrics. Part I. Backed cloths, J. Text. Inst. 89 (3) (1998) 532−545, part I.

[16] X. Chen, P. Potiyaraj, CAD/CAM for complex woven fabrics. Part II. Multi-layer fabrics, J. Text. Inst. 90 (1) (1999) 73−90, part I.

[17] G. Ping, D. Lixin, Algorithms for computer-aided construction of double weaves: application of the Kronecker product, J. Text. Inst. 90 (2) (1999) 158−176, part I.

[18] S.V. Lomov, et al., Modelling 3D fabrics and 3D reinforced composites: challenges and solutions, Text. Res. J. 81 (1) (2011) 26−41.

[19] S.V. Lomov, Modelling the geometry of textile reinforcements for composites: WiseTex, in: P. Boisse (Ed.), Composite Reinforcements for Optimum Performance, Woodhead Publishing, Oxford, 2011, pp. 200−238.

[20] S.V. Lomov, et al., Model of internal geometry of textile composite reinforcements: data structure and virtual reality implementation, J. Text. Inst. 98 (1) (2007) 1−13.

[21] K. Searles, G. Obegard, M. Kumosa, Micro- and mesomechanics of 8-harness satin woven fabric composite. I. Evaluation of elastic behaviour, Compos. A 32 (2001) 1627−1655.

[22] M. Karahan, et al., Internal geometry evaluation of non-crimp 3D orthogonal woven carbon fabric composite, Compos. A 41 (2010) 1301−1311.

[23] D.S. Ivanov, et al., Local compressibility of draped woven fabrics, in: 15th European Conference on Composite Materials (ECCM-15), electronic edition, 2012. Venice.

[24] D.S. Ivanov, et al., Failure analysis of triaxial braided composite, Compos. Sci. Technol. 69 (2009) 1372−1380.

[25] S.G. Ivanov, et al., Meso-FE models of tight 3D woven structures, in: 15th European Conference on Composite Materials (ECCM-15), electronic edition, 2012. Venice.

[26] S.V. Lomov, et al., Full field strain measurements for validation of meso-FE analysis of textile composites, Compos. A 39 (2008) 1218−1231.

[27] S.A. Grishanov, et al., The simulation of the geometry of two-component yarns. Part II. Fibre distribution in the yarn cross-section, J. Text. Inst. 88 (4) (1997) 352−372, part 1.

[28] T. Kurashiki, et al., On a numerical simulation of the mechanical behaviour for laminated woven fabric composites under tensile loading, in: Proceedings of the 7th International Conference on Textile Composites (TexComp-7), 2004, pp. 1−4. Yonezawa. p. (Textile 13).

[29] J. Whitcomb, C.D. Chapman, X. Tang, Derivation of boundary conditions for micro-mechanics analyses of plain and satin woven composites, J. Compos. Mater. 34 (9) (2000) 724−747.

[30] D.S. Ivanov, et al., Unit cell modelling of textile laminates with arbitrary inter-ply shifts, Compos. Sci. Technol. 72 (1) (2011) 14−20.

[31] D.S. Ivanov, et al., Stress distribution in outer and inner plies of textile laminates and novel boundary conditions for unit cell analysis, Compos. A 41 (4) (2010) 571−580.

[32] N.V. De Carvalho, S.T. Pinho, P. Robinson, Reducing the domain in the mechanical analysis of periodic structures, with application to woven composites, Compos. Sci. Technol. 71 (2011) 969−979.

[33] S. Sihn, E. Iarve, A.K. Roy, Three-dimensional stress analysis of textile composites: Part I. Numerical analysis, Int. J. Solids Struct. 41 (2004) 1377−1393.

[34] S. Sihn, E. Iarve, A.K. Roy, Three-dimensional stress analysis of textile composites: Part II. Asymptotic analysis, Int. J. Solids Struct. 41 (2004) 1395−1410.

[35] J. Fish, Q. Yu, Two-scale damage modeling of brittle composites, Compos. Sci. Technol. 61 (2001) 2215−2222.

[36] W.-G. Jiang, S.R. Hallett, M. Wisnom, Development of domain superposition technique for the modeling of woven fabric composites, in: P.P. Camanho (Ed.), Mechanical Response of Composites, Springer, 2008.

[37] G.N. Naik, V.K. Ganeshi, Prediction of on-axes elastic properties of plain weave fabric composites, Compos. Sci. Technol. 45 (1992) 135−152.

[38] M.G. Kollegal, S. Sridharan, Strength prediction of plain woven fabrics, J. Compos. Mater. 34 (2000) 240−257.

[39] M.G. Kollegal, S.N. Chatterjee, G. Flanagan, Progressive failure analysis of plain weaves using damage mechanics based constitutive laws, Int. J. Damage Mech. 10 (2001) 301−323.

[40] J. Whitcomb, J. Noh, C. Chapman, Evaluation of various approximate analyses for plain weave composites, J. Compos. Mater. 33 (1999) 1958−1980.

[41] V. Carvelli, C. Poggi, A homogenization procedure for the numerical analysis of woven fabric composites, Compos. A 32 (10) (2001) 1425−1432.

[42] S.C. Quek, et al., Compressive response and failure of braided textile composites: part 2 — computations, Int. J. Non-Linear Mech. 39 (4) (2004) 649−663.

[43] A. Miravete, et al., 3D mesomechanical analysis of three-axial braided composite materials, Compos. Sci. Technol. 66 (15) (2006) 2954−2964.

[44] S.V. Lomov, et al., Meso-FE modelling of textile composites: road map, data flow and algorithms, Compos. Sci. Technol. 67 (2007) 1870−1891.

[45] M. Kästner, G. Haasemann, V. Ulbricht, XFEM-modelling and simulation of the inelastic material behaviour of textile-reinforced polymers, Int. J. Numer. Methods Eng. 86 (2011) 477−498.

[46] D. Goyal, et al., Effect of various parameters on effective engineering properties of 2 x 2 braided composites, Mech. Adv. Mater. Struct. 12 (2) (2005) 113−128.

[47] D. Goyal, J.D. Whitcomb, Effect of fiber properties on plastic behavior of 2x2 biaxial braided composites, Compos. Sci. Technol. 68 (3−4) (2008) 969−977.

[48] I. Tsukrov, et al., Finite element modeling to predict cure-induced microcracking in three-dimensional woven composites, Int. J. Fract. 172 (2011) 209−216.

[49] F. Stig, S. Hallstrom, A modelling framework for composites containing 3D reinforcement, Compos. Struct. 94 (2012) 2895−2901.

[50] D. Goyal, J.D. Whitcomb, Load flow in plain woven composites, J. Compos. Mater. 42 (25) (2008) 2761−2777.

[51] J. Varghese, et al., Hierarchical analysis of woven composite DCB specimen, J. Compos. Mater. 41 (8) (2007) 931−950.

[52] S. Dai, P.R. Cunningham, Multi-scale damage modelling of 3D woven composites under uni-axial tension, Compos. Struct. 142 (2016) 298−312.

[53] J. Llorca, et al., Multiscale modelling of composite materials: a road map towards virtual testing, Adv. Mater. 23 (2011) 5130−5147.

[54] K. Woo, Y.W. Suh, J.D. Whitcomb, Phase shift effect on the stress distribution for satin weave composites, J. Compos. Mater. 36 (2002) 271−286.

[55] D. Bigaud, P. Hamelin, Stiffness and failure modelling of 2D and 3D textile-reinforced composites by means of imbricate-type elements approaches, Comput. Struct. 80 (2002) 2253−2264.

[56] X. Tang, J.D. Whitcomb, Progressive failure behaviour of 2D woven composites, J. Compos. Mater. 37 (14) (2003) 1239−1259.

[57] M. Zako, Y. Uetsuji, T. Kurashiki, Finite element analysis of damaged woven fabric composite materials, Compos. Sci. Technol. 63 (2003) 507−516.

[58] G. Nicoletto, E. Riva, Failure mechanisms in twill weave laminates: FEM predictions vs experiments, Compos. A 35 (2004) 787−795.

[59] S.V. Lomov, et al., Homogenisation of a sheared unit cell of textile composites: FEA and approximate inclusion model, Revue Européenne de Mécanique Numérique (former Revue européenne des éléments finis) 14 (6−7) (2005) 709−728.

[60] P. Potluri, A. Manan, Mechanics of non-orthogonally interlaced textile composites, Compos. Appl. Sci. Manuf. 38 (4) (2007) 1216−1226.

[61] R.L. Karkkainen, B.V. Sankar, A direct micromechanics method for analysis of failure initiation of plain weave textile composites, Compos. Sci. Technol. 66 (2006) 137−150.

[62] R.L. Karkkainen, J.T. Tzeng, Micromechanical strength modeling and investigation of stitch density effects on 3D orthogonal composites, J. Compos. Mater. 43 (25) (2009) 3125−3142.

[63] H. Huang, A.M. Waas, Compressive response of Z-pinned woven glass fiber textile composite laminates: modeling and computations, Compos. Sci. Technol. 69 (2009) 2338−2344.

[64] C. El Hage, et al., Analytical and numerical modeling of mechanical properties of orthogonal 3D CFRP, Compos. Sci. Technol. 69 (2009) 111−116.

[65] D.S. Ivanov, et al., Strain mapping analysis of textile composites, Opt. Lasers Eng. 47 (2009) 360−370.

[66] M.P. Rao, B.V. Sankar, G. Subhash, Effect of Z-yarns on the stiffness and strength of three-dimensional woven composites, Compos. B 40 (2009) 540−551.

[67] B. Owens, J. Whitcomb, J. Varghese, Effect of finite thickness and free edges on stresses in plain weave composites, J. Compos. Mater. 44 (2010) 675−692.

[68] S. Daggumati, et al., Local damage in a 5-harness satin weave composite under static tension: Part II − meso-FE modelling, Compos. Sci. Technol. 70 (13) (2010) 1934−1941.

[69] S. Daggumati, et al., Local strain in a 5-harness satin weave composite under static tension: part I − experimental analysis, Compos. Sci. Technol. 71 (8) (2011) 1171−1179.

[70] S. Li, et al., A unit cell for FE analysis of materials with the microstructure of a staggered pattern, Compos. A 42 (2011) 801−811.

[71] V. Šmilauer, et al., Multiscale simulation of fracture of braided composites via repetitive unit cells, Eng. Fract. Mech. 78 (2011) 901−918.

[72] A. Adumitroaie, E.J. Barbero, Stiffness and strength prediction for plain weave textile reinforced composites, Mech. Adv. Mater. Struct. 19 (2012) 169−183.

[73] E.J. Barbero, et al., Finite element modeling of plain weave fabrics from photomicrograph measurements, Compos. Struct. 73 (2006) 41−52.

[74] E. Bedogni, et al., Creating finite element model of 3D woven fabrics and composites: semi-authomated solution of interpenetration problem, in: 15th European Conference on Composite Materials (ECCM-15), electronic edition, 2012. Venice.

[75] A.R. Melro, et al., Numerical simulation of the non-linear deformation of 5-harness satin weaves, Comput. Mater. Sci. 61 (2012) 116−126.

[76] N.V. De Carvalho, S.T. Pinho, P. Robinson, Numerical modelling of woven composites: biaxial loading, Compos. Appl. Sci. Manuf. 43 (8) (2012) 1326−1337.

[77] A. Doitrand, et al., On the influence of fabric layer shifts on the strain distributions in a multi-layer woven composite, Compos. Struct. 145 (2016) 15−25.

[78] L. Wang, et al., Progressive failure analysis of 2D woven composites at the meso-micro scale, Compos. Struct. 178 (2017) 395−405.

[79] L. Wang, et al., Experimental and numerical investigation on mechanical behaviors of woven fabric composites under off-axial loading, Int. J. Mech. Sci. 141 (2018) 157−167.

[80] D. Goyal, J.D. Whitcomb, X.D. Tang, Validation of full 3D and equivalent tape laminate modeling of plasticity induced non-linearity in 2 x 2 braided composites, Compos. A − Appl. Sci. Manuf. 39 (5) (2008) 747−760.

[81] D. Goyal, J.D. Whitcomb, Analysis of stress concentrations in 2 x 2 braided composites, J. Compos. Mater. 40 (6) (2006) 533−546.

[82] T. Wehrkamp-Richter, N.V. De Carvalho, S.T. Pinho, A meso-scale simulation framework for predicting the mechanical response of triaxial braided composites, Compos. Appl. Sci. Manuf. 107 (2018) 489−506.

[83] G. Grail, et al., Consistent finite element mesh generation for meso-scale modeling of textile composites with preformed and compacted reinforcements, Compos. Appl. Sci. Manuf. 55 (2013) 143−151.

[84] K.C. Warren, et al., Progressive failure analysis of three-dimensional woven carbon composites in single-bolt, double-shear bearing, Compos. B Eng. 84 (2016) 266−276.

[85] A.K. Pickett, J. Sirtautas, A. Erber, Braiding simulation and prediction of mechanical properties, Appl. Compos. Mater. 16 (6) (2009) 345−364.

[86] E.V. Iarve, et al., Independent mesh method-based prediction of local and volume average fields in textile composites, Compos. Appl. Sci. Manuf. 40 (12) (2009) 1880−1890.

[87] R.D.B. Sevenois, et al., Avoiding interpenetrations and the importance of nesting in analytic geometry construction for representative unit cells of woven composite laminates, Compos. Sci. Technol. 136 (2016) 119−132.

[88] S. Daggumati, et al., Local strain in a 5-harness satin weave composite under static tension: Part II − meso-FE analysis, Compos. Sci. Technol. 71 (8) (2011) 1217−1224.

[89] E. D'Amato, Finite element modelling of textile composites, Compos. Struct. 54 (2002) 467−475.

[90] G. Anzelotti, G. Nicoletto, E. Riva, Mesomechanic strain analysis of twill-weave composite lamina under unidirectional in-plane tension, Compos. Appl. Sci. Manuf. 39 (8) (2008) 1294−1301.

[91] Z.T. Kier, et al., Estimating mechanical properties of 2D triaxially braided textile composites based on microstructure properties, Compos. B Eng. 68 (2015) 288−299.

[92] M. Pankow, et al., Modeling the response, strength and degradation of 3D woven composites subjected to high rate loading, Compos. Struct. 94 (5) (2012) 1590−1604.

[93] Y. Zhou, Z. Lu, Z. Yang, Progressive damage analysis and strength prediction of 2D plain weave composites, Compos. B Eng. 47 (2013) 220−229.

[94] A. Doitrand, et al., Mesoscale analysis of damage growth in woven composites, Compos. Appl. Sci. Manuf. 96 (2017) 77−88.

[95] S.V. Lomov, et al., Meso-level textile composites simulations: open data exchange and scripting, J. Compos. Mater. 48 (2014) 621−637.

[96] A. Wendling, et al., Consistent geometrical model of interlock fabrics, Finite Elem. Anal. Des. 90 (2014) 93−105.

[97] A. Song, et al., Accounting for sheared textile composite unit cell properties in macro scale FE simulations, in: 22nd International Conference on Composite Materials (ICCM22), Melbourne, Australia, 2019.

[98] B. El Said, et al., Multi-scale modelling of strongly heterogeneous 3D composite structures using spatial Voronoi tessellation, J. Mech. Phys. Solids 88 (2016) 50−71.

[99] B. El Said, et al., An iterative multiscale modelling approach for nonlinear analysis of 3D composites, Int. J. Solids Struct. 132−133 (2018) 42−58.

[100] Y. Miao, et al., Mechanics of textile composites: micro-geometry, Compos. Sci. Technol. 68 (2008) 1671−1678.

[101] I. Tsukrov, J. Novak, Micromechanical modelling of transverse moduli of unidirectional composites with non-circular elastic fibres, in: C.A. Brebbia, W.P. de Wilde (Eds.), High Performance Structures and Composites, WIT Press, Southampton, Boston, 2002, pp. 212−220.

[102] Y. Mahadik, S.R. Hallett, Finite element modelling of tow geometry in 3D woven fabrics, Compos. A 41 (2010) 1192−1200.

[103] S.D. Green, et al., Mechanical modelling of 3D woven composites considering realistic unit cell geometry, Compos. Struct. 118 (2014) 284−293.

[104] S. Joglekar, M. Pankow, Modeling of 3D woven composites using the digital element approach for accurate prediction of kinking under compressive loads, Compos. Struct. 160 (2017) 547−559.

[105] A.J. Thompson, et al., High fidelity modelling of the compression behaviour of 2D woven fabrics, Int. J. Solids Struct. 154 (2018) 104−113.

[106] G. Nilakantan, B.N. Cox, O. Sudre, Generation of realistic stochastic virtual microstructures using a novel thermal growth method for woven fabrics and textile composites, in: Proceedings of American Society for Composites 32nd Technical Conference, 2017.

[107] F. Robitaille, et al., Authomatically generated geometric descriptions of textile and composite unit cells, Compos. A 34 (4) (2003) 303−312.

[108] G. Hivet, P. Boisse, Consistent 3D geometrical model of fabric elementary cell. Application to a meshing preprocessor for 3D finite element analysis, Finite Elem. Anal. Des. 42 (2005) 25−49.

[109] G. Hivet, P. Boisse, Consistent mesoscopic mechanical behaviour model for woven composite reinforcements in biaxial tension, Compos. B Eng. 39 (2) (2008) 345−361.

[110] N. Isart, et al., Internal geometric modelling of 3D woven composites: a comparison between different approaches, Compos. Struct. 132 (2015) 1219−1230.

[111] N. Isart, et al., Geometric model for 3D through-thickness orthogonal interlock composites, Compos. Struct. 119 (2015) 787−798.

[112] I. Straumit, et al., Identification of the flax fibre modulus based on an impregnated quasi-unidirectional fibre bundle test and X-ray computed tomography, Compos. Sci. Technol. 151 (2017) 124−130.

[113] Y. Liu, et al., Prediction of linear and nonlinear behavior of 3D woven composite using mesoscopic voxel models reconstructed from X-ray micro-tomography, Compos. Struct. 179 (2017) 568−579.

[114] I. Straumit, S.V. Lomov, M. Wevers, Quantification of the internal structure and automatic generation of voxel models of textile composites from X-ray computed tomography data, Compos. A 69 (2015) 150−158.

[115] A. Vanaerschot, et al., Stochastic framework for quantifying the geometrical variability of laminated textile composites using micro-computed tomography, Compos. A 44 (2013) 122−131.

[116] A. Vanaerschot, et al., Experimentally validated stochastic geometry description for textile composite reinforcements, Compos. Sci. Technol. 122 (2016) 122−129.

[117] A. Vanaerschot, et al., Stochastic characterisation methodology for 3-D textiles based on micro-tomography, Compos. Struct. 173 (2017) 44−52.

[118] A. Vanaerschot, et al., Multi-scale modelling strategy for textile composites based on stochastic reinforcement geometry, Comput. Methods Appl. Mech. Eng. 310 (2016) 906−934.

[119] R.G. Rinaldi, et al., Generating virtual textile composite specimens using statistical data from micro-computed tomography: 3D tow representations, J. Mech. Phys. Solids 60 (8) (2012) 1561−1581.

[120] T. Kurashiki, et al., Mechanical behaviors of non-crimp fabric composites based on multi-scale analysis, in: 17th International Conference on Composite Materials (ICCM-17), IOM Communications Ltd, Edinburgh, 2009.

[121] T. Kurashiki, et al., Effects of stitching parameters on damage development for non-crimp fabric composites under tensile loading, in: 15th European Conference on Composite Materials (ECCM-15), electronic edition, 2012. Venice.

[122] S.A. Tabatabaei, S.V. Lomov, I. Verpoest, Assessment of embedded element technique in meso-FE modelling of fibre reinforced composites, Compos. Struct. 107 (2014) 436−446.

[123] S.A. Tabatabaei, S.V. Lomov, Eliminating the volume redundancy of embedded elements and yarn interpenetrations in meso- finite element modelling of textile composites, Comput. Struct. 152 (2015) 142−154.

[124] S.A. Tabatabaei, et al., Full-field strain measurements and meso-FE modelling of hybrid carbon/self-reinforced polypropylene, Compos. Struct. 132 (2015) 864−873.

[125] O. Vorobiov, S.A. Tabatabaei, S.V. Lomov, Mesh superposition applied to meso-FE modelling of fibre reinforced composites: cross-comparison of implementations, Int. J. Numer. Methods Eng. 111 (2017) 1003−1024.

[126] J. Crookston, et al., Modelling mechanical performance including damage development for textile composites using a grid-based FE method with adaptive mesh refinement, in: Proceedings of the 8th International Conference on Textile Compoosites (TexComp-8), electronic edition, 2006. Nottingham.

[127] G. Fang, et al., Smoothing artificial stress concentrations in voxel-based models of textile composites, Compos. Appl. Sci. Manuf. 80 (2016) 270−284.

[128] C.C. Chamis, Mechanics of composite materials: past, present and future, J. Compos. Technol. Res. 11 (1) (1989) 3−14.

[129] S.G. Abaimov, A.A. Khudyakova, S.V. Lomov, On the closed form expression of the Mori-Tanaka theory prediction for the engineering constants of a unidirectional fiber-reinforced ply, Compos. Struct. 142 (2016) 1−6.

[130] A.F. Kregers, Y.G. Melbardis, Determination of the deformability of three-dimensional reinforced composites by the stiffness averaging method, Polym. Mech. 14 (1978) 3−8.

[131] G. Huysmans, I. Verpoest, P. Van Houtte, A poly-inclusion approach for the elastic modelling of knitted fabric composites, Acta Mater. 46 (9) (1998) 3003−3013.

[132] G. Huysmans, I. Verpoest, P. Van Houtte, A damage model for knitted fabric composites, Compos. A 32 (10) (2001) 1465−1475.

[133] S.V. Lomov, et al., Textile geometry preprocessor for meso-mechanical models of woven composites, Compos. Sci. Technol. 60 (2000) 2083−2095.

[134] S.V. Lomov, et al., Textile composites: modelling strategies, Compos. A 32 (10) (2001) 1379−1394.

[135] S.V. Lomov, et al., Predictive analyses and experimental validations of effective elastic properties of 2D and 3D woven composites, in: 13th European Conference on Composite Materials (ECCM-13), 2008. Stockholm.

[136] K. Birkefeld, et al., Characterization of biaxial and triaxial braids: fiber architecture and mechanical properties, Appl. Compos. Mater. 19 (2012) 259−273.

[137] A. El Mourid, R. Ganesan, M. Levesque, Comparison between analytical and numerical predictions for the linearly viscoelastic behavior of textile composites, Mech. Mater. 58 (2013) 69−83.

[138] J.D. Eshelby, The determination of the elastic field of an ellipsoidal inclusion and related problems, Proc. Royal Soc. (1957) 376−396. A-241.

[139] T. Mura, Micromechanics of Defects in Solids, Kluwer Academic Publishers, Dordrecht, 1987, p. 586.

[140] D.S. Ivanov, S.V. Lomov, I. Verpoest, Finite element modelling of inter-ply delamination and intra-yarn cracking in textile laminates, in: Proceedings of 32nd SAMPE-Europe SEICO Conference, Paris, CD edition, 2011.

[141] L. Gorbatikh, S.V. Lomov, Damage accummulation in textile composites, in: R. Talreja, J. Varna (Eds.), Modeling Damage, Fatigue and Failure of Composite Materials, Elsevier (Woodhead Publishers), Cambridge, 2016, pp. 41−60.

[142] L. Gorbatikh, et al., On modelling of damage evolution in textile composites on meso-level via property degradation approach, Compos. A 38 (2007) 2433−2442.

[143] P.A. Zinoviev, S.V. Tsvetkov, Mechanical properties of unidirectional organic-fiber-reinforced plastics under hydrostatic pressure, Compos. Sci. Technol. 58 (1) (1998) 31−39.

[144] E. Hinton, A.S. Kaddour, P.D. Soden, Failure Criteria in Fibre Reinforced Polymer Composites: The World-wide Failure Exercise, Elsevier, Amsterdam, 2004.

[145] A. Puck, H. Schurmann, Failure analysis of FRP laminates by means of physically based phenomenological models, Compos. Sci. Technol. 62 (2002) 1633−1662.

[146] S. Murakami, Mechanical modeling of material damage, J. Appl. Mech. 55 (1988) 280.

[147] A. Puck, J. Kopp, M. Knops, Guidelines for determination of the parameters in Puck's action plane strength criterion, Compos. Sci. Technol. 62 (2002) 371−378.

[148] S.V. Lomov, et al., Experimental methodology of study of damage initiation and development in textile composites in uniaxial tensile test, Compos. Sci. Technol. 68 (2008) 2340−2349.

[149] P. Ladeveze, G. Lubineau, On a damage mesomodel for laminates: micromechanics basis and improvement, Mech. Mater. 35 (2003) 763−775.

[150] S.V. Lomov, et al., A comparative study of tensile properties of non-crimp 3D orthogonal weave and multi-layer plain weave E-glass composites. Part 1: materials, methods and principal results, Compos. A 40 (2009) 1134−1143.

[151] D.S. Ivanov, et al., A comparative study of tensile properties of non-crimp 3D orthogonal weave and multi-layer plain weave E-glass composites. Part 2: comprehensive experimental results, Compos. A 40 (2009) 1144−1157.

Manufacturing processes for composite materials and components for aerospace applications

A. McIlhagger, E. Archer, R. McIlhagger
Ulster University, Newtownabbey, Ulster, United Kingdom

3.1 Introduction

Throughout the last 40 years of using polymer composites in the aerospace sector, designers and manufacturing engineers have progressed from relatively small, lightly loaded components and sections of structure, such as ailerons and fairings to heavily stressed and critical items, such as the main wing and fuselage of the Boeing 787, the Airbus A400 M and the Airbus A350 aircraft, which are constructed from up to 50% (53% in the case of the A350) carbon-fiber-reinforced polymer composite (by weight of aircraft), and in which the main wings and fuselage are largely manufactured from composite materials.

Early manufacturing processes for lightly stressed components were small scale, involving significant elements of manual intervention in the process. They relied on the low density and high stiffness and strength of the raw materials to deliver the required performance. As the size, stress values, and criticality of the parts all increased, manual input has declined dramatically, substituted by complex, sophisticated robotic machinery. The robots have delivered consistency, freedom from defects, and increased processing speed to cope with the manufacture of wings and fuselage sections of large civil aircraft. However, the essentials of this prepreg route have remained unchanged, and there are still issues of the cost effectiveness of this route. In parallel, manufacturing researchers are pursuing lower cost options. In this chapter, the prepreg route in its various guises will be described and the state-of-the-art in alternative processes contrasted with it.

In the past, the principal drivers for the use of composites for aircraft components were:

- Reduced weight
- Cost reduction
- Improved performance

The emphasis has now shifted toward environmental issues. Hence, the prime drivers are now:

- Reduced fuel burn
- Reduced pollution
- Reduced noise

In order to achieve these aims, smaller, more efficient engines are used producing, all things being equal, less thrust, and thus, for force balance, the aircraft must produce less drag. While the form drag (due to the shape of the aircraft) remains essentially unchanged, the reduction must come from a reduced induced drag. For the performance characteristics to remain stable, the lift/drag (L/D) must be the same, and hence, less lift is generated. Again for force balance, with less lift and reduced drag (L/D fixed under similar conditions) then, if the payload accommodation is to remain the same, the structural weight of the aircraft must be reduced. The direct implication of this will be reduced operating costs.

Taylor (2000) [1] states that "increasing the use of composites to replace aluminum in the manufacture of airframes brings about numerous performance advantages such as the potential for weight reduction (due to higher specific strength and modulus), increased flexibility of design (due to the ability to build performance in specific directions), greater corrosion resistance and improved fatigue resistance. Weight reduction leads to improved fuel efficiency." Furthermore, the reduced number of fasteners on composite structures give a more aerodynamic surface to the aircraft compared to riveted aluminum.

This chapter begins by looking at key property and process requirements for composites before going on to look first at developments in processes using preimpregnated fibers (known as prepegs). It then looks at newer, alternative processes, such as resin transfer molding (RTM) and vacuum-assisted resin injection (VARI) molding.

3.2 Key property and process requirements

High fiber volume is essential for good aircraft structure performance. It is also important that the distribution of both fiber and resin is uniform throughout the component. To illustrate, the simple rule of mixtures (ROM) approach for the calculation of longitudinal modulus falls into the mechanics of materials category; the modulus of elasticity in the longitudinal direction (E_L), which is the direction parallel to the fibers, is given as:

$$E_L = E_l^f V_f + E_m(1 - V_f)$$

where V_f is the fiber volume fraction of the composite, E_l^f is the modulus of the fiber and E_m is the modulus of the resin. The typical V_f values for aerospace autoclaved prepreg components are approximately 54%, aerospace RTM components could be

57%, and some new resin infusion and advanced pultrusion processes could be above 60%. Although the simple ROM approach predicts an increase in performance with increased V_f, in reality, some important material properties, such as compression after impact strength begin to diminish as the resin content becomes insufficient to support the fibers.

One of the major difficulties associated with composite manufacture is that of void formation during impregnation and cure [2]. As these gaseous voids become entrapped within the matrix, stress concentrations can be established within the matrix. These may originate in a number of ways, including:

- During the mixing of the resin formulation.
- During filling of the cavities in components of more complex shape.
- Due to the complex nature of the textile reinforcement since air can become entrapped in the interstices of the fabric structure. This can be particularly evident when coarse yarns (or tows) are used or in complex three-dimensional (3-D) structures, e.g., braided or woven, and could be most prevalent at the tool/composite interface.
- During the complex chemical reactions which take place during the cure of thermosetting resins, as volatile gases are released and become encapsulated in the crosslinked resin [3].

A critical requirement of any process is that it is able to minimize void formation and ensure uniform distribution of resin as well as fibers throughout the component. These are major factors, alongside cost and flexibility in manufacturing different types of component, in assessing the merits of any particular manufacturing technique. These process variations must be understood at the design stage. For example, variation in fiber volume fraction can have a negative effect on the structural performance of the component which must be allowed for in the design by applying a B-basis knockdown factor to the allowable stress on the aircraft structure. On the other hand, if efforts are made to control V_f tightly, a negative impact on part thickness control could result, creating significant difficulties at the assembly stage where shimming might be required. In general, V_f is related to component thickness by:

$$V_f = \frac{A_W}{\rho_f t}$$

where A_W is the areal weight of the fibers, ρ_f is the density of the fiber and t is the component thickness.

Selection of both manufacturing process type and resin/fiber system will be influenced by the specific properties required for different parts of the aircraft. High fiber strength and stiffness combined with low density are obvious general requirements for all parts of the aircraft structure. These properties have been best achieved from composites produced using layup of unidirectional preimpregnated fibers (known as prepreg) coupled with autoclave cure. The high levels of composite stiffness and strength achieved by prepreg technology, combined with the low density of the constituents, make components manufactured this way suitable for wing and fuselage structures. Compression properties, in particular, will reduce if the fiber volume fraction is low. The upper wing skin and parts of the spar structure, which are placed

under compression loading will, therefore, benefit most from the use of unidirectional prepreg material where control of fiber distribution is good.

Other parts of the aircraft are not so severely stressed and require different sets of properties. As an example, leading edges of the wings, empennage and nose cone all have a high risk of bird strike and will require high composite toughness and resistance to impact and delamination. Optimized compression strength will be of less importance. The degree of fiber crimp, strength and volume fraction in the matrix can all be at less demanding values than for the wing skins or fuselage. Other parts of the aircraft with more complex geometries, such as fuselage doors, fairings, pressure bulkheads, and landing gear doors might be manufactured using processes more suited to forming these complex, relatively small-scale components than can be achieved using prepreg processes.

As has been noted, early examples of polymer composite manufacture on aircraft often used prepreg coupled with manual layup techniques followed by an autoclave cure. This process can produce composites with straight fibers, high and uniform volume fraction, and freedom from voids and porosity. Such composites, thus achieve optimum stiffness and static strength. While the production cost may have been competitive with aluminum for limited production runs, generally the cost of manufacturing structures with composites via this labor-intensive route was greater than with aluminum. The performance advantages of composites in terms of stiffness and strength to weight had to be weighed against the increased cost of manufacture. There has been, therefore, an increasing focus on reducing the cost of composite parts by reducing the costs of both materials and manufacturing processes [4].

Many of the alternative processes to prepreg production reduce cost via elimination of the autoclave stage, forming the composite by weaving, winding stitching or assembling a dry fiber preform which is then infused or infiltrated with a fluid resin to produce the final component. Composite components produced via these processes do not achieve the same levels of stiffness and strength as those produced via the prepreg route. Although their properties may not be as good as composites manufactured using prepreg technology, there will be components, where the reduced process cost makes them competitive with aluminum, and the non-optimal stiffness and strength do not matter. These alternative processes have other advantages, e.g., fiber arrangements can be multidirectional (e.g., a 3-D fiber architecture), giving significant improvements in delamination and impact resistance, a particular weakness of prepreg composites.

3.3   Prepreg/autoclave processes

Manufacturers of composite structures have traditionally used prepreg tape to manufacture structural components. Fibers are initially combined into unidirectional tows (bundles) of fibers combined into fabrics, e.g., by weaving or knitting. The vast majority of the tows employed in woven, braided or knitted reinforcements comprise low

twist or untwisted continuous filament yarns. Three-dimensional technical textiles can be produced by weaving [5], knitting [6], and braiding [7], or as noncrimp fabrics.

Sheets of fibers are soaked or coated in the partially cured resin. Controlled preimpregnation using dip coating and lick roll technology is used to apply a uniform amount of uncured resin to the reinforcement (Fig. 3.1). The resin contains both the base matrix resin and hardeners. The sheets are protected on both sides by the backing paper or film to stop them sticking. They must be stored at low temperatures to avoid the further curing and crosslinking of the resin matrix, which occurs at room temperature. Rolls of prepreg are stored under refrigerated conditions for a given period of time before the shelf life of the product expires. This is normally 90 days at $-18°C$ for aerospace quality materials. A sophisticated materials handling system is required to track all the materials to ensure that out-of-life prepreg is not used.

Prior to processing, rolls are removed and allowed to thaw and condition. After reaching room temperature, the fabric is cut into shaped plies, taking into account fiber orientation. Computer-based nesting is used to optimize fabric utilization. These plies are labeled to ensure they are used in the correct sequence. Plies of prepreg are cut into the appropriate shape either by hand or by an automated process, such as a Gerber cutter system. Plies are placed in a precise order and orientation on the surface of a tool made in the shape of the component to be manufactured. Since the layup sequence and orientation of the plies is critical to the performance of the composite, the plies must be hand laid into the thoroughly degreased and clean molding tool correctly. Constant inspection and signing-off of the layup at each stage is necessary to ensure performance and quality. Where the component comprises a large number of plies, frequent debaulking is required; i.e., the layup is compressed under vacuum, after which a further series of plies are laid-in.

Once the layup is completed, a layer of release film is laid on top of the ply layup to prevent the resinous stack of plies from adhering to the fibrous breather cloth which is used to absorb any excess resin and distribute the applied pressure evenly over the layup. Since a single tool surface is utilized, a good finish is secured on only one surface of the component, the other surface being in contact with the release film.
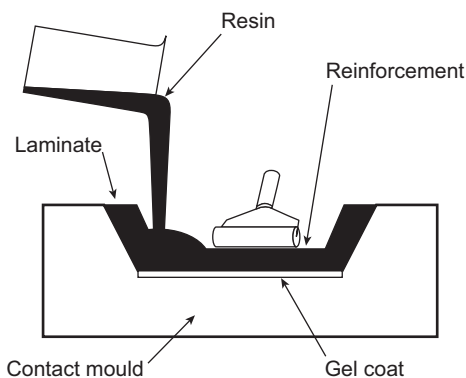
Figure 3.1 Hand layup.

However, caul plates can be used to produce a good surface finish on both sides of the component, even for reasonably complex shapes. Under these conditions, the pressure applied between the caul plate and tool surface holds the reinforcement in position, allowing the resin to flow in the space around the outer edge of the reinforcement before being drawn into the reinforcement, completely wetting it out. Thickness variations using this technique are much less pronounced than for matched tooling under pressure unless very stiff tooling is used. It is essential to ensure that the layup is contamination free. Such contamination can seriously impair the performance of the composite component. A clean room is required, and protective clothing should be worn at all times for both production of defect-free components and also for health and safety reasons.

The vacuum bagging system is used for producing noncritical components (Fig. 3.2). The complete assembly is enclosed in a sealed bag. Alternatively, the bagging layer is sealed to the surface of the tool surround beyond the boundaries of the component. A vacuum connector is inserted into this bagging film so that the ply stack can be consolidated under approximately 1 atm of vacuum. After confirming the integrity of the seal, the bagged assembly, while still under vacuum, is placed in a computer-controlled autoclave which is programmed to follow a particular processing cycle of both temperature and pressure [8].

The cycle is so designed that the maximum flow is achieved up to and including the hold period so that the fabric can be completely wetted-out and the interstices and the interfilament regions in the fabric structure completely filled with resin. The application of pressure, through inert nitrogen gas, at a very early stage in the cycle consolidates the composite structure and minimizes the risk of fire and explosion. The autoclave is typically operated at a maximum of approximately 1 bar to consolidate the plies into a "homogeneous" layer. However, this low pressure may sometimes be insufficient to compact the layers adequately to produce a high-performance component with high fiber volume fraction and low void content, and higher pressures may be required. As the temperature increases to the maximum, the resin commences crosslinking through an exothermic chemical reaction. Heat-up rates, typically at $2-5°C/min$, are kept slow to ensure that exothermic reactions are kept under control [8]. Dielectric analysis, differential scanning calorimetry, and thermo-gravimetric analysis can be used to establish the correct set-up conditions.
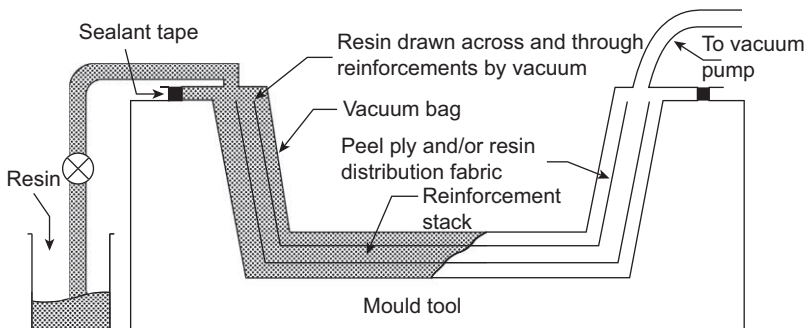
Figure 3.2 Vacuum bag resin infusion.

Good quality in a composite component requires that the cure cycle is carefully adhered to and key stages checked during processing. Cure monitoring is essential for ensuring the optimum mechanical and thermal properties of composites materials balanced against reducing manufacturing costs. Once the cure cycle has been completed, and the component cooled, also at a slow rate, the excess resin around the periphery is trimmed off and holes drilled where necessary (e.g., for bolting components together). Finally, the various components are put together to form the final assembly.

This prepreg route can be used to manufacture high quality, small to medium scale composite components for aerospace applications. (n.b. Manufacture of large wing skins, wing spars and fuselage sections in transport aircraft is performed instead by AFP and ATL processes; variants of the filament winding process, and will be described in Section 3.5) The fiber volume fraction for carbon fiber composites is typically in the region of 60% and the void content <1%. Nondestructive quality control is performed using ultrasound scans or X-ray micrographs to confirm this.

While prepreg processing provides high-performance composites, it is expensive. Costs include:

- To guarantee the quality of the component and the generation of high added-value waste material
- The need for low-temperature storage space
- The limited shelf life of prepreg
- The labor-intensive nature of the manual ply layup procedure both in terms of implementation and inspection to guarantee the quality of the component
- The large capital outlay required, e.g., for the autoclave

As noted, autoclaves have to be large enough to accommodate components, and they need to process several components of uniform thickness to be both cost effective and ensure effective curing. The autoclave can often form a bottle-neck for composites manufacturing since commercial autoclaves are large, and full loads have to be assembled, to be viable. Since components of similar thickness must be processed under the same cure cycle, good production scheduling is crucial to the success of the operation.

3.4 Filament winding

There are many other processes that have been developed with prepreg technology. Filament winding is a simple and effective method for producing parts, such as pipes and cylindrical containers in a wide range of sizes using both prepreg and other methods [9]. Part diameters ranging from 25 mm to 6 m are commonly fabricated. The process consists of wrapping bands of continuous fiber or roving over a mandrel in a controlled operation (Fig. 3.3). The production cycle for most filament wound composites can be subdivided into the following stages:

- winding of a preform
- heating of a preform with the mandrel up to the temperature of binder polymerization
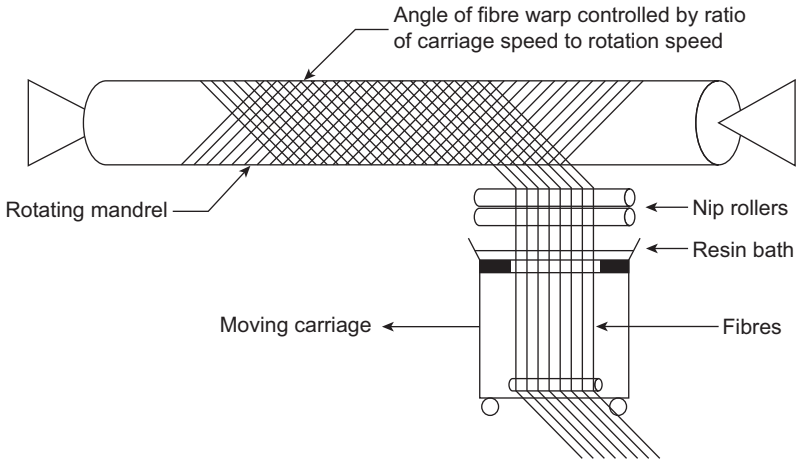
Figure 3.3 Filament winding.

- curing at constant or variable temperature
- cooling
- removal of the article from the mandrel

Many layers of the same or different patterns can be placed on the mandrel. The repeated patterns and reinforcement spacing are subject to close control. During winding, fiber tension generates pressure between layers of uncured composite. This pressure influences the compaction and void content of the article, which in turn controls the strength and stiffness of component. The resin may be added before winding (to produce a prepreg) or added during or after the winding operation. Finishing operations, such as machining or grinding, are usually not necessary.

Many high performance applications adopted in aircraft use epoxy-based resin systems. Silicones, phenolics, and polyimides are limited to special high temperature or electrical applications. Although thermosetting resins, such as epoxy, are commonly used in filament winding, there has been recent research into using thermoplastic matrix materials [9].

The following major processing factors influence filament wound composite properties:

- helix angle
- resin content and distribution
- winding tension
- condition of the impregnated strand
- variation in strand bandwidth
- position of the strand
- curing cycle

Defects, such as voids, dry spots, resin-rich areas, premature failures, localized failure regions, and nonuniform or incomplete cures can occur. Most aerospace components are held to within 2% weight tolerance, and for strength, an excessive variation can result in uneven stress distribution, resulting in component failure.

Resin content is closely related to the winding tension. A certain amount of flow is beneficial in removing entrapped air or other volatiles, but excessive tension can produce significant differences in the amount of resin in the inner and outer layers. Winding tension is thus, a critical parameter in controlling and limiting void content, which, in excess, can decrease interlaminar shear strength, lower compressive strength, and reduce resistance to buckling. Aerospace filament winding has become highly specialized and is designed for superior performance at a premium price.

3.5 Automated prepreg processes: automated fiber placement and automated tape layup

Manufacture of large composite aircraft structures (e.g., upper and lower wing skins and spars and fuselages for aircraft, such as the Boeing 787 and Airbus A350 with wingspans greater than 30 m) requires composites with the highest performance obtained using unidirectional prepreg material with autoclave cure. The aerospace sector also requires consistently accurate dimensional and shape tolerances and production rates, which are significantly better than those obtained with the manual layup. The main automated processes developed for these applications are:

- automated fiber placement (AFP)
- automated tape layup (ATL)

In the AFP process, multiheaded robot machinery lays down multiple strands of prepregged fiber on either flat tools, curved mandrels or complete cylindrical mandrels or drums (as applied in manufacture of fuselage sections of the Boeing 787). The process is shown in Fig. 3.4. The ATL variant of the process lays down tapes of unidirectional prepreg up to 300 mm wide across the mandrel. The AFP process uses smaller width ribbons of prepreg a few millimeters wide and can cope with more complex component shapes than ATL but cannot achieve the same laydown rates as smaller tape widths are involved. During the laydown process, the fibers or tapes are heated to promote tack and aid consolidation. At intervals, the laydown is suspended and the partially completed component consolidated under pressure. After completion of the layup, the sections of the structure are autoclaved under pressure.

The ATL and AFP processes are thus, a cross between filament winding with its elaborate automated patterns of fiber laydown and unidirectional prepreg layup with its reliance on the autoclave. The use of automated robotic machinery for the layup gives increased layup speed (vital to economically manufacture these large items in feasible timescale), consistency and freedom from errors compared with manual techniques, as well as ensuring precision in the placement of the tows and tapes.

Manufacture of upper and lower wing covers, spars and fuselages for aircraft, such as Boeing 787 and Airbus A350 relies on AFP using elaborate and high capital cost robotic machinery. The empennages (vertical stabilizer and horizontal stabilizer) of the Boeing 777, Airbus A340 and A380 are also manufactured using AFP. Before autoclaving, both wing skins and fuselage sections have stringer stiffeners attached.
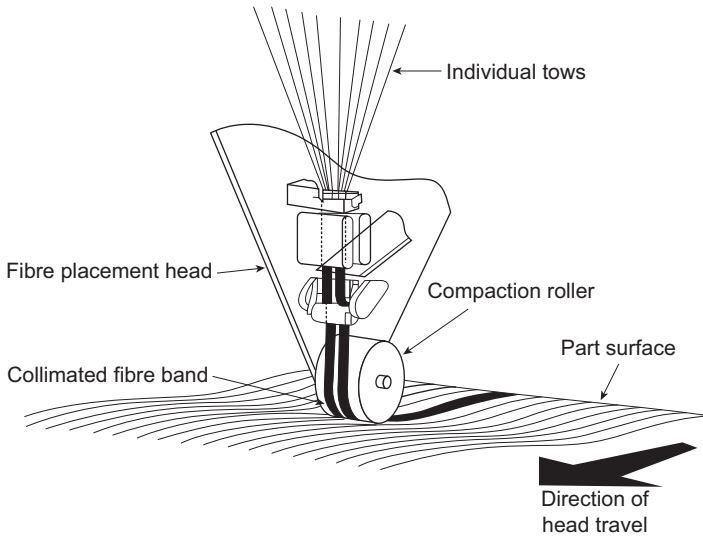
Figure 3.4 Automated fiber placement.

These are laid up separately, once again using automated layup of nonwoven unidirectional prepreg, positioned on to the skin and cocured with the skin to produce a complete skin-stringer fuselage section, panel or wing skin. Front and rear spars for the main wing are produced using similar techniques of AFP plus cocuring of separately manufactured stiffeners applied to the very different geometry of a C spar.

Even with modern autoclaves accommodating sections of structure up to 10−12 m long, it is not possible to manufacture wings and fuselage in a single piece and one operation. Instead, they are manufactured in parts and then joined. Bonding processes and the mechanical reliability of adhesive bonds are not yet sufficiently mature for aircraft regulators to contemplate the elimination of mechanical fasteners. Joining of the wings and fuselages is, therefore, accomplished by a mixture of mechanical fasteners and adhesive bonding.

This means that another mechanical property required for the composite material for present-day aircraft designs and manufacturing techniques is the strength of mechanically fastened joints under both static loads and in fatigue loading. Each A350 wing spar is manufactured in three sections, and these are first drilled using multiaxis machining centers. Approximately 16,000 holes are required for the six sections of the two spars. The upper and lower wing skins and stringers are bolted together also using mechanical fastening. On the 787 fuselage, the sections of fuselage barrels are bolted and bonded together via circumferential joints. On the A350 fuselage, composite panels are bolted and bonded to composite and metallic frames.

The A380 aircraft, although it has metallic wings and fuselage, is constructed using almost 30% polymer composite by weight. Many of these parts also are formed using the ATL or AFP processes. These include the center wing box, the tail cone, the vertical tailplane, and the horizontal tailplane. Other parts of the aircraft use other manufacturing techniques because the shape or properties required are better achieved

with that technique. For example, the rear pressure bulkhead is manufactured of non-crimped fabric with a resin film infusion process. The floor beams of the upper deck are of pultruded constant cross-section carbon fiber composites, and the flap track panels use RTM carbon fiber polymer composite. Leading edges and noses require above all else toughness with little stiffness or strength requirement, and glass/thermoplastic composite is used to confer this.

The ATL and AFP process requires high capital cost equipment, as well as the use of expensive fiber and toughened resin systems for the polymer composite. Hence, despite the current level of investment in these processes, a major driver for future composite process development is, therefore, further manufacturing and material cost reduction. While larger wide-body aircraft, such as the B787 and A350 can cost effectively exploit the stiffness and strength of polymer composites using current ATL and AFP processes production rates and costs, smaller composite aircraft with higher production rates in long runs are unlikely to be able to compete with metallic alternatives without further manufacture cost reduction.

3.6 Resin-infusion processes

3.6.1 Manual layup and sprayup techniques

The cost limitations of prepreg processing have led to the development of alternative techniques in which dry fabric is infused with resin as part of the manufacturing process [10].

Advantages of resin-infusion processes (sometimes referred to as "out of autoclave processes") include:

- no capital investment in expensive autoclaves is required although mold costs may be higher
- cold storage areas are not necessary, and hence, high value-added materials do not need to be held in stock
- shelf-life constraints are eliminated
- when dry preforms are used, expensive nesting, cutting-out, and hence, wastage are minimized, and labor-intensive hand layup is dispensed with.

Scott and Heath (1992) [11] have reported that cost savings ranging from 25% to 40% are possible with liquid molding raw materials when compared to prepreg. This is substantial as up to 50% of an autoclave component cost can be associated with the raw materials.

There are a number of ways in which fibers or reinforcements can be impregnated with thermosetting resin during production. In the early days of composite manufacture, the resin system was hand mixed and then applied by brush to each layer and consolidated using pressure applied through a hand-held roller.

The sprayup process is ideal for low to medium volume applications and is particularly well suited for efficient fabrication of large shapes. The decision to choose sprayup over hand layup is based on both the mechanical properties required and

the processing constraints. This process has been superseded in some applications by other advanced fabrication techniques, such as RTM which are discussed in later sections.

3.6.2   Matched-die molding

To achieve a more uniform distribution of resin throughout the reinforcement, more automated systems have been developed [12]. In matched-die molding, premixed resin and hardener are injected under pressure from a pressure pot into the reinforcement placed in a closed matched cavity tool [13]. The resin spreads out radially from the point of injection, permeating through the reinforcement until the cavity is completely filled with resin.

   In this process, the flow paths must be fully understood and predictable. Effective control of the filling operation is required to ensure resin "racing" or "tracking" does not occur. If this is not controlled, the resin flow front will race ahead (or fall behind) before re-joining the pressure flow front, leading to unimpregnated enclosed dry regions. Resin starved areas can be created even in very simple geometric configurations in which the resin front impinges on the cavity boundary wall when the flow front can no longer expand in the radial direction. Two such fronts on adjacent walls will result in the flow converging on a point within the reinforcement. This region will remain dry, i.e., not impregnated with resin.

   Such problems have led to a considerable amount of effort to model and predict the precise point where the molten resin front is with respect to time [13−15]. These approaches, applied at the design stage, have permitted fill procedures to be developed by which resin-starved areas are eliminated through the use of accurately positioned vents and/or different resin injection points. These predictive approaches require greater knowledge of the properties of the reinforcements, particularly their permeability which, depending upon the nature of the reinforcement, may be different in the longitudinal and transverse directions. Modeling of the isothermal flow Q in volume/Sec of resin of constant viscosity μ through textile reinforcements with isotropic permeability K is based on DArcy's equation:

$$Q = \frac{-KA}{\mu} \frac{(P_b - P_a)}{L}$$

where K is the permeability, μ the resin viscosity, $(P_b-P_a)/L$ is the pressure P drop per unit length L, and A is the area of the cross section.

   For random mat nonwoven reinforcements, permeability is isotropic in-plane while, for other textile structures, the permeability will be different in different directions, depending upon the nature of the textile structure (number and size of tows, warp and weft densities, etc). This differential permeability will result in complex flow patterns in the tool, making flow prediction even more important, although the use of DArcy's equation then becomes an oversimplification.

3.6.3   VARI molding

The development of the matched-die molding process is to vacuum assist the resin into the tool. Dry reinforcements are placed in an open tool. The layup is sealed by a flexible vacuum bag, and vacuum is applied. The resin is forced under pressure into the tool, thus wetting out the fiber. Curing takes place from room temperature up to 180°C. This approach is known as VARI (vacuum assisted resin infusion) [16]. Using vacuum assistance initially to evacuate the cavity and then to draw the degassed resin into the reinforcement can produce high-performance composites.

Investigations into different combinations of gating and pressure/vacuum injection have shown that peripheral gating and vacuum injection provide the most effective route to achieve this aim [6]. In this arrangement, the flow surrounds the reinforcement, and then the flow front converges toward the vacuum exit point. The position of this is not critical since initial vacuum removal of all the air from the sealed tool permits the inflow of resin throughout the reinforcement. The progression of the fill of a rectangular plaque with the exit point deliberately off-set has been described by Abraham and McIlhagger (1995) [17]. Venting is much less critical. The liquid molding route with vacuum assistance can be used to produce structural composites with high fiber volume fraction and low void content using either ply layup or more complex 3D reinforcements. The process is less costly if near-net-shape textile reinforcements are employed.

3.6.4   RTM

The further development of the use of a vacuum to improve processing is RTM (resin transfer molding). The process is shown in Fig. 3.5. A key reason for using the RTM route as a manufacturing route is to reduce costs. The simple definition of RTM is "the injection of liquid resin at low viscosity, under vacuum or low pressure, into prearranged reinforcement materials or preform, which are contained in a closed mold die" [15]. Potter (1999) [18] provides a history of the RTM process over the last 60
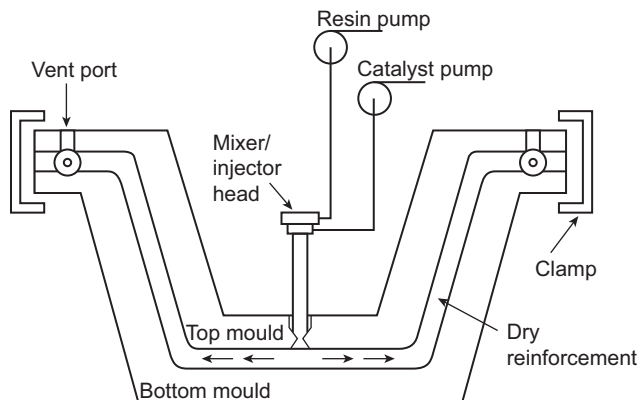
Figure 3.5 Resin transfer molding (RTM).

years and identifies the developments that have taken place over this period. The process is described in detail by Ref. [19].

In the RTM process, the fabric is placed inside the cavity between two matched molds with their inner surfaces having the shape of the final component. Fabric plies are stacked to the required orientation and sequence inside the mold, which is then sealed and clamped. Liquid resin is injected into the mold, flowing through the open spaces of the fabric until the mold is completely filled. When heated and pressure or vacuum is applied, the resin flows to completely fill the interstices in the reinforcement and the spaces between the filaments. After injection, the mold is heated to cure the matrix. Once cured, the mold can be opened and the component removed for finishing. This is a much more rapid method which overcomes the time-consuming process of deaerating the resin system to ensure void-free composite manufacture. It can be used for mass production of components, including complex 3D reinforcements.

The need for low capital cost tooling and process flexibility was first appreciated in the automotive industry. The RTM method was extensively developed by the automotive industry in the 1980s. In the 2000s, through the development of high-strength resin systems and more advanced pumping systems, RTM has advanced to new levels. These recent developments have promoted this technology as a practical manufacturing option for high-strength composite designs in the aerospace industry. Brinkman et al. (1995) [20], for example, concluded that "the inherent cost savings and reduced equipment dependency of RTM therefore make it an excellent composite fabrication candidate for general aviation hardware manufacturers."

Aerospace Technologies of Australia (ASTA) Components first recognized the potential of the RTM process for the manufacture of aerospace structures to reduce the cost and undertook the development of the RTM process for aerospace applications. ASTA Components now manufactures various composite structures for Boeing and Airbus aircraft, such as rudders for Boeing 757 and 777, landing gear doors for Airbus A330/A340, F/A-18 flap shroud and landing gear doors. The last, for example, is 15% lighter compared to the conventional sandwich version and has incorporated features, such as molded counter sink holes and ribbed hard point attachments. Other aircraft components such as radomes, bullet fairings, and propeller blades have been produced by RTM [15].

One advantage of RTM is the wide range of process variants, which range from relatively simple vacuum impregnation processes, requiring little by way of capital equipment, to more complex hybrid RTM operations (discussed in Section 3.10). This makes it possible to design and manufacture a wide range of different component shapes.

Another important advantage of RTM, compared to prepreg, is that complex 3D structures can be produced with through-thickness reinforcement, which simply cannot be made using prepreg. Complex components can be manufactured in a single step, combining multiple, detailed components into one configuration. Bushings and inserts can be molded in. One method of creating 3D structures is by weaving on a conventional Jacquard loom. These 3D preforms can be placed directly in the RTM tooling.

Other advantages of RTM include component quality [19]:

- Mechanical properties are similar to those of prepreg.
- A good surface finish is produced on both sides of a component.
- It has low part variability and good dimensional tolerances.
- There is good control of fiber/resin ratio, typically 55%−70% by weight. This produces parts that are lightweight and high in strength.
- Preforms can be manufactured in batches with no special storage conditions required.

In addition, RTM has a number of cost and process advantages:

- Low capital investment costs. Because the method of heat transfer is integrated into the mold die, the need for an autoclave is eliminated. The initial capital investment costs of RTM are low when compared with the many other molding processes.
- Cost savings from using cheaper dry, bulk materials which do not need special handling requirements, such as freezer storage.
- Extended shelf life of raw materials (especially carbon fabrics).
- Reduced cycle times.
- Near-net molded components, resulting in reduced postmolding finishing processes and less material scrap.
- Minimal training costs. The basic injection operation of RTM is straightforward and easily learned. Hence, minimal training is required to bring operators online.
- Low worker exposure. In most cases, RTM materials can be used with minimal chemical exposure to workers and their environment. Many high-performance resin systems are stable and release low volatiles. Since RTM is processed within a closed system, workers are exposed to the resin only when loading the dispensing equipment.
- Abraham and McIlhagger (1996) [21] compared the RTM and autoclave processing routes and found that the main advantage of the autoclave route was that the higher consolidation pressure used led to higher values of fiber volume fraction which favorably influenced component mechanical properties. They also confirmed that the RTM method offers materials and labor cost savings compared with conventional autoclaving as well as operational, health, and safety benefits.

However, the RTM process is not free from disadvantages, which include the following:

- Unidirectional layups are difficult to use and may result in reduced structural performance or increased weight or both.
- There is high initial tooling expenditure.
- Large components require complex/innovative tooling.
- Resin injection process requires a tight control of process parameters.
- There is limited flexibility to modify the tools for any design changes of the component.
- There is a possible reduction in the mechanical properties of the structures due to binders or tackifiers in preforming fabrics.

As has been noted, the utilization of matched tooling in RTM increases mold costs. In addition, great care must be exercised to ensure that both sides of the tool are sufficiently stiff to resist plate deflection, thus introducing thickness variations in the component. Such variations will result in fiber volume fraction and performance variations throughout the composite structure. Stiffer tooling also has a large thermal

mass which will, in turn, necessitate longer cycle times to complete the cure of the component. One of the most serious problems in RTM is the presence of voids in the finished component [15]. In common with all fabrication processes, it is important to maintain voidage in the final laminate as low as possible. Since RTM (generally) involves no further consolidation, the impregnation process needs to be controlled with some care.

3.6.5 Variants of VARI and RTM processes

A number of variations of VARI and RTM processes have been developed to reduce processing times/costs or for particular applications [10,19]. These include:

- vacuum-assisted resin transfer molding (VARTM)
- resin film infusion (RFI)
- light RTM (LRTM)
- seemann's composite resin infusion molding process (SCRIMP)
- vacuum-induced preform relaxation (VIPR)
- fast remotely actuated channeling (FASTRAC)
- structural reaction injection molding (S-RIM)
- coinjection resin transfer molding (CIRTM)
- compression resin transfer molding (CRTM)
- resin infusion between double flexible tooling (RIDFT)

These processes are described briefly:

- VARTM: In this process (which is a variation of the VARI process), the preform is placed in an open rigid tool (Fig. 3.6). The layup is sealed in a flexible vacuum bag. As a vacuum is applied, the resin is drawn into the preform, which is compacted on the tool surface. The general advantages of vacuum processes, such as VARTM are discussed below.
- RFI: In this process, instead of injecting the film into the mold, sheets of resin are produced as thin films and placed on the bottom or top or both of the preform. Tool inserts are placed around the preform, and the assembly is placed in a vacuum bag. When the tool is heated and pressurized, the resin film or films melt, flow into the preform and are cured. Advantages include higher fiber volume fractions and less expensive molds.
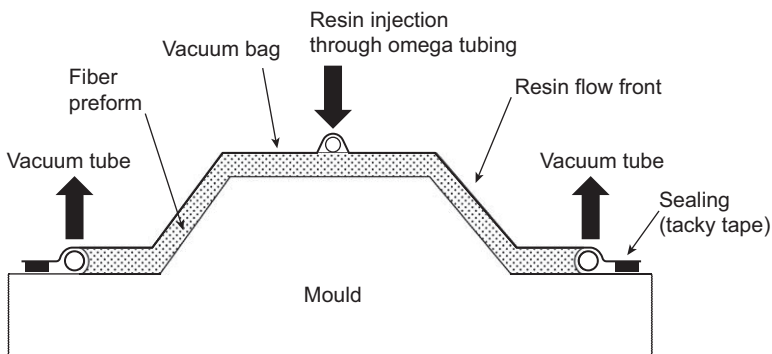
Figure 3.6 Vacuum-assisted resin transfer molding (VARTM).

- LRTM: In this process, the upper mold is made from a semi-transparent composite shell, sometimes supported by a steel structure. Advantages include lower tooling costs and shorter production cycles.
- SCRIMP: This process involves placing a peel-ply and distribution medium between the fiber preform and the vacuum bag (Fig. 3.7). Advantages include speeding up the filling process, i.e., resin infusion.
- VIPR: This process is the development of VARTM and SCRIMP (Fig. 3.8). It involves placing a vacuum chamber over the vacuum bag. Advantages include reduced filling time and the ability to direct the flow to regions which are difficult to fill.
- FASTRAC: This process involves the use of a primary and secondary vacuum bag together with a noncontacting tool to allow the resin to penetrate the preform more rapidly and completely (Fig. 3.9).
- S-RIM: This process uses separate resin components and catalysts, which are mixed just before injection into the mold.
- CIRTM: This process allows two or more resins to be simultaneously injected into the mold. Advantages include the ability to create multilayer and multiresin structures.
- CRTM: Also known as injection compression molding, the process involves a gap between the mold surface and the fiber perform (Fig. 3.10). Resin is injected into the gap, and the mold closed to compress the resin into the fiber preform. This reduces the injection pressure and filling time required in RTM.
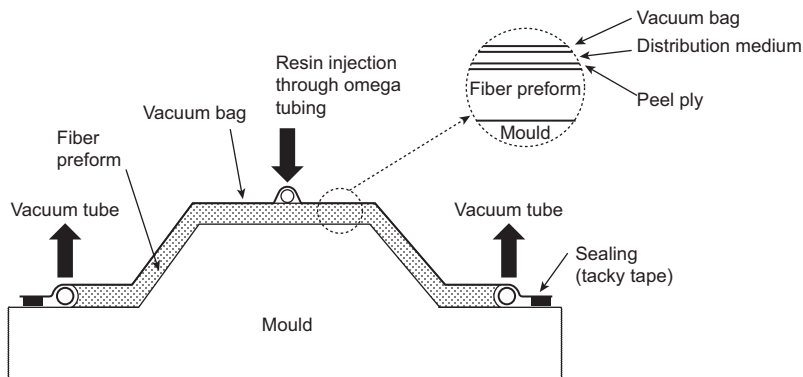
Figure 3.7 Seeman's composite resin infusion molding (SCRIM).
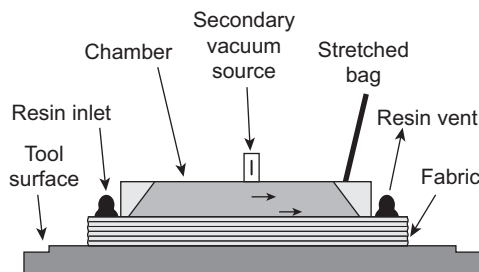
Figure 3.8 Vacuum induced preform relaxation (VIPR).
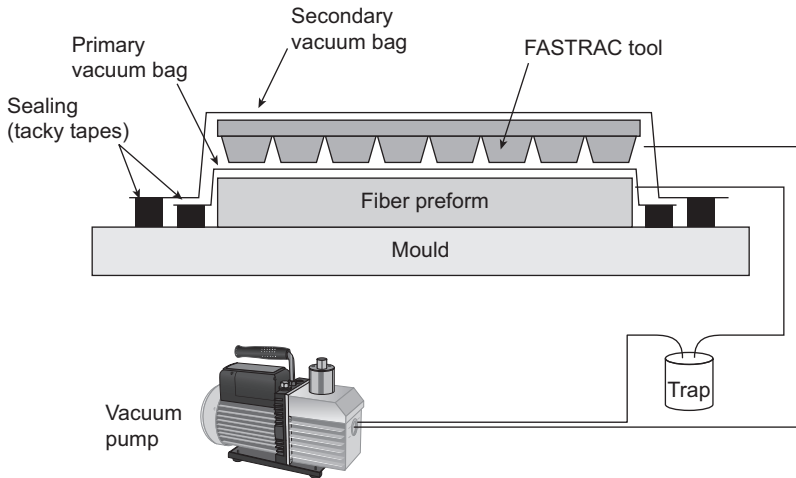
Figure 3.9 Fast remotely channeling (FASTRAC) process.
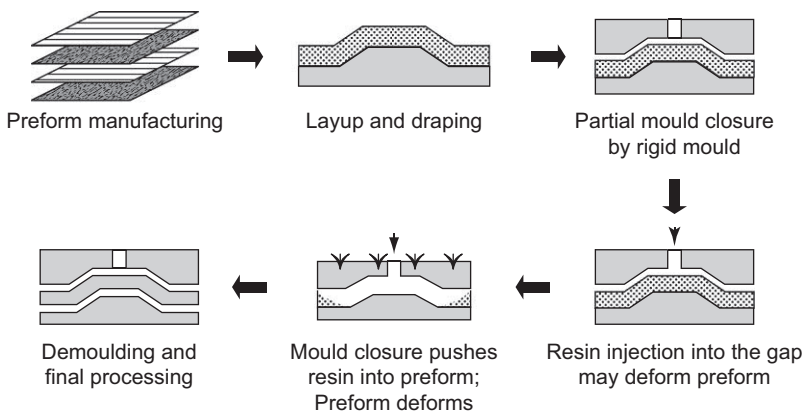
Figure 3.10 Compression resin transfer molding (CRTM).

- RIDFT: In this process, the resin is injected into a fiber preform placed between two flexible tools. The vacuum is used to shape the saturated preform into the shape of the component.

Two of the most popular of these processes are CRTM, which is reviewed by Bickerton and Kelly (2012) [22] and VARTM, which is discussed by Hsiao and Heider (2012) [23]. The use of vacuum to develop resin-infusion processes has been one of the most successful developments in reducing the problem of voidage, as well as speeding up the process. Vacuum-based processes have enjoyed enormous growth in popularity over the last few years, primarily because they enable the cost-effective fabrication of relatively large, complicated structures. Vacuum-based processes require less expensive consumables, such as bagging materials and

distribution media. Hayward and Harris (1990) [24] investigated the effects of vacuum assistance and reported a reduction in voidage during positive pressure RTM. Abraham and McIlhagger (1996) [21] considered several injection strategies and gating arrangements and found these to affect the degree of visual porosity and molding translucency. The qualitative comparison showed that vacuum impregnation and peripheral gating produced the best quality moldings. Clearly, the properties of vacuum impregnated moldings are also strongly dependent upon the fiber volume fraction that is achieved. Unlike conventional RTM, which is carried out in a fixed height cavity, the use of a flexible membrane to close the cavity means that the degree of fabric compaction (thus, the fiber volume fraction) depends upon the pressure difference across the membrane.

3.6.6 Pultrusion

Pultrusion is a cost-effective automated process for manufacturing continuous, constant cross-section composite profiles [25,26]. It is similar to the extrusion process used for manufacturing metallic aircraft stringers except the material is pulled through a die instead of being pushed through (Fig. 3.11). Raw materials are a liquid resin mixture (containing resin, fillers and specialized additives) and flexible textile reinforcing fibers.

The basic process is as follows:

- Continuous fibers (tows) are pulled off storage spools.
- They are drawn through a liquid resin bath.
- After removal of excess resin, the resin-impregnated tows are pulled through a heated die in the shape of the final component.
- As the material passes through the die, it assumes the shape of the component and is cured.
- The cured component leaves the die and is cut to the appropriate length.
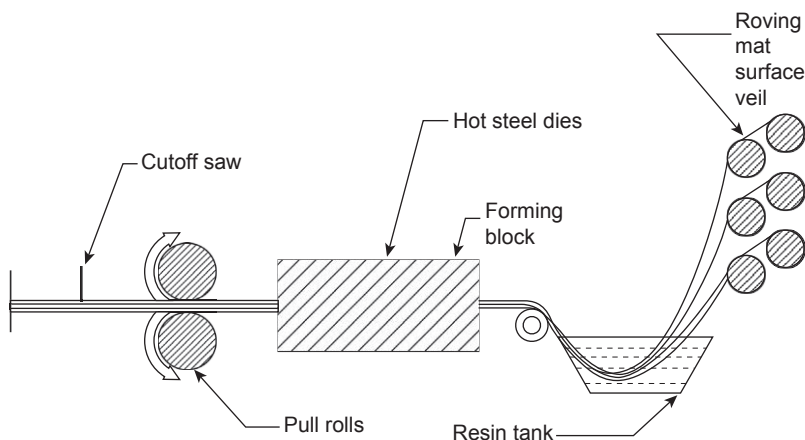
Figure 3.11 Pultrusion.

The fibers can be oriented to react best to the applied load. The woven cloth can be folded over or placed off-axis as it passes through one or more forming devices. As the reinforcements are saturated with the resin mixture "wet-out" in the resin bath and pulled through the die, the gelation, or hardening of the resin is initiated by the heat from the die, and a rigid, cured profile is formed that corresponds to the shape of the die. A variant of the process involves forcing the resin under pressure directly onto the reinforcements within an enclosed injection die before they pass into the heated pultrusion die.

Often overlooked by manufacturers of aerospace parts, pultrusion is clearly a viable candidate for certain applications, where the very low cost and the automated process can deliver high-performance constant cross-section parts. It has been demonstrated, for example, that pultruded parts could be suitable for low-cost unmanned aerial vehicles (UAV), e.g., hollow wing sections [27]. The 555-passenger Airbus A380 uses pultruded profiles for the stiffeners and stringers of the huge vertical tail. Pultruded components have also been used for high-strength floor beams in aircraft [28].

3.7 Process monitoring

The manufacturing of composites has traditionally been as much of an art as a science. This is because information directly related to internal process variables, such as the degree of cure of the epoxy resin has not been available. Typically external process parameters, such as mold temperature and resin supply pressure were known, but no information was available regarding the actual state of the curing epoxy. The curing process has been identified as the most critical and costly stage in the manufacturing of composite structures. Mijović et al. (1993) [29] have argued that a significant aspect of composite processing still in need of fundamental research relates to the development and implementation of a special class of in situ sensors capable of relaying fundamental information about the mechanism and rate of chemical reactions during cure.

Joshi et al. (1999) [30] illustrate the problem of effective control through the example of the curing of thermosetting resins as an exothermic reaction. The temperature profiles in the curing part depend not only on the heat supplied to the tool but also on the heat generated by the curing resin. The total mass fraction of resin in the mold and the resin system used to determine the generated heat, with the exothermic reaction associated with a low thermal conductivity of the resin potentially lead to excessively high localized temperatures in the part. This can result in nonuniform cure and an increase in the residual thermal stresses leading to degradation of the matrix. They conclude that "it is therefore necessary to study the curing of a component along with a chosen tooling assembly to obtain an optimum cure cycle."

Recent developments in sensor technologies for in situ monitoring have made it possible to obtain some insight into the state of the curing resin. Parameters are calculated from sensor measurements and analytical models developed in terms of the epoxy cure behavior [31]. It is clear that it would be more beneficial if the composite part could be continually monitored during the curing process. Online cure

monitoring [32] holds great appeal for materials and process engineers, with advantages, such as:

- The online sensor data eliminate the need for off-line collection and the analysis of control samples.
- Online sensing allows continuous verification of the progress of reactions against a known processing model, and hence, provides the basis for a closed-loop "smart" process control system.
- Variations can be identified and resolved, e.g., from batch to batch or between process cycles.

The aerospace industry is continually developing higher temperature resins but does not have the sensors that can operate at these high temperatures. This industry desires a better understanding of what is happening to the whole part and not just a section. Embedded sensors have been utilized for through the thickness readings, but serious concerns about performance properties are expressed due to the intrusive nature of these sensors. A major factor is the need to tailor the sensors to meet processing requirements.

3.8   Conclusions

Prepreg production processes for aircraft can achieve the best properties but at a relatively high cost. Alternative lower cost processes, such as VARTM have been developed, but while they have superior performance in some areas, such as toughness, through-thickness properties, and impact resistance, they have not, however, achieved the performance levels of which the prepreg route components are capable. While smaller scale, lightly stressed components on the aircraft could be made by a variety of the lower cost techniques, the major aircraft structural elements in existing and projected aircraft of main wings, fuselage and empennage are exclusively manufactured using prepreg as the starter material and high capital cost robotic layup and autoclave techniques to process it. Unless raw material and process costs can be reduced, the benefits of composites will be realized only on a limited range of aircraft types.

References

[1] A. Taylor, RTM material developments for improved processability and performance, SAMPE J. 36 (4) (July/August 2000) 17−24.
[2] J.R. Lowe, M.J. Owen, C.D. Rudd, Void formation resin transfer moulding, in: Proceedings of the 4th International Conference on Automated Composites, ICAC95, Nottingham, Institute of Materials, pp. 227−234.
[3] B.J. Hill, R. McIlhagger, Resin impregnation and prediction of fabric properties, in: A. Miravete (Ed.), 3−D Textile Reinforcements in Composite Materials, Woodhead Publishing Limited: Cambridge (UK).

 [4] C. Harries, J. Starnes, M. Stuart, Design and manufacturing of aerospace composite
     structures: state-of-the-art assessment, J. Aircr. 39 (2002) 545−560.
 [5] B.J. Hill, R. McIlhagger, C.M. Harper, W. Wenger, Woven integrated multilayered
     structures for engineering preforms, Compos. Manuf. 5 (1) (1994) 25−30.
 [6] B. Gommers, I. Verpoest, Tensile behaviour of knitted fabric reinforced composites, in:
     Proceedings of the 10th International Conference on Composite Materials (ICCM10), vol.
     IV Whistler: Canada, pp. 309−316.
 [7] W. Li, M. Hammad, A. El-Shiek, Structural analysis of 3D braided preforms for com-
     posites. Part 1 the 4 step process, J. Text. Inst. 81 (4) (1990) 491−514.
 [8] P. Hubert, G. Fernlund, A. Poursartip, Autoclave processing for composites, in: S. Advani
     K.T. Hsiao (Eds.), Manufacturing Techniques for Polymer Matrix Composites (PMCs),
     Woodhead Publishing Limited: Cambridge (UK).
 [9] J. Mack, R. Schledjewski, The filament winding process in thermoplastics, in: S. Advani,
     K.T. Hsiao (Eds.), Manufacturing Techniques for Polymer Matrix Composites (PMCs),
     Woodhead Publishing Limited: Cambridge (UK).
[10] J. Schlimbach, A. Ogale, Out-of-autoclave curing processes for polymer matrix compos-
     ites, in: S. Advani, K.T. Hsiao (Eds.), Manufacturing Techniques for Polymer Matrix
     Composites (PMCs). Woodhead Publishing Limited: Cambridge (UK).
[11] F.N. Scott, R. Heath, Resin Transfer Moulding for Civil Aircraft Manufacture, SAMPE
     European Chapter.
[12] K.N. Kendall, C.D. Rudd, M.J. Owen, V. Middleton, Characterisation of the resin transfer
     moulding process, Compos. Manuf. 3 (2) (1992) 235−249.
[13] T. Creasy, Sheet forming in polymer matrix composites, in: S. Advani, K.T. Hsiao (Eds.),
     Manufacturing Techniques for Polymer Matrix Composites (PMCs), Woodhead Publish-
     ing Limited: Cambridge (UK).
[14] P. Ferland, D. Guittard, F. Trochu, Concurrent methods for permeability measurement in
     resin transfer moulding. Modelling and simulation of resin transfer moulding, Polym.
     Compos. 17 (1) (1996) 149−153.
[15] B. Lui, S. Bickerton, G. Advani, Modelling and simulation of resin transfer moulding-gate
     control, venting and dry spot prediction, Compos. Part A 27a (2) (1996) 135−141.
[16] F.L, Matthews, R.D, Rawlings, Composite Materials: Engineering and Science, Woodhead
     Publishing Limited: Cambridge (UK).
[17] D. Abraham, R. McIlhagger, Vacuum assisted resin transfer moulding for high perfor-
     mance carbon fibre composites, in: Proceedings of the 4th International Conference on
     Automated Composites, ICAC95, Nottingham, pp. 299−306.
[18] K.D. Potter, The early history of the resin transfer moulding process for aerospace ap-
     plications, Compos. Part A Appl. Sci. Manuf. 30 (5) (May 1999) 619−621.
[19] E. Sozer, P. Simacek, S. Advani, Resin transfer molding (RTM) in polymer matrix
     composites, in: S. Advani, K.T. Hsiao (Eds) Manufacturing Techniques for Polymer
     Matrix Composites (PMCs), Woodhead Publishing Limited: Cambridge (UK).
[20] B.G. Brinkman, C. Cadenas, R. Phillips, A. Arnold, K. Bowman, Evaluation of tackifier
     agents for resin transfer molding, in: 40th International SAMPE Symposium, May 8−11,
     1995, pp. 1523−1530.
[21] D. Abraham, R. McIlhagger, A review of liquid injection techniques for the manufacture of
     aerospace composite structures, Polym. Polym. Compos. 4 (6) (1996) 437−443.
[22] S. Bickerton, P. Kelly, Compression resin transfer moulding (CRTM) in polymer matrix
     composites, in: S. Advani, K.T. Hsiao (Eds.), Manufacturing Techniques for Polymer
     Matrix Composites (PMCs), Woodhead Publishing Limited: Cambridge (UK).

[23] K.T. Hsiao, D. Heider, Vacuum assisted resin transfer molding (VARTM) in polymer matrix composites, in: S. Advani, K.T. Hsiao (Eds.), Manufacturing Techniques for Polymer Matrix Composites (PMCs), Woodhead Publishing Limited: Cambridge (UK).

[24] J.S. Hayward, B. Harris, Effect of process variables on the quality of RTM mouldings, SAMPE J. 26 (3) (May/June 1990) 39−46.

[25] S. Joshi, The pultrusion process in polymer matrix composites, in: S. Advani, K.T. Hsiao (Eds.), Manufacturing Techniques for Polymer Matrix Composites (PMCs), Woodhead Publishing Limited: Cambridge (UK).

[26] T. Starr, Pultrusion for Engineers, Woodhead Publishing Limited: Cambridge (UK).

[27] S. Black, Pultruding costs out of aerospace parts, High Perform. Compos. (March 2009).

[28] A. Mouritz, Introduction to Aerospace Materials, Woodhead Publishing Limited: Cambridge (UK).

[29] J. Mijović, M. Kenny, A. Maffezzoli, A. Trivisano, F. Bellucci, F. Nicolais, The principles of dielectric measurements for in situ monitoring of composite processing, Compos. Sci. Technol. 49 (3) (1993) 277−290.

[30] S.C. Joshi, X.L. Liu, Y.C. Lam, A numerical approach to the modeling of polymer curing in fibre-reinforced composites, Compos. Sci. Technol. 59 (1999) 1003−1013.

[31] I.K. Partridge, G.M. Maistros, Dielectric cure monitoring for process control. Compr. Compos. Mater 5 413−426.

[32] A. McIlhagger, D. Brown, B. Hill, The development of a dielectric system for the on-line cure monitoring of the resin transfer moulding process, Compos. Part A Appl. Sci. Manuf. 31 (12) (December 2000) 1373−1381.

Manufacturing defects in composites and their effects on performance

Ramesh Talreja
Department of Aerospace Engineering, Department of Materials Science and Engineering, Texas A&M University, College Station, TX, United States

4.1   Introduction

Lightweight structures in aerospace applications are mostly made of polymer matrix composites. The size and shape of the structure, and its usage, e.g., as primary or secondary structure in aircraft, dictate the choice of the manufacturing process. While the early aerospace applications in defense were mainly performance driven, the cost of manufacturing today is of increasing concern. Therefore, the traditional design approach of 'defect-free' structures must be revisited. In fact, no structure is without defects; a low threshold of measurable defects is essentially taken to define the defect-free condition. If the cost of manufacturing is to be managed, i.e., reduced in a controlled way, then the effects of defects must be assessed. This requires a mechanics-based knowledge base on the characterization of defects and quantification of their effects on specific performance characteristics. Reducing the cost of manufacturing further requires that the manufacturing process be quantified with parameters that can be varied to minimize cost.

This chapter reviews a few common manufacturing defect types for illustration. A cost-effective manufacturing strategy is then described, followed by a discussion of the role of manufacturing defects in affecting the performance of the composite part that has been produced. Three examples are given to illustrate how the manufacturing defects can be characterized, and their effect on the relevant performance characteristics can be evaluated. This mechanics-based analysis methodology can be utilized in other cases and can become what may be called a *defect engineering framework* for cost-effective manufacturing of composite structures.

4.2   Defects in composite materials

Composite materials can be manufactured by a variety of methods. Polymer matrix composites (PMCs), for instance, can be processed by compression molding, liquid molding, injection molding, resin infusion, etc. and can be joined by adhesive bonding, mechanical fastening, fusion bonding, etc. For a good overview of the processing and manufacturing of PMCs, see Månson et al. [1]. Each processing and manufacturing

route will induce defects. A systematic way to categorize defects is to group them into a matrix, fiber, and interface defects. Thus, matrix defects can be incomplete curing and voids; fiber defects can be misalignments, waviness and broken fibers and irregularities of fiber distribution in the matrix; and interfaces can carry defects as unbonded regions on fiber surfaces and between layers (delamination). These defects will be discussed next.

Voids are the most common type of *matrix defects* and are found in virtually all PMC parts, whether manufactured by autoclave, liquid compression molding, or resin transfer molding (RTM). The void formation can be, to some extent, controlled by manufacturing process parameters such as vacuum pressure, resin viscosity, cure temperature, and consolidation pressure. In one study [2], for example, void morphology and spatial distribution in a circular disc of glass/epoxy were studied in an RTM process in which the resin was injected under pressure into a mold containing fiber bundle preform. The voids were found to vary in size, shape, and spatial location. These characteristics were found to depend on the resin flow kinematics in the mold. Fig. 4.1 taken from that work shows representative images of voids.

Fig. 4.2 shows voids in a unidirectional carbon/epoxy composite made by the autoclave technique [3]. The two sections, cut parallel and perpendicular to the fiber

Matrix   Fiber   Void
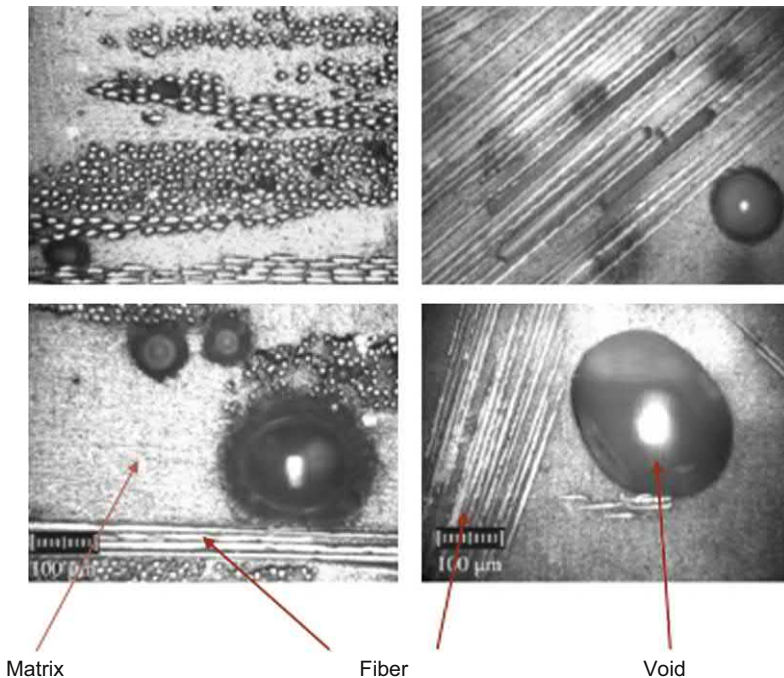
Figure 4.1 Representative microscopic images of voids resulting in an E-glass/epoxy composite from an RTM process.
From Y.K. Hamidi, L. Aktas, M. Cengiz Altan, Formation of microscopic voids in resin transfer moulded composites, J. Eng. Mater. Technol. Trans. ASME (126) (2004) 420−426.

(a)   (b)

A section parallel to the fiber direction   A section perpendicular to the fiber direction
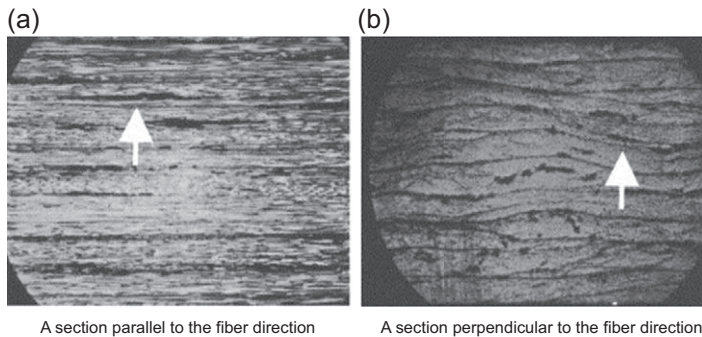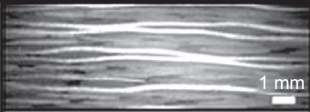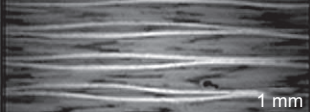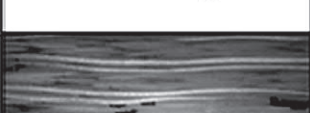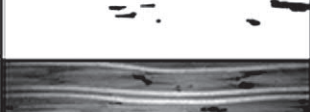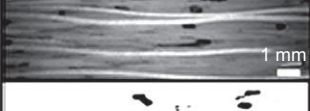
Figure 4.2 Voids in a unidirectional carbon/epoxy composite made by the autoclave process. From K.J. Bowles, S. Frimpong, Void effects on the interlaminar shear strength of unidirectional graphite-fibre-reinforced composites, J. Compos. Mater. (26) (1992) 487−1509.

direction, display the voids that appear as elongated cylindrical-shaped entities lying mostly between the plies. These voids are typical of the autoclave process where they form as a consequence of trapped air in ply interfaces during the composite layup or by evaporation of water and volatiles inside the prepregs during curing. The vacuum and applied pressure during the curing process cause vapor and volatiles to diffuse into existing air pockets. Reducing voids in the autoclave process generally increases the cost of manufacturing and can become prohibitive for large structures. For this reason, the autoclave process is not used for structures such as wind turbine blades.

One of the ways considered to reduce the cost of manufacturing by the autoclave technique is to eliminate external pressure and use vacuum pressure only. One study looked at the effect of moisture formation resulting from dissolved moisture in the prepregs [4]. Significant voids resulted in this case when the pressure was not applied. Fig. 4.3 shows an example of the voids formed. On the other hand, eliminating vacuum in the autoclave technique also produces voids. An example of this is shown in Fig. 4.4 [5].

Fiber defects, as noted above, are fiber misalignment and waviness, and broken fibers. In composites, where fibers are assumed to be straight, parallel and oriented in intended directions, deviations due to misalignment and waviness can reduce initial properties, particularly compression strength and stiffness and lead to reductions in aircraft design limit load and design ultimate load capability in service. Fig. 4.5 illustrates the level of misalignment found in a typical as-delivered unidirectional prepreg [6]. A study of the effect of fiber waviness in unidirectional composites under axial compression [7] showed that the stiffness and strength reduced severely due to this type of defect. Stress analysis and experimental observations indicated that the interlaminar shear stress developed due to fiber waviness was responsible for delamination and subsequent failure. Fig. 4.6 taken from that work illustrates occurrence of delamination (separation of individual layers that were intentionally made with wavy fibers) and final failure in axial compression. In an experimental and analytical study of the failure of unidirectional composites loaded in combined compression and shear, Vogler et al. [8] also found a significant effect of

VBO laminates		Volid content (Vol %)	Thickness (mm)
As received	1 mm	<<.1	5.08 ± 0.01
70% RH	1 mm	0.08 ± 0.08	5.13 ± 0.01
80% RH	1 mm	1.00 ± 0.29	5.31 ± 0.05
90% RH	1 mm	2.62 ± 0.48	5.48 ± 0.02

Figure 4.3 Voids resulting in a composite laminate from dissolved moisture in the prepregs in an autoclaving process where vacuum bagging was used, but no external pressure was applied. From L.K. Grunenfelder, S.R. Nutt, Void formation in composite prepregs — effect of dissolved moisture, Compos. Sci. Technol. (70) (2010) 2304—2309.

fiber waviness on strength. The mechanism of failure, in this case, was microbuckling-induced kink band formation. A severe example of fiber defect is shown in Fig. 4.7 where tangled fibers are seen in a carbon/epoxy prepreg [9]. It is difficult to predict quantitatively the effects of such defects on design stresses except by testing to measure the degradation. If the manufacturing process control
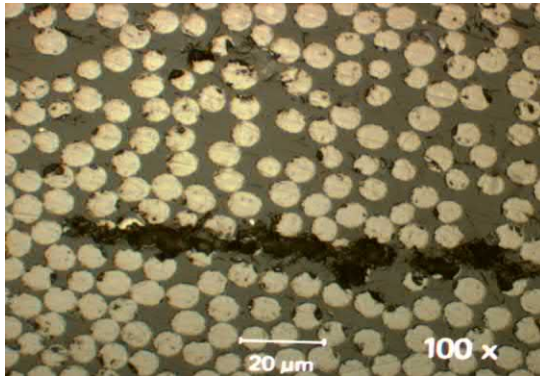
Figure 4.4 An example of voids formed between prepregs when the vacuum is eliminated from the standard autoclave technique for manufacturing composite laminates.
From Y. Huang, J. Varna, R. Talreja, The effect of manufacturing quality on transverse cracking in cross ply laminates, in: D. Bhattacharrya, R.J.T. Lin, T.S. Srivatsan (Eds), Proceedings of Processing and Fabrication of Advanced Materials XIX, PFAM-19, New Zealand, Auckland, pp. 552−559.

Figure 4.5 Level of fiber misalignment in a typical as-delivered unidirectional prepreg.
From K. Potter, B. Khan, M. Wisnom, T. Bell, J. Stevens, Variability, fibre waviness and misalignment in the determination of the properties of composite materials and structures, Compos. Appl. Sci. Manuf. (39) (2008) 1343−1354.

makes the occurrence of such defects possible, then designers must ensure that the ultimate design strength can be achieved in the presence of such defects.

Interface defects are largely caused by inadequate conditions for generating bonds at interfaces between fibers and matrix and between layers of composites during
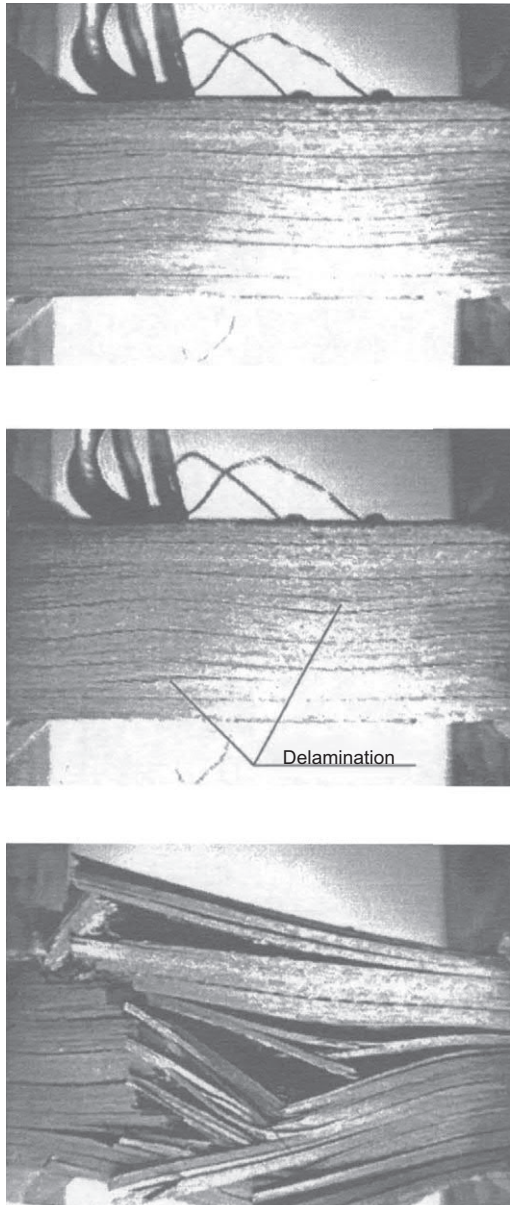
Figure 4.6 Illustration of the fiber waviness effect on failure under axial compression of a unidirectional carbon/epoxy composite. Top: graded waviness of fibers before loading; Middle: occurrence of delamination under compression; Bottom: final failure.
From H.M. Hsiao, I.M. Daniel, Effect of fibre waviness on stiffness and strength reduction of unidirectional composites under compressive loading, Compos. Sci. Technol. (56) (1996) 581−593.

Figure 4.7 A region of entangled fibers in a carbon/epoxy prepreg.
From R.D. Adams, P. Cawley, A review of defect types and non-destructive testing techniques for composites and bonded joints, NDT Int. 21 (1988) 202−222.

manufacturing. If the resin is infused into a fiber preform, it may not wet the entire fiber surface, resulting in unbonded regions of the fiber surface. If preimpregnated layers of composites (prepregs) are stacked in a manufacturing process, then air can be trapped between the layers. The pockets of air in the interlaminar region can flatten during the consolidation of layers resulting in planes of no contact, and therefore, no bond, between layers. These defects are often called *delaminations*, although this term more appropriately describes separation (debonding) of bonded layers at interfaces.

4.3 Modeling with defects

A given manufacturing process results in a composite part that is specific to that process and can be described by its **material state**. The conventional representation of the material state is by homogenization that produces direction-dependent overall properties (e.g., anisotropic elastic constants). Explicit knowledge of the size and distribution of fibers is not retained in this representation. This is adequate and efficient if the purpose is to determine initial deformation characteristics, such as deflections and rotations of the produced composite part. When service loading is applied, the composite part suffers damage that in many cases initiates from the manufacturing-induced defects. Stress analysis using homogenized material state is then inadequate in analyzing the formation and progression of failure. A new approach to the representation of the material state is needed (discussed next).

Instead of the conventional homogenization, the material state description should retain the knowledge of the heterogeneities in a statistical sense to the degree that their effects on the local stress states generated at the microlevel are properly represented. Additionally, the defects described in Section 5.2 should be incorporated in the material state description along with the other heterogeneities (e.g., fibers and differently oriented layers) in a manner that the perturbations in the local stress field are explicitly

attributable to the defects. This can allow evaluation of the defects from the viewpoint of failure initiation and progression.

4.4 Implications for cost-effective manufacturing

Fig. 4.8 depicts the overall methodology of a cost-effective design. Manufacturing plays a central role in this methodology since a substantial part of the total cost of a structure lies in steps such as processing, machining, and assembly. On completion of these steps, the manufactured part is characterized by its geometry and the material state described in Section 4.3. This characterization may require various efforts such as polymer process modeling, microscopy, and nondestructive inspection. The quantified material state enters into the next group of items placed in the box labeled as properties/performance evaluation. Of particular note is the explicit separation of information concerning the material state ('microstructure') into the 'homogenized' and 'defects' parts. This is a departure from the traditional design approach where defects are not considered as a variable in the material state but only as a threshold for 'accept/reject' criteria. For instance, in some aerospace applications, a 2% void content is used as a threshold to accept or reject a manufactured part. In the strategy proposed here, the defects are viewed as a result of a well-defined manufacturing process, and it is assumed that they can be varied by controlled variation of the manufacturing parameters. The role of defects in determining the properties and performance (i.e., degradation of properties in service) is a key to assessing the effectiveness, and thereby the cost-effectiveness, of the manufacturing process. However, to ensure that each aircraft can achieve design ultimate and design limit strength values, the manufacturing process must be well in statistical process control producing a level of defects that will guarantee
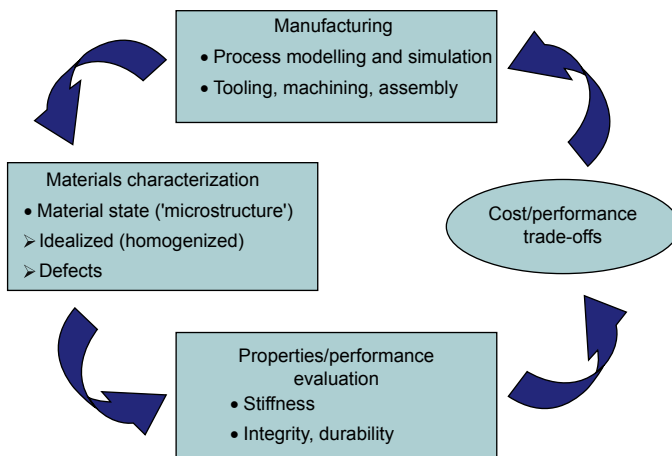
Figure 4.8 Cost-effective design process for composite structures.

that design ultimate and limit strengths are consistently achieved. The outcome of the properties/performance evaluation enters in the last piece of the iterative process for cost reduction where cost/performance trade-offs are done. Conducting these trade-offs requires balancing the manufacturing cost with the properties and the level of the achieved performance.

4.5   Mechanics-based analysis of defects

4.5.1   *Effect of voids on effective elastic properties*

Traditionally the analysis of the effects of voids on the effective elastic properties is conducted by using inclusion theories where the inclusions are assigned zero properties [10]. Typically, the voids are distributed as embedded entities in the homogenized composite and the reduction in the elastic properties caused by their presence is estimated. Simulating the geometry of actual voids in a unidirectional composite, Huang and Talreja [11] showed that such estimates were generally not accurate. Basically, instead of cutting out a volume in a homogenized composite and replacing it with a void, as is commonly done, this work displaced the fibers locally in the composite to accommodate the void. This approach produced the effect of voids more accurately. A parametric study of the effects of voids in that work also showed that the void shape generally has significant effects on the matrix-dominated elastic properties, such as the modulus transverse to fibers (both in-plane and out-of-plane) and the shear modulus. An example of the through-thickness elastic modulus reduction [12] and its comparison with model prediction [11] is shown in Fig. 4.9.
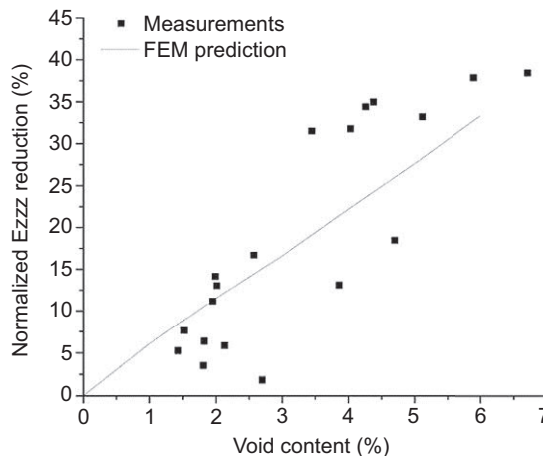
Figure 4.9 Percentage reduction in the through-thickness elastic modulus (Ezz) induced by voids. Modeling prediction [11] compared with test data from Ref. [12].

4.5.2   Effect of voids on delamination growth

If delamination exists in a composite part either as an initial interlaminar defect or induced by service loading, such as lateral impact, then it is common to assess the effect on the failure of the part by fracture mechanics methods. These methods typically analyze the propensity of the delamination, viewed as a crack, to grow unstably to failure. The driving force for crack growth, or the strain energy release rate (SERR) of the delamination crack front, is compared with the fracture toughness, i.e., the resistance to crack growth, of the material in the interface in which the delamination lies. Thus if G is the SERR of a given delamination crack, then $G = G_c$ is the criterion for incipient unstable crack growth (fracture). G_c, the interface fracture toughness is evaluated by certain standard experimental techniques. Generally, the loading conditions on the structural part could result in a mixed-mode delamination growth, in which case the SERR and the fracture toughness will have different values corresponding to each mode. For most PMCs, the mode I (opening mode) fracture toughness is the lowest of the three possible crack growth modes. To evaluate the failure potential of existing delamination, therefore, one commonly uses the opening mode fracture criterion $G_I = G_{Ic}$.

Depending on the manufacturing process, voids can be produced in the interfacial region between the composite layers, or in the layers themselves, or both. For delamination growth, the overall void content is of little consequence. What matters is the presence of voids in the delaminated (cracked) interface. Ricotta et al. [13] demonstrated this in a study of delamination growth by analyzing the so-called *double cantilever beam* (DCB) specimen containing voids ahead of the crack tip (Fig. 4.10).

Fig. 4.11 shows the computed effect of the presence of circular voids in the interface as a function of the distance D of the nearest void from the crack tip. As seen, the effect of the nearest void has the most influence on the SERR, while adding more voids has an increasingly lesser effect. In Fig. 4.12, the effect of multiple voids as a function of the distance of the additional voids from the nearest void to the crack tip is illustrated. The results shown for a fixed distance of the first void from the crack tip indicate that the additional voids enhance the SERR, but as they move away from the first void,
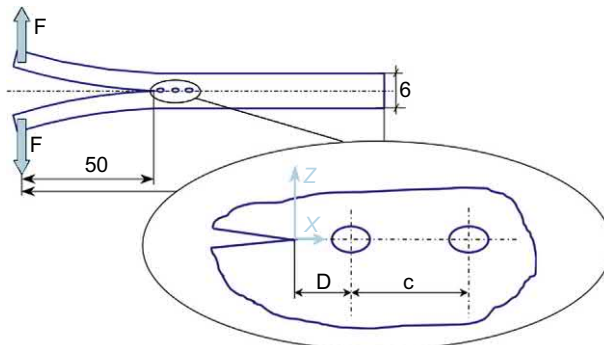
Figure 4.10 A schematic of a DCB specimen with voids ahead of the crack tip.
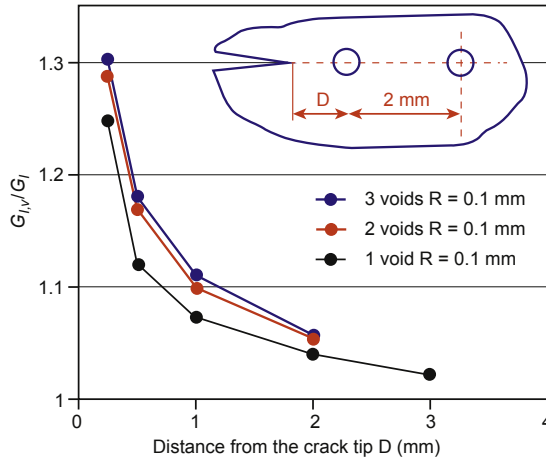
Figure 4.11 Variation of SERR ($G_{I,v}$) with the distance D from the crack tip of the nearest circular void of 0.1 mm radius. Effect of up to three voids of mutual distance 2.0 mm is also shown.
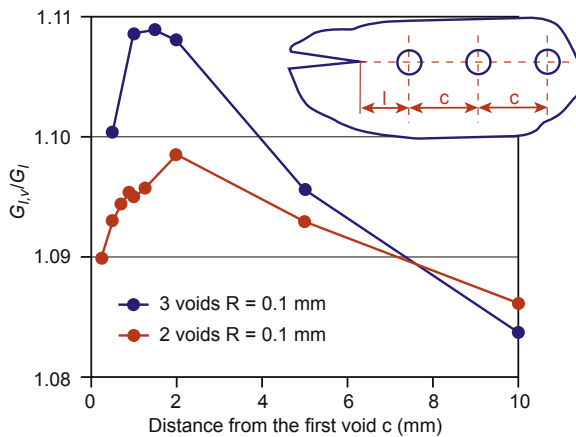
Figure 4.12 Effect on the SERR ($G_{I,v}$) of the mutual spacing c of the voids with the distance of the nearest void being fixed.

that enhancement decreases. More results of the parametric study of the effects of the voids on SERR are given in Ref. [13].

4.5.3   Effect of defects on progressive intralaminar cracking

The first failure mechanism in multidirectional composite laminae is matrix cracking along fibers within plies. This mechanism described as transverse cracking, or intralaminar cracking is often the basis of design, i.e., the applied load level is kept below the threshold for initiation of these cracks. These cracks do not cause the failure of the

laminate but lead to other mechanisms that eventually cause failure. The transverse cracking process in laminates progresses in stages commonly described as noninteractive and interactive. In the noninteractive stage, the cracks initiate from defects in the plies, the largest defect (with most favorable orientation and size) initiating the first crack. As the load is increased, more cracks initiate from smaller defects at random locations. The noninteractive stage shows an increasing rate of crack formation with loading until the cracks begin interacting, i.e., the perturbation in the local stress field induced by one crack is affected by the presence of another crack. The subsequent cracks form between the preexisting cracks at locations where the stress exceeds the material strength (with or without defects). Thus, in this interactive stage, the role of manufacturing defects diminishes as the stress field becomes increasingly affected by the cracks of reducing mutual spacing. In Fig. 4.13 the transverse cracks as seen from the edge of a specimen are shown. Fig. 4.13(a) shows an array of parallel cracks in the 90 degrees plies of a cross-ply laminate, while in Fig. 4.13(b) one sees the same type of parallel cracks within transverse bundles of an 8-harness woven fabric composite.

For investigating the effect of manufacturing defects on the transverse cracking process, a study was recently conducted to test how different irregular manufacturing processes influence the progressive transverse cracking in cross-ply laminates [5]. Composite laminates with a thermosetting polymer matrix are manufactured in the aerospace industry commonly by the autoclaving process. In this process, a prespecified temperature and pressure variation is followed along with the application of vacuum to draw out air from the composite part. The process cost is elevated due
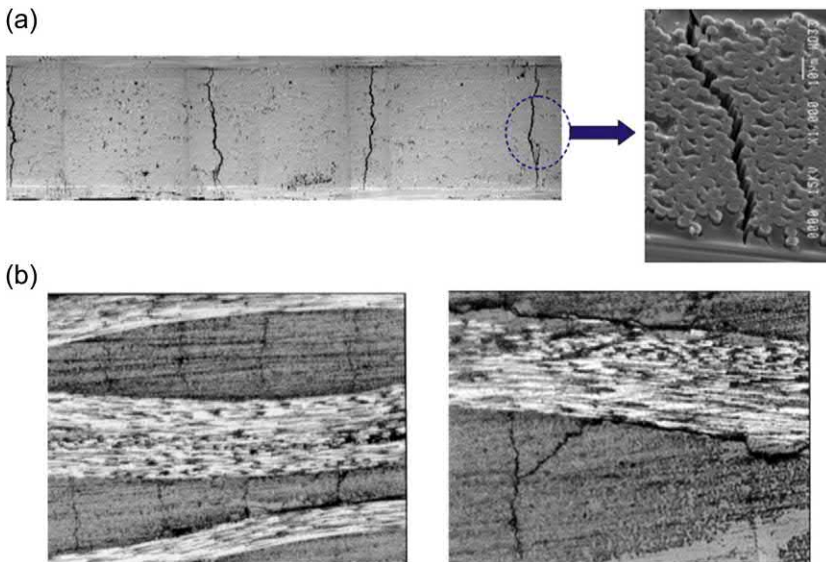
Figure 4.13 (a) Transverse cracks in 90 degrees plies of a cross-ply laminate; (b) cracks within transverse bundles of an 8-harness woven fabric composite.

to the requirement of placing the mold in a closed space in which the part is subjected to controlled temperature, pressure, and vacuum. The cost could be reduced if the application of vacuum or pressure could be omitted without adversely affecting the part quality. It is expected that omitting vacuum or pressure will result in voids and possibly other defects such as inadequate wetting of the fibers by resin prior to curing.

Three plates of a $(0/90)_s$ laminate were fabricated in an autoclave using prepregs of HexPly M10/38%/UD300/CHS. Plate 1 was produced by the standard process with the exception that the air was intentionally left entrapped between prepregs by not applying consolidation pressure during the lamination (stacking of prepregs) process. For plate 2, the standard process was followed, except no vacuum was applied during the curing process. For plate 3, the standard process was strictly followed. The coupons cut from the laminated plates were subjected to monotonic axial tension.

The study [5] focused on the noninteractive stage of the transverse cracking process and accounted for the random defects by a statistical description of strength. Specifically, Weibull distribution was used to represent the random strength, and the two parameters of the probability distribution function were estimated from the test data. The result of the analysis is presented in Fig. 4.14, where the crack density (average number of cracks per unit specimen length) is plotted against the applied axial stress. Three different curves illustrate the differences due to the defects induced by the three manufacturing processes. At the same applied stress, plate 1 made with air-entrapped layups consistently has highest crack density, followed
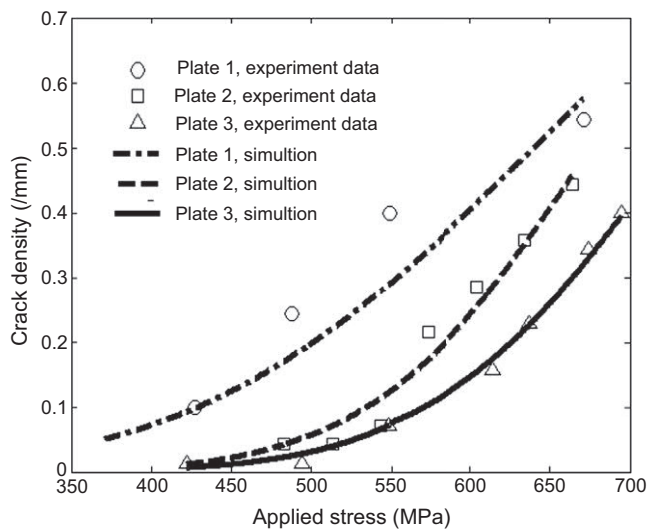
Figure 4.14 Variation of the density of transverse cracks in cross-ply laminates produced by three manufacturing processes. The manufacturing process for the lowest curve (Plate 3) is the standard autoclave process (specified by the manufacturer), while in Plate 2 vacuum was not applied, and Plate 1 was not consolidated by external pressure, trapping air between layers.

by plate 2 cured without applying vacuum, while plate 3 made by the standard process has the lowest crack density. Also, the onset stress for the initiation of the transverse crack is much lower for plate 1.

4.6   Summary

This chapter has briefly reviewed some of the common forms of defect found in composites structures and their effects on some mechanical properties. A good engineering design should not only meet the performance specifications required of the composite structure, but it should do so at the lowest cost feasible for that structure. The traditional design focuses on meeting performance requirements and uses quality control measures to accept or reject the manufactured part. This is not going to be feasible for acceptance of large wings and fuselage structures — the cost will be prohibitive, and instead, the service performance of composite aircraft structures must rely on manufacture with consistent levels of defect severity produced by a process that is strictly within manufacturing process control. This can be accomplished if the effects of defects on mechanical performance are evaluated. Three examples given here illustrate that average measures of defects, e.g., void volume fraction, are inadequate for this purpose. Instead, the size, shape, and location of defects need to be accounted for to do a proper assessment of performance. The manufacturing process must be understood sufficiently well to allow process modification to control the level of defects produced.

References

[1] J.A.E. Månson, M.D. Wakeman, N. Bernet, Composite processing and manufacturing — an overview, in: R. Talreja, J.A.E. Månson, A. Kelly, C. Zweben (Eds), Comprehensive Composite Materials, vol. 2, Elsevier, 577−607.
[2] Y.K. Hamidi, L. Aktas, M. Cengiz Altan, Formation of microscopic voids in resin transfer moulded composites, J. Eng. Mater. Technol. Trans. ASME 126 (2004) 420−426.
[3] K.J. Bowles, S. Frimpong, Void effects on the interlaminar shear strength of unidirectional graphite-fibre-reinforced composites, J. Compos. Mater. 26 (1992) 1487−1509.
[4] L.K. Grunenfelder, S.R. Nutt, Void formation in composite prepregs — effect of dissolved moisture, Compos. Sci. Technol. 70 (2010) 2304−2309.
[5] Y. Huang, J. Varna, R. Talreja, The effect of manufacturing quality on transverse cracking in cross ply laminates, in: D. Bhattacharrya, R.J.T. Lin, T.S. Srivatsan (Eds). Proceedings of Processing and Fabrication of Advanced Materials XIX, PFAM-19, New Zealand, Auckland, pp. 552−559.
[6] K. Potter, B. Khan, M. Wisnom, T. Bell, J. Stevens, Variability, fibre waviness and misalignment in the determination of the properties of composite materials and structures, Compos. Appl. Sci. Manuf. 39 (2008) 1343−1354.

[7] H.M. Hsiao, I.M. Daniel, Effect of fibre waviness on stiffness and strength reduction of unidirectional composites under compressive loading, Compos. Sci. Technol. 56 (1996) 581−593.

[8] T.J. Vogler, S.-Y. Hsu, S. Kyriakides, Composite failure under combined compression and shear, Int. J. Solids Struct. 37 (2000) 1765−1791.

[9] R.D. Adams, P. Cawley, A review of defect types and non-destructive testing techniques for composites and bonded joints, NDT Int. 21 (1988) 208−222.

[10] J.G. Berryman, Role of porosity in estimates of composite elastic constants, Trans. ASME J. Energy Resour. Tech. 116 (1994) 87−96.

[11] H. Huang, R. Talreja, Effect of void geometry on elastic properties of unidirectional fibre reinforced composites, Compos. Sci. Technol. 65 (2005) 1964−1981.

[12] Z. Guerdal, A.P. Tomasino, S.B. Biggers, Effects of processing induced defects on laminate response: interlaminar tensile strength, SAMPE J. 27 (1991) 3−49.

[13] M. Ricotta, M. Quaresimin, R. Talreja, Mode 1 strain energy release rate in composite laminates in the presence of voids, Compos. Sci. Technol. 68 (2008) 2616−2623.

Part Two

Composite performance in aerospace structural design

Buckling and compressive strength of laminates with optimized fiber-steering and layer-stacking for aerospace applications

5

Richard Butler, Andrew T. Rhead, Mark W.D. Nielsen
Materials and Structures Research Centre, Department of Mechanical Engineering, University of Bath, Bath, United Kingdom

5.1   Introduction

A high proportion of aerospace structures consist of relatively thin panels that are stiffened by stringers and frames or ribs. These panels are prone to buckle under compressive load, and in order to prevent delamination due to interlaminar shear stress, buckling is usually prevented up to ultimate levels of load.

Compared with aluminum, composites have the capacity to deliver significant weight saving, largely because of improved specific stiffness. For example, Fig. 5.1 compares the panel buckling efficiency of aluminum with optimized carbon fiber-reinforced polymer (CFRP) laminates, illustrating theoretical improvements of 30%−40%. However, impact damage—which may not be visible on the surface of laminated composites—can occur from such objects as runway debris, hailstones, and dropped tools. Current regulations specify that during design, this barely visible impact damage (BVID) must be assumed within most components. This means that weight savings may reduce for more highly loaded panels.

In this chapter, we will describe the different kinds of elastic coupling effects that can arise in anisotropic composite laminates before developing expressions that are used to determine laminate buckling loads. We then illustrate the optimization (or elastic tailoring) of laminates using straight fibers, followed by a presentation of the potential advantage of a new manufacturing technique that incorporates in-plane steering of fibers to achieve curved, elastically tailored, tows. Finally, we use an analytical model to examine the damage tolerance of a variety of straight fiber stacking sequences, highlighting improvements in compressive strength that can be made when plies are either stacked in sequences that maximize damage tolerance or use nonstandard ply orientations.
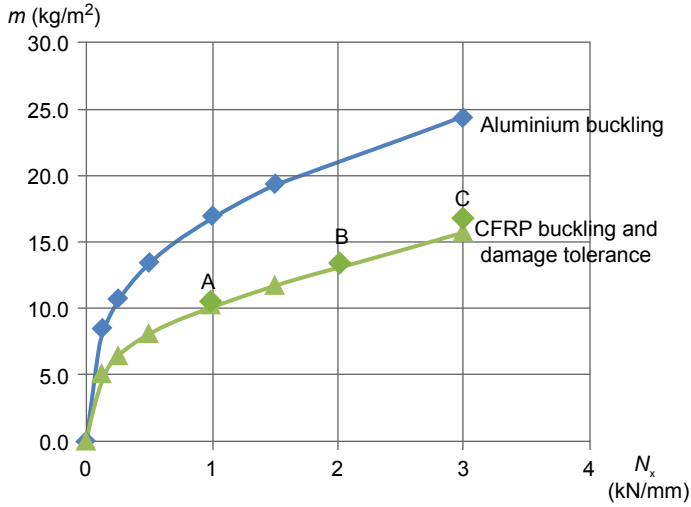
Figure 5.1 Panel efficiency of optimized CFRP compared with aluminum for a 250 mm wide, 750 mm long, simply supported panel. N_x is compressive load capacity per unit width and m is mass per unit planform area. The limiting strain, accounting for damage tolerance, is 3,600 μm/m. Panels (a−c) are described in Table 5.3.

5.2 Elastic properties of laminates

An individual straight fiber layer (lamina) has orthotropic elastic properties, i.e., properties that can be defined along orthogonal axes, one of which is aligned with the fiber direction. Most current practices involve the use of layers with 0, +45, −45, and 90 degrees fiber directions. The freedom to adjust the orientation of fibers within individual layers of composite laminates sets them apart from metal components. Ordering these layers into different lay-up sequences to produce a laminate can dramatically change the overall mechanical behavior, influencing the in-service structural performance. Here we consider the different forms of elastic coupling that can arise between in-plane forces (and deformations) and out-of-plane (bending and twisting) moments (and curvatures).

The elastic coupling of a thin-walled laminate can be described by the well-known Classical Laminate Theory and **ABD** matrix notation:

$$
\begin{bmatrix} N_x \\ N_y \\ N_{xy} \\ M_x \\ M_y \\ M_{xy} \end{bmatrix} = \begin{bmatrix} A_{11} & A_{12} & A_{16} & B_{11} & B_{12} & B_{16} \\ & A_{22} & A_{26} & B_{12} & B_{22} & B_{26} \\ & & A_{66} & B_{16} & B_{26} & B_{66} \\ & & & D_{11} & D_{12} & D_{16} \\ & sym. & & & D_{22} & D_{26} \\ & & & & & D_{66} \end{bmatrix} \begin{Bmatrix} \varepsilon x \\ \varepsilon_y \\ \gamma_{xy} \\ -\partial^2 w/\partial x^2 \\ -\partial^2 w/\partial y^2 \\ -2\partial^2 w/\partial x \partial y \end{Bmatrix} \tag{5.1}
$$
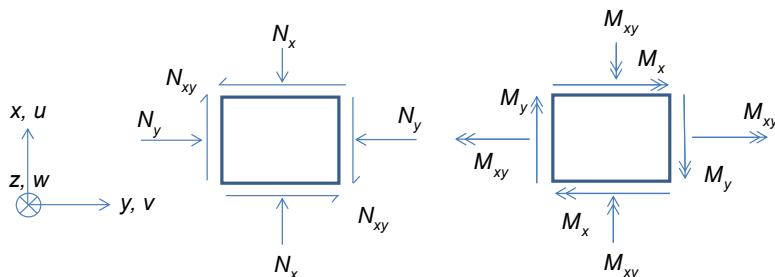
Figure 5.2 Sign convention for displacements, forces, and moments.

where the sign convention for membrane forces and bending and twisting moments is shown in Fig. 5.2 and ε_x, ε_y and γ_{xy} are the direct strains in x and y and the shear strain, respectively.

Eq. (5.1) is always symmetric and the terms on the leading diagonal are always present, as are A_{12} and D_{12}, due to Poisson's ratio effects. Other terms within the **ABD** matrices are referred to as the elastic coupling terms, summarized in Table 5.1. Although elastic coupling can be advantageous (in aeroelastic applications, for example) it is not generally desirable in compressively loaded structures since it can give rise to greater vulnerability to buckling or structural instability.

In order to minimize coupling, the aerospace industry usually selects laminates that are both balanced (i.e., they have as many +45 degrees layers as they have −45 degrees layers) and symmetric about their midplane. Balancing eliminates extension-shear coupling, whereas symmetry eliminates all **B**-matrix terms, preventing coupling between in-plane and out-of-plane deformation/load. Grouping of more than four layers of the same orientation is not normally permitted to avoid large interlaminar stresses, and at least 8% of each of the 0, +45, −45 and 90 degrees fiber orientations is usually required.

The laminates covered by the above rules are hygro-thermally curvature stable, meaning their curvatures do not vary with changes in temperature and moisture. This is an important characteristic for manufacture so that laminates are warp-free

Table 5.1 Description of different forms of elastic coupling arising in Eq. (5.1).

Term(s)	Elastic coupling	Example laminate
A_{16}, A_{26}	Extension-shear	$[+45/0/+45/0]_S$
B_{11}, B_{22}	Extension-bending	$[0/0/90/90]_T$
B_{16}, B_{26}	Extension-twist and shear-bending	$[+45/+45/−45−45]_T$
B_{66}	Shear-twist	$[+45/+45/0/0]_T$
D_{16}, D_{26}	Bend-twist	$[+45/+45/−45/−45]_S$
All	Fully coupled	$[+45/+45/0/0]_T$
None	Fully uncoupled	$[+45/−45/−45/+45]_A$

Note that subscript S denotes symmetry about laminate centerline, A denotes antisymmetry, whereas, T signifies that the total laminate is defined by the sequence.
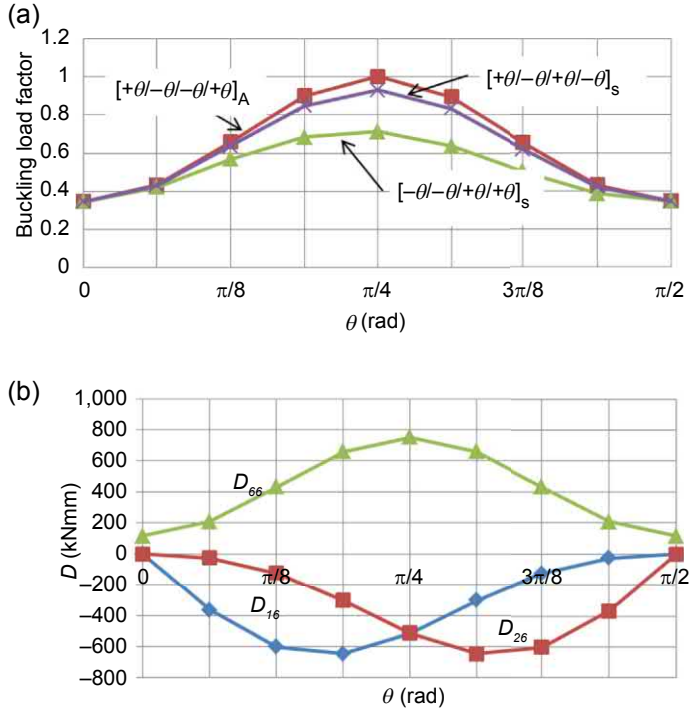
Figure 5.3 Influence of bend-twist coupling on buckling load of laminate. (a) Variation of buckling load factor with fiber angle θ for laminates with varying bend-twist coupling. (b) Selected D-matrix terms for $[-\theta/-\theta/+\theta/+\theta]_S$ laminate.

following high-temperature curing of the resin. The rules eliminate all terms in Table 5.1, apart from bend-twist coupling D_{16} and D_{26}. The influence of these terms on the buckling of a simply supported laminate is illustrated in Fig. 5.3(a). In the most severe case, for the $[-\theta/-\theta/+\theta/+\theta]_S$ laminate, where $-\theta$ plies are all outermost (maximizing bend-twist coupling) the knockdown to buckling capacity reaches over 25% when $\theta = 45$ degrees. Fig. 5.3(b) shows that this occurs when the sum of D_{16} and D_{16} is maximum. With this in mind, it may be important to design laminates that are fully uncoupled. The research was conducted by Refs. [1,2] into the removal of all elastic coupling for laminates up to 21 plies thick; Table 5.2 shows that most of these laminates are nonsymmetric.

5.3   Buckling analysis

The out-of-plane equilibrium of a plate subject to in-plane forces N_x, N_y, and N_{xy} which give rise to buckling instability is defined by

$$\frac{\partial^2 M_x}{\partial x^2} + 2\frac{\partial^2 M_{xy}}{\partial x \partial y} + \frac{\partial^2 M_y}{\partial y^2} - N_x\frac{\partial^2 w}{\partial x^2} - 2N_{xy}\frac{\partial^2 w}{\partial x \partial y} - N_y\frac{\partial^2 w}{\partial y^2} = 0 \qquad (5.2)$$

Table 5.2 Number of symmetric, antisymmetric and nonsymmetric fully uncoupled laminates with 7 through 21 plies [2].

	Number of plies, n														
	7	8	9	10	11	12	13	14	15	16	17	18	19	20	21
Symmetric	—	—	—	—	—	4	—	12	4	33	50	110	120	352	344
Antisymmetric	2	1	6	6	24	21	84	76	288	268	1002	934	3512	3290	12,392
Nonsymmetric	—	—	—	—	—	—	—	—	68	59	780	559	4934	4284	35,521

Assuming that there is no coupling between in-plane and out-of-plane deformation (i.e., the **B** matrix of Eq. 5.1 is null), substitution for bending moments defined in Eq. (5.1) gives

$$D_{11}\frac{\partial^4 w}{\partial x^4} + 4D_{23}\frac{\partial^4 w}{\partial x \partial y^3} + 2(D_{12} + 2D_{33})\frac{\partial^4 w}{\partial x^2 \partial y^2} + 4D_{13}\frac{\partial^4 w}{\partial x^3 \partial y} + D_{22}\frac{\partial^4 w}{\partial y^4} +$$

$$\left(N_x\frac{\partial^2 w}{\partial x^2} + 2N_{xy}\frac{\partial^2 w}{\partial x \partial y} + N_y\frac{\partial^2 w}{\partial y^2}\right) = 0$$

$$(5.3)$$

Most aerospace structures, such as wing and fuselage panels, are long compared with cross-sectional dimensions. Hence, strip models, making prismatic assumptions in the solution of Eq. (5.3), are computationally efficient in many applications. Approaches that find buckling loads by minimizing potential energy for assumed mode shapes have been developed [3].

In this chapter, we use a method that solves Eq. (5.3) by using exact, periodic formulations [4]. Here, the eigenvalue analysis is executed on a transcendental stiffness matrix derived from the solution of the governing differential equations of the constituent strips, which are assumed to undergo a deformation that varies sinusoidally to infinity in the longitudinal direction. The out-of-plane buckling displacement w is assumed to be of the form

$$w = \text{Re}\left[F(y)e^{\left(\frac{i\pi x}{\lambda}\right)}\right]$$

$$(5.4)$$

For $F(y)$ written as

$$F(y) = f_1(y) + i \cdot f_2(y)$$

$$(5.5)$$

the buckling displacement w is

$$w = f_1(y)\cos\frac{\pi x}{\lambda} - f_2(y)\sin\frac{\pi x}{\lambda}$$

$$(5.6)$$

The displacement shape assumed in Eq. (5.6) provides an infinite periodic solution to the governing differential Eq. (5.3) if the panel and the loading are uniform in the x direction. The functions $f_1(y)$ and $f_2(y)$ allow various boundary conditions to be applied on the longitudinal edges of panels, including free, simple, clamped, and elastic supports. The displacement amplitudes u, v, w, and rotation about the x axis, ψ are calculated repeatedly for a user-specified set of half-wavelengths λ, where u and v are shown in Fig. 5.2. The half-wavelengths are defined by the length of the plate L divided by the number of half-wavelengths assumed along the length of the plate. The resulting transcendental eigenvalue problem requires an iterative solution that is performed using

the Wittrick-Williams algorithm [5] to ensure that no eigenvalues are missed. The lowest buckling load found for a range of values of λ is taken as the critical buckling for the panel.

For orthotropic panels ($D_{13} = D_{23} = 0$) with no shear loading, f_2 is zero, and the buckling displacements in Eq. (5.6) satisfy the simply supported boundary conditions at the end of a finite length panel, see Fig. 5.4. For laminates with bend-twist coupling and/or shear loading, f_2 is not zero. In this case, the functions f_1 and f_2 are such that the nodal lines of the buckling mode are skewed and not straight and do not coincide with simply supported, finite length panels, see Fig. 5.5. This so-called VIPASA-type analysis, therefore, provides conservative results compared with the case forcing the node lines to be straight along the transverse supports. The conservativeness is overcome by coupling the VIPASA stiffness matrices for different wavelength responses through a numerical method, producing VICON-type analysis [6], which gives a good approximation to panels of finite length with transverse supports. VIPASA is more efficient than VICON in terms of computational cost for optimization. In the wing box and fuselage structures, the skin panels are continuously supported by the adjacent panels and other structures so that VIPASA has a practical application, where shear loads and bend-twist coupling are negligible.

5.4 Buckling optimization of straight fiber laminates

The minimum-weight design of the straight fiber laminates for buckling constraints involves the selection of an optimized stacking sequence with a discrete number of layers. This is a complex problem that has been solved using a range of approaches, including genetic algorithms [7], continuous methods [8] and [9], bi-level methods
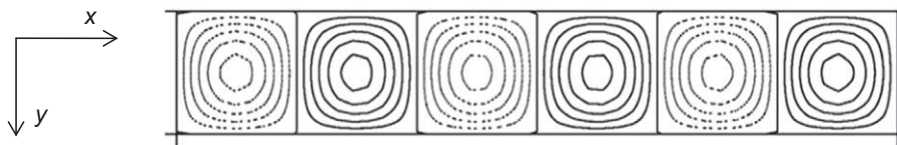
Figure 5.4 Buckling mode shape when $f_2 = 0$ in Eq. (5.6), for orthotropic laminate with no shear load, simply supported along longitudinal edges.
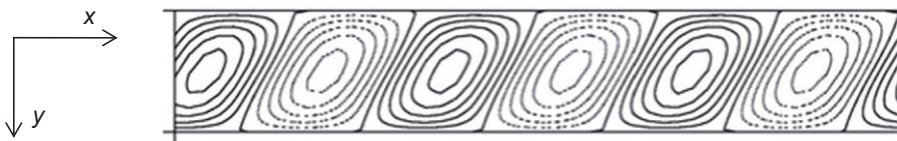
Figure 5.5 Mode produced by Eq. (5.6) for bend-twist coupled laminate.

[10], and [11], and lamination parameters [12]. In Table 5.3 we illustrate the continuously optimized laminate designs obtained using VICONOPT [9] for designs A, B, and C indicated in Fig. 5.1. We also show two sets of discrete (rounded) solutions for 0.125 mm thick plies, where the second set satisfies the ply grouping rules described above, requiring the addition of more 90 degrees plies. Note that the percentage of 0 degree plies increases with an increasing load to satisfy the damage tolerant strain limit of 3600 μm/m, and that the outermost positioning of ±45 degrees plies is required to maintain the buckling resistance.

5.5   Variable angle fibers using continuous tow shearing

Variable Angle Tow (VAT) composites have been applied to elastic tailoring of laminated structures to improve structural efficiency of composites panels in the aerospace sector. Compared with conventional straight fibers, VAT composites allow the designer to vary the fiber angle as a function of position throughout the structures, resulting in variable stiffness and strength without adding extra plies [13−15].

In order to bring VAT panels from design to application scenarios, a variety of manufacturing techniques have been developed. Conventional Automated Fiber Placement (AFP) techniques use tow head turning to control the angle change [16], reduce the overlap, and cut-off, to improve the quality of the VAT panels.

Two methods can be used to lay tows in terms of a reference tow path when AFP is applied; parallel paths and shifted (similar) paths. The advantage of parallel paths is that no gaps or overlaps will occur between tows, resulting in a laminate with uniform thickness and (theoretically) without any defects. However, the disadvantage is that the steering radius of parallel tows may result in the violation of the maximum allowable tow curvature. A geometric singularity can also occur, as shown in Fig. 5.6(a). Shifted paths keep each tow path the same as the reference tow path, resulting in tow overlaps and/or tow gaps, as shown in Fig. 5.6(b). The tow overlap occurs when the two courses are moved closer to eliminate the gap. An overlap (or gap) produces local thickening (or thinning) which is accompanied by localized out-of-plane fiber waviness, as well as, locally resin-rich areas, which may decrease the structural strength. Tow cutting can be used to reduce tow gaps and keep the panel mass as low as the one obtained from the design stage but produces fiber discontinuity. For both parallel and shifted cases, fiber wrinkling is caused by localized buckling in the internal radius of the AFP tows subject to in-plane bending.

A collaborative project between the universities of Bristol and Bath has developed a Continuous Tow Shearing (CTS) technique [17] for fiber placement, which uses the deformable characteristic of dry tows in shear and can significantly reduce process-induced defects compared with the AFP techniques, which use in-plane bending deformation. In addition, the design flexibility is increased by reducing the minimum radius of curvature of each tow path. The CTS technique offers smooth thickness distribution rather than the discontinuous thickness caused by tow overlapping in AFP. CTS also reduces process-induced defects, such as fiber wrinkling, resin-rich areas, and fiber

Table 5.3 Ply percentages and total laminate thickness T for optimum CFRP buckling designs A, B and C shown in Fig. 5.1. The continuous designs were obtained assuming a (blocked) stacking sequence of $[45/-45/-45/45/0/90/90/0/-45/45/45/-45]_T$.

Optimum design	$N_x = 1.0$ kN/mm (A)				$N_x = 2.0$ kN/mm (B)				$N_x = 3.0$ kN/mm (C)			
	0°	**±45 degrees**	**90 degrees**	**T (mm)**	**0°**	**±45 degrees**	**90 degrees**	**T (mm)**	**0°**	**±45 degrees**	**90 degrees**	**T (mm)**
Continuous	20	74	6	6.486	42	54	4	8.266	61	39	0	9.618
Rounded	21	75	4	6.625	43	54	3	8.375	58	42	0	10.125
Rounded (rules)	20	73	7	6.875	41	51	8	8.875	54	39	7	10.875
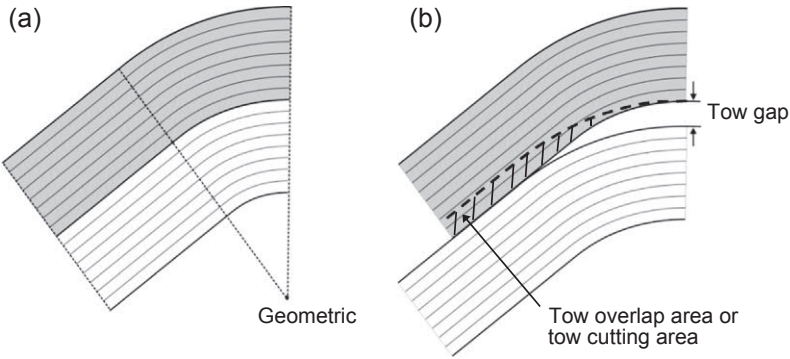
Figure 5.6 Illustration of two AFP tow path methods: (a) parallel paths and (b) shifted paths.

discontinuity compared with the conventional AFP techniques, which use in-plane bending to steer tows. In contrast, the CTS technique uses dry tows combined with an *in-situ* impregnation to provide shearing capability and prevent the fiber splitting. In its dry state, the tow can be continuously sheared along the fiber path with in-plane shearing deformation.

The CTS technique can achieve a minimum radius of tow path of 30 mm. When the tow is sheared, the thickness is changed according to the shear angle. Assuming that the fiber volume of the tow element is not changed, the thickness change of the tow element before and after the shear deformation is shown in Fig. 5.7. The tow shearing
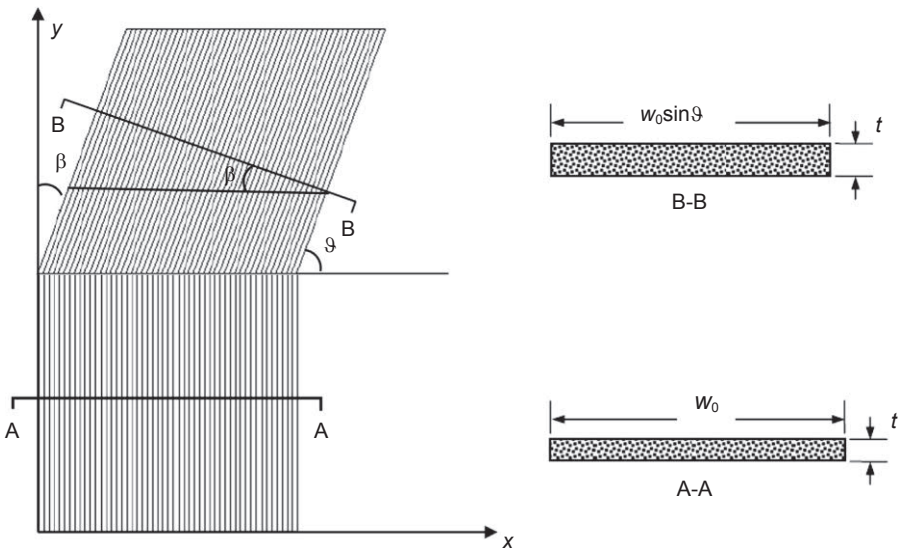
Figure 5.7 Thickness change of tow element due to shear deformation in the CTS method. The tow element with cross-section A-A shows tow thickness before shear, whereas B-B shows the thickness change after shear. Note that β is the tow shearing angle and θ is the tow angle defined in the VIPASA model.

angle is defined as β, and the angle θ is the tow (fiber) angle, relative to the x-axis. The relationship between the two angles is

$$\theta = 90° - \beta \tag{5.7}$$

The function of $f(t_0, \theta)$ is used to denote the change of the sheared tow thickness t according to the average tow thickness t_0 before shearing and the tow angle θ. Because

$$t_0 w_0 = tw \tag{5.8}$$

and

$$w = w_0 \sin \theta \tag{5.9}$$

the sheared tow thickness t is given by

$$t = \frac{t_0}{\sin \theta} \tag{5.10}$$

The formula is singular when $\theta = 0$. Therefore, θ will not be allowed to be equal to zero degrees for manufacturability reasons. In practice, the tow angle that the tow head of the prototype CTS machine can handle is 15 degrees $\leq \theta \leq$ 90 degrees.

Gürdal et al. studied two cases of tow paths, which linearly vary along the longitudinal x direction or the transverse y direction. They showed that due to redistribution of the longitudinal compressive load N_x, fiber angle variation in the y direction is more efficient than variation in the x direction in the case of initial buckling. In this chapter, therefore, we focus on variation in the direction transverse to load, in order to achieve the best structural efficiency while retaining the prismatic conditions. We apply an efficient optimization strategy for the design of VAT panels with minimum mass while satisfying the buckling load and CTS manufacturing constraints. We use a gradient-based method, which suits the continuity of tow paths. Local optima can be readily avoided by selecting different starting points covering all the design space. The optimization treats the fiber angles as design variables, and the VIPASA buckling analysis is selected since it suits a transverse variation of angle. As VIPASA is fast, requiring 0.1% of FEM computation time, its use in optimization is very efficient.

VAT panels are divided into a number of strips of equal width, and the fiber angle θ_i of each strip is free to vary while satisfying buckling constraints. Antisymmetry is imposed about the panel centerline, as shown in Fig. 5.8. The figure illustrates that the fiber path $\theta(y)$ is represented as the fiber angle θ_i in each strip. The number of strips for buckling analyses was checked to ensure mesh convergence while maintaining computational efficiency.

Fig. 5.9 compares the average thickness of optimum designs obtained using VICONOPT with straight fiber laminates (SF), and variable angle tows obtained using either CTS or AFP techniques, where the latter assumes shifted (similar)
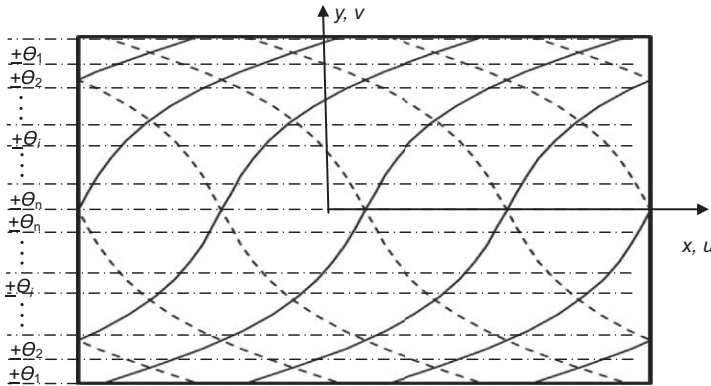
Figure 5.8 VIPASA definition of the VAT panel. θ_i is the fiber orientation angle in each strip for a VAT ply.
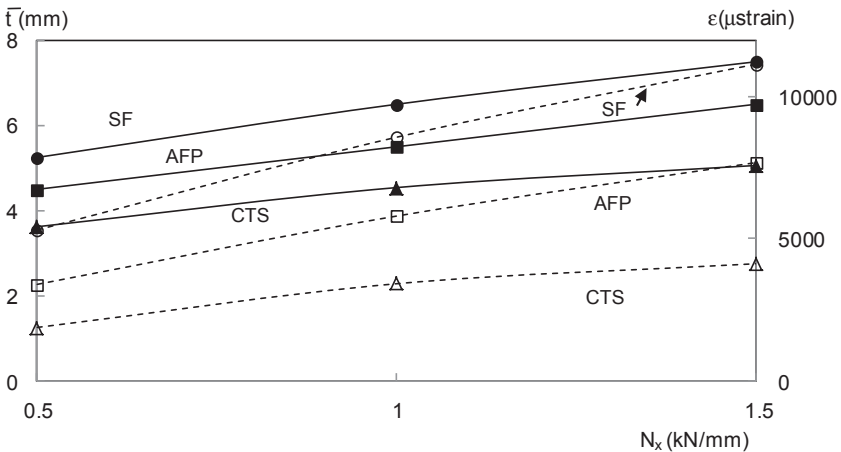
Figure 5.9 Comparison of the average thickness $\bar{t}$ (*solid lines*) and buckling strains (*dashed*) for Straight Fiber optimum designs and variable fiber angle designs obtained using Continuous Tow Shearing and Automated Fiber Placement. In all cases, the panels are 250 mm wide and 750 mm long with simple supports.

tow paths obtained by tow cutting, see Fig. 5.6(b). The results show that AFP produces weight savings of 10%−20%, whereas, in the case of CTS, the saving can be as much as 35%. The fiber path for one of the CTS designs, Fig. 5.10, shows that the axial load (applied as uniform end shortening) is redistributed from the unsupported panel center to the simply supported boundary. We can also see from Fig. 5.9 that the buckling strains for the CTS designs are considerably lower than the comparable AFP values. However, these CTS designs are likely to have low strength due to the absence of fibers in x and y directions, and the presence of very high, localized values of Poisson's ratio [18,19].
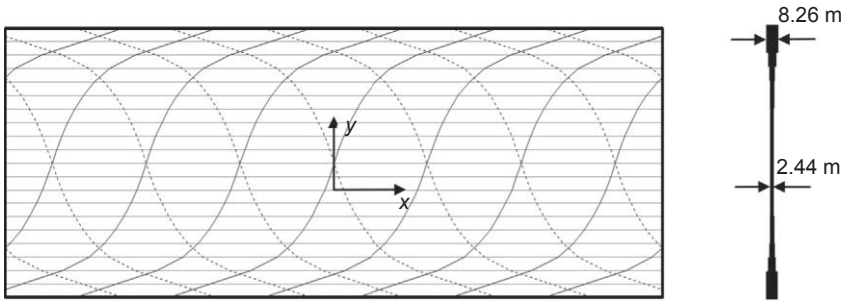
Figure 5.10 Optimum fiber path and cross-section of the CTS panel for $N_x = 1.0$ kN/mm in Fig. 5.9.

5.6 Compression after impact and damage tolerance

When laminated CFRP structures are impacted, below surface delaminations can occur, which can reduce static strength by 60%. Consequently, airworthiness regulations state that, provided the level of impact required to cause BVID is due to a realistically expected event (defined as having a probability of occurrence of 1 in 10^5 flying hours) it must be assumed that BVID is present and that the structure must tolerate this damage at ultimate levels of load without failing. At present, the propagation of BVID is suppressed in design by applying empirically derived limits for allowable stress and strain at ultimate levels of load. Various analytical techniques have been developed to predict the Compression After Impact (CAI) strength of laminates containing delamination. These include two-dimensional models [20] that calculate the total strain energy release rate for propagation of a thin, postbuckled elliptical plate with orthotropic properties and relate this to the energy required to create a fracture surface under Mode I (peeling) load conditions.

In this chapter, a computationally efficient, analytical CAI model [21] is applied to select laminate stacking sequences that offer improved damage tolerance when compared with a baseline laminate. This extends the previous CAI model [22]; and [23] to now include evaluation of the full 2D sublaminate Strain Energy Release Rate (SERR). The model uses a simple approximation of BVID morphology and calculates the threshold strain ε^{th} below which propagation of the delamination damage will not initiate under any general load. The underlying principle is to find the difference in energy in the postbuckled sublaminate, see Fig. 5.11, immediately before and after the growth of delamination and to compare this difference to the Mode I fracture energy required to create a new area of delamination. If sufficient energy is available, then a new area of delamination is created, and propagation of the delamination will occur. Growth is assumed to extend the delamination to a longer elliptical morphology. A thin-film assumption is made that has the effect of allowing no bending energy to be released from the lower unbuckled base laminate.

First, the general strain state is converted to its principal strain directions, and the buckling strain state ε^C of each sublaminate created by delamination is calculated using VICON-type analysis. Each delaminated sublaminate is modeled as a thin
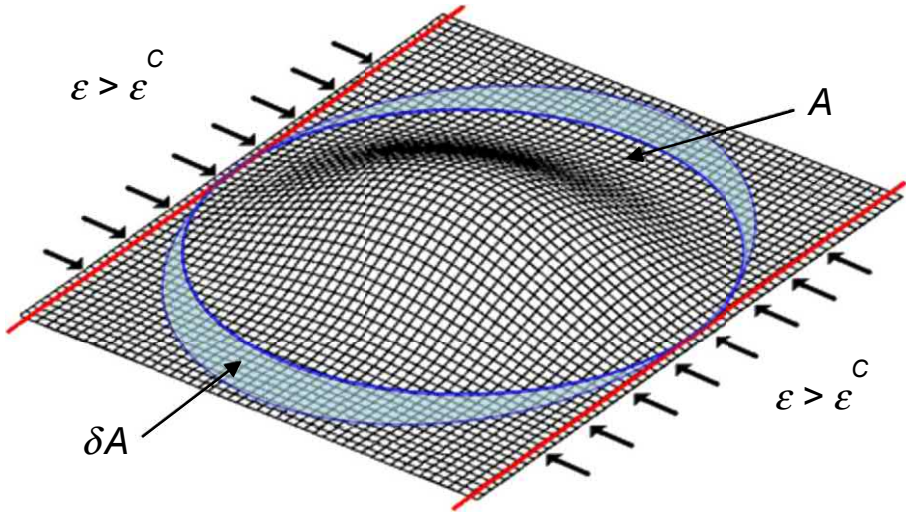
Figure 5.11 Postbuckling of circular sublaminate above delamination area A and elliptical propagation of delamination δA.

film, such that the boundary along the circular perimeter of the delamination is assumed to be clamped, see Fig. 5.11. Circular sublaminates are modeled as a series of strips, the edges of which are constrained by nodes approximating a circular boundary. For the results presented later, 36 node points are applied at intervals of 10 degrees around the circular perimeter, creating 18 different width strips defined by vertical lines spanning the nodes from top to bottom of the circular boundary. Here, constrained implies that no buckling displacement or rotation is allowed at the nodes, thus, approximating a fully clamped boundary. The strips are loaded according to the biaxial loads applied to the thin film with compression in the strip direction of the full laminate. It should be noted that VICON buckling analysis is fully general and can analyze the complex unbalanced and asymmetric sublaminates that can arise in the delaminated sublaminate.

The propagation model, which accounts for the full energy available in the sublaminate at propagation, is applied at each possible interface in turn up to a depth of 25% of the total thickness away from the face of the laminate. For the case of enclosed delaminations, multiple delaminations which are representative of impact damage can be approximated by single delamination at a critical interface. Thus, at each application, it is assumed that only the delamination being examined is present in the laminate and that all secondary effects relating to multiple delaminations being present in the laminate are ignored. Prior to propagation, the thin buckled sublaminate is considered to contain bending energy and membrane energy which are associated with a generalized area A, see Fig. 5.11. Following propagation of the buckled delamination, this area becomes $A + \delta A$, and the corresponding updated membrane and bending energies are calculated. Energy for propagation is also available in the form of membrane energy released from the section of the sublaminate of

area δA which becomes delaminated during propagation. This comparison results in the following equation for SERR [21],

$$\left(F_{th}^2 + 2F_{th} - 3\right)u_T = G_{IC} \tag{5.11}$$

$$u_T = \left\{\left(A_{11}\varepsilon_x^c + A_{12}\varepsilon_y^c\right)\varepsilon_x^c + \left(A_{12}\varepsilon_x^c + A_{22}\varepsilon_y^c\right)\varepsilon_y^c\right\} \tag{5.12}$$

Here, F_{th} is the threshold load factor above the buckling strain state at which propagation occurs. The A_{11}, A_{12} and A_{22} terms are the in-plane stiffness components of the sublaminate in principal strain directions and are the only active in-plane stiffness terms under biaxial strain (A_{13}, A_{23} can be nonzero but do not contribute to u_T). The terms ε_x^C and ε_y^C are the buckling strains in the principal directions. Both combine to form a 2D energy expression u_T. By comparing the difference in energies to G_{IC}, the SERR required to cause Mode I failure of the resin, it is possible to approximately predict the threshold strain ε_x^{th}, below which a propagation of delamination will not occur.

$$\varepsilon_x^{th} = \varepsilon_x^C\left(\sqrt{4 + \frac{G_{IC}}{u_T}} - 1\right) \tag{5.13}$$

The sublaminate at which the lowest threshold strain for propagation is determined will be the first to propagate. Eq. (5.13) is independent of growth direction and only calculates the strain that corresponds to there being sufficient energy available for release per unit area to cause Mode I failure of the resin. Note that the assumption is made that propagation initiates under Mode I conditions, which corresponds to the situation of propagation at the edge of the delamination closest to the loading edge. For propagation, transverse to the load, it is understood that propagation is mixed mode (the Mode II contribution being particularly large for $90°$ dominated sublaminates). However, applying a G_{IC} condition should be conservative since less energy needs to be developed in the sublaminate to cause propagation i.e., typically $G_{IIC} > 2G_{IC}$. The results of Eq. (5.13) have been compared with a range of experimental tests [21] showing agreement to within 12% for balanced sublaminates in which delamination propagation occurred before intraply cracking.

The use of Eq. (5.13) in laminate design is illustrated for two different stacking sequences in Fig. 5.12 where it can be seen that the four ± 45 degrees surface plies in the $[(45/-45/45/-45)_2/(90/0/90/0)_2]_S$ laminate provide enhanced damage tolerance under uniaxial loading. This is due to the combined effect of delayed buckling (Fig. 5.12(a)) and reduced SERR with a lower stiffness of the surface plies in the axial direction. In the case of the $[45/0/-45/90]_{4S}$ laminate, the near-surface presence of the $0°$ ply has the opposite effect. HTA12K/977-2 material properties were used; $E_{11} = 147\,\text{GPa}$, $E_{22} = 8.5\,\text{GPa}$, $G_{12} = 4.9\,GPa$, $\nu_{12} = 0.3$, $G_{IC} = 478\,\text{J/m}^2$ and $t = 0.125\,\text{mm}$.

The most damage-tolerant laminates have outer layers that are softer in the loading direction, with central layers dominated by stiffer plies. This configuration produces
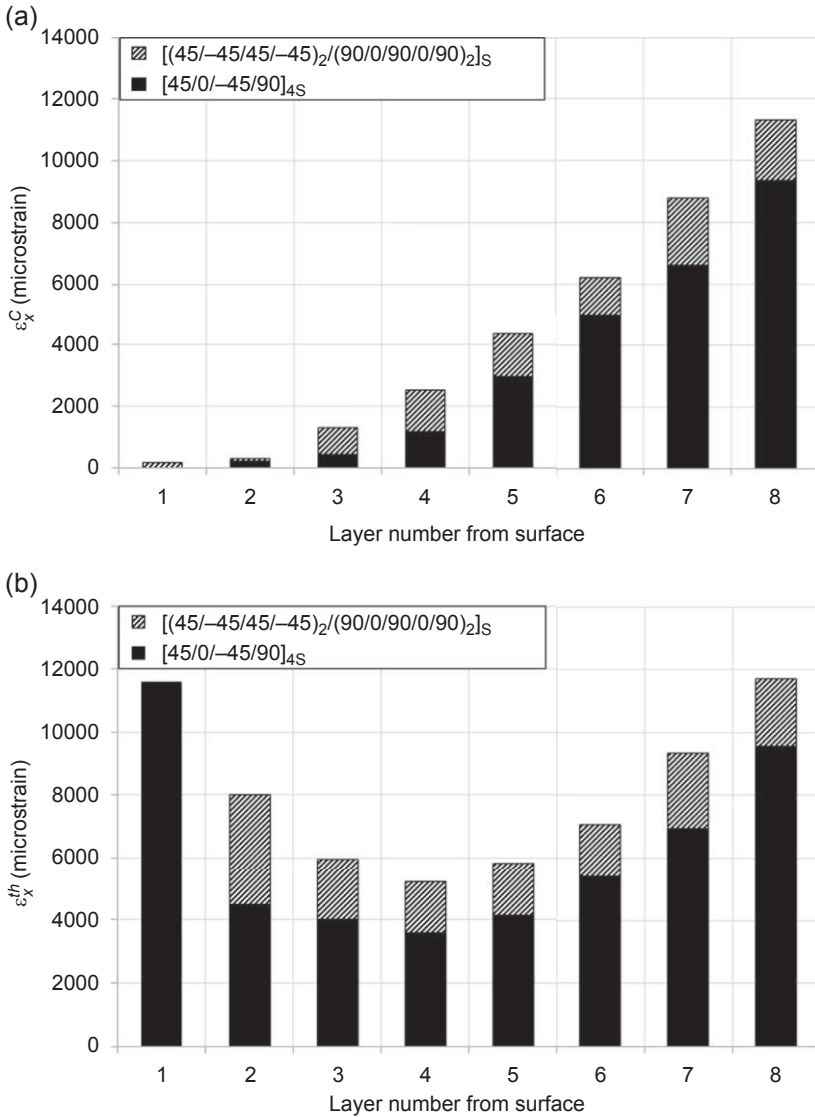
Figure 5.12 Comparison of (a) buckling strains and (b) threshold strains for first four interfaces of $[45/0/-45/90]_{4S}$ and $[(45/-45/45/-45)_2/(90/0/90/0)_2]_S$ laminates. A 30 mm diameter delamination is assumed at each interface in turn.

higher buckling strains for the thin, outer sublaminates, and also means they accrue strain energy more slowly in the postbuckled regime. Stiffer plies in the core of the laminate increase the effective modulus, raising the threshold stress. If sublaminates have large numbers of plies orientated in the main load direction, the threshold strain will drop significantly, leading to a nonoptimal solution.

In the damage tolerance design problem, before a stacking sequence is decided upon and without knowledge of the given impact scenario, it is impossible to know the severity and morphology of impact damage. A worst-case damage must then be assumed for any given stack. The worst-case scenario may not necessarily be the largest delamination. The delamination size that causes the greatest SERR and lowest propagation strain, does not correspond to the lowest buckling strain, see Fig. 5.13. The minimum threshold strain $\varepsilon_x^{th,min}$ can be found analytically by using the plate model applying $d\varepsilon_x^{th}/d\varepsilon_x^C = 0$ to Eq. (5.13). Since this minimum does not require computation of a buckling strain and knowledge of damage size and morphology, it is possible to consider the minimum threshold strain for each possible sublaminate for a given laminate. Thus, for any iterative stack in design optimization, the worst-case propagation strain can be known from assuming this worst-case damage condition. Stable propagation occurs to the left of the minimum on Fig. 5.13 i.e., it will take further loading to propagate the delamination further. In contrast to unstable propagation (right of the minimum on Fig. 5.13), where the loading to cause propagation is reduced with increase in delamination size. If the most severe delamination is not the largest and larger than critical delaminations propagate stably, it could be argued that the largest delamination size is not the most critical because the damage can still grow without significant failure of the full structure.

Design loadings vary with different parts across an aircraft, and it is more likely that components will be under multiaxial loads than a simple uniaxial loading condition. There must, of course, be a compressive component for the buckling-driven delamination propagation mechanism to occur. Fig. 5.14 shows results from a parameter study investigating the plate model minimum threshold strain for a range of combinations of biaxial
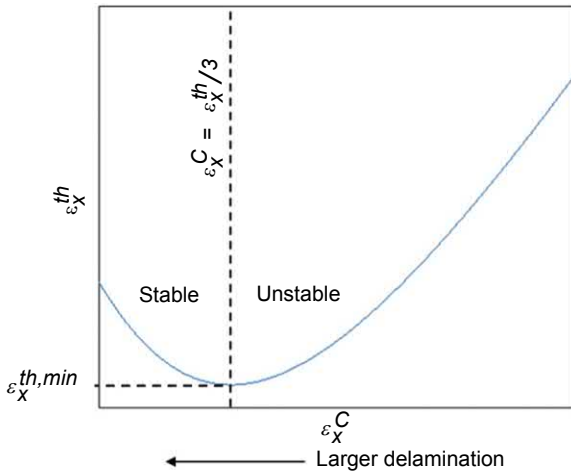
Figure 5.13 Variation of threshold strain ε_x^{th} with buckling strain ε_x^C given by Eq. (5.13), for any arbitrary sublaminate. The minimum threshold strain $\varepsilon_x^{th,min}$ represents the worst-case delamination scenario [24].
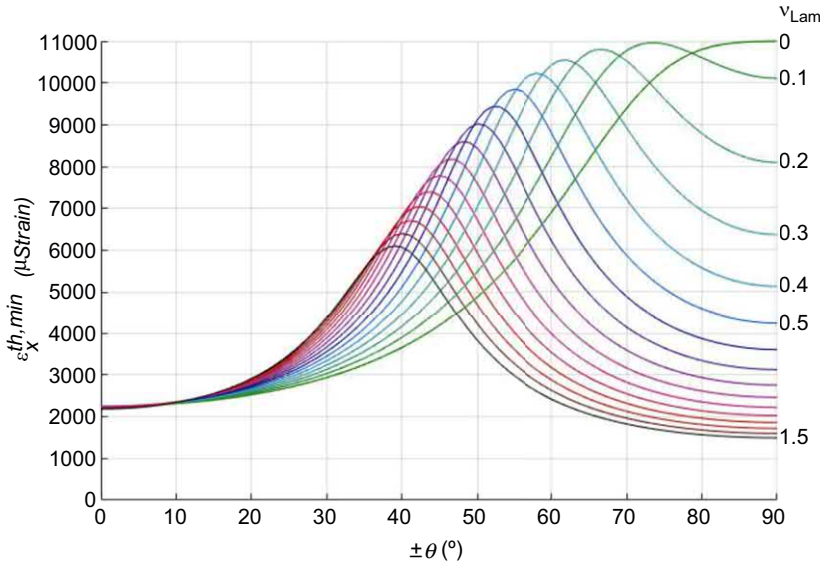
Figure 5.14 Minimum threshold strain of $\pm\theta$ sublaminates ($T_{sub} = 0.5$ mm) under different biaxial strain states defined by the full laminate Poisson's ratio $\nu_{Lam} = -\varepsilon_y/\varepsilon_x$. Note that these strain results scale with $1/\sqrt{T_{sub}}$. For example, a 1 mm thick sublaminate would propagate at 71% of the values shown.

strain states and sublaminate angles. M21/T700GC material properties were used; $E_{11} = 136$ GPa, $E_{22} = 8.9$ GPa, $G_{12} = 4.5$ GPa, $\nu_{12} = 0.35$, $G_{IC} = 550$ J/m^2 and $t = 0.25$ mm. The results in Fig. 5.14 indicate that nonstandard angles produce greater damage tolerance performance than standard angles for the majority of strain states. This is intuitive as the stiffness of the sublaminate should be tailored to the loading in order to minimize the SERR, and nonstandard angles offer greater stiffness tailoring, especially for the low numbers of plies near the surface. Generally, angles should not be orientated in the main strain direction, and optimal plies can be seen to align transversely to this direction.

5.7   Conclusion

The primary objective of design in aerospace composites is to minimize weight for a given loading requirement. For thin laminates subject to compression, this means ensuring sufficient buckling stiffness while maintaining material strength in the presence of in-service damage. In effect, stress levels (i.e., applied running load/laminate thickness) are maximized.

Here, we have shown that buckling stresses for lightly loaded (thin) panels are relatively low (N_x/T values in Table 5.3 are less than 280 MPa). Note that increased stiffening could be used in such cases to reduce effective panel widths, but this comes

with increased manufacturing costs. Alternatively, fibers can be steered in the plane of the panel to increase the load in the vicinity of supports (Compare maximum stress levels in Fig. 5.9 for straight fiber design where $\sigma = 1500/7.5 = 200$ MPa with effective stress of steered CTS design, where $\sigma = 1500/5.1 = 294$ MPa). However, such a design does not include the need to satisfy damage tolerance requirements.

The use of a simple, analytical approach to damage tolerance enables the selection of optimum stacking sequences. The approach assumes that laminates are locally rigid, without accounting for the interaction of local damage with laminate buckling modes. Nevertheless, results suggest that current design practice, which ignores the effect of stacking sequence on compressive strength, has plenty of room for improvement. Nonstandard angles specifically show improvement over the use of standard angles for the majority of laminate loading scenarios.

Future work should explore the above findings in the context of large-scale, semi-monocoque aerospace structures. Actual in-service experience of the material will be vital in assessing whether the design approach can be made more sophisticated by, for example, accounting for better means of detection (health monitoring), improving the damage resistance and damage tolerance of constituent materials, and/or taking a statistical, risk-based approach to the likelihood of damage in the first place.

Glossary

AFP	Automated Fiber Placement
BVID	Barely Visible Impact Damage;
CAI	Compression After Impact
CFRP	Carbon Fiber Reinforced Plastic
CTS	Continuous Tow Shearing
FEM	Finite Element Method
SERR	Strain Energy Release Rate
VAT	Variable Angle Tow;
VICON	VIpasa with CONstraints
VICONOPT	VICON with OPTimization
VIPASA	Vibration and Instability of Plate Assemblies, including Shear and Anisotropy

References

[1] P. Bartholomew, Ply stacking sequences for laminated plates having in-plane and bending orthotropy, Fibre Sci. Technol. 10 (No. 4) (1977) 239−253.

[2] C.B. York, Characterization of nonsymmetric forms of fully orthotropic laminates, J. Aircr. 46 (No. 4) (2009) 1114−1125.

[3] D.J. Dawe, T.J. Craig, Buckling and vibration of shear deformable prismatic plate structures by a complex finite strip method, Int. J. Mech. Sci. 30 (No. 2) (1988) 77−99, https://doi.org/10.1016/0020-7403(88)90063-X.

[4] W.H. Wittrick, F.W. Williams, Buckling and vibration of anisotropic or isotropic plate assemblies under combined loadings, Int. J. Mech. Sci. 16 (1974) 209−239.

[5] W.H. Wittrick, F.W. Williams, An algorithm for computing critical buckling loads of elastic structures, J. Struct. Mech. 1 (No. 4) (1973) 497−518.

[6] M.S. Anderson, F.W. Williams, C.J. Wright, Buckling and vibration of any prismatic assembly of shear and compression loaded anisotropic plates with an arbitrary supporting structures, Int. J. Mech. Sci. 25 (1983) 585−596.

[7] B. Liu, R.T. Haftka, M. Akgün, A. Todoroki, Permutation genetic algorithm for stacking sequence design of composite laminates, Comput. Methods Appl. Mech. Eng. 186 (2000) 357−372.

[8] G.N. Vanderplaats, CONMIN − a Fortran Program for Constrained Function Minimisation, User's Manual, 1973. NASA TM X-62282.

[9] R. Butler, F.W. Williams, Optimum design using VICONOPT, a buckling and strength constraint program for prismatic assemblies of anisotropic plates, Comput. Struct. 43 (No. 4) (1992) 699−708.

[10] W. Liu, R. Butler, H.A. Kim, Optimization of composite stiffened panels subject to compression and lateral pressure using a bi-level approach, J. Struct. Multidiscip. Optim. 36 (No. 3) (2008) 235−245.

[11] R. Butler, W. Liu, Optimisation of stiffened panels using finite strip models, in: B.G. Falzon, M.H. Aliabadi (Eds.), Buckling and Postbuckling Structures, Imperial College Press, London, UK, 2008, pp. 225−257.

[12] P. Weaver, in: B.G. Falzon, M.H. Aliabadi (Eds.), Anisotropic Elastic Tailoring in Laminated Composite Plates and Shells, Imperial College Press, London, UK, 2008, pp. 177−224.

[13] M.W. Hyer, R.F. Charette, The Use of Curvilinear Fiber Format in Composite Structure Design, 1989. AIAA paper no. 1989-1404.

[14] Z. Gürdal, R. Olmedo, In-plane response of laminates with spatially varying fiber orientation: variable stiffness concept, AIAA J. 31 (4) (1993) 751−758.

[15] E. Lund, Buckling topology optimization of laminated multi-material composite shell structures, Compos. Struct. 91 (2009) 158−167.

[16] A.W. Blom, M.M. Abdalla, Z. Gürdal, Optimization of course locations in the fiber-placed panels for general fiber angle distributions, Compos. Sci. Technol. 70 (2010) 564−570.

[17] B.C. Kim, K. Potter, P.,M. Weaver, Continuous tow shearing for manufacturing variable angle tow composites, Compos. Appl. Sci. Manuf. 43 (No. 8) (2012) 1347−1356.

[18] A.T. Rhead, R. Butler, W. Liu, N. Baker, The influence of surface ply fibre angle on the compressive strength of composite laminates containing delamination, Aeronaut. J. 116 (No. 1186) (2012) 1315−1330.

[19] A.T. Rhead, R. Butler, W. Liu, B.C. Kim, S.R. Hallett, Compression after impact strength of a buckling resistant, tow steered panel, in: 19th International Conference on Composite Materials (ICCM19), Montreal, July−August, 2013.

[20] H. Chai, C.D. Babcock, Two-dimensional modelling of compressive failure in delaminated laminates, J. Compos. Mater. 19 (No. 1) (1985) 67−98.

[21] R.S. Choudhry, A.T. Rhead, M.W.D. Nielsen, R. Butler, A plate model for compressive strength prediction of delaminated composites, Compos. Struct. 210 (2019) 509−517.

[22] A.T. Rhead, R. Butler, Compressive static strength model for impact damaged laminates, Compos. Sci. Technol. 69 (No. 14) (2009) 2301−2307.

[23] R. Butler, A.T. Rhead, W. Liu, N. Kontis, Compressive strength of delaminated aerospace composites, Philos. Trans. R. Soc. A Phil. Trans. 370 (2012) 1759−1779.

[24] M.W.D. Nielsen, Design of Aerospace Laminates for Multi-Axis Loading and Damage Tolerance, Ph.D. thesis, University of Bath, 2017.

Further reading

[1] D. Bushnell, PANDA2 − program for minimum mass design of stiffened, composite, locally buckled panels, Comput. Struct. 25 (1987) 469−605.

[2] A.T. Rhead, R. Butler, N. Baker, Analysis and compression testing of laminates optimised for damage tolerance, Appl. Compos. Mater. 18 (No. 1) (2011) 85−100.

[3] F.W. Williams, D. Kennedy, M.S. Anderson, Analysis features of VICONOPT, an exact buckling and vibration program for prismatic assemblies of anisotropic plates, in: 31st AIAA Structural Dynamics and Materials (SDM) Conference, Paper No. 90-0970, Long Beach, California, April 1990.

[4] F.W. Williams, D. Kennedy, R. Butler, M.S. Anderson, VICONOPT: program for exact vibration and buckling analysis of prismatic plate assemblies, AIAA J. 29 (No. 11) (1991) 1927−1928.

Postbuckling analysis and optimization of laminated composite plates with applications in aerospace

6

Zhangming Wu [1, 2]
[1]School of Mechanical Engineering & Mechanics, Ningbo University, China;
[2]School of Engineering, Cardiff University, Cardiff, United Kingdom

6.1 Introduction

In aerospace applications, thin plate-like structures are widely used and often undergo large transverse deflections and have to carry considerable loads. In conventional design practices, buckling is often considered as a final failure of structural members. However, there may be considerable load capacity, particularly for plate-like structures, beyond buckling limit before final failure occurs. Therefore, it has been a common practice in aerospace to further explore the load-carrying capacity, or, in other words, the weight-savings by allowing the structures to operate in their postbuckling regime. The further load-carrying capacity of thin-walled plates/structures in the postbuckling regime makes them very attractive in the design of lightweight aero-structures, which have continuously been in demand in the aerospace industry. For example, lighter, thinner, still stronger skins can be used in wings and fuselages. On the other hand, solid knowledge and deep understanding of the postbuckling behavior of the thin-walled plates/structures must be acquired before performing the optimal design of such nonlinear structural performance [1]. Laminated composite materials are increasingly used in the aviation and aerospace industry as the primary load-carrying components, due to their high strength-to-weight ratios and large stiffness tailoring flexibility. Driven by advanced manufacturing technologies, many novel composite materials with increased design flexibility and functionality, such as functionally graded materials, variable angle tow composites, and 3D-printed composites, have been developed. These novel composite materials provide extensive opportunities for designers to obtain desirable postbuckling performance for future aerospace structures.

Postbuckling is a nonlinear elastic behavior of a structure after it enters buckling, and will induce the stretching-bending coupling irrespective of material anisotropy. Therefore, the stretching of the middle surface of the plate due to out-of-plane displacement must be considered in the postbuckling analysis [2]. The fundamental nonlinear strain−displacement relations and the partial differential equations for the large deflection of thin plates were derived by von Kármán. Approximate solutions

for the postbuckling behavior of isotropic plates under compression was first obtained by Cox [3] and Marguerre [4] using the energy method, in which one-term displacement function and Airy's stress function was assumed. Later, Levy [2] obtained an exact solution by expanding the Airy's stress function and the out-of-plane deflection in terms of independent Fourier series. The energy method expressed with Airy's stress function has been widely used in the postbuckling analysis of isotropic or orthotropic composite laminated plates by Coan, Yamaki, Prabhakara and Chia, and Shin et al. [5−8]. On the other hand, only a few research works [9−11] were reported to apply the energy method expressed in terms of three displacement variables to solve the postbuckling problem. Harris [12] derived a closed-form expression for the evaluation of initial postbuckling strength of orthotropic composite plates via a Taylor series expansion near the critical buckling point. Diaconu and Weaver [13,14] also developed approximate closed-form postbuckling solutions for infinitely long composite plates with high flexural/twisting anisotropy. The perturbation method provides an alternative but very effective way to solve the nonlinear problem asymptotically. Koiter [15,16] is the most well-known researcher who applied this asymptotic approach and established reliable postbuckling analysis of plates and shells. He also approved that the third and fourth perturbation terms actually governed the nonlinear behavior. Stein [17] also derived an asymptotical solution for the postbuckling behavior of isotropic rectangular plates through taking a loading factor as the perturbation parameter, and he also analyzed the phenomenon of buckle wavelength change [18]. Later, Chandra and Raju (1972) extended Stein's model for orthotropic plates. Shen and Zhang [19,20] derived the asymptotic solutions for a series of different postbuckling problems of rectangular plates using a maximum deflection based perturbation parameter. More recently, Wu et al. [21] applied a similar perturbation technique to derive a more accurate closed-form solution for the postbuckling analysis of orthotropic composite laminates. Although finite element methods dominate the structural analysis since last decade, there remain strong research interests in both academic and industrial fields in developing advanced and efficient modeling methods for the postbuckling analysis of composite plates, e.g., closed-form solutions [12−14,21], semi-analytical methods [7,22], and other rapid numerical methods (e.g., DQM [23]).

The optimization of postbuckling behavior of composite laminates is a challenging task, because it often suffers from high computational costs in tracing the nonlinear post-buckling equilibrium path. In the post-buckling optimization of laminated composite plates, it is needed to determine the post-buckling behavior of a large number of lamination configurations. Therefore, most previous works exploit analytical/semi-analytical formulations or other approximate schemes that can rapidly determine the nonlinear structural responses, so as to incorporate optimization procedures. Dickson and Biggers [24] developed a program (POSTOP) to perform the optimum design of metal or composite panels with open-section stiffeners under combined loadings. In their program, analytical/semi-analytical solutions were adopted for the buckling and postbuckling analysis, and a modified feasible-direction method was applied for the optimization procedure. Shin et al. [25] presented a work on the minimum-weight optimum design of specially orthotropic laminates with respect to the postbuckling performance. The postbuckling analysis of composite laminates was performed using a Marguerre-type energy method, and the phenomenon of mode jumping is

considered in the optimization process. Bushnell [26] also implemented the function for the postbuckling design in his PANDA2 program, in which the postbuckling problem was solved in a semi-analytical way. In addition, an optimization strategy was introduced to retreat or remove the cases with nonconvergent solutions. Bisagni and Vescovini [27] developed an efficient semi-analytical postbuckling model based on the mixed variational principle to carry out the optimization of the nonlinear postbuckling behavior of composite structures using a genetic algorithm. Other routines/tools integrated with efficient modeling methods were also developed and used for the postbuckling optimum design, such as NLPANOPT [28,29], VICONOPT [30,31]. As an alternative to analytical solutions, the high computational costs are reduced in some works by the application of response surface methodologies that offer a global approximation scheme to predict the postbuckling behavior using a less number of sampled points [32,33]. More recently, based on a newly derived closed-form solution, Wu et al. [21] implemented a very efficient two-level optimization routine for the design of postbuckling behavior of orthotropic composite plates using the lamination parameters as the intermediate design variables.

Conventional straight-fiber laminates offer a limited tailoring option by designing the stacking sequence with constant ply-angles along the thickness direction. The advent of new advanced fiber/tow placement machines enable the steering of tow paths (namely VAT − Variable Angle Tow) in the plane of composite laminates and result in variable stiffness structures [34,35]. The development of tow steering technology enables the stiffness properties of composite materials to vary from one point to another. As such, it offers a fully three-dimensional tailoring capacity. Previous research has shown the substantial potential of utilizing the VAT laminates to improve composite structural performance, particularly the buckling and postbuckling load-carrying capability [22,23,35−37]. Despite the benefits of VAT laminates, the postbuckling optimization of such variable stiffness laminates is a particular challenge, as it involves a large number of design variables and large computational effort required by an optimization process. These challenges in the optimal design of the nonlinear postbuckling behavior of VAT composite plates necessitate the development of new efficient modeling and effective optimization strategies. Several optimization works on the postbuckling performance of VAT composite plates have been proposed, which are based on either using genetic algorithms (GA) [37] or a two-level optimization framework [38,39]. More recently, Wu et al. [38] designed an effectively "Buckle-Free" composite panel through the optimal design of the postbuckling behavior of variable thickness, variable angle tow composite laminates.

In this chapter, we will first present the fundamental theory for the postbuckling analysis of composite laminates based on the von Kármán large deflection equations and classical lamination theory (CLT). Subsequently, some recent developed analytical or numerical techniques will be introduced in deriving the closed-form solutions or the semi-analytical/analytical models for the postbuckling analysis of composite panels. With the efficient postbuckling models, a two-level optimization framework that applies the lamination parameters as the intermediate design variables will be introduced in the optimal design of nonlinear postbuckling behavior of composite panels. Lastly we will demonstrate and discuss some case studies on the postbuckling

optimization with the consideration of failure criteria, highlighting the benefits provided by the elastic tailoring of local or global composite anisotropy to enhance the structural efficiency.

6.2 Fundamental theory

6.2.1 Constitutive equations of composite laminates

One of the most distinct advantages of fiber-reinforced composite laminates in structural design is their extensive flexibility in elastic stiffness tailoring. The stiffness properties of a composite laminate are denoted by $\mathbf{A}$, $\mathbf{B}$, $\mathbf{D}$ matrices, which are the in-plane, coupling, and bending stiffness, respectively. Based on the Classical Lamination Theory (CLT), the constitutive equation for a composite laminate is defined as,

$$\begin{bmatrix} \mathbf{N} \\ \mathbf{M} \end{bmatrix} = \begin{bmatrix} \mathbf{A} & \mathbf{B} \\ \mathbf{B} & \mathbf{D} \end{bmatrix} \begin{bmatrix} \varepsilon^0 \\ \kappa \end{bmatrix} \tag{6.1}$$

The term ε^0 is the midplane strain, κ is the curvature, and N, M are in-plane stress and bending moment resultants, respectively. Alternative to Eq. (6.1), the constitutive equation is also often expressed in a partially inverted form given by Mansfield [40] for the convenient derivation of the equations in terms of transverse deflection and force function,

$$\begin{bmatrix} \varepsilon^0 \\ \mathbf{M} \end{bmatrix} = \begin{bmatrix} \mathbf{a} & \mathbf{b} \\ -\mathbf{b}^T & \mathbf{D}^* \end{bmatrix} \begin{bmatrix} \mathbf{N} \\ \kappa \end{bmatrix} \tag{6.2}$$

where $\mathbf{a} = (a_{ij}) = \mathbf{A}^{-1}$, $\mathbf{b} = (b_{ij}) = -\mathbf{A}^{-1}\mathbf{B}$, $\mathbf{D}^* = \left(D_{ij}^*\right) = \mathbf{D} - \mathbf{BA}^{-1}\mathbf{B}$. For VAT composite laminates, their values vary with respect to the coordinates x and y. As only the symmetric laminates are considered in this section, there is no stretching−bending coupling and the coupling matrix $\mathbf{B} = \mathbf{0}$, $\mathbf{b} = \mathbf{0}$, and $\mathbf{D}^* = \mathbf{D}$. By introducing the material invariants and the lamination parameters [41], the stiffness A_{ij}, D_{ij} (i, j = 1,2,6) can be expressed as follows,

$$\begin{pmatrix} A_{11} \\ A_{22} \\ A_{12} \\ A_{66} \\ A_{16} \\ A_{26} \end{pmatrix} = h \begin{bmatrix} 1 & \xi_1^A & \xi_2^A & 0 & 0 \\ 1 & -\xi_1^A & \xi_2^A & 0 & 0 \\ 0 & 0 & -\xi_2^A & 1 & 0 \\ 0 & 0 & -\xi_2^A & 0 & 1 \\ 0 & \xi_3^A/2 & \xi_4^A & 0 & 0 \\ 0 & \xi_3^A/2 & -\xi_4^A & 0 & 0 \end{bmatrix} \begin{pmatrix} U_1 \\ U_2 \\ U_3 \\ U_4 \\ U_5 \end{pmatrix} \tag{6.3}$$

$$\begin{pmatrix} D_{11} \\ D_{22} \\ D_{12} \\ D_{66} \\ D_{16} \\ D_{26} \end{pmatrix} = \frac{h^3}{12} \begin{bmatrix} 1 & \xi_1^D & \xi_2^D & 0 & 0 \\ 1 & -\xi_1^D & \xi_2^D & 0 & 0 \\ 0 & 0 & -\xi_2^D & 1 & 0 \\ 0 & 0 & -\xi_2^D & 0 & 1 \\ 0 & \xi_3^D/2 & \xi_4^D & 0 & 0 \\ 0 & \xi_3^D/2 & -\xi_4^D & 0 & 0 \end{bmatrix} \begin{pmatrix} U_1 \\ U_2 \\ U_3 \\ U_4 \\ U_5 \end{pmatrix} \tag{6.4}$$

$$\xi_{1,2,3,4}^A = \int_{-1}^{1} \left[\cos\left(2\theta(\overline{z})\right) \ \cos\left(4\theta(\overline{z})\right) \ \sin\left(2\theta(\overline{z})\right) \ \sin\left(4\theta(\overline{z})\right) \right] d\overline{z} \tag{6.5}$$

$$\xi_{1,2,3,4}^D = \frac{3}{2} \int_{-1}^{1} \left[\cos\left(2\theta(\overline{z})\right) \ \cos\left(4\theta(\overline{z})\right) \ \sin\left(2\theta(\overline{z})\right) \ \sin\left(4\theta(\overline{z})\right) \right] \overline{z}^2 d\overline{z}$$

where the terms U_1, ..., U_5 are the material invariants, and $\xi_{1,2,3,4}^A$ and $\xi_{1,2,3,4}^D$ are the in-plane and out-of-plane lamination parameters, respectively. $\theta(\overline{z})$ is the variation function of the fiber orientation angles along the normalized thickness $\overline{z}$. As shown in Eqs. (6.3–6.5), the laminate stiffness properties can be arbitrarily tailored through a specific design of the fiber-angle distribution function $\theta(\overline{z})$, either through changing the layer fiber orientation angles or the stacking sequence arrangement. This characteristic of a composite laminate provides an extensive design flexibility to enhance the structural performance through an optimization process of a laminate layup, namely stiffness tailoring.

6.2.2 Governing equations

The von Kármán large deflection equations that define the nonlinear relationship between the midplane strains and midplane displacements are given by (Bulson, 1970) [42].

$$\varepsilon_x^0 = \frac{\partial u_0}{\partial x} + \frac{1}{2}\left(\frac{\partial w}{\partial x}\right)^2, \ \varepsilon_y^0 = \frac{\partial v_0}{\partial x} + \frac{1}{2}\left(\frac{\partial w}{\partial y}\right)^2, \ \gamma_x^0 = \frac{\partial u_0}{\partial y} + \frac{\partial v_0}{\partial x} + \left(\frac{\partial w}{\partial x}\right)\left(\frac{\partial w}{\partial y}\right) \tag{6.6}$$

Applying Eq. (6.6) on the *condition of compatibility* leads to the following expression,

$$\frac{\partial^2 \varepsilon_x^0}{\partial y^2} + \frac{\partial^2 \varepsilon_y^0}{\partial x^2} - \frac{\partial^2 \gamma_{xy}^0}{\partial x \partial y} = \left(\frac{\partial^2 w}{\partial x \partial y}\right)^2 - \frac{\partial^2 w}{\partial x^2}\frac{\partial^2 w}{\partial y^2} \tag{6.7}$$

The stretching behavior of a plate can be modeled by introducing the *Airy's stress function* (Φ) to model the stress resultants $\mathbf{N}$ (N_x; N_y; N_{xy}), which are then expressed as,

$$N_x = \Phi_{,yy} \quad N_y = \Phi_{,xx} \quad N_{xy} = -\Phi_{,xy} \tag{6.8}$$

On the basis of Eqs. (6.2, 6.6−6.8), we rewrite the *compatibility* and *equilibrium* equations for a plate in terms of the out-of-plane deflection w and the *Airy's stress function* Φ as,

$$\frac{\partial^2}{\partial y^2}\left[a_{11}\Phi_{,yy} + a_{12}\Phi_{,xx} - a_{16}\Phi_{,xy}\right] + \frac{\partial^2}{\partial x^2}\left[a_{12}\Phi_{,yy} + a_{22}\Phi_{,xx} - a_{26}\Phi_{,xy}\right]$$

$$- \frac{\partial^2}{\partial x \partial y}\left[a_{16}\Phi_{,yy} + a_{26}\Phi_{,xx} - a_{66}\Phi_{,xy}\right] = \left(w_{,xy}\right)^2 - \left(w_{,xx}\right)\left(w_{,yy}\right)$$

$$\tag{6.9}$$

$$\frac{\partial^2}{\partial x^2}\left[D_{11}w_{,xx} + D_{12}w_{,yy} + 2D_{16}w_{,xy}\right] + \frac{\partial^2}{\partial y^2}\left[D_{12}w_{,xx} + D_{22}w_{,yy} + 2D_{26}w_{,xy}\right]$$

$$+ 2\frac{\partial^2}{\partial x \partial y}\left[D_{16}w_{,xx} + D_{26}w_{,yy} + 2D_{66}w_{,xy}\right]$$

$$+ \Phi_{,yy}w_{,xx} + \Phi_{,xx}w_{,yy} - 2\Phi_{,xy}w_{,xy} = 0$$

$$\tag{6.10}$$

If the variable stiffness composite plates are considered, the expansion of both *compatibility* and *equilibrium* equations of (6.9) and (6.10) involve additional higher order derivative terms with respect to the in-plane flexibility and bending stiffness coefficients [23,35], respectively. It will be more tedious if one directly solves these two coupled governing equations by applying the Galerkin method or the principle of virtual work (displacement) to solve this postbuckling problem for the variable stiffness composite plates.

6.3 Postbuckling analysis

6.3.1 Asymptotic closed-form solutions

A closed-form asymptotic solution for the postbuckling problem of straight fiber, constant stiffness composite plates is derived using the perturbation method [21]. A simply supported laminated plate is subjected to biaxial loading. The ratio between the longitudinal loading N_{x0} and transverse loading N_{y0} is denoted by k. The four edges

are assumed to remain straight during the loading and deformation, which are constant in-plane displacement boundary conditions:

$$u_{,y}(0, y) = u_{,y}(a, y) = v_{,x}(x, 0) = v_{,x}(x, b) = 0 \tag{6.11}$$

For satisfying the boundary conditions and consider nonlinear structural behavior in the postbuckling regime, the out-of-plane deflection, and the Airy stress function are expressed in the following perturbation forms.

$$
\begin{aligned}
w(x, y) = \varepsilon \left[w_1 \sin\frac{m\pi x}{a} \sin\frac{n\pi x}{b} \right] + \varepsilon^3 \left[w_3 \sin\frac{m\pi x}{a} \sin\frac{n\pi x}{b} \right. \\
\left. + w_3 \sin\frac{m\pi x}{a} \sin\frac{n\pi x}{b} + w_3 \sin\frac{m\pi x}{a} \sin\frac{n\pi x}{b} \right] + \mathcal{O}\left(\varepsilon^5\right)
\end{aligned}
\tag{6.12}
$$

$$
\begin{aligned}
\Phi(x, y) = -\phi_x^{(0)}\frac{y^2}{2} - \phi_y^{(0)}\frac{x^2}{2} + \varepsilon^2 \left[-\phi_x^{(2)}\frac{y^2}{2} - \phi_x^{(2)}\frac{x^2}{2} + \phi_{20}^{(2)} \cos\frac{2m\pi x}{a} \right. \\
\left. + \phi_{02}^{(2)} \cos\frac{2n\pi y}{b} \right] + \varepsilon^4 \left[-\phi_x^{(4)}\frac{y^2}{2} - \phi_x^{(4)}\frac{x^2}{2} + \phi_{20}^{(4)} \cos\frac{2m\pi x}{a} + \phi_{02}^{(4)} \cos\frac{2n\pi y}{b} \right. \\
\left. + \phi_{22}^{(4)} \cos\frac{2m\pi x}{a}\cos\frac{2n\pi y}{b} + \phi_{40}^{(4)} \cos\frac{4m\pi x}{a} + \phi_{04}^{(4)} \cos\frac{4n\pi y}{b} \right. \\
\left. + \phi_{24}^{(4)} \cos\frac{2m\pi x}{a}\cos\frac{4n\pi y}{b} + \phi_{42}^{(4)} \cos\frac{4m\pi x}{a}\cos\frac{2n\pi y}{b} \right] + \mathcal{O}\left(\varepsilon^6\right)
\end{aligned}
\tag{6.13}
$$

where ε is the perturbation parameter, m and n are the number of half-waves of w in the x and y directions, respectively. Note, the zeroth-, second-, and fourth-order terms of out-of-plane displacement w and the first- and third-order terms of the Airy function Φ are eliminated due to the orthogonality condition [43]. Substituting the expressions of Eqs. (6.12) and (6.13) into the postbuckling governing equations [Eqs. (6.9) and (6.10)] result in a set of linear nonhomogeneous equations, where the unknown coefficients $(w_1, w_3, \ldots, \phi_{20}^{(2)})$ can be determined using a step-by-step procedure [19,20]. The difference between Zhang and Shen's model [25] and the present method is the assumption for truncating the higher-order terms $(\mathcal{O}\left(\varepsilon^5\right), \mathcal{O}\left(\varepsilon^6\right), \cdots)$ in the derivation of closed-form expressions of these unknown coefficients and the choice of perturbation parameter ε. I have found that retaining more terms for mode shape assumption [Eq. (6.12)] is beneficial to accurately capturing the nonlinearity of the postbuckling behavior of composite laminates in the moderately deep range. In Zhang and Shen's model [20], the coefficient w_3 is assumed to be zero, and the perturbation parameter is chosen by truncating the expansion of the maximum transverse deflection. In this work, the perturbation parameter is chosen from the in-plane stress resultant

along the longitudinal direction at the boundary N_{x0}. The in-plane stress resultant N_{x0} is given by the following series:

$$N_{x0} = N_x^0 + \varepsilon^2 N_x^{(2)} + \varepsilon^4 N_x^{(4)} + \dots \tag{6.14}$$

In Eq. (6.14), the term $\varepsilon^4 N_x^{(4)}$ and higher-order perturbation terms are ignored. The perturbation parameter is then defined as,

$$\varepsilon^2 = \frac{N_{x0} - N_x^{cr}}{N_x^{(2)}} \tag{6.15}$$

Substituting the coefficients in Eqs. (6.12−6.15) into Eqs. (6.9−6.10), the end-shortening strain and maximum out-of-plane deflection function are written as

$$\varepsilon_x = (a_{11} + ka_{12})N_x^{cr} + \left(N_{x0} - N_x^{cr}\right)\left[(a_{11} + ka_{12}) + \frac{2a_{11}a_{22}\left(1 + k\alpha^2\right)}{a_{22} + a_{11}\alpha^4}\right]$$

$$+ \left(N_{x0} - N_x^{cr}\right)^2 \frac{6b^2}{(n\pi)^2} \frac{\left(1 + k\alpha^2\right)^2}{a_{22}^3 + 3a_{11}a_{22}^2\alpha^4 + 3a_{11}^2 a_{22}\alpha^8 + a_{11}^3\alpha^{12}} \cdot \tag{6.16}$$

$$\left[\frac{a_{11}a_{22}^3\left(1 + k\alpha^2\right)}{-8kD_{11} + 16(D_{12} + 2D_{66}) + (80 - 72k\alpha^2)\alpha^2 D_{22}}\right.$$

$$\left. + \frac{a_{11}^3 a_{22}\alpha^{10}\left(1 + k\alpha^2\right)}{(72 - 80k\alpha^2)D_{11} + 16k\alpha^4(D_{12} + 2D_{66}) - 8\alpha^4 D_{22}}\right]$$

$$w_{max} = \frac{4b}{n\pi}\left[\frac{\left(N_{x0} - N_x^{cr}\right)\left(1 + k\alpha^2\right)a_{11}a_{22}\alpha^2}{a_{22} + a_{11}\alpha^4}\right]^{\frac{1}{2}}\left\{1 + \left(\frac{b}{n\pi}\right)^2\right.$$

$$\left[\frac{\left(N_{x0} - N_x^{cr}\right)\left(1 + k\alpha^2\right)^2 a_{11}a_{22}\alpha^2}{2(a_{22} + a_{11}\alpha^4)^2}\right] \cdot$$

$$\left[\frac{\left(a_{22} - 2a_{11}\alpha^4\right)/\left(a_{11}\alpha^2\right)}{-8kD_{11} + 16(D_{12} + 2D_{66}) + (80 - 72k\alpha^2)\alpha^2 D_{22}}\right. \tag{6.17}$$

$$\left.\left. + \frac{\alpha^6\left(a_{11}\alpha^4 - 2a_{22}\right)/\left(a_{22}\right)}{(72 - 80k\alpha^2)D_{11} + 16k\alpha^4(D_{12} + 2D_{66}) - 8\alpha^4 D_{22}}\right]\right\}$$

where $k = N_{x0}/N_{y0}$ is the specified loading ratio, N_x^{cr} is the critical buckling load of the plate, and $\alpha = (na/mb)$ is the buckling mode parameter. Note, the accuracy of the postbuckling model given by Eqs. (6.16) and (6.17) for biaxial compressive loaded plates with highly orthotropic material (with a large E_1/E_2 ratio) is not satisfactory when the load factor k and the aspect ratio a/b are both very large. From the numerical

experience, Eqs. (6.16) and (6.17) are able to give sufficiently accurate postbuckling solution for highly orthotropic material when $k < 0.5$ and $a/b < 5$. The nonlinearity of the postbuckling equilibrium path is explicitly defined in terms of the composite stiffness matrices a_{ij}, D_{ij}, the plate aspect ratio, load factor k, and the increased portion of external loading $\left(N_{x0} - N_x^{cr}\right)$. If the nonlinear terms (with respect to the applied compression loading) are ignored and only the linear terms are retained, Eq. (6.16) reduces to the exact same form as Harris's postbuckling model [12]. A unidirectional laminate $[0]_s$ was chosen for the postbuckling model validation. It was found, in general, that the asymptotic perturbation method yields the least accurate solutions for the $[0]_s$ laminates with the material properties that were highly orthotropic (the ratio of E_1/E_2 was large). Fig. 6.1 illustrates the postbuckling equilibrium paths of a $[0]_s$ square plate given by various analytical models and the FEM. The plot (a) gives the normalized strains $\varepsilon_x/\varepsilon_x^{iso}$ as a function of the normalized axial loads N_{x0}/N_x^{iso}, and the plot (b) shows the normalized maximum transverse displacement w_{max}/h as a function of the normalized axial loads N_{x0}/N_x^{iso}. It can be seen that, for this extreme case, the closed-form model given by Eqs. (6.16) and (6.17) is able to accurately capture the nonlinear structural behavior in deep postbuckling regime.

6.3.2 Semi-analytical model based on a mixed variational principle

Applying the energy method or a variational formulation to derive the semi-analytical model for the analysis of the nonlinear postbuckling behavior of composite structures has attracted lots of interest in previous research works [10,25]. This approach is particularly attractive for the postbuckling analysis of variable stiffness composite laminates because the derivative terms of stiffness coefficients can be avoided, and it results in an analogous modeling procedure with that for straight fiber laminates. In this article, a single variational formula expressed in terms of the *Airy's stress*
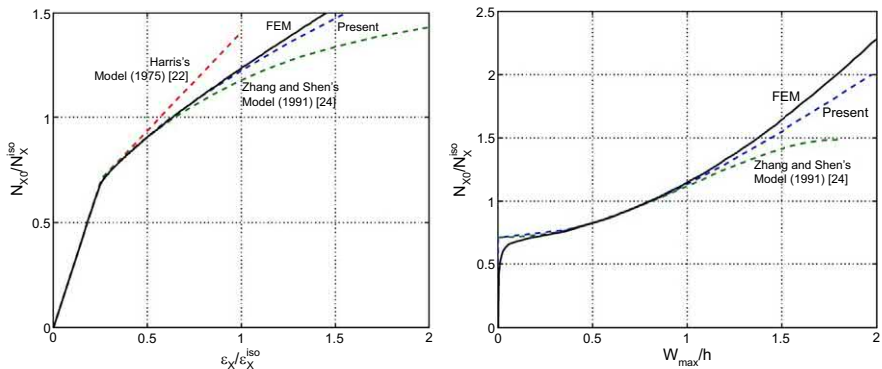
Figure 6.1 Postbuckling model validation and comparison on a composite laminate $[0]_s$.

function and transverse deflection function is proposed to model the postbuckling behavior of composite plates, which is defined as [27,33],

$$
\mathbf{\Pi}^* = -\frac{1}{2} \iint_S \left[a_{11} \left(\frac{\partial^2 \Phi}{\partial y^2} \right)^2 + 2a_{12} \frac{\partial^2 \Phi}{\partial x^2} \frac{\partial^2 \Phi}{\partial y^2} + a_{22} \left(\frac{\partial^2 \Phi}{\partial x^2} \right)^2 + a_{66} \left(\frac{\partial^2 \Phi}{\partial x \partial y} \right)^2 \right.
$$

$$
\left. -2a_{16} \frac{\partial^2 \Phi}{\partial y^2} \frac{\partial^2 \Phi}{\partial x \partial y} - 2a_{26} \frac{\partial^2 \Phi}{\partial x^2} \frac{\partial^2 \Phi}{\partial x \partial y} \right] dxdy
$$

$$
+\frac{1}{2} \iint_S \left[D_{11} \left(\frac{\partial^2 w}{\partial x^2} \right)^2 + 2D_{12} \frac{\partial^2 w}{\partial x^2} \frac{\partial^2 w}{\partial y^2} + D_{22} \left(\frac{\partial^2 w}{\partial y^2} \right)^2 + 4D_{66} \left(\frac{\partial^2 w}{\partial x \partial y} \right)^2 \right.
$$

$$
\left. +4D_{16} \frac{\partial^2 w}{\partial x^2} \frac{\partial^2 w}{\partial x \partial y} + 4D_{26} \frac{\partial^2 w}{\partial y^2} \frac{\partial^2 w}{\partial x \partial y} \right] dxdy
$$

$$
+\frac{1}{2} \iint_S \left[\frac{\partial^2 \Phi}{\partial y^2} \left(\frac{\partial w}{\partial x} \right)^2 + \frac{\partial^2 \Phi}{\partial x^2} \left(\frac{\partial w}{\partial y} \right)^2 - 2 \frac{\partial^2 \Phi}{\partial x \partial y} \frac{\partial w}{\partial x} \frac{\partial w}{\partial y} \right] dxdy
$$

$$
+\int_{c_1} \left[M_{vo} \frac{\partial w}{\partial v} - \left(V_{z0} + \frac{\partial M_{vs0}}{\partial s} \right) w \right] ds + \int_{c_2} [u_0 N_{xv} + v_0 N_{yv}] ds
$$

$$(6.18)$$

where c_1 and c_2 denote the portion of boundaries over which stresses and displacements are prescribed, respectively. The descriptors s and v indicate the tangential and normal direction respectively, along a specified boundary. One of the advantages of applying this method to model the postbuckling behavior of composite laminates is able to deal with the mixed boundary conditions, directly. For the VAT laminates, the displacement along a stress-free boundary is generally unknown and difficult to determine [36]. For applying the Rayleigh−Ritz method, the transverse deflection function w and the *Airy's stress function* Φ are assumed to have the following series forms,

$$
w(x,y) = \sum_{r=0}^{R} \sum_{s=0}^{S} W_{rs} X_r(x) Y_s(y) \tag{6.19}
$$

$$
\Phi(x,y) = \Phi_0(x,y) + \sum_{p=0}^{P} \sum_{q=0}^{Q} \phi_{pq} X_p(x) Y_q(y) \tag{6.20}
$$

where $X_r(x)$, $Y_s(y)$, $X_p(x)$, $Y_q(y)$ are shapes functions for the transverse deflection w and stress function Φ, respectively. In the authors' previous works, the Legendre Polynomials are applied, which had been approved to have the advantages in capturing

local structural behavior. Substituting Eqs. (6.19−6.20) into Eq. (6.18) and applying the Rayleigh−Ritz method, a set of nonlinear algebraic equations are obtained and expressed in the following tensor form,

$$K_{pi}^{mm}\phi_p + K_{li}^{mc}c_l + K_{li}^{md}d_l + K_{rsi}^{mb}W_rW_s = 0$$

$$K_{pi}^{cm}\phi_p + K_{li}^{cc}c_l + K_{li}^{cd}d_l + K_{rsi}^{cb}W_rW_s = F_i^x$$

$$K_{pi}^{dm}\phi_p + K_{li}^{dc}c_l + K_{li}^{dd}d_l + K_{rsi}^{db}W_rW_s = F_i^y$$

$$K_{ri}^{bb}W_r - K_{rpi}^{bm}W_r\phi_p - K_{rli}^{bc}W_rc_l - K_{rli}^{bd}W_rd_l = 0$$

$$(6.21)$$

where K_{pi}^{mm}, K_{li}^{mc}, ... represent various stiffness matrices for a composite plate in the postbuckled state. The letters (b; m; c; d) in the superscript of each stiffness matrix (K) denote bending, membrane, the boundaries of loaded edges and transverse edges, respectively. A combination of two letters represents coupling effects, for example, K_{rsi}^{mb} denotes the nonlinear coupling between stretching and bending. The explicit expressions of the elements in each matrix can be found in Ref. [22]. A numerical routine based on Eqs. (6.19−6.21) was implemented for the prebuckling, buckling, and postbuckling analysis of composite plates, including a specific routine for analyzing the VAT composite laminates. First, the values of each stiffness matrix in Eq. (6.21) are computed. The integrations in the stiffness matrices, such as K_{ri}^{bb}; K_{pi}^{mm}; K_{li}^{mc}; ..., that may contain the variable stiffness terms are evaluated numerically. A modified Newton−Raphson method [22] is applied to solve the nonlinear algebraic equations and determine the postbuckling equilibrium paths. In the Newton−Raphson method, the applied load (displacement) is subdivided into a series of small incremental load steps, and in each step, the unknown coefficients of the deflection function (w) and stress function (ϕ, c; d) are obtained by an iterative procedure. It is to be noted that the initial step sizes are usually required to be sufficiently small to ensure convergence. The Jacobian matrix of Eq. (6.21) can also be derived analytically to improve the computational efficiency.

6.3.3 Postbuckling stiffness indices

We normalized the postbuckling solutions with respect to a homogeneous quasi-isotropic laminate to benchmark the postbuckling analysis of composite laminates. The equivalent Young's modulus E_{iso}, Poisson's ratio v_{iso} and bending stiffness D_{iso} of the quasi-isotropic laminate are given by Ref. [14],

$$D_{iso} = \frac{E_{iso}h^3}{12(1 - v_{iso}^2)}, \quad v_{iso} = \frac{U_4}{U_1}, \quad E_{iso} = U_1(1 - v_{iso}^2)$$

$$(6.22)$$

where U_1; U_2; U_4 are material invariants as given in Eq. (6.3). The applied loads and end-shortening strains in the postbuckling equilibrium paths are normalized with

respect to that of this quasi-isotropic laminate at its critical buckling state. This quantity, namely, the relative stiffness (denoted by K_r), reflects the proportion of stiffness that remains in the postbuckling regime against its initial prebuckling stiffness (K_{pre}) [13]. The relative stiffness, however, does not convey any information regarding laminate configurations. In order to perform the layup comparison and consider the stiffness in both pre and postbuckling regimes simultaneously, two other quantities are defined in this work to characterize the postbuckling behaviors of VAT laminates. One is the normalized postbuckling stiffness (K_{post}), which is defined as the slope of the initial postbuckling range normalized by the prebuckling stiffness (K_{iso}) of a quasi-isotropic laminate. The other is the normalized overall stiffness (K_o) that is directly quantized by the end-shortening strain (ε_x^{iso}) under a certain load condition (N_{x0}), which is often chosen to be in the range of one to three times the critical buckling load of the quasi-isotropic laminate (N_x^{iso}). The formulae for calculating these stiffness indices are expressed as,

$$K_{pre} = \frac{N_x^{cr}}{\varepsilon_x^{cr}} = a\frac{N_x^{cr}}{\Delta_x^{cr}}, \quad K_r = \frac{1}{K_{pre}}\left(\frac{dN}{d\varepsilon}\right)$$

$$\tag{6.23}$$

$$K_{post} = \frac{1}{K_{iso}}\left(\frac{dN}{d\varepsilon}\right), \quad K_0 = \frac{1}{K_{iso}}\frac{N_x^0}{\varepsilon_x}$$

where N_x^{cr}, ε_x^{cr}, Δ_x^{cr} are the critical buckling load, strain, and displacement, respectively.

6.4 Two-level postbuckling optimization of composite structures based on lamination parameters

6.4.1 Two-level optimization framework

6.4.1.1 Optimization criteria

In the post-buckling optimization problem, the objectives are to minimize either the end-shortening strain $\varepsilon_x = \Delta_x/a$ along the loading direction or the maximum transverse deflection w_{max} under a prescribed service load N_{x0}. As the applied loading condition is identical for each optimal design, the overall structural strength, or the load-carrying capacity, directly relates to the resultant end-shortening strain ε_x or the maximum transverse deflection w_{max}. Their evaluation is based on the postbuckling equilibrium paths, which are the load versus end-shortening curves and the nonlinear load versus transverse deflection curves.

6.4.1.2 Feasible region of lamination parameters

In this chapter, only specially orthotropic composite laminates are considered for postbuckling optimization. In other words, there are no in-plane and out-of-plane

couplings ($\boldsymbol{B} = \boldsymbol{0}$), no extension-shear coupling ($A_{16} = 0, A_{26} = 0$) and no flexural-twisting coupling ($D_{16} = 0, D_{26} = 0$). Therefore, two in-plane and two out-of-plane lamination parameters $(\xi_1^A, \xi_2^A), (\xi_1^D, \xi_2^D)$ are sufficient to define the stiffness matrices in Eqs. (6.3) and (6.4). An outer boundary of the feasible region of lamination parameters was often employed in previous optimization works [13]. In the plate postbuckling problem, a strong coupling between the in-plane stiffness and the out-of-plane stiffness was present. Consequently, an accurate boundary of the feasible region of lamination parameters is important for obtaining realistic composite layups. In the previous work by Wu et al. [44], a set of new explicit closed-form expressions that can accurately define the interdependent feasible region. The nonlinear constraints for these four coupled lamination parameters are expressed as,

$$5\left(\xi_1^A - \xi_D^A\right)^2 - 2\left(1 + \xi_2^A - 2\left(\xi_1^A\right)^2\right) \le 0$$

$$\left(\xi_2^A - 4t\xi_1^A + 1 + 2t^2\right)^3 - 4\left(1 + 2|t| + t^2\right)^2\left(\xi_2^D - 4t\xi_1^D + 1 + 2t^2\right) \le 0$$

$$\left(\xi_2^A - 4t\xi_1^A + 1 + 2t^2\right)^3 - 4\left(1 + 2|t| + t^2\right)^2\left(\xi_2^D - 4t\xi_1^D + 1 + 2t^2\right) \le 0$$

$$\tag{6.24}$$

where $t = [-1; -0.75; -0.5; -0.25; 0; 0.25; 0.5; 0.75; 1]$, or for better accuracy,

$t = [-1; -0.8; -0.6; -0.4; -0.2; 0; 0.2; 0.4; 0.6; 0.8; 1]$. These $19 \sim 23$ equations in Eqs. (5–7) are able to accurately bound the feasible region of the four lamination parameters $\xi_{A,D}^{1,2}$.

6.4.1.3   Two-level optimization

A two-level optimization procedure is applied to perform the optimal design of the postbuckling behavior of composite plates, both constant stiffness (straight fiber) and variable stiffness (VAT) laminates. At the first step, a gradient-based mathematical programming technique is used to determine the optimal values (distributions for VAT composites) of lamination parameters, which give the desired postbuckling performance/strength. At the second step, a genetic algorithm (GA) is employed as an optimizer to obtain the actual layups, including the stacking sequence and fiber orientation angles, from the target values (distributions) of lamination parameters.

First-level optimization
In the postbuckling response of composite laminated plates, the optimization problem is expressed as.

Minimize:

$$\varepsilon_x(\boldsymbol{\xi}) / \varepsilon_x^{iso} \text{ or } w_{max}(\boldsymbol{\xi})/h \tag{6.25}$$

Design variables:

$$\xi = \left[\xi_1^A,\ \xi_2^A,\ \xi_1^D,\ \xi_2^D\right]\ \text{(at each control point for VAT laminates)}$$

Subjected to:

$$g_j(\xi) \leq 0 \tag{6.26}$$

where g_j are the constraint functions defined in Eq. (6.24) that define the feasible region of these four lamination parameters.

At the first level, for the postbuckling optimization of variable stiffness (VAT) composite laminates, B-spline functions are employed to define the spatial variation of lamination parameters (variable stiffness). A given degree of B-spline curve/surface is determined by a set of control points and a prescribed knot vector. The control points are distributed over the plate domain, and the design variables (lamination parameters) are associated with each control point. As illustrated in Fig. 6.2, the design flexibility is adjusted by altering the number and position of control points, the degree, and the knot vector of the spline functions. Compared with the discretized finite element approach, using B-splines to represent the spatial variation of lamination parameters requires fewer design variables and leads to a continuous and smooth distribution. In addition, the convex hull property of B-splines enforces the spatially varying lamination parameter across the planform of the plate to be fully constrained inside the feasible region, provided that the lamination parameters at the control points satisfy all the nonlinear constraints.

The first-level postbuckling optimization problem in Eq. (6.25), which is defined in terms of the lamination parameters, can be effectively solved using a gradient-based mathematical programming algorithm. The GCMMA (Globally Convergent Method of Moving Asymptotes) approach had been approved to be an effective algorithm in our previous works [21,37,38]. In a GCMMA approach, the objective function and
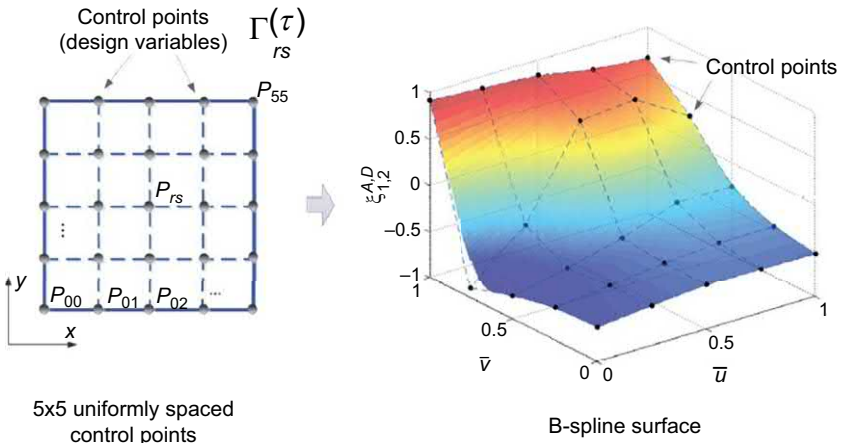
Figure 6.2 Illustration of B-spline surface constructing by five-by-five uniformly spaced control points.

the nonlinear constraints are approximated by convex separable forms in a local region as,

$$\bar{f}_i^{(\mu,v)}(\xi) = \sum_{j=1}^{4} \left(\frac{p_{ij}^{(\mu,v)}}{\alpha_j^{(\mu)} - \xi_j} + \frac{q_{ij}^{(\mu,v)}}{\xi_j - \beta_j^{(\mu)}} \right) + r_i^{(\mu,v)} \tag{6.26}$$

where μ and v denote the indices of the "outer" and "inner" iterations, respectively. For the detailed expression of each variable in Eq. (6.26), refer to Svanberg's work. The approximating formula of Eq. (6.26) for the objective function and nonlinear constraints is shown to be convex separable and conservative with respect to each design variable (lamination parameters). The advantages of applying the GCMMA approach is that the feasible constraints can be strictly satisfied in an optimization process, and there is a strong likelihood of finding the globally optimal solution.

Second-level optimization

The second-level optimization process is applied to retrieve a realistic composite layup. For simulating the specially orthotropic composite laminates, an antisymmetrical stacking sequence with specially orthotropic properties ($[B] = 0$, $A_{16}, A_{26} = 0$, $D_{16}, D_{26} = 0$) is used. For instance, the stacking sequence with a 16-layer composite laminate $[\pm \theta_1 / \mp \theta_1 / \pm \theta_2 / \mp \theta_1]_{AS}$ possesses two independent ply orientations. Larger design freedoms can be achieved in the second-level optimization process by adding more design layers. Subsequently, a genetic algorithm (GA) is used to determine the fiber orientation angles for each design layer, which results in lamination parameters matching the desired results closely. The fitness function is expressed as a mean value of the least-square distance between the obtained lamination parameters and the target lamination parameters. The optimization problem is formulated as follows:

Minimum:

$$\Delta \xi(\theta_i) = \left[\sum_i^2 w_i^A \left(\xi_i^A - \tilde{\xi}_i^A \right)^2 + \sum_i^2 w_i^D \left(\xi_i^D - \tilde{\xi}_i^D \right)^2 \right]$$

$$\xi_{1,2}^{A,D} \leftarrow [\theta_1, \ \theta_2, \theta_3, \theta_4]$$

Subjected to: $-\pi/2 \leq \theta_i \leq \pi/2$ \hfill (6.27)

where θ_i is the fiber angle at each design layer, and w_i^A and w_i^D are the weights to distinguish the relative importance between $\xi_{1,2}^A$ and $\xi_{1,2}^D$. Based on our trial-and-error experiences, the population size was set to be at least 20–30 times the number of design variables, whereas, the number of generations is usually set to 50–100, depending on the population size. The crossover and mutation probabilities were chosen to be 0.7 and 0.04.

For retrieving the VAT laminate layup from a target lamination parameters distribution, each VAT layer is parameterized by the fiber angles defined at a set of control points. A smooth nonlinear variation (NLV) of fiber orientation angles over the plate domain is generated using Lagrangian polynomials, as given in Ref. [36]. Subsequently, a GA is used to determine the fiber orientation angles at all the control points of each VAT layer. The fitness function of second-level optimization is expressed as a mean value of the least square distance between the obtained stiffness variation and the target stiffness variation at a large number of grid points over the plate domain.

$$\text{Minimize: } \Delta \xi = \frac{1}{N_p} \sum_j \Delta \xi_j$$

$$\Delta \xi_j = \left[\sum_i^2 w_i^A \left(\xi_i^A - \tilde{\xi}_i^A \right)^2 + \sum_i^2 w_i^D \left(\xi_i^D - \tilde{\xi}_i^D \right)^2 \right]_{(j)}$$

$$\xi_{1,2}^{A,D} \leftarrow \left[T_1^k, \cdots, T_n^k, \cdots, T_N^k \right]$$

$$\text{Subjected to: } -\pi/2 \leq T_n^k \leq \pi/2 \tag{6.28}$$

where T_n^k is the fiber angle at the control point for the kth ply. The total number of grid points Np is chosen to be 1000 ~ 2000 in total for a two-dimensional variation.

6.4.2 Postbuckling optimization of straight-fiber composite laminates

Fig. 6.3 illustrates the postbuckling optimization results under the case of the biaxial compressive loading conditions ($k = 0.2$). The left plot presents the optimal layups that give the minimum end-shortening strain. As shown in the left plot of Fig. 6.3, the layup $[\pm 35/\mp 35/\pm 20/\mp 20/0_8]_{AS}$ gave the minimum end-shortening strain for the axial loading $N_{x0} = 1.5N_x^{iso}$. $[\pm 50/\mp 50/\pm 10/\mp 10/0_8]_{AS}$ was the optimized layup for the minimum end-shortening strain when axial loading $N_{x0} = 1.5N_x^{iso}$ or $N_{x0} = 2.5N_x^{iso}$. It shows that a large proportion of 0 degree plies in a laminate is also important for minimizing the end-shortening strains for biaxial compressive loading cases. In the right plot of Fig. 6.3, the optimal layup $[(\pm 45/\mp 45)_2/\pm 75/\mp 75/0_4]_{AS}$ shows the minimum of maximum transverse deflections when $N_{x0} = 1.5N_x^{iso}$, $[\pm 60/\mp 60/\pm 90/\mp 90/0_4]_{AS}$ are the optimized layups for $N_{x0} = 2N_x^{iso}$ and $[\pm 70/\mp 70/\pm 90/\mp 90/0_4]_{AS}$ for $N_{x0} = 2.5N_x^{iso}$, respectively. It is interesting to observe that the inner layers of all of these layups are always a combination of $[90_n/0_n]$ which is beneficial for a laminate to minimize its membrane strains, and hence, its nonlinear (in the von Kármán sense) maximum transverse deflection.
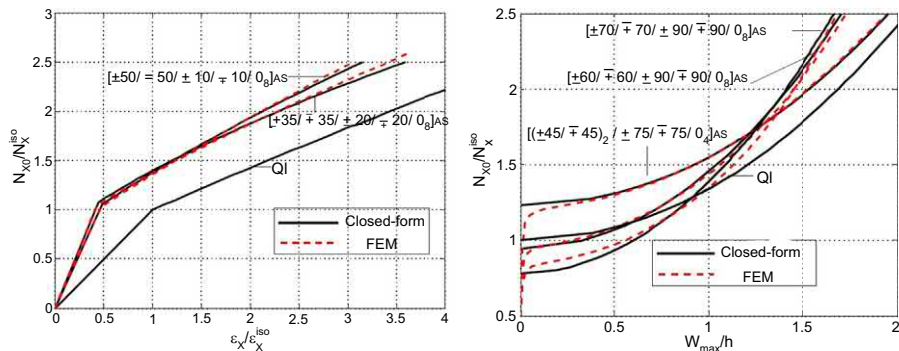
Figure 6.3 Optimal layups of a square plate under biaxial compression (k = 0.2) for minimizing ε_x (left plot) or minimizing w_{max} (right plot) (QI, Quasi-Isotropic).

6.4.3 Postbuckling optimization of variable angle tow composite laminates

The two-level optimization method is also applied to perform the optimal design of postbuckling behavior of compressive loaded, simply supported, and square VAT composite plates. The optimal layups which give the minimum end-shortening strain or the maximum transverse displacement may be different when the level of axial compressive load N_{x0} is changed. Herein, in the optimization of VAT laminates for giving the minimum end-shortened strain ε_x, the value of the compressive axial load N_{x0} is set to be 2.5 times of the critical buckling load ($2.5N_{iso}$) of an equivalent quasi-isotropic laminate. The optimal variations (7×7 control points) of the four lamination parameters of the VAT plate that gives minimum end-shortening strain ε_x. The postbuckling equilibrium paths for the optimized constant stiffness and VAT laminates are compared and illustrated in Fig. 6.4. The layup $[45/0_6]_s$ gives the minimum end-shortening strain among the constant stiffness laminates. VAT #1 is the optimal design using a direct GA approach [37], and VAT #2 is the optimal design result using the two-level optimization approach. It was shown that there is approximately 21% increment for the optimal design layup VAT #2 compared with the best straight-fiber layup $[45/0_6]_s$. The right plot in Fig. 6.5 illustrates the optimal fiber-angle varying distributions which are retrieved from the left-hand side target distribution of lamination parameters. The numerical results also demonstrate the robustness and computational efficiency of the proposed two-level optimization methodology for the postbuckling design of VAT laminates.

6.4.4 Postbuckling optimization of variable thickness, variable angle tow composite laminates, toward "buckle-design" concept

This section presents the optimal postbuckling designs for VAT panels with independent thickness variation, which provides a very large design flexibility of general
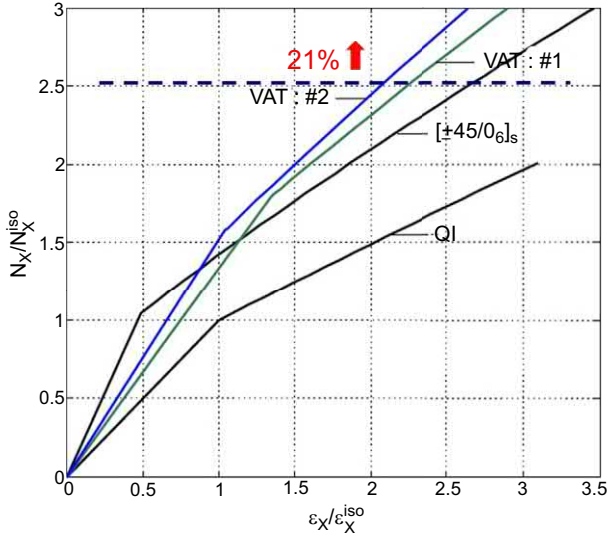
Figure 6.4 Postbuckling behavior comparison on the normalized axial loads versus normalized axial strain.

variable stiffness tailoring. The postbuckling optimization problem with the general variable stiffness tailoring considers the stiffness variation that is defined in terms of four lamination parameters ($\xi_{1,2}^{A,D}$) and a thickness variable associated with each control point of the B-spline function. The first-level postbuckling optimization is then formulated as,

$$\text{Minimize: } \varepsilon_x^0\left(\Gamma_{mn}^{(\tau)},\ h_{mn}\right)$$

$$\text{subjected to: } -1 \leq \Gamma_{mn}^{(\tau)} \leq 1$$

$$g_i\left(\Gamma_{mn}^{\tau}\right) \leq 0$$

$$h_L \leq h_{mn} \leq h_U \qquad\qquad\qquad (6.29)$$

$$\frac{1}{ab} \int\limits_{-a/2}^{a/2} \int\limits_{-b/2}^{b/2} h(x,y)dxdy - h_0 \leq 0$$

First, for the purpose of simplicity, one-dimensional stiffness variation along y direction (within 7 control points defining the B-spline function) is allowed in the post-buckling optimization. Fig. 6.6(a) illustrates different one-dimensional optimal post-buckling results (from VAT panels #3 to #6) that are obtained by setting different
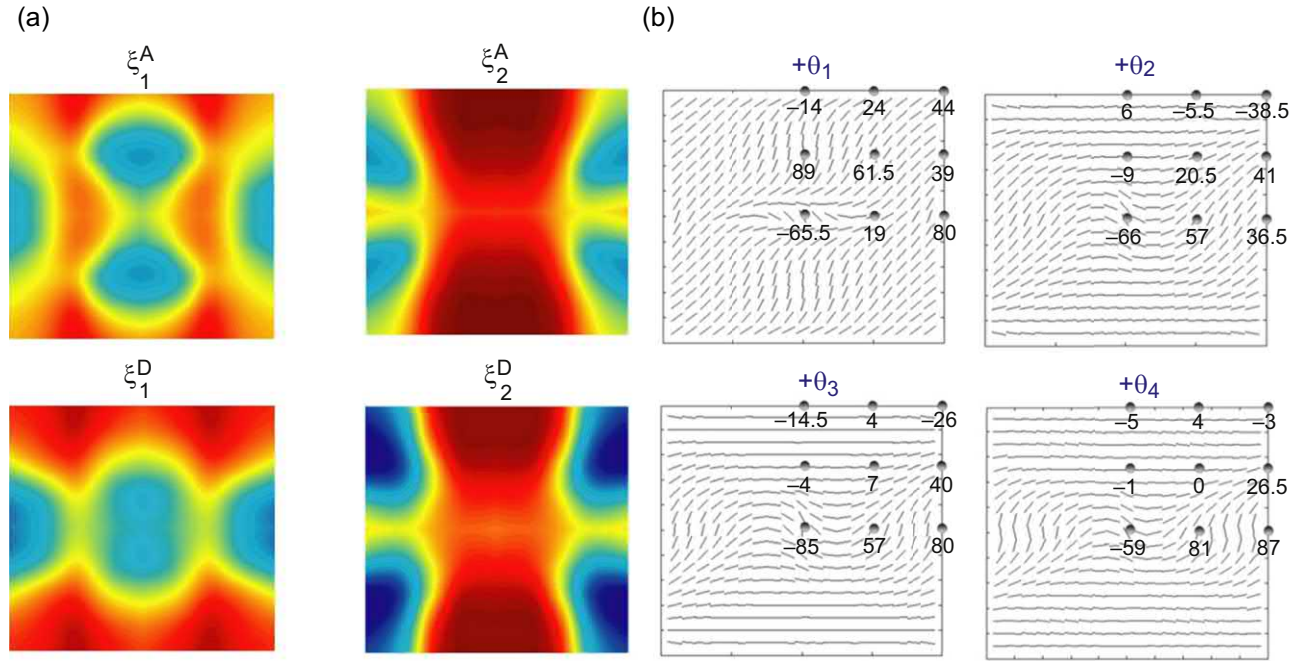
Figure 6.5 (a) Optimal lamination parameter distribution for minimizing ε_x of a square simply supported plate; (b) The optimum nonlinear variation (3×3 control points for each layer) of fiber-orientation distribution for minimizing ε_x of the square simply supported VAT plate design.

(a)

(b)
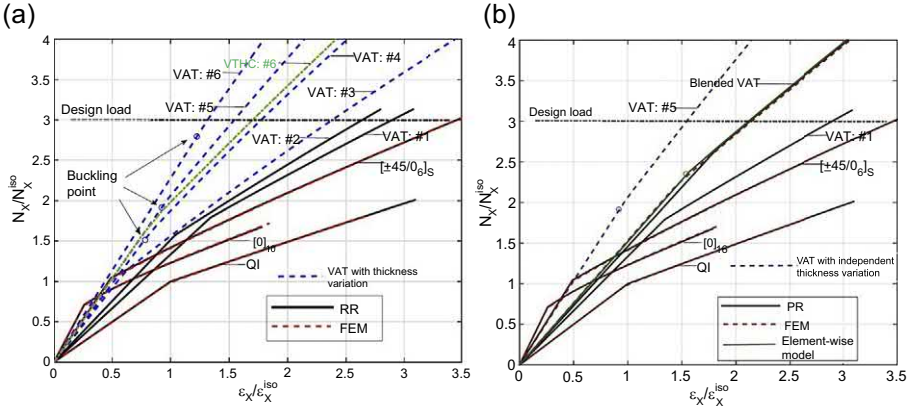
Figure 6.6 Postbuckling responses of the optimal VAT layups with different thickness variation patterns for a square panel under a given uniaxial compressive loading ($N_{x0} = 3 N_x^{iso}$) for minimizing the end-shortening strain: (a) VAT#1-2: constant thickness, VAT#1 = 3−6: different thickness variation; (b) A blended VAT panel design compared with other VAT plates.

ranges of thickness variation. The upper bound of the thickness variation is set to be $h_U = 4h_0$, which is the maximum thickness build-up given by a CTS-manufacturing lamina with 75 °shear angle. The VAT panels #3, #4, #5 and #6 are the optimal results when the lower bound of thickness variation is chosen to be $h_L = 0.9h_0, 0.7h_0, 0.5h_0$ and $0.25h_0$, respectively. From the postbuckling results shown in Fig. 6.6(a) for the VAT panels #3 to #6, it can be seen that the postbuckling performance (overall axial stiffness) of the VAT panels can be substantially improved through inducing an independent thickness variation in the variable stiffness design. Moreover, the reduction in axial compressive stiffness of VAT panels #4 to #6 after entering the postbuckling regime is extremely low. The critical buckling points for the VAT panels #4 to #6 become less clear and are denoted by small circles in Fig. 6.6. Therefore, the "Buckle-Free" design concept is eventually achieved. These results (VAT panels #3 to #6) also indicate that substantial benefits are received in the postbuckling behavior design of VAT panels through general stiffness tailoring. Nevertheless, the VAT panel #6 is already approaching an ideal "Buckle-Free" panel design. VAT panels #4 to #6 are the optimal results from the first-level optimization process, of which, only the variable stiffness distributions are given.

A blended panel design scheme is then considered and optimized to match the target stiffness distribution of VAT panel #5 that is obtained from the first-level optimization process. As shown in Fig. 6.7(a), this blended panel is split into three parts that consist of one constant thickness central element and two outer elements with a large amount of thickness build-up. It was also noticed that the thickness variation pattern in the outer regions in Fig. 6.7(a) is similar to the thickness build-up of a CTS laminate with large shear angles along the edges. Therefore, a blended panel design scheme with eight AFP-manufacturing constant thickness plies ($\left[\pm\theta_1^{AFP}\right]_{2s}$)
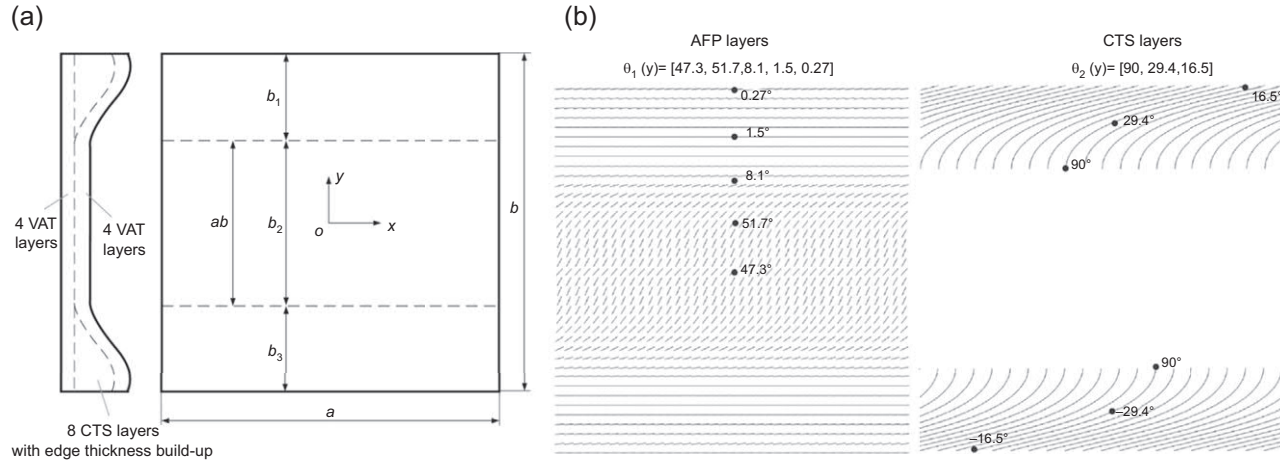
Figure 6.7 Illustration of a blended VAT panel design with eight constant thickness VAT plies $\left(\left[\pm\theta_1/\pm\theta_1\right]_s\right)$ over the entire plate and eight segmentally placed CTS plies at the outer regions ($\left[\pm\theta_2/\pm\theta_2\right]_s$). Optimized tow trajectories of constant thickness VAT (AFP-manufactured) plies (θ_1 defined by five control points) and CTS plies (θ_2 defined by three control points).

over the entire plate and eight segmentally placed CTS composite plies at the outer regions $\left(\left[\pm\theta_2^{\mathrm{CTS}}\right]_{2s}\right)$ is designed, and the curvilinear tow paths are illustrated in Fig. 6.7(b). The width ratio (α) of the central element is determined first from the thickness variation of VAT panel #5, that is $\alpha = b_2/b = 0.5586$ for this case. Subsequently, the second-level optimization process, as stated in Eq. (6.28) is carried out to determine the optimal fiber angles at the control points prescribed for the AFP layers ($\pm\theta_1$) and the CTS layers ($\pm\theta_2$). The second-level optimization solution enables the blended VAT panel to possess the closest stiffness variation to that of the VAT panel #5. Fig. 6.7(b) shows the optimal results for the tow (fiber) trajectories of the AFP layers and CTS layers, which are both varying along y direction and are characterized by five and three control points, respectively. As shown in Fig. 6.7, the constant-thickness AFP layers cover the entire panel, while CTS layers only placed at two outer regions for the blended VAT panel. The large axial compressive stiffness of this blended VAT panel benefits from a large amount of 0-degree fiber placement at the outer regions and the edge thickness build-up pattern given by the segmental CTS layers.

References

[1] C. Kassapoglou, Design and Analysis of Composite Structures: With Applications to Aerospace Structures, second ed., John Wiley & Sons, 2013.

[2] S. Levy, Bending of Rectangular Plates with Large Deflection, National Advisory Committee for Aeronautics (United States Advisory Committee for Aeronautics), Washington, DC, United States, 1942, p. 19.

[3] H.L. Cox, The Buckling of Thin Plates in Compression. British A.R.C., R. & M., 1933, p. 1554.

[4] K. Marguerre, The apparent width of the plate in compression. NACA, 1937. No. 833.

[5] J.M. Coan, Large-deflection theory for plates with small initial curvature loaded in edge compression, in: American Society of Mechanical Engineers — Meeting A-2, Nov 26—Dec 1, 1950, American Society of Mechanical Engineers (ASME), New York, NY, United States, 1950.

[6] M.K. Prabhakara, C.Y. Chia, Postbuckling behaviour of optimized rectangular composite laminates, J. Mech. Eng. Sci. 15 (1) (1973) 25—33.

[7] D.K. Shin, O.H. Griffin, Z. Gürdal, Postbuckling response of laminated plates under uniaxial compression, Int. J. Non-Linear Mech. 28 (1) (1993) 95—115.

[8] N. Yamaki, Postbuckling behavior of rectangular plates with small initial curvature loaded in edge compression, in: ASME Meeting, Nov 30—Dec 5, 1958, American Society of Mechanical Engineers (ASME), New York, NY, United States, 1958.

[9] M. Feng, An energy theory for postbuckling of composite plates under combined loading, Comput. Struct. 16 (1) (1983) 423—431.

[10] O. Seresta, M. Abdalla, Z. Gurdal, Optimal design of laminated composite plate for maximum postbuckling strength, in: 46th AIAA/ASME/ASCE/AHS/ASC Structures, Structural Dynamics and Materials Conference, American Institute of Aeronautics and Astronautics, 2005.

[11] N. Sherbourne Archibald, K. Bedair Osama, Plate-Stiffener assemblies in uniform compression. Part II: postbuckling, J. Eng. Mech. 119 (10) (1993) 1956−1972.

[12] G.Z. Harris, The buckling and post-buckling behaviour of composite plates under biaxial loading, Int. J. Mech. Sci. 17 (3) (1975) 187−202.

[13] C.G. Diaconu, P.M. Weaver, Approximate solution and optimum design of compression-loaded, postbuckled laminated composite plates, AIAA J. 43 (4) (2005) 906−914.

[14] C.G. Diaconu, P.M. Weaver, Postbuckling of long unsymmetrically laminated composite plates under axial compression, Int. J. Solids Struct. 43 (22) (2006) 6978−6997.

[15] W.T. Koiter, On the Stability of Elastic Equilibrium (in Dutch), Delft University, 1945.

[16] W.T. Koiter, Elastic Stability of Solids and Structures, Cambridge University Press, 2009.

[17] M. Stein, Loads and Deformations of Buckled Rectangular Plates, National Aeronautics and Space Administration (NASA), Washington, DC, United States, 1959, p. 71.

[18] M. Stein, Phenomenon of Change in Buckle Pattern in Elastic Structures, National Aeronautics and Space Administration (NASA), Washington, DC, United States, 1959, p. 22.

[19] S. Hui-shen, Z. Jian-wu, Perturbation analyses for the postbuckling of simply supported rectangular plates under uniaxial compression, Appl. Math. Mech. 9 (8) (1988) 793−804.

[20] J.W. Zhang, H.S. Shen, Postbuckling of orthotropic rectangular plates in biaxial compression, J. Eng. Mech. 117 (5) (1991) 1158−1170.

[21] Z. Wu, G. Raju, P. Weaver, Analysis and design for the moderately deep postbuckling behavior of composite plates, J. Aircr. 54 (1) (2016) 327−335.

[22] Z. Wu, G. Raju, P.M. Weaver, Postbuckling analysis of variable angle tow composite plates, Int. J. Solids Struct. 50 (10) (2013) 1770−1780.

[23] G. Raju, Z. Wu, P. Weaver, Postbuckling response of variable angle tow composite plates under shear load, in: 54th AIAA/ASME/ASCE/AHS/ASC Structures, Structural Dynamics, and Materials Conference, American Institute of Aeronautics and Astronautics, 2013.

[24] J.N.B. Dickson, S.B. Biggers, POSTOP: postbuckled open-stiffener optimum panels-theory and capability, NASA-CR-172259 26 (1984) 172259.

[25] D.K. Shin, Z. Gürdal, J.O.H. Griffin, Minimum weight design of laminated composite plates for postbuckling performance, Appl. Mech. Rev. 44 (11S) (1991) S219−S231.

[26] D. Bushnell, Optimization of composite, stiffened, imperfect panels under combined loads for service in the postbuckling regime, Comput. Methods Appl. Mech. Eng. 103 (1) (1993) 43−114.

[27] C. Bisagni, R. Vescovini, Fast tool for buckling analysis and optimization of stiffened panels, J. Aircr. 46 (6) (2009) 2041−2053.

[28] C.A. Perry, Z. GÜRdal, J.H. Starnes, Minimum-weight design of compressively loaded stiffened panels for postbuckling response, Eng. Optim. 28 (3) (1997) 175−197.

[29] F.G. Stoll, Zafer, J.H. Starnes Jr., A method for the geometrically nonlinear analysis of compressively loaded prismatic composite structures, NASA-CR-184846 26 (1991) 184846. NAS 1.

[30] W. Liu, et al., Bilevel optimization and postbuckling of highly strained composite stiffened panels, AIAA J. 44 (11) (2006) 2562−2570.

[31] M. Lillico, et al., Analysis and testing of a postbuckled stiffened panel, AIAA J. 40 (5) (2002) 996−1000.

[32] L. Lanzi, V. Giavotto, Post-buckling optimization of composite stiffened panels: comsputations and experiments, Compos. Struct. 73 (2) (2006) 208−220.

[33] C. Bisagni, L. Lanzi, Post-buckling optimisation of composite stiffened panels using neural networks, Compos. Struct. 58 (2) (2002) 237−247.

[34] C. Wu, Z. Gurdal, J. Starnes, Structural response of compression-loaded, tow-placed, variable stiffness panels, in: 43rd AIAA/ASME/ASCE/AHS/ASC Structures, Structural Dynamics, and Materials Conference, American Institute of Aeronautics and Astronautics, 2002.

[35] Z. Gürdal, B.F. Tatting, C.K. Wu, Variable stiffness composite panels: effects of stiffness variation on the in-plane and buckling response, Compos. Appl. Sci. Manuf. 39 (5) (2008) 911−922.

[36] Z. Wu, et al., Buckling analysis and optimisation of variable angle tow composite plates, Thin-Walled Struct. 60 (2012) 163−172.

[37] Z. Wu, P.M. Weaver, G. Raju, Postbuckling optimisation of variable angle tow composite plates, Compos. Struct. 103 (2013) 34−42.

[38] Z. Wu, G. Raju, P.M. Weaver, Optimization of postbuckling behaviour of variable thickness composite panels with variable angle tows: towards "Buckle-Free" design concept, Int. J. Solids Struct. 132−133 (2018) 66−79.

[39] G. Raju, et al., Optimal postbuckling design of variable angle tow composite plates, AIAA J. 56 (5) (2018) 2045−2061.

[40] E.H. Mansfield, The Bending and Stretching of Plates, Cambridge University Press, 1989.

[41] R.M. Jones, Mechanics of Composite Materials, 1986, p. 538.

[42] P.S. Bulson, The stability of flat plates, Chatto & Windus, 1970.

[43] B. Budiansky, Theory of buckling and post-buckling behavior of elastic structures, in: C.-S. Yih (Ed.), Advances in Applied Mechanics, Elsevier, 1974, pp. 1−65.

[44] G.R. Zhangming Wu, P.M. Weaver, Framework for the buckling optimization of variable-angle tow composite plates, AIAA J. 53 (12) (2015) 3788−3804.

Stiffness & strength of composite structural elements **7**

C. Kassapoglou
Delft University of Technology, Delft, The Netherlands

7.1 Introduction

A successful design of a composite structure hinges, among other things, on accurate estimates of its stiffness and strength.

In principle, knowledge of the stiffness and strength of the individual constituents, fibers and matrix, should allow accurate determination of the corresponding properties in the resulting composite structure. However, despite a lot of progress over the last few decades, there are still no analytical models that can accurately bridge the different scales from the individual fiber and matrix (micromechanics) to the actual structure (macroscopic scale). This problem is particularly pronounced by the lack of analytical methods that accurately predict failure in composites.

These difficulties have led to the development of models that start from a longer scale than the individual fiber and matrix, the scale of an individual ply. Based on this, models predicting the stiffness of composite laminates or structures are quite accurate. Strength models, on the other hand, need further development.

In Section 7.2, the structural elements are described briefly in order to give the reader a better understanding of the size and complexity that they entail. Then, some of the more representative models for predicting stiffness and strength of these elements, made from uni-directional tape material, are outlined in Section 7.3. A brief discussion of woven composites with emphasis on the differences of composites made with tape material is given in Section 7.4. In Section 7.5, some models for incorporating manufacturing anomalies, such as voids are presented. Additional sources discussing the topics presented in this chapter in more detail are provided in Section 7.6. Finally, a brief presentation of some future trends is given in Section 7.7.

7.2 Definition of structural elements

Composite airframe structures consist of special-purpose parts (e.g., skins, spars, etc.) which, in turn, are made of smaller structural elements that are put together to create the various parts. The subdivision into structural elements is subjective, and often, a matter of convenience. However, using commonality of purpose and shape as the distinguishing characteristics, the following classification into structural elements can be made:

1. Skins. Flat or curved parts carrying primarily in-plane and pressure loads
2. Stiffeners, stringers. One-dimensional parts carrying the load along their axis

3. Fittings and joints. Complex, usually three-dimensional, parts used to connect other structural elements, and typically, carrying loads in multiple directions

4. Frames. Two-dimensional parts consisting of webs, stiffeners, and caps carrying bending and shear loads

5. Bulkheads. Two-dimensional parts carrying pressure and bending loads

6. Ribs, decks, intercostals. Two-dimensional parts carrying in-plane loads (tension, compression, and shear) and used to connect and support other structural elements.

Some representative structural elements are shown in Fig. 7.1. As already mentioned, this classification is a matter of convenience. It does not mean that one cannot subdivide some of these elements into smaller components. For example, a stiffener or a frame can be broken down into webs and flanges. Nor does it mean one cannot lump some of these to form more complex elements, such as stiffened skins for example (Fig. 7.1b).
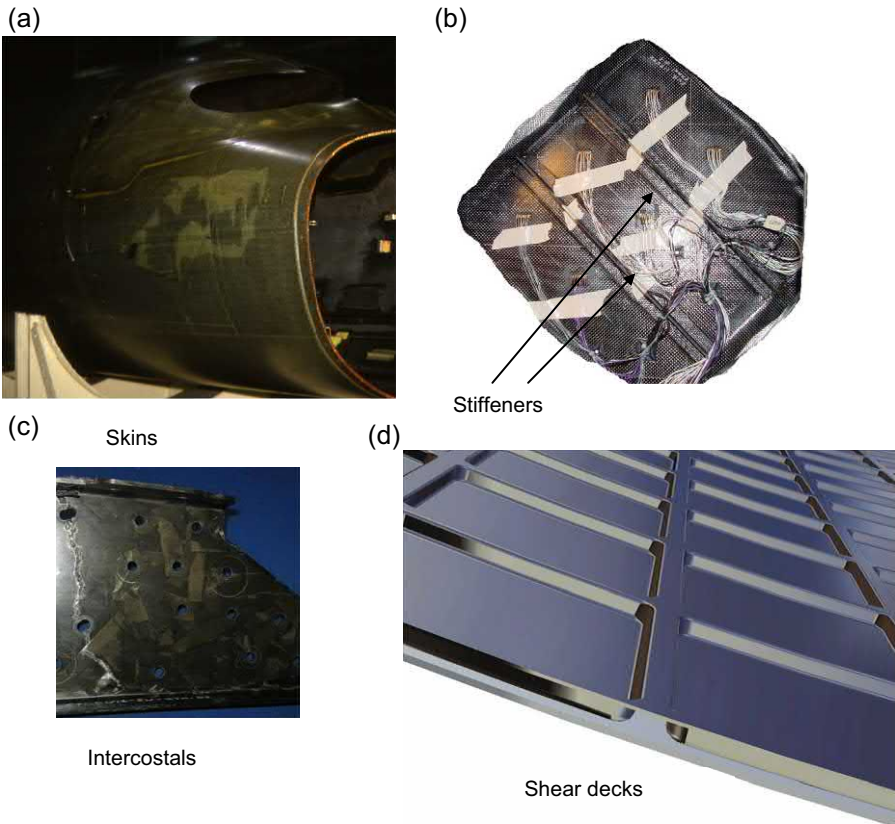
Figure 7.1 Structural elements; Skins (a Top left), Stiffeners (b Top right), Intercostals (c Bottom left), Shear decks (d Bottom right).

The deformation of these structural elements under a given loading is a function of their respective stiffness. These elements are combined to make specific airframe parts. It is, therefore, expected that one could combine the analysis methods of the individual structural elements with a model of the load transfer at the connections or joints between elements, to develop an accurate model for the structural response of airframe parts. While this, in principle, is possible and it is done often, in practice, the accuracy of the developed model, especially for the strength, requires additional modeling efforts and methodology development. Even then, analysis of some parts, such as three-dimensional fittings does not provide accurate predictions for their strength, and additional testing is required. This testing either replaces the analysis methods altogether or provides inputs for tuning analytical models to match test results.

The emphasis, in this chapter, is placed on relatively thin parts and is mainly based on plane stress situations, where one of the dimensions is small relative to the others, and the deformations are in the linear range. Thicker parts require additional analysis methods, which are not discussed here in detail.

7.3   Modeling approaches

As already referred to in Section 7.1, it is important to select the basic building unit that will be used to create the model for the more complex structure. Here, the individual ply or lamina is selected as the basic unit.

It is assumed that the properties of an individual ply are known in some coordinate system. In addition, the following assumptions are made:

1. The fibers and matrix can be treated together as a homogeneous material with smeared properties
2. There is a perfect bond between fibers and matrix
3. There is a perfect bond between plies
4. Plane sections remain plane.
5. Sections perpendicular to the neutral axis remain perpendicular after deformation

The first assumption allows the development of "averaged" stiffness values for each ply which depend on the individual stiffnesses of the fibers and matrix. The second and third assumptions are necessary for the development of the weighted stiffnesses for each ply and for each laminate. They can be relaxed when dealing with some failure modes, such as fiber pull-out and delamination. The last two assumptions form the Kirchhoff hypothesis and ensure small deflections and rotations.

For simplicity, it will be assumed that the structure consists of laminates made with uni-directional tape plies and linear stress-strain response. The equations derived are, in general, valid for other material forms, such as fabrics with some differences that will be pointed out in subsequent sections.

The basic approach [1−4] starts with a single orthotropic ply. In the coordinate system of the ply, with one axis parallel to the fibers and one perpendicular to the fibers, in the plane of the ply, the stiffness properties are assumed to be known. These stiffness values may be obtained from analytical modeling at lower scales using micromechanics or may be obtained experimentally with ply coordinates 1 and 2, as opposed to the laminate coordinates x and y (see Fig. 7.2).

7.3.1 The single-ply coordinate system

A single orthotropic ply in the ply coordinate system (Fig. 7.2) is characterized by the following stress-strain relationships:

$$
\begin{Bmatrix} \sigma_1 \\ \sigma_2 \\ \tau_{12} \end{Bmatrix} = \begin{bmatrix} Q_{11}^{(0)} & Q_{12}^{(0)} & 0 \\ Q_{12}^{(0)} & Q_{22}^{(0)} & 0 \\ 0 & 0 & Q_{66}^{(0)} \end{bmatrix} \begin{Bmatrix} \varepsilon_1 \\ \varepsilon_2 \\ \gamma_{12} \end{Bmatrix} \tag{7.1}
$$

The ply stiffnesses $Q_{ij}^{(0)}$ are, in turn, obtained from four experimentally measured stiffness properties:

- E_L, the longitudinal Young's modulus parallel to the fibers,
- E_T, the transverse Young's modulus perpendicular to the fibers,
- G_{LT}, the in-plane shear modulus, and
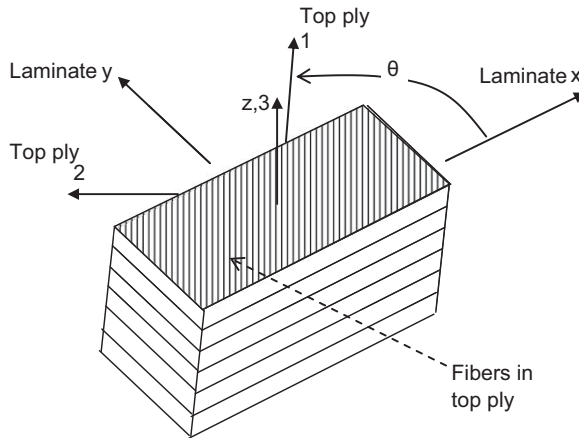
Figure 7.2 Ply and laminate coordinate systems.

– ν_{LT} the major Poisson's ratio showing the amount of contraction (or expansion) in the direction perpendicular to the fibers due to a tension (or compression) load in the direction parallel to the fibers

By considering the response of a single ply to the different types of loading corresponding to the above stiffness properties, one can show that:

$$Q_{11}^{(0)} = \frac{E_L}{1 - \nu_{LT}\nu_{TL}}$$

$$Q_{22}^{(0)} = \frac{E_T}{1 - \nu_{LT}\nu_{TL}}$$

(7.2a-d)

$$Q_{12}^{(0)} = \frac{\nu_{LT}E_T}{1 - \nu_{LT}\nu_{TL}} = \frac{\nu_{TL}E_L}{1 - \nu_{LT}\nu_{TL}}$$

$$Q_{66}^{(0)} = G_{LT}$$

Note that, as Eq. (7.2c) implies, the minor Poisson's ratio ν_{TL} is related to the major Poisson's ratio via the relation:

$$\nu_{TL} = \nu_{LT}\frac{E_T}{E_L}$$

(7.3)

which is a direct consequence of the symmetry of the stiffness tensor.

Eqs. (7.1) and (7.2) give the stress-strain response of a single ply in its own coordinate system, where one axis is parallel and the other perpendicular to the fibers. In practice, the plies making up a laminate are oriented in different directions (see Fig. 7.2) following the requirements of the design. It is, therefore, necessary to transform stiffness properties, stresses, and strains from the basic ply coordinate system to other coordinate systems, such as the laminate coordinate system.

7.3.2   The laminate coordinate system

In the laminate coordinate system, the stress-strain equations for a single ply can be written in the form:

$$\begin{Bmatrix} \sigma_x \\ \sigma_y \\ \tau_{xy} \end{Bmatrix} = \begin{bmatrix} Q_{xx} & Q_{xy} & Q_{xs} \\ Q_{xy} & Q_{yy} & Q_{ys} \\ Q_{xs} & Q_{ys} & Q_{ss} \end{bmatrix} \begin{Bmatrix} \varepsilon_x \\ \varepsilon_y \\ \gamma_{xy} \end{Bmatrix}$$

(7.4)

Note that in the laminate coordinate system a single ply is not necessarily ortho-tropic. As a result, additional stiffness terms Q_{xs} and Q_{ys} appear. The stiffness proper-ties Q_{xx}, Q_{xy}, etc., can be determined as a function of the stiffness properties $Q_{11}^{(0)}$, $Q_{12}^{(0)}$, etc., that were used in Eq. (7.1) and (7.2). This is done by starting by rotating strains from the ply to the laminate coordinate system using the standard transformation relation:

$$
\begin{Bmatrix} \varepsilon_1 \\ \varepsilon_2 \\ \gamma_{12} \end{Bmatrix} = \begin{bmatrix} \cos^2\theta & \sin^2\theta & \sin\theta\cos\theta \\ \sin^2\theta & \cos^2\theta & -\sin\theta\cos\theta \\ -2\sin\theta\cos\theta & 2\sin\theta\cos\theta & (\cos^2\theta - \sin^2\theta) \end{bmatrix} \begin{Bmatrix} \varepsilon_x \\ \varepsilon_y \\ \gamma_{xy} \end{Bmatrix} \quad (7.5)
$$

where θ is the orientation of the fibers in the ply in question with θ defined positive, as shown in Fig. 7.2.

In addition, the stress transformation relation is also needed:

$$
\begin{Bmatrix} \sigma_1 \\ \sigma_2 \\ \tau_{12} \end{Bmatrix} = \begin{bmatrix} \cos^2\theta & \sin^2\theta & 2\sin\theta\cos\theta \\ \sin^2\theta & \cos^2\theta & -2\sin\theta\cos\theta \\ -\sin\theta\cos\theta & \sin\theta\cos\theta & (\cos^2\theta - \sin^2\theta) \end{bmatrix} \begin{Bmatrix} \sigma_x \\ \sigma_y \\ \tau_{xy} \end{Bmatrix} \quad (7.6)
$$

The transformation matrix involving θ in Eqs. (7.5) and (7.6) is not exactly the same because in Eq. (7.5) the engineering strain γ_{12} instead of the tensorial strain $\varepsilon_{12}(=\gamma_{12}/2)$ is used.

Using Eqs. (7.5) and (7.6) to substitute in Eq. (7.1) gives:

$$
\begin{bmatrix} \cos^2\theta & \sin^2\theta & 2\sin\theta\cos\theta \\ \sin^2\theta & \cos^2\theta & -2\sin\theta\cos\theta \\ -\sin\theta\cos\theta & \sin\theta\cos\theta & (\cos^2\theta - \sin^2\theta) \end{bmatrix} \begin{Bmatrix} \sigma_x \\ \sigma_y \\ \tau_{xy} \end{Bmatrix} = \begin{bmatrix} Q_{11}^{(0)} & Q_{12}^{(0)} & 0 \\ Q_{12}^{(0)} & Q_{22}^{(0)} & 0 \\ 0 & 0 & Q_{66}^{(0)} \end{bmatrix}.
$$

$$
\begin{bmatrix} \cos^2\theta & \sin^2\theta & \sin\theta\cos\theta \\ \sin^2\theta & \cos^2\theta & -\sin\theta\cos\theta \\ -2\sin\theta\cos\theta & 2\sin\theta\cos\theta & (\cos^2\theta - \sin^2\theta) \end{bmatrix} \begin{Bmatrix} \varepsilon_x \\ \varepsilon_y \\ \gamma_{xy} \end{Bmatrix}
$$

$$
(7.7)
$$

The inverse of the first matrix on the left-hand side of Eq. (7.7) can be determined as:

$$
\begin{bmatrix}
\cos^2\theta & \sin^2\theta & 2\sin\theta\cos\theta \\
\sin^2\theta & \cos^2\theta & -2\sin\theta\cos\theta \\
-\sin\theta\cos\theta & \sin\theta\cos\theta & (\cos^2\theta - \sin^2\theta)
\end{bmatrix}^{-1}
$$

$$
=
\begin{bmatrix}
\cos^2\theta & \sin^2\theta & -2\sin\theta\cos\theta \\
\sin^2\theta & \cos^2\theta & 2\sin\theta\cos\theta \\
\sin\theta\cos\theta & -\sin\theta\cos\theta & (\cos^2\theta - \sin^2\theta)
\end{bmatrix}
$$

By premultiplying both sides of Eq. (7.7) by this inverse matrix, gives:

$$
\left\{
\begin{array}{c}
\sigma_x \\
\sigma_y \\
\tau_{xy}
\end{array}
\right\}
= [T]^{-1}\left[Q^{(0)}\right][R]
\left\{
\begin{array}{c}
\varepsilon_x \\
\varepsilon_y \\
\gamma_{xy}
\end{array}
\right\}
\tag{7.8}
$$

where

$$
[T]^{-1} =
\begin{bmatrix}
\cos^2\theta & \sin^2\theta & -2\sin\theta\cos\theta \\
\sin^2\theta & \cos^2\theta & 2\sin\theta\cos\theta \\
\sin\theta\cos\theta & -\sin\theta\cos\theta & (\cos^2\theta - \sin^2\theta)
\end{bmatrix}
$$

$$
\left[Q^{(0)}\right] =
\begin{bmatrix}
Q_{11}^{(0)} & Q_{12}^{(0)} & 0 \\
Q_{12}^{(0)} & Q_{22}^{(0)} & 0 \\
0 & 0 & Q_{66}^{(0)}
\end{bmatrix}
$$

$$
[R] =
\begin{bmatrix}
\cos^2\theta & \sin^2\theta & \sin\theta\cos\theta \\
\sin^2\theta & \cos^2\theta & -\sin\theta\cos\theta \\
-2\sin\theta\cos\theta & 2\sin\theta\cos\theta & (\cos^2\theta - \sin^2\theta)
\end{bmatrix}
$$

Carrying out the matrix multiplications on the right-hand side of Eq. (7.8) gives:

$$\left\{ \begin{array}{c} \sigma_x \\ \sigma_y \\ \tau_{xy} \end{array} \right\} = \left[Q^{(\theta)} \right] \left\{ \begin{array}{c} \varepsilon_x \\ \varepsilon_y \\ \gamma_{xy} \end{array} \right\} \tag{7.9}$$

where, with reference to Eq. (7.4), the entries of the matrix $Q^{(\theta)}$ are given by:

$$Q_{xx}^{(\theta)} = m^4 Q_{11}^{(0)} + n^4 Q_{22}^{(0)} + 2m^2 n^2 Q_{12}^{(0)} + 4m^2 n^2 Q_{66}^{(0)}$$

$$Q_{yy}^{(\theta)} = n^4 Q_{11}^{(0)} + m^4 Q_{22}^{(0)} + 2m^2 n^2 Q_{12}^{(0)} + 4m^2 n^2 Q_{66}^{(0)}$$

$$Q_{xy}^{(\theta)} = m^2 n^2 Q_{11}^{(0)} + m^2 n^2 Q_{22}^{(0)} + \left(m^4 + n^4 \right) Q_{12}^{(0)} - 4m^2 n^2 Q_{66}^{(0)}$$

$$Q_{ss}^{(\theta)} = m^2 n^2 Q_{11}^{(0)} + m^2 n^2 Q_{22}^{(0)} - 2m^2 n^2 Q_{12}^{(0)} + \left(m^2 - n^2 \right)^2 Q_{66}^{(0)} \tag{7.10}$$

$$Q_{xs}^{(\theta)} = m^3 n Q_{11}^{(0)} - mn^3 Q_{22}^{(0)} + \left(mn^3 - m^3 n \right) Q_{12}^{(0)} + 2 \left(mn^3 - m^3 n \right) Q_{66}^{(0)}$$

$$Q_{ys}^{(\theta)} = mn^3 Q_{11}^{(0)} - m^3 n Q_{22}^{(0)} + \left(m^3 n - mn^3 \right) Q_{12}^{(0)} + 2 \left(m^3 n - mn^3 \right) Q_{66}^{(0)}$$

with $m = cos\theta$ and $n = sin\theta$.

Eq. (7.9) or (7.4) and (7.10) provide the stiffnesses of a ply with fibers oriented at an angle θ in the laminate coordinate system.

The above discussion concentrated on plane stress conditions. In a three-dimensional situation, a 0 degree ply is defined with nine stiffness parameters: E_{11}, E_{22}, E_{33}, G_{12}, G_{13}, G_{23}, ν_{12}, ν_{13}, and ν_{23}. Here, as before, 1 denotes the direction parallel to the fibers, 2 is perpendicular to the fibers, and 3 is the out-of-plane direction. For orthotropic plies, $E_{22} = E_{33}$, $G_{12} = G_{13}$, and $\nu_{12} = \nu_{13}$. These properties are determined experimentally and can be used to obtain ply compliances. For a 0 ply:

$$S_{11}^0 = \frac{1}{E_{11}}$$

$$S_{12}^0 = -\frac{\nu_{12}}{E_{11}}$$

$$S_{66}^0 = \frac{1}{G_{12}}$$

$$S_{22}^0 = \frac{1}{E_{22}}$$

$$S_{13}^0 = -\frac{\nu_{13}}{E_{11}}$$

$$S_{23}^0 = -\frac{\nu_{23}}{E_{22}}$$

$$S_{33}^0 = \frac{1}{E_{33}}$$

$$S_{44}^0 = \frac{1}{G_{23}}$$

$$S_{55}^0 = \frac{1}{G_{13}}$$

(7.11)

These can then be used to obtain the compliances of a ply or arbitrary in-plane orientation θ as follows:

$$S_{11} = S_{11}^0 \cos^4\theta + \left(2S_{12}^0 + S_{66}^0\right)\sin^2\theta\cos^2\theta + S_{22}^0\sin^4\theta$$

$$S_{12} = \left(S_{11}^0 + S_{22}^0 - S_{66}^0\right)\sin^2\theta\cos^2\theta + S_{12}^0\left(\sin^4\theta + \cos^4\theta\right)$$

$$S_{13} = S_{13}^0\cos^2\theta + S_{23}^0\sin^2\theta$$

$$S_{22} = S_{11}^0\sin^4\theta + \left(2S_{12}^0 + S_{66}^0\right)\sin^2\theta\cos^2\theta + S_{22}^0\cos^4\theta$$

$$S_{23} = S_{13}^0\sin^2\theta + S_{23}^0\cos^2\theta$$

$$S_{33} = S_{33}^0$$

$$S_{16} = 2S_{11}^0\cos^3\theta\,\sin\theta - 2S_{22}^0\,\cos\theta\sin^3\theta + \left(2S_{22}^0 + S_{66}^0\right)\left(\cos\theta\,\sin^3\theta - \cos^3\theta\,\sin\theta\right)$$

$$S_{26} = 2S_{11}^0\,\cos\theta\sin^3\theta - 2S_{22}^0\cos^3\theta\,\sin\theta + \left(2S_{22}^0 + S_{66}^0\right)\left(\cos^3\theta\,\sin\theta - \cos\theta\,\sin^3\theta\right)$$

$$S_{36} = 2\left(S_{13}^0 - S_{23}^0\right)\cos\theta\,\sin\theta$$

$$S_{44} = S_{55}^0\sin^2\theta + S_{44}^0\cos^2\theta$$

$$S_{45} = \left(S_{55}^0 - S_{44}^0\right)\sin\theta\,\cos\theta$$

$$S_{55} = S_{55}^0\cos^2\theta + S_{44}^0\sin^2\theta$$

$$S_{66} = 4\left(S_{11}^0 + S_{22}^0 - 2S_{12}^0\right)\sin^2\theta\cos^2\theta + S_{66}^0\left(\sin^4\theta + \cos^4\theta - 2\sin^2\theta\,\cos^2\theta\right)$$

(7.12)

7.3.3 Laminate stiffness

The ply stiffness values obtained in the previous section can be used to determine the stiffness of a laminate. In general, one can view the laminate stiffnesses as a weighted average of the ply stiffnesses, where the weights change depending on whether the laminate undergoes pure stretching, pure bending, or combination of the two.

7.3.3.1   Force and moment resultants

It is convenient to define force and moment resultants, which are sum totals of the individual stress contributions integrated over the entire laminate thickness. Specifically, the force resultants are:

$$N_x = \int_{-\frac{h}{2}}^{\frac{h}{2}} \sigma_x dz$$

$$N_y = \int_{-\frac{h}{2}}^{\frac{h}{2}} \sigma_y dz \tag{7.13}$$

$$N_{xy} = \int_{-\frac{h}{2}}^{\frac{h}{2}} \tau_{xy} dz$$

and the moment resultants are:

$$M_x = \int_{-\frac{h}{2}}^{\frac{h}{2}} \sigma_x z dz$$

$$M_y = \int_{-\frac{h}{2}}^{\frac{h}{2}} \sigma_y z dz \tag{7.14}$$

$$M_{xy} = \int_{-\frac{h}{2}}^{\frac{h}{2}} \tau_{xy} z dz$$
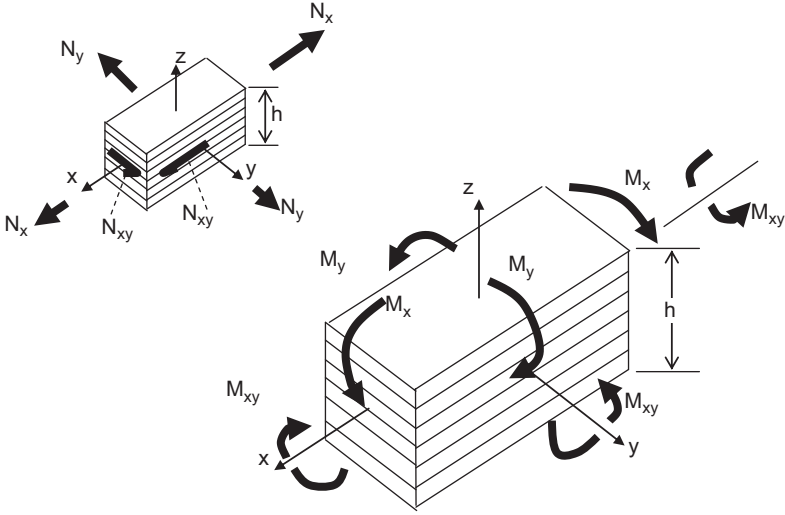
Figure 7.3 Sign convention for forces and moments.

where the sign convention for positive force and moment resultants is given in Fig. 7.3.

Consider the case of a laminate under membrane forces N_x, N_y, and N_{xy}. Then, direct integration through the thickness of Eq. (7.4) gives:

$$\left\{ \begin{array}{c} \displaystyle\int_{-h/2}^{h/2} \sigma_x dz \\[2em] \displaystyle\int_{-h/2}^{h/2} \sigma_y dz \\[2em] \displaystyle\int_{-h/2}^{h/2} \tau_{xy} dz \end{array} \right\} = \int_{-h/2}^{h/2} \begin{bmatrix} Q_{xx} & Q_{xy} & Q_{xs} \\ Q_{xy} & Q_{yy} & Q_{ys} \\ Q_{xs} & Q_{ys} & Q_{ss} \end{bmatrix} dz \left\{ \begin{array}{c} \varepsilon_x \\ \varepsilon_y \\ \gamma_{xy} \end{array} \right\} \tag{7.15}$$

Now using Eq. (7.13), the left-hand side of Eq. (7.15) can be shown to equal $\{N_x, N_y, N_{xy}\}^T$. The integrals on the right-hand side can be transformed to summations through the thickness of the laminate recognizing that the corresponding stiffnesses Q_{xx}, Q_{xy}, etc., are constant through the thickness of each ply but not necessarily equal from one ply to the next. Therefore, letting:

$$A_{11} = \sum_{k=1}^{n} Q_{xx}(z_k - z_{k-1})$$

$$A_{12} = \sum_{k=1}^{n} Q_{xy}(z_k - z_{k-1})$$

$$A_{16} = \sum_{k=1}^{n} Q_{xs}(z_k - z_{k-1})$$

$$A_{22} = \sum_{k=1}^{n} Q_{yy}(z_k - z_{k-1})$$

$$A_{26} = \sum_{k=1}^{n} Q_{ys}(z_k - z_{k-1})$$

$$A_{66} = \sum_{k=1}^{n} Q_{ss}(z_k - z_{k-1}) \tag{7.16}$$

with z_0 at the bottom of the laminate, Eq. (7.15) can be rewritten in the form:

$$\begin{Bmatrix} N_x \\ N_y \\ N_{xy} \end{Bmatrix} = \begin{bmatrix} A_{11} & A_{12} & A_{16} \\ A_{12} & A_{22} & A_{26} \\ A_{16} & A_{26} & A_{66} \end{bmatrix} \begin{Bmatrix} \varepsilon_x \\ \varepsilon_y \\ \gamma_{xy} \end{Bmatrix} \tag{7.17}$$

Now for a laminate undergoing pure bending, the strains through the thickness of the laminate follow the standard linear distribution:

$$\varepsilon_x = -z\frac{\partial^2 w}{\partial x^2} = z\kappa_x$$

$$\varepsilon_y = -z\frac{\partial^2 w}{\partial y^2} = z\kappa_y \tag{7.18}$$

$$\gamma_{xy} = -2z\frac{\partial^2 w}{\partial x \partial y} = z\kappa_{xy}$$

where κ_x, κ_y, and κ_{xy} are the laminate curvatures.

Using Eq. (7.18) to substitute in Eq. (7.4) and multiplying both sides by z and integrating, gives:

$$\begin{Bmatrix} \int_{-h/2}^{h/2} \sigma_x z\, dz \\ \int_{-h/2}^{h/2} \sigma_y z\, dz \\ \int_{-h/2}^{h/2} \tau_{xy} z\, dz \end{Bmatrix} = \int_{-h/2}^{h/2} \begin{bmatrix} Q_{xx} & Q_{xy} & Q_{xs} \\ Q_{xy} & Q_{yy} & Q_{ys} \\ Q_{xs} & Q_{ys} & Q_{ss} \end{bmatrix} \begin{Bmatrix} z^2\kappa_x \\ z^2\kappa_y \\ z^2\kappa_{xy} \end{Bmatrix} dz \tag{7.19}$$

Using Eq. (7.14), the left-hand side of Eq. (7.19) can be shown to equal $\{M_x, M_y, M_{xy}\}^{\mathrm{T}}$. The integrals in the right-hand side can be transformed to summations over all plies in the laminate, recognizing the fact that the stiffnesses Q_{xx}, Q_{yy}, etc. are constant through each ply. Therefore, letting:

$$D_{11} = \sum_{k=1}^{n} \frac{Q_{xx}}{3}\left(z_k^3 - z_{k-1}^3\right)$$

$$D_{12} = \sum_{k=1}^{n} \frac{Q_{xy}}{3}\left(z_k^3 - z_{k-1}^3\right)$$

$$D_{16} = \sum_{k=1}^{n} \frac{Q_{xs}}{3}\left(z_k^3 - z_{k-1}^3\right)$$

$$D_{22} = \sum_{k=1}^{n} \frac{Q_{yy}}{3}\left(z_k^3 - z_{k-1}^3\right) \tag{7.20}$$

$$D_{26} = \sum_{k=1}^{n} \frac{Q_{ys}}{3}\left(z_k^3 - z_{k-1}^3\right)$$

$$D_{66} = \sum_{k=1}^{n} \frac{Q_{ss}}{3}\left(z_k^3 - z_{k-1}^3\right)$$

with z_0 at the bottom of the laminate, Eq. (7.19) can be rewritten in the form

$$\left\{\begin{array}{c} M_x \\ M_y \\ M_{xy} \end{array}\right\} = \begin{bmatrix} D_{11} & D_{12} & D_{16} \\ D_{12} & D_{22} & D_{26} \\ D_{16} & D_{26} & D_{66} \end{bmatrix} \left\{\begin{array}{c} \kappa_x \\ \kappa_y \\ \kappa_{xy} \end{array}\right\} \tag{7.21}$$

Eqs. (7.17) and (7.21) describe the response of a laminate when the stretching and bending behaviors are decoupled. This would be the case of symmetric laminates, where plies symmetrically located with respect to the mid-plane of the laminate have the same material, thickness, and orientation. For general laminates, however, membrane and bending behaviors are coupled. In such a case, the in-plane forces N_x, N_y, and N_{xy} cause bending curvatures κ_x, κ_y, and κ_{xy}. In an analogous fashion, bending moments M_x, M_y, and M_{xy} cause membrane strains ε_{xo}, ε_{yo}, and γ_{xyo} with the additional subscript "o" referring to straining of the mid-plane of the laminate. For the case relating membrane forces to bending curvatures, Eq. (7.18) can be

substituted in the right-hand side of Eq. (7.4). Then, integrating both sides with respect to z, gives:

$$
\left\{
\begin{array}{c}
\displaystyle\int_{-h/2}^{h/2} \sigma_x dz \\[3ex]
\displaystyle\int_{-h/2}^{h/2} \sigma_y dz \\[3ex]
\displaystyle\int_{-h/2}^{h/2} \tau_{xy} dz
\end{array}
\right\}
=
\int_{-h/2}^{h/2}
\begin{bmatrix}
Q_{xx} & Q_{xy} & Q_{xs} \\
Q_{xy} & Q_{yy} & Q_{ys} \\
Q_{xs} & Q_{ys} & Q_{ss}
\end{bmatrix}
\left\{
\begin{array}{c}
z\kappa_x \\
z\kappa_y \\
z\kappa_{xy}
\end{array}
\right\} dz
\tag{7.22}
$$

Letting now:

$$
B_{11} = \sum_{k=1}^{n} \frac{Q_{xx}}{2} \left(z_k^2 - z_{k-1}^2 \right)
$$

$$
B_{12} = \sum_{k=1}^{n} \frac{Q_{xy}}{2} \left(z_k^2 - z_{k-1}^2 \right)
$$

$$
B_{16} = \sum_{k=1}^{n} \frac{Q_{xs}}{2} \left(z_k^2 - z_{k-1}^2 \right)
$$

$$
\tag{7.23}
$$

$$
B_{22} = \sum_{k=1}^{n} \frac{Q_{yy}}{2} \left(z_k^2 - z_{k-1}^2 \right)
$$

$$
B_{26} = \sum_{k=1}^{n} \frac{Q_{ys}}{2} \left(z_k^2 - z_{k-1}^2 \right)
$$

$$
B_{66} = \sum_{k=1}^{n} \frac{Q_{ss}}{2} \left(z_k^2 - z_{k-1}^2 \right)
$$

where z_0 is at the bottom of the laminate and using Eq. (7.13) gives:

$$\begin{Bmatrix} N_x \\ N_y \\ N_{xy} \end{Bmatrix} = \begin{bmatrix} B_{11} & B_{12} & B_{16} \\ B_{12} & B_{22} & B_{26} \\ B_{16} & B_{26} & B_{66} \end{bmatrix} \begin{Bmatrix} \kappa_x \\ \kappa_y \\ \kappa_{xy} \end{Bmatrix} \tag{7.24}$$

Eq. (7.17), (7.20), and (7.24) can be combined to give the constitutive relations for a general laminate. This is done by writing the total strains in the laminate as the sum of the mid-plane strains and the bending strains due to curvature:

$$\varepsilon_x = \varepsilon_{xo} + z\kappa_x$$
$$\varepsilon_y = \varepsilon_{yo} + z\kappa_y \tag{7.25}$$
$$\gamma_{xy} = \gamma_{xyo} + z\kappa_{xy}$$

The final relations combining (7.17), (7.20), (7.24), and (7.25) are:

$$\begin{Bmatrix} N_x \\ N_y \\ N_{xy} \\ M_x \\ M_y \\ M_{xy} \end{Bmatrix} = \begin{bmatrix} A_{11} & A_{12} & A_{16} & B_{11} & B_{12} & B_{16} \\ A_{12} & A_{22} & A_{26} & B_{12} & B_{22} & B_{26} \\ A_{16} & A_{26} & A_{66} & B_{16} & B_{26} & B_{66} \\ B_{11} & B_{12} & B_{16} & D_{11} & D_{12} & D_{16} \\ B_{12} & B_{22} & B_{26} & D_{12} & D_{22} & D_{26} \\ B_{16} & B_{26} & B_{66} & D_{16} & D_{26} & D_{66} \end{bmatrix} \begin{Bmatrix} \varepsilon_{xo} \\ \varepsilon_{yo} \\ \gamma_{xyo} \\ \kappa_x \\ \kappa_y \\ \kappa_{xy} \end{Bmatrix} \tag{7.26}$$

7.3.3.2 Special classes of laminates

Some special classes of laminates are worth mentioning at this point. Symmetric laminates were already defined earlier. For symmetric laminates, the B matrix is zero ($B_{ij} = 0$). Balanced laminates are laminates in which for every $+\theta$ ply ($\theta \neq 0$ or 90) there is another $-\theta$ ply somewhere in the stacking sequence. For such laminates, $A_{16} = A_{26} = 0$ which means there is no stretching-shearing coupling: A force N_x or N_y does not cause a shear strain γ_{xyo} and a shear force N_{xy} does not cause axial strains ε_{xo} and ε_{yo}. Finally, specially orthotropic laminates are laminates for which in addition to A_{16} and A_{26} being zero, also $D_{16} = D_{26} = 0$. The last condition implies there is no bending-twisting coupling, which means that bending moments do not twist the laminate and an applied torque does not cause pure bending, only twisting. Antisymmetric laminates (for each $+\theta$ there is a $-\theta$ at its symmetric location with respect to the mid-plane) are the general laminates that satisfy $D_{16} = D_{26} = 0$.

To use Eq. (7.26), one must know the strains and/or curvatures in a laminate.

Usually, these are not known. Instead, the forces and moments are known, and the strains are needed. This would be a typical situation for failure analysis. This means that Eq. (7.26) must be inverted to give the strains and curvatures as a function of the applied loads:

$$
\begin{Bmatrix} \varepsilon_{xo} \\ \varepsilon_{yo} \\ \gamma_{xyo} \\ \kappa_x \\ \kappa_y \\ \kappa_{xy} \end{Bmatrix} = \begin{bmatrix} \alpha_{11} & \alpha_{12} & \alpha_{16} & \beta_{11} & \beta_{12} & \beta_{16} \\ \alpha_{12} & \alpha_{22} & \alpha_{26} & \beta_{21} & \beta_{22} & \beta_{26} \\ \alpha_{16} & \alpha_{26} & \alpha_{66} & \beta_{61} & \beta_{62} & \beta_{66} \\ \beta_{11} & \beta_{21} & \beta_{61} & \delta_{11} & \delta_{12} & \delta_{16} \\ \beta_{12} & \beta_{22} & \beta_{62} & \delta_{12} & \delta_{22} & \delta_{26} \\ \beta_{16} & \beta_{26} & \beta_{66} & \delta_{16} & \delta_{26} & \delta_{66} \end{bmatrix} \begin{Bmatrix} N_x \\ N_y \\ N_{xy} \\ M_x \\ M_y \\ M_{xy} \end{Bmatrix} \tag{7.27}
$$

It can be shown that:

$$
[\alpha] = [A]^{-1} + [A]^{-1}[B]\Big[[D] - [B][A]^{-1}[B]\Big]^{-1}[B][A]^{-1} \tag{7.28}
$$

$$
[\beta] = -[A][B]\Big[[D] - [B][A]^{-1}[B]\Big]^{-1} \tag{7.29}
$$

$$
[\delta] = \Big[[D] - [B][A]^{-1}[B]\Big]^{-1} \tag{7.30}
$$

The ABD stiffness matrix terms can be used to determine the so-called *engineering elastic constants*. These are the stiffness values one would measure experimentally in the laboratory for a given laminate. For example, a uniaxial tension test would determine the laminate Young's modulus and Poisson's ratio. It is important to note that these values are not the same when the loading is changed to compression. Even more important is the fact that, in general, the stiffness properties corresponding to the membrane behavior are not the same to those corresponding to the bending behavior. Thus, the Young's modulus when a laminate is tested under tension is not the same as the Young's modulus measured during a bending test. For the case of a symmetric laminate (B matrix is zero) on can show using Eqs. (7.26) and (7.27) that:

$$
E_{xm} = \frac{1}{ha_{11}}
$$

$$
E_{ym} = \frac{1}{ha_{22}}
$$

$$
G_{xym} = \frac{1}{ha_{66}}
$$

$$\nu_{xym} = -\frac{a_{12}}{a_{11}}$$

$$\nu_{yxm} = -\frac{a_{12}}{a_{22}}$$

$$E_{xb} = \frac{12}{h^3 d_{11}}$$

$$E_{yb} = \frac{12}{h^3 d_{22}}$$

$$G_{xyb} = \frac{12}{h^3 d_{66}}$$

$$\nu_{xyb} = -\frac{d_{12}}{d_{11}}$$

$$\nu_{yxb} = -\frac{d_{12}}{d_{22}}$$

(7.31)

where h is the laminate thickness, a_{ij} refers to the corresponding entry of the inverse of the A matrix and d_{ij} refers to the corresponding entry of the inverse of the D matrix of the laminate.

The above discussion was specific to the plane stress assumptions, where no out-of-plane stresses are present. For a more general situation, the three-dimensional stiffness values of a laminate can be obtained as a thickness-weighted average of the ply compliances given by Eq. (7.12):

$$\frac{1}{S_{ij}} = \frac{1}{h} \sum_1^N \frac{t^{(k)}}{S_{ij}^{(k)}}$$

(7.32)

where i and $j = 1,2,\ldots6$, h is the laminate thickness, for a laminate with N plies. $t^{(k)}$ and $S_{ij}^{(k)}$ are the thickness and compliance of the kth ply.

The three-dimensional properties of a laminate given by Eq. (7.11), (7.12), and (7.32) are needed in situations where out-of-plane stresses develop. Besides the obvious case of out-of-plane loadings, such as the local indentation and the associated solution of contact stresses in an impact problem, out-of-plane stresses typically arise near free edges of laminates, in the immediate vicinity of ply drops and near matrix cracks or delaminations. Typical examples are shown in Fig. 7.4. The red lines indicate regions in the vicinity of which out-of-plane stresses σ_z, τ_{xz}, and τ_{yz} develop (with z the out-of-plane coordinate).
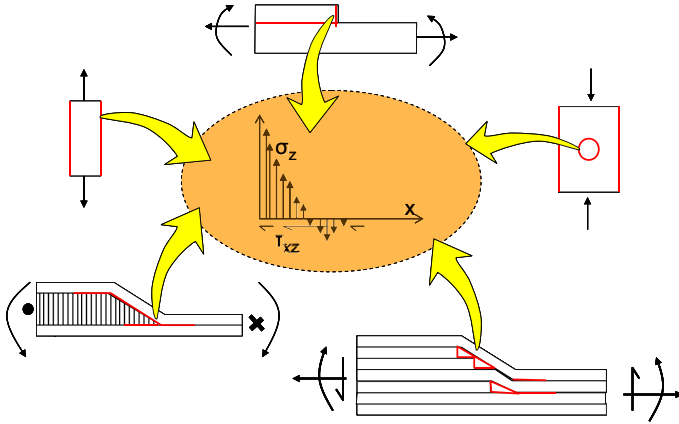
Figure 7.4 Structural details where 3-D stresses develop.

7.3.4 The use of lamination parameters to define laminate stiffnesses

The stiffness formulation in the previous sections has been used extensively in the past and has been very useful. It suffers, however, from two major drawbacks. The first is that it uses thickness explicitly as a variable which, due to the fact that the material forms can only come in integral multiples of individual ply thicknesses, is discontinuous. This makes the design effort, where the thickness of the structure must be minimized, very cumbersome. With this limitation, layup optimizers must make use of special approaches based typically on Genetic Algorithms [5,6] which, sometimes have difficulty in converging and/or converge to a local optimum point instead of the global optimum.

The second drawback is that individual ply angles are needed as inputs in the design process. This limits design flexibility and speed of convergence as it is difficult to come up with robust algorithms, which can change the angles that contribute the most to the stiffness all the while observing design guidelines, such as layup symmetry, balance, a minimum percentage of plies in certain directions, etc.

An alternative modeling approach which deals with these drawbacks is the use of lamination parameters. It makes use of the composite material invariants U_1-U_5. These were proposed by Tsai and Pagano [7] to allow an alternative way to write Eq. (7.10):

$$Q_{xx}^{(\theta)} = U_1 + U_2 \cos 2\theta + U_3 \cos 4\theta$$

$$Q_{yy}^{(\theta)} = U_1 - U_2 \cos 2\theta + U_3 \cos 4\theta$$

$$Q_{xy}^{(\theta)} = U_4 - U_3 \cos 4\theta$$

$$Q_{ss}^{(\theta)} = U_5 - U_3 \cos4\theta$$

$$Q_{xs}^{(\theta)} = \frac{U_2}{2}\sin2\theta + U_3 \sin4\theta$$

$$Q_{ys}^{(\theta)} = \frac{U_2}{2}\sin2\theta - U_3 \sin4\theta$$

(7.10a)

The invariants U_1-U_5 are defined as:

$$U_1 = \frac{1}{8}\left(3Q_{11}^{(0)} + 3Q_{22}^{(0)} + 2Q_{12}^{(0)} + 4Q_{66}^{(0)}\right)$$

$$U_2 = \frac{1}{2}\left(Q_{11}^{(0)} - Q_{22}^{(0)}\right)$$

$$U_3 = \frac{1}{8}\left(Q_{11}^{(0)} + Q_{22}^{(0)} - 2Q_{12}^{(0)} - 4Q_{66}^{(0)}\right)$$

(7.33)

$$U_4 = \frac{1}{8}\left(Q_{11}^{(0)} + Q_{22}^{(0)} + 6Q_{12}^{(0)} - 4Q_{66}^{(0)}\right)$$

$$U_5 = \frac{1}{8}\left(Q_{11}^{(0)} + Q_{22}^{(0)} - 2Q_{12}^{(0)} + 4Q_{66}^{(0)}\right)$$

The following matrices can then be defined:

$$\Gamma_0 = \begin{bmatrix} U_1 & U_4 & 0 \\ U_4 & U_1 & 0 \\ 0 & 0 & U_5 \end{bmatrix}, \Gamma_1 = \begin{bmatrix} U_2 & 0 & 0 \\ 0 & -U_2 & 0 \\ 0 & 0 & 0 \end{bmatrix}, \Gamma_2 = \begin{bmatrix} 0 & 0 & \frac{1}{2}U_2 \\ 0 & 0 & \frac{1}{2}U_2 \\ \frac{1}{2}U_2 & \frac{1}{2}U_2 & 0 \end{bmatrix}$$

$$\Gamma_3 = \begin{bmatrix} U_3 & -U_3 & 0 \\ -U_3 & U_3 & 0 \\ 0 & 0 & -U_3 \end{bmatrix}, \Gamma_4 = \begin{bmatrix} 0 & 0 & U_3 \\ 0 & 0 & -U_3 \\ U_3 & -U_3 & 0 \end{bmatrix}$$

(7.34)

With the help of these matrices, the lamination parameters V_i^A, V_i^B, V_i^D, (i = 1–4), which were introduced by Tsai and Pagano [7] are determined as:

$$V_1^A, V_2^A, V_3^A, V_4^A = \frac{1}{n} \sum_{i=1}^{n} [\cos2\theta_i, \sin2\theta_i, \cos4\theta_i, \sin4\theta_i]$$

$$V_1^B, V_2^B, V_3^B, V_4^B = \frac{2}{n^2} \sum_{i=1}^{n} \left(\left(\frac{n}{2} - i + 1\right)^2 - \left(\frac{n}{2} - i\right)^2 \right) [\cos2\theta_i, \sin2\theta_i, \cos4\theta_i, \sin4\theta_i]$$

$$V_1^D, V_2^D, V_3^D, V_4^D = \frac{4}{n^3} \sum_{i=1}^{n} \left(\left(\frac{n}{2} - i + 1\right)^3 - \left(\frac{n}{2} - i\right)^3 \right) [\cos2\theta_i, \sin2\theta_i, \cos4\theta_i, \sin4\theta_i]$$

$$(7.35)$$

where n is the number of plies in the laminate, and i is the ith ply. For the special case of symmetric and balanced laminates, V_2^A, V_4^A, and V_i^B, i = 1–4, are zero and V_2^D, V_4^D are negligible (especially for large n). In such cases, the number of lamination parameters is reduced from 12 for general laminates, to 4. Given the fact that the lamination parameters involve trigonometric functions as shown in Eq. (7.35), they are limited in the values they can attain. For example, V_1 and V_3 are constrained to lie in the region shown in Fig. 7.5. The three corners define the 0, 90, and ±45 laminates.
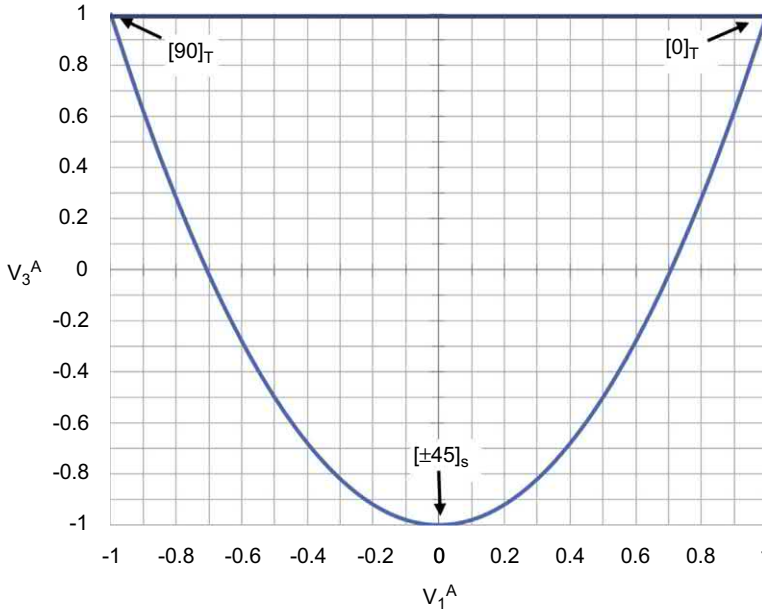
Figure 7.5 Feasible region for V_1^A and V_3^A (inside the curve is shown).

It can be shown that the matrices *A* from Eq. (7.16), *B* from Eq. (7.20) and *D* from Eq. (7.23), which define the stiffness response of a laminate in Eq. (7.26) can now be written as:

$$\mathbf{A} = h\left(\mathbf{\Gamma}_0 + \mathbf{\Gamma}_1 V_1^A + \mathbf{\Gamma}_2 V_2^A + \mathbf{\Gamma}_3 V_3^A + \mathbf{\Gamma}_4 V_4^A\right)$$

$$\mathbf{B} = \frac{h^2}{4}\left(\mathbf{\Gamma}_0 + \mathbf{\Gamma}_1 V_1^B + \mathbf{\Gamma}_2 V_2^B + \mathbf{\Gamma}_3 V_3^B + \mathbf{\Gamma}_4 V_4^B\right) \qquad (7.36)$$

$$\mathbf{D} = \frac{h^3}{12}\left(\mathbf{\Gamma}_0 + \mathbf{\Gamma}_1 V_1^D + \mathbf{\Gamma}_2 V_2^D + \mathbf{\Gamma}_3 V_3^D + \mathbf{\Gamma}_4 V_4^D\right)$$

where h is the laminate thickness.

Analogous expressions can also be obtained for other stiffness values, such as the engineering constants of Eq. (7.31).

It can be seen that the lamination parameters V_i^A, V_i^B, V_i^D are dimensionless continuous variables. This means that the *A*, *B*, and *D* matrices are now defined as continuous variables, and the laminate thickness h is also treated as a continuous variable. This, of course, introduces a problem when lamination parameters are used to design a laminate. The resulting lamination parameters do not always correspond to a laminate whose thickness is an integral multiple of the ply thickness of the material(s) used. Some approximation, discussed below, will be necessary.

The usefulness of this approach was first demonstrated by Miki [8] and Miki and Sugiyama [9]. Optimum lamination parameters for different problems can be obtained using formal optimization e.g., [10, 11]. The great advantage is that optimizers using continuous variables (such as gradient-based approaches) can be used instead of approaches, such as Genetic Algorithms that are set up to deal with discontinuous variables, are slower and do not necessarily converge to a global optimum.

This approach is very effective in dealing with the fiber steering problem where the fiber orientation within each ply is a function of location. Such an approach allows increased tailoring of the design and leads to significantly improved performance [12−14]. However, as already mentioned, the use of lamination parameters has a disadvantage: The need to translate the resulting lamination parameters to a useable stacking sequence. Not every lamination parameter combination can be translated to a set of ply angles. As a result, approximation schemes have been developed using, for example, a nonlinear least square solution approach [15] or a combination of Genetic Algorithms and a Gradient-based optimizer [16].

7.3.5   Ply strength

Determining the strength of a single ply is useful for two reasons. First, because in limited cases, laminates consisting of a single ply that repeats are used (typically fabric plies used in laminates with a single loading condition). Second, because many of the laminate strength theories make use of the individual ply strengths.

7.3.5.1   Failure modes

The failure of a ply depends on the loading and the strength of its constituents, the fibers, and matrix. At the macroscopic level, five different failure modes are recognized for a ply:

- tension strength parallel to the fibers, denoted by X^t
- compression strength parallel to the fibers, denoted by X^c
- tension strength perpendicular to the fibers, denoted by Y^t
- compression strength perpendicular to the fibers denoted by Y^c
- in-plane shear strength denoted by S

It is important to note that these quantities do not correspond to a simple or single damage mechanism. For example, tension failure parallel to the fibers may involve some combination of fiber breakage, matrix failure along the failed fibers, and failure of the fiber/matrix interface. The actual sequence of events depends on the relative strength and stiffness of fibers and matrix and the strength of the fiber/matrix bond (fiber matrix interface). Similarly, compression failure parallel to the fibers involves fiber kinking or very short wavelength buckling of fibers with the matrix acting as an elastic foundation, accompanied by matrix failure. Finally, for pure shear loading of an unidirectional ply, resolving the load to a biaxial tension and compression combination combines the failure modes already mentioned in a very complex sequence of events.

The complexity of damage formation and evolution makes it very difficult to model failure by accurately tracking damage from the creation of the first type of damage to the final failure. For this reason, one resorts to ply-level failure strength as described above. Then, the failure of a ply occurs if the applied stress exceeds the corresponding failure strength. In an analogous fashion, one can use ultimate strains instead of strengths to predict failure. Five failure strains, ε_{xu}^t, ε_{xu}^c, ε_{yu}^t, ε_{yu}^c, and γ_{xy}^u are used for the five macroscopic failures defined above: tension or compression parallel to the fibers, tension or compression perpendicular to the fibers and shear.

7.3.5.2   Linear stress-strain response

One important comment about the linear stress-strain response is in order. For typical composite materials, the stress-strain response parallel to the fibers under tension and compression is nearly linear. However, tension and compression perpendicular to the fibers and shear exhibit high nonlinearity, raising the question as to what value one could use for the ultimate strength and strain values. For example, referring to the schematic shear stress-strain plot of Fig. 7.6, one must decide on the values that should be used. Using τ_{ult} would give a good measure of the ultimate strength, but if it is combined with the shear modulus G corresponding to the linear portion of the curve, it will result in the shear strain failure that equals γ_e. This strain is significantly lower than the ultimate strain γ_{ult} and has important implications, for example, for the state of postbuckled skins under shear. Still, it is used as a conservative approach in practice. At the other extreme, using γ_{ult} to predict failure, again within the context of a linear model would require the use of a shear modulus equal to the slope of line OA in Fig. 7.6,
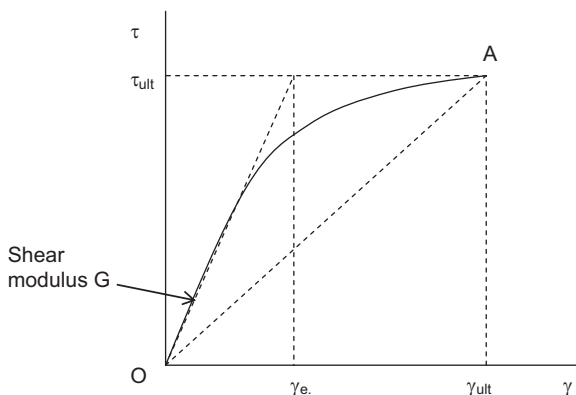
Figure 7.6 Schematic of shear stress-strain plot.

which is significantly lower than the actual value of G, in order to ensure that the shear stress equals zero when the shear strain equals zero. This would alter the predicted or simulated load distribution in the structure as a lower shear modulus would divert the load to an adjacent structure. This discussion suggests that for situations with significant departures from nonlinearity, a good model accounting for this nonlinearity might be the best and most accurate method to use.

7.3.6 Laminate strength theories

Traditionally, laminate strength theories are based on ply strengths and models that use them to predict when a laminate would fail. The complexities associated with the failure of a single ply are compounded in this case by the fact that damage created in one ply can interact with damage in other plies and evolve very differently depending on the laminate. For example, matrix cracks may evolve to delaminations or may branch out to adjacent plies, as shown in Fig. 7.7.

7.3.6.1 Typical failure analysis procedures

As at this stage, accurate modeling of failure after the first damage is very complicated and not very accurate. For general laminates, failure theories used in practice conservatively equate final failure with failure of the first ply in the laminate. The procedure requires determination of the stresses or strains in each ply in the ply axes and use of one of the many failure criteria. The steps followed in a typical failure analysis are as follows:

1. Use Eq. (7.27) to obtain mid-plane strains and curvatures in the laminate
2. Use Eq. (7.26) to obtain strains in the laminate as a function of through the thickness location
3. For each ply, obtain stresses in laminate axes using Eq. (7.4). In cases where bending is present, this should be done at the top and bottom of each ply to ensure that the critical location in each ply is found.
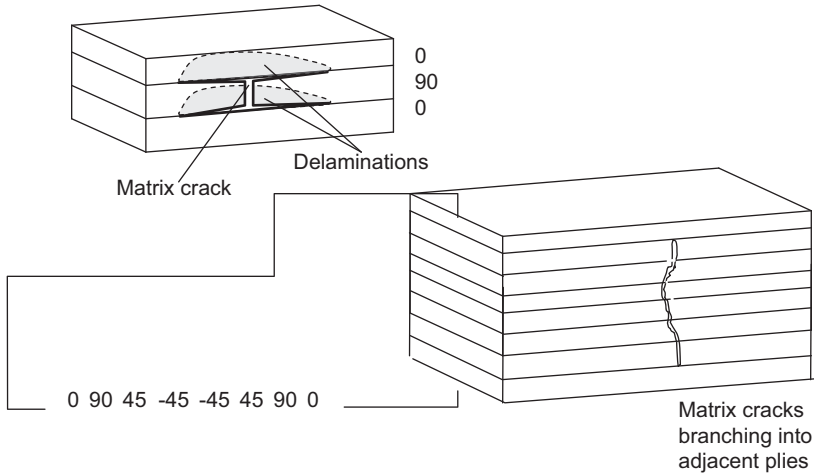
Figure 7.7 Matrix cracks triggering delaminations versus matrix cracks branching into other matrix cracks in adjacent plies.

4. For strain-based failure criteria, use Eq. (7.5) to obtain strains in ply axes. Apply corresponding failure criterion
5. For stress-based failure criteria, use Eq. (7.6) to obtain stresses in ply axes. Apply corresponding failure criterion

7.3.6.2   First-ply failure theories

7.3.6.2.1   Maximum stress

In this case, each of the stresses present in a ply is compared to its corresponding failure values X^t, X^c, Y^t, Y^c, and S presented in Section 7.3.3. The failure criterion takes the form:

$$\frac{\sigma_x}{X} \geq 1$$

$$\frac{\sigma_y}{Y} \geq 1 \qquad\qquad (7.37)$$

$$\frac{|\tau_{xy}|}{S} \geq 1$$

where X in the first criterion of Eq. (7.37) equals X^t if σ_x is tensile and X^c if it is compressive. Similarly, Y in the second criterion of Eq. (7.37) equals Y^t if σ_y is tensile and Y^c if it is compressive.

One advantage of the maximum stress failure criterion is that it gives an indication of the type of failure mode. By checking which criterion of Eq. (7.37) is satisfied, one

can determine whether the fibers or the matrix failed and whether it is a tension, compression, or shear failure. Of course, this is a macroscopic assessment as the failure criterion in this form does not allow a more detailed determination of failure initiation. For example, a shear failure determined by the last criterion of Eq. (7.37) cannot be traced down to a matrix failure due to local tension or compression, nor can it be determined whether the matrix crack was parallel or perpendicular to the fibers.

7.3.6.2.2 Maximum strain

This is completely analogous to the maximum stress criterion, but instead of stresses, strain values are used:

$$\frac{\varepsilon_x}{\varepsilon_x^{ult}} \geq 1$$

$$\frac{\varepsilon_y}{\varepsilon_y^{ult}} \geq 1 \qquad\qquad (7.38)$$

$$\frac{|\gamma_{xy}|}{\gamma_{xy}^{ult}} \geq 1$$

The denominators in the first two criteria of Eq. (7.38) are the tensile or compressive ultimate strains in the corresponding direction depending on whether ε_x or ε_y is tensile or compressive, respectively. It should be noted that for a material that is linear to failure, the predictions from the maximum strain criterion would differ from those from the maximum stress criterion only by a factor depending on the Poisson's ratios ν_{xy} and ν_{yx}. As with the maximum stress criterion, the maximum strain criterion provides some feedback on the type of failure mode occurring.

7.3.6.2.3 Tsai-Hill

The maximum stress and maximum strain failure criteria consider each stress component individually. This is a simplification. Test results show that if more than one stresses are present in a ply, they can combine to give failure earlier (or later) than the maximum stress or maximum strain failure criterion would predict. One example that shows this effect is the case of an uni-directional ply under shear on which tensile or compressive stress is applied parallel to the fibers. The situation is shown in Fig. 7.8(b).

In the case of Fig. 7.8(a), the presence of tensile load perpendicular to the fibers precipitates failure earlier because the matrix between the fibers undergoes a combined tension and shear load. On the other hand, under compression, as in Fig. 7.8(b), the matrix can withstand significantly higher load prior to failure. Thus, for a given shear load, the magnitude of the compression load to cause failure will be higher than that of the corresponding tension load or, for a situation where the magnitude of the transverse load (tension or compression) is kept constant, the shear load needed to cause failure is higher.
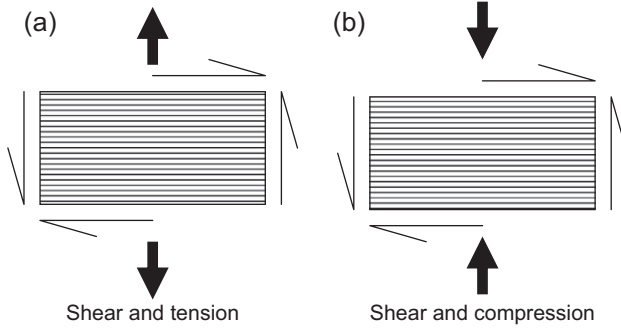
Figure 7.8 Shear combined with tension or compression on an uni-directional ply.

Working on metals, Hill [16] introduced a failure criterion for combined loading situations in metals:

$$F_x \sigma_x^2 + F_y \sigma_y^2 + F_{xy} \sigma_x \sigma_y + F_s \tau_{xy}^2 = 1 \qquad (7.39)$$

which, with an appropriate definition of the coefficients, can be shown to degenerate to the von Mises yield failure criterion for metals.

In an attempt to apply similar concepts in composites, Tsai proposed the use of a failure surface defined using Eq. (7.39) but with a proper redefinition of the coefficients in that equation. The corresponding expression is:

$$\frac{\sigma_x^2}{X^2} - \frac{\sigma_x \sigma_y}{X^2} + \frac{\sigma_y^2}{Y^2} + \frac{\tau_{xy}^2}{S^2} = 1 \qquad (7.40)$$

where X, Y, and S are the yield stresses along the fibers, perpendicular to the fibers and in shear of an uni-directional ply.

This criterion has been used widely and quite successfully in many cases but it is important to note that (a) it is more of a curve fit than a model accounting for actual failure mechanisms in a composite and (b) it does not differentiate between tension and compression failure strength, which, in a composite, can have very different magnitudes.

7.3.6.2.4   Tsai-Wu

In a further refinement of the Tsai-Hill failure criterion, Tsai and Wu [17] proposed a criterion that accounts for the differences in the magnitude of tension and compression strengths in the form:

$$\frac{\sigma_x^2}{X^t X^c} + \frac{\sigma_y^2}{Y^t Y^c} - \sqrt{\frac{1}{X^t X^c} \frac{1}{Y^t Y^c}} \sigma_x \sigma_y + \left(\frac{1}{X^t} - \frac{1}{X^c} \right) \sigma_x + \left(\frac{1}{Y^t} - \frac{1}{Y^c} \right) \sigma_y + \frac{\tau_{xy}^2}{S^2} = 1$$

$$(7.41)$$

with X and Y the strengths parallel and perpendicular to the fibers and the superscripts "t" and "c" corresponding to tension or compression. S is the shear strength for an uni-directional ply as before.

Despite the improvement in differentiating between tension and compression strength values, the Tsai-Wu failure criterion remains a curve fit and does not capture well the mechanism of failure, nor the failure load itself, especially in cases of combined loading with biaxial compression being one of the major problem areas [18]. However, it has been shown to work well in many cases, especially when substantiated, and if necessary, modified, by experimental results.

7.3.6.2.5 Other failure criteria

As alluded to above, failure criteria, in general, have difficulty in predicting the failure of composite structures other than in few simple cases mainly under single load. The difficulty stems from the fact that initial failure, which usually is a matrix crack, does not coincide with the final failure. However, this initial failure evolves into other failure modes, such as delaminations or fiber breakage until the final collapse of the structure. This suggests that a reliable failure theory must have two main characteristics (1) it must model the constituents, fibers, and matrix separately so it can capture their individual failures accurately and (2) it must be able to track damage from failure onset through its evolution to other damage types to final failure.

Recognizing that most failure criteria are limited in their accuracy [19,20], researchers worldwide have undertaken collaborative efforts to evaluate different failure criteria to determine their accuracy and applicability in order to find the best one [21]. These efforts, in particular, the worldwide failure exercise in Ref. [21], have underlined the fact that despite the large number (over 20) failure criteria, there is no single one that seems to capture failure of composites accurately for a wide range of loading situations and materials. However, they have pointed out that certain criteria are more accurate and/or have a wider range of applicability than others. Most notable among these are the Puck criterion and the LaRC 03 failure criterion. In addition, recent work has shown that the onset theory (originally named as Strain Invariant Failure Theory or SIFT) is very accurate in predicting failure onset.

7.3.6.2.6 The Puck criterion

The Puck criterion [22] differentiates failure modes by determining the critical fracture plane, where the stresses combine for the failure of either the matrix or the fiber. Failure can only be caused by stresses acting on the fracture plane. Six different loading situations are considered for an individual ply: (1) Tension along the fibers, (2) Compression along the fibers, (3) Tension perpendicular to the fibers, (4) Compression perpendicular to the fibers, (5) Shear 12 or 13 loading with the fibers aligned with the 1 direction, and (6) Shear 23 loading with the fibers in the 1 direction (note: 1 is parallel to the fibers, 2 is in-plane perpendicular to the fibers). The Puck criterion requires knowledge or determination of the critical fracture plane, as well as the slope of the fracture surfaces at specific locations. In addition, a parameter determining load sharing between fibers and matrix under transverse loading is needed. When these parameters are accurately known, usually through experiments, accurate predictions for failure are obtained.

7.3.6.2.7   LaRC 03 failure criterion

The LaRC 03 failure criterion [23] consists of a family of six criteria. It is an extension of the Puck [22] and Hashin [24] failure criteria. Like the Puck criterion, it focuses on the fracture plane, which is determined by maximizing the Mohr-Coulomb stresses. In the LaRC 03 criterion, failure due to matrix compression is the result of local interaction of shear stresses on a fracture plane. This perspective comes from soil mechanics situations, where the compression strength is different than the tensile strength. It is particularly useful in cases where, on a certain plane in the material, there are both normal and shear stresses acting. The interaction line that defines failure in shear versus normal stress space is the Mohr-Coulomb line, and the two stresses are Mohr-Coulomb stresses. The inclination of the fracture plane must be known in order to apply this criterion. The standard "ply strength values" X, Y, (tension or compression) and S are used as inputs in the LaRC 03 criterion. It is important to note that using this criterion for composite laminates requires use of the *in-situ* strength values for X, Y, and S. These can be significantly different from the values one obtains from standard tests because, in a laminate, plies are constrained by adjacent plies of different orientations, and typically, exhibit significantly higher values for Y and S than obtained in tests of individual 0/90 specimens [25]. Predictions obtained with this criterion on uni-directional laminates are in good agreement with the test results [23].

7.3.6.2.8   Onset Failure Theory (originally Strain Invariant Failure Theory)

This is an approach that explicitly accounts for fibers and matrix, and their respective failure strains under different types of loading [26−28]. This is done by relating the applied strains to strains applied to the fiber and matrix and using strain invariants to predict the onset of failure. Finite element models are used to go from the global strains to the local fiber and matrix strains. This process is called micromechanical enhancement [27]. Representative Volume Elements representing the possible ways fibers may be distributed in the matrix are used. Extensive work has been done in Refs. [26−28] and other references (see Section 7.6) to determine the minimum number of unit cells needed and at what locations the strains should be calculated in order to obtain a lower bound on the strain to failure of typical composite structures. In principle, for each constituent, fiber, and matrix, there are two invariants, the dilatational, which, for small strains, is the sum of the normal strains, and the distortional, which is analogous to the expression of the von Mises yield criterion expressed in terms of strain. Since failure onset in typical composite materials is always a matrix crack, the matrix strain invariants are critical. If accurate values of the strain invariants are available (they should be measured experimentally), the predictions of the method for the onset of failure are very accurate.

7.3.6.2.9   First-ply failure using lamination parameters

The lamination parameters introduced in Section 7.3.4 cannot be used to predict laminate strength directly. Even if the conversion process from lamination parameters to a stacking sequence takes place, some type of a failure criterion would have to be used. Following such a procedure would eliminate most of the advantages of using lamination parameters to design or optimize a laminate. As an alternative, Ijsselmuiden et al. [29] proposed a method that uses the Tsai-Wu failure criterion to determine a

conservative strain envelope inside which the Tsai-Wu criterion is guaranteed to not predict failure for any stacking sequence of the chosen material. The Tsai-Wu criterion is written in terms of laminate strains, and the angle θ is varied from 0 to 90°. For each value of θ, a different failure curve is obtained. The envelope of all curves which define the range of strains which do not cause failure according to the Tsai-Wu criterion is determined by solving two polynomial equations for the first and second strain invariants. It should be noted that, although this method uses strain invariants, it is different from the method described in the previous section. In the Onset Theory of the previous section, the strain invariants are compared to material allowable values, whereas, here, the Tsai-Wu failure criterion is applied. This method is conservative because, by construction, it would work for any stacking sequence of the chosen material. It, however, allows the use of lamination parameters, and thus, strength optimization can still be done using them, avoiding the problems encountered when operating with actual laminate layups.

These recent developments show significant improvement in the accuracy and applicability of the failure criteria and point to the importance of incorporating physical mechanisms in the failure model. Some of these models may, currently, require some parameters that are experimentally determined and may come at a significant computational cost as criteria, such as the LaRC 03 are extended to the post first-ply failure of laminates, but are the most promising for predicting the final collapse of the material in realistic composite structures.

Most of the criteria discussed so far, focus on predicting some form of failure onset, typically the first-ply failure. As referred to above, this does not necessarily coincide with final failure or collapse of a laminate. There may be significant additional load carrying capability, which can be very important for damage tolerance considerations.

Considering the difficulties that the existing failure criteria have in accurately predicting the first-ply failure, it would appear futile to discuss the post first-ply failure modeling. However, the concepts and approaches used can be very valuable in providing a framework that can be used in conjunction with more accurate failure criteria as they develop.

In the general approach, the loads are applied incrementally until the first-ply failure occurs. The type of failure, matrix or fiber, determines the properties of the failed plies that must change to reflect the damage created. This is subjective and can cover a range of possibilities. The most conservative approach would completely discard affected properties for the failed plies. So for fiber failure, E_{11} would be set to zero. For matrix failure, E_{22} and G_{12} would be set to zero. Then, the loads would be incremented until another ply fails, and the procedure would be repeated to complete failure of the laminate. Less conservative approaches attempt to only partially discount stiffness values of the failed ply and even differentiate between tension and compression moduli. These methods can be reasonably accurate if they are accompanied by selected tests that help better define "adjustment" factors for the stiffness properties of failed plies. However, they are limited in applicability and accuracy because they are affected by the first-ply failure criterion used to trigger the failure sequence and because they do not correctly capture damage modes, such as delamination and the interaction between them, such as matrix cracks causing delaminations in adjacent ply interfaces.

Significant improvements in modeling have been achieved with the use of extended finite element methods (x-FEM) coupled with more accurate constitutive properties and continuum damage mechanics [30,31]. In these and similar approaches, improved failure criteria, such as the LaRC 03 are combined with accurate stress-strain curves obtained experimentally, which track the full load cycle past the linear region and following failure and unloading. These are obtained for different failure modes, such as fiber pull-out, fiber kinking, etc. and allow more accurate adjustment of properties in computational models. In addition, delaminations are tracked with the use of cohesive elements in a finite element framework. There are some issues with damage interaction and how the load is redistributed in the vicinity of damage, but this type of modeling appears to be the most promising to date. It should be noted that the computational demands for fully carrying out analysis of even relatively simple situations, such as low-speed impact, are very high.

7.3.7   Notched strength of composite laminates

Flaws in composite structures are inevitable. Of particular interest are the notches, such as holes, cracks, or impact damage. Unlike metals, composites exhibit notch sensitivity. For high applied loads there is very little load redistribution in composites while in metals, yielding allows a significant reduction in the stresses in the vicinity of the flaw to values much lower than their linear elastic counterparts. As such, composites, show, in general, a steep reduction in strength with flaw size while the corresponding strength reduction in metals is smaller. These flaws and their effect on the strength of composite structures are analyzed elsewhere in this book. Here, a few overview comments are in order.

First, a linear analysis (for holes and cracks, for example) shows much higher stresses (infinite for a crack) than are actually present. This is due to the fact that a linear analysis does not account for the damage or process zone created at the edge of the flaw which redistributes the stresses to some extent. For this reason, analysis in the presence of flaws using a linear model requires the use of some characteristic or averaging distance [32,33] at which, or over which stresses are evaluated and compared to the un-notched strength values.

Second, for uni-axial loading situations, the use of 45/-45 fibers provides excellent load distribution around the notch. The stress concentration factor due to the presence of the notch is drastically reduced. However, the exclusive use of 45/-45 fibers results in laminates with low un-notched strength. So a combination of fibers aligned with the primary load direction (for example, 0° fibers) and 45/-45 fibers would give the highest notched strength by reducing the stress concentration factor while maintaining adequate un-notched strength.

Finally, of great importance are finite width effects. The strength of a composite laminate in the presence of a hole, a crack, or impact damage is drastically reduced as the size of the notch covers a significant percentage of one of the dimensions of the structure. Finite width correction factors have been obtained by Tan for holes [34].

7.3.7.1   The effect of a hole on laminate strength

For putting things in perspective, the effect of a hole on the tensile or compressive strength of a laminate is discussed here in more detail. This is the case of an "open hole," that is a hole that does not have a fastener in it. Such holes are used often in design to model other types of notches (cracks, impact damage) as circular holes of an effective diameter. In addition, holes (6−7 mm in diameter) are used as the notch of preference in demonstrating limit load capability in a composite aircraft part. Thus, being able to predict the tension or compression strength of a laminate in the presence of a hole can be very important in the design of a component made of composite materials. The situation, for a laminate under tension or compression, is shown in Fig. 7.9.

The case of an infinite plate with an elliptical hole was solved by Lekhnitskii [35]. By using anisotropic elasticity and treating the plate as homogeneous, he determined the stresses anywhere in an infinite composite plate with a hole. Due to the stress concentration effect created by the hole, the highest stresses are on the hole boundary. It is important to note that, unlike metals, where the critical location is at $\theta = 90$ degrees (see Fig. 7.9) the critical location for a composite plate is a function of the stacking sequence. It can be shown that Lekhnitskii's solution on the hole edge becomes:

$$\sigma_\theta(r=a) = \frac{-K\cos^2\theta + \left(1 + \sqrt{2K-m}\,\right)\sin^2\theta}{\sin^4\theta - m\sin^2\theta\cos^2\theta + K^2\cos^4\theta} \tag{7.42}$$

where

$$K = \sqrt{\frac{E^L_{xm}}{E^L_{ym}}}, \quad m = 2\nu^L_{xym} - \frac{E^L_{xm}}{G^L_{xym}}$$

with E^L_{xm}, E^L_{ym}, G^L_{xym}, and ν^L_{xym} laminate (membrane) stiffness properties given by Eq. (7.30).
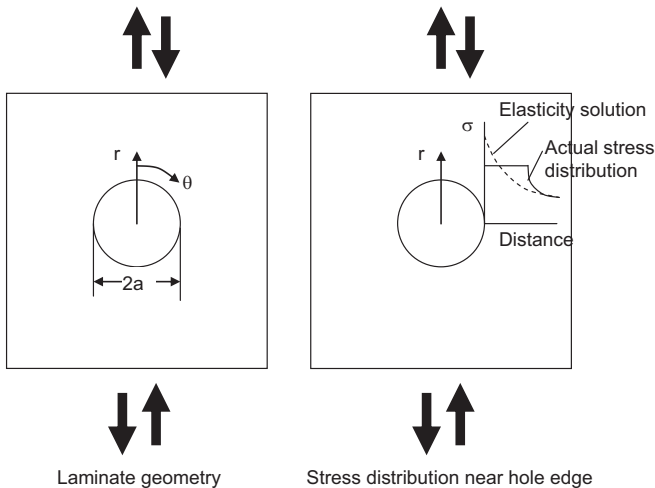
Figure 7.9 Composite laminate with a hole under tension or compression.

As K and m change, the location of the maximum value of the circumferential stress σ_θ changes. The quantity multiplying σ in the right-hand side of Eq. (7.42) is the stress concentration factor SCF. The SCF for a composite can be as high as seven to nine for a laminate consisting of all 0 plies. This happens because the orthotropy ratio E^L_{xm}/E^L_{ym} is maximized for such laminates. Also, in the case of a quasi-isotropic laminate, $E^L_{xm} = E^L_{ym}$ and $E^L_{xm} = 2(1+\nu^L_{xym})G^L_{xym}$. Substituting in Eq. (7.42) and evaluating at $\theta = 90$ yields the well-known result for isotropic materials, SCF = 3.

It should be noted that the above equation, which is based on the assumption of a homogeneous plate, is independent of the stacking sequence. Rearranging the plies in a laminate in any order will give the same answer. This means that interlaminar stresses, which for some stacking sequences can be very important, are neglected.

The stress predicted by Eq. (7.42) is very conservative. A laminate will have damage onset when the right-hand side of Eq. (7.42) exceeds the stress at which first damage will occur, but this damage onset almost never coincides with final failure. As mentioned above, some stress redistribution takes place as damage starts and evolves. This is shown schematically on the right of Fig. 7.9. Therefore, Eq. (7.42) cannot be used to predict final failure of a laminate with a hole. For this reason, alternative methods have been proposed.

7.3.7.2   Alternative methods to predict final failure of laminate with a hole

Whitney and Nuismer [36] recognized that the stress value predicted by elasticity at the hole edge is of no use for predicting final failure. They suggested that failure occurs when the damage zone created at the edge of the hole reaches a size such that further stable growth of the damage zone is not sustainable. They postulated two approaches: In the first, there should be a characteristic distance d_o away from the hole edge at which one should evaluate the stress using the linear elastic solution. If the stress at that point equals the undamaged strength of the laminate, the laminate with the hole fails. In the second they proposed that the linear elastic circumferential stress be averaged over a characteristic distance a_o (different than d_o). If that average equals the undamaged failure strength, the laminate with a hole fails. Both of these characteristic distances are assumed to be material constants. However, it was found that these distances vary with stacking sequence, but they do not seem to vary a lot with hole size for a given stacking sequence. Still, the approach gives reasonable predictions. The typical value for d_o is approximately 1 mm for first-generation thermoset composite materials.

An improvement over the Whitney-Nuismer approach was that by Garbo and Ogonowski [37]. They solved the case of a fastener hole using complex elasticity and recovered the case of an open hole as a special case. They still use a characteristic distance as is done in the Whitney-Nuismer approach, but their method is applied to every single ply. In addition, it allows for any type of combined in-plane loading instead of uniaxial tension or compression.

Soutis, Fleck, and Smith [38], proposed the use of linear elastic fracture mechanics and the principle of superposition to determine the failure strength of composites with holes in particular under compression. This approach essentially models the damage developing at the edge of the hole as a crack with loaded surfaces. This is a one-parameter model as the crack surface stress must be determined by tests.

A method to use the Whitney-Nuismer approach [36] but analytically predict the averaging distance was proposed by Kassapoglou [39,40]. The size of the damage region next to the hole edge is estimated by assuming the stress in the damaged region is constant and obtained by equality of strain energy density with the linear solution. The estimated size of the damage region is then used in the determination of the averaging distance. Typical results for an AS/3501-6 quasi-isotropic laminate are shown in Fig. 7.10. Note that for compression, fiber kinking next to the hole edge must also be taken into account (see Eq. 7.45 below).
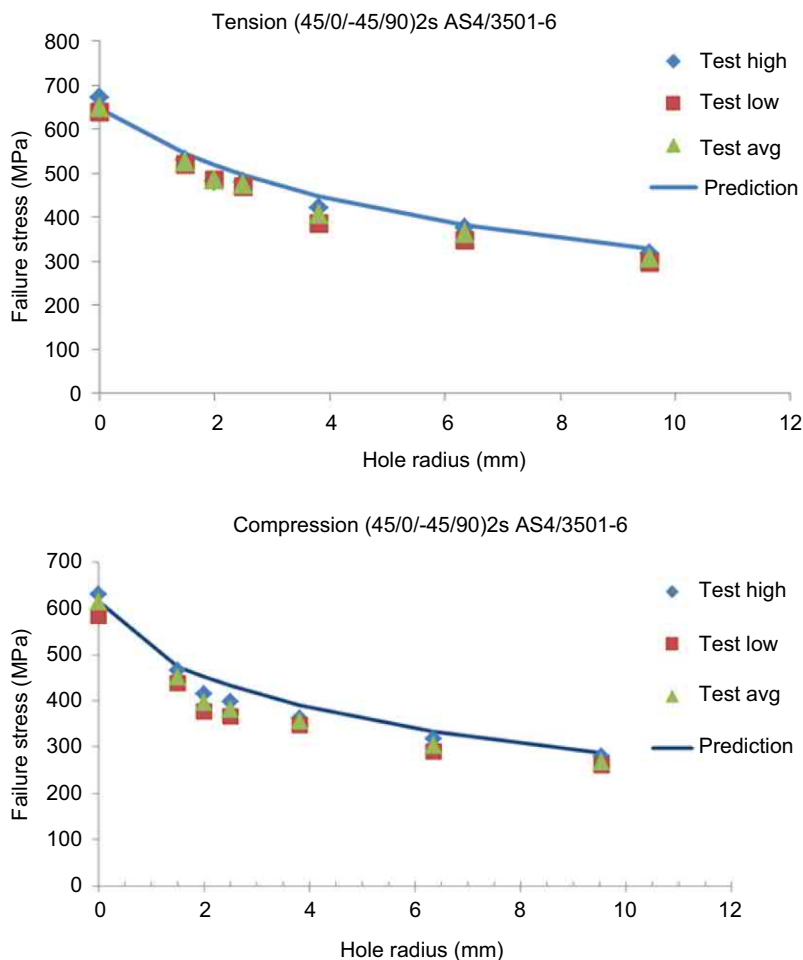
Figure 7.10 Strength as a function of hole size for quasi-isotropic AS/3501-6 laminate.

The above methods vary in accuracy and complexity, and it is up to the user to determine which method suits best a particular application. The topic is very much an open research topic, and the methods just described are some of the more promising in dealing with the problem.

7.4 Woven composite materials

In addition to laminated composite structures using uni-directional tape plies as the building blocks, fabric materials, woven, braided, knitted, stitched, etc., are also used in practice. In general, woven materials are used because (a) they conform more easily to complex shapes avoiding manufacturing flaws, such as delaminations, fiber bridging, "pinched" material, etc., (b) they can align fibers, which are the main load-carrying constituents, in directions of significant secondary loads, such as the out-of-plane loads (c) they improve damage resistance (e.g., impact damage) by minimizing interply failure (delaminations). At the same time, these advantages of woven composite materials come at a price: reduced in-plane stiffness and strength properties in some situations. For example, 2-D braided composites compared to their uni-directional tape equivalents [41] have shown lower transverse stiffness, and compression, shear, and bearing strengths with the drop in shear strength approaching 50% for some configurations. On the other hand, open hole and filled hole tension strengths were significantly higher than those for the equivalent tape laminates.

7.4.1 Stiffness models

In general, a woven fabric form has at its base a repeating unit. Modeling the stiffness and strength of the repeating unit is one of the methods for analyzing such structures. However, this does not allow for variations to or deviations from the nominal pattern in the repeating unit cell or representative volume element. These deviations may result in the significant departure of the response of the overall structure from the nominal response. One can account for these deviations by using the Monte-Carlo simulations that will provide a range for the structural property (stiffness) of interest.

Alternatively, tests can be used to obtain the basic stiffness properties of the material form and their corresponding range measured by some statistical property, such as the standard deviation. In two-dimensional cases where there are no significant loads in the out-of-plane direction, the basic orthotropic stiffness properties in Eq. (7.1) can be measured experimentally. Then, the Classical Laminated-Plate theory, described in the previous sections for determination of stiffness, can be used effectively to model these structures. Alternatively, the four basic stiffnesses for 3D woven composites can be obtained, with reasonable accuracy, by assuming that Young's moduli in the 1 and the 2 directions are those corresponding to a 0/90 laminate as obtained by the rule of mixtures and the Poisson's ratio ν_{12} is very small. For the shear modulus G_{12}, the rule of mixtures underestimates the value. It should also be noted that minor adjustments to E_{11}, and E_{22} to account for the 3D reinforcement improve the prediction of the rule of mixtures [42].

However, especially for three-dimensional structure, or even, in two-dimensional structure with significant out-of-plane loads, the stiffness-averaging of the Classical Laminated-Plate theory is not sufficient. In such cases, a specialized finite element model, such as the binary model by Cox, Carter, and Fleck [43] can be used. In this model, the Monte Carlo simulation allows the user to randomly orient tows and assign strength properties to the different components.

It is important to note the effect of scales here. Any analytical model that is based on a repeating volume element or some form of property averaging is only valid over a length scale that is significantly larger than the size of the repeating volume element or the pattern that makes up the structure. For typical 3-D woven fabrics, this means that stiffness properties are averaged over lengths of 10−15 mm.

7.4.2   Strength models

As one might expect from the discussion in Section 7.3 on failure criteria for laminates, most macroscopic failure criteria that are not based on some physical representation of damage phenomena are not very accurate or do not apply to a wide range of laminates and/or loading situations. This situation is even more pronounced for woven composites where the presence of yarns in different directions (warp, stuffer, filler), fiber or yarn waviness, damage caused to the fibers during the weaving process, variations in the fiber volume distribution and the existence of flaws, complicate the situation significantly.

Final in-plane failure under tension is caused by fiber breakage. Under compression, the dominating mechanism is kink-band formation and fiber microbuckling. The stress σ_b at which fibers buckle is given by

$$\sigma_b = \frac{\tau_{my}}{\phi} \tag{7.43}$$

where τ_{my} is the yield shear stress of the matrix and φ is the misalignment angle. Note that when $\varphi = 0$, there is no misalignment, and there is no kink band formation (σ_b equals infinity).

For typical 3D woven fabrics, the misalignment angle can be assumed to be normally distributed with mean equal to zero and a standard deviation around 5-6 degrees [44].

In the presence of shear stresses, kink band formation is still possible, but now the buckling stress is reduced [44]:

$$\sigma_b = \frac{\tau_{my} - \tau}{\phi} \tag{7.44}$$

where τ is the applied shear stress in the plane of interest (for example, transverse shear stress in the 13 plane). Note that the absolute values of τ and φ should be used in the right-hand side of Eq. (7.44).

Budiansky [45] showed, under certain assumptions that Eq. (7.44) takes the form:

$$\sigma_b = \frac{\left(G + E_T \tan^2\beta\right)\dfrac{\tau_{my}}{G}}{\varphi_m\sqrt{\left(\dfrac{G + E_T \tan^2\beta}{G}\right) + \dfrac{\tau_{my}}{G}}} \tag{7.45}$$

where G, E_T are the shear and transverse moduli, respectively, of the composite, and β the kink band rotation angle and $\varphi_m + \varphi$ is the inclination angle of the kink band with respect to the axis of the fibers.

7.4.3   The effect of flaws on the strength of woven fabrics

The discussion of flaws from Section 7.3 carries over to woven fabrics also. There is, however, an additional important aspect related to scaling. The microscopic structure of woven fabrics builds into these structures an inherent flaw size effect. That is, due to misalignment and waviness of fibers, nonuniform fiber volume distribution, damage to the fibers during the weaving process, etc., the strength of a nominally pristine woven fabric is lower than the ideal strength one would obtain for this geometry. This means that if the flaw size is smaller than the size of a few representative volume elements, its effect will be "masked" by the microstructure of the material and it will not cause any reduction to the un-notched strength. Only when the size is greater than a threshold size, (typically the size of one or two representative volume elements) will the presence of a notch (a hole, crack, etc.) register as a measurable reduction in strength.

For accurate modeling of woven fabrics with flaws, finite element models with cohesive elements are recommended.

The above is by no means an exhaustive account. It is only meant to alert the reader to several issues that must be accounted for when modeling the stiffness and strength of composite structures.

7.5   Modeling effect of anomalies

Several types of anomalies or flaws occur during manufacturing and service of composite structures. Excluding the holes which were discussed in section 7.3, impact damage and delaminations, which are discussed within the context of damage tolerance in this book, the main types of anomalies are:

-   Resin rich/resin poor areas.
-   Small distributed voids/porosity
-   Larger isolated voids
-   Fiber waviness

7.5.1   Porosity

Porosity is discussed here briefly as an example. The size of individual pores or voids is assumed to be small, so each of them is completely encased by the matrix in

the composite. The voids are assumed to be spherical and are modeled as cracks of the same size. Then, the matrix properties in the presence of porosity can be determined by considering a new material with the basic matrix properties and randomly interspersed cracks. This problem has been solved by Budiansky and O'Connel [46] within a different context, but their results can be applied here also. The Poisson's ratio of the porous matrix is found iteratively as the solution to:

$$D = \frac{45}{16} \frac{(\nu - \nu_v)(2 - \nu_v)}{(1 - \nu_v^2)(10\nu - \nu_v(1 + 3\nu))} \tag{7.46}$$

where ν is the Poisson's ratio of the nonporous matrix, assumed isotropic, ν_v is the sought-for Poisson's ratio of the matrix with porosity and D is a measure of crack density given by:

$$D = n(2R_v)^3 \tag{7.47}$$

where R_v is the typical radius of a spherical void and n is the number of voids per unit volume.

The Young's and shear moduli E_v and G_v of the porous matrix respectively can be found to be:

$$\frac{E_v}{E} = 1 - \frac{16}{45} \frac{(1 - \nu_v^2)(10 - 3\nu_v)}{2 - \nu_v} D \tag{7.48}$$

$$\frac{G_v}{G} = 1 - \frac{32}{45} \frac{(1 - \nu_v)(5 - \nu_v)}{2 - \nu_v} D \tag{7.49}$$

It is important to note that the size of the voids R_v does not affect the values of the stiffness properties of the porous matrix because as R_v changes the number of voids per unit volume n changes accordingly thus canceling out this effect.

Once the new matrix properties accounting for porosity are known, the ply-level stiffnesses can be determined using micromechanics and then the Classical Laminated Plate Theory outlined in previous sections can be used.

7.5.2   Larger voids as delaminations

Larger voids can be modeled as delaminations. Their effect on stiffness can be accounted for by combining the sublaminates into which they divide the original laminate to determine the corresponding stiffness properties (combination of springs in parallel and/or in series). For example, with reference to Fig. 7.11, the laminate stiffness in the x direction accounting for individual voids can be approximated by:

$$E_x = \frac{1}{h} \left[\sum_{k=1}^{n} (Q_{11})_k t_k - \sum_{j=1}^{3} \left[\sum_{k=1}^{n} (Q_{11})_k t_k - \frac{1}{h} \sum_{m=1}^{n+1} (Q_{11})_m t_m \right] \frac{2s_j}{L} \right] \tag{7.50}$$
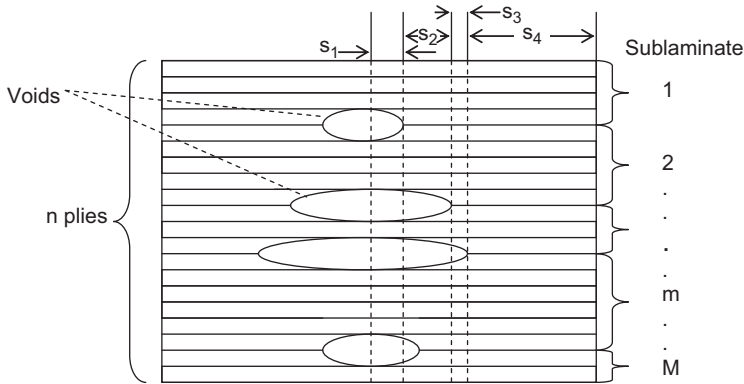
Figure 7.11 Individual voids dividing a laminate into sublaminates and sections.

where h is the laminate thickness, n is the total number of plies in the laminate, the subscript k denotes the kth sublaminate, Q_{11} is axial stiffness ($=E_{11}/(1-\nu_{12}\ \nu_{21})$), s_j denotes the length of the jth section in the cross-section of interest, L is the total length of the cross-section, and j denotes the cross-section on which the calculations are performed.

7.6 Future trends

7.6.1 Trends in failure analysis

Work continues in progressive damage modeling. Recent trends suggest that probabilistic methods, including micromechanical models [47] and xFEM, allowing the introduction of cracks or other damage in a finite element mesh independent of the mesh pattern [48] yield very promising results and good correlation with tests is obtained as damage evolves during the test.

7.6.2 New design concepts

7.6.2.1 Grid-stiffened structures

Ever since the Vickers Wellington bomber in the 1940s, the increased damage tolerance and structural efficiency of grid-stiffened structures have made this concept worth revisiting a number of times. The main problem with such construction has always been the cost. The development of automated fabrication processes, such as the Automated fiber/ Tow Placement (ATP), makes the cost-efficient fabrication of such structures possible. Currently, there are on-going efforts in Russia, the United States, and Europe where composite grid-stiffened fuselage barrels are being designed and fabricated [49−51]. The analysis of such structures requires special attention to the effect of the grid on stiffness and strength. Models range from simple homogeneous models with smeared properties to detailed three-dimensional finite element models that can capture the interlaminar stresses between grid and skins and predict grid-skin separation.

7.6.2.2   Variable stiffness laminates

Another advantage of using the new ATP technology for the fabrication of composite structures is that it makes possible the construction of composite parts with continuously varying fiber orientation in each ply. Optimization methods, based mostly on lamination parameter formulations, are used to determine the optimum fiber paths to minimize weight, maximize stiffness, place natural frequencies accurately, etc. A significant improvement over optimum results with straight fibers has been documented [52−55]. Examples of variable stiffness laminates are shown in Fig. 7.12.

(a)   (b)

Portion of cylinder   Flat panel
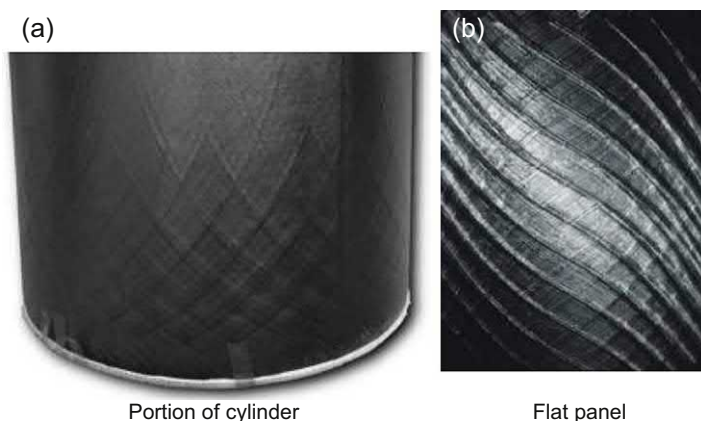
Figure 7.12 Variable stiffness composite parts (made in a program by TUDelft and NLR).

7.6.2.3   AP-PLY laminates

Another area where the advent of ATP has opened up new design possibilities is the creation of panels where different plies can be selectively interwoven through the thickness of the laminate. Such laminates are called AP-PLY laminates [56,57]. This is done with almost no increase in fabrication time and ensuring minimal waviness of the interweaving plies or tows. During lay-up of a certain ply, tows are placed in the tool with a predetermined spacing between them. Then, tows corresponding to subsequent plies are placed in the tool again, leaving gaps between them. Subsequently, tows from the first ply that was laid down are placed in the tool filling some of the gaps left originally. Different patterns, interweaving two or more plies and over areas as small as a tow width and as large as the design might dictate, are possible. The resulting patterns, some of which can be seen in Fig. 7.13, have several advantages over conventional laminates: (a) They provide fabric-like behavior without the loss of in-plane strength associated with fabric materials. So, they can be used as outer plies of laminates for improved damage resistance (containing damage due to impact) or for better definition of entrance and exit holes during drilling for fasteners. (b) They provide increased damage tolerance for impact damage situations through the
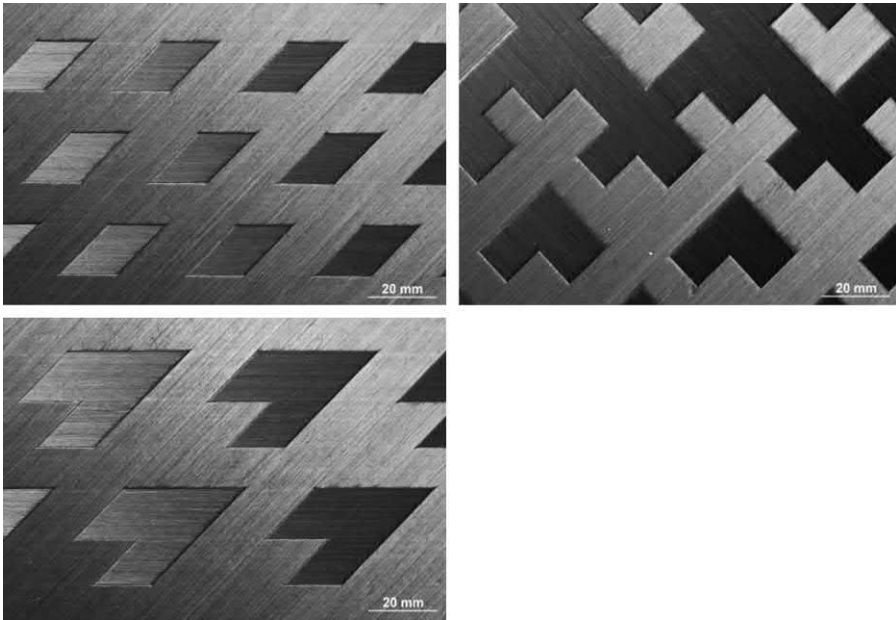
Figure 7.13 AP-PLY laminates created with the ATP process.

interweaving of plies and redistributing the impact energy between matrix cracks, delaminations with different sizes and at different through-the-thickness locations, and fiber breakage. (c) They increase "formability" by allowing a laminate to better conform to a curved surface.

References

[1] S.W. Tsai, Mechanics of composite materials, Part II - theoretical aspects, in: Report AFML-TR-66-149, Part II, Air Force Materials Laboratory Research and Technology Division, Wright-Patterson Air Force Base, Ohio, November, 1966.

[2] S.W. Tsai, H.T. Hahn, Introduction to Composite Materials, Technomic Publishing Co, Westport CT, 1980.

[3] R.M. Jones, Mechanics of Composite Materials, McGraw-Hill Book Co, Washington DC, 1975.

[4] J.E. Ashton, J.C. Halpin, P.H. Petit, Primer on Composite Materials: Analysis, Technomic, 1969.

[5] S. Nagendra, D. Jestin, Z. Gürdal, R.T. Haftka, L.T. Watson, Improved Genetic Algorithm for the Design of Stiffened Composite Panels, Computers and Structures, 1996, pp. 543−555.

[6] R. Le Riche, R.T. Haftka, Improved Genetic Algorithm for Minimum Thickness Composite Laminate Design, Composite Engineering, 1995, pp. 143−161.

[7] S.W. Tsai, N.J. Pagano, Invariant Properties of Composite Materials, Composite Materials Workshop, Technomic, 1968.

[8] M. Miki, Material Design of Composite Laminates with Required In-Plane Elastic Properties, ICCM-IV, Tokyo, 1982, pp. 1725−1731.

[9] M. Miki, Y. Sugiyama, Optimum design of laminated composite plates using lamination parameters, AIAA J. 31 (1993) 921−922.

[10] C.G. Diaconu, M. Sato, H. Sekine, Layup optimization of symmetrically laminated thick plates for fundamental frequencies using lamination parameters, Struct. Multidiscip. Optim. 24 (2002) 302−311.

[11] S.T. Ijsselmuiden, M.M. Abdalla, Z. Gürdal, Optimization of variable stiffness panels for maximum buckling load using lamination parameters, AIAA J. 48 (2010) 134−143.

[12] Z. Gürdal, R.A. Olmedo, /Composite laminates with spatially varying fiber orientations: variable stifness panel concept, AIAA J. 31 (No. 4) (April 1993) 601−608.

[13] D.C. Jegley, B.F. Tatting, Z. Gürdal, Tow-steered panels with holes subjected to compression or shear loading, in: Proceedings of the 46th AIAA/ASME/AHS/ASC Structures, Structural Dynamics and Materials (SDM) Conference, Austin, TX, USA, April 2005.

[14] A. Ahmad, M.M. Abdalla, Z. Gürdal, Optimal design of tow-placed fuselage panels for maximum strength with buckling considerations, J. Aircr. 47 (3) (2010) 775.

[15] S. Setoodeh, A.W. Blom, M.M. Abdalla, Z. Gürdal, Generating curvilinear fiber paths from lamination parameters distribution, in: Proceedings of 47th AIAA/ASME/ASCE/ AHS/ASC Structures, Structural Dynamics and Materials Conference, 2006 paper AIAA-2006-1875, Newport RI.

[16] R. Hill, The Mathematical Theory of Plasticity, Oxford University Press, London, 1950.

[17] S.W. Tsai, E.M. Wu, A general theory of strength for anisotropic materials, J. Compos. Mater. (1971) 58−80.

[18] L.J. Hart-Smith, An Inherent Fallacy in Composite Interaction Failure Criteria, Composites 24 (1993) 523−524.

[19] M.N. Nahas, Survey of failure and post-failure theories of laminated fiber-reinforced composites, J. Compos. Technol. Res. 8 (1986) 138−153.

[20] B.J. Quinn, C.T. Sun, A critical evaluation of failure analysis methods for composite laminates, in: Proceedings of 10th DoD/NASA/FAA Conf. on Fibrous Composites in Structural Design, V, 1994, pp. V21−V37.

[21] M. Hinton, P.D. Soden, A.-S. Kaddour, Failure Criteria in Fiber-Reinforced-Polymer Composites: The Worldwide Failure Exercise, Elsevier, 2004.

[22] A. Puck, H. Schürmann, Failure analysis of FRP laminates by means of physically based phenomenological models, Compos. Sci. Technol. 62 (2002) 1633−1662.

[23] C. Dávila, P.P. Camanho, C.A. Rose, Failure criteria for FRP laminates, J. Compos. Mater. 39 (2005) 323−345.

[24] Z. Hashin, Failure criteria for unidirectional fiber composites, J. Appl. Mech. 47 (1980) 329−334.

[25] G.J. Dvorak, N. Laws, "Analysis of progressive matrix cracking in composite laminates: − II first ply failure", J. Compos. Mater. 21 (1987) 309−329.

[26] J.H. Gosse, S. Christensen, Strain invariant failure criteria for polymers in composite materials, in: 42nd AIAA/ASME/ASCE/AHS/ASC Structures, Structural Dynamics, and Materials Conference. Anaheim, CA, 2001.

[27] D.L. Buchanan, J.H. Gosse, J.A. Wollschlager, A.J. Ritchey, R.B. Pipes, Micromechanical enhancement of the macroscopic strain state for advanced composite materials, Compos. Sci. Technol. 69 (2009) 1974−1978.

[28] A.J. Ritchey, J.S. Dustin, J.H. Gosse, R.B. Pipes, Self-consistent micromechanical enhancement of continuous fiber composites, in: B. Attaf (Ed.), Advances in Composite Materials − Ecodesign and Analysis, 2011, pp. 607−624.

[29] S.T. Ijsselmuiden, M.M. Abdalla, Z. Gürdal, Implementation of strength-based failure criteria in the lamination parameter design space, AIAA J. 46 (2006) 1826−1834.

[30] P. Maimí, P.P. Camanho, J.A. Mayugo, C.G. Dávila, A continuum damage model for composite laminates: Part I - constitutive model, Mech. Mater. 39 (2007) 897−908.

[31] P. Maimí, P.P. Camanho, J.A. Mayugo, C.G. Dávila, A continuum damage model for composite laminates: Part II - computational implementation and validation, Mech. Mater. 39 (2007) 909−919.

[32] J.M. Whitney, R.J. Nuismer, Stress fracture criteria for laminated composites containing stress concentrations, J. Compos. Mater. 8 (1974) 253−265.

[33] J.C. Brewer, P.A. Lagacé, Quadratic stress criterion for initiation of delamination, J. Compos. Mater. (1988) 1141−1155.

[34] S.C. Tan, Finite width correction factors for anisotropic plate containing a central opening, J. Compos. Mater. 22 (1988) 1080−1097.

[35] S.G. Lekhnitskii, Theory of Elasticity of an Anisotropic Elastic Body, Translated by P. Fern, Holden Day Inc, San Francisco, 1963.

[36] J.M. Whitney, R.J. Nuismer, Stress fracture criteria for laminated composites containing stress concentrations, J. Compos. Mater. 8 (1974) 253−265.

[37] S.P. Garbo, J.M. Ogonowski, Effect of Variances and Manufacturing Tolerances on the Design Strength and Life of Mechanically Fastened Composite Joints", 1981. AFWAL-TR-81-3041.

[38] C. Soutis, N.A. Fleck, P.A. Smith, Failure prediction technique for compression loaded carbon fibre-epoxy laminate with open holes, J. Compos. Mater. 25 (1991) 1476−1498.

[39] C. Kassapoglou, Modeling the Effect of Damage in Composite Structures, Wiley, 2015 (chapter 2).6.

[40] C. Kassapoglou, Static and fatigue analysis of notched composite laminates, J. Compos. Mater. 50 (2016) 4307−4317.

[41] P.J. Minguet, C.K. Gunther, A comparison of graphite/epoxy tape laminates and 2-D braided composites mechanical properties, NASA CR 4610 (July 1994).

[42] B. Cox, Failure Models for Textile Composites, August 1995. NASA CR 4686.

[43] B. Cox, W.C. Carter, N.A. Fleck, "A binary model of textile composites − I Formulation", Acta Metall. Mater. 42 (1994) 3463−3479.

[44] A.S. Argon, Fracture of Composites: Treatise of Material Science and Technology, Vol 1, Academic Press, New York, 1972.

[45] B. Budiansky, Micromechanics, Comput. Struct. 16 (1983) 3−12.

[46] B. Budiansky, R.J. O'Connell, Elastic moduli of a cracked solid, Int. J. Solids Struct. (1976) 81−97.

[47] E.V. Iarve, D. Mollenhauer, T.J. Whitney, R. Kim, Strength prediction in composites with stress concentrations: classical weibull and critical failure volume methods with micromechanical considerations, J. Mater. Sci. 41 (2006) 6610−6621.

[48] E.V. Iarve, M.R. Gurvich, D.H. Mollenhauer, C.A. Rose, C.G. Dávila, Mesh-independent matrix cracking and delamination modeling in laminated composites, Int. J. Numer. Methods Eng. (2011).

[49] S.M. Huybrechts, S.E. Hahn, T.E. Meink, Grid-Stiffened Structures: A Survey of Fabrication, Analysis and Design Methods, in: Proceedings of 12th International Conference on Composite Materials (ICCM), Paris France, 1999.

[50] V.V. Vasiliev, V.A. Barynin, A.F. Razin, "Anisogrid composite lattice structures − development and aerospace applications", Compos. Struct. 94 (2012) 1117−1127.

[51] C. Trautvetter, Spectrum Aeronautical Unveils the Newest Entry to VLJ Market, Aviation International News, October 2005 (online version).

[52] Z. Gürdal, R.A. Olmedo, /Composite laminates with spatially varying fiber orientations: variable stifness panel concept, AIAA J. 31 (No. 4) (April 1993) 601−608.

[53] D.C. Jegley, B.F. Tatting, Z. Gürdal, "Tow-steered panels with holes subjected to compression or shear loading, in: Proceedings of the 46th AIAA/ASME/AHS/ASC Structures, Structural Dynamics and Materials (SDM) Conference, Austin, TX, USA, April 2005.

[54] A. Ahmad, M.M. Abdalla, Z. Gürdal, Design tailoring for pressure pillowing using tow-placed steered fibers, J. Aircr. 45 (2) (2008) 630−640.

[55] A. Ahmad, M.M. Abdalla, Z. Gürdal, Optimal design of tow-placed fuselage panels for maximum strength with buckling considerations, J. Aircr. 47 (3) (2010) 775.

[56] M.H. Nagelsmit, C. Kassapoglou, Z. Gürdal, AP-ply: a new fibre placement architecture for fabric replacement, SAMPE J. 47 (2012) 36−45.

[57] M.H. Nagelsmit, C. Kassapoglou, Z. Gürdal, Fiber placement process for AP-PLY composite components, in: Proceedings SAMPE SETEC, Leiden NL, 2011, pp. 195−202.

Sources of further information and advice

Laminate design

[1] Z. Gürdal, R.T. Haftka, P. Hajela, Design and Optimization of Laminated Compposite Materials, Wiley, 1999.

[2] S. Setoodeh, M.M. Abdalla, Z. Gürdal, Design of Variable Stiffness Laminates Using Lamination Parameters, Composites Part B, 2006, pp. 301−309.

Failure criteria and Worldwide failure exercise

[3] Z. Hashin, A. Rotem, A fatigue failure criterion for fiber reinforced materials, J. Compos. Mater. 7 (1973) 448−464.

[4] L.J. Hart-Smith, A Re-examination of the analysis of in-plane matrix failures in fibrous composite laminates, Compos. Sci. Technol. 56 (1996) 107−121.

[5] L.J. Hart-Smith, The role of biaxial stresses in discriminating between meaningful and illusory composite failure theories, Compos. Struct. 25 (1993) 3−20.

[6] R.J. Nuismer, "Continuum Modeling of Damage Accumulation and Ultimate Failure in Fiber Reinforced Laminated Composite Materials", Research Workshop, Mechanics of Composite Materials, Duke University, Durham NC, 1978, pp. 55−77.

[7] Y.S. Reddy, J.N. Reddy, Three-dimensional finite element progressive failure analysis of composite laminates under axial extension, J. Compos. Technol. Res. 15 (1993) 73−87.

[8] V. Laš, R. Zemčík, T. Kroupa, R. Kottner, Failure prediction of composite materials, Bulletin of Applied Mechanics 4 (2008) 81−87.

[9] M. Hinton, S. Kaddour, P. Smith, S. Li, P. Soden, "Failure Criteria in Fiber Reinforced Polymer Composites: Can Any of the Predictive Theories Be Trusted?", in: Presentation to NAFEMS World Congress, Boston, May 23−26, 2011, 2011.

[10] L.J. Hart-Smith, Application of the strain invariant failure theory (SIFT) to metals and fiber-polymer composites, Philos. Mag. 90 (2010) 4263−4331.

[11] R.B. Pipes, J.H. Gosse, An onset theory for irreversible deformation in composite materials, in: 17th International Conference on Composite Materials, ICCM-17), 2009.

Post first-ply failure, progressive failure of composite laminates

[12] C.G. Dávila, D.R. Ambur, D.M. McGowan, Analytical prediction of damage growth in notched composite panels loaded in compression, J. Aircr. 37 (5) (2000) 898−905.

[13] N.F. Knight Jr., C.C. Rankin, F.A. Brogan, STAGS computational procedure for progressive failure analysis of laminated composite structures, Int. J. Non-Linear Mech. 37 (4) (2002) 833−849.

[14] P.P. Camanho, C.G. Dávila, D.R. Ambur, NASA TP 2001-211041 (2001).

[15] C.G. Dávila, P.P. Camanho, M.F. de Moura, Mixed-Mode Decohesion Elements for Analyses of Progressive Delamination," AIAA Paper No. 2001-1486, Presented at the AIAA/ASME/ASCE/AHS/ASC 42nd Structures, Structural Dynamics, and Materials Conference, Seattle, WA, April 16-19, 2001.

[16] D. Mollenhauer, L. Ward, E. Iarve, S. Putthanarat, K. Hoos, S. Hallett, X. Li, Simulation of discrete damage in composite overheight compact tension specimens, Composites Part A 43 (2012) 1667−1679.

Modeling woven and braided materials

[17] J.-M. Yang, C.-L. Ma, T.-W. Chou, Fiber inclination model of three-dimensional textile structural composites, J. Composite Mateials 17 (1981) 25−31.

[18] A.F. Kregers, G.A. Teters, Determination of the elasto-plastic properties spatially reinforced composites by the stiffness averaging method, Mech. Compos. Mater. 20 (1986) 472−484.

[19] T.L. Normal, C. Anglin, D. Gaskin, M. Patrick, Effect of open hole on tensile failure properties of 2D triaxial braided textile composites and tape equivalents, k NASA CR 4676 (June 1995).

[20] J. Delbrey, Database of mechanical properties of textile composites, NASA CR 4747 (August 1996).

[21] C.C. Poe, C.E. Harris (Eds.), Mechanics of Textile Composites Conference, NASA Conference Publication, October 1995, 3311, Parts 1 and 2.

Further reading

[22] E.J. Barbero, Introduction to Composite Materials Design, second ed., CRC Press, Taylor & Francis Group, Boca Raton FL, 2011 chapters 5 and 6.

Appendix 1: Glossary

anomaly	:	Flaw.
balanced laminate	:	Laminate with no stretching/shearing coupling (usually for every $+\theta$ ply there is a $-\theta$ ply of the same thickness and material).
characteristic distance	:	A distance near a hole in a laminate related to the size of the distance: damage region and used to predict failure.
coupling	:	Situation where one type of behavior (for example tension) affects another (for example shear).
curvature	:	Measure of the local amount of bending or twisting in a laminate (units 1/length).
delamination	:	Disbond between plies caused by high interlaminar stresses.
failure criterion	:	Typically, a phenomenology-based equation that attempts to predict the failure of a ply given a certain loading situation.
flaw	:	Any departure of the resulting laminate from the nominal expected.
fiber kinking or micro-buckling	:	Phenomenon, where under local compression, the matrix is no longer stabilizes the fibers and they buckle forming a kink-band.
force resultant	:	Stress averaged over the laminate thickness.
fracture plane	:	Plane along which fracture occurs in a laminate.
kink band	:	Band of fibers rotated at an angle due to micro-buckling.
moment resultant	:	Stress times distance averaged over the laminate thickness.
interlaminar stresses	:	Out-of-plane stresses developing between plies in a laminate.
laminate	:	Collection of plies stacked together in a sequence that gives the desired performance.
laminate axes	:	Axis system with axes parallel and perpendicular to the edges of a rectangular laminate.
lamination parameters	:	Nondimensional parameters which define uniquely the in-plane, out-of-plane and coupling stiffness matrices of a laminate.
micromechanics	:	Branch of mechanics where the properties of individual constituents, such as matrix and fiber, are used to estimate the structural performance of a composite.
notch	:	Any form of local discontinuity (hole, crack, impact damage …)

orthotropy	:	Situation where a material exhibits different properties in different directions with no shearing/stretching coupling.
ply (or lamina)	:	Single layer of composite material used to make laminates.
ply axes	:	Axis system with axes parallel and perpendicular to the fibers in a specific ply quasi-isotropic.
Laminate	:	Laminate with the same in-plane stiffness in any direction.
specially orthotropic laminate	:	Symmetric laminate with no stretching/shearing and no bending/tropic laminate: twisting coupling.
symmetric laminate	:	Laminate in which plies located symmetrically with respect to the laminate: midplane have exactly the same orientation, thickness, and material.
a_{ij} (i,j = 1,2,6)	:	Inverse of A matrix.
A_{ij} (i,j = 1,2,6)	:	In-plane membrane stiffnesses of a laminate (units: force/length).
B_{ij} (i,j = 1,2,6)	:	Membrane/bending coupling stiffnesses of a laminate (units: force).
D	:	Measure of crack density in matrix with cracks.
d_{ij}	:	Inverse of D matrix.
D_{ij} (i,j = 1,2,6)	:	ending stiffnesses of a laminate (units: force x length).
E_{ij} (i,j = 1,2,3)	:	Young's moduli of a single three-dimensional layer.
E, E_v	:	Young's modulus in non-porous and porous matrix.
E_L, E_T	:	Young's modulus of a single ply in the longitudinal and transverse directions.
F_x, F_y, F_{xy}, F_s	:	Coefficients in Tsai-Hill failure criterion.
G, G_v	:	Shear modulus in non-porous and porous matrix.
G_{12}, G_{13}, G_{23}	:	Shear moduli of a three-dimensional layer.
G_{LT}	:	Shear modulus of a single ply.
h	:	Laminate thickness.
K	:	Square root of orthotropy ratio (used for stress around the hole).
m	:	$\cos\theta$ and stiffness parameter in equation for stress around a hole.
M_x, M_y, M_{xy}	:	Moment resultants in laminate axes (units: moment/width).
n	:	$\sin\theta$, number of voids per unit volume in a porous matrix, and total number of plies in a laminate with voids.
N_x, N_y, N_{xy}	:	Force resultants in laminate axes (units: force/width).
Q_{ij} (i = 1,2,6)	:	Ply stiffnesses in ply axes.
Q_{xx}, Q_{yy},…	:	Ply stiffnesses in laminate axes.
[R]	:	Rotation matrix (function of θ).
R_v	:	typical radius of spherical void in a porous matrix.
S		Ply shear strength.

S_{ij} (i,j = 1−6)	:	Compliances (inverses of Young's moduli) of a single three-dimensional layer.
[T]	:	Transformation matrix (function of θ).
U_1-U_5	:	Invariants describing the stiffness properties of a laminate.
V_i^A, V_i^B, V_i^D	:	Lamination parameters (trigonometric functions of θ) (i = 1−4).
x	:	One of the laminate coordinates.
X^t, X^c	:	Ply tension and compression strengths parallel to the fibers.
y	:	One of the laminate coordinates.
Y^t, Y^c	:	Ply tension and compression strengths perpendicular to the fibers.
z	:	One of the laminate coordinates.
α_{ij} (i,j = 1,2,6)	:	ntries of inverse of laminate stiffness matrix relating to membrane behavior.
β_{ij} (i,j = 1,2,6)	:	Entries of inverse of laminate stiffness matrix relating to membrane/bending coupling.
Γ_0- Γ_4	:	Matrices in terms of laminate invariants used in the definition of lamination parameters.
δ_{ij} (i,j = 1,2,6)	:	Entries of inverse of laminate stiffness matrix relating to bending behavior.
ε_1 ε_2 γ_{12}	:	Normal (ε) and shear (γ) strains in ply axes.
ε_x ε_y γ_{xy}	:	Normal (ε) and shear (γ) strains in laminate axes.
ε_x^{ult} ε_y^{ult} γ_{xy}^{ult}	:	Ultimate normal strains (ε) and shear strain (γ).
θ	:	Angle of orientation of fibers in a ply relative to the laminate x axis.
κ_x, κ_y, κ_{xy}	:	Laminate curvatures (units: 1/length).
ν, ν_v	:	Poisson's ratio of non-porous and porous matrix.
ν_{12} ν_{13} ν_{23}	:	Poisson's ratios of a three-dimensional layer.
ν_{LT}, ν_{TL}	:	Major and minor Poisson's ratios for a single ply.
σ_b	:	fiber buckling stress.
σ_1 σ_2 τ_{12}	:	Normal (σ) and shear (τ) stresses in ply axes.
σ_x σ_y τ_{xy}	:	Normal (σ) and shear (τ) stresses in laminate axes.
τ_m	:	Matrix yield stress in shear.
φ	:	Fiber misalignment angle.

Fracture mechanics of polymer composites in aerospace applications

8

Andreas J. Brunner

Empa, Swiss Federal Laboratories for Materials Science and Technology, Dübendorf, Switzerland

8.1   Introduction and overview

Fiber-reinforced polymer-matrix (FRP) composites with typical fiber volume fractions of 50%−60% are increasingly used in high-performance aircraft and spacecraft structures, mainly based on their comparatively high specific strength and stiffness which derive from their relatively low density. This trend is expected to continue due to the increasing demand for energy-saving propulsion systems for aircraft and spacecraft for which weight reductions are a key element. An important issue for these applications are impact resistance and durability under the rather severe service conditions in the aerospace environment.

FRP composites are prone to damage from initiation and propagation of delaminations in the matrix layer between the fibers or from fiber-matrix debonding. Fracture mechanics of FRP composites has to consider the anisotropic morphology of the material, which affects the location of the delaminations [1]. Delaminations located in the matrix between the planes defined by the fiber layup or the fiber plies are hence, called *interlaminar*. Initiation of such delaminations or of fiber-matrix debonding is, e.g., caused by the impact of "foreign" objects (e.g., bird strike, dropping of tools, collision with other vehicles), followed by propagation and growth due to cyclic thermo-mechanical service loads, if the applied stresses are large enough. Post-impact strength and fatigue of FRP composites are further discussed in detail in Chapter 12 of this book. Delaminations can also initiate from processing induced defects in FRP composite parts, such as machining, cutting or drilling (see, e.g., Lasri et al. [2], Shetty et al. [3]). Residual stresses from processing and manufacturing (e.g., near voids), or at material discontinuities and geometric features, e.g., edges, holes and ply drop-offs, also provide initiation sites for delaminations or contribute to their propagation and growth.

This has spurred research into improving delamination resistance or fracture toughness of FRP laminates. A key requirement for that is the development of test methods for the characterization of their fracture and fatigue fracture behavior. Fracture mechanics is the scientific discipline dealing with the behavior of cracks in materials under applied loads, stresses, or deformations. Fracture mechanics tests for quantifying

delamination resistance determine the change in strain energy per unit area of delamination, i.e., the strain energy release rate which is denoted by the symbol G. Assessing the long-term performance of FRP composites for aerospace applications, notably of their delamination resistance, also requires consideration of the effects of the respective service load spectra and of the related environmental exposure.

Most FRP composites have a comparatively high specific stiffness and show essentially linear-elastic behavior under mechanical loads. Therefore, delamination propagation in FRP composites can be analyzed with the methods of Linear Elastic Fracture Mechanics (LEFM). This avoids the complexity of dealing with elastic-plastic or plastic fracture mechanics in this class of materials in most cases [4]. Test methods for determining LEFM data are usually developed and standardized for the basic loading modes (Fig. 8.1).

These are tensile opening (labeled mode I), in-plane shear (labeled mode II) and transverse shear or twisting (labeled mode III). Of course, in structural applications, loading often occurs in mixed modes rather than in one of the pure basic modes. Test methods are further divided into quasi-static (typical load rates of a few mm/min), intermediate and high rates (around 1 m/s and several m per second, respectively) and cyclic load tests (with a choice of tension-tension, tension-compression or compression-compression loads) at constant or variable frequency and constant or variable load or displacement amplitude. The R-ratio describes the ratio between minimum and maximum stress (essentially load). The symbol R is also used for displacement ratio if the test is performed under displacement control rather than load control. A frequently used R-ratio value is $R = 0.1$, roughly corresponding to a ground-air-ground cycle, but higher R-ratio values (up to about 0.7) and lower (e.g., -1) are investigated as well. The scope of standardized fracture mechanics test methods usually specifies interlaminar delamination resistance or fracture
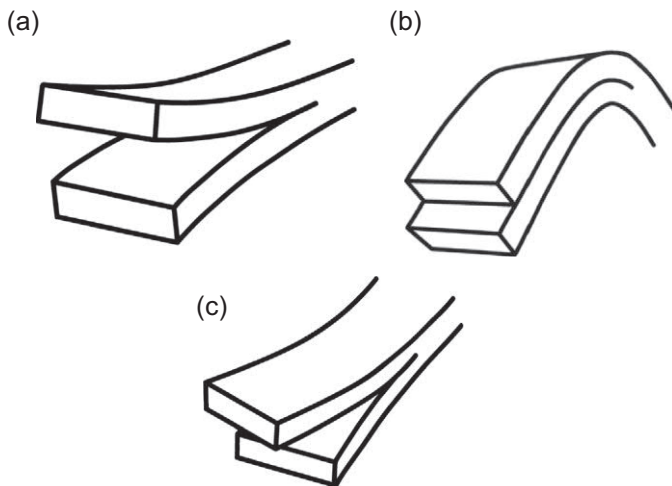
Figure 8.1 Schematic presentation of basic loading modes. (a) Mode I tensile opening; (b) mode II in-plane shear; and (c) mode III transverse twisting.

toughness of FRP composites with carbon- or glass-fiber reinforcements (CFRP and GFRP, respectively), which are the typical materials used in round robin testing for the development of the standard test procedures.

Besides interlaminar delamination propagation (i.e., extension of the delamination in the polymer matrix between fiber layers, or fiber plies), delaminations can also propagate in the intralaminar direction (i.e., between fibers, but normal to the orientation of the fiber plies), or even in translaminar direction (i.e., normal to the fiber ply orientation, resulting in fiber or fiber ply breaking). A schematic of these types of delaminations is shown in Fig. 8.2.

FRP composites in some applications use hybrid fiber reinforcements (e.g., a mixture of carbon and glass fibers, or one of these with fibers made from another material). "Fibers" as reinforcement can be "continuous" or "short" and are embedded in a polymer matrix. Continuous fibers can be fully or mainly aligned in one single direction (if "fully" aligned, the laminates are called *unidirectional*), in different planar directions (this is called *multidirectional*), or even in three spatial dimensions (e.g., emulating "textile"-type reinforcements). "Short" fibers have lengths in the range between a few centimeters and fractions of 1 mm down to about 0.1 mm; however, the fracture and fatigue fracture of short fiber or of particle or of nanoparticle-reinforced composites will not be discussed here in detail. For toughness testing of short fiber polymer composites see, e.g., ISO 13586-2018 and ISO 17281-2018, both originally developed for fracture of neat, unreinforced polymers, but now including polymer
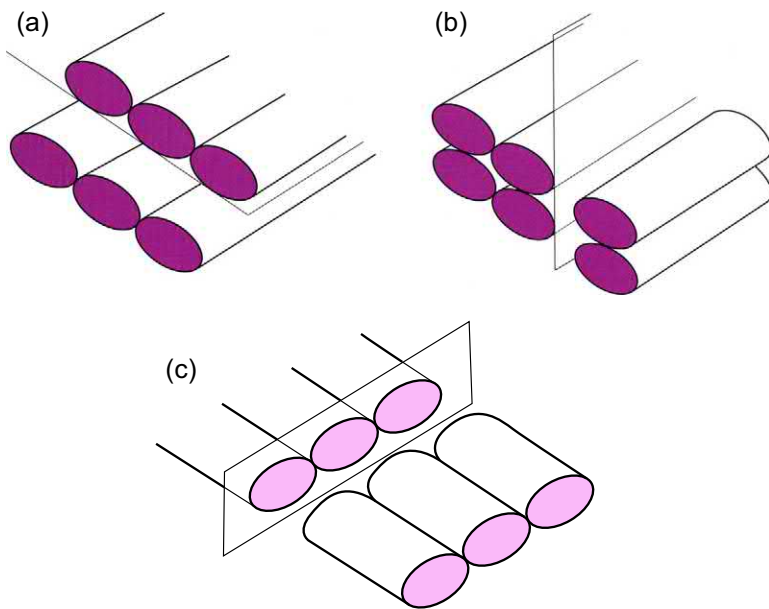
Figure 8.2 Schematic presentation of (a) interlaminar (between fiber plies); (b) intralaminar (normal to fiber plies); and (c) translaminar (cutting fiber) delamination in fiber-reinforced composite laminates.

composites with short fibers. In these two standards, short fibers are specified to have lengths in the range between 0.1 and 7.5 mm. Both describe LEFM tests, the first at quasi-static and the other at moderate loading rates around 1 m/s, respectively. Examples of testing short FRP composites are given, e.g., by Friedrich [5], Friedrich et al. [6], Nikpur et al. [7], Fernberg [8] or Rizov et al. [9]. Matrix polymers for FRP composites can be either thermoset (e.g., epoxies) or thermoplastic polymers.

Other fiber materials for FRP composites include basalt and aramid fibers. Basalt fiber composites were investigated in early research, essentially going back to work by Subramanian and Shu in the 1970ies, detailed, e.g., in Subramanian and Shu [10], and further explored by, e.g., Czigány [11], Sarasini et al. [12] and others, but not included in the scope of the test standards. Turan Demirci et al. [13] recently observed increased mode I toughness in basalt fiber-epoxy composites when adding SiO_2 nanoparticles. The fracture behavior of aramid fiber composites (fiber trade names, e.g., are Kevlar or Twaron) was investigated in the 1990ies, by, e.g., Kim and Mai [14] and others, and, as in the case of basalt fibers, was not considered in the standardization efforts. While aramid fiber composites are advantageous in ballistic and impact loading situations (see, e.g., Priyanka et al. [15] and references therein), they may be of limited use in many quasi-static fracture cases, due to their sensitivity to moisture uptake. The effects of aramid or basalt fiber-reinforcement on fracture toughness and delamination resistance is receiving some attention again recently; often, these fibers are used in hybrid fiber composites [16]. The current status of basalt-fiber polymer composites, including toughness or delamination resistance testing, has been reviewed by Fiori et al. [17] and Dhand et al. [18] and that of aramid fiber composites by Sockalingam et al. [19]. The effects of various types of aramid based components (interleaved thin films, particles, and chopped fibers) on quasi-static mode I and mode II delamination resistance of FRP composites were discussed in two papers by Yasaee et al. [20,21]. Aramid nanofibers showed improved fracture performance when implemented in continuously reinforced aramid FRP (reinforcement Kevlar KM2 fabric, style 706 scoured, CS-800 with a plain 0°/90° weave and Epon 862 matrix). The aramid nanofibers were prepared and then dispersed in the curing agent (Epikure 3230) as discussed by Patterson et al. [22]. These results indicate that the standard test procedures developed so far likely are applicable to essentially specimens made with other fiber materials, besides glass or carbon, as well. However, introducing new fiber types or additives into FRP composites for aerospace components and structures (as envisaged, e.g., by Zhang et al. [23]) requires certification of materials which can be a time-consuming and costly procedure. The essential aspects of certification of FRP composites for aerospace applications are discussed, e.g., by Leckey et al. [24], or Schmid Fuertes et al. [25].

In the context of fracture toughness and delamination resistance of aerospace structures, there are other types of fiber laminates worth mentioning that are already used in certain aircraft structures. The main group is the fiber-metal laminates (FML). Depending on the type of fiber, FML are called *Aramid-Reinforced Aluminum Laminate* (ARALL), *Carbon-Reinforced Aluminum Laminate* (CARALL), or *Glass Laminate Aluminum-Reinforced Epoxy* (GLARE). GLARE, for example, is used in parts of the fuselage of the Airbus A380 aircraft as discussed by, e.g., Wu and Yang [26].

Their fracture and fatigue fracture performance are not detailed here, for this see, e.g., Alderliesten [27] and references therein. A recent paper discusses a setup for quasi-static and fatigue fracture testing of asymmetric composite/metal assemblies under mode I loading [28].

Another type of laminate that has the potential for use in aerospace structures are FRP composites with nano-modified matrix; this has been reviewed, e.g., by Gohardani et al. [29] and Kostopoulos et al. [30]. One example of an aircraft structure with nano-modified FRP is the F-35 fighter aircraft for which the use of an epoxy matrix with carbon nanotubes (CNT) in wingtip fairings was announced in 2011, as noted in the reviews cited above. An example for space application of CNT is NASA's Juno spacecraft launched in August 2011 with CNT-sheets. These were implemented to improve protection against electrostatic discharge (ESD) which, however, is not a structural application. The same CNT-technology, on the other hand, is used on carbon fiber-wrapped pressure vessels produced by NASA. The available literature indicates that FRP composites with nano-modified matrix polymers likely can be characterized by existing fracture tests or fatigue fracture tests under development. Whether 3D printed short fiber epoxy composites (see, e.g., [31]) or continuous fiber composites with thermoplastic (see, e.g., [32]) or thermoset matrix (see, e.g., [33]) will be introduced into aerospace FRP composite structures soon, is highly questionable. However, in the long term and after certification of the materials, FRP composite parts made by additive manufacturing may find their application niches, e.g., for structural repair. Likely, the fracture behavior of these materials can be characterized by the available fracture mechanics test procedures for FRP composites.

In spite of extensive developments over the last 30 years, not all possible combinations of loading modes, load-rate as well as polymer types and fiber layups have yielded standards yet. The status of delamination resistance test developments has been reviewed by Gillespie [34], Tay [35], Davies [36] or Brunner et al. [37]. Selected challenges in the field of fracture and fatigue fracture of FRP composites have recently been compiled by Brunner [38], and the most relevant ones will be discussed in this chapter in detail.

This chapter will first discuss fracture mechanics applications to FRP composites for aerospace structures, and then compile the different test methods by type of load. This is followed by a section with literature data to highlight selected effects from processing and material layup and type. Further sections will discuss nonunidirectional reinforcement, briefly note the status of modeling and simulation of fracture and fatigue fracture tests, then review testing under environmental conditions relevant for aerospace applications and conclude with an outlook on materials delamination resistance and fracture test development trends.

Sources of information are websites of the International Organization for Standardization (ISO), the American Society for Materials and Testing International (ASTM) and the Japanese Standardization Agency (JSA) that issues Japan Industrial Standards (JIS) documents; scientific and technical journals; and information from materials manufacturers and users available through the internet. An important source of information on composites testing and materials data is the former (United States) Department of Defense Composite Materials Handbook MIL-HDBK-17 Version F

[39−41] issued by ASTM and its latest revision Composite Materials Handbook 17 Version G [42] that has been edited by a nonprofit organization (CMH17) and is available, e.g., through SAE International.

8.2   Applications of fracture mechanics to FRP composites used in aerospace

Fracture mechanics testing of FRP composites for aerospace applications may serve several, quite different purposes. Qualification and certification of FRP composites for aerospace applications require extensive test efforts (see, e.g., [24, 43]) for which fracture mechanics tests have, so far, played a secondary role. Fracture mechanics testing for quality control of processing and manufacturing is of interest to materials producers and suppliers. Determination of materials data for manufacturer's data sheets and application guidelines is a related purpose. Comparative materials characterization is, on the one hand, of interest to materials developers, but on the other, also important for the selection of materials for the set of requirements posed by the specific application and its service conditions. FRP structural design can be based on fracture mechanics criteria and test data, as discussed by, e.g., Martin [44]. However, this is not state-of-the-art, as shown, e.g., by the EUROCOMP Design Code and Handbook [45] or the U.S. Department of Defense Composite Materials Handbooks (2002). Volume 1 "Polymer Matrix Composites Guidelines for Characterization of Structural Materials" [39] that do list fracture mechanics test methods but without guidelines on the use of fracture mechanics data for structural design in Volume 3 "Materials usage, design and analysis" [41]. The latest edition of the Composite Materials Handbook 17 Version G [42] addresses these issues, however, in a fairly general way that requires additional information and engineering experience for implementing fracture mechanics data or methodology into the structural design with FRP composites. Approaches for determining design and lifing allowables for FRP aerospace structures or components based on fatigue fracture testing are discussed, e.g., by DorMohammdi et al. [46], Jones et al. [47], or Yao et al. [48]. While these purposes quite likely can be served by laboratory-scale specimen testing, design verification for complex FRP structural elements may still require structural element or full-scale structural tests.

Increasing use of simulations with, e.g., finite element and other numerical methods, in the development and design of FRP structures and their validation will require sufficiently accurate fracture mechanics data. Examples for this are modeling, e.g., impact behavior and crash resistance, but also delamination propagation under a complex spectrum of thermo-mechanical or combined mechanical and environmental loads, for examples see, e.g., Tay [35] or Hadavinia and Ghasemnejad [49]. Even with further advances in modeling and simulating structural behavior, damage accumulation and fracture induced failure, experimental design verification will not become obsolete; at least in the near and intermediate future and experimental materials' characterization tests will always provide the basic data for that.

Use of fracture mechanics test methods for failure analysis of FRP composite elements is feasible, but to the best knowledge of the author, no examples of this have been published. The main challenge here is the preparation of suitable test specimens from structural elements and the creation of the starter cracks. ISO 15024 does provide some information on mode I starter crack preparation for nonstandard specimens in informative appendix "B.8 Guidelines for wedge precracking" and that procedure can be adapted for other specimen geometries. Diamond wire sawing (see, e.g., [50]) is another approach, and a comparison of different precracking methods is discussed, e.g., by Burda et al. [51]. There are two issues to be considered: First, precracks should ideally simulate "natural" cracks assumed to be "sharp" (e.g., defined by a notch-tip radius of a "few" micrometers; typically 10 μm are considered an upper limit) and, second, different precracking methods may yield different fracture process zones and hence different extent and possibly type of damage close to the crack tip.

The variety of damage mechanisms and the resulting complex damage accumulation and failure behavior of FRP composites as well as the material variability are typically accommodated via the use of safety factors in the design of structural elements (even in designs that are not based on fracture mechanics). Combining fracture mechanics data from materials or structural element tests with suitable simulation or damage models may provide a path toward lighter and simultaneously more reliable FRP structures in the future. As discussed below in more detail, for structural applications in aerospace, the quantification of the scatter in the experimental data from standard tests is essential to determine safe design limits. This challenge has not been completely solved yet, mainly due to the fact that not all sources of scattering have been identified and quantified.

One advantage of structural designs with FRP composites is that the layup, that is, the number of plies (fiber layers) and the orientation of the fibers in each ply relative to other plies can be chosen according to the strength and/or stiffness requirements for the specific application. This frequently results in multidirectional layups. Another solution is the use of three-dimensional reinforcements, e.g., braided or woven, but also preparing composites by stitching, tufting, or inserting Z-pins in the through-thickness direction (see, e.g., [52−57]). Z-pinned FRP composites have found applications in composite structures in fighter aircraft, namely in the air inlet ducts and engine bay doors of the F/A-18E/F Super Hornet [58]).

The industry-specific fracture mechanics test procedures for FRP composites, e.g., Airbus Industries Test Methods (AITM) or Boeing Support Specification (BSS) are essentially based on test procedures developed by national or international standardization agencies. The scope of the standard test methods published so far focusses on unidirectionally reinforced FRP laminates, i.e., composites with fibers aligned in one direction only. Published research, discussed in detail below, does indicate that the standard test methods may not be applicable for all types of nonunidirectional or multidirectional layup. Therefore, the question of how fracture mechanics data from tests on unidirectionally reinforced FRP composites can be applied to the selection of materials or to designing engineering structures deserves attention. One published example of fracture mechanics-based design and life-time prediction are rotor hub flexbeams [59]. The discussion compares finite element model

predictions with test results and explicitly notes the need for mode I and mode II fatigue delamination propagation data for which no standards are yet available. Wimmer et al. [60] discuss the numerical simulation of delaminations based on a combination of strength and fracture mechanics criteria and Chen et al. [61] predict delamination behavior in braided composite T-shaped specimens.

From the perspective of test laboratories, simple, quick, and easily analyzed test methods are desirable. These aspects are especially important for cyclic fracture mechanics tests. The determination of threshold values, i.e., applied load or displacement levels for which no delamination propagation is observed, typically require long test duration (several million cycles at frequencies of a few and, at most, around 10 Hz). Increasing test frequency beyond 10 Hz may result in significant thermal effects due to "self-heating" of specimens. Threshold values are of importance in fracture mechanics based composites design for the so-called *no growth* approach [44], since the typical plots of delamination length increment per cycle as a function of applied "load" (either expressed as a G_{max} or a ΔG value) yield rather steep slopes and frequently significant scatter (for mode I fracture of FRP laminates see, e.g., [62−64] in the so-called *Paris plot* [65]. However, detailed analysis of mode I cyclic fatigue tests [63] has indicated that threshold values in some experiments may be apparent rather than real in the sense that they reflect limited experimental resolution in load and displacement measurements or in the observed delamination length increment. At a delamination rate of 10^{-8} mm/cycle, one million cycles yield an average increment of 10 μm. At least five million cycles are needed to reach 50 μm of delamination length increment (roughly the diameter of a human hair) that is estimated to be a lower limit of resolution for such measurements at best, even if a traveling microscope (maximum specified magnification of 70× in ASTM D5528) is used.

From a cost perspective, automated fracture mechanics testing, data acquisition, and analysis with minimal operator effort and also requiring minimal operator qualification are preferred. Quality assurance testing and even more statistical process control demand quickly available test results and possibly in large quantities, while design and life-time estimates based on cyclic fatigue require rather long test durations and hence yield large amounts of data. Unless other tests are used instead of fracture mechanics data for quality assurance and process control which, however, may be limited in their correlation with fracture behavior, automated testing, and data analysis quite likely offer the best solution. Eliminating operator-dependent effects, e.g., the subjective visual reading of delamination length by the so-called *effective delamination length* back-calculated from specimen compliance (load and displacement data from the test machine) and independent measurement of the elastic modulus (see Blackman et al. [66] or ISO 15114 for details) improves reproducibility. This approach can easily be implemented in automated analysis. Digital image or video acquisition and analysis can provide an alternative or complementary record to machine-based compliance data for delamination length determination. The cost for high-resolution digital cameras with large memory has decreased significantly in recent years, and there are increasing numbers of publications on this topic (see, e.g., [67]). Digital Image Correlation (DIC), which yields images of the stress fields on the specimens' surface is also explored for characterizing delamination initiation and propagation

(see, e.g., [68−70]). For these reasons, if fracture mechanics tests are going to be used in the aerospace industry, extensive automation of testing, data and image acquisition as well as data analysis is expected to be the key factor.

8.3 Fracture mechanics test methods for FRP composites

8.3.1 Quasi-static test methods

An overview of quasi-static fracture mechanics test methods for continuous fiber, unidirectional FRP composites is given in Table 8.1. For mode I, several test standards first issued many years ago, namely JIS K7086 "Testing methods for interlaminar

Table 8.1 Quasi-static fracture mechanics test methods for FRP composites.

Mode	Standard test method	Standard test in preparation	Remarks
I	JIS K 7086 ASTM D 5528 ISO 15024	−	Applicability to nonunidirectional FRP composites not fully assessed, intralaminar see Macedo et al. [77] trans-laminar see Laffan et al. [78]
	ISO 13586-2018		Short fiber composites
II	JIS K 7086	−	3-ENF specimen
	ASTM D7905	−	3-ENF specimen
	ISO 15114	−	C-ELS specimen
III	Not available	ASTM round robins 1999 ff. (no current ASTM work item)	de Morais et al. [79], Browning et al. [80, 81], Szekrényes [82], Ge et al. [83]
I/II	ASTM D 6671	ESIS round robins 1994 ff. (under development for standardization in ISO)	ESIS investigates a fixed ratio (4:3) mixed-mode I/II test (FRMM)
I/III	Not available	−	Pereira and de Morais [84], Szekrényes [85]
II/III	Not available	−	de Morais and Pereira [86], Kondo et al. [87], Szekrényes and Vicente [88], Canturri et al. [89]
I/II/III	Not available		Davidson and Sediles [90]

fracture toughness of carbon fiber reinforced plastics" (1993) which also includes a mode II test procedure; ASTM D5528 "Standard test method for mode I interlaminar fracture toughness of unidirectional fiber-reinforced polymer matrix composites" (first issued 2001), and ISO 15024 "Fiber-reinforced plastic composites − Determination of mode I interlaminar fracture toughness, G_{IC}, for unidirectionally reinforced materials" (2001). Quasi-static mode II has been standardized in ASTM D7905/D7905M (2017) "Standard Test Method for Determination of the Mode II Interlaminar Fracture Toughness of Unidirectional Fiber-Reinforced Polymer Matrix Composites" and ISO 15114 (2014) "Fiber-reinforced plastic composites - Determination of the mode II fracture resistance for unidirectionally reinforced materials using the calibrated end-loaded split (C-ELS) test and an effective crack length approach." The European aerospace series standards EN 6033 "Carbon fiber-reinforced plastics − Test method − Determination of interlaminar fracture toughness energy − mode I − G_{IC}" (2015) and EN 6034 "Carbon fiber-reinforced plastics − Test method − Determination of interlaminar fracture toughness energy − mode II − G_{IIC}" (2015) are equivalent to AITM 1−0005 "Fiber-reinforced plastics - Determination of interlaminar fracture toughness energy - Mode I − GIc" and AITM 1−0006 "Fiber reinforced plastics - Determination of interlaminar fracture toughness energy - Mode II − GIIc," respectively. EN 6033 and AITM 1−005 use a different analysis than the mode I standards noted above, i.e., the area method, which is also used by the Chinese standard HB 7402-1996 "Test method for mode I interlaminar fracture toughness G_{IC} of carbon fiber-reinforced composite laminates" published by China Aviation Industry Standards and intended for aerospace materials construction. The HB 7402 standard requires a unidirectionally reinforced DCB specimen, 25 mm wide, with piano hinges, and quasi-static loading at rates between 1 and 2 mm/min. BSS 7273 "GIC interlaminar fracture toughness fiber reinforced composites" is another quasi-static test procedure for mode I. Mixed-mode I/II delamination testing is described in ASTM D6671 "Standard test method for mixed mode I-mode II interlaminar fracture toughness of unidirectional fiber reinforced polymer matrix composites" (2006). Fracture toughness testing under quasi-static loads for short fiber-reinforced composites with thermoplastic matrix, i.e., for typical injection molding materials is standardized for mode I tensile opening load from notched specimens (compact tension − CT−or single-edge notched bending - SENB) in ISO 13586 "Plastics - Determination of fracture toughness (GIC and KIC) − Linear elastic fracture mechanics (LEFM) approach" (2018). Depending on the fiber orientation with respect to the notch, specimens have to be machined from injection-molded plates taking into account the different possible fiber orientations with respect to the direction of injection. In aerospace applications, the focus is mainly on continuous FRP laminates, with few exceptions (Jayakrishna et al. [71], Kurkin and Sadykova [72]). However, besides the references cited in the introduction, also Mandell et al. [73], Agarwal and Giare [74], Lindhagen and Berglund, [75], and Walker and Hu [76] provide more information on the fracture of short fiber composites.

For loading modes or mode combinations for which no standards do yet exist, selected literature providing the state of research is listed in Table 8.1.

Intralaminar delamination, i.e., delamination normal to fiber plies does seem to yield increased delamination resistance compared to interlaminar delamination between fiber plies (see Macedo et al. [77]). A recent investigation of intralaminar fracture on IM7/8552 CFRP with a Double-Edge-Notched (DEN) specimen [91] found no changes in compressive and tensile steady-state values of R-curves when testing at low temperatures of $-50°C$, but a significant decrease when testing at higher temperatures of $+100°C$ compared with the respective behavior at room temperature. Kuhn et al. [68] investigated mode I intralaminar fracture at high-loading rates (also on IM7/8552 CFRP) with a Split Hopkinson bar, extending previous work by Catalanotti et al. [92] with Double-Edge Notched Tensile (DENT) specimens and concluded that quasi-static Fracture Mechanics theory is applicable for analyzing high-rate test data (up to 60 s^{-1}) and that the fracture toughness of the material was increasing with increasing load rate. Catalanotti et al. [93] further investigated mode II intralaminar fracture with a modified Iosipescu specimen and concluded that the steady-state value was 34.4 kJ/m^2 and the corresponding length of the fracture process zone is 4.95 mm. Intralaminar fracture under mode I loading on CFRP with thermoplastic polyphenylene sulfide (PPS) matrix was investigated by Pappas et al. [94]. The DCB specimens showed large-scale bridging (LSB) and thus significantly higher energy release rates than the corresponding interlaminar specimens (however, determined previously by another group, i.e., not necessarily on identical material from the same production). To complement the quasi-static tests on intralaminar FRP composites, Sato et al. [95] reported data from cyclic mode I fatigue fracture on toughened intralaminar and interlaminar CFRP. Interlayer toughening was performed by adding polyamide particles (PA12). The conclusion was that observed larger crack growth resistance of un-toughened intralaminar composites did not hold at zero crack extension, i.e., the higher resistance effect was due to fiber-bridging and that interlayer toughening did not affect the intralaminar fatigue resistance.

Translaminar fracture, defined as "fiber breaking" delamination, e.g., with 5% or more fibers in through-thickness direction, has been reviewed by Dickinson et al. [96] and Laffan et al. [78] and both conclude that more research is required. Nevertheless, the fiber breaking will result in significant effects on delamination resistance. Recently, Chabchoub et al. [97] investigated translaminar mode I fracture initiation and propagation in woven carbon fiber thermoplastic (CF-PPS) at elevated temperatures and used Acoustic Emission to validate the onset of microscopic cracking. Syed Abdullah et al. [98] tested the translaminar fracture of Vectran-Epoxy composites using a modified Compact-Tension (CT) specimen and reported high toughness values (around $130-145$ kJ/m^2 for initiation and $250-260$ kJ/m^2 for propagation). Bullegas et al. [99] even introduced microcrack cuts to "engineer" translaminar fracture in quasi-isotropic and cross-ply laminates in order to improve their damage resistance and compared model and experimental results. The observed improvements in fracture toughness were attributed to crack deflection by the microcracks and resulting pull-out, debonding, and friction effects.

8.3.2 Cyclic test methods

Cyclic fracture mechanics tests are summarized in Table 8.2.

There is one standard test, ASTM D6115 "Standard test method for mode I fatigue delamination growth onset of unidirectional fiber-reinforced polymer matrix composites" (1997 - reapproved 2019). Cyclic fatigue delamination propagation is currently an active area with several round robins organized by ASTM and ESIS. First results from round robin testing unidirectional CFRP epoxy laminates (IM7/977-2, IM7/977-3, AS4/PEEK) under cyclic fatigue mode I loading have been published by Brunner et al. [62] and Stelzer et al. [63].

Table 8.2 Cyclic fatigue fracture mechanics test methods for FRP composites.

Mode	Standard test	Standard test in preparation	Remarks
I tension-tension	ASTM D 6115	ESIS TC4 round robins 2009 ff. ASTM D30.06 round robin 2010	ASTM D 6115 delamination onset only, propagation in round robins
I tension-compression	Not available		
I compression-compression	Not available		Katerelos et al. [100]
II no shear reversal	Not available	ESIS TC4 round robin(s) 2011 ff.	Delamination propagation
II shear reversal	Not available		Dahlen and Sprenger (1994) no shear reversal versus shear reversal [101]
III	Not available		Miura et al. (2009) cryogenic temperature test [102]
I/II	Not available	ESIS round robin (preliminary tests)	Shindo et al. (2011) cryogenic temperature test [103], Jaeck et al. [104], Rubiera et al. [105]
I/III	Not available		Miura et al. [106]
II/III	Not available		Takeda et al. (2013) cryo-genic temperature test [107]
I/II/III	Not available		

A crucial issue is the determination of the threshold values, and their associated scatter, which are, as noted above, important for structural design. This resulted in a debate on scatter in the test data and how to account for that (see, e.g., [108−110]). Possible sources of scatter due to microscopic damage mechanisms in FRP composites are compiled and discussed by Alderliesten et al. [111]. The authors attempt to identify extrinsic sources (e.g., test setup, load cell range with insufficient measurement resolution, operator experience, machining variation in specimen width and cutting quality, or excessive variation in laminate plate thickness) and their causes in order to reduce the scatter due to these, while simultaneously keeping the full range of intrinsic sources that reflect material variability and inhomogeneity from processing (e.g., waviness and longer-range variation in fiber orientation, matrix porosity, inclusion of foreign particles, and residual stresses).

The standard test specimens for determination of delamination resistance are usually specified with unidirectional fiber layup and that yields effects from fiber-bridging, especially in tensile mode I or mode combinations with a certain amount of mode I. Fiber-bridging is the main cause for the delamination behavior described by the R-curve (R for resistance curve), i.e., a graph of G_c versus delamination length a. Fiber-bridging effects, however, are reduced or almost absent in delamination resistance testing of FRP composites with nonunidirectional layups. This leads to the question whether the test data from standard tests (or the test procedures under development for cyclic fatigue fracture provide so-called *conservative* data (considered to provide safe limits) for the design of composite structures or components. The only application where fibere-bridging and the respective increase in delamination resistance with increasing delamination length is effective and hence is desirable are FRP composite wind rotor blades which contain mostly unidirectionally aligned fibers along the blade [112].

If, on the other hand, fiber-bridging is affecting data from testing specific, often standardized test specimens, such as in quasi-static and cyclic fatigue fracture mode I tests, the question how these effects could be quantified and accounted for in order to establish safe design limits and the related scatter bands is intensely debated in research literature. An early proposal was put forward in Japan in the 1990ies by Hojo et al. (discussed by Hojo and Aoki [113]). The procedure analyzed G-constant mode I cyclic fatigue fracture tests (e.g., similar to those described by Russell and Street [114]) and established the curve representing essentially zero delamination length increase in the Paris-graph (i.e., unaffected by fiber-bridging) from these. More recently, another, potentially simpler experiment that, in principle, yields design and lifing allowables for FRP structures was proposed by Yao et al. [48, 115, 116], The procedure consists of testing single DCB-specimens sequentially at different load levels. In the Paris graph, this results in several curves that are shifted to the right with increasing delamination length. An extrapolation procedure will then yield data from which the delamination resistance due to fiber-bridging is eliminated. This method looks very promising and maybe could, in the future, even be used to account for variable amounts of fiber-bridging for FRP structures with specific layups. However, validation of the basic approach is still required in round robin testing and this is currently underway within ESIS TC4.

Cyclic fatigue fracture loading can, as noted above, be performed under tension, tension-compression, or compression-compression. Delamination growth under monotonic or cyclic compression has been discussed by Kardomateas [117] for mode I, mode II and mixed-mode I/II, partly based on experimental results published earlier. Mode I cyclic compression-compression tests on CFRP impacted CFRP plates have been performed by Katerelos et al. [100]. The analysis relies on nondestructive testing (ultrasonic C-scan) and modeling for quantification of the delamination resistance. Rhee et al. [118] report compressive fracture toughness experiments on thick CFRP (nonwoven graphite/epoxy prepreg tape, type CU125NS manufactured by Hankuk Fiber) under hydrostatic pressure. Compressive failure modes at high loading rates are discussed by Kuhn et al. [119]. For tension-compression fatigue of a GFRP epoxy composite, Gamstedt and Sjögren [120] claim that tension-compression fatigue is more detrimental than tension-tension fatigue to transverse and multidirectional laminates and combine FEM and experiments for their analysis.

In mode II tests, there is a choice between test parameters yielding no shear reversal or shear reversal. Dahlen and Springer [101] had noted differences in the position and slope of the Paris plot between the two for two types of CFRP epoxy laminates (IM7/ 977-2, T300/976).

Other cyclic fatigue loading modes have been explored in fracture mechanics research. Donaldson and Mall [121] explored mode III cyclic fatigue, but the split cantilever beam specimen has been shown to yield varying mode II and mode III contributions even in quasi-static tests [122]. Tests on GFRP woven epoxy were performed at low temperatures under mode III cyclic fatigue loading [102], mixed-mode I/II loading [103], and mixed-mode I/III [106]. Recently, mixed-mode I/II fatigue fracture testing of FRP composites at room temperature has been investigated by Jaeck et al. [104] and Rubiera et al. [105].

8.3.3   High-rate test methods

In aerospace applications, loading rates higher than those used in quasi-static tests are also of importance, e.g., in situations where the impact of objects occurs. High-rate tests are summarized in Table 8.3.

High-rate fracture mechanics tests are often divided into so-called *intermediate* (around 1 m/s) and "high-rate" tests (several m/s) which include impact speeds. At loading rates of several m/s, dynamic effects come into play and have to be considered in data analysis. For short fiber-reinforced composites (defined as containing fibers in the length range between 0.1 and < 7.5 mm in the ISO standard) ISO 17281 (2018) "Plastics − Determination of fracture toughness (GIC and KIC) at moderately high loading rates (1 m/s)" can be used since it covers the same range of materials as ISO 13586 (2018). Clearly, this class of tests is the least developed so far. High-rate testing of FRP composites was investigated by Blackman et al. for mode I [123], for mode II [128], and mixed-mode I/II [133]. The challenges of high-rate testing of FRP were also discussed, e.g., by Hamouda and Hashmi [134]. Recent literature seems to indicate a trend toward the use of a wedge-type test (originally proposed by Glessner et al. [135] for quasi-static DCB tests) for

Table 8.3 High-rate fracture mechanics test methods for FRP composites.

Mode	Standard test	Standard test in preparation	Research
I	Not available	ESIS TC4 round robin 2009 (results not published)	1 m/s and several m/s (up to 10 m/s); Blackman (1995) [123], selected literature data compiled by Kusaka et al. (1998) [124], Thorsson et al. (2018) [125], Liu et al. (2018) [126], Isakov et al. (2019) [127]
	ISO 17281 (2002)		Short fiber composites (ISO 17281-2018)
II	Not available		Blackman (1996) [128], selected literature data compiled by Kusaka et al. [129], Jacob et al. [130], Zabala et al. [131]
III	Not available		Pennas et al. [132]
I–II	Not available		Blackman et al. [133], Jacob et al. [130]
I–III	Not available		
II–III	Not available		
I–II–III	Not available		

higher-rate mode I DCB specimens. High-rate mode I fracture with loading speeds up to 15 m/s using a wedge-type setup on standard DCB specimens is discussed and analyzed by Isakov et al. [127]. The unidirectional CFRP specimens were made from Toray Torayca prepreg 3252S-10. The data is analyzed based on optical tracking of the DCB arm and linear elastic beam theory. This allows for calculating G_{IC} without load measurements. A similar mode I wedging setup with speeds up to 3.6 m/s applied to an unspecified CFRP laminate was described by Thorsson et al. [125]. They noted a decrease in toughness and fracture mode with increasing load-rate. As an alternative to DCB specimens, compact-tension (CT) specimens of IM7/8552 on a Hopkinson bar were used by Hoffmann et al. [69] for characterizing rate-dependence under mode I, and a significant reduction in G_{IC} was noted for high-rates. Zabala et al. [131] investigated the rate dependence of a unidirectional CFRP (Toray GV 170 U and epoxy SiComin SR 8100/SD 8822) under mode II with a 4-ENF setup. No significant rate dependence was observed up to 0.19 m/s, the maximum load-rate of the hydraulic test machine. This is consistent with the results reported by Kusaka et al. on the rate dependence of one CFRP epoxy (T300/2500) in mode I [124] and of two CFRP epoxy (T300/2500 and IM600/133) in mode II tests [129] from quasi-static to impact rates yielding a moderate rate-dependence in both

cases. It has to be noted that a 25 μm thick starter film was used, which is thicker than recommended by current standards (ISO 15024 and ASTM D5528).

A special case of high-rate and high-energy impact fracture testing was investigated by Yazid Yahya et al. [136] using explosive blasts on CFRP woven epoxy (EP121) plates. It was concluded that delamination and fiber fracture absorbed relatively little energy in this case. Again, additional information and references can be found in [37]. Recent literature dealing with rate dependence and the resulting effects in FRP composites comprises, e.g., [137] developing a continuum mechanics approach for dynamic fracture under different modes; Yasaee et al. [55] confirmed previously reported results that mode II delamination values of FRP epoxy composites showed a minor increase with increasing strain rate, but a large effect if Z-pins were used; Liu et al. [138] presenting a CZM model explaining experimentally observed variation due to rate-dependence; and Miao and Tippur [70] comparing effects of fiber orientation on delamination initiation and growth for two different load-rates (and using optical measurements for analysis). Special cases of high-rate fracture of FRP composites were discussed by Kuhn et al. for fiber compressive failure [119] and for intralaminar fiber tensile failure [68].

8.4   Fracture mechanics test data for selected FRP composites

The literature published on fracture mechanics testing of FRP in the last 40 years comprises a large database on delamination resistance or fracture toughness of different types of FRP. An early review [139] compiled the data available at that time. Selected data from quasi-static mode I and mode II tests on FRP were compared by O'Brien [140] and quasi-static mode I test data from carbon-fiber epoxy and poly-ether-ether-ketone (PEEK) by Brunner [141]. Mechanical properties of FRP composites are compiled in the Composite Materials Handbook Version F [39−41] as well as version G [42], but this does not comprise fracture mechanics data. Hence, there is no comprehensive and up-to-date database on available data or literature.

Data on unidirectional CFRP epoxy (IM7/977-1), a high-performance aerospace type laminate from ESIS TC4 round robins under quasi-static mode I, mode II and fixed-ratio mixed-mode I/II loading have been published by Brunner et al. [142], Davies et al. [143] and Blackman et al. [144]. The data are summarized in Figs. 8.3−8.5.

Available data are shown for three initiation points, namely nonlinear, visual and maximum load or 5% compliance change (as defined in ISO 15024) and average propagation (defined as an average of all data except initiation points) and maximum propagation point. Comparing initiation and propagation will give an indication whether the resistance curve (R-curve), i.e., G_C for the respective mode versus delamination length is strongly increasing or not (see, e.g., [145]). Recently, this CFRP laminate (with modified epoxy 977-2 or 977-3) has been used in cyclic fatigue mode I and mode II round robins [64, 146], summarized in Fig. 8.6 and complemented by
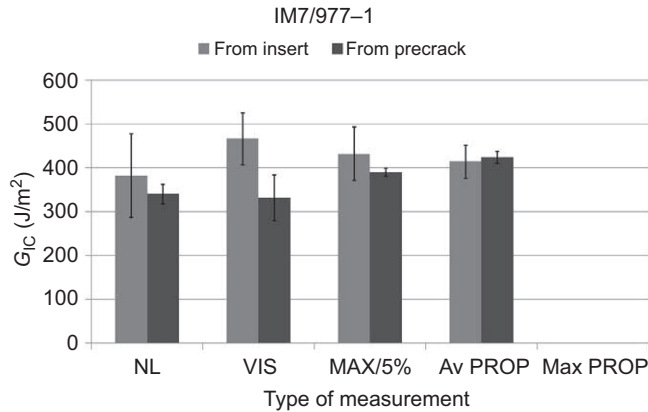
Figure 8.3 Delamination resistance of carbon fiber-epoxy (IM7/977-1) under quasi-static mode I loading; nonlinear (NL), visual (VIS) and maximum load or 5% compliance change (MAX/5%) are initiation values (defined in ISO 15024), and available average and maximum propagation (Av PROP and Max PROP) values are also shown for indicating resistance curve (R-curve) effects. The plot of values is from a table presenting ESIS TC4 round robin results in [142].
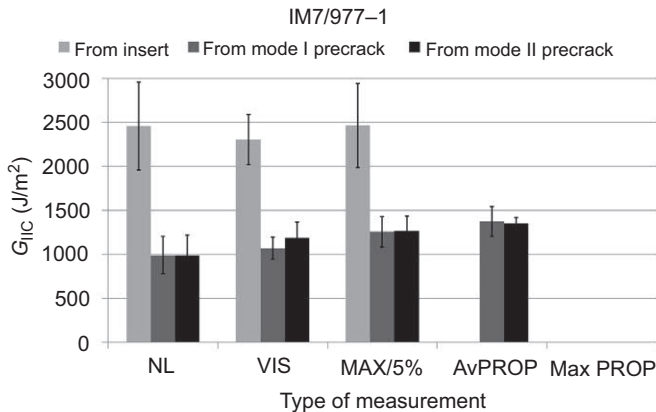
Figure 8.4 Delamination resistance of carbon fiber-epoxy (IM7/977-1) under quasi-static mode II loading; nonlinear (NL), visual (VIS) and maximum load or 5% compliance change (MAX/5%) are initiation values (defined in ISO 15,024), and available average and maximum propagation (Av PROP and Max PROP) values are also shown for indicating resistance curve (R-curve) effects. The plot of values is from a table presenting ESIS TC4 round robin results in [143].

quasi-static and cyclic mode I and mode II fatigue data [62, 101] and one data set from preliminary fixed-ratio mixed-mode I/II testing at the authors' laboratory. From different possible presentations of the Paris-plot, the delamination rate (increase in delamination length per cycle) da/dN versus the maximum G-value, G_{max}, is used for presenting cyclic fatigue data here. The delamination rate da/dN could also be plotted versus ΔG, the change in applied G-value, but that can be affected by
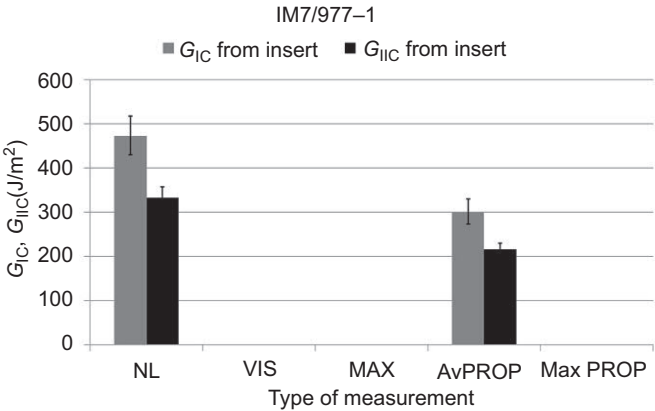
Figure 8.5 Delamination resistance of carbon fiber-epoxy (IM7/977-1) under quasi-static mixed-mode I/II loading with a fixed ratio of mode I to mode II of 4:3; nonlinear (NL), visual (VIS) and maximum load or 5% compliance change (MAX/5%) are initiation values (defined in ISO 15024), and available average and maximum propagation (Av PROP and Max PROP) values are also shown to indicate resistance curve (R-curve) effects. The plot of values is from a table presenting ESIS TC4 round robin results in [144].
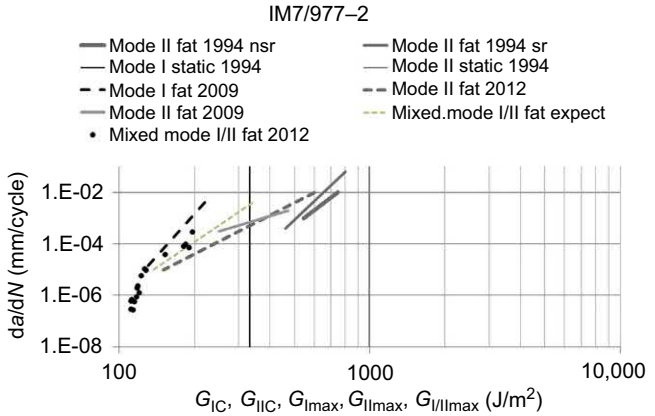
Figure 8.6 Double logarithmic plot of delamination rate da/dN versus G_{Imax} and G_{IImax}, respectively, from cyclic fatigue (fat) with an R-ratio of 0.1 of carbon fiber epoxy (IM7/977-2) under mode I and mode II from ESIS TC4 round robins (2009, 2012), and under fixed-ratio mixed-mode I/II from preliminary single-specimen testing (*black dots*) at the author's laboratory; expected values for fixed-ratio mixed-mode I/II (mixed-mode I/II fat expect) were calculated from cyclic fatigue mode I and mode II round robin data (2009 and 2012, respectively), quasi-static (static) and cyclic fatigue mode I and mode II values from literature (Dahlen and Springer [101]) (nsr = no shear reversal; sr = with shear reversal) are shown for comparison.

interfacial interference (see, e.g., [147] for details). It is interesting to note that Dahlen and Springer [101] tested mode II fatigue once with shear reversal and once without shear reversal and obtained somewhat differing results (especially slopes) in the Paris plot. The single data set from preliminary fixed-ratio mixed-mode I/II testing agrees fairly well with the expectation (mode I to mode II ratio of 4.3) calculated from the experimental data for mode I and mode II fatigue, at least down to a $G_{I/IImax}$ around 120 J/m^2. The mixed-mode I/II analysis used corrected beam theory following [148] with a value of 5 mm for the Δ_I-correction (average from earlier round robin testing at the authors' laboratory) and a ratio of 0.42 times Δ_I for the Δ_{II}-correction. Whether the change in slope for cyclic fatigue under mixed-mode I/II loading below 120 J/m^2 is an indication of threshold behavior or an artifact from possible compressive stresses from the clamping in the test setup (see, e.g., [148]) for a schematic), is not clear. Such effects have been observed in the round robin on cyclic fatigue under mode II loading and tentatively been attributed to compressive stresses from the three-point bending and end-loaded split test setups (Brunner et al. 2012, unpublished results). Fig. 8.7 compares the slopes of Paris plots for cyclic mode I fatigue delamination on CFRP (IM7/977-3), and Fig. 8.8 shows the Paris plot from an ASTM round robin (Brunner 2010, unpublished data) for comparison with Fig. 8.7. IM7/977-3 has a lower toughness than IM7/977-2, and this is reflected in the Paris plot. There is some scatter in all Paris plots, and the relatively steep slopes make use of the data for design difficult.

Cartié et al. [149] investigated the effect of hydrostatic pressure between 0.4 and 90 MPa on the delamination resistance under quasi-static mode I and mode II load for IM7/977-2. They conclude that no significant effect was observed for mode I (the data may suggest a modest decrease), but noted a slight increase mode II with increasing pressure (Fig. 8.9). Comparison with Fig. 8.7 indicates that quasi-static
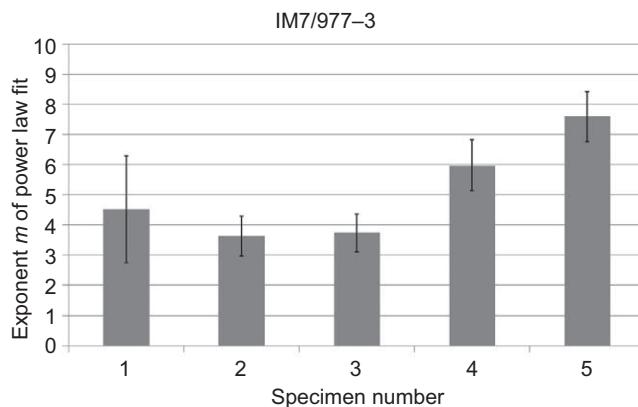
Figure 8.7 Exponent m of the power-law fit (A*Gm) to the double logarithmic plot of delamination rate da/dN versus GImax from cyclic mode I fatigue with an R-ratio of 0.1 of five specimens of carbon fiber epoxy (IM7/977-3) from the ASTM round robin. Unpublished data from the author's laboratory, 2010.

IM7/977–3

—Mode I static ·····+s.d. ·····−s.d. —Mode I fatigue
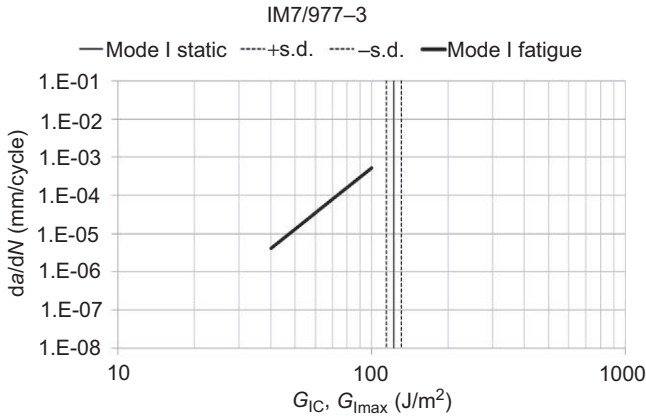
Figure 8.8 Double logarithmic plot of delamination rate da/dN versus G_{Imax} from cyclic mode I fatigue with an R-ratio of 0.1 of carbon fiber epoxy (IM7/977-3) with quasi-static (static) values from the ASTM round robin. Unpublished data from the author's laboratory, 2010.

IM7/977–2

■ Mode I init   ■ Mode I prop   ■ Mode II init   ■ Mode II prop
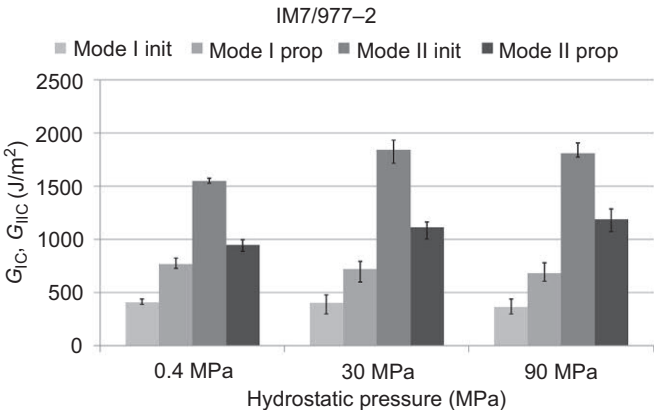
Figure 8.9 Delamination resistance of carbon fiber-epoxy (IM7/977-2) under quasi-static mode I and mode II loading as a function of hydrostatic pressure. Shown are average initiation (init) and average propagation (prop) values. The error bars represent minimum and maximum values, not standard deviations. Data plotted from a table presented in [149].

values [101] for IM7/977-2 under mode I (around 333 J/m^2) and mode II (around 994 J/m^2) at ambient pressure tend to be lower than values at elevated pressure but the laminates were prepared and tested in different laboratories more than 10 years apart.

It is of interest to compare the data for fiber-reinforced laminates with thermoset matrix, e.g., epoxy, with data obtained on laminates with thermoplastic matrix materials. An early comparison with GFRP epoxy, CFRP epoxy and poly-ether-ether-ketone (PEEK) under quasi-static and cyclic fatigue mode I, mode II, and

mixed-mode I/II have been published by Prel et al. [150] and a similar investigation by Hojo et al. [151]. The results indicate that for quasi-static tests, the carbon fiber epoxy yields the lowest initiation and propagation values, followed by GFRP epoxy and that CFRP PEEK shows the highest values. There is an increase in G_C values when going from quasi-static mode I to mode II. This is consistent with the assumption that mode I constitutes a lower bound (at least for quasi-static loading, see below for cyclic fatigue).

Recent cyclic fatigue delamination testing under mode I [64] has shown that thermoplastic CFRP PEEK yields higher values than CFRP epoxy, but also shows considerably larger scatter (Fig. 8.10). The data in Fig. 8.10 are complemented by literature values on cyclic mode I and mode II fatigue for the same laminate (Martin and Murri [147]) and quasi-static values from O'Brien [140]).

Test development also investigated the effect of artificial starter cracks, essentially thin polymer or metal films, on the resulting fracture mechanics data and specifically on the initiation values. Perez and Davidson [152], for example, compiled data on several precracking methods, namely three- and four-point end-notched flexure testing, for quasi-static mode II testing of carbon fiber epoxy (IM7/8552-1 and T800H/3900-2) using three-point end-notched flexure. They observed no significant difference between the two precracking methods, but also a dependence on the dynamic crack advance during precracking. Mode I and mode II precracking using the respective test methods and mode I wedge precracking using a clamp to stop the precrack at defined location (partly verified by nondestructive tests) are briefly described and compared by Brunner [145].
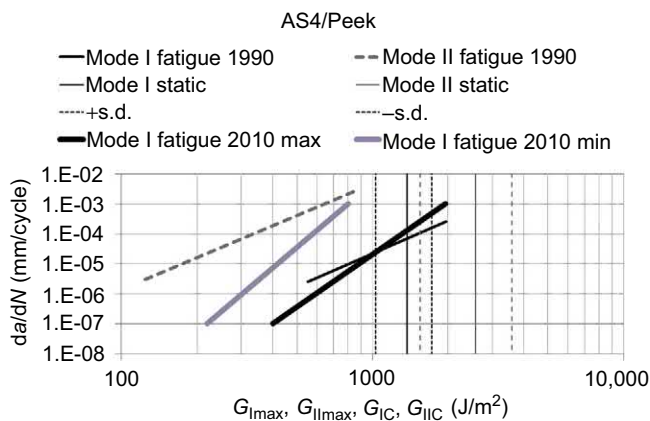
Figure 8.10 Double logarithmic plot of delamination rate da/dN versus G_{Imax} and G_{IImax}, respectively, from cyclic fatigue with an R-ratio of 0.1 of a carbon fiber thermoplastic (AS4/PEEK) under mode I loading from an ESIS TC4 round robin. The min and max lines indicate the scatter band of tests from five laboratories; cyclic fatigue mode I and mode II values and averaged quasi-static mode I and mode II values [140] are shown for comparison (s.d., standard deviation).

There have been attempts at improving the delamination resistance by modifying the interlaminar layer between fibers. Interleaving, i.e., insertion of a toughening layer has proven fairly effective, first data were compiled by Sela and Ishai [139], and later investigations reported by, e.g., Armstrong−Carroll et al. [153], and Hojo et al. [154, 155]. The latter group observed significant improvements of the fatigue delamination resistance under mode I using a heterogeneous interlayer with polyamide particles (in T800H/3900-2) and for a special ionomer CFRP thermoplastic (UT500/111). A 50 μm thick self-same epoxy interleaf improved mode II cyclic fatigue delamination resistance but not that under mode I cyclic fatigue loading.

Improving fiber-matrix adhesion has also been explored for achieving higher toughness [156]. Quasi-static mode II delamination resistance of CFRP epoxy with AT400 fibers after anodic oxidation was increased by about 30% and under cyclic mode II cyclic fatigue at higher delamination propagation rates but not in the near-threshold regime.

Processing of the FRP laminates can affect delamination resistance, e.g., by variation of the forming temperature of CFRP thermoplastic (IM6/PEEK) laminates [157]. Lower forming temperature (+360°C) yielded lower mode I and mode II delamination resistance than +380°C (recommended manufacturer value), while higher temperatures (+400 to +440°C) resulted in improved interfacial strength with corresponding improvements in mode II delamination resistance. Cure pressure for woven CFRP epoxy was varied in three steps (0.69, 0.31 and 0.10 MPa) by Li et al. [158] and affected physical and mechanical properties, including interlaminar fracture toughness of the laminates. A comparison of different processes (autoclave vs. proprietary Quickstep) for a unidirectional CFRP epoxy (T800H/3900-2) indicated similar quasi-static mode I values (554 and 527 J/m^2, respectively) but a significantly increased fatigue performance for the latter [159].

The available data for unidirectionally reinforced laminates are typically interpreted such that mode I values do seem to constitute a lower bound compared to the other modes, specifically mode II, at least for quasi-static tests. For cyclic fatigue delamination tests, it has been shown by Martin and Murri [147] that mode II fatigue for CFRP PEEK yields lower values than mode I in the Paris plot. At present, it is not clear whether this is limited to certain types of composite laminates, e.g., thermoplastics, or whether this is specific for mode II fatigue. The recent round robin data for mode II fatigue delamination propagation in IM7/977-2 laminates do suggest a possible "cross-over" from mode I to mode II as the lowest curve for sufficiently low values of G_{max} (Brunner, unpublished data 2012). For other test types there are only scant data.

The assumption of a lower bound represented by pure mode I data is hence a possible route to avoid the complexity of different modes and mode combinations in design. However, for cyclic fatigue, this is not always the case as shown by the cyclic delamination fatigue in mode II data for one type of CFRP thermoplastic composite noted above. Therefore, there is a need for further cyclic fatigue testing and comparative data analysis. In addition, the question of how cyclic fatigue fracture test data from unidirectional FRP laminates with significant fiber-bridging relate to other layups, e.g., cross-ply, multidirectional or three-dimensionally reinforced

laminates has to be discussed for different loading modes and likely also for high-rate tests. From the results of the tests discussed above, it can still be hypothesized that other quasi-static modes or mode combinations will not yield lower values than mode I for unidirectional laminates. This seems to hold even though fiber-bridging effects in quasi-static mode I tests on unidirectional FRP specimens are contributing more significantly to the delamination resistance than in other modes or mode combinations. Further research on how to account for fiber-bridging in the various modes, including cyclic fatigue fracture, is hence necessary. Only with experimental data and a sufficient understanding of the effects can the implications of fiber-bridging for FRP structural design be assessed and reliable safety factors be defined.

8.5 Fracture mechanics testing of non-unidirectional FRP composites

In FRP composite applications, nonunidirectional or multidirectional fiber layups are more frequently used than the strongly anisotropic, unidirectional laminates typical of the scope of standard test methods. An early review of interlaminar fracture toughness or delamination resistance listing literature data for unidirectional and nonunidirectional laminates under mode I and mode II loading was published by Sela and Ishai [139]. Values for G_{IC} for various carbon fiber epoxy laminates determined at different laboratories range from about 60 to 4600 J/m^2, and for G_{IIC} from about 150 to 2050 J/m^2. Quite likely, the large scatter can be attributed to a combination of layup, specimen type, test rig, and test parameters. In the 1990ies, some of these effects were investigated in detail within the framework of round robins with several participating laboratories. One example is cross-ply laminates, i.e., composites with alternating layers oriented at 0° and 90°. These have been investigated under quasi-static mode I loading in round robins by ESIS TC4. The round robin results on symmetric and asymmetric cross-ply IM7/977-2 laminates have been presented and discussed by Brunner [160]. In a few cases, the delamination was observed to partly or fully deviate from the center 90° layers into the adjacent 0° plies. Partial deviation inside the specimens could not be observed on the edges but resulted in a strongly decreasing R-curve. A typical feature in cross-ply was the observation of a delamination path oscillating between the 0° plies adjacent to the center 90° layer. This resulted in strongly increasing R-curves for symmetric and asymmetric cross-ply layup (Figs. 8.11 and 8.12), which could not be explained by the nominal increase in delamination length [161]. A tentative explanation is a combination of mode I and mixed-mode delamination or combined interlaminar and intralaminar propagation, and hence the values may have to be regarded as "apparent" rather than real mode I.

Trakas and Kortschot [162] used carbon fiber epoxy (AS4/3501-6) specimens modified with Teflon edge delaminations in a study comparing unidirectional and 0°/90° and 90°/90° interfaces under mode I, mode II, and mode III loading. Delamination resistance decreased for all modes when going from unidirectional to cross-ply and 90°/90°. The tests were complemented with Scanning Electron Microscopy of
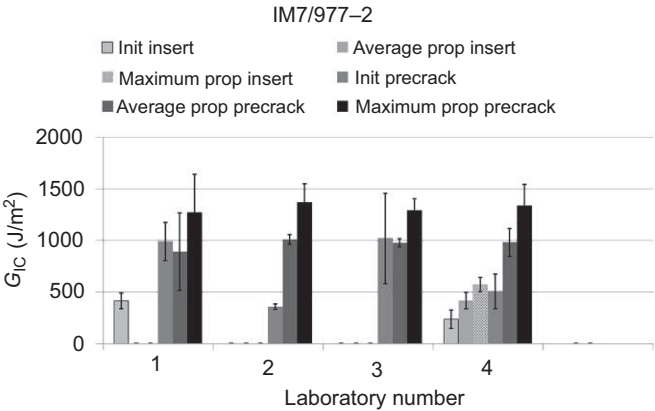
Figure 8.11 Delamination resistance of symmetric cross-ply carbon fiber-epoxy (IM7/977-2) under quasi-static mode I loading, average initiation (init), average propagation (prop) and maximum prop values (averages from two to five laboratories and standard deviations) for testing from a starter crack thin-film insert and from a mode I precrack. Data plotted from ESIS TC4 round robin analysis [160].
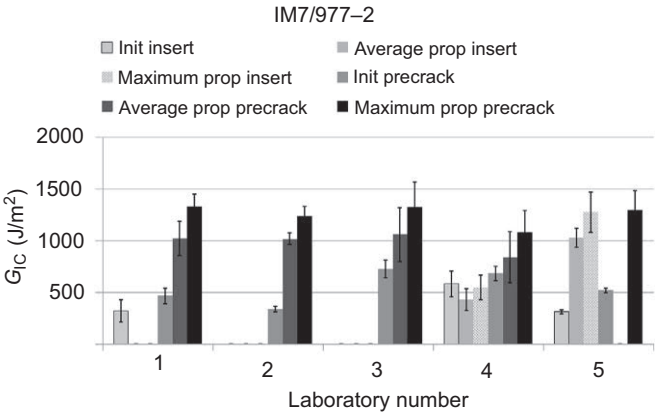
Figure 8.12 Delamination resistance of asymmetric cross-ply carbon fiber-epoxy (IM7/977-2) under quasi-static mode I loading, average initiation (init), average propagation (prop) and maximum prop values (averages from two to five laboratories and standard deviations) for testing from a starter crack thin-film insert and from a mode I precrack. Data plotted from ESIS TC4 round-robin analysis [160].

the fracture surfaces but did not yield a direct quantitative correlation with the measured values of G_c. It was noted that G_c could be used as a material property for design as long as the layup (ply orientation) and mode of fracture corresponded to those in the intended use.

Prombut et al. [163] used carbon fiber epoxy (T700/M21) laminates in asymmetric double cantilever beam (ADCB) and asymmetric mixed-mode flexure (AMMF)

specimens beside standard mode I, mode II and mixed-mode flexure specimens in their investigation and complemented experiments with numerical simulations. Although they succeeded in preventing jumps in the delamination plane and achieved reasonable crack front profiles, they concluded that more work would be needed to establish a crack propagation criterion for the 0°/45° interface.

Andersons and König [164] reviewed the literature on the dependence of fracture toughness on interface ply orientation and delamination growth direction for glass and carbon fiber laminates. They list a number of factors that affect the delamination analysis of multidirectional laminates, among them mode mixity and the question of mode partitioning, residual stresses, the distribution of the energy release rate along the delamination front, contributions from intra-laminar damage, and inelastic deformation due to reduced specimen stiffness. They concluded that the conventional tests on unidirectional laminates could overestimate or underestimate the delamination resistance of composite laminates, depending on layup and loading mode, specifically for shear. For mode I, unidirectional laminates do seem to give conservative values, and the data can hence be used for design. However, in view of the recent debate about effects of fiber-bridging on delamination propagation and the resulting R-curve behavior, it has become clear that the "standard" test data obtained from unidirectionally reinforced FRP laminates will not provide "conservative" limits for FRP structural design in all cases. The main application where fiber-bridging is used is wind rotor blades [112] made with primarily unidirectional laminates along the length of the blade (mainly glass-fiber, but also hybrid glass-carbon-fibers in larger components exceeding about 100 m in length). For nonunidirectional or multidirectional laminate layups the delamination propagation in FRP structures may yield significantly less fiber-bridging and hence faster propagation beyond the initial delamination length, e.g., higher da/dN for a given level of the applied load. This will shift the data curves in the Paris−or the Hartman-Schijve-graphs upward and hence yield less damage-tolerant designs.

Multidirectional laminates frequently found in applications are quasi-isotropic laminates with typical fiber orientations of 0°, ±45°, and 90° in a specific stacking sequence. Fracture mechanics testing of multidirectional laminates has been extensively investigated and discussed. Choi et al. [165] investigated symmetric −45 °/0°/+45° multidirectional CFRP epoxy laminates (prepared from unidirectional prepreg tape Fiberdux 6376C) under quasi-static mode I, mode II, and mixed-mode I/II loading with the starter crack located between −45° and +45°. Initiation values of G_C were always larger for the multidirectional laminates than for corresponding 0°/0° composites. Propagation of delaminations typically yielded crack jumps to other planes with extensive fiber-bridging and crack splitting. Mode II and mixed-mode I/II also involved partly unstable delamination growth. Compliance calibration-based analysis yielded good agreement with modified beam analysis. The dependence of interlaminar fracture Energy G_C on delamination length turned out to be complex, reflecting the observed delamination behavior. Compared with mode I loading, R-curve effects were less pronounced in mode II and mixed-mode I/II tests. Gong et al. [166] investigated quasi-homogeneous, symmetric and anti-symmetric GFRP and CFRP epoxy laminates (prepared from balanced fabric GFRP, and quasi-unidirectional and unidirectional sheet

CFRP prepregs) with different number of plies and ply thicknesses and with a range of ply orientations (0°, 15°, 30°, 45°, 90°) under quasi-static mode I loading and compared different methods for data analysis. They noted that simple beam theory values differed from those of various experimental compliance-based approaches and recommended the latter for multidirectional laminates. Finite element analysis showed a dependence of the normalized G_I value along the width of the specimens which depended on the aspect ratios (thickness to width and crack length to width) and which decreased with increasing specimen width (from 5 to 180 mm). In multidirectional specimens with 0°/0° interface, the G_{IC}-values increased with increasing ply angle of the adjacent plies. No significant difference was found for symmetric and anti-symmetric layups for 30°/30° lay-ups.

Sebaey et al. [167, 168] used numerical simulations for the development of special stacking sequences for multidirectional laminates and verified experimentally in quasi-static mode I tests on six selected layups that crack jumping could be prevented by increasing flexural stiffness of the beams in CFRP laminates (made from AS4/8552 prepreg). The delaminations involved fiber tearing. The measured toughness depended on the amount of fiber-bridging and on the interface angle, but fiber-bridging was noted to dominate over angle mismatch effects.

Peng et al. [169] investigated mode I delamination in four multidirectional laminates (0°/5°, +45°/−45°, 90°/90°, and 0°/45°) made from carbon fiber bismaleimide prepreg (type T700/QY811) under cyclic fatigue loads. Quasi-static tests on the same laminates had shown increasing R-curves with increasing delamination lengths for all interface types. The fatigue fracture curves, i.e., a modified Paris-equation, showed different exponents for the different interfaces, the lowest for 90°/90° and the highest for +45°/−45°.

Zhao et al. [170] developed a numerical cohesive zone model for simulating mode I and mixed-mode I/II delamination in multidirectional laminates and the numerical results agreed with experimental data within a few percent. This approach was extended in a later paper [171]. Quasi-static delamination in angle-ply or multidirectional laminates was recently also investigated by Gong et al. [172] and Blondeau et al. [173], both comparing experiments with cohesive zone modeling. Mode I fatigue fracture in multidirectional laminates is extensively discussed, e.g., by Yao et al. [115, 116, 174].

In all of the laminates mentioned above, the number of plies with a given orientation can be varied and optimized for the strength or stiffness requirements for the FRP composite elements or structures, resulting in a different thickness of the respective layer.

While off-angle and some multidirectionally reinforced FRP laminates may still have fibers aligned in one single direction or orientation in each ply (and just have different fiber orientation from ply to ply), there are more complex fiber arrangements that also need to be considered. A comparison between unidirectionally reinforced and plain weave CFRP epoxy laminates (IM7/8552) for quasi-static mode I, mode II, and mixed-mode I/II [175] found similar initiation values, but clearly higher propagation values of delamination resistance for the woven CFRP. Woven fiber mats, three-dimensional fiber preforms, or third dimension reinforcement of FRP composites (see, e.g., [54]) with fibers aligned in one plane have been developed and can be tested

for their fracture mechanics properties. The typical approach for testing these is to apply a standard test method developed for unidirectionally reinforced FRP composites and to assess the difference in delamination resistance compared to the standard laminate. So far, that approach has yielded (nominal) numbers, but their interpretation is not completely clear. One example of three-dimensional reinforcement are Z-anchor CFRP composites [176] and cyclic mode I fatigue delamination resistance of Z-anchor CFRP epoxy has been observed to increase significantly by Hojo et al. [177].

Another example with an aerospace application of three-dimensional FRP composites are z-pinned laminates [178, 179] which have been used in some fighter aircraft [58]. However, Z-pin through-thickness reinforcement will affect other mechanical properties of the FRP laminates [58, 180]. As discussed by Robinson et al. [181] Z-pinned laminates under quasi-static mode I loading seem to yield a "developing" and "fully developed bridging state" and data analysis and interpretation may have to be modified from that in the standard test procedure in order to obtain meaningful values. Mixed-mode I/II loading of z-pin-reinforced composites yields a complex failure sequence with different behavior of the mode I and mode II components [182]. Delamination of Z-pinned CFRP laminates (IM7/977-2) with CFRP pins (T600/ BMI) has been investigated under quasi-static mode I loading with acoustic emission monitoring [178] as a function of pin areal density and with two separate Z-pinned areas. The delamination passed through the pinned area at areal densities of 2% or less but was stopped by 4% areal density. The unstable delamination growth resulting from the high stored energy after passing through the pinned area could be stopped by a second pinned area of density of 0.5% or higher. Cyclic fatigue under mode I and mode II loading of Z-pinned laminates (IM7/977-2) was investigated by Brunner et al. [183], again with acoustic emission monitoring. It was concluded that cyclic fatigue loading under load control yielded delamination propagation for mode I (Fig. 8.13) and mode II (Fig. 8.14) independent of pin density, if sufficiently high
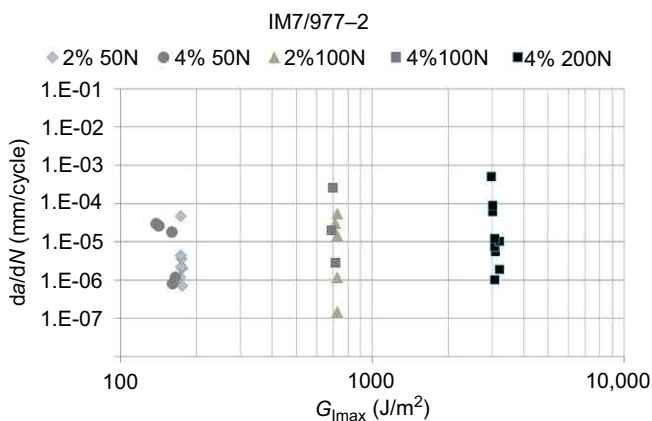
Figure 8.13 Double logarithmic plot of delamination rate da/dN versus G_{Imax} from mode I cyclic fatigue under load control with an R-ratio of 0.1 of Z-pin-reinforced carbon fiber epoxy (IM7/977-2). Shown are selected data points for loads of 50, 100 and 200 N. Unpublished data from [183].
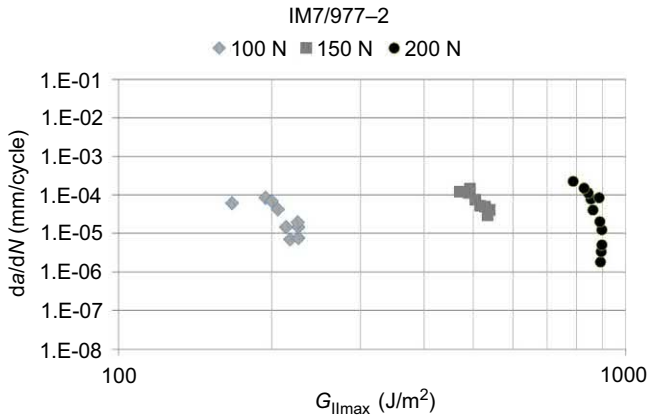
Figure 8.14 Double logarithmic plot of delamination rate da/dN versus G_{IImax} from mode II cyclic fatigue under load control with an R-ratio of 0.1 of Z-pin-reinforced carbon fiber epoxy (IM7/977-2). Shown are selected data points for loads of 100, 150 and 200 N. Unpublished data from [183].

loads are applied. Contrary to the quasi-static mode I tests, no change in failure mode was observed for cyclic mode I fatigue at 4% pin density. The steep, almost vertical slopes in Figs. 8.13 and 8.14 are similar to Paris plots obtained for mode II cyclic fatigue delamination resistance of unidirectional CFRP epoxy (IM7/977-2) when the crack tip was either close to the clamp in the ELS-test rig or in the three-point bending ENF (see, e.g., [66] for test setups) close to the center loading fin (Brunner et al., unpublished results, 2012). Cyclic mode I fatigue behavior under displacement control may be affected by pin pull-out, which poses a resistance against the full closing of the crack opening. At constant applied load, the delamination propagation speed slowed down with the increasing number of cycles but did not stop. 4% pin density proved more efficient in improving delamination resistance than 2%. Thermography showed cyclic heat spikes synchronous with the test frequency in the Z-pinned area while no heating was observed for the same type of laminate without Z-pins.

Other techniques for three-dimensional reinforcements that provide improved delamination resistance are stitching [184] and tufting [185]. Quasistatic mode I, mode II and mixed-mode I/II test on CFRP weave epoxy (5H G0926/RTM6) with Kevlar stitching yarn yielded significant improvements under mode I loading [186]. Mode II did not show unstable crack growth for stitched specimens (contrary to unstitched specimens), and stitching yarns were not broken. For some specimens bending failure was observed. Under mixed-mode I/II, stitching yarns are broken, but still result in improved delamination resistance. There are arguments that indicate that mode I delamination resistance of through-thickness reinforced laminates may be reduced at higher crack velocities [187]. The question whether linear elastic fracture mechanics concepts are applicable to through-thickness reinforced composites is discussed in detail by Cox and Massabò [188].

Quasi-static mode I and mode II tests on three-ply polyester thread stitched CFRP weave epoxy laminates (5H T300/RTM6) showed larger mode I delamination resistance for large diameter threads initially (about 100%), but the difference reduced to 36% for larger delamination lengths [189]. For mode II tests, there was no significant difference initially. Stitch distribution does seem to have an effect, and hence, there is potential for optimization. Tufting yielded improvements in mode I delamination resistance in CFRP fabric epoxy (5H satin WEAVE-RITE/977-20) comparable to that of Z-pinning, but this also required some optimization of the tuft spacing. Tufting also resulted in a significant improvement in compression after impact. This was also observed by Heβ and Himmel [190] for stitched CFRP epoxy with noncrimped fabric (HTA/RTM6 and HTS/RTM6) but delamination and compression after impact resistance had to be balanced with in-plane mechanical properties for optimal stitching density.

Another topic of interest in the context of aerospace applications of FRP composites is testing nonstandard specimen geometries differing from the typical straight beam-type specimens defined in the standards. Approaches for delamination testing curved composite specimens taken, e.g., from typical thin-walled cylindrical GFRP shells, have been developed by, e.g., Beckert et al. [50], or Ozdil et al. [191, 192]. Hojo and Aoki [193] explored the effects of specimen thickness in mode I delamination resistance measurements (DCB-specimen). They manufactured laminates with a nominal thickness of 8 mm, effectively 8.9 mm thick CFRP epoxy (T800/3631) and 8.3 mm thick CFRP thermoplastic (AS4/PEEK) laminates and then milled specimens with 3, 4 and 5 mm thickness in addition to the 8 mm thick specimens. Initiation values determined from 6 to 8 mm long precracks (prepared manually by wedging) did not show any thickness dependence for both types of laminates. Propagation values for thicker specimens were slightly higher than those for thin specimens. However, there was a difference between values for CFRP epoxy for specimens prepared from two different plates, which were attributed to differences in fiber orientation. This is again, an example that processing and manufacturing may play an important role in delamination resistance performance. Thick section FRP composites may require the development of new test methods or modification of existing test procedures for measuring delamination and damage behavior, as shown, e.g., by El Hajjar and Haj-Ali [194] for pultruded glass polyester composites.

8.6 Fracture mechanics simulation and modeling approaches for FRP composites

Some examples of modeling and simulation of fracture in FRP composites have been noted in the literature cited above already. The application of modeling and simulation to fracture of FRP composites had been reviewed, e.g., by Gillespie [34] or Tay [35] for both, coupon testing and structural behavior and by Liu [138] for continuum damage mechanics. Results often depend on the specific type of structure and load case.

Examples are filament-wound composite pipes [195], and a composite box section for which analytical solutions and FEM are compared with experimental data [49]. In the following, selected papers illustrating the status of modeling and simulation of fracture and fatigue fracture of FRP composites are briefly noted. A full review of this topic is beyond the scope of this chapter. Early simulations used the Virtual Crack Closure Technique (VCCT), see, e.g., [86] for mixed-mode I/II delamination, [196] for applying it to mode II ENF tests, or [197] for investigating load-rate dependence of mode I fracture. A review on VCCT applied to damage modeling in FRP composites was published in [198] and a model benchmark in [199]. For modeling delamination testing of FRP composites Cohesive Zone Models (CZM) are now extensively discussed in literature (see, e.g., [200]), Liu et al. [197] and Soto et al. [201] present a discussion of analytical expressions for the cohesive zone length which is used for determining the mesh size. Recently, so-called *extended* FEM (XFEM) is also applied to fracture of FRP composites, see e.g., [202, 203], the latter combined XFEM with CZM. Dimitri et al. [204] compare CZM and Finite Fracture Mechanics modeling of Mode I delamination with a DCB-specimen and conclude that with generalized zero-thickness contact interface elements an excellent agreement between the methods can be achieved.

Peridynamics is a special continuum mechanics alternative to VCCT or FEM modeling of FRP composite behavior, and it has been applied to modeling dynamic fracture [205] or fatigue life prediction [206]. A direct comparison with other modeling and simulation tools applied to fracture or fatigue fracture of FRP composites would be of interest, among other aspects also with respect to the computational effort. Other modeling approaches are discussed, e.g., by Corbetta et al. [207] comparing different strain energy release rate models for prediction, by Gong et al. [208] investigating an energy-based approach, or by Allegri [209] questioning whether artificial neural networks might be preferable to empirical power-law fitting, Carreras et al. [210] provide a benchmark for modeling delamination in a DCB-specimen under quasi-static and fatigue loading. It is expected that simulation and modeling comparisons with different methods and codes using benchmark cases are essential for establishing validated models yielding realistic results. One exercise on simulating the quasi-static mode I load-displacement and load-delamination length curves in a DBC-specimen from materials data organized by members of ESIS TC4 is currently underway, and a similar exercise for mode I fatigue fracture is in preparation.

8.7 Fracture mechanics testing under aerospace environmental conditions

Fracture mechanics testing of FRP composites under environmental exposure that corresponds to service conditions for aerospace applications has received scant attention so far, and there are no specific standard test procedures. Most of the published research focuses on fracture mechanics testing at cryogenic temperatures [103, 211, 212, 213]. The aerospace environment, however, includes hygro-thermal cycling, solar

irradiation (ultraviolet), and, in space the absence of an atmosphere, extreme temperature variations, significant ionizing radiation (X-ray and gamma-ray), magnetic fields, neutral or ionized atomic or molecular species (reactive oxygen), elementary particles, and micrometeorites and in some locations space debris moving at high speeds (several km/s). For FRP composite aircraft structures, foreign object impact and resulting damage, as well as exposure to certain fluids, such as kerosene, hydraulic or de-icing fluids, or to oil and grease may have to be considered (see, e.g., the discussions in "Long-Term Durability of Polymeric Matrix" (2012) edited by Pochiraju et al. [214]). There is some information on fluid exposure effects on fracture properties of CFRP. Hooper and Subramanian [215], for example, discuss effects of long-term soaking exposure (200 days) in distilled water and jet fluids (Jet A commercial jet fuel, and JP-4 military jet fuel) on CFRP (HYE1337AU from ICI Fiberite, noted to be equivalent to AS4/3501-6) and conclude that these result in some degree of toughening compared to dry specimens. For mode I cohesive fracture of the epoxy matrix and a significant amount of fiber breaks were identified as main factors for the toughening behavior. For mode II, water exposure did not change the fracture pattern much, but jet fuel absorption did. Landry et al. [216] investigated mode II fatigue fracture in CFRP (G40-800/5276-1) and noted an increase in delamination rate for distilled water, hydraulic fluid (Aero-Shell Fluid 41) and de-icing fluid (UCAR ADF XL 54), as well as a decrease in the number of cycles to delamination onset. The effects were most pronounced for de-icing fluids. It has to be noted that a 26 μm thick PTFE film was used as starter crack, twice as thick as recommended in current standards. Moutsompegka et al. [217] consider effects of de-icing fluid (SAFEWAY KF from Clariant) in different concentrations (de-icing fluid diluted in demineralized water) on mode I and mode II fracture toughness of composite bonded joints (FM 300-2 adhesive and HexPly M21E/IMA composite), and noted a decrease in both after the exposure. Yavas et al. [218] discuss contamination by one type of aviation hydraulic fluid (MIL-PRF-87257) on an adhesive/composite adherend system (Hysol EA9394 adhesive and Hexcel IM7-G/8552 composite). Quasi-static mode I and mode II toughness (the latter tested for de-icing fluid only) were noted to decrease in the bonded joints. Most of the published data, hence, seems to indicate degradation of FRP and adhesive bond properties due to exposure to these fluids. Malinowski et al. [219] also investigated CFRP adhesive bonds subject to different treatments focusing on repair issues and potential effects of applying improper procedures. Thermal treatment simulating external heat sources or lightning impact effects were combined with exposure to de-icing fluids and improper cure. The study further investigated the applicability of different NDT-methods for detecting the defects in the bonded joints. X-ray microcomputed tomography indicated porosity bond-lines but failed to clearly distinguish contaminated and reference bond-lines, whereas nonlinear ultrasonics was able to do that.

Another type of environmental exposure is the formation of microbial films on CFRP in certain environments. First, this seemed to be of more concern in naval transportation, as discussed by Wagner et al. [220]. Composites, resins, and fibers were exposed to sulfur/iron-oxidizing, calcareous-depositing, ammonium-producing, hydrogen-producing, and sulfate-reducing bacteria with no noticeable effects on epoxy

resin, carbon fibers, and CFRP epoxy composites. Gu [221] reviewed the information available on biodegradation of polymers and composites for space applications and noted degradation due to fungal and bacterial action in experiments covering a wide range of temperature and humidity conditions. Fracture toughness or delamination resistance, however, was not investigated explicitly in these studies. It is likely that degradation of CFRP composites due to microbial biofilm formation may later result in deterioration of toughness and delamination resistance, but clarifying this will require a significant research effort. It is noted here that microbial degradation of CFRP composites may play a role in developments toward future, environmentally safer, recycling or disposal strategies of CFRP structures, such as aircraft fuselage, wings, or stabilizers, and Gu [222] pointed out possible pitfalls that have to be considered when developing biodegradation methods for FRP composites. Currently, recycling of FRP composites, in general, is a research area that has not been explored much yet, for respective methods and strategy see, e.g., [223, 224].

While constituents of the aerospace environment and appropriate models are known, understanding of the interaction of components and their synergy is still lacking [225]. Each of these or combinations of aerospace exposures lead to aging and/or damage initiation and accumulation in the FRP composites that may require monitoring and maintenance, but ultimately limits the service life of the FRP component or structure. Specific effects from space environment on FRP composites and related property measurements are noted in the revised edition of the Composite Material Handbook (Version G, [42]). However, the information presented is not focusing on environmentally induced toughness or delamination resistance changes. Maji and Mahnke [226] summarize the literature on space environment effects, mainly radiation, on FRP composites and in most cases, note degradation in mechanical and thermomechanical properties. The toughness or delamination resistance is not noted explicitly in this overview, nor in the overview by Edwards et al. [225]. Voicu [227] did not observe the formation of delaminations in CFRP (3k Carbon fiber fabric reinforcement 0/90°, twill2x2 with M49 epoxy matrix) in three-point flexure testing after exposure to UV, gamma radiation and thermal cycles corresponding to conditions in Low Earth Orbit (LEO). Moon et al. [228] used a combination of simulated high vacuum, atomic oxygen, UV exposure, and thermal cycling for 20 h (equivalent to the STS-4 space shuttle exposure in LEO). Tensile testing of CFRP specimens (T700 fibers in phenolic novolac epoxy and bisphenol-A epoxy matrix), some modified with Multi-Walled Carbon nanotubes (MWCNT) showed effects on tensile strength and stiffness (fracture mechanics properties were not investigated).

There are two basic approaches for fracture mechanics testing under specific environmental conditions or their combinations. The first is to subject the FRP composites to certain exposures for a given duration and then test the fracture mechanics properties after a sufficient conditioning period under laboratory conditions (e.g., +23°C and 50% relative humidity). This determines the resulting aging and damage as a function of intensity and duration of exposure. The second is to perform the test at the specific exposure condition, again as a function of intensity and duration. The latter clearly is more difficult and requires load, displacement and delamination length measurements at the specified condition as basic information for calculating fracture mechanics

quantities, except when a compliance-based effective crack length is used that elimi-
nates the need for delamination length readings. Aging effects in FRP composites may
be quite complex, e.g., depending on specimen size and surface preparation even for
relatively simple accelerated thermal aging of an aerospace CFRP (IM7/8552)
laminate as discussed by Dao et al. [229].

As noted above, fracture mechanics tests on FRP composites have been performed
at low temperatures by, e.g., [103, 221, 222, 223, 230]. Data for carbon fiber/epoxy
laminates (IM7/977-2) from at cryogenic, room and elevated temperatures indicating
increasing mode I delamination resistance with increasing temperature and a slight
decrease below room temperature are summarized in Fig. 8.15 [231, 232]. Results
for GFRP laminates mainly with woven reinforcement are not limited to quasi-static
mode I and mode II tests, but include mixed-mode I/II and cyclic fatigue tests under
mode I, mode II, and mixed-mode I/II [103, 221, 222, 233]. For plain weave CFRP
laminates (T300/XB5082) Cantwell [230] reported improved delamination resistance
for mode II (as well as for interlaminar shear strength) at temperatures below room
temperature down to −194°C, but no observable effect for mode I, in spite of
improved toughness for pure epoxy specimens under mode I loading. Compared
with room-temperature, Horiguchi et al. [233] reported improved mode II delamina-
tion resistance on glass-cloth/epoxy laminates at −196°C (liquid nitrogen) and further
improvements at −269°C (liquid helium). Improved delamination resistance in woven
glass/epoxy laminates under cyclic fatigue mixed-mode I/II loading was noted in
[103]; however, the improvement was more pronounced at −196°C (liquid nitrogen)
than at −269°C (liquid helium).

Environmental effects, such as humidity and temperature on fracture behavior of
FRP composites have been investigated since the 1980ies (see, e.g., [234]) but have
not been included in the standard test methods. These typically require conditioning
at a specified temperature, e.g., for obtaining a "dry" condition (with parameters as
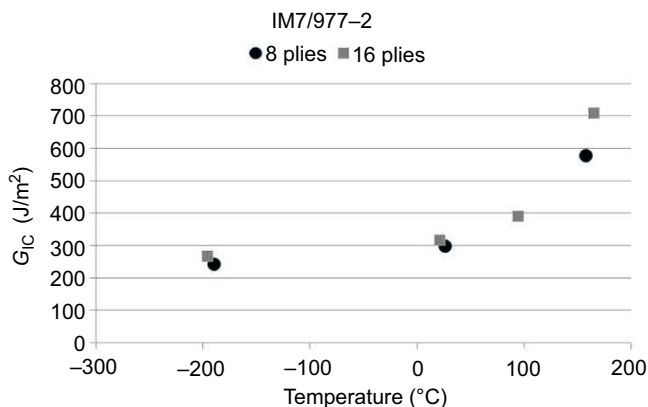
Figure 8.15 Dependence of the delamination resistance under quasi-static mode I loading for
carbon-fiber-reinforced epoxy (IM7/977-2) on test temperature (after sufficient conditioning)
for two laminate thicknesses [231]; with increasing temperatures, the delamination resistance
is increasing.

recommended by manufacturer according to clause eight of ISO 15024 or in following Procedure D of ASTM D5229 according to clause 10.2 of ASTM D5528) but some standards allow agreeing on conditioning in different climates (e.g., ASTM D5528, clause 10.1). Vieille [235] investigated the ductile or brittle transition in the failure of woven-ply reinforced carbon PPS laminate (T300 3K 5HS) weave by cyclic loading of SEN specimens at +120°C. A translaminar failure with fiber breaks and matrix cracks near the crack tip was observed. For cyclic fatigue fracture, ESIS TC4 procedures recommended to condition to test climate (e.g., +23°C, 50% relative humidity). Since test duration in cyclic fatigue can be significant, keeping the test climate, whatever it is, sufficiently constant (e.g., within the margins of ±2°C and ±5% relative humidity set by ISO 291) is strongly recommended in order to avoid effects from a variation of ambient conditions on the test results. Temperature and humidity effects on FRP composites are further discussed in Chapter 9 of this book.

Effects from thermal cycling between −175 and +120°C under vacuum (at 1.3 mPa simulating space environment) on carbon-fiber-reinforced epoxy laminates (made from M40J, M55J, and M60J unidirectional prepregs) have been investigated by Park et al. [236]. They found that the density of the materials decreased after 2,000 cycles, and they observed significant degradation in mechanical properties. Interlaminar fracture toughness has not been determined, but properties affecting it (e.g., fiber-matrix adhesion) have been shown to decrease.

Hygro-thermal effects on fracture toughness of FRP composites have, e.g., been investigated for mode I, mode I and mixed-mode I/II [237]. For a carbon-fiber-reinforced epoxy with thermoplastic particulate interlayers, with dry and moisture-saturated conditions at temperatures ranging from −43 to +98°C plus one test at +125°C in dry condition, increasing matrix ductility was observed for increasing temperature and moisture. This correlated with an increase in mode I toughness and a decrease in mode II toughness. Effects of combined hygro-thermal cycles of carbon-fiber-reinforced composites, e.g., simulating aircraft operating at high altitudes (low temperatures, e.g., below −50°C and very low relative humidity, e.g., a few percent) and landing in tropical zones (high temperatures at and above +30°C and high relative humidity near 100%) on fracture toughness or delamination resistance have not been investigated in published research to the best knowledge of the author. It is expected that large temperature variations resulting in corresponding stresses from the coefficient of linear thermal expansion (typically around 10^{-6}/°C) would dominate over the hygric stresses on the typical time scales for aircraft operation (up to 14 h at low humidity alternating with a few hours at high humidity). Hygro-thermo-mechanical aging effects on fracture behavior have been compared to those induced by hygro-thermal aging by Zenasni et al. [238] for woven glass (ST220-2/2 twill/PEI, SS303-8H satin/PEI) and woven carbon fiber poly-ether-imide composites (CD342-8H satin/PEI). They observed differences in moisture uptake and delamination behavior. The two GFRP fiber laminates showed similar moisture uptake (saturation around 0.21%), while CFRP showed a value of around 0.3%. After hygro-thermal aging (at +70°C and 95% relative humidity) the 8H laminates proved more resistant than the 2/2 twill under mode I and mode II loading. Hygro-thermo-mechanical aging in special loading devices under the same conditions yielded initial increases in mode

I delamination resistance (up to about 30 days). For mode II, the 8H GFRP showed initial increases under hygro-thermal and hygro-thermo-mechanical aging, while the other laminates showed decreasing mode II delamination resistance with time.

Fire resistance of FRP composites is also of concern in aerospace applications; a review [239] found severe degradation in postfire flexural properties for FRP epoxy composites, which were induced by delamination formation due to resin combustion.

Effects of electromagnetic radiation of different frequency, and hence energy, or of particle irradiation on the fracture of FRP composites have only scantly been investigated. Electron irradiation of a carbon-fiber epoxy composite (T300/934) was investigated by Funk and Sykes [240] on standard size and miniature specimens under mode I and mode II loading at three test temperatures ($-157°$C, room-temperature, $+121°$C). The irradiation with 1 MeV electrons and a radiation dose of 1×10^{10} rad in high vacuum of 1.3×10^{-7} mbar simulated about 30 years in a geosynchronous orbit. Although the results showed a significant effect of test temperature, electron irradiated specimens yielded a higher delamination resistance. Dynamic-Mechanical-Thermal Analysis (DMTA) and Scanning Electron Microscopy (SEM) indicated that this was due to irradiation-induced matrix changes. Similar experiments were performed by Takeda et al. [241] under mode I and mixed-mode I/II on carbon- and glass-fiber-reinforced epoxy composites. Electron irradiation was performed in the air up to total absorbed doses of 120 MGy, resulting in heating of the specimens to about $+70°$C. The delamination resistance decreased with increasing dose in both types of composites. The fracture tests were again complemented by DMTA and SEM indicating degradation of the glass fiber epoxy interface (silane coupling agent) in addition to matrix degradation. For CFRP, only matrix degradation was observed. Gamma irradiation with doses up to 27.2 MGy was investigated by Sekulic et al. [242] for unidirectional CFRP epoxy (HTS/HexPly 6376 NCHR). In some specimens, irradiation was followed by annealing. DMTA indicated some changes in transition temperature for a certain irradiation dose range, but less for others, which correlated with changes in delamination resistance. The experiments discussed above all indicate a complex interaction between irradiation and temperature, which would have to be taken into account in irradiation test development. Arnaout et al. [243] discuss electric charging effects in typical geostationary orbits on dielectric materials but do not consider CFRP composites in their investigation. Effects on composites from space environment (absence of atmosphere, irradiation with particles and electromagnetic waves, temperature variation, etc.) are discussed in the new Composite Materials Handbook (Version G, [42]), but again in rather general terms. First, it is pointed out that FRP are more sensitive to environmental exposure than metals, specifically with respect to temperature (for aircraft, $+82°$C is considered the worst case) and moisture (85% relative humidity again being the worst case for aircraft), and second, the (comparatively) "extreme" aerospace environment is noted. UV exposure is another important effect for FRP composites. For space applications, the impacts of micrometeorites and of space debris, e.g., from other spacecraft [244] will also contribute to damage of FRP composites and hence to aging.

A special electromagnetic environment relevant to aircraft operating in the atmosphere is the effect of lightning. Artificial lightning tests on CFRP epoxy laminates

(IM600/133) by Hirano et al. [245] have yielded fiber damage, resin deterioration, and internal delaminations. There is a nonlinear relationship between the delamination area and the electrical action integral (defined as time integral over the square of the electrical current). Delamination resistance or changes in delamination resistance after lightning action has not been quantified, but the material has been damaged, and delaminations have initiated. Feraboli and Miller [246] performed similar experiments on another CFRP epoxy laminate (G30-500 12k HTA/7714A) and quantified mechanical property changes (tensile and compressive strength, E-modulus) after lightning strikes. Again, delaminations were noted but delamination resistance or its change not quantified. In aircraft design, copper meshes are implemented into the CFRP structures in order to mitigate the effects of lightning strikes, but these require proper attention in case of later repair [247]. A combination of characterization methods was used by Yamashita et al. [248] to assess simulated lightning strike effects on quasi-isotropic, thermoplastic CFRP laminates and chopped carbon fiber tape-reinforced thermoplastics (TR505 PAN-based fiber and PA6 matrix). Recent research on lightning effects in CFRP laminates applied modeling or simulation approaches [249−251] to replace the experimental setups and the complex characterization methods, see, e.g., Zou et al. [252] discussing aircraft models based on EMA3D electromagnetic simulation software. Recent experimental approaches are discussed by Abdelal and Murphy [253] using a CFRP epoxy (IM600/133, with a 32-ply quasi-isotropic layup $[45°/0°/-45°/90°]_{4S}$) and simulating that with FEM with a user material subroutine in Abaqus. Lightning effects on thin-ply CFRP are presented by Yamashita et al. [248] testing a thermoplastic CFRP (fiber type TR50S from Mitsubishi Rayon Co. Ltd. and a PA6 Diamiron C from Mitsubishi Plastics Co. Ltd.) with a high-speed camera and posttest ultrasonics for damage characterization. Lightning effects on FRP composites are further discussed in Chapter 18 of this book.

A general perspective on requirements for all material classes, not only FRP composites, used in aerospace applications and, specifically, on the challenges of the operating environments, is given by Zhang et al. [23]. The conclusion for composites is that, beside PMC, other composite matrix materials (metal matrix composites; MMC or ceramic matrix materials; CMC) may provide a better performance, either by better balancing mechanical properties by specific fiber selection or addition of other species, e.g., graphene platelets. These approaches are deemed important by the authors also in order to improve the toughness of composites. However, as noted earlier, composites for aerospace applications will, in general, have to be certified, and that may delay introducing new materials into aerospace structural designs, even if their performance is better.

8.8   Conclusions and outlook

The present contribution discusses test standards and test development for determining fracture mechanics data of fiber-reinforced polymer-matrix (FRP) laminates. The focus is on experimental work. Major factors that affect delamination resistance, besides

loading mode, are fiber and polymer types, fiber orientation and layup, processing, conditioning, and aging. This is illustrated by selected test data for a high-performance CFRP epoxy (IM7 fiber with different 977 epoxy resin types). Modeling of fracture behavior of FRP composites is not treated in detail, but cited references discuss some examples of that. Modeling and simulation are expected to become more important in fracture mechanics based structural design with FRP composites and to also play an important role in test development and data analysis. Modeling is used, e.g., to assess the influence of friction in test setups, to determine mode mixing contributions, or to predict fracture behavior. Tay [35] provides more information on various early aspects of modeling and simulation in fracture mechanics of FRP composites. As briefly discussed above, the number of publications providing results of modeling or simulation of quasi-static fracture of FRP composites is increasing, and this trend will continue. So far, there is little published on modeling or simulation of cyclic fatigue fracture (see, e.g., [254, 255]) or of fracture under high-rate loads (e.g., [68, 256]). Analogous to experimental studies, round robin exercises of modeling and simulation will be necessary to assess the reproducibility of the results and to identify the computationally most efficient codes. Such an exercise aiming at reproducing the quasi-static behavior of a unidirectionally reinforced CFRP by calculating loads and the delamination length increments as a function of displacement has been started by members of ESIS TC4 in 2018, but analysis and publication of the results will take some time. An extension of this is planned for dealing with the simulation of cyclic fatigue fracture under mode I loads for the same material, aiming at reproducing the da/dN versus G_{max} graph (Paris curve).

Fracture mechanics testing of FRP composites so far has played a minor role in material selection, materials qualification, and structural design for aerospace applications. However, due to current demands for energy-saving transportation and propulsion systems, it is expected that fracture mechanics-based designs will become standard in aerospace structural engineering in the near to intermediate future. However, this requires providing a suitable education for material scientists and engineers. Damage accumulation and fatigue behavior of FRP composites and hence delamination propagation due to cyclic thermo-mechanical service loads are current research topics. Exposure of aircraft and space structures to special environmental conditions may require more detailed investigations in the future for assuring sufficient service life of the composite laminates.

Materials development for the improvement of performance, specifically of damage and delamination resistance of FRP composites have received and still receive significant attention. Among the concepts investigated are interleaving and use of three-dimensional reinforcements (both discussed above), as well as matrix toughening, recently via the addition of nanoscale and/or microscale fillers. These comprise a range of materials, e.g., carbon nanotubes, layered silicate clays, silica nanospheres, carbon black, graphene, and microscale inorganic fillers. Polymer nanocomposites have been prepared with combinations of different nanoscale additives or combinations of nano- and microscale fillers [257], but those have not yet been explored as a matrix in FRP laminates. Ashrafi et al. [258] reported an increase in mode I and mode II delamination resistance from incorporation of single-wall carbon nanotubes into the epoxy matrix

for a CFRP laminate which proved more effective than multi-wall carbon nanotubes at similar weight fraction, while Tang et al. [259] observed an increase in delamination resistance under quasi-static mode I, but a decrease under quasi-static mode II loading when incorporating silica nanoparticles (Nanopox F400) into a CFRP epoxy laminate (UT70-20/Araldite F). Nano-modified epoxy with functionalized layered silicate clay (Cloisite 30B) as the matrix has been reported to increase the impact behavior of GFRP epoxy laminates [260], and that possibly suggests improved delamination resistance of nano-modified CFRP under high-rate loading. Thermoplastic nanofiber interlayers deposited on the carbon fiber fabric investigated by Zhang et al. [261] provide another approach for toughened CFRP epoxy laminates (C12K/MY0510), but among three types tested, only poly(c-caprolactone) nanofibers proved efficient. So far, the existing standard test methods have proven applicable for determining fracture mechanics data for FRP laminates with nano-modified polymer matrix materials. However, an important issue in processing, manufacturing, testing, and disposal of these composites is the release of nanoparticles into the environment and the associated potential health risks to persons that may be exposed. A recent review [262] points out that it is too early for a definitive assessment of the nano-risks, and further research will be needed. One aspect that is important for all current or future developments of FRP composites for aerospace applications, either on the material side (e.g., nanoscale additives or interleaving) or in manufacturing processes (e.g., additive manufacturing) is the certification for use.

The question as to whether delamination resistance can be quantitatively characterized using existing standard test procedures or whether modified or new standard procedures have to be developed also applies to other types of FRP composites. Currently, available data indicate that three-dimensional reinforcements typically result in "high" values of G_C compared with the unidirectional laminate made from the same fiber and matrix. Whether the high delamination resistance of three-dimensional FRP laminates do represent material values or are "apparent" values, e.g., depending on specific test and specimen parameters, is still debated (see, e.g., [181]). More generally, the applicability of linear elastic fracture mechanics to through-thickness reinforced FRP composites may be questionable [188].

As an outlook, it is expected that test development for fracture toughness, and delamination resistance measurements on FRP composite laminates will move from tests, which have been standardized for unidirectional glass- and carbon-fiber-reinforced laminates, i.e., quasi-static mode I, mode II and mixed-mode I/II loading, to cyclic fatigue and high rate tests for the same laminate types and modes. For mode I and mode II cyclic fatigue, test procedures are under development, and for mixed-mode I/II, preliminary tests have been performed indicating the basic feasibility. Whether and, if necessary, how fiber-bridging effects (which play an important role in unidirectional FRP laminates) have to be taken into account in other modes and mode mixes as well in order to obtain safe design limits, is at present still debated. In parallel or at a later stage, the applicability of the test procedures to nonunidirectional and multidirectional reinforced laminates will have to be investigated. Again, first trial tests have been performed in some cases. Implementation of contactless optical monitoring of experiments, e.g., with digital imaging or video and advanced

image analysis will provide valuable data records that can be analyzed in detail for the determination of delamination lengths or for automation of data analysis, and both will likely reduce the scatter in the data. The second line of test development will focus on environmental exposure and its effects, probably first dealing with quasi-static and cyclic fatigue loading for mode I. The use of fracture mechanics data in structural composite designs will have to be developed further, and it is expected that experimental and modeling fracture mechanics research and material developments in combination with proper education or training will yield economically feasible composite aerospace structures for safe long-term use. The Hartman-Schijve type analysis of fatigue fracture data of FRP composites seems to work well for life prediction of composite components and structures as discussed, e.g., by Jones et al. [48]. This is in-line with the experience from composite structural design in another high-performance application, namely Formula 1 racing cars [263]. For recycling or environmentally friendly disposal of aerospace FRP composite components and structures [223] after their service life, delamination resistance, or matrix toughness might play a role depending on the methods used, but this will require significant research efforts before suitable technologies can be successfully and economically implemented on a large scale.

Appendix: glossary

3ENF	three-point bending ENF (specimen)
4ENF	four-point bending ENF (specimen)
ΔG	Difference in energy release rate (usually between maximum and minimum, Gmax-Gmin)
μm	mmicrometre (10^{-6} m)
ADCB	symmetric Double Cantilever Beam (specimen)
AITM	Airbus Industries Test Method.
AMMF	Asymmetric Mixed-Mode Fracture.
ARALL	Aramide-Reinforced Aluminum Laminate.
ASTM Intl	American Society for Testing and Materials International.
BSS	Boeing Support Specification.
CARALL	Carbon-Reinforced Aluminum Laminate.
CFRP	Carbon Fiber-Reinforced Polymer-Matrix.
CMC	Ceramic-Matrix Composite(s)
CMH, CHM17	Composite Materials Handbook, Composite Materials Handbook-17.
CNT	Carbon Nano-Tube(s)
CT	Compact Tension (specimen)
CZM	Cohesive Zone Model.
da/dN	delamination length increment per cycle.
DCB	Double Cantilever Beam (specimen)
DEN	Double-Edge-Notched (specimen)
DENT, DEN-T	Double-Edge-Notched Tensile (specimen)
DIC	Digital image Correlation.
DMTA	Dynamic Mechanical Thermal Analysis.

ELS	End-Loaded Split (specimen)
EN	European Standard.
ENF	End-Notched Flexure (specimen)
ESD	Electro-Static Discharge.
ESIS	European Structural Integrity Society.
EUROCOMP	European Composites Design Code and Standard.
FEA	Finite Element Analysis.
FEM	Finite Element Method.
FML	Fiber Metal Laminate(s)
FRP	Fibee-Reinforced Polymer-Matrix.
G_C, G	critical energy release rate and energy release rate, respectively (the additional subscripts G_{IC}, G_{IIC}, G_{IIIC}, $G_{I/IIC}$, $G_{I/IIIC}$ and $G_{I/II/IIIC}$ refer to quasi-static fracture modes (I = tensile opening, II = in-plane shear and III = transverse shear or twist and respective mixed modes), and G_{Imax}, G_{IImax} and $G_{I/IImax}$ refer to the maximum applied energy release rate (stress) in the respective pure or mixed mode)
GFRP	Glass Fiber-Reinforced Polymer-Matrix.
GLARE	Glass Laminate Aluminum-Reinforced Epoxy.
ISO	International Organization for Standardization.
J	Joule (unit of energy)
JIS	Japan Industrial Standards.
JSA	Japanese Standards Association.
K_{IC}	stress intensity factor.
LEFM	Linear Elastic Fracture Mechanics.
LSB	Large-Scale Bridging (fibers)
MGy	Mega-Grey (unit of radiation energy dose, 1 Gy = 1 J/kg)
MIL-HDBK	(United States Department of Defense) Military Handbook.
MMB	Mixed-Mode Bending (specimen)
MMC	Metal-Matrix Composite(s)
MPa	Mega-Pascal (unit of pressure, 1 MPa = 1 N/mm^2)
MWCNT	Multi-Walled Carbon Nano-Tube(s)
N	Newton (unit of force)
NASA	National Aeronautics and Space Administration (USA)
PA6 PA12	Poly-Amide-6, Poly-Amide-12.
PAN	Poly-Acrylo-Nitrile (polymer)
PEEK	Poly-Ether-Ether-Ketone (polymer)
PEI	Poly-Ether-Imide (polymer)
PPS	Poly-Phenylene Sulfide (polymer)
PTFE	Poly-Tetra-Fluoro-Ethylene (polymer)
R curve	resistance curve (plot of values of energy release rate G vs. delamination length a)
R ratio	ratio between the minimum and maximum load/stress or displacement (in cyclic fatigue tests)
RTM	Resin Transfer Molding.
SAE Intl	Society of Automotive Engineers, International.
SEM	Scanning Electron Microscopy.
SENB	Single Edge Notch Bending (specimen)
TC	Technical Committee.

| VCCT | Virtual Crack Closure Technique. |
| XFEM | Extended Finite Element Method. |

Acknowledgments

References

[1] J.G. Williams, The fracture mechanics of delamination tests, J. Strain Anal. 24 (1989) 207−214. https://doi.org/10.1243/03093247V244207.

[2] L. Lasri, M. Nouari, M. El Mansori, Wear resistance and induced cutting damage of aeronautical FRP components obtained by machining, Wear 271 (2011) 2542−2548. https://doi.org/10.1016/j.wear.2010.11.056.

[3] N. Shetty, S.M. Shahabaz, S.S. Sharma, S. Divakara Shetty, A review on finite element method for machining of composite materials, Compos. Struct. 176 (2017) 790−802. https://doi.org/10.1016/j.compstruct.2017.06.012.

[4] J.G. Williams, Introduction to linear elastic fracture mechanics, in: D.R. Moore, A. Pavan, J.G. Williams (Eds.), Fracture Mechanics Testing Methods for Polymers, Adhesives and Composites, ESIS Publication 28, Elsevier, 2001, pp. 3−10.

[5] K. Friedrich, Microstructural efficiency and fracture toughness of short fiber/thermoplastic matrix composites, Compos. Sci. Technol. 22 (1985) 43−74. https://doi.org/10.1016/0266-3538(85)90090-9.

[6] K. Friedrich, R. Walter, H. Voss, J. Karger-Kocsis, Effect of short fibre reinforcement on the fatigue crack propagation and fracture of PEEK-matrix composites, Composites 17 (1986) 205−216. https://doi.org/10.1016/0010-4361(86)91004-9.

[7] K. Nikpur, Y.F. Chen, J.L. Kardos, Fracture toughness of unidirectional short-fiber reinforced epoxy composites, Compos. Sci. Technol. 38 (1990) 175−191. https://doi.org/10.1016/0266-3538(90)90005-P.

[8] P. Fernberg, Toughness of Short Fiber Composites − an Approach Based on Crack-Bridging, Ph.D. Thesis, Luleå University of Technology, 2002, pp. 1−148.

[9] V. Rizov, T. Harmia, A. Reinhardt, K. Friedrich, Fracture toughness of discontinuous long glass fiber reinforced polypropylene: an approach based on a numerical prediction of fiber orientation in injection molding, Polym. Polym. Compos. 13 (2005) 121−130. https://doi.org/10.1177/096739110501300201.

[10] R.V. Subramanian, K.H. Shu, Silane coupling agents for basalt fiber reinforced polymer composites, in: H. Ishida, H.G. Kumar (Eds.), Molecular Characterization of Composite Interfaces, Polymer Science and Technology, vol. 27, Springer, 1985, pp. 205−236.

[11] T. Czigány, Basalt fiber reinforced hybrid polymer composites, Mater. Sci. Forum 473−474 (2005) 59−66. https://doi.org/10.4028/www.scientific.net/MSF.473-474.59.

[12] F. Sarasini, J. Tirillò, M. Valente, T. Valente, S. Cioffi, S. Iannace, L. Sorrentino, Effect of basalt fiber hybridization on the impact behavior under low impact velocity of glass/basalt woven fabric/epoxy resin composites, Compos. A Appl. Sci. Manuf. 47 (2013) 109−123. https://doi.org/10.1016/j.compositesa.2012.11.021.

[13] M. Turan Demirci, N. Tarakçıoğlu, A. Avcı, A. Akdemir, I. Demirci, Fracture toughness (Mode I) characterization of SiO_2 nanoparticle filled basalt/epoxy filament wound composite ring with split-disk test method, Compos. B Eng. 119 (2017) 114−124. https://doi.org/10.1016/j.compositesb.2017.03.045.

[14] J.K. Kim, Y.W. Mai, High strength, high fracture toughness fibre composites with interface control a review, Compos. Sci. Technol. 41 (1991) 333−378. https://doi.org/10.1016/0266-3538(91)90072-W.

[15] P. Priyanka, A. Dixit, H.S. Mali, High-strength hybrid textile composites with carbon, Kevlar, and E-glass fibers for impact-resistant structures. A review, Mech. Compos. Mater. 53 (2017) 685−704. https://doi.org/10.1007/s11029-017-9696-2.

[16] Y. Swolfs, I. Verpoest, L. Gorbatikh, Recent advances in fibre-hybrid composites: materials selection, opportunities and applications, Int. Mater. Rev. 64 (2019) 181−215. https://doi.org/10.1080/09506608.2018.1467365.

[17] V. Fiori, T. Scalici, G. Di Bella, A. Valenza, A review on basalt fibre and its composites, Compos. B Eng. 74 (2015) 74−94. https://doi.org/10.1016/j.compositesb.2014.12.034.

[18] V. Dhand, G. Mittal, K.Y. Rhee, S.J. Park, D. Hui, A short review on basalt fiber reinforced polymer composites, Compos. B Eng. 73 (2015) 166−180. https://doi.org/10.1016/j.compositesb.2014.12.011.

[19] S. Sockalingam, S.C. Chowdhury, J.W. Gillespie, M. Keefe, Recent advances in modeling and experiments of Kevlar ballistic fibrils, fibers, yarns and flexible woven textile fabrics − a review, Text. Res. J. 87 (2017) 984−1010. https://doi.org/10.1177/0040517516646039.

[20] M. Yasaee, I.P. Bond, R.S. Trask, E.S. Greenhalgh, Mode I interfacial toughening through discontinuous interleaves for damage suppression and control, Compos. A Appl. Sci. Manuf. 43 (2012a) 198−207. https://doi.org/10.1016/j.compositesa.2011.10.009.

[21] M. Yasaee, L.P. Bond, R.S. Trask, E.S. Greenhalgh, Mode II interfacial toughening through discontinuous interleaves for damage suppression and control, Compos. A Appl. Sci. Manuf. 43 (2012b) 121−128. https://doi.org/10.1016/j.compositesa.2011.09.026.

[22] B.A. Patterson, M.H. Malakooti, J.J. Lin, A. Okorom, H.A. Sodano, Aramid nanofibers for multiscale fiber reinforcement of polymer composites, Compos. Sci. Technol. 161 (2018) 92−99. https://doi.org/10.1016/j.compscitech.2018.04.005.

[23] X.S. Zhang, Y.G. Chen, J.L. Hu, Recent advances in the development of aerospace materials, Prog. Aerosp. Sci. 97 (2018) 22−34. https://doi.org/j.paerosci.2018.01.001.

[24] C.A.C. Leckey, J.P. Seebo, P. Juarez, Challenges of NDE simulation tool validation, optimization, and utilization for composites, SPIE, AIP Conf. Proc. 1706 (2016), 120011-1 − 120001-8, https://doi.org/10.1063/1.4940596.

[25] T.A. Schmid-Fuertes, T. Kruse, T. Körwien, M. Geistbeck, Bonding of CFRP primary aerospace structures − discussion of the certification boundary conditions and related technology fields addressing the needs for development, Compos. Interface 22 (2015) 795−808. https://doi.org/10.1080/09276440.2015.1077048.

[26] G.C. Wu, J.M. Yang, The mechanical behavior of GLARE laminates for aircraft structures, JOM 57 (2005) 72−79. https://doi.org/10.1007/s11837-005-0067-4.

[27] R.C. Alderliesten, in: J.R. Barber, A. Klarbring (Eds.), Fatigue and Fracture of Fibre Metal Laminates. Solid Mechanics and Its Applications 236, Springer, 2017, pp. 1−300. https://doi.org/10.1007/978-3-319-56227-8.

[28] G. Zambelis, T. Da Silv Botelho, O. Klinkova, I. Tawfiq, C. Lanouettea, A new approach in testing fatigue fracture mechanics properties in asymmetrical bonded composite/metal assemblies, Compos. B Eng. 158 (2019) 390−399. https://doi.org/10.1016/j.compositesb.2018.09.073.

[29] O. Gohardani, M. Chapartegui Elola, C. Elizetxea, Potential and prospective implementation of carbon nanotubes on next generation aircraft and space vehicles: a review of current and expected applications in aerospace sciences, Prog. Aerosp. Sci. 70 (2014) 42−68. https://doi.org/10.1016/j.paerosci.2014.05.002.

[30] V. Kostopoulos, A. Masouras, A. Baltopoulos, A. Vavouliotis, G. Sotiriadis, L. Pambaguian, A critical review of nanotechnologies for composite aerospace structures, CEAS Space J. 9 (2017) 35−57. https://doi.org/10.1007/s12567-016-0123-7.

[31] J.R. Raney, R. Jordan, B.G. Compton, J. Mueller, T.J. Ober, K. Shea, et al., Rotational 3D printing of damage-tolerant composites with programmable mechanics, Proc. Natl. Acad. Sci. U.S.A. 115 (2018) 1198−1203. https://doi.org/10.1073/pnas.1715157115.

[32] M.A. Caminero, J.M. Chacón, I. García Moreno, J.M. Reverte, Interlaminar bonding performance of 3D printed continuous fibre reinforced thermoplastic composites using fused deposition modelling, Polym. Test. 68 (2018) 415−423. https://doi.org/10.1016/j.polymertesting.2018.04.038.

[33] W.F. Hao, Y. Liu, H. Zhou, H.S. Chen, D.N. Fang, Preparation and characterization of 3D printed continuous carbon fiber reinforced thermosetting composites, Polym. Test. 65 (2018) 29−34. https://doi.org/10.1016/j.polymertesting.2017.11.004.

[34] J.W. Gillespie, Damage tolerance of composite structures: the role of interlaminar fracture mechanics, J. Offshore Mech. Arct. 113 (1991) 247−252. https://doi.org/10.1115/1.2919927.

[35] T.E. Tay, Characterization and analysis of delamination fracture in composites: an overview of developments from 1990 to 2001, Appl. Mech. Rev. 56 (2003) 1−31. https://doi.org/10.1115/1.1504848.

[36] P. Davies, Review of standard procedures for delamination resistance testing [Chapter 3], in: S. Sridharan (Ed.), Delamination Behaviour of Composites, Woodhead Publishing, 2008, pp. 65−86. https://doi.org/10.1533/9781845694821.1.65.

[37] A.J. Brunner, B.R.K. Blackman, P. Davies, A status report on delamination resistance testing of polymer-matrix composites, Eng. Fract. Mech. 75 (2008) 2779−2794. https://doi.org/10.1016/j.engfracmech.2007.03.012.

[38] A.J. Brunner, Scatter, scope and structures: what fatigue fracture testing of fiber polymer composites is all about, Proc. 39th Risø Int. Symp. Mater. Sci., IOP Conf. Ser. Mater. Sci. Eng. 388 (2018) 1−19. https://doi.org/10.1088/1757-899X/388/1/012003.

[39] Department of Defense Handbook, Composite Materials Handbook, MIL-HDBK 17-1F Volume 1 'Polymer Matrix Composites Guidelines for Characterization of Structural Materials', 2002.

[40] Department of Defense Handbook, Composite Materials Handbook, MIL-HDBK 2F Volume 2 'Polymer Matrix Composites Material Properties', 2002.

[41] Department of Defense Handbook, Composite Materials Handbook, MIL-HDBK-3F Volume 3 'Polymer Matrix Composites Material Usage, Design and Analysis', 2002.

[42] Composite Materials Handbook 17, 2017. www.cmh17.org.

[43] F.W.J. van Hattum, F. Regel, M. Labordus, Cost reduction in manufacturing of aerospace composites, Plast. Rubber Compos. 40 (2011) 93−99. https://doi.org/10.1179/174328911X12988622801052.

[44] R.H. Martin, Incorporating interlaminar fracture mechanics into design, Proc. Inst. Mech. Eng. L J. Mater. Des. Appl. 214 (2000) 91−97. https://doi.org/10.1243/1464420001544870.

[45] J.L. Clarke (Ed.), EUROCOMP Design Code and Handbook Structural Design of Composites, Taylor & Francis, 1996, 0419194509.

[46] S. DorMohammdi, C. Godines, F. Abdi, D. Huang, M. Repupilli, L. Minnetyan, Damage-tolerant composite design principles for aircraft components under fatigue service loading using multi-scale progressive failure analysis, J. Compos. Mater. 51 (2017) 2181−2202. https://doi.org/10.1177/0021998317691812.

[47] R. Jones, A.J. Kinloch, J.G. Michopoulos, A.J. Brunner, N. Phan, Delamination growth in polymer-matrix fibre composites and the use of fracture mechanics data for material characterisation and life prediction, Compos. Struct. 180 (2017) 316−333. https://doi.org/10.1016/j.compstruct.2017.07.097.

[48] L.J. Yao, R.C. Alderliesten, R. Jones, A.J. Kinloch, Delamination fatigue growth in polymer-matrix fibre composites: a methodology for determining the design and lifing allowables, Compos. Struct. 196 (2018) 8−20. https://doi.org/10.1016/j.compstruct.2018.04.069.

[49] H. Hadavinia, H. Ghasemnejad, Effects of Mode-I and Mode-II interlaminar fracture toughness on the energy absorption of CFRP twill/weave composite box sections, Compos. Struct. 89 (2009) 303−314. https://doi.org/10.1016/j.compstruct.2008.08.004.

[50] W. Beckert, B. Lauke, K. Friedrich, Delamination toughness computation for curved thermoplastic composites, Appl. Compos. Mater. 1 (1994/1995) 395−400. https://doi.org/10.1007/BF00568044.

[51] I. Burda, M. Barbezat, A.J. Brunner, Mode I fracture testing of pultruded glass fiber-reinforced epoxy rods: test development and influence of precracking method and manufacturing, Eng. Fract. Mech. 149 (2015) 287−297. https://doi.org/10.1016/j.engfracmech.2015.08.009.

[52] A.P. Mouritz, K.H. Leong, I. Herszberg, A review of the effect of stitching on the in-plane mechanical properties of fibre-reinforced polymer composites, Compos. A Appl. Sci. Manuf. 28 (1997) 979−991. https://doi.org/10.1016/S1359-835X(97)00057-2.

[53] A.P. Mouritz, Review of Z-pinned composite laminates, Compos. A Appl. Sci. Manuf. 38 (2007) 2383−2397. https://doi.org/10.1016/j.compositesa.2007.08.016.

[54] A.P. Mouritz, Compression properties of z-pinned composite laminates, Compos. Sci. Technol. 67 (2007) 3110−3120. https://doi.org/10.1016/j.compscitech.2007.04.017.

[55] M. Yasaee, M. Galal, A. Pellegrino, N. Petrinic, S.R. Hallett, Strain rate dependence of mode II delamination resistance in through thickness reinforced laminated composites, Int. J. Impact Eng. 107 (2017) 1−11. https://doi.org/10.1016/j.ijimpeng.2017.05.003.

[56] M.F. Funari, F. Greco, P. Lonetti, R. Luciano, R. Penna, An interface approach based on moving mesh and cohesive modeling in Z-pinned composite laminates, Compos. B Eng. 135 (2018) 207−217. https://doi.org/10.1016/j.compositesb.2017.10.018.

[57] A.R. Ravindran, R.B. Ladani, C.H. Wang, A.P. Mouritz, Synergistic mode II delamination toughening of composites using multiscale carbon-based reinforcements, Compos. A Appl. Sci. Manuf. 117 (2019) 103−115. https://doi.org/10.1016/j.compositesa.2018.11.011R.

[58] A.P. Mouritz, P. Chang, M.D. Isa, Z-pin composites: aerospace structural design considerations, J. Aerosp. Eng. 24 (2011) 425−432. https://doi.org/10.1061/(ASCE)AS.1943-5525.0000078.

[59] G.B. Murri, Testing and life prediction for composite rotor hub flexbeams, Int. J. Fract. 28 (2006) 1124−1135. https://doi.org/10.1016/j.ijfatigue.2006.02.029.

[60] G. Wimmer, C. Schuecker, H. Pettermann, Numerical simulation of delamination in laminated composite components — A review combination of a strength criterion and fracture mechanics, Compos. B Eng. 40 (2009) 158−165. https://doi.org/10.1016/j.compositesb.2008.10.006.

[61] J. Chen, E. Ravey, S. Hallett, M. Wisnom, M. Grassi, Prediction of delamination in braided composite T-piece specimens, Compos. Sci. Technol. 69 (2009) 2363−2367. https://doi.org/10.1016/j.compscitech.2009.01.027.

[62] A.J. Brunner, N. Murphy, G. Pinter, Development of a standardised procedure for the characterisation of interlaminar delamination propagation in advanced composites under fatigue mode I loading conditions, Eng. Fract. Mech. 76 (2009) 2678−2689. https://doi.org/10.1016/j.engfracmech.2009.07.014.

[63] S. Stelzer, A.J. Brunner, A. Argüelles, N. Murphy, G. Pinter, Mode I delamination fatigue crack growth in unidirectional fiber reinforced composites: development of a standardized test procedure, Compos. Sci. Technol. 72 (2012) 1102−1107. https://doi.org/10.1016/j.compscitech.2011.11.033.

[64] S. Stelzer, A.J. Brunner, A. Argüelles, N. Murphy, G.M. Cano, G. Pinter, Mode I delamination fatigue crack growth in unidirectional fiber reinforced composites: results from ESIS TC4 round-robins, Eng. Fract. Mech. 116 (2014) 92−107. https://doi.org/10.1016/j.engfracmech.2013.12.002.

[65] P. Paris, F. Erdogan, A critical analysis of crack propagation laws, Trans. ASME Ser. D J. Basic Eng. 85 (1963) 528−533.

[66] B.R.K. Blackman, A.J. Brunner, J.G. Williams, Mode II fracture testing of composites: a new look at an old problem, Eng. Fract. Mech. 73 (2006) 2443−2455. https://doi.org/10.1016/j.engfracmech.2006.05.022.

[67] I. Simon, L. Banks-Sills, V. Fourman, Mode I delamination propagation and R-ratio effects in woven composite DCB specimens for a multi-directional layup, Int. J. Fatigue 96 (2017) 237−251. https://doi.org/10.1016/j.ijfatigue.2016.12.005.

[68] P. Kuhn, G. Catalanotti, J. Xavier, M. Ploeckl, H. Koerber, Determination of the crack resistance curve for intralaminar fiber tensile failure mode in polymer composites under high rate loading, Compos. Struct. 204 (2018) 276−287. https://doi.org/10.1016/j.compstruct.2018.07.039.

[69] J. Hoffmann, H. Cui, N. Petrinic, Determination of the strain-energy release rate of a composite laminate under high-rate tensile deformation in fibre direction, Compos. Sci. Tehcnol. 164 (2018) 110−119. https://doi.org/10.1016/j.compscitech.2018.05.034.

[70] C.Y. Miao, H.V. Tippur, Fracture behavior of carbon fiber reinforced polymer composites: an optical study of loading rate effects, Eng. Fract. Mech. 207 (2019) 203−221. https://doi.org/10.1016/j.engfracmech.2018.12.035.

[71] K. Jayakrishna, V.R. Kar, M.T.H. Sultan, M. Rajesh, Materials selection for aerospace components. Chapter 1, in: Sustainable Composites for Aerospace Applications, 2018, pp. 1−18. https://doi.org/10.1016/B978-0-08-102131-6.00001-3.

[72] E.I. Kurkin, V.O. Sadykova, Application of short fiber reinforced composite materials multilevel model for design of ultra-light aerospace structures, Process Eng. 185 (2017) 182−189. https://doi.org/10.1016/j.proeng.2017.03.336.

[73] J.F. Mandell, A.Y. Darwish, J.F. McGarry, Fracture testing of injection-molded glass and carbon fiber reinforced thermoplastics, in: C.C. Chamis (Ed.), Test Methods and Design Allowables for Fibrous Composites, vol. 734, ASTM Special Technical Publication, 1981, pp. 73−90. https://doi.org/10.1520/STP29304S.

[74] B.D. Agarwal, G.S. Giare, Fracture toughness of short fibre composites in modes II and III, Eng. Fract. Mech. 15 (1981) 219−230. https://doi.org/10.1016/0013-7944(81)90119-3.

[75] J.E. Lindhagen, L.A. Berglund, Application of bridging law concepts to short fiber composites Part 1: DCB test procedures for bridging law and fracture energy, Compos. Sci. Technol. 60 (2000) 871−883. https://doi.org/10.1016/S0266-3538(00)00004-X.

[76] L. Walker, X.Z. Hu, Mode I delamination behavior of short fibre reinforced carbon fibre/epoxy composites following environmental conditioning, Compos. Sci. Technol. 63 (2003) 531−537. https://doi.org/10.1016/S0266-3538(02)00224-5.

[77] F.S. Macedo, A.B. Pereira, A.B. de Morais, Mixed bending-tension (MBT) test for mode I interlaminar and intralaminar fracture, Compos. Sci. Technol. 72 (2012) 1049−1055. https://doi.org/10.1016/j.compscitech.2012.03.023.

[78] M.J. Laffan, S.T. Pinho, P. Robinson, A.J. McMillan, Translaminar fracture toughness testing of composites: a review, Polym. Test. 31 (2012) 481−489. https://doi.org/10.1016/j.polymertesting.2012.01.002.

[79] A.B. de Morais, A.B. Pereira, M.F.S.F. de Moura, A.G. Magalhães, Mode III interlaminar fracture of carbon/epoxy laminates using the edge crack torsion (ECT) test, Compos. Sci. Technol. 69 (2009) 670−676. https://doi.org/10.1016/j.compscitech.2008.12.019.

[80] G. Browning, L.A. Larsson, J.G. Ratcliffe, Redesign of the ECT test for mode III delamination testing. Part I: finite element analysis, J. Compos. Mater. 44 (2010) 1867−1881. https://doi.org/10.1177/0021998309356606.

[81] G. Browning, L.A. Larsson, J.G. Ratcliffe, Redesign of the ECT test for mode III delamination testing. Part II: experimental study, J. Compos. Mater. 45 (2010) 2633−2640. https://doi.org/10.1177/0021998311401115.

[82] A. Szekrényes, The influence of crack length and delamination width on the mode-III energy release rate of laminated composites, J. Compos. Mater. 45 (2012) 279−294. https://doi.org/10.1177/0021998310376097.

[83] Y.Y. Ge, X.J. Gong, A. Hurez, E. De Luycker, Test methods for measuring pure mode III delamination toughness of composite, Polym. Test. 55 (2016) 261−268. https://doi.org/10.1016/j.polymertesting.2016.08.025.

[84] A.B. Pereira, A.B. de Morais, Mixed-mode I/III interlaminar fracture of carbon/epoxy laminates, Compos. A Appl. Sci. Manuf. 40 (2009) 518−523. https://doi.org/10.1016/j.compositesa.2009.02.003.

[85] A. Szekrényes, Interlaminar fracture analysis in the G_I-G_{III} plane using prestressed transparent composite beams, Compos. A Appl. Sci. Manuf. 40 (2009) 1621−1631. https://doi.org/10.1016/j.compositesa.2009.07.009.

[86] A.B. de Morais, A.B. Pereira, Mixed mode II/III interlaminar fracture of carbon/epoxy laminates, Compos. Sci. Technol. 68 (2008) 2022−2027. https://doi.org/10.1016/j.compscitech.2008.02.023.

[87] A. Kondo, Y. Sato, H. Suemasu, Y. Aoki, Fracture resistance of carbon/epoxy composite laminates under mixed mode II and III failure and its dependence on fracture morphology, Adv. Compos. Mater. 20 (2011) 405−418. https://doi.org/10.1163/092430411X568197.

[88] A. Szekrényes, W.M. Vicente, Interlaminar fracture analysis in the G_{II}−G_{III} plane using prestressed transparent composite beams, Compos. A Appl. Sci. Manuf. 43 (2012) 95−103. https://doi.org/10.1016/j.compositesa.2011.09.022.

[89] C. Canturri, E.S. Greenhalgh, S.T. Pinho, The relationship between mixed-mode II/III delamination and delamination migration in composite laminates, Compos. Sci. Technol. 105 (2014) 102−109. https://doi.org/10.1016/j.compscitech.2014.10.001.

[90] B.D. Davidson, F.O. Sediles, Mixed-mode I-II-III delamination toughness determination via a shear-torsion bending test, Compos. A Appl. Sci. Manuf. 42 (2011) 589−603. https://doi.org/10.1016/j.compositesa.2011.01.018.

[91] R.F. Pinto, G. Catalanotti, P.P. Camanho, Measuring the intralaminar crack resistance curve of fibre reinforced composites at extreme temperatures, Compos. A Appl. Sci. Manuf. 91 (2016) 145−155. https://doi.org/10.1016/j.compositesa. 016.10.004.

[92] G. Catalanotti, A. Arteiro, M. Hayati, P.P. Camanho, Determination of the mode I crack resistance curve of polymer composites using the size-effect law, Eng. Fract. Mech. 118 (2014) 49−65. https://doi.org/10.1016/j.engfracmech.2013.10.021.

[93] G. Catalanotti, J. Xavier, Measurement of the mode II intralaminar fracture toughness and R-curve of polymer composites using a modified Iosipescu specimen and the size effect law, Eng. Fract. Mech. 138 (2015) 202−214. https://doi.org/10.1016/j.engfracmech. 2015.03.005.

[94] G. Pappas, L.P. Canal, J. Botsis, Characterization of intralaminar mode I fracture of AS4/ PPS composite using inverse identification and micromechanics, Compos. A Appl. Sci. Manuf. 91 (2016) 117−126. https://doi.org/10.1016/j.compositesa.2016.09.018.

[95] N. Sato, M. Hojo, M. Nishikawa, Intralaminar fatigue crack growth properties of conventional and interlayer toughened CFRP laminate under mode I loading, Compos. A Appl. Sci. Manuf. 68 (2015) 202−211. https://doi.org/10.1016/j.compositesa.2014.09. 031.

[96] L.C. Dickinson, G.L. Farley, M.K. Hinders, Translaminar reinforced composites: a review, J. Compos. Technol. Res. 21 (1999) 3−15. https://doi.org/10.1520/CTR10607J.

[97] M. Chabchoub, D. Bouscarrat, B. Vieille, C. Gautrelet, M. Beyaoui, M. Taktak, et al., Investigations on the mode I translaminar failure and determination of fracture toughness in woven-ply carbon fibers thermoplastic composites at high temperatures, Appl. Acoust. 128 (2017) 55−63. https://doi.org/10.1016/j.apacoust.2017.01.028.

[98] S.I.B. Syed Abdulla, L. Iannucci, E.S. Greenhalgh, On the translaminar fracture toughness of Vectran/epoxy composite material, Compos. Struct. 202 (2018) 566−577. https:// doi.org/10.1016/j.compstruct.2018.03.004.

[99] G. Bullegas, J. Benliel, P.L. Fenelli, S.T. Pinho, S. Pimenta, Towards quasi isotropic laminates with engineered fracture behaviour for industrial applications, Compos. Sci. Technol. 165 (2018) 290−306. https://doi.org/10.1016/j.compscitech.2018.07.004.

[100] D.G. Katerelos, A. Paipetis, V. Kostopoulos, A simple model for the prediction of the fatigue delamination growth in impacted composite panels, Fatigue Fract. Eng. Mater. Struct. 27 (2004) 911−922. https://doi.org/10.1111/j.1460-2695.2004.00798.x.

[101] C. Dahlen, G.S. Springer, Delamination growth in composites under cyclic loads, J. Compos. Mater. 28 (1994) 732e81. https://doi.org/10.1177/002199839402800803.

[102] M. Miura, Y. Shindo, F. Narita, S. Watanabe, M. Suzuki, Mode III fatigue delamination growth of glass fiber reinforced woven polymer laminates at cryogenic temperatures, Cryogenics 49 (2009) 407−412. https://doi.org/10.1016/j.cryogenics.2009.05.004.

[103] Y. Shindo, M. Miura, T. Takeda, N. Saito, F. Narita, Cryogenic delamination growth in woven glass/epoxy composite laminates under mixed-mode I/II fatigue loading, Compos. Sci. Technol. 71 (2011) 647−652. https://doi.org/10.1016/j.compscitech.2011.01.006.

[104] I. Jaeck, L. Carreras, J. Rennart, A. Turon, F. Martin de la Escalera, Y. Essa, Experimental methodology for obtaining fatigue crack growth rate curves in mixed-mode I-II by means of variable cyclic displacement tests, Int. J. Fatigue 110 (2018) 63−70. https://doi.org/10. 1016/j.ijfatigue.2018.01.016.

[105] S. Rubiera, A. Argüelles, J. Viña, C. Rocandio, Study of the phenomenon of fatigue delamination in a carbon-epoxy composite under mixed mode I/II fracture employing an asymmetric specimen, Int. J. Fatigue 114 (2018) 74−80. https://doi.org/10.1016/j.ijfatigue.2018.05.015.

[106] M. Miura, Y. Shindo, T. Takeda, F. Narita, Mixed-mode I/III fatigue delamination growth in woven glass/epoxy composite laminates at cryogenic temperatures, J. Compos. Mater. 48 (2014) 1251−1259. https://doi.org/10.1177/0021998313484951.

[107] T. Takeda, M. Masaya, S. Yasuhide, N. Fumio, Fatigue delamination growth in woven glass/epoxy composite laminates under mixed-mode II/III loading conditions at cryogenic temperatures, Cryogenics 58 (2013) 55−61. https://doi.org/10.1016/j.cryogenics.2013.10.001.

[108] R. Jones, S. Pitt, A.J. Brunner, D. Hui, Application of the Hartman−Schijve equation to represent Mode I and Mode II fatigue delamination growth in composites, Compos. Struct. 94 (2012) 1343−1351. https://doi.org/10.1016/j.compstruct.2011.11.030.

[109] R. Jones, S. Stelzer, A.J. Brunner, Mode I, II and mixed Mode I/II delamination growth in composites, Compos. Struct. 110 (2014) 317−324. https://doi.org/10.1016/j.compstruct.2013.12.009.

[110] A. Mujtaba, S. Stelzer, A.J. Brunner, R. Jones, Thoughts on the scatter seen in cyclic Mode I fatigue delamination growth in DCB tests, Compos. Struct. 160 (2017) 1329−1338. https://doi.org/10.1016/j.compstruct.2016.11.002.

[111] R.C. Alderliesten, A.J. Brunner, J.A. Pascoe, Cyclic fatigue fracture of composites: what has testing revealed about the physics of the processes so far? Eng. Fract. Mech. 203 (2018) 186−196. https://doi.org/10.1016/j.engfracmech.2018.06.023.

[112] M. McGugan, G. Pereira, B.F. Sørensen, H. Toftegaard, K. K. Branner, Damage tolerance and structural monitoring for wind turbine blades, Phil. Trans. Math. Phys. Eng. Sci. 373 (2035) (2015) 1−16. https://doi.org/10.1098/rsta.2014,0077.

[113] M. Hojo, T. Aoki, Characterization of fatigue R-curves based on G_{max} constant delamination tests in CF/PEEK laminates, Proc. 20th Int. Conf. Comp. Mats. (2015) 1−8.

[114] A.J. Russell, K.N. Street, A constant ΔG test for measuring mode I interlaminar fatigue crack growth rates, in: J.D. Whitcomb (Ed.), Composite Materials: Testing and Design (Eighth Conference), ASTM STP 972, American Society for Testing and Materials, 1988, pp. 259−277.

[115] L.J. Yao, Y. Sun, L.C. Guo, M.Y. Zhao, L.Y. Jia, R.C. Alderliesten, et al., A modified Paris relation for fatigue delamination with fibre bridging in composite laminates, Compos. Struct. 176 (2017) 556−564. https://doi.org/10.1016/j.compstruct.2017.05.070.

[116] L.J. Yao, H. Cui, Y. Sun, L.C. Guo, X.M. Chen, M.Y. Zhao, R.C. Alderliesten, Fibre-bridged fatigue delamination in multidirectional composite laminates, Compos. A Appl. Sci. Manuf. 115 (2018) 175−186. https://doi.org/10.1016/j.compositesa.2018.09.027.

[117] G.A. Kardomateas, Predicting the growth of internal delaminations under monotonic or cyclic compression, Key Eng. Mater. 120−121 (1996) 441−462. https://doi.org/10.4028/www.scientific.net/KEM.120-121.441.

[118] K.Y. Rhee, S.J. Park, J.H. Lee, On the application of η-factor approach to determine compressive fracture toughness of fiber-reinforced composites under hydrostatic pressure environment, Compos. Sci. Technol. 63 (2003) 829−837. https://doi.org/10.1016/S0266-3538(02)00283-X.

[119] P. Kuhn, G. Catalanotti, J. Xavier, P.P. Camanho, H. Koerber, Fracture toughness and crack resistance curves for fiber compressive failure mode in polymer composites under high rate loading, Compos. Struct. 182 (2017) 164−175. https://doi.org/10.1016/j.compstruct.2017.09.040.

[120] E.K. Gamstedt, B.A. Sjögren, Micromechanisms in tension-compression fatigue of composite laminates containing transverse plies, Compos. Sci. Technol. 59 (1999) 167−178. https://doi.org/10.1016/S0266-3538(98)00061-X.

[121] S.L. Donaldson, S. Mall, Delamination growth in graphite/epoxy composites subjected to cyclic mode III loading, J. Reinf. Plast. Compos. 8 (1989) 91−103. https://doi.org/10.1177/073168448900800106.

[122] R.H. Martin, Evaluation of the split cantilever beam test for mode III delamination testing, in: T.K. O'Brien (Ed.), Composite Materials: Fatigue and Fracture, vol. 1110, ASTM Special Technical Publication, 1991, pp. 243−266. https://doi.org/10.1520/STP17722S.

[123] B.R.K. Blackman, J.P. Dear, A.J. Kinloch, H. MacGillivray, Y. Wang, J.G. Williams, P. Yayla, The failure of fibre composites and adhesively bonded fibre composites under high rates of test. Part I Mode I loading-experimental studies, J. Mater. Sci. 30 (1995) 5885−5900. https://doi.org/10.1007/BF01151502.

[124] T. Kusaka, M. Hojo, Y.W. Mai, T. Kurokawa, T. Nojima, S. Ochiai, Rate dependence of mode I fracture behaviour in carbon-fibre/epoxy composite laminates, Compos. Sci. Technol. 58 (1998) 591−602. https://doi.org/10.1016/S0266-3538(97)00176-0.

[125] S.I. Thorsson, A.M. Waas, J. Schaefer, B. Justusson, S. Liguore, Effects of elevated loading rates on mode I fracture of composite laminates using a modified wedge-insert fracture method, Compos. Sci. Technol. 156 (2018) 39−47. https://doi.org/10.1016/j.compscitech.2017.12.018.

[126] H.F. Liu, H.L. Nie, C. Zhang, Y.L. Li, Loading rate dependency of Mode I interlaminar fracture toughness for unidirectional composite laminates, Compos. Sci. Technol. 167 (2018) 215−223. https://doi.org/10.1016/j.compscitech.2018.07.040.

[127] M. Isakov, M. May, P. Hahn, H. Paul, M. Nishi, Fracture toughness measurement without force data − application to high rate DCB on CFRP, Compos. A Appl. Sci. Manuf. 119 (2019) 176−187. https://doi.org/10.1016/j.compositesa.2019.01.030.

[128] B.R.K. Blackman, A.J. Kinloch, Y. Wang, J.G. Williams, The failure of fibre composites and adhesively bonded fibre composites under high rates of test. Part II Mode I loading - dynamic effects, J. Mater. Sci. 31 (1996) 4451−4466. https://doi.org/10.1007/BF00366341.

[129] T. Kusaka, M. Hojo, S. Ochiai, T. Kurokawa, Rate-dependent mode II interlaminar fracture behavior of carbon fiber/epoxy composite laminates, Mater. Sci. Res. Int. 5 (1999) 98−103.

[130] G.C. Jacob, J.M. Starbuck, J.F. Fellers, S. Simunovic, R.G. Boeman, The effect of loading rate on the fracture toughness of fiber reinforced polymer composites, J. Appl. Polym. Sci. 96 (2005) 899−904. https://doi.org/10.1002/app.21535.

[131] H. Zabala, L. Aretxabaleta, G. Castillo, J. Aurrekoetxea, Dynamic 4 ENF test for a strain rate dependent mode II interlaminar fracture toughness characterization of unidirectional carbon fibre epoxy composites, Polym. Test. 55 (2016) 212−218. https://doi.org/10.1016/j.polymertesting.2016.09.001.

[132] D. Pennas, W.J. Cantwell, P. Compston, The influence of strain-rate on the mode III interlaminar fracture of composite materials, J. Compos. Mater. 41 (2007) 2595−2614. https://doi.org/10.1177/0021998307078690.

[133] B.R.K. Blackman, J.P. Dear, A.J. Kinloch, H. MacGillivray, Y. Wang, J.G. Williams, The failure of fibre composites and adhesively bonded fibre composites under high rates of test. 3. Mixed mode I/II and mode II loadings, J. Mater. Sci. 31 (1996) 4467−4477. https://doi.org/10.1007/BF00366342.

[134] A.M.S. Hamouda, M.S.J. Hashmi, Testing of composite materials at high rates of strain: advances and challenges, J. Mater. Process. Technol. 77 (1998) 327−336. https://doi.org/10.1016/S0924-0136(97)00436-6.

[135] A.L. Glessner, M.T. Takemori, M.A. Vallance, S.K. Gifford, Mode I interlaminar fracture toughness of unidirectional carbon-fiber composites using a novel Wedge−Driven delamination design, in: P.A. Lagace (Ed.), Composites Materials: Fatigue and Fracture, ASTM STP 1012, American Society for Testing and Materials, 1989, pp. 181−200.

[136] Y.M. Yazid, W.J. Cantwell, G.S. Langdon, G.N. Nurick, The blast resistance of a woven carbon fiber-reinforced epoxy composite, J. Compos. Mater. 45 (2011) 789−801. https://doi.org/10.1177/0021998310376103.

[137] A. Shojaei, G.Q. Li, P.J. Tan, J. Fish, Dynamic delamination in laminated fiber reinforced composites: a continuum damage mechanics approach, Int. J. Solids Struct. 71 (2015) 262−276. https://doi.org/10.1016/j.ijsolstr.2015.06.029.

[138] P.F. Liu, J.Y. Zheng, Recent developments on damage modeling and finite element analysis for composite laminates: a review, Mater. Des. 31 (2010) 3825−3834. https://doi.org/10.1016/j.matdes.2010.03.031.

[139] N. Sela, O. Oshai, Interlaminar fracture toughness and toughening of laminated composite materials: a review, Composites 20 (1989) 423−435. https://doi.org/10.1016/0010-4361(89)90211-5.

[140] T.K. O'Brien, Composite interlaminar shear fracture toughness GIIC: shear measurement or sheer myth?, in: R.B. Bucinell (Ed.), Composite Materials: Fatigue and Fracture, vol. 1330 ASTM Special Technical Publication, 1998, pp. 3−18. https://doi.org/10.1520/STP13263S.

[141] A.J. Brunner, Fracture testing of polymer-matrix composites. Proceedings 10th Portuguese Conference on Fracture, 2006, pp. 1−11.

[142] A.J. Brunner, B.R.K. Blackman, P. Davies, Mode I delamination [Chapter 4.1], in: D.R. Moore, A. Pavan, J.G. Williams (Eds.), Fracture Mechanics Test Methods for Polymers, Adhesives and Composites, Elsevier, 2001, pp. 271−305. https://doi.org/10.1016/S1566-1369(01)80038-8.

[143] P. Davies, B.R.K. Blackman, A.J. Brunner, Mode II delamination [Chapter 4.2], in: D.R. Moore, A. Pavan, J.G. Williams (Eds.), Fracture Mechanics Test Methods for Polymers, Adhesives and Composites, Elsevier, 2001, pp. 307−333. https://doi.org/10.1016/S1566-1369(01)80039-X.

[144] B.R.K. Blackman, A.J. Brunner, P. Davies, Delamination fracture of continuous fibre composites: mixed-mode fracture [Chapter 4.3], in: D.R. Moore, A. Pavan, J.G. Williams (Eds.), Fracture Mechanics Test Methods for Polymers, Adhesives and Composites, Elsevier, 2001, pp. 335−359. https://doi.org/10.1016/S1566-1369(01)80040-6.

[145] A.J. Brunner, Experimental aspects of mode I and mode II fracture toughness testing of fibre-reinforced polymer-matrix composites, Comput. Methods Appl. Mech. Eng. 185 (2000) 161−172. https://doi.org/10.1016/S0045-7825(99)00257-1.

[146] A.J. Brunner, S. Stelzer, G. Pinter, G.P. Terrasi, Mode II fatigue delamination resistance of advanced fiber-reinforced polymer-matrix laminates: towards the development of a standardized test procedure, Int. J. Fatigue 50 (2013) 57−62. https://doi.org/10.1016/j.ijfatigue.2012.02.021.

[147] R.H. Martin, G.B. Murri, Characterization of mode I and mode II delamination growth and thresholds in AS4/PEEK composites, in: S.P. Garbo (Ed.), Composite Materials: Testing and Design, vol. 1059, ASTM Special Technical Publication, 1990, pp. 251−270. https://doi.org/10.1520/STP24115S.

[148] B.R.K. Blackman, A.J. Kinloch, F.S. Rodriguez-Sanchez, W.S. Teo, The fracture behaviour of adhesively-bonded composite joints: effects of rate of test and mode of loading, Int. J. Solids Struct. 49 (2012) 1434−1452. https://doi.org/10.1016/j.ijsolstr.2012.02.022.

[149] D. Cartié, P. Davies, M. Peleau, I.K. Partridge, The influence of hydrostatic pressure on the interlaminar fracture toughness of carbon/epoxy composites, Compos. B Eng. 37 (2006) 292−300. https://doi.org/10.1016/j.compositesb.2005.12.002.

[150] Y.J. Prel, P. Davies, M.L. Benzeggagh, F.-X. de Charentay, Mode I and mode II delamination of thermosetting and thermoplastic composites, in: P.A. Lagace (Ed.), Composite Materials: Fatigue and Fracture, ASTM STP 1012, 1989, pp. 251−269. https://doi.org/10.1520/STP10419S.

[151] M. Hojo, S. Ochiai, C.-G. Gustafson, K. Tanaka, Effect of matrix resin on delamination fatigue crack growth in CFRP laminates, Eng. Fract. Mech. 49 (1994) 35−47.

[152] C.L. Perez, B.D. Davidson, Evaluation of precracking methods for the end-notched flexure test, AIAA J. 45 (2007) 2603−2611. https://doi.org/10.2514/1.24188.

[153] E. Armstrong-Carroll, B. Iskandarani, I. Kamel, T.M. Donnellan, The influence of interleaf deformation behaviour and film resin adhesion on the fracture toughness of interleaved composites, in: W.W. Stinchcomb, N.E. Ashbaugh (Eds.), Composite Materials: Fatigue and Fracture, vol. 1156, ASTM Special Technical Publication, 1993, pp. 299−317. https://doi.org/10.1520/STP24737S.

[154] M. Hojo, S. Matsuda, M. Tanaka, S. Ochiai, S. Murakami, Mode I delamination fatigue properties of interlayer-toughened CF/epoxy laminates, Compos. Sci. Technol. 66 (2006) 665−675. https://doi.org/10.1016/j.compscitech.2005.07.038.

[155] M. Hojo, T. Ando, M. Tanaka, T. Adachi, S. Ochiai, Y. Endo, Modes I and II interlaminar fracture toughness and fatigue delamination of CF/epoxy laminates with self-same epoxy interleaf, Int. J. Fatigue 28 (2006) 1154−1165. https://doi.org/10.1016/j.ijfatigue.2006.02.004.

[156] M. Hojo, S. Matsuda, S. Ochiai, N. Tsujioka, Y. Nakanaishi, Z. Maekawa, et al., Mode II interlaminar properties under static and fatigue loadings of for CF/epoxy laminates with different fiber-surface treatment, Adv. Compos. Mater. 10 (2001) 237−246. https://doi.org/10.1163/156855101753396717.

[157] P.-Y.B. Jar, R. Mulone, P. Davies, H.H. Kausch, A study of the effect of forming temperature on the mechanical behavior of carbon-fibre/PEEK composites, Compos. Sci. Technol. 46 (1993) 7−19. https://doi.org/10.1016/0266-3538(93)90076-S.

[158] W.W. Li, A. Crosky, Effect of cure pressure on the behavior of woven carbon/epoxy composite laminates, Int. J. Mater. Prod. Technol. 19 (2003) 275−283. https://doi.org/10.1504/IJMPT.2003.002511.

[159] J. Zhang, B.L. Fox, Manufacturing influence on the delamination fracture behavior of the T800H/3900-2 carbon fiber reinforced polymer composites, Mater. Manuf. Process. 22 (2007) 768−772. https://doi.org/10.1080/10426910701385432.

[160] A.J. Brunner, Experimental study of delamination in cross-ply laminates [Chapter 9], in: S. Sridharan (Ed.), Delamination Behaviour of Composites, Woodhead Publishing, 2008, pp. 281−309. https://doi.org/10.1533/9781845694821.3.281.

[161] A.J. Brunner, P. Flüeler, Prospects in fracture mechanics of 'engineering' laminates, Eng. Fract. Mech. 72 (2005) 899−908. https://doi.org/10.1016/j.engfracmech.2004.08.002.

[162] K. Trakas, M.T. Kortschot, The relationship between critical strain energy release rate and fracture mode in multidirectional carbon-fiber/epoxy laminates, in: E.A. Armanios (Ed.), Composite Materials: Fatigue and Fracture, vol. 1285, ASTM Special Technical Publication, 1997, pp. 283−304. https://doi.org/10.1520/STP19933S.

[163] P. Prombut, L. Michel, F. Lachaud, J.J. Barrau, Delamination of multidirectional composite laminates at 0°/θ° ply interfaces, Eng. Fract. Mech. 73 (2006) 2427−2442. https://doi.org/10.1016/j.engfracmech.2006.05.013.

[164] J. Andersons, M. König, Dependence of fracture toughness of composite laminates on interface ply orientations and delamination growth direction, Compos. Sci. Technol. 64 (2004) 2139−2152. https://doi.org/10.1016/j.compscitech.2004.03.007.

[165] N.S. Choi, A.J. Kinloch, J.G. Williams, Delamination fracture of multidirectional carbon fiber/epoxy composites under mode I, mode II and mixed-mode I/II loading, J. Compos. Mater. 99 (1999) 73−100. https://doi.org/10.1177/002199839903300105.

[166] X.J. Gong, A. Hurez, G. Verchery, On the determination of delamination toughness by using multidirectional DCB specimens, Polym. Test. 29 (2010) 658−666. https://doi.org/10.1016/j.polymertesting.2010.04.007.

[167] T.A. Sebaey, N. Blanco, J. Costa, C.S. Lopes, Numerical investigation to prevent crack jumping in double cantilever beam tests of multidirectional composite laminates, Compos. Sci. Technol. 71 (2011) 1587−1592. https://doi.org/10.1016/j.compscitech.2011.07.002.

[168] T.A. Sebaey, N. Blanco, J. Costa, C.S. Lopes, Characterization of crack propagation in mode I delamination in multidirectional CFRP laminates, Compos. Sci. Technol. 72 (2012) 1251−1256. https://doi.org/10.1016/j.compscitech.2012.04.011.

[169] L. Peng, J.Y. Zhang, L.B. Zhao, R. Bao, H.Q. Yang, B.J. Fei, Mode I delamination growth of multidirectional composite laminates under fatigue loading, J. Compos. Mater. 45 (2011) 1077−1090. https://doi.org/10.1177/0021998310385029.

[170] L.B. Zhao, Y. Gong, J.Y. Zhang, Y.L. Chen, B.J. Fei, Simulation of delamination growth in multidirectional laminates under mode I and mixed mode I/II loadings using cohesive elements, Compos. Struct. 116 (2014) 509−522. https://doi.org/10.1016/j.compstruct.2014.05.042.

[171] L.B. Zhao, Y. Wang, J.Y. Zhang, Y. Gong, Z. Lu, N. Hu, J.F. Xu, An interface-dependent model of plateau fracture toughness in multidirectional CFRP laminates under mode I loading, Compos. B Eng. 131 (2017) 196−208. https://doi.org/0.1016/j.compositesb.2017.07.077.

[172] Y. Gong, L.B. Zhao, J.Y. Zhang, Y. Wang, N. Hu, Delamination propagation criterion including the effect of fiber bridging for mixed-mode I/II delamination in CFRP multidirectional laminates, Compos. Sci. Technol. 151 (2017) 302−309. https://doi.org/10.1016/j.compscitech.2017.09.002.

[173] C. Blondeau, G. Pappas, J. Botsis, Influence of ply-angle on fracture in antisymmetric interfaces of CFRP laminates, Compos. Struct. 216 (2019) 464−476. https://doi.org/10.1016/j.compstruct.2019.03.004.

[174] L.J. Yao, H. Cui, Y. Sun, R.C. Alderliesten, R. Benedictus, M.Y. Zhao, Fibre bridging effect on the Paris relation for mode I fatigue delamination growth in composites with consideration of interface configuration, Compos. Struct. 159 (2017) 471−478. https://doi.org/10.1016/j.compstruct.2016.09.082.

[175] I. Paris, P.J. Minguet, T.K. O'Brien, Comparison of delamination characterization for IM7/8552 composite woven and tape laminates, in: C.E. Bakis (Ed.), Composite Materials: Testing and Design, vol. 1436, ASTM Special Technical Publication, 2003, pp. 372−390. https://doi.org/10.1520/STP38422S.

[176] T. Ishikawa, Overview of trends in advanced composite research and applications in Japan, Adv. Compos. Mater. 15 (2006) 3−37. https://doi.org/10.1163/156855106776829383.

[177] M. Hojo, K. Nakashima, T. Kusaka, M. Tanaka, T. Adachi, T. Fukuoka, et al., Mode I fatigue delamination of Z-anchor-reinforced CF/epoxy laminates, Int. J. Fatigue 32 (2010) 37−45. https://doi.org/10.1016/j.ijfatigue.2009.02.025.

[178] D.D.R. Cartié, A.J. Brunner, I.K. Partridge, Effects of mesostructure on crack growth control characteristics in Z-pinned laminates, in: B.R.K. Blackman, A. Pavan, J.G. Williams (Eds.), Fracture of Polymers, Composites and Adhesives II, Elsevier, 2003, pp. 503−514. https://doi.org/10.1016/S1566-1369(03)80120-6.

[179] D.D.R. Cartié, M. Troulis, I.K. Partridge, Delamination of Z-pinned carbon fibre reinforced laminates, Compos. Sci. Technol. 66 (2006) 855−861 [neu 180]https://doi.org/10.1016/j.compscitech.2004.12.018.

[180] C.A. Steeves, N.A. Fleck, In-plane properties of composite laminates with through thickness pin reinforcement, Int. J. Solids Struct. 43 (2006) 3197−3212. https://doi.org/10.1016/j.ijsolstr.2005.05.017.

[181] P. Robinson, S. Das, Mode I DCB testing of composite laminates reinforced with z-direction pins: a simple model for the investigation of data reduction strategies, Eng. Fract. Mech. 71 (2004) 345−364. https://doi.org/10.1016/S0013-7944(03)00116-4.

[182] K.L. Rugg, B.N. Cox, R. Massabò, Mixed mode delamination of polymer composite laminates reinforced through thickness by z-fibers, Compos. A Appl. Sci. Manuf. 33 (2002) 177−190. https://doi.org/10.1016/S1359-835X(01)00109-9.

[183] A.J. Brunner, G.P. Terrasi, D.D.R. Cartié, Fatigue testing of Z-pin reinforced carbon-fibre laminates, in: Proceedings 12th International Conference on Fracture ICF-12, 2009, pp. 1−8, 01199.

[184] O. Ishai, Interlaminar fracture toughness of selectively stitched thick carbon fibre polymer fabric composite laminates, Plast. Rubber Compos. 29 (2000) 134−143. https://doi.org/10.1179/146580100101540888.

[185] G. Dell'Anno, D.D. Cartié, I.K. Partridge, A. Rezai, Exploring mechanical property balance in tufted carbon fabric/epoxy composites, Compos. A Appl. Sci. Manuf. 38 (2007) 2366−2373. https://doi.org/10.1016/j.compositesa.2007.06.004.

[186] W. Trabelsi, L. Michel, R. Othomene, Effects of stitching on delamination of satin weave carbon-epoxy laminates under mode I, mode II and mixed mode I/II loadings, Appl. Compos. Mater. 17 (2010) 575−595. https://doi.org/10.1007/s10443-010-9128-0.

[187] N. Sridhar, R. Massabò, B.N. Cox, I.J. Beyerlein, Delamination dynamics in through thickness reinforced laminates with application to DCB specimens, Int. J. Fract. 118 (2002) 119−144. https://doi.org/10.1023/A:1022884410968.

[188] B.N. Cox, R. Massabò, Towards standardization for through-thickness reinforcement of laminates, in: S. Loud, V. Karbhari, D.O. Adams, A.B. Strong (Eds.), Proceedings 45th International SAMPE Symposium, 2000, pp. 1526−1537.

[189] K.P. Plain, L.Y. Tong, An experimental study on mode I and II fracture toughness of laminates stitched with a one-sided stitching technique, Compos. A Appl. Sci. Manuf. 42 (2011) 203−210. https://doi.org/10.1016/j.compositesa.2010.11.006.

[190] H. Heβ, N. Himmel, Structurally stitched NCF CFRP laminates. Part 1: experimental characterization of in-plane and out-of-plane properties, Compos. Sci. Technol. 71 (2011) 549−568. https://doi.org/10.1016/j.compscitech.2010.11.012.

[191] F. Ozdil, L.A. Carlsson, Characterization of mode I delamination growth in glass/epoxy composite cylinders, J. Compos. Mater. 34 (2000) 398−419. https://doi.org/10.1106/TP78-3H2H-8NV2-1F9H.

[192] F. Ozdil, L.A. Carlsson, Characterization of mixed mode delamination growth in glass/epoxy composite cylinders, J. Compos. Mater. 34 (2000) 420e41. https://doi.org/10.1106/7PBL-9NM1-A3XQ-3DVE.

[193] M. Hojo, T. Aoki, Thickness effect of double cantilever beam specimen on interlaminar fracture toughness of AS4/PEEK and T800/epoxy laminates, in: W.W. Stinchcomb, N.E. Ashbaugh (Eds.), Composite Materials: Fatigue and Fracture, vol. 1156, ASTM Special Technical Publication, 1993, pp. 281−298. https://doi.org/10.1520/STP24736S.

[194] R. El-Hajjar, R. Haj-Ali, Mode-I fracture toughness testing of thick section FRP composites using the ESE(T) specimen, Eng. Fract. Mech. 72 (2005) 631−643. https://doi.org/10.1016/j.engfracmech.2004.03.013.

[195] Z. Zou, S.R. Reid, S. Li, P.D. Soden, Application of a delamination model to laminated composite structures, Compos. Struct. 56 (2002) 375−389. https://doi.org/10.1016/S0263-8223(02)00021-1.

[196] J. Bonhomme, V. Mollón, J. Viña, A. Argüelles, Modelling ENF test procedure by means of the two-step extension method. Influence of friction forces, Polym. Test. 30 (2011) 856−860. https://doi.org/10.1016/j.polymertesting.2011.08.001.

[197] Y. Liu, F.P. van der Meer, L.J. Sluys, Cohesive zone and interfacial thick level set modeling of the dynamic double cantilever beam test of composite laminate, Theor. Appl. Fract. Mech. 96 (2018) 617−630. https://doi.org/10.1016/j.tafmec.2018.07.004.

[198] A.C. Orifici, I. Herszberg, R.S. Thomson, Review of methodologies for composite material modelling incorporating failure, Compos. Struct. 86 (2008) 194−210. https://doi.org/10.1016/j.compstruct.2008.03.007.

[199] A.C. Orifici, R. Krueger, Benchmark assessment of automated delamination propagation capabilities in finite element codes for static loading, Finite Elem. Anal. Des. 54 (2012) 28−36. https://doi.org/10.1016/j.finel.2012.01.006.

[200] N. Nguyen, A.M. Waas, A novel mixed-mode cohesive formulation for crack growth analysis, Compos. Struct. 156 (2016) 253−262. https://doi.org/10.1016/j.compstruct.2015.11.015.

[201] A. Soto, E.V. González, P. Maimi, A. Turon, J.R. Sainz de Aja, F.M. de la Escalera, Cohesive zone length of orthotropic materials undergoing delamination, Eng. Fract. Mech. 159 (2016) 174−188. https://doi.org/10.1016/j.engfracmech.2016.03.033.

[202] S. Yazdani, W.J.H. Rust, P. Wriggers, An XFEM approach for modelling delamination in composite laminates, Compos. Struct. 135 (2016) 353−364. https://doi.org/10.1016/j.compstruct.2015.09.035.

[203] R. Higuchi, T. Okabe, T. Nagashima, Numerical simulation of progressive damage and failure in composite laminates using XFEM/CZM coupled approach, Compos. A Appl. Sci. Manuf. 95 (2017) 197−207. https://doi.org/10.1016/j.compositesa.2016.12.026.

[204] R. Dimitri, P. Cornetti, V. Manti, M. Trullo, L. De Lorenzis, Mode-I debonding of a double cantilever beam: a comparison between cohesive crack modeling and Finite Fracture Mechanics, Int. J. Solids Struct. 124 (2017) 57−72. https://doi.org/10.1016/j.ijsolstr.2017.06.007.

[205] W. Hu, Y.D. Ha, F. Bobaru, Modelling dynamic fracture and damage in a fiber-reinforced composite lamina with peridynamics, Int. J. Multiscale Com. 9 (2011) 707−726. https://doi.org/10.1615/IntJMultCompEng.2011002651.

[206] Y.L. Hu, E. Madenci, Peridynamics for fatigue life and residual strength prediction of composite laminates, Compos. Struct. 160 (2017) 169−184. https://doi.org/10.1016/j.compstruct.2016.10.010.

[207] M. Corbetta, A. Saxena, M. Giglio, K. Goebel, An investigation of strain energy release rate models for real-time prognosis of fiber-reinforced laminates, Compos. Struct. 165 (2017) 99−114. https://doi.org/10.1016/j.compstruct.2017.01.002.

[208] Y. Gong, L.B. Zhao, J.Y. Zhang, N. Hu, A novel model for determining the fatigue delamination resistance in composite laminates from a viewpoint of energy, Compos. Sci. Technol. 167 (2018) 489−496. https://doi.org/10.1016/j.compscitech.2018.08.045.

[209] G. Allegri, Modelling fatigue delamination growth in fibre-reinforced composites: power-law equations or artificial neural networks? Mater. Des. 155 (2018) 59−70. https://doi.org/10.1016/j.matdes.2018.05.049.

[210] L. Carreras, J. Renart, A. Turon, J. Costa, B.L.V. Bak, E. Lindegaard, et al., A benchmark test for validating 3D simulation methods for delamination growth under quasi-static and fatigue loading, Compos. Struct. 210 (2019) 932−941. https://doi.org/10.1016/j.compstruct.2018.12.008.

[211] Y. Shindo, H. Horiguchi, R. Wang, H. Kudo, Double cantilever beam measurement and finite element analysis of cryogenic mode I interlaminar fracture toughness of glass-cloth/epoxy laminates, J. Eng. Mater. Technol. 123 (2001) 191−197. https://doi.org/10.1115/1.1345527.

[212] Y. Shindo, A. Inamoto, F. Narita, K. Horiguchi, Mode I fatigue delamination growth in GFRP woven laminates at low temperatures, Eng. Fract. Mech. 73 (2006) 2080−2090. https://doi.org/10.1016/j.engfracmech.2006.03.015.

[213] Y. Shindo, S. Takahashi, T. Takeda, F. Narita, Watanabe, Mixed-mode interlaminar fracture and damage characterization in woven fabric-reinforced glass/epoxy composite laminates at cryogenic temperatures using the finite element and improved test methods, Eng. Fract. Mech. 75 (2008) 5101−5112. https://doi.org/10.1016/j.engfracmech.2008.07.009.

[214] K.V. Pochiraju, G.P. Tandon, G.A. Schoeppner (Eds.), Long-Term Durability of Polymeric Matrix, Springer, 2012, pp. 1−677. https://doi.org/10.1007/978-1-4419-9308-3.

[215] S.J. Hooper, R. Subramanian, Effects of water and jet fuel absorption on mode I and mode II delamination of graphite/epoxy, in: Composite Materials: Fatigue and Fracture. Fourth volume, ASTM STP 1156, Stinchcomb WW, Ashbaugh NE, American Society for Testing and Materials, Philadelphia, 1993, pp. 318−340.

[216] B. Landry, G. LaPlante, L.R. LeBlanc, Environmental effects on mode II fatigue delamination growth in an aerospace grade carbon/epoxy composite, Compos. A Appl. Sci. Manuf. 43 (2012) 375−385. https://doi.org/10.1016/j.compositesa.2011.11.015.

[217] E. Moutsompegka, K.I. Tserpes, P. Polydoropoulou, C. Tornow, M. Schlag, K. Brune, et al., Experimental study of the effect of pre-bond contamination with de-icing fluid and ageing on the fracture toughness of composite bonded joints, Fatigue Fract. Eng. Mater. Struct. 40 (2017) 1581−1591. https://doi.org/10.1111/ffe.12660.

[218] D. Yavas, X. Shang, A.F. Bastawros, Mode-I fracture toughness and surface morphology evolution for contaminated adhesively bonded composite structures, Compos. Struct. 203 (2018) 513−522. https://doi.org/0.1016/j.compstruct.2018.07.014.

[219] P.H. Malinowski, T. Wandowski, W.M. Ostachowicz, A. Christopoulos, I. Koulalis, K. Kitsianos, et al., Study of CFRP Adhesive Bonds Influenced by Factors Encountered during Aircraft Operations. Proc SPIE 10598, Sensors and Smart Structures Technologies for Civil, Mechanical, and Aerospace Systems, 2018, 105980C, https://doi.org/10.1117/12.2294616.

[220] P.A. Wagner, B.J. Little, K.R. Hart, R.I. Ray, Biodegradation of composite materials, Int. Biodeterior. Biodegrad. 38 (1996) 125−132. https://doi.org/10.1016/S0964-8305(96) 00036-4.

[221] J.D. Gu, Microbial colonization of polymeric materials for space applications and mechanisms of biodeterioration: a review, Int. Biodeterior. Biodegrad. 59 (2007) 170−179. https://doi.org/10.1016/j.ibiod.2006.08.010.

[222] J.D. Gu, Biodegradation testing: so many tests, but very little new innovation, Appl. Environ. Biotech. 1 (2016) 92−95. https://doi.org/10.18063/AEB.2016.01.007.

[223] D. Rodrigues Vieira, R. Kennedy Vieira, M. Chang Chain, Strategy and management for the recycling of carbon fiber-reinforced polymers (CFRPs) in the aircraft industry: a critical review, Int. J. Sustain. Dev. World 24 (2017) 214−223. https://doi.org/10.1080/ 13504509.2016.1204371.

[224] K. Wong, C. Rudd, S. Pickering, X.L. Xiao, Composites recycling solutions for the aviation industry, Sci. China Technol. Sci. 60 (2017) 1291−1300. https://doi.org/10. 1007/s11431-016-9028-7.

[225] D.L. Edwards, A.P. Tighe, M. Van Eesbeek, Y. Kimoto, K.K. de Groh, Overview of the natural space environment and ESA, JAXA, and NASA materials flight experiments, MRS Bull. 35 (2010) 25−34. https://doi.org/10.1557/mrs2010.613.

[226] A.K. Maji, S.A. Mahnke, A Review of the Degradation of Composites in Mid Earth Orbit. Proc 9th Biennial Conf Eng, Construction, and Operations in Challenging Environments, Earth & Space, 2004, pp. 567−572. https://doi.org/10.1061/40722(153)79.

[227] R. Voicu, CFRP composite behaviour under extreme environment exposure, Mater. Plast. 53 (2016) 465−469.

[228] J.B. Moon, C.G. Kim, Inter-lamina shear strength of MWNT-reinforced thin-ply CFRP under LEO space environment, Compos. Res. 30 (2017) 7−14. https://doi.org/10.7234/ composres.2017.30.1.007.

[229] B. Dao, J. Hodgkin, J. Krstina, J. Mardel, W. Tian, Accelerated aging versus realistic aging in aerospace composite materials II. Chemistry of thermal aging in a structural composite, J. Appl. Polym. Sci. 102 (2006) 3221−3232. https://doi.org/10.1002/app. 24573.

[230] W.J. Cantwell, The interlaminar fracture behaviour of carbon fibre reinforced plastics at low temperatures, Proc. Inst. Mech. Eng. G J. Aerosp. Eng. 210 (1996) 1−7, in: https:// doi.org/10.1243/PIME_PROC_1996_210_339_02.

[231] M.S. Oliver, W.S. Johnson, Effect of temperature on mode I interlaminar fracture of IM7/ PETI-5 and IM7/977-2 laminates, J. Compos. Mater. 43 (2009) 1213−1219. https://doi. org/10.1177/0021998308104147.

[232] W.S. Johnson, M.M. Pavlick, M.S. Oliver, Determination of Interlaminar Toughness of IM7/977-2 Composites at Temperature Extremes and Different Thicknesses, Georgia Institute of Technology, 2005, pp. 1−27. Final report.

[233] K. Horiguchi, Y. Shindo, H. Kudo, S. Kumagai, End-notched flexure testing and analysis of mode II interlaminar fracture behaviour of glass-cloth/epoxy laminates at cryogenic temperatures, J. Compos. Technol. Res. 24 (2002) 239−245. https://doi.org/10.1520/ CTR10930J.

[234] I. Chou, Effect of fiber orientation and moisture absorption on the interlaminar fracture toughness of CFRP laminates, Adv. Compos. Mater. 7 (1998) 377−394. https://doi.org/ 10.1163/156855198X00264.

[235] B. Vieille, Evolution of the strain energy release rate during ductile or brittle failure in woven-ply reinforced thermoplastic laminates under high temperature, Polym. Compos. 40 (2019) 121−131. https://doi.org/10.1002/pc.24612.

[236] S.Y. Park, H.S. Choi, W.J. Choi, H. Kwon, Effect of vacuum thermal cyclic exposures on unidirectional carbon fiber/epoxy composites for low earth orbit space applications, Compos. B Eng. 43 (2012) 726−738. https://doi.org/10.1016/j.compositesb.2011.03.007.

[237] B.D. Davidson, M. Kumar, M.A. Soffa, Influence of mode ratio and hygrothermal condition on the delamination toughness of a thermoplastic particulate interlayered carbon/epoxy composite, Compos. Appl. Sci. Manuf. A40 (2009) 67−79. https://doi.org/10.1016/j.compositesa.2008.10.006.

[238] R. Zenasni, A.S. Bachir, I. Viña, A. Argüelles, J. Viña, Effects of hygrothermomechanical aging on the interlaminar fracture behavior of woven fabric fiber/PEI composite materials, J. Compos. Mater. 19 (2006) 385−398. https://doi.org/10.1177/0892705706059743.

[239] A.P. Mouritz, Post-fire flexural properties of fibre-reinforced polyester, epoxy and phenolic composites, J. Mater. Sci. 37 (2002) 1377−1386. https://doi.org/10.1023/A:1014520628915.

[240] J.G. Funk, G.F. Sykes, The effects of radiation on the interlaminar fracture toughness of a graphite/epoxy composite, J. Compos. Technol. Res. 8 (1986) 92−97. https://doi.org/10.1520/CTR10328J.

[241] N. Takeda, M. Tohdoh, K. Takahashi, Interlaminar fracture toughness degradation of radiation-damaged GFRP and CFRP composites, Adv. Compos. Mater. 4 (1995) 343−354. https://doi.org/10.1163/156855195X00195.

[242] D.R. Sekulic, M.V. Gordic, I.M. Djordjevic, Z.S. Petrovic, M.M. Stevanovic, Irradiation and annealing effects on delamination toughness in carbon/epoxy composites, J. Nucl. Mater. 383 (2009) 209−214. https://doi.org/10.1016/j.jnucmat.2008.09.009.

[243] M. Arnaout, T. Paulmier, B. Dirassen, D. Payan, Study of radiation induced conductivity and photoconduction phenomenon for materials used in space environment, J. Electrost. 84 (2016) 48−53. https://doi.org/10.1016/j.elstat.2016.09.001.

[244] W.P. Schonberg, Protecting earth-orbiting spacecraft against micro-meteroid/orbital debris impact damage using composite structural systems and materials: an overview, Adv. Space Res. 45 (2010) 709−720. https://doi.org/10.1016/j.asr.2009.11.014.

[245] Y. Hirano, S. Katsumata, Y. Iwahori, A. Todoroki, Artificial lightning testing on graphite/epoxy composite laminates, Compos. A Appl. Sci. Manuf. 41 (2010) 1461−1470. https://doi.org/10.1016/j.compositesa.2010.06.008.

[246] P. Feraboli, M. Miller, Damage resistance and tolerance of carbon/epoxy coupons subjected to simulated lightning strike, Compos. A Appl. Sci. Manuf. 40 (2009) 954−967. https://doi.org/10.1016/j.compositesa.2009.04.025.

[247] H. Kawakami, P. Feraboli, Lightning strike damage resistance and tolerance of scarf-repaired mesh-protected carbon fiber composites, Compos. A Appl. Sci. Manuf. 42 (2011) 1247−1262. https://doi.org/10.1016/j.compositesa.2011.05.007.

[248] S. Yamashita, T. Sonehara, J. Takahashi, K. Kawabe, T. Murakami, Effect of thin-ply on damage behaviour of continuous and discontinuous carbon fibre reinforced thermoplastics subjected to simulated lightning strike, Compos. A Appl. Sci. Manuf. 95 (2017) 132−140. https://doi.org/10.1016/j.compositesa.2017.01.010.

[249] T. Ogasawara, Y. Hirano, A. Yoshimura, Coupled thermal−electrical analysis for carbon fiber/epoxy composites exposed to simulated lightning current, Compos. A Appl. Sci. Manuf. 41 (2010) 973−981. https://doi.org/10.1016/j.compositesa.2010.04.001.

[250] Y.L. Guo, D. Qi, J.L. Chen, X.L. Yao, X.S. Yi, Y. Jia, Comparison between temperature and pyrolysis dependent models to evaluate the lightning strike damage of carbon fiber composite laminates, Compos. A Appl. Sci. Manuf. 97 (2017) 10−18. https://doi.org/10.1016/j.compositesa.2017.02.022.

[251] Y.Q. Wang, Multiphysics analysis of lightning strike damage in laminated carbon/glass fiber reinforced polymer matrix composite materials: a review of problem formulation and computational modelling, Compos. A Appl. Sci. Manuf. 101 (2017) 543−553. https://doi.org/10.1016/j.compositesa.2017.07.010.

[252] T.C. Zou, J. Wang, K. Mao, Z.Y. Feng, Simulation of lightning protection for composite civil aircrafts, Process Eng. 17 (2011) 328−334. https://doi.org/10.1016/j.proeng.2011.10.036.

[253] G. Abdelal, A. Murphy, Nonlinear numerical modelling of lightning strike effect on composite panels with temperature dependent material properties, Compos. Struct. 109 (2014) 268−278. https://doi.org/10.1016/j.compstruct.2013.11.007.

[254] G. Allegri, M.R. Wisnom, A non-linear damage evolution model for mode II fatigue delamination onset and growth, Int. J. Fatigue 43 (2012) 226−234. https://doi.org/10.1016/j.ijfatigue.2012.03.016.

[255] B.L.V. Bak, A. Turon, E. Lindgaard, E. Lund, A simulation method for high-cycle fatigue-driven delamination using a cohesive zone model, Int. J. Numer. Methods Eng. 106 (2016) 163−191. https://doi.org/10.1002/nme.5117.

[256] M. May, Measuring the rate-dependent mode I fracture toughness of composites − a review, Compos. A Appl. Sci. Manuf. 81 (2016) 1−12. https://doi.org/10.1016/j.compositesa.2015.10.033.

[257] L.-C. Tang, H. Zhang, S. Sprenger, L. Ye, Z. Zhang, Fracture mechanisms of epoxy-based ternary composites filled with rigid-soft particles, Compos. Sci. Technol. 72 (2012) 558−565. https://doi.org/10.1016/j.compscitech.2011.12.015.

[258] B. Ashrafi, J.W. Guan, V. Mirjalili, Y.F. Zhang, L. Chun, P. Hubert, et al., Enhancement of mechanical performance of epoxy/carbon fiber composites using single-walled carbon nanotubes, Compos. Sci. Technol. 71 (2011) 1569−1578. https://doi.org/10.1016/j.compscitech.2011.06.015.

[259] Y.H. Tang, L. Ye, D.H. Zhang, S.Q. Deng, Characterization of transverse tensile, interlaminar shear and interlaminate fracture in CF/EP laminates with 10 wt% and 20 wt% silica nanoparticles in matrix resins, Compos. A Appl. Sci. Manuf. 42 (2011) 1943−1950. https://doi.org/10.1016/j.compositesa.2011.08.019.

[260] F. Aymerich, A. Dalla Via, M. Quaresimin, Energy absorption capability of nanomodified glass/epoxy laminates, Process Eng. 10 (2011) 780−785. https://doi.org/10.1016/j.proeng.2011.04.129.

[261] J. Zhang, T. Yang, T. Lin, C.H. Wang, Phase morphology of nanofibre interlayers: critical factor for toughening carbon/epoxy composites, Compos. Sci. Technol. 72 (2012) 256−262. https://doi.org/10.1016/j.compscitech.2011.11.010.

[262] K. Savolainen, L. Pyllkänen, H. Norppa, G. Falck, H. Lindberg, T. Tuomi, et al., Nanotechnologies, engineered nanomaterials and occupational health and safety - A review, Saf. Sci. 48 (2010) 957−963. https://doi.org/10.1016/j.ssci.2010.03.006.

[263] G. Savage, Enhancing the exploitation and efficiency of fibre-reinforced composite structures by improvement of interlaminar fracture toughness, Eng. Fail. Anal. 13 (2006) 198−209. https://doi.org/10.1016/j.engfailanal.2004.12.047.

The response of aerospace composites to temperature and humidity

9

F.R. Jones, J.P. Foreman
University of Sheffield, Sheffield, United Kingdom

9.1   Introduction

Polymer matrix composites have matured over recent years with their application as major structural components of aircraft, such as the wing box on the Airbus A380. Most recently the Boeing 787 Dreamliner utilises 90% by volume of composite materials of which much is employed in load bearing applications. The main advantage of fiber composites arises from their high specific strength and stiffness, which means that low weight structures can be designed. Energy costs have driven the demand for low weight structural composites. The gradual replacement of non-structural components has also provided designers with the confidence to increase the number of applications. However, composites have a long track record going back to the beginnings of the plastics industry, more than 100 years ago, where phenolic resin—paper cores were essential to the development of electrical applications, and fabric-reinforced phenolic moldings became popular for more complex shaped artifacts. However, more critical was the use of "fiberglass" for the hulls of leisure boats in the 1950s, military ships in the 1970s and pipes for transporting both potable drinking water (without taint) and corrosive effluents. Here, the durability and corrosion resistance of glass fiber—reinforced plastic (GFRP) provided the main driver. The development of carbon fiber composites since the 1960s spurred academic and industrial studies so that full understanding of the micromechanics of failure has been achieved over several decades [1,2].

A composite consists of a reinforcement, which is mainly a high-performance fiber or micro- or nano-sized inorganic particle dispersed in a polymeric matrix. The latter can be acicular, such as carbon nanotubes. Most recently, hybrid systems have been developed to reduce the volume fraction of the polymer matrix, which has the lowest modulus of all components. The polymer is also the most sensitive to the absorption of aqueous and organic fluids. The effect of environments is also complicated by the morphology of the matrix, which often involves a phase-separated thermoplastic in a thermoset resin. In some aerospace laminates, heterogeneous rubber or thermoplastic particles are used in the interlaminar regions as toughening agents. A further complication is the formation of interphases between the reinforcement and matrix, which represents a region of the mixed polymer at the reinforcement interface [3].

This chapter is concerned with the effect of absorption of moisture (and other organics) on the micromechanics of failure of aerospace composite materials.
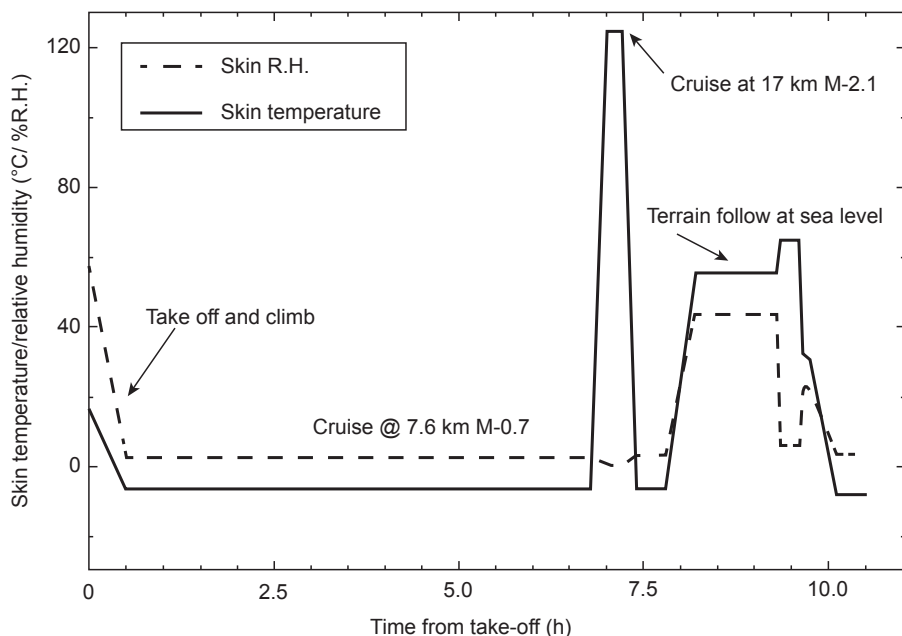
Figure 9.1 Schematic of skin temperature and local relative humidity during a typical flight of a military jet [4].

Fig. 9.1 shows a schematic temperature and humidity profile of a military aircraft on a typical flight sortie [4]. On the ground, the relative humidity (RH) is high but decreases on take-off; however, one may encounter flight at sea level where humidity rises. Also, an aircraft's skin temperature depends on speed and elevation. Of note is the rapid rise in skin temperature during the supersonic flight to temperatures in excess of 120°C, referred to as thermal spiking. To understand the effects of these flight variables, we will discuss Fickian diffusion and the sensitivity of polymers and fibers to aqueous and non-aqueous environments. We will also describe the effect of thermal spiking on moisture absorption since this could be a major source of residual stress in an aerospace composite.

9.1.1 Moisture absorption

Organic matrix polymers are sensitive to water ingress. Therefore, in humid environments, moisture diffuses into polymer matrix composites to differing degrees. The extent of moisture absorption depends on the molecular structure of the polymer. This aspect is described in Section 9.2. Dissolved water can plasticize the matrix and reduce the glass transition temperature, T_g, and hence service temperature of the composite significantly. In conjunction with this, hydrolytic degradation can reduce the thermo-mechanical properties further. For aerospace structures, in particular, the rate of absorption and its temperature dependence is especially critical since the life of an aircraft is several decades.

Most structural composites are highly anisotropic, consisting of unidirectional materials where the mechanical properties in the longitudinal (or 0°) direction are fiber dominated, while in the transverse (or 90 degrees) direction they are matrix dominated. Therefore, moisture absorption has a larger effect on the transverse properties of a typical composite system. Despite this, the strength of a 0° composite is also affected by moisture ingress since the reloading of a broken fiber occurs through shear stress transfer from the "interphasal" matrix. For achieving isotropy, unidirectional plies are stacked at a set of angles, such as 0°, ±45 degrees and 90 degrees to form a laminate. In this situation, moisture ingress will modify the residual stress state in the individual laminae.

Whereas the thermodynamic properties of the resin and environment will determine the maximum extent of moisture absorption, diffusion is a kinetic property, which is temperature-dependent. Normally, the latter is considered to be Fickian in nature. For highly polar polymers, other diffusion models need to be considered, but for most structural composite materials, the Fickian laws are applicable.

9.1.2 Fickian diffusion

Fickian laws were developed for thermal equilibration, but thermal diffusion is significantly faster than moisture diffusion by a factor of $\sim 10^6$. This means that a 12 mm thick composite can take 13 years for moisture equilibration at 350 K, while thermal equilibration would take only 15 s. The consequence of this is that a typical aerospace structure will take many years in service before the structure has become saturated with water. Thus, engineers need to deal with property gradients resulting from moisture absorption. However, this is complicated by the variations in temperature and RH at different storage and holding locations and during flight. As a result of this, water will tend to move within a structure in response to environmental fluctuations. For instance, at these locations with a high ambient temperature, moisture will diffuse deeper into the structure as each molecule has higher energy. Correspondingly, during flight missions, the structure will experience low RH at high altitudes, and the moisture will tend to move in the opposite direction. However, this effect is inhibited by the low rates at low temperatures [5,6].

The distribution of water throughout the composite will arise from an averaging of a series of moisture profiles over time. The solution to Fick's second law, which defines the diffusion constant (D) for moisture uptake, is given by Eq (9.1):

$$D = \frac{\pi d^2}{16 M_\infty^2} \left(\frac{M_2 - M_1}{t_2^{1/2} - t_1^{1/2}} \right)^2 \tag{9.1}$$

where M_1 and M_2 are the moisture contents at times t_1 and t_2; d is the thickness of the specimen. The experimental measurement of D uses coupons where diffusion through all the faces occurs so that an edge correction is required for the calculation of a true one-dimensional (1D) diffusion constant [5−8].

For the prediction of the time required for moisture equilibration of a structure, the diffusion constant, D, for each material is required, but their measurement is time-consuming because the equilibrium moisture content (M_∞) has to be determined in long-term tests. Therefore, accelerated tests are used. As with other kinetic processes, D is related to temperature (T) according to the Arrhenius equation,

$$D = A \exp(-E_a/RT) \tag{9.2}$$

where E_a is the activation energy for moisture transport, and A is the pre-exponential factor.

While many resin systems exhibit Fickian diffusion, others show non-Fickian behavior. The experimental reabsorption diffusion curve shown in Fig. 9.2 represents a smooth process which is linear over the first 60% before reaching equilibrium. For the resin system used, Fickian diffusion could only be obtained after preconditioning because often the early stage of moisture absorption deviates from Fickian kinetics. This creates difficulties in the calculation of a precise diffusion constant. It is thought that the non-Fickian behavior results from the reorganization of the network, as the material becomes plasticized [9−11].

Fig. 9.2 also illustrates this point where the moisture concentration in the first absorption appears to approach equilibrium, but then after a longer period, the moisture sorption accelerates. Much work on the thermal spiking phenomenon (see Section 9.5) has confirmed that the relaxation of the network occurs in the presence of water making more polar sites available which can bind additional water molecules.
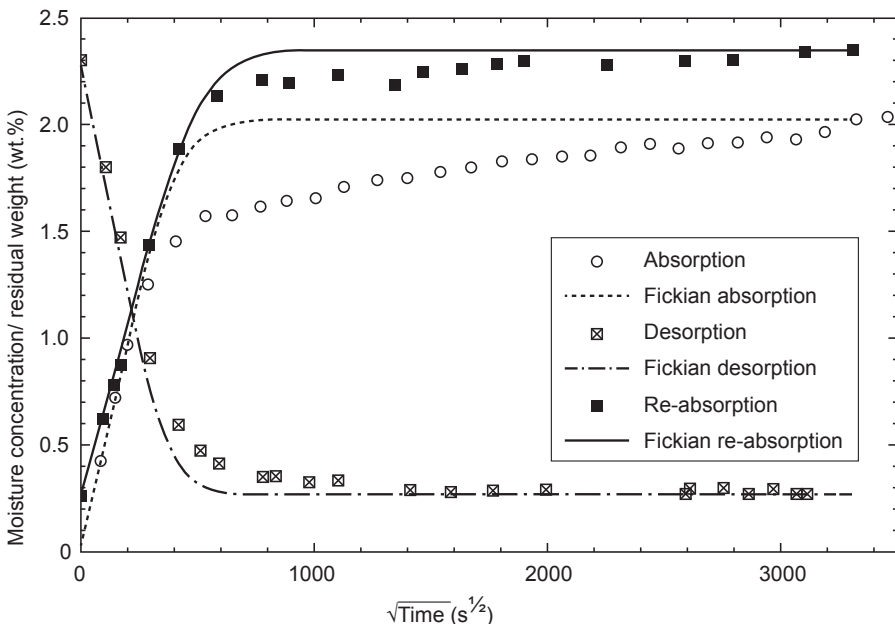
Figure 9.2 Isothermal absorption and reabsorption curves for the bismaleimide epoxy resin Narmco Rigidite 5245 at 90% RH at 45°C. Calculated theoretical Fickian first absorption and desorption curves are also shown [4].

Composite materials are typically anisotropic, so the diffusion constants in the longitudinal and transverse directions can differ. These are related to each other through Eq (9.3):

$$D = D_x \left[1 + \frac{d}{l} \left(\frac{D_y}{D_x} \right)^{\frac{1}{2}} + \frac{d}{b} \left(\frac{D_z}{D_x} \right)^{\frac{1}{2}} \right]^2 \tag{9.3}$$

where D_x, D_y, and D_z are the diffusion constants through the thickness, d, along the length, l, and across the breadth, b.

For a unidirectionally reinforced $0°$ ply, D_z and D_x are equivalent, both occurring at 90 degrees to the fibers. Therefore, Eq. (9.3) becomes:

$$D = D_x \left[1 + \frac{d}{b} + \frac{d}{l} \left(\frac{D_y}{D_x} \right)^{\frac{1}{2}} \right]^2 \tag{9.4}$$

It is possible to measure the influence of the fibers on the diffusion because, with a poor interfacial bond between the fiber and the resin, rapid transport will take place at the interface and can be differentiated from the resin-dominated diffusion at 90 degrees to the fibers. If D_y is greater than D_x, then capillary diffusion at a poor interfacial bond must be occurring. For perfectly bonded fibers, D_x will be significantly larger than D_y because of the relatively higher surface area of resin in the 90 degrees direction. Typical values of the diffusion constant are 10^{-6} mm^2/s for resin and 10^{-7} mm^2/s for composite.

9.1.3 Prediction of moisture content and time dependence

We can predict the distribution of moisture in a laminate using Fickian diffusion kinetics. Fig. 9.3 shows the calculated distribution of moisture in a carbon fiber laminate of thickness 0.94 mm after 3 days at 96% RH and 50°C. As a result of Fickian analysis, we can observe that it would take 13 years to reach equilibrium if the material had a thickness of 12 mm. However, this does not reflect the actual environment since the temperature and RH can change.

9.1.4 Moisture distribution in a laminate

Fig. 9.4 shows how the moisture profile in a laminate through-thickness changes as a result of a thermal excursion. Since the rate of moisture diffusion is controlled by an activation process (Eq. 9.2) at higher temperatures, the moisture will desorb from the surface, whereas, subsurface moisture will move into structure. Therefore, over several cycles, the moisture profile will even out through the thickness.
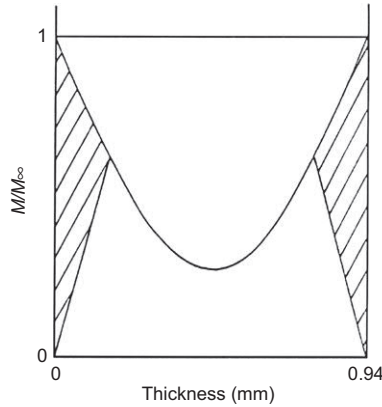
Figure 9.3 Theoretical moisture distribution within a unidirectional carbon fiber laminate from Narmco Rigidite 5245C, after 3 days at 50°C and 96% RH (curved line) and after a rapid thermal excursion to 150°C (the "spiked" curve) The shaded area indicates the water that has moved out of the laminate during the thermal excursion [7].
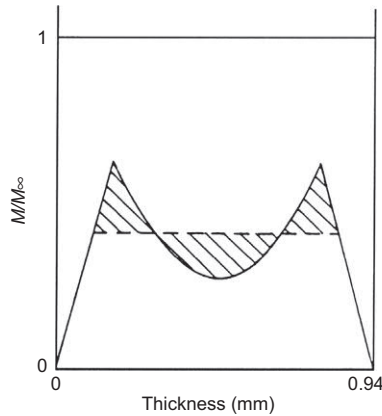
Figure 9.4 Theoretical moisture distribution within a unidirectional carbon fiber laminate from Narmco Rigidite 5245C, after 3 days at 50°C and 96% RH and a rapid thermal excursion to 150°C. The shaded area indicates the water that has moved into the laminate during the thermal excursion [7].

9.1.5 Interfacial stability during moisture absorption

The durability of a composite material to moisture ingress can often be determined by the maintenance of interfacial integrity. Therefore, it is useful to study diffusion in different directions of a unidirectional composite.

Eq. (9.4) can be used to calculate the diffusion constants in the direction parallel, D_x, and at 90 degrees, D_y and D_z. Rearrangement gives

$$D^{\frac{1}{2}} = \left(1 + \frac{d}{b}\right)D_x^{\frac{1}{2}} + \left(\frac{d}{l}\right)D_y^{\frac{1}{2}} \tag{9.5}$$

Therefore, a plot of Eq. (9.5) enables D_x and D_y to be estimated from the diffusion constants for coupons of differing geometry. In this way, the degradation of the interface under aggressive environments in accelerated tests can be identified. However, interfacial degradation to moisture should be avoided by correct selection of fiber and sizing in separate experiments. Often, single-filament tests, such as fragmentation, pull-out, or microdroplet, can be used to assess the interfacial stability of certain combinations of fibers and resin. With aerospace carbon fibers, the oxidative fiber treatment coupled with epoxy resin sizes in epoxy matrices provides a "good" interface. It should be remembered that a perfect interface will lead to brittle failure and that partial debonding or interphasal yield is required for tough performance [3].

9.2 Moisture sensitivity of matrix resins

Moisture diffuses into polymers to differing degrees, which is a function of the morphology and molecular structure. The following aspects are critical:

1. The polarity of the molecular structure
2. The degree of cross-linking
3. The degree of crystallinity in the case of a thermoplastic matrix (although certain modified thermosets can also have a crystalline component)
4. The presence of residuals in the material

While (1−3) are clearly variables of the matrix, the presence of residuals (4) is not so obvious since this refers to unreacted hardeners and other impurities. Impurities, such as calcium, sodium or potassium salts arise from inclusions in fillers or as contaminants on the surface of reinforcing fibers. The sodium and potassium content of glass fibers has been steadily reduced over recent years because they were widely acknowledged as responsible for the water sensitivity of glass fiber composites in aqueous environments.

Table 9.1 gives typical values of the diffusion constant for a series of thermosetting matrices where the effect of polarity of the resin on the equilibrium on moisture concentration is illustrated. Epoxy resins are the network product of the reaction of a multifunctional epoxide monomer with a hardener. One of the important aspects of composite materials which needs to be recognized is that the material is synthesized at the same time that the component is manufactured. The precise chemistry of the final network can be uncertain but is a function of the chemical structures of the epoxide and hardener and/or catalyst, which determine the mechanism of cure. In this way, the cured resins can have differing polarities.

For example, an anhydride hardener (with tertiary amine accelerator) will produce a "polyester"-type structure with low polarity, whereas, an amine hardener will form a β-hydroxyl amine network with high polarity. Hydrogen bonding of water molecules at these sites enhances the concentration of moisture which can be absorbed. However, with catalytic curing agents, polyether structures of relatively low polarity will form. Since it is quite common to use mixed curing agents for composite matrices, the cured network will have a complex structure where its polarity is strongly dependent on the

Table 9.1 Typical moisture diffusion coefficients and maximum moisture concentrations of aerospace epoxy matrix resins [8,10].

Resin	M_∞/ wt %	$D/10^{-7}$ mm²/s	Relative humidity/%	T/°C
Epoxy: General purpose (DGEBA)	6.9	2.8	96	50
Epoxy: Dow DEN 431 (epoxy novolak)	0.48	5.99	11	50
Epoxy aerospace: Narmco 5245	1.96	11.0	96	45
	1.38	14.7	75	45
	0.8	19.4	46	45
	0.54	17.2	31	45
Epoxy−cyanate ester: Primaset PT30/DEN 431	2.96	3.62	96	50
	2.19	4.85	75	50
	1.44	6.34	46	50
	1.04	6.12	31	50
	0.70	5.46	16.5	50
	0.48	5.99	11	50

degree of incorporation of the individual components and the chemical mechanisms employed. In Table 9.1, it is clearly shown how the choice of resin and curing mechanism strongly influences the moisture sensitivity.

9.2.1 Epoxy resins

Fig. 9.5 shows an example of the cured structure of a thermoset resin using two different epoxide monomers with two different amine hardeners. The epoxies are triglycidyl *p*-aminophenol (TGAP) and tetraglycidyl 4,4-diaminodiphenylmethane (TGDDM), which are tri- and tetra-functional, respectively ($n = 3$ and $n = 4$, respectively); and the two hardeners are 4,4-diamino-diphenylsulfone (DDS) and dicyandiamide (DICY).

9.2.2 Advanced matrix resins

As shown in Table 9.2, thermoplastic matrices, such as polyethersulphone (PES) and polyetheretherketone (PEEK) absorb much less moisture than the advanced epoxies. PEEK is an example of a partially crystalline linear polymer with very low moisture absorption. Thermoplastics that are relatively nonpolar and absorb low concentrations of moisture are also used as "flow-control" additives and/or toughening agents in advanced epoxy resins and help provide a reduction in moisture sensitivity.
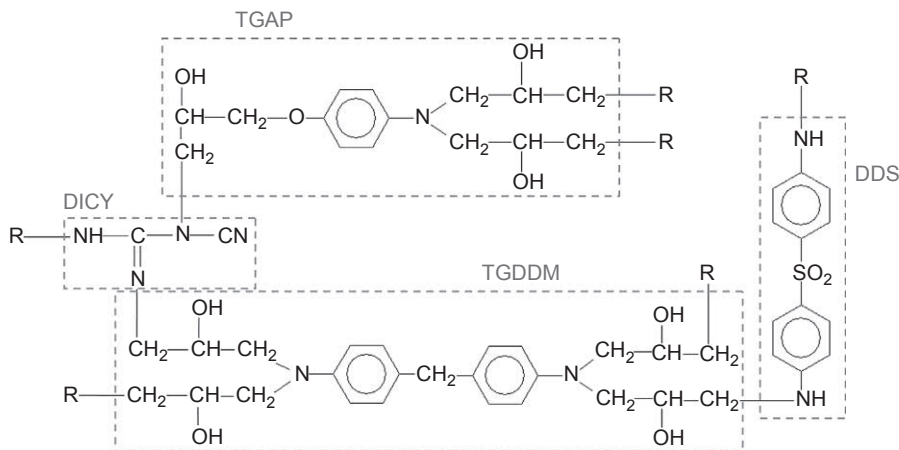
Figure 9.5 Typical chemical structure of a cured epoxy resin showing the use of two epoxies and two hardeners. *R* represents a connection to the 3D network.

In recent times, commodity thermoplastics have become significant contenders as matrices for glass fiber composites where environmental resistance is sought; for example, polypropylene is now available in a prepreg form for fusion bonding. Since it has low polarity and is also partially crystalline, moisture absorption is very low.

9.3 Mechanism of moisture retention in aerospace epoxies

9.3.1 Chemical aspects

The epoxy amine cure mechanism begins with an energetically favorable ring opening of the unstable epoxide group by a primary amine, resulting in the formation of a hydroxyl group and secondary amine. This is followed by the less favorable reaction of an epoxide group with a secondary amine or the even less favorable reaction of an epoxide group with a hydroxyl group (etherification).

If each monomer reacted only twice ($n = 2$), a simple linear polymer is created, but this is clearly not the case in thermosetting resin systems. In theory, each TGAP monomer can react three times through its epoxide groups and further three times through the resultant hydroxyl groups, bringing its maximum theoretical functionality to six ($n = 6$). However, in practice, this is highly unlikely to occur partly due to the etherification reaction being energetically less favorable and partly due to the dramatic decrease in mobility each monomer experiences as the number of times it has reacted increases. When a monomer is unreacted, it is free to migrate through the monomer−polymer−network system. After it has reacted once, its translational freedom has been removed, and each subsequent reaction reduces its mobility further until it is firmly locked into the 3D network. At this point, its ability to react with other species present in the network is significantly hindered.

Table 9.2 Moisture content of carbon fiber composites from thermosetting and thermoplastic matrices; also shown is the benefit of modifying epoxy resin with thermoset and thermoplastic modifiers to reduce M_∞.

Resin	Type	Modifier	M_∞/ wt %	Relative humidity/%	T/°C
Fibredux 924E[a]	Epoxy thermoset	None	2.44	96	50
924C	Epoxy	PES	1.72	96	50
927C	Epoxy	Cyanate ester/PI	0.98	96	50
Narmco rigidite 5255C	Epoxy	BMI	0.82	96	50
APC 2	PEEK thermoplastic	None	0.02	50	23 (350 h)
APC 2	PEEK	None	0.23	100 (immersion)	100 (360 h)
PMR 15	BMI thermoset	None	0.32	96	50

BMI, bismaleimide; *PES*, polyethersulfone; *PI*, polyimide.
[a]Calculated from data on cast resins (6.95%).

Epoxy resins used in composite manufacturing are intentionally prepared with an excess of epoxy compared to hardener. This is done to ensure that the hardener is completely reacted during cure and is not allowed to remain in the network and cause plasticization. A mixture with an epoxy−hardener ratio of 1:1 would not be able to fully cure due to the mobility arguments given in this chapter. The epoxy excess means that there will be a significant number of unreacted and relatively polar functional groups present in the cured 3D network.

Each time a monomer reacts more than twice ($n > 2$), it is considered to have chemically cross-linked, creating a permanent covalent link between adjacent polymer chains. Multifunctional epoxy resins, such as TGAP and TGDDM form networks with diamines, such as DDS and DICY, with a significant number of cross-links present. Extensive cross-linking adds to the strength and stiffness of the cured resin but produces a brittle material with little inherent toughness. This can be a problem if the etherification reaction is able to occur to a significant level. A highly cross-linked 3D network will contain enclosed areas where no further reactions are possible, leading to the so-called *free volume*.

It is clear that the type and ratio of functional groups present in the network will affect its polarity and degree of cross-linking [12−14] and hence its moisture absorption characteristics. While the original monomers are practically frozen in place as a fused network, diluents introduced into the system are capable of diffusing deep into the network. In the case of water, the additional molecules either merge to form discrete micro-phases located in the free volume or hydrogen-bonded to polar functional groups on the polymer chain. The ratio of water present in the free volume
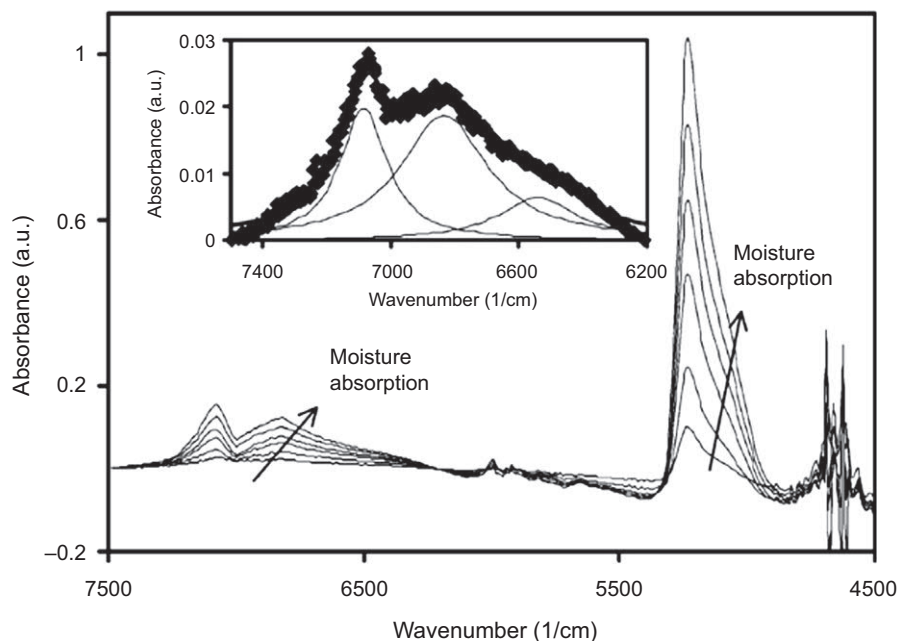
Figure 9.6 NIR difference spectra for diglycidyl ether of bisphenol-A (DGEBA)−
diethylenetriamine (DETA) with absorbed moisture levels varying between 0.46% and 2.69%.
The inset shows a deconvoluted analysis with peaks at 7085, 6834 and 6541/cm, which
correspond to free water and singly and doubly hydrogen-bonded water, respectively [15].

to hydrogen-bonded water, can be estimated using near-infrared spectroscopy (NIR),
such as described by Mijovic and Zhang [15]. While free and hydrogen-bonded water
have different characteristic peaks, as shown in Fig. 9.6, it is difficult to obtain a
precise ratio.

The absorbed water has a distinct and often undesirable effect on the thermo-
mechanical properties of the resin. Discrete pockets of water will plasticize the
network by dissipating thermo-mechanical energy via the translational degrees of
freedom associated with unattached molecules. Correspondingly, individual water
molecules hydrogen-bond to appropriate sites, such as hydroxyl and amino groups
in particular. Here, while there is an increase in binding energy due to the hydrogen
bond, there is also increased energy dissipation because each individual water mole-
cule imparts extra degrees of freedom to the system. In the case of small diluents,
such as water, which have a high value of specific degrees of freedom, this energy
balance favors dissipation which accounts for the deleterious effect such molecules
have on thermo-mechanical properties. For larger diluents, such as unreacted mono-
mers and oligomers, the situation is less clear as these molecules will have a lower
value for the specific degrees of freedom.

Hydrogen bonding of water molecules to the cross-linked network in moisture-
affected epoxies is further complicated by the likelihood that the absorbed water can
hydrogen-bond more than once, as shown in Fig. 9.7. Several analyses of such systems
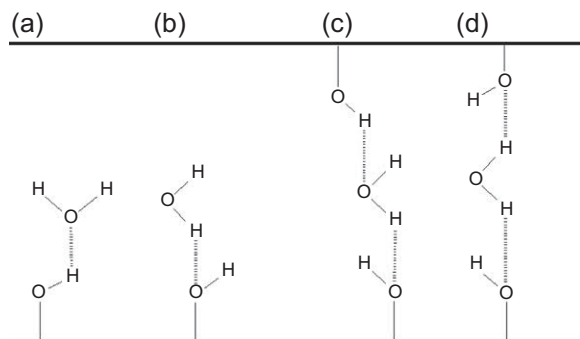
Figure 9.7 Variation in hydrogen bonding between absorbed water and polymer backbone. (a) Singly bound water as acceptor; (b) singly bound water as donor; (c) doubly bound water as donor and acceptor; (d) doubly bound water as donor twice. Hydroxyl groups are shown from the polymer backbone, but amino groups are also possible as donor and acceptor.

suggest that the proportion of absorbed moisture that is doubly hydrogen-bonded to the network may be as high as 20% [15]. Whether the doubly bonded water preferentially acts as a donor and acceptor or as a donor twice is unclear, as is whether it is doubly bonded to a single polymer chain or between two adjacent chains (creating a further weaker cross-link). There appears to be no evidence to suggest that water is capable of hydrogen bonding more than twice per molecule in such systems.

9.3.2 Predictive modeling

There are a number of models which can be used to predict the effect that absorbed diluents, in particular, water, have on a cured polymeric resin. One of the most powerful of these is Group Interaction Modeling (GIM), a continuum-type model with a set of versatile input parameters based on the number and type of chemical functional groups present in the network. This allows the complex chemistry of amine-cured epoxy resins to be catered for while retaining the speed afforded by using a set of linked constitutive equations of state for property prediction.

GIM is particularly suitable for predicting the change in polymer properties observed upon introduction of a diluent into a thermosetting resin. First, the model deals with chemical cross-linking by reducing the degrees of freedom assigned to each mer unit with a cross-linked site. Secondly, the addition of diluents is accounted for by modifying the input parameters of the system according to the amount and type of extra molecules present. For example, water which is free to migrate through the network has a significantly higher number of translational degrees of freedom than a monomer which has reacted two or more times and is locked into the 3D network. Additionally, hydrogen bonding is accounted for by increasing the binding energy of the system for each hydrogen bond. In this way, multiple hydrogen bonding can be catered for in the property prediction routines.

The fundamental equation of state central to GIM is a modified Lennard–Jones potential function which describes the interaction energy between adjacent polymers,

E. This function has powers of six and three instead of the normal 12 and six because volume, *V*, is proportional to the square of the interchain separation distance, *r*. In a polymer, the chain length is significantly larger than *r* and is therefore assumed to be invariant. E_{coh} refers to the zero point cohesive energy, and V_0 is the zero point volume

$$E = E_{coh}\left[\left(\frac{V_0}{V}\right)^6 - 2\left(\frac{V_0}{V}\right)^3\right] \tag{9.6}$$

The potential function shown in Eq. (9.6) is used as the basis for the prediction of a series of thermo-mechanical properties for the polymer as a function of temperature, strain, strain rate, and pressure. Similarly, an equation for the prediction of the glass transition temperature of the polymer is derived by assuming the change from glassy to rubbery properties is centered on the temperature T_g, at which the attractive force between adjacent polymers is zero. At this point, large-scale motion becomes possible, resulting in a significant dissipation of stored energy which is lost as heat. Eq. (9.7) uses GIM principles to predict T_g using a remarkably limited set of inputs, including degrees of freedom, *N* and the Debye temperature, θ_1.

$$T_g = 0.224\theta_1 + \frac{0.0513E_{coh}}{N} \tag{9.7}$$

Eq. (9.7) predicts T_g via a baseline stiffness (the Debye temperature, often 550 K for phenylene-containing polymers) and a balance between attractive, binding energy (E_{coh}) and repulsive, thermal energy (the latter being governed by the degrees of freedom, *N*). A simplistic approach to achieving a higher T_g would be to increase E_{coh} without increasing *N* too much. Clearly, this is easier said than done, and it is worth repeating that thermoset resins with high T_g are also liable to be brittle. Correspondingly, an easy way of reducing T_g is to increase *N* without a significant simultaneous increase in E_{coh}. This is the exact situation which occurs when small molecules infiltrate a thermoset network. Water, in particular, adds significantly to the degrees of freedom of the system (translational freedom) but only makes a modest increase in the cohesive energy (hydrogen bonding). Overall, the T_g is reduced as much as 20°C for each 1% absorbed water present in the system.

By assigning values of E_{coh} and *N* for the epoxy, hardener, and water, the effect of adding increasing amounts of water to a cured epoxy can be modelled using GIM via Eq. (9.7). A typical set of parameters are given in Table 9.3 for TGAP cured with DDS.

Along with the composition of the cured resin (the epoxy−hardener ratio) and corrections to *N* (for cross-linking or translational freedom) and E_{coh} (for hydrogen bonding), the GIM prediction of T_g for dry TGAP−DDS is approximately 298°C. Each 1% of water added to the system reduces the predicted T_g in line with experimental values. The model predictions and experimental values can be seen in Fig. 9.8, where there is good agreement between the two sets of data. Experimental values are measured by dynamic mechanical thermal analysis (DMTA) and are presented as broad ranges as there is often significant scatter in the T_g of moisture-affected samples.

Table 9.3 GIM parameters for TGAP cured with DDS.

Functional group	N	E_{coh} (J/mol)
CH_2	2	4500
Phenylene	3	25,000
N	2	9000
CH(OH)	2	20,800
SO_2	2	45,000
O	2	6300
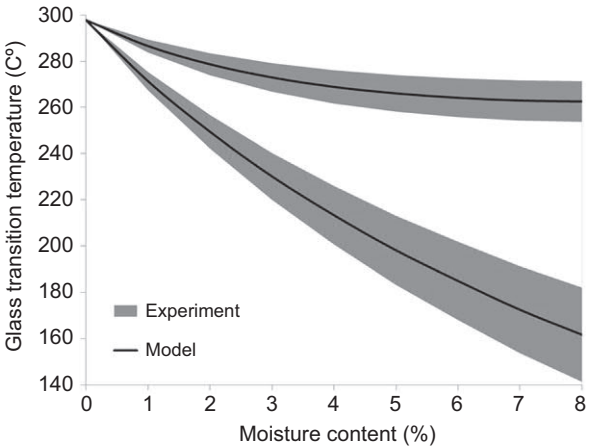
Figure 9.8 Schematic diagram showing the effect of absorbed moisture content on the glass transition temperature(s) in TGAP-DDS resin. The two broad ranges in experimental measurements illustrate the development of a secondary T_g peak. The GIM calculations using the parameters for singly (upper) and doubly (lower) hydrogen-bonded water predict this effect well.

The clear change from a T_g with one peak in the DMTA plot to two on the absorption of water is common to many epoxy resins, including DGEBA, TGAP, and TGDDM which represent functionalities of $n = 2$, 3 and 4. While the exact origin of this splitting of the T_g peak is still yet to be understood, the possibility that it is a result of absorbed water being singly and doubly hydrogen-bonded to the polymer network can be explored using GIM. The two solid lines in Fig. 9.8 are predictions of the change in T_g due to increasing moisture using one and two hydrogen bonds per water molecule. E_{coh} is increased, and N decreased to account for the extra hydrogen bond. The agreement with experimental values between the two sets of model parameters over a range of moisture contents adds weight to the argument that the peak splitting is caused by hydrogen bonding to differing levels.

9.4   Anomalous effects

9.4.1   Role of impurities and unreacted resin components

Cured resins behave as semi-impermeable membranes allowing water to diffuse but acting as a barrier to larger molecules so that osmosis can occur. Therefore, if the resin contains water-soluble impurities, thermodynamics will drive the water into the resin. Osmotic pressure (π) is a colligative property and is directly proportional to the molal concentration of the impurity. As shown in Eq. (9.8):

$$\pi = RT\,c \qquad\qquad\qquad (9.8)$$

where c is the molal (mol/kg) concentration of solubilized inclusions, T is the temperature, and R is the gas constant.

Since the moisture can plasticize and soften the resin, the pressure which develops at the inclusion will cause a blister to form. In the case of glass fiber−reinforced materials, this has been referred to as "boat pox." This is especially prevalent in fresh-water areas as opposed to sea environments because c in Eq. (9.8) will be the difference between the concentrations of impurities in the "resin" and the environment. In unsaturated polyester resins, the impurities leading to osmosis are likely to be residual acids and anhydrides or glycols from the synthesis of the unsaturated polyester. In the case of glass fiber composites, some aqueous-based sizings can also cause osmosis at the interface. Therefore, the selection of fiber "finish" is very important in the manufacture of a composite destined for use in aqueous (e.g., chemical plant or marine) environments. With advanced composite materials, osmosis is less of a problem but can occur. Dicyandiamide (DICY) is commonly used as a "latent" curing agent for epoxy resins. With a melting point of 160°C, solid DICY can be dispersed into the resin. Curing will only begin when the DICY melts. Accelerators are available which reduce the cure temperature. However, to achieve a satisfactory cure, without the formation of encapsulated DICY particles, it is essential to disperse them finely throughout the prepreg material; this is often referred to as micronization. If this is not done efficiently, enhanced moisture absorption can be observed. In some cases, this can lead to blistering. Furthermore, the hydrolysis products can provide an alkaline environment which can degrade glass fibers [7,8].

Chen and Birley [16,17] demonstrated that the residual stress state could contribute to the absorption of water, providing a thermodynamic mechanism akin to osmosis. Blisters were shown to occur at the interface between the gel-coat and structural resins, and they were attributed to localized residual stresses. To avoid blister formation on immersion in water or other aqueous environments, the presence of impurities, which can act as osmotic centers, needs to be minimized, and the properties of any gel-coat or surface finish should be matched to those of the structural resins.

9.5   Thermal spiking

Moisture absorption is also affected by brief excursions to elevated temperatures, which can lead to an enhancement of the concentration of absorbed moisture. This is referred to as thermal spiking. Thermal spikes as short as a minute can cause a significant increase in moisture content. A typical moisture absorption curve measured during the presence of a series of thermal spikes is given in Fig. 9.9. Above a maximum spike in temperature (Fig. 9.10), the moisture content falls [9]. This suggests that the matrix is responsible, and this is confirmed in Fig. 9.11, where it can be seen that the "thermal spiking" phenomenon is associated with the matrix and is not a consequence of combining the reinforcement with the resin.

9.6   Thermo-mechanical response of resins

Water molecules plasticize polar polymers, such as epoxy and other advanced resins used as matrices for fiber composites so that absorption of moisture can cause the glass transition temperature T_g, to be reduced significantly. This effect is illustrated in Fig. 9.12 [4] and therefore has an impact on the maximum service temperature available to a specific composite system. A rule of thumb for epoxy resins is that T_g is reduced on average by 20 K for each 1% of moisture absorbed [18]. Thus, a resin with 7% absorbed moisture at saturation can have its glass transition temperature reduced by 140 K.
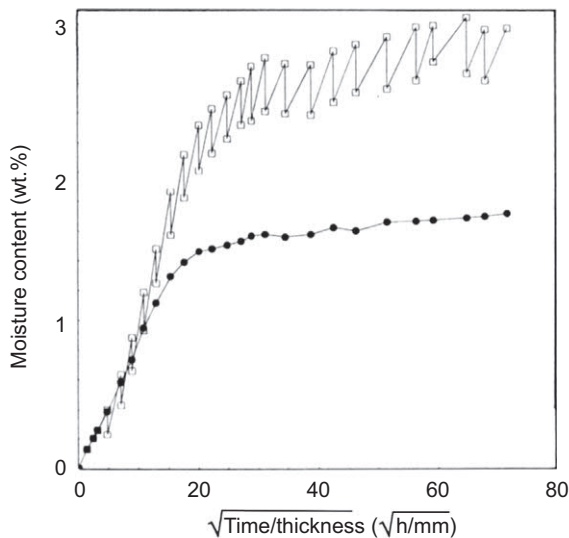
Figure 9.9 Illustration of the effect of thermal spiking to 140°C on the moisture absorption of a Fibredux 924C unidirectional laminate in 96% RH at 50°C. The individual points represent the actual moisture content immediately before and after a thermal spike. The continuous line is for the isothermal control under identical humid conditions [7].
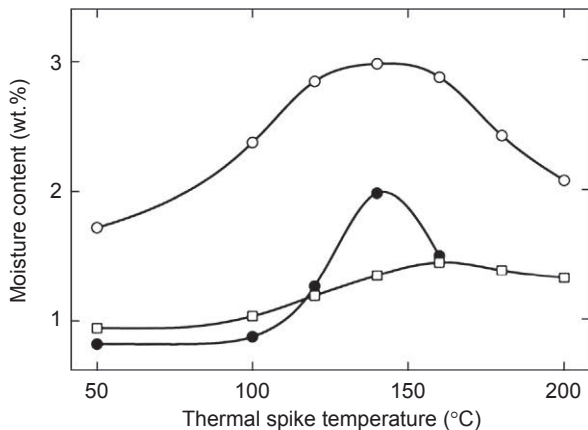
Figure 9.10 Moisture enhancement after thermal spiking of carbon fiber laminates conditioned at 50°C and 96% RH with 22 thermal spikes. Narmco Rigidite (●); Fibredux 927D (□); Fibredux 924C (○) [7].
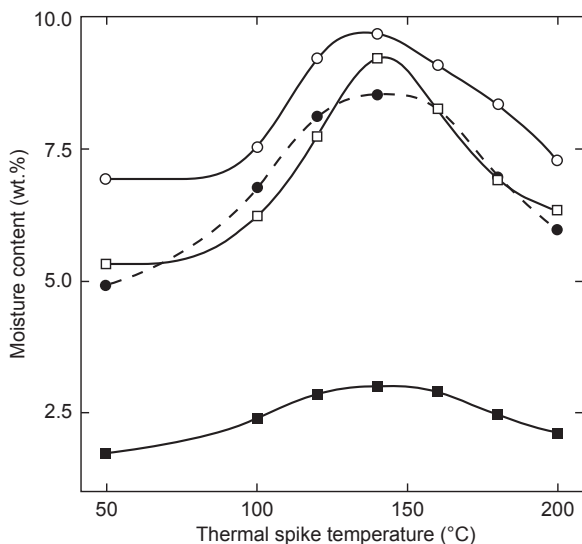
Figure 9.11 Moisture enhancement of matrix resins: Unmodified epoxy Fibredux 924E (○); thermoplastic modified epoxy Fibredux 924T (□); Fibredux 924T within a composite (estimated) (●); carbon fiber Fibredux 924C composite (■) [7].

A typical cured aerospace epoxy resin is highly cross-linked and may contain a dispersed non-polar thermoplastic or rubber which reduces the equilibrium moisture content and limits the reduction in T_g. As shown in Table 9.2, more advanced systems, such as an epoxy–cyanate ester blend, absorb lower concentrations of water at equilibrium. However, the water is not uniformly distributed so that the epoxy phase is still
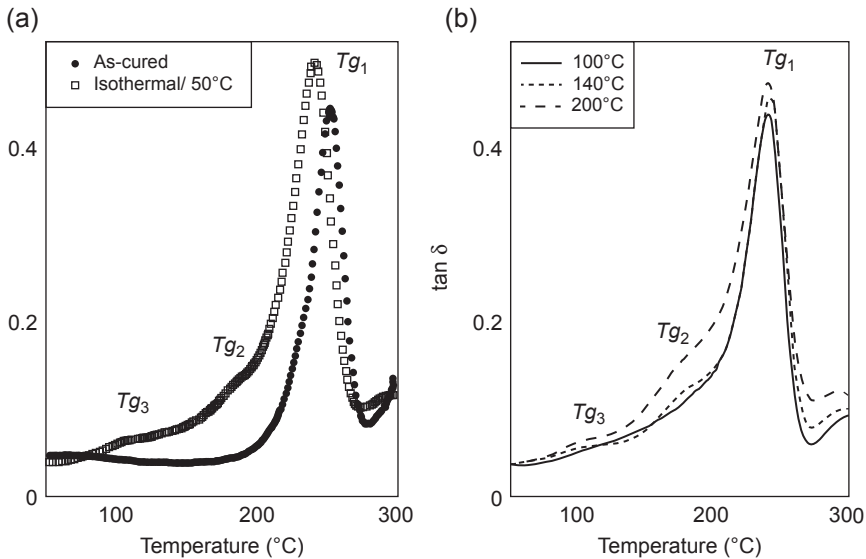
Figure 9.12 DMTA tan δ spectra of a cured, untoughened Fibredux 924 base epoxy resin showing the reduction of T_g with water absorption and the development of secondary peaks (T_{g2}, T_{g3}) on moisture absorption: (a) isothermally and (b) dynamically in the presence of thermal excursions to 100, 140 and 200°C [4].

plasticized to the same extent. Fig. 9.12 shows that the different component epoxies and/or hardeners are plasticized differentially with the development of additional relaxation peaks. We discussed the different degrees of water molecule hydrogen bonding as a function of network polarity in this chapter.

The maximum service temperature will also be affected since the resin modulus will tend to drop at the lowest relaxation temperature. Some modified systems also exhibit a larger reduction in T_g because of modifier hydrolysis, especially during thermal excursions. Therefore, an additional safety margin should be added to the highest service temperature. Since the T_g of a thermoset is a direct function of the cure or post-cure temperature, a resin cured at 150°C may have a long-term maximum useful temperature of only 100°C. This represents the design service temperature of the structure, although moisture equilibrium will be reached after several years.

The shear modulus of rubber is inversely proportional to the average network chain length according to the Gaussian theory of rubber elasticity [19]. Therefore, the examination of the storage modulus (E'_R) above the T_g provides the evidence for network hydrolytic resistance. Fig. 9.13 shows that the storage modulus (E'_R) of a thermally cured cyanate ester AroCy L10 falls as a result of thermal spiking at temperatures above 50°C in humid environments. The rubbery modulus is not affected by simple plasticization. Therefore, this resin is clearly susceptible to hydrolysis. The choice of hardener is critical, as shown in Fig. 9.13, where the thermally co-cured epoxy−cyanate ester is shown to be hydrolytically stable [9,20].
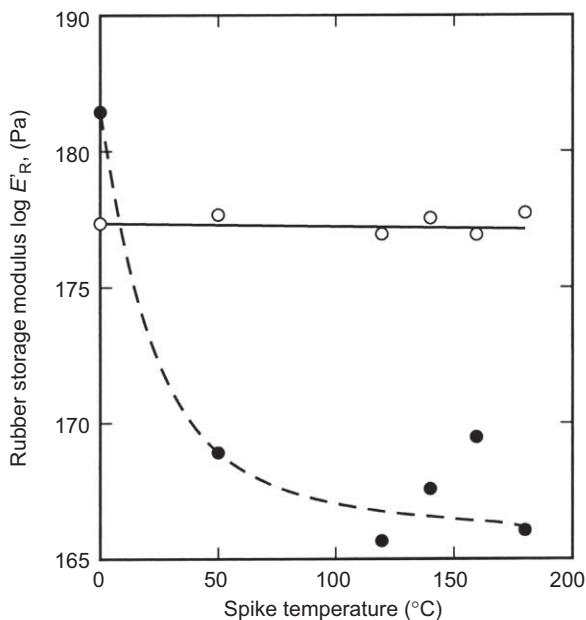
Figure 9.13 The rubber storage modulus of two cyanate ester resins as a function of moisture absorption with thermal spiking temperature illustrating the hydrolytic instability of the thermally cured AroCy L10 (●) compared to the stability of an epoxy-cured AroCy L10 (○) [7,19].

9.7 Effect of moisture on composite performance

9.7.1 Thermal stresses

Aerospace laminates are made from plies of embedded continuous fibers at different orientations. This is because of the anisotropy of the individual plies. That is, the thermal and mechanical properties are strongly dependent on the orientation of the fibers to the applied load. For example, the expansion coefficient parallel to the fibers (α_l) is significantly less than the expansion coefficient transversely to the fibers (α_t) while the modulus of a longitudinal ply (E_l) is significantly higher than the modulus of a transverse ply (E_t). Therefore, the matrix shrinkage at 90 degrees to the fibers, on cooling, is constrained so that a tensile thermal stress will develop in the plies transversely to the fibers while compressive stresses will be in the longitudinal or fiber direction. The stress-free temperature (T_1) is also an important parameter which determines the magnitude of the residual thermal stress. It is a function of the matrix glass transition temperature, and/or the cure or postcure temperature.

The tensile thermal strain in the longitudinal (l) direction of the transverse (t) ply (ε_{tl}^{th}) of a 0/90/0 laminate at temperature T_2 is given by Eq. (9.9):

$$\varepsilon_{tl}^{th} = \frac{E_l b (\alpha_t - \alpha_l)(T_1 - T_2)}{E_l b + E_t d} \tag{9.9}$$

where b and d are the thicknesses of the 0° ply and semi-90° plies.

In a 0°/90 degrees/0° laminate, Eq. (9.9) applies to the inner ply, but the thermal strain in the transverse direction of outer 0° plies will be slightly different and given by Eq. (9.10). The tensile thermal strain in the transverse (t) direction of the longitudinal (l) ply (ε_{lt}^{th}) is given by

$$\varepsilon_{lt}^{th} = \frac{E_l d(\alpha_t - \alpha_l)(T_1 - T_2)}{E_t b + E_l d} \tag{9.10}$$

The first failure of a composite, such as a simple 0°/90° /0° laminate usually occurs by transverse or matrix cracking of the 90° or transverse ply. Since the residual thermal stress in this direction is tensile, the first-ply failure will occur at a lower applied strain [21].

To balance the tensile thermal stresses, the plies will go into compression in the longitudinal direction. Thus, the thermal strain in the longitudinal (l) direction of the longitudinal (l) plies (ε_{ll}^{th}) is given by

$$\varepsilon_{ll}^{th} = -\frac{E_t}{E_l}\varepsilon_{tl}^{th} \tag{9.11}$$

Therefore, the 0° plies will fail at a slightly higher strain because of the induction of compressive stress into the fibers.

Furthermore, the thermal strain in the transverse (t) direction in the transverse (t) ply (ε_{tt}^{th}) is given by Eq. (9.12):

$$\varepsilon_{tt}^{th} = -\frac{E_t}{E_l}\varepsilon_{lt}^{th} \tag{9.12}$$

Under multidirectional stresses, such as an impact load, the fibers in the transverse plies will fail at a higher resolved strain.

9.7.2 Thermal cracking

The failure strain of a unidirectional fiber composite in the transverse direction is normally low because the matrix resins have relatively low failure strains while the large difference between the moduli of the components magnifies the strain in the matrix under stress. Thus, in an angle ply laminate, the first failure event occurs in the transverse ply or plies. Reloading of the transverse ply via shear stress transfer at the ply interfaces leads to multiple cracking before the fibers reach their failure strain. Since the thermal strain in these plies is tensile, the first-ply cracking of the laminate is less than that of an isolated 90 degrees ply.

Eq. (9.13) describes this observation:

$$\varepsilon_{tlu} = \varepsilon_{tu} - \varepsilon_{tl}^{th} \tag{9.13}$$

Transverse multiple cracking will be initiated on cooling after cure when ε_{tl}^{th} exceeds the ply failure strain (ε_{tu}). This can occur when either the stress-free temperature (usually, the glass transition temperature of the matrix) and/or the matrix expansion coefficient are high in magnitude. Thermal cracking can occur for similar reasons when the properties of the matrix change as a result of a thermal excursion.

Thermal fatigue is the phenomenon whereby the material exhibits damage resulting from multiple excursions to different thermal environments. The stresses will also be multidirectional, and in a composite laminate, the tensile stresses at 90 degrees to the fibers in all plies will vary during the heating cycles. Provided that there is no change in the expansion coefficients of the two plies, the material will be stable and transverse cracks will not form. However, if α_t is sensitive to temperature, there is a potential for thermal cracking at $90°$ to the fibers in all plies. Generally, thermal cycling of dry composite materials to temperatures lower than the cure temperature does not normally lead to thermal cracking during the cooling cycle.

9.7.3 Effect of moisture absorption

The resin matrix in a composite absorbs water in service. As discussed in this chapter, this process is kinetically slow, so the concentration of water in the resin will vary with time and location. Thermal cycling will tend to move the water into the structure. Furthermore, the absorption of the water causes the polymer to expand; however, in a composite, the swelling is constrained in an analogous way to that described for thermal contraction. Thus, the process of conditioning in moist environments leads to a reduction in the magnitude of the thermal strain present in the laminate.

The degree of swelling can be described quantitatively in analogous equations. For example, the swelling strain in the transverse ply in the longitudinal direction (ε_{tl}^s) is given by

$$\varepsilon_{tl}^s = \frac{E_l b (\beta_t - \beta_l)(M_1 - M_2)}{E_l b + E_t d} \tag{9.14}$$

where M_1 and M_2 are the initial and final moisture concentrations, respectively.

As a result, the thermal strain in a laminate (composite) will relax (i.e., reduced) on moisture diffusion. The extent of moisture swelling by resins used for composites can vary significantly, so the effect on the residual stress state differs widely. However, the major problem is not the benefits associated with thermal stress relaxation, but the fact that the plasticization of the matrix may enhance its expansion coefficient. Therefore, on cooling, a wet resin matrix either from its cure temperature or after a thermal cycle can, according to Eq. (9.9), lead to higher values of ε_{lt}^{th} and ε_{lt}^{th}. Fig. 9.14 shows how the transverse thermal strain in the 90 degrees ply reduced on isothermal moisture
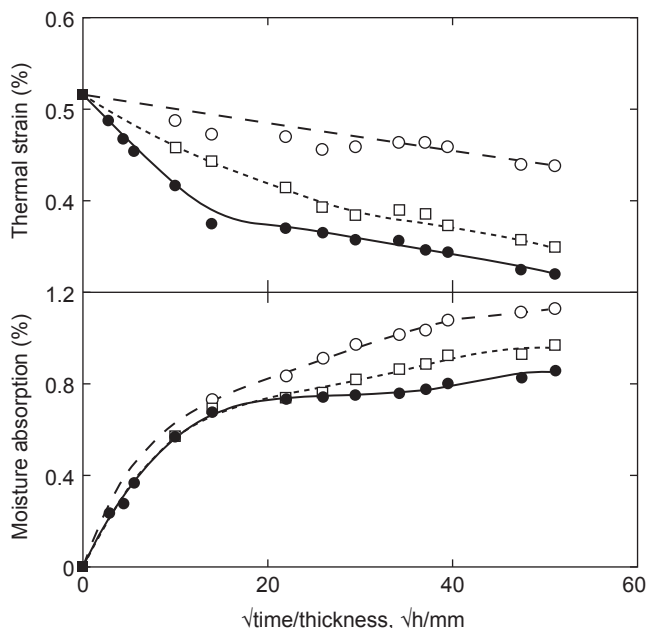
Figure 9.14 Effect of moisture absorption at 50°C and 96% RH on the thermal strain in a balanced 0°/90 degrees/0° 927C laminate estimated from the curvature of an unbalanced 0°/90 degrees beam [3]. Control (●); 120°C spike (□); 140°C spike (○) [7,22].

absorption and restrained matrix swelling but in the presence of a thermal excursion the combination of cooling from the elevated temperature and higher matrix expansion coefficient results in a much lower effect of moisture absorption. For some matrices, thermal spiking can enhance the residual thermal strain and cause thermal cracking [22].

The higher degree of contraction of a wet cross-linked polymer (which will be constrained) tends to arise from the appearance of a secondary relaxation peak or peaks in the expansion coefficient temperature profile. The thermal response will mirror any changes which occur in the DMTA spectrum. This may have its origin in the number of different types of polar groups present in the cured polymer matrix and their mechanism of interaction with water. Moisture absorption will decrease T_g and hence T_1, but since this is not usually exceeded in a thermal excursion, its influence on the thermal strain is limited. That means that during a thermal excursion, even to temperatures below the glass transition temperature or postcure temperature of the material, the higher constrained contraction on subsequent cooling may induce a higher residual thermal strain.

In Fig. 9.15 [23,24], the additional contraction, which manifests itself as an increase in residual thermal strain on cooling, is represented by the difference between the areas under the two curves. In the next cycle, moisture absorption may lead to further swelling of the material and a reduction in the thermal strain. However, after a
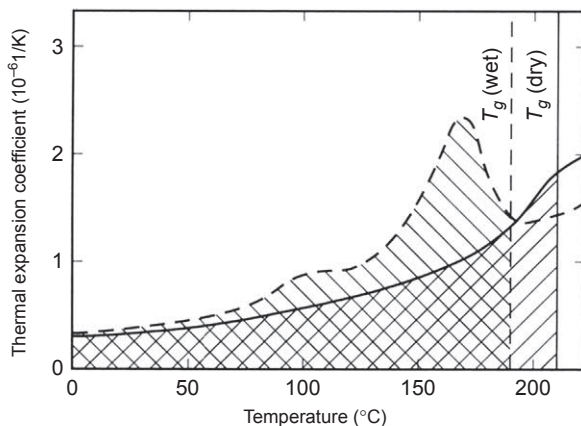
Figure 9.15 Temperature dependence of the transverse thermal expansion coefficients of a bismaleimide modified epoxy resin−based carbon fiber composite (Narmco Rigidite 5245C): dry (continuous curve) and wet (dashed curve). The hatching illustrates the differing constrained shrinkages (and hence, thermal strain) for wet and dry laminates [23,24].
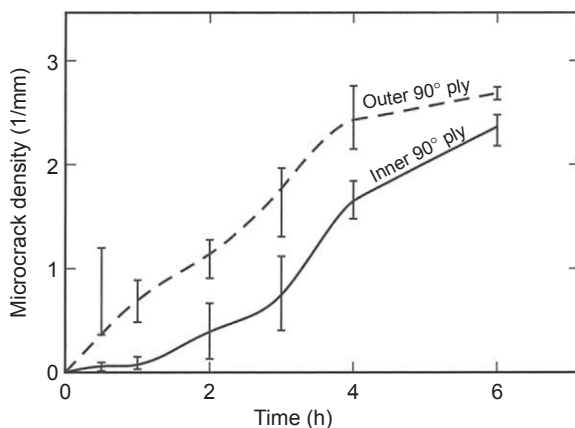
Figure 9.16 Thermal transverse cracking of a 0°/90 degrees/0° laminate from PMR15 during aging at 390°C [25].

subsequent thermal cycle, the thermal strain will be again enhanced. If the thermal stresses which are induced into the material exceed the transverse cracking strain of the individual ply, then thermal cracks will form. Because of the 3D nature of the thermal stresses, thermal cracking occurs in every ply. As shown in Fig. 9.16, thermal cracking of the plies will occur differentially because the moisture absorption will not be uniformly distributed throughout the material. In Fig. 9.16, the thermal cracking occurred more rapidly in the outer ply [25]. Matrix cracking during thermal cycling of PMR 15 composites is complicated by the release of volatiles during cure, which become occluded in the matrix. This causes the thermal expansion coefficients of

the plies and the stress-free temperature to vary during thermal cycling because these volatiles slowly desorb over a number of thermal cycles. As a result, the composites exhibit thermal cracking (or thermal fatigue) on cooling from each thermal excursion [26].

9.8   Fiber-dominated properties

Fiber choice is complex where cost often outweighs performance. For industrial composites, E glass therefore dominates. In aerospace, where cost can be spread over a longer life, often with savings in maintenance and service, carbon and other high-performance fibers are selected. For example, the high-modulus carbon fibers provide the highest dimensional stability of satellite dishes, where performance is critical.

9.8.1   Carbon fibers

Carbon fibers are commonly used in aerospace structures. There are various grades of carbon fiber ranging in modulus between 220 and 490 GPa for those prepared from polyacrylonitrile precursors. The in-plane theoretical modulus of graphite is 1000 GPa so that the perfection of the orientation of the graphite crystals to the fiber axis is responsible for the lower practical values. As a result, the stress−strain curve of an individual filament of high-strength carbon fiber ($E_f \approx 220-240$ GPa) will show increasing modulus with strain. From a strength perspective, there are no reports of static fatigue.

For pitch precursors, the refinement and spinning processes lead to larger crystals with better alignment to the fiber axis and hence a higher modulus.

With respect to the effect of environments, carbon fibers can be largely considered to be inert since they are stable to higher temperatures than the resin matrices can withstand. At temperatures above 300°C, the fibers begin to degrade in oxidizing atmospheres, but most polymers have a lower maximum service temperature. The advanced polyimides and PMR (polymerization of monomer reactants) systems can survive temperatures up to ≈ 450°C, but these are usually in short-term applications [27]. It is also unlikely that composites will be in contact with damaging solvents, such as concentrated oxidizing acids, such as sulfuric and/or nitric acids.

The fibers are not resistant to the temperatures encountered in metal and ceramic matrix composite melt processing, and protective coatings or low-temperature manufacturing routes are needed.

9.8.2   Advanced polymer fibers

Aerospace composite structures can also employ high-performance polymeric fibers, such as the aramids: Kevlar (DuPont) or Twaron (Teijin Twaron), poly(p-phenylene-2,6-benzobisoxazole) (PBO) (Toyobo) and high-modulus polyethylene

(PE) (Dynema, Certran, and Spectra). Generally, ultra-high-molecular-weight PE (UHMWPE) can be considered to be inert to most environments except that the service temperature is limited to <130°C.

Aramid fibers are aromatic polyamides. Therefore, the presence of the polar and hydrolysable amide group introduces the potential for moisture absorption up to 5%. As a result, these fibers exhibit time-dependent loss of strength or static fatigue in aqueous environments [28,29]. The fibers are spun from sulfuric acid solution so that residuals might be responsible. These fibers are also highly susceptible to hydrolysis in alkaline environments. As with other polymers, aramid fibers are susceptible to oxidation, especially in the presence of ultraviolet (UV) light. Fortunately, the degradation products help to protect the fibers since they act as a UV screen. However, protective coatings should be used for ropes and cables. Furthermore, the matrix for composites needs to prevent moisture from reaching the fibers and to screen out UV rays. Van Dingenen [30] has examined strength retention under these demanding environments. For composite applications, the sizing of aramid fibers has to provide chemical coupling between the fiber and the matrix for interfacial integrity as well as limiting moisture ingress.

PBO fibers may also be thermally sensitive, which has been attributed to acidic contaminants from the spinning solvent [31].

9.8.3 Glass fibers

The strength of a glass or other brittle material is determined by the presence of Griffith flaws [32]. By drawing glass into fibers, the population of flaws of critical dimension is reduced. Therefore, there will be a statistical distribution of strengths, which is commonly described using the Weibull model. However, Bartenev [33] and Metcalfe and Schmitz [34] have shown that fibers have three populations of flaws of different dimensions which are considered responsible for the length dependence of strength. Thus, commercial E-glass fibers typically have an average strength of 3 GPa with wide distribution as indicated by a Weibull modulus of ~4. Protective coatings (called *sizes*) are essential for protection from damage during processing. The site also contains adhesion promoters which ensure durable interfaces. This is discussed in detail elsewhere [3,35].
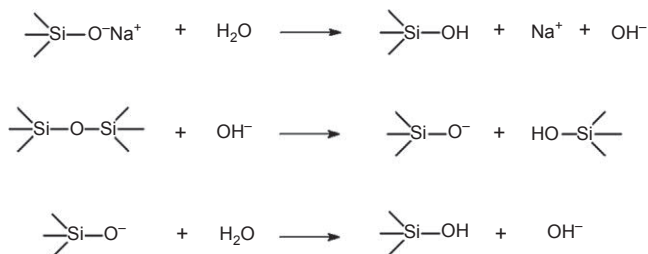
Figure 9.17 The mechanism of hydrolytic degradation of the silica network in E glass and related fibers, showing the catalytic role of Na^+ and $OH-$ ions.

Glass fibers exhibit time-dependent fracture under a static load, which is referred to as static fatigue [36]. Since there is no time dependence of strength in a vacuum, it is considered that water is involved in the reduction in strength. Thus, a stress corrosion mechanism in "condensed" water is inferred. The chemical reactions associated with this process are given in Fig. 9.17.

Thus, the sodium ions present in the E glass act as a catalyst for the degradation of the silica network, which is propagated by hydroxyl ions. The static fatigue of glass fibers involves three stages which operate at differing applied loads, according to the Charles mechanism [37].

Stage I is a stress-dominated region at high stresses where crack propagation is fast compared to the rate of reaction with water (i.e., fiber corrosion at the crack or flaw tip). The rate of diffusion of sodium ions to the surface is rate determining, and the fracture is dominated by the mechanical loading.

Stage II is the stress corrosion region where the rate of corrosion is similar to the rate of crack propagation. Therefore, the crack remains sharp and propagates into the weakened glass.

Stage III is the stress-assisted corrosion region where the effect of stress on the failure time is much less significant because the rate of hydrolysis of the silica network is higher than the rate of crack growth. The corrosive effect leads to a rounding of the crack tip. This reduces the potential for crack propagation according to the Irwin equation:

$$\sigma_{\max} = 2\sigma_a \left(\frac{x}{\rho}\right)^{\frac{1}{2}} \tag{9.15}$$

where σ_a is the applied stress and $\sigma_{\max}$ is the stress at a crack tip of depth, x, and radius, ρ.

A typical bundle of E-glass fibers can have a typical lifetime of $10^6 - 10^7$ min at an applied strain of $\approx 0.5\%$. This provides a lifetime of 2−20 years. Therefore, provided the fibers are protected from both mechanical damage and moisture diffusion, a composite could be expected to have a minimum lifetime, at 0.5% strain in the fibers, of approximately 20 years. From Eq. (9.1), one-sided exposure to water would extend the life of a 10 mm thick composite to $\approx$ 120 years and two-sided diffusion ≈ 30 years. Loss of interfacial integrity will lead to more rapid diffusion of the environment and will accelerate the degradation.

9.8.3.1 Thermal effects

The strength of E-glass composites is strongly affected by excursions to temperatures above 300°C. Feih et al. [38,39] have studied these effects in the context of durability on exposure to fire. Fig. 9.18 shows how the strength is retained up to approximately 300°C while at 350°C a strong temperature dependence has been observed.

The most likely mechanism involves the reversible hydrolysis of the silica network, which is shown in Figs. 9.19. Below $\sim$ 300°C, surface silanol groups will tend to
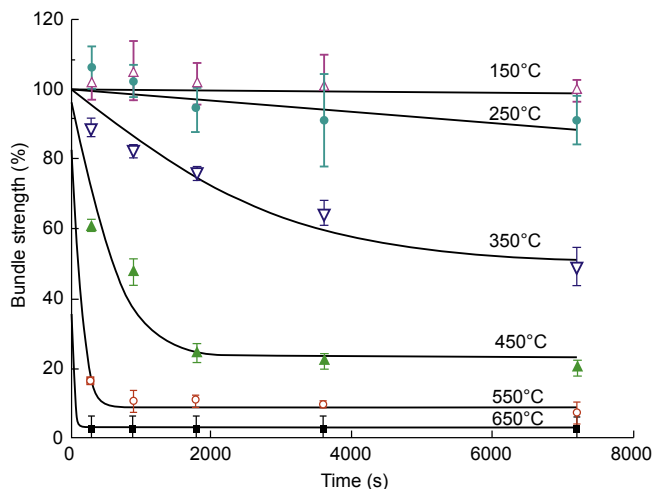
Figure 9.18 The effect of time at temperature on E-glass fiber bundle strength [35,38].

Figure 9.19 Mechanism of reversible hydrolysis of silica network in E glass and related fibers. Below 300°C, the reaction moves to the right; but at ≈ 350°C, hydrolytic degradation dominates [35].

condense to form siloxane bonds, whereas, above this temperature, hydrolysis dominates [35,38].

The change from strength stability below 300°C can be attributed to the thermodynamics of the above reaction. As with any chemical reaction, the rate of hydrolysis is a function of the presence of catalysts. Since the alkali metal glass modifiers (sodium−potassium) catalyze hydrolysis, alkali metal-free glasses are expected to show more resistance to high temperatures.

Recently, Owens Corning has replaced its E-glass fibers with boron-free formulations (Advantex). These fibers have similar mechanical properties to E glass but are believed to exhibit similar durability to ECR glass fibers which were developed for corrosion-resistant applications.

9.8.3.2 Environmental stress corrosion cracking (ESCC) of glass fibers

E-glass fibers have a reduced lifetime under load in the presence of moisture, but this is even more severe in a corrosive environment [40−42]. The rate of strength degradation in non-loaded E-glass fibers is maximized at a pH close to zero (i.e., in dilute aqueous mineral acids). Only in highly alkaline environments (pH ≈ 13) is a similar reduction in strength observed. Under load, ESCC of E-glass filaments also has a

$$SiO_2 + H_2O \underset{K_1}{\rightleftarrows} H_2SiO_3 \underset{K_2}{\rightleftarrows} H^+ + HSiO_3^- \underset{K_3}{\rightleftarrows} 2H^+ + SiO_3^{2-}$$
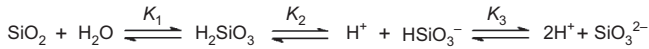
Figure 9.20 Hydrolysis and ionization of a silica network at differing pH [43].

maximum degradation rate in an environment of pH $\approx$ 0.2 (0.5 M H_2SO_4) [41]. ESCC occurs in acidic environments because the network modifiers (Ca, Na, Al, K, and Fe) are leached from E glass to leave the silica network largely intact. Therefore, for the fiber to fracture, a crack needs to propagate through the weakened glass sheaf which retains a covalently bonded structure.

In alkaline environments, hydrolysis of the silica network occurs sequentially with pH, as shown in Fig. 9.20 [43].

Thermodynamically, step 1 with equilibrium constant (K_1) occurs at a pH $\approx$ 10, and step 2 (K_2) at pH $\approx$ 12.5.

Therefore, at high pH, found with aqueous alkalis, a rapid hydrolysis of the silica network occurs. Any cracks can be blunted through corrosive mechanisms or ion precipitation. Therefore, weakening of the fibers is more important in alkaline environments, and brittle ESCC fractures are not normally observed (except when stress concentrations occur as a result of a crystallization pressure at the boundary between parts of the composite with a degraded and nondegraded interface) [44].

ECR and boron-free glass fibers have improved durability over E glass so that ESCC of glass fiber composites is less likely when modern glasses are employed. The design of glass fiber composites for resistance to stress corrosion cracking has been discussed in detail elsewhere [7,8].

9.9   Non-aqueous environments

Organic solvents are used in paints, in paint strippers, and as degreasing agents, so the resistance of organic polymer-based composites to these materials should be discussed. Cross-linked thermoset resins or crystalline thermoplastics do not dissolve in common organic solvents. However, the amorphous regions of the thermoplastics and the cured thermosets used as composite matrices will swell after contact. The solvent will tend to dissolve (i.e., diffuse) into the polymer in an analogous mechanism to moisture diffusion but at a higher rate. The degree of swelling will be maximized in contact fluids with a similar solubility parameter as the polymer matrix. The solubility parameters of the matrix and the solvent can be estimated using simple additive principles [45]. The concept of solubility parameters is simply described by Eq. (9.16):

$$\delta_{solvent} = \delta_{polymer} \tag{9.16}$$

where $\delta_{solvent}$ and $\delta_{polymer}$ are the solubility parameters.

The maximum plasticization of the matrix will occur under these conditions, which will lead to a high potential to creep under off-axis loads. The residual stress state will also be significantly modified, as discussed in this chapter.

Schulte [46,47] has demonstrated how different organic solvents, such as hydraulic fluid encountered in the aerospace structures, lead to a reduction in the secant modulus of $\pm 45°$ glass fiber laminate under flexural fatigue and the number of cycles to failure. The matrix, in this case, was a polyetherimide (PEI) which is plasticized by the ingress of the fluid. A reduction in the matrix modulus means that the shear strength of the matrix will also be reduced with the consequence that the failure mechanism in flexure will change from matrix-fracture to delamination.

Matrix swelling also contributes to the loss of durability in the $0°$ composite where plasticization causes buckling in the compressive face of the coupon [46,47]. This occurs because, in compression, the plasticized matrix is unable to support the reinforcement.

The reader should be reminded that PEI is an amorphous polymer and is much more susceptible to solvents than partially crystalline polymers, such as PEEK, which are used for structural composites.

Weatherhead [48] and Jones [7] provide a survey of the durability of resins to a range of environments.

9.10   Composite unidirectional properties

From the discussion in this chapter, it can be seen that the degradation of the fibers will lead to a reduction of the $0°$ strength of a ply or composite. However, in order to reach the fibers, diffusion of the environment through the matrix is anticipated. As described in this chapter, this can be a slow process unless the degradation of the interface has occurred, which promotes the ingress of the environment. Assuming that interfacial failure has not occurred, then the interaction of the environment with the matrix is important. If chemical degradation occurs, it is probable that the matrix will be embrittled and premature failure can occur, initiated by matrix cracking, or fiber breaks propagating into the degraded resin. Environmental stress corrosion cracking of glass fiber composites often arises from low-strain fiber breaks propagating into the matrix. Good design often uses ductile barrier resins in combination with the structural resin.

9.10.1   Tensile strength

Foreman and Behzadi [49−52] modelled the effect of matrix ductility on the unidirectional tensile strength of a carbon fiber composite. Fig. 9.21 shows how ductility of an epoxy resin leads to higher $0°$ strength. Interestingly, the best prediction is achieved when the viscoelasticity of the matrix is included in the model. Absorbed moisture and other solvents will increase the ductility of the matrix. The absorption of water or an organic solvent can be expected to plasticize the resin matrix. The reduction of the Tg and/or generation of lower temperature relaxation peaks will tend to reduce the yield strength of the matrix. As a result, ingress of small quantities of water or other environments will provide stress redistribution mechanisms near a fiber break. The tensile strength of the composite might increase. The complication arises from changes
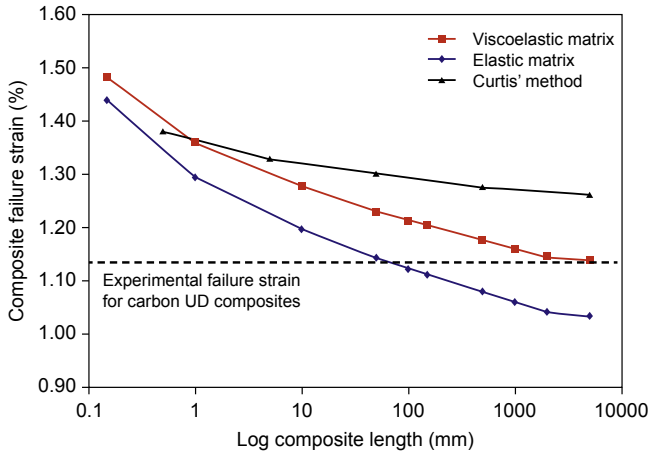
Figure 9.21 Plot of the relationship between the predicted unidirectional (UD) carbon fiber composite failure strain and composite length. The data are presented for a viscoelastic TGAP−DDS matrix and a purely elastic matrix. The dotted line represents a typical experimental failure strain for a UD carbon fiber composite [49].

in the residual stress state, which will tend to negate the thermal compressive stress in the fibers and reduce the strain to first fiber fracture.

Furthermore, the absorption of water by the interphasal polymer can reduce its yield strength below the interfacial bond strength. Thus, the "apparent" interfacial shear strength will be reduced, and a yield front, rather than a debond, will propagate along with the fiber interface modifying the stress transfer micromechanics at a fiber break. A consequence is that the stress concentrations in adjacent fibers to the fiber break will be reduced, and the probability of the formation of a flaw of critical dimensions is also reduced. The number of interacting fiber breaks associated with a flaw of critical dimensions will increase.

9.10.2 Compressive strength

In compression, the mechanism of failure changes from fiber fracture to fiber buckling. Here, the modulus of the matrix is a critical factor in supporting the fiber and by prevention of kinking (of the fibers) in a shear band. Soutis [53] has discussed the modeling of these types of failure using Eqs. (9.17) and (9.18):

$$\sigma = \frac{\tau_y \left[1 + \left(\frac{\sigma_{ty}}{\tau_y} \right)^2 \tan^2 \lambda \right]^{1/2}}{\phi_\theta + \phi} \tag{9.17}$$

where τ_y and σ_{ty} are the in-plane shear and transverse yield stresses of the composite, respectively. ϕ_0 is the assumed fiber misalignment angle in the kink band, ϕ is the additional fiber rotation in the kink band under a remote compressive stress σ, and λ is the band orientation angle.
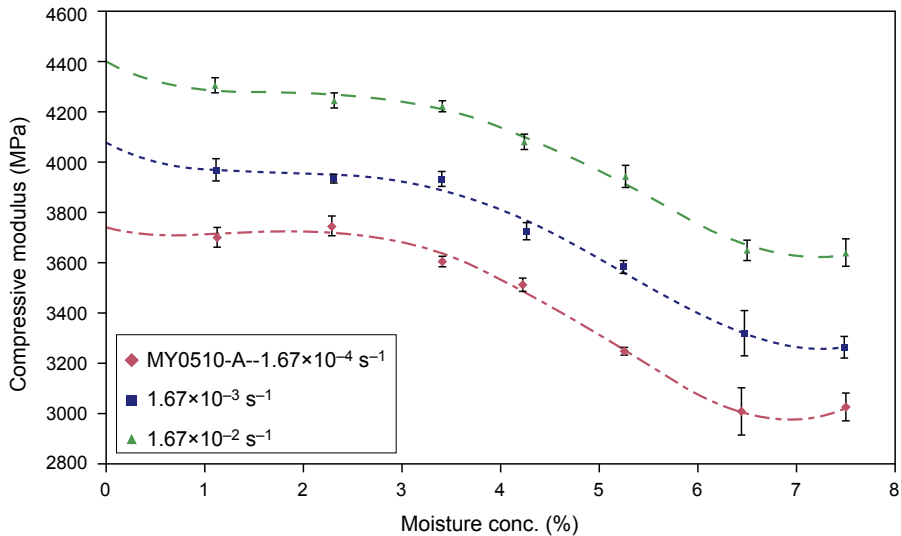
Figure 9.22 The effect of water absorption on the compression modulus of TGAP epoxy resin cured with DDS. The experiments were conducted at different three strain rates at 22°C [54].

$$\tau(\gamma) = \tau_{ult}\left[1 - \exp\left(-\frac{G_{12}\gamma}{\tau_{ult}}\right)\right] \tag{9.18}$$

where G_{12} is the elastic shear modulus, γ is the shear strain, and τ_{ult} is the shear strength.

Fig. 9.22 shows how the compressive modulus of a TGAP−DDS epoxy resin is reduced by moisture absorption. At the highest strain rate, the compressive modulus fell from 4.4 to 3.6 GPa on the absorption of 7% water. It is also noticed that initial moisture absorption is not so deleterious. This is because the unoccupied volume (sometimes referred to as *free volume* 'free volume') will be filled first before plasticization occurs.

The reduction in compressive modulus will have an effect on the compressive yield strength, as shown in Fig. 9.23. The trend is different in that it is a continuous decrease. This is most likely a result of the load state near the yield point when the water molecules become mobilized. The compressive properties of unidirectional carbon fiber composites have been studied by Soutis [53], where the reduction in shear yield strength and compressive modulus causes fiber kinking to occur at lower stresses. Table 9.4 shows the measured and predicted compressive strengths of 0° carbon fiber (T800) Fiberdux 924 epoxy composites in the presence of absorbed moisture. This shows that absorbed moisture and/or possible organic cleaning solvents cause the deterioration of the compressive properties of composite materials.

The compressive properties of a composite under all loading conditions are strongly affected by moisture absorption because of the reduction in shear properties of the matrix polymer. The design of artifacts with polymer matrix composites needs to reflect the limitations of these materials in compression, especially in service where environmental conditioning is likely.
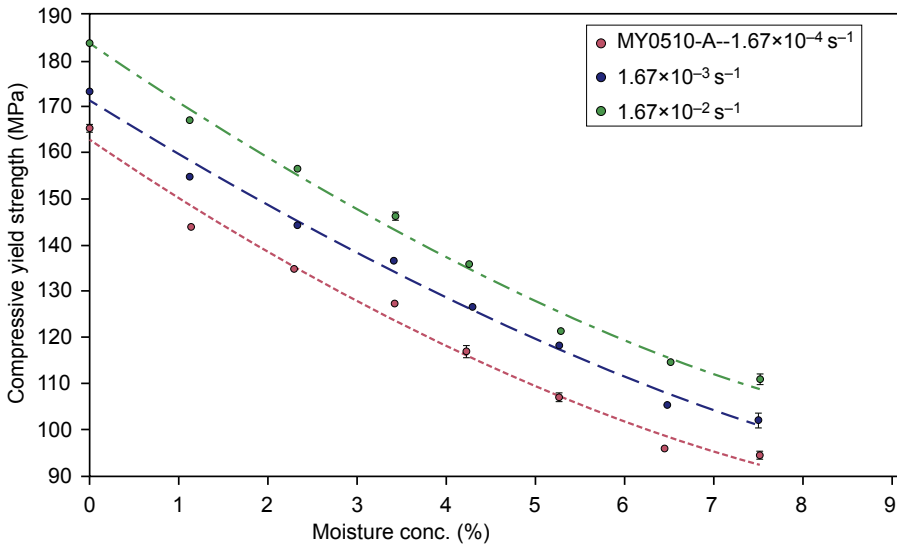
Figure 9.23 The effect of water on the compressive yield strength of TGAP epoxy resin cured with DDS. The experiments were conducted at different strain rates at 22°C [54].

9.11 Conclusions

This chapter reviews the state of knowledge regarding moisture absorption by aerospace composites in service. The discussion centers on the generic use of epoxy resins as matrices for polymer matrix composites. Some reference to other matrices is also made, but we have limited this in order for the main principles to be understood. Moisture ingresses into these resins relatively slowly so that the effects on the mechanical properties are complex. The moisture mainly influences the thermo-mechanical properties of the matrix, and so we concentrate on how thermal strains, tensile, and compressive properties of the composites are affected.

In order to achieve these objectives, we discussed the diffusion of moisture into these materials using Fickian kinetics and recognized that for composites based on glass or carbon fibers, the changes in matrix properties are critical. Using Group Interaction Modelling, the mechanisms responsible for these changes are confirmed. Of relevance to this book is the point that for many aerospace epoxy resins, moisture absorption can lead to additional relaxation peaks in their thermo-mechanical response. As a result, the service temperature of polymer matrix composites will be reduced. Thus, the compressive properties are strongly affected because the matrix carries the shear stresses which develop. Fortunately, the diffusivity is such that sufficient water is only absorbed over many years.

One means of reducing the time scale of moisture absorption is to subject the structure to rapid thermal excursions. Because the original structure of the cured epoxy resin is in a nonequilibrium state, thermal spiking can lead to more rapid moisture absorption. Relaxation of the matrix structure will occur as a result of these moisture and thermal events. Other mechanisms which lead to enhanced moisture concentrations are discussed in the context of matrix resin and fiber selection.

Table 9.4 Measured compressive strength properties of T800/924C unidirectional (0°) laminates at a range of temperatures at 95% relative humidity [53].

Test temperature (°C)	Compressive strength (MPa) Expt	Compressive strength (MPa) prediction	Young's Modulus[a] (GPa)	Shear strength (MPa)	Shear yield stress (MPa)	Shear modulus[b] (GPa)
20-dry	1415	(1411)	160	110	40	6.0
20-wet	1060	(1040)	—	(89)	(29.5)	(5.4)
50-dry	1230	(1235)	155	105	35	5.8
50-wet	930	(917)	—	(78)	(26)	(5.4)
80-dry	1137	(1129)	149	98	32	5.4
80-wet	828	(829)	—	(69)	(23)	(4.9)
100-Dry	973	(953)	136	90	28	4.9
100-Wet	654	(653)	—	(54)	(18.5)	(4.5)

Moisture content, $M_\infty = 1.42\%$. Assumed initial fiber misalignment, $\phi_0 = 1.75$ degrees; kink band inclination angle, $\lambda = 15$ degrees; the value of ϕ_0 is not affected by the environmental test conditions. ( ) estimates from Eqs. (9.17) and (9.18) and the measured unidirectional compressive or shear strength properties.
[a]Secant axial modulus measured at 0.25% axial strain.
[b]Secant shear modulus measured at 0.5% shear strain.

The effect of moisture absorption on composite performance has been discussed in terms of changes in thermal strain in cross-ply laminates and the introduction of transverse cracks during thermal excursions. The nature of the failure of unidirectional plies under tensile and compressive loads is also discussed in detail.

The conclusions of this chapter should be kept in mind when considering the failure mechanisms described in other parts of this book when selecting the matrix resins and reinforcing fibers for the design of durable composite structures.

References

[1] L. Nicolais, A. Borzacchiello, S.M. Lee (Eds.), Wiley Encyclopedia of Composites, second ed, John Wiley & Sons, Hoboken, New Jersey, 2012.

[2] D. Middleton, Composite Materials in Aircraft Structures, Longman, Harlow, 1990.

[3] F.R. Jones, The Interphase in Fibre Composite Materials, vol. 3, Wiley Encycl Compos, 2012, pp. 1396−1402.

[4] J.A. Hough, Enhanced Moisture Absorption in Advanced Composites [Ph.D. Thesis], University of Sheffield, 1997.

[5] G.S. Springer, Environmental Effects on Composite Materials, vol. 1, Technomic, Westport, USA, 1981.

[6] C.H. Shen, G.S. Springer, J. Compos. Mater. 10 (1976) 2−20.

[7] F.R. Jones, Durability of reinforced plastics in liquid environments, in: G. Pritchard (Ed.), Reinforced Plastics Durability, Cambridge, Woodhead, 1999, pp. 70−110.

[8] F.R. Jones, The effects of aggressive environments on long-term behaviour, in: B. Harris (Ed.), Fatigue in Composites, Cambridge, Woodhead, 2003, pp. 117−146.

[9] Z.D. Xiang, F.R. Jones, Compos. Sci. Technol. 57 (1997) 451.

[10] S.K. Karad, F.R. Jones, D. Attwood, Polymer 43 (2002) 5209−5218.

[11] S.K. Karad, F.R. Jones, D. Attwood, Polymer 42 (2002) 5643−5649.

[12] J.P. Foreman, F.R. Jones, D. Porter, S. Behzadi, Polymer 49 (25) (2008) 5588−5595.

[13] J.P. Foreman, D. Porter, S. Behzadi, F.R. Jones, Compos Part A 41 (9) (2010) 1072−1076.

[14] J.P. Foreman, D. Porter, S. Behzadi, K.P. Travis, F.R. Jones, J. Mater. Sci. 41 (20) (2006) 6631−6638.

[15] J. Mijovic, H. Zhang, Macromolecules 36 (4) (2003) 1279−1288.

[16] F. Chen, A.W. Birley, Plast., Rubber Compos. Process. Appl. 15 (1991) 161.

[17] F. Chen, A.W. Birley, Plast., Rubber Compos. Process. Appl. 15 (1991) 169.

[18] W.W. Wright, Composites 12 (1981) 201.

[19] S.K. Karad, D. Attwood, F.R. Jones, Compos A 33A (2002) 1665−1675.

[20] L.R.G. Treloar, The Physics of Rubber Elasticity, third ed., Clarendon Press, Oxford, 1975.

[21] J.E. Bailey, P.T. Curtis, A. Parvizi, Proc. R. Soc. Lond. A366 (1979) 599.

[22] Calota E, Jones FR. Unpublished data; 1997.

[23] F.R. Jones, Handbook of Polymer-Fibre Composites, Longman, Harlow, 1994.

[24] P.M. Jacobs, F.R. Jones, S.W. Tsai, in: G. Springer (Ed.), Composite Design, Manufacture and Application (ICCM VIII), vol. 2, SAMPE, Corina, CA, USA, 1991.

[25] Z.D. Xiang, F.R. Jones, M.S. Found, Effect of isothermal ageing on thermomechanical stability of carbon fibre reinforced PMF-15 resin matrix composites, in: Experimental Techniques and Design in Composites Materials, Sheffield Academic Press, 1995, pp. 406−420.

[26] P.M. Simpson, F.R. Jones, Composites 22 (1991) 105.

[27] Z.D. Xiang, F.R. Jones, Compos. Sci. Technol. 47 (1993) 209.

[28] A. Howard, N.J. Parratt, Life prediction for aromatic polyamide reinforcements, in: W.C. Harrington, J. Strife, A.K. Dhingra (Eds.), ICCM 5, Warrendale, PA, USA, 1985, pp. 277−292.

[29] M. Horio, T. Kaneda, S. Ishikana, K. Shimamura, J Fibre Sci Technol Jpn 40 (1984) 1285.

[30] J.L.J. van, Dingegen Gel spun high performance polyethylene fibres, in: J.W.S. Hearle (Ed.), High Performance Fibres, Woodhead, Cambridge, 2001.

[31] A. Pegoretti, M. Traina, Liquid crystalline organic fibres and their mechanical behaviour, in: A.R. Bunsell (Ed.), Handbook of Tensile Properties of Textile and Technical Fibres, vol. 12, Cambridge, Woodhead, 2009, pp. 354−436.

[32] A.A. Griffiths, Philos. Trans. R. Soc. Lond. A221 (1920) 163.

[33] G.M. Bartenev, The Structure and Mechanical Properties of Inorganic Glasses, Walters-Noordhoff, Groningen, 1970.

[34] A.G. Metcalfe, G.K. Schmitz, Glass Technol. 13 (1972) 5.

[35] N.T. Huff, F.R. Jones, The structure and properties of glass fibres, in: S.J. Eichhorn, et al. (Eds.), Handbook of Textile Fibre Structure. Natural, Regenerated, Inorganic and Specialist Fibres 2, Cambridge, Woodhead, 2009, pp. 307−352.

[36] W.F. Thomas, Phys. Chem. Glasses 1 (1960) 4−18.

[37] R.J. Charles, J. Appl. Phys. 29 (1958) 1549.

[38] S. Feih, A.P. Mouritz, Z. Mathys, A.G. Gibson, J. Compos. Mater. 41 (2007) 2387−2410.

[39] S. Feih, K. Manatpon, Z. Mathys, A.G. Gibson, A.P. Mouritz, J. Mater. Sci. 44 (2009) 392−400.

[40] H. Sekine, P.W.R. Beaumont, Compos. Sci. Technol. 58 (1998) 1665−1689.

[41] D.R. Cockram, Glass Technol. 22 (1981) 211−214.

[42] F.R. Jones, J.W. Rock, J. Mater. Sci. Lett. 2 (1983) 415−418.

[43] P.G. Fox, Mechanisms of environmentally sensitive cracking in glasses, in: Proc. Congr. On Mechanisms of Environmental Stress Cracking, Metals Soc, London, 1977, pp. 268−282.

[44] P.A. Sheard, Transverse and Environmental Cracking of Glass Fibre Reinforced Plastics, University of Surrey, 1986 [Ph. D. thesis].

[45] D.W. van Krevelen, K. Te Nijenhuis, Properties of Polymers, Elsevier, 2009.

[46] K.L. Schulte, Cyclic mechanical loading, in: G. Pritchard (Ed.), Reinforced Plastics Durability, vol. 5, Cambridge, Woodhead, 1999, pp. 151−185.

[47] K. Schulte, A. Mulkers, H.D. Berg, H. Schoke, Environmental influence on the fatigue behaviour of amorphous glass/thermoplastic matrix composites, in: S. Degallaix, C. Bathias, R. Fongeres (Eds.), International Conf. On Fatigue of Composites, 1997, pp. 339−346.

[48] R.G. Weatherhead, FRP Technology, Fibre Reinforced Resin Systems, Applied Science Publishers, London, 1980.

[49] S. Behzadi, P.T. Curtis, F.R. Jones, Compos. Sci. Technol. 69 (2009) 2421.

[50] J.P. Foreman, S. Behzadi, D. Porter, P.T. Curtis, F.R. Jones, J. Mater. Sci. 43 (20) (2008) 6642−6650.

[51] J.P. Foreman, S. Behzadi, S.A. Tsampas, D. Porter, P.T. Curtis, F.R. Jones, Plast Rubber Compos 38 (2−4) (2009) 67−71.

[52] J.P. Foreman, S. Behzadi, D. Porter, F.R. Jones, Philos. Mag. 90 (2010) 4227−4244.

[53] C. Soutis, Plast Rubber Compos 38 (2009) 55−60.

[54] S. Behzadi, Role of Matrix Yield in Composite Performance, University of Sheffield, UK, 2006 [Ph. D. Thesis].

Fatigue of polymer composites 10

Ramesh Talreja

Department of Aerospace Engineering, Department of Materials Science and Engineering, Texas A&M University, College Station, TX, United States

10.1 Introduction

The recent success of polymer composites in civil aviation is attributed not only to fuel savings by lightweight properties of these materials but also to their high fatigue resistance. The higher fatigue limit of unidirectional composites in cyclic axial tension compared to that of Al alloys, when measured in strain, has allowed higher design loads in composite structures. However, the fatigue performance of polymer composites in different loading combinations and different laminate configurations differ significantly. Optimal designs cannot, therefore, be achieved by arbitrarily setting the allowable strain levels to low values. The alternative of testing to find safe design values is not cost-effective. The mechanisms underlying fatigue failure of the constituents and their interfaces must, therefore, be understood, and this knowledge incorporated in predictive models. Addressing this problem is exacerbated by new developments in fibers and polymers and by a variety of manufacturing methods to construct composite structures.

Beginning with the paper in 1981 [1], this author introduced a conceptual framework for the interpretation of the fatigue behavior of composites called a fatigue life diagram (FLD). In its baseline form, the FLD separates the fatigue failure in three regions based on the underlying dominant mechanisms. One region denoted as Region I, characterizes the fiber-failure dominant mechanism, where failure is heavily governed by the statistical nature of the fiber failure, and therefore, the resulting composite fatigue shows negligible dependence on load cycles. Region II is controlled by progressive mechanisms, such as irreversible deformation of the matrix and matrix crack growth, leading to damage accumulation culminating in a critical condition of ultimate failure. Finally, Region III is where failure mechanisms do not progress to criticality within a prespecified large number of load cycles because of local obstacles to growth imparted by fiber-architectural features and interfaces. The demarcation between Region II and Region III forms the fatigue limit. The FLD clarifies the relative significance of these regions for a given combination of fibers and matrix.

10.2 Construction of FLDs

Let us begin with Region I, which, as stated above, signifies the fiber failure dominated mechanism. Fig. 10.1 depicts three failure scenarios under a tensile load P. Fig.10.1(a)
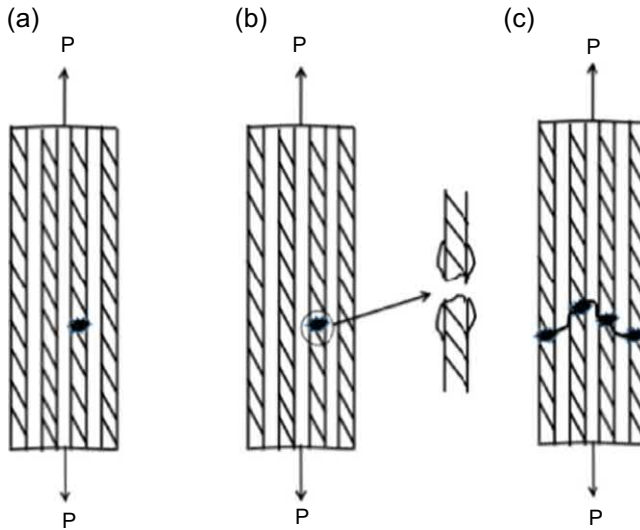
Figure 10.1 Fiber failure scenarios under a tensile load P. (a) A dry fiber bundle with the weakest fiber failure; (b) A fiber composite with the weakest fiber failure and debonding over a short length; (c) Composite failure from the linkage of failed fiber regions.

shows a dry fiber bundle in which the first fiber failure is indicated at the weakest point. At the instant of this fiber failure, the load is shared equally by the surviving fibers, and on increasing the load, the next failure occurs at the weakest point in these fibers. If, however, the load is not increased but is reduced to some value, say zero, and reapplied, no further fiber failures occur. Thus, there is no fatigue failure process. This assumes that fibers do not have a fatigue degradation mechanism.

Consider now the scenario depicted in Fig. 10.1(b) where a unidirectional composite is loaded in axial tension and the first fiber has failed at a certain value of P. The failed fiber will likely also debond over a length depending on the interfacial characteristics. If the load P is reduced to zero and reapplied to this value, the question arises: will another fiber fail? To answer this question, we note first that on the failure of the first fiber, not all other fibers but a few fibers in close vicinity of the failed fiber are affected. This leads to what is known as local load sharing, the extent of which depends on the debonded length of the failed fiber. Thus, in the local load sharing, an affected fiber can fail if its strength is exceeded at some point over its affected length. If this occurs, it will occur instantaneously, if no time dependency of deformation exists in the fibers, matrix, or interfaces. To avoid unnecessary complication at this point, we assume that all deformation is time-independent. If the load P is reduced to zero and reapplied to the previous value, no further failure is possible unless an irreversible deformation has occurred. Such deformation will redistribute the stresses in the local load sharing region during the unloading and reloading process and create a new stress field, which can result in new fiber failure. Due to the statistical nature of fiber failures, however, there is no certainty that the next fiber failure will occur in the second or a

subsequent load cycle. Thus, a random process of fiber failure ensues. More significantly, the critical condition in which the failed fibers in the local load sharing region connect through the matrix and interface cracks, leading to an unstable growth of the connecting failure plane, occurs much more randomly. In fact, this condition of composite failure depicted in Fig. 10.1(c), is of such random nature that it may be rightly described as a chaotic process because of its high sensitivity to the initial condition, i.e., the first fiber failure. This also means that a well-defined progression in the fiber failure process that can be described by a rate equation does not exist. Therefore, the final failure event is for all purposes cycle-independent.

Region I of an FLD corresponding to the fiber failure dominant mechanism is sketched in Fig. 10.2. The vertical axis of the FLD is the maximum strain ε_{max} applied to the composite in the fiber direction. Although the load P is applied and reapplied, the first applied maximum strain makes a proper reference for the load level since it is the same irrespective of the fiber volume fraction, while fiber stress is not. Fig. 10.2 shows Region I as a scatter band centered around the mean strain to static (first load application) failure ε_c of the composite. The scatter band shown in the figure is for 5% and 95% probabilities of failure, as an example. The scatter band is shown flat (horizontal) to indicate that the initial (static) statistical variability does not change with the number of load cycles applied. As described and argued above, if on the first application of the tensile load the composite does not fail, but at least one fiber within the composite fails, then the composite can fail at any number of subsequent cycles. This will then lead to the scatter band of composite failure becoming independent of the number of cycles. It is possible, however, that the width of the scatter band changes (possibly reduces) with the number of cycles applied, but an analysis to determine that change is currently not feasible.

Consider now the case where the first application of load (ε_{max}) is below the scatter band depicted in Region I. The composite failure then will be less likely to be dominated by fiber failures. Instead, the irreversible deformation and crack formation mechanisms in the polymer matrix and at the fiber/matrix interfaces will gain more
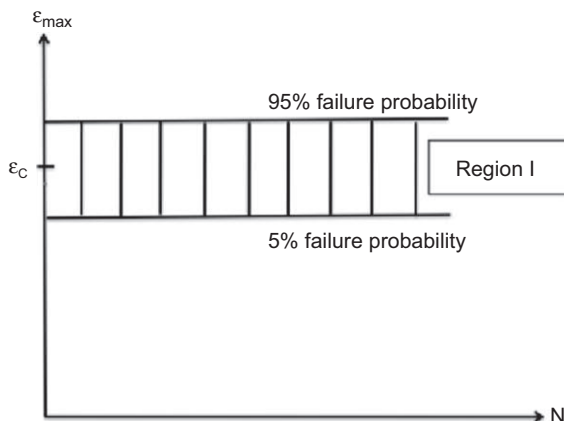
Figure 10.2 Region I of a fatigue life diagram.

prominence. These mechanisms were studied extensively and reported in Ref. [2] for a carbon/epoxy (AS4/8552) unidirectional composite loaded in cyclic tension at the load ratio (P_{min}/P_{max}) of R = 0.1 and cyclic frequency of 10 Hz. Surface replicas were collected periodically at different load levels using cellulose acetate films. After replication, the films were hardened and coated with a layer of carbon by sputtering. They were then observed under a microscope. Fig. 10.3 shows a series of micrographs showing the progression of a crack on the specimen surface and Fig. 10.4 shows more clearly how a crack is bridged by fibers. The crack opening profile evident in Fig. 10.3 has the crack-tip region squeezed, which can be attributed to the closing pressure on crack surfaces induced by the bridging fibers.

The study [2] also indicated the effect of fiber/matrix debonding on the fiber-bridged matrix cracking as the operating progressive failure mechanism in Region II. The progression of this cracking mechanism is governed by fiber breakage, which is accelerated when a greater length of fibers is exposed to an enhanced stress by debonding, thereby increasing their propensity to failure. With sufficient debonding,
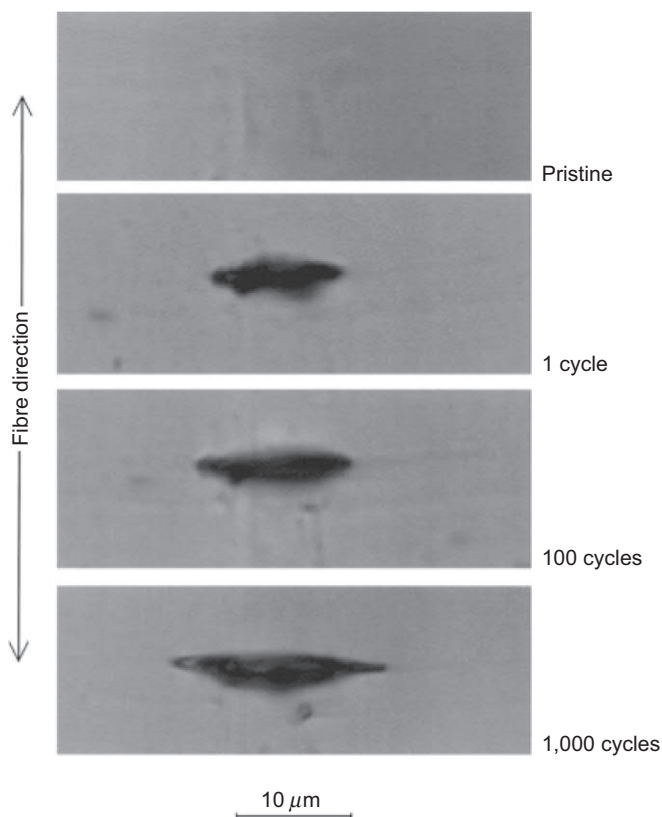
Figure 10.3 Micrographs of surface replicas showing a matrix crack at different applied load cycles [2].
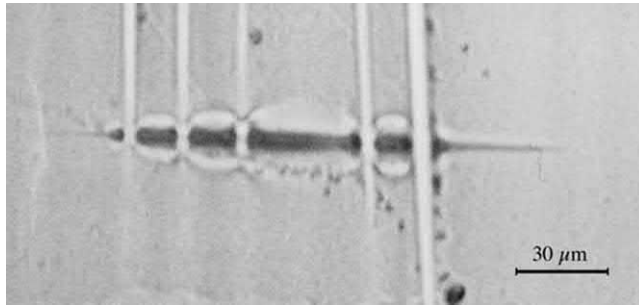
Figure 10.4 Micrograph showing a matrix crack bridged by fibers [2].

the progressive failure mechanism is then essentially fiber breakage, whose unstable progression leads to the composite failure.

Fig. 10.5 illustrates the appearance of Region II in the FLD. The random rate of fiber breakage leads to the scatter band in Region II, as indicated.

Finally, Region III represents the cracking mechanisms that have such low driving forces that the energy barriers placed by fibers in the crack paths cannot be overcome to reach the critical state of unstable growth. Fig. 10.6 shows this region of the FLD with the insert in the figure illustrating a matrix crack arresting mechanism. The fatigue limit, below which Region III lies, is the limiting state of the progressive mechanisms in Region II.

Fig. 10.7 is now the entire FLD for a unidirectional composite under axial fatigue where the three regions of the FLD (Figs. 10.2, 10.5 and 10.6) have been put together. The effect of increasing the stiffness of fibers is indicated in the FLD. This effect is a consequence of the bridging action of fibers running across a growing matrix crack (insert in Fig. 10.5) and the constraining effect on the matrix cracks by the surrounding fibers (insert in Fig. 10.6).

Fig. 10.8 shows the actual fatigue life data with superimposed FLDs for a lower fiber stiffness case (glass/epoxy) and a higher fiber stiffness case (carbon/PEEK). As can
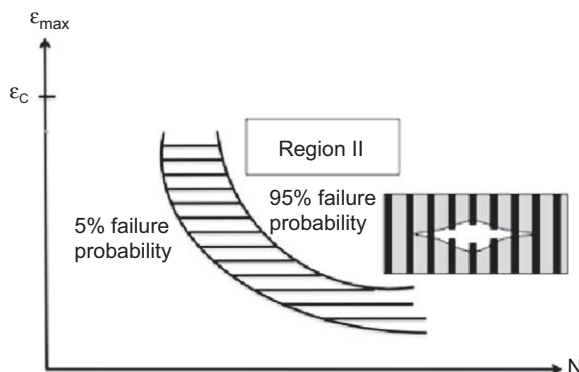
Figure 10.5 Region II of the fatigue life diagram.
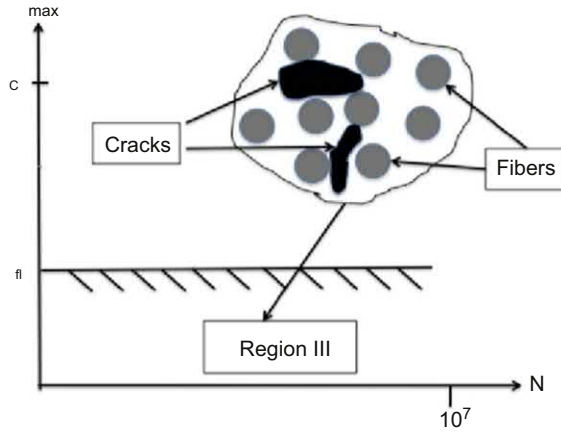
Figure 10.6 Region III of fatigue life diagram indicating the mechanism of matrix crack arrest by fibers.
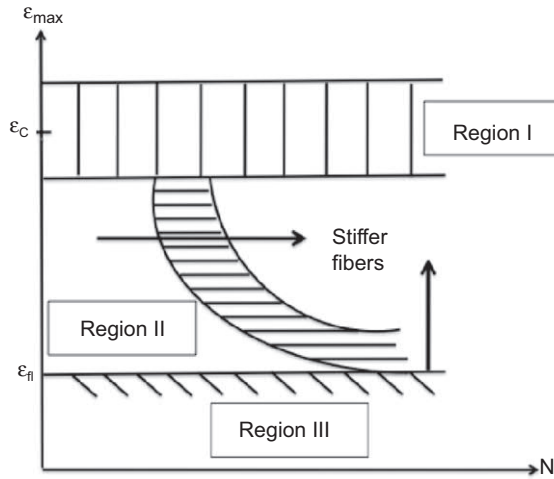
Figure 10.7 The baseline fatigue life diagram of unidirectional composites under cyclic tension.

be seen, the trends predicted by the conceptual FLD (Fig. 10.7) are confirmed by these data. It is also noteworthy that the glass/epoxy data for three different fiber volume fractions ($V_f = 0.16$, 0.33 and 0.5) fall together within the same Region II scatter band. It is recalled that the fatigue testing was done conventionally, i.e., with load control, and the data when plotted on the stress basis (as S−N plots) fall as three separate curves, each corresponding to one fiber volume fraction.

The fatigue limit, as shown in Fig. 10.8(a) is the fatigue limit reported by the authors [3] obtained by testing neat epoxy in *strain control*. The runouts (with arrows) shown in Fig. 10.8(a) suggest that the glass/epoxy composite fatigue limit is slightly higher, in accordance with the FLD in Fig. 10.7. For carbon/PEEK data in
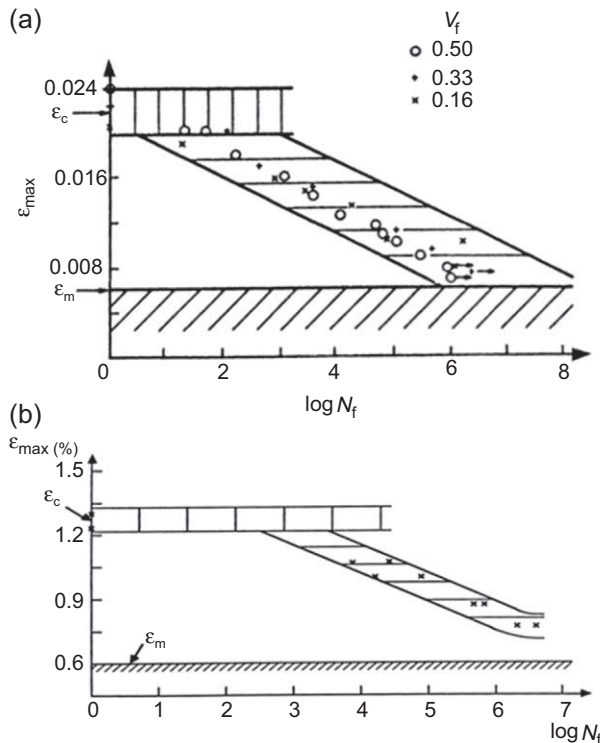
Figure 10.8 Fatigue life data and superimposed FLDs for a glass/epoxy composite (a) at three fiber volume fractions [3] and for a carbon-PEEK composite (b) [4].

Fig. 10.8(b) the same fatigue limit of epoxy ($\varepsilon_m = 0.6\%$) is also indicated for reference, as the PEEK fatigue limit has not been reported. It is expected that PEEK being tougher than epoxy will have a higher fatigue limit. In any case, the carbon/PEEK data shown in Fig. 10.8(b) show a fatigue limit higher than 0.6% strain. A comparison of carbon/PEEK and carbon/epoxy in Ref. [2] showed the fatigue limit values of 0.75% and 0.85%, respectively. The lower value of the fatigue limit for carbon/PEEK is attributed to more extensive debonding observed in this composite [2]. Again, this is in accordance with the expected trend predicted by the FLD (Fig. 10.7).

10.3 Modeling of FLD trends

Some of the qualitative trends in the fatigue behavior of unidirectional composites in cyclic tension emerge logically from the FLD, e.g., the direct dependence of Region I on the fiber strain to failure and the effect of fiber stiffness on Region II and Region III as indicated in Fig. 10.7. There have, however, been efforts to pin down the trends by quantitative modeling. Experimental evidence gathered by surface replicas

(Figs. 10.2 and 10.3) [2] indicated that the fiber-bridged cracks attributed to Region II (Fig. 10.2) tended to stop growing unless, as described above, a progressive fiber breakage occurred. It was found that the fiber/matrix debond length grew with fatigue cycles, exposing the increasing length of the debonded fiber to enhanced stress, as well as affecting the neighboring fibers. A shear-lag model was used to determine the stress transfer from the broken fiber to the neighboring fibers, and the Weibull distribution was assumed for the probability of fiber failure [5]. Although quantitative fatigue life prediction could not be made, the trends regarding how Region II would change with the cyclic rate of fiber/matrix debonding and the Weibull shape parameter were inferred [5].

An approach to fiber failure progression in fatigue was put forth recently [6] in which the fiber/matrix interface failure is represented by a cohesive zone model for static strength and the Paris relationship (power-law) for mode-II fatigue crack growth is assumed for the debond crack growth. The statistical fiber failure is given a Weibull distribution, and the fiber bundle failure is modeled by a hierarchical scaling method developed earlier [7]. While evaluating various material parameters entering the models is a challenge, with reasonably assumed values, the prediction of fatigue life in tension-tension loading by the approach seems to confirm the proposed FLD (Fig. 10.9). Strictly speaking, it is noted that Region I of the FLD is not the same as that in Fig. 10.7, where the idealized behavior does not assume cycle dependency. The authors [6] predict low dependency on cycles in this region because of low debond growth rate and high rate of fiber failures. The debond crack growth dictates the slope of Region II in their model. Finally, the mode-II fatigue crack growth threshold of debond cracks determines the fatigue limit.

The uncertainty in model inputs and their effects on fatigue life prediction was discussed by the authors [6]. Assuming a cohesive zone for the static shear failure of the
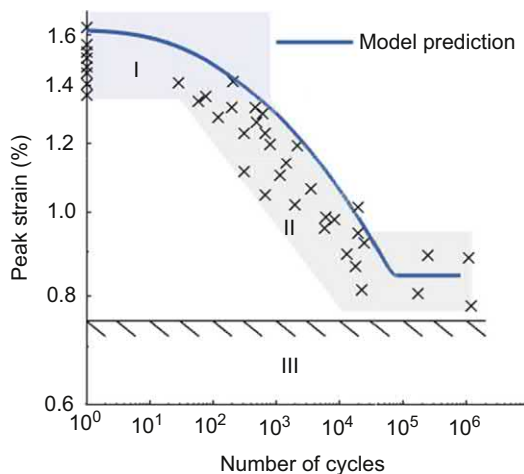
Figure 10.9 Model prediction by Ref. [6] compared to experimental data reported in Ref. [2]. The three regions of FLD in Fig. 10.6 have been superimposed on the data.

fiber/matrix interface has inherent uncertainty, as the material constants entering this model cannot be obtained independently. For debond growth, assuming a mode-II crack growth rate also induces uncertainty since the driving forces for a debond crack on the surface of a fiber embedded in a composite cannot be accurately reproduced in a test specimen devised for measuring crack growth rates. Finally, applying Weibull parameters found in a single fiber test, where the fiber is under uniform stress, to debonded fibers in a cluster of other debonded fibers introduces difficulties, which necessitate simplifying assumptions, leading to inaccuracies. At best, therefore, the type of modeling in Ref. [6] provides a useful trend analysis such as the effect of the mode-II crack growth threshold on the fatigue limit, the effect of the shear strength of the fiber/matrix interface and the crack growth resistance on the slope of the fatigue life scatter band.

Another recent work [8] also conducts modeling of the fatigue failure process in UD composites under cyclic axial tension starting with a broken fiber surrounded by matrix and accompanied by fiber/matrix debond of a certain length. The debond crack is assumed to grow as a mode-II crack following the Paris relationship. Additionally, in the debonding process, the role of interfacial frictional shear stress is considered. The fibers affected by the broken and debonded fiber are placed around this fiber in a hexagonal pattern, and the enhanced stress in these fibers is evaluated from the singular stress field at the debond crack tip. Failure of these fibers is then assessed assuming Weibull distribution for fiber strength.

A novel feature of [8] is that the fiber breakage process is assumed to cease when none of the six fibers surrounding the broken and debonded fibers reaches its failure condition expressed as the probability of failure (1/6, i.e., one out of six failing). This provides a way to estimate the fatigue limit. With this model of fatigue limit, the effects of parameters, such as the fiber volume fraction (based on a hexagonal fiber pattern), as well as the fiber/matrix interfacial characteristics, expressed as frictional shear stress and fracture energy can be evaluated. These effects are shown in Fig. 10.10, reproduced from Ref. [8]. It is noted that there is no unique way to estimate the interfacial characteristics, and this introduces a source of the inherent uncertainty in modeling fatigue behavior, where the irreversibility underlying fatigue is attributed to the interface.

In both models cited above, the role of the matrix in the process of stress transfer from the broken and debonded fiber to the surrounding fibers is not explicitly considered. It is known from observations and analysis that a debond crack can deviate into the matrix if favorable conditions exist for that to occur. A study [9] of failure in UD composites from a local fracture plane under monotonic axial tension looked at two scenarios: one, where a broken fiber exists from manufacturing and the other where a fiber fails at a weak point during loading. While in the first case the matrix crack formed at the broken fiber end was found to grow normal to the fiber axis, in the second case, the initial (assumed) debond crack kinks out in the matrix toward the neighboring fibers. The consequence of fiber failure progression, evaluated in probabilistic terms, was found to be higher when matrix cracking was considered than when it was ignored. It is expected that this will also be the case under cyclic loading.
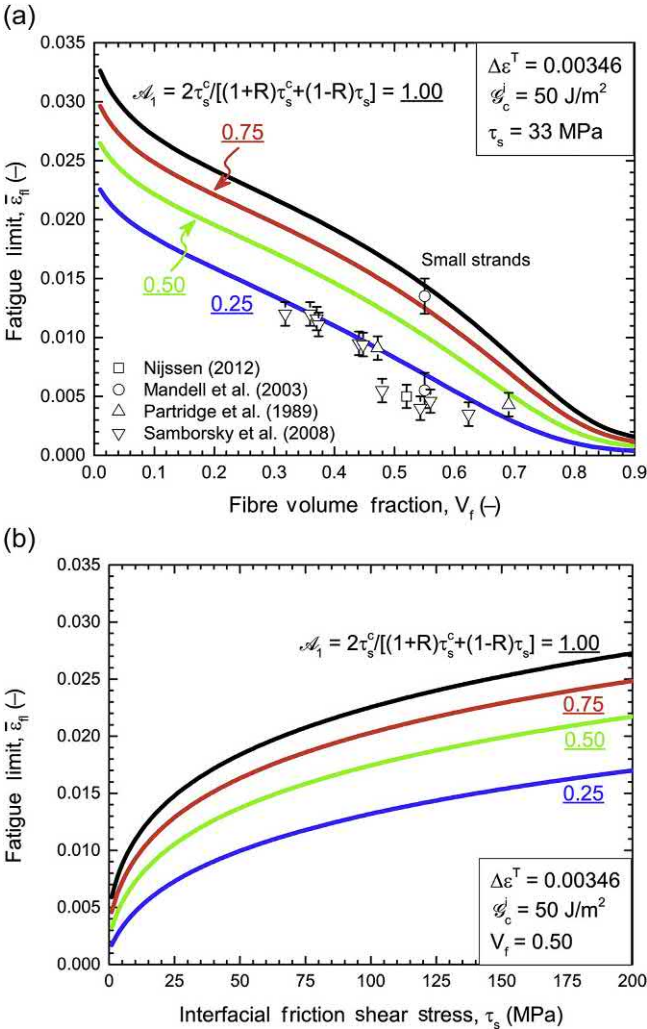
Figure 10.10 Variation of the fatigue limit with (a) fiber volume fraction, (b) interfacial frictional shear stress, and (c) interfacial fracture energy [8]. The function A_1 shown in the figures is the frictional prefactor [8] that depends on the R-factor, the frictional shear stress, and its critical value, as indicated.
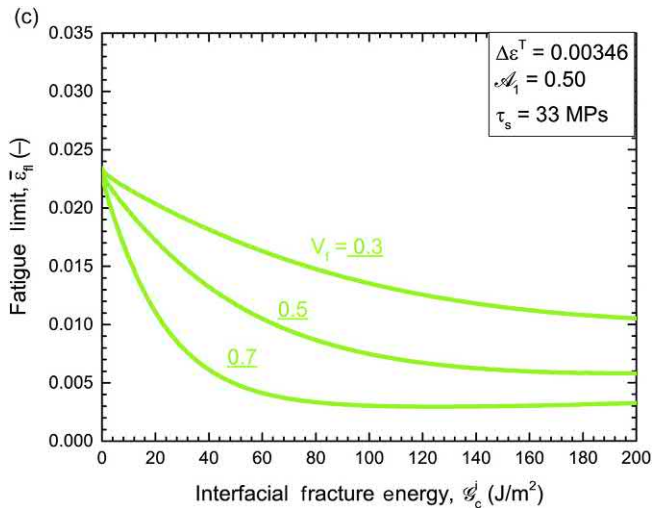
Figure 10.10 cont'd.

10.4 Fatigue of laminates

In straight-fiber laminates subjected to in-plane cyclic loading, the individual plies will be subjected to biaxial cyclic stressing. In the material coordinates of a ply, the three stress components viz., the normal stress in the fiber direction σ_1, the normal stress transverse to the fiber direction σ_2, and the in-plane shear stress σ_{12}, will generally vary cyclically in various in-phase and out-of-phase combinations. It is obvious that testing and analysis of fatigue in all such combinations is a tremendous task. The approaches taken often in the literature are to resort to phenomenological criteria, commonly used for quasi-static failure, and predict fatigue life by simply generalizing to cyclic loading. A literature survey of such approaches was given in Ref. [10]. In Ref. [11], a critical assessment of common phenomenological models for fatigue life prediction was made, and using a large set of data from the literature, it was shown that such models are not reliable. Since then, unfortunately, more phenomenological models have appeared in the literature, and the reliability of life prediction by such models remains uncertain.

In Ref. [11], a way forward to address fatigue behavior by the mechanisms path was laid out. Resorting to the FLD concept, the progressive mechanisms of fiber-bridged matrix cracking and interfiber matrix cracking (including fiber/matrix debonding) were identified as the dominant ply fatigue mechanisms. It was emphasized that through systematic studies of these mechanisms by experiments and observations, modeling strategies could develop. Several such studies have been conducted and models proposed for the interfiber matrix cracking under cyclic loading [12–16]. As the ply cracks approach the ply/ply interfaces, the diversion and deflection of these cracks take place, leading to delamination. The delamination cracks then grow under cyclic loading. In the initial stage of the delamination fatigue, the interaction with the

ply cracks is expected. This interaction needs to be studied before proper models for it can be developed.

After sufficient delamination has occurred, the separated plies behave without the constraint from the previously bonded plies. In this phase of the fatigue process, the focus should shift to the most load-bearing ply (or set of plies), whose failure will cause the final failure of the laminate. Here, the FLD for UD composites, discussed above, will be a useful guide to modeling the final failure stage.

The issue of the fatigue limit of a given laminate has not been addressed sufficiently so far. Generally speaking, there are two ways to approach the fatigue limit, one by asking at what applied load the progressive fatigue mechanism slows down to not fail the composite in a prescribed large number of cycles (10^6, 10^7, etc.), and second, to identify conditions for not initiating a progressive mechanism. The two approaches will produce upper and lower bounds to the fatigue limit, respectively. As an example, if transverse cracking in 90-degree plies is the first failure mechanism under axial tension of a cross-ply laminate, then its progression with load cycles is the key to determining the fatigue limit. Thus, if a model is set up for describing the cyclic rate of transverse crack density, then the fatigue limit will fall naturally from the model. This is then the first approach stated above, providing the upper bound of the fatigue limit. To find the lower limit, one would need to determine the conditions for the formation of a transverse crack. The upper bound approach was demonstrated in Ref. [17] for cross-ply laminates under cyclic axial tension.

10.5   Concluding remarks

This chapter has focused on the fundamentals of the fatigue failure process in composite materials. Without reviewing all works in fatigue, the emphasis has been placed on clarifying the roles of failure mechanisms, and for this purpose, a conceptual framework proposed by the author in 1981 called a fatigue life diagram (FLD) has been revisited. It is shown how easily the FLD reveals the effects of fiber stiffness and fiber failure strain on the fatigue behavior of UD composites. The trends induced in the fatigue life and the fatigue limit by the progressive fiber failure mechanism have been modeled recently, and these have been discussed to identify further improvements needed in the models. The implications of the FLD concept on understanding fatigue of laminates has then been discussed. An example of how this was utilized for axial tension fatigue of cross-ply laminates suggests a direction for addressing other laminates by mechanisms-based approaches.

References

[1] R. Talreja, Fatigue of composite materials: damage mechanisms and fatigue life diagrams, Proc. R. Soc. Lond. A378 (1981) 461−475.

[2] E.K. Gamstedt, R. Talreja, Fatigue damage mechanisms in unidirectional carbon-fibre-reinforced plastics, J. Mater. Sci. 34 (1999) 2535−2546.

[3] C.K.H. Dharan, Fatigue failure in graphite fibre and glass fibre-polymer composites, J. Mater. Sci. 10 (1975) 1665−1670.

[4] P.T. Curtis, An investigation of the tensile fatigue behaviour of improved carbon fibre composite materials, in: Proceedings of the Sixth International Conference on Composite Materials, ICCM-6, Imperial College, London, 1987, pp. 4.54−64.

[5] E.K. Gamstedt, Effects of debonding and fiber strength distribution on fatigue-damage propagation in carbon fiber-reinforced epoxy, J. Appl. Polym. Sci. 76 (2000) 457−474.

[6] M. Alves, S. Pimenta, A computationally-efficient micromechanical model for the fatigue life of unidirectional composites under tension-tension loading, Int. J. Fatigue 116 (2018) 677−690.

[7] S. Pimenta, S.T. Pinho, Hierarchical scaling law for the strength of composite fibre bundles, J. Mech. Phys. Solids 61 (2013) 1337−1356.

[8] B.F. Sørensen, S. Goutianos, Micromechanical model for prediction of the fatigue limit for unidirectional fibre composites, Mech. Mater. 131 (2019) 169−187.

[9] L. Zhuang, R. Talreja, J. Varna, Tensile failure of unidirectional composites from a local fracture plane, Compos. Sci. Technol. 133 (2016) 119−127.

[10] J. Degrieck, W. Van Paepegem, Fatigue damage modelling of fibre-reinforced composite materials: a review, Appl. Mech. Rev. 54 (2001) 279−300.

[11] M. Quaresimin, L. Susmel, R. Talreja, Fatigue behaviour and life assessment of composite laminates under multiaxial loadings, Int. J. Fatigue 32 (2010) 2−16.

[12] M. Quaresimin, P.A. Carraro, On the investigation of the biaxial fatigue behaviour of unidirectional composites, Compos. B Eng. 54 (2013) 200−208.

[13] M. Quaresimin, P. Carraro, Damage initiation and evolution in glass/epoxy tubes subjected to combined tension-torsion fatigue loading, Int. J. Fatigue 63 (2014) 22−35.

[14] M. Quaresimin, P.A. Carraro, L.P. Mikkelsen, N. Lucato, L. Vivian, P. Brønsted, B.F. Sørensen, J. Varna, R. Talreja, Damage evolution under cyclic multiaxial stress state: a comparative analysis between glass/epoxy laminates and tubes, Compos. B Eng. 61 (2014) 282−290.

[15] (a) M. Quaresimin, P.A. Carraro, A damage based model for crack initiation in unidirectional composites under multiaxial cyclic loading, Compos. Sci. Technol. 99 (2014) 154−163;
(b) M. Quaresimin, P.A. Carraro, L. Maragoni, Early stage damage in off-axis plies under fatigue loading, Compos. Sci. Technol. 128 (2016) 147−154.

[16] J.A. Glud, P.A. Carraro, M. Quaresimin, J.M. Dulieu-Barton, O.T. Thomsen, L.C.T. Overgaard, A damage-based model for mixed-mode crack propagation in composite laminates, Compos. Appl. Sci. Manuf. 107 (2018) 421−431.

[17] N.V. Akshantala, R. Talreja, A micromechanics based model for predicting fatigue life of composite laminates, Mater. Sci. Eng. A285 (2000) 303−313.

Impact, post-impact strength, and post-impact fatigue behavior of polymer composites

11

Glyn Davies [1], *Philip Irving* [2]
[1]Imperial College, London, United Kingdom; [2]School of Aerospace, Transport and Manufacture, University of Cranfield, Cranfield, United Kingdom

11.1   Introduction

Of the countless papers on composites in the past 30 years, possibly the topic addressed most has been impact damage and residual strength. Why has this been so? The first all-composite aircraft were agile combat aircraft whose specification could not have been met without the superior specific stiffness of carbon/epoxy composites. The uncertainty of how to design these revolutionary structures was compounded by the fear of "Barely Visible Impact Damage" known universally as BVID. Impact damage on metallic structures was well known. The incident energy was relatively easily absorbed by the elastoplastic response of light alloys, and after absorption, the effect was visible as a dent, which could then be repaired. Composites were different. Conventional carbon fibers and epoxy resins were virtually linearly elastic to failure, whether fiber or matrix. The failure modes, such as fiber fracture in tension, compression kinking, matrix cracking, and delamination, did not absorb much energy. The recovery could be purely elastic with little or no changes to the surface profile. Thus, the damage could be "barely visible" and remain undetected on visual inspection. For structures designed to resist compression, the most serious form of undetected subsurface damage, was delamination, liable to provoke local buckling, triggering unstable propagation, and significantly degrading static strength. Therefore, Compression-After-Impact (CAI) was an obligatory strength test for certification of military aircraft.

This chapter will describe the behavior of impact response and damage and the subsequent consequences on fatigue strength. For in-depth treatments of these topics, the reader is referred to the publications of Abrate [1], Davies and Olsson [2], Cantwell and Morton [3] and Bogenfield et al. [4].

The nature of all forms of impact damage is best characterized in terms of incident velocity, which may span several orders of magnitude and the impacting mass. There are many different structural consequences depending on the specific combination of mass and velocity. At one extreme is the high mass and ultralow-velocity (quasi-static)

impact of catering and baggage handling equipment with the aircraft. The low-velocity impact is understood to be in the range of 4–10 m/sec with energies up to 50J. Dropped tools during manufacture or service are in this category. Impact due to runway debris can be classified as intermediate velocity but again with energies of order 50J. Bird strikes can occur at "medium" velocities of 100–250 m/s but with much higher energy.

Ballistic impact due to ordnance or missile fragments can be classified as "high velocity" in the range 250 to 2000 m/s. These projectiles may have a mass only a few grams, but their energy is now 10–20 kJ. At these speeds, the impact event will be so short that the structure will have no time to respond in global flexure or shear, and the main issue is whether complete penetration occurs. Body armor, using various composite/ceramic materials, for example, is designed to resist penetration.

The term "hypervelocity" has come to be applied to satellite and spacecraft which may be struck by micrometeorites at velocities of the order 30–70 km/s. Here the impact time is measured in nanoseconds; conventional heat transport is impossible, and both the meteorite and the impacted structure will vaporize [5]. Indeed the aim of protective shielding is to encourage this so that only a gaseous cloud hits the payload.

11.2   Nature of impact damage

Many different forms of laminated composite damage can take place, as shown in Fig. 11.1 for a laminate with 0° and 90 degrees layers.

Some modes may dominate: for example, for large bending strains in a flexible structure, fiber fracture in tension, and fiber kinking in compression will dominate near both surfaces. Matrix cracks can cause delamination when they reach a ply interface. If the structure is stiff enough to resist with a significant force, then local indentation damage and shear-driven delamination in the interior will occur. Fig. 11.2a schematically shows the different modes of delamination. The "peanut" shapes [3] develop because compression under the impact site partially suppresses delamination growth. Fig. 11.2b shows the development of a cone of interply and intraply damage spreading out from the dent marking the impact site.
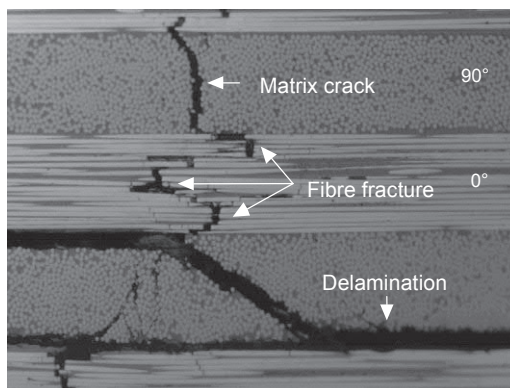
Figure 11.1 Different forms of damage in a composite laminate after impact.
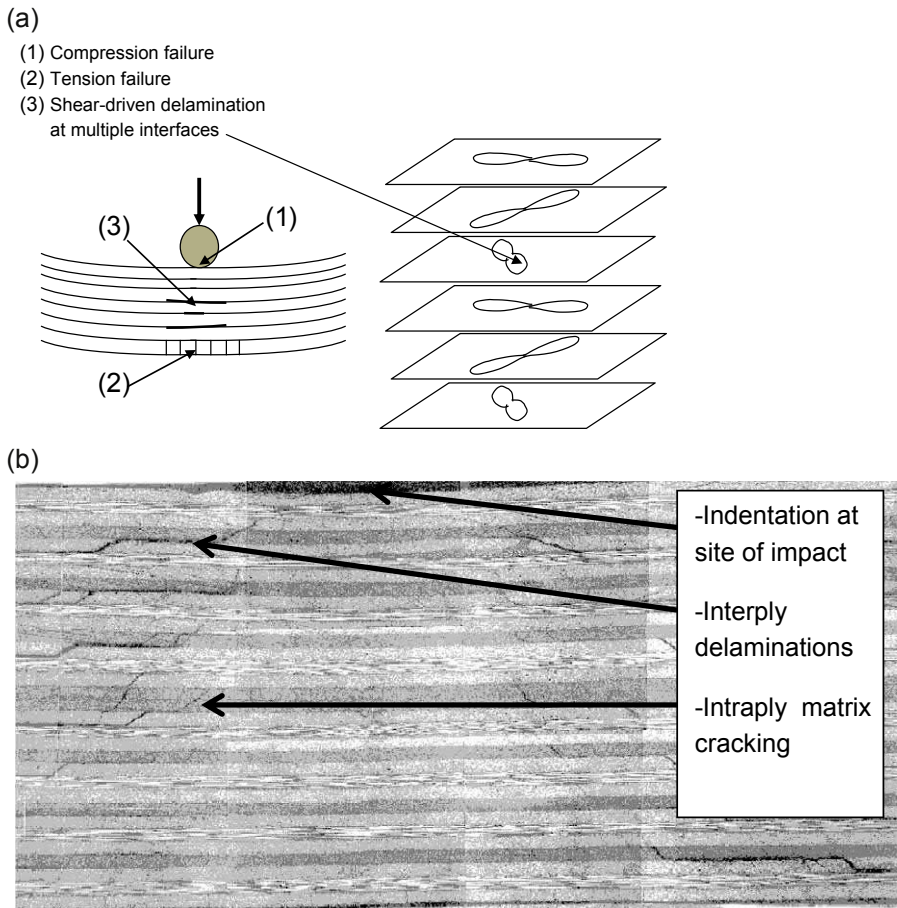
Figure 11.2 (a) Schematic illustration of different failure modes under impact event. (b) Section through impact damage in 32 ply quasi-isotropic laminate subjected to 30J impact showing matrix cracks and delaminations propagating away from the original impact site [6].

An indentation results from permanent local deflection, in addition to the global flexural response. After low-velocity impacts achieving modest loads, the indentation depth is only a few tenths of a millimeter. For larger impacts particularly on stiff structures, matrix cracking and delamination together result in the redistribution of the contact pressure over a larger area forming a dent that can be 0.5−1.0 mm deep and 5−10 mm across. The local surface indentation is the only indication to aircraft inspectors that subsurface damage exists. Subsurface damage accompanying the smallest dent, which can be reliably detected, is the Barely Visible Impact Damage (BVID) value. The degradation in compression strength caused by undetected delaminations at the BVID level is of significant airworthiness regulatory concern (see Chapter 19).

The local dent deflection reduces with time after impact as local residual stresses created during impact reduce. Indentation shape depends to a degree on the geometry
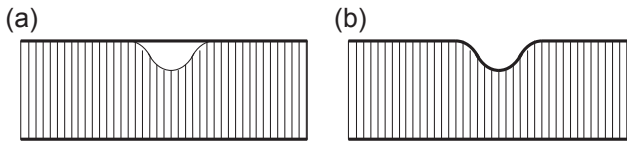
Figure 11.3 Residual deformation of a sandwich panel after impact.

of the impactor [6]; laboratory testing generally uses standardized 16 mm diameter hemispheres. Of course in service, impacting objects may be of arbitrary shape and size and consequently the relation between visible dent size, shape, and subsurface damage may be only approximately defined.

Impact response of sandwich panels depends on the relative stiffnesses of the skin and core and also on the strength of the skin/core interface. Fig. 11.3 shows the two extremes; Fig. 11.3a shows the dangerous invisible type, where the skin springs back covering the damage. Fig. 11.3b shows the effect of a strong skin-core bond, causing a visible dent.

The low to medium velocity response of laminates depends on whether the impact is a small mass with intermediate velocity or a large mass with a low velocity. Fig. 11.4, Davies and Olsson [2], shows the response of a clamped 125 × 125 × 6 mm flat laminate impacted at 10J with large and small mass impactors. The duration of the large mass impact is comparable with the plate's fundamental mode and the load, deflection, and strains, in both x and y directions, are essentially in phase. The maximum values will occur when all the kinetic energy has been absorbed, and the impactor is stationary. This state can be simulated by a static test. For small masses, the corresponding quantities are out of phase, the maximum force and strains occur in a short time, which results in a wave-controlled local response of the laminate. The impact force and in consequence, the delaminations will be larger.

The response and extent of damage will depend, in general, on the nature of the structure, which may not be the same as a simple plate. For stiffened compression panels, if impacted between stiffeners, the response will be similar to that described above. Impact over a stiffener will result in a much higher force with a resulting stiffener response similar to that of a long beam. The shear stresses (which can cause stiffener debonding) can extend along the stiffener with little diffusion into the surrounding panel skins, Davies et al., [7]. Impact on a curved panel with edge supports can also be different for impact on the convex face. This stiffer structure will experience higher impact forces and consequently increased delaminations [8].

Features in the load-time trace can be associated with fracture events. For example, Fig. 11.5 Cartie et al. [9] shows a typical initial load maximum in the trace marked at point A. This is the threshold force to initiate delamination. Impacts producing a force less than this do not result in delamination damage. The load at point A is a characteristic of the composite system and the local geometry and is independent of the impact energy. If the threshold force at A is exceeded, the load-time curve after this point develops significant load oscillations (between points B and C in Fig. 11.5), as delaminations and matrix cracks are propagated through the laminate, and local compliance suddenly increases following a growth increment. Eventually, the overall maximum

1.5 kg impactor
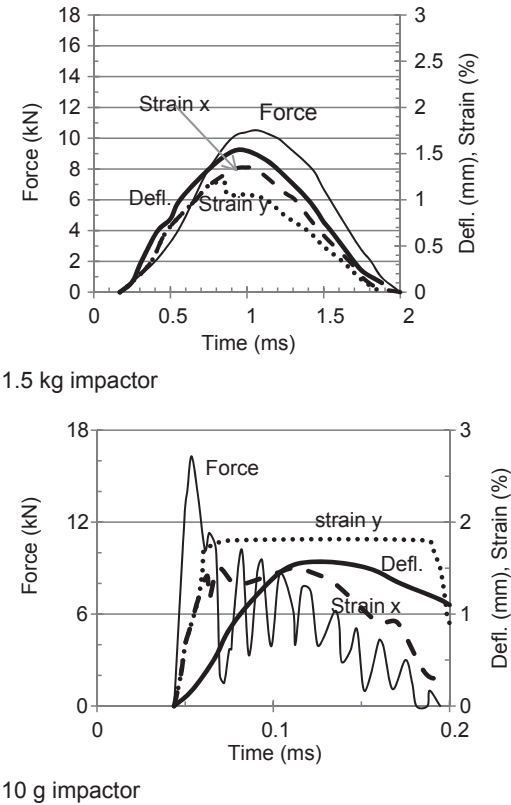
10 g impactor

Figure 11.4 Load, strain, and deflection responses due to a 10J impact by Top 1.5 kg and Bottom 10 g impactors on a polymer composite plate. Strain x and strain y refer to in−plane direction strains. Deflection directions are out-of-plane (z direction).
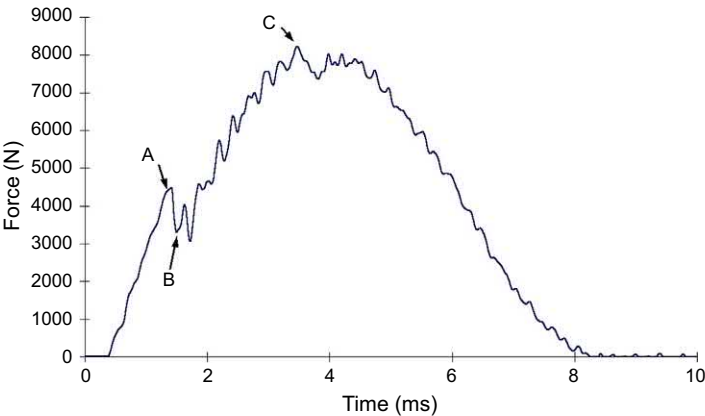
Figure 11.5 Force-time trace during a 20 J impact on 32 ply quasi-isotropic laminate of IMS/ 922 [9].
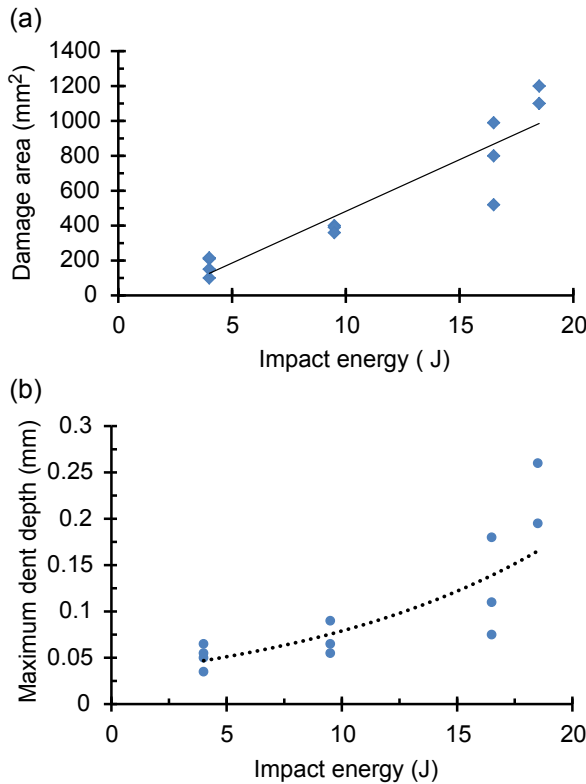
Figure 11.6 (a) Relation between impact energy and delamination area for 16 ply quasi-isotropic cfrp composite HTA/985. (b) Same impact events as in 11.6a, but showing dent depth as a function of impact energy. Panettieri et al. [10].

load is achieved at point C, and the force reduces as elastic recovery occurs and delamination growth in consequence stops.

For low-velocity impact on stiff structures, many experiments have shown the following damage characteristics, e.g., Refs. [9—11]:

- Increased impact energy produces an increased delamination area and increased dent depth, as shown in Figs. 11.6a and 11.6b.
- Multiple delaminations develop under the impact site, with their area increasing with the distance from the impacted surface forming a cone; see Fig. 11.2b.
- The threshold value of force to create dents and delamination damage is a constant (termed Pc) for the laminate system and the local geometry, independent of the impact energy.
- Both Pc and delamination damage area are strongly dependent on the mode II fracture toughness G_{IIC} of the laminate system in question, as shown in Fig. 11.7.

During aircraft assembly or internal maintenance operations inside the wing and fuselage skins, stiffeners and other design features are oriented so that accidental impact on their free edge rather than out of plane impacts on their surface is a possibility. The effects of such edge impact damage and the reduction in strength and stiffness, which
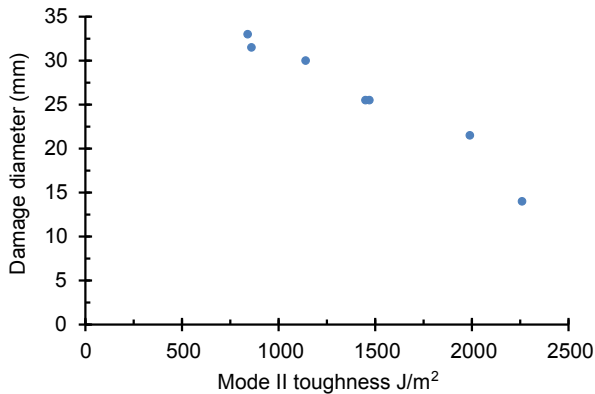
Figure 11.7 Relation between projected delamination width after 10.8 J impact and the shear toughness G_{IIC}. 32 ply quasi-isotropic composite using IM7 fiber and resins of a range of toughness values. Nettles et al. [11].

it can cause have been the subject of much recent research. While the local crushing damage is more visually detectable than for face-on impacts, as for face impacts, through-thickness inspection using NDT is required to establish the extent of subsurface damage. The energy required for inducing edge impact damage is significantly smaller than the 7.6 J per mm of thickness recommended by ASTM D7136 to induce damage after face-on impact. In this stiff edge-on orientation, there is little or no elastic deformation, and almost all energy is available to create crush or delamination damage [12,13].

Ballistic impact velocities up to 2000 m/s result in damage due to the transverse dilatational waves inducing strains of order V/C_Z, Godwin and Davies [14], where V is the impact velocity and Cz is the velocity of the through-thickness waves. ($C_Z = \sqrt{E/\rho}$, where E is the through-thickness modulus and ρ the density.) Thus, for a wave speed of 2000 m/s an impact velocity of 70 m/s will induce compressive strains of order 3% even before any further flexural response. The high inertial resistance will cause a high impact force and a consequent "shear out" plug unless the structure is more than (say) 10 mm thick. The impact event is short and no structural modes are excited at all. Strain rates may exceed 100/sec at which the material properties for glass and aramids will change, but for carbon/epoxy this will not happen until rates exceed 1000/sec. Because penetration is important for ordnance applications, experimental studies have centered on resisting penetration completely. This "ballistic limit" is usually defined by the V_{50} parameter, implying a value at which at least 50% of tests will not penetrate. It will depend on target thickness, fiber surface treatments, and interlaminar toughness.

11.3 Residual strength after impact: observations

Probably the most serious design case and the most discussed is that of BVID and its effect on CAI strength. It is discussed by literally hundreds of studies—see reviews [1–4]. Several types of failure in compression may occur and are illustrated in Fig. 11.8.
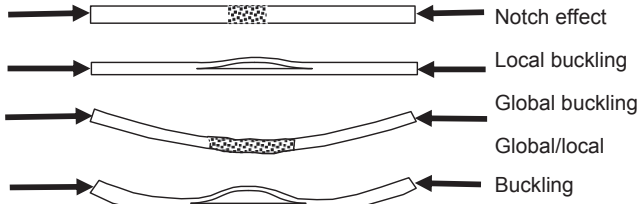
Figure 11.8 Failure mechanisms for "compression-after-impact."

(1) Notch effect. There may be fiber and matrix damage through the thickness, causing a local loss of stiffness. This has the same effect as an insertion or hole that causes a stress concentration, but probably the Kt value is less than that of a circular hole (Kt = 3).

(2) Local Buckling. The shear-driven delaminations can reduce the buckling strength of sublaminates by an order of 4, so that local buckling can release enough energy to propagate the buckling envelope in an unstable fashion.

(3) Global Buckling. Can occur in the presence of delamination just due to the local reduction in flexural stiffness.

(4) Global/Local Buckling. A combination of (2) and (3).

The many tests on coupons (with supported edges), and on stiffened compression panels, demonstrate that impact damage can reduce residual strength by more than 70%, depending on the size of impact damage [15]. Fig. 11.9 shows the results of a series of tests by Olsson [16] conducted on panels of various thicknesses, edge support conditions, and materials. The decrease in residual strength with increasing delamination width is dramatic. There is a modest increase in residual strength for samples with toughened epoxy (6376) and thermoplastic PEEK matrices. Increasing sample thickness promotes increased residual strength. These general characteristics of CAI behavior have been repeatedly confirmed since the work of Olsson in 1999. The work of Nettles and Scharber [11] in 2018 demonstrates for identical impacts on QI laminates with a range of toughness values that shear toughness G_{IIC} determines
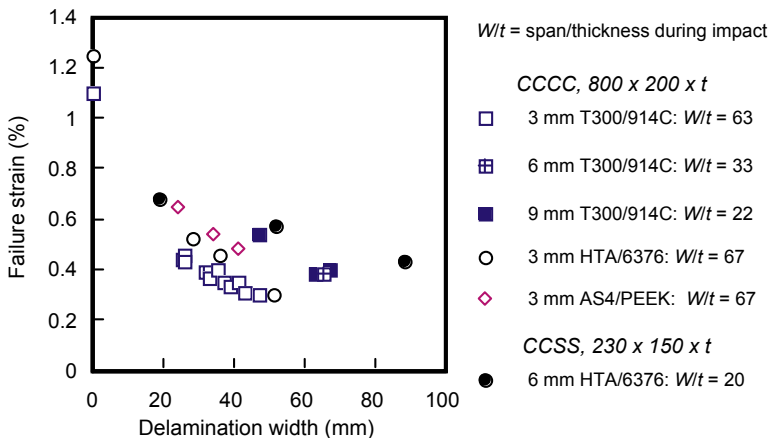
Figure 11.9 Influence of delamination width on compression failure strain [16].

delamination width (Fig. 11.7), and in turn, delamination width determines CAI, providing fiber type, layup, geometry, and impact energy are all held constant. Toughness has little role in the compression buckling failure itself.

The behavior of structural elements like stiffened compression panels can differ from these simple coupon tests. For example, the buckling modes along a panel will have crests and node lines, spaced at half-wave-lengths of the order of the stiffener pitch. The delamination will be promoted for impact at a crest but can be retarded for impact at a node line. Impact actually above a stiffener will produce a much higher force than mid-panel impact, and can cause stiffener debonding along a considerable length of the stiffener. This may propagate under compression loading and effectively double the distance between stiffeners, causing a 75% reduction in the postbuckling load [17].

It is usually assumed that low-velocity impact damage is caused by dropped tools or similar maintenance accidents when the structure is not loaded. This may not be so; for example, impact by runway debris on take-off, or ballistic impact in flight. Compression strength during impact under load has received relatively little attention. Zhang and Davies [18] have conducted tests and simulations on panels with and without preload. Applied compression can reduce the stiffness of panels and so reduce the impact force and amount of damage. However, if the applied strain is near the material's strain to failure, then the damage as impact-induced strains occur, can be greater than in the unloaded panel. These effects depend on panel size, thickness, stiffness, and boundary conditions, but can be quantified by three nondimensional parameters:

- The ratio of the applied preload to the panel's initial buckling load.
- The ratio of the maximum impact force to the critical value of force (Point A in Fig. 11.5).
- The ratio of the applied preload strains to the material compressive failure strain.

It was found that the failure load with preload was only marginally less (14%) than the usual CAI load even when all the above three parameters were near to unity.

Sandwich panels exhibit all the failure modes of monolithic laminates. However, because of these structures' high flexural stiffness, global buckling is not an issue, and the assumption frequently made of delamination growth due to skin-core separation and "outward" skin buckling is not supported by experiments [19]. More usual is inward skin buckling initiated by the inward dent (Fig. 11.3b) Progressive core crushing can take place as the applied load increases further.

11.4 Residual strength and damage extent after impact: predictive models

11.4.1 Simple analytical approach

Even if Finite Element codes are easy and cheap to use, designers will warm to simple analysis, especially if the failure mechanisms are clear and related to obvious physical properties. A first step is to find the extent of damage caused by the known energy of an impact. In Davies and Robinson [20], a simple model was derived for a quasi-isotropic lay-up by assuming it behaved in an axisymmetrical fashion. If delamination is driven
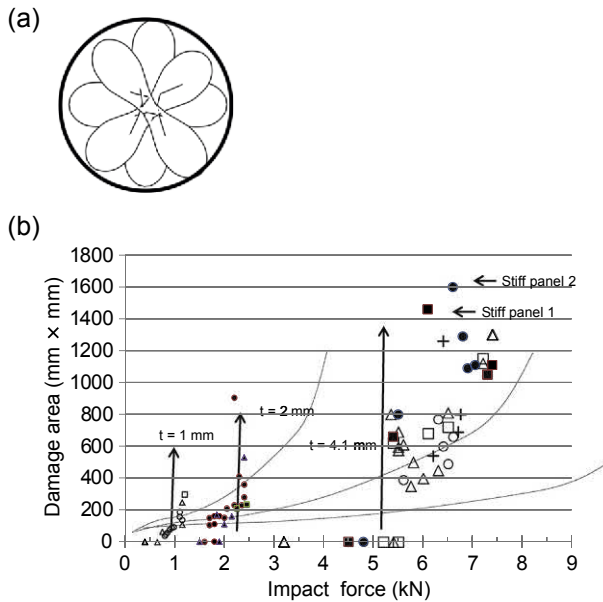
Figure 11.10 (a) Envelope of all the "peanut" shaped delaminations. (b) Delamination damage area as a function of measured impact force for a range of sample thicknesses.

by interlaminar shear, it could be assumed that the shear stress τ at a distance of r from the impact force P on a laminate of thickness t is given by $\tau = P/2\pi rt$. The delamination area is then proportional to P^2. It was assumed that the delamination was in mode II shear and that all the "peanut" delamination shapes in Fig. 11.2 could be represented by single circular delamination located at mid thickness with an area of the projected envelope of the array, as shown in Fig. 11.10a.

The resulting analysis (Eq. 11.1) showed that there existed a threshold critical force Pc (point A in Fig. 11.5), below which no delamination occurred.

$$Pc^2 = 8\pi^2 E t^3 G_{IIC}/9(1-\nu^2)$$ (11.1)

where G_{IIC} is the mode II fracture toughness, E the elastic modulus of the laminate, ν Poisson's ratio and t the laminate thickness.

It was found that Eq. (11.1) was remarkably accurate for impacts on a large number of plates and coupons of three thicknesses and several boundary conditions including stiffened panels.

Fig. 11.10b shows the damage areas for these tests, together with the thresholds, indicated as arrows, according to Eq. (11.1), for the three thicknesses t = 1, 2, and 3 mm. The absence of damage below the threshold forces is clear. Clearly, delamination is a fracture mechanics controlled mechanism. A more general version of Eq. (11.1) has been proposed by Suemasu and Majima [21] for "n" delaminations, all of them axisymmetrical, where the number nine in (11.1) is replaced by 3(n+2).

Eq. (11.1) predicts the threshold for damage initiation but not its ultimate width or area or the degradation in compression strength which results. These can be measured experimentally in the laboratory, but for design calculations on aircraft structures, numerical models are required.

11.4.2 Numerical techniques to predict impact damage extent and CAI strength

Theoretical models for residual strength of panels impacted at low-velocity incorporate the failure mechanisms (Fig. 11.8): of notch effect and sublaminate buckling under global and local situations. The notch models deploy a theoretical soft inclusion to represent the damage. The use of such inclusions to model impact damage has been evaluated for tensile [22] and compression [23] loading. Sublaminate buckling has been modeled by Xiong et al. [24] and the growth of such buckles in compression by Flanagan [25].

For high-velocity impact, a composite plate does not have time to develop flexural and shear deformations; instead, it can perforate, absorbing energy by a mixture of strain energy, matrix and fiber failure, delamination, forming of petals, hole enlargement, and friction when a "plug" is formed. Very simple models prove to be remarkably accurate for perforation prediction.

Numerical approaches to predict impact behavior and residual strength of polymer composite operate by solving the equations of motion for the displacements $\mathbf{r}(t)$

$$M\ddot{r} + C\dot{r} + Kr = R(t) \tag{11.2}$$

where the mass matrix M, the damping matrix C and the stiffness matrix K will be assembled by the code, once the elements have been chosen, and generated for the particular geometry. The applied forces R(t) will normally be zero during the impact event, but the same routine can be used on the damaged structure to apply (say) the compressive loading, at a convenient rate, until failure occurs.

The most popular commercial software codes used are ABAQUS and DYNA3-D, both in explicit form viz:

$$\ddot{r} = M^{-1}[R(t) - C\dot{r} - Kr]. \tag{11.3}$$

The variation of $\ddot{r}$ over a small time interval ∂t is assumed linear and the solution at a time $t + \partial t$ is found in terms of $r(t)$, treating the right-hand side of (11.3) as a constant, to be updated at time $t + \partial t$. The mass matrix is usually "lumped" as a pure diagonal, so no inversion is needed. The advantage of this explicit strategy is that all the terms in **Kr** can be non-linear. The material properties can be changing, and the displacements can be large (or unstable). The only disadvantage of this method is that it will be numerically unstable if the time step ∂t is not as small as the time for a stress wave to cross the smallest finite element. This, of course, will be small, but in impact problems, a large number of small time-steps will be needed anyway to capture the correct physics.

The same can be true for CAI simulation if unstable propagation occurs. In this last case, the loading is best applied in increments and the damping chosen to be critical so that the static solution is reached as quickly as possible.

The degradation of composite laminate strength can be modeled using simple criteria of strength for fibers and matrix before delamination occurs. Fig. 11.11 shows the test force-time history for a 200 × 200 mm plate together with various numerical FE (77) predictions (Davies et al., [26]). The linear elastic case successfully predicts the time of the force maximum but underestimates its size by a factor of 3. The finite element prediction overestimates the force but does get the departure from the linear solution correctly. The fully degraded solution (with much fiber failure) matches the experimental history. Delamination was confined to one interface near the mid-plane as the C-scan image indicates.

If delamination mechanisms are to be accurately simulated, then cohesive interface elements are needed. Commercial codes have these, incorporating strength criteria for initiation of the crack, and thereafter, a fracture-based propagation. In using such cohesive elements at the crack front, it should be remembered that the cohesive zone may be less than 1 millimeter in size, and the finite element size chosen to cope with this. Fig. 11.12 compares experimental ultrasound scans of a "peanut" shaped delamination with numerical predictions made using 0.2 mm elements. The process zone (with partial crack opening) is indicated [27]. Validation of the use of cohesive elements has been shown by Ref. [28] and by Davies and Zhang [18] on stiffened compression panels with impacts between and over stiffeners. Numerical models of composite laminates are now at the stage where impact behavior of the more complex woven composites can be successfully addressed. Woven composites are attractive in that they can be more easily draped and have the additional capability for absorbing impact energy, [29].
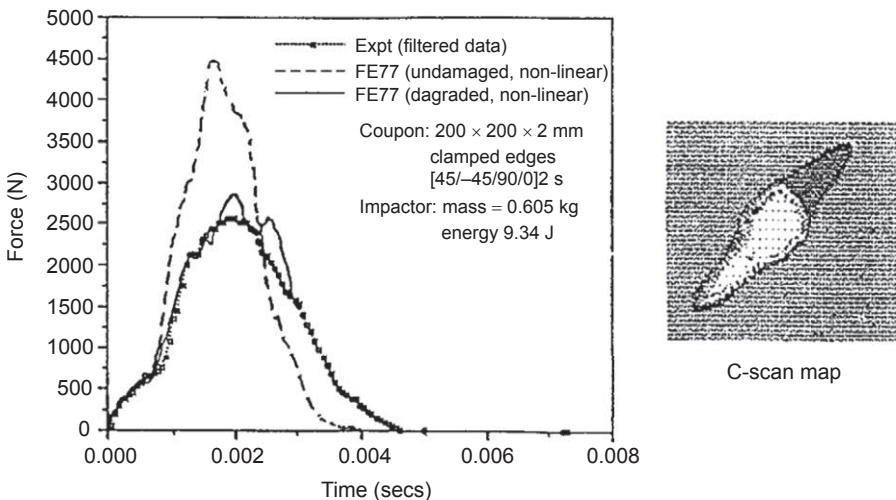
Figure 11.11 Experimental and modeled impact force-time histories as predicted by numerical models [26].
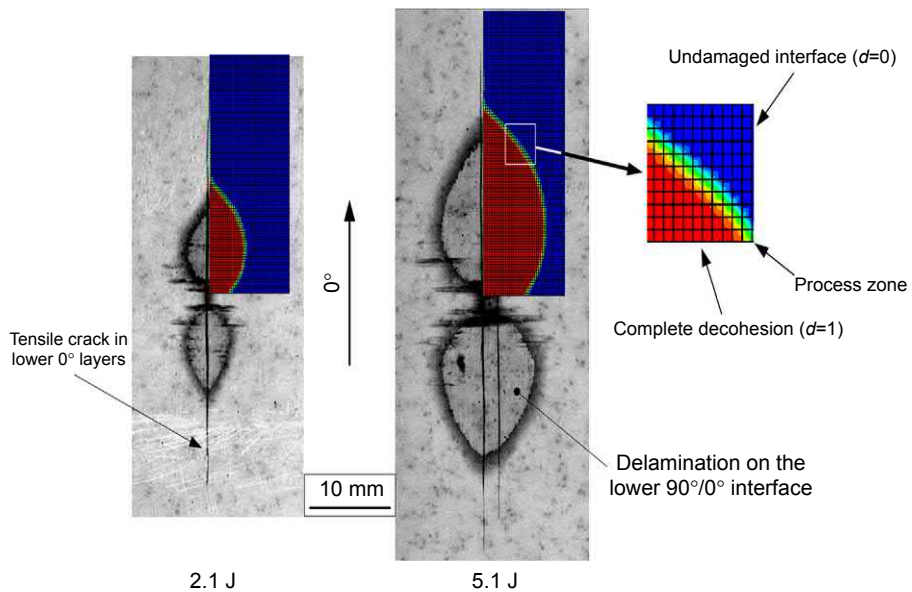
Figure 11.12 Peanut shaped delaminations after impact showing measured (Black and White) and predicted (in color) delamination geometry [27].

Developments in computing speed and software innovations post-2015 have permitted numerical models for prediction of impact damage and compression strength degradation to routinely predict impact damage and compression strength reduction on simple coupon laminates to within a small percentage of accuracy. Increasing accuracy and fidelity have been enabled by increasingly complex models requiring lengthy computation time. This can be in excess of 24 h for impact and compression failure on a simple coupon-even using multiple CPU computer arrays. Selected examples of modeling work performed in the period 2015−18 include [4,30−36]. Fig. 11.13 shows examples of simulated local compressive buckling failure in impact damaged composite from Sun & Hallett [32].

Bogenfeld et al. [4] give a detailed summary of recently published models, computation time and accuracy. They conclude that to accurately model delamination extent and local indentation even on small coupons, mesoscale models with stacked solid or shell elements are required. Along with extensive computation time, sophisticated models require increasing numbers of material property parameters—to be supplied by experiment. Neither time nor properties may be available for use in routine damage tolerant design calculations in which the performance of candidate composite systems and layups are explored. Use of less sophisticated models requiring fewer properties and less computation time may be thus compelled, with consequent compromises in accuracy and reliability of the results. Modeling of larger, geometrically complicated structures can be made feasible by noting that most of the larger structure is not subject to damage and can be treated elastically, whereas the damaged area remains local and can be treated using a more sophisticated model of local behavior. Accuracy of
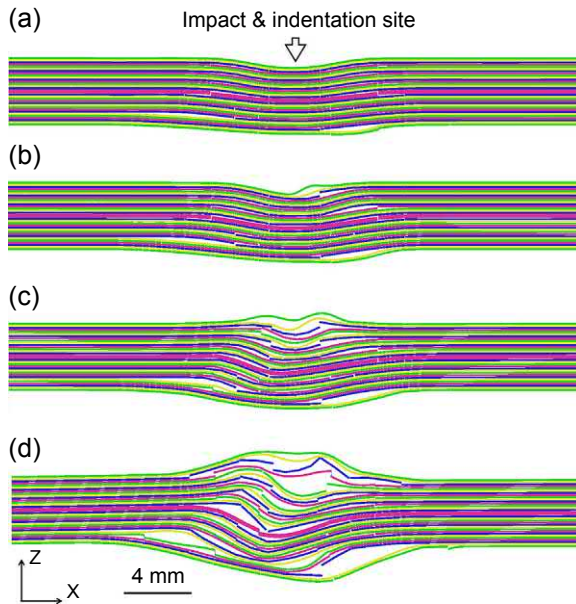
Figure 11.13 Simulated development of Compression After Impact failure via local buckling instability as the global load is increased from case (a) to (d), from Sun & Hallett [32].

strength predictions for damaged structures is not yet as good as predictions for simple coupons [4].

As an example of damage tolerant design calculations exploiting numerical models, Dubary et al. [31] use a Discrete Ply Model to calculate delamination area, dent depths, and CAI values for impacts on a range of laminate types, using the data to derive CAI values at dent depths of 0.5 mm—the value assumed for visual inspection BVID. Thus, laminate types with optimum CAI strengths at BVID could be identified and used for material selection and design calculations. The authors note that 36 h on a 20 CPU array is required for analysis of a single impact. Future model development needs to reduce this considerably if numerical modeling is to be directly used in practical design and materials selection.

High-velocity impact can introduce additional modeling challenges. Ballistic impact and bird strike can produce extremely distorted structures (and the bird). Hypervelocity impact needs to cope with gross distortions of the impactor and the impacted object. Conventional FE codes cannot cope with gross distortions since the shape functions across the elements are no longer accurate. An alternative strategy, which commercial codes are now incorporating, is the use of SPH. (Smooth Particle Hydrodynamics; Libersky et al. [37]). This is a *meshless* method which allows complete freedom in the disposition of a node, relating only to other nodes immediately surrounding it, and choosing local curve fitting to suit the accuracy required. Hypervelocity impact on satellite barriers is an ideal candidate for this method. As mentioned earlier, satellites need a barrier to break up micrometeorites which can impact at velocities in excess of 70 km/s. The SPH code needs to model the breakup of the micrometeorite as it passes

through the first barrier and converts its energy to a debris cloud. Tests are not possible at these velocities, but for the Columbus International Space Station, tests conducted at 3 km/s agreed well with the SPH simulations [38].

11.5 Post impact fatigue behavior of polymer composite laminates

11.5.1 General

The fatigue response of impact damaged laminates is important because impact-induced delaminations may grow under service fatigue loads, further reducing the residual static strength. In-plane fatigue loading in aircraft structures can be either tension−tension; compression-tension, or compression−compression. Fuselage structures are largely in tension fatigue, lower wing skins are largely tension with excursions into compression on landing, and upper wing skins largely compression with occasional excursions into tension during landing. For both static and fatigue compression, impact-induced local delamination clusters promote local buckling under in-plane compression resulting in mode I opening and modes II (and III) shear displacements at delamination tips (Fig. 11.14).

Chapter 8 of this book describes the behavior of single delaminations propagating under static and cyclic loads under Mode I opening and Mode II shear. Experiments to measure delamination crack growth rates under these conditions have established that the major controlling parameter is strain energy release rate range ΔG, (or G_{max} for minimum loads of zero) There are now emerging protocols and standards for this type of test (see Chapter 8) together with significant quantities of delamination growth data for a large number of polymer composite systems. Delamination crack growth rates in both modes I and II are now routinely characterized by plotting G against delamination growth rate, as shown in Fig. 11.15. This shows schematically the characteristic delamination crack growth behavior with a minimum threshold value of G, G_{th} necessary for growth, a region where da/dN the growth rate is proportional to G^n n
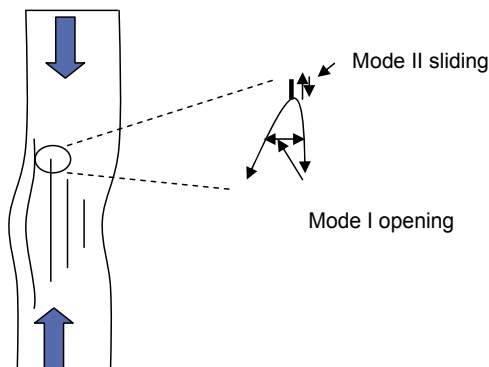
Figure 11.14 Schematic illustration of mode I and II displacements at a delamination tip under in-plane compression loading.
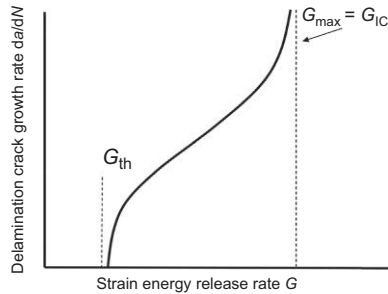
Figure 11.15 Schematic illustration of the relation between strain energy release rate G and delamination crack growth rates as established via tests on the standard geometry DCB and ENF samples, showing the threshold for growth at G_{th} and static fracture at $G = G_{IC}$.

being a constant, and a region of the accelerating growth rate as G_{max} approaches G_{IC} or G_{IIC} the static composite toughness.

While laboratory measurements of fatigue growth rates of single delaminations from starter defects are valuable to characterize intrinsic material behavior under well-defined conditions, growth of delaminations within damage clusters typified by Figs. 11.1 and 11.2 is a more complex situation. Location of individual delaminations within the impact cluster is often known only approximately, and the close proximity of delaminations to each other implies there will be interactions between them, influencing the strain energy release rate at delamination tips. In addition, measurement of internal delamination dimensions is significantly less accurate than in DCB and ENF samples, where the single delamination is visible at the sample edge. Together, these factors ensure significant variability in fatigue life of impact damaged samples. Ogasawara et al. [39] have demonstrated a progressive reduction in Weibull modulus (increasing variability) from 61.8 for undamaged composite compression strength, to 19.4 for CAI strength, to between two and three for fatigue life scatter of impact damaged samples.

11.5.2 In-plane fatigue life of impacted composites

Tension-tension loading in fatigue is found experimentally to be comparatively benign in its effects on life (for example [40,41]) in comparison with loadings dominated by compression cycles which have more severe effects [42]. For example, Melin et al. [42] showed that fatigue tests of impact damaged laminates in tension-compression fatigue at R-values (minimum load/maximum load) of −1 and −5 have almost identical stress-life (S−N) curves when lives are plotted in terms of maximum compression stress. Fig. 11.16 shows this for the two data sets. Tests at an R value of −1 have a mean stress of zero and equal excursions into tension and compression, whereas tests at R = −5 will have stress cycles with tension excursions only 20% of the size of the compression ones. The similarity of the S−N curves implies that tensile load excursions are contributing little to the fatigue damage.

The damaging effect of compression is entirely consistent with the local buckling behavior of the delaminations when loaded in this way. The local strain energy release rates at delamination tips will depend on whether or not there are shear components in
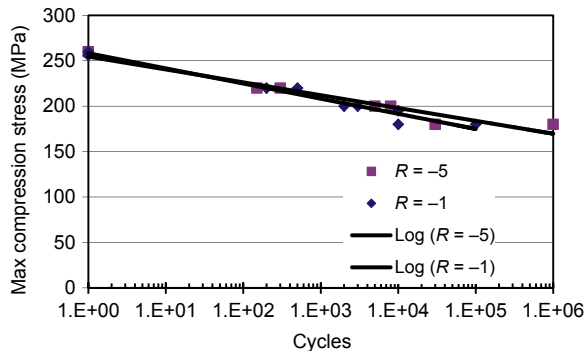
Figure 11.16 Maximum compression stress versus fatigue cycles for tension-compression fatigue at R = −1 and R = −5; adapted from the data of Melin et al. [42].

mode II or mode III present. To the extent that the size and morphology of initial delamination damage are only approximately known, there will be a range of possible G values at delamination tips for each delamination, growth in fatigue occurring if the G resulting from the combined displacements exceeds G_{th}.

Stress-life fatigue behavior of damaged composites under in-plane compression − compression loading has been investigated by Refs. [43−50] using samples with minimum detectable damage (BVID) and also samples with larger (visible) damage. Quantified impact damage size-is often not specified in many test series. When specified it is characterized variously as dent depth, delamination area or damage width and/or length. This vagueness sometimes makes meaningful data comparison between different authors difficult.

Fatigue life data universally shows increasing fatigue life with decreased maximum compressive stress; the larger the initial damage area, the greater the reduction in the S−N curve compared with pristine material. Static strength reductions (CAI) of about 15% are found for BVID damage compared with the undamaged compression strength. Larger (visible) damage with delaminations up to 30%−40% of the sample width produces further reductions in static CAI of up to 30%−40%. For composite matrices of low to intermediate toughness, the degradation in stress-life fatigue data echos the static strength reduction irrespective of the life. Cyclic stresses producing a defined life of say 10^5 cycles are progressively reduced with increased initial damage width. S−N trend lines are parallel to each other and to the undamaged pristine one [44]. An example of this behavior from the work of Isa et al. [43] is shown in Fig. 11.17a. In contrast, S−N data for samples with tough matrices [41,44] show a diminishing effect of impact damage with increased fatigue life; S−N lines of pristine and damaged samples tend to converge at lives in excess of 10^6 cycles. For these materials, the worst effects of impact damage are for the static loading case; the effect of fatigue is more benign. This behavior is shown in Fig. 11.17b. At long lives, fatigue strengths of the damaged and pristine samples are almost identical e.g. [41,43].

For epoxy matrix composites, if maximum cyclic stresses are normalized with respect to the static composite CAI strength, then S−N data for samples with different damage width come approximately together. This is shown in Fig. 11.18 from the

(a)

(b)
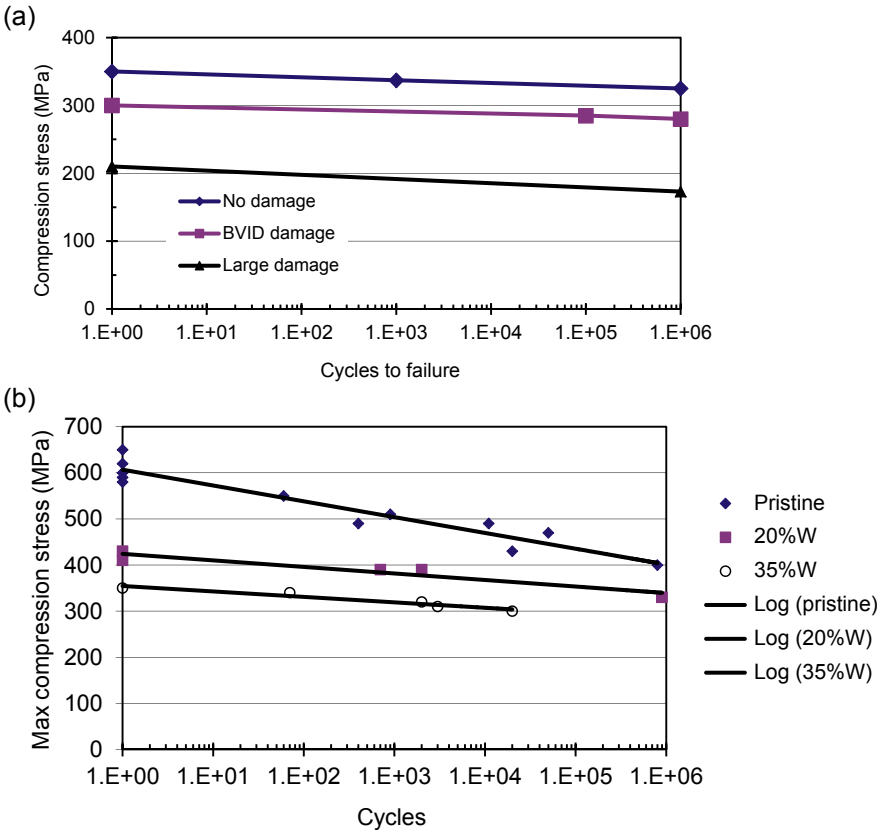
Figure 11.17 a & b; Maximum compression stress versus cycles to failure for pristine and for impact damaged QI samples with damage occupying 20% and 35% sample width. (a) shows data for epoxy matrix composites, and (b) shows data for tougher PEEK matrix samples. Adapted from data of Isa et al. [43] and Uda [44].
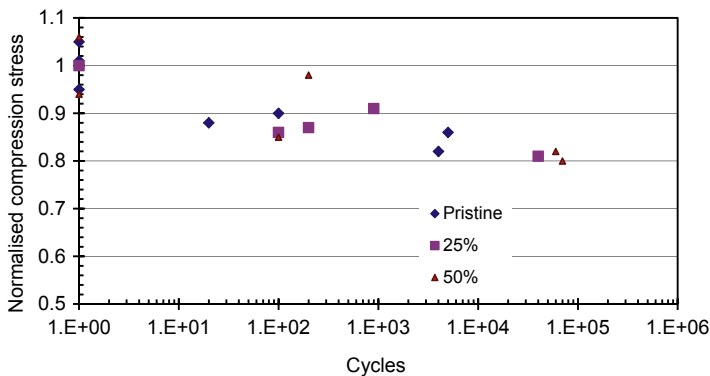
Figure 11.18 Normalized stress versus cycles for failure with compression stress normalized against CAI strength; 25% and 50% refer to damage as a % of sample width. Data from Uda et al. [46].

work of Uda et al. [44] where S−N lines for pristine, and impact damage covering 25% and 50% of the fatigue sample width are plotted. The extrapolated fatigue strength at lives in excess of 10^6 cycles in Fig. 11.18 is about 70%−75% of the static strength, irrespective of the damage size.

Many investigators have shown that there is a fatigue endurance limit of between 60% and 70% of the static CAI strength for constant amplitude cycling in compression of impact damaged samples [41,50]. If the damaged laminate is cycled at maximum compressive stresses less than this, there is no failure. The 60%−70% figure appears to hold good irrespective of the extent of the damage. It is also found that there is no degradation in residual strength [50] with increasing cycles if the laminate is fatigued at compression stress cycles less than 60%, implying there is no fatigue-induced delamination growth at stresses less than 60%−70% of static CAI.

There is little information available for the effects of variable amplitude loading on the fatigue of damaged samples, except for the detailed study of Mitrovich [41] who has investigated the effects of low-high and high-low block programs and also TWIST aircraft wing spectrum, all in compression. One major conclusion was that application of high-low blocks where the initial blocks exceeded 70% of the CAI, caused rapid delamination growth under the high load block, which continued under the smaller stresses of the low block. These were less than 30% of the CAI static strength. Stresses of 30% CAI would not have caused growth had they been applied first in a low − high sequence. Thus, stresses to initiate fatigue damage growth within delamination clusters was greater than those required to propagate it.

11.5.3 Fatigue delamination growth from impact damage

Observations using C scan and other NDT techniques during fatigue of impact damaged laminates show that at cyclic stresses above the threshold of 60%−70% of static CAI, delamination growth occurs and eventually results in sample failure via buckling instability. Behavior reported by different investigators are sometimes inconsistent, with some reports finding zero delamination growth until just before failure, and no change in the residual compression strength throughout the life [43], and others [41,44,45] finding that delamination growth occurs throughout life. The differences may be related to the size of the cyclic stresses applied, but may also be related to experimental difficulties in monitoring damage growth. Small increments of growth at low stresses may not be detected by the NDT technique used. In the traditional C scan ultrasound, only the outline of the projected area of the delamination array can be imaged. Growth of small internal delaminations cannot be monitored. There is currently inadequate understanding of factors controlling the onset of impact damage growth in fatigue.

For example, little or no delamination growth was detected during the first 90%−95% of fatigue life in the work of Isa et al. [43]. Beyond this point, the rapid growth of delaminations took place, resulting in sample failure after a very few further cycles. This behavior is illustrated in Fig. 11.19a, showing data for two levels of impact damage at maximum stresses between 85% and 94% of static CAI strength. Delamination growth has also been observed much earlier in life [41,51]. An example
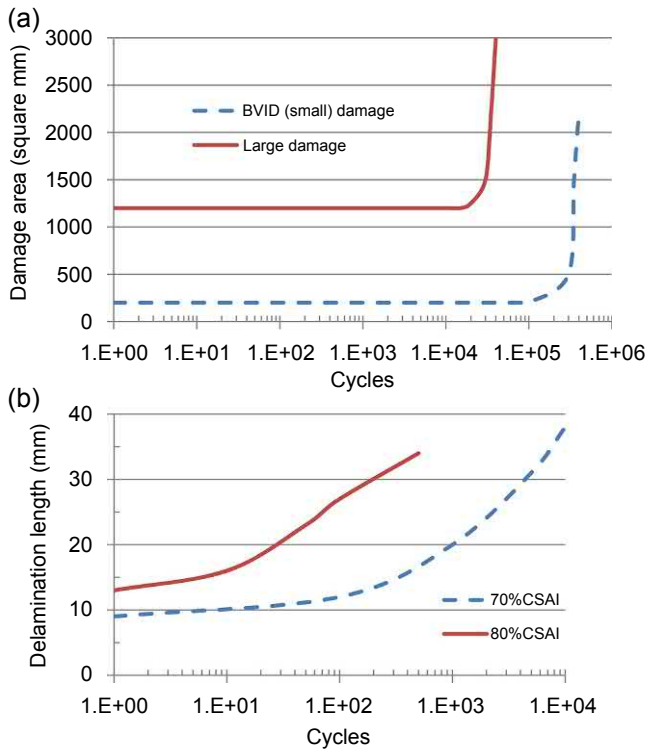
Figure 11.19 Delamination growth within impact damage versus fatigue cycles under zero to compression loading; (a) From Isa et al. [43] showing zero growth in the area until near end of life under stresses 85% of static CAI. (b) From Mitrovich et al. [41] showing delamination length growth from the start of fatigue cycling under stresses 70% and 80% of static CAI.

of this behavior is shown in Fig. 11.19b from the work of Mitrovich [41] under stresses between 70% and 80% of static CAI.

The observations of Mitrovich [41] on high-low block loading fatigue suggest that in some circumstances initial fatigue delamination growth from the impact damage may require either prolonged cycling or high stresses to begin, but once started delaminations can grow at smaller stress values than were required for initiation. All observations agree that once started, delamination growth rates are rapid with perhaps only 10^4 cycles required to cause final failure. Observations of the delamination growth process reveal that growth occurs first in the width of the projected damaged area, perpendicular to the applied compressive stress [40,41,52], and preferentially from delaminations nearest the laminate side opposite the impacted one.

Strain energy release rates G at delamination tips have been calculated using finite element analysis for single delaminations located within the composite laminate thickness [41,53,54]. It is found that under compression-compression loading, both G_I and G_{II} strain energy release rates decline with increasing delamination length (measured parallel to the loading direction). Fig. 11.20 shows the calculated changes in $G_{II,}$ the
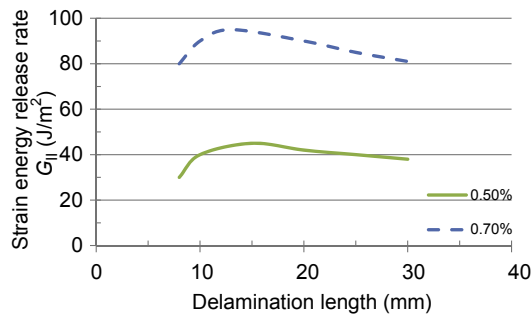
Figure 11.20 Calculated values of mode II strain energy release rate G_{II} versus delamination length for idealized single delamination two plies from the outer laminate surface; laminate subjected to strains of 0.5% and 0.7% in-plane compressive strain, from Mitrovich [41].

shear mode strain energy release rate with increasing delamination length for a single delamination two plies from the surface of a QI lay-up. There is an initial increase in G_{II} value with increased delamination length, followed by a steady fall with further growth.

A reduction in strain energy release rate with increased delamination length implies that growth rates should follow the same trend. This has been confirmed experimentally by Mitrovich [41] and Zhang et al. [54]. If data in Fig. 11.19b is replotted with a linear cycles scale, instead of a logarithmic one, the decrease in growth rate with increased length can be more obviously seen (Fig. 11.21). Growth rates calculated from these data together with observations from tests at other stress levels are shown in Fig. 11.22. A trend of decreased growth rates with increased delamination length is confirmed. This figure also shows the importance of maximum stress level. An increase in cyclic compression stress from 60% to 80% of static CAI increases the delamination growth rate by a factor approaching 100. Also shown on this curve are growth rates at 30% of CAI, obtained after delamination growth had been started by cycling at 80% CAI. As Fig. 11.20 shows, stress is a major parameter determining G the strain energy release rate; thus, growth rates from impact damage are strongly dependent on G, echoing the well-established dependencies between G and growth rate found for single delaminations in DCB and ENF samples (see Chapter 8).
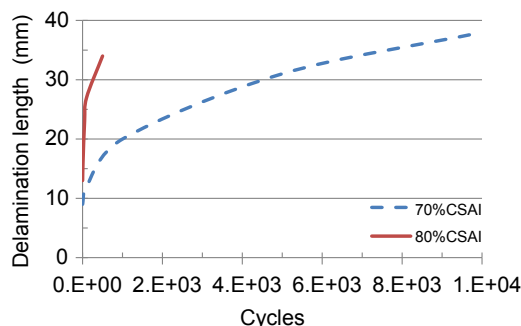
Figure 11.21 Data from Fig. 11.19 [41] replotted on a linear cycles scale showing a decrease in delamination growth rate with increasing delamination length and fatigue cycles.
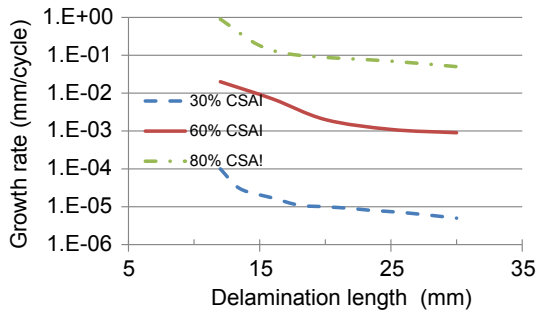
Figure 11.22 Measured delamination growth rates versus delamination length from Ref. [41] showing decrease in growth rates as delamination extends and sensitivity of growth rate to maximum compressive stress.

The work of Butler et al. [53] also suggests a link between these two very different types of tests via the G value of delaminations. However the interactions between the strain fields of individual delaminations, and the mode II contributions to delamination growth were not incorporated, and the correlation requires further research, particularly into the contribution of modes II and III shear modes to the overall G at impact clusters of delaminations.

A similar approach by Mitrovich [41] but using mixed-mode strain energy release rates was used to predict growth in delaminations within impact damaged areas with a variant on the expression:

$$\frac{dL}{dN} = m_1 \left(\frac{G_I}{G_{IC}} \right)^{n_1} + m_2 \left(\frac{G_{II}}{G_{IIC}} \right)^{n_2} \tag{11.4}$$

Where dL/dN is the delamination growth rate.

m_1, m_2, n_1, n_2 are all experimental constants.

G_{IC}, G_{IIC} are critical values of strain energy release (static toughness) rate in modes I and II for the composite system.

G_I and G_{II} are the current applied levels of strain energy release rate in fatigue.

These results imply that both CAI strength and the fatigue limit of impact damaged laminates will be dependent on the static toughness values in modes I and II for comparable impact damage levels.

11.6   The damage-resistant structure: designing against impact and fatigue

11.6.1   Resistance to impact

Having described the many modes of impact damage, their debilitating effects, and the use of analytical and numerical methods to predict damage and residual strengths, it is of relevance to discuss what can be done to alleviate this weakness where the residual compressive strength may be low. There are two strategies: first, to increase the
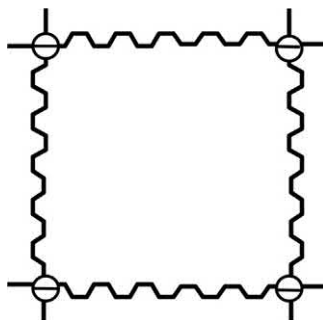
Figure 11.23 Plan form of subfloor posts in a proposed helicopter [55].

toughness and through-thickness strength of laminates, and second, to design energy-absorbing structures where the final (collapsed) state is not important.

Increasing the fracture toughness of resin is possible to a certain extent, but a more drastic solution is to increase the through-thickness resistance by adding reinforcement. Such a technique is the commercial product ("Z" pins) using tiny pins driven into the laminate before curing. This is expensive and can lower some undamaged in-plane strengths. A better alternative is the use of stitching, particularly for stiffened compression panels. The industry has invested significantly in developing this technique [56].

An energy-absorbing composite can be deliberately designed. Energy absorption in ductile metallic structures is well established since plasticity is an excellent mechanism. The most effective energy absorbing mechanism in brittle composites is complete debonding of all fibers. This was demonstrated by Hull [57]. Clever detailed design is necessary to ensure that large scale fiber debonding is excited. Specific energy absorption of order 75 kJ/kg is possible, compared with 15−30 kJ/kg for mild steel and light alloys. The ultimate need for good energy absorption is the subfloor in a helicopter. Here, there is a large mass on the roof, and the passenger cabin should keep its shape in a crash landing. Thus, to avoid using super-stiff fuselage frames, a good energy-absorbing subfloor is needed. Johnson and Kohlgruber [55] describe a successful grillage design shown schematically in Fig. 11.23.

The orthogonally intersecting grillage posts have their vertically corrugated shear webs to keep the buckling stress high. At the four corner intersections, there are cylindrical-section tubes, all having tailored edges to trigger fiber debonding mechanisms. By using hybrid composite configurations, specific energies greater than 70 kJ/kg have been achieved.

11.6.2 Resistance to fatigue delamination growth

There is considerable experimental evidence (see Chapter 8) that together with increases in static CAI strength, fatigue delamination growth rates in coupon samples are reduced by increased composite G_{IC} and G_{IIC} toughness values. As threshold stress ranges for fatigue failure are 70% of the static CAI strength, and CAI is increased with increased toughness, increased toughness will increase both the fatigue strength of impact damaged samples and the fatigue cycles occupied by delamination crack growth.

Even for composites with the toughest matrices currently available, delamination growth rates are too rapid for damage tolerance of aircraft structures via regular inspection for slow damage growth during service to be a viable design technique. As noted in chapter 19, civil aircraft certification for airworthiness must rely instead on demonstration of zero crack growth during testing of the damaged structure. It is unclear at the moment whether pinning, stitching, and 3D weaving techniques will be as successful in inhibiting the growth of delaminations in fatigue, as they are in improving resistance to static damage growth. This remains an area for future research.

11.7 Conclusions

1. The extent of damage due to impact is found to depend not just on the material properties but on the dynamic response of the impacted structure, that is, its mass, stiffness, and the impact velocity.
2. Ballistic damage occurs with little structural response; low-velocity damage is possibly the most serious since impact damage can cause extensive shear-driven delamination entirely inside the structure, leading to reductions in the residual compressive strength of up to 60%.
3. Analytical methods exist to predict damage extent approximately. For low-velocity impact, a critical force exists, below which, no damage occurs. It depends on the mode II fracture toughness and is independent of the impact energy and structural stiffness.
4. If the critical force is exceeded, finite element models can predict subsurface delamination size, morphology and surface dent depth from input data of material properties, laminate characteristics, and structural compliance. Finite element models can accurately predict subsequent degradation of static compression strength—the CAI value.
5. Compression strength reduction is largely dependent on the extent of impact damage with material properties and structural compliance contributing to compression strength only via impact behavior.
6. Accurate FE analysis to predict CAI strength requires the use of sophisticated complex models requiring calculation times in excess of 24 h even on multi CPU arrays. Their routine use for design calculations of damage tolerance capability in composite aircraft awaits further increments in computing speed and software code.
7. For high velocities of impact, the ballistic limit depends on the induced stress and strain and the mass ratio.
8. Fatigue life and fatigue strength of pristine samples are reduced by impact damage with the reduction being dependent on the size of impact damage. The static CAI strength is a strong indicator of fatigue strength. For zero to compression fatigue loading, the long-life fatigue limit is between 0.6 and 0.7 of the static CAI.
9. For composites with tough matrices, the reduction in static strength produced by the impact is greater than the reduction in long-life fatigue strength. At lives $> 10^6$ cycles, there is little difference in fatigue strength between pristine laminates and ones damaged at BVID.
10. The fatigue failure process is one of delamination growth, followed by unstable buckling failure. In long-life fatigue, there is a significant incubation period before the delamination growth is detected. Once delamination growth begins the remaining life is short, prohibiting damage tolerance design via slow crack growth. The delamination growth rates decline marginally with increasing length but increase markedly with increasing compression stress. The finite element calculations of strain energy release rates at internal delamination

tips show a similar decrease with increasing delamination length and are highly sensitive to applied stress.

11. The proportion of fatigue life occupied by delamination growth is a small fraction of the total. The onset of delamination growth is sensitive to load history; the initiation of growth appears to be more difficult than its propagation.

11.8   Future trends

(1) Conditions determining the threshold for delamination growth and growth onset are poorly understood. As fatigue delamination growth rates are fast and the fraction of life occupied by growth is small, it is vital for safe aircraft operation that conditions determining the threshold are understood and can be used to predict safe design stresses.

(2) There have been very few studies of the influence of variable amplitude loading on fatigue life and delamination crack growth from impact damaged samples. More studies and a better understanding of this important design situation are required.

(3) Degradation of compression strength with increased visibility of damage is an important aspect of damage tolerance and structural airworthiness of polymer composite aircraft, as discussed in chapter 20. The relationships between the size of visible surface damage, the extent of subsurface damage, degradation in static strength and fatigue life, still lack the predictive capability necessary for the design of composite aircraft structures. Significant experimental and modeling work is required to fill this gap.

(4) Numerical models needing significantly reduced computer processing time are required before they can be used in routine design studies.

(5) Research to improve the toughness, stiffness, and strength of polymer composite laminates has continued for many years to improve the resistance of polymer composites to impact damage. New laminates will require their static and fatigue damage tolerance to be characterized so that the new materials can be exploited in a safe, airworthy manner.

References

[1] S. Abrate, Impact on Composite Structures, Cambridge Univ. Press, 1998.

[2] G.A.O. Davies, R. Olsson, Impact on composite structures, Aeronautical Jnl 108 (2004) 541−563.

[3] W.J. Cantwell, J. Morton, The impact resistance of composite materials: a review, Composites 22 (15) (1991) 347−362.

[4] R. Bogenfield, J. Kreikemeier, T. Wille, Review and benchmark study on the analysis of low velocity impact on composite laminates, Engng Failure Anal. vol. 86 (2018) 72−99.

[5] C.E. Andersen, 'Hypervelocity impact': proc. Of symposium at noordvijk, Netherlands, Int. Jnl. of Impact Engng. 29 (2003).

[6] L. Cook, Visual Inspection Reliability for Composite Aircraft Structures, Ph D thesis Cranfield University, 2009.

[7] G.A.O. Davies, D. Hitchings, J. Wang, Prediction of threshold impact energy in quasi-isotropic carbon/epoxy composite laminates under low-velocity impact, Compos.Sci.and Tech. 60 (1) (2000) 1−7.

[8] G.A.O. Davies, D. Hitchings, The separate roles of fibre damage and delamination in compression-after-impact strength of composite panels, in: 5th EUROMECH Solid mechanics Conf. Thessaloniki, Greece, 2003.

[9] D.D.R. Cartie, P.E. Irving, Effect of resin and fibre properties on impact and compression after impact performance of cfrp, Composites 33 (2002) 483−493.

[10] E. Panettieri, D. Fanteria, C. Froustey, Low velocity impact tests on carbon epoxy composite laminates: a bench mark study, Composites Part B 107 (2016) 9−21.

[11] A.T. Nettles, L. Scharber, The influence of G_I and G_{II} on the compression after impact strength of carbon fibre/epoxy laminates, J. Compos. Mater. 52 (8) (2018) 991−1003.

[12] T. Rhead, D. Marchant, R. Butler, Compressive strength of composite laminates following free edge impact, Compos. Part A 41 (9) (2010) 1056−1065.

[13] S.I. Thorsson, S.P. Sringeri, A.M. Waas, B.P. Justusson, Experimental investigation of composite laminates subject to low velocity edge-on impacts and compression after impact, Compos. Struct. 186 (2018) 35−346.

[14] W. Godwin, G.A.O. Davies, Impact behaviour of thermoplastic composites, in: C. Brebbia (Ed.), Composite Material Technology, Springer Verlag, 1988.

[15] J.C. Pritchard, P.J. Hogg, The role of impact damage in post-impact compression testing, Composites 21 (6) (1990) 503−511.

[16] R. Olsson, 'A Review of Impact Experiments at FFA during 1986 to 1988', the Aero, Research Institute of Sweden, 1999.

[17] J.F.M. Wiggenrad, X. Zhang, G.A.O. Davies, Impact damage prediction and failure analysis of heavily loaded, blade-stiffened composite wing panels, Compos. Struct. 45 (2) (1990) 81−103.

[18] G.A.O. Davies, X. Zhang, Predicting impact damage of stiffened compression panels, Aeronautical Jnl 104 (2000) 97−103.

[19] G.A.O. Davies, D. Hitchings, J. Ankersen, Prediction of delamination and debonding in modern aerospace composite structures, Compos. Sci.and Tech. 66 (2005) 846−854.

[20] G.A.O. Davies, P. Robinson, 'Predicting Failure by Debonding/delamination' in Debonding/Delamination of Composites', AGARD Conf. Proc. 530, AGARD Neuilly sur Seine, France, 1992.

[21] H. Suemasu, O. Majima, Multiple delaminations and their severity in circular axisymmetrical plates subjected to transverse loadings', Jnl. Compos. Matls. 30 (4) (1996) 441−453.

[22] A. Sjögren, Y. Krasnikov, J. Varsna, Determination of elastic properties of impact damage in carbon fibre/epoxy laminates, Composites, Part A 32 (9) (2001) 353−360.

[23] P. Berbinau, C. Filiou, C. Soutis, Stress and failure analysis of composite laminates with inclusions under multi-axial compression-tension loading, Applied Compos.Materials. 8 (5) (2000) 307−326.

[24] Y. Xiong, C. Poon, P.V. Straznicky, H. Vietinghoff, A prediction method for the compressive strength of impact damaged composite laminates', Compos. Struct. 30 (4) (1995) 357−367.

[25] G. Flanagan, Two-dimensional delamination growth in composite laminates under compression loading, in: Composite Materials: Testing and Design, 8th vol, Whitcomb,J.D, 1988, pp. 10−190. ASTM STP 1206.

[26] G.A.O. Davies, X. Zhang, Impact damage prediction in composite structures, Int. Jnl. of Impact Engng. 6 (1) (1995) 149−170.

[27] F. Aymerich, F. Dore, P. Priolo, Simulation of multiple delaminations in impacted cross-ply laminates using a finite element model based on cohesive interface elements, Compos. Sci. Technol. 69 (2009) 1699−1709.

[28] X. Zhang, F. Bianchi, H. Liu, Predicting low-velocity impact damage in composites by a quasi-static load model with cohesive interface elements, The Aeronautical Jnl 116 (1186) (2012) 1350−1367.

[29] L. Iannuci, R. Duchaene, M. Willows, J.A. Degrieck, Failure modes for the analysis of thin woven glass composite structures under impact loadings, Comput. Struct. 79 (8) (2001) 785−799.

[30] X.C. Sun, S.R. Hallett, Barely visible impact damage in scaled composite laminates: experiments and numerical simulations, Int J impact Engng 109 (2017) pp178−195.

[31] N. Dubary, C. Bouvet, S. Rivallant, Ratsifandrihanaj, Damage tolerance of an impacted laminate, Compos. Struct. 206 (2018) 261−271.

[32] X.C. Sun, S.R. Hallett, Failure mechanisms and damage evolution of laminated composites under compression after impact (CAI): experimental and numerical study, Composites 104 (2018) 41−59.

[33] W. Tan, B.G. Falzon, L.N.S. Chiu, M. Price, Predicting low velocity impact damage and compression after impact (CAI) behaviour of composite laminates, Composites 71 (2015) 212−226.

[34] S. Rivallant, C. Bouvet, E.A. Abdallah, B. Broll, J.J. Barrau, Experimental analysis of cfrp laminates subject to compression after impact: the role of impact induced cracks in failure, Compos. Struct. 111 (2014) 147−157.

[35] A. Soto, E.V. Gonzalez, P. Maimi, J.A. Mayugo, P.R. Pasquali, P.P. Camanho, A methodology to simulate low velocity impact and compression after impact in large stiffened panels, Compos. Struct. 204 (2018) 223−238.

[36] Y. Feng, Y. He, H. Zhang, X. Tan, A. Tao, J. Zheng, Effect of fatigue loading on impact damage and buckling/post buckling behaviours of stiffened composite panels under axial compression, Compos. Struct. 164 (2017) 248−262.

[37] L.D. Libersky, A.G. Petschek, SPH with strength of materials, in: Advances in the Free Lagrange Method, ed. Trease, Fritts and Growley, Springer Verlag, Berlin, 1993.

[38] N. Robertson, Hypervelocity Impact: Simulation of Impact on a Space Vehicle Shielding Structure, Royal Aero. Soc. Conference on Impact and Damage Tolerance in Composite Materials, London, 2012.

[39] T. Ogasawara, S. Sugimoto, H. Katoh, T. Ishikawa, Fatigue behaviour and lifetime distribution of impact damaged carbon fibre/toughened epoxy composites under compressive loading" Advanced Composite Materials vol. 22, 2013, pp. 65−78.

[40] H.T. Hahn, J. Bartley-Cho, S.G. Lim, "The effect of loading parameters on fatigue of composite laminates" Part II, DOT/FAA/AR-96/76, 1996.

[41] M. Mitrovich, H.T. Hahn, G.P. Carman, P. Shyprykevich, Effect of loading parameters on the fatigue behaviour of impact damaged composite laminates, Compos. Sci. Technol. 59 (1999) 2059−2078.

[42] L.G. Melin, J. Schon, T. Nyman, Fatigue testing and buckling characteristics of impacted composite specimens, Int. J. Fatigue 24 (2002) 263−272.

[43] M.D. Isa, S. Feih, A.P. Mouritz, Compression fatigue properties of z-pinned quasi isotropic carbon epoxy laminate with barely visible impact damage, Compos. Struct. 93 (2011) 2269−2276.

[44] N. Uda, K. Ono, K. Kunoo, Compression fatigue failure of cfrp laminates with impact damage, Compos. Sci. Technol. 69 (2009) 2308−2314.

[45] M.S. Rosenfeld, L.W. Gause, Compression fatigue behaviour of graphite epoxy in the presence of stress raisers, in: Fatigue of Fibrous Composite Materials ASTMSTP, vol. 723, ASTM, Philadelphia PA USA, 1981, pp. 174−196.

[46] D.D. Symonds, G. Davis, Fatigue testing of impact damaged T300/914 Carbon fibre reinforced plastic, Compos. Sci. Technol. 60 (2000) 379−389.

[47] G. Clark, T.J. Van Baricum, Load Spectrum Modification Effects on Fatigue of Impact Damaged Carbon Fibre Composite Coupons Composites, vol. 18, 1987, pp. 243−251.

[48] M.R.L. Gower, R.M. Shaw, Assessment of the applicability of compression after impact (CAI) and open hole tension (OHT) methods for use under fatigue loading, in: 13th European Conference on Composite Material, Stockholm Sweden, 2008.

[49] H.T. Hahn, M. Mitrovic, O. Turkgenc, The Effect of Loading Parameters on Fatigue of Composite Laminates: Part III, FAA Report DOT/FAA/AR-99/22, Office of Aviation Research, Washington, 1999.

[50] A. Nettles, A. Hodge, J. Jackson, An examination of the compressive cycle loading aspects of damage tolerance for polymer matrix launch vehicle hardware, J. Compos. Mater. 45 (2011) 437.

[51] A.S. Chen, D.P. Almond, B. Harris, Impact damage growth in composites under fatigue conditions monitored by Acoustography, Int. J. Fatigue 24 (2002) 257−261.

[52] L.G. Melin, J. Schon, Buckling behaviour and delamination growth in impacted composite specimens under fatigue loads and experimental study, Comp. Sci. Tech. 61 (2001) 1841−1852.

[53] R. Butler, D.P. Almond, G.W. Hunt, B. Hu, N. Gathercole, Compressive fatigue limit of impact damaged composites laminates, Composites 38 (2007) 1211−1215.

[54] L. Zhang, R. Wang, W. Liu, C. Chen, X. He, Delamination growth behaviour in carbon fibre reinforced plastic angle ply laminates under compression fatigue loads, J. Reinf. Plast. Compos. 31 (2012) 259−267.

[55] A.F. Johnson, D. Kohlgruber, Design and performance of energy absorbing subfloor structures in aerospace applications. Materials and Structures for Energy Absorption, I.Mech. E. Seminar S672, London, 2000.

[56] A. Velicki, P. Thrash, Damage arrest design approach using stitched composites, Aeronautical Jnl 115 (1174) (2011).

[57] D. Hull, Energy Absorption of Composite Materials under Crash Conditions, ICCM4, Japan, 1982.

Design and failure analysis of composite bolted joints for aerospace composites

12

C.T. McCarthy, M.A. McCarthy
University of Limerick, Limerick, Ireland

12.1   Introduction

Large commercial aircraft, such as the Airbus A380 or Boeing 747−800, contain about six million parts, three million of which are fasteners (e.g., bolts, rivets). Fasteners for composite aircraft applications are very expensive, and so the cost element involved in aircraft assembly, due to fastener requirements, is enormous. In addition, fasteners significantly reduce structural efficiency, due to stress concentrations at bolt-holes, and add significant weight to structures. Hence, efficient design of bolted joints for composite aircraft, in terms of maximizing joint strength while simultaneously minimizing fastener requirements, presents a major technical challenge to aircraft manufacturers. As a result, the composite bolted joint design has been a major topic of research for over 30 years, and many hundreds of papers on the subject exist (e.g., see Refs. [1−59]).

This chapter presents both experimental and finite element approaches that are commonly used to assist in the design and failure analysis of composite bolted joints. The work presented mostly stems from the authors' work in the field over the past decade. Results from both local (i.e., detailed) finite element and global (i.e., efficient) closed-form and finite element approaches are presented, and experimental results from the open literature are used to both calibrate and validate the modeling procedures. The primary variable under consideration is bolt-hole clearance, which is chosen as it induces significant three-dimensional stresses into the joint, and significantly alters the bolt-load distribution in multibolt joints, and so provides a rigorous test case for analysis.

The chapter opens with a general overview of composite bolted joint design, including the common terminology used, the modes in which composite joints fail and a description of the particular joining types being addressed in this Chapter A brief overview of the design and modeling technique is then presented. Following this, an analysis of single-bolt joints is carried out where the effects of bolt-hole clearance and friction are investigated. The analysis of load distribution in multibolt joints is then carried out, including failure predictions using bearing-bypass diagrams and issues around modeling large joint assemblies. Finally, a progressive failure analysis is carried out on multibolt joints. The chapter concludes with some further sources of information and future trends in this research field.

12.1.1   *General overview of composite joint design*

As mentioned, large commercial aircraft contain about three million fasteners, and so a multitude of bolted joint configurations exist. However, despite this diversity, there is a basic commonality in the stresses set up by the fastener or bolt load at a particular bolt-hole, and the effect of other loaded bolt-holes on this stress distribution [1]. This allows simplified coupon tests to be used in establishing design criteria and data for these various joint configurations. The intent then is to combine a suitable number of test/model results to represent the actual situation.

An example of reducing a complex primary structural joint down to a coupon test is shown in Fig. 12.1, Fig. 12.1(a) shows the design of a hybrid composite-metal wing-box that was proposed in the Technology Application to Near Term Business Goals and Objectives (TANGO) [2] project. Fig. 12.1(b) shows an actual skin-stringer joint that could be used to connect the outer composite wingbox to the inner metallic wing-box. A representative "benchmark" for this type of joint is shown in Fig. 12.1(c). Testing and analysis would be carried out on this "benchmark" structure to gain an insight into its behavior and failure mechanisms. To date, most research has been carried out at a coupon level on "benchmarks" similar, but often simpler, to that shown in Fig. 12.1(c). Very little testing and analysis for actual aircraft joints have been reported in the open literature, which is due to the extremely high costs and complexity associated with such work. Hence, this chapter will mostly concentrate on the design and analysis of coupon type composite bolted joints. However, consideration is given to large joint assemblies (20 bolts), which is now possible to analyze using the global finite element or closed-form approaches.
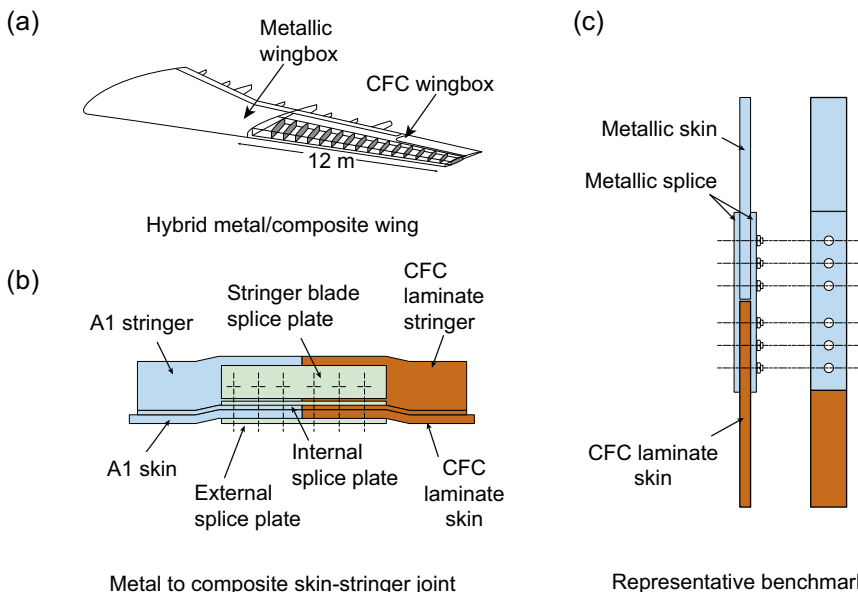
Figure 12.1 (a) Proposed hybrid composite-metal wingbox, (b) metal to composite skin-stringer joint, and (c) proposed representative benchmark joint [2]. CFC, carbon fiber composite.
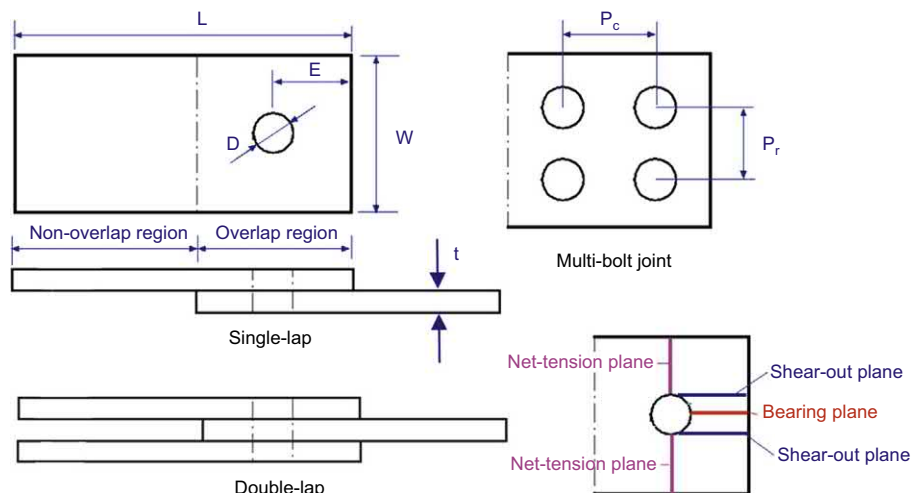
Figure 12.2 Definition of joint geometric design parameters.

12.1.2 Terminology used in bolted joint design

Fig. 12.2 shows an illustration of some commonly used joint geometric design parameters. The length, L, usually consists of two regions: the overlap region and the nonoverlap region. The length of the overlap region is defined by the portion of the laminate that is in contact with another laminate, while the length of the nonoverlap region is simply the remaining portion. The laminate−laminate contact interface is often referred to as the "shear plane" or "faying surface." The diameter, width, thickness, and edge distance are defined as D, W, t, and E, respectively, as illustrated in Fig. 12.2. In the case of multibolt joints, two additional parameters are used: the distance (i.e., pitch) between bolt-hole centers along the loading direction, P_c (i.e., the column pitch), and transverse to the loading direction P_r (i.e., the row pitch). Generally, two types of lap configurations exist, single-lap and double-lap, as shown in Fig. 12.2. Failure modes are generally associated with failure planes, and these planes are referred to as the bearing plane, the net-tension plane, and the shear-out plane, which are again highlighted in Fig. 12.2.

12.1.3 Bolted joints failure modes

The design of composite joints requires a sound understanding of the different failure modes. At a coupon level, there are generally six ways in which a composite bolted joint can fail, referred to as bearing, net-tension, shear-out, cleavage, fastener pull-through, and bolt failure, as illustrated in Fig. 12.3(a)−(f), respectively. Failure can also occur in more than one mode, either simultaneously or consecutively. The joint geometry predominantly controls the failure mode. However, other factors, such as material type, ply orientation, bolt torque, and loading configuration also
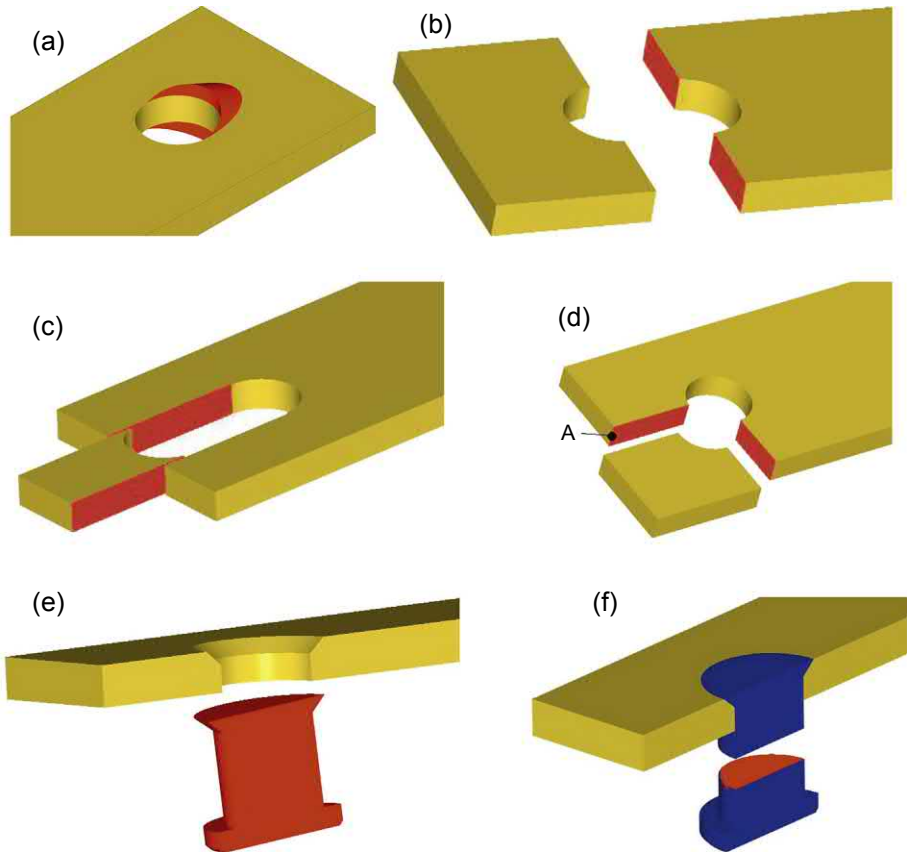
Figure 12.3 Failure modes in composite bolted joints:(a) bearing failure, (b) net-tension failure, (c) shear-out failure, (d) cleavage failure, (e) fastener pull-through, (f) bolt failure.

contribute, and each failure mode results from entirely different damage mechanisms occurring in the laminate and/or the bolt.

12.1.4   Problem description

12.1.4.1   Joint geometries

The single-bolt, single-lap joint, shown in Fig. 12.4(a), was used for the initial analysis on bolted joints carried out in this chapter, as extensive experimental and numerical results for this joint configuration were available from the literature [14−17]. The joint geometry is based on the ASTM standard D 5961/D 5961 M-96, [18]. The geometric ratios, w/d = 6, e/d = 3, and d/t = 1.6, were designed to induce bearing failure. For examining the load distribution in multibolt joints, the single-bolt joint, as in Fig. 12.4(a) was extended to include three fasteners, as shown in Fig. 12.4(b).
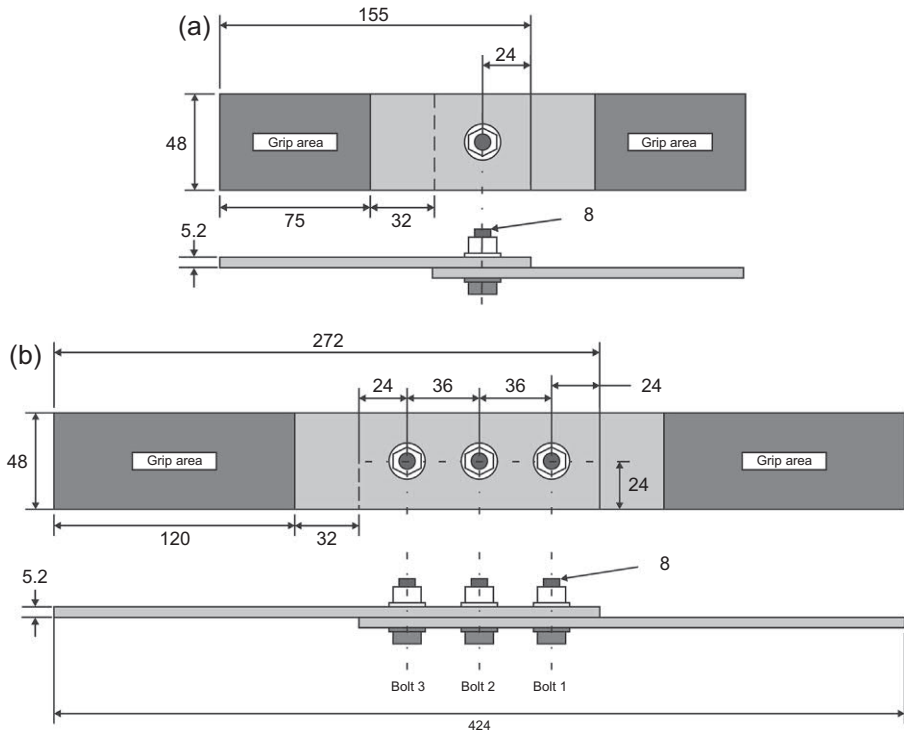
Figure 12.4 Joint geometries (all dimensions in millimetres): (a) single-bolt, single-lap joint; (b) three-bolt, single-lap joint [17,42].

Following the analysis on these joints, this chapter also considers the analysis of complex load distributions in large joint assemblies [19], and this will be assessed through a global finite element analysis of a 20-bolt joint (see Fig. 12.5) in both single-lap and double-lap joint configurations. All these aforementioned joint configurations were used as benchmark studies in the EU Framework five project BOJCAS (Bolted Joints in Composite Aircraft Structures) [19].

12.1.4.2 Materials

In this work, all joints were fabricated using a carbon fiber/epoxy composite material manufactured by Hexcel composites, with designation HTA/6376. In the single-bolt and three-bolt, single-lap joints, both laminates had a quasi-isotropic layup with stacking sequence $[45/0/-45/90]_{5s}$. Each ply had a thickness of 0.13 mm, yielding a total laminate thickness of 5.2 mm. In the double-lap three-bolt joints, the splice plates were manufactured from 16 plies, giving a nominal thickness of 2.08 mm, while the skin plate was manufactured from 32 plies and was nominally 4.16 mm thick. In the 20-bolt joints, the 3.12 and 6.24 mm thickness laminates had stacking sequences of $[\pm45/0/90]_{3s}$ and $[\pm45/0/90]_{6s}$, respectively. Unidirectional lamina material properties
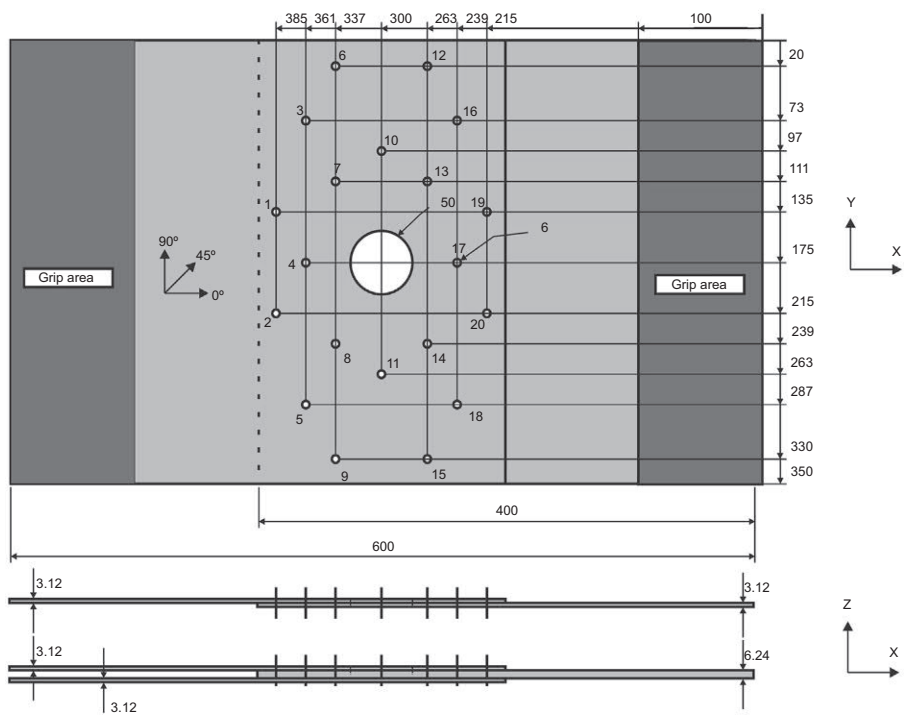
Figure 12.5 Twenty-bolt, single-lap, and double-lap joints with a bolt numbering system [19].

Table 12.1 Material properties.

Material	E_{11} (GPa)	E_{22} (GPa)	E_{33} (GPa)	G_{12} (GPa)	G_{13} (GPa)	G_{23} (GPa)	ν_{12}	ν_{13}	ν_{23}
HTA/ 6376	140	10	10	5.2	5.2	3.9	0.30	0.30	0.50
Titanium	110	110	110	42.6	42.6	42.6	0.29	0.29	0.29
Steel	210	210	210	80.8	80.8	80.3	0.30	0.30	0.30

are listed in Table 12.1. The variables E_{ii}, G_{ij}, and ν_{ij} refer to the modulus, shear modulus and Poisson's ratio in the principal material directions i, j (i, $j = 1, 2, 3$), respectively. The 6 and 8 mm diameter bolts were made from aerospace-grade titanium alloy, while the nuts and washers were manufactured from steel. Both the titanium and steel parts were modeled as isotropic bodies, and the material properties are listed in Table 12.1.

Table 12.2 Bolt-hole clearances used.

Clearance code	Nominal clearance (µm)
C1	0
C2	80
C3	160
C4	240

12.1.4.3 Bolt-hole clearance

As discussed previously, the main geometrical variable under investigation in this work is bolt-hole clearance. Due to manufacturing tolerances on both the bolts and the holes, it is inevitable that some bolt-hole clearance exists in bolted joints. In this work, clearance is defined as the algebraic difference between the bolt diameter and bolt-hole diameter, and the bolt-hole clearances chosen for this study are listed in Table 12.2. For a nominal 8 mm hole diameter, they represent percentage clearances of 0%, 1%, 2%, and 3% and are respectively coded C1−C4. Clearances C1 and C2 are within current aerospace tolerances, while C3 and C4 are slightly outside. The latter two are thus of interest in examining the possible effects of out-of-tolerance aerospace holes (or fasteners), and also in nonaerospace applications. For further details on the rationale for choosing these clearances, see McCarthy et al. [14]. The clearances were obtained experimentally using four reamers of different diameters, specially manufactured for this study to a tight tolerance by an aerospace supplier.

12.2 Finite element model

A typical finite element mesh for the joint is shown in Fig. 12.6. Five separate parts were meshed—two laminates, two washers, and a combined bolt-nut. The meshing of the laminates is similar to that used by Ireman [21], with a relatively high radial mesh density near the hole and under the washer, where high-strain gradients exist. Wedge elements were used to form the core of the bolt.

   The boundary conditions are also shown in Fig. 12.6. In order to avoid potential rigid body modes, light springs were applied to the components not fully constrained, such as the bolt, washers, and bottom laminate. For the finger-tight (bolt torque = 0.5 Nm) experiments modeled here, a bolt prestress of 7.2 MPa was applied (by artificially heating the washer in a separate load-step), while for the highly torqued joints (bolt torque = 16 Nm) a 227 MPa prestress was applied. For further details on bolt tightening, refer to McCarthy et al. and Lawlor [15,25]. Both contact and friction were considered between each contacting interface in the model. See McCarthy et al. and [15,17] for full details on contact and friction modeling in composite bolted joints.
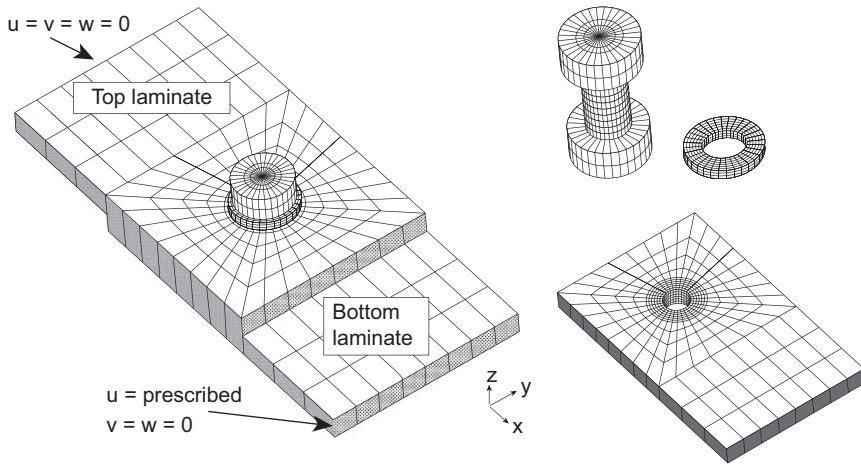
Figure 12.6 Finite element model with boundary conditions [15].

12.3   Analysis of single-bolt joints

12.3.1   Effects of bolt-hole clearance

Fig. 12.7 shows the initial part of the load-displacement curves obtained from experiments and simulations on neat-fit (i.e., C1 clearance in Table 12.2) and 240 µm (i.e., C4 clearance in Table 12.2) clearance single-bolt, single-lap joints, with best-fit lines. From the figure, a reduction in slope (stiffness) due to increasing clearance is clearly visible in the experimental and numerical results. The delay in load take-up for the C4 clearance joint is similar for the experiment and simulation. The C4 joint has a slight tendency to stiffen as load increases, which again is visible in both the experimental and numerical results. This is not exhibited by the C1 joint. Above about 9 kN the slope in the experimental plot drops due to the development of damage in the joint; this is not reflected in the model, as no damage model was implemented for this case (note that damage is considered in Section 12.5).

The joint stiffness was measured between 2 and 7 kN, for which the experimental load-displacement curves were essentially linear. Table 12.3 lists the change in stiffness as the clearance is varied from neat-fit (C1) to 240 µm (C4), for both the experiments and the finite element models. It is evident that as clearance increases, joint stiffness decreases, and it is also evident that the finite element models provide an accurate prediction of this loss in stiffness.

The explanation for these variations in stiffness lies in the development of the contact area between the bolt and the laminate. Fig. 12.8 shows the growth of the contact area between the bolt and one of the laminates in the C1 clearance joint. It can be seen that the contact area gets up to its final value quite quickly, with a contact angle of 160−170 degrees, which is fairly constant through the thickness. In the experiment, the bolt was found to leave a silver-colored imprint on the inside of the hole, as shown in Fig. 12.8(d) (highlighted for clarity). This is an indication of the maximum contact area that developed during the experiment and was found to match that predicted by the finite element model closely.
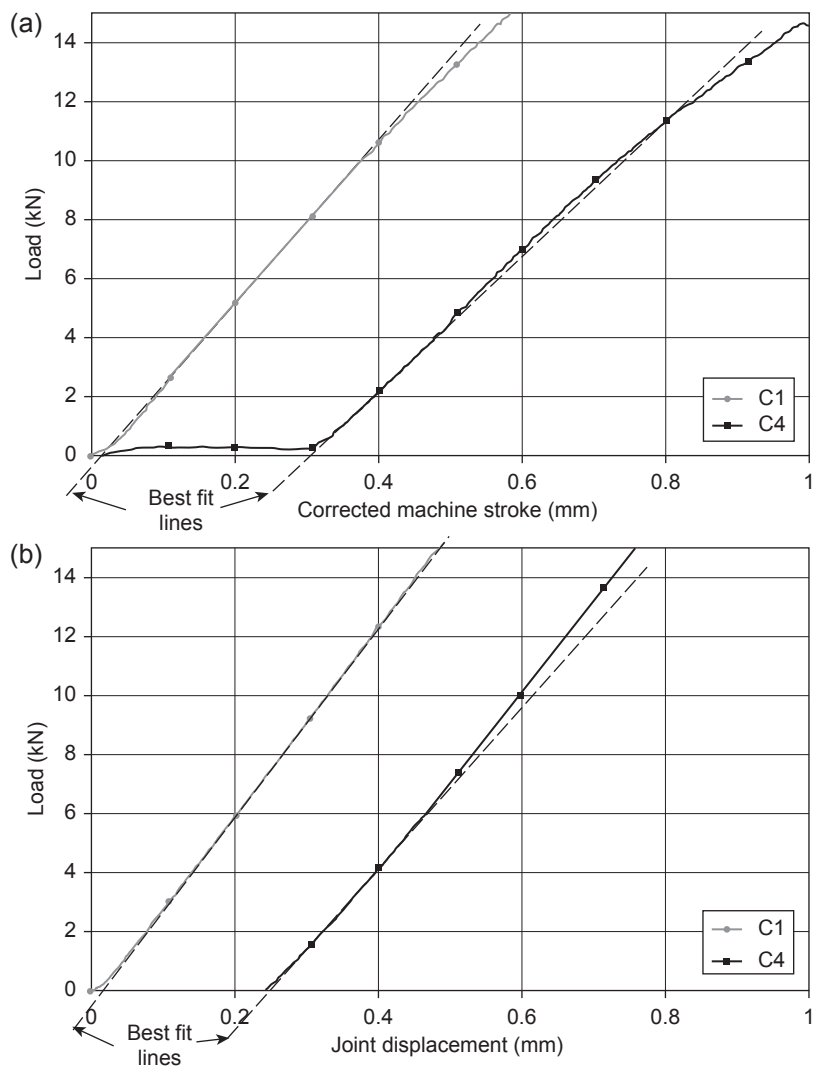
Figure 12.7 Load-displacement curves for a C1 and C4 clearance joint with quasi-isotropic -lay-up: (a) experiments, (b) simulations [16].

Table 12.3 Reduction in joint stiffness as a function of bolt-hole clearance − simulations versus experiments.

	C1	C2	C3	C4
Model stiffness (kN/mm)	31.56	30.14	28.96	27.98
Percentage change from C1 (models)	−	−4.5%	−8.24%	−11.34%
Percentage change from C1 (experiments)	−	−1.9%	−7.3%	−10.4%
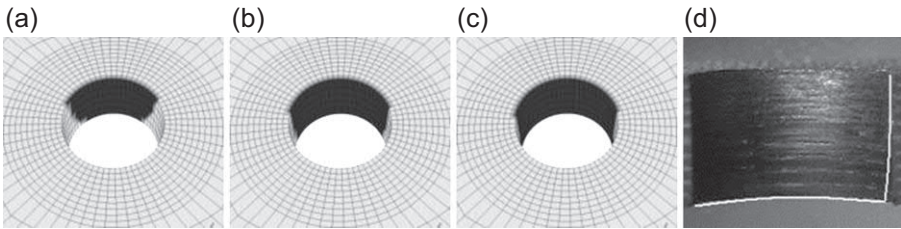
Figure 12.8 Development of the contact area in the C1 joint: (a) initial contact, (b) intermediate, (c) final contact, (d) experiment contact [16].
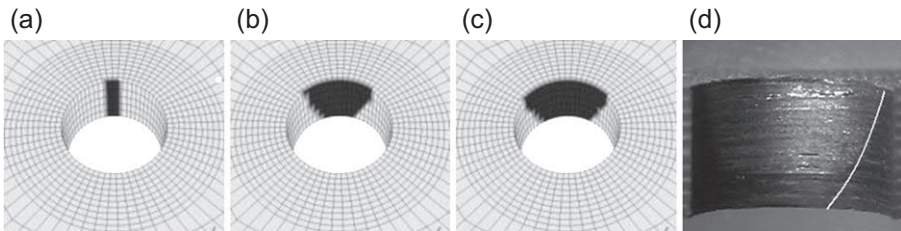
Figure 12.9 Development of the contact area in the C4 joint:(a) initial contact, (b) intermediate, (c) final contact, (d) experiment [16].

In contrast, in the C4 joint, shown in Fig. 12.9, significant contact is not made until the clearance is taken up, and initial contact is over a very small contact arc. As the load increases, the bolt tilts, and the contact area grows quite gradually. Even at high loads, the contact area is still much less than in the C1 joint, with a value of 100−105 degrees at the shear plane, reducing to 55−60 degrees at the free face of the laminate. This result highlights the importance of using a *three-dimensional* analysis method to examine the effects of clearance in single-lap joints. Note that the contact area in the model again agrees well with the imprint left by the bolt in the experiment. The gradual nature of the increase in contact area explains the continuing stiffening of the C4 joint with increasing load, while the lower final contact area explains the lower stiffness of the C4 joint compared to the C1 joint.

12.3.2   Effects of friction

For the friction study, the bolt was torqued to the recommended in-service level of 16 Nm, thus providing a high degree of lateral constraint. Two different bolt-hole clearances were tested. The first, being a control case, had a neat-fit (i.e., C1) clearance while the other had a 240 μm (i.e., C4) clearance and was chosen to provide some finite relative slipping between the composite parts, thus presenting a rigorous test for the friction models. Note that the bolts were initially centered in the holes using a custom-built assembly jig. For further details of the experimental methods refer to Ref. [14].

From these experiments, load-displacement curves were obtained, as shown in Fig. 12.10(a). Fig. 12.10(b) and (c) show close-ups of the initial behavior for the
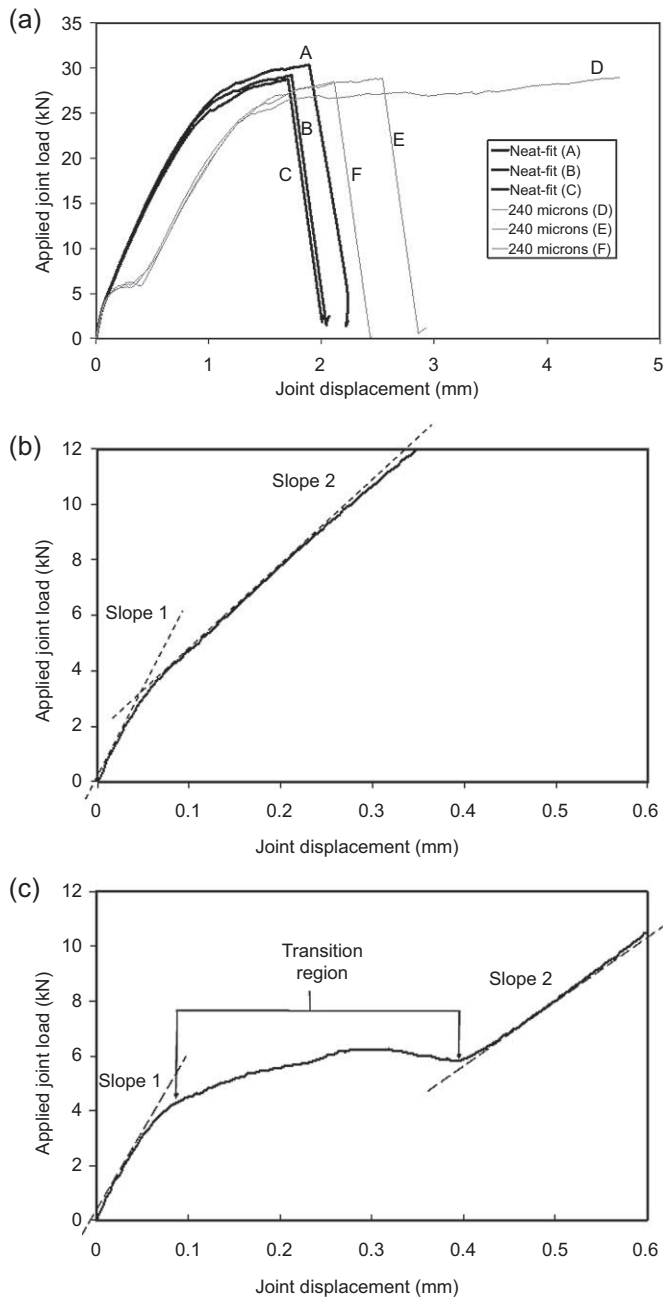
Figure 12.10 Experimentally determined load versus joint displacement for neat-fit and 240 μm clearance single-lap joints: (a) all tests, (b) initial stages − neat-fit, (c) initial stages − 240 μm [17].

neat-fit and 240 μm clearance joints, respectively. From these curves, the following characteristics can be noted:

1. All tests initially show fairly linear behavior up to about 2 kN applied load. The slope (marked "*Slope 1*" in Fig. 12.10(b) and (c)) is similar for both clearances. This is most likely because this region is dominated by static friction forces, which would be independent of bolt-hole clearance, and therefore, the same for all joints.
2. Above 2 kN, the joints begin to slip, and the behavior transitions to a new region of quasi-linearity with a reduced slope "*Slope 2*." In the transition region, the clearance is taken up in the 240 μm clearance joints; because the bolts were initially centered in the holes, no bolt-hole contact is made until the end of the transition region.
3. There is good repeatability between the tests with virtually no distinction between the initial slopes (Slope 1) in any test, while Slope 2 in the neat-fit clearance cases had an average value of 50.37 kN/mm with a standard deviation of 0.99 (2%) and in the 240 μm clearance cases had an average value of 37.06 kN/mm with a standard deviation of 1.74 (4.7%). The difference in Slope 2 for the two clearance cases was due to differences in the developing contact area between the bolt and the hole, as described in Section 12.3.1 above.

As expected, the 240 μm clearance joints are particularly interesting because there are three distinct regions of behavior, as the load increases: the first dominated by static friction, then the transition region dominated by kinetic friction, then a final region in which the stiffness is due to bolt-hole contact forces as well as friction.

The finite element model described in Section 12.2 was used here to model the friction experiments described above. However, to simulate the 16 Nm torque, a bolt prestress of 227 MPa was applied. This value was obtained experimentally from the axial gauges in the shank of a specially manufactured instrumented bolt, as discussed previously. For comparison, both the *continuous* and s*tick-slip* [26] friction models (available in MSC Marc finite element code) was used to account for friction between the contacting interfaces. The friction coefficients were chosen to be 0.1, 0.3 and 0.45 between the bolt/laminate, washer/laminate and laminate/laminate interfaces, respectively. More details on friction coefficient selection can be found in Ref. [17].

The load-deflection response from both friction models (i.e., the continuous and stick-slip friction models) are shown in Fig. 12.11 together with the experimental curve. Both friction models represent the behavior in the experiment reasonably well. The sharp change from static friction (*Slope 1*) to kinetic friction (*transition region*) is slightly better represented by the *stick-slip* friction model. This is because the *continuous* model does not model static friction exactly—there is always some relative movement between parts because the model never forces the parts to truly "stick." The load-displacement curve for the stick-slip model with the laminate−laminate friction coefficient reduced to 0.42 results in generally excellent agreement with the experiment. The model prediction using this reduced friction coefficient for the C1 joint is shown in Fig. 12.11(b). Again excellent agreement is obtained.

The finite element model can provide fundamental insight into the breakdown of load transfer in the joint. Fig. 12.12(a) shows a free body diagram of the forces acting on the laminate in the direction of the applied load (i.e., the *x*-direction in Fig. 12.6).
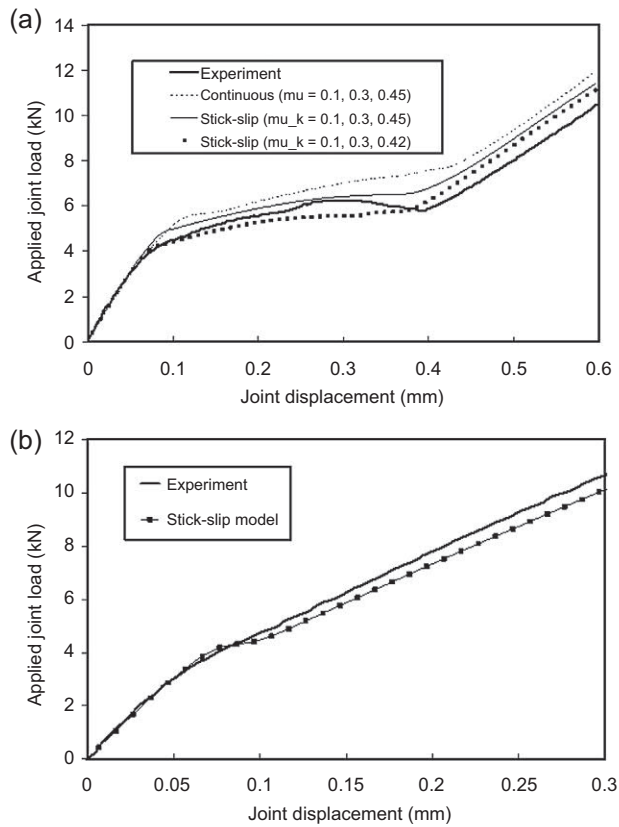
Figure 12.11 Load-displacement curves for (a) C4 clearance joint and (b) C1 clearance joint [17].
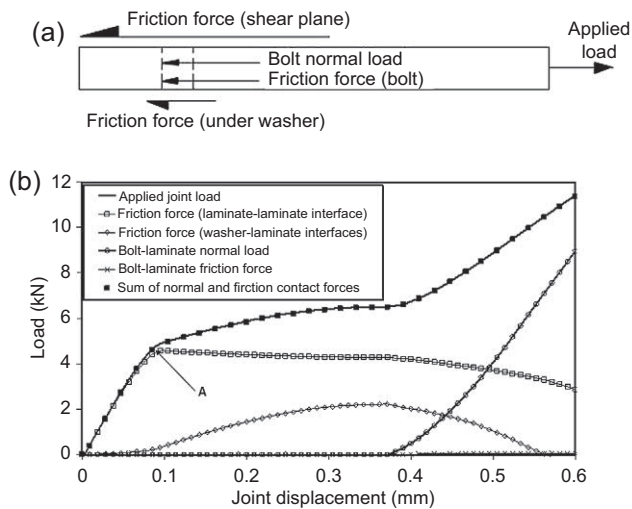
Figure 12.12 Component of loads acting on one laminate in the single-lap joint in the loading (x) direction. (a) Free body diagram of force components in loading direction, (b) loads from a finite element model using stick-slip friction model [17].

Fig. 12.12(b) shows the component of each of these forces in the *x*-direction for a C4 clearance joint, and the following observations can be made:

- Friction forces between the two composite laminates dominate the initial slope of the load-displacement curve
- At approximately 0.08 mm joint displacement, the nonfixed laminate starts to slip. At this point (point A, Fig. 12.12(b)) the laminate−laminate friction changes from static to kinetic friction and starts to reduce in magnitude
- Also at 0.08 mm joint displacement, the friction forces under the washer start to increase, reaching a maximum just before the bolt contacts the laminate. The increase in washer−laminate friction force is most likely due to the tipping of the bolt in the hole, and the resultant "digging in" of the washer into the laminate
- The friction force between the bolt and the laminate possesses a very small component in the *x*-direction, which is due primarily to the friction force along the longitudinal axis of the bolt, which because of tipping, is not exactly perpendicular to the *x*-direction
- At approximately 0.38 mm joint displacement the bolt starts to transfer load, at which point the friction forces between the composite laminates and under the washer start to decrease significantly

This analysis shows that as far as the load-displacement curve is concerned, the dominant friction coefficient is that between the laminates, except toward the end of the "transition" region where the washer-laminate coefficient becomes significant. This exercise also shows the insight that can be gained with finite element analysis, since this load breakdown would be very difficult to obtain experimentally.

12.3.3 3D stress analysis in protruding-head joints

The effects of clearance on the stress distribution in the laminate around the hole boundary are presented first for a model in which homogeneous anisotropic material properties for the laminates were used. This is the approach often used in previous studies and gives an overview of the effects of clearance without the complexity present in the layered stress results, which are given later. Fig. 12.13 shows the radial and tangential stresses at the hole for the quasi-isotropic lay-up in both a neat-fit (i.e., C1 clearance) and 240 μm (i.e., a C4 clearance) clearance joints. The applied load level for these graphs was 5 kN, which was within the elastic range of the experiments. The stress is seen to vary through the thickness being highest at the shear plane, or faying surface. Clearance is seen to have the following effects. The peak radial stress increases with increasing clearance (due to the load being distributed over a smaller contact area). The location of the maximum tangential stress varies with clearance, generally being near the end of the contact region. This also implies that the direction of the peak tangential stress changes. The magnitude of the peak tangential stress increases slightly with increasing clearance.

All of these findings are in agreement with previous two-dimensional studies on clearance [39−41]. In addition, it can be seen that compressive tangential stress exists at the back of the hole ($\theta \cong \pm 180$ degrees) in both clearance cases, and at the bearing plane ($\theta \cong 0°$) in the C4 clearance case.

The ply-level radial stress distribution for a model with layered properties is shown for the C1 clearance, quasi-isotropic joint in Fig. 12.14. The highest radial stress occurs in layer No. 2, which is the second ply from the shear plane and is orientated at 0 degree
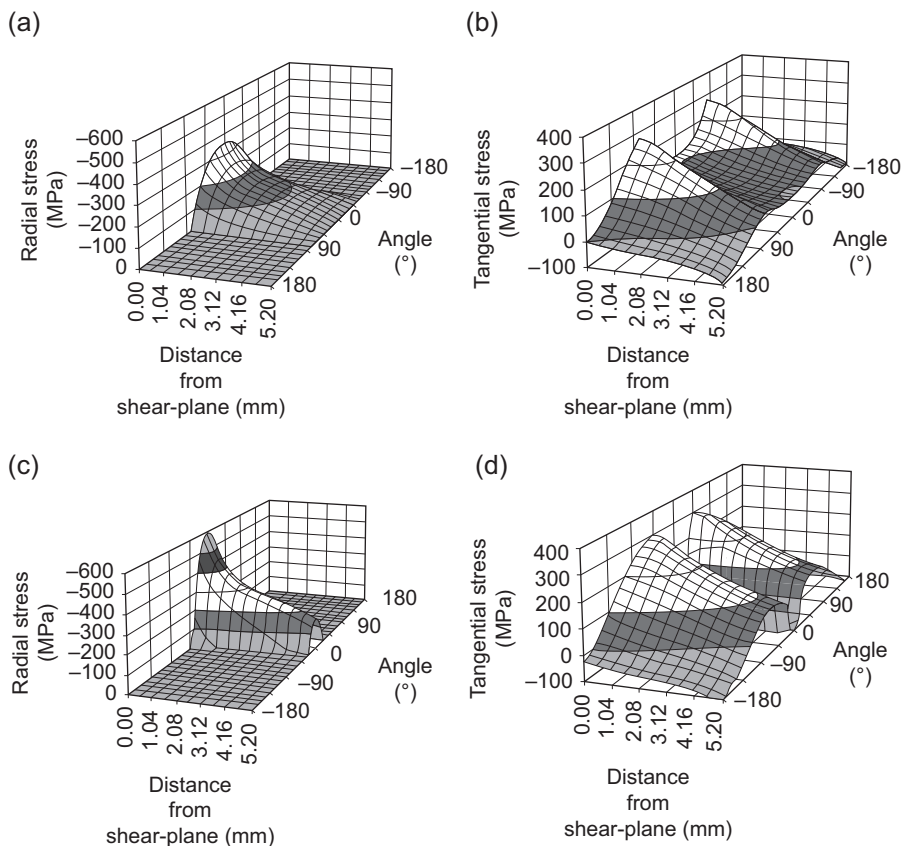
Figure 12.13 Radial and tangential stresses in C1 and C4 clearance joints (quasi-isotropic lay-up) with homogeneous, orthotropic material properties, at 5 kN applied load: (a) radial stress, C1 clearance, (b) tangential stress, C1 clearance, (c) radial stress, C4 clearance, (d) tangential stress, C4 clearance. From [16]
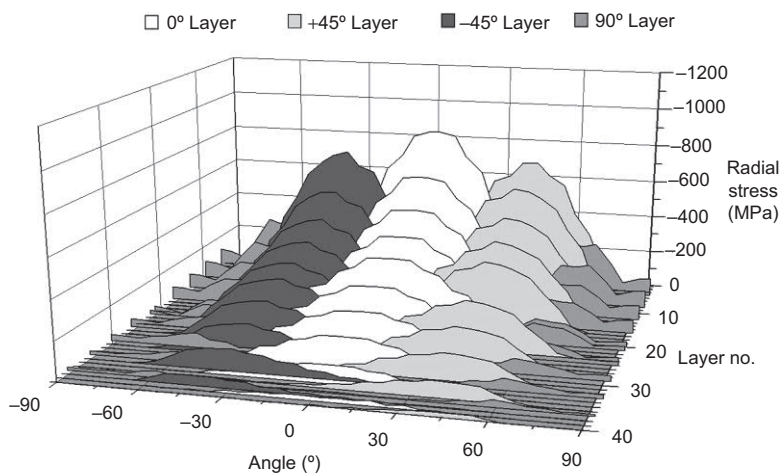
Figure 12.14 Radial stress distribution in each layer of the C1 clearance quasi-isotropic ([45/0/−45/90]$_{5s}$) joint at 5 kN applied load. Layer No. 1 is located at the shear plane [16].
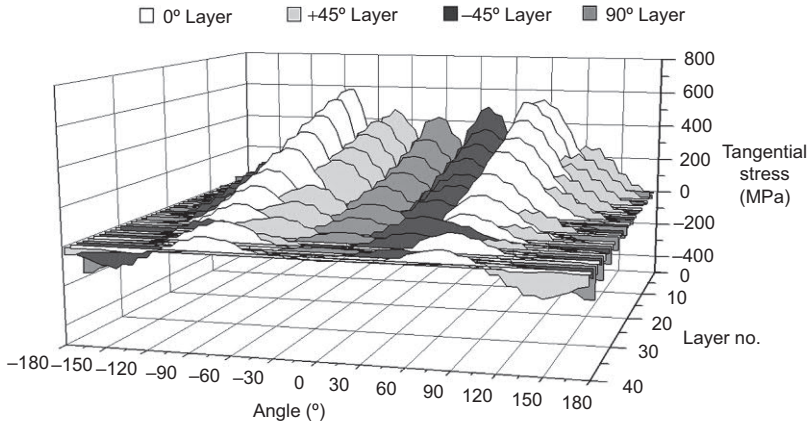
Figure 12.15 Tangential stress distribution in each layer of the C1 clearance quasi-isotropic ([45/0/−45/90]$_{5s}$) joint at 5 kN applied load. Layer No. 1 is located at the shear plane [16].

with the loading direction. As can be seen, all the 0 degree plies are most highly stressed at the 0 degree location (the bearing plane), all the +45 degrees plies are most highly stressed near the +45 degrees location, and all the −45 degrees plies are most highly stressed near the −45 degrees location. The 90 degrees plies experience their highest stresses at an angle less than ±90 degrees, which varies through the thickness; the angle is less than ±90 degrees since the contact angle is less than 180 degrees.

The tangential stresses around the hole boundary for the C1 quasi-isotropic joint are shown in Fig. 12.15. The tangential stress in each layer is positive except for some plies near the free surface of the laminate at the back of the hole ($\theta \cong \pm180$ degrees). The highest tangential stresses overall occur in all the 0 degree plies near the ±90 degrees location (net-section plane). The highest tangential stresses in the +45 degrees plies occur near the −45 degrees location because the +45 degrees plies are stiffest in the tangential direction at this point. The opposite is also true for the −45 degrees plies. A second, but the lower peak is also experienced in the +45 and −45 degrees plies at locations of 135 and −135 degrees, respectively. Again this is due to the plies being stiffest at these locations. Finally, the stresses in the 90 degrees plies are highest at the 0 degree location, once again due to their high stiffness in the tangential direction at this location. Thus, for the C1 quasi-isotropic joint, the highest tangential stresses occur in each ply at locations along the hole boundary, where they are stiffest in the tangential direction.

The radial stress distribution for the C4 clearance, quasi-isotropic joint is shown in Fig. 12.16. Similarly to the C1 joint (Fig. 12.14), the highest radial stresses occur in 0 degree layer nearest the shear plane (layer No. 2), but the stress in this ply is much higher in the C4 case. Interestingly, quite high stress levels exist in the C4 joint all the way through the thickness, whereas in the C1 joint (Fig. 12.14) the stresses tend to drop off to very low levels as the free surface of the laminate (i.e., ply No. 40) is approached. Fig. 12.16 shows that the radial stresses in the 0 degree plies are highest at the 0 degree location, as for the C1 case. However, differently from the C1 case, the +45 and −45 degrees plies do not peak at their stiffest locations, but at an angle of approximately +15 and −15 degrees, respectively. This is due to the contact
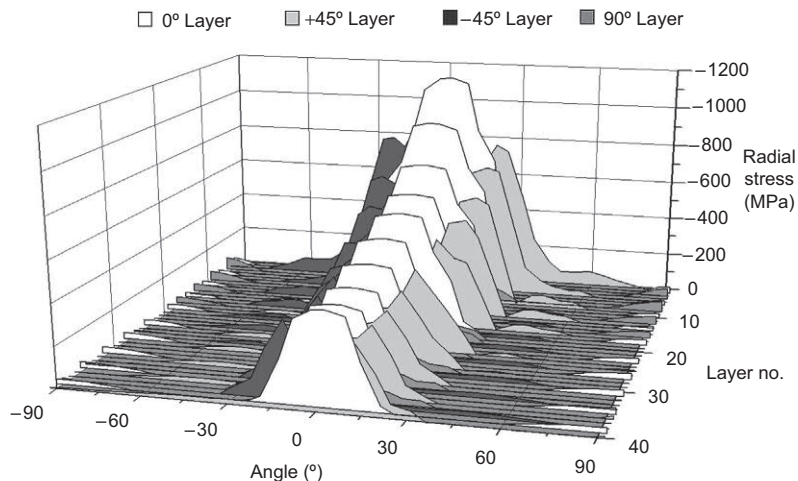
Figure 12.16 Radial stress distribution in each layer of the C4 clearance quasi-isotropic ([45/0/−45/90]$_{5s}$) joint at 5 kN applied load. Layer No. 1 is located at the shear plane [16].
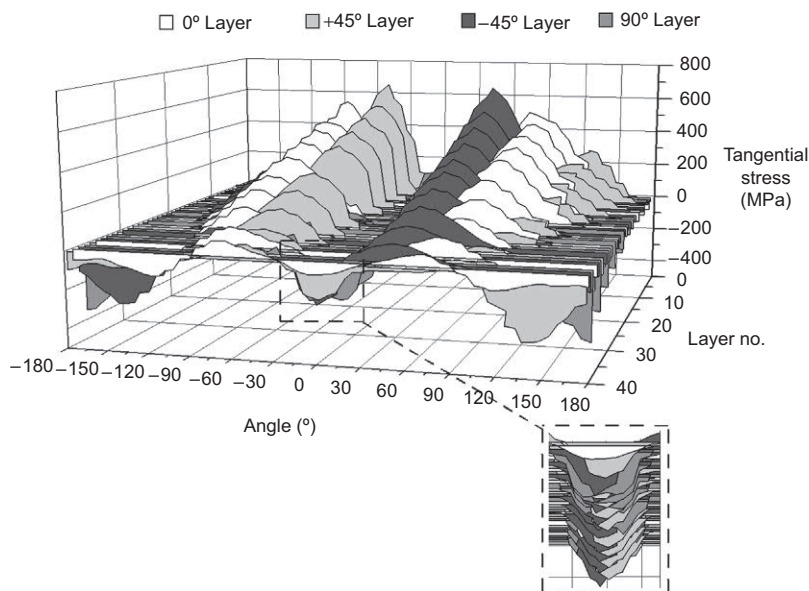
Figure 12.17 Tangential stress distribution in each layer of the C4 clearance quasi-isotropic ([45/0/−45/90]$_{5s}$) joint at 5 kN applied load. Layer No. 1 is located at the shear plane [16].

pressure being applied over a reduced contact angle. The peak radial stress value for these plies is also increased compared to the C1 case.

The tangential stresses around the hole boundary for the C4 quasi-isotropic joint are shown in Fig. 12.17. Different from the C1 joint (Fig. 12.15), the tangential stresses are negative in a region bounded by the ±30 degrees location in all plies except for two 90

degrees plies located nearest the shear plane. In addition, the negative tangential stresses at the back of the hole ($\theta \cong \pm 180$ degrees) experienced in the C1 case are more pronounced in the C4 case. This is in line with the findings for homogeneous properties above. The peak tangential stress has also increased slightly and unlike the C1 case, occurs in the $+45$ and -45 degrees plies, not in the 0 degree plies. This is in line with the finding from the previous section that the peak tangential stress shifts toward the bearing plane (0 degree location) in the presence of clearance.

12.4 Analysis of multibolt joints

12.4.1 Bolt-load distribution in joints

Load-distributions in single-lap, multibolt joints are now presented—for further details see Ref. [42]. The specimen geometry is shown in Fig. 12.4(b); also shown in this figure is the hole numbering used. All tests were carried out with protruding-head bolts, torqued to 0.5 Nm (finger-tight), with steel washers both on the nut and head side. The clearances chosen for this study were the same as in the single-bolt joint study (see Table 12.2). For the present study, two different clearance variations were examined and are listed in Table 12.4. In the first case, the clearance was neat-fit at each bolt and is designated C1_C1_C1. In the second case, a small 80 μm clearance was present at bolt-hole No. 3, and this case is designated C1_C1_C2. Both cases were examined in a load distribution study involving tests in the linear elastic loading regime for the joints.

For measuring the load distribution, standard aerospace bolts were fitted with strain gauges. Both shear and axial load could be measured. A three-dimensional finite element model with linear elastic material properties was developed for calculation of load distribution prior to initiation of material failure and comparison with instrumented bolt results. Model details are similar to those of the single-bolt model above, with a full-contact analysis being performed for all bolts, washers, and holes.

Fig. 12.18 shows the load distribution from the instrumented bolts for the C1_C1_C1 (all holes neat-fit) case and the C1_C1_C2 case (80 μm clearance in Hole 3 — see Fig. 12.4 for hole numbering). Shown also are results from the three-dimensional finite element model where the agreement between the experimental

Table 12.4 Joint clearance cases examined.

Case code	Nominal clearance (μm)		
	Hole 1	Hole 2	Hole 3
C1_C1_C1	0	0	0
C1_C1_C2	0	0	80
C4_C1_C1	240	0	0
C3_C3_C1	160	160	0
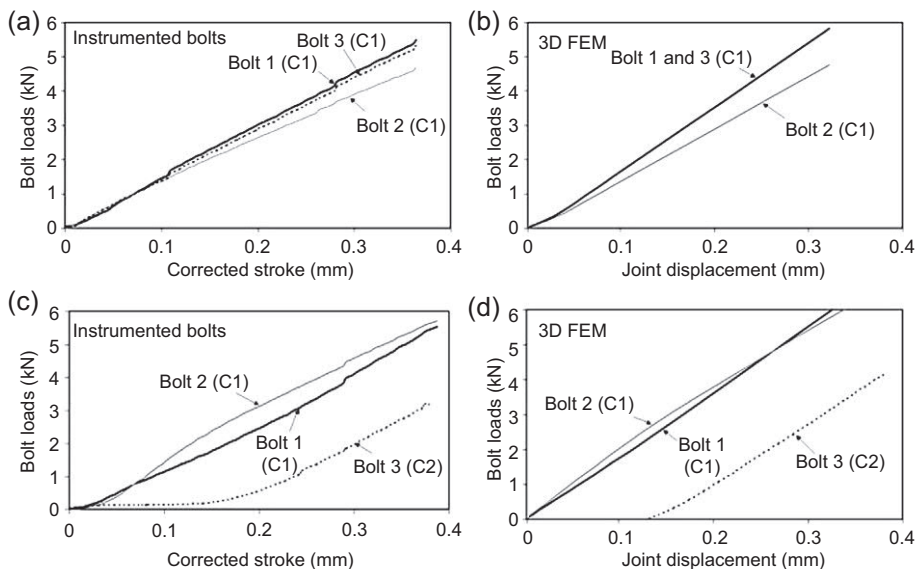
Figure 12.18 Load distribution for clearance cases C1_C1_C1 and C1_C1_C2 from instrumented bolts and three-dimensional finite element analysis. (a) C1_C1_C1 experimental, (b) C1_C1_C1 finite element analysis, (c) C1_C1_C2 experimental, (d) C1_C1_C2 finite element analysis. From [42].

and numerical results in terms of load distribution between the bolts is considered very good.

The usual assumption in such a three-bolt joint is that the outer two bolts take an equal load, while the inner bolt takes less load [42]. This was borne out in the C1_C1_C1 case (Fig. 12.18), with the outer two bolts each taking ∼35% of the load at 15 kN applied load. However, in the C1_C1_C2 joint, it can be seen that even a small change in clearance conditions can change the distribution significantly (note: the C2 clearance is within allowable aerospace tolerances). In this case, the bolt in the largest clearance hole (Bolt 3) initially does not take any load, since it has been centered in the hole by the positioning jig. Bolt 2 (the center bolt) takes the most load. Once Bolt 3 begins to pick up load, the percentage load taken by Bolt 2 begins to drop, and one might speculate that if the joint remained elastic to high enough loads the load distribution might approach that in the C1_C1_C1 case. However, at 15 kN applied load, Bolt 3 still takes only about 22% of the load, with 78% of the load being shared equally by Bolts 1 and 2. Later tests showed initial damage occurs at 20 kN, so it is unlikely that the Bolt 3 load ever overtakes the Bolt 2 load in the C1_C1_C2 case.

12.4.2 Failure prediction using bearing-bypass diagrams

For this study, two different joint configurations were considered. The first was a C1_C1_C1 joint with neat-fit clearances at each bolt-hole, and the other (C4_C1_C1) had a 240 μm clearance at bolt-hole No. 1, as shown in Table 12.4.

Three tests to failure on the C1_C1_C1 joint configuration were carried out in Ref. [42]. The study found that one joint failed in net-tension at hole 1 in the lower laminate at a joint load of 80 kN, while another failed by net-tension at hole 3 in the top laminate at 84 kN. The third joint tested failed by bolt failure at 76 kN. It should be noted that bearing damage was evident at holes where bolt failure occurred. However, as this damage mode is noncatastrophic, high loads are transferred through the bolt until high joint loads, causing bolt failure. The predicted bearing/bypass diagram is shown in Fig. 12.19 [44]. A star is placed where the bearing/bypass stress curve intersects the ultimate failure envelope and indicates the failure mode and stress level at which the joint fails. The failure load is determined by evaluating the joint load at which the bearing/bypass stress curve intersects the failure envelope. As can be seen, bearing failures are predicted to initiate (inner envelope) at hole 3 in the bottom laminate and hole 1 in the top laminate simultaneously, which occurred at a joint
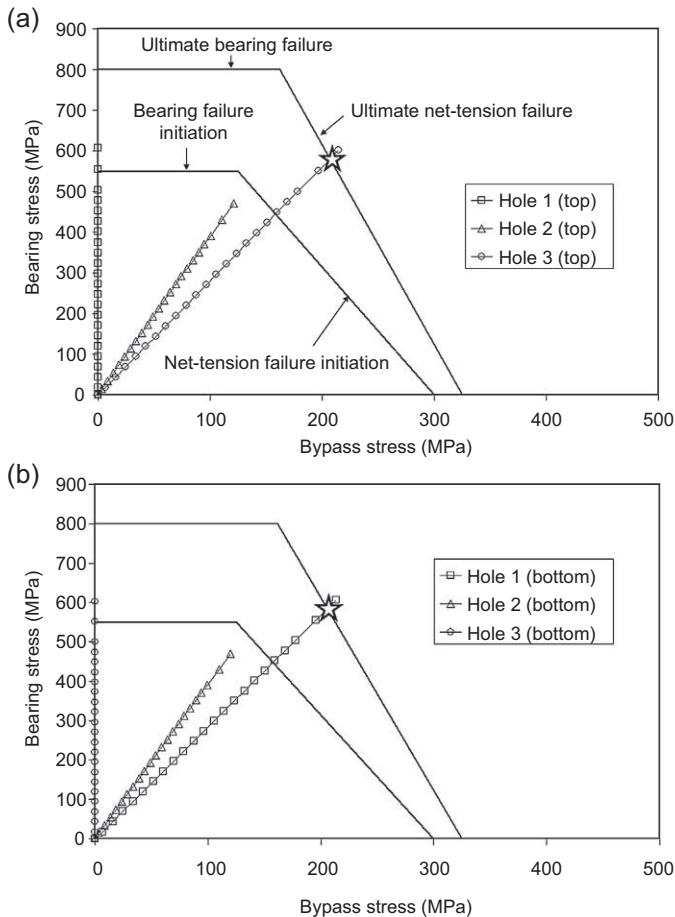
Figure 12.19 Bearing bypass diagram for C1_C1_C1 joint: (a) top laminate, (b) bottom laminate [44].

load of 62 kN. Ultimately, failure is subsequently predicted to occur by net-tension at hole 1 in the bottom laminate or hole 3 in the top laminate, which is in agreement with the experiments. This occurred at 67.4 kN, which underestimates the average experimental value by 17.8%.

Three tests to failure on the C4_C1_C1 joint configuration were also carried out in Ref. [42]. Similarly to the C1_C1_C1 joint, one joint failed in net-tension at hole 1 in the bottom laminate at 78 kN, and another failed in net-tension at hole 3 in the top laminate at 82 kN. The third joint tested failed by bolts 2 and 3 failing simultaneously at a joint load of 79 kN. The predicted bearing/bypass diagram is shown in Fig. 12.20. As can be seen, a bearing failure initiates at hole 3 in the bottom laminate, and this occurred at a joint load of 56 kN, which is approximately 10% lower than in the C1_C1_C1 joint. In addition, failure is also predicted to initiate in bearing at hole 2 in the top and bottom laminate at a higher load of 62 kN. Ultimate failure was
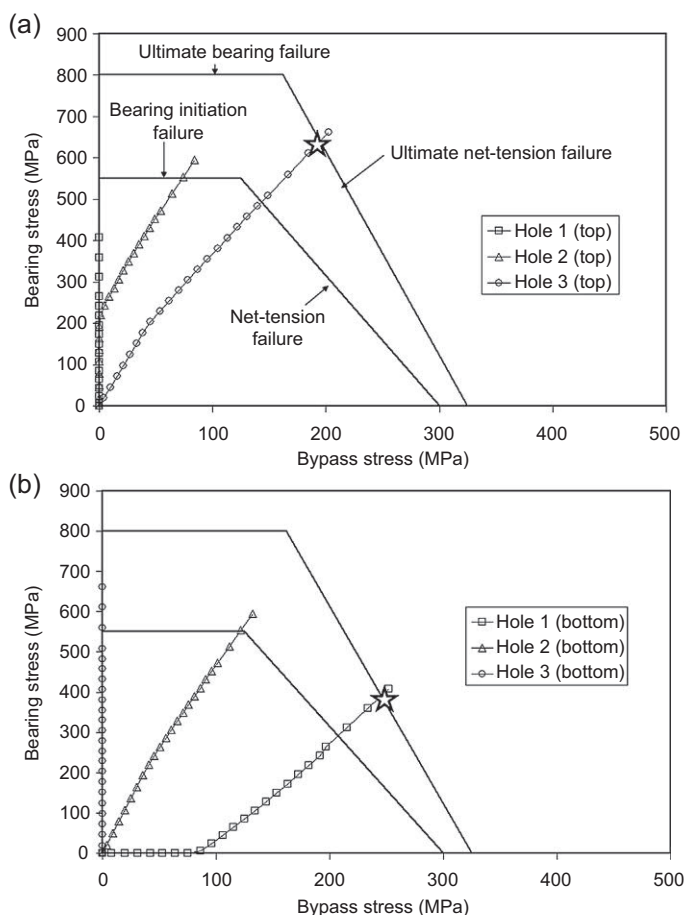
Figure 12.20 Bearing bypass diagram for C4_C1_C1 joint: (a) top laminate, (b) bottom laminate [44].

predicted to occur by a net-tension failure at hole 3 in the top laminate at a joint load of 67.2 kN. However, it is interesting to note that at a slightly higher load level (68 kN) the hole 1 bottom laminate bearing/bypass stress curve intersected the failure envelope at a different location. Hence, although the bypass stress is considerably higher at hole 1 in the bottom laminate than at hole 3 in the top laminate, the combination of bearing and bypass stresses at these holes result in essentially equal probabilities of failure, which explains the experimental observation. In summary, the failure sequence for this joint is bearing failure initiation at hole 3 in the bottom laminate at 56 kN, followed by bearing failure initiation at hole 2 in the top and bottom laminates at 62 kN and finally, net-tension failure at hole 3 in the top laminate (or possibly hole 1 in the bottom laminate) at 67.2 kN. The predicted ultimate failure load is an underestimation of 16% compared to the experimental result, but the location of failure and failure mode are in good agreement.

12.4.3 Modeling large joint assemblies

Modeling large joint assemblies using three-dimensional finite element analysis, like that described in Section 12.1.4.1 above, is still not yet feasible in an industrial environment where many joint configurations may need to be analyzed and assessed very quickly. Hence, to model large joint assemblies, global finite element approaches, like that described in Refs. [31−34,36,37], can provide designers with rapid design tools that can produce bolt-load distributions and stresses in composite panels quickly.

The capability of a global method (described in Ref. [34]) to model complex load distributions is assessed here through a global FE analysis of a 20-bolt joint, shown in Fig. 12.5, in both single-lap and double-lap joint configurations. The presence of a hole at the center of the structure gives rise to a more complex load distribution i.e., an increased presence of bolt-load components in both in-plane (i.e., X and Y) directions. As stated previously, this joint configuration was used as benchmark studies in the EU Framework 5 project BOJCAS [19]. As before, the joint was fabricated using a carbon fiber/epoxy composite material manufactured by Hexcel composites, with designation HTA/6376. The 3.12 and 6.24 mm thickness laminates had stacking sequences of $[\pm45/0/90]_{3s}$ and $[\pm45/0/90]_{6s}$, respectively. The 6 and 8 mm diameter bolts were made from aerospace-grade titanium alloy and the material properties, and are again listed in Table 12.1. The joint configurations analyzed are presented in Table 12.5. The single-lap joints were loaded to 250 kN, while a compressive load of 200 kN was applied to the double-lap joint.

Table 12.5 Joint configurations.

Joint	Joint type	Description	Loading
A	Single-lap	All bolts present	Tension
B	Single-lap	Bolt 13 removed	Tension
C	Single-lap	Bolts 19 and 20 removed	Tension
D	Double-lap	All bolts present	Compression

12.4.4   Load distribution in large joint assemblies and effects of missing fasteners

The results from the load distribution analysis on the 20-bolt joint are illustrated in Fig. 12.21, where the percentages of the total joint load carried by each fastener in the structure are presented together with bolt-hole contact angles. Comparison with load distributions from experimental results was not possible, as results from tests involving instrumented fasteners were not available. However, load distribution results from the fully validated numerical approach of Friberg [48,49] were available and have thus been used for the purposes of comparison. Regarding Joint A (see Table 12.5), excellent agreement between the global model and Friberg's Method [49] was obtained in terms of the load sharing capacity of each individual fastener. A degree of fluctuation in the percentage of the load carried is seen between Bolts 6 and 10. It should be noted that the fasteners located quite close to the hole at the center of the structure (such as Bolts 7, 8, 10, 11, 11, and 14) experience relatively low bolt loads. In terms of the bolt-load angles (which were computed from components of bolt-load acting in the X and Y directions at each fastener location), good agreement was also obtained between the global model and Friberg's model [49]. It can be clearly seen that bolts located away from the hole at the center of the structure experience high contact angles, while bolts located on the X-axis of symmetry experience very low contact angles.

In Joint B, the presence of a missing fastener at location 13 results in a notable change in the load distribution. The fasteners located in the lower half of the structure take a higher portion of the overall joint load and experience slightly higher contact angles. This effect was captured quite well by both the global model and Friberg's Method. In Joint C, missing bolts at locations 19 and 20, results in a redistribution of the load to Bolts 16, 17, and 18 and again good agreement was obtained between both methods of load distribution analysis. This would suggest that the removal of bolts results in a localized effect, where bolts which are located close to open holes carry more load.

12.5   Failure analysis of joints

12.5.1   Progressive damage analysis

In order to perform a progressive failure analysis of composite materials, it is essential that the failure mode (i.e., fiber failure, matrix failure, etc.) be evaluated so that the appropriate material properties can be degraded accordingly. For example, if fiber failure is detected, the longitudinal modulus, E_{11}, could be reduced to simulate the loss of load-carrying capacity in that direction, whereas the transverse moduli, E_{22} and $E_{33,}$ could be considered to be unaffected and consequently not altered. A well-known failure theory that can predict failure mode, as well as failure load, and had been used previously for failure analysis of bolted joints [50−52] is the theory developed by Hashin [53], that was adopted herein. Once failure is detected at a material point,
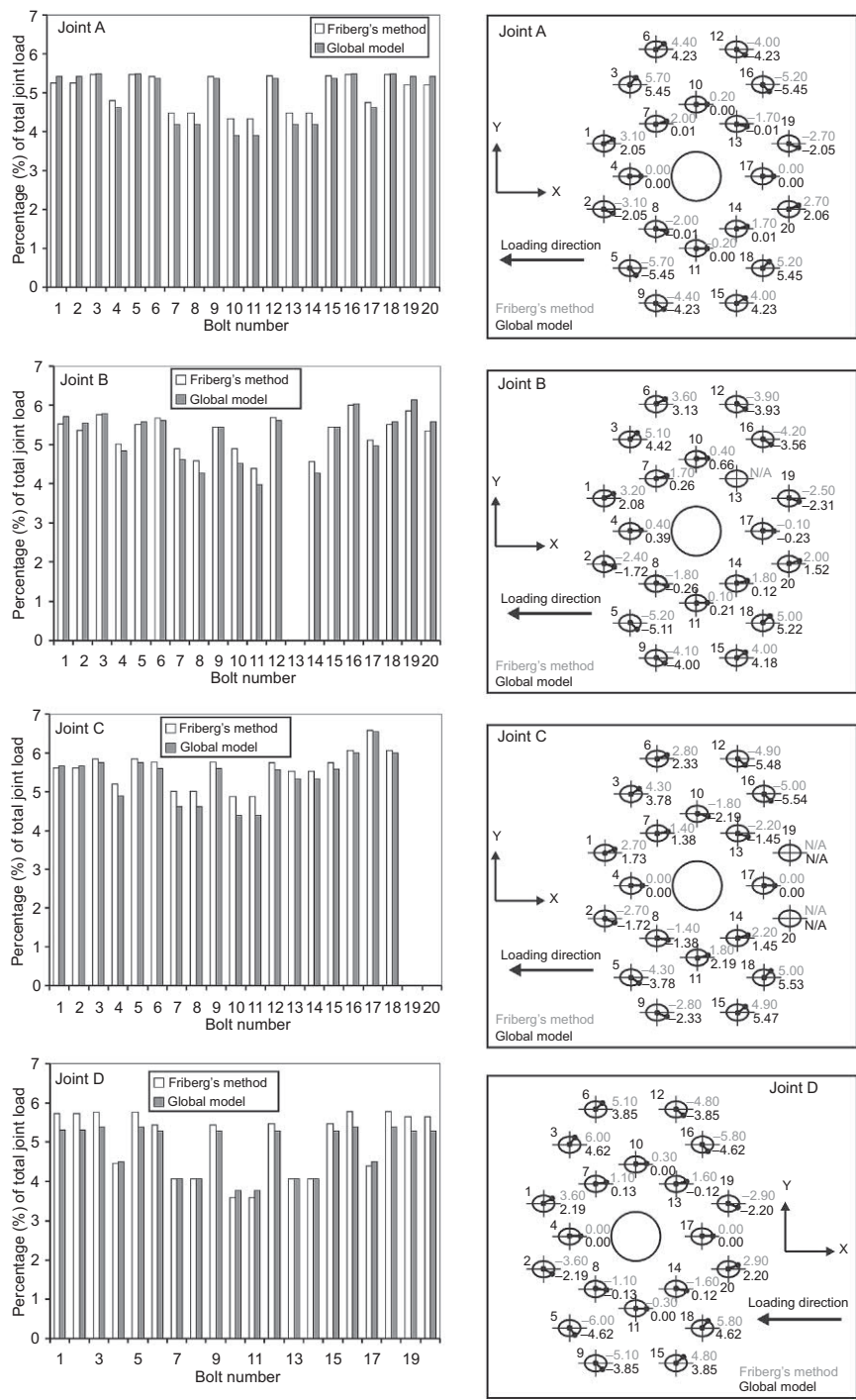
Figure 12.21 Load distributions in 20-bolt joints — percentage of load carried by each bolt and bolt-load angles redrawn from [49].

Table 12.6 Material strength data for HTA/6376 [52].

S_{11}^T MPa	S_{11}^C MPa	S_{22}^T MPa	S_{22}^C MPa	S_{33}^T MPa	S_{33}^C MPa	S_{12} MPa	S_{23} MPa	S_{31} MPa
2200	1600	70	250	50	300	120	50	120

the material properties are reduced according to the damage law imposed. Full details of the damage modeling approach, including the property reduction scheme used herein, are given in Ref. [55]. For completeness, Table 12.6 lists the strength data for the material used in this study (HTA/6376). These strengths are typical mean values, and no reduction due to scattering or defects has been made.

12.5.2 Damage modeling in multibolt joints

The joint under investigation in this study is shown in Fig. 12.22(a). It is of double-lap configuration and consists of three bolts "in-line," six washers, three nuts, two splice plates (outer plates), and one skin plate (middle plate). Protruding-head bolts were used and were torqued to a low value (0.5 Nm) to represent a finger-tightened condition. Hence, friction was not considered in the analysis. Again, the laminates were made from a carbon fiber/epoxy matrix system (HTA/6376), and were stacked in a quasi-isotropic configuration $[45/0/-45/90]_{ns}$. The splice plates were manufactured from 16 plies giving a nominal thickness of 2.08 mm. The skin plate was manufactured from 32 plies and was nominally 4.16 mm thick. After assembly, the joint was subjected to a tensile load, applied quasi-statically.

The ABAQUS finite element model is shown in Fig. 12.22(b). Due to symmetry, only one-quarter of the joint was modeled, with symmetric boundary conditions at the symmetry planes, as shown. The gripped areas in Fig. 12.22(a) were not modeled as they were assumed to be perfectly clamped. The washers were not modeled discretely. Instead, the outer diameter of the bolt head and nut were set equal to the outside diameter of the washer (14 mm). Pre-stress was introduced to the bolts using a PRE-TENSION SECTION option available in ABAQUS. In the experiment, the skin plate was held stationary, and the splice plates were loaded by applying a displacement quasi-statically to their ends. For simulating this loading, prescribed displacements were applied to the end of the skin and splice plate, as shown in Fig. 12.22(b). Again, light springs were attached to the bolts and splice plate to prevent rigid body motions.

By using the unidirectional stiffness properties of the composite material (HTA/6376) in Table 12.1, the laminates were modeled with one orthotropic solid element per ply in the thickness direction, leading to 16 elements through-thickness for both the splice plate and skin plate. As before, the titanium bolts were modeled with isotropic material properties, with material constants $E_b = 110$ GPa, $\nu_b = 0.29$. Linear 8-node hexahedral brick elements with a reduced integration scheme were used for the laminates and bolts. This element formulation was used to reduce the cost of the analysis and size of the output files, which were very large.
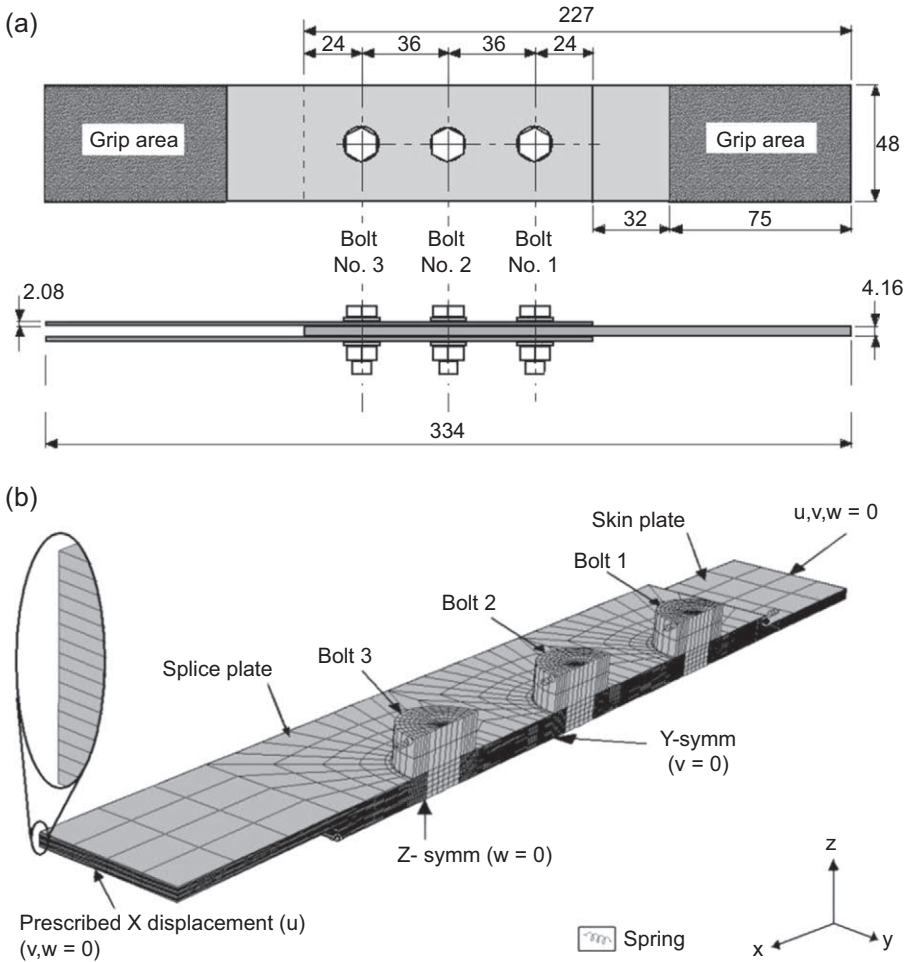
Figure 12.22 (a) Double-lap, multi-bolt specimen geometry (all dimensions in mm), (b) corresponding 3D finite element model with boundary conditions. From [55].

12.5.3 Load-redistribution after bearing failure in multibolt joints

Results from two joints with different clearance configurations are presented here. The first joint, designated C1_C_C1, represented the control case having a neat-fit at each hole. The second joint, designated C3_C3_C1 (see Table 12.4 for the clearance codes), had a 160 μm clearance at holes 1 and 2 and a neat-fit at hole 3.

The bolt-load distribution for C1_C1_C1 joint, as determined from the experiment and the finite element model, is shown in Fig. 12.23. In agreement with previous studies [56–58], the two outer bolts (bolts 1 and 3) carry the highest amount of load during the linear portion of the loading history. However, at approximately
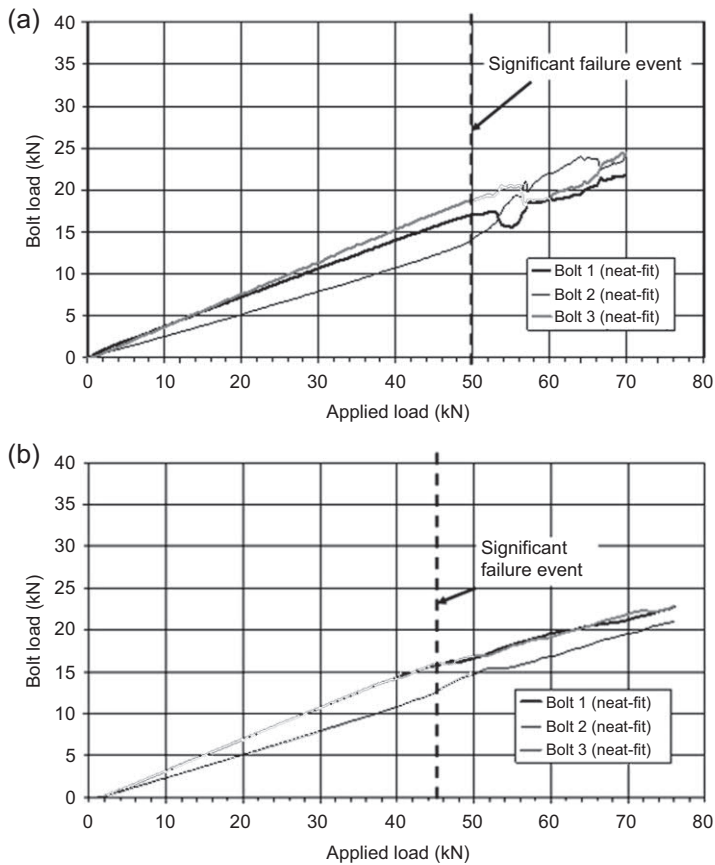
Figure 12.23 Bolt-load distribution in the C1_C1_C1 double-lap joint: (a) Experiment, (b) simulation [55].

45 kN (50 kN in the experiment), a significant disruption of the bolt-load distribution occurs. The experiments revealed that this was due to bearing failure at holes 1 and 3. This causes a reduction in the load carried at these two holes and consequent transfer of load to hole 2. At about 52 kN, the simulation indicates bearing failure of hole 2 (the experiment possibly predicts such a failure at 56 kN), and thereafter, the load distribution starts to even out (which is evident from both the simulation and the experiment).

The bolt-load distribution for the C3_C3_C1 joint (i.e., 160 µm clearances at hole 1 and 2, neat-fit at hole 3) is shown in Fig. 12.24. Because of the 160 µm clearance at holes 1 and 2, bolt 3 carries the entire applied load until a joint load of approximately 10 kN. At this point, bolt 1 followed by bolt 2 starts to pick up the load, but bolt 3 still remains the most highly loaded. At a joint load of approximately 27 kN (37 kN in the experiment), bearing failure occurs at hole 3. Thereafter, the experiment and simulation both predict that the load evens out, with the experiments predicting a more dramatic redistribution of the load.
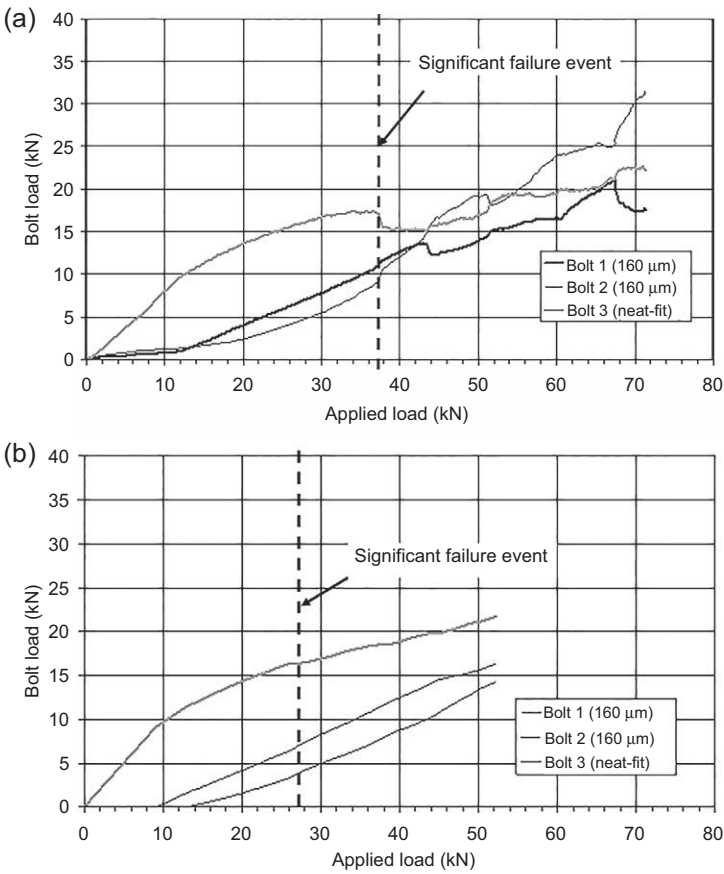
Figure 12.24 Bolt-load distribution in the C3_C3_C1 double-lap joint: (a) Experiment, (b) simulation [55].

Table 12.7 Experimental and finite element predictions of first significant failure (bearing failure at one or more holes).

	Experiments		Simulations	
Joint code	**Load at first significant failure (kN)**	**Percentage difference from joint A**	**Load at first significant failure (kN)**	**Percentage difference from joint A**
C1_C1_C1	50.5	—	45	—
C3_C3_C1	37.8	−25.1%	27	−40%

Table 12.7 shows a summary of the first significant failure loads determined from the experiments and simulations. Both the experiments and simulations show that bolt-hole clearance has a strong effect on the load at which first significant failure (i.e., bearing failure at one of the holes) occurs. This "initial strength" is relevant for

the design of aircraft structures for limit load, so clearance is evidently a highly significant variable for aircraft design. The C3_C3_C1 joint experimental result shows a 25.1% decrease in initial strength, compared to the neat-fit control case (i.e., C1_C1_C1 joint). The finite element model predicts a 40% decrease.

12.5.4 Progression of damage in multibolt joints

In this section, the effects of clearance on the damage response of the C1_C1_C1 double-lap joint (i.e., a control case) and the C3_C3_C1 double-lap joint (i.e., a worst-case scenario in the sense that all the load is initially carried by one bolt) are investigated. The progression of damage in the joints is shown at the applied load levels of 10, 30, and 50 kN for the four different failure modes considered, i.e., tensile matrix failure; compressive matrix failure; tensile fiber failure and compressive fiber failure. These load levels were chosen so that the damage could be tracked from initiation up to the point of extensive damage.

12.5.4.1 Damage progression in the C1_C1_C1 joint

The progression of damage at hole 1, hole 2 and hole 3 in the C1_C1_C1 joint is shown in Figs. 12.25−12.27, respectively. The pictures show the damage in each mode in both the splice plate (top plate in the figures) and the skin plate (bottom plate in the figures). At 10 kN, no damage is detected in any mode at any hole. At 30 kN, significant compressive matrix failure is present at holes 1 and 3 (with somewhat
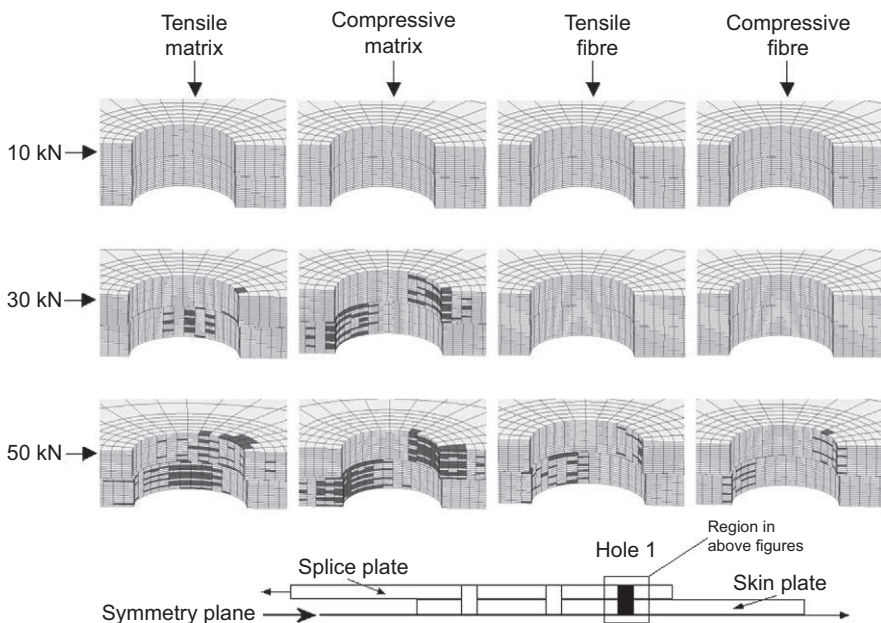
Figure 12.25 Progression of damage at hole 1 (neat-fit clearance) in the C1_C1_C1 joint [55].
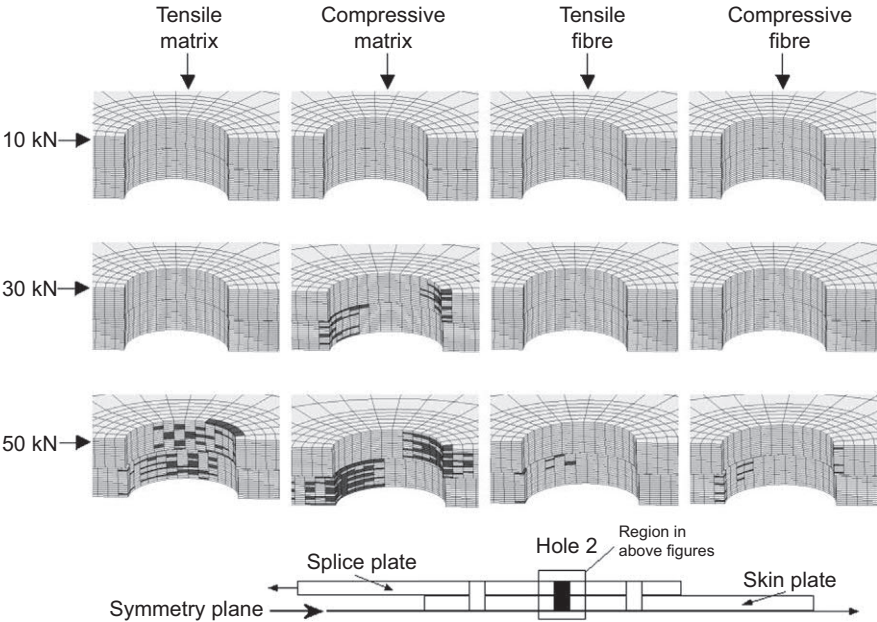
Figure 12.26 Progression of damage at hole 2 (neat-fit clearance) in the C1_C1_C1 joint [55].
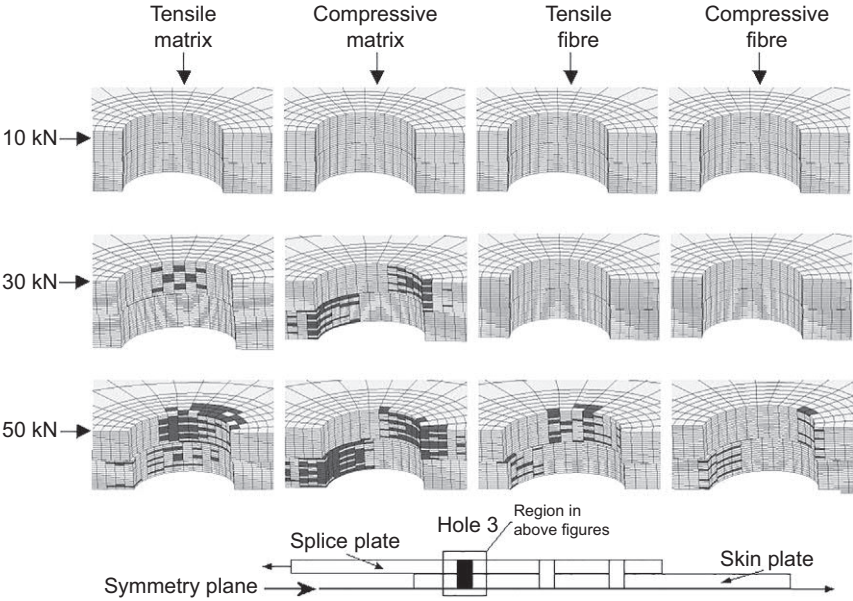
Figure 12.27 Progression of damage at hole 3 (neat-fit clearance) in the C1_C1_C1 joint [55].

less at hole 2) in both the skin and splice plates. Considerable tensile matrix failure is also present at hole 1 in the skin plate and at hole 3 in the splice plate. By 50 kN, significant tensile fiber failure near the net-tension plane exists at hole 1 in the skin plate and hole 3 in the splice plate. In addition, compressive fiber failure has occurred at each hole in each laminate at the bearing plane (considerably more in holes 1 and 3 than hole 2). This indicates bearing failure at holes 1 and 3 and imminent bearing failure at hole 2. The above observations are consistent with the findings on bolt loads in the previous section, where it was found that bolts 1 and 3 took more load than bolt 2, and bearing failure occurred in holes 1 and 3 at 45 kN after which some load transferred to bolt 2. The fiber and matrix tension failures are of interest since they provide a pointer to the ultimate failure mode of the joint in the experiment, which, in this case, was by net-tension failure at hole 3 in the splice plates. Unfortunately, the models generally failed to provide a convergent solution all the way to ultimate failure, due to severe distortion of the damaged elements, and so ultimate failure load prediction was not possible.

An interesting feature of these figures is the difference in damage states at holes with the same bearing load but different bypass loads. For example, contrast holes 1 and 3 in the splice plate at 50 kN applied load. The bearing (bolt) load at hole 1 is obtained from Fig. 12.23(b) as approximately $17/2$ kN or 8.5 kN (division by two occurs because there are two splice plates sharing the bolt load). The bearing load at hole 3 is the same. However, the bypass load at hole 1 in the splice plate is zero, while the bypass load at hole 3 is $(50\text{-}17)/2$ kN or 16.5 kN. If the fiber failures at holes 1 and 3 in the splice plate (top plate in Figs. 12.6 and 12.27) at 50 kN applied load are now compared, it can be seen that the compressive fiber failure state is very similar at both holes, while the tensile fiber failure state is very different with much more failures around hole 3, especially at the net-tension plane. Thus, by explicitly modeling each bolt and hole in a multibolt joint, the correct bypass stresses are obtained. Finally, for this joint configuration, the first fiber failure was detected at a joint load of approximately 38 kN, which is 7 kN less than the load for first bearing failure. Thus, if fiber damage is to be avoided, the load for this joint should be kept below 38 kN.

12.5.4.2   Damage progression in the C3_C3_C1 joint

The progression of damage at hole 1, hole 2 and hole 3 in the C3_C3_C1 joint is shown in Figs. 12.28−12.30, respectively. As can be seen, in contrast to the C1_C1_C1 joint, considerable compressive matrix damage is present at hole 3 at just 10 kN applied load, which is due to all the load initially being taken by bolt 3, while clearance is taken up at holes 1 and 2 (note that the bolts were initially centered in the holes). At 30 kN, compressive fiber failures are present in the splice plate at hole 3, indicating bearing failure. At 50 kN, bearing failure is also evident at hole 1 in the splice plate, but no compressive fiber failures exist for hole 2 indicating no bearing failure at hole 2. These findings are all consistent with the progression of the bolt loads in Fig. 12.24(b). Thus, the failure sequence for this joint is bearing failure at hole 3, followed by bearing failure at hole 1 and eventually bearing failure at hole 2 (if ultimate failure due to net tension does not occur first).
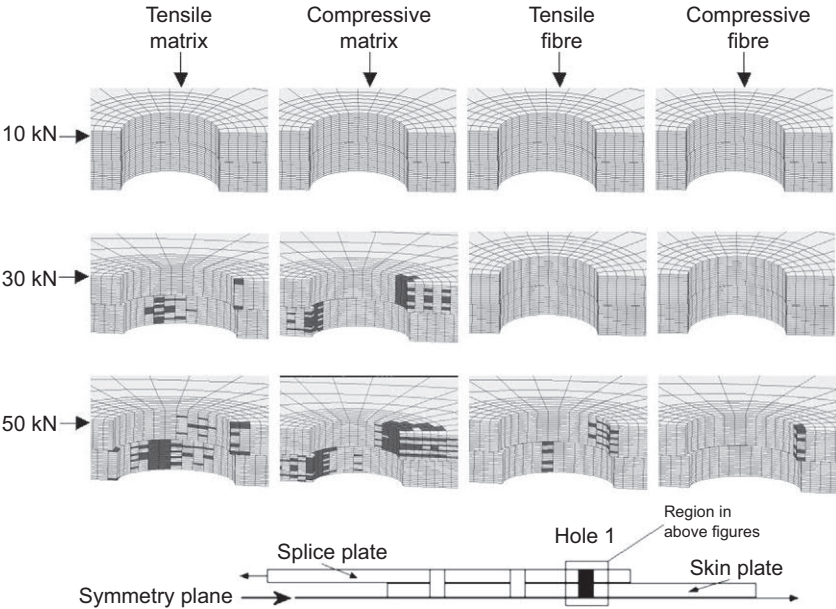
Figure 12.28 Progression of damage at hole 1 (160 μm clearance) in the C3_C3_C1 joint [55].
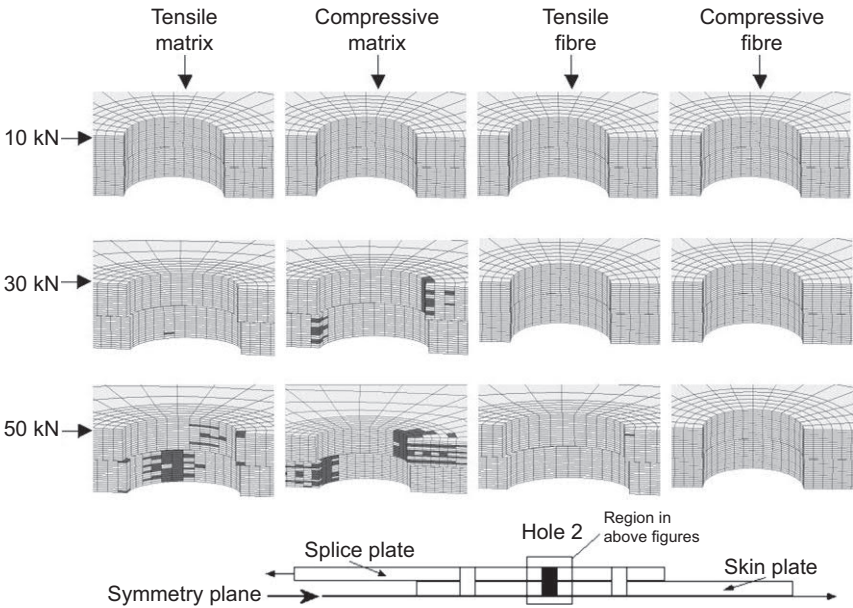
Figure 12.29 Progression of damage at hole 2 (160 μm clearance) in the C3_C3_C1 joint [55].
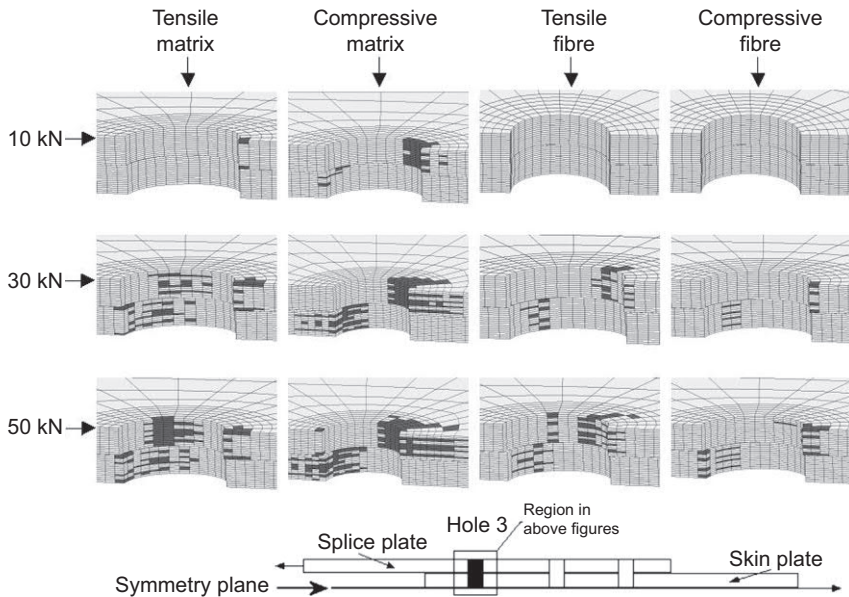
Figure 12.30 Progression of damage at hole 3 (neat-fit clearance) in the C3_C3_C1 joint [55].

First, fiber failure was detected in this joint at 17 kN, which is 55.3% less than the neat-fit control case (i.e., the C1_C1_C1 joint). This highlights that joints with variable clearance incur significant joint damage at much lower loads than joints with all neat-fit bolt-holes.

12.6 Future trends

A future trend in composite bolted joint design is the use of more advanced continuum damage mechanics approaches to model joint failure so that nonlinear shear behavior and gradual stiffness degradation can be implemented. An important element of joint failure is delamination, and many efforts are being undertaken to implement delamination in finite element models. However, for bolted joints analysis this poses many problems due to the large number of delamination interfaces in thick laminates, coupled with the fact that delamination normally occurs at the bolt-hole where significant contact mechanics are also at play. This makes modeling very challenging since newly formed delamination surfaces can potentially become new contact surfaces as the joint deforms during failure. In addition, mitigating mesh-sensitivity effects in damage modeling is a significant current and future challenge. It needs to be proved that any numerical predictions of joint strength are independent of the underlying mesh used for the analysis. A number of approaches exist for mitigating mesh-sensitivity effects, such as crack-band models, nonlocal approaches and damage delay procedures, but as yet, no one technique has been shown to be the most suitable approach for bolted joints analysis.

Another approach that is recently receiving considerable attention is multiscale and multilevel joint analysis. In this approach, a global model is used to model the entire structure, where the fastener region is modeled approximately. By using this global model as a driver, a local model of the joint is constructed where many details are included, such as the bolt, washer, composite material, contact and friction, and material damage in both the fastener and surrounding composite. However, efficient approaches are still needed to provide a methodology to facilitate feedback from the local model to the global model, so that more accurate global predictions of the structural response to load would be possible.

Joints represent the "weak-link" in any structure and are, in most cases, the location where structural failure initiates. For safety-critical structures, such as primary load-bearing joints in aircraft, it would be highly advantageous to be able to monitor the health of joints in real time throughout their design life. In the aerospace sector, the demand to maintain airworthiness by performing regular inspections becomes clear when realizing that the design life of, say, a typical short-range jet aircraft is approximately 50,000 flights. This example illustrates the extensive loading history, which the structure, with special emphasis on its joints, has to withstand during its operational life, including many accidently induced damages and cracks. The recently introduced Structural Health Monitoring (SHM) concept is aimed toward real-time structural airworthiness assessment as an alternative to traditionally scheduled maintenance inspections. Applying this concept to structural joints will enable structural airworthiness deterioration to be monitored in real-time, significantly reducing maintenance costs by increasing the presently scheduled maintenance intervals. Furthermore, it is also expected that by adopting the SHM concept, new aircraft design will require fewer access panels to gain access for inspections, especially in the wing, further significantly increasing the structural efficiency. For secondary, noncritical joints, it would also be advantageous to be able to check joint health during routine inspections. Hence, joint health monitoring tools are urgently required, and so research in this area is due to receive a considerable amount of attention in the near future.

Finally, and as stated previously, approximately half of an aircraft's parts are fasteners. There is an enormous drive in the industry to reduce fastener requirements, and so novel joining approaches will form a significant base for future research. However, bolting will probably never be fully replaced, so novel approaches to optimize bolt patterns to both reduce the number of bolts and increase the strength of the joint still remains a major challenge.

12.7   Conclusions

This chapter has presented both local and global finite element approaches to assist in the design and failure analysis of composite bolted joints. The primary variable under consideration was bolt-hole clearance, which was chosen as it induces significant three-dimensional stresses into the composite laminates, and significantly alters the bolt-load distribution in multibolt joints, and so provides a rigorous test case. It was

shown that bolt-hole clearance significantly increases the stresses at the bolt-hole, and this causes both matrix and fiber damage to occur earlier in the loading history. Hence, for limit load design, or design that requires no fiber damage, clearance should be considered an important parameter. However, it was found that bolt-hole clearance did not have a significant effect on the ultimate failure load of joints, which was due to the extensive bearing damage that takes place in the joints which masks any initial clearance effect and redistributes loads to other fasteners in multibolt joints.

12.8   Further sources of information

12.8.1   Conferences

The 21st International Workshop on Computational Mechanics of Materials, held at the University of Limerick, Ireland, in 2011, hosted a special session on joining of composites. The annual *Composites Structures* conference also regularly presents many interesting papers on joining of composites. The International Conference on Composite Materials (ICCM) runs every 2 years, and many excellent technical papers on joining composites are usually presented.

12.8.2   Websites

Excellent websites for composites, in general, are the JEC website (www.jeccomposites.com) and the Net-Composites website (www.netcomposites.com). Two good bolting websites are due to Bolt Science (www.boltscience.com) and Nord-lock (www.nord-lock.com). Dedicated composite bolted joints websites are less common, but the EU Framework five Project *BOJCAS (Bolted Joint in Composite Aircraft Structures)* [19] produced a website which can be found at the following URL (http://www.smr.ch/bojcas/). The author's personal website (www.fem-ireland.ie) provides a list of many journal papers on the subject.

12.8.3   Interest groups and industries

Many industries, including automotive, aerospace, civil, rail, marine, high-speed machinery, process plant industries, and high-end sports equipment, are currently concerned with composite bolted joints. The aerospace sector is now heavily implementing carbon fiber into wing and fuselage structures, and companies, such as Airbus and Bombardier are carrying out significant research in the field in collaboration with the authors and others. In the automotive sector, BMW is releasing the i3 electric car, which will be the first mass-produced composite car and is due for launch in 2013.

    Some interest groups include the CEN/TC250 and the AGARD advisory group. The Working Group N°4 (WG4) of the CEN/TC250 "Fiber Reinforced Polymers," standard is the currently drafting a Eurocode on the structural use of fibre-reinforced composite materials, with one section devoted to joining. The advisory group AGARD (Advisory Group for Aerospace Research and Development) has produced excellent

conference proceedings on the *Behavior and Analysis of Mechanical Fastened Joints in Composite Structures*, which can be downloaded freely from (www.dtic.mil/cgi-bin/GetTRDoc?AD=ADA199171). Standard bearing tests methods are given by SACRM SRM 9−89, prEN 6037 (1995), ISO 12,815 (2013), ASTM D5961 (1996) Procedures A, B and ASTM D5961 (2008) Procedures C and D.

12.8.4   International journals and books

The international journal *Composite Structures* provides a wealth on papers on composite bolted joints. Other journals, such as *Composites Science and Technology, Composites, Part A & B* and the *Journal of Composite Materials* all have excellent papers on composite bolted joints in their archives. The recently published book *Composite Joints and Connections: Principles, Modelling and Testing* [57] is a dedicated text on composite joints and connections and is highly recommended as an introduction to the subject.

References

[1] L.J. Hart-Smith, Mechanical-Fastened Joints for Advanced Composites − Phenomenological Considerations and Simple Analysis, Plenum Press, New York.

[2] TANGO, Technology Application to the Near-Term Business Goals and Objectives of the Aerospace Industry. EU Framework V project, Contract No. G4RD-CT-2000−00241.

[3] P.P. Camanho, S. Bowron, F.L. Matthews, Failure mechanisms in bolted CFRP, J. Reinf. Plast. Compos. 17 (3) (1998) 205−233.

[4] T.A. Collings, On the bearing strength of CFRP laminates, Composites 13 (1982) 241−252.

[5] C. Cooper, G.J. Turvey, Effects of joint geometry and bolt torque on the structural performance of single bolt tension joints in pultruded GRP Sheet material, Compos. Struct. 32 (1995) 217−226.

[6] P.A. Smith, M.F. Ashby, K.J. Pascoe, Modeling clamp-up effects in composite bolted joints, J. Compos. Mater. 21 (1987) 878−897.

[7] C.T. Sun, Y. Yan, F.K. Chang, Lateral Constraining Effect on Bolted Composite Joints, AIAA, New York, USA.

[8] H. Wang, C. Hung, F.K. Chang, Bearing failure of bolted composites joints. part I: experimental characterisation, J. Compos. Mater. 30 (12) (1996) 1285−1313.

[9] R. Starikov, J. Schon, Quasi-static behaviour of composite joints with protruding-head bolts, Compos. Struct. 51 (2001) 411−425.

[10] L.J. Hart-Smith, Bolted joints in graphite-epoxy composites, NASA Contract. Rep. (1976). NASA CR-144899.

[11] G. Kretsis, F.L. Matthews, The strength of bolted joints in glass fibre/epoxy laminates, Composites 16 (1985) 92−105.

[12] W.H. Chen, S.S. Lee, Numerical and experimental failure analysis of composite laminates with bolted joints under bending loads, J. Compos. Mater. 29 (1) (1995) 15−36.

[13] V.P. Lawlor, W.F. Stanley, M.A. McCarthy, Characterisation of damage development in single shear bolted composite joints, Plastics Rubber Compos. 31 (3) (2002) 126−133.

[14] M.A. McCarthy, V.P. Lawlor, W.F. Stanley, C.T. McCarthy, Bolt-hole clearance effects and strength criteria in single-bolt, single-lap, composite bolted joints, Compos. Sci. Technol. 62 (10−11) (2002) 1415−1431.

[15] M.A. McCarthy, C.T. McCarthy, V.P. Lawlor, W.F. Stanley, Three-dimensional finite element analysis of single-bolt, single-lap composite bolted joints: part I − model development and validation, Compos. Struct. 71 (2) (2005) 140−158.

[16] C.T. McCarthy, M.A. McCarthy, Three-dimensional finite element analysis of single-bolt, single-lap composite bolted joints: part II − effects of bolt-hole clearance, Compos. Struct. 71 (2) (2005) 159−175.

[17] C.T. McCarthy, M.A. McCarthy, W.F. Stanley, V.P. Lawlor, Experiences with modelling friction in composite bolted joints, J. Compos. Mater. 39 (21) (2005) 1881−1908.

[18] ASTM, Standard Test Method for Bearing Response of Polymer Matrix Composite Laminates, ASTM Standard D 5961/D 5961M − 96.

[19] M.A. McCarthy, BOJCAS: bolted joints in composite aircraft structures, Air Space Eur. 3/4 (3) (2001) 139−142.

[20] P.J. Gray, C.T. McCarthy, A highly efficient user defined finite element for load distribution analysis of large scale bolted composite structures, Comp. Sci. Tech. 71 (2011) 1517−1527.

[21] T. Ireman, Three-dimensional stress analysis of bolted composite single-lap joints, Compos. Struct. 43 (1998) 195−216.

[22] L. Tong, Bearing failure of composite bolted joints with non-uniform bolt to washer clearance, Compos. A 31 (2000) 609−615.

[23] P.D. Herrington, M. Sabbaghian, Effect of radial clearance between bolt and washer on the bearing strength of composite bolted joints, J. Compos. Mater. 26 (12) (1992) 1826−1843.

[24] Version 6.9 ABAQUS Analysis User's Manual. Dassault Systèmes.

[25] V.P. Lawlor, An Experimental Study of the Effects of Variable Bolt-Hole Clearance on the Mechanical Behaviour of Composite Bolted Joints, Ph.D. thesis, University of Limerick, Ireland, 2014.

[26] MSCMarc, MSC Marc User's Manual Volume a: Theory and User Information, MSC Software Corporation.

[27] A. Winistörfer, J.T. Mottram, Finite element analysis of non-laminated composite pin-loaded straps for civil engineering, J. Compos. Mater. 35 (7) (2001) 577−601.

[28] J.W. Ju, R.L. Taylor, A perturbed Lagrangian formulation for the finite element solution of nonlinear frictional contact problems, J. De Mechanique Theorique et Appliquee 7 (S1) (1988) 1−14.

[29] B. Andersson, A splitting method for fast solution of 3D contact problems in bolted joints (interim report), in: Deliverable Number D4.3-5, BOJCAS, EU Contract # G4RD-CT-1999−00036, Programme: Growth, New Perspectives in Aeronautics, 2001.

[30] J. Ekh, Three-dimensional stress analysis (interim report), in: Deliverable Number D4.1-1, BOJCAS, EU Contract # G4RD-CT-1999−00036, Programme: Growth, New Perspectives in Aeronautics, 2001.

[31] M.A. McCarthy, C.T. McCarthy, G.S. Padhi, A simple method for determining the effects of bolt-hole clearance on load distribution in single-column, multi-bolt composite joints, Compos. Struct. 73 (1) (2006) 78−87.

[32] M.B. Tate, S.J. Rosenfeld, Preliminary Investigation of the Loads Carried by Individual Bolts in Bolted Joints. NACA TN 1051.

[33] W.D. Nelson, B.L. Bunin, L.J. Hart-Smith, Critical Joints in Large Composite Aircraft Structure, NASA CR-3710.

[34] P.J. Gray, C.T. McCarthy, A global bolted joint model for finite element analysis of load distributions in multi-bolt composite joints, Compos. B-Eng. 41 (4) (2010) 317−325.

[35] R.C. Stephens, Strength of Materials: Theory and Examples, Edward Arnold Ltd, London, 1970.

[36] C.T. McCarthy, P.J. Gray, An analytical model for the prediction of load distribution in highly torqued multi-bolt composite joints, Compos. Struct. 92 (2) (2011) 287−298.

[37] P.J. Gray, C.T. McCarthy, An analytical model for the prediction of through-thickness stiffness in tension-loaded composite bolted joints, Compos. Struct. 94 (8) (2012) 2450−2459.

[38] I. Lapczyk, J.A. Hurtado, Progressive damage modelling in fibre-reinforced materials, Compos. A-Appl. Sci. Manuf. 28 (2007) 2333−2341.

[39] M.W. Hyer, E.C. Klang, D.E. Cooper, The effects of pin elasticity, clearance, and friction on the stresses in a pin-loaded orthotropic plate, J. Compos. Mater. 21 (3) (1987) 190−206.

[40] R.A. Naik, J.H. Crews Jr., Stress analysis method for a clearance-fit bolt under bearing loads, AIAA J. 24 (8) (1986) 1348−1353.

[41] H.Y. Ko, B.M. Kwak, Contact analysis of mechanically fastened joints in composite laminates by linear complementarity problem formulation, Compos. Struct. 40 (3−4) (1998) 187−200.

[42] M.A. McCarthy, V.P. Lawlor, W.F. Stanley, An experimental study of bolt-hole clearance effects in single-lap, multi-bolt composite joints, J. Compos. Mater. 39 (9) (2005) 799−825.

[43] L.J. Hart-Smith, Design and empirical analysis of bolted or riveted joints, in: Joining Fibre Reinforced Plastics, Elsevier Science, pp. 227−269.

[44] C.T. McCarthy, M.A. McCarthy, M.D. Gilchrist, Predicting failure in multi bolt composite joints using finite element analysis and bearing by pass diagrams, Key engineering materials 293−294 (2005) 591−598.

[45] J.H. Crews Jr., R.A. Naik, National Aeronautics and Space Administration, NASA TM 89153.

[46] D. Hachenberg,. Personal Communication, Airbus, Deutschland.

[47] P. Ball, Personal Communication, Airbus, UK.

[48] M. Friberg, Fastener Load Distribution and Interlaminar Stresses in Composite Laminates [Licentiate Thesis], Royal Institute of Technology, Stockholm, 2000.

[49] M. Friberg, Final description of global design methods developed. BOJCAS Tech. Rep., Deliverable No: D2.3−4.

[50] P.P. Camanho, F.L. Matthews, A progressive damage model for mechanically fastened joints in composite laminates, J. Compos. Mater. 33 (1999) 2248−2280.

[51] T.H. Kermanidis, G. Labeas, K.I. Tserpes, S. Pantelakis, Finite Element Modelling of Damage Accumulation in Bolted Composite Joints Under Incremental Tensile Loading, ECCOMAS, Barcelona, 2000.

[52] C.L. Hung, F.K. Chang, Bearing failure of bolted composite joints. Part II: model and verification, J. Compos. Mater. 30 (1996) 1359−1400.

[53] Z. Hashin, Failure criteria for unidirectional fiber composites, J. Appl. Mech. 47 (1980) 329−334.

[54] M. Friberg, Personal Communication, SAAB.

[55] C.T. McCarthy, M.A. McCarthy, Progressive damage analysis of multi-bolt composite joints with variable bolt-hole clearances, Compos. B 36 (2005) 290−305.

[56] R.L. Ramkumar, E.S. Saether, K. Appa, Strength Analysis of Laminated and Metallic Plates Bolted Together by Many Fasteners, Air Force Wright Aeronautical Laboratories Technical Report, AFWAL-TR-86−3034.

[57] W.X. Fan, C.T. Qiu, Load distribution of multi-fastener Laminated composite joints, Int. J. Solids Struct. 30 (21) (1993) 3013−3023.

[58] M.A. McCarthy, C.T. McCarthy, Finite element analysis of the effects of clearance on single-shear, composite bolted joints, Plastics Rubber Compos. 32 (2) (2002) 65−70.
[59] P. Camanho, L. Tong, Composite Joints and Connections: Principles, Modelling and Testing, Woodhead Publishing, 2011.

Further reading

[1] F.K. Chang, K.Y. Chang, A progressive damage model for laminated composites containing stress concentrations, J. Compos. Mater. 21 (1987) 834−855.
[2] D.W. Sleight, Progressive Failure Analysis Methodology for Laminated Composite Structures, NASA/TP-19999−209107, Washington DC, 20546-0001.

Design and testing of crashworthy aerospace composite components

A.F. Johnson [1], R.S. Thomson [2], M. David [3], M.W. Joosten [4], M. Waimer [5]
[1]Composites Consultant, Stuttgart, Germany; [2]Advanced Composite Structures Australia, Port Melbourne, VIC, Australia; [3]ARC Training Centre for Automated Manufacture of Advanced Composites, School of Mechanical and Manufacturing Engineering, UNSW, Sydney, NSW, Australia; [4]Deakin University, Geelong, VIC, Australia; [5]German Aerospace Center (DLR), Stuttgart, Germany

13.1　Introduction

This chapter presents the current state of the art in the design, analysis, and test of crashworthy aircraft structures manufactured from composite materials. Carbon fiber composites are well established for aircraft structures due to their high specific stiffness and strength, their inherent fatigue and corrosion resistance, and suitability for the fabrication of large structures. After initial success in general aviation aircraft and executive jets (Beechcraft Starship, Hawker Beechcraft 390 Premier), followed by military helicopters (EC Tiger, NH90), composites are now being used for primary wing and fuselage structures in large transport aircraft, such as the Boeing 787 and Airbus A350 XWB. A critical safety issue for the design of primary aircraft structures is vulnerability and damage tolerance due to crash loads and foreign object impacts from bird strike, hail, tire rubber, and metal fragments. New composite aircraft structures are particularly vulnerable to impact damage, due to the thin composite skins and the generally brittle behavior of carbon fiber reinforced epoxy resins. A major concern for the aircraft industry is to develop a viable strategy for design and certification of large composite aircraft structures subjected to crash and impact loads. Previous experience with design of metallic structures under crash loads shows that impact energy is absorbed by plastic deformation and plastic hinge formation in the structure, which is not usually relevant to the orthotropic elastic behavior with brittle failure at low strains observed in carbon/epoxy composite structures. Thus, new design concepts are required for crashworthy aircraft structures in composite materials that exploit alternative failure mechanisms, such as fiber fragmentation and delamination to absorb impact energy in the structure.

For aircraft structures, the first structural design requirements for better crash protection were established for light fixed-wing aircraft and military helicopters in the Aircraft Crash Survival Design Guide (ACSDG) [1] and the MIL-STD-1290A [2]. The principles established there for crashworthy aircraft structures are now embedded

in the Federal Aviation Administration (FAA) 14 CFR Airworthiness Standards [3] and EASA Certification Specifications [4] as civil airworthiness requirements for small transport aircraft CFR 23/CS 23, large transport aircraft CFR 25/CS 25, small rotorcraft CFR 27/CS 27 and large rotorcraft CFR 29/CS 29, as discussed further in Section 13.2. The main requirements for structural crashworthiness are to design the aircraft structure to absorb crash energy for a specified survivable crash scenario so as to protect the occupant space, provide restraint systems to limit occupant loads and accelerations and to provide an escape route through sufficient postcrash structural integrity. As with crashworthy automotive vehicles, active and passive crash safety systems composed of energy-absorbing components, primary aircraft structure and seat restraint systems are designed to work together to absorb crash kinetic energy and bring occupants to rest without serious injury. A typical crashworthy aircraft structure requires a stiff safety cage to protect occupants, combined with energy-absorbing structural elements that dissipate crash energy and lower occupant crash loads. Composite structures have the ability to absorb impact energy through a controlled failure in progressive crushing as demonstrated in the design of carbon fiber reinforced F1 racing car components, discussed in Ref. [5]. By tailoring the fiber type, matrix type, fiber—matrix interface, fiber stacking sequence, and fiber orientation, composite crashworthy structures have been shown to have excellent energy absorption (EA) performance characteristics. The challenge for the aircraft designer is to develop composite fuselage structures that meet the appropriate airworthiness structural requirements, without excessive weight or cost penalties being required for the crashworthiness special conditions.

The FAA route to certification adopted by civil aircraft manufacturers is based on the well-known test pyramid for aircraft structures, as set out for composite aircraft in Ref. [6]. Hachenberg [7] discusses the corresponding design procedures, which foresee five levels of tests from material characterization test specimens in Level 1 up to full aircraft structures in Level 5. This is a "building block" approach as each level strongly relies on the results obtained at the level just below. The complexity of the test specimens and the subsequent costs increase considerably on the next higher level, although the number of specimens is reduced. Such an approach has proven its robustness and efficiency in the last decades and has been applied for most major civil aircraft developments. However, large-scale crash testing of composite aircraft fuselage structures and structural elements is too costly due to the number of crash scenarios, the wide range of composite materials and crash concepts in consideration. Thus, there is considerable interest in design and certification by analysis for composite structures or in practice using analysis to support a reduced structural crash test program.

This requires the development and validation of computational methods to support the design of a composite aircraft under the full range of flight and service loads defined in the airworthiness specifications. For the structural crash behavior, improved composites damage and failure models with appropriate finite element (FE) codes are needed and should be validated by materials and structural crash tests at each level of the test pyramid. The successful introduction of polymer composites for the development of commercial transport aircraft and helicopters that meet crashworthy regulations requires an industry-wide initiative. This has prompted the FAA

to form a Crashworthiness Working Group of the CMH-17 (Composite Materials Handbook, formerly MIL-HDBK-17) [8] with representatives from the aerospace and automotive industries, software companies, academia, and national aerospace laboratories. It aims to develop standards for the energy-absorbing characteristics of polymer composite material systems with guidelines and practices for experimental testing and design of composite energy absorbers and crashworthy composite structures. The building block approach is being actively promoted, which includes test procedures for composite energy-absorbing materials and elements, see Ref. [9], design analysis methods for elements [10], with future work on aircraft subfloor structures in discussion.

The plan of this chapter is as follows. Section 13.2 gives an overview of crashworthy requirements and design concepts for aircraft structures with a focus on composite fixed-wing aircraft and rotorcraft. Section 13.3 reviews failure mechanisms and EA in composite crash absorber elements. After discussion of composites mesoscale ply damage and delamination models used for FE simulation of crush failures, design, and analysis methods for composite energy-absorbing elements are then presented together with validation by crush tests. This is followed in Section 13.4 by the design of carbon/epoxy energy-absorbing composite subfloor frame structures for a helicopter. This crashworthy concept study was carried out in a collaborative research project between the Cooperative Research Center for Advanced Composite Structures (CRC-ACS) and the German Aerospace Center (DLR) focusing on the development of novel designs and improved methods of design synthesis for crashworthy helicopter structures. This illustrates the building block approach to design and includes a detailed comparison of design predictions with laboratory crash tests on a prototype subfloor frame structure. This led to a design concept for an energy-absorbing transverse subfloor beam for retrofitting into a metallic helicopter airframe structure, which was crash tested by NASA Langley within a full-scale crash test program. Section 13.5 discusses recent developments and trends in composites damage modeling for use in energy-absorbing structures under dynamic and crash loads, followed by concluding remarks and outlook in Section 13.6. The chapter concentrates on structural crashworthiness for polymer composite materials, that is, the design of composite crashworthy elements and their application to aircraft subfloor structures. For wider aspects of aircraft safety, the reader is referred to other sources of information on current developments in airframe design, crashworthy seat and restraint systems, postcrash fire protection, etc.

13.2   Crashworthy design concepts for aircraft structures

13.2.1   Design philosophy and requirements for airframe crash resistance

Aircraft fuselage structures are designed to be crashworthy in survivable crash scenarios following principles established from crash tests and developed in research

programs over several decades, as discussed in ACSDG [1,11−13]. The main requirements in a crash are that crash energy should be absorbed in the lower part of the fuselage, while the passenger cabin remains intact to allow safe evacuation of passengers. In a crash, the aircraft will have both a horizontal and vertical velocity component. The kinetic energy associated with the horizontal component is mainly absorbed by friction between the sliding structure and the ground, including structural damage and possible soil deformation during the slide out. The crash loads associated with the vertical component of the impact velocity have to be absorbed mainly by controlled structural deformation and failure. Although for fixed-wing aircraft and many rotorcraft crash scenarios the horizontal velocity component will usually be much higher than the vertical component in a crash, it is the vertical crash loads that are more critical for the occupants and require crashworthy design concepts.

Improved airframe and occupant safety are achieved through the design of a crash management system that is dependent on the type of aircraft. Large transport aircraft with a high volume cargo hold below the cabin floor are able to absorb crash energy through controlled plastic deformation of lower fuselage frames and the vertical cargo hold struts. However, light fixed-wing general aviation aircraft, small passenger airplanes, and rotorcraft, have little crushable airframe structure below the passenger floor. Here a system approach is required involving landing gear, energy-absorbing subfloor structures, survivable cabin protection cage, crashworthy seats, occupant restraint systems, crashworthy fuel systems, etc. Fig. 13.1 shows the principles of crashworthy design concepts for such aircraft, based on a stiff structure to protect
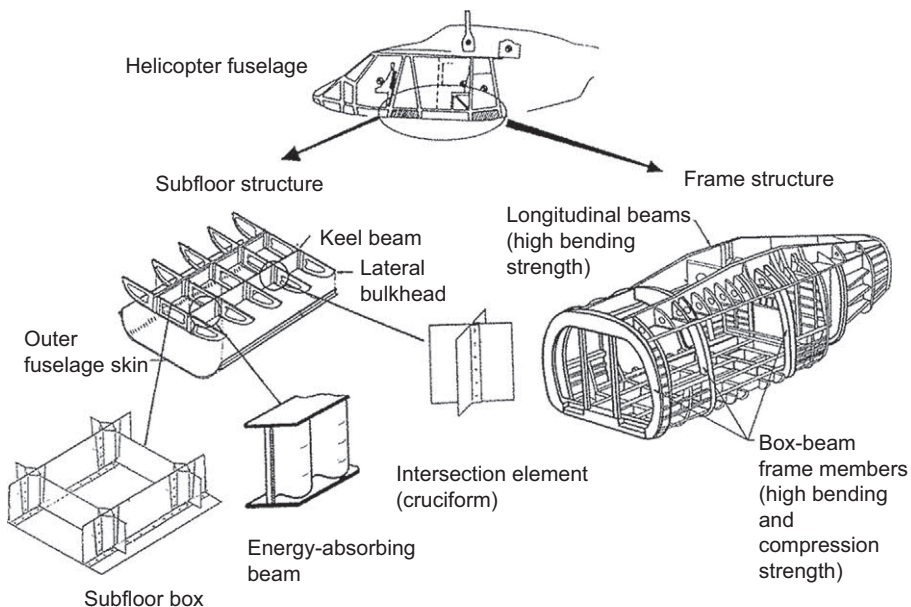
Figure 13.1 Design concept for crashworthy airframe structure [11], with acknowledgements to Taylor & Francis Ltd. www.informaworld.com.

the cabin and occupants composed of frames and longitudinal beams supporting the outer skin and cabin floor. Below the cabin floor is a subfloor structure of keel beams and lateral bulkheads forming subfloor boxes, which may be as low as 200 mm in height, where beam elements are designed to crush down to absorb crash energy. Under vertical crash loads, frame and shell structures above the cabin floor are required to provide a survivable cabin space with high mass retention to prevent intrusion from engines, transmissions, rotor hubs, wings, etc. The subfloor structures are designed to maintain cabin floor structural integrity, absorb crash energy, and reduce dynamic load pulses transmitted to occupants through the cabin floor.

The design of safe, crashworthy subfloor structures is dependent on crash severity and what is considered to be a survivable crash. For large civil transport aircraft, crashworthiness requirements are set out in CFR and CS paragraphs 25.561, 25.562 [3,4], which presume an acceptable level of crashworthiness based on experience with traditionally-configured large metallic airplanes. 25.561 presumes ultimate inertia forces for which the applicant must demonstrate the protection of each occupant. Thus, 25.561 does not define a survivable crash velocity, which has to be obtained from service experience with the aircraft type, such as accident data or fuselage section crash tests. For new composite aircraft such as the Boeing 787, this is defined in a Special Condition SC 25-07-05-SC [14], which requires that the composite fuselage exhibit an equivalent safety level to existing metallic aircraft. Fuselage drop tests on metallic transport aircraft, see for example [15], have shown that a vertical crash velocity of 9.2 m/s (30 ft/s) is survivable, which becomes the required limit of survivability for the Boeing 787 aircraft structure. Paragraph 25.562 requires more stringent tests on passenger seats and harness systems, with specified occupant injury criteria limits at vertical crash velocity 10.7 m/s (35 ft/s) and horizontal velocity 13.4 m/s (44 ft/s).

The corresponding structural crashworthiness requirements for civil helicopters are CFR and CS paragraphs 27.561 for small rotorcraft and 29.561 for transport rotorcraft [3,4]. In addition, seats and restraint systems must satisfy 27.562, 27.785 for small rotorcraft and 29.562, 29.783 and 29.785 for transport rotorcraft. As per these paragraphs, the rotorcraft can be damaged under emergency landing conditions on land or water; however, the airframe has to be designed to such loads that the occupant is protected against severe injuries. Occupants and mass items in the cabin should be limited to maximum decelerations of 20 g vertical and 16 g horizontal. Inertia loads with reduced factors of 12 g horizontal and 12 g vertical are applied to heavy mass items such as engines, gearboxes, and rotors. In transport helicopters, the airframe must also provide protection for subfloor tank failure, if the tanks are subjected to crash loads. Survivable emergency landing conditions for the occupant are specified in paragraphs 27.562 and 29.562, in the form of compliance tests for seats and restraint systems with a 77 kg anthropomorphic test dummy (ATD). The two crash conditions specified are 12.8 m/s (42 ft/s) horizontal with nominal seat position, and 9.1 m/s (30 ft/s) vertical on a seat inclined upward at 60 degrees to the impact direction. Occupant injury criteria such as head accelerations with maximum HIC factor 1000, lumber load limit 6.7 kN, etc. are specified and are measured in the seat tests. For military helicopters, the crashworthy requirements are in MIL-STD-1290A [2] and ADS-36 [16], which are both based on the

ACSDG [1]. Impact conditions in MIL-STD-1290A require occupant survivability for a vertical impact velocity of 12.8 m/s (42 ft/s) on a rigid surface, although the aircraft structure may be damaged. This is a more severe crash condition than the 9.1 m/s defined in the civil requirements. However, with the landing gear retracted, the survivable vertical impact velocity in MIL-STD-1290A is reduced to 7.9 m/s (26 ft/s). This shows that for higher crash velocities, it is expected that other systems, such as the landing gear or airbags would absorb crash energy to reduce the EA requirement for the fuselage subfloor structure.

13.2.2   Use of composites in crashworthy subfloor structures

Composite structural elements have been shown to be capable of high specific energy absorption (SEA) under crash loads through appropriate design and initiation of appropriate failure modes, see for example [5,11]. The challenge is to design a crashworthy aircraft structure such as a subfloor in composites with dual functionality for complying with flight structural loads and providing crash EA under emergency loads. The drop test on an Airbus A320 fuselage section at 7.0 m/s reported by Ref. [17], which complied with the CS 25.561 crashworthy requirements, showed that crash energy in the metallic fuselage was absorbed mainly through plastic hinge formation in frame bending below the cabin floor and in the cabin floor struts. Considerable research has gone on to provide equivalent levels of EA for composite fuselages, which lack the ductility of aluminum, and a number of composites concepts have been developed for fixed-wing transport aircraft. Waimer et al. [18] analyzed the failure mechanisms in transport aircraft fuselage drop tests, including the A320 test, and developed a composite fuselage concept with kinematic hinges at critical positions in the lower fuselage frames composed of carbon fiber-reinforced polymer (CFRP)/titanium hybrid laminate inserts. These were combined with composite segment absorber elements located below a stiff cargo hold floor that absorbed initial crash energy before the kinematic frame hinges were triggered at higher crash velocities. An alternative concept for a large transport aircraft fuselage is described by Ref. [19] in which a composite crash absorber was integrated into the Z-struts that connect the passenger floor to the lower frames at the cargo floor. Under crash conditions when the cargo floor is flattened, the hollow circular CFRP Z-struts are loaded in compression, where they are extruded through a metallic end fixture causing longitudinal splitting and fragmentation with high EA.

In business jets and commuter aircraft, there is less space below the cabin floor, which requires more efficient EA systems. A retrofit concept with energy-absorbing keel beams for a general aviation Lear Fan 2100 aircraft was developed and crash tested, as reported in Refs. [20,21]. A modular sandwich beam concept was developed based on glass and aramid fabric/epoxy skins with hollow glass fiber reinforced plastic (GRP) box cores or foam-filled GRP block cores, which showed high EA in preliminary crush tests. The block core sandwich beams were fitted to the aircraft fuselage section, replacing the aluminum keel beams, before crash testing at NASA Langley with added floor beams, two seats, and ATDs at vertical impact velocity of 9.45 m/s. However, the crashworthy concept was not successful in the

test due to fracture of the fuselage frames above the floor level, with no significant sandwich beam crushing due to the loss of stiffness in the cabin floor needed to resist the beam crush forces.

Another design study was carried out in the EU CRASURV Project [22] to provide a composite crashworthy subfloor structure for a commuter aircraft, as reported in Ref. [23]. The subfloor configuration was based on an Alenia ATR 42/72 aircraft with composite ring frames, transverse floor beams and inclined struts supporting the floor beams at points beneath the seat rails and connected to the frames below. The struts were replaced by longitudinal sine wave beams at a 10 degrees angle with respect to the vertical plane to provide crash EA. The ring frame was modified by continuing the upper part into the transverse floor beam to provide a stiff floor structure, with the lower part hinged at the transverse floor beam and in two parts connected by splice plate at the bottom of the frame. This was to prevent bending moments from the impact point being transmitted to the upper frame. Upon impact, the lower frame should split into two parts that would rotate upward allowing the sine wave beams to make ground contact and absorb the crash energy by controlled crushing. The subfloor structure was manufactured at NLR and crash tested at 7.1 m/s with 640 kg added mass and 19.9 kJ impact energy at CEAT. However, the crashworthy concept did not function correctly in the test; the lower frame split on contact as required, but instead of rotating, the lower frame halves buckled and caused the sine wave beams to slip sideways so that without transverse support they were not loaded in axial compression by ground contact and did not absorb the crash energy. Very valuable experience was gained from these two fixed-wing crashworthy concept studies, which highlight the difficulty of successfully integrating EA structural elements into the aircraft subfloor structure and correctly triggering crush failures.

For rotorcraft structures, it was indicated above that crash survivability is required in crash scenarios with high vertical impact velocity components, up to 12.8 m/s for the case of military specifications. It is also apparent that rotorcraft airframe structures use design concepts as in Fig. 13.1, with relatively large cabin volume and small subfloor volume with typical subfloor heights of 200−300 mm. Due to the low height of the subfloor, highly efficient composite absorbers are needed to absorb crash energy. Furthermore, the presence of fuel tanks and control systems in the subfloor boxes reduces available space for energy-absorbing devices. It follows that rotorcraft crash survivability requires a systems approach. After ground impact, the landing gear or skids should absorb the first part of impact energy, followed by the crashworthy subfloor structural elements. If peak loads are too high, they are transmitted through the cabin floor into the seat rails and the crashworthy seat with occupant restraint system. The stroking seat design may use hydraulic dampers or energy-absorbing devices designed into the seat frames, which should reduce the occupant accelerations and transmitted spinal forces. Finally, the restraint system with seat belts and possibly airbags is designed to protect the occupant from injury through contact with the cabin structure.

The severity of the crash loads on rotorcraft airframe structures has led NASA to consider alternative concepts to increase the volume of a structure to be able to absorb crash energy. This has led to the deployable energy absorber (DEA) concept

developed and validated by Kellas and Jackson [24]. The DEA concept is a composite honeycomb structure that can be deployed to provide EA, much like an external airbag system. The aramid/epoxy honeycomb is initially folded flat and located on the external lower fuselage. On ground impact it is triggered to unfold into a block of honeycomb, which then crushes down to absorb crash energy, thus protecting the fuselage. The device has been retrofitted on an MD-500 helicopter, and two full-scale crash tests were carried out with and without the DEA with velocity components 7.9 m/s (26 ft/s) vertical and 12.2 m/s (40 ft/s) horizontal [25]. It was found that the helicopter with the DEA showed no structural crash damage, while the baseline helicopter had damage to keel beams and subfloor structure as well as buckled and fractured seat frames. The peak floor decelerations were reduced from 40 to 14 g when the DEA was used, which demonstrates its effectiveness.

The focus of this chapter is on composite structures, which due to their high SEA compared with metallic beam and plate structures are of particular interest for the helicopter subfloor. Composite subfloor box concept structures were developed in CRASURV [22] and validated by an extensive design, manufacture, and crash test program as discussed further in Refs. [11,26,27]. The generic subfloor boxes, see insert sketch in Fig. 13.1, consisted of keel beam elements with lateral bulkheads and dimensions ca 600 × 600 mm, with height 180 mm. Crash EA was achieved by utilizing sine wave or trapezoidal corrugated webs in the beams. They are efficient at carrying shear and compression loads in normal flight, with high EA under crushing loads when suitably triggered. Beams were fabricated from hybrid carbon fabric/aramid fabric/epoxy laminates, ca. 2 mm thick, which provided good postcrash structural integrity through hybridization with the more ductile aramid fibers. Critical for a successful design are the intersection/cruciform elements at the box corners, which act as hard points in a crash and transmit high forces to the seat rails, requiring special trigger concepts. Fig. 13.2 shows a successful DLR prototype subfloor box before and after a vertical crash test on a rigid base at 9.2 m/s in which 21.2 kJ of energy was absorbed by the structure at failure.

(a)   (b)

Test structure   Damaged structure after test
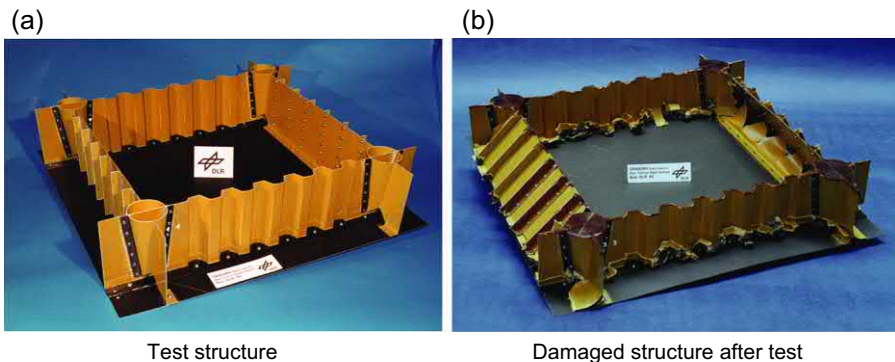
Figure 13.2 Hybrid composite subfloor box (a) before and (b) after drop test at 9.2 m/s, with 501 kg added mass and 21.2 kJ impact energy [28].

This work has been extended recently in a joint DLR/CRC-ACS research project to develop composite helicopter frame structures with integrated EA capability under crash loads, as reported in Refs. [29–31], which is the main subject of this chapter. Due to the complexity and cost of developing composite crashworthy structures, the building block approach was used at each stage of the test/design pyramid to reduce the structural crash test program, as schematically shown in Fig. 13.3. An important feature here is to develop composite materials failure models at Level 1, use these to design and validate energy-absorbing structural elements and components at Levels 2 and 3, before applying them to design the frame structure at Level 4. Further details of EA concepts for composite structural elements are now presented in Section 13.3, with the design and dynamic testing of the crashworthy helicopter frame concept in Section 13.4 of this chapter.

13.3 Design of composite structural elements under crash loads

13.3.1 Energy-absorbing mechanisms in composite structural elements

Although CFRP is generally brittle in its tensile behavior with low failure strains, it has been shown that composite structural elements that fail in other failure modes such as local compression, shear, microbuckling or delamination have the ability to absorb energy through a controlled progressive crush failure. The key is to initiate a progressive crush mode of failure where the absorbed energy is considerably higher than that measured in brittle failures. This is achieved by trigger mechanisms (also known as crush initiators) introduced into a structural element, which reduce peak crush forces and invoke a progressive failure mode that propagates through the structure. Many different progressive failure modes have been observed that depend significantly on
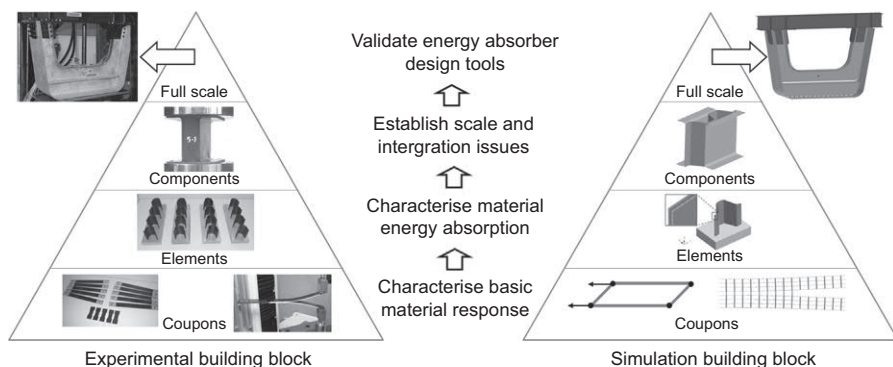
Figure 13.3 Building block approach with test and simulation pyramids as basis for the design of a crashworthy helicopter frame structure.

fiber type, matrix type, fiber–matrix interface, fiber stacking sequence and fiber orientation, specimen geometry, mode of loading, design of trigger, strain rate, temperature effects, etc. Research on energy-absorbing failure modes has continued for over 30 years covering all aspects from composites micromechanics, through macromechanics at the ply/laminate level, up to trigger concepts and design at the structural level.

Early work by Refs. [32–37] showed that glass or CFRP tubes loaded in axial compression through a beveled or chamfered tube end (a chamfer trigger) could fail in a progressive crush mode, provided tube wall thickness was high enough to prevent premature global or local buckling failures. Through this work, the main crush failure mechanisms were identified as a splaying or fragmentation mode. Splaying is initiated at a chamfer trigger by delaminations at the crush front that cause plies to bend or splay outward leading to axial splitting and bending or transverse shear failures. Depending on the ductility of the composite, the splayed plies or fronds will be short due to fragmentation, or long. Fragmentation of the shorter fronds at the crush front leads to a debris wedge, which then drives the delamination failures and leads to a steady crush failure mode with high EA. This is a basic mechanism of composite tube absorbers under axial crush loads. An important step in the development of crashworthy composite structures was to show that similar failure mechanisms could be triggered in nontubular structural elements, such as open circular segments and sine wave webs [27,36], and box sections [38].

To measure and understand the EA and failure mechanisms of composite structural elements requires the development of new test procedures and appropriate test specimens. Feraboli [9] reviews current test procedures and discusses the characteristics of flat plate and corrugated specimens for axial crush tests. The EA properties to be measured are obtained from specimens that fail in a steady crush mode, requiring specially designed support fixtures or self-supporting specimens, such as tubes and cylindrical profiles. DLR has developed chamfered tube segment specimens, see Ref. [28], which are easier to fabricate than tubes, are self-stabilizing without lateral supports and give reproducible axial crush failures under both quasi-static and dynamic loading conditions. Quasi-static tests on the chamfered tube segment specimens are discussed here, and dynamic crush tests are described further in Ref. [39]. The test specimens consist of a half-circle cylindrical segment with flanges at the longitudinal free edges to inhibit local buckling in axial compression. They were manufactured from Hexply M18/1/43%/G939-220gsm 4HS carbon fabric/epoxy prepreg with eight fabric plies and a [0/90/0/90]s layup. Dimensions are length 75 mm, diameter 50 mm at flanges, nominal thickness 2.0 mm. The trigger mechanism was a 45 degrees outside chamfer, which initiates a steady crush process at the chamfer tip. The base of the segment specimens is fixed in a support clamp to a lower steel platen mounted on the load cell of a quasi-static test machine. The chamfered edge is loaded in axial compression by a steel plate attached to the crosshead, which loads the specimen at 1 mm/s. Axial force time and crosshead displacement time are measured in the test for typical crush distances of 50 mm.

Fig. 13.4 shows images from the film of the crush test showing three phases, crushing down of trigger, splaying of the laminate into inner and outer laminae with a central delamination crack, followed by axial splitting of laminae bundles
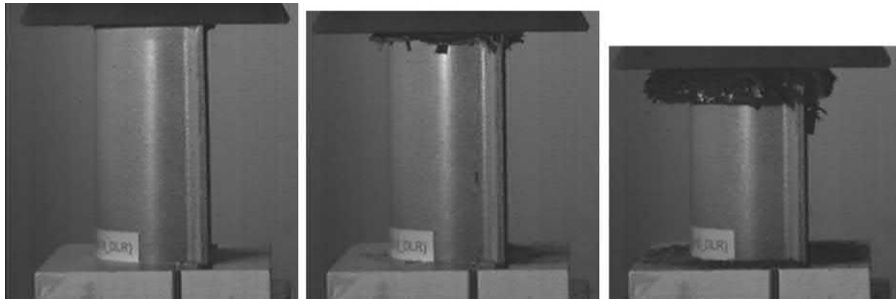
Figure 13.4 Quasi-static crush test sequence on carbon fabric/epoxy tube segment.

(a) (b)
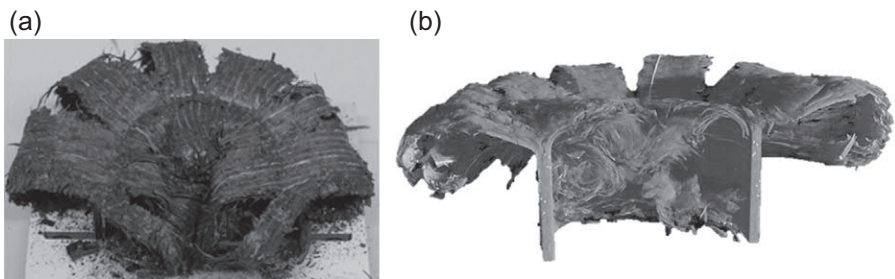
Figure 13.5 Carbon fabric/epoxy segment specimen after quasi-static crush test. (a) Crushed segment; (b) High resolution computed tomography scan of crush front.

into petal-like fronds, as described in more detail in Ref. [40] and seen in the final crushed specimen in Fig. 13.5(a). The steady-state crush phase consists of frond formation driven by the central delamination crack with a debris wedge, Fig. 13.5(b), which shows a high resolution computed tomography (HRCT) X-ray scan of the segment wall cross-section at the crush front. The measured crush force—displacement curve of the segment specimen is plotted in Fig. 13.6 up to a displacement of 40 mm. The curve indicates a rapidly increasing load with a peak at about 2 mm displacement, which corresponds to loading the chamfer trigger. This is followed by a sharp drop in load as the trigger fractures with load falling to a constant mean value in the steady-state crushing phase. This steady crush is the basic mechanism used in the development of composites energy-absorbing structures. Key parameters for the design of such devices are the steady-state crush force (SSCF), the EA, defined as the area under the crush force—displacement curve and SEA, which is the energy absorbed per unit mass of fractured material. These data are shown in the first row of Table 13.1 with SSCF of 24 kN and SEA of 87.1 kJ/kg, which are typical values for quasi-static DLR segment tests with M18/1 carbon fabric prepreg materials. In an extended study of these specimens with different laminate layups and manufacturing variants reported in Ref. [41];
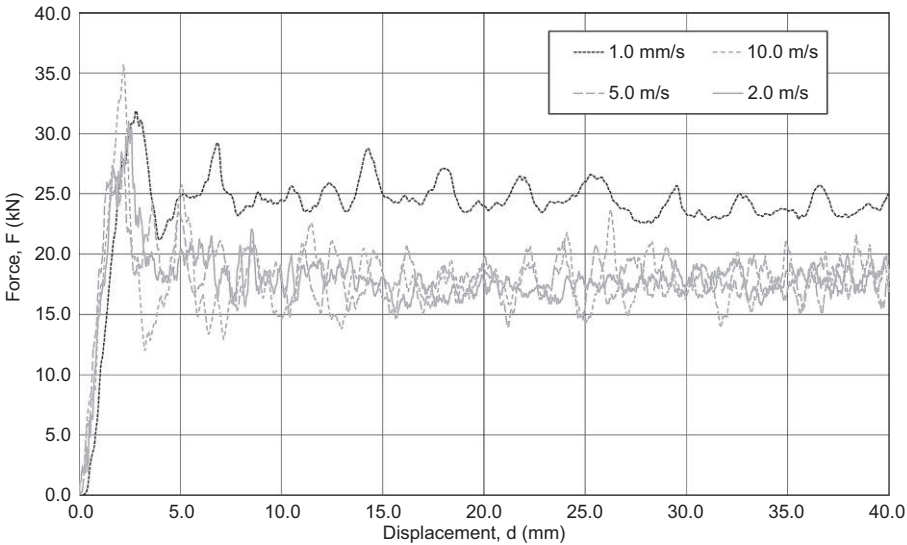
Figure 13.6 Crush force−displacement curves for carbon fabric/epoxy segment specimens at different loading rates.

Table 13.1 Energy absorption performance of carbon fiber reinforced polymer segments at different loading rates.

Loading rate (m/s)	Peak crush force (kN)	SSCF (kN)	Crush distance (mm)	Energy absorbed (kJ)	SEA (kJ/kg)
0.001	31.86	24.03	58.48	1.420	87.11
2.00	31.01	17.71	49.29	0.891	67.89
5.00	27.88	17.80	45.67	0.825	67.53
10.00	35.69	18.04	41.62	0.741	67.04

the SEA range of 79.4−90.6 kJ/kg was measured as layup was varied with different proportions of 0 degree and 45 degrees fabric plies to the load axis.

Fig. 13.6 also includes equivalent force−displacement curves on similar segment specimens tested dynamically at higher loading rates at velocities 2, 5 and 10 m/s in the Instron VHS 100/20 High Strain Rate Test machine at the DLR, see Ref. [39] for more details. This shows that the dynamic specimens exhibited a steady crush response after triggering at an initial peak load. The most interesting feature of the curves is that the three dynamic curves were very similar, with no obvious dependence on the test velocity, and all were significantly below the quasi-static test curve. Table 13.1 summarizes the main results of the quasi-static and dynamic tests.

This shows a reduction of 22% in SEA and 26% in SSCF at 2 m/s compared with the quasi-static values. These results are in line with previous tests done at the DLR on crash elements and are explained by the more brittle behavior of the composite at higher rates causing shorter fronds at the crush front, which fragment sooner, absorbing less energy. The data are important for the designer since composite absorbers are designed for crash loads, and it is apparent that reliance on quasi-static tests for the development of EA structures is nonconservative.

The chamfered half-tube segments exhibit high SEA but are not suitable themselves as structural energy absorbers, due to their idealized shape. The segment crush tests are relatively easy to perform with high reproducibility, and the tests are mainly used for screening new composite materials and lay-ups for use in crash energy absorbers. They are the basic elements of sine wave and corrugated webs that are used in crashworthy subfloor structures as described by Refs. [27,36]. Current interest is now to study EA behavior for a range of composite channel shapes, which can then be the basis of more advanced EA structures. A detailed study of carbon fabric/epoxy profiles with corrugated webs [9] and several channel sections cut from box sections, including the full box, C-channels and right angle corner sections [42] has been undertaken in the CMH-17 Crashworthiness Working Group [8]. Quasi-static tests on the channel sections fabricated from a Toray T700/2510 woven fabric prepreg composite indicated SEA values ranging from 80 kJ/kg for the corrugated webs, 62 kJ/kg for a small right angle corner section, down to 37 kJ/kg for a box section and large C-channel. This follows from the different failure modes that are shape-dependent. The corrugated web crushed down similar to the DLR segments and had high SEA, whereas in the C-channel the unsupported sidewalls bend outward and caused a global splaying failure mode with energy absorbed by tearing along the channel corners.

To increase the level of complexity, a variety of integrated composite structures, involving circular and trapezoidal segments bonded and/riveted to backing plates, or used as the core with sandwich skins, were investigated by CRC-ACS, as reported in Refs. [29,43−45]. These test articles were designed to generate information on the effect of integrating crush elements with the surrounding structure. Tests were conducted to study both the difference between bonded and mechanically fastened components and the effects of different load introduction paths. This led to the development of an EA web segment that is discussed further in Section 16.3.3 and is the basic element of the concept subfloor structure described in Section 16.4.

13.3.2 Composites damage and delamination models

The segment crush tests provide data on crush failure mechanisms that may then be applied in design studies on crashworthy structures. Physical phenomena associated with impact damage and progressive collapse of composite structures are complex, and predictive models and simulation tools for design and analysis are urgently required to reduce the dependence on structural crash testing programs. A mesoscale composite model is used in the work presented here in which the composite laminate is

modeled by layered shell elements. The shells are composed of composite plies assumed to be homogeneous orthotropic elastic or elastic−plastic damaging materials whose properties are degraded by microcracking prior to ultimate failure. The ply properties assigned were based on a composite ply damage model for unidirectional (UD) composites with shear plasticity [46], which was extended to fabric plies by Ref. [47]. The ply model introduces three scalar damage parameters d_1, d_2, d_{12}, which have values $0 \leq d_i \leq 1$ and represent modulus reductions under different loading conditions due to microdamage in the material. For fabric, plies d_1 and d_2 are associated with damage or failure in the principal fiber directions and d_{12} with in-plane shear damage. The ply model is completed by assuming damage evolution equations that have a specific form requiring additional parameters to be determined from specimen tests as discussed further in Ref. [48]. For in-plane shear, ply deformations are controlled by matrix behavior that may be inelastic, or irreversible, due to the presence of extensive matrix cracking or resin plasticity. On unloading, this can lead to permanent deformations in the ply. A plasticity model is included for the shear plasticity with an elastic domain function and hardening law, which requires additional cyclic shear tests for the plies to determine a power-law plastic hardening function. Failure in the ply is controlled by fiber failure strains in tension or compression or by reaching ply shear failure as determined by the shear damage energy at failure.

The tests above on crush coupon specimens have shown the importance of interply delamination in controlling failure mode and EA. The mesoscale FE models were extended in Refs. [47,49] to include stacked shell elements for the composite laminate connected through cohesive interfaces to model delamination failure. This can be described as a 2.5D FE model, where the stacked shell technique allows a composite laminate to split into plies or sublaminates when the cohesive interface fails, and delamination occurs. The cohesive interface is controlled by interface traction− displacement law, such that interface contact is broken when the interface energy dissipated reaches the mixed-mode delamination energy criteria. The proposed delamination model is applied to model interface fracture between composite plies, in which measured fracture energies G_{IC} and G_{IIC} from through-thickness tension and shear tests on composite laminates with an interface crack are the main materials parameters required. This contact interface is an efficient way of modeling delamination, with the advantage that the critical integration time step is relatively large since it depends on the area size of the shell elements and not on the interply thickness. The ply damage and failure models have been implemented in the commercial explicit crash and impact code PAM-CRASH [50] in collaboration with the software company Engineering Systems International. They have been tested and validated extensively for modeling impact damage in composite structures [48] and for simulation of crushing failures and EA in composite structural elements [29,40,51,52]. Note that the models discussed here have been based mainly on composites quasi-static test properties, although as seen in Fig. 13.6, polymer composites exhibit rate-dependent behavior under dynamic crash loads. Development of dynamic failure models is currently an active research field, which is discussed in future trends in Section 13.5.

13.3.3 Design analysis of crash elements

13.3.3.1 DLR crush segments

This subsection is concerned with the application of the mesoscale composites models to simulate crush behavior of crash elements and their validation by comparison with crush test data. The numerical model selected for the segment test specimen consists of four stacked shells, as seen in the inset detail to Fig. 13.7. Each shell in the stack is a four-node layered composite shell that represents a ply or sublaminate ply group, with mesh size 1 mm. In the model here, each stacked shell represents two carbon fabric/epoxy plies. The ply properties assigned were based on the mesoscale fabric ply model discussed in Section 13.3.2. Material parameters were obtained from coupon tests previously conducted at DLR on the carbon fabric/epoxy material. The four stacked shells were connected using three cohesive interfaces whose failure behavior was characterized by the delamination model. The required interface fracture energy properties G_{IC} and G_{IIC} were determined, respectively, from double cantilever beam and end notched flexure tests conducted at CRC-ACS. Just as the chamfered edge is the key to initiate stable crushing in the segment specimen, the FE model requires a numerical trigger to produce a stable crush analysis, as seen in Fig. 13.7. This consists of a rigid element called a separation wedge, which mimics the behavior of the debris in the HRCT scan image Fig. 13.5(b). The elements representing the chamfer are then offset so that contact with the separation wedge initiates a central delamination crack in the stacked shells of the segment wall. The contact distance and friction coefficient between the segment shells and wedge are varied to control the delamination crack length, which in turn influences the degree of splaying in the fronds. Fig. 13.7 shows the segment simulation in the steady crush phase, which approximates quite well to the observed failure mode in the test segment shown in Fig. 13.5. A critical test of the FE model is to compare computed crush load—displacement curves with test data, as seen in Fig. 13.8. These results are encouraging since the numerical simulations show an initial peak contact force, which after triggering drops to a steady crush force level close to that measured in the test, with similar good agreement in EA determined from the area under the force—displacement curves. Further details of the simulation results and data
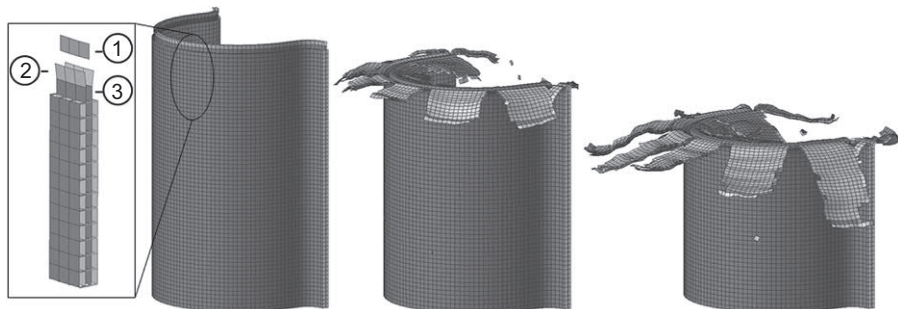
Figure 13.7 Finite element model of DLR carbon fabric/epoxy tube segment under axial crush showing chamfer trigger model and crush sequence.
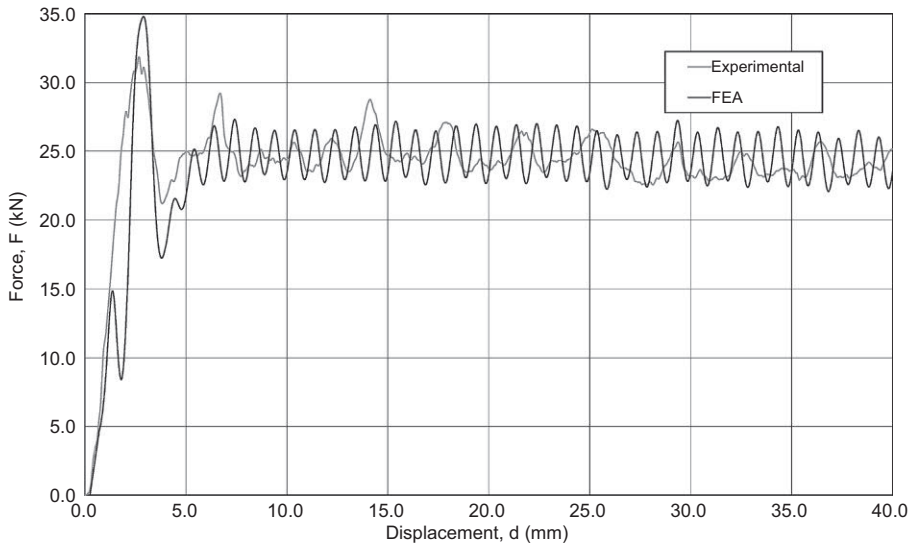
Figure 13.8 Comparison of crush force test data with finite element simulation for DLR segment.

requirements with further application of the model to C-channels specimens from the CMH-17 Crashworthiness Working Group can be found in Refs. [40,51].

13.3.3.2 EA web segment

The EA web segment shown schematically in Fig. 13.9 is composed of a corrugated trapezoidal shear web (one and a half waves) with two C-sections bonded to the outer edges, and plates bonded to the top and bottom to produce a segment of the energy-absorbing web. This was shown to have good EA properties and be suitable for integration into the composite subfloor structure described in Section 13.4. A three-layer stacked shell model was used for the corrugated trapezoidal core, which is the main crushable EA component. The two plate and C-sections contributed approximately 20% to the EA of the structure and for computational efficiency were modeled with single-layered shell elements. Cohesive interfaces were used to represent the behavior of the adhesive used to bond the web segment together. The upper plate was modeled as a rigid body and a constant velocity field applied to the plate. The lower plate was fixed in all degrees of freedom based on experimental observations. A self-contact was applied to all layered shells, and three node-to-segment contacts were used to ensure that the shells of the C-sections, corrugated core and the upper and lower plates interact without penetration throughout the failure process.

The simulated crushing response of the EA web segment is shown in Fig. 13.10. It should be noted that the model is shown with the upper plate removed to allow the internal failure mode to be observed. The corrugated core exhibited a failure mode similar to that observed for hat-shaped crush elements tested in Ref. [43], where the two C-sections splayed out from the corrugated core as the crushing element progressively failed. A comparison of the experimental and predicted load−displacement
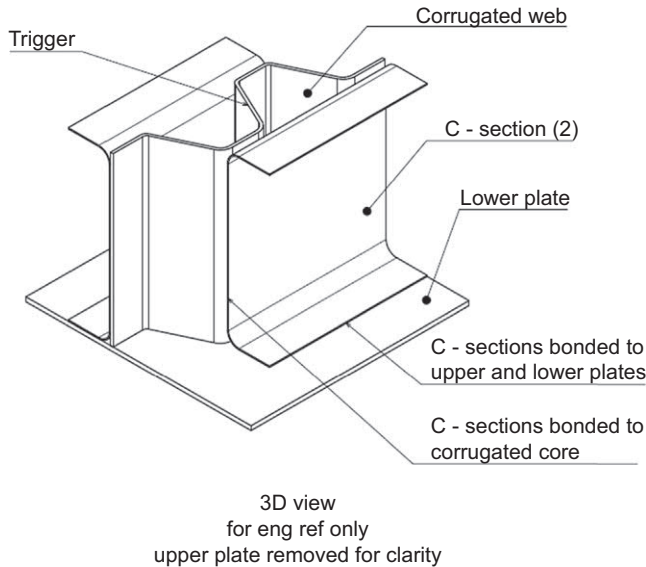
Figure 13.9 Schematic representation of the energy absorption web segment.
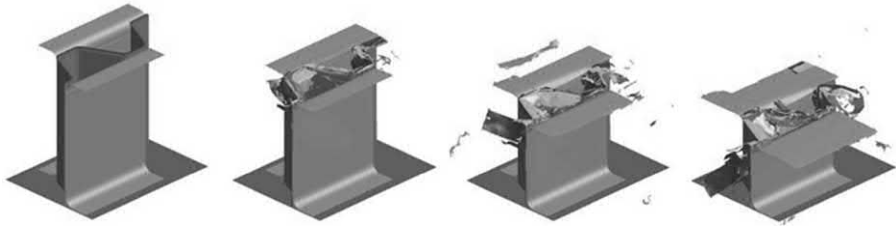
Figure 13.10 Simulated crushing sequence for the energy absorption web segment.

response for the EA web segment is shown in Fig. 13.11. In the early stages of loading the numerical model shows good agreement with the experimental data. After 15.0 mm of stroke, it underpredicts the crushing load due to the C-sections exhibiting a "tearing" type of failure close to the bonded interface at the corrugated core, which was not observed during experimental tests. Overall, the numerical model provided a good approximation of the crushing response of the EA web segment and with the test data shows that this is a robust EA element that is suitable for use in energy-absorbing subfloor structures.

13.4 Design and crash test of composite helicopter frame structure

13.4.1 Frame structure design concept

A composites concept structure was designed and manufactured following the building block approach set out in Fig. 13.3, to demonstrate energy-absorbing concepts
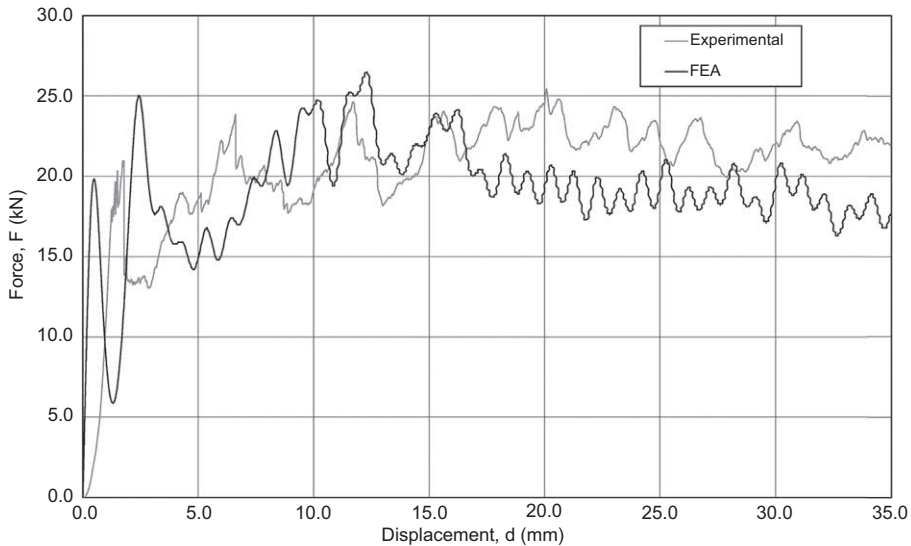
Figure 13.11 Comparison of crush force test data with finite element simulation for energy absorption web segment.

and to validate the modeling methods. The structure chosen represents the lower half of a helicopter fuselage frame that was designed to the crashworthy concepts discussed in Section 13.2.1, with main components shown schematically in Fig. 13.12. These are a stiff semirigid upper frame to provide survivable space for the occupants and a sacrificial EA subfloor, together with an outer skin laminate not shown in the figure. The overall dimensions of the structure were 450 mm (height) × 700 mm (width) × 200 mm (depth), with the height of the lower frame structure 170 mm, of which the subfloor absorber element had a height 85 mm. Dimensions were chosen to reduce manufacturing and testing costs and could represent a quarter-scale model of a typical transport helicopter frame. The structure shown in Fig. 13.13 was manufactured from a woven carbon fabric/epoxy prepreg. The subcomponents were bonded together. The outer skin was mechanically fastened by rivets and bonded to the energy-absorbing structure and upper frame. Three structures were designed and manufactured by CRC-ACS for testing at the DLR.

The upper frame structure was composed of back-to-back flanged C-sections bonded together. The composite materials used were Hexply M18/1/43%/G939-220gsm 4HS fabric, laminate thickness in the webs and flanges varied between 8 and 18 plies, chosen to provide the high structural stiffness required by the frame with additional reinforcement at load introduction points. The EA subfloor was a corrugated core sandwich based on the trapezoidal core EA web segments discussed above in Section 13.3.3. The corrugated web used a ply-drop trigger and was sandwiched between two C-sections. The trapezoidal core elements were also fabricated from Hexply M18/1/43%/G939-220gsm 4HS fabric with a thickness of five plies. The webs of the subfloor C-sections were two plies with two additional plies added
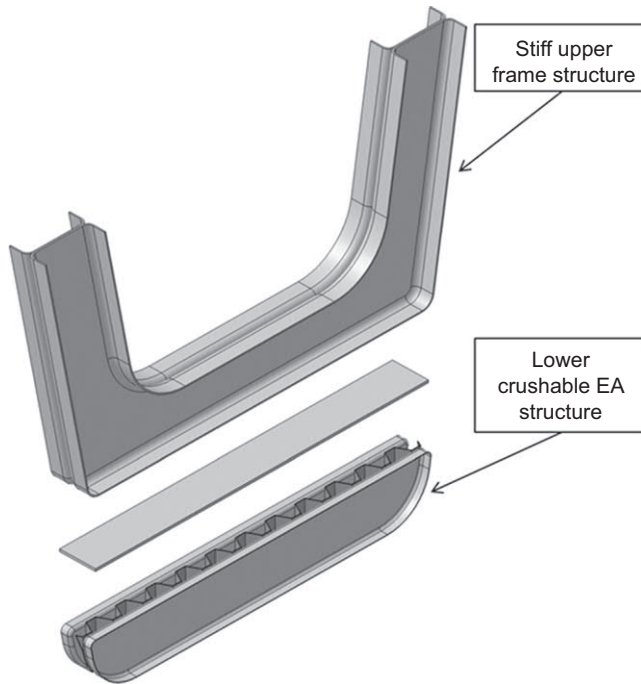
Figure 13.12 Schematic of crashworthy frame concept structure.

Figure 13.13 As manufactured frame structure with details of energy absorption subfloor.

to the flanges so that the thickness transition between web and flange was a weak point that functioned as a triggering mechanism under vertical crash loads. The manufactured trapezoidal core web sandwiched by the C-sections with the upper cover plate is shown in the inset details of Fig. 13.13. The outer skin laminate ranged in thickness from 6 to 10 plies, with the additional reinforcements at the base.

A simplified global FE model was developed first to support the design concept, as discussed further in Ref. [31]. The stiff frame structure was modeled conventionally by composite shell elements, with the EA subfloor modeled using nonlinear springs based

on data from web segment crush tests. This allowed a rapid estimate of structural crash performance and was a basis for the choice of composite ply layups in the frame and subfloor structures. The upper frame was designed to sustain the expected peak dynamic loads transferred through the energy-absorbing elements. The frame geometry and layup were optimized to maximize structural efficiency. The global model was also used to design the supporting structure and interface attachment for the drop tower crash tests discussed in Section 13.4.2.

13.4.2 Quasi-static and crash test results

Three tests, one quasi-static crush test, and two vertical drop tests were performed on the frame structures. The purpose of the quasi-static crush test was to observe failure modes and establish the baseline performance and energy-absorption characteristics of the structure. The dynamic crash tests were to evaluate the crash performance of the structure at two impact energies and provide data for validation of the FE simulation methods to substantiate the building block design methodology. For supporting the frame structure for testing and providing a means of load introduction, the two arms of the frame structure were attached at the top to a steel I-beam through riveted brackets attached to the flanges of the composite frame.

Quasi-static and dynamic tests were conducted at the DLR Institute of Structures and Design, Stuttgart. The quasi-static test was conducted in a Zwick 1494 servo-hydraulic uniaxial loading frame (max. loads ±500 kN, max. crosshead displacement 850 mm) with the structure test setup as shown in Fig. 13.14(a). Vertical compression loads were applied by the test machine crosshead via a load cell to the test structure through the I-beam and measured at the load cell and on the load platform. The test was performed initially at a crosshead velocity of 5 mm/min for the first 20 mm of crosshead displacement, then increased and maintained at 20 mm/min until final collapse at 62 mm crosshead displacement. From the measured load-deflection curve,

(a)   (b)
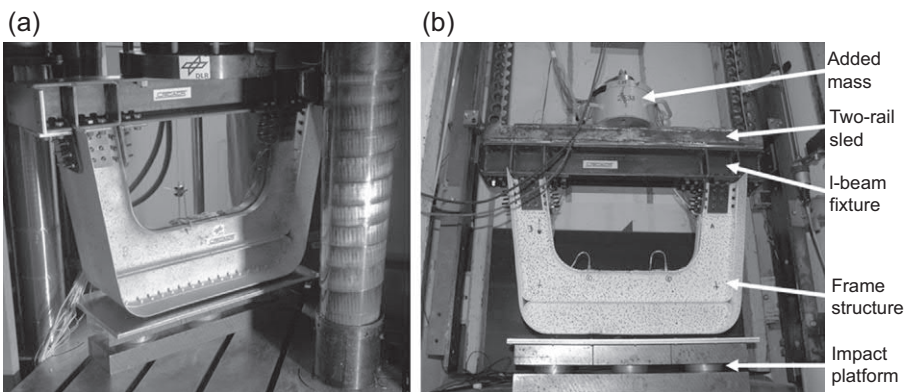
Figure 13.14 Test setup for frame structure. (a) Quasi-static crush test, (b) dynamic drop test.

the absorbed energy at failure can be calculated, which was measured to be 6.3 kJ at 62 mm displacement. This energy represents an upper limit for EA in the crash tests, which gives a guideline for appropriate crash test conditions for the frame structure.

The two crash tests (Dynamic 1 and Dynamic 2) were performed in the DLR drop tower shown with test structure in Fig. 13.14(b). A target impact velocity of 8.0 m/s was chosen, which is in accordance with the landing gear retracted vertical crash requirement of 7.9 m/s defined in MIL-STD-1290A as discussed in Section 13.2.1. The impact velocity in the drop test is determined from the drop height in the tower, with added mass being chosen to provide the required crash kinetic energy for the structure. Two crash scenarios were investigated in tests Dynamic 1 and Dynamic 2 with masses corresponding to 50% and 85% of the EA capacity of the structure, respectively. The structures were instrumented with strain gauges and accelerometers, and the tests were recorded using high speed (HS) video.

For the dynamic tests on larger structures, load measurements on a load cell attached to the I-beam are not very reliable, due to system and structure vibrations. These crash loads were thus measured as response loads on a specially designed base platform. The impact platform, designed and built specifically for use in both quasi-static and dynamic crash tests, is shown schematically in Fig. 13.15 and can be seen on the test fixture in Fig. 13.14(b). Impact Plate 1 is aluminum and spans the width of the structure. Impact Plate 2 consists of three separate steel plates with a force transducer below each segment. The locations of these force transducers were aligned to the load path, as indicated in Fig. 13.15. This partitioning reduces the occurrence of undesirable vibrations in the impact platform during the period of the crash test. A steel base plate of identical thickness to Impact Plate 2 completes the impact base platform.

A summary of the test conditions and results is detailed in Table 13.2, which shows total mass inclusive of drop sled, I-beam, added mass and mass of frame structure, the absorbed energy by the frame structure and the crush distances. The
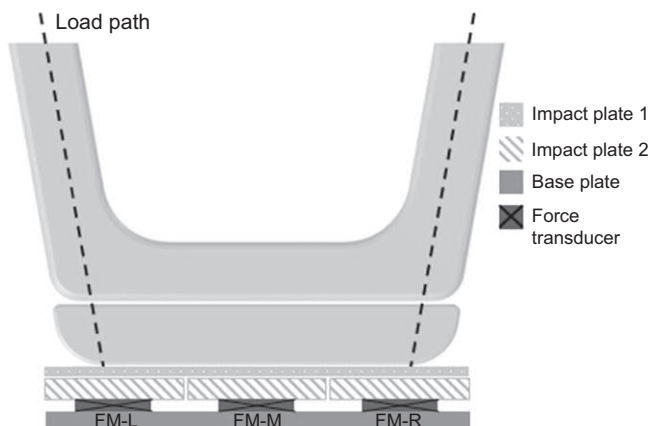
Figure 13.15 Schematic of impact platform.

Table 13.2 Summary of the parameters and results in frame tests.

	Test		
Quantity	Quasi-static	Dynamic 1	Dynamic 2
Mass (kg)	n/a	98	159
Impact velocity (m/s)	n/a	8.05	8.0
Impact energy (kJ)	n/a	3.2	5.1
Absorbed energy (kJ)	6.3	2.8	5.1
Crush distance (mm)	62	32	56
Peak load (kN)	123	121	120
Steady crush load (kN)	113	104	101

measured force—displacement curves from the quasi-static and dynamic tests are presented in Fig. 13.16. The load levels plotted for each of the tests conducted are a summation of the three force transducers in the impact platform. These curves exhibit characteristics typical of those seen in Section 13.3 for progressively crushed composite energy absorbers, with a rapid rise to a peak load at which the absorber elements are triggered, followed by a fairly steady crush force. The response of the structure in all three tests was similar, although the measured steady-state crush load was approximately 10% lower in the dynamic tests, which was also observed in the previous element tests in Fig. 13.6. It is apparent that the failure behavior is the same in the two dynamic tests; however, Dynamic 1 has absorbed the crash kinetic
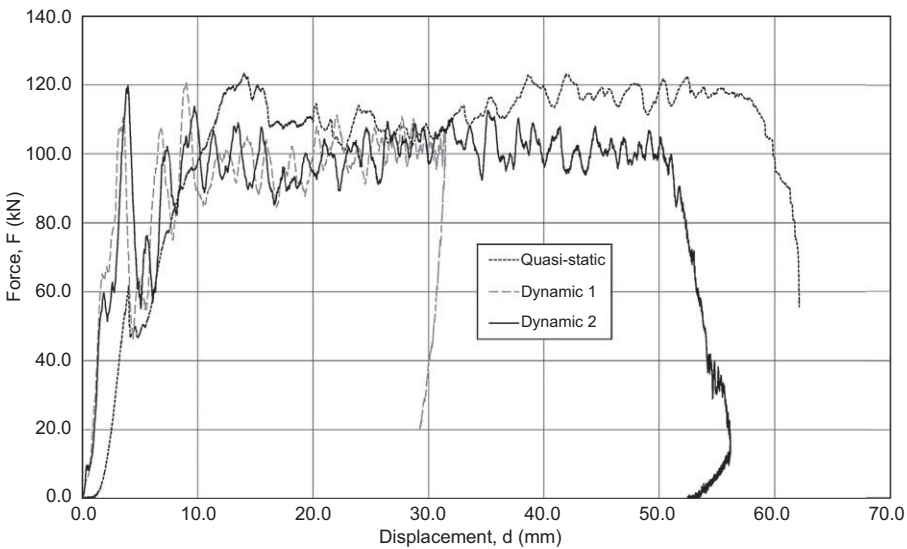
Figure 13.16 Force—displacement responses measured in quasi-static and dynamic frame tests.

energy at 32 mm, while for the higher energy Dynamic 2 test steady crushing of the EA subfloor continues up to 56 mm. In the latter case, this represents a crush distance of about 65% of the height of the trapezoidal absorber elements.

The HS video films of the tests show the sequential failure modes observed and give an insight into the effectiveness of the design concept and triggering of the EA subfloor. Sequences from the videos and details of the strain gauge data are given in Ref. [31]. Fig. 13.17 compares images of the final damage of the EA subfloor for each test. In the quasi-static test, the structure was loaded most severely, and the test was finally stopped at the first crack in the stiff upper frame. Fig. 13.17(a) shows the final failure in which the sacrificial EA structure was almost fully crushed from the bottom upward. Contact of the outer skin fastener heads with the flange of the non-crushing frame caused bending that resulted in the large transverse crack that can be observed in the figure.

The Dynamic 1 test structure in Fig. 13.17(b) exhibited significantly less damage compared to the quasi-static test due to the lower crash energy applied. The integrity of the upper frame was maintained, and the damage was limited to the EA subfloor component, which crushed progressively from the bottom upward. The Dynamic 2 test structure was subjected to higher impact energy that caused very significant crushing of the energy absorber coupled with separation and buckling of the face sheets, as shown in Fig. 13.17(c). It was observed that failure of the bond line between the flange of the upper frame section and the flange of the face sheets in the subfloor crushing section occurred near the end of the drop test, and separation of these two parts initiated at the two corner sections and progressed inward. Further-more, separation of the skin panel caused by the failure of several fasteners leading to excessive skin buckling was also observed. The upper frame was relatively undam-aged as specified in the design requirement.

The manufacture and crash tests on the frame concept structure demonstrated the success of the concept at the crash energy levels in the test. The upper frame remained intact and was stiff enough to maintain cabin volume and provide the required resisting force at floor level for crushing the sacrificial EA trapezoidal sub-floor absorber elements. The trapezoidal sandwich absorber elements were triggered
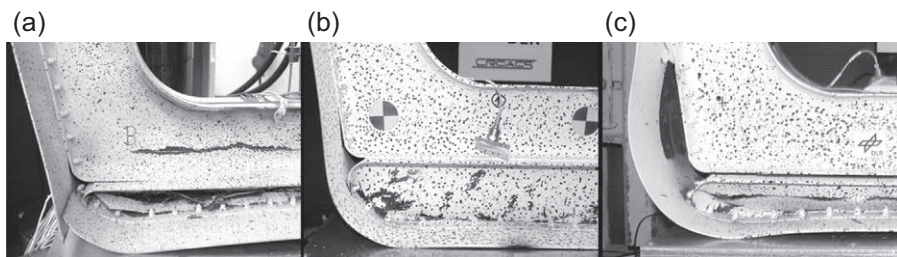
Figure 13.17 Subfloor of frame structure showing final damage at end of each test. (a) Quasi-static test, (b) dynamic 1, (c) dynamic 2.

successfully to prevent excessive peak loads and exhibited the required steady crush behavior until the structure was brought to rest.

13.4.3 Crash modeling and damage prediction

Experience has shown that when modeling crash and impact events, it is important to include details of the test rig in the FE model since dynamic force measurements are influenced by system vibrations (see Ref. [53]). To simulate the crash tests, a detailed FE model of the frame structure, together with the main items of the drop tower sled and three-part impact platform, was developed, as shown in Fig. 13.18. The modeling method for the EA substructure used a three-layered, stacked shell composite mesomodel, as discussed in Section 13.3.3 and shown in the inset diagram in Fig. 13.18, while the remainder of the composite structure used single-layered composite shell elements. The configuration and boundary conditions of the numerical model were as in the experimental test. A gravitational acceleration field of 9.81 m/s^2 and an initial velocity of 8.05 m/s were applied to the entire model. The FE model was developed to better represent the transfer of inertia during the crash simulation and replaces an earlier model without test fixture shown in Ref. [31]. To reflect the mass distribution, center of gravity and inertia of the entire system more precisely, the I-beam and two-rail sled were included, with the I-beam fastened to the sled using eight metallic brackets with point link elements to represent riveted fasteners. These link elements are referred to as PLINK elements in the PAM-CRASH [50] code and can model separation at a given rivet failure load, as described in Ref. [54]. The riveted outer skin connection to the frame C-section flanges was also modeled by PLINK elements, which included rivet
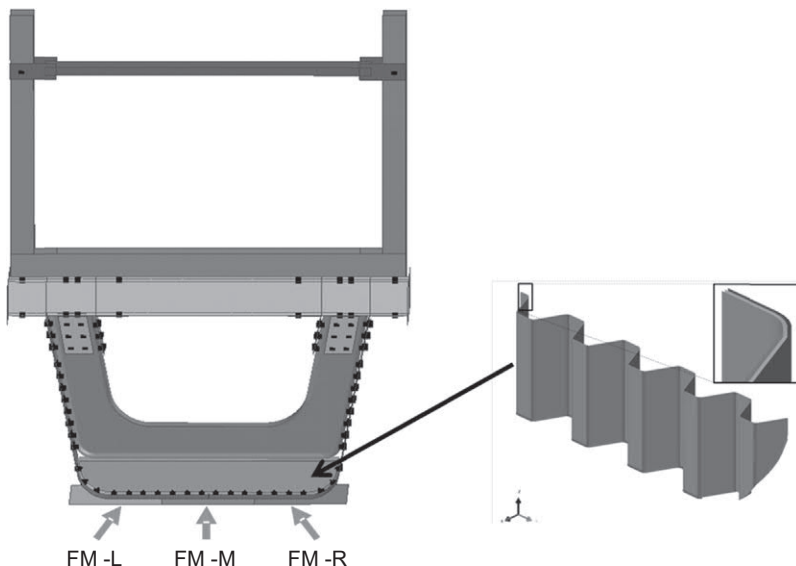
Figure 13.18 Finite element model of frame structure with drop sled and impact platform.

tails as rigid bodies as they prevented the webs splaying outward during crushing and contained the failed material. This containment role of the webs contributed to the overall crushing response observed in the tests (see Ref. [29]).

The accuracy of the refined FE model was assessed qualitatively and quantitatively through comparison of predicted load—displacement response, failure behavior, and strain response with test data. Fig. 13.19 compares the final damage state of the frame structure in the crash test Dynamic 1 (left side) with results from the FE simulations (right side), showing good agreement in deformation with separation and buckling of the outer skin at the frame/absorber interface. Fig. 13.20 shows crush failure in the EA subfloor structure, comparing an HRCT scan of the crushed trapezoidal elements (left side) with the FE simulation (right side) of the subfloor, which included rigid body rivet models. The FE model correctly exhibited the crushing in the lower 35 mm of the subfloor section, together with the buckling and ply damage progressing ahead of the crush front. The upper part of the EA section showed no significant failure, and adhesive interfaces remained intact. A comparison of measured and predicted dynamic strains at six locations on the upper frame was also made, with satisfactory agreement, as reported in Ref. [30].

The measured and simulated force—displacement and energy—displacement curves for Dynamic 1 are shown in Fig. 13.21. The total force shown is the sum of the forces from the left, middle, and right load cells. There were some discrepancies in the initial force predictions during triggering of the absorber, but the subsequent steady crushing was accurate. This suggests that refinements are needed to model the trigger, as discussed in the crush segment models in Section 13.3.3. An overview of test results and FE predictions for both dynamic tests is presented in Table 13.3. The overall quantitative comparison is very good, demonstrating that the models were capable of accurately predicting the steady-state crushing loads
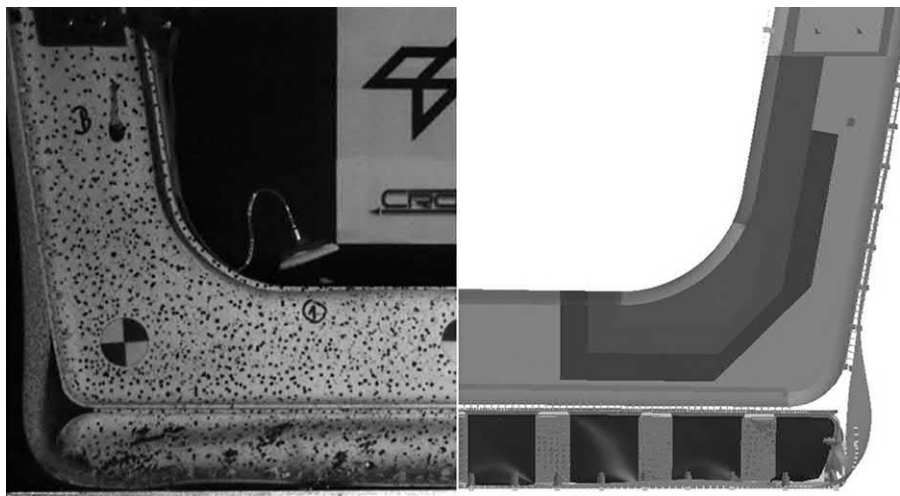
Figure 13.19 Comparison of deformations in test and finite element simulation of Dynamic 1.

HRCT-scan

Figure 13.20 Comparison of subfloor damage from high resolution computed tomography scan and finite element simulation of Dynamic 1.
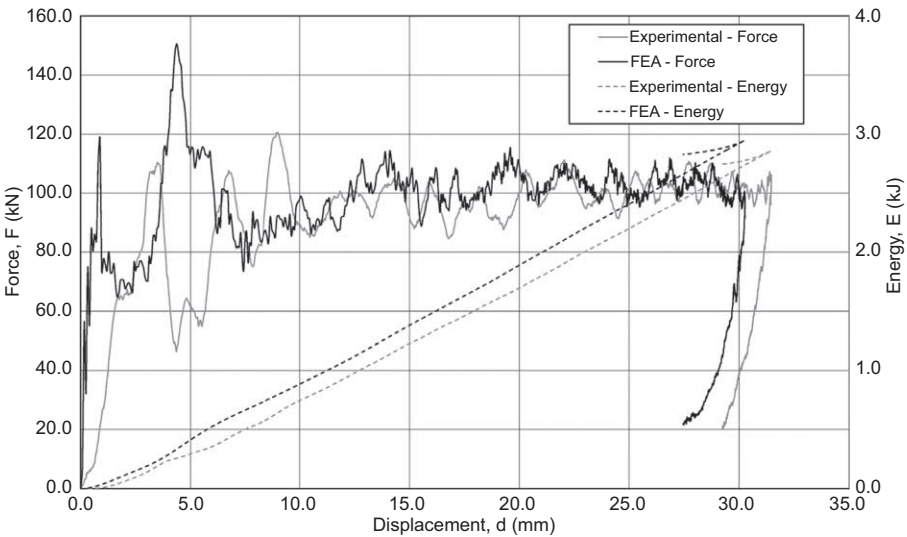
Figure 13.21 Comparison of measured and simulated force−displacement curves and absorbed energy for the frame structure in Dynamic 1.

and EA. The numerical models overpredicted the peak load due to the initiation of local buckling in the C-section webs in the test, which coincided with crushing in the corrugated web. Predicting the precise failure sequence, including the triggering with complex structural interactions and material failure remains a challenge for composite crashworthy structures.

Table 13.3 Summary of results from crash tests and finite element (FE) simulations on the frame structure.

Quantity	Dynamic 1		Dynamic 2	
	Test	**FE**	**Test**	**FE**
Absorbed energy (kJ)	2.83	2.93	5.10	5.10
Crush distance (mm)	31.5	30.3	56.0	52.0
Peak load (kN)	121	150	120	142
Steady crush load (kN)	104	105	101	99.2

13.4.4 Retrofit helicopter subfloor crash structure

The experience gained with the design and analysis of the EA composite frame structure was then applied to develop a retrofit helicopter subfloor crash concept structure for integration into a helicopter fuselage crash test. NASA Langley Research Center obtained two Boeing Vertol CH-46E Sea Knight helicopters from the US Navy for full-scale crash tests in the Transport Rotorcraft Airframe Crash Testbed (TRACT) research program. The TRACT 1 & 2 rotorcraft crash tests were carried out on soft soil at the NASA Landing and Impact Research (LandIR) Facility in 2013 and 2014, see Ref. [55] for full details. The CH-46E airframe was in a baseline configuration in the TRACT 1 test, fitted out with energy-absorbing seats, occupant dummies, etc. and tested under combined crash conditions of 7.62 m/s vertical and 10.05 m/s forward velocity. The main aim was to provide data on airframe and occupant kinematics in a crash under realistic conditions. The TRACT 2 test was performed later under the same nominal crash conditions to determine whether significant improvements in crashworthiness could be achieved, with the airframe modified so that existing aluminum shear panels in the mid-cabin region were retrofitted with composite energy-absorbing subfloor structures. NASA designed and developed two EA subfloor transverse beam structures reported in Ref. [56]: the "conusoid," made up of conical-shaped elements with hybrid carbon/aramid fabric reinforcement; the "sinusoid," a sinusoidal-shaped sandwich beam with the same hybrid fabric skins and a polymer foam core. A third subfloor transverse beam structure was designed, developed, and manufactured by CRC-ACS/DLR in collaboration with NASA and delivered to them for retrofitting in the TRACT 2 crash test. The Composite Subfloor System (CSS) chosen was an EA subfloor beam based on the trapezoidal EA elements used successfully in the helicopter frame structure in §13.4. The location of the three composite transverse beam subfloor structures in the helicopter floor is indicated in the NASA TRACT 2 test report [55].

Fig. 13.22 shows a schematic of the CSS concept structure, which follows closely the crashworthy frame concept structure developed in Fig. 13.12. It consists of a stiff upper I-beam manufactured from back to back C-sections which supports the cabin floor, with sacrificial energy-absorbing beam structure based on trapezoidal EA
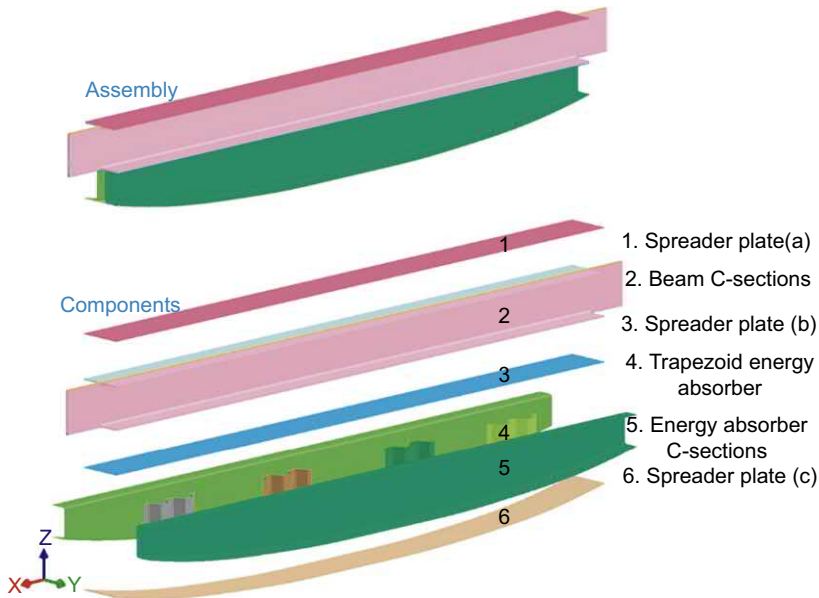
Figure 13.22 Composite sub-floor system (CSS) [57].

elements as the core, sandwiched between C-sections webs. The individual components of the CSS are:

1. Spreader plate (a)
2. I-Beam C-sections (two back-to-back)
3. Spreader plate (b)
4. Four trapezoid energy absorbers
5. Energy absorber C-sections
6. Spreader plate (c)

The complete structure was manufactured from Hexcel M18-1/43%G939-220gsm 4HS carbon fiber/epoxy fabric, with sub-components of the energy absorber bonded together, and skins mechanically fastened and bonded to the energy-absorbing structure and upper beam C-section flanges. Dimensions of the CSS are length ca 1500 mm, with maximum height ca 230 mm at the midpoint, and thickness ca 100 mm. Particular attention was given to the design of the trapezoidal EA elements.

The trapezoid core concept structure in §13.4 develops a steady-state crush load of approximately 180−200 N/mm width. Based on information from the TRACT 1 crash test, the requirement for the CSS was a steady-state crush load of 80−100 N/mm width. Reducing the thickness of the trapezoidal web below the five plies used previously was not an option as buckling is induced over crushing. Therefore, a segmented energy-absorbing element concept was proposed in the CSS, as seen in Fig. 13.22, which shows four trapezoidal web elements across the beam length each composed of two trapezoid cycles. Preliminary design studies were used to select the absorber

configuration and verify that the required energy-absorbing response was achieved, as discussed in Ref. [57].

This was based on an FE model of a 2-cycle trapezoid sandwich element 143 mm wide, height 120 mm, with the same five ply M18 layup in the web developed in §13.3 and using the same composite ply data. The web was modeled with three stacked shells and two cohesive interfaces, with face skins modeled as single-layered shells with appropriate laminate thicknesses. A steady crush simulation was performed, similar to that shown in Figs. 13.10 and 13.11, initiated through a numerical trigger by off-setting the bottom nodes in the trapezoidal web stacked shells. The predicted mean crush force up to 95 mm displacement was 24.1 kN or 170 N/mm so that an energy absorber with trapezoidal core across the whole span would be too stiff to be triggered in the crash test. It was considered that four 2-cycle trapezoidal elements were required in the EA beam substructure. Other possible configurations could be eight 1-cycle trapezoid elements distributed along the absorber structure.

Following the TRACT 1 crash test, an undamaged section of the CH-46E airframe was fitted with seats, occupant dummies and added masses for use in a drop test to evaluate the NASA conusoid and sinusoid energy-absorbing concepts, as reported in Ref. [56]. Drop test results were then used by NASA in a barrel test FE model to validate designs for the conusoid and sinusoid absorber beams, as described in Ref. [58]. Parameter studies to design the CSS beam were carried out in a similar way by integrating detailed FE models of CSS concept beams into a cabin fuselage barrel section model converted to PAM-CRASH from the LS-Dyna model provided by NASA, as shown in Fig. 13.23.
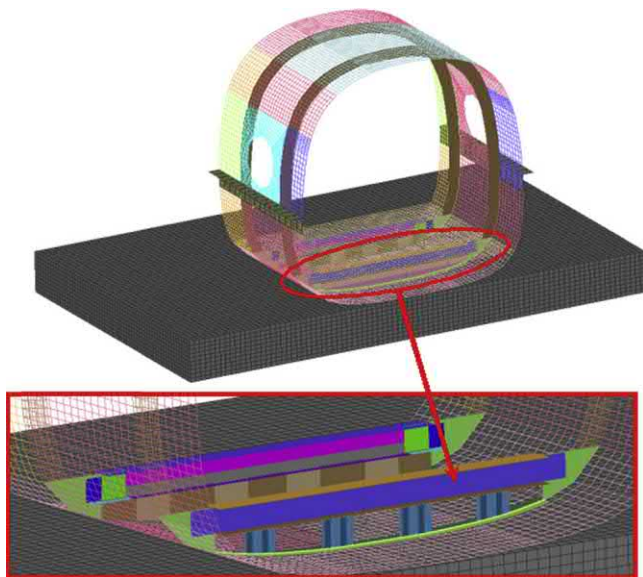
Figure 13.23 Barrel Section FE model with the CSS subfloor beam incorprated at FS220 [57,58].

Two concepts of the CSS beam considered for detailed analysis are 2-cycle trapezoidal core elements at four equally spaced locations (EA1), or eight 1-cycle trapezoids uniformly spaced across the absorber beam (EA2). Two frame positions in the cabin floor were considered as possible locations for the CSS beams, referred to as Frame Section (FS) 190 and 220, see [55, Fig. 13.9]. Note that the seat and mass distribution in the cabin depends on frame position, which influences the dynamic loads on the absorber elements during a drop or crash test. FE simulations were carried out for a drop test on the barrel section with vertical impact velocity 7.62 m/s, equal to the vertical component in the TRACT 1 test, for beam concepts EA1 and EA2, at locations FS 190 and 220. Fig. 13.24 shows typical simulation results of beam deformations in EA1 and EA2 when situated at FS 220, which is a location for two seats and occupant dummies above the beam. In Fig. 13.24(b), the C-Section core skin is omitted in the visualization to show the extent of damage and crushing in the trapezoidal absorbers. Results show that the transverse I-beams are deflected in bending, with the absorber beam crushed down along its length and trapezoidal elements crushing from the triggered lower edges. The lower spreader plate in contact with the aluminum floor skin shows extensive local deformations from contact with soft soil, particularly for EA1. Further details such as FE predictions of accelerations, section forces and energy absorption in the CSS beams are given in Ref. [57].

Fig. 13.25 shows predictions of section forces at FS 190 and 220 for absorber concepts EA1 and EA2 in a simulated barrel drop test at 7.62 m/s. Note that a simplified absorber model was used at FS 190, in which the cohesive interfaces were not included in the trapezoidal web, which may explain the different behavior to that seen in the full FE model used at FS 220. At FS 220 there is an initial peak force ca 165 kN at about 3−4 ms, which falls rapidly at 6 ms as the trapeze elements are triggered to crush, followed by a steady crush force ca 100 kN up to 20 ms. Concept EA2 had higher peak forces on impact, with lower steady crush forces than EA1. Analysis of predicted accelerations in the crash dummies above the CSS at FS 220 showed peak values of 135 g with EA2 floor beams, compared with 110 g with EA1 floor beams. Total energy absorbed was very similar in the two concepts, with small differences in the partition of energy between trapezoidal absorbers, beams, spreaders, and the aluminum skin. The higher initial peak accelerations would cause increased occupant loads at the seat
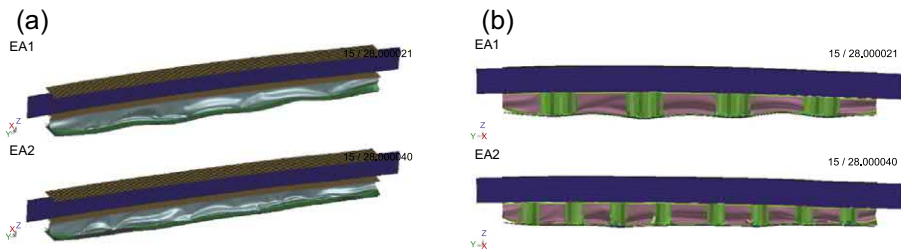
Figure 13.24 FE simulation of EA1 and EA2 beam structures in drop test on soft soil at 7.62 m/s [57] (a) Isometric view (b) Nearside EA C-sections omitted.
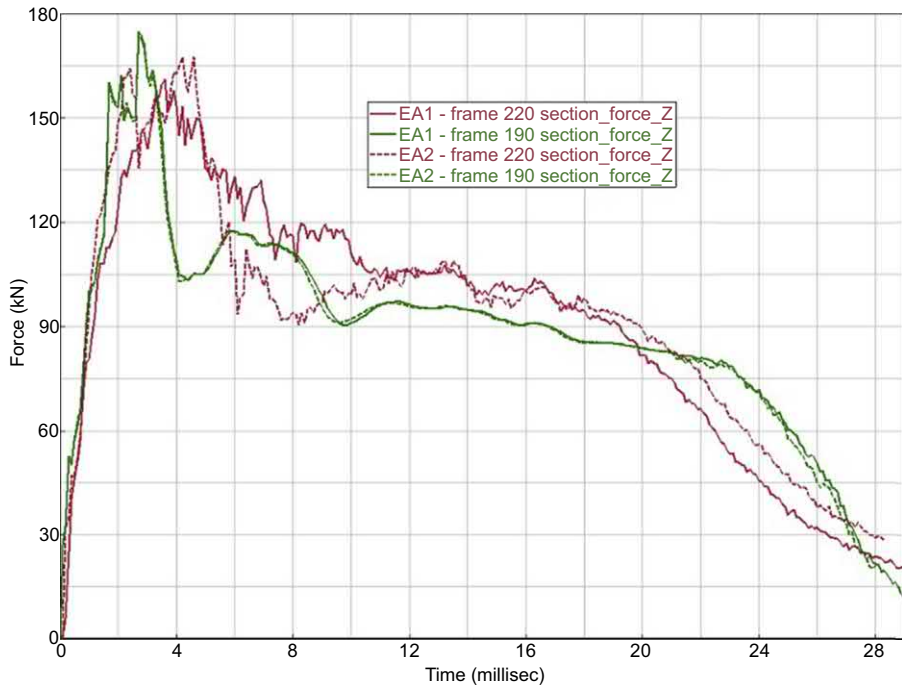
Figure 13.25 Predicted z-direction section forces in CSS structures EA1 and EA2 in barrel drop test at 7.62 m/s [57].

locations. It was concluded that concept EA1 is preferred as it should provide better occupant protection through lower peak accelerations. This led to the design of a floor beam structure based on four equally spaced 2-cycle trapezoidal absorbers in the EA sandwich core. This CSS structure was manufactured at CRC-ACS, delivered to NASA and retrofitted into the TRACT 2 helicopter crash test structure.

Full details of the TRACT 2 crash test with fuselage retrofitted with NASA sinusoid beam at FS 254, conusoid beam at FS 286, and the CRC-ACS/DLR CSS beam at FS 220 are given in Ref. [55]. The TRACT 2 test was successfully carried out with impact conditions of 7.7 m/s vertical and 10.3 m/s horizontal, very close to those in the TRACT 1 test, with 95% of 360 channels of airframe and ATD data collected. This provided a unique opportunity to assess full-scale crashworthiness of a large rotorcraft fitted with seats and crash dummies under combined longitudinal and vertical impact conditions. An evaluation of the performance of the NASA subfloor structures is discussed in Ref. [56], with the response of the CSS in Ref. [59]. Here the TRACT 2 test results were inconclusive for validating the crashworthiness of the retrofitted composite beams as seen in damaged subfloor structure, Fig. 13.21 of NASA report [56], which states:

> "Results from the TRACT 2 full-scale crash test were also complicated by anomalies. Moist soil increased the coefficient of friction and reduced the stopping distance of the

test article by half, compared with the TRACT 1 test. Due to excessive damage of
the outer belly skin, the composite energy absorbers failed to crush and rotated
globally as they became separated from the floor and outer skin."

Due to the softer soil conditions the TRACT 2 airframe slid forward only 1.3 m in
impact compared with 2.4 m in the first test, which caused part of the subfloor to
plow into the soil surface causing excessive shear forces on the fuselage skin which frac-
tured in places. Subfloor structural integrity was lost and the seats with occupant
dummies located at FS 220, where the CSS was installed, lost their attachment to the
floor and rotated severely resulting in the CSS floor beam being loaded in transverse
shear rather than axial compression. Fig. 13.26 shows the FSS floor beam removed
from the airframe after the TRACT 2 test. Inspection of the structure showed that the
stiff I-beam had little damage, the absorber C-section skins had triggered at the absorber
base, but there was no evidence of crushing in the trapezoidal elements. Closer inspec-
tion indicated some permanent transverse shear damage in the trapezoidal core. Due to
the subfloor kinematics in the airframe crash test, it was not possible to initiate the axial
compression crush failure mode in the CSS beam structure, so that the floor beams were
not able to dissipate crash energy and reduce occupant crash loads as intended. Similar
conclusions apply to the NASA sinusoid and conusoid absorbers which were located
close by in the same mid-floor region, as discussed in Ref. [56].

In conclusion, the retrofit program has shown that composite subfloor EA structures
can be designed, manufactured and shown to have high crash energy absorption when
tested in idealized laboratory conditions, for example in drop tests on rigid surfaces,
where the absorber elements are loaded uniaxially. This was demonstrated with the
EA frame structure described in §13.4. The challenge is to design and develop
energy-absorbing structures which function in real crash conditions where there
may be multiaxial dynamic loads, and interaction with nonrigid surfaces which deform
and influence crash kinematics. A key to future progress is to develop robust simula-
tion tools able to predict the response of composite absorber structures under a wide
range of dynamic load conditions to demonstrate their envelope of validity. Further-
more, a better understanding of the global crash response of aircraft structures is ur-
gently needed from full-scale crash tests and crash simulation tools to provide a
framework for the integration of detailed crash models for structural assemblies.

(a)   (b)
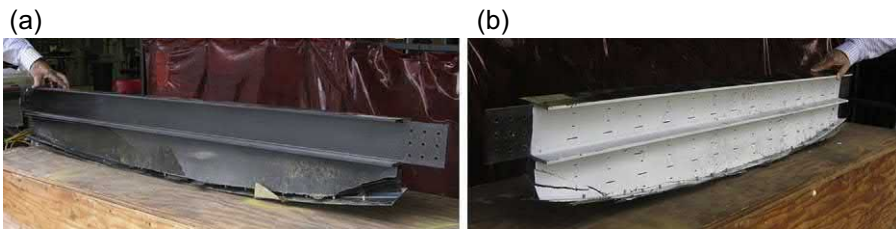
Figure 13.26 CSS floor beam structure after removal from TRACT 2 airframe crash test [59],
(a) Front side (b) Rear side.

13.5   Future trends in damage and crash modeling

Damage and crash models, although they follow the building block approach, often require a model or application-specific calibration to capture observed failure modes in specific structural applications and load cases. Hence, they may not be "truly predictive," and detailed studies are required to understand model limitations and define their envelopes of validity. In a recent study [60], the predictive capability of the mesoscale composite modeling approach, described in Section 13.3.3, was investigated based on a test campaign on CFRP crash absorber elements at the structural level. Aim of this study was to obtain agreement over a range of crash absorber variants and crush failure modes with a fixed set of simulation parameters. When validated in this way, simulation methods should provide robust, reliable analysis of design variants, which have not been tested experimentally and whose failure modes are to be determined.

A composite crash absorber is considered, which is integrated into a transport aircraft fuselage frame to provide an energy-absorbing crushable cargo floor strut, as shown in Fig. 13.27(a). It consists of a bolted assembly of an L-shaped strut with a half-tube absorber based on the DLR crush segment design of Section 13.3.1. The combination of the self-supporting absorber and the flat L-strut, which triggers failure through buckling under axial load, provides a basis to validate simulation models as different failure modes occur in both assembled parts. The L-strut design includes constant laminate thickness and variants with a local thickness reduction, which may exhibit progressive crushing or catastrophic failure. The chamfer angle φ at the lower edge of the half-tube absorber Fig. 13.27(b) causes a steadily increasing axial crush load when triggered by the L-strut buckling. The chosen material was a woven carbon fabric/epoxy with mass 286 g/m^2 and ply thickness 0.25 mm. Test structures were manufactured with laminate thicknesses 1 mm (layup [45°, 0°]$_S$) and 2 mm (layup [45°, 0°, 45°, 0°]$_S$, and chamfer angles φ = 60°, 75°.
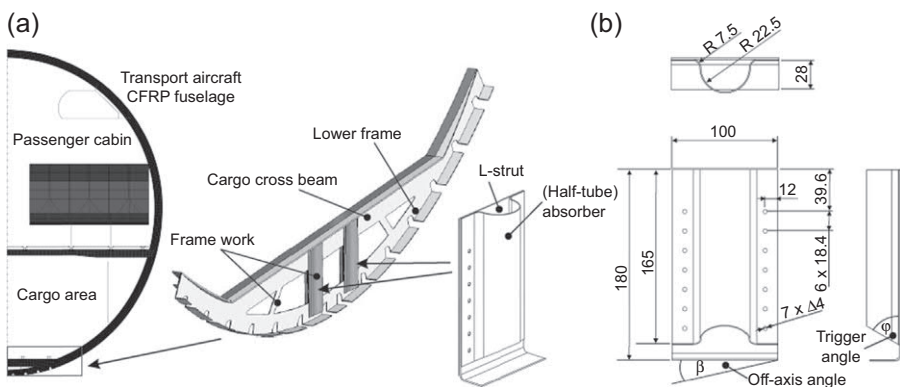
Figure 13.27 Absorber strut in crashworthy aircraft fuselage structure, (a) Sub-cargo floor frame structure, (b) Strut absorber geometry, see Ref. [60], with acknowledgements to Elsevier Ltd.

In this study, the mesoscale intralaminar model with stacked shells and cohesive interfaces discussed in § 13.3.1 was further developed by replacing 4-node shell elements by continuum shell elements with reduced integration (type SC8R). The 8-node continuum shells give a better representation of laminate stacking with respect to cohesive elements between shells and their penalty contact interactions. The simulations were performed in Abaqus/Explicit using an intralaminar material model for fabric composite plies available as VUMAT abq_ply_fabric described in Ref. [61]. This provides an orthotropic linear elastic material formulation and a maximum stress-based damage initiation for the longitudinal fiber directions, with damage evolution based on fracture energies. For in-plane shear, damage evolution and plasticity are included in the model. A calibration procedure for the intralaminar composite material model was developed using cyclic shear tests for shear damage and plasticity parameters, with coupon crush tests for determination of fracture energies.

The cohesive interface is simulated in Abaqus/Explicit using solid elements of type COH3D8 and follows the cohesive zone (CHZ) model discussed in Ref. [62]. A bi-linear traction-separation law is used which requires interface fracture toughness properties measured under through thickness tension G_{IC} and shear $G_{IIC,}$ in combination with a power-law failure mode interaction. A calibration procedure for the normal and shear cohesive layer stiffness values in the stacked laminate was developed in Ref. [60] to determine penalty values, which are a compromise between too high model compliance and numerical instability from too stiff input values.

A study was made of the FE mesh influence on simulation of progressive crushing by comparing regular structured meshes with unstructured and skewed meshes. Structured meshes typically cause load spikes for each element row that undergoes simultaneous failure and elimination at the crush front, and mesh adaptions can prevent this and lead to smoother progressive failure. It was shown that with a skewed mesh, crush simulations could be improved and mesh dependent force spikes prevented. This is important as unrealistic force spikes may cause rupture of the analyzed structure away from the crush zone so that complex crash structures can be simulated and potential failure in the back-up structure reliably identified.

As detailed in Ref. [60] the simulation method was able to represent failure modes observed in a wide range of dynamic crush tests with the L-strut absorber, which included different delamination effects and failure modes. In some tests, the structure collapsed after a certain crush displacement due to local ply drop-off and thickness reductions in the L-strut design. This effect was dependent on other design parameters, such as stiffness of the attached half-tube absorber. The simulations were able to predict observed failure modes for a range of design variants identified in the experiments. Fig. 13.28 compares a test sequence during an axial crush test with simulated deformation and failure of an L-strut absorber, together with a detailed comparison of measured and simulated load-displacement curves at the test machine cross-head load transducer. The test case shown is for a 4-ply 1 mm thick absorber element, with a 60 degrees trigger angle. The simulations predict well the failure sequence observed in which the L-strut buckles at the J-trigger, the load plate then crushes down the half-tube chamfer, before a steady crush of the half tube section with backing plate. There is also an acceptable agreement between measured and simulated load-displacement
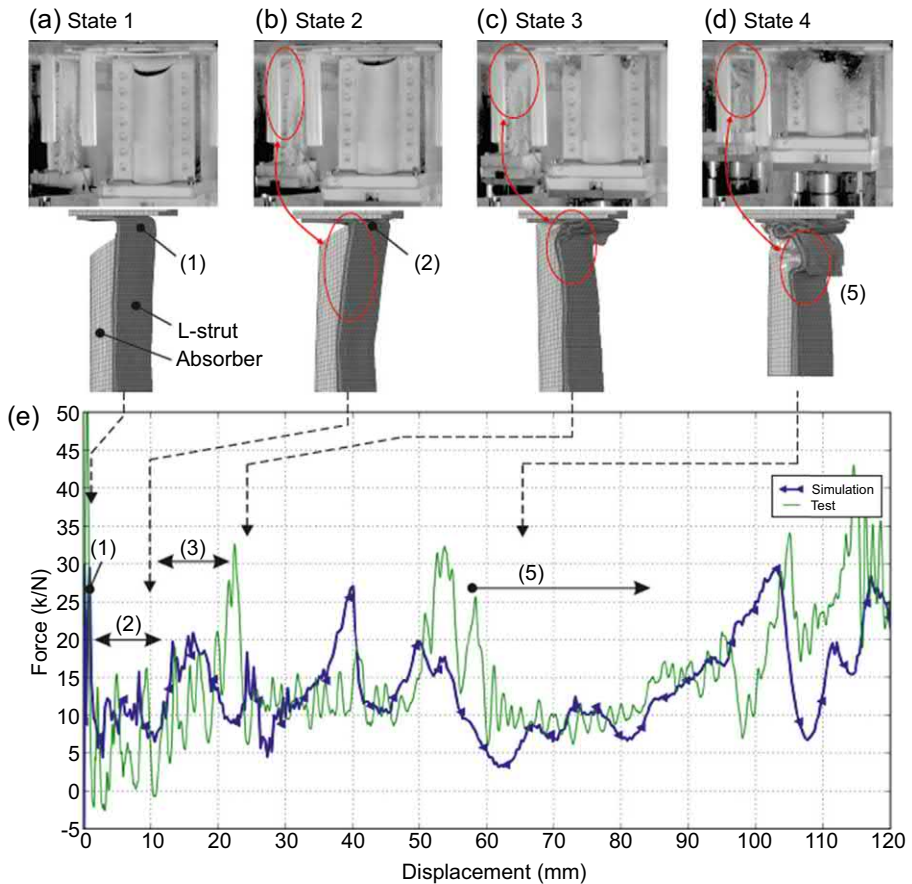
Figure 13.28 Validation of simulation results with crush sequence and force-displacement curves (1 mm CFRP layup, chamfer $\varphi = 60$ degrees) [60], with acknowledgements to Elsevier Ltd.

curves over a crush length of 120 mm. The study demonstrates the maturity of the mesoscale modeling approach with continuum shell elements and its application to absorber element design at structural levels.

Further developments with composite laminates using different mesoscale ply damage and delamination models are continuing in a research collaboration between the German Aerospace Center (DLR) and the University of British Columbia (UBC). The objective is to establish a robust simulation framework using different FE codes and damage models to support the effective design of crashworthy composite components using the building block approach with reduced reliance on experiments. In this work, the UBC sub-laminate continuum damage model CODAM2 [63], implemented as MAT_219 in LS-DYNA, is compared with a ply-based Ladevèze CDM model [46], implemented in Abaqus/Explicit by the DLR as the user VUMAT subroutine ABQ_DLR_UD [64]. Intraply damage and failure were studied under tension in

notched UD composite laminates such as center-notched and over-height compact tension (OCT) tests [65]. More recently, damage models for UD laminates under compression are being validated on compact compression (CC) tests as well as progressive crushing at different structural scales [66,67]. Here the UD intraply models are applied within the building block approach to predict progressive axial crushing and energy absorption in triggered flat plate laminates, C-sections and a lower lobe aircraft fuselage section. This work is contributed to the ongoing Crashworthiness Working Group (CWG) of the Composite Materials Handbook CMH-17 [8], to support standards and procedures for simulation to support certification of aircraft structures.

The composites damage and failure models discussed in the chapter have assumed rate-independent behavior, and materials properties used for validation studies are from quasi-static specimen tests. However, a test series on carbon fabric/epoxy segment specimens shown in Fig. 13.6 compares quasi-static crush behavior with dynamic crush tests at 2, 5 and 10 m/s. Mean dynamic steady crush force was about 26% lower and SEA 22% lower in the dynamic tests compared with quasi-static properties, which shows the importance of dynamic effects on crash behavior. This applies to crash structures seen in Fig. 13.16 and Table 13.2, where steady crush loads in dynamic crash tests on the frame structure at 8 m/s are about 10% below values measured in the quasi-static crush test, with similar reductions in SEA. Standard practice in the crash analysis of composite structures has been to neglect dynamic effects on composites properties. Reasons are the lack of international test standards for measuring rate-dependent composites properties and a lack of reliable materials test data. In particular for the influence of strain rate on interlaminar fracture toughness, as this behaviour can drive a change in failure mode.

Dynamic failure models for composites are not well understood, and only limited models are available in current commercial FE codes. Rate dependent properties of UD carbon/epoxy materials have been studied systematically in Refs. [68,69] using split Hopkinson bar impact tests for strain rates in the range $100-350$ s^{-1}, which are appropriate for crash analysis studies. Carbon fibers are highly elastic so that fiber tensile properties show low rate dependence. Epoxy matrix-dominated properties such as in-plane shear and both longitudinal and transverse compression properties show significant rate dependence. By adjusting composites properties to allow for rate dependence, with reduced shear failure strain, it was demonstrated in Ref. [70] that simulated segment crush failures at high rates in Fig. 13.6 had more brittle failure and increased fragmentation, which caused lower steady crush stresses. The influence of loading rate on simulation of structural crash response is being addressed in the current work of the CMH-17 CWG with some rate-dependent materials tests and dynamic crush tests on triggered plates and composite sections.

Polymer composites are sensitive to the environment such as temperature and moisture, which are known to influence stiffness, failure modes, and strength properties. For the design of crashworthy structures, which in aircraft operate over a wide range of environmental conditions, it is important to understand what influence environmental effects might have on crush failure modes and SEA. This was studied in Ref. [71] in quasi-static crush tests on carbon fabric/epoxy hat-shaped crush elements,

similar to the corrugated web profile seen in Fig. 13.9, with temperatures in the range -35 to $70°C$ for dry specimens and those conditioned at 50% and 95% relative humidity (RH). An important conclusion was that both hot/wet and cold/dry conditions reduce the quasi-static crush performance and SEA of carbon/epoxy specimens compared with tests at ambient temperature. This was due to a more brittle failure mode at low temperatures causing fragmentation (similar to the influence of high rates), while high temperatures lowered carbon/epoxy stiffness and strength properties. Further studies are needed to characterize the environment on polymer composite properties and provide data for damage and failure models under development for impact and crash analysis of structures. There is a potential for high fidelity multiphysics simulations to develop the required inputs as a function of temperature, moisture, loading rate etc. To include resin behaviour, these simulations could include analysis of RVE micromodels with the aim of providing inputs at the macro-scale.

13.6   Concluding remarks

This chapter has discussed recent progress on design, FE analysis, and test of composite materials and structures under crash loads and their use in the development of crashworthy composite aircraft structures. Aircraft crash requirements and crashworthy design concepts for composite aircraft structures were reviewed, and the "building block" approach to design and certification of composite structures was presented. This is based on test/simulation pyramids with structures of different levels of complexity, from materials test specimens, through structural elements of increasing complexity up to large structural assemblies and full aircraft structures. For reducing the number of expensive crash tests at each level, crash analysis methods are developed and validated by crash tests on smaller structures at lower levels of the test pyramid before being applied to the design of large crashworthy structures—thus reducing the number of large-scale crash tests required for certification. Because of the complex failure modes observed in crash tests on composite structural elements, a key aspect of this design strategy is to develop reliable computational methods for prediction of crash and impact damage in composite materials. The methods discussed in the chapter are based mainly on explicit FE codes with mesoscale composites models for ply damage, together with delamination failure models as cohesive interfaces between plies or laminated shell elements. The cohesive interface fractures and plies separate when the interface energy dissipated reaches the mixed-mode delamination failure energy criteria.

The chapter then focused on the application of this building block approach to design, manufacture, and crash testing of a composite helicopter frame structure. Improved methods for the design of energy-absorbing structures from composite materials were developed and validated first on idealized structural elements such as half-tube segments under axial crush loads, then used for the development of an energy-absorbing web section. The analysis methods were based on the explicit FE software PAM-CRASH^{TM} [50], with mesoscale damage and delamination models. Additional FE code features, such as link elements to simulate riveted fasteners, and

adhesive interface models are required, as structural complexity increases. For crash elements, novel numerical triggers were developed to initiate and propagate a numerically stable crush failure mode. This work was then applied to the design of a demonstrator energy-absorbing structure in carbon fabric/epoxy, suitable for integration into a helicopter fuselage subfloor as part of the crash management system. Final validation of the design concept and FE simulation tools was achieved through the manufacture of test articles for the frame section. Quasi-static and dynamic crash tests were carried out, and the results compared with predictions from FE simulation. Comparisons of the failure modes, peak force, steady-state crush force, SEA, and crush distance showed good agreement between the test and analysis.

These same concepts were then used in the design of a crashworthy composite transverse floor beam which was retrofitted into the airframe of a metallic CH-46E helicopter and crash tested in the NASA TRACT program [55]. Although the crashworthiness of the concept structure had been established under vertical crash test conditions on a rigid surface, it was not possible to trigger the EA crush behavior in the full-scale airframe crash test on soft soil. This test highlighted the challenge to scale up the design of crashworthy concept structures from laboratory tests in order to function successfully under real aircraft crash conditions. Design and test of EA subfloor structures is just the start, as global crash mechanics will determine what failure modes are initiated in aircraft and influence EA and crash safety as seen in the TRACT test program.

The chapter demonstrated that the building block approach can be used to design composite energy-absorbing structures at the lower levels of the test pyramid, Fig. 13.3. Computational methods support the process by predicting performance, reducing reliance on testing, and help to optimize the design of crashworthy composite structures. At the highest levels of the test pyramid, large scale crash tests on complete aircraft or fuselage sections are required for certification, since computational methods to simulate full-scale aircraft crash response are at an early stage in their development. Once "virtual" crash testing tools are available to support full-scale aircraft crash tests, it will allow a full range of crash scenarios to be investigated with a reduction in development and certification costs for next-generation aircraft structures.

Although considerable progress has been made in the last decade, it should nevertheless be pointed out that it will take many years for composites modeling in dynamic FE codes to reach the same level as that currently achieved in the crash and impact analysis of metallic structures. The reasons are historical. Metal plasticity was understood, and established mathematical models date from the middle of the 20th century. Furthermore, the automotive industry was the "driver" for the development of complete vehicle FE models in crash codes, so that considerable resources have been invested in modeling, development of test methods, code implementations, validations, etc. for metal structures. Similar resources are only now being made available for composites materials and structures. In addition, the diversity of composite materials, the complex anisotropic failure behavior, the lack of standardized materials and dynamic test procedures and the smaller more specialist market for composites, all contribute to delay in establishing good, reliable composites models in FE crash codes suitable for direct application to the design of crashworthy aircraft structures.

Problems being addressed in current research programs include introducing temperature-and-rate-dependent effects into the composites materials models. Test data presented in the chapter showed that crash EA was generally reduced at higher loading rates. The more brittle behavior of polymer composites at higher rates plays a role, but other factors such as friction in the debris wedge at crush fronts or the observed temperature increase at the crush front are also important. Temperature, moisture content, and strain rates are known to modify composite properties and can influence the failure mode and the energy absorbed. This highlights the need for better experimental techniques, such as optical techniques for full-field characterization of local failure behavior, to determine critical material parameters used to support improved damage models and code developments.

Since fine-scale detailed damage models are mainly required in zones of failure at the crush front or at critical joints and boundaries, much coarser global models are required for undamaged parts of the structure and for modeling crash kinematics. Future work is required to develop and improve multiscale computational strategies and code coupling techniques linking fine-scale FE models with global structural models for the prediction of crash and impact damage in large aircraft structures. An important research activity for certification of crashworthy structures is to develop efficient stochastic analysis methods for use with explicit FE codes. Since crash events are stochastic in nature, through the variability of structural mass, crash velocity, impact position and impact angle, crash surface, etc., a single crash simulation with one set of conditions is not sufficient for certification procedures. Introducing materials variability and manufacturing defects in stochastic analyses would allow localized reductions in strength to be included. In this case, a certification strategy based on stochastic analysis with variation in crash conditions and material variability would allow failure envelopes to be determined for specific crash scenarios. Then it may be possible to assess crashworthiness under realistic multiaxial crash conditions to establish structural integrity for the worst case rather than for a single crash scenario. The increased computational costs are necessary to give confidence in the analysis methods with the goal of certification by simulation.

Acknowledgments

References

[1] S.P. Desjardins, R.E. Zimmermann, A.O. Bolukbasi, N.A. Merritt, ACSDG Aircraft Crash Survival Design Guide, vol. I−IV. USAAVSCOM TR 89-D-22A-E.

[2] MIL-STD-1290A (AV), Military standard for light fixed and rotary-wing aircraft crash resistance, Department of Defense, Washington, DC.

[3] FAA 14 CFR airworthiness standards: part 23 normal, utility, acrobatic and commuter category airplanes, part 25 transport category airplanes, part 27 normal category rotorcraft, part 29 transport category rotorcraft, Federal Aviation Administration. www.airweb.faa. gov.

[4] EASA certification specifications: CS 23 normal, utility, aerobatic and commuter aeroplanes, CS 25 large aeroplanes, CS 27 small rotorcraft, CS 29 large rotorcraft, European Aviation Safety Agency. www.easa.europa.eu.

[5] C. Bisagni, G. Dipietro, L. Fraschini, D. Terletti, Progressive crushing of fibre-reinforced composite structural components of a formula one racing car, Compos. Struct. 68 (2005) 491−503.

[6] AC20-107B, Advisory circular on composite aircraft structure, Federal Aviation Administration.

[7] D. Hachenberg, The role of advanced numerical methods in the design and certification of future composite aircraft structures, in: World Congress on Computational Mechanics, WCCM V, Vienna.

[8] CMH-17, Rev. G, vol. 3, Ch. 14 Crashworthiness and energy absorption, in: Proceedings of the Crashworthiness Working Group, ASTM International, West Conshohocken, PA, USA.

[9] P. Feraboli, Development of a corrugated test specimen for composite materials Energy absorption, J. Compos. Mater. 42 (2008) 229−256.

[10] B. Wade, F. Deleo, P. Feraboli, A. Byar, M. Rucki, M. Rassaian, Toward the development of a standard for characterizing the energy absorption of composite materials, in: ICCM17, 17th Int. Conf. Compos. Mater., Paper F11-1, Edinburgh, UK, 2007.

[11] C.M. Kindervater, D. Kohlgrüber, A.F. Johnson, Composite vehicle structural crashworthiness − a status of design methodology and numerical simulation techniques, Int. J. Crashworthiness 4 (1999) 213−230.

[12] K.E. Jackson, R.L. Boitnott, E.L. Fasanella, L.E. Jones, K.H. Lyle, A history of full-scale aircraft and rotorcraft crash testing and simulation at NASA Langley research center, in: 4th Triennial. Int. Fire & Cabin Safety Res. Conf., November 15−18, 2004, Lisbon, Portugal, 2004.

[13] K.E. Jackson, Y.T. Fuchs, S. Kellas, Overview of the NASA subsonic rotary wing aeronautics research program in rotorcraft crashworthiness, J. Aerosp. Eng. 22 (3) (2009) 229−239.

[14] SC 25-07-05-SC, Special conditions: Boeing model 787-8 airplane; crashworthiness, U. S Fed Regist (June 2007) 72 (111). Docket No. NM368, Federal Aviation Administration.

[15] A. Abramowitz, T.G. Smith, T. Vu, J. Zvanya, Vertical Drop Test of an ATR 42-300 Airplane. FAA Document DOT/FAA/AR-05/56, March 2006.

[16] ADS 36, Aeronautical design standard 36: Rotary-Wing crash resistance, US Army.

[17] F. Le Page, R. Carciente, A320 Fuselage Section Vertical Drop Test, Part 2: Test Results; CEAT Report N° S95 5776/2, EU Research project, Crashworthiness for Commercial Aircraft, 1995.

[18] M. Waimer, D. Kohlgrüber, D. Hachenberg, H. Voggenreiter, The kinematics model − a numerical method for the development of a crashworthy composite fuselage design of transport aircraft, in: 6th Trien. Int. Aircraft Fire & Cabin Safety Res. Conf., Atlantic City, NJ, USA.

[19] S. Heimbs, F. Strobl, P. Middendorf, Integration of a composite crash absorber in aircraft fuselage vertical struts, Int. J. Veh. Struct. Syst. 3 (2011) 87−95.

[20] K.E. Jackson, A comparative analysis of three composite fuselage concepts for crash performance, in: Proc. Amer. Helicopter Soc, 52nd Annual Forum, Washington DC, USA.

[21] A.F. Johnson, C.M. Kindervater, K.E. Jackson, Multifunctional design concepts for energy absorbing composite fuselage sub-structures, in: Proc. Amer, Helicopter Soc., 53rd Annual Forum, Virginia Beach, VA, USA.

[22] CRASURV, Commercial aircraft − design for crash survivability, EU FP4 RTD Project IMT AREA 3 (3A5.6).

[23] J.F.M. Wiggenraad, A.L.P.J. Michielsen, D. Santoro, F. Lepage, C.M. Kindervater, F. Beltran, Development of a Crashworthy Composite Fuselage Structure for a Commuter Aircraft, NLR-TP-99532, National Aerospace Laboratory, Amsterdam.

[24] S. Kellas, K.E. Jackson, Deployable system for crash-load attenuation, in: Proc. Amer. Helicopter Soc., 63rd Annual Forum, Virginia Beach, VA, USA.

[25] S. Kellas, K.E. Jackson, Multi-terrain vertical drop tests of a composite fuselage section, J. Am. Helicopter Soc. 55 (4) (2010), 042002−1 to 042002−7.

[26] A.F. Johnson, C.M. Kindervater, H.G.S.J. Thuis, J.F.M. Wiggenraad, Crash resistant composite subfloor structures for helicopters, in: AGARD FVP Symposium: Advances in Rotorcraft Technology, Ottawa.

[27] D. Kohlgrüber, A. Kamoulakos, Validation of numerical simulation of composite helicopter sub-floor structures under crash loading, in: Proc. Amer. Helicopter Soc., 54th Annual Forum, Washington, DC, USA, pp. 340−349.

[28] A.F. Johnson, D. Kohlgrüber, Design and performance of energy absorbing subfloor structures in aerospace applications, in: IMechE Seminar S672, 'Materials and Structures for Energy Absorption', Inst. of Mech. Engrs, London.

[29] M.W. Joosten, S. Dutton, D.W. Kelly, R.S. Thomson, A.F. Johnson, Developing crashworthy composite helicopter structures: a building block approach, in: 14th Austral. Int. Aerosp. Congr. (AIAC 14), Melbourne, Australia.

[30] M. Joosten, M. David, C. Kindervater, R.S. Thomson, Improved design methods for crashworthy composite helicopter structures, in: ICAS 2012, 28th Int, Congress Aeronautical Sciences, Brisbane, Australia, 2012.

[31] C. Kindervater, R.S. Thomson, A.F. Johnson, M. David, M. Joosten, Z. Mikulik, et al., Validation of crashworthiness simulation and design methods by testing of a scaled composite helicopter frame section, in: Proc. Amer. Helicopter Soc., 67th Annual Forum, Virginia Beach, VA, USA.

[32] A.H. Fairfull, D. Hull, Effects of specimen dimensions on the specific energy absorption of fibre composite tubes, in: ICCM6 6th Int. Conf. Compos. Mater., London, pp. 3.36−3.45.

[33] G.L. Farley, R.M. Jones, Crushing characteristics of continuous fibre-reinforced composite tubes, J. Compos. Mater. 26 (1992) 37−50.

[34] H. Hamada, S. Ramakrishna, H. Satoh, Crushing mechanism of carbon fibre/PEEK composite tubes, Composites 26 (1995) 749−755.

[35] D. Hull, A unified approach to progressive crushing of fibre-reinforced composite tubes, Compos. Sci. Technol. 40 (1991) 377−421.

[36] C.M. Kindervater, H. Georgi, Composite strength and energy absorption as an aspect of structural crash resistance, in: N. Jones, T. Wierzbicki (Eds.), Structural Crashworthiness and Failure, Elsevier, London.

[37] A.G. Mamalis, D.E. Manolakos, G.A. Demosthenous, M.B. Ioannidis, Analysis of failure mechanisms observed in axial collapse of thin-walled circular fibreglass composite tubes, Thin-Walled Struct. 24 (1996) 335−352.

[38] A.G. Mamalis, D.E. Manolakos, G.A. Demosthenous, M.B. Ioannidis, The static and dynamic axial crumbling of thin-walled fibreglass composite square tubes, Compos. B 28 (1997) 439−451.

[39] M. David, A.F. Johnson, H. Voggenreiter, Analysis of crushing response of composite crashworthy structures, Appl. Compos. Mater. 20 (2013) 773−787.

[40] A.F. Johnson, M. David, Failure mechanisms in energy-absorbing composite structures, Philos. Mag. 90 (31/32) (2010) 4245−4261.

[41] A. Jackson, S. Dutton, A.J. Gunnion, D. Kelly, Effect of manufacture and laminate design on energy absorption of open carbon fibre/epoxy sections, in: ICCM17, 17th Int. Conf. Compos. Mater. Paper F11-2, Edinburgh, UK.

[42] P. Feraboli, B. Wade, F. Deleo, M. Rassaian, Crush energy absorption of composite channel section specimens, Compos. A 40 (2009) 1248−1256.

[43] A. Jackson, M. David, A.J. Gunnion, D.W. Kelly, S. Dutton, Dynamic and quasi-static crush testing of closed carbon-fibre/epoxy elements, in: ICAS 2010, 27th Int. Congress Aeronautical Sciences, Nice, France.

[44] M.W. Joosten, S. Dutton, D.W. Kelly, R.S. Thomson, Experimental and numerical investigation of the crushing response of an open section composite energy absorbing element, Compos. Struct. 93 (2010) 682−689.

[45] M.W. Joosten, S. Dutton, D. Kelly, R.S. Thomson, Experimental evaluation of the crush energy absorption of triggered composite sandwich panels under quasi-static edgewise compressive loading, Compos. A 41 (2010) 1099−1106.

[46] P. Ladeveze, E. Le Dantec, Damage modelling of the elementary ply for laminated composites, Compos. Sci. Technol. 43 (1992) 257−267.

[47] A.F. Johnson, A.K. Pickett, P. Rozycki, Computational methods for predicting impact damage in composite structures, Compos. Sci. Technol. 61 (2001) 2183−2192.

[48] A.F. Johnson, Modelling impact damage in composite structural elements, in: P. Beaumont, C. Soutis (Eds.), Multiscale Modelling of Composite Materials and Systems, Woodhead, Cambridge, pp. 401−429.

[49] L. Greve, A.K. Pickett, Delamination testing and modelling for composite crash simulation, Compos. Sci. Technol. 66 (2006) 816−826.

[50] PAM-CRASH™ FE Code, Engineering Systems International, Rungis Cedex, France.

[51] A.F. Johnson, M. David, Failure mechanisms and energy absorption in composite elements under axial crush, Key Eng. Mater. (2012) 488−489.

[52] M.W. Joosten, S. Dutton, D.W. Kelly, R.S. Thomson, Evaluation of a predictive stacked-shell analysis methodology for the analysis of energy absorbing composite crush elements, in: 14th Eur. Conf. Compos. Mater. (ECCM14), Budapest, Hungary.

[53] M.A. McCarthy, J.R. Xiao, C.T. McCarthy, A. Kamoulakos, J. Ramos, J.P. Gallard, et al., Modelling of bird strike on an aircraft wing leading edge made from fibre metal laminates − part 2: modelling of impact with SPH bird model, Appl. Compos. Mater. 11 (2004) 317−340.

[54] G. Pearce, D. Kelly, A.F. Johnson, R.S. Thomson, Influence of dynamic loading on fastened composite joints, in: P. Camanho, L. Tong (Eds.), Composite Joints and Connections, Woodhead, Cambridge, 2011, pp. 257−294.

[55] M.S. Annett, J.D. Little, Evaluation of the second transport rotorcraft airframe crash testbed (TRACT 2) full scale crash test, in: Proc. 71st AHS International Forum, Virginia Beach, VA, 2015.

[56] J.D. Littell, K.E. Jackson, M.S. Annett, E. Fasanella, M. Seal, The development of two composite energy absorbers for use in a transport rotorcraft airframe crash testbed (TRACT 2) full-scale crash test, in: Proc. 71st AHS International Forum, Virginia Beach, VA, 2015.

[57] A. Chhor, M. David, L. Mulcahy, M. Vuong, R. Thomson, Design of a Retrofit Energy Absorbing Sub-floor for a Helicopter, CRC-ACS TR 14051, Cooperative Research Centre for Advanced Composite Structures Ltd, Melbourne, Australia, 2014.

[58] K.E. Jackson, E.L. Fasanella, Design Testing and Simulation of Crashworthy Composite Airframe Structures at NASA Langley Research Center, Ch 8.15, Comprehensive Composite Materials II, vol. 8, Elsevier, 2018.

[59] L. Mulcahy, B. Cartright, A. Chhor, R. Thomson, Simulation of a Helicopter Crash Test, CRC-ACS TR 15052, Cooperative Research Centre for Advanced Composite Structures Ltd, Melbourne, Australia, 2015.

[60] M. Waimer, M.H. Siemann, T. Feser, Simulation of CFRP components subjected to dynamic crash loads, Int. J. Impact Eng. 101 (2017) 115−131.

[61] Dassault Systemes Simulia Corp., VUMAT for Fabric reinforced composites, Abaqus support document, QA Article: QA00000008519.

[62] A. Turon, C.G. Davila, P.P. Camanho, J. Costa, An engineering solution for mesh size effects in the simulation of delamination using cohesive zone models, Eng. Fract. Mech. 74 (2007) 1665−1682.

[63] A. Forghani, N. Zobeiry, A. Poursartip, R. Vaziri, A structural modelling framework forprediction of damage development and failure of composite laminates, J. Compos. Mater. 47 (20−21) (2013) 2553−2573. https://doi.org/10.1177/0021998312474044.

[64] D. Schueler, N. Toso-Pentecôte, H. Voggenreiter, Simulation of high velocity impact on composite structures − model implementation and validation, Appl. Compos. Mater. 23 (4) (2016) 857−878. https://doi.org/10.1007/s10443-016-9489-0.

[65] J. Reiner, T. Feser, D. Schueler, M. Waimer, R. Vaziri, Comparison of two progressive damage models for studying the notched behaviour of composite laminates under tension, Compos. Struct. 207 (2019) 385−396.

[66] N. Zobeiry, R. Vaziri, A. Poursartip, Characterization of strain-softening behaviour and failure mechanisms of composites under tension and compression, Compos. A 68 (2015) 29−41.

[67] T. Feser, M. Waimer, N. Schueler Toso-Pentecôte, J. Reiner, N. Zobeiry, S. Abouali, R. Vaziri, Simulation of dynamic crushing of composite structures using two intra-Laminar damage models implemented in LS-DYNA and ABAQUS/explicit, in: Aerospace Structural Impact and Dynamics International Conference (ASIDIC), 17−19 October 2017, Wichita, USA, 2017.

[68] H. Koerber, P.P. Camanho, High strain rate characterisation of unidirectional carbon− epoxy IM7-8552 in longitudinal compression, Compos. A (2011). https://doi.org/10.1016/j.compositesa.2011.01.002.

[69] H. Koerber, X. Xavier, P.P. Camanho, High strain rate characterisation of unidirectional carbon-epoxy IM7-8552 in transverse compression and in-plane shear using digital image correlation, Mech. Mater. 42 (2010) 1004−1019.

[70] M. David, A.F. Johnson, Effect of strain rate on the failure mechanisms and energy absorption in polymer composite elements under axial loading, Compos. Struct. 122 (2015) 430−439.

[71] M.W. Joosten, C. Hirth, R. Thomson, H. Koerber, Effect of environmental conditions on the failure mechanisms and energy absorption of open-section crush elements under quasi-static loading, Compos. Struct. 209 (2019) 747−753.

The blast response of composite and fiber-metal laminate materials

14

G.S. Langdon [1], W.J. Cantwell [2]
[1]Blast and Impact Survivability Research Unit, Department of Mechanical Engineering, University of Cape Town, Rondebosch, Western Cape, South Africa; [2]Department of Aerospace Engineering, Khalifa University of Science and Technology (KUST), Abu Dhabi, United Arab Emirates

14.1 Introduction

Due to the rise in subversive activity, the need to protect people, equipment, and structures from explosions has greatly increased. In 2016, terrorist attacks caused the deaths of at least 25,673 people [1]. Bombings and explosions comprised 54% of these attacks. When ranking the 50 worst terrorist attacks in 2016 by the number of deaths, bombings/explosions accounted for 44% of the worst attacks [1]. Accidental explosions, such as the tragic events in Chinese industrial parks [2,3], Russian apartment blocks [4], and in an Indian power plant [5], are of grave concern and receive a lot of attention in the press. Even small explosions can result in severe injury or death, such as the "exploding electronic cigarette" incidents noted in the United States [6].

The effects of explosions are often disastrous, particularly in confined spaces, such as onboard an aircraft. Accidental explosions have also occurred, such as explosions in the engine [7] and the fuel tanks [8]. These are tragic events that often cause fatalities. Fortunately, there have been very few explosions in aircraft. In addition to accidental explosions, the potential terrorist threat has been high in the public conscientiousness since the devastating 9/11 attacks in the US.

Composite materials offer the potential for superior strength and stiffness properties, as their properties can be tailored to match the load and deflection orientations at the design stage. Due to mass limitations, composite materials are finding increasing use in the design and manufacture of primary structures in the aircraft industry. Composite materials are currently being used in the manufacture of a range of primary load-bearing structures in the aerospace industry, with examples, including the fuselage sections of the A350 XWB and the Boeing 787 aircraft. Given the possibility of explosions occurring within such structures, there is a clear need to understand the response of laminated composite materials to conditions associated with blast loading. However, despite this distinct need, an examination of the literature indicates that there are relatively few investigations in this area [9].

In this chapter, the characteristics of air explosions are briefly described, and various blast protection paradigms are discussed. The blast behavior of plain composites and multilayered structures are then discussed. Plain composites typically comprise polymeric resins with fiber reinforcement, such as carbon fiber-reinforced epoxy resins. Multilayered systems include composite sandwich structures and hybrid composite-metal structures, known as fiber-metal laminates.

14.2   Characteristics of explosions in the air

An explosion is defined as a rapid release of energy in a fleeting period of time [10]. The cause of the explosion may be mechanical, chemical, or nuclear. Nuclear explosions are of little relevance to research on aircraft safety, but the former two explosion sources are relevant. For example, a mechanical cause of explosions is the rupture of a pressure vessel [10,11], such as the rapid depressurization of an aircraft [12] that has suffered a breach in its structural integrity. Chemical explosions can have many causes, such as vapor cloud explosions and the detonation of explosives. The former are usually accidental and can be prevented on aircraft through careful design of the fuel systems. The latter are the result of deliberate terrorist activity. Considerable effort is being spent on preventing explosives from entering an aircraft by employing improved chemical detection systems, better screening of potential terrorists, and more vigilant airport security. Although this is to be commended, it is still necessary to understand the effects of explosions on the structural materials used in the aircraft industry.

An explosive detonation in the air is followed by a shock wave that rapidly compresses the surrounding air, creating high pressure, short-duration blast wave, which, in turn, can have destructive effects on objects in its path. The pressure magnitude and duration of the blast wave initially depend upon the source of the explosion, but are also influenced by the propagation media, distance traveled, degree of confinement (creating reflections, causing quasi-static pressure accumulation, and preventing dissipation of the explosive energy) and proximity to the ground. The distance between the explosion source and the object of interest (the target) is known as the standoff distance. Increasing the standoff distance causes the pressure magnitude to decrease and the blast duration to increase. A short standoff distance blast is referred to as a near field explosion, and it is extremely difficult to approximate the complex pressure profiles using simple closed forms.

As the standoff distance increases, the explosion is termed as a far-field explosion. If the explosion is unconfined, these are lower pressure, longer duration blasts with a characteristic shape, as shown in Fig. 14.1 [10,13]. The properties of the pressure profile can be determined by using Hopkinson-Cranz scaling laws, where pressure and duration are expressed as variables of the Hopkinson scaled distance Z, given in Eq. (14.1).

$$Z = \frac{R}{W^{1/3}} \tag{14.1}$$

Where R = standoff distance (m), W = TNT equivalent charge mass (in kg)
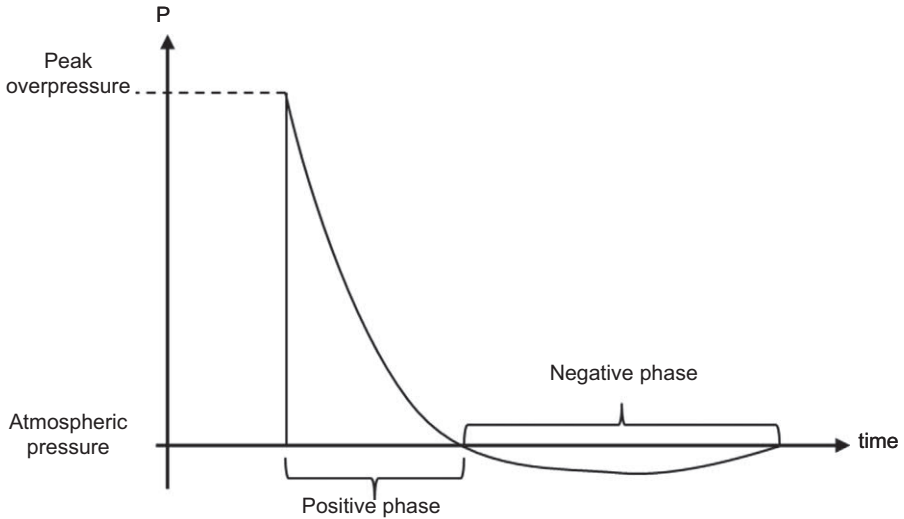
Figure 14.1 Schematic showing a typical pressure profile for far-field unconfined air-blast loading.

It is evident from Fig. 14.1 that an unconfined far-field explosion is characterized by a rapid rise in pressure, up to the peak overpressure and a gradually decaying slope. The phase of the loading that has a pressure greater than atmospheric is referred to as the positive phase (as shown in Fig. 14.1). The subsequent negative (suction) phase is usually longer in duration and is often neglected. However, for glazed structures, the negative phase cannot be neglected. Many expressions have been proposed to describe the relationship between peak overpressure, specific impulse, duration, and Z. Two of the more common expressions are given in Eqs. (14.2) and (14.3) for side-on pressure [10].

$$p_s = \frac{6.7}{Z^3} + 1 \; bar \; (p_s > 10 \; bar)$$

$$p_s = \frac{0.975}{Z} + \frac{1.455}{Z^2} + \frac{5.85}{Z^3} - 0.019 \; bar \; (0.1 \le p_s < 10 \; bar) \qquad (14.2)$$

$$p_s = \frac{14.072}{Z} + \frac{5.540}{Z^2} - \frac{0.357}{Z^3} + \frac{0.00625}{Z^4} \; bar \; (0.05 \le Z < 0.3)$$

$$p_s = \frac{6.194}{Z} - \frac{0.326}{Z^2} + \frac{2.132}{Z^3} \; bar \; (0.3 \le Z < 1)$$

$$p_s = \frac{0.662}{Z} + \frac{4.05}{Z^2} + \frac{3.288}{Z^3} \; bar \; (1 \le Z < 10) \qquad (14.3)$$

Since explosions usually occur outdoors, there are possible environmental effects that should be accounted for, such as atmospheric pressure. Sachs scaling law [10] accounts for some of these effects, but a full discussion of this is beyond the scope of this chapter.

Explosion characteristics in an aircraft cannot be determined using simplified empirical forms, such as those given in Eqs. (14.2) and (14.3). Various explosion scenarios (including analysis of, for example, different charge locations onboard an aircraft, and the effect of altitude on cabin pressure) should be modeled using hydrodynamic models. Examples of explosion modeling using commercially available codes, such as Autodyn and more recently, LS Dyna, are given in Refs. [14–16] respectively. An explosion onboard an aircraft is clearly a confined explosion, with the effect that the energy and the pressure involved are considerably higher than those for an unconfined blast [17–19]. The spatial and temporal blast loading characteristics are highly variable—depending upon (among other things) the location of the explosion, the aircraft geometry, and the propagation media (for example, was the explosion in free air, in a partially filled luggage container, or perhaps inside a recently filled fuel tank?). Altitude may be a factor in mechanical explosions. Rapid depressurization of the aircraft can only occur during flight when a pressure mismatch between the internal and external skins of the aircraft develops at high altitude, whereas chemical explosions could occur either on the ground or in the air.

14.3   Paradigms of blast protection

Approaches to blast protection can be categorized as active (deployed upon detection of an explosion) or passive (always present). An example of an active mitigation system is the water deluge system used on offshore oil and gas platforms [20]. Upon detection of a gas leak, the entire area is showered with carefully sized water droplets to prevent ignition and remove the energy from a vapor cloud explosion. An active system can only work if the imminent explosion can be detected and a suitable system deployed in time. These systems work offshore because the gas leak, which accumulates relatively slowly, can be detected easily and the water system deployed. Several researchers have worked on the detection and deployment of mitigation devices for explosive detonations with military applications [21,22]. Such systems have yet to be deployed in the military, and (at the time of writing) no such detection systems are available for the case of explosive detonation onboard an aircraft. For such a system to be viable, it would need to be robust and inexpensive to install and operate.

Passive mitigation systems are, therefore, the only viable option for the aircraft industry to consider at present. These can be divided into four blast protection paradigms:

1. Sacrificial systems—these absorb energy and prevent the load from transferring to the structure that is being protected. The use of cellular metals as cladding materials has been investigated [23,24] with possible application to the hull of a mine-resistant vehicle. However, such systems require a (heavy) protective faceplate and need a thick core to be effective.

Hence, this type of system is impractical for blast protection onboard aircraft, where weight and volume are critical.

2. Impedance mismatch: it is theoretically possible to pair up materials having different impedances to prevent stress wave transmission to the structure to be protected. No practical systems employing this principle exist.

3. Interfering with the blast wave transmission: it is possible to place obstacles into the path of the blast wave, which could either deflect the wave or throttle the flow. The V-shaped hull on a landmine protected vehicle employs this principle [25], deflecting the blast impulse sideways, and thereby, preventing the vehicle from gaining significant vertical momentum (that is, reducing ground lift). Other examples of this include filters [26], barriers [27], and perforated plates [28], which restrict the blast wave propagation resulting in a lower pressure impinging upon the primary structure. While such systems might be useful for protection of ventilation shafts and tunnels from explosion effects, they would not be effective onboard an aircraft.

4. Containment: in this case, the explosion is contained within an area which must not rupture. Blast walls [29] on offshore platforms operate on this principle, separating out parts of the platform and protecting personnel behind the barrier. This is the most relevant paradigm for aircraft protection, with unit load devices being an ideal example. A likely location of an explosive detonation is within a suitcase stored in a unit load device (an aircraft luggage container). If the unit load device (ULD) could contain the explosion, then the aircraft would sustain minimal damage, if any, and would still be able to land safely. It is important that the materials used to construct a containment system for aircraft must be strong, ductile, and have high rupture strains (in addition to being lightweight).

14.4 Explosion loading of fuselage structures

It is evident from the above discussion on explosions in free air and the effect of confinement that it is necessary to understand the potential loading scenarios that may develop onboard an aircraft due to an explosion. There is also a need to prioritize which blast loading scenarios an aircraft may be vulnerable to, from both a structural and a security perspective. Which areas of an aircraft may be vulnerable to the smuggling of explosives on board? Which areas are structurally vulnerable and require additional protection?

Composites and multilayered materials are highly sensitive to the spatial distribution of the loading, and if the design is to account properly for explosion scenarios onboard a future aircraft the potential loading threats must be known beforehand (or can be reliably estimated). There has been some recent work by Kotzakolios et al. [15] on finite element modeling of the response of FML fuselage structures to blast loading using LS Dyna. Fuselage structures comprising either aluminum alloy or GLARE 3, with geometry typical of the Airbus A320 aircraft design, were analyzed. Four explosion scenarios were examined—100 g spheres of C4 plastic explosive were positioned at different locations in the fuselage to determine the vulnerability of the aircraft for each scenario [15]. No justification or risk analyses for the chosen locations were provided. Interestingly, the two materials exhibit the most severe damage under different

loading cases. Unfortunately, no experimental results were reported for the validation of the modeling.

It is understandable that little work of this nature has been published in the open literature for individualized aircraft, but it would be helpful to researchers if some more generalized information were available. This would enable researchers to perform experimentally relevant work and to concentrate their modeling efforts in the correct direction.

14.5   The blast performance of plain composites

An important step toward understanding the blast response of composite materials involves characterizing the failure and fracture processes that result from the air-blast loading. A number of workers have investigated the failure mechanisms in blast-loaded composite materials [30−34]. Franz et al. [30] conducted tests on single and multiple panel E-glass chopped strand mat/polyester structures. They observed three distinct failure modes, matrix cracking, delamination, and penetration, and found that the resistance to delamination/debonding decreases with increasing areal density and thickness of the laminates. They proposed that the damage resistance of a layered structure could be enhanced by using a graded structure, in which the front surface layers were based on laminates exhibiting high energy absorption and damping characteristics, while the rear layers should offer higher flexural rigidity for sufficient mechanical support and structural stiffness [30]. Comtois et al. [31] used PE4 explosive in a blast chamber to load 2 mm thick quasi-isotropic glass and carbon fiber-reinforced epoxy laminates. The explosive mass was varied from 0.5 to 1.0 g and the standoff distance from 54 to 500 mm. Damage in the form of delamination and fiber fracture tended to occur at the edges of the panel because of the constraints applied by the supports. The authors showed that the conditions under which the panels were supported had a significant effect on the development of damage within the laminates, with damage in adhesively bonded laminates being less than that in clamped structures [31]. They also noted that there was less fiber damage at the supports in the carbon fiber composites than in their glass fiber counterparts.

Yahya et al. [32−35] used a ballistic pendulum to conduct blast tests on a range of glass and carbon fiber-reinforced composites. The fracture processes in the panels were initially assessed by examining the proximal and distal surfaces of the panels following blast loading. Fig. 14.2 shows photographs of a number of 4.2 mm thick laminates subjected to impulses between 3.3 and 6.1 Ns. Following an impulse of 3.3 Ns, a small rear surface fiber crack, propagating across the 0 fibers, was apparent. Additionally, an array of fine cracks was in evidence on the loaded face, associated with local fiber buckling. The laminate subjected to an impulse of 3.7 Ns displayed front surface fiber buckling, rear surface fiber fracture as well as extensive shear fracture of the rear surface fibers along the perimeter of the unsupported area, Fig. 14.2(c) [35]. Rear surface fiber damage was considerable at impulses of 6 Ns and above, with extensive fiber fracture being in evidence across both fiber directions.

(a)

(b)

Fibre crack

(c)
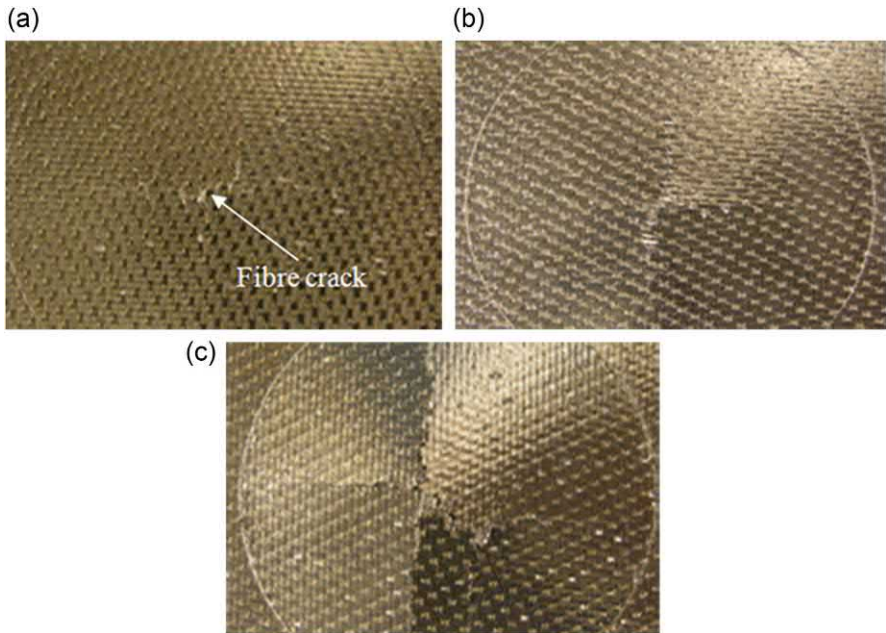
Figure 14.2 Rear surfaces of 4.2 mm thick carbon fiber reinforced PEI panels following air blast testing [35].

The test specimens shown in Fig. 14.2 were subsequently sectioned to highlight the failure processes within the test samples, Fig. 14.3 [35]. Damage in the panels subjected to the two lowest impulses took the form of fiber fracture in the rear surface plies and buckling failure of the top surface fibers. It is interesting to note that virtually no delamination was observed in these samples. An impulse of 5.0 Ns produced top surface fiber fracture, a small amount of delamination and fiber fracture in the lowermost plies. This damage resulted from the flexural response of the target during the blast event. Finally, at 6.1 Ns, fiber fracture has extended through the laminate thickness and a small area of delamination was evident close to the midplane of the sample [35]. The lack of delamination in these samples is surprising and is clearly related to the very high values of interlaminar fracture toughness reported in the previous section. It is possible that the very high values of interlaminar fracture energy associated with the current thermoplastic-matrix systems may reduce their energy-absorbing capacity under this form of extreme loading [33].

Similar failure mechanisms were observed in glass fiber-reinforced panels [33,35]. Fig. 14.4 shows cross-sections of 4.5 mm thick glass fiber-reinforced PEI composite subjected to impulses between 7.9 and 9.4 Ns. Here, delamination between the central plies and localized fiber fracture is in evidence following blast loading. It is evident that the difference between the impulse associated with the damage threshold and that to cause gross through-thickness damage is small. This is particularly evident when the length of fiber fracture is plotted against impulse, Fig. 14.5 [35]. Here,
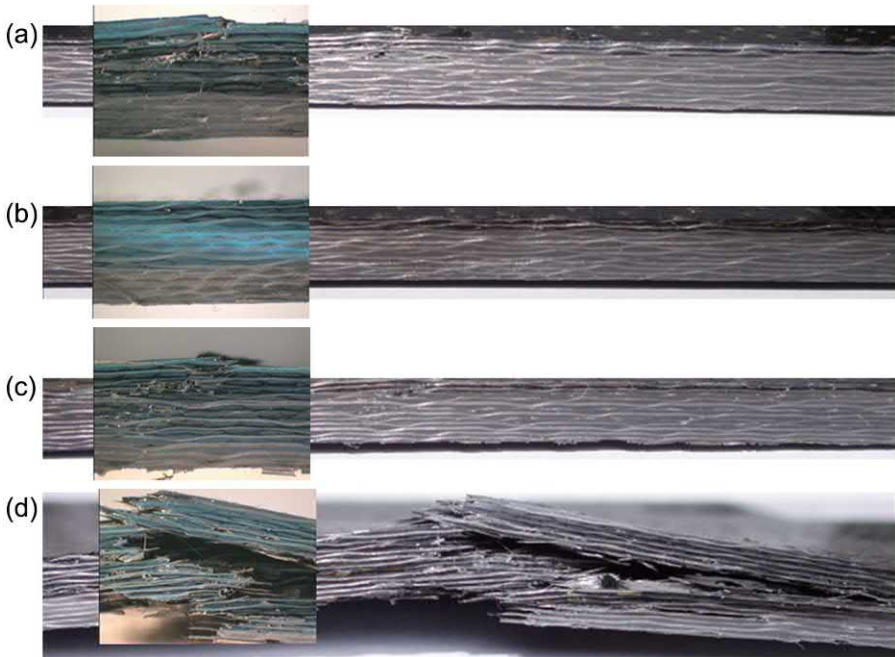
Figure 14.3 Cross-sections of 4.2 mm thick carbon fiber reinforced PEI panels following air blast testing [35]. (a) Impulse = 3.3 Ns. (b) Impulse = 3.7 Ns. (c) Impulse = 5.0Ns. (d) Impulse = 6.1 Ns.

Laminates A, B, and C refer to 2.2, 4.2, and 6.2 mm thick laminates, respectively, and Laminate F corresponds to a 4.5 mm thick GF/PEI plate. An examination of the figure indicates that fiber damage propagates extremely quickly once the threshold for the onset of such damage is exceeded. This observation agrees with the findings of Tekalur et al. [36], who found that carbon fiber-reinforced vinylester composites showed no signs of external damage prior to complete failure of the panel.

Fig. 14.6 shows the impulse required to cause complete through-thickness rupture of the laminates, around the clamped periphery of the panels, as a function of laminate thickness. The arrows in the figure signify that these laminates had not completely failed. For each of these laminates, the level of damage suggested that the failure threshold was close to the value indicated in Fig. 14.6 [30]. From the figure, the impulse to cause target failure increases with increasing plate thickness. Included in Fig. 14.6 (crosses) are the impulses required to initiate rear surface fiber damage in the panels. The figure indicates this threshold impulse is very close to that required to trigger a complete failure of the panel. Fig. 14.6 also suggests that glass fiber composites offer a superior blast resistance to carbon fiber systems [30]. Similarly, Tekalur et al. [36] showed that glass fiber-reinforced composites exhibited delamination-type damage at relatively high shock pressures; carbon fiber systems failed in a brittle manner under similar loading conditions. In an attempt to modify the failure mechanisms in blast-loaded composite materials, Gargano et al. [37] studied the effect of

Figure 14.4 Cross-sections of 4.5 mm thick glass fiber reinforced PEI panels following air blast testing [35]. (a) Impulse = 7.9 Ns. (b) Impulse = 8.0 Ns. (c) Impulse = 9.0 Ns. (d) Impulse = 9.4 Ns.

varying the fiber-matrix interfacial strength on the blast resistance of carbon fiber/vinylester laminates. Two types of fiber-sizing agents were used, one that resulted in a strong fiber-matrix bond, and the other that yielded a weak bond with the surrounding polymer. It was shown that the impulse required to initiate damage is significantly higher, and the resulting level of damage is smaller when in laminates exhibiting increased fiber-matrix adhesion. The possibility of suppressing delamination crack growth was investigated by Kerber et al. [38] who conducted an experimental study to investigate the damage resistance of 3D composites subjected to shock-wave loading associated with an air blast. Here, laminates based on a noncrimp fabric were manufactured with increasing amounts of through-thickness fibers and their response compared to that of a plain 2D woven laminate. It was shown that, when subjected to high impulses, the delamination resistance of the 3D composites increases with the level of through-thickness reinforcement. It was also observed that the 3D composites remained intact under high blast impulses, whereas the 2D systems shattered completely.

Polyurea (PU) is an elastomeric polymer that is being increasingly used as a coating material, usually onto metals for applications, such as hangar floors and landing gear components, to reduce exposure to chemicals. Researchers have proposed this for as a potential blast-resistant coating after it was demonstrated that it improved the
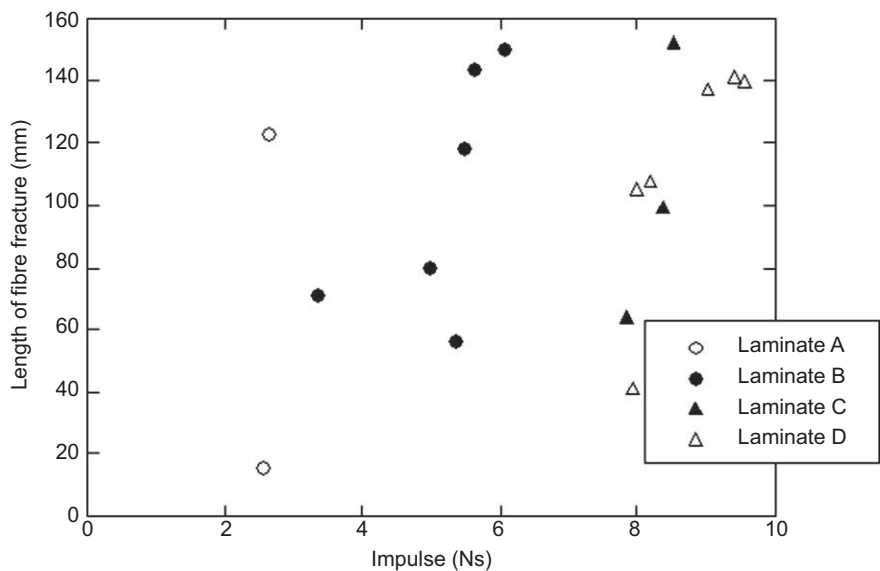
Figure 14.5 The variation of the length of fiber fracture with an impulse for 2.2, 4.2 and 6.2 mm thick CF/PEI plates (Laminates A to C respectively) and a 4.5 mm thick GF/PEI plate (Laminate F) [35].
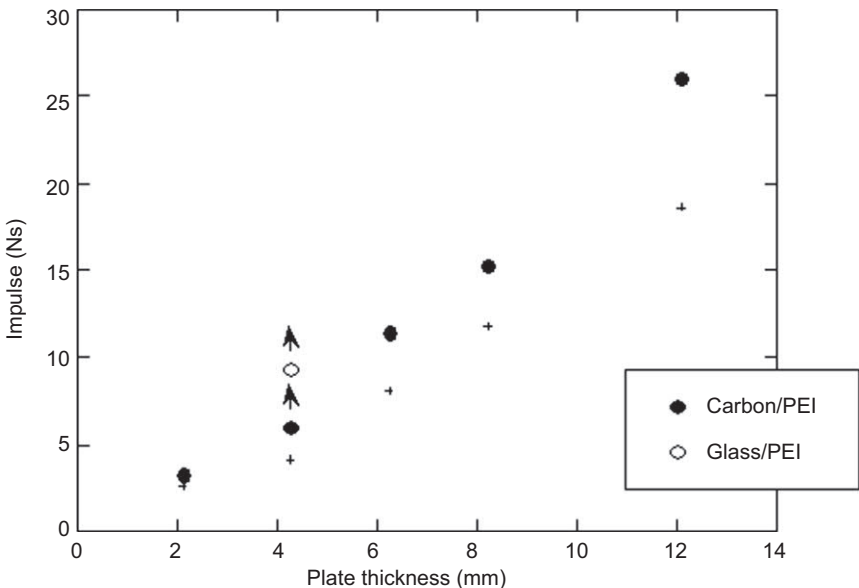
Figure 14.6 The variation of the impulse required to cause complete failure of the composites as a function of plate thickness. The arrows indicate that the panels had not failed completely [35].

properties of concrete structures subjected to explosions [39]. In the composites arena, Tekalur et al. [40] modified an E-glass vinyl ester composite by bonding a layer of PU to the face of the composite. They showed that positioning the PU layer on the surface facing the blast resulted in a significant enhancement of the blast resistance of the composite. Similarly, Ha et al. [41] showed that adding a PU layer to a carbon fiber-reinforced plastic improved the material's ability to strengthen blast-loaded reinforced concrete structures. This is a potentially interesting development for aircraft composites, as PU has a wide operating range of operating temperatures, and worthy of further exploration.

In addition, there is also the possibility of tailoring the properties of plain composites further by adding particles (such as metallic fillers [42,43], carbon nanotubes [44] or urea-formaldehyde [45]) to the composite layers to create multifunctional and self-healing materials. So, von Klemperer and Maharaj [42] added copper and aluminum powder fillers to carbon fiber epoxy laminates to improve the electromagnetic shielding capacity of the composite panels. Blast tests on the laminates [43] showed that the laminates with filler particles outperformed their plain composite counterparts, although the margin was small.

Recently, there has been a growing interesting in the possibility of using natural fibers in the manufacture of dynamically loaded engineering structures. Basturk et al. [46] conducted an experimental and numerical investigation on the blast response of composites based on basalt fibers. The laminates were manufactured using a resin infusion technique and fully clamped for subsequent blast testing. The Galerkin method was employed to develop nonlinear differential equations in the time domain with the resulting predictions being in good agreement with the experimental data. In general, natural fiber composites have inferior properties to their synthetic counterparts (that is, carbon fiber and glass fiber). However, the use of natural materials and biocomposites may offer reduced dependence on fossil fuels, lower disposal energy consumption, and a generally lower harmful impact on human health and the environment [47]. This makes natural fiber composites an attractive alternative, particularly, where structural rigidity and strength are of secondary importance. At present, they are unlikely to replacement glass and carbon fiber composites in aircraft structures.

Rather surprisingly, very little work has been undertaken to investigate the load-bearing properties of composite materials damaged by blast loading. A study by Black et al. [48] on glass fiber/epoxy laminates involved using a shock tube to induce increased levels of damage within the composite laminates, the effect of which was characterized via NDT analyses and compression testing. As expected, increased shock damage caused a corresponding reduction in load-bearing capability. The authors developed a combined damage parameter based on the individual failure mechanisms that were observed in the laminates after testing. The residual compressive strength of the blast-loaded panels exhibited a linear dependence on the proposed damage parameter.

A number of workers have attempted to model the blast response of composite plates [49−54] Turkmen [49] used the Runge-Kutta-Verner analysis to solve the equation of motion of curved glass and carbon fiber cylindrical panels and compared the resulting predictions with both experimental data and the results of finite element

analysis. Good agreement was obtained between the experimental and predicted responses in the longitudinal direction; however, discrepancies were observed in the circumferential direction. Yuksel and Turkmen [50] extended this work to consider the blast response of laminated GFRP hemispheres, with a qualitative agreement being obtained between the numerical and experimental results. Dolce et al. [51] used a three-dimensional finite element analysis to model damage due to an air blast on a carbon fiber-reinforced plastic. The blast load was modeled by assuming a fluid-structure interaction between the Eulerian blast and the Lagrangian structure [51]. Agreement between the model and the experimental data was good in terms of both the residual displacements and resulting damage.

Batra and Hassan [52] modeled the blast resistance of AS4/PEEK composites using the finite element method. The problem formulation included the development of damage as a result of fiber fracture, fiber/matrix debonding, matrix cracking, and delamination. They showed that approximately 15% of the total work done is dissipated in these failure modes. The model was used to show how the energy absorbed in the various failure modes was strongly dependent on the laminate stacking sequence. Fig. 14.7 presents a bar chart summarizing the predictions of the energy absorbed by the principal failure modes in four-ply AS4/PEEK laminates [52]. Although delamination represented the principal energy-absorbing failure process for many stacking
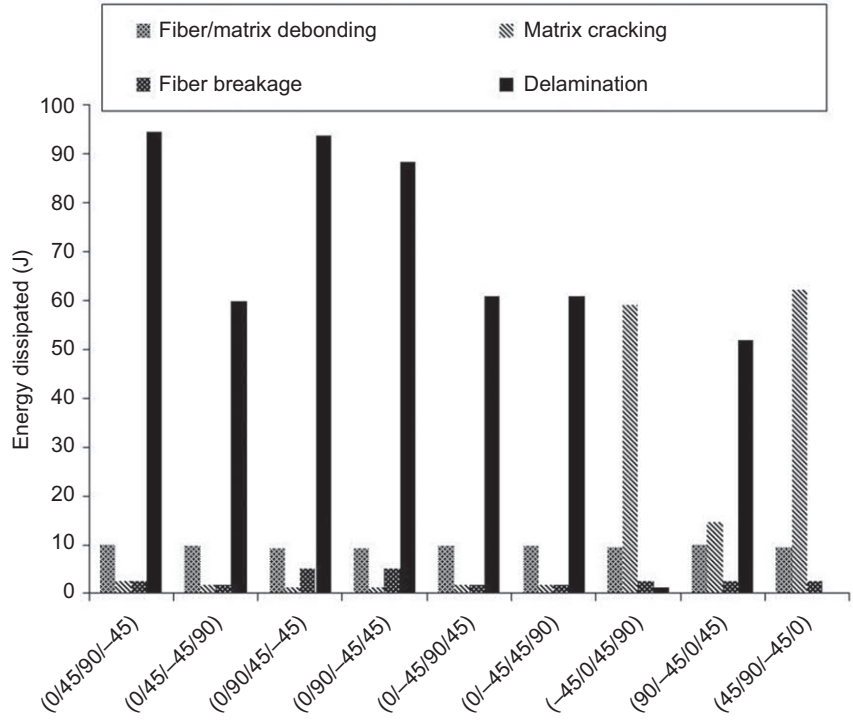
Figure 14.7 Predictions of the energy dissipated in the four primary failure modes observed in four-ply AS4/PEEK laminates based on different stacking sequences [52].
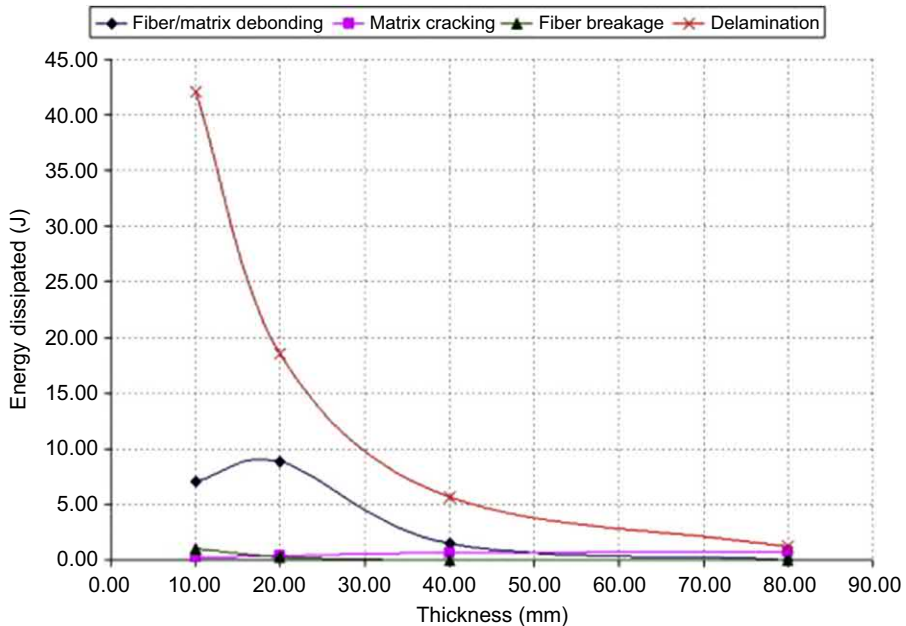
Figure 14.8 Summary of the predicted energy dissipated in different failure modes as a function of laminate thickness for AS4/PEEK [52].

sequences, it was negligible in a [-45,0,45,90] laminate. The authors also investigated the influence of target thickness on delamination in the laminates. It was assumed that the target consisted of four uniform plies with differing thickness according to the overall desired laminate thickness. They predicted that the central deflection of the plate decreased exponentially with target thickness, leading to a similar reduction in the energy dissipated in delamination, Fig. 14.8. Finally, increasing the stiffness of the reinforcing fiber altered the rate of damage development within the target and serves to delay the onset of matrix cracking [52]. Eren et al. [55] modeled the blast resistance of sisal fiber-reinforced epoxy composites and compared their response to that predicted for a glass fiber-reinforced epoxy composite. Modeling was conducted to simulate both single and multiple blasts. The authors showed that the natural fiber composites exhibited an inferior blast response to that of the more conventional glass fiber system, although they argued that their low cost, low density, and biodegradable characteristics still made them attractive candidates for certain applications.

14.6 The blast performance of multilayered systems

14.6.1 Composite sandwich panels

Sandwich panels typically comprise a relatively soft core sandwiched between two stiff outer face sheets. The addition of a core increases the bending stiffness by

increasing the second moment of area of the structure without significant weight penalty. Thus, such structures have high specific strength and stiffness, as well as acoustic damping properties, making them attractive materials for aerospace applications. For example, 8% of the wetted surface of the Boeing 707 is based on sandwich structures, a figure that rose to 46% in the Boeing 757 and 767 aircraft [56]. In addition, the fuselage of the Boeing 747 is based largely on Nomex honeycomb structures, as are the floors, ceiling, and side panels [56]. Similarly, the Beech Starship is recognized as being the first all sandwich aircraft, having carbon/Nomex and aramid/Nomex throughout its structure. Sandwich structures, based primarily on honeycomb cores, are also finding widespread use in the walls of luggage compartments, structures that can potentially be subjected to blast loads from concealed explosives [57].

There is an enormous possibility for potential combinations of face sheet and cores, including the variation of geometry (thickness of face sheets and core), material (resin, reinforcement, core material), bonding and manufacturing methods. Arora et al. [58] present the transient response measurements from the blast tests on sandwich panels with E-glass fiber epoxy face sheets and polymeric foam (Corecell) cores. The panels were considered to be representative of full-scale panels used in marine transport, with an exposed target area of 1.6 × 1.3 m. The panels were loaded by detonating 30 kg spheres of PE4 at several meters from the panel. Transient strain and displacement field data were captured using high-speed photography and digital image correlation [58]. Asymmetric panel deformation was observed due to the boundary support of the panels. Finite element models were constructed using Abaqus to understand the influence of the boundary conditions on the panel response. Damage initiated on the front face sheet, due to cracking, and was accompanied by localized delamination. Core shear cracking and interfacial failure were also evident. The rear face sheets did not exhibit visible tearing and cracking failures [58].

Gardner et al. [59] presented test results on shock-loaded sandwich panels comprising E-glass vinylester face sheets and a Corecell polymeric foam core. Tests on panels with stepwise graded density cores and with polyurea interlayers were also examined. Digital image correlation was used to capture the dynamic response of the panels. The results showed that polyurea core improved the performance of the panels when placed on the rear side of the panel. Core compression, face sheet delamination, and core cracking were all observed.

Langdon et al. [60] tested glass fiber vinylester composite panels having an equivalent mass to sandwich panels having the same composite in the face sheet and a PVC foam core. While vinylester polymers are not aerospace resins, the research method and results are of interest to those concerned with blast testing sandwich structures for aerospace applications. The panels had a 200 mm diameter exposed area and were loaded by detonating a plastic explosive in close proximity to the panels [60]. Delamination of face sheets, core compression, core fragmentation, and fiber rupture were observed [60], as shown in a typical example in Fig. 14.9. Finite element modeling of the panel response was also performed. The tests showed that, in this particular case, the plain composite panels offered superior resistance to blast loading since they could be subjected to higher charge mass explosions without rupture. The FE analysis and the experiments showed that this was due to the higher velocity
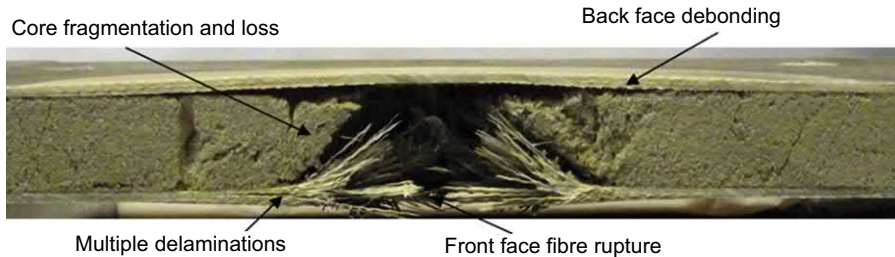
Figure 14.9 Photograph of a cross-section of a blast loaded polymeric sandwich panel with glass fiber vinylester face sheets and a PVC foam core (Impulse = 19.1 Ns, 10 g PE4 charge) [60].

transferred to the front face sheet during the blast loading, which resulted in face sheet failure. The high velocities caused fiber fracture in the front face sheet that exposed the soft core to the blast loading, which resulted in core fragmentation. Although the panels were destined for use in marine applications, the work highlights both the requirement for careful design of composite panels and the complex interplay between the geometric and material properties of these structural materials.

Ma et al. [61] studied the blast response of aluminum honeycomb sandwich panels based on basalt fiber/aluminum alloy FML skins. Basalt was selected for its excellent mechanical properties and environmentally friendly characteristics. The authors investigated several designs based on different graded honeycomb core designs. It was shown that these natural fiber-reinforced structures offer a superior blast resistance to similar panels manufactured using aluminum alloy skins. It was also demonstrated that the blast resistance of the sandwich panels depended on the geometric dimensions of the target, the grading of the core, as well as the intensity of the blast.

Although much of the published work on the blast response of sandwich panels has focused on flat laminates, only a limited number of works have investigated the effect of blast loading on curved sandwich panels [62,63]. Langdon et al. [62] investigated the influence of curvature and load direction on the blast response of curved glass fiber/epoxy laminates and sandwich panels. Lower impulse levels were transferred when the convex side of the curved panels was oriented toward the blast. Laminate panels exhibited superior performance when compared to equivalent mass sandwich panels as the rupture threshold of the laminates was much higher. Increasing the front face sheet thickness in sandwich panels was recommended, but not investigated. Hoo Fatt and Sirivolu [63] developed an analytical model to predict the blast response of shallow shell composite sandwich structures with a double curvature. Here, Lagrange's equations of motion were used to predict the response of shells with an isotropic and a transversely isotropic elastic-plastic core. The authors conducted a detailed parametric study, where it was shown that the blast resistance of the double-curved panels increases as the curvature ratio decreases.

From an aerospace perspective, the work reported above indicates important considerations for the use of composite sandwich panels in blast-resistant applications. Some of the important considerations are the front face sheet thickness, the

equivalence of plain composite laminates, coating technology, energy absorption characteristics of the core, and the delamination resistance of the composite face sheets.

14.6.2   Fiber-metal laminates

Several workers have investigated the blast resistance of multilayered systems based on combinations of thin layers of composite material and metal alloy. Fiber-metal laminates (FMLs) are hybrid structural materials comprising interleaved thin metal sheets and fiber-reinforced polymer laminates. They were developed as a lightweight alternative to monolithic metals for the aircraft industry, particularly for improved fatigue resistance. The only commercially used FML is GLARE©, which comprises thin aluminum alloy sheets and glass fiber-reinforced epoxy (a thermoset). A cross-section view through GLARE 3 is shown in Fig. 14.10. Although the initial use of GLARE© in an aircraft was to improve the fatigue properties of the aircraft components [64], GLARE© has also been used because of its improved impact properties, relative to monolithic aluminum of the same areal density [65,66]. An increase in the ballistic limit of 15% has also been reported for GLARE© when compared to equivalent mass monolithic aluminum alloy [66].

Composite and fiber-metal laminate materials are finding increased use in the aircraft industry. For example, Airbus has, for some time, been using GLARE© to improve fatigue crack growth resistance, in an attempt to introduce life cycle cost savings. GLARE© has been used as a material in the upper fuselage and leading edges of the Airbus A380. Boeing has preferred to use fiber-reinforced composites, such as CFRP, in its aircraft—a notable example being the 787.

There are various types of GLARE©, depending upon the layup of the constituents, but only two that are regularly used in impact applications—GLARE 3 and GLARE 5 [64]. Typically, GLARE is manufactured using 2024-T3 sheets and S2 glass fiber-reinforced epoxy prepreg. The distinct types of GLARE refer to the different possible layups of the glass fiber in the composite layers. GLARE 5 was proposed as a material to replace aluminum for unit load devices (aircraft luggage containers) but has not been widely adopted. Fleisher [67] showed that a GLARE unit load device would contain
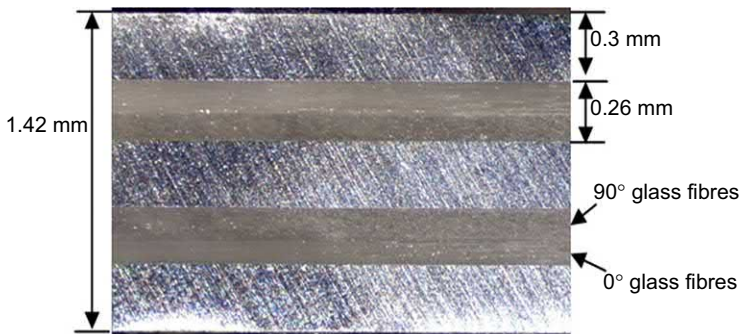
Figure 14.10 Cross-section view of GLARE 3 [68].

blast loads comparable to those responsible for destroying Pan Am Flight 103 over Lockerbie in December 1988. The GLARE device has been certified for use onboard an aircraft but the higher cost (with no life cycle cost savings) of the GLARE containers compared to their aluminum counterparts has limited their use. From a research and design perspective, the details released in Ref. [67] are incomplete—they do not report information about the precise design and the experimental details, making the findings difficult to replicate or use.

Langdon et al. [68] reported results from blast loading experiments on GLARE 3 panels. The panels were square, with an exposed area of 200 mm by 200 mm. The loading was generated by detonating plastic explosive (PE4) disks at a standoff distance of 200 mm from the panel surface and directing the blast waves down a square section tube in front of the panel. The size and mass of the PE4 disks were varied. The panels behaved similarly to monolithic metal plates, exhibiting large plastic deformation with a classic yield line formation pattern typical of fully clamped plates subjected to uniform impulsive loading. When presented in dimensionless form, the results indicated that GLARE might potentially offer superior blast resistance to other metals and composites [68]. However, when the explosive charge was moved closer to the panels, failure was catastrophic as the material could not withstand such highly localized loading.

Researchers across different institutions recently collaborated as part of an EU funded project known as project VULCAN [69−72] to study the response of aerospace materials, including GLARE, to dynamic loading. Mediavilla et al. [69,70] performed experiments to elucidate the dynamic crack propagation and fracture response of an aerospace aluminum alloy, CFRP, and GLARE. Results from experiments on notched plates subjected to loading arising from an explosive line charge are reported in Ref. [69]. Both the aluminum and GLARE exhibited ductile crack propagation, whereas fracture of CFRP panels was brittle. Unfortunately, limited test data were presented, making it impossible to judge which material was better, as the explosive charge failure threshold was not reported. However, since ductile crack propagation proceeds more slowly and involves energy absorption through plastic deformation, this may be more desirable for an aircraft. Tensile tests were performed on GLARE and aluminum alloy specimens over the strain rate range 3×10^{-4} s^{-1} to 300 s^{-1} [70]. No significant rate sensitivity was observed across this range. Pressurized barrel tests [69,70] were performed to gain insight into the dynamic crack propagation. The crack speeds were measured during the barrel tests and showed that higher speeds were measured in the CFRP material (up to 2000 m/s) [70]. The high propagation speed indicated a more brittle failure mechanism in the CFRP compared to GLARE and aluminum alloy. This was attributed to the lower toughness of CFRP [70].

Other types of FMLs, based on fiber-reinforced thermoplastic polymers, have been developed by Guillen and Cantwell [73]. These are mostly based upon polypropylene, which is not suitable for aerospace applications as the polymer is in a rubbery state above −20°C. However, blast testing of these FMLs has been performed as reported by Langdon and coworkers [74−78]. Langdon et al. [74] performed a preliminary investigation on small scale FML panels manufactured from aluminum alloy and three different composite materials. The results indicated that, in nondimensional form, the

midpoint displacements of the different configurations of FML panel were similar to those obtained for monolithic aluminum plates [74]. This was an unexpected result given the completely different failure mechanisms observed in the different types of the panel [74]. The main focus of subsequent work has been on the blast response of aluminum alloy, and woven glass fiber polypropylene (GFPP) based FML panels as reported in Refs. [75−78]. Localized [75,77,78] and uniformly distributed [76] blast loading experiments have been performed on the GFPP based FMLs, with large plastic deformation, debonding, rupture, and petaling failures reported [75−78]. Typical failure modes for blast loaded FML panels are illustrated in the photographs shown in Fig. 14.11. Fig. 14.11(a−c) are from FML panel tests reported in Ref. [76] on FMLs with two metal layers and one composite block (known as the 2/1 configuration). The panels with unidirectional plies exhibited delamination failures (Fig. 14.11(a) and (b)), whereas the woven plies do not exhibit delamination (Fig. 11(c)). Fiber fracture and aluminum rupture were evident at higher loads (Fig. 11(a) and (c)). Fig. 11(d) shows a photograph of a panel cross-section typical of tests on thicker FMLs with woven GPP layers, as reported in Refs. [75−78]. Debonding, fiber fracture, and large inelastic displacement of the aluminum are characteristic failure modes in these panels.

The spatial distribution of the blast loading produced different responses in the FML panels. Uniformly loaded FMLs exhibited higher impulses to tearing and did not exhibit the centralized fiber fracture and panel rupture failures observed in the locally loaded panels [73]. A photograph of a cross-section from an FML panel
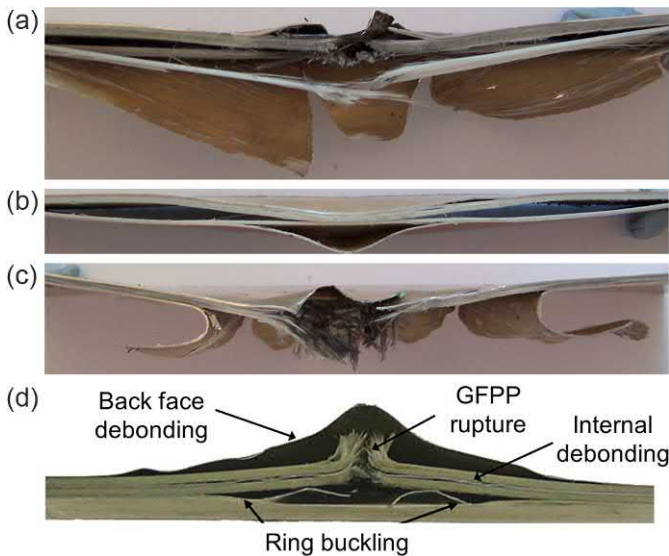
Figure 14.11 Photographs of cross-sections from FML panels subjected to localized air-blast loading (a) 2/1 FML with unidirectional GFPP layers, (b) 2/1 FML with unidirectional GFPP layers, (c) 2/1 FML with woven GFPP layers, (d) 3/2 FML with woven GFPP layers [74,75].

Figure 14.12 Photograph of a cross-section from a GFPP based FML panel subjected to uniformly distributed air-blast loading [76].

subjected to uniformly distributed loading is shown in Fig. 14.12. The debonding failures are located at both the panel edges and the in the central region. The whole section appears "wavy" due to the elastic rebound of the composite constrained by the plastically deformed aluminum layers. However, despite the differences in panel failure mechanisms, the nondimensional analysis showed the midpoint displacements from both the uniform and localized blast tests could be fitted to a linear trend of increasing normalized displacement with increasing nondimensional impulse [75,78].

Langdon et al.'s investigations on blast-loaded GFPP FMLs [75−78] showed that the rear face of the FML frequently debonded from the rest of the panel. Since the first failure was interfacial debonding between the composite layers and the aluminum alloy rear panel, Langdon et al. [79] examined ways to improve this interfacial debonding strength. Improving the adhesion properties of the aluminum−composite interface in FML panels will contribute to the development of blast resistant epoxy-based FMLs. Various surface treatments, resin systems, adhesive additives, and glass fiber types were examined. The interfacial bond strength, determined from single-leg bend tests, was highest when a combination of bead blasting and silane treatment was employed. The surface treatments had no discernible effect on the quasi-static tensile properties. The blast tests showed that fiber configuration and bond strength played a role in blast resistance, but that bond strength (and particularly resin type) was more prominent. However, in terms of blast performance, the improved FML panels were still inferior to GLARE.

Modeling the response of FMLs to blast loading is particularly challenging because of the large number of layers, the possibility of multiple failure modes and the difficulties in defining the spatial distribution of the blast loading pressure on the panel surface. Work by Karagiozova et al. [80,81] on GFPP based FMLs, subjected to localized blast loading, showed that the function of the composite is to spread the loading over a wider region of the panel, thus enabling higher energy absorption. The woven composite was simplified as two orthotropic layers. Delamination and interfacial debonding were modeled using cohesive elements. Subsequently, Soutis et al. [72] used the same approach to model the delamination within GLARE panels subjected to air-blast loading using the LS Dyna finite element code. Soutis et al. [72] reported modeling predictions for the response of clamped quadrangular GLARE panels subjected to explosion loading. The loading is generated by detonating spheres of C4 explosive 200 mm away from the target plates. The target plates had an exposed area of 600 mm by 600 mm. Aluminum, glass fiber, and GLARE panels were all tested and analyzed. The predictions were performed using LS-Dyna, and are compared to blast loading perforation tests. Good correlation is reported [72].

Following the approach by Karagiozova [80,81], Vo et al. [82,83] have also modeled the low impulse blast, and impact behavior of GFPP based FMLs. Numerical simulation results [82,83] compared favorably with experiments reported in Refs. [75−78]. Vo et al. [83] numerically investigated the influence of aluminum alloy type on the overall response. Four alloys were investigated. Vo et al. [83] showed that midpoint panel displacement could be decreased by increasing the yield stress of the aluminum alloy, but that debonding area increased with alloy yield strength. The papers by Karagiozova et al. [80,81] and Vo et al. [82,83] mention the lack of strain rate dependent properties for GFPP as a limiting feature in their work. To address this, Sitnokova et al. [84,85] undertook a numerical study to model the various failure modes observed in aluminum/glass fiber polypropylene FMLs. This work was based on the earlier experimental study by Langdon and coworkers [75−78]. In an initial study [84], perforation-type failure in FMLs based on several stacking sequences was modeled using Abaqus/Explicit. The composite was treated as an orthotropic elastic material up to failure initiation and ensuing damage using an instant failure rate-dependent model. Good agreement between the observed and predicted perforated panels was observed for the range of laminates considered. In a subsequent study, Sitnokova et al. [85] modeled both perforated and nonperforated FML panels. Here a simple model based on continuum damage mechanics was used to describe the response of the FMLs. The blast load was modeled as a pressure function on the front surface of the panel. It was argued that this procedure accounted for both the temporal and spatial distribution of the blast. The finite element models were used to predict both perforation and nonperforation damage in the aluminum/glass fiber polypropylene laminates. Good agreement was observed between the predicted and observed damage modes, although the level of accuracy decreased in thicker laminates based on a larger number of plies [85].

More recently, Nwankwo et al. [86] developed a three-dimensional constitutive analysis to model the blast response of Langdon et al.'s [75−78] glass/PP fiber-metal laminates. The authors stated that to describe the behavior of these materials under extreme conditions fully, it is extremely important to capture the highly nonlinear transient effects, including delamination, debonding, tearing, plastic deformation, and the fracture of the component materials. Two concepts were proposed in the context of characterizing the blast behavior, these being the efficiency of charge and the effectiveness of the target. It was shown that for the configuration studied, the efficiency of the charge was 99.5%, suggesting that the system took the full impulse associated with the charge. The effectiveness of the target is defined as the impulse corresponding to a threshold damage level divided by the nondimensional impulse. It was argued that the lower the efficiency parameter, the more severe the observed damage and degree of perforation [86].

14.7   Conclusions

The blast response of composite materials has become increasingly important as these materials are employed more frequently in modern aircraft. When considering blast

response, it is vital that a careful assessment of the blast loading scenarios for each aircraft design is made, as the loading is complicated by the degree of confinement, geometrical variations, and the multiplicity of potential explosion scenarios. Recent experimental and numerical investigations concerning the blast behavior of fiber-reinforced polymers and fiber-metal laminates have shown that the composites are better able to contain explosion loading that is uniformly distributed. In addition to the nature of the loading, the failure progression and ultimate rupture loads of composite materials depend upon many factors, including the materials, geometrical configurations, overall panel thickness, and stacking sequence. Failure modes in blast loaded composite, and fiber-metal laminates include delamination, interfacial debonding, fiber fracture, plastic deformation of the metal layers, and rupture. Woven composites appear to offer better damage tolerance to blast loading, with fewer delamination failures. Coatings and filler materials could offer a potential improvement in blast response in the future and are avenues of future research. At present, natural fiber composites cannot replace carbon fiber or glass fiber-based composites for load-bearing structures in an aircraft due to their inferior properties.

References

[1] Institute for Economics and Peace, Global Terrorism Index 2017: Measuring and Understanding the Impact of Terrorism, January 2, 2019. Online article. Available from: http://visionofhumanity.org/app/uploads/2017/11/Global-Terrorism-Index-2017.pdf.
[2] BBC, China Industrial Park Explosion Kills 19, July 13, 2018. Online article. Available from: https://www.bbc.com/news/world-asia-china-44816715.
[3] BBC, Tianjin Chemical Blast: Deadly Disaster Marked One Year on, August 12, 2016. Online article. Available from: https://www.bbc.com/news/world-asia-37019025.
[4] O. Holmes, Russia Explosion: Baby Pulled Alive from Tower Block Rubble, The Guardian, January 1, 2019. Online article. Available from: https://www.theguardian.com/world/2019/jan/01/baby-girl-pulled-alive-from-collapsed-russian-tower-block.
[5] R.K. Singh, Death Toll Rises at Indian Power Plant 7 Months after Start. Bloomberg, November 2, 2017. Online article. Available from: https://www.bloomberg.com/news/articles/2017-11-02/explosion-at-indian-coal-power-plant-kills-29-injures-85.
[6] E. Rosenberg, Exploding Vape Pen Caused Florida Man's Death, Autopsy Says. Washington Post, May 17, 2018. Online article. Available from: www.washingtonpost.com/news/to-your-health/wp/2018/05/16/man-died-after-a-vape-pen-exploded-and-embedded-pieces-into-this-head-autopsy-says/?utm_term=.2e9cfda7d079.
[7] L. Stack, M. Stevens, Southwest Airlines Engine Explodes in Flight, Killing a Passenger, the New York Times, April 17, 2018. Online article. Available from: https://www.nytimes.com/2018/04/17/us/southwest-airlines-explosion.html.
[8] National Transportation Safety Board, Aircraft Accident Report: In-Flight Break-Up over the Atlantic Ocean TWA Flight 800, Boeing 747-131, N93119, Near East Moriches, New York, July 1996. Aircraft Accident Report NTSB/AAR-00/03. Washington DC, 2000.
[9] M. Porfiri, N. Gupta, A review of research on impulsive loading of marine composites, in: I.M. Daniel, E.E. Gdoutos, Y.D.S. Rajapakse (Eds.), Major Accomplishments in Composite Materials and Sandwich Structures, an Anthology of ONR Sponsored Research, Springer, 2009, pp. 169−194.

[10] P.D. Smith, J.G. Hetherington, Blast and Ballistic Loading of Structures, Butterworth Heinmann, 1994.

[11] G.K. Schleyer, Predicting the effects of blast loading arising from a pressure vessel failure: a review, Proc. Inst. Mech. Eng. E J. Process Mech. Eng. 218 (4) (2004) 181−190.

[12] M.C. Simmons, G.K. Schleyer, Pulse pressure loading of aircraft structural panels, Thin-Walled Struct. 44 (5) (2006) 496−506.

[13] P.W. Cooper, Explosives Engineering, Wiley-VCH, 1996. ISBN 0471186368.

[14] B.M. Luccioni, R. D Ambrosini, R.F. Danesi, Analysis of building collapse under blast loads, Eng. Struct. 26 (2004) 63−71.

[15] T. Kotzakolios, D.E. Vlachos, V. Kostopoulis, Blast response of metal composite laminate fuselage structures using finite element modelling, Compos. Struct. 93 (2011) 665−681.

[16] A. Dacko, J. Tocyski, Structural response of a blast loaded fuselage, J. KONES Power Transp. 17 (1) (2010) 101−109.

[17] J.A. Gatto, S. Kranaric, Pressure Loading on a Luggage Container Due to an Internal Explosion, Int Conf Structures Under Shock and Impact IV, Computational Mechanics Publications, Southampton, Boston, 1996, pp. 61−77.

[18] C. Kingery, R. Schumacher, W. Ewing Jr., Internal Pressure from Explosions in Suppressive Structures, Memorandum Report ARBRL-MR-02848, Ballistic Research Laboratory, Aberdeen Proving Ground, Mary land, United States, 1978.

[19] W.A. Keenan, J.E. Tancreto, Blast Environment from Fully and Partially Vented Explosions in Cubicles, Technical Report R828, Civil Engineering Laboratory, Naval Construction Battalion Center, California, United States, 1975.

[20] G.O. Thomas, On the conditions required for explosion mitigation by water sprays, Trans. Ins. Chem. Eng. 78 (B) (2000) 339−354.

[21] H.N.G. Wadley, K.P. Dharmasena, M.Y. He, R.M. McMeeking, A.G. Evans, T. Bui-Thanh, R. Radovitzky, An active concept for limiting injuries caused by blast, Int. J. Impact Eng. 37 (2010) 317−323.

[22] Advanced Blast & Ballistic Systems Ltd, 2012. www.advanced-blast.com/technology.php.

[23] A.G. Hanssen, L. Enstock, M. Langseth, Close-range blast loading of aluminium foam panels, Int. J. Impact Eng. 27 (6) (2002) 593−618.

[24] G.S. Langdon, D. Karagiozova, M.D. Theobald, G.N. Nurick, G. Lu, R.P. Merrett, Fracture of aluminium foam core sacrificial cladding subjected to air blast loading, Int. J. Impact Eng. 37 (2010) 638−651.

[25] S. Chung Kim Yuen, G.S. Langdon, G.N. Nurick, E.G. Pickering, V.H. Balden, Response of V-shape plates to localised blast load: experiments and numerical simulation, Int. J. Impact Eng. 46 (2012) 97−109.

[26] A. Britan, G. Ben-Dor, O. Igra, H. Shapiro, Shock waves attenuation by granular filters, Int. J. Multiph. Flow 27 (4) (2001) 617−634.

[27] S. Berger, O. Sadot, G. Melamud, I. Anteby, Y. Kiviti, A. Britan, G. Ben-Dor, Attenuation of shock waves by barriers in tunnels and corridor type structures, in: Proc. 2nd Design and Analysis of Protected Structures, 2006, pp. 71−77.

[28] G.S. Langdon, G.N. Nurick, N.J. du Plessis, The influence of separation distance on the performance of perforated plates as a blast wave shielding technique, Eng. Struct. 33 (12) (2011) 3537−3545.

[29] G.S. Langdon, G.K. Schleyer, Inelastic deformation and failure of profiled stainless steel blast wall panels: Part I, experimental investigations, Int. J. Impact Eng. 31 (4) (2005) 341−369.

[30] T. Franz, G.N. Nurick, M.J. Perry, Experimental investigation into the response of chopped strand mat glassfibre laminates to blast loading, Int. J. Impact Eng. 27 (2002) 639−667.

[31] J.L.R. Comtois, M.R. Edwards, M.C. Oakes, The effect of explosives on polymer matrix composite laminates, Compos. A. 30 (1999) 181−190.

[32] M.Y. Yahya, W.J. Cantwell, G.S. Langdon, G.N. Nurick, The blast behaviour of fibre reinforced thermoplastic laminates, J. Compos. Mater. 42 (2008) 2275−2297.

[33] M.Y. Yahya, W.J. Cantwell, G.S. Langdon, G.N. Nurick, The blast resistance of a woven carbon fiber-reinforced epoxy composite, J. Compos. Mater. 45 (2011) 789−801.

[34] M.Y. Yahya, W.J. Cantwell, G.S. Langdon, G.N. Nurick, The blast behaviour of fibre reinforced composite materials, in: Proc. 7th International Conference on Shock and Impact Loans on Structures, 2007, pp. 691−698.

[35] M.Y. Yahya, in: PhD Thesis, University of Liverpool, 2008.

[36] S.A. Tekalur, K. Shivakumar, A. Shukla, Mechanical behaviour and damage evolution in E-glass vinyl ester and carbon composites subjected to static and blast loads, Compos. B 39 (2008) 57−65.

[37] A. Gargano, K. Pingkarawat, V.L. Pickerd, M.E. Ibrahim, A.P. Mouritz, Effect of fibre-matrix interfacial strength on the explosive blast resistance of carbon fibre laminates, Compos. Sci. Technol. 138 (2017) 68−79.

[38] A. Kerber, A. Gargano, K. Pingkarawat, A.P. Mouritz, Explosive blast damage resistance of three dimensional textile composites, Compos. A 100 (2017) 170−182.

[39] Fatt MS Hoo, X. Ouyang, R.J. Dinan, Blast response of walls retrofitted with elastomer coatings, Struct. Mater. 15 (2004) 129−138.

[40] S.A. Tekalur, A. Shukla, K. Shivakumar, Blast resistance of polyurea based layered composite materials, Compos. Struct. 84 (2008) 271−281.

[41] J.-H. Ha, N.-H. Yi, J.K. Choi, J.-H.J. Kim, Experimental study on hybrid CFRP-PU strengthening effect on RC panels under blast loading, Compos. Struct. 93 (2011) 2070−2082.

[42] D.M. CJ von Klemperer, Composite electromagnetic interference shielding materials for aerospace applications, Compos. Struct. 91 (4) (2009) 467−472.

[43] C.J. von Klemperer, G.S. Langdon, D. Maharaj, D. Shivute, Magnetic filler powders to improve electromagnetic shielding of FRP laminates, in: 17th Int Conf on Composite Materials, Edinburgh, United Kingdom, July 2009.

[44] V. Kostopoulos, A. Baltopoulos, P. Karapappas, A. Vavouliotis, A. Paipetis, Impact and after-impact properties of carbon fibre reinforced composites enhanced with multi-wall carbon nanotubes, Compos. Sci. Technol. 70 (4) (2010) 553−563.

[45] E.N. Brown, S.R. White, N.R. Sottos, Microcapsule induced toughening in a self-healing polymer composite, J. Mater. Sci. 39 (2004) 1703−1710.

[46] S. Bastürk, S. Süsler, H. Uyanik, H.S. Türkmen, V. Lopresto, S. Genna, Z. Kazanci, Experimental and numerical analysis of a laminated basalt composite plate subjected to blast load, in: 20th Int. Conf. on Composite Materials, Copenhagen, Denmark, July 2015.

[47] S. Gabriel, G.S. Langdon, C.J. von Klemperer, S. Chung Kim Yuen, The effect of blast loading on composites containing sustainable materials, in: 3rd Int Conf on Composites, Biocomposites and Nanocomposites, Port Elizabeth, South Africa, November 2018.

[48] M. Black, S. Kishore, J. LeBlanc, P. Lockhart, A. Shukla, Non-destructive imaging and residual strength of composite materials after exposure to blast loading, J. Dyn. Behavior. Mats 4 (2018) 408−424.

[49] H.S. Turkmen, Structural response of laminated composite shells subjected to blast loading: comparison of experimental and theoretical methods, J. Sound Vib. 49 (2002) 663−678.

[50] H.M. Yuksel, H.S. Turkmen, Air blast-induced vibration of a laminated spherical shell, Proc. Phys. 111 (2007) 537−542. Springer.

[51] F. Dolce, M. Meo, A. Wright, M. French, M. Bernabei, Structural response of laminated composite plates to blast load, Plastics Rubber Compos. 39 (2010) 180−188.

[52] R.C. Batra, N.M. Hassan, Blast resistance of unidirectional fiber reinforced composites, Compos. B 39 (2008) pp513−536.

[53] H.S. Turkmen, Z. Mecitoglu, Nonlinear structural response of laminated composite plates subjected to blast loading, AIAA J. 37 (1999) 1639−1647.

[54] A. Forghani, R. Vaziri, Computational modeling of damage development in composite laminates subjected to transverse dynamic loading, J. Appl. Mech. 76 (2009).

[55] Z. Eren, Z. Kazanci, H.S. Turkmen, Repeated air blast response of sisal fibers reinforced bio-composites, Process Eng. 167 (2016) 197−205.

[56] J.R. Vinson, in: O.T. Thomson, et al. (Eds.), Sandwich Structures: Past, Present and Future, Advancing With Sandwich Structures and Materials, 2005, pp. 3−12.

[57] S.M. Lee (Ed.), Handbook of Composite Reinforcements, Wiley VCH, 1992.

[58] H. Arora, P.A. Hooper, J.P. Dear, Dynamic response of full-scale sandwich composite structures subject to air-blast loading, Compos. A. 42 (2011) 1651−1662.

[59] N. Gardner, E. Wang, P. Kumar, A. Shukla, Blast mitigation in a sandwich composite using graded core and polyurea interlayer, Exp. Mech. 52 (2012) 119−133.

[60] G.S. Langdon, D. Karagiozova, C.J. von Klemperer, G.N. Nurick, A. Ozinsky, E.G. Pickering, The air-blast response of sandwich panels with composite face sheets and polymer foam cores: experiments and predictions, Int. J. Impact Eng. 54 (2013) 64−82.

[61] X. Ma, X. Li, S. Li, R. Li, Z. Wang, G. Wu, Blast response of gradient honeycomb sandwich panels with basalt fiber metal laminates as skins, Int. J. Impact Eng. 123 (2019) 126−139.

[62] G.S. Langdon, C.J. von Klemperer, G. Sinclair, I. Ghoor, Influence of curvature and load direction on the air-blast response of singly curved glass fiber reinforced epoxy laminate and sandwich panels, in: A.P. Mouritz, Y.D.S. Rajapakse (Eds.), Chapter 6 in Explosion Blast Response of Composites, Woodhead Pub, 2018.

[63] M.S. Hoo Fatt, D. Sirivolu, Blast response of double curvature, composite sandwich shallow shells, Eng. Struct. 100 (2015) 696−706.

[64] A.D. Vlot GLARE − A History of Development of a New Aircraft Material, Springer, 2001.

[65] P. Compston, W.J. Cantwell, C. Jones, N. Jones, Impact perforation resistance and fracture mechanisms of a thermoplastic based fiber-metal laminate, J. Mater. Sci. Lett. 20 (2001) 597−599.

[66] M.S. Hoo Fatt, C. Lin, D.M. Revilock Jr., D.A. Hopkins, Ballistic impact of GLARE™ fiber−metal laminates, Compos. Struct. 61 (1−2) (2003) 73−88.

[67] H.J. Fleisher, Design and explosive testing of a blast resistant luggage container, in: Proc. Struc. Under Shock and Impact Conf. IV, 1996, pp. 51−59.

[68] G.S. Langdon, Y. Chi, G.N. Nurick, P. Haupt, Response of GLARE© panels to blast loading, Eng. Struct. 31 (2009) 3116−3120.

[69] J. Mediavilla Varas, O.R. van der Meulen, F. Soetens, M. Sagimon, Dynamic crack propagation of Glare and CFRP fuselage materials, in: 10th Deformation and Fracture of Composites Conf, DFC10), Sheffield, UK, 2009.

[70] J. Mediavilla Varas, F. Soetens, E. Kroon, J.E. van Aanhold, O.R. van der Meulen, M. Sagimon, Fracture and strain rate behavior of airplane fuselage materials under blast loading, in: Proc. 14th Int. Conf. Expt. Mech. (ICEM14), France, 2010.

[71] G. Mohamed, C. Soutis, A. Hodzic, J.C. Craveur, S. Pormente, Interaction of hybrid pressurised cylindrical structures subjected to blast loading, Plastics Rubber Compos. 41 (2) (2012) 69−76.

[72] C. Soutis, G. Mohamed, A. Hodzic, Modelling the structural response of GLARE panels to blast load, Compos. Struct. 94 (2012) 954−965.

[73] J.F. Guillen, W.J. Cantwell, The influence of cooling rate on the fracture properties of a thermoplastic- based fibre-metal-laminates, J. Reinf. Plast. Compos. 21 (8) (2002) 749−772.

[74] G.S. Langdon, W.J. Cantwell, G.N. Nurick, The blast response of novel thermoplastic-based fibre-metal laminates − some preliminary results and observations, Compos. Sci. Technol. 65 (6) (2005) 861−872.

[75] G.S. Langdon, G.N. Nurick, S.L. Lemanski, M.C. Simmons, W.J. Cantwell, G.K. Schleyer, Failure characterisation of blast-loaded fibre-metal laminate panels based on aluminium and glass-fibre reinforced polypropylene, Compos. Sci. Technol. 67 (7−8) (2007) 1385−1405.

[76] G.S. Langdon, G.N. Nurick, W.J. Cantwell, The response of fibre-metal laminates subjected to uniformly distributed blast loading, Eur. J. Mech − A Solids 27 (2) (2008) 107−115.

[77] G.S. Langdon, S.L. Lemanski, G.N. Nurick, M.C. Simmons, W.J. Cantwell, G.K. Schleyer, Behaviour of fibre-metal laminates subjected to localised blast loading: Part I − experimental observations and failure analysis, Int. J. Impact Eng. 34 (7) (2007) 1202−1222.

[78] S.L. Lemanski, G.N. Nurick, G.S. Langdon, M.C. Simmons, W.J. Cantwell, G.K. Schleyer, Behaviour of fibre-metal laminates subjected to localised blast loading: Part II − quantitative analysis, Int. J. Impact Eng. 34 (7) (2007) 1223−1245.

[79] G.S. Langdon, C.J. von Klemperer, G.F. Volschenk, T. van Tonder, R.A. Govender, The influence of interfacial bonding on the response of aluminium and glass fibre metal laminate panels subjected to air-blast loading, J. Mech. Eng. Sci. 232 (8) (2018) 1402−1417.

[80] D. Karagiozova, G.S. Langdon, G.N. Nurick, in: D. Reddy (Ed.), Modelling the Behaviour of Fibre−Metal Laminates Subjected to Localised Blast Loading, Theoretical, Modelling and Computational Aspects of Inelastic Media, International Union of Theoretical and Applied Mechanics, 2008, pp. 319−328.

[81] D. Karagiozova, G.S. Langdon, G.N. Nurick, S. Chung Kim Yuen, Simulation of the response of fibre-metal laminates to localised blast loading, Int. J. Impact Eng. 37 (6) (2010) 766−782.

[82] T.P. Vo, Z.W. Guan, W.J. Cantwell, G.K. Schleyer, Low-impulse blast behaviour of fibre-metal laminates, Compos. Struct. 94 (2013) 954−965.

[83] T.P. Vo, Z.W. Guan, W.J. Cantwell, G.K. Schleyer, Modelling of the low-impulse blast behaviour of fibre−metal laminates based on different aluminium alloys, Compos. B 44 (2012) 141−151.

[84] E. Sitnikova, Z.W. Guan, G.K. Schleyer, W. Cantwell, Modelling of perforation failure in fibre metal laminates subjected to high impulsive blast loading, Int. J. Solids Struct. 51 (2014) 3135−3146.

[85] E. Sitnikova, Z.W. Guan, W. Cantwell, The analysis of the ultimate blast failure modes in fibre metal laminates, Compos. Sci. Technol. 135 (2016) 1−12.

[86] E. Nwankwo, A.S. Fallah, M. Moatamedi, L.A. Louca, Numerical simulation of the dynamic response of pulse-loaded fibre-metal-laminated plates, Int. J. Protect. Struct. 7 (4) (2016) 469−494.

Repair of damaged aerospace composite structures

<div style="text-align:right">**15**</div>

E. Archer, A. McIlhagger
Ulster University, Newtownabbey, Ulster, United Kingdom

15.1 Introduction

The repair of composite aircraft structures is similar to that of other advanced composite repair techniques [1]. With all aircraft repairs, however, closer attention is usually paid to the balance between weight and safety factors, aerodynamics, quality control, and substantiation. The approach taken will depend on a number for factors, but initially, a different set of priorities might be applied to an in-service repair versus a manufacturing repair. The task of repair begins only after the extent of the damage has been established by skilled personnel using inspection methods and damage assessment. A repair has the objective of restoring a damaged structure to an acceptable capability in terms of strength, durability, stiffness, functional performance, safety, cosmetic appearance, or service life. Ideally, the repair will return the structure to its original capability and appearance.

Repairs to manufacturing damage must address structural requirements (strength, stiffness, static, fatigue, durability) and cosmetic requirements (customer will not accept a visible repair on their expensive aircraft). However, the time required to complete the repair is not usually an issue unless it delays dispatching a component. Material cost and availability is not a major driver for manufacturing repairs where there is predictable usage, and large volume reduces purchase cost. It may, however, be a major issue for in-service repairs. Aircraft operators will request alternatives to costly or scarce materials.

Repairs to in-service damage must also address structural requirements, but in this case, the time to complete the repair is of the utmost importance (any delay to aircraft departures or a flight cancellation is very expensive). Generally, the cosmetic appearance of the repair is not a major consideration, but modern composite aircraft are often sold on the assumption that the smoother air washed surfaces as a result of fewer fasteners compared to metallic structures will provide fuel savings, so an into wind step is generally not desirable. The size of the repair and the local changes in weight can be insignificant to the total component weight, but in weight-sensitive structures, such as aerodynamic or hydrodynamic control surfaces, the effect to the mass balance can be highly significant. The effective change in local weight must be controlled to within certain limits, and in some cases, rebalancing of the component may be necessary.

Common manufacturing defects include anomalies, such as porosity, microcracking, and delamination resulting from processing discrepancies as well as inadvertent edge cuts, surface gouges and scratches, damaged fastener holes, and impact damage.

Damage can also occur in detail parts or components during assembly, transport, or during operation.

A list of sources of manufacturing defects includes:

- improper curing or processing
- improper machining
- mishandling
- improper drilling
- tool drops
- contamination
- improper sanding
- substandard material
- inadequate tooling
- mislocation of holes or details

During the manufacture of a new aircraft, FAR Part 121.707 -Alteration and repair reports, require the airframe manufacturer to keep a copy of each report of a major repair available for inspection. Airplane operators, therefore, require a record of major predelivery repairs. For economical and logistical reasons, they have a need to know about any predelivery repairs that will affect their maintenance operations. In response to these customer requirements, original equipment manufacturers (OEMs) compile a Significant Rework Log for each airplane and deliver it with the airplane. Rework/repair is deemed significant when it may have an impact on the way the airplane operator will perform repair, maintenance, or overhaul, or affect the inspection program that the airplane operator must follow.

The main characteristic of in-service damage is that it occurs during service in a random manner. A list of sources of in-service damage threats is given below:

- hail
- runway debris
- ground vehicles, equipment, and structures
- lightning strike
- tool drops
- bird strike
- turbine blade separation
- fire
- wear
- rain erosion
- ultraviolet exposure
- hygrothermal cycling
- oxidative degradation
- repeated loads
- chemical exposure

For damage sustained to aircraft structural composite materials, the repair methodology depends on the size of the damage and other factors. An aircraft's Structural Repair Manual (SRM) is a set of repair data for common damage events. It is provided by the OEM at the time of the airplane delivery and approved by the relevant

regulatory authority. It will indicate limitations and provide repair scheme designs if the damage is within these limits. Generally, the repair procedures are as follows:

1. Within damage size limitations, the procedure is laid out in the SRM.
2. Outside the damage size limitations, an engineering decision is required for the design of the repair scheme by the aircraft airworthiness design authority.

The typical procedures followed for the restoration of damaged composite airframes are to:

1. Find the damage,
2. Determine the extent of damage by an appropriate nondestructive inspection (NDI) method,
3. Remove the damage,
4. Fabricate the repair scheme,
5. Apply the repair scheme and
6. Restore aircraft surface finish.

There are several reasons why the ability to repair composites is considered to be a problem. Inappropriate designs adopted in the early years of composite aircraft structures (thin skin honeycomb sandwich construction) exposed composites' weaknesses during service (e.g., prone to impact damage and water migration through the skins into Nomex core, which can cause further damage, especially during freeze-thaw cycling) and required major repair. Also, these thin laminates prevented the use of an operator's preferred in-service repair methods of mechanically fastened repairs. Currently, many operators and maintenance organizations lack knowledge and experience of repairing composite structures, and hence, composites are deemed "hard" to repair. Composites have different properties and behave differently from metal, and unfortunately, there is little standardization on the repair materials and processes. Also, a need to store "lifed" materials, some of which need refrigeration, is also a cost burden on the repair organization. With the increased use of composite materials, certificating authorities are increasingly concerned about skill base and experience levels in maintenance organizations. Many of the legacy repair methods are not rapid and efficient enough to meet the program needs for effective fleet support. They are also not applicable to new airplane programs, especially those incorporating new materials and structural concepts, such as the Boeing 787, Airbus A350, or Bombardier C Series.

15.2 Assessment of repair and nondestructive tests

In many instances, uncertainties associated with existing damage, as well as economic considerations necessitate reliance on inspection and repair programs to ensure the required structural capability is maintained. During the design of composite structural components, consideration should be given to the inspection methods available to both the manufacturer and the customer. Typical composite in-process NDI methods available to the manufacturer are visual, through-transmission ultrasonics, pulse-echo ultrasonics, X-ray, and other advanced NDI methods, such as enhanced optical schemes

and thermography. Most airlines use visual inspections supplemented with both mechanical (i.e., some form of tap test) and electronic (i.e., pulse-echo and low-frequency bond testing) to locate damage. When airplane operators are forced to use inspection methods that are subjective, i.e., the tap test, they are handicapped by lack of knowledge of damage sizes and criticality. This is a significant problem for operators, and while sandwich structural configurations can be very efficient from a performance point of view, they tend to be fragile, easily damaged, and difficult to inspect.

15.2.1   Damage scenario

With metals, impact energy is dissipated through plastic deformation, and the structure still retains a good deal of structural integrity. Laminated composite materials, however, are susceptible to transverse impact loading, which causes laminas to become delaminated or skins and the core of sandwich panels to become disbonded [2]. This delamination causes a considerable reduction in tensile, shear, and especially compressive strength [3], depending on the impact energy level, impactor shape, morphology, and velocity. The process and consequences are described in detail in chapter 11 of this book. Blunt impacts can induce subsurface damage without visible surface damage [4]; it is, thus, difficult to identify such damage during visual inspections [5]. Impact loads can cause delamination, dents, and punctures, as well as micro-damage, such as matrix-cracking and fiber breakage. Although the surface damage may not be readily evident at the time of impact, it can cause severe internal damage and weakening of the resin-dominated properties and could develop into a catastrophic failure of the component. During the design and certification stages, much time and energy are devoted to ensuring a robust airframe. From testing a large range of different layups and thickness for different energy levels, curves are created which act as design allowables for different components. A composite layup will have an allowable design curve, where allowable stress (or strain) varies with thickness for a given impact energy level up to open-hole allowables. Most composite components are designed for specific damage resistance, damage tolerance, and durability criteria, to alleviate the effects of the expected damage. Further information regarding bird strike damage is given in FAR Part 25.631.

During the design stage, an energy level defines the severity of an impact. Statistical studies are used to determine the maximum amount of energy a component can be expected to withstand without affecting the structural integrity. This could typically be the equivalent of an 18 lb toolbox being dropped from waist height, but there are various zones with different energy levels on the aircraft. Barely visible impact damage (BVID) is a defined amount of damage that a component must be able to withstand without affecting the structural integrity. Typically this is 1 mm dent depth; this amount of damage may not be visible on a preflight inspection or even at scheduled maintenance. As in the case of metal aircraft, ultimate strength and damage tolerance philosophies are used to maintain the reliable and safe operation of composite structures. The Federal Aviation Authority (FAA) guidelines for discrete source damage are stated in DOT/FAA/AR-02/121. They state [6]:

1. Structure containing likely damage or defects that are not detectable during manufacturing inspections and service inspections must withstand Ultimate Load and not impair the operation of the aircraft for its lifetime (with appropriate factor).
2. Structure containing the damage that is detectable during maintenance inspections must withstand a once per lifetime load, which is applied following repeated service loads occurring during an inspection interval (with appropriate factor).
3. All damage that lowers strength below Ultimate Load must be repaired when found.
4. A structure damaged from an in-flight, discrete source, which is evident to the crew must withstand loads that are consistent with continued safe flight.
5. Any damage that is repaired must withstand Ultimate Load.

The repair design must also be compatible with other associated systems on the aircraft. Typically these systems are as follows:

1. *Fuel System Sealing.* In modern platforms, the fuel is carried within the structure as an integral part of the structure, i.e., the "wet wing" of an aircraft. Hence, any repair to a structure that is in direct contact with the fuel system must seal the fuel tank, cater for out-of-plane fuel pressure forces, and not contaminate the fuel system during the repair process.
2. *Lightning Protection.* Some composite structure has provision for conducting lightning strikes by use of flame-sprayed coatings, bonded metallic strips, wire mesh, etc. A repair to the structure must restore the electrical continuity, as well as the structural strength. Bolted repairs around fuel tanks must avoid creating an electrical path. If the electrical conductivity of the parent structure is required for lightning protection, then this must also be repaired. Thus, the repair must also incorporate the same degree of electrical conductivity for lightning protection.
3. *Mechanical System Operation.* Any component that is required to move during the operation of the platform or is in close proximity to a moving component, and is subsequently repaired, must ensure that the repair does not impede component operation. For example, retracting aircraft flaps must be repaired such that the repair still provides adequate retraction clearance.

Once the extent of the damage has been assessed, the materials and processes used in the original part fabrication must be determined. Generally, the specifications are available from the OEM. However, if the original specifications are not available, an engineering analysis must be conducted to determine the designed ultimate loads, fatigue, and environmental exposure requirements per Federal Aviation Regulations (FARs) 23.305, 23.307 and 23.573. Even if the specifications are available, however, the specified processes may not be readily duplicable. For example, a part which was manufactured with a preimpregnated resin system cured at 85 psi pressure in an autoclave may not be repairable in this fashion unless it can be disassembled and transported to a facility with the capabilities. Even if it could be transported to an autoclave, it may not be feasible for the completed component with subassemblies to be exposed to the temperatures and pressures of the autoclave without being totally disassembled and supported within the manufacture's original tooling [1]. Furthermore, the elevated pressure used to manufacture skin panels might crush honeycomb stiffened parts of the assembly. Generally, repairs are conducted with only the use of vacuum-induced pressures and localized heating. The reduction in pressure can cause lower fiber volume fraction, so the mechanical strength of the vacuum bagged layup will not be equivalent to the higher pressure laminate; this may require compensating

the repair laminate with an additional ply, which often prevents the repair from being totally flush with the parent material. It should also be remembered that the vacuum pressure applied by the vacuum bag will be less at higher altitude repair centers than at sea level.

15.3 Repair

If the damage is assessed to be negligible by the NDT method, usually, a simple cosmetic repair is sufficient to seal the area. Negligible damage, in the terms of airframes, is usual, but not limited to scratches, chips, or very small holes. In this case, the area would be filled and sealed with a repair epoxy, sanded level with the surface, and painted. The purpose of this is purely cosmetic and to protect it from the elements. It is often the case that small areas of damage are detected in-service, which in themselves do not threaten the integrity or mechanical properties of the component as a whole; if left unrepaired, however, they may lead to further rapid propagation of the damage through moisture ingress and fatigue. Similarly, skin damage to honeycomb panels, core replacement in honeycomb panels or fastener hole elongation may be repaired by potting or filling. In such a repair scheme the damage may not necessarily be removed. However, it is important to remove any absorbed moisture. Absorbed moisture could present long-term problems, such as corrosion or repair scheme loss. The damaged area is filled with a suitable potting compound (neat resin or mixed with chopped fiber) and then sealed with a layer of composite. When applying a potting compound, the weight and balance requirements should be checked, especially, if applied to flight control surfaces. Alternatively, simple patch type repairs can be carried out, with the minimum of preparation, to protect the component until it can be taken out of service for a proper structural repair. These temporary repairs should be subject to regular inspection. For repair of delaminations, resin injection might be adequate. If however, the damage is found to be more serious but considered repairable, then bonded or bolted repairs are the most common methodologies to provide an effective load transfer through the material. All of these common methods are frequently employed and well developed. The one key limitation, however, is they are all "high skill" jobs and are labor intensive, rendering them both expensive and time consuming. The final classification of serious damage confirms the part is not viable to effect a repair; the damaged part must be removed from the structure and replaced.

In order to develop repair concepts for a broad range of damage scenarios, the repair design philosophy is focusing on more generic repairs that are not damage-specific. This approach will be beneficial because generic designs and corresponding repair procedures can be developed for various levels of damage which are, within certain limits, independent of specific damages. Another aspect of the approach is to provide operators with multiple options for a given repair situation. Options might include, as examples, temporary versus permanent repair, bonded composite patches versus bolted composite or metal patches, or wet layup or prepreg patches versus precured bonded patches. An operator's choice might depend on the severity of the damage, the time

available to perform the repair, the operator's facilities and capabilities, inspection/overhaul schedules and/or current field environmental conditions.

There are four basic levels of generic repair scheme designs:

1. Filling and sealing the damaged area (cosmetic repair)
2. Filling the damaged area and applying a doubler patch (semi-structural repair)
3. Bonding a flush patch to the damaged area (structural repair)
4. Bolting a patch to the damaged area (structural repair)

15.3.1 Resin injection

Resin injection can be applied for the repair of skins that have disbonded from the honeycomb core on honeycomb sandwich panels, to repair delaminations between plies of a solid laminate with no damage to the surface, or for small disbonds. Local stiffness and stability may be restored by the injection of resin into the damaged area. This is achieved by drilling two small holes in the surface of the laminate, down to the defect. One hole is used to inject the resin while the other acts as a vent or vacuum port. Generally, toughened resins are more viscous than is favorable for easy injection. Also, drilling the holes can possibly make the damage worse by giving any cracks a high-stress path to follow [7,8].

15.3.2 Chopped fiber

During the assembly stage of composite aircraft components, it is occasionally necessary to repair a laminated component due to defective drilling of holes. These defects could be oversized holes, misaligned holes, incorrect geometric tolerance, etc. A common repair strategy for secondary structures is to fill the damaged hole with a combination of chopped fibers and an epoxy resin system, which subsequently cures to a solid material, allowing a new hole to be drilled as required to meet product conformance.

15.3.3 Bonded patch repair

The bonded repair can take the form of either an external patch, internal patch, or a flush scarf or stepped repair as described in MIL-HDBK-17-3F 3. The internal patch usually is not an option due to accessibility. For simplicity, the external lap is commonly used on internal component repairs, such as bulkheads and inner skins. To maintain aerodynamic cleanliness and to minimize moment-induced failure modes; however, the flush scarf repair is preferred [1]. Furthermore, on composite control surfaces (flaps, ailerons, etc.) that have critical mass balance limitations, the lighter weight flush scarf repair is often the only acceptable means of repair, but a high-level skill and longer time are required to prepare the damaged area for repair.

To apply an external or internal patch (single lap joint) the surface is cleaned and lightly abraded prior to laying up the repair. Single lap shear joints are not as structurally efficient as scarf joints or step joints. For implementing the flush repairs, the

process begins with the removal of the damage and the careful creation of a hole by the scarf or step method. Drying the laminate prior to applying the repair scheme is important. The patch is designed and fabricated to fit in the hole. In this case, either a precured (or hard-patch) and secondarily bonded repair patch or cocured (soft-parch) repair patch is adhesively bonded to the damaged area. Cocured patches are generally stronger. Baker [9] refers to the hard-patch method as a form of scarf repair that involves preforming the patch in a mold, then using adhesive to bond it into the scarf cavity when cured, instead of forming the patch in place. This methodology has several substantial advantages when compared to the industry standard soft patch approach as the patch can be formed in the same manner as the parent component, e.g., autoclaved, the advantages of which have been discussed already [10]. Another alternative is to CNC machine hard patch to the contour of the outer mold line and scarf cavity and then secondarily bonded into the scarf cavity. Options for the patch material include composite laminate, titanium alloy sheet laminate, or solid titanium alloy [11].

15.3.4 Honeycomb

As the structural severity of the damage increases, particularly for thin skins and honeycomb sandwich panels, some load transfer over the damaged region will be required to restore structural integrity. Such a repair scheme, Fig. 15.3, is both cosmetic and semi-structural. The damage is usually removed and so is any absorbed moisture, the damaged honeycomb core is replaced or a foaming resin plug inserted. Over the repair region, a doubler is bonded in place. The hole plug must be of low modulus so as to not attract load, and hence, the load is transferred from the parent laminate into the doubler and out again into the parent laminate. Often the inner skin is repaired with a simple external lap and replacement core cocured in place with potting compound around the perimeter. If the core is honeycomb, the replacement should be of the same material with matching cell size and orientation. Large areas of core replacement with potting compound should be avoided to keep from inducing a failure due to increased local stiffness or increase in mass on components such as engine cowls [1] (See Figs. 15.1, 15.2 and 15.4).
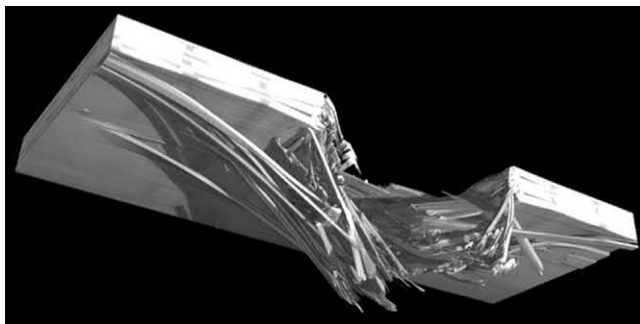
Figure 15.1 Typical through penetration of a 3 mm carbon fiber laminate impacted with an energy of 40 J.
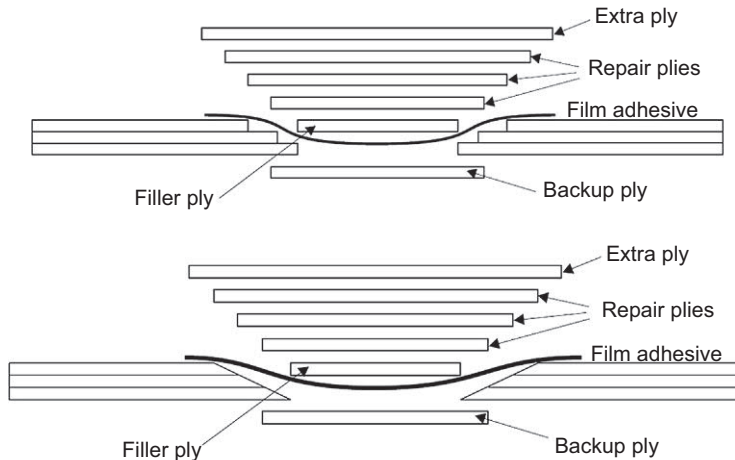
Figure 15.2 Typical flush stepped and scarf repair.
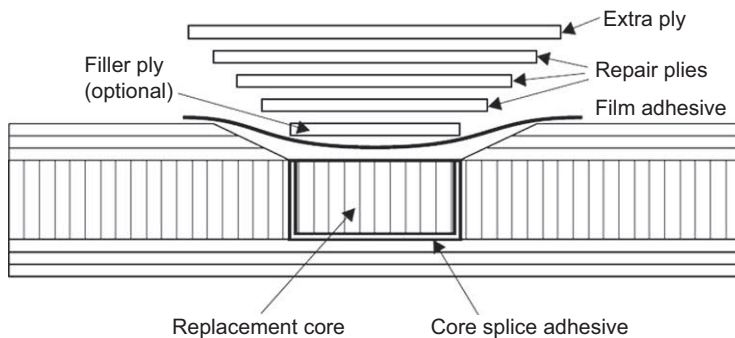
Figure 15.3 Typical repair to honeycomb sandwich panel.

15.4 Typical repair procedure

An industry-standard scarf repair first involves removal of topcoat and primer and then using a hand-held pneumatic router or grinder to machine the damaged portion of the laminate into a circular shape. The sides of the circular cutaway must then be machined to a taper at the required angle. Two approaches can be employed, either stepped or scarfed. The scarfed joint is theoretically superior (better stress distribution), but little difference is seen in practice. The joint face is sanded to a constant taper ratio. Thickness of laminate and predominant nature of loading (tension or compression) impact the optimal taper ratio (different OEMs use different taper ratios, but typically they are between 20:1 and 50:1 but could be as high as 100:1) [12]; however, OEMs usually simplify things and base all their repairs upon a single taper ratio. A final solvent wipe is performed followed by a further inspection, such

as a water break test; the area is then dried before layup begins. Most repair material systems cure at temperatures above the boiling point of water, which can cause a disbond at the skin-to-core interface wherever trapped water resides. Depending on the resin system used, the repair will require curing at elevated temperatures. These could be as low as $50-60°C$ for some room temperature wet layup resins to $180°C$ for some prepreg systems. Some special repair prepreg systems have been developed with lower cure ($120°C$) prepregs optimized for repair use such as Hexply M20. If the repair is to a sandwich construction, the inner skin and core are repaired in a first step. A nonstructural backing may have to be applied to support the inner layup during cure.

For repairs to be made *in situ* (without removing the component), a vacuum bagging system is generally used. This is an integral part of the process as heating elements are used to cure the prepreg resin in the repair material. This process occurs under vacuum to optimize the resin distribution and to also provide a force to bond the patch to the surface of the parent component. A typical vacuum bag schematic is shown in MIL-HDBK 17-3F 3. The best vacuum bag schedule will vary from one repair layup to another, with different repair layups requiring different bleeder ply schedules. In the case of flat laminates, heat is usually applied by means of temperature-controlled electric heating blankets in conjunction with a vacuum bag arrangement. These blankets can also be manufactured to fit complex double curvature aircraft surfaces, or a temporary oven might be constructed. In order to substantiate the repair quality, a process control panel should be fabricated within the repair vacuum bag and cured simultaneously. When the repair is completed, the process panel can be tested to verify the process results [1]. Clearly, this process is severely limited on a large scale as the accuracy and uniformity of the hand-machined scarf cavity and level of cosmetic finish is entirely dependent on the skills and experience of the operator. Another important limitation to consider is the pressure and temperature that can be achieved using a vacuum bagging system. For manufacturing a patch, equivalent to the quality of the original auto-claved part, it is imperative that the patch is cured under autoclave conditions. To account for the loss in performance, extra plies are added to the repair scheme; this has the negative effect of prevent a "flush" repair from being totally free from protrusion.

15.4.1   Bolted patch repair schemes

For thicker laminated sections, restoration of the design load-carrying capacity can be provided with a bolted patch repair. This repair process is to remove the damage and create a hole with circular ends, remove any moisture, drill the locating fastener holes in the parent laminate, and attach the repair panel, which could be of inner, flush, and outer patch types. The patch panels and fasteners should be coated with a sealing compound and fitted wet. Bolted repairs can comprise an external or an internal patch that results in a single shear joint, or two patches, one on each side that leads to a double
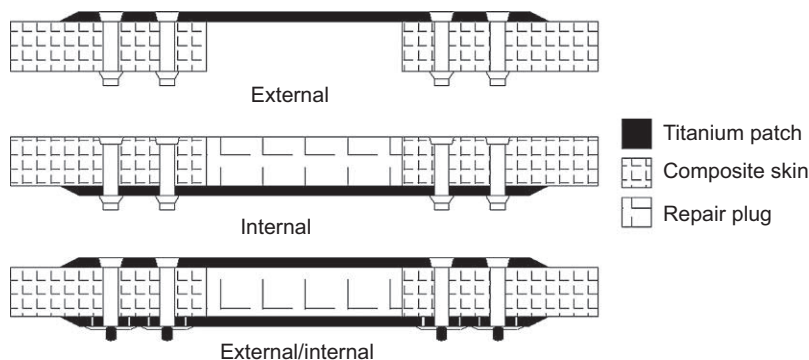
Figure 15.4 Bolted repairs (Ref: MIL-HDBK 17).

shear joint, see Fig. 15.4. In both cases, the load is transferred through the fasteners and the patch by shear forces, but in the case of the two-patch repair, transfer load eccentricity is minimized.

Bolted repair procedure consists of six distinct steps: (1) patch preparation and pilot drilling holes, (2) laying out hole pattern on the parent skin and pilot drilling skin holes, (3) the transfer of the holes in the skin to the patch if the patch covers some existing skin holes, (4) drilling/reaming of patch and skin, (5) patch and fastener installation and (6) sealing of the repair. For complex repairs, multirow fastener patterns will be required to gradually introduce the load from the part being repaired into the repair patch. It is virtually impossible to distribute the load evenly between all the fasteners in a multiple-row pattern, but careful design of patch geometry, fastener diameter, and spacing can alleviate the high loads at the first fasteners. Such complex repairs are not usually identified in the approved repair manuals or procedures (SRM, TO or TM) and normally need engineering input for design. Care should be taken to prevent galvanic corrosion, and as with composite joints, special titanium, monel, or stainless steel fasteners are required.

External Patch with Backup Plate: This concept uses an external chamfered metal patch bolted to the panel being repaired. The bolts thread into nut plates mounted on metal backup plates that are on the side of the repaired panel. The backup plate can be split into two or more pieces and slipped through the opening.

External Patch with Blind Fasteners: This concept is similar to the previous one, except that the backup plates are not used. Blind fasteners are not as strong as bolts and nutplates, but if acceptable strength can be restored, this concept is easier to use.

Bolted Internal Doubler: This concept has been used as a standard repair for metal structures. Access to the backside is required to install the doubler. The doubler cannot be installed through the hole as a separate piece because the doubler has to be continuous to carry loads in all directions. The filler is used to provide a flush outer surface and is not designed to carry loads.

Table 15.1 Repair design criteria, part configuration and logistic requirements will dictate whether the repair should be bolted or bonded (Ref: MIL-HDBK-17.3).

Condition	Bolting	Bonding
Lightly loaded, thin (<0.10 in. (2.5 mm))		×
Highly loaded, thick (>0.10 in. (2.5 mm))	×	×
High peeling stresses	×	
Honeycomb structure		×
Dry and clean adherend surfaces	×	×
Wet and/or contaminated adherend surfaces	×	
Sealing required	×	×
Disassembly required	×	
Restore unnotched strength		×

15.4.2 Bonded versus bolted

Repair design criteria, part configuration, and logistic requirements will dictate whether the repair should be bolted or bonded. Depending on the layup and material, composites can exhibit low bearing strength. Due to the bearing loads induced by mechanical fasteners, bolted repairs are not generally acceptable on thin laminates or sandwich structures. According to Baker and Jones [13], bolted repairs should not be used on laminates less than 8 mm thick. In reality, however, they are used on laminates greater than 3 mm thick. Adhesive bonded patched repairs are very attractive due to their high efficiency, more uniform stress distribution, and good fatigue behavior. Bonded repairs enable the joining of thin sheets with minimal stress concentrations while providing an aerodynamically smooth repaired area with few irregularities. Also, bonded repairs can be more aesthetically pleasing with minimal weight increase and some control of joint and repair stiffness (Table 15.1).

However, the disadvantages of bonded repairs are that surface preparation is critical and sometimes difficult, and the processing and material storage are environmentally sensitive regarding temperature, time, and humidity. Also, NDI is required, which increases the cost, skill, equipment need, and time to complete the repair. Bonded repairs are sometimes severely size restricted and might require recurring inspections. Also, deep damages require removal of a lot of undamaged parent material and bonded repair must elevate the repair area to a uniform temperature, so care must be taken to alleviate heat sink.

Bolted repairs require similar skills and processes to repair of metal structure meaning materials, equipment and skills are more readily available, so there is an opportunity to save considerable time without the requirement to scarf the surface. Also, this brings better confidence in the process and the design. The disadvantage of bolted repairs is that it is difficult to design repairs for sandwich structures and

for thin sheets due to high bearing stresses. If dissimilar materials are used, there is the potential for thermal stresses, stiffness, and strength mismatches and environmental deterioration. Bolted repairs generally incur an increase in weight, and are, therefore, less structurally efficient and the aerodynamic smoothness more likely to be compromised even for "flush" schemes. With composites, a greater edge distance is required than in metal structure, and a drilled hole through the complete thickness is required regardless of damage depth. Mechanically fastened repairs require care and accuracy in the drilling of holes and the alignment of parts during assembly. Fastener hole breakout is a characteristic problem, commonly solved by using a layer of woven fabric as the outermost ply for all laminates during initial component manufacture.

In summary, bonded repairs are the preferred approach for manufacturing repairs to both honeycomb sandwich and monolithic secondary structure. However, for the FAA and European Airworthiness and Safety Administration, the main reason for withholding certification of bonded repairs for the primary structure is the lack of certainty over bond quality, as it is not possible to assess strength and durability of bonded joints without destructive testing.

15.5 Analysis of repair

Most repairs are basically designed as a joint to transfer the load into and out of a patch. In the case of the bonded repair, a simple method of determining the load sharing ratio with a bonded repair, and the parent laminate is illustrated by Hart and Smith [14]. For ensuring that the repair configuration will have adequate strength and stiffness, the repair joint must be analyzed to predict its strength. As stated before, if the damage is outside of information available in the SRM, a repair scheme must be designed. However, as FAR requires the use of data "Approved" by the FAA or data "Acceptable" to the FAA when performing structural repairs, aircraft operators will be reliant upon the OEM for composite repair data. More information regarding repair to structure susceptible to widespread fatigue damage is given in AC 25.571-1D stating that analysis must be supported by test evidence. Further information on the repair approval process is given in appendix 5 of AC 120-93.

Composite panel repair has been extensively studied for the last 40 years and many researchers have reported that aircraft structures can be repaired to restore between 80% and 100% of the parent [15] laminate strength. In practice, however, the composite laminate strength in the overlap section of a scarfed lap joint is usually reduced when compared with the parent laminate strength due to discontinuous fibers across the overlap length, as well as, stress concentrations in the bond line and laminates. In addition, the bond strength could vary due to variations of the material or geometrical and processing properties [16]. It is important to note that the structural behavior of bonded repairs relies heavily on processing factors (i.e., surface properties, adhesion, and curing conditions) rather than mechanics (i.e., stress and strain) alone [17]. By comparison, the performance of mechanically fastened composite joints mainly depends on the mechanical

factors, such as bolt load and bolt-composite mechanical interactions [18]. This difference is a major challenge to provide strong, durable, and reliable bonded repairs, especially for primary structural components.

For the analysis of adhesively bonded joints, approaches based on analytical or numerical methods are used, but the majority of the existing analytical models for adhesively bonded joints use two-dimensional macro mechanics, which assume plane stress or strain state and neglect the stresses generated across the third direction in the adherends. Considering that the transverse mechanical properties of composite laminates are relatively low in comparison to the in-plane mechanical properties of the laminate, joint failure could be an adherend failure in transverse tension before the failure of the adhesive occurs [19]. The design of bonded repairs (as with bonded joints), therefore, should aim to provide a shear dominant stress state and induce minimum peel (i.e., through-thickness out-of-plane) stresses in the adhesive layer to improve the joint strength [20]. In general, bonded scarf patches, with no eccentricity of the load and minimal peel stresses, are the most efficient joints for bonded repair. If a sandwich structure is repaired, the core forms a substrate, which provides support for the out-of-plane loads. This is why bonded repairs are very efficient for sandwich structures [21].

Any repair must be capable of supporting the design loads that are applied to the original structure. The two major aspects of supporting design loads are strength restoration and stability requirements; the greatest concern is often structural instability under compressive loading so the repair design must consider how to restore structural stiffness. Damage analysis will indicate where structural instability exists. Generally, the stiffness and placement of repair material should match the parent material as closely as possible. This avoids any recalculations of the overall dynamic behavior of the component, such as flutter or structural load redistribution. However, if damage analysis indicates that local structural instability is likely, then some form of structural doubler patch is applied to restore local stiffness. The restored stiffness should be equivalent to the undamaged stiffness such that [22]:

$$E_{restored1} = \frac{E_{lam_1} * h}{t_r}$$

$$= \frac{E_{p_1} t_p + E_{deg_1} t_{damage}}{t_r}$$

$$= \text{Effective Patch Stiffness} + \text{Effective Degraded Stiffness}$$

where:

$E_{l\,am_1}$ = Laminate Effective Principal Stiffness
h = laminate thickness
t_r = thickness of the repaired region
E_{p_1} = patch stiffness
t_p = patch thickness
E_{deg_1} = degraded region stiffness
t_{damage} = depth of the damaged region

Any permanent repair must be designed to support applied loads at the ultimate design load level at the extremes of temperature excursions, moisture levels, and barely visible damage levels. Also, structural repairs may be more susceptible to damage caused by repeated loads during their service lives. This is because the repair process is not as well controlled, and the repairs themselves create discontinuities in areas that are exposed. Bonded repairs should be well sealed as they can develop disbonds after being weakened by environmental effects. In a recent study on repair by bonding external patches, Cheng et al. [23] found that high-stress concentration along the transverse edges of circular patches and/or at the longitudinal edges of the hole leads to early damage initiation in the parent plate. It is shown that the damage progression depends on the repair patch. This study considered various patches of different stacking sequences placed on both sides of the parent plate. Finite element analysis was used to optimize patched repairs.

The design analysis of a scarf may be considered similar to a single lap bonded joint, detailed analysis of which can be found in MIL-HDBK 17-3F 3. However, the analysis of a bonded joint is made complex by the modulus difference of the adhesive compared to the adherends and the relative thicknesses of both, which causes a nonlinear distribution of the shear forces in a lap joint with peak stresses at the ends [1]. Scarf repairs provide a more uniform stress distribution; however, to achieve this, an adequate scarf angle is required [24] shown in Fig. 15.5.

Scarf repairs can be modeled to a first approximation as a simple scarf joint. If the patch matches the parent material in stiffness and expansion coefficient, simple theory gives:

$$\tau = \frac{P * \sin 2\,\theta}{2 * t}$$

where τ is the adhesive shear stress, P the applied load per unit width, t the laminate thickness, and θ the scarf angle. The required minimum value of scarf angle θ for an applied load P can be obtained from the following, taking τ_P as the peak or allowable adhesive shear stress:

$$P = E * \varepsilon_U * t = \frac{2 * \tau_P * t}{\sin 2\theta}$$

where E is the laminate modulus and ε_U the allowable laminate strain. For small scarf angles, the condition for reaching the allowable strain ε_U in the adherends is:

$$\theta < \frac{\tau_P}{E * \varepsilon_U}$$

Figure 15.5 Scarf joint analysis geometry.
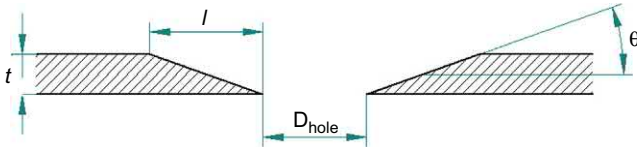
Figure 15.6 Scarf repair length geometry.

Taking ε_U, as 4000 microstrains at design ultimate stress for the composite component τ_P, for hot/wet conditions as 13 MPa for film adhesive and E as 70 GPa, typical of a composite laminate used in aircraft structure gives $\theta \leq 3$ degrees. From the above, we can also calculate the repair scheme patch length, as shown in Fig. 15.6:

$$l_{Patch} = \frac{2 * t}{\sin \theta} + D_{hole}$$

where:

t = laminate thickness
D_{hole} = the hole diameter

In practice, a general rule of thumb for scarfing is to remove 12.7 mm per ply. Ply thickness varies depending on the materials used in the original structure, but for carbon fiber unidirectional tape, it can be as thin as 0.127 mm. Clearly, a scarf repair on a structure of 6.35 mm thickness (50 plies thick) would approximately translate to a scarf of ~635 mm.

Clearly, these are simple approaches and do not optimize the repair for a complex multiload path structure. In recent research, Engels and Becker [25] proposed a laminate plate being repaired by elliptical patches. This is done by first cutting the damaged section to an elliptical shape and then repairing the surface with the same shaped patches of the relevant larger size. Similarly, Wang and Gunnion [26] postulate that a constant scarf angle in every direction may be overly conservative for orthotropic laminates that make up the majority of aircraft external structures. However, the extra complexity involved would further challenge the current repair provision. Soutis and Hu [27] determined that scarf geometry based on 2D stress analysis could differ from a 3D configuration. In a 2D analysis, once the bond line fails, the joint can no longer carry the load, while in the 3D arrangement the load-carrying laminate will have the strength of the plate with a scarfed cut-out or hole. Using a nonlinear shear-lag analysis and 3D finite element analysis to estimate the compressive failure load of the repaired laminate, Hu and Soutis [28] found the compressive loading mode was more severe than the tensile mode owing to the instability of delaminated plies, instability of the patch and skin strength reductions occurring under elevated temperatures and absorbed moisture conditions. In this study, the predicted strength was within 10% of the experimental data.

15.5.1 Analysis of bolted repair

Analysis of a bolted repair follows the analysis of a bolted joint. The behavior of composites in bolted joints differs considerably from what occurs with metals. The brittle nature of composites necessitates more detailed analysis to quantify the level of various stress peaks as stress concentrations. Composite joint design is more sensitive to edge distances and hole spacing than metal joint designs and requires specialized fasteners. Interference fit fasteners or rivets must not be used but expanding sleeves can be installed as required.

The estimation of the transferred load through the repair is the first stage in the repair analysis. Generally, the load cases must be sought from the aircraft manufacturer, but on special occasions, especially for temporary repairs, loads can be approximated by reverse engineering, utilizing the known design of the parent structure. Care should be taken to use conservative approximations that are based on the maximum load that can be sustained by the geometry and layup of the parent structure. After the load transferred through the repair is known, the distribution of this load between the various fasteners, parent structure, and the patch has to be evaluated.

A failure analysis should also be conducted as the parent part of the joint may not be adequate to accommodate the mechanically fastened joint. It may not have the adequate thickness or the proper layup to provide the bearing resistance. As the layup cannot be changed, the only recourse is to bond additional plies. However, care must be taken so as not to end up with a highly unsymmetrical layup. Care must also be taken to properly estimate the bearing/by pass ratio and to consider all possible laminate failure in order to avoid increasing the damage by failing the periphery of the repair. Analysis techniques follow Volume 3, Sections 6.2.2.2 and 6.3.2.3 of the MIL-HDBK-17.

Other important variables are patch structure (composite material, layup, and thickness according to the analytical results) and fastener stiffness which should be determined by test or analysis and subsequently used in the analysis of the overall repair. Fastener tensile and shear stresses should be determined as to their adequacy for static strength and for fatigue loading. Fastener selection is addressed in Chapter 11.

15.6 Conclusion and future trends

Regarding the current composite airframes, Boeing claims their rapid composite repair technique for the 787 offers temporary repair capability to get an airplane flying again quickly, despite minor damage that might ground an aluminum airplane. The 787 SRM specifies three types of composite repair: traditional vacuum debulked bonded scarfed repair, the company's patented quick composite repair technique and conventional bolted repair [29]. Looking to the future, EADS Innovation has been working on automation that might eventually carry out an entire repair cycle encompassing damage detection, surface preparation, repair patch creation, patch application, and finally quality assurance checking. Meanwhile, the German Aerospace Research Center DLR has been investigating the automation of resin-infused repairs. The aim is to develop scarf repair capability including damage removal by computer-controlled

milling, impregnation of a dry preform laid into an excised site, and subsequent cure. DLR claims the method is particularly appropriate for curved areas, reducing complexity and avoiding the need to produce special tooling. Laser specialists clean-LASER and SLCR, also in Germany, are separately working on systems to prepare repair sites. GKN Aerospace (Isle of Wight, U.K.) and SLCR Lasertechnik (Düren, Germany) have agreed to develop automated laser repair for composite structures on aircraft [30]. By looking beyond state of the art, research on structural health monitors using techniques, such as embedded fiber optic strain sensing and self-healing composites using microvascular systems of repair networks have been demonstrated. Whatever the future holds, the approach for the composite structure design teams needs to be based upon input and knowledge gained from a working relationship established with the airline maintenance personnel. This can be accomplished through repair workshops, or inquiries, involving airline and OEM customer support personnel, engineering personnel and involvement with the Commercial Aircraft Composite Repair Committee (CACRC). CACRC meets twice per year, under the auspices of the SAE International, alternating between Europe and North America. The remit is to address issues experienced by aircraft operators when maintaining composite components on commercial aircraft. Delegates are drawn from airlines, OEMs, regulatory authorities, material suppliers and maintenance and repair organizations.

References

[1] L.L. Mansberger, General Aviation Composite Repair, The University of Texas. Available from: Arlingtonmansbergeraircraft.com.
[2] E. Archer, J. Broderick, S. Buchanan, A.T. McIlhagger, Internal strain measurement and impact response of three-dimensional angle interlock woven carbon fibre composites, J. Reinf. Plast. Compos. 32 (12) (2013) 912−924.
[3] J.C. Prichard, P.J. Hogg, The role of impact damage in post-impact compression testing, Composites 21 (6) (1990) 503−511.
[4] P. Kumar, B. Rai, Delaminations of barely visible impact damage in CFRP laminates, Compos. Struct. 23 (4) (1993) 313−318.
[5] U. Polimeno, M. Meo, Detecting barely visible impact damage detection on aircraft composites structures, Compos. Struct. 91 (4) (2009) 398−402.
[6] J. Xie, Y. Lu, Study on airworthiness requirements of composite aircraft structure for transport category aircraft in FAA, Proc. Eng. 2nd Int. Symp. Aircr. Airworth. 17 (2011) 270−278. ISAA.
[7] A.A. Baker, R.J. Chester, G.R. Hugo, T.C. Radtke, Scarf repairs to highly strained graphite/epoxy structure, Int. J. Adhesion Adhes. 19 (1999) 161−171.
[8] V. Sabelkina, S. Malla, M.A. Hansena, R.M. Vandawakerb, M. Derrisob, Investigation into cracked aluminum plate repaired with bonded composite patch, Compos. Struct. 9 (1) (2007) 55−66.
[9] A.A. Baker, Development of a Hard-Patch Approach for Scarf Repair of Composite Structure. Defence Science and Technology Organisation Report TR-1892, 19.
[10] D. Bitton, A.A. Baker, I. Hertzberg, Development of a Hard-Patch Approach for Scarf Repair of Composite Structure. CRC-ACS Report TM 05080.

[11] B. Whittingham, A.A. Baker, A. Harman, D. Bitton, Micrographic studies on adhesively bonded scarf repairs to thick composite aircraft structure, Compos. A 40 (9) (2009) 1419−1432.

[12] B.A. Strong, Fundamentals of Composites Manufacturing, Soc. Manuf. Eng. Mich. 2007, pp. 495−497.

[13] A.A. Baker, R. Jones, Bonded Repair of Aircraft Structures, Martinus Nijhoff, Dordrecht.

[14] L.J. Hart-Smith, Design Methodology for Bonded-Bolted Composite Joints, AFWAL-TR-81−3154.

[15] S.H. Myhre, J.D. Labor, Repair of advanced composite structures, J. Aircr. 18 (1981) 546−552.

[16] A. Baker, Bonded composite repair of fatigue-cracked primary aircraft structure, Tenth Int. Conf. Compos. Struct. 47 (1−4) (1999) 431−443.

[17] A.J. Kinloch, Adhesives in engineering, in: Proceedings of the Institution of Mechanical Engineers, Part G. Journal of Aerospace Engineering, vol. 211, 1997, pp. 307−335.

[18] E.W. Godwin, F.L. Matthews, A review of the strength of joints in fibre reinforced plastics: part 1. Mechanically fastened joints, Composites 11 (3) (1980) 155−160.

[19] M.D. Banea, L.F.M. daSilva, Adhesively bonded joints in composite materials: an overview, in: Proceedings of the Institution of Mechanical Engineers, Part L. Journal of Materials: Design and Applications vol. 223, 2016, pp. 1−18 (1).

[20] A.J. Gunnion, I. Herszberg, Parametric study of scarf joints in composite structures, Compos. Struct. 75 (1) (2006) 364−376.

[21] K.B. Katnama, L.F.M. da Silva, T.M. Young, Bonded repair of composite aircraft structures: a review of scientific challenges and opportunities, Prog. Aerosp. Sci. 61 (2013) 26−42.

[22] L.J. Hart-Smith, Effects of Flaws and Porosity on Strength of Adhesive-Bonded Joints, Douglas Aircraft Co.

[23] P. Cheng, X.J. Gong, S. Aivazzadeh, Design and Optimization of Composite Laminates Repaired by External Patches, in 18th International Conference on Composite Materials, Korea, pp. 21−26.

[24] B.C. Hoskin, A.A. Baker (Eds.), Composite Materials for Aircraft Structures, AIAA Education Series, AIAA, New York.

[25] H. Engels, W. Becker, Closed-form analysis of external patch repairs of laminates, Compos. Struct. 56 (3) (2002) 259−268.

[26] C.H. Wang, A.J. Gunnion, Optimum shapes of scarf repairs, Compos. A 40 (9) (2009) 1407−1418.

[27] C. Soutis, F.Z. Hu, Failure analysis of scarf-patch-repaired composite laminates loaded in compression, AIAA J. 38 (4) (2000) 734−740.

[28] F.Z. Hu, C. Soutis, Strength prediction of patch repaired CFRP laminates loaded in compression, J. Compos. Sci. Technol. 60 (7) (2000) 1103−1114.

[29] K. Wood, In-situ composite repair builds on basics, in: High-Performance Composites, 2008.

[30] G. March, Meeting the Challenge of Composite Fuselage Repair, 14 May, May/June Issue of Reinforced Plastics Magazine.

Nondestructive testing of aerospace composites

R.H. Bossi [1], G.E. Georgeson [2]
[1]The Boeing Company (retired), Seattle, WA, United States; [2]The Boeing Company, Seattle, WA, United States

16.1 Introduction

Nondestructive Testing (NDT), Nondestructive Inspection (NDI), and Nondestructive Evaluation (NDE) are concerned with the techniques and measurements that provide data on the condition of the materials and structures at the time of manufacturing and during the in-service experience. The NDT/I/E methods are generally speaking discrete inspections performed during manufacture and at specified intervals or events during the service life of a structure.

This chapter describes the basics of NDT/I/E for polymer-based composite fiber-reinforced structures. Today NDT/I/E methods are used primarily to detect manufacturing defects or damage. The future direction, however, is to use these tools for material state condition assessment and prognosis of remaining structural life. Additionally, there are opportunities to employ NDT/I/E methods at earlier stages in the manufacturing process of composites to reduce final inspection time and cost.

16.2 NDT, NDI, and NDE methods for polymer composite structures

Nondestructive methods of testing, inspecting, or evaluating a product utilize physical measurements that do not alter the condition or life of the product for its continued use. Nondestructive Testing (NDT) and Nondestructive Inspection (NDI) are generally considered synonymous, with both being related to the use of measurements tools per specification and assessment against specified criteria. Nondestructive Evaluation (NDE) and Nondestructive Characterization (NDC) are terms intended to convey the use of nondestructive measurements for material condition, property or state assessment, especially in a quantitative manner. For this text, the acronym NDT will be used to represent all these uses.

16.2.1 Quality assurance and NDT

The fabrication of polymer composite structures used in aerospace applications follows a set of processing procedures. Imbedded in those procedures are a number of

measurements, observations, and records of the raw materials, assembly process steps, and curing settings that document the Quality Assurance (QA) of the final product. NDT provides a particular verification of the quality of the structure that combined with other QA requirements will verify that a structure is fit for service. NDT is required at various levels and coverages, depending on the component designation as primary or secondary structure. The primary structure is a structure where the failure could result in loss of the air vehicle or life, and therefore, usually requires 100% area coverage with instrumented NDT. The secondary structure is the structure where failure does not affect flight safety and may or may not require inspection beyond visual or partial instrumented NDT coverage, depending on the manufacturing process control capabilities.

NDT is critical to the quality assurance of primary polymer composite structure in the aerospace industry. Above all, NDT is concerned with the safety of users of these structures, and aircraft accident prevention. The reliability and sensitivity to relevant defects with qualified NDT equipment and methods—utilized by qualified NDT personnel—is essential to ensuring life-critical airworthiness.

NDT is the means of assuring that the design requirements for the as-built structure are met and its response to all possible in-service conditions are reliably assured. This is done by direct correlative testing of NDT capability compared to structural modeling and destructive testing of composite sub-, mid-, and full-scale structures. Structures are designed to be able to handle a certain level or size of flaws or damage during their use. The selected NDT method must be shown to reliably detect flaws or damage, the size of which would produce damage growth under any possible in-service loading conditions. In the end, design "allowables"—tying together flaw size and location, structural modeling, and mechanical testing, and NDT flaw detection capability—form the basis for general structural airworthiness. Various ultrasonic methods have historically been utilized in the defining of allowables for composites, which explains why the vast majority of primary composite structure product is inspected with some form of ultrasound testing.

Composite manufacturing process specifications are written to define acceptable NDT methods and requirements for flaw sensitivities. The NDT system and method cost, inspection coverage speed, and relevant flaw sensitivities need to be taken into account early in the composite structural design process and manufacturing planning. If this does not happen, the structure can end up being uninspectable at sensitivities required, or very costly or time-consuming to inspect. Collaborative engagement of the NDT community with the designers and fabricators is essential to ensure that the design, manufacturing, and NDT operations work together to produce an optimized, cost-effective, and reliable product.

The qualification of NDT equipment for composite inspection is accomplished utilizing physical NDT reference standards that represent the structures under test and their potential flaws. After initial qualification of the system, regular checks of the equipment in operation are performed by rescanning the standards to look for changes in defect sensitivity that need to be addressed before continuing.

A final important piece in product assurance is the certification of the personnel who are conducting the NDT and analyzing the results in order to make a

determination on product fitness for service. The American Society for Nondestructive Testing (ASNT) provides training and certification for various operational levels of NDT personnel (as recommended in the SNT-TC-1A document published by ASNT) for a broad range of NDT methods. There are three levels of capability and responsibility:

Level I technicians are able to carry out calibrations and perform test procedures under the supervision of a certified Level II or Level III personnel. Level II technicians can calibrate, perform tests without supervision, and make test assessments when required. Level III personnel are responsible for the training, qualification, and certification of the companies' nondestructive testing Level I and Level II technicians. The Level III also develops inspection procedures and acceptance criteria. Employer-based certification requires the employer to create their own written certification document and choose a subset of SNT-TC-1A requirements based upon the company needs. The National Aerospace Standard NAS-410 also provides for employer or third party certification, with required specific training and experience hours on aerospace parts.

Both primary and secondary polymer composite structure may require in-service NDT. While a metal structure may require some frequency of inspection due to fatigue life and potential cracking, polymer composites are generally designed to only require an in-service inspection as a result of damage or unplanned events. Visual observation of damage may trigger an instrumented NDT inspection for measurement of the damage or degradation to determine repair or replacement.

The two major categories of polymer composite used in aerospace are laminates and sandwich structure, which require some differences in NDT inspection methods. At the time of manufacture, the main issues are porosity, delaminations, foreign materials, disbonds, cracks, and wrinkles. Sandwich parts that contain honeycomb core may also have core quality or adhesive issues. Depending on the manufacturing process, these features may have different probabilities of occurrence. In service, the main damage of interest will be delaminations, disbonds, cracking, moisture ingress, and heat damage. Fig. 16.1 shows these primary defects of interest at the time of manufacture and defects that can be a result of an in-service activity.
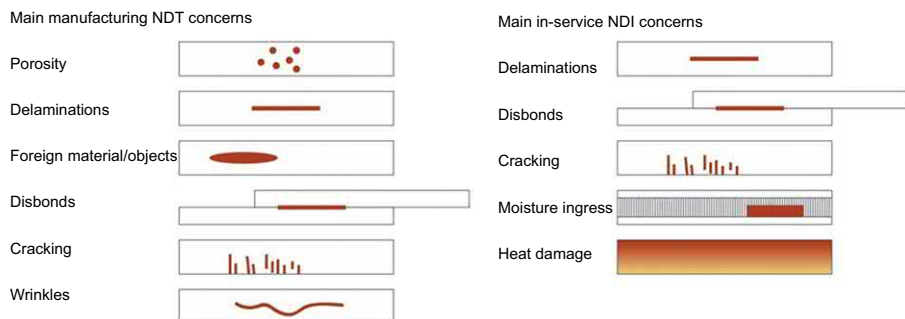
Figure 16.1 Primary defects of interest at the time of manufacturing and in-service.

The NDT technology that will be applied may be different for the two scenarios: at manufacture or in-service. At manufacture, the defect size criteria are smaller than the criteria that will be applied in-service. Porosity and wrinkles will not develop in-service, so sensitivity to them is not necessary for the field. If a repair is made, then the repair will be inspected with concern for porosity and wrinkles. At the time of manufacture, there will be the opportunity to have NDT equipment designed to be specifically suited to inspect the product form. This equipment can be fully automated, have high resolution, and must operate at sufficient speed to keep up with the production rate. In the field, the inspections may need to be performed in difficult-to-access locations and harsh environments. Field inspections will also need to be carried out at low cost and relatively quickly.

The form of the structure determines the types of features of concern and the NDT techniques that may be applied to detect and measure them. Table 16.1 summarizes some general thoughts and considerations on the NDT of polymer composite structure. ASTM also provides guidance on NDT for polymer composites [1]. Ultrasound is the predominate method for composite laminate inspection, especially during manufacture. In sandwich structure, the core material-to-face sheet bond, core condition, and fluid ingress are the usual concerns, and a range of NDT methods can be selected to address them.

Ultrasound inspection is used at the time of manufacture for sandwich structure, but tap testing and low-frequency bond testers are perhaps the predominate methods for sandwich structure in-service inspection, with radiography, thermography, and shearography being used in a number of applications. Shearography and thermography are used for sandwich and laminate structures, and usually for in-service applications with some production applications. Acoustic emission is used during structural load testing. Table 16.1 also identifies 3D polymer structure and bonds as additional categories. The baseline techniques of visual, ultrasound, thermography, shearography, and radiography apply to these forms, but do have some differences in application because of the configuration and the type and morphology of features to be detected.

The combination of the material form, the structure type, manufacturing process control, and whether the inspection is performed at the time of production or later in-service will all influence the selection of the specifics of the NDT method and inspection criteria. Structure shape and defect orientation play large roles in the selection of the method and the specific instrument variations. For example, radii inspection at the web to caps or flanges for stringers, ribs, and spars are critical locations for defect detection but also represent a difficult region for inspection coverage. Table 16.2 provides a summary that considers the effectiveness of the various NDT methods for finding defects of interest. Even for recommended methods, Table 16.2 is subject to a number of caveats depending on part specifics such as thickness, geometry, and location of the defect. Those listed as limited applicability may be successful under some circumstance, but generally, are not recommended or included in the specification. Some of these issues will be mentioned in the next section on methods discussion.

Table 16.1 Polymer composite inspection.

Category of polymer composite	Inspection issues	Comments on NDT inspection methods

Laminate
  Hand layup
  Tape layup
  Fiber placement
  Resin transfer molding
	At manufacture
	  Consolidation,
	  Porosity,
	  Fiber to resin ratio,
	  Inclusions,
	  Microcracks
	  Delamination,
	  Wrinkles
	In-service
	  Impact damage
	  Heat damage
	  Lightning strike
		• Visual - Visually inspect the surface for dry plies, wrinkles, and other surface damage. Strong backlighting visual inspection is often used on fiberglass for detection of voids, resin pockets and cracking
		• Tap testing − Coin tapping on laminate structure is not recommended but will detect near-surface internal damage if it is of sufficient size.
		• Ultrasound - Through Transmission Ultrasound (TTU) or Pulse Echo (PE) ultrasound is the primary method for the acceptance of composite laminate materials using an automated scanning system with water coupled piezoelectric transducers and acceptance standards. Many variations are applicable depending on the material, configuration, thickness, and sensitivity requirements.
		• X-ray − Radiography can be used for engineering evaluation for cracking, density variations, and tracer yarn detection for ply orientation. Computed tomography (CT) is used for complex structure configurations for assembly, density, and delamination.
		• Thermography - Thermography is sensitive to delamination and inclusions. It is applicable to relatively thin (<0.1 inch) materials.
		• Acoustic Emission (AE) − AE is used for pressure vessel testing and structural health monitoring.
		• Shearography - Shearography is used for impact damage, wrinkles, delamination, fiber bridging
		• Electromagnetic - Eddy current is not commonly applied to composites, but does have sensitivity to fiber and matrix variations. Microwave and other electromagnetic methods are applicable to glass fiber composites and can be sensitive to moisture or resin degradation effects.

Continued

Table 16.1 Continued

Category of polymer composite	Inspection issues	Comments on NDT inspection methods

Sandwich
  Honeycomb core
  Foam core
	At manufacture
	  Face sheet consolidation,
	  Face sheet to core bond,
	  Crushed core
	  Inclusions,
	  Wrinkles
	In-service
	  Moisture ingress
	  Impact damage
	  Environmental damage
	  Lightning strike
		• Visual - Visually inspect surface for dry plies, wrinkles, and other surface damage.
		• Tap testing − Tapping for face sheet delamination and fluid ingress is common but only recommended for thin (3−5 ply for example) face sheets.
		• Ultrasound - TTU is the primary method for sandwich structure at manufacture. In-service resonance or bond testing methods are common.
		• X-ray - Radiography can be used for face sheet to core fillet quality, crushed core, and moisture ingress.
		• Thermography −Thermography detects damage and water ingress.
		• Shearography - Shearography can be used to detect damage, delamination, water ingress

3D performs and other forms such as braided, stitched, chopped fiber or tape	At manufacture
	  Porosity
	  Resin pockets
	In-service
	  Impact damage
	  Environmental damage
		• Visual - Visually inspect for surface conditions.
		• X-ray − Radiography for density variations and computed tomography (CT) for complex structure configurations.
		• Ultrasound - TTU or PE ultrasound may be used but can be difficult to penetrate some 3D forms.

Bonds
  Film or paste
  Secondary or co-bond
	At manufacture
	  Unbond
	  Porosity
	  Thickness
	In-service
	  Disbond
		• Ultrasound − TTU or PE validates the bond is completed. Bond testers check for disbonds.
		• X-ray − Radiography can be used to detect voids in bonded joints.
		• Thermography − Thermography detects disbonds.
		• Shearography - Shearography can detect some types of poorly bonded and disbonded elements.

Table 16.2 NDT method applications for composites (R, Recommended; L, limited applicability).

NDT method	Porosity	Laminate delamination/ disbond	Skin to core disbond	Cracks	Surface damage	Water ingress	Wrinkles
Visual					R		R
Tap test		L	R				
Ultrasound TTU	R	R	R			R	
Ultrasound PE	R	R		L			R
Bond testers		R	R			L	
Radiography	L	L		R		R	L
Thermography	L	R	R			R	
Shearography	L	R	R			L	L
Electromagnetic		L		L			
Acoustic emission[a]		R		R			

[a]requires loading of the structure.

16.3 Probability of detection

The selection of any NDT method for a particular inspection will be due to some extent on the probability of detection (POD) for that method. The POD is a measure of the reliability of the method to detect a particular type of flaw size [2,3]. POD curves are created from empirical studies to show the reliability of a method for the detection of features or defects. A useful curve for POD's is the 90% POD with 95% confidence, referred to as 90/95 POD. Fig. 16.2 is a notional POD curve which shows how one method may perform more reliably than another for the detection of particular flaw sizes. Probability of detection curves can be expensive to experimentally develop because they require test samples with known defect sizes and numerous inspection tests by different operators to develop credible statistics. Model assisted based POD methods are being developed to reduce this burden [4].

Depending on the requirements and costs, one method may be chosen over another, provided it registers sufficient reliability. For example, while visual inspection is unreliable for small defects compared to an instrument inspection, in some aerospace in-service applications it can be more cost-effective or practical to use visual inspection on a frequent basis than a more sensitive and costly instrument inspection less frequently to achieve the same service reliability of a component. It is common to specify that inspections require a signal to noise of SNR > 2.5 for the system sensitivity to the detection criteria of designated features in a calibration standard. Under a normal curve distribution, this would provide better than 98.7% detectability.
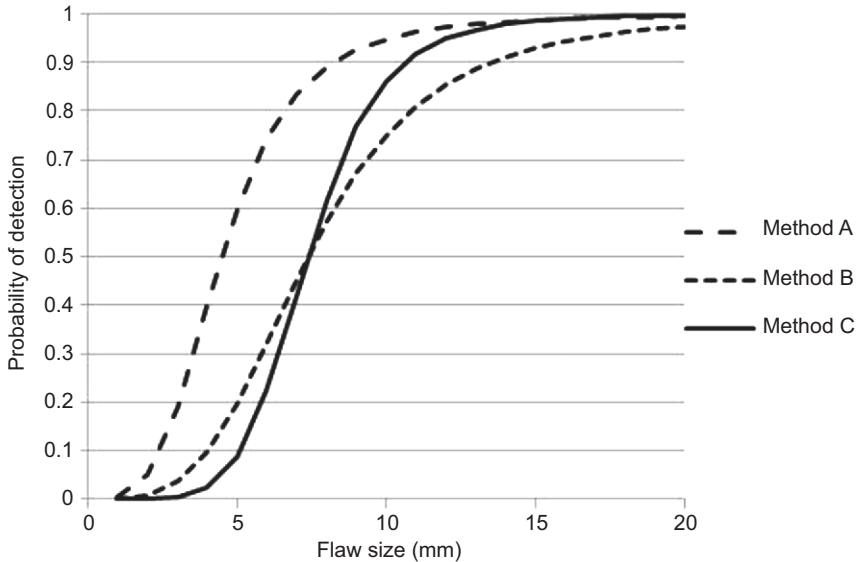
Figure 16.2 Notional probability of detection curve for three methods.

16.4 Visual and tap testing

Visual inspection/observation and recording is a fundamental task of the QA activity in the polymer composite processing activities and specification requirements. Visual testing of the finished surface in polymer composites is important not only as an inspection in itself but as an aid to any required additional instrumented NDT. Visual inspection is primarily performed at optical wavelengths suitable for the human eye. The principal features of interest are surface damage, surface porosity, dry ply, mark-off, bow waves, resin-rich areas, and wrinkles [5,6]. Surface damage may be in the form of indentations or cracks. Dry ply is a surface condition where fibers are not covered by sufficient resin, leaving very small pockets on the surface which can become surface porosity. Mark-off can be resin-dominated ridges formed by improper tooling or bagging. Bow waves are material waviness near edges or step changes. Resin rich surface zones are indicative of nonuniformity or subsurface variations such as wrinkles. Wrinkles can be visually detected if they extend to the edge of the part, and the edge is trimmed. They can also be detected on the surface as a slight out-of-plane change or by a slight change in the fiber or resin pattern of the surface layer.

Illumination is a critical issue for visual inspection, particularly the intensity and angle of the light. It is important to orient the light to optimize detection. Visual inspection may be enhanced by additional tools such as borescopes for looking into cavities and magnifiers or microscopes for close up inspections. Camera recording is an additional important visual inspection that can be performed as a part of composite fabrication monitoring activities. Digital video magnifiers and video borescopes are effective tools for improving detail inspections. One additional method that is of particular interest is digital image correlation. This method uses two cameras oriented for parallax imaging of surface patterns on a test object. The relative motion of the surface patterns by the two cameras during loading or mechanical testing can be used to calculate a full-field surface strain that provides much greater information on the part performance than discreet strain sensors [7,8].

While not actually a visual test, tap testing is often performed in junction with visual testing. A coin is often used. However, NDT personnel have developed specific tools for tapping to assist them. In the tapping method, the inspector listens for a lower frequency thud to indicate a structural defect such as delaminations. Solid structures should have a higher frequency ring. The method is particularly effective on honeycomb structure with a thin (3−6 ply) skin to determine when a disbond has occurred. As the thickness increases the sensitivity decreases. Tap testing should not be used on composite laminates greater than 1 mm thick [9]. Instrumented tap testers are also available that provide quantitative information that may improve defect sensitivity in some cases [10,11].

16.5 Ultrasonic testing

Ultrasonic testing (UT) uses mechanical waves to test objects for their quality. The ultrasound wave is generated by mechanical vibration from a transducer that

converts an electrical signal into mechanical motion and vice versa. By inputting a short pulse of electrical energy or a tone burst to the transducer, it generates a pressure pulse that—when coupled to the composite part—will create an ultrasound wave in the structure under test. The wave will travel in the composite material at a particular frequency band and velocity. For the most common specifications for composite inspection, the center frequency used will usually be between 1 and 5 MHz. The typical velocity of the ultrasound across the laminate stack is close to 2.8 mm/μs. At 1 MHz, this represents a wavelength of 2.8 mm and at 5 MHz a wavelength of 0.56 mm. Common composite ply thickness could be in the range of 0.1−0.35 mm. Higher frequencies will reduce the wavelength, making the inspection more sensitive to small features and interpretation of individual plies but at the expense of signal penetration depth. The frequency and wavelength are related by

$$\lambda = f/c \tag{16.1}$$

where λ is the wavelength, f is the frequency, and c is the wave speed. The transmission of the ultrasound is subject to attenuation that is represented by

$$A = A_0 e^{-\alpha x} \tag{16.2}$$

where A is the pressure amplitude after transmission, A_0 is the initial pressure amplitude, α is the attenuation coefficient in nepers per unit distance, and x is the transmitted distance [12]. The attenuation of ultrasound through a composite is a measure of material consolidation. From Eq. (16.2), the attenuation over a distance x can be calculated as

$$\text{UT attenuation} = \alpha x = \ln(A_0/A) \tag{16.3}$$

In practice, ultrasound attenuation is measured in decibel (dB) units and hence

$$\text{UT attenuation in dB} = 20 \log_{10}(A_0/A) \tag{16.4}$$

A change of signal strength by a factor of 2 is 6 dB, and by a factor of 10 is 20 dB. The attenuation of the ultrasound depends on frequency. For example, at 5 MHz in a composite laminate, the attenuation could be in the range of 1.5−2 dB/mm while at 1 MHz, the values could be half of that. The values are subject to the specifics of the fibers, resin, fiber to resin ratio, ply type, and layup. They are also subject to specifics of the ultrasonic inspection equipment. As consolidation is compromised by porosity, the attenuation will increase. The measurement of porosity level by ultrasonic attenuation is used for acceptance of the composite product. Calibration curves must be developed for the specific equipment and the level of dB loss as a function of porosity for each thickness of composite established. A typical criterion is that less than 2% porosity is acceptable for the manufacturing processes. Greater than 4% porosity can result in a significant knockdown in performance.

The detection of features in composite laminate, such as delamination or inclusions is a function of the transmission or reflection of the ultrasound across the material. This is dependent on the acoustic impedance difference between the materials at the feature interface. The acoustic impedance Z is defined as

$$Z = \rho v \tag{16.5}$$

where ρ is material density and v is the particle velocity (aka, acoustic velocity). The transmission pressure amplitude at an interface is given by

$$T = 2Z_2/(Z_2 + Z_1) \tag{16.6}$$

and the reflection pressure amplitude is given by

$$R = (Z_2 - Z_1)/(Z_2 + Z_1) \tag{16.7}$$

where Z_1 is the acoustic impedance of the first material and Z_2 is the acoustic impedance of the second material at the interface [13]. The acoustic impedance of a polymer composite, for example, is on the order of 470,000 g/cm^2-s while air is only 40 g/cm^2-s. In view of Eqs. (16.6 and 16.7), a composite to air interface will have a transmission pressure coefficient of 0.00,017 and a reflection pressure coefficient of 0.9998. This very low transmission and very high reflection explain why de-laminations are easy to detect with ultrasound. Inclusions that are not bonded into the composite will be easy to detect. However, inclusions will only be detectable depending on the significance of the acoustic impedance difference with the composite.

16.5.1 UT methods

UT includes many variants. The principal methods of ultrasound include through transmission ultrasound (TTU), pulse-echo (PE), and pitch-catch. Additionally, ultra-sound methods can include guided wave, resonance, and bond testing methods. Within these designations are a number of subtle distinctions on what can be done and how the signal can be used. Fig. 16.3 roughly shows the configuration of TTU, PE, Pitch Catch, and guided waves methods.

The TTU method is one of the most frequently used methods for UT of composites. In this method, an ultrasonic signal is sent from a transmitting transducer to a receiving transducer penetrating the composite to be inspected. The signal strength received is a measure of the part quality as measured by the acoustic attenuation. Decreasing quality by such effects as porosity, inclusions, wrinkles, etc. will increase the acoustic atten-uation and reduce the measured signal strength. Decreasing the ultrasound frequency from, say, 5−1 MHz will also decrease the attenuation of the composite, making the inspection method more penetrating for thicker composites, but also less sensitive to subtle features such as some types of inclusions. Delamination and disbonds will
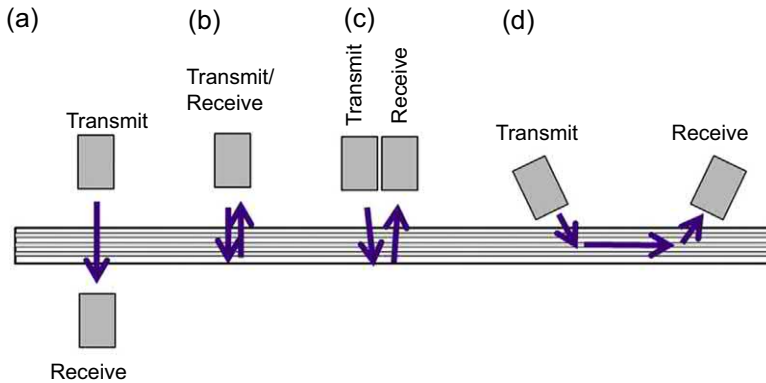
Figure 16.3 Typical ultrasonic configurations: (a) TTU; (b) PE; (c) Pitch Catch and (d) guided waves.

nearly block the signal making them easy to detect. The penetration power of TTU makes it particularly useful for sandwich structure composites with honeycomb or foam cores or very thick or attenuative structure. The drawback to TTU is that access to both sides of the part is required. The two transducers must be aligned with each other and also be normal to the surface such that the scanning system must maintain the orientation on curved parts. The signal that is detected by the receiving transducer is usually plotted as a function of position and is called a *C-scan* display. The TTU *C-scan* display will show where a feature may be located in the surface area of a part, but it does not indicate the depth of the feature.

The PE method is one-sided, using a single transducer as both the transmitter and the receiver. At any single point, the output that is obtained is called an *A-scan*, which is a plot of signal amplitude versus time. The *A-scan* is commonly used by inspectors to interpret the condition of the part under examination. The signal is a time base response from reflections within the part. The typical interpretation is to check for a strong echo from the back wall of the part to show good transmission. Also, the inspector will look for echo indications from internal locations between the front surface and the back wall in the part to indicate inclusions or delamination. If the part has porosity, the back wall echo will be reduced or lost, although there may not be a significant reflection from the scattered internal porosity as there could be from an inclusion or delamination. Interpretation of the *A-scan* will provide the depth location of defects from the "time of flight" (TOF) display based on the velocity of the material. The interpretation of the strength of an internal reflection signal relative to the loss of the back signal reflection is used by inspectors to assess the defect type.

The PE method can be used with a handheld instrument at any particular point on a part, or in a scanning mode with the transducer, either riding on the surface, moved in a water tank or scanned with a water squirter system. When a one dimensional (line) scan is made and an image of distance versus time with the signal amplitude shown in gray scale the output is called a *B-scan*. *B-scans* are useful for identifying internal
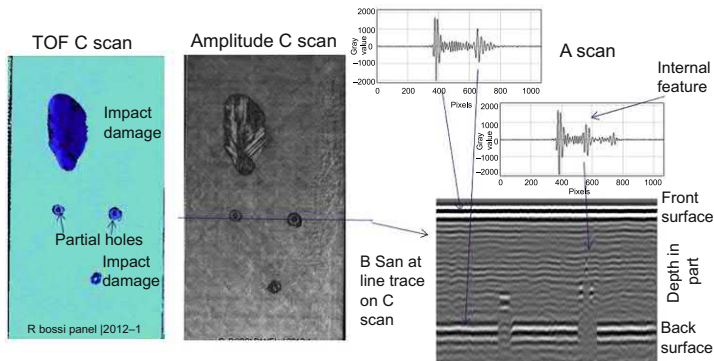
Figure 16.4 Ultrasonic signal display options of *A, B, and C-scans*.

echo locations produced by inclusions, feature steps in part, such as ply drops, or out of plane distortions, such as wrinkles. In standard ultrasonic system electronics there will be a "time gate" that will zone regions of the *A-scan* where an amplitude will be measured. When a value from the time gate, such as the signal intensity at the back wall of the part, is plotted as a function of x and y position on the part, the output is called an amplitude *C-scan*, which is similar to the TTU *C-scan*. The gate may also be an internal gate between the front and back wall, or a full gate that is the signal after the front surface but includes the back wall. A signal, such as a peak value, in the gate, will be recorded for the *C-scan* display. The *C-scans* from these different gate configurations may be slightly different depending on the defect type and its effect on the reflected signal. Another common plot is the TOF *C-scan*, where the grayscale is the depth (the time between the near surface and return signals multiplied by velocity and divided by two) in the part at which the reflected signal is greater than a prescribed threshold above the noise floor. Often inspectors display both the amplitude and TOF *C-scans* to interpret the data. In PE mode applications, the placement of the gate and threshold level can make a significant difference in the ability to detect defects of interest. Specifications, standards, and procedures established by designated experts (NDT Level III) are used to calibrate inspection systems to be sure the settings will result in images of sufficient sensitivity to critical defect types. Fig. 16.4 shows these differences in data display used for interpretation of the features detected in a 22 ply composite laminate containing two impact areas and two partially drilled holes.

In the pitch-catch method, two ultrasound transducers are used, one as a transmitter and one as a receiver. However, unlike the TTU method, the pitch-catch transducers may be on the same side of the part or oriented in a number of ways for the ultrasound to progress from one transducer to the other. The interpretation is usually based on changes in detected signal strength or frequency and calibrated against a known test sample.

Ultrasound can operate in a variety of modes, including longitudinal, transverse, guided waves, or surface waves [14,15]. Of these modes, the longitudinal wave is the most common used for TTU and PE *C-scans* for composites. Transverse waves

are often used in metallic inspections, such as welds because of the generally isotropic behavior of metals and the shorter wavelength of shear waves relative to longitudinal waves to provide higher sensitivity. For polymer composites, the significant anisotropy in the layup makes shear waves more difficult to use effectively. Guided waves, which include Lamb waves, are used in composite inspection. These waves are sometimes referred to as structural waves and can require considerable interpretation when used for NDT. Guided waves are discussed in the SHM chapter of this book. Surface or Rayleigh waves are useful for detecting surface cracks in metals but have not seen much application for composites.

Two other options for ultrasound that are commonly used are resonance and bond testing, both of which use lower frequencies than TTU or PE and are used almost exclusively for in-service applications. In the resonance mode, the ultrasonic transducer is used in a continuous or repeated tone burst operation. Placing the transducer on a part will cause an impedance change to the transducer operation. The impedance effect is picked up as a change in the amplitude and phase of the transducer signal as it is moved over the part. Resonance scanning can be very sensitive to changes in the composite thickness or sandwich structure quality. The frequency used for resonance inspection is usually in the low hundreds of kilohertz. In the bond testing instrument configuration, a pitch-catch arrangement is typically used with low-frequency transmission, often in the tens of kilohertz range, from the transmitter to the receiver on a single side of the structure. Bond testing is most applicable to thin laminate layers bonded to other structure, such as the face sheets of a sandwich structure.

As mentioned earlier, ultrasound for composite inspection is most commonly generated by piezoelectric transducers that convert electrical signals into mechanical motion and vice versa. The generated frequency is controlled by the crystal thickness of the piezoelectric, the construction of the transducer housing, and the electrical signal characteristics. The transducers can be made in a variety of sizes and with lenses for focusing the ultrasound if desired. Larger diameter transducers will have greater power but may not be suited for small feature detection or operation near edges. Transducers with beams in the 6−12 mm diameter (0.25−0.5 inch) range are commonly used in composite inspections. For detailed inspections, they may be focused to something on the order of 1−2 mm (0.04−0.08 inch) in size on a depth of interest in the part. Transducers are usually categorized as broadband or narrowband depending on whether they are damped to have a narrow pulse with broad frequency content or allowed to ring to have a higher output at a specific frequency. The broadband transducers are typically used for pulse-echo applications because they can resolve depth features, particularly at near and far surfaces. The narrow-band transducers offer significantly higher power and are useful for TTU applications on highly attenuative or thick structure. For efficient inspection, the ultrasound from the transducer must be coupled to the part. Typically, water coupling is used by either immersion scanning systems, water squirter, or bubbler systems. Fig. 16.5 shows examples of ultrasonic scanning systems for composites. In Fig. 16.5(a), the composite part is immersed in a water tank for scanning, which provides excellent coupling. Water bubbles must be removed from the tank and the surface of the part. In Fig. 16.5(b) water squirters

(a)   (b)
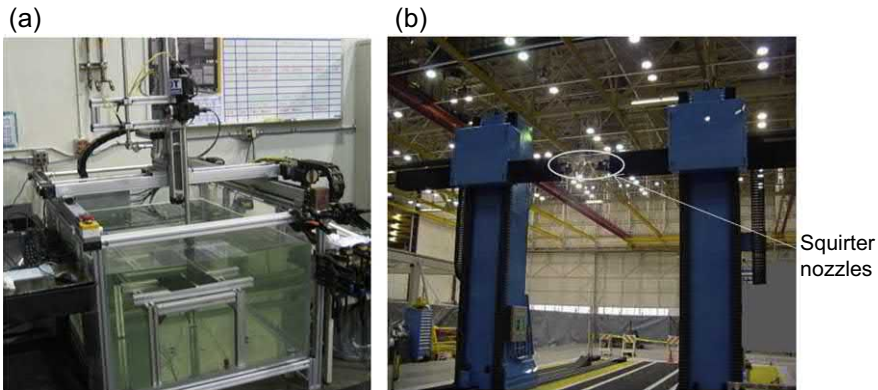
Squirter
nozzles

Figure 16.5 Example ultrasonic scanning systems (a) laboratory immersion tank with test samples, (b) water squirter.

that use high-pressure water flow around the transducer in a nozzle are attached at the end of a pair of opposing articulating arms on large gantry towers to stream the water coupling to the part. The water may include a surfactant to improve wetting, although that may not be allowed on many composites. Scanning may also be performed with a surface following transducer in contact or in a water bubbler such that there will be a water layer present on the composite surface for coupling. Sometimes it is sufficient to use a water mist on the surface and a transducer with a rubber shoe or housing to slide over the surface.

It is possible to use air as the coupling for a noncontact inspection using piezo-electric transducers. The noncontact application of ultrasound is desirable to avoid the issues with water couplant systems involving the handling of the water and uni-form surface wetting. However, the high impedance mismatch between air and solids causes a significant loss of acoustic energy at the interface resulting in poorer signal to noise available for the inspection. At low frequency, 50−500 kHz, transducers can be made that will transmit sufficient intensity to be useful. Air coupled ultrasound is used on sandwich structure applications, where lower frequencies are typically used anyway, and where critical defect sizes may be relatively large, on the order of 25 mm (1 inch).

The rate of automated inspection of parts using mechanical scanning systems will depend on the pulse repetition rate of the transducer, the required data spacing for feature detection, and the speed of the mechanical system. In most cases, the time of transit through the part for inspection will be a few to tens of microseconds, which means that pulse repetition rates of tens to possibly hundreds of kilohertz would be acceptable. The data spacing for most composite inspection is usually one-third of the smallest required feature size detection. This means that for a minimum feature detection on the order of 6 mm (0.25 inches) the data spacing would be 2 mm (0.080 inches). Finer data spacing is used in development activities or for interpreta-tion of detected abnormal features. Depending on how often the mechanical scanner must change direction, the overall composite inspection will have a wide scanning

rate range. For single transducer scanning methods, the rate can be in the range of 10−40 square feet/hour. For increasing the rate, the scanning system may use multiple transducers arranged for specific purposes. In the case of composite structures that have radii, such as angle or I beams, transducer arrays may be set at prescribed orientations to be normal to the curvature at specific locations in the radii, and the part moved past them.

An improvement over the individual transducers is the phased array transducer systems that may have many elements such as 16 to over 128 elements in a linear arrangement [13,16]. The phased array electronic systems will pulse multiple small (e.g., 1 mm wide) elements in a timed sequence to create an ultrasonic beam with directional or focused properties based on the time phasing of the transducer pulses and the relative spacing of the elements. When phased array instruments use the phasing to send the beam at angles different from normal to the surface it is referred to as a sector or *S-scan*. When the array of transducers elements are pulsed with the intent of creating a sequence of normal beams to the surface, the array is performing an electronic or *E-scan*. Often the sequencing will utilize four to eight elements in the array for each beam and then step along the array to create the multiple ultrasonic beams in sequence. As an example, an array with 1.5 mm wide elements may pulse 4 elements simultaneously to create a 6 mm wide transducer beam. The pulsing sequence may be in steps as small as 1 element to create beams that are scanned at only 1.5 mm apart for fine resolution or stepped by four elements, so the beams are 6 mm apart depending on the needs of geometry in a particular part. With these methods, modern scanners can inspect composite structures with rates of over 150 square feet per hour, and in some cases, up to more than four times that amount [17]. It is possible to produce the transducer element in a 2D format, creating an area imager [18]. Such a device is particularly useful for rapid field inspection of small areas of suspected damage.

Another method of generating ultrasound uses the photothermoelastic effect from laser energy [19,20]. A laser pulse of proper wavelength and sufficient intensity on the surface of a composite will be absorbed and generate an ultrasonic pulse in the material. The surface motion from the ultrasound reflection signal can be detected by laser interferometric measurements. Laser UT has several advantages. The method is noncontact and can be quite rapid depending on the laser repetition rate (typically 100−600 Hz). The ultrasound is generated in the part normal to the surface although the beam may come from an angle, which makes the scanning of complex contour shapes very easy. The scanning system can use mirrors to scan the beam at a distance from the part, reducing the mechanical system. There is a limitation to the amount of off-normal angle that can be tolerated, so the systems usually cover approximately ±30 degrees before being repositioned for additional coverage on a part. For parts that are highly contoured or have sharp angles, a second scan is sometimes performed with a new orientation of the beam relative to the part. The drawbacks to laser UT are the higher system cost relative to piezoelectric systems, and limitations for the generation of ultrasound in some materials. Because it is only a one-sided approach, laser UT is not typically applicable to sandwich structure for the core inspection.

16.6   Thermography

Thermography or infrared testing uses the heat transfer rate of materials as a means to detect subsurface features by measurement of the surface temperature or surface temperature rates of change [1,21]. For the aerospace industry, composite inspection thermography has generally not been chosen as the manufacturing inspection method of choice because of the limitations in the sensitivity to measure porosity and inclusions at specification levels for critical structure. In less critical applications, thermography may be applied at the manufacturing level. Once a composite part has been put into service, thermography can be very useful for the detection of in-service damage, where porosity or inclusions are not relevant defects. Impact damage causing delamination and cracks in composite laminate, sandwich structure disbonds, or honeycomb water ingress are excellent applications of thermography.

Thermography is usually performed as an area inspection and can be relatively fast. The method requires some form of stimulation to the sample that generates heat, and then a measurement of the surface irradiance or temperature. Fig. 16.6 shows the basic effect of thermography that is used to assess material conditions. A surface is heated in some manner in Fig. 16.6(a). That surface will emit infrared radiation (Fig. 16.6(b)). As heat is transferred internally in the part, the surface emissions will change with time. As shown in Fig. 16.6(c), if an internal feature exists, it will alter the heat flow, resulting in a change in the surface infrared emission. An infrared camera is the most common method of measurement of the surface temperature within a field of view over time. A general rule of thumb for thermography, due to the heat flow effects, is that the size of the feature that needs to be detected should be greater than its depth in the part.

Thermography may be applied passively or actively. In the passive mode, heating by natural surroundings can be used as the source. For example, as an aircraft coming down from high altitude warms up, thermographic images of the structure can be used to visualize some subsurface conditions. In the active mode, various moderate heat sources or controlled rate sources may be used. In many cases, moderate heating with a hairdryer or heat blanket for a few seconds is sufficient in generating heat into a composite for sufficient sensitivity to detect subsurface features. Sandwich structure is often inspected in this manner. Controlled heat sources can be used in a method called lock-in thermography where the heat source, such as a halogen lamp, is used
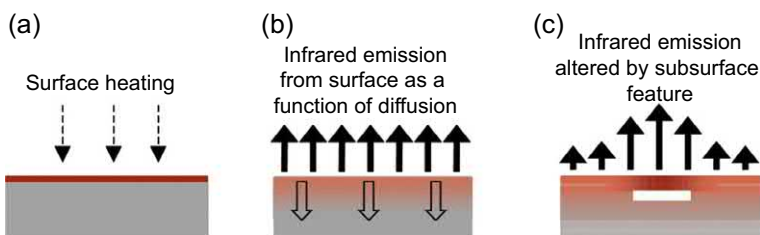
Figure 16.6 Thermographic inspection method (a) surface heating, (b) surface emission and heat transfer, (c) effect of an internal feature on surface emission.

with a temporal variation of input to the surface that has the effect of creating a phase lag in the camera images between areas of features and background [22]. The lock-in thermography method is effective for separating out surface emissivity effects of the sample and optimizing the sensitivity to a particular depth in a part based on the rate of heat input fluctuation and the heat transfer in the part. The lock-in method may require more sampling time than other thermography methods in order to maximize sensitivity and detect small defects deep in a part.

Perhaps the most common method of controlled active thermography for composites is flash thermography where a very short time burst of energy is used to impart heat onto the surface. The transient surface temperature will then be monitored by the infrared camera.

In the flash thermography application, the surface temperature change with time is given by

$$T_s(t) - T_s(0) = Q/K\rho C(\pi t)^{1/2} \tag{16.8}$$

where T_s is the surface temperature, t is the time, Q is the input energy, K is the thermal conductivity, ρ is the density, and C is the specific heat of the material. The change in temperature with time will be a straight line on a logarithmic plot with a slope of 0.5. However, when a discontinuity or the back surface is encountered, the slope will change. Using Thermographic Signal Reconstruction (TSR) from the sequence of thermographic images taken on the infrared camera, a significant improvement in sensitivity can be obtained for thermography [22]. The processing of the images is a pixel by pixel assembly of the surface temperature decay. This curve can then be interpreted by differentiation for the first derivative inflection point and second derivative maximum. This data can be used to tell the time at which an inflection occurred, and thus the depth of the internal feature or back wall.

The rate of heat transfer in composites is particularly suited to this TSR method of inspection, and the resulting highly sensitive images can be obtained over the area of inspection in a few seconds. Fig. 16.7 shows the thermographic TSR second derivative image of the 22 ply (4 mm thick) composite sample from Fig. 16.4 with subsurface features. Fig. 16.7 includes a picture of the thermography system, curves of the temperature decay with time for regions in the sample and an image of the second derivative of the temperature decay at about 16 s after the pulse. Fig. 16.8 shows both a radiographic and a thermographic image of a honeycomb sandwich structure with water ingress. While the radiographic image provides finer detail in this case, the difficulty of the inspection relative to the speed and ease of thermography makes thermography of interest wherever it is demonstrated to have sufficient sensitivity.

In recent years, composite fabricators have considered the use of infrared thermography as a tool for in-process monitoring. Of particular interest is the monitoring of green plies for Foreign Object Debris (FOD). In-process IR thermography has been shown to be very effective for finding FOD. Fig. 16.9 shows how much better IR can detect a tape layer, even subsurface, than a visual image.
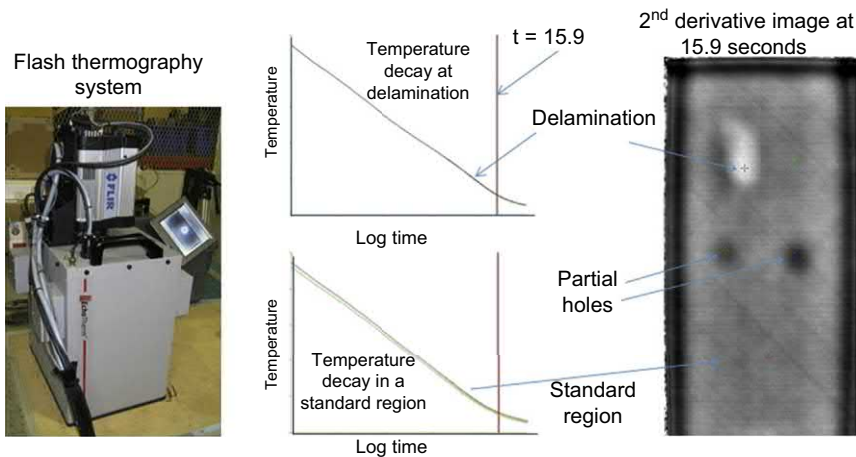
Figure 16.7 Example thermographic inspection of a composite sample.
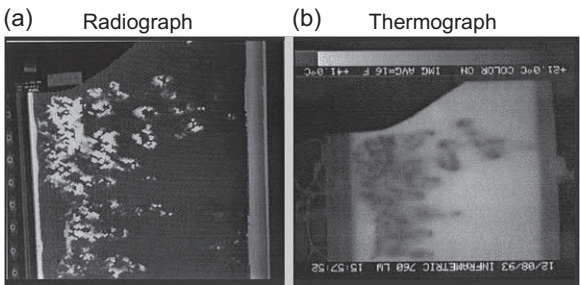
Figure 16.8 Example inspection of composite honeycomb with water inclusion comparing a radiographic and thermographic image.
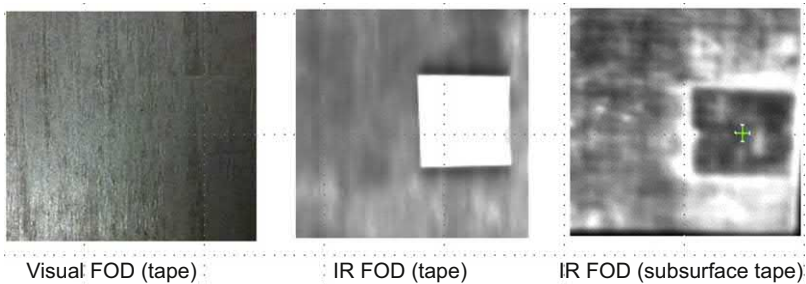
Figure 16.9 IR imaging on surface and subsurface plies enhance the detectability of FOD during composite ply or fiber placement application compared to visual.

Figure 16.10 Dynamic IR thermography system schematic using a line heater to monitor for on-surface or near-surface defects.
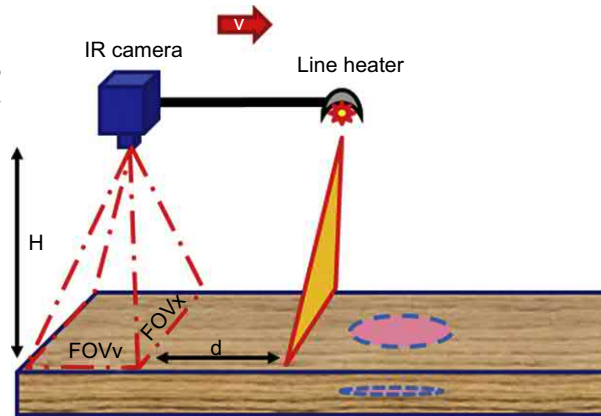
End-item FOD detection requires higher UT detection sensitivities than delaminations or disbonds do. If avoidance of FOD can be assured during fabrication, UT inspection requirements can be relaxed, which simplifies and reduces end item inspection time, and enables quick repair in the green stage rather than the much more costly repair of a cured part. IR FOD detection feasibility has been demonstrated on a composite aerospace structure for essentially all of the FOD of interest, for the allowable flaw size.

A dynamic thermal imaging schema is shown in Fig. 16.10 for ply by ply FOD inspection. By using IR cameras mounted on gantries, a ply laydown can be inspected for FOD at speeds on the order of 100 in/s. A line of heat is used to generate a thermal response that is imaged using a stand-off IR camera positioned a selected distance (d) behind the heat line. Automated defect recognition algorithms that size and locate FOD in near real-time can be used.

Subsurface (beneath a ply or two) FOD, fuzzballs and "void-like" layup anomalies are detected in addition to surface FOD. Examples of gaps, porosity, twisted plies, and ply ends are shown in Fig. 16.11. Thermal signatures of these various features permit anomaly classification and on-the-fly decision-making. The result is that the IR thermography FOD scanning system also eliminates the need for time-consuming and labor-intensive manual visual inspection for anomalies between applied layers of composite.

16.7 Shearography

Shearography is an optical interferometric technique that is finding increasing application for composite inspection [23,24]. Fig. 16.12 shows a schematic of the shearography process. Coherent laser light is scattered from the test surface and passed through a shearing optic that splits the scene into two identical but displaced images before the image is focused on the detector. Each resolution element of the detector receives
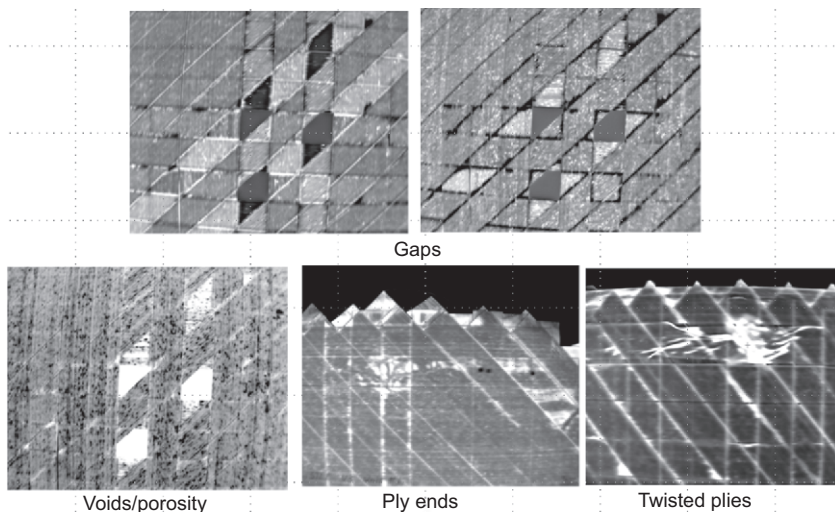
Figure 16.11 Various types of in-process flaws that can be rapidly detected with IR thermography.

energy from two distinctly different locations on of surface being imaged. The separation distance and direction between two positions on the object create the shear vector. The light from each point will be focused on the same pixel in the CCD camera by the shearing optic consisting of the beam splitter and adjustable mirrors creating interference. When the object is stressed the two points that contribute to the speckle phase information at a resolution element undergo an out-of-plane motion relative to each other altering the phase relationship of the light and changing the intensity response in the image. The difference before and after stressing will show surface displacement indications that can identify subsurface features.

The stressing of the part may be performed by several means, such as vacuum, thermal, or vibration loading. In production, shearography is most often used with vacuum rooms, pulling only 1 or 2 psi. For in-service applications, shearography is used with vacuum heads, thermal heating, or vibration. Shearography is most useful on honeycomb and foam structures. It can detect features in the laminate to 0.1″ depth and sometimes more. Fig. 16.13 shows the use of a large shearography system on the
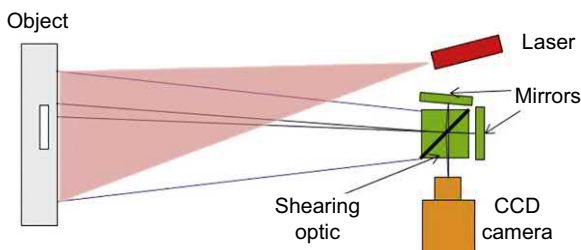
Figure 16.12 Configuration for a shearography system.

(a)   (b)

Shearography system   Image of disbonds
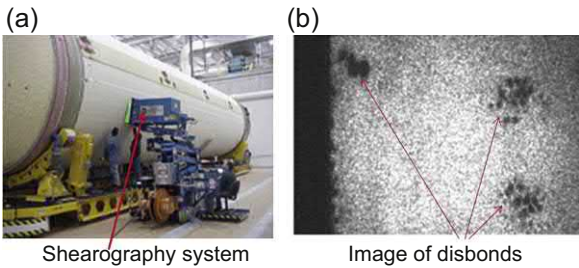
Figure 16.13 Shearography examples: (a) shearography system inspecting a rocket body, (b) shearography image shows foam insulation disbonds.

exterior of a rocket body checking for bonded insulation defects. The associated image shows disbonds of the outer foam insulation from the skin. Much smaller and portable shearography systems are available for field inspections.

16.8   Radiography

Radiography uses penetrating radiation to inspect materials for changes in density or thickness [25]. Fig. 16.14 shows how X-ray transmission through an object will change its intensity as a function of an internal void. The transmitted beam intensity is recorded by an imaging detector system, such as a film or a digital imaging system. The general equation for the attenuation of the radiation beam is given by

$$I(E) = I_0(E)e^{-\mu(E)x} \tag{16.9}$$

where $I(E)$ is the transmitted beam intensity as a function of energy E, $I_0(E)$ is the initial X-ray beam spectrum intensity, $\mu(E)$ is the material linear attenuation
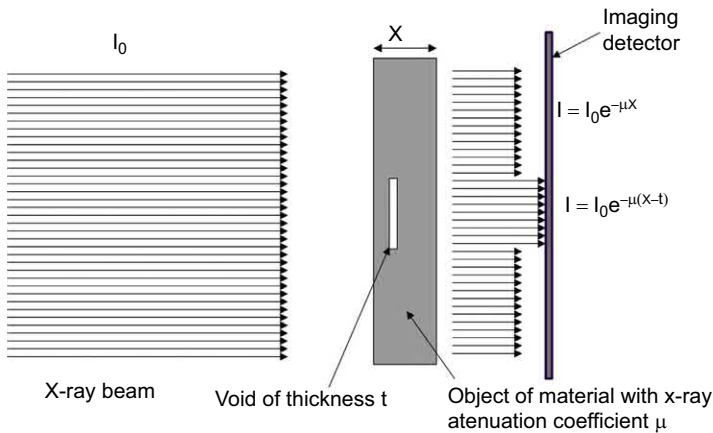
Figure 16.14 X-ray transmission through a sample for detection of internal features.
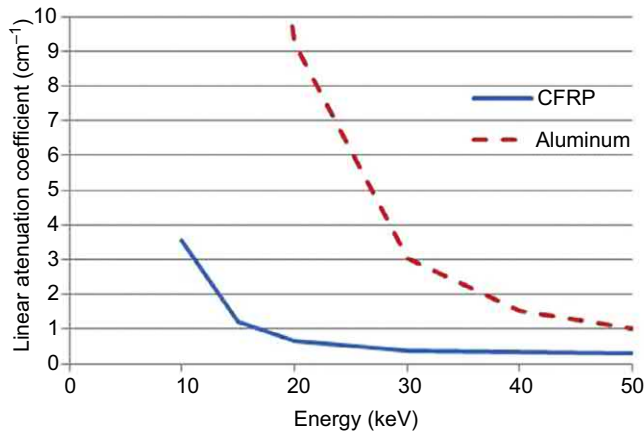
Figure 16.15 X-ray linear attenuation coefficient estimates for CFRP and aluminum.

coefficient, and x is the thickness. In most cases, μ is closely related to material density and radiography is referred to as a "density multiplied by thickness" measurement due to the μx term in the exponent. Because μ is a function of energy, the sensitivity of X-ray inspection is dependent on the X-ray energy chosen for the inspection.

Fig. 16.15 shows a plot of estimated linear attenuation coefficients up to 50 keV for Carbon Fiber Reinforced Plastic (CFRP) and aluminum. At an effective energy of approximately 20 keV the attenuation coefficient for CFRP is of the order of $0.66\ cm^{-1}$. By differentiating Eq. (16.9)

$$dI/dx = -\mu I_0 e^{-\mu x} \tag{16.10}$$

and upon rearrangement, Eq. (16.10) becomes

$$dI/I = -\mu\, dx \tag{16.11}$$

an approximate 1 ply (approx. 0.19 mm) change in thickness will represent about a 1.2% change in intensity.

While radiography can be very sensitive to volumetric features, it is not sensitive to planar defects such as delamination. Fig. 16.16 shows a digital X-ray arrangement and radiograph of the CFRP panel from Figs. 16.4 and 16.7. The 22 ply panel contains 20 plies of CFRP tape and 1 ply of fiberglass fabric on each side. The partial holes are clearly detectable, but the delamination for impact damage is not. A penetrameter of 0.125 mm thickness is included in the image to show the sensitivity, including the detection of holes in the penetrameter as small as 0.25 mm. When delaminations lead to cracking then radiography can detect the damage.

Although radiography is not usually selected for laminate damage detection, it is useful for volumetric features, such as water intrusion in a honeycomb sandwich
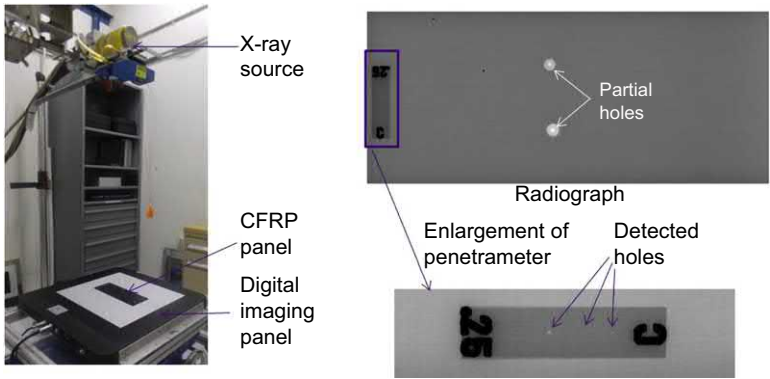
Figure 16.16 X-ray inspection example for CFRP panel.
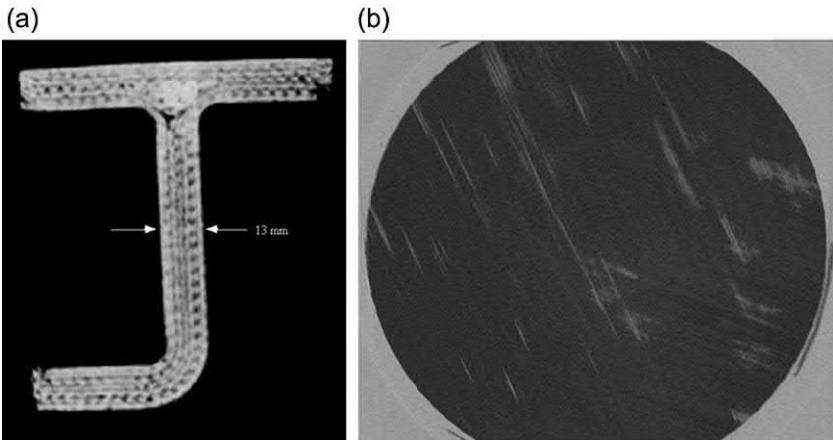
Figure 16.17 CT scan images of CFRP (a) woven J structure, (b) porosity in laminate.

structure as was shown in the example of Fig. 16.8(a). An extension of radiography for 3D volumetric inspection is computed tomography. In computed tomography, data is taken with many radiographic projection views from around an object, and the computer reconstructs the data to create a volumetric data set [26]. Image planes through the data set will reveal the internal configuration and material variations. The reconstructed image is basically a map of the linear attenuation coefficient of the sample in small volume elements. Fig. 16.17 shows two examples of CT images. Fig. 16.17(a) shows a woven J structure. Fig. 16.17(b) is a CT image of an approximately 20 mm diameter coupon from a laminate structure containing porosity. The CT slice cuts at a slight angle through two plies and the porosity lies along the fibers for each orientation.

16.9 Electromagnetic methods

Electromagnetic methods, such as eddy current, capacitance, microwaves, and tera-hertz radiation are not traditional inspection methods for composites, but they can be used in some circumstances [27]. Microwaves (300 MHz−300 GHz, 1000−1 mm) and terahertz (300 GHz−3 THz, 1−0.1 mm) are applicable to fiberglass composite inspection and have been successful at the detection of damage and internal features [28−36]. However, electromagnetic radiation at these wavelengths does not penetrate conductive materials. For CFRP, which is mildly conductive, they are only useful for sensing very near the surface. Capacitance measurements can be used to measure dielectric property changes in composites such as moisture uptake or cure condition.

Eddy current inspection is typically performed in metallic components for cracks or thickness inspections. The method uses a changing magnetic field to create eddy currents in the substrate under test. The eddy currents create a secondary field back in the eddy current coil. Changes in the substrate that affect the eddy current flow will alter the secondary electromagnetic fields, and therefore, affect the originating coil impedance. Measurement of the impedance changes of the initiating coil or of a separate pickup coil will allow the detection of material changes such as cracks. The standard depth of penetration for eddy current inspection is given by:

$$\delta = (\pi f \mu_r \mu_0 \sigma)^{-1/2} \tag{16.12}$$

where f is the coil operating frequency (Hz), μ_r is the relative permeability of the material being tested, μ_0 is the permeability of free space ($\mu_0 = 4\pi \times 10^{-7}$ H/m), and σ is the conductivity (S/m). The low conductivity of composites means that the inspection should penetrate into the material and could allow small high-frequency coils to be applied for penetration. Fig. 16.18 shows an example of scanning with an eddy current based system at 700 kHz on a cracked composite part. The part is a hat-stiffened skin with a crack along the edge of the hat. The eddy current scan shows the edges with a change in signal due to the cracking. The photograph is taken from what would be considered the back side, while the eddy current scan is taken from the skin side.

16.10 Bond inspection

The assembly of composite structural elements into a complete integrated structure will often involve bonding processes. These may be cobonds or secondary bonds. In cobonds, a cured composite is assembled with a film adhesive to an uncured laminate layup. The assembly is cured in an oven or autoclave. Secondary bonds are bonds between two cured laminates. The adhesive may be film or paste, and the cure may be in an oven or at room temperature. Composite repair following a damage event usually involves a cobond by scarfing out the damaged area, laying in a film adhesive, adding

Figure 16.18 Eddy current inspection of a cracked hat stiffener composite (a) photograph with the crack location marked in white (b) eddy current scan.

Photograph

Eddy current scan

Cracked edge
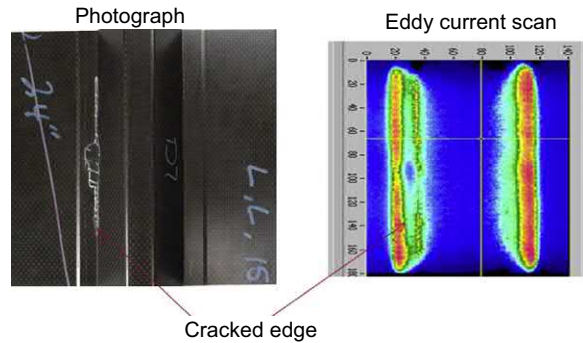
prepreg layers, bagging and curing. Cobonds and secondary bonds will be inspected by many of the methods used for laminate inspection, checking for voids or disbonds. The choice of method depends on the configuration.

The inspection of bonds may have an added requirement that the strength of the bonds be verified. This is often achieved by proof testing the structure or mechanically testing a witness coupon assembled simultaneous with the bond. The search for a nondestructive method to evaluate bonds for strength has been difficult. Numerous attempts have been made to find a correlation between ultrasonic or other NDT methods with bond strength [37−40]. Nondestructive methods have not been completely successful because the strength parameter is measured in the plastic regime of material while nondestructive testing is performed in the elastic regime. Sufficiently strong stress waves that can actually fail weak bonds have been found to provide a local proof test validation method to assess the adhesive strength in composite bonds [41−43].

16.11   Summary and conclusions

This chapter has discussed the modes of damage which can occur with polymer composites. Failure occurs progressively under tension, compression, or shear and polymer composites are particularly prone to low-velocity impacts, which may result in damage which is not obvious to the naked eye. This emphasizes the need to test polymer composite aircraft structures both at the time of manufacture and in-service. The methodologies currently employed for NDT/NDI/NDE of aircraft structures have been detailed, and examples are shown. The precise method used for a given application will depend on the economic cost, subject to a sufficient probability of detection of any damage.

16.12   Future trends

Future trends in NDT of composites are expected to be transformative for the entire industry. In the manufacturing arena, robotics and other flexible automation will

replace current higher cost, large footprint stationary scanning systems. Waterless stand-off NDT sensors, such as Infrared Thermography and Laser Ultrasound, are being advanced to inspect complex shapes, thinner laminates, and edges, without having to touch the part or deal with water collection and recirculation issues. NDT will be moved earlier into the manufacturing processes and be better integrated so that feedback will reduce costly flaws and repairs and improve designs. Process monitoring and process control with NDT sensors are gaining interest, as is modeling of NDT aproaches for faster and better integration before fabrication starts. Automated defect analysis and artificial intelligence (AI) will be developed and utilized to increase manufacturing throughput by reducing time-consuming manual interactions and taking better advantage of the data collected.

Manufacturing and in-service NDT data and analysis will be better integrated in the future. 2-D and 3-D NDT data mapping on the structure will be used for improved life-cycle utilization of the data, including maintenance decision-making and prognostics. Some future NDT capabilities aimed at reducing composite in-service costs will include structural health monitoring (SHM) using new on-board NDT sensors, surgical NDT tools and methods for inspection hard-to-access areas, and web-based "remote expert" NDT, where the inspection is guided or completed by an off-site expert with limited or no on-site NDT support. UAV-based visual inspection is expected to provide pre-NDT assessments of where and when a full NDT must be performed. Rapid methods for moving NDT results to finite element analysis and performance prediction are also being developed. Finally, automated crawling platforms carrying various NDT sensors or sensor arrays will be developed enough to reduce manual inspections for commercial and military aircraft and other composite structures.

References

[1] ASTM-International, in: Standard Guide for Nondestructive Testing of Polymer Matrix Composites Used in Aerospace Applications, 2009.
[2] A.P. Berens, NDE reliability data analysis, in: Metals Handbook Volume 17: Nondestructive Evaluation and Quality Control, ninth ed., ASM International, 1988, pp. 659−701.
[3] MIL-HDBK-1823A, Nondestructive Evaluation System Reliability Assessment, US Dept. of Defense MIL-HDBK-1823A, 2009.
[4] B. Thompson, A unified approach to the model-assisted determination of probability of detection, Mater. Eval. 66 (6) (June 2008) 667−673.
[5] D. Bailey, Visual testing of composite materials, in: Visual and Optical Testing, second ed., vol. 8, American Society for Nondestructive Testing, 1993, pp. 328−330.
[6] M.W. Algaier, R. Cameron, Visual testing. Nondestructive Testing Handbook, third ed., American Society for Nondestructive Testing, 2010.
[7] T.J. Schmidt, G.K. Tyson, Full-field dynamic displacement and strain measurement using advanced 3D image correlation photogrammetry − part I, Exp. Tech. 27 (3) (2003) 47−50.
[8] M.A. Sutton, J.-J. Orteu, H.W. Schreier, Image Correlation for Shape, Motion, and Deformation Measurements, Springer, NY, 2009.
[9] F.C. Campbell, Manufacturing Processes for Advanced Composites, Elsevier, 2004.

[10] G. Georgeson, S. Lea, J. Hansen, Electronic tap hammer for composite damage assessment, in: SPIE Proc. Nondestructive Evaluation of Aging Aircraft, Airports, and Aerospace Hardware, 1996.

[11] FAA, Impact Damage Characterization and Damage Tolerance of Composite Sandwich Airframe Structures − Phase II," DOT/FAA/AR-02/80 Final Report, October 2002.

[12] G.L. Workman, D. Kishoni, in: Ultrasonic Testing, third ed., American Society for Nondestructive Testing, 2007.

[13] J. Krautkramer, H. Krautkramer, Ultrasonic Testing of Materials, Springer-Verlag, 1983.

[14] J.L. Rose, Ultrasonic Waves in Solid Media, Cambridge University Press, 1999.

[15] S.I. Rokhlin, D.E. Chimenti, P.B. Nagy, Physical Ultrasonics of Composites, Oxford University Press, 2011.

[16] B.M. Lempriere, Ultrasound and Elastic Waves, Academic Press, 2002.

[17] R.H. Bossi, G.E. Georgeson, Nondestructive testing of composites, Mater. Eval. 78 (No. 8) (August 2018) 1049−1060.

[18] E. Skaglund, "Ultrasound NDT of Drilled Holes Using 2D Array System," 58th Annual A4A NDT Forum, Fort Lauderdayle, FL, 2015.

[19] ASM, ASM Handbook, vol. 21 Composites, 2001. Materials Park, OH.

[20] ASNT, Laser based nondestructive testing methods, in: second ed.Special Nondestructive Testing Methods, Vol. 9 of Nondestructive Testing Handbook, vol. 9, American Society for Nondestructive Testing, 2003.

[21] X.P.V. Maldague, in: Infrared and Thermal Testing, third ed., American Society for Nondestructive Testing, 2001.

[22] S.M. Shepard, J.R. Lhota, B.A. Rubadeux, D. Wang, T. Ahmed, Materials characterization using reconstructed thermographic data, in: QNDE 2002 V22 Review of Progress in Quantitative Nondestructive Evaluation, vols. 22a and 22b, Western Washington Univesity, Bellingham, WA, 2002, pp. 1270−1276.

[23] J.W. Newman, Holographic and shearographic applications in aerospace manufacturing, Mater. Eval. 63 (7) (July 2005) 746−750.

[24] ASTM-International, Standard practice for shearography of polymer matrix composites, in: Sandwich Core Materials and Filament-Wound Pressure Vessels in Aerospace Applications, 2007.

[25] R. Bossi, F. Iddings, G. Wheeler, in: Radiographic Testing, third ed., American Society for Nondestructive Testing, 2002.

[26] R. Bossi, P. Burstein, J. Nelson, Computed tomography, in: R. Bossi, F. Iddings, G. Wheeler (Eds.), Nondestructive Testing Handbook Vol 12 Radiographic Testing, third ed., American Society for Nondestructive Testing, 2002.

[27] S.S. Udpa, in: Electromagnetic Testing, third ed., American Society for Nondestructive Testing, 2001.

[28] R. Zoughi, Microwave Non-destructive Testing and Evaluation, Kluwer Academic Publishers, Dordrecht, The Netherlands, 2000.

[29] A. Bahr, R. Zoughi, N. Qaddoumi, Microwave, in: Nondestructive Evaluation, Marcel Dekker, Inc, 2002, pp. 645−720.

[30] D. Mittleman, Sensing with Terahertz Radiaton, Springer Verlag, New York, 2003.

[31] J. Beckmann, H. Richter, U. Zscherpel, U. Ewert, J. Weinzierl, L.-P. Schmidt, F. Rutz, M. Koch, H. Richter, H.W. Hubers, Imaging Capability of Terahertz and Millimeter-Wave Instrumentations for NDT of Polymer Materials, ECNDT, 2006.

[32] P. Ramuhalli, N. Qaddoumi, R. Botsko, Microwave Testing, vol. 3, American Society for Nondestructive Testing, 2004.

[33] J.K.F. Schmidt, J.J.R. Little, W. Ellingson, A.W. Green, Optimizing a portable microwave interference scanning system for nondestructive testing of multi-layered dielectric materials, in: QNDE 2009 V29 Review of Progress in Quantitative Nondestructive Evaluation, 2009, pp. 1249−1256.

[34] P. Lopato, T. Chady, K. Goracy, Image and signal processing algorithms for THz imaging of composite materials, in: QNDE 2009 V29 Review of Progress in Quantitative Nondestructive Evaluation, Univ Rhode lsland, Kingston, RI, 2009, pp. 766−773.

[35] C.D. Stoik, M.J. Bohn, J.L. Blackshire, Nondestructive evaluation of aircraft composites using dielectric properties and imaging in the terahertz spectrum, in: QNDE 2008 V28 Review of Progress in Quantitative Nondestructive Evaluation, 2008, pp. 418−425.

[36] U. Ewert, J. Beckmann, L.S. von Chrzanowski, G. Brekow, D. Brackrock, Time of flight diffraction (ToFD) with THz radiation - an alternative to the ultrasound, in: QNDE 2010 V30 Review of Progress in Quantitative Nondestructive Evaluation, CAI, San Diego, 2010, pp. 541−548.

[37] P. Cawley, Low-frequency NDT techniques for the detection of disbonds and delaminations, Insight − Br. J. Non-Destr. Test. 32 (9) (September 1990) 454−461.

[38] S.I. Rokhlin, D. Marom, Nondestructive testing of adhesively bonded joints, J. Acoust. Soc. Am. 87 (2) (1990) 532−542.

[39] M.A. Drewry, R. Smith, A. Phang, D. Yan, P. Wilcox, D. Roach, Ultrasonic techniques for detection of weak adhesion, Mater. Eval. 67 (9) (September 2009) 1048−1058.

[40] R. Heslehurst, Optical NDT of adhesively bonded joints, Mater. Eval. 67 (7) (July 2009) 837−842.

[41] R. Bossi, K. Housen, C. Walters, D. Sokol, Laser bond testing, Mater. Eval. 67 (7) (July 2009) 819−827.

[42] M. Perton, A. Blouin, Z. Gu, J.P. Monchalin, E. Gay, L. Berthe, M. Boustie, M. Arrigoni, Laser Shock Waves for Adhesive Bond Testing, " SAMPE Proceeding, Seattle, WA, May 2010.

[43] R. Bossi, D. Lahrman, D. Sokol, C. Walters, Laser Bond Inspection for Adhesvie Bond Strength, SAMPE Proceeding, Long Beach, CA, May 2009, 2011.

Structural health monitoring (SHM) of aerospace composites

17

Victor Giurgiutiu
University of South Carolina, Columbia, SC, United States

17.1   Introduction

Structural health monitoring (SHM) relies on sensors that can be permanently placed on the structure and monitored over time, either in a passive or in an active way. These sensors should be affordable, lightweight, and unobtrusive so as to not impose cost and weight penalty on the structure and to not interfere with the structural strength and airworthiness.

Nondestructive Testing (NDT), Nondestructive Inspection (NDI), and Nondestructive Evaluation (NDE) are concerned with the techniques and measurements that provide data on the condition of the materials and structures at the time of manufacturing and in-service. The NDT/I/E methods are generally speaking discrete inspections performed during manufacture and at specified intervals or events during service of a structure.

The tools used for NDT/I/E and for Structural Health Monitoring (SHM) can be quite complementary, and in many cases, they may be used in what might be considered a similar fashion, i.e., employing SHM on-board sensors as *in situ* NDT/I/E by engaging in sensor acquisition at specified intervals. Chapter 16 describes the basics of NDT for polymer composite structures, while SHM is discussed in Chapter 17. Today NDT methods are used primarily to detect manufacturing defects or damage. The future direction, however, is to use these tools for material state condition assessment and prognosis of the remaining structural life.

This chapter starts with a brief overview of the composite damage situations. This is followed by a description of the major methods applied to composite structures during in-service inspection.

17.2   Composite damage

Advanced composite materials are made of high-strength fibers embedded in a polymeric matrix. Glass fiber-reinforced polymer (GFRP), and carbon fiber-reinforced polymer (CFRP) are among the most common composite materials. The damage and failure of metallic structures is relatively well understood; the in-service damage and failure of metallic structures occurs mostly due to fatigue cracks that propagate under cyclic loading. In contrast, the damage of composite materials occurs in many more

ways than that of metals [1]. Composites fail differently under tension than they fail in compression, and the effect of fastener holes is much more complicated than in metals. In addition, the composites are prone to hidden damage from low-velocity impact (e.g., the drop of a hand tool on a wing, or large hail impact on a radome, etc.); such damage can be barely visible and may go undetected, but its degradation effect on the composite structure strength can be dramatic. In order to satisfy the aircraft damage tolerance requirements [2], one has to demonstrate that a composite aircraft structure possesses adequate residual strength in the presence of assumed worst-case damage, such as, for example, caused by a low-velocity impact on a composite structure [3,4].

Tension, compression, and shear are the three fundamental modes in which a composite lamina may fail. As the composite material is made up of multiple laminae (layers, plies) of various orientations, the stresses in the lamina principal directions vary from lamina to lamina. As the load is increased, so do the various stresses in the laminae, and failure values may be attained in a certain lamina in a certain principal direction without the overall laminate experiencing actual failure; in other words, the failure of the composite laminate is a progressive phenomenon. This progressive damage evolution is subcritical for a while but eventually leads to the ultimate failure of the composite laminate.

17.2.1   Tension damage in composites

When subjected to axial tension, the composite material displays progressive failure through several damage mechanisms taking place sequentially. Consider, for example, the cross-ply laminate of Fig. 17.1: as an axial load is applied in the longitudinal (L) direction, the 0-degree ply is loaded along its reinforcing fibers, whereas the 90-degree ply is loaded across the fibers. Because the strength of the polymeric matrix is much less than that of the fibers, the across-the-fiber strength of the lamina is much lower than the along-the-fiber strength. Hence, matrix cracking of the 90-degree ply occurs at an early stage in the loading cycle (Fig. 17.1). As the tension load increases, further damage occurs in the form of delaminations between the 0- and 90-degree plies due to 3-D effects at the interface between the two plies with radically different properties. The matrix cracks existing in the transverse ply act as discontinuities generating 3-D disbonding stresses that promote delaminations. The same 3-D effects will lead to splitting of the 0-degree plies at higher tension loads. If the load continues to increase, the 0-degree plies will eventually fail due to fiber fracture, at which point no load can be supported any longer [6].

This simple 0/90 example indicates that internal damage in a composite laminate can happen at relatively low stress levels in the form of matrix cracking; this is followed, at intermediate levels, by interlaminar delamination and lamina splitting. If the applied stress is cyclic, as in fatigue loading, then these low-level damage states can increase and propagate further and further into the composite with each load cycle. The reinforcing fibers have high strength and good load carrying properties, but the matrix cracking, delamination, and lamina splitting mechanisms usually lead to in-service composite structures becoming operationally unfit and requiring replacement.
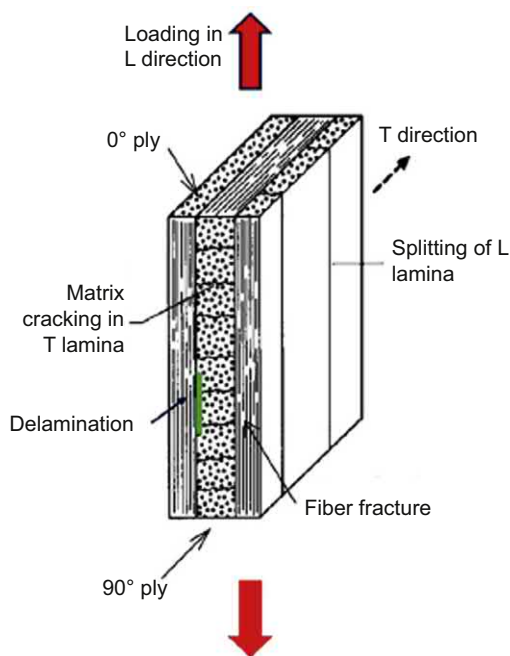
Figure 17.1 Longitudinal tension of a 0/90 composite laminate: The highlight of several damage modes: matrix cracking in transverse (T) lamina; splitting of longitudinal (L) laminae; delamination between T and L laminae [5].

17.2.2 Compression damage in composites

When subjected to axial compression, the composite fails through the loss of elastic stability (buckling). At the global scale, buckling can be avoided by the appropriate sizing of the component length versus its bending stiffness such that loss of elastic stability does not occur for the given boundary conditions and operational load levels. At the local scale, the composite material itself can fail under compression through the microbuckling mechanism (Fig. 17.2). The high-strength fibers encased in the polymeric matrix can be viewed as beams on elastic foundation, where the elastic support is provided by the matrix stiffness. Under axial compression, such a beam on an elastic foundation would eventually buckle and take an undulatory shape (Fig. 17.2(a)). The compressive stress values at which such buckling occurs are dictated by the fiber bending stiffness and matrix compression stiffness. As the compressive load is further increased, the microbuckling is further exacerbated until local failure occurs in the form of *kink bands* (Fig. 17.2(b)).

For a given composite material system with a certain fiber/matrix combination, the microbuckling compressive strength is fixed and cannot be altered through structural design. In order to modify the microbuckling compressive strength, one has to address the very constituents of the composite material system. For example, the thicker boron fibers have a higher compression buckling strength than the thinner carbon fibers; for this reason, boron fiber composites may be preferred in places where material compression strength is the critical factor.
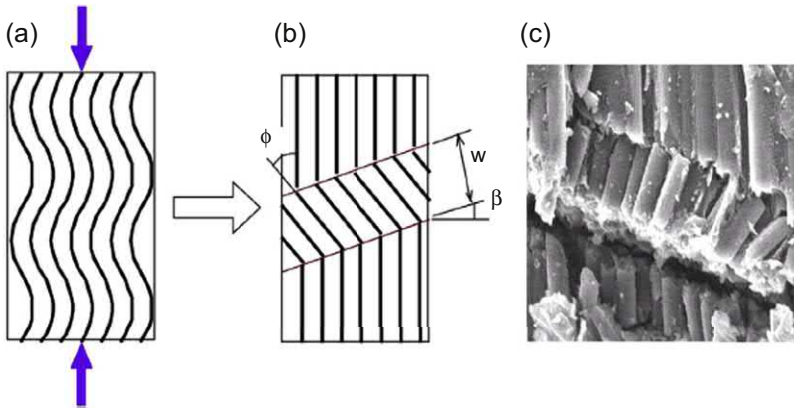
Figure 17.2 Compression damage of fiber composites through microbuckling: (a) undulations of buckled fibers; (b) kink band local failure schema; (c) micrograph of kink band formation in T800/924C carbon-fiber composite [5].

17.2.3   Fastener hole damage in composites

Mechanical fasteners used in riveted and bolted joints are prevalent in metallic aircraft structures, where they offer a rapid and convenient method of assembling large structures from smaller components. The load-bearing mechanisms of metallic joints are well understood and easily predicted. The use of mechanical fasters in composite structures is also allowed, but this comes with significant strength and fatigue penalties. Nonetheless, mechanical fasteners are still widely used in the construction of current composite structures, especially when load transfer has to be achieved between composite and metallic components. A typical example is illustrated in Fig. 17.3(a), where the load from a composite wing skin is transferred into an aluminum metallic bracket through a 9-bolt junction. When in service, each hole in the composite skin would be subjected to both tension and/or compression loading that may, under certain circumstances, promote damage initiation and damage progression [7].

Under tension (Fig. 17.3(b)), the composite joint may fail in one of three major modes: (i) tear failure; (ii) bearing failure; and (iii) shear-out failure. Of these, tear failure is unlikely to happen because the fiber reinforcement is strongest in tension. The shear-out failure would happen if the fibers are predominant in the tension direction; shear-out failure can be counteracted through material design by the addition of 45-degree reinforcement. The bearing failure is more difficult to prevent because it is a compression-type loading that has to be taken up by the polymeric matrix and by the fibers under compression. Bearing failure may occur through matrix crushing, or fiber microbuckling, or both.

Under compression (Fig. 17.3(c)), the composite joint may fail in three major modes: overall buckling of the component; local buckling of the region weakened by the hole; fiber microbuckling at the areas of highest compression strength. The overall compression buckling can be prevented by proper component design. Local
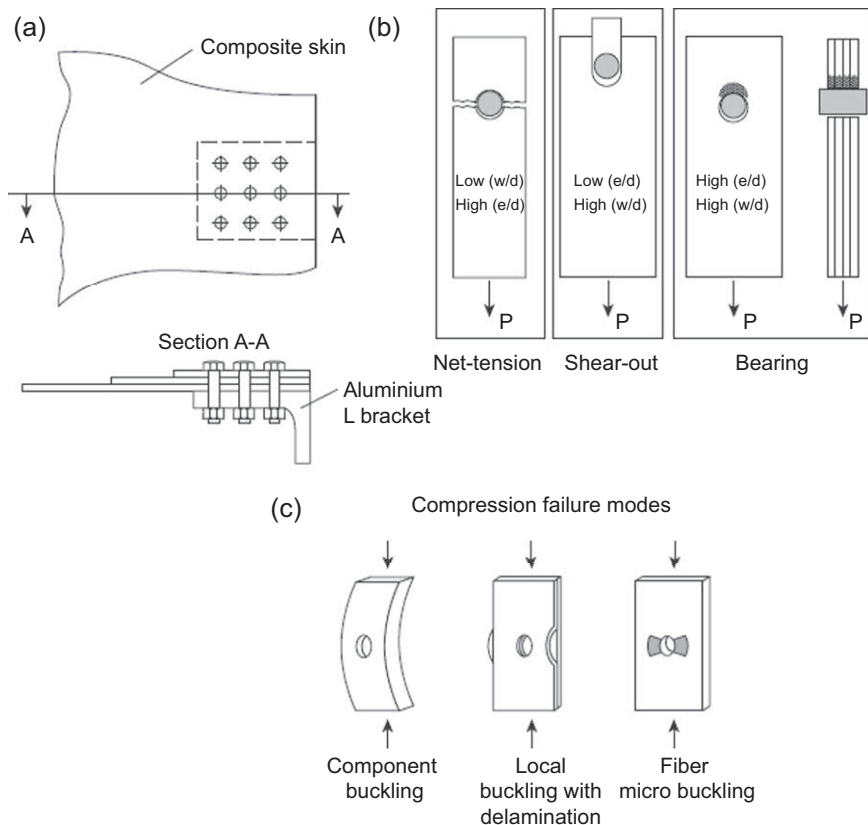
Figure 17.3 Composite damage due to fastener holes: (a) typical bolted junction between a composite wing skin and metallic connection; (b) failure modes in a bolted joint under tension [5]; (c) compressive failure modes in a plate with an open hole.

buckling and fiber microbuckling may also be prevented by design, but damage accumulation during cyclic loading would eventually weaken it.

The use of mechanical fasteners in fiber composites is somehow counter-intuitive, but expedient. The very premise of fiber composites assumes the load to be carried through the high-strength fibers embedded in a relatively weak polymeric matrix. This type of load-carrying capability benefits from a smooth and continuous load "flow" and is averse to sudden changes in material properties and geometries, such as those imposed by a fastener hole. Ideally, composite joints should be done through adhesive bonding with a gradual transition from one component into the next. However, mechanical fasteners are often used for a variety of reasons, and one has to assess the consequences of such a design decision: fastener holes drilled in the composite structures produce sudden discontinuities, interrupt the fiber flow, and act as stress concentrators. They also act as crack and delamination initiators due to microdamage introduced during the hole drilling process. Special attention can be given to creating

stress-free holes by designing local reinforcement; damage-free holes can also be manufactured with special tooling. However, these aspects come with the added cost and may not always be implemented in practice.

17.2.4   Impact damage in composites

Composite aerospace structures are prone to a particular type of damage that is not critical in metallic aerospace structures, i.e., **low-velocity impact damage**. Such damage may occur during the manufacturing or in-service due to, say, a hand tool being dropped onto a thin-wall composite part. When such an impact happens on a conventional metallic structural part, either the part is not damaged at all, or, if it is damaged, then it shows clearly as an indent or scratch. In composite structures, a similar impact may damage the structure without leaving any significant visible marks on the surface (so-called *barely visible damage*). In this case, the impact result takes the form of **delaminations** in the composite layup (Fig. 17.4). A more drastic impact may also show spalling on the backside while having no visible marks on the front side.

Delamination due to barely visible impact damage may not have a large effect on the tensile strength of the composite, but it can significantly **diminish the composite compression strength** (delaminated plies have a much weaker buckling resistance than the same plies solidly bonded together). Both component buckling strength and local buckling strength may be affected; when a fastener hole is present, as depicted in Fig. 17.3(c), this effect maybe even worse. For this reason, manufacturing companies place a strong emphasis on testing the **open-hole compression strength after the impact** of their composite structures.

Worst-case impact damage is defined as the damage caused by an impact event (e.g., a 1-in hemispherical impactor) at the lesser of the following two energy levels: (a) 100 ft-lb, or (b) energy to cause a visible dent (0.1-in deep). A schematic of the various damage mechanisms that take place in a laminated composite under low-velocity impact is shown in Fig. 17.4; they can be summarized as [8]: (a) front face damage (crater); (b) transverse cracks; (c) delaminations; (d) back face fiber breakage.
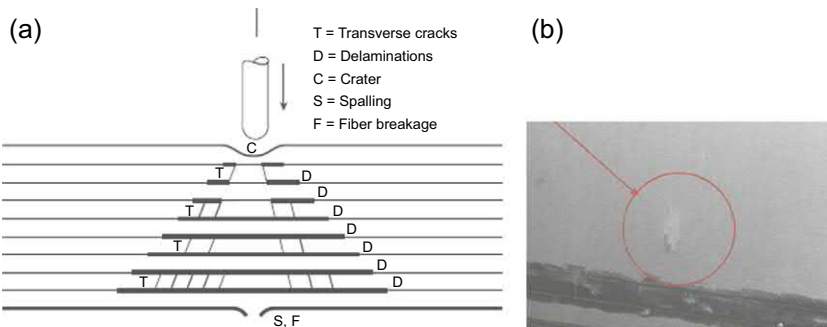
Figure 17.4 Impact damage effects on laminated composites (a) schematics of various damage mechanisms; (b) photo of composite surface.

The front face damage may in many practical instances be barely visible. The impactor shape may have a significant effect on damage details (Fig. 17.5).

17.2.5 Fatigue damage of composites

Composite fatigue is substantially more complicated than that of metals [9]. Damage progression in a cross-ply laminated composite under fatigue loading was studied in Ref. [10]; the following stages were identified in a unidirectional laminate under cyclic tension (Fig. 17.6):

1. Matrix cracking
2. Crack coupling and interfacial debonding
3. Delamination
4. Fiber breaking and composite fracture

The evolution of damage through these phases depends on the cyclic fatigue loading level; three loading levels can be identified with respect to the damage produced in the composite [10]:
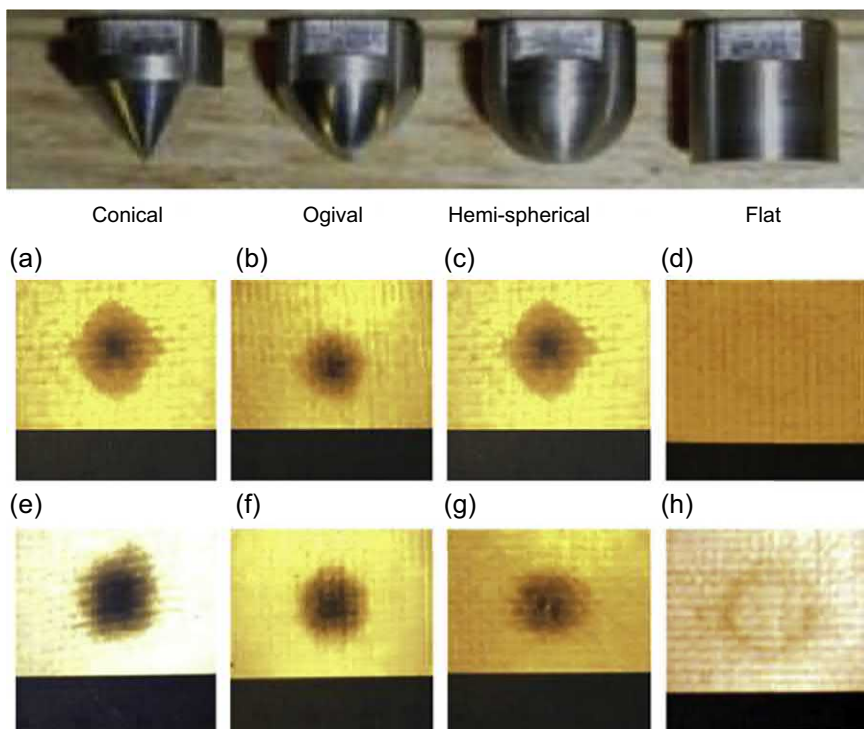
Figure 17.5 Effect of impactor size and type on the resulting damage in a laminated GFRP composite. Top row: various impactor shapes. Middle and bottom rows: back-illuminated images of the impact area for each impactor shape at 4 and 6 J impact energy, respectively [8].

Loading Level 1: matrix cracks begin to develop while the fibers remain intact. Under cyclic loading, these cracks propagate until they reach a fiber/matrix interface or some other inhomogeneity. If the cyclic load is sufficiently low, these cracks will not propagate any further, and no more fracture surfaces will be created until the fatigue limit of the fibers is reached, and overall composite failure occurs.

Loading Level 2: If the cyclic load is at a higher level, then the matrix cracks may not stop at the fiber/matrix interface as they did in Level 1. Several things could happen at this stage: (a) when the matrix crack reaches a fiber, the stress concentration may cause the fiber to break, forming a larger crack. (b) If the stress concentration is not sufficiently high for the fiber to break, a separation of the fiber and matrix could occur, and the crack propagates along the fiber/matrix interface. The damage propagating through the (a) and (b) mechanisms reaches new fiber/matrix interfaces and may cause further fiber fractures or fiber/matrix separation. Eventually, the degradation of the composite will be sufficiently large to cause a fracture.

Loading Level 3: If the cyclic fatigue load is near the ultimate strength, some fibers will fail immediately due to the statistical spread of their individual strengths. As the cyclic loading continues, more fibers will break throughout the composite; when enough fibers have failed in a particular area, a crack will form, leading to a rapid fracture of the composite. At this level of loading, the final fracture will occur quickly, and the damage progression trend shown in Fig. 17.6, will no longer take place.

The orientation of the laminae in the composite laminate may modify the damage evolution. In a generic situation, the individual lamina is subjected to off-axis loading
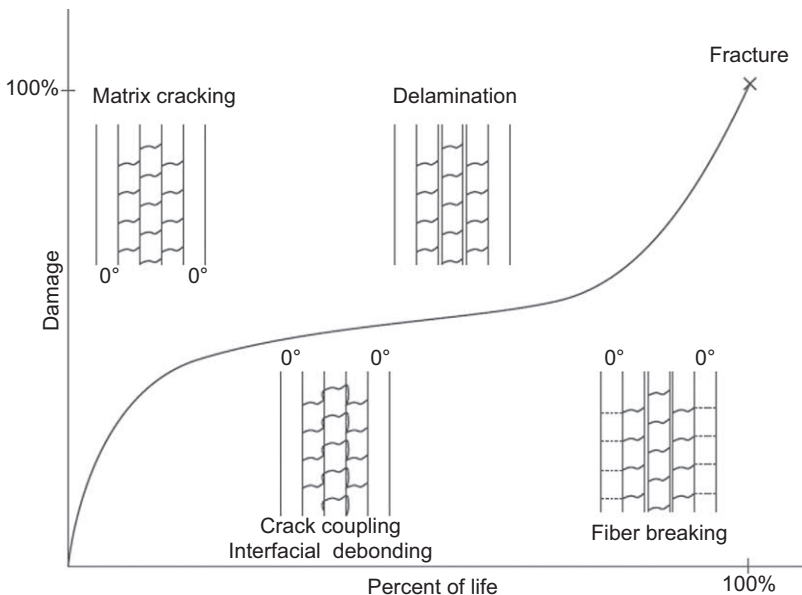
Figure 17.6 Conceptual description of the evolution of fatigue damage in a cross-ply laminated composite.

that is projected onto the lamina principal axes and may cause matrix cracks to form parallel to the fibers. These cracks can propagate freely down the length of the fiber either in the matrix or in the fiber/matrix interface. Debonds between the fibers and matrix eventually will occur. The damage occurring in a composite laminate is a complex phenomenon that is governed by the processes taking in each individual lamina. A generic scenario may look as follows:

(a) Small microcracks develop in the matrix mainly between fibers that are not parallel to the loading direction.
(b) As the cyclic loading continues, the microcracks grow and become macroscopic cracks. At this point, the material has reached the Characteristic Damage State (CDS) as marked in Fig. 17.6.
(c) The cracks in the matrix will spread through the ply in which they began.
(d) Stress concentrations cause microcracks to develop on either side of the initial ply.
(e) Stress concentrations between plies cause local delaminations.
(f) Once delaminations have formed, the damage increases rapidly up to complete failure.

Because of this progressive fatigue damage behavior, a composite structure subject to high fatigue loads should be periodically inspected to monitor the damage progression just as a metallic structure is monitored under current inspection guidelines. Properly designed composite aerospace structure operates below the threshold for significant fatigue damage during the design lifetime.

17.2.6 Damage in composite sandwich structures

The carbon fiber-reinforced polymer (CFRP) sandwich panels are much more susceptible to impact damage than glass fiber-reinforced polymer (GFRP) panels, and the predominant type of damage is different: fiber breaking for CFRP sandwich and core crushing for GFRP sandwich.

Fig. 17.7 shows the various types of damage that can happen in a composite sandwich under the impact, i.e.,:

- Front skin damage: (a) skin indentation; (b) skin cracking; (c) resin crushing; (d) fiber breaking; (e) delamination
- Foam core damage: (a) core crushing; (b) core cracking.
- Interface damage: debonding at the skin/core interface

Fig. 17.7(b) shows the mapped indentation profile on a GFRP/foam core sandwich after a 10 J impact. The indentation depth and the crater ridge swelling can be as high as 0.1 mm.

Skin Damage: On the front face (impact side), an indentation occurs. This type of damage is invisible to the naked eye for very low energy impact but may become barely visible at a threshold that depends on the materials used, the structure arrangement, and the attachment of the coupon to the sample holder of the impact machine. For larger energy, the indentation is easily visible, and its detection does not need the use of sophisticated NDE techniques. It is crucial to be able to detect the barely visible damage because it can be accompanied by severe internal damage reducing the local mechanical strength. As shown in Fig. 17.7(b), the indentation obtained
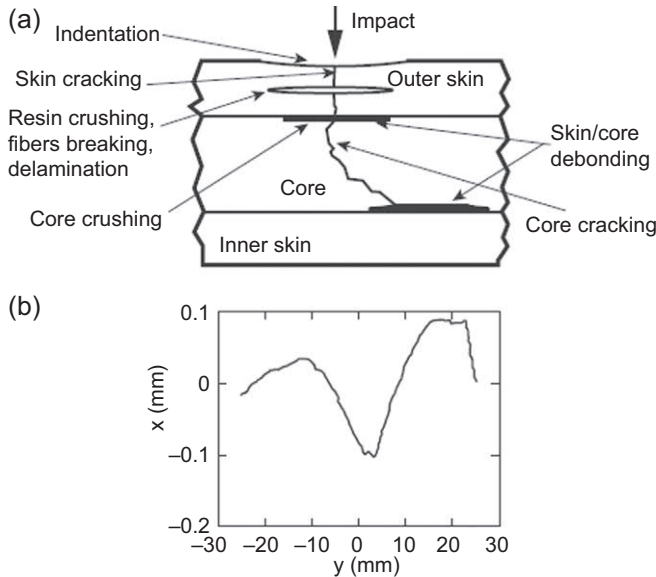
Figure 17.7 Impact damage on composite/foam sandwich: (a) various types of possible damage; (b) Indentation profile after a 10 J impact on a GFRP/foam core sandwich [11].

may be barely visible, even for a 10 J impact. The maximum depression of the surface is less than 0.1 mm over an extent of 40 mm. In fact, for radome sandwich structure, due to the nature of the skin, the visual inspection can sometimes detect the damage by a slight change in the surface color. The surface alterations, which by themselves have no influence on the mechanical resistance of the structure, can be accompanied by more critical damage: matrix cracking, matrix crushing, fiber breaking, and delamination. The occurrence of such types of damage strongly depends on the nature of the skin material.

Interface Damage: In parallel with the damage of the skin, the skins/core interfaces can be damaged by debonding. For carbon/epoxy skins and foam core, debonds are nonexistent in spite of the presence of delaminations and fiber breaking of the front face skin. As shown in Fig. 17.7(a), for a higher level of impact energy, debonding can occur at the core/rear-face skin interface too.

Core Damage: In the case of lightweight foam, two types of damages take place: core cracking in relation with skin cracking, and core crushing located underneath debonds.

17.2.7 Damage in adhesive composite joints

Adhesive composite joints offer unquestionable manufacturing and cost advantages over mechanical fasteners. In addition, the adhesive joining of composite parts seems more appropriate than drilling holes, as discussed in Section 17.5. However, the reliability of adhesive bonding cannot always be guaranteed due to a variety of reasons. Hence,

delamination damage in composite joints is probably the most frequently occurring damage, and the consequences may be quite severe. If the joint is part of a fail-safe construction, then the occurrence of delamination reduces the stiffness of the structure, and hence, the load-carrying capability of the structure. If the joint is not in a fail-safe construction, then the consequences of the joint failure may be dramatic.

17.3   SHM sensors

Some of the sensor types that have been considered for SHM applications are:

- Conventional resistance strain gages
- Fiber optic sensors, e.g., fiber Bragg gratings (FBG) strain sensors
- Piezoelectric wafer active sensors (PWAS)
- Electrical properties sensors: resistance, impedance, dielectric, etc.

These sensors may operate in static and dynamic regimes, depending on the physical principle that is employed in monitoring the structure. Other damages measuring methods based on large-area measurements (ultrasonic C-scans, scanning Doppler laser velocimetry, thermography, etc.) have been used in SHM development for definition and confirmation of damage and/or for understating the proposed SHM approach; however, they do not seem appropriate for permanent installation onto the monitored structure and will not be discussed under the heading of SHM sensors.

17.3.1   Resistance strain gages

The conventional resistance strain gages are well known [12] and need not be detailed here. Their physical principle relies on converting a relative strain change into a relative resistance change that is read with a precision instrument (e.g., a Wheatstone bridge). The strain-induced resistance change maybe due to purely geometric effects (e.g., foil strain gages), or may be enhanced by the piezo-resistive effect exhibited by some materials. Conventional resistance strain gages operate well in both static and dynamic regimes. The signal bandwidth is limited only by the bandwidth and signal to noise ratio (SNR) of the electronic conditioning equipment because the strain gage coverts directly the strain change into a resistance change. The strain gage technology is well developed and relatively matured; known difficulties with using strain gage for long-term monitoring under various environmental conditions are usually related to the adhesion between the gage and the structure and with the adverse effect of the environment onto the electrical wire connections that may result in strain drift or even signal loss.

17.3.2   Fiber optic sensors

Fiber optic sensors offer several advantages for structural health monitoring: (a) immune to electromagnetic interference (EMI); (b) corrosion resistance;

(c) possibility of multiplexing several sensors on the same optical fiber; (d) the promise of direct embedment into the composite material along with the reinforcing fibers, etc. Fiber optic sensors also have several limitations that have impeded their widespread usage: (i) the need for considerable optoelectronic equipment to convert the optical changes into actual readings of the physical quantity being monitored (strain, or other material property); (b) bandwidth limited by the bandwidth of the optoelectronic equipment that has to perform complicated processing of the optical signal; etc. Fiber optic sensors have known extensive development in recent years, and the methods used for the demodulation and interpretation of the optical signal are very diverse and still evolving.

Optical fiber has a central core surrounded by an annular cladding and a protective coating (Fig. 17.8). Due to the phenomenon of total internal reflection (the cladding has a lower refractive index than the core), the light wave is confined in the core and travels over large distances with very little loss (Fig. 17.8(a)).

The overall diameter of a typical optical fiber varies between 120 μm and 250 μm; when embedded in a composite, optical fibers may create a discernible discontinuity (Fig. 17.8(b)); development of small-diameter optical fibers (e.g., 52 μm) for embedment into composites has also been reported [15]. Single-mode fibers have a small core ($\sim 10\,\mu m$) and only accommodate the fundamental guided lightwave mode; multimode fibers have larger cores ($\sim 50\,\mu m$ to $100\,\mu m$) and permit the propagation of multiple modes (Fig. 17.8c). Either a single-mode or multimode optical fiber can be used for constructing an individual fiber optic sensor. Yet a single-mode optical fiber with a smaller core is more strain sensitive than a multimode optical fiber [14]. A comprehensive review of fiber optics sensors for structural health monitoring is provided in Refs. [16–20]. The fiber-optic sensing mechanisms for SHM applications can be
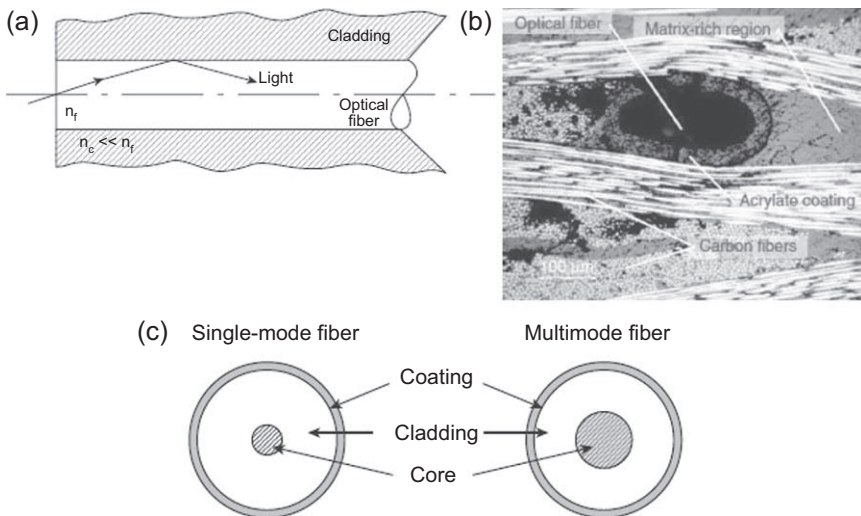
Figure 17.8 Fiber optic essentials: (a) total internal reflection principle; (b) optical fiber embedded in a CFRP composite [13]; (c) single-mode and multimode fibers [14].

one of four types [17]: (a) intensity modulation; (b) polarization modulation; (c) phase modulation; (d) scattering modulation; (e) spectral modulation.

Intensity modulation is one of the simplest to measure because it only requires a photodetector to assess the light intensity. The intensity of the light wave traveling through an optical fiber can be modified by microbending of the optical fiber, by a change in the coupling of the fiber with the surrounding medium, or by the fracture of the optical fiber. A photodetector is used to measure the intensity of the light transmitted through the fiber or reflected back to the input. One drawback of these simple optical sensors is that they cannot be multiplexed into sensor networks.

Polarization modulation: The cross-section of the optical fiber has a fast axis and a slow axis, which are mutually perpendicular. Two light waves individually polarized about each of these axes will not usually interfere with each other, and their intensity can be separately measured using polarizing filters. External stimuli, such as pressure or twisting of the fiber may induce transfer between the two polarized modes, which may be quantified and used for measurement.

Phase modulation: mechanical strain or thermal expansion changes the optical path length through the fiber and hence affects the light wave phase. Interferometric methods are used to measure the phase shift between the light wave traveling through the sensor and a reference wave split from the same source. The reference fiber can be exposed to some of the external effects, such as to decouple these effects from those to be measured by the sensing fibers. For example, if mechanical strain and temperature changes are both present, the reference fiber can be exposed to temperature only, whereas the measuring fiber is exposed to both strain and temperature, such that the resulting relative phase between the two fibers will be due only to the strain effects. Optoelectronic interferometers that convert the phase shift into some numerical readout are commercially available [21]. However, the phase modulation measurements remain particular to a single fiber and multiplexing of several sensors on the same fiber is not generally possible.

Scattering modulation: The fused silica material used in the optical fiber has intrinsic scattering properties (Fig. 17.9(a)) that affect the light wave propagating through it. Several backscatter waves are possible: Rayleigh, Brillouin, Raman, Stokes (Fig. 17.9). Brillouin scattering occurs due to interactions with acoustic waves known as phonons; its frequency shift can be related to applied strain or temperature. The weak Brillouin can be amplified by stimulating acoustic waves through the use of a second pulsed laser connected to the opposite end of the optical fiber. By scanning the frequency of the pulsed laser, the relative frequency shifts at which the stimulated Brillouin scattering occurs can be identified and converted into the applied strain or temperature. The time of arrival of the scattered light is analyzed to determine the location of each Brillouin scattering event. In this manner, the strain or temperature distribution along an optical fiber can be measured. The strain and temperature resolution are around $5\,\mu\varepsilon$ and $0.25°C$; nominal spatial resolution with a single laser source is about 5 m. The use of advanced signal processing techniques, e.g., Brillouin optical correlation domain analysis, has been shown to improve the spatial resolution significantly [18].

Spectral modulation: Spectral modulation is achieved through Fabry−Perot interferometers (FPI) or fiber Bragg gratings (FBG). Such sensors typically act as filters, transmitting certain wavelengths, and radiating or reflecting others. Changes in mechanical strain, temperature, or other external parameters are converted into a shift of the characteristic wavelength of such a filter. The decoding of the wavelength-encoded signal is commonly done by one of three methods: (i) with an optical spectrum analyzer; (ii) with a tunable laser source that scans a band of wavelengths; or (iii) with a wavelength-tunable filter. Other, more complex methods based on three-way couplers or fast Fourier transforms have also been developed for high-rate data acquisition and sensor multiplexing. The cavity-based FPI sensors are manufactured by inserting into a capillary tube the two ends of a cleaved fiber separated by a small distance (Fig. 17.9(b)). The cavity acts as a wavelength filter; if a strain is applied, the cavity size changes and its center frequency shifts. This wavelength shift is decoded into a strain. The FBG sensors achieve similar results through a grating pattern imprinted directly onto the fiber with ultraviolet (UV) light, as discussed next.

Figure 17.9 (a) Spectrum of intrinsic scattering for fused silica fiber; (b) Fabry-Perot cavity constructed between the two ends of cleaved optical fiber.
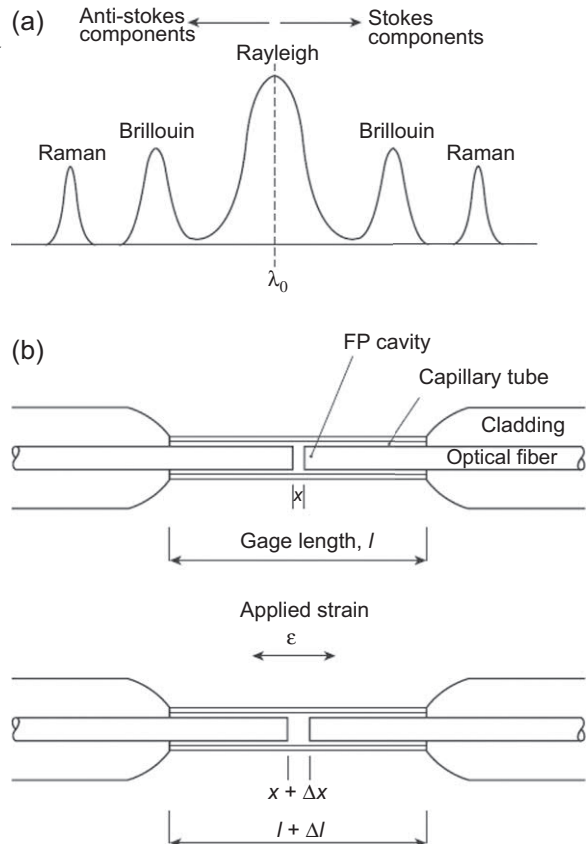
17.3.3 Fiber Bragg grating (FBG) sensors

FBG sensors have gained considerable popularity; they are simple to manufacture by UV imprinting of a grating pattern directly onto the fiber; the sensor diameter is the same as the fiber diameter; several different FBG sensors can be imprinted at different locations on the same fiber and can be individually addressed and multiplexed.

The FBG sensor (Fig. 17.10) is a permanent periodical perturbation (grating) in the index of refraction of the optical fiber core inscribed at selected locations using high-intensity UV light. This periodic perturbation with pitch Λ acts as a wavelength filter with a narrowband reflection spectrum centered on the Bragg wavelength $\lambda_B = 2\eta_{eff}\Lambda$ (Fig. 17.10(b)).
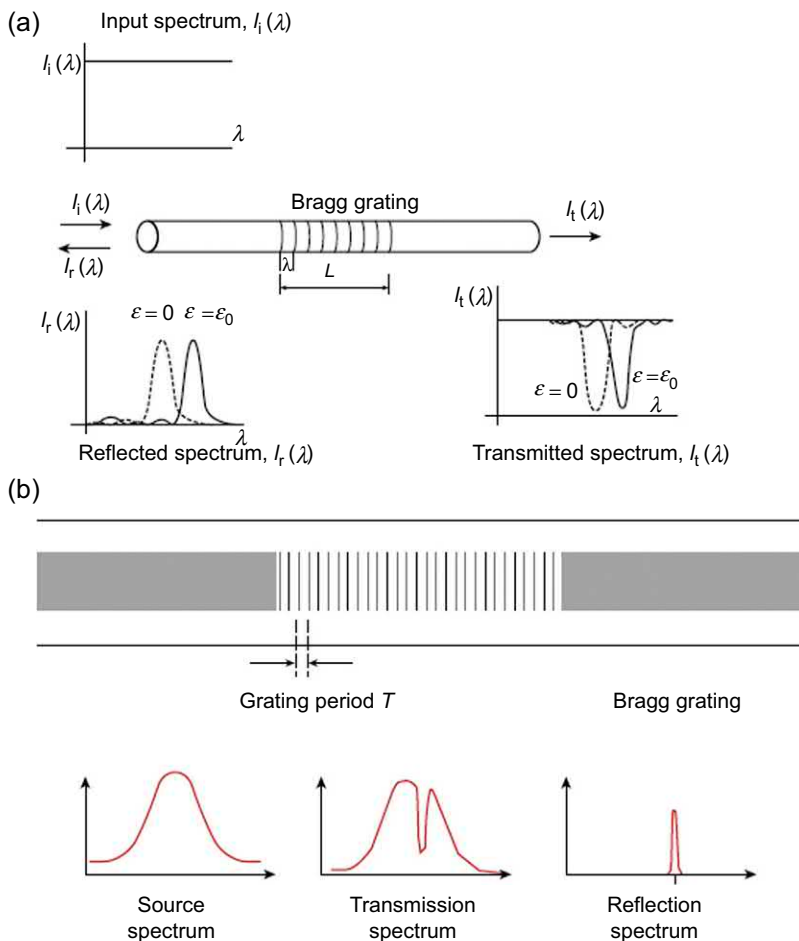
Figure 17.10 (a) Principles of fiber Bragg grating (FBG) optical sensors; (b) details showing the notch in the transmission spectrum and the peak in the reflection spectrum at the Bragg wavelength λ_B [22].

When the mechanical strain $\Delta\varepsilon$ and temperature change ΔT are present, the Bragg wavelength shifts with

$$\Delta\lambda_B = \Delta\lambda_{BS} + \Delta\lambda_{BT} = \lambda_B(1 - \rho_\alpha)\Delta\varepsilon + \lambda_B(1 + \xi)\Delta T \qquad (17.1)$$

where ξ is the thermo-optic coefficient and ρ_α is the effective strain-optic coefficient, which is a function of the Poisson ratio ν of the fiber and the Pockels constant ρ_{ij}, i.e.,

$$\rho_\alpha = n_{eff}^2/2[\rho_{12} - \nu(\rho_{11} - \rho_{12})] \qquad (17.2)$$

If the temperature is constant, only the strain effect is present and Eq. (17.1) simplifies to

$$\Delta\lambda_B = \lambda_B(1 - \rho_\alpha)\Delta\varepsilon \qquad (17.3)$$

Eq. (17.3) shows that the relative wavelength shift is proportional to the strain, i.e.,

$$\frac{\Delta\lambda_B}{\lambda_B} = \kappa\,\Delta\varepsilon \qquad (17.4)$$

where κ is the FBG strain gage factor. The theoretical value of κ for pure silica glass has been calculated to be around $\kappa \approx 0.78$ [23].

Besides the center frequency shift, the FBG spectrum develops other, more intricate changes representative of proximal structural damage. For example, the processing and detailed analysis of the FBG spectrum has been used to extract the effect of nonuniform strain field in the proximity of matrix cracks and delaminations [24,25].

Conditioning equipment for the FBG sensor should be able to convert the various optical processes inside the FBG sensor into an actual strain reading at the equipment output. This process is often referred to as "demodulation" or "decoding" of the optical signal. Refs. [19,26] describe a number of strategies for decoding the Bragg wavelength of the signal reflected from an FBG sensor and extracting a strain reading: optical spectral analyzers; scanning fiber filters; unbalanced fiber interferometers in combination with wavelength division multiplexers; wavelength-swept lasers; CCD arrays combined with a dispersive element; photorefractive crystals, etc. Some of these methods are appropriate for static and quasi-static strain measurements, some can operate in the dynamic range, and a few could operate at ultrasonic frequencies (Fig. 17.11). The individual addressing of several FBG sensors engraved on the same optical fiber is achievable through wavelength domain multiplexing (WDM); the switching between various optical fibers can be attained through time-domain multiplexing (TDM). A large system that employs several optical fibers with a number of FBG sensors on each fiber would have to use a WDM-TDM combination [19].

17.3.4   Piezoelectric wafer active sensors (PWAS)

Piezoelectric wafer active sensors (PWAS) are small, lightweight, and relatively low-cost transducers based on the piezoelectric principle that couples the electrical and mechanical variables in the material (mechanical strain S_{ij}, mechanical stress T_{kl}, electrical field E_k, and electrical displacement D_j) in the form

$$S_{ij} = s_{ijkl}^E T_{kl} + d_{kij}E_k$$

$$D_j = d_{jkl}T_{kl} + \varepsilon_{jk}^T E_k$$

(17.5)

where s_{ijkl}^E is the mechanical compliance of the material measured at zero electric field ($E = 0$), ε_{jk}^T is the dielectric permittivity measured at zero mechanical stress ($T = 0$), and d_{kij} represents the piezoelectric coupling effect. The direct piezoelectric effect converts the stress applied to the sensor into an electric charge. Similarly, the converse piezoelectric effect produces strain when a voltage is applied to the sensor.

In a PWAS, the electrical field E_3 is applied across the PWAS thickness in the three directions. The prevalent piezoelectric coupling is between in-plane strain in the 1 and 2 directions and out-of-plane electrical field in the third direction.

Frequency	1 Hz	100 Hz	1 kHz	1 MHz
Response time	1 s	10 ms	1 ms	1 μs
Application field	Strain, temperature monitoring of large structures	Vibration monitoring of large structures	• Acceleration monitoring • Seismograph • Vibration monitoring of power cables, suspension cables, pipelines	• Impact monitoring • Hydrophobes • Acoustic emission monitoring
Detection method (FBG equipment)	• Scanning gratings moved by stepper motors • Tunable laser and power meter	Fabry-perot tunable filter driven by piezo actuator		

Wave length sweeping by mechanical moving parts

Conversion of wave length shift into optical power change by optical filtering without neck moving parts

Figure 17.11 Various methods for FBG sensor conditioning as a function of needed detection frequency and application type.

At ultrasonic frequencies, PWAS can sense and excite guided Lamb waves traveling long distances along the thin-wall shell structures of aircraft and space vehicles (Fig. 17.12).

PWAS are made of thin, inexpensive piezoceramic wafers electrically poled in the thickness direction and provided with top and bottom electrodes. Typical PWAS are 7-mm squares or discs with a 0.2-mm thickness (Fig. 17.13). PWAS can be bonded to the structure with strain-gage installation methodology. They have also been experimentally inserted between the layers of a composite layup, but this option has raised some structural integrity issues that are still being examined. The PWAS transducers are called differently by various authors: "piezos," "piezo wafers," "PZTs," etc. In this article, we will consistently call them "PWAS" (same in singular and in plural) or "PWAS transducers."

When permanently attached to the structure, PWAS provide bidirectional energy transduction from the electronics into the structure, and from the structure back into the electronics. PWAS have been extensively used for SHM demonstrations because they directly convert electric energy into elastic energy and vice-versa, and thus, require very simple instrumentation: effective measurements of composite impact waves and guided-waves transmission/reception have been achieved with experimental setups consisting of no more than a signal generator, a digitizing oscilloscope, and a PC [27]. The commercially available SMART layer technology [28,29] has facilitated the use of these sensors in both academic and industrial SHM research.

Figure 17.12 Coupling between piezoelectric wafer active sensors and Lamb waves in a thin-wall structure: (a) symmetric mode; (b) antisymmetric mode.
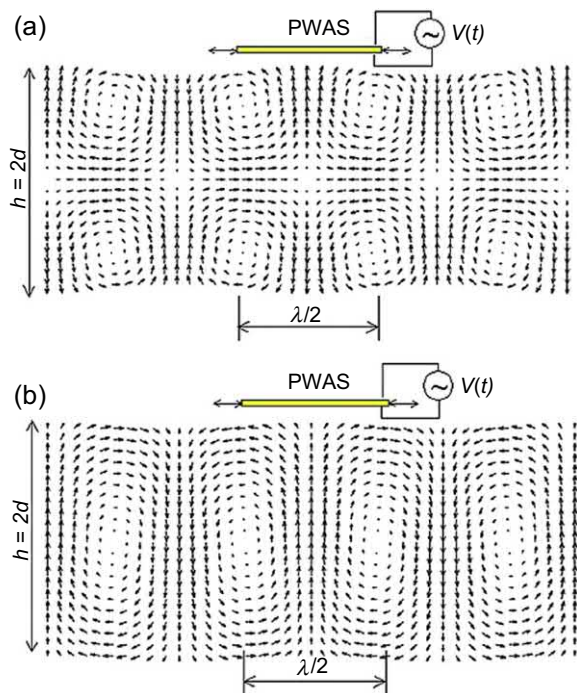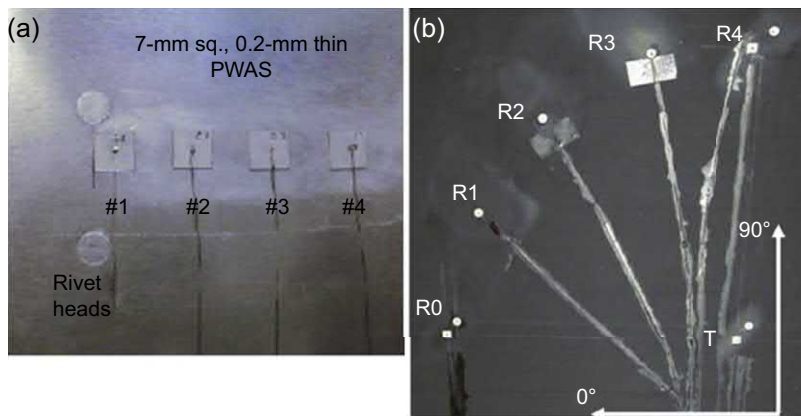
Figure 17.13 Piezoelectric wafer active sensors (PWAS) installation: (a) 7-mm square PWAS on a metallic structure; (b) 7-mm round and square PWAS on a composite structure.

As shown in Fig. 17.14, PWAS transducers can serve several purposes [27]: (a) high-bandwidth strain sensors; (b) high-bandwidth wave exciters and receivers; (c) resonators; (d) embedded modal sensors with the electromechanical (E/M) impedance method. By application types, PWAS transducers can be used for (i) **active sensing of far-field damage** using pulse-echo, pitch-catch, and phased-array methods, (ii) **active sensing of near-field damage** using high-frequency E/M impedance method and thickness-gage mode, and (iii) **passive sensing of damage-generating events** through detection of low-velocity impacts and acoustic emission at the tip of
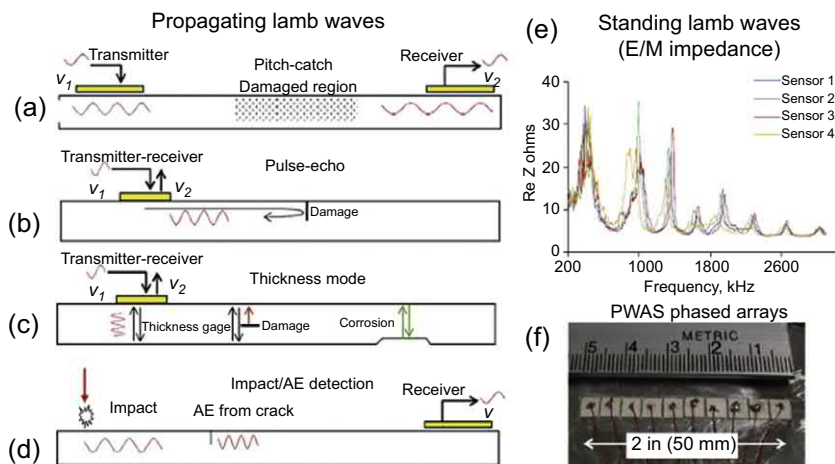
Figure 17.14 Use of piezoelectric wafer active sensors (PWAS) for damage detection with propagating and standing guided waves in thin-wall structures: (a) pitch-catch; (b) pulse-echo; (c) thickness mode; (d) impact and acoustic emission (AE) detection; (e) electromechanical (E/M) impedance; (f) PWAS phased array [27].

advancing cracks. By using Lamb waves in a thin-wall structure, one can detect a structural anomaly, i.e., cracks, corrosions, delaminations, and other damages. Because of the physical, mechanical, and piezoelectric properties of PWAS transducers, they act as both transmitters and receivers of Lamb waves traveling through the structure. Upon excitation with an electric signal, the PWAS generate Lamb waves in a thin-wall structure. The generated Lamb waves travel through the structure and are reflected or diffracted by the structural boundaries, discontinuities, and damages. The reflected or diffracted waves arrive at the PWAS, where they are transformed into electric signals.

PWAS transducers can be used in either traveling wave mode or standing wave mode. Details are given next.

17.3.5   Travelling-wave SHM methods with PWAS transducers

Fig. 17.14(a) illustrates the **pitch-catch method**. An electric signal applied at the transmitter PWAS generates, through piezoelectric transduction, elastic waves that travel into the structure and are captured at the receiver PWAS. As long as the structural region between the transmitter and receiver is in pristine condition, the received signal will be consistently the same; if the structure becomes damaged, then the received signal will be modified. Comparison between the historically stored signals and the currently read signal will indicate when changes (e.g., damage) take place in the structure. The pitch-catch method may be applied to situations in which the damage is diffuse and/or distributed, such as corrosion in metals or degradation in composites. By extension of the pitch-catch method to several pitch-catch pairs in a network of PWAS ("sparse array") placed around a structural region of interest, one achieves **ultrasonic tomography** through a round-robin process. Processing of the data collected during the round-robin process yields an image of the monitored region indicating the damaged area. Fig. 17.14(b) illustrates the **pulse-echo** method. In this case, the same PWAS transducer acts as both transmitter and receiver. A tone-burst signal applied to the PWAS generates an elastic wave packet that travels through the structure and reflects at structural boundaries and cracks and abrupt discontinuities. In a pristine structure, only boundary reflections are present, whereas, in a damaged structure, reflections from cracks also appear. By comparing historical signals, one can identify when new reflections appear due to the presence of damage. This comparison may be facilitated by the differential signal method.

Fig. 17.14(c) illustrates the use of PWAS transducers in **thickness mode**. The thickness mode is usually excited at much higher frequencies than the guided wave modes discussed in the previous two paragraphs. For example, the thickness mode for a 0.2-mm PWAS is excited at around 12 MHz, whereas the guided wave modes are excited at tens and hundreds of kHz. When operating in thickness mode, the PWAS transducer can act as a thickness gage. In metallic structures, thickness mode measurements allow the detection of damage that affects the structural thickness, e.g., corrosion, which can be detected from the other side of the structure, which is not exposed to the corrosive environment. In composite structures, thickness mode measurements may detect cracks which are parallel to the surface, such as delaminations. A limitation of the

thickness mode approach is that detection can only be made directly under the PWAS location or in its proximity. In this respect, this method is rather localized, which may be alright for monitoring well-defined critical areas, but insufficient for large area monitoring.

Fig. 17.14(d) illustrates the detection of **impacts and acoustic emission (AE) events**. In this case, the PWAS transducer is operating as a passive receiver of the elastic waves generated by impacts or by AE events. By placing several PWAS transducers in a network configuration around a given structural area, one can set up a "listening" system that would monitor if impact damage or AE events take place. Because the PWAS is self-energized through piezoelectric transduction, the listening system can stay in a low-energy dormant mode until triggered by the incoming waves. The signals recorded by the PWAS network can be processed to yield the location and amplitude of the impact and/or AE event.

17.3.6   Standing-wave SHM methods with PWAS transducers

When a structure is excited with sustained harmonic excitation of a given frequency, the waves traveling in the structure undergo multiple boundary reflections and settle down in a **standing-wave pattern** known as **vibration**. Structural vibration is characterized by resonance frequencies at which the structural response goes through peak values. The structural response measured over a frequency range, including several resonance frequencies, generates a vibration spectrum or frequency response function. When damage occurring in a structure induces changes in its dynamic properties, the vibration spectrum also changes. However, the conventional vibration analysis methods are not sensitive enough to detect small incipient damage; they can only measure structural dynamics up to several kHz, which is insufficient for the small wavelength needed to discover incipient damage. An alternative approach, which is able to measure structural spectrum into the hundreds of kHz and low MHz range, is offered by the electromechanical (E/M) impedance method [27]. The electromechanical impedance method measures the electrical impedance $Z(\omega)$, of a PWAS transducer using an impedance analyzer. The real part of the impedance $\mathrm{Re}(Z)$ reflects the mechanical behavior of the PWAS, i.e., its dynamic spectrum and its resonances. When the PWAS is attached to a structure, the real part of the impedance measured at the PWAS terminals reflects the dynamics of the structure on which the PWAS is attached, i.e., the structural dynamic spectrum and its resonances. Thus, a PWAS attached to a structure can be used as a structural−identification sensor that directly measures the structural response at very high frequencies. Fig. 17.14(e) illustrates the E/M impedance spectrum measured in the MHz range.

17.3.7   Phased PWAS arrays and embedded ultrasonic structural radar

A natural extension of the PWAS pulse-echo method is the development of a PWAS phased array (Fig. 17.14(f)), which is able to scan a large area from a single

location. Phased arrays were first used in radar applications because they allowed the replacement of the rotating radar dish with a fixed panel equipped with an array of transmitter-receivers which were energized with prearranged phase delays. When simultaneous signals are emitted from an array of transmitters, the constructive interference of the propagating waves creates a beam positioned broadside to the array. If prearranged phase delays are introduced in the firing of the signals of individual array elements, then the constructive interference beam can be steered to different angular positions. Thus, an azimuth and elevation sweep can be achieved without mechanical rotation of the radar platform. The phased array principle has gained wide utilization in ultrasonics, both for medical applications and for nondestructive evaluation, because ultrasonic phased arrays permit the sweeping of large volumes from a single location.

The PWAS phased arrays utilize the phased array principles to create an interrogating beam of guided waves that travel in a thin-wall structure and can sweep a large area from a single location [27,30]. The embedded ultrasonics structural radar (EUSR) methodology uses the full matrix of captured signals collected by the PWAS phased array to recreate a virtual sweeping of the monitored structural area. The associated image represents the reconstruction of the complete area as if the interrogating beam was actually sweeping it. When no damage is present, the only echoes are those arriving from the natural boundaries of the interrogated area; if the damage is present, its echo reflection is imaged on the EUSR screen indicating its location in (R, θ) or (x, y) coordinates. PWAS phased arrays have been used to monitor crack growth during fatigue testing [31].

A remarkable property of PWAS transducers is their frequency and size-dependent tuning with various guided Lamb waves traveling in the structure, as predicted by the following formula [30].

$$
\begin{aligned}
\varepsilon_x(x, t) = & -i \frac{a\tau_0}{\mu} \sum_{\xi^S} \left(\sin \xi^S a\right) \frac{N_S(\xi^S)}{D'_S(\xi^S)} e^{i(\xi^S x - \omega t)} \\
& -i \frac{a\tau_0}{\mu} \sum_{\xi^A} \left(\sin \xi^A a\right) \frac{N_A(\xi^A)}{D'_A(\xi^A)} e^{i(\xi^A x - \omega t)}
\end{aligned}
\tag{17.6}
$$

where ξ is the wavenumber and a is the PWAS half-length. The superscripts S and A signify the symmetric and antisymmetric modes, $D(\xi)$ is the LHS of the Rayleigh-Lamb equation [27], and D' is the derivative of D with respect to ξ. The summations in Eq. (17.6) cover all the symmetric and antisymmetric Lamb wave modes that exist for a given frequency-thickness value fd. It is apparent from Eq. (17.6) that, for a PWAS of given length $2a$, certain frequencies will maximize the $\sin \xi a$ terms for certain modes, whereas other frequencies will vanish the $\sin \xi a$ for other modes, since, at a given frequency, the Lamb wave modes have different wavelengths. Eq. (17.6) has been verified experimentally in both metallic and composite structures (Fig. 17.15).
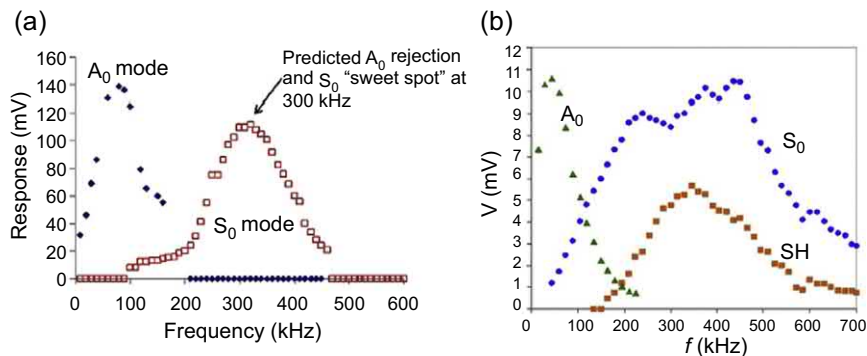
Figure 17.15 Experimental frequency tuning results: (a) maximum S_0 response at around 300 kHz due to A_0 rejection in a 1-mm aluminum plate; (b) similar rejection of A_0 mode in a CFRP composite plate [27].

17.3.8   Electrical properties sensors

The electrical SHM of composites relies on the material itself to act as the sensor. Carbon fibers are electrically conductive; the epoxy resin is an insulator. The carbon fiber-reinforced polymer (CFRP) composite is somehow conductive because the densely packed carbon fibers may touch each other. As damage (e.g., cracks and delamination) takes place in the composite, the electric conductivity is expected to change. The glass fiber-reinforced polymer (GFRP) composite is a nonconductive insulator with certain dielectric properties. Damage in GFRP composites creates microcracks and even sizable delaminations, which change the dielectric properties of the composite since the dielectric permittivity of air is smaller than that of GFRP. Ingress of water, which has a dielectric permittivity higher than GFRP, will again change the overall dielectric properties of GFRP composites.

These intuitive concepts stand at the foundation of the electrical SHM methods for composite materials. This approach is deemed "self-sensing" because it relies entirely on measuring a material property (i.e., electrical characteristic) and does not require an additional transduction sensor; the only instrumentation that needs to be installed on the composite structure consists of the electrodes. In the case of composite transport aircraft, the conductive screen skins currently used to mitigate lightning strike could potentially also serve as the measuring electrodes. Electrical SHM methods range from the simple measurement of the electrical resistance measurements up to more sophisticated methods, such as electrical potential mapping, dielectric measurement, electrochemical impedance, etc.

17.4   SHM methods and systems

Structural health monitoring of composites can be done in a variety of ways, and attempting a classification is a daunting task. From the point of view of the sensor

location, two major trends have emerged: (i) proximal/local sensor placement in the vicinity of a structural region of interest (hot spot); (ii) remote sensor placement, such as to interrogate a large structural area. Fig. 17.16 illustrates how these options could be achieved with piezo and fiber-optics; other sensors (resistance strain gages, electrical properties sensors, etc.) could also be used for either local or remote structural monitoring.

The methods that can be used for structural health monitoring depend, to a certain extent, on the physical principles of the sensors and/or of the structural interrogation approaches. However, two broad categories emerge: (a) passive sensing, and (b) active sensing. The former just monitors some structural/material property or the occurrence of damaging event; the latter actively interrogates the structure with ultrasonic or electromagnetic waves similar to the conventional NDE approaches.
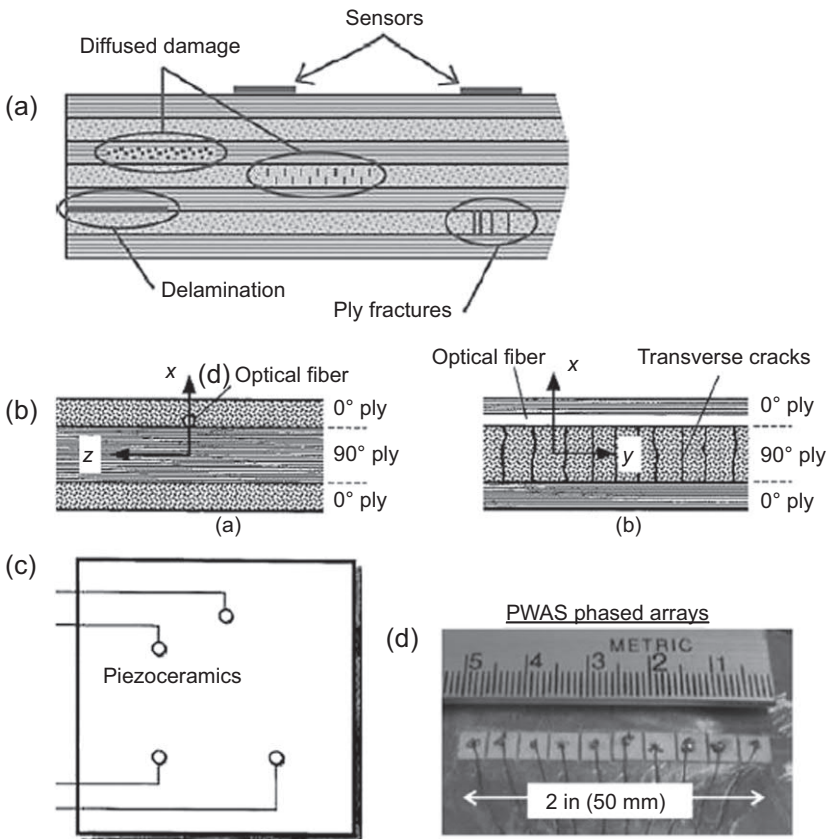
Figure 17.16 Possible sensor configurations for composites SHM: (a) local detection with piezo sensors [32]; (b) local detection with optical fiber sensors [24]; (c) sparse array of piezo-sensors guided-waves tomography for remote detection [33]; (d) phased-arrays of piezo-sensors for remote guided-waves scanning.

17.4.1 Strain monitoring as passive SHM method

Passive sensing SHM is done by using sensors to just "listen" to structural signals and monitor them over time. The premise of strain SHM is that presence of damage will generate a redistribution of mechanical strain in the structure which can be monitored and interpreted. A sudden rise of strains in a safety-critical part of the structure should trigger an alarm of impending failure, whereas, a sudden drop in strain may be indicative that, due to damage, the monitored part no longer carries its expected share of the load. Strain redistribution in the damage vicinity may be measured and interpreted as indicative of damage presence and extent (Fig. 17.17).

For example, delamination in a composite layup produces strain distribution in the surrounding area, which is substantially different from that in a pristine zone [34]. Strain monitoring can be done with conventional electrical resistance strain gages or with fiber optics. The latter offers the capability of having several measuring locations that can be individually addressed on the same fiber. Ref. [34] used conventional strain gages to monitor delamination in a composite T-joint. The strain gages were placed on the outside of the joint in zones deemed sensitive to strain redistribution due to delaminations.
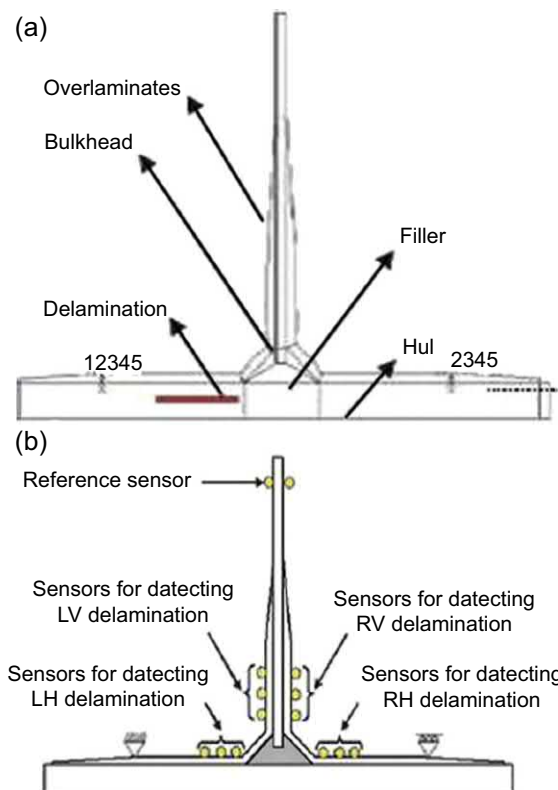
Figure 17.17 Delamination monitoring with conventional strain gages: (a) composite T-joint susceptible to delamination failure; (b) placement of strain gages for detecting delaminations in the horizontal and vertical sections [34].
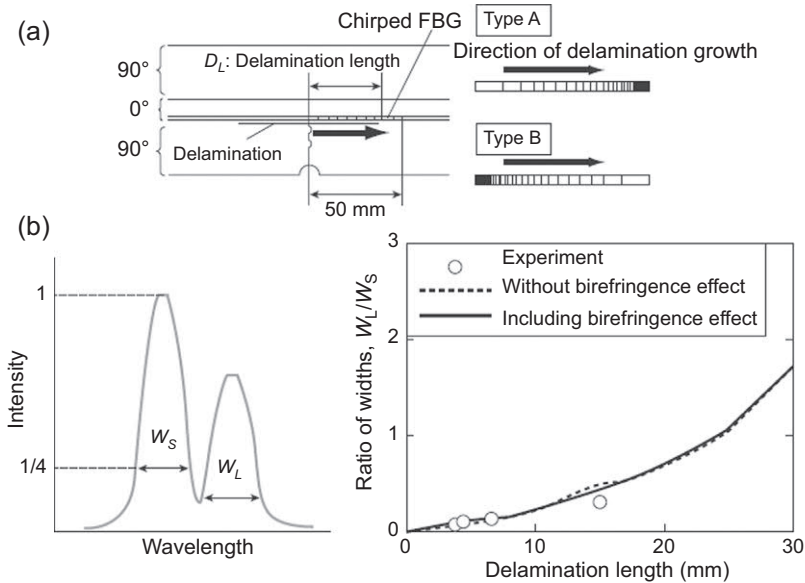
Figure 17.18 Chirped FBG sensor embedded in a cross-ply CFRP laminate to monitor occurrence and growth of delamination under four-point bending: (a) location of a sensor; (b) optical spectrum details used for quantifying delamination growth [36].

Ref. [35] used both conventional strain gages and fiber optics FBG sensors to measure strain in an aircraft wing section having CFRP composite skins with both cocured and cobonded stiffeners. Strain changes due to proximal damage (delamination between skin and stiffeners) or global damage (loosening of the spar/skin bolts) were recorded. Ref. [36] used special FBG sensors (chirped FBG) inserted in a cross-ply CFRP laminate to monitor the occurrence and growth of delamination under four-point bending. The changes in the optical spectrum of the chirped FBG were processed to yield the delamination occurrence and growth (Fig. 17.18).

In an early paper [24], Tanaka's group at the University of Tokyo, Japan discussed the detection of transverse cracks in CFRP composites using embedded FBG sensors (Fig. 17.19). An uncoated optical fiber containing 10-mm long FBG sensor was laid along the loading direction at the bottom of the longitudinal ($0°$) ply.

The strain was measured both with the FBG sensor and with a conventional resistance strain gage. The specimen was loaded in a tensile machine. Good agreement between the strain values measured by FBG sensors and conventional strain gage was observed (Fig. 17.20). Transverse cracks appeared in the $90°$ plies as the longitudinal strain was increased. During various loading stages of the experiment, the position and the number of the transverse cracks in the specimen was determined using an edge replica technique. It was found that the transverse crack density increases with longitudinal strain, as expected. As the crack density increased under increasing load, it was noticed that the reflected FBG spectrum became distorted, in addition to being shifted. This phenomenon was explained through a detailed analysis of the modified strain
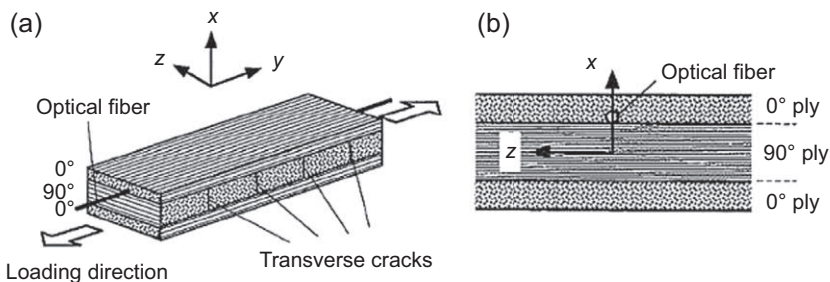
Figure 17.19 Longitudinal embedding of an optical fiber with an FBG sensor for detecting transverse cracks in a cross-ply CFRP specimen: (a) general view; (b) placement of the optical fiber [24].

distribution due to transverse cracks presence. From simulation studies, it was concluded that the distortion of the spectrum can be correlated with the crack density, which could offer a baseline-free method for transverse cracks detection.

The spectrum width at the half-maximum was proposed as a quantitative indicator of transverse crack density. However, it was noticed in practice that the residual thermal stresses resulting from the initial CFRP processing might pose a problem because the spectrum had already split into two peaks and became much broader before the tensile load was even applied. Hence, this proposed baseline-free method could be used only if the FBG sensor could be embedded without the nonaxisymmetric residual thermal stresses being present. Nonetheless, the direct measurement of actual strain with the FBG sensor can be used as a baseline-based method of inferring the crack density from the strain values, although this would have to rely on an initial baseline measurement of the crack-free state before loading. This topic was further studied by the same team to assess the effect of coating [37] and to test special small-diameter FBG sensors with 52 μm outside diameter [16].
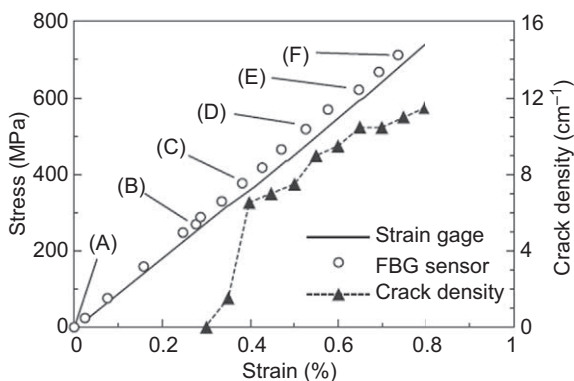
Figure 17.20 Longitudinal strain measured by FBG sensor and conventional strain gage and density of transverse cracks in a cross-ply CFRP specimen [24].

Ref. [38] reports the monitoring of the buckling of a composite panel with FBG sensors. The FBG sensors were used as strain sensors, and buckling was detected by the change in the local strain measured by the FBG sensors. Three blade-stiffened CFRP panels with cocured stiffening webs were tested under compressive load. Several FBG sensors were surface bonded on two of the stiffened panels and embedded into the stiffener webs of the third panel. The FBG sensors measured the strain distribution in the stiffener web and in the skin panels. The buckling onset was detected, and the postbuckling behavior could be tracked.

Monitoring of operational loads and strain on actual vehicles has been reported by several authors. Ref. [39] reports multichannel FBG strain monitoring systems installed on a sailing yacht and a turboprop aircraft. Ref. [40] reports fiber optic multipoint strain measurement on two full-scale CFRP vehicles, an American's Cup class yacht and an experimental reentry vehicle. Ref. [26] describes multipoint FBG strain measurements on a sea-going GFRP ship. The FBG sensors were installed at various locations to measure operational loads during sea trials. Both FBG strain rosettes and individual FBG sensors were used. Typical strain recordings are illustrated in Fig. 17.21; strains due to wave-drive sagging and hogging of the whole ship and due to resonant whipping of the hull can be distinguished in these signals are shown in Fig. 17.21(a); equivalent stress resultants postcalculated from the strain data and FEM modeling are shown in Fig. 17.21(b).

Ref. [42] reports a space-qualified FBG system, which uses FBG sensors to monitor the strains in a filament wound CFRP tank during pressure testing. Ref. [41] describes a space-qualified on-board FBG system used to monitor the strain on a CFRP composite LH2 tank installed on a reusable launch vehicle (RLV) test article. The FBG sensors were installed on the CFRP composite tank with UV-cured polyurethane adhesive that showed good performance at cryogenic temperatures. The system (which weighs less than 2 kg) was installed, flown, and tested on the RLV; typical recorded data is shown in Fig. 17.22.

17.4.2   Impact monitoring as passive SHM method

Both impact and acoustic emission (AE) events generate ultrasonic waves; hence, they benefit from the commonality of sensor installation. However, the frequency bands in which the two events take place are different; the impacts are more strongly felt as relatively low-frequency flexural waves (e.g., tens of kHz), whereas the AE events happen in a higher frequency band (e.g., $150 - 300$ kHz).

Monitoring of damage-inducing impacts on a composite structure and determination of their location and amplitude has received considerable attention. The basic method named "passive sensing diagnostics" (PSD) in Ref. [43], consists of using a sparse array of sensors (strain gages, piezo wafers, FBG, etc.) that capture the guided waves generated by the impact. The captured signals are processed to determine the impact location and amplitude. The guided waves generated by the impact are highly dispersive and multimodal (Fig. 17.23). This makes the time-of-flight determination through signal processing quite challenging, especially in composite structures with complicated structural features. Two algorithmic approaches have been explored for
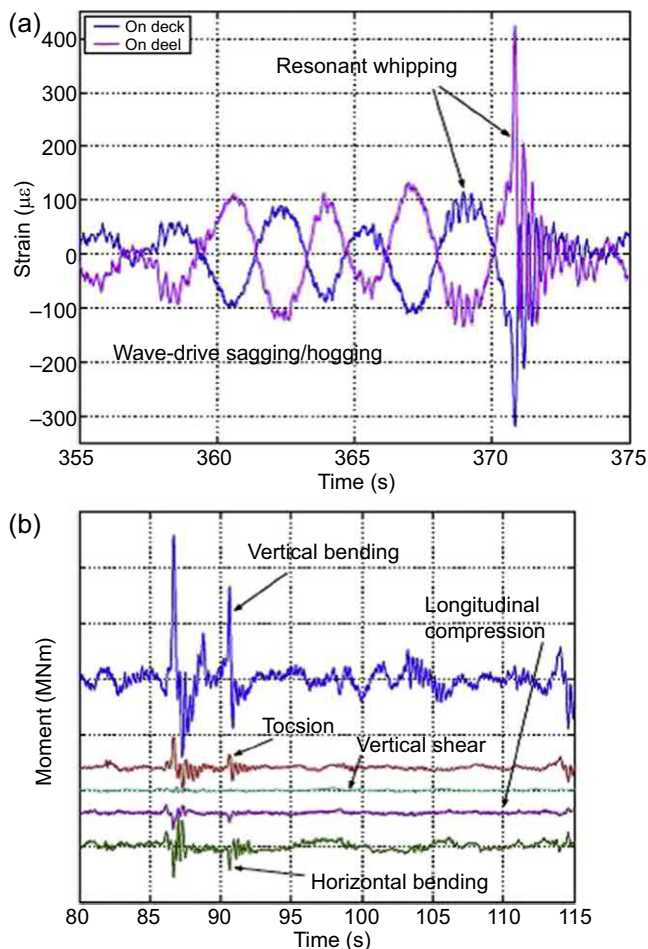
Figure 17.21 Typical strain signals recorded with FBG sensors: (a) strains due to wave-drive sagging and hogging, as well as resonant whipping; (b) stress resultants calculated from the strain data [26].

impact identification: (a) model based; (b) data driven. The direct use of directional sensors has also been recently reported.

The use of fiber optic FBG sensors is attractive because a single optical fiber can carry several FBG sensors, which can be independently interrogated; hence, the installation cabling issues are greatly simplified if FBG sensors are used instead of the more conventional transducers. In addition, fiber optics sensors are immune to electromagnetic interference, which can confer an advantage in certain applications.

The model-based approach to impact detection relies on a structural model that can simulate the signals to be received by the sensors for a given impact of assumed amplitude time history $F(t)$ and location (x, y). The structural model varies from simple
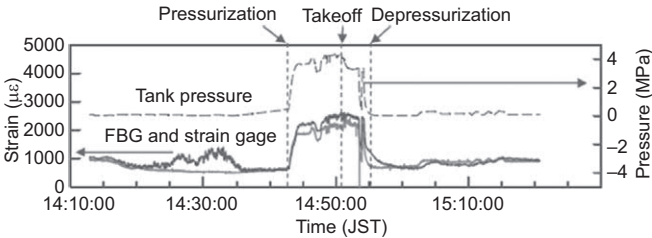
Figure 17.22 Space-qualified FBG strain measurement system installed on a composite LH2 tank [41].

composite plate flexure [44], through more-complicated models of stiffened plate [45], and FEM meshing of complicated composite structures [46]. The simulated and the measured time series were compared, and the model parameters (impact location, amplitude, and time-history) were adjusted through a two-stage optimization/fitting process [47,48] (Fig. 17.24).

An alternative approach is to perform experimental system ID instead of modeling the actual physical structure. Ref. [49] performed the system ID with the ARX technique (auto-regressive with exogenous inputs) and constructed a numerical model of the physical system based on a finite set of experiments. In the training stage, a set of experiments were conducted on the specimen; each experiment consisted of applying a known impact to a known location on the structure and recording the time-series corresponding to the impact force and the signals received at the sensors. The recorded time-series data was used in the ARX algorithm to determine the model
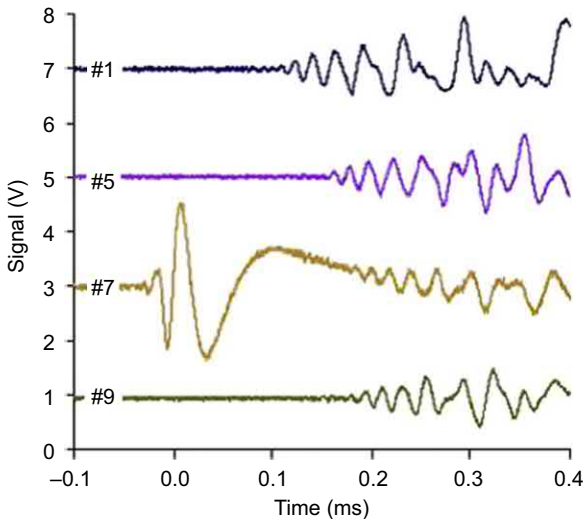
Figure 17.23 Typical impact signals received at various locations with PWAS transducers (PWAS #7 is closest to the impact).

parameters and implicitly the structural transfer functions between the impact location and the sensors. In the validation stage, the ARX was used to synthesize sensor signals and compared them with the original experimental data; a good agreement was observed [49].

Finally, the validated ARX model was used to detect impact at locations and time-history different from those used in the training stage. The detection accuracy in terms of location and force time-history was evaluated. More recent developments of this approach [46] used a FEM simulation instead of actual hardware to construct the system ID model; again, a force of known time-history was applied at given locations on the FEM structure, and the response of the sensors was simulated. The simulated sensors response was used as input the system ID algorithm. A two-step optimization using genetic algorithms (GA) was applied to fit the system ID model to the FEM-generated signals. This approach permitted the exploration of a wide parameter space in simulation in order to find the most appropriate sensors network configuration that would give an acceptable probability of detection (POD) of the impact with manageable sensor-installation costs.
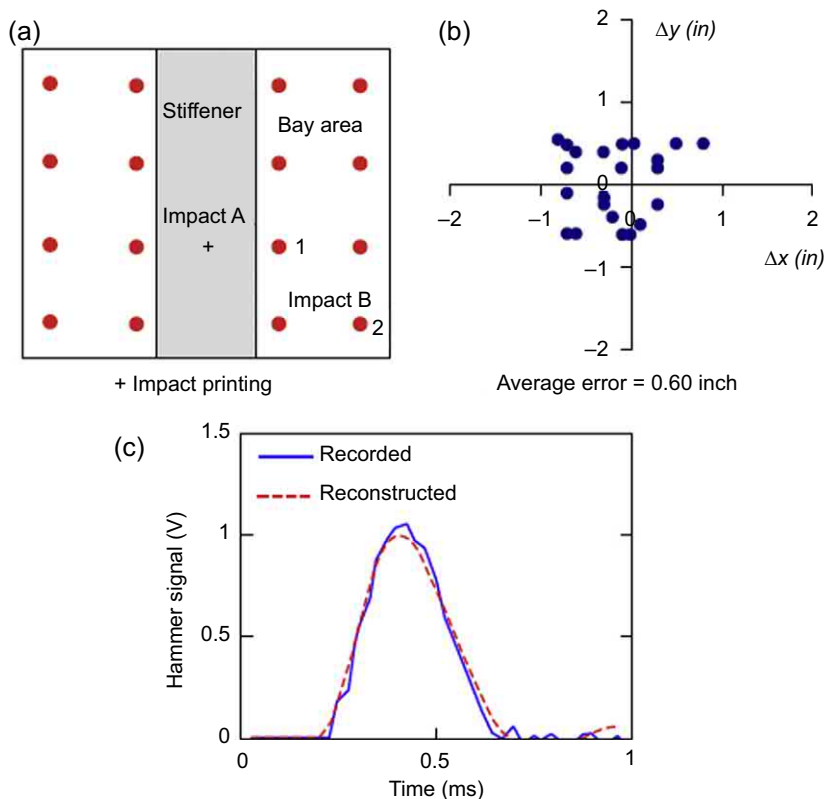
Figure 17.24 Impact identification on stiffened composite panel using a system ID approach: (a) impact locations; (b) impact localization spread; (c) force reconstruction [49].

Structural models for complicated composite structures may not be detailed enough to handle wave propagation simulation. Hence, techniques that do not require a structural model and rely entirely on the measured data are of interest. Data-driven techniques have been investigated by several researchers: Ref. [50] used an artificial neural network (NN) for impact detection in a CFRP composite plate instrumented with four piezo wafer sensors. NN training was done with an initial set of 100 low-energy impacts (0.3 J) applied on the nodes of a 10-by-10 grid covering most of the plate. The second set of 30 low-energy impacts was performed at randomly selected sites on the same grid. The third set consisted of only one single severe-energy impact (10 J) that produced an indentation on the front face of the panel, cracking on the back face, and internal delaminations between the plies. Finally, the fourth set of low-energy impacts was performed to teach the NN the "feel" of a damaged panel. Features extracted from the signals were used to train the NN algorithm. The mean detection error was 5% (17 radial mm on a 340 mm by 340 mm plate). Further work by the same team, which includes a more complicated NN, larger set of features, and the use of genetic algorithm (GA) optimization is reported in Refs. [51,52]. Other artificial intelligence techniques, e.g., case-based reasoning (CBR) have also been explored [15].

The use of directional sensors can greatly simplify impact detection and localization. Directional sensors overcome the time-of-flight triangulation difficulty posed by the multimodal dispersive character of the guided waves generated by the impact event. Only two directional sensors are needed to locate an impact; each sensor generates a ray indicating the direction of the presumptive wave source and the impact is easily located at the intersection of these two rays (Fig. 17.25(a)).

Several directional sensors types have been proposed, one based on fiber optics [53], the other based on piezo wafers [54]. Ref. [53] reports a rosette constructed from three FBG optical sensors arranged in a triangular pattern (Fig. 17.25(b)). Strain gage rosette principles are used to resolve the principal directions and obtain the sensing ray direction. Ref. [54,55] report a piezo rosette constructed from three macro-fiber composite (MFC) sensors arranged in a star pattern (Fig. 17.25(c)). Both methods obtained good impact localization without any structural model, neural net, or signal baseline (Fig. 17.26). Piezo rosettes constructed from thin rectangular wafers of PMN crystals cut and poled in the $[011]_c$ direction have also been reported [56].

17.4.3   Acoustic emission monitoring as passive SHM method

Acoustic emission (AE) can be monitored with both piezo transducers and fiber optics sensors. The piezo-based AE sensors are relatively well established in conventional ultrasonic NDE; however, these conventional AE sensors are not quite appropriate for deploying in large numbers on a flight structure due to both cost and size. The compact SHM sensors (both piezo and optical) have also been shown capable of AE monitoring: Ref. [52,57,58] used piezo wafer sensors, whereas Ref. [59,60] used optical fiber Bragg gratings (FBG) sensors for AE emission monitoring. Existing
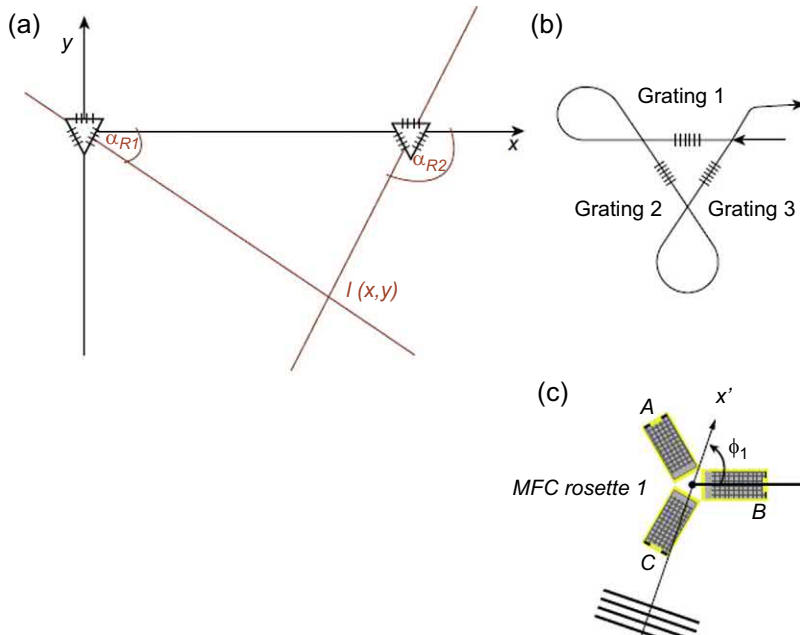
Figure 17.25 Impact localization with directional sensors: (a) localization is obtained at the intersection of two directional sensor rays; (b) FBG rosette directional optical sensor [53]; (c) MFC rosette directional piezo sensor [54].

AE monitoring methodology for signal capturing and interpretation (noise filtering, AE events counting algorithms, etc. [61]) can also be used with SHM sensors.

Ref. [57] reports that the impact response recorded by a piezo wafer sensor mounted on a CFRP plate seems to show two separate wave types (Fig. 17.27): (a) a stress wave due to the initial impact; and (b) a superposed high-frequency wave packet similar to an AE burst due to the composite laminate suffering damage (delaminations and splits) due to impact.

A similar situation in which the signal received by the piezo wafer transducer during an impact event on a composite structure seems to contain two distinct components (impact generated waves and AE waves) was also reported in Ref. [52]. As illustrated in Fig. 17.28, the higher-order wavelet-transform components of the signal from a 3.7 J impact (Fig. 17.28(b)) show AE bursts that were not present in the signal from a lower-energy impact (Fig. 17.28(a)). The interpretation of these signals was as follows: the 3.7-J impact produced internal damage (and hence AE signals) but the lower-energy impact did not.

Ref. [60] describes the use of a dual-demodulator FBG system to measure both the strain and the acoustic emission signal emanating from the damage created in a cross-ply laminated composite under tensile loading. One FBG sensor, one electrical strain gage (ESG), and one PZT sensor were mounted on a CFRP cross-ply composite specimen (Fig. 17.29). The dual demodulation was achieved with a tunable Fabry-Perot
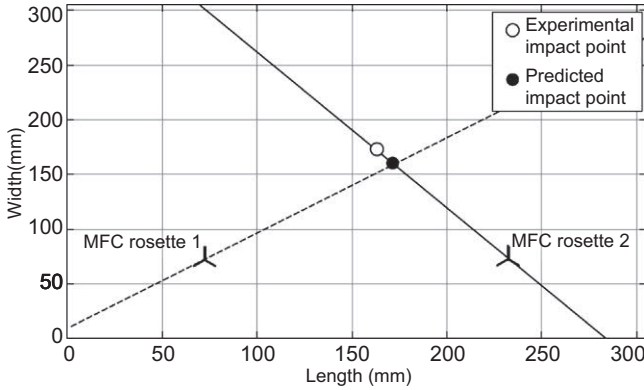
Figure 17.26 Model-free impact localization on quasi-isotropic CFRP woven composite panel using directional piezo sensors MFC rosettes [55].

filter (TFPF) for quasi-static strain and a Mach-Zehnder interferometer (MZI) for strain waves. The quasi-static strain and the strain wave signals measured by the FBG sensor showed sudden strain shifts accompanied by high-frequency strain waves in the hundreds of kHz range occurring when transverse cracks propagated in the transverse layer of the cross-ply composite (Fig. 17.30). Note that the FBG signal in Fig. 17.30 is proportional to the dynamic strain whereas the PZT signal is proportional to the strain rate.

17.4.4 Acousto-ultrasonics active SHM method

Active sensing SHM consists of "interrogating" the structure with wave transmitters and picking up the structural response with wave receivers. The waves used in active SHM may be elastic or electromagnetic. In the former case, one distinguishes
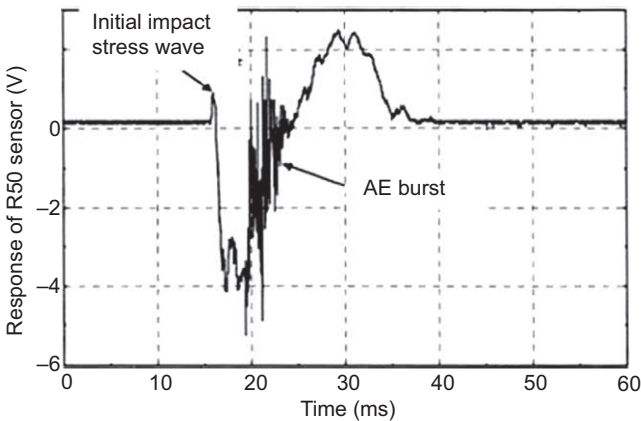
Figure 17.27 Impact response recorded by a piezo wafer sensor mounted on a CFRP plate: two separate wave types are apparent, an initial impact stress wave and a high-frequency wave packed similar to an AE burst [57].
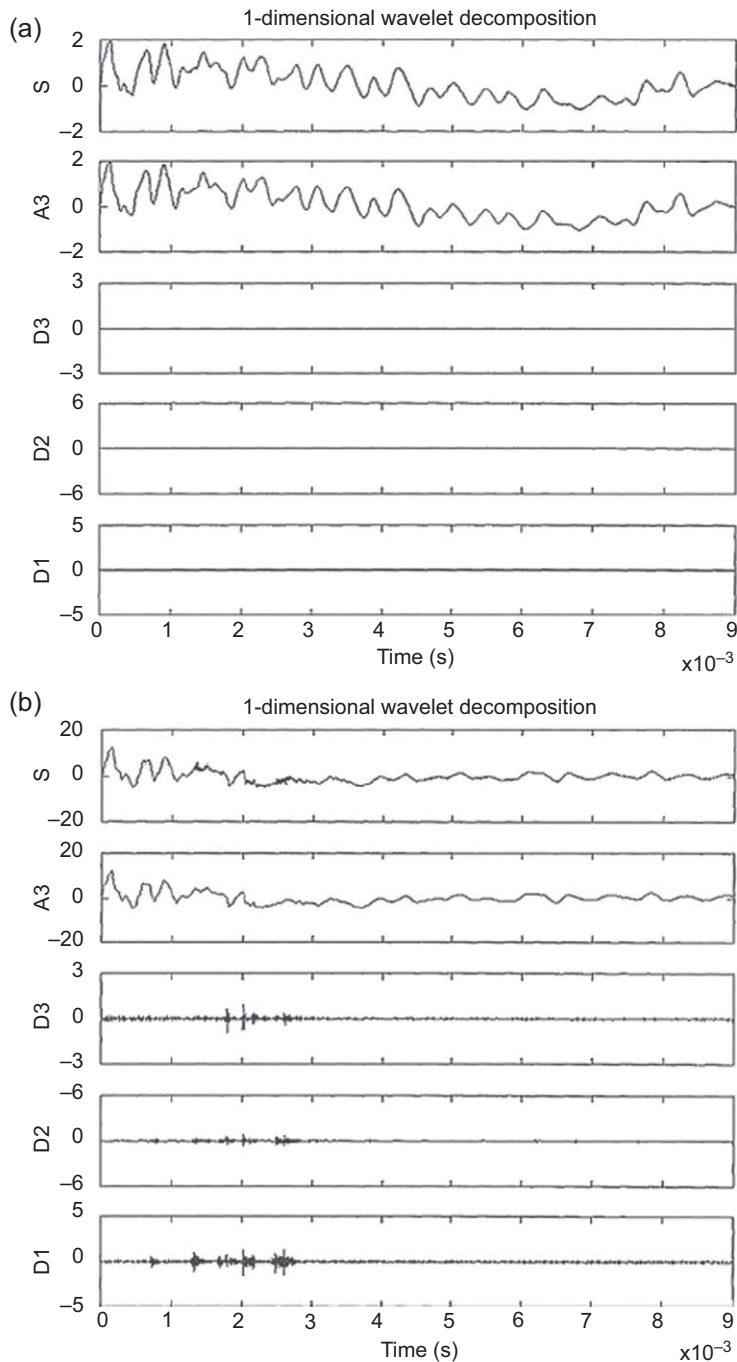
Figure 17.28 Wavelet transform (WT) decomposition of the received signal during impact on a $[0_4/90_4]_S$ CFRP laminate: (a) 0.1-J impact does not produce internal damage; (b) 3.7-J impact produces internal damage which generates acoustic emission (AE) waves that are picked up in the WT decomposition levels D1, D2, D3 [62].
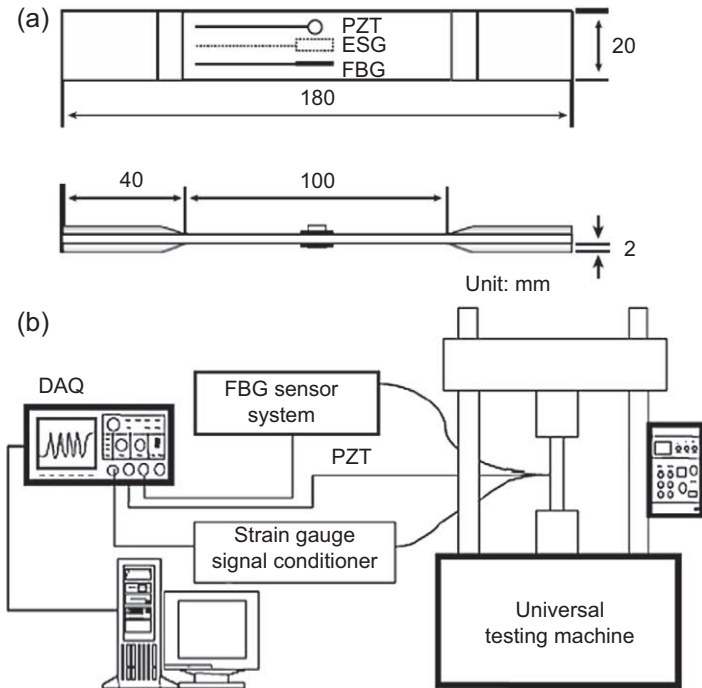
Figure 17.29 Simultaneous measurement of static strain and strain waves in a cross-ply composite using FBG sensors and dual-demodulator system: (a) specimen instrumented with FBG sensor, PZT sensor, and electrical strain gage (ESG); (b) experimental setup schematics [60].

methods based on (a) frequency response function; (b) acousto-ultrasonics; (c) electromechanical impedance spectroscopy; (d) directional guided waves. In the latter case, one has a variety of electric, magnetic, and electromagnetic methods used for monitoring the composite electrical properties.

Acousto-ultrasonics [63] is a guided-wave pitch-catch method. The "acousto" part in the name reminds of the reception of guided waves generated by the acoustic emission (AE) process at a propagating crack. The term "ultrasonics" infers that this is an active technique in which ultrasonic waves are generated by the transmitter; thus, this technique is different from the AE technique that is just a passive technique.

Acousto-ultrasonics requires two ultrasonic guided-wave probes, a transmitter, and a receiver [30]. In SHM work, the transmitter has usually been a piezoelectric wafer; the receiver has traditionally been also a piezoelectric wafer, which imparts reciprocal transmitter-receiver capabilities to the setup and enables guided-waves tomography. The use of different receivers, e.g., fiber optics FBG sensors, has also been reported [64]; this option is attractive because a single optical fiber can carry several FBG sensors that can be independently interrogated; hence, the installation cabling is greatly simplified. In addition, fiber optics sensors are immune to electromagnetic interference, which can confer an advantage in certain applications. However, FBG cannot
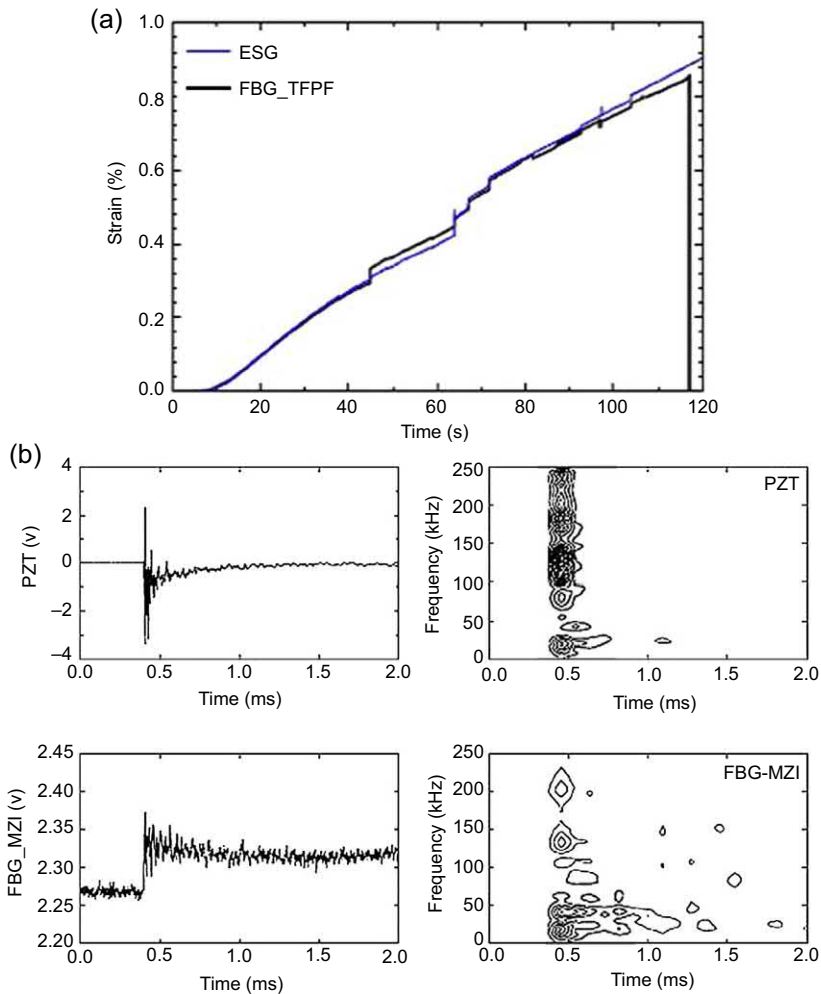
Figure 17.30 (a) Quasi-static strain measured with the TFPF-demodulated FBG sensor signal; (b) strain wave signals measured with the MZI-demodulated FBG sensor compared with that measured by the PZT sensor [60].

usually act as a transmitter, and this imposes limitations on the methodology; reports of using optical fiber for guided waves excitation also exist, but these attempts are still confined to the laboratory [65].

The acousto-ultrasonics approach, aka "active damage diagnostics" (ASD) [43], has received extensive attention in composites SHM; ASD is the operating principle of the SMART Layer technology [28,29]; this technique has been extensively used to image impact damage and delamination in laminated composites that compared quite well with X-ray and C-scan imaging (Fig. 17.31). Its principles are illustrated in Fig. 17.32: a unit damage identification cell (UDIC) is defined by four piezo wafer

(a) X ray picture with damage

Estimated Damage

Real Damage

PZT

[0₂/45₂/-45₂/90₂]s

(b)

$(0_4/90_4)s$

	a	b	↗
Estimated	1.4	0.6	2°
Real	1.2	0.5	0°

Unit: inch

$(0_2/45_2/-45_2/90_2)s$

	a	b	↗
Estimated	0.9	0.5	27°
Real	0.8	0.4	32°

a : semi-major axis of the damage.
b : semi-minor axis of the damage.
↗ : angle between semi-major axis and 0°
   fibre direction
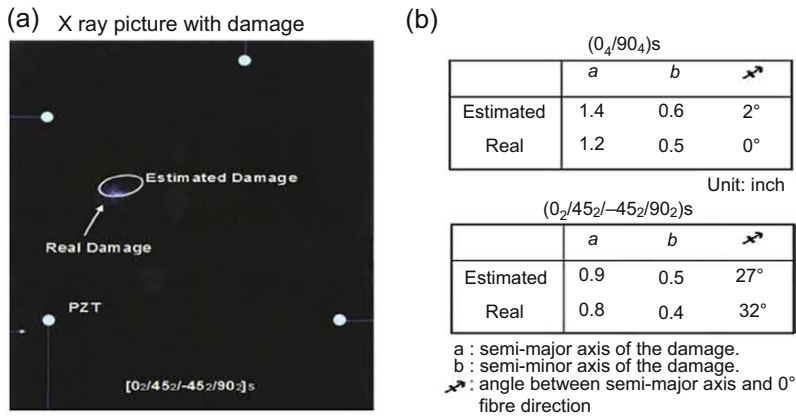
Figure 17.31 Impact damage identification in a composite panel with the embedded pitch-catch method: (a) "real damage" detected by X-rays superposed with the "estimated damage" computed from the data; the location of the four piezo wafer transducers "PZT" is also shown; (b) comparison between estimation and real damage size is described by an ellipse with parameters a, b, θ [33].

transducers that can act as both transmitters (actuators) and receivers (sensors) of ultrasonic guided waves [33]. A round-robin pitch-catch process takes place between the four transducers. The transducer acting in actuator mode generates a diagnostic wave that interacts with the composite structure and is modified by the damage. The wave is received at the other three transducers acting as receivers. The six possible transducer pairs define six path-dependent signals. For each path, a scatter signal is defined as the difference between a baseline signal, previously recorded on a pristine specimen, and the current signal recorded on the damaged specimen. The set of recorded pitch-catch signals is processed through a computer algorithm to yield the damage image and estimate its size and location (Fig. 17.31)

A large variety of damage imaging algorithms has been reported in the literature. Ref. [33] used a structural model based on axisymmetric flexure-like guided waves at relatively low frequency-thickness product values; these waves are highly dispersive, and their speed tends to zero as frequency tends to zero; hence, a reduction in effective plate thickness due to damage effects a strong reduction in the wave speed. The wave speed reduction factor was assumed to be constant within a damaged area. This structural model was used to predict the scattered wave signal from a damage assumed to be an ellipse of semi-axes (a, b), inclination θ, and location (x, y). A two-step fitting algorithm was used, first for the time of flight (TOF), next for the damage location, size, and shape. The algorithm was calibrated for a number of composite layups and damage types [66] and incorporated in the SMART Suitcase commercial software [65]. Other more elaborate structural models (both analytical and FEM) for considering the complicated interaction of guided waves with defects in layered composites are possible (Fig. 17.33).

The guided wave tomography has been extensively used in conventional ultrasonic NDE, and some sophisticated data-driven imaging algorithms have been developed (e.g., Ref. [68]). Similar approaches have been tried for acousto-ultrasonics SHM imaging [69,70]. Ref. [67] performs a comprehensive comparative study of various tomographic imaging algorithms: fan-beam filtered back-projection (FBP), interpolated FBP, algebraic reconstruction technique (ART) with Bessel−Kaiser basis functions, probabilistic reconstruction algorithm (PRA), etc. The use of their own RAPID algorithm that accounts for wave scattering and reflection from damage using a probabilistic damage detection concept where the final tomogram is a superposition of ray ellipses was recommended. The ray ellipses are initially constructed using simulated multi-mode guided wave propagation in the composite; they can be modified based on experimental data for a more accurate representation of defects.

A considerable number of references discuss imaging algorithms that are entirely data-driven and do not require a structural model. Similar to the passive damage diagnostic approach, neural networks (NN) have been proposed that would be trained on a number of damage scenarios and then used to identify actual damage; however, this data-driven approach seems to require a large number of tests and could be cost prohibitive.

Another model-free method for active damage detection is based on directional transducers. For passive sensing, Section 17.4.1 has already discussed the use of
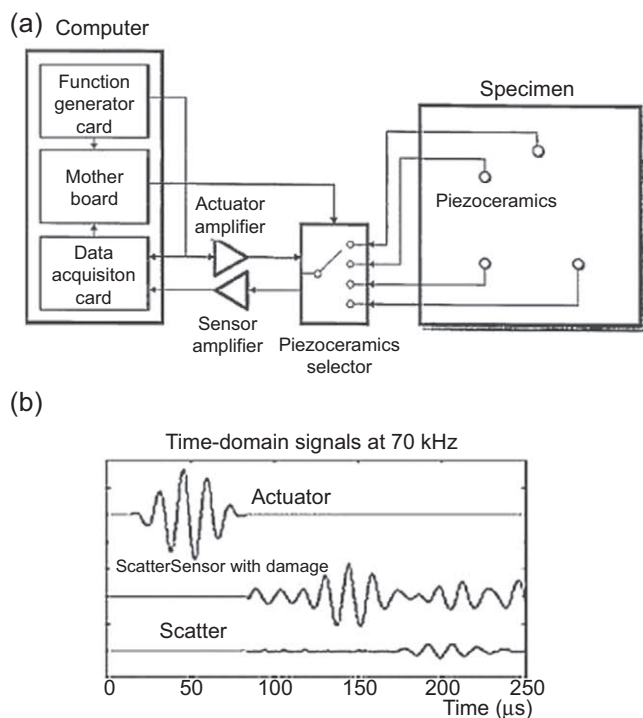
Figure 17.32 Schema of acousto-ultrasonics damage imaging in a composite: (a) experimental setup; (b) scatter signal definition [33].
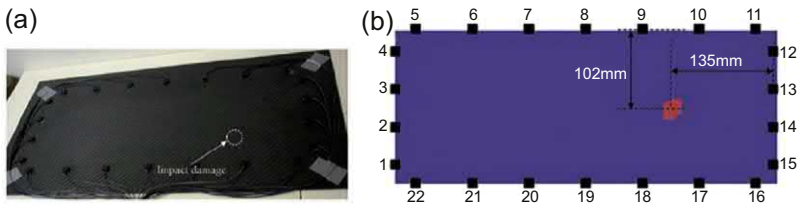
Figure 17.33 Imaging tomogram of impact damage in a composite plate: (a) photo showing damage location and sensors setup; (b) reconstructed tomogram showing predicted damage location and size [67].

directional strain rosettes (both piezo and optical) to effectively detect an acoustic source without the need for a structural model. For active sensing, directional transmission, as well as the reception of a guided wave can be achieved with phased-array transducers. Ref. [67] reviews the main imaging techniques for guided-wave SHM and identifies the phased-array principles as the other major approach besides tomography. Ref. [71] constructed *in situ* phased-arrays of piezo wafer active sensors tuned to low-dispersion S0 waves. The EUSR[1] phased-array SHM concept which performs the phased-array reconstruction in postprocessing, and thus, does not need multi-channel measuring capabilities, was proposed. The EUSR phased-array SHM was used to image *in situ* the actual crack growth during fatigue testing of an aluminum plate [31]. Extension to two-dimensional phased-array scanning was studied for different array geometries and was demonstrated experimentally for a rectangular array [72] (Fig. 17.34).

Ref. [67] demonstrated the simultaneous imaging of multiple crack and hole damage sites using a single circular-fence phased-array placed at the center of an aluminum plate. Ref. [73] studied the extension of phased array principles to composite structures
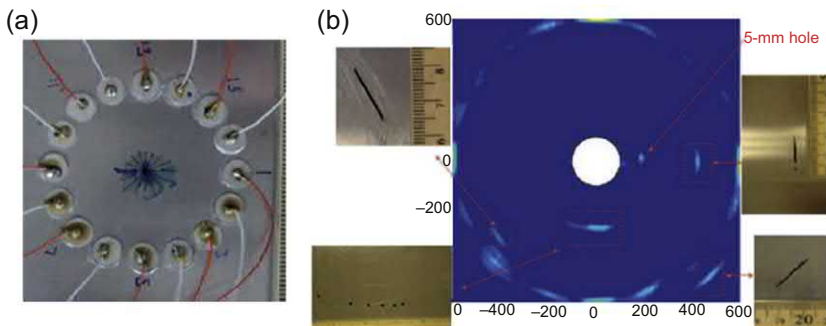
Figure 17.34 *in situ* phased array for monitoring multiple damages on an aluminum plate: (a) circular-fence array of piezo wafer active sensors placed at plate center; (b) simultaneous imaging of multiple crack and hole damage sites on the plate [67].

---

[1] Embedded ultrasonic structural radar.

and developed appropriate signal processing algorithm (experimental results of actual damage imaging in a composite specimen have still not been published).

Directional transducers, such as macro-fiber composite (MFC), can be placed along the desired directions for ultrasonic interrogation. In addition, MFC transducers can be arranged in rosette configurations and then be excited with phased signals such that a beam steering effect is achieved. An extensive theoretical and experimental study of the capabilities of directional MFC transducers and MFC rosettes is given in Ref. [74].

Another method of constructing transducers with intrinsic beam steering capabilities for large area SHM imaging is described in Ref. [75]. A steerable directional transducer is constructed with eight independently addressable sectors arranged around the circle at 45° pitch (Fig. 17.35(a)). Each sector has an actuator outer part and a sensing inner part. An interdigitated electrode pattern was printed on a copper-clad Kapton film using photolithography. 0.2-mm thick PZT–5A piezoceramic rings were diced into wedge-shaped fibers such that a fiber width of 0.36 mm was achieved at the inner radius. The fibers and electrodes were bonded together and cured in an autoclave and then poled (Fig. 17.35(b)). The steering of the directional sensor is achieved by switching between the individual sector. Calibration experiments were performed on an aluminum plate; the SLDV measured wave field for various excitation directions agreed very well with the theoretical predictions.

A directional SHM transducer that does not require phase-array delays or connection switching to achieve steering is described in Ref. [76]. This directional sensor achieves tuning into the preferential direction at certain discrete frequencies, which are the solution of a frequency-wavenumber equation. The transducer consists of a skew array of piezo wafer active sensors placed at pitch values d_1, d_2 and angles α, β about the 1 and 2 axes, respectively (Fig. 17.36(a)). The transducer achieves directivity at certain frequencies; Fig. 17.36(b) illustrates the directionality measured with SLDV on an isotropic aluminum: 45°@105 kHz, 120°@150 kHz, −17°@200 kHz,
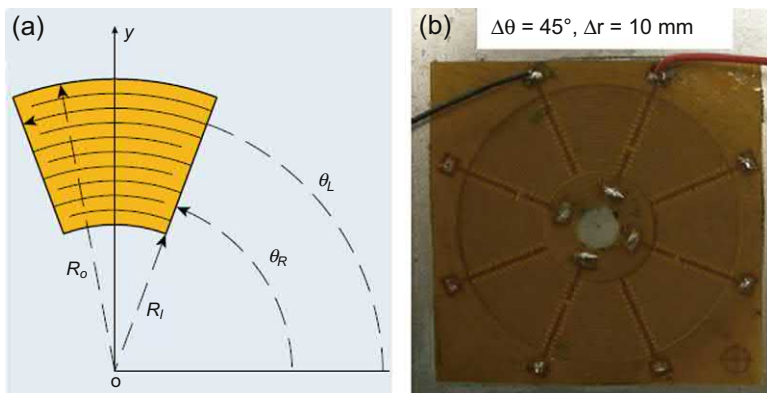
Figure 17.35 Directionally steerable CLOVER transducer for 2-D SHM scanning: (a) schematic illustrating the geometry of an individual sector; (b) actual implementation [75].
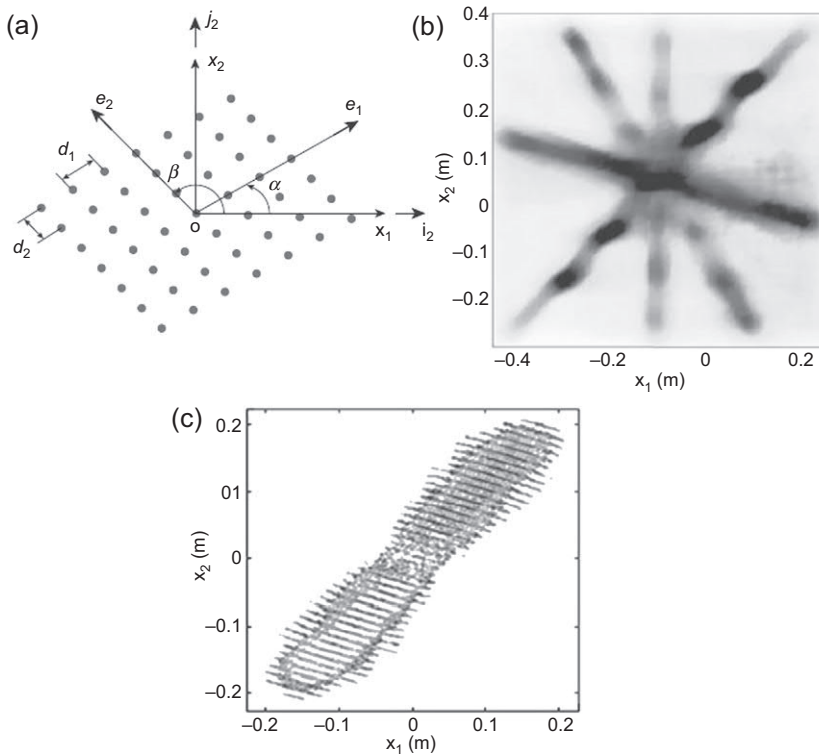
Figure 17.36 Frequency-steerable direction SHM sensor: (a) grid pattern of the sensor elements; (b) preferential steering directions highlighted simultaneously through broadband excitation on an aluminum plate as measured with an SLDV; (c) directional wave pattern achieved on a composite plate at the first steering frequency: guided wave simulation in an unidirectional GFRP plate [76].

88°@280 kHz. Thus, the transducer directionality is controlled by the excitation frequency in discrete steps.

Ref. [76] also addresses directionality in a composite plate, which is more difficult to achieve because of the inherent anisotropy of the medium. Fig. 17.36(c) shows such directional pattern obtained through guided wave simulation in a unidirectional a GFRP plate. A further extension of this concept to achieve continuous steering through a double spiral shape is presented in Ref. [77].

Piezo-optical acousto-ultrasonics uses piezo transmitters and FBG sensor receivers. Ref. [78] describes a piezo-optical approach to detect impact delaminations in CFRP composites; a pitch-catch method based on the mode conversion between symmetric and antisymmetric guided waves modes at the delamination is used. A 3.4 − mm thick CFRP quasi-isotropic plate with artificial midplane delamination was tested. Piezo actuators were placed on both sides of the plate such that symmetric and antisymmetric modes could be independently excited. It was found that the

pristine 3.4 mm quasi-isotropic CFRP specimen accommodates three guided wave modes (quasi A_0, S_0, A_1) at 300 kHz. However, the delaminated region is composed of thinner branches, say 1.7 mm each. In these thinner plates, only two guided wave modes (quasi A_0 and S_0) propagate at 300 kHz. Hence, the A_1 mode, which is present in the pristine plate, cannot propagate in the top and bottom branches of the delaminated plate. Thus, mode conversion takes place at the beginning of the delaminated region, and the A_1 mode converts into S_0 and A_0 modes. Conversely, at the end of the delamination region, when the thickness changes back from 1.7 mm to 3.4 mm, some of the energy of the S_0 and A_0 modes will be converted into a reemerging A_1 mode. Therefore, if there is delamination in the middle of the thickness of the laminate, it is expected that the frequency dispersion curves of the Lamb waves that pass through the delaminated area will change because of the mode conversions at both tips of the delamination.

When antisymmetric modes were used (A_0, A_1), the A_1 mode was converted into the S_0 mode in the delaminated area (Fig. 17.37(a)). In this case, the dispersion of the group velocity differs between the A_1 mode in the pristine region of 3.4 mm thickness and the S_0 mode in the delaminated region of 1.7 mm thickness, as plotted in (Fig. 17.37(b)). Since the S_0 mode is faster than the A_1 mode, the arrival time of the A_1 mode at the FBG sensors decreases with the increase of the delamination length. Furthermore, this difference in the velocity increases as the frequency decreases. Hence, the frequency dispersion of the received A_1 mode is expected to change, depending on the delamination length. This phenomenon was investigated numerically and experimentally, and a damage index based on the A_1 conversion was proposed for quantifying the delamination damage. A similar mode conversion phenomenon measured with scanning Doppler laser vibrometry was reported in Ref. [79]; the generation of standing waves that persist only in the delamination region was also observed [79].

Ref. [80] describes the use of a hybrid PZT/FBG system for active detection of impact delamination damage in a composite plate using acousto-ultrasonic tomography. Fig. 17.38 shows a schematic of the sensor layout. The advantage of the FBG sensors is that several of them can be laid out on the same optical fiber, hence, reducing the
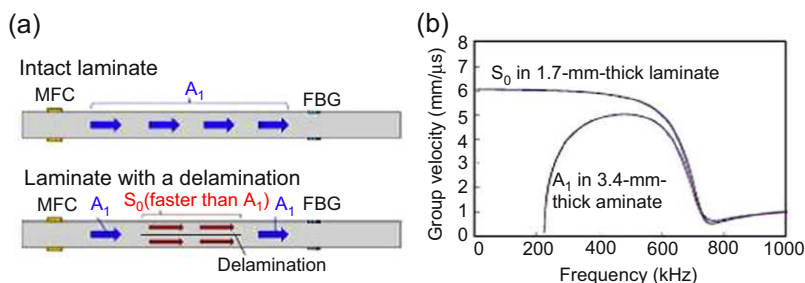
Figure 17.37 Conversion between A_1 mode and S_0 mode at the start and end of the delaminated region: (a) wave propagation schematic; (b) group velocity changes due to effective thickness change [78].
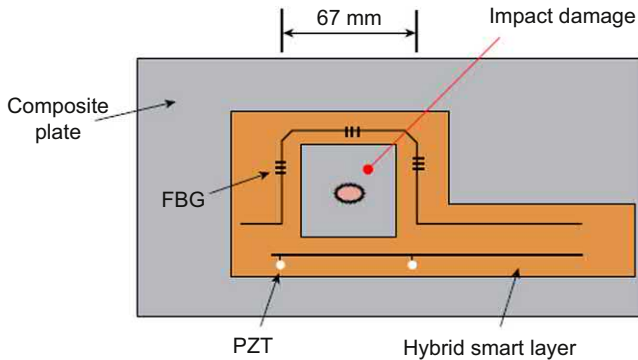
Figure 17.38 Hybrid PZT/FBG system for the detection of impact delamination damage in a CFRP composite plate [80].

number of cable connections. As indicated in Fig. 17.38, the FBG sensors surround the impact damage area and hence collect signals from several directions. Fig. 17.39 shows the imaging of the damage through the guided-waves interrogation system compared with conventional X-ray.

17.4.5   Vibration monitoring active SHM method

Finding damage from changes in structural vibration is one of the longest-researched SHM approach [81]. Structural vibration is characterized by resonance frequencies at which the structural response goes through peaks. At each resonance, the structure vibrates in salient modes. The structural response measured over a frequency range containing several resonance frequencies generates a vibration spectrum or frequency response function. At a generic frequency that is not a resonant, the structure motion follows an operational deflection shape. If a structure suffers damage, then its dynamic properties (resonance frequencies and mode shapes, damping, operational deflection shapes, etc.) also change.

A pertinent survey article [82] classifies the vibration-based damage identification methods into four categories: (i) natural frequency-based methods; (ii) mode shape-based methods; (iii) curvature/strain mode shape-based methods; (iv) other methods based on modal parameters. Although most of these methods can tell that some damage is present from vibration changes, the finding of damage location and size proves to be very challenging. This fact is not surprising because vibration assessment is a global method, whereas damage is a local event. Damage-induced local changes have only limited influence on the global scale. In other words, loss of structural strength at a local scale may cause structural failure in virtue of the "weakest link" principle but may not be detected at the global scale before the failure actually occurs. An additional difficulty is that, in practical applications, the vibration changes due to damage may be confounded by those due to environmental vibrations or by temperature/humidity changes that affect the structural vibration but do not represent damage.
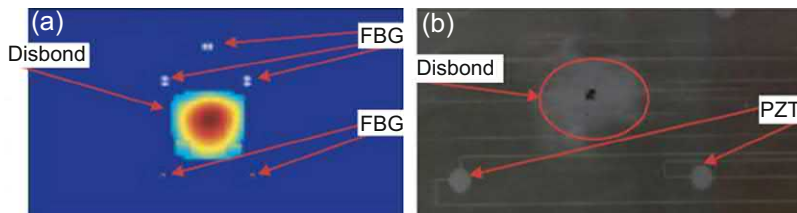
Figure 17.39 Detection of impact delamination damage in a CFRP composite plate using a hybrid PZT/FBG system (a) reconstructed tomographic image; (b) X-ray image [80].

Most of the vibration-based SHM work reported to date is model-based; a common approach is to have a detailed structural model that is fitted to a pristine structure over the frequency range of interest. For detecting damage, the model is manipulated by introducing simulated damage at various locations until the vibration measured on the damaged structure is being reproduced by the model. A variety of optimization methods for model updating have been tried [82] to achieve this data-fitting goal. This approach was used by Ref. [83] to detect low-energy impact damage in quasi-isotropic 3.12-mm thick CFRP beams. The beams were shaken with burst random excitation, and frequency response function (FRF) was measured at 33 points Doppler laser velocimeter (DLV) filtered in the $0 - 1.6\,\text{kHz}$ band. A modal identification package was used to obtain the modal parameters; a damage-induced decrease of natural frequencies and increase of modal damping were observed. A detailed FEM model was used in a topological optimization loop to construct the damage scenario that best fits the measured vibration data. Fig. 17.40 shows a FEM-generated image of the damaged specimen; the FEM damage zones compare well with the ultrasonic C-scan of the actual specimen.

The curvature/strain modes method hold the promise of detecting damage from the processing of experimental data without a structural model. The premise of the method
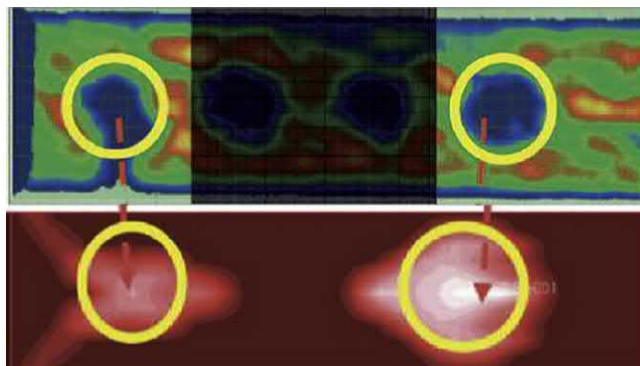
Figure 17.40 Vibration-based identification of impact damage in quasi-isotropic CFRP through model updating: top picture shows the ultrasonic C-scan of the specimen; the bottom picture shows the damage areas fitted in the FEM model [81].

is that damage in thin-wall structures induces local discontinuities that strongly affect the curvature of the flexural modes of the structure [84]. The curvature of the modes (i.e., the curvature modes) can be determined through space-wise double differentiation of the measured displacement/velocity/acceleration modes. They can also be measured directly with surface mounted strain gages.

If the modal displacement is measured on a dense grid with a scanning Doppler laser velocimeter (SLDV) then curvature modes method can be quite effective. Ref. [85] demonstrates its successful application on a composite beam with a couple of saw-cut notches. The beam was excited with a surface mounted piezoceramic wafer. The curvature mode shapes are determined through space-wise double differentiation of the measured displacement; a strain energy ratio (SER) is calculated at each grid point. A method for self-baselining is also proposed. This method does not require measurements on a pristine structure; the baseline is simply determined from the damaged structure itself under the hypothesis that damage is a local phenomenon that sharply modifies the curvature modes of the structure in a local region. Hence, a baseline is obtained through low-order smoothing of the measured data such that higher order variations are eliminated. If the data is very dense, this can be achieved simply through undersampling [85]. Other possible approaches are low-order curve fitting, spline interpolation [85], wavelet transform, etc.

However, SHM applications of the curvature-modes method require the use of *in situ* sensing instead of the SLDV approach. Ref. [86] describes the use of surface-mounted flexible piezo sensors made of polyvinylidene fluoride (PVDF) place at 16 locations on a cross-ply CFRP beam. Vibration excitation was done with a piezoceramic wafer mounted at the end of the beam energized by a sine signal swept up to 2 kHz. Various damages were applied on separate specimens (saw-cut notches; delaminations simulated by Teflon inserts; impact). A set of pristine specimens were used to construct a baseline database of curvature modes. Subsequently, data were taken on the damaged beams. Further processing of these experimental results was done in Ref. [87]. The method showed promise although the experimental data suffered from considerable scatter.

Considerable effort has been dedicated to applying statistical signal processing methods to vibration signals [88]. Ref. [89] describes shaker tests performed on a composite wing instrumented with FBG sensors and accelerometers. The wing had sandwich construction with composite faces and foam core. Consecutive low-velocity 7-J impacts were applied in a certain zone of the wing, which was surrounded with FBG sensors. Vibration signals were recorded during stochastic Gaussian excitation in the $0-1500$ Hz range. The FBG sensors were sampled at 3906 Hz. The vibration time-series signals were processed with statistical method aimed at revealing the nonlinear response features associated with impact damage [89].

17.4.6 Frequency transfer function active SHM method

The frequency transfer function SHM method resembles the vibration SHM methods in the fact that it uses the spectral representation of the data. However, its implementation is different; the frequency transfer function (FRF) between two structurally

mounted piezo wafers is determined directly through sweep-sine or broadband random excitation. The complex quantity measured in this way is also known as transmittance. FRF SHM methods can be either model-based or model free.

A model-based FRF SHM method is described in Ref. [62]. The analysis is performed in two steps: (a) direct problem; (b) inverse problem. The direct problem is stated as follows: given a composite structure with known damage, find the FRF between a given pair of actuator-sensor wafer transducers. For solving the direct problem, a model of a composite structure with attached piezo wafer transducers was constructed, e.g., the actuator-sensor pair depicted in Fig. 17.41. The model is used to predict the FRF between the two transducers. Next, delamination damage is introduced into the model, and a new FRF is predicted (Fig. 17.41). If the structure has several transducers, then all the possible combinations are used to determine a set of FRF data.

The inverse problem is more challenging: given a measured FRF between actuator-sensor pairs, find the location and size of the damage in the composite structure. For solving the inverse problem, one has to sift through all the possible combinations of damage size and location and then select the one that best fits the measured data. Ref. [62] describes in quite a detail this two-step process consisting of building the model, conducting experiments, and then iteratively adjusting the model to determine the best possible approximation of the size and location of the damage. It was found that the method was successful in determining delaminations that were greater than
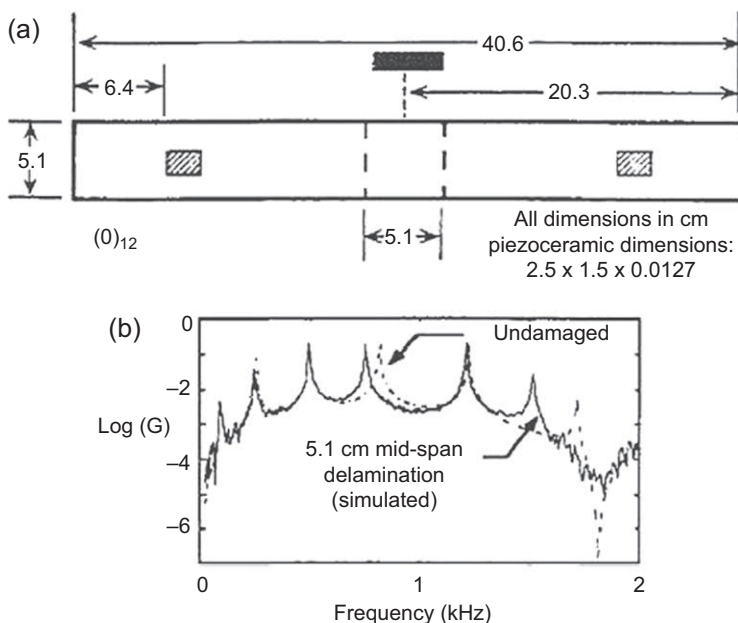
Figure 17.41 Model-based FRF SHM: (a) composite specimen geometry; (b) frequency response function (FRF) up to 2 kHz showing changes due to damage [62].
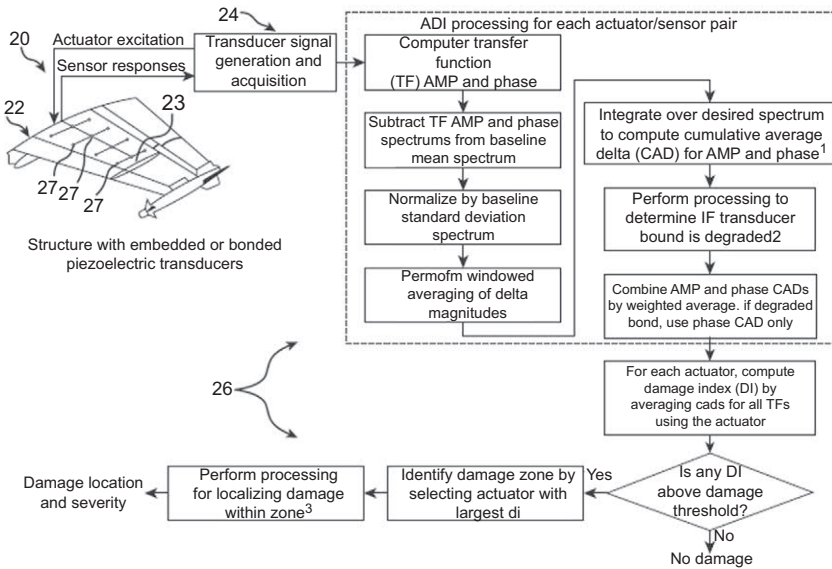
Figure 17.42 Model-free frequency transfer function SHM system based entirely on statistical signal processing [90].

approximately 10% of the beam length but had difficulty with smaller delaminations. It was found that experimental noise can obscure the subtle changes in the amplitude response produced by delaminations.

Ref. [90] describes a model-free FRF SHM method named active damage interrogation (ADI). It also consists of multiple actuator-sensor pairs of piezo wafer transducers mounted on the structure. Broadband signals (white noise or chirp up to 100 kHz) are transmitted between all the possible pairs in a round-robin process, and the associated transfer functions magnitude and phase spectra are calculated (Fig. 17.42). The data is further processed with statistical methods to determine a comprehensive damage indication metric or damage index (DI) for each actuator. The damage is then localized to a damage zone by identifying the actuator with the highest DI. Further processing of an array of DI values can be performed to localize the damage further within the damage zone. A more recent revisiting of this approach through numerical modeling and improved placement of the transducers is reported in Ref. [91].

17.4.7 Electromechanical impedance spectroscopy active SHM method

The electromechanical (E/M) impedance spectroscopy is a high-frequency standing waves method capable of detecting small local damage in the vicinity of the transducer. The essence of the E/M impedance technique consists of using an electrical impedance analyzer to measure the impedance, $Z(\omega)$, of a PWAS transducer firmly

attached to the monitored structure. As proven through theoretical developments and experimental tests [27], the real part of the impedance $\mathrm{Re}(Z)$ reflects the mechanical behavior of the structure on which the PWAS is attached, i.e., its follows the dynamic spectrum and the resonances of the structure [92,93]. Thus, a PWAS attached to a structure can be used as a structural−identification sensor that directly measures the local structural spectrum at very high frequencies. Electromechanical impedance spectroscopy (EMIS) has been shown to be very effective in the detection of proximal disbonds [94] and delaminations [32]. It has also been used to monitor material state change in composite specimens during fatigue testing [95,96].

Detection of delaminations has been tried by both traveling guided waves and by standing ultrasonic guided waves. In the former case, mode conversion and scatter at the delamination boundary modifies the traveling wave pattern. In the latter case, disbonds and delamination manifest high-frequency "breathing" modes that were not present in the pristine structure.

Conventional vibration analysis methods, which measure structural dynamics up to several kHz, are not sensitive enough to detect damage that is much smaller than the structural scale, such as local delaminations in a composite structure. These local resonances would manifest as new peaks in the high-frequency spectrum of the local structure. Local vibration measuring techniques that can sense the high-frequency breathing mode of the disbonded area and its effect on the dynamics of the surrounding structure are needed. Laser Doppler velocimeter (LDV) measurements have verified that piezoelectric wafer sensors attached to the structure can excite the high-frequency breathing modes of a disbonded or delaminated area [79,85,97]. A method to directly measure this high-frequency local vibration spectrum is offered by the E/M impedance method, which can measure the structural spectrum into the hundreds of kHz and low MHz range [27].

Fig. 17.43 shows the application of EMIS for the detection of 20-mm long delamination on a $2-\mathrm{mm}$ thick L-section bonded stiffener [94]; PWAS transducer a2,
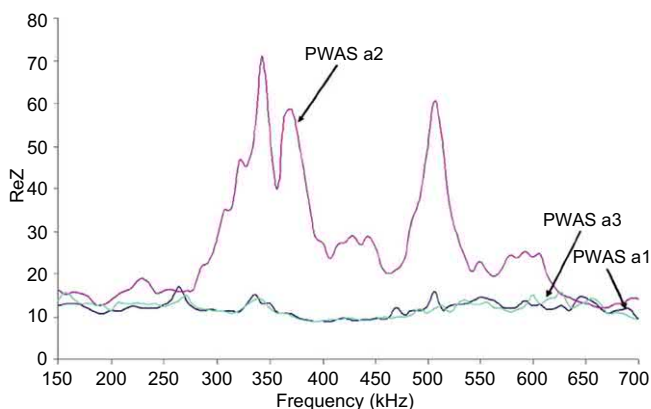
Figure 17.43 E/M impedance spectrum showing new resonant frequencies due to disbond (PWAS a2) that were not present in a well-bonded region on the same member.

which is placed in a zone proximal to the delamination displays new resonances associated with disbond vibration at $\sim 350\,\mathrm{kHz}$ and $\sim 510\,\mathrm{kHz}$. In the same time, these new resonances are not present in the spectrum measured by the witness PWAS transducers a1 and a3 that were placed on the same stiffener but some 70 mm away on either side of the disbond. The fact that the a1 and a3 spectra are almost identical confirms the consistency of the EMIS method.

A comprehensive analysis of the use of EMIS for damage detection in laminated composites was presented in Ref. [32]. Fig. 17.44 shows the experimental setup and the analytical model. A transfer-matrix method approach was used to compute the high-frequency dynamics of the delaminated composite beam and then predict the E/M impedance at the piezoelectric sensor. An extensive parameter study of the effect of delamination length, position, and depth location on the E/M impedance spectrum was performed. The effect of the PWAS transducer location relative to the disbond was also studied. The prediction results were compared with experiments performed on quasi-isotropic CFRP beams.

The EMIS method was used by several authors to measure disbonds and delamination: Ref. [98] discusses FEM simulation of EMIS disbond detection in bonded composite repairs; ref. [99] reports the measurement EMIS for disbonding detection of CFRP composite strips used for strengthening and rehabilitation of concrete structures. EMIS was also used for monitoring progressive changes in a composite material during cyclic fatigue loading: Ref. [100] describes how EMIS was applied to ceramic matrix composites during axial fatigue and compared the results with acoustic emission readings; Ref. [95] reports EMIS being used to monitor woven GFRP specimens
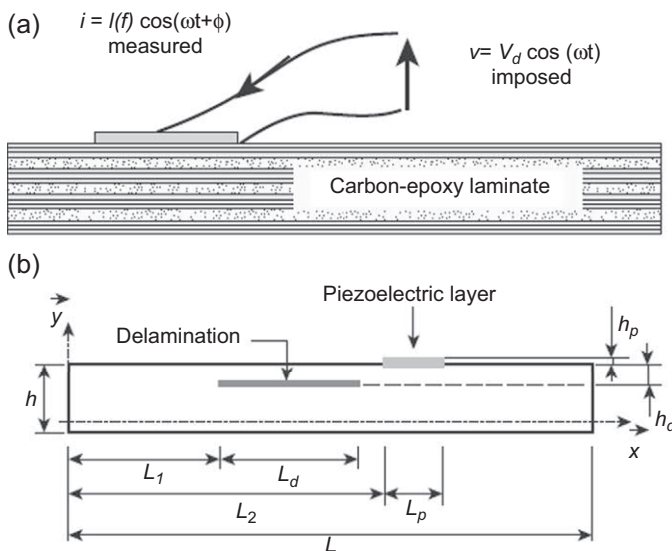
Figure 17.44 Modeling of electromechanical impedance spectroscopy for delamination detection in CFRP composites: (a) experimental setup; (b) analytical model [32].

undergoing flexural fatigue; Ref. [96] compares EMIS measurements and FEM predictions at high ultrasonic frequencies (hundreds of kHz to tens of MHz).

17.4.8   Electrical properties monitoring active SHM method

The electrical SHM of composites relies on the material itself to act as a sensor. As mentioned in Section 15, the carbon fibers are electrically conductive, whereas the glass fibers and the epoxy matrix are insulators. Hence, the electrical SHM of composites will be performed differently for CFRP than for GFRP, as detailed next.

When a unidirectional CFRP composite specimen is stretched, its longitudinal resistance decreases. This phenomenon (which may be due to both a transverse Poisson effect and carbon fiber piezo-resistivity) is reversible, and the resistance returns to its initial value as the load is released. However, if damage occurs, irreversible resistance changes may occur. Fig. 17.45 shows the variation of longitudinal electrical resistance during tension-tension fatigue testing of a unidirectional CFRP composite specimen. The reversible cyclic changes of resistance are due to the reversible cyclic strains. The permanently increased resistance at cycle # 218,281 may be due to permanent damage, e.g., matrix and some fiber fracture in the specimen. Ref. [101] correlated the appearance of residual electrical resistance changes with optical microscope observation on the side of a cross-ply specimen. It was concluded that residual electrical resistance change became elevated just after the onset of matrix cracking at 0.25% strain.

Impact damage detection by electrical resistance monitoring of CFRP composites has been given a lot of attention. The methods fall into two large categories: (a) monitoring of an average damage state of the whole panel by performing overall resistance measurements; and (b) damage location through more elaborate measurements and data processing. Ref. [102] describes a conductivity mapping approach that employs an array of electrodes surface-mounted on the CFRP composite. Measurements taken between one electrical contact and all of its neighbors in the array
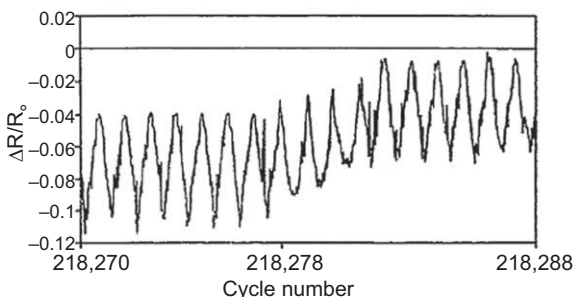
Figure 17.45 Variation of longitudinal electrical resistance during tension−tension fatigue testing of a unidirectional CFRP composite specimen. The cyclic change of resistance is due to reversible cyclic strain; the permanent increased in resistance around cycle # 218,281 may be due to permanent damage, e.g., some fiber fracture [103].

Figure 17.46 Electrical resistance monitoring with surface mounted electrodes: (a) surface mounted electrodes pattern; (b) schema of delamination and matrix cracking phenomena in relation to the electrode placement [104].
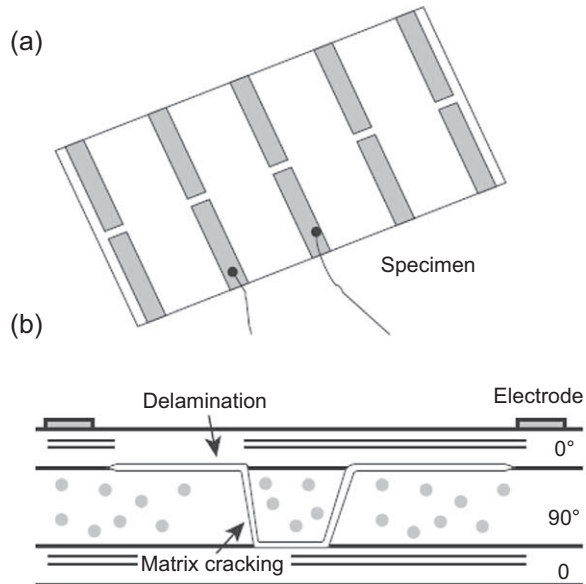
could give conductivity values in all the corresponding directions. By plotting the conductivity values over the specimen area and looking for anomalies in the conductivity surface, one could identify possible damage zones. Detection of fiber fracture and matrix damage (transverse cracking and delamination) was demonstrated. The method was shown capable of detecting surface-breaking severe damage but unable to detect barely visible mild damage.

Ref. [104] uses a "response surface" technique to process the electrical resistance measurements. A large number of cross-ply and quasi-isotropic specimens were tested such that statistical data processing could be applied. Copper-foil electrodes mounted on one side of the CFRP specimens during prepreg layup were cocured with the specimen (Fig. 17.46). Impact-induced matrix cracking and delaminations were detected. Probability of location estimation and error bands were computed [104]. The extension of this method to woven CFRP composites is described in Ref. [105].

Ref. [106] describes multiphysics FEM simulation of two electrical conductivity techniques for delamination detection in CFRP composites: (a) the circular array method (Fig. 17.47(a)); and (b) the matrix array method (Fig. 17.47(a)). It was concluded that the matrix array method was more effective and gave a smaller error in detecting delamination than the circular array method [106]. However, the matrix array method may be affected by severe impacts that may produce damage to the electrode strips mounted on the specimen surface. If this happens, the surviving electrodes, which were more remote from the damage may be used to measure the large-scale electrical resistance changes as in the circular array method.

The electrical potential method uses the array of contact electrodes to measure the electrical potential with respect to a reference point or the ground. Since the potential
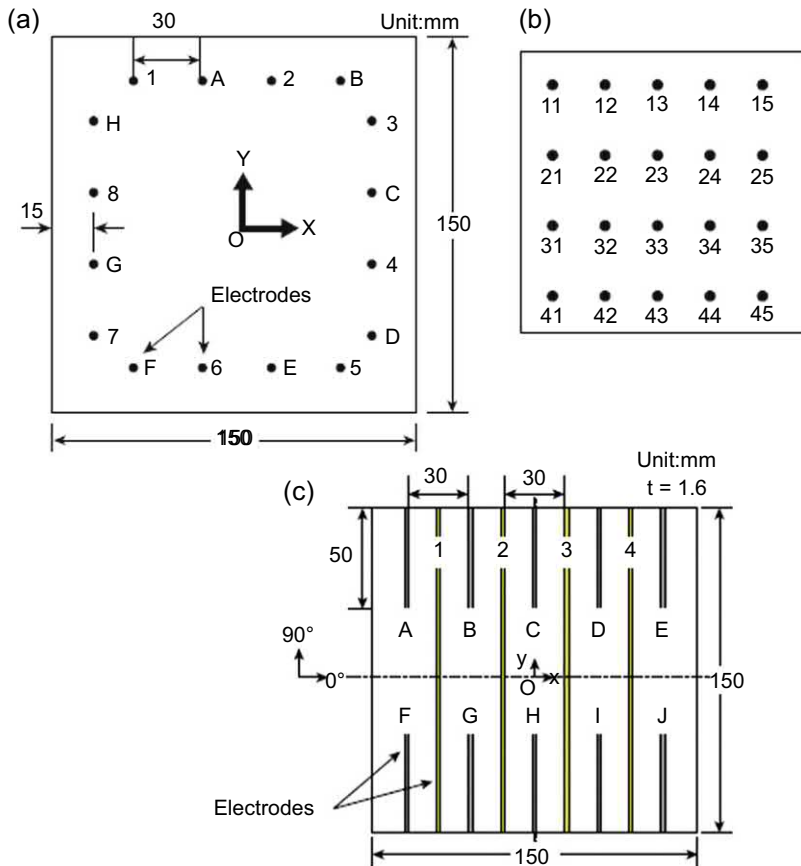
Figure 17.47 CFRP specimen dimensions and placement of electrodes: (a) circular array method [106]; (b) grid array method [107]; (c) matrix array method [106].

depends on the direction of electric current flow, the electrical potential would be done for all possible current flow configurations (electrical tomography). Circular or grid arrays may be used (Fig. 17.47(a,b)). Ref. [108] describes a numerical and experimental study of using the electrical potential method to detect impact-induced delaminations in a CFRP quasi-isotropic laminate using a surface-mounted circular array. Comparison of calculated and measured data revealed that the measured and calculated contours of equipotential change surrounding impact damage seem similar but are different in details. In both simulation and experiment, the potential changes are concentrated in a two-lobe region elongated in the surface fiber directions.

An extensive study of the electrical potential method is described in Ref. [107]. Different methods of electric current injection were considered (use only one specimen surface; use both specimen surfaces and send current across thickness; use the specimen side edges). The relative orientation of electric current injection with respect to the direction of specimen fibers in the top layer was also investigated. A comparative

study of the electrical resistance and electrical potential methods for damage detection in CFRP quasi-isotropic specimens of various thicknesses (i.e., 8, 16, 24 plies) is described in Ref. [109]. It was found that both the electrical resistance and the electrical potential methods were effective for damage sensing in thin (8-ply) composites. In this case, the potential method was found superior to the resistance method, which showed some inconsistency in the variation of readings with increasing impact energy for the segments not containing the impact point. The superiority of the potential method over the resistance method for the 8-ply composite was explained in terms of the current path distortion resulting from the impact damage. For the 16-ply and 24-ply composites, the resistance method was effective, whereas the potential method was not. This means that the potential method does not work when the distance of separation between the applied current line and the potential gradient line is excessive. A distance of 2.10 mm (16 plies) in the through-thickness direction was found excessive, whereas a distance of 1.05 mm (8 plies) was not.

Since GFRP composites are nonconducting dielectrics, their electrical SHM is done with frequency domain methods. Ref. [110] describes the measurement of changes in the dielectric constant of GFRP composites due to delamination and water seepage. The method rests on the different values of the relative permittivity of air ($\varepsilon_{air} \approx$ 1), water ($\varepsilon_{water} \approx 81$) in comparison with that of GFRP composite ($\varepsilon_{GFRP} = 3.12$). GFRP plate specimens (12.5 mm thick) were fabricated with built-in delaminations (thin pockets) placed at different depths (2.0; 3.5; 4.0; 5.5; 6.0; 7.5 mm). The pockets could be filled with water and sealed. The measurements were done with a capacitance meter connected between two surface-applied electrodes. Sensing of delamination depth was explored for both dry and wet pockets. It was found that the presence of delaminations (both dry and wet) could be detected well when they are close to the surface, but less well as their position is more and more removed from the specimen surface.

Ref. [111] used electrochemical impedance spectroscopy (ECIS) to monitor woven GFRP composites during cyclic fatigue loading in flexure. The ECIS readings were taken at various stages during the fatigue life; the ECIS testing was done inside an environmental chamber. The damage began with matrix cracking on the tensile side of the specimen; the pattern of matrix cracking is associated with tow geometry of the fiber weave pattern. Fracture of the specimen occurs when the damage propagates through the thickness of the specimens to create a continuous fracture path across the fibers. The process of progressive damage and fracture path creation in this insulating heterogeneous material is related to a process of conduction paths creation due to moisture infiltration during damage development.

The measured data is presented in Fig. 17.48. Each curve represents an x-y plot of the Re-Im parts of the impedance for various frequency values in the 1 kHz to 10 kHz range. Low excitation frequencies (i.e., down to 1 kHz) produce data to the right of Figure 48b, and high excitation frequencies (i.e., up to 10 kHz) produce the data on the left-hand side of Fig. 17.48(b) and toward the origin of the graph. It is apparent that the undamaged specimen is effectively a dielectric, and its impedance is dominated by the capacitive response with the reactance $X_C(\omega) = 1/i\omega C$. In this case,
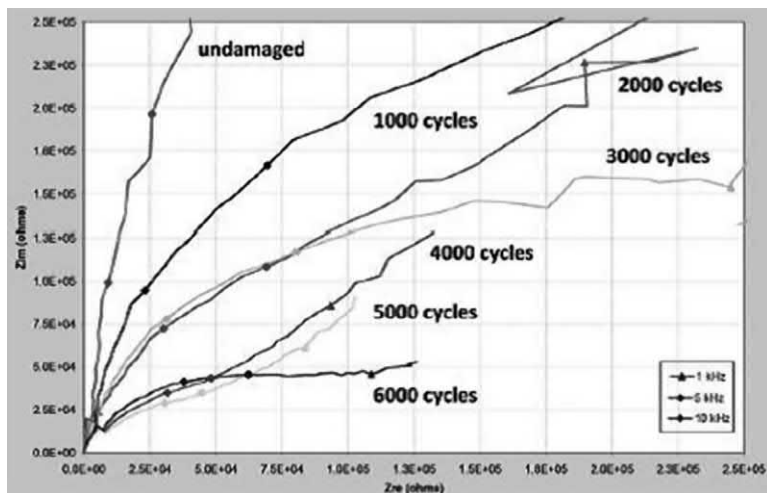
Figure 17.48 Electrochemical impedance spectroscopy (ECIS) Nyquist plot of Re-Im imped-ance curves at various stages during low-cycle flexure fatigue testing of woven GFRP (specimen failure occurred at ~7000 cycles) [111].

the real part of the impedance represents the internal energy-dissipation losses during cyclic excitation.

As the frequency ω increases, the capacitive reactance diminishes, and the curve aims toward the axis origin. As damage progresses and conductive paths are created in the damaged material, the relative proportion between the real and imaginary parts of the impedance changes. The greatest difference in Fig. 17.48(b) data seems to be between the results for the undamaged specimen, and the results for the specimen
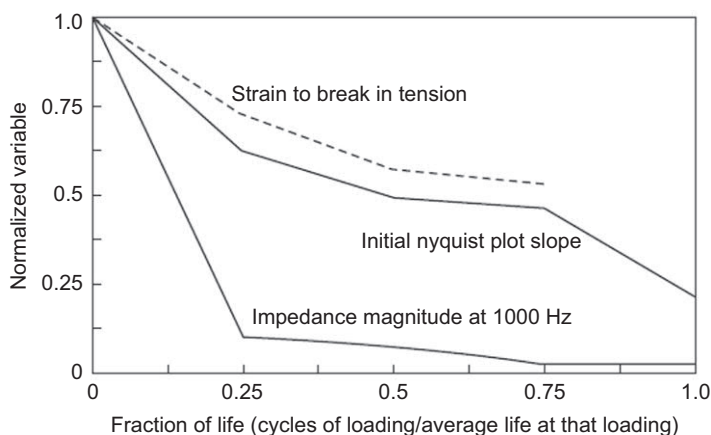
Figure 17.49 Comparison of normalized progressive damage accumulation as a function of the fraction of life of the tested specimens [111].

cycled to only 1000 cycles, which represent the first 14% or so of the specimen life. As damage progresses, the lower-frequency imaginary component of the impedance (to the right of Fig. 17.48(b)) drops sharply in magnitude, indicating a sharp decrease in capacitive reactance.

It is apparent that the ECIS method is remarkably sensitive to the details of internal damage development in woven GFRP composites; in addition, the actual progress of the degradation in terms of life and remaining strength can be related to ECIS data. Fig. 17.49 compares of different ways to quantify damage development in terms of loading cycles: (a) initial slope of the Nyquist plot; (b) impedance magnitude at a fixed frequency, say at 1000 Hz; (c) remaining strain. Averaged multispecimen data recorded at 25%, 50%, 75%, and 100% of life are shown. The two selected ECIS characteristics (initial Nyquist slope and impedance magnitude at a fixed frequency) show a clear relationship with the fractional life variable; in fact, they seem good damage indicators, especially of early damage onset. However, many other characteristics could have been selected in the robust ECIS data set.

Electromagnetic methods for finding defects and damage in composite materials rely on the response of these materials to the excitation by electromagnetic fields. Dielectric composites, such as GFRP materials, can be interrogated with the use of an electric field whereas conductive composites, such as CFRP materials can be interrogated with a magnetic field.

Fig. 17.50(a) shows the detection of an internal defect (zone of missing foam) in a GFRP sandwich specimen by illumination with an electric field (e.g., with an electric antenna in near field) and by measuring the total electric component of the electric field crossing through the material. Fig. 17.50(b) shows the magnetic imaging of delamination in a CFRP plate. Both measurements were performed in the transmission mode with excitation and detection fields being of the same type: electric→electric for GFRP and magnetic→magnetic for CFRP.
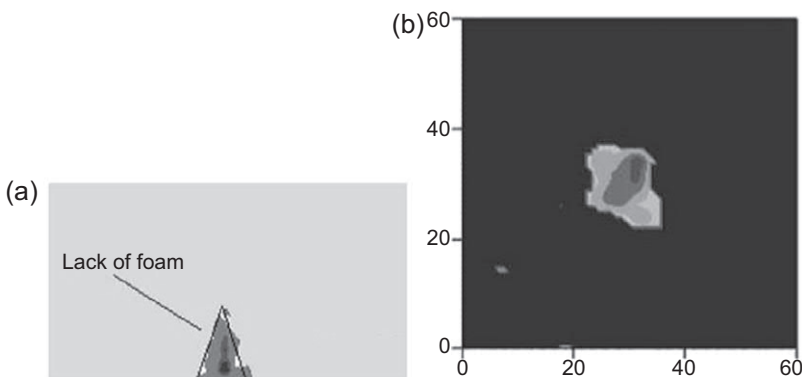
Figure 17.50 Electromagnetic methods for imaging of damage or defects in composite materials: (a) electric imaging of a GFRP sandwich specimen showing the detection of a zone with missing foam; (b) magnetic imaging of delamination in CFRP plate [112].

Eddy currents (EC) technique are well developed for damage detection in metallic structures. Recent studies have shown that they can also be used in CFRP composites [113]. CFRP permeability and conductivity influence the EC penetration depth. EC methods permit the determination of textural parameters like layer orientation and gap sizes between roving, the detection of foreign polymer particles; fuzzy balls and visualization of undulations can also be done with this method. The detection of a 4.48° fiber misalignment was shown possible; other textural features can also be automatically found and classified. This technique holds the promise of *in situ* sensing through MWM-array eddy current technology [114].

A hybrid electromagnetic method is also possible for CFRP composites in which a modulated high-frequency electric excitation is applied, and the magnetic response of the material is recorded. Ref. [112] describes such a hybrid method applied to a CFRP composite plate and compares its efficacy with the acousto-ultrasonic method. The instrumented CFRP specimen is depicted in Fig. 17.51. The specimen was a 16-ply cross-ply CFRP plate. An acousto-ultrasonic SMART layer was embedded in the midplane, and a hybrid electromagnetic layer HELP© with a 20 mm × 20 mm mesh was applied to one side of the specimen. A 700 kHz high-frequency electric excitation with full 1 kHz modulation width was applied. The damage was applied in the form of impacts, and electric spark burns to simulate lightning strikes. The impacts I1 and I2 were of 2 and 4 J, respectively. The burns were applied with high-energy sparks (30 V, 5 A) of various energies: 120 J, 40 J, 80 J, 400 J for B1, B2, B3, B4, respectively. The hybrid electromagnetic and acousto-ultrasonic imaging results are compared in Fig. 17.52(a).

The hybrid electromagnetic HELP© method could detect all damages but I1, whereas the acousto-ultrasonic SMART layer method could only detect damages I1, I2, B4. The fact that the HELP© method could not detect the low-energy damage I1 is attributed to the fact that this mild impact only produced delamination but no composite breakage; this indicates that the HELP© may not be able to detect mild delaminations. It is also noticed that the lowest-energy burn B2 (40 J) is only slightly visible in Fig. 17.52(a), which may be indicative that this slight burn damage is probably at the detection threshold of this method.
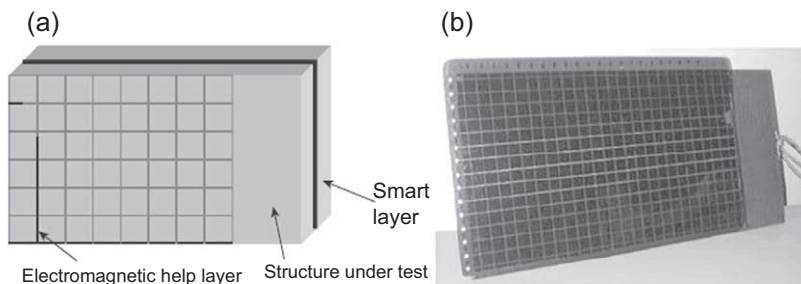
Figure 17.51 CFRP plate specimen instrumented with hybrid electromagnetic layer HELP© and with acousto-ultrasonic SMART layer: (a) schematic; (b) photograph [112].
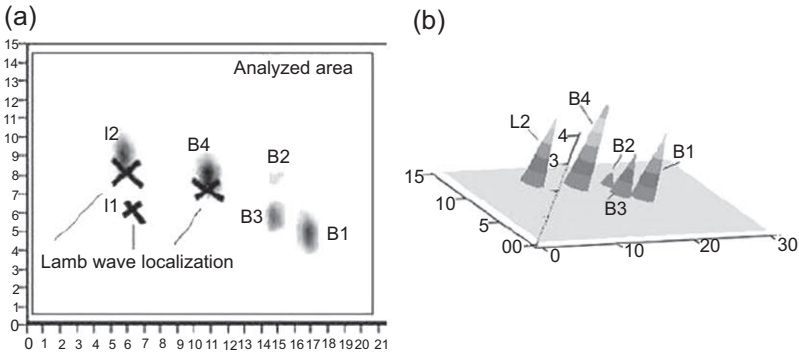
Figure 17.52 Comparative detection of impacts (I1, I2) and burns (B1, B2, B3, B4) on a CFRP plate instrumented with hybrid electromagnetic layer HELP© and with acousto-ultrasonic SMART layer: (a) image showing that the HELP© method could detect all damages but I1 whereas the Lamb wave-based SMART layer method could only detect I1, I2, and B4 damages; (b) image showing the detection levels of the electromagnetic HELP© method [112].

The fact that the SMART layer method could not detect the B1, B2, B3 burns may be attributed to the fact that these damages were only superficial changes that did not affect sufficiently the guided wave propagation used in the acousto-ultrasonic method. The severe damage B4 (400 J electric spark) was detectable with this method because it produced sufficient local changes in the material to scatter the guided waves used in the acousto-ultrasonic method.

17.4.9   Direct methods for impact damage detection

A number of publications describe attempts to directly detect the composite impact damage with damage-sensitive embedded sensors or through composite self-
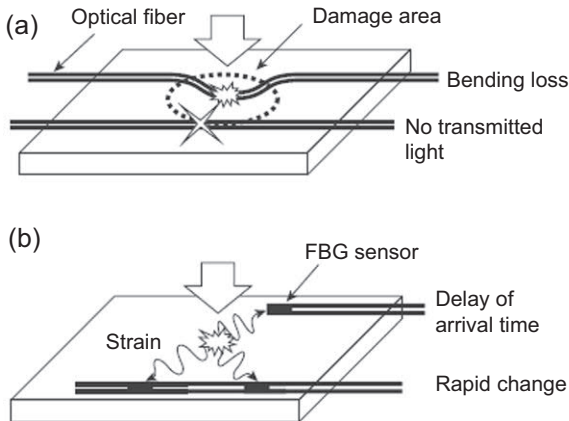
Figure 17.53 Measuring impact response in a composite with fiber optics through the change of optical intensity due to fiber microbending and fiber fracture [115].

sensing. Ref. [115] uses optical intensity sensors consisting of small diameter (40 μm) multimode optical fibers with a polyimide coating, which change their transmission characteristics when suffering microbending due to structural damage (Fig. 17.53(a)).

Ref. [116] describes a method for the detection of damage in GFRP composites using conventional reinforcing E-glass fibers that were made to act as light guides and dubbed reinforcing fiber light guides (RFLG). These reinforcing-fiber light guides were used to detect damage induced in the composite by impact, indentation, and flexure. The E-glass fibers were converted into light guides by applying an appropriate cladding material. The coating resins were epoxy-based and polyurethane-based resin systems. These self-sensing fibers or reinforcing-fiber light guides were surface mounted and also embedded at two specified locations within 16-ply glass fiber-reinforced epoxy prepreg composites.

The data demonstrated that the self-sensing concept could be used to study *in situ* and in real-time the failure processes in glass fiber-reinforced composites. The characterization of failure modes observed when the composites with the self-sensing light guides were subjected to impact, indentation and flexural loading was attempted. The damaged areas in the GFRP composite were located by means of the "bleeding" light emanating from the broken self-sensing E-glass fibers (Fig. 17.54). The RFLG approach was further refined by developing a sol-gel cladding fabrication technique [117].

The use of the triboluminescent effect to capture impact damage events in a CFRP panel is described in Ref. [118]. Hollow silica capillaries were incorporated into CFRP composite panels; the composite prepreg was doped with Terbium triboluminescent compound. After curing of the composite, the silica capillaries were filled with rhodamine 6G in benzyl alcohol and sealed. The panels were again impacted in the drop-weight tower, with the resulting light emission recorded (Fig. 17.55).
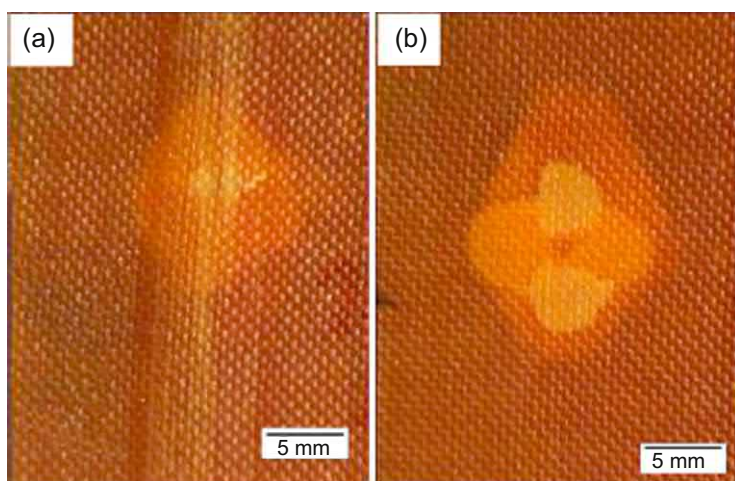
Figure 17.54 Detection of 2 J impact delamination in a GFRP composite with RFLG fibers placed on the top surface: (a) front face; (b) back face [116].
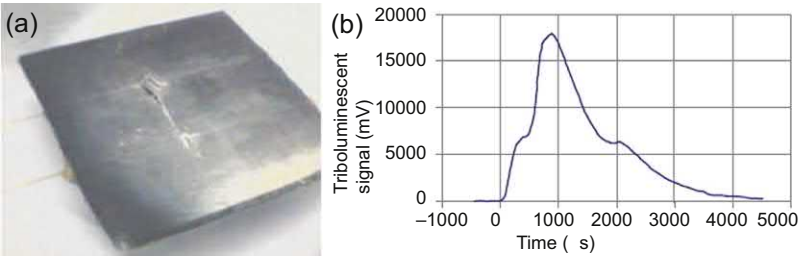
Figure 17.55 Use of triboluminescence to detect the impact on a CFRP panel: (a) CFRP panel showing the place of impact and two photoluminescent hollow silica fibers used to capture the triboluminescence phenomenon; (b) triboluminescent signal captured during impact [118].

Refs. [11,119] describe the use of optical time-domain reflectometry (OTDR) and fiber Bragg gratings (FBG) to detect impact damage in GFRP sandwich specimens. The optical fibers were embedded in the sandwich core at various depth (Fig. 17.56). The principle of the detection method consists in the fact that deformation and damage due to impact leaves areas of permanent strain around the impact zone. The OTDR and FBG methods were employed to detect such changes in comparison with the preimpact baseline. It was concluded that both methods are able to detect the permanent strain changes produced by the impact provided the sensors are in the proximity of the impact zone.

17.5 Summary, conclusions, and suggestions for further work

This chapter started with a review of the modes of damage that can occur in polymer composites. Failure occurs progressively under tension, compression, or shear and polymer composites are particularly prone to low-velocity impacts that may result in damage which is not obvious to the naked eye. This emphasizes the need to test
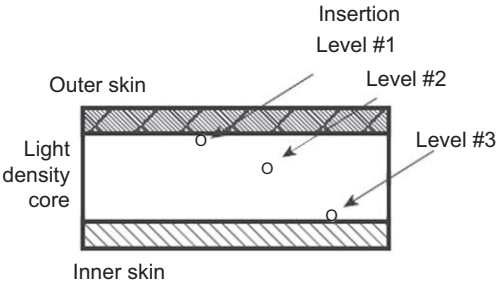
Figure 17.56 Thickness-wise locations of the optical fibers for OTDR and FBG damage detection in a GFRP-face/rigid-foam sandwich [11].

polymer composite aircraft structures both at the time of manufacture and in-service. A brief review of the main means and methods for the emerging field of structural health monitoring (SHM) of safety-critical composite structures was presented. The different physical principals employed by each approach have been detailed for the various sensor types, which may either focus on a specific (small) area or cover large areas of the structure. Examples have also been presented to illustrate the practical interpretation of the sensor derived data.

Considerable further research is, however, needed to mature the development of SHM sensors and methods in order to achieve a viable and practical implementation of this promising new technology. Future work should cover the development of new sensors, improvement of sensor data interpretation, and a great effort in the predictive simulation of how the SHM system would function such that its fundamental parameters can be fine-tuned before actual implementation.

References

[1] C. Soutis, P.W.R. Beaumont, Multi-scale Modelling of Composite Material Systems: The Art of Predictive Damage Modelling, Woodhead Publishing Ltd., 2005.

[2] MIL-STD-1530B, "Standard Practice: Aircraft Structural Integrity Program (ASIP)," United State Air Force Aeronautical Systems Division, WPAFB, 1530B, USA MIL STD, Dayton, OH, 2004.

[3] E. Demuts, R.S. Whitehead, R.B. Deo, Assessment of damage tolerance in composite, Compos. Struct. 4 (1) (1985) 45−58.

[4] J.W. Lincoln, USAF experience in the qualification of composite structures, in: Composite Structures; Theory and Practice, vol. 1383, ASTM, 2000, pp. 3−11.

[5] C. Soutis, Private Communication, 2013.

[6] M. Kashtalyan, C. Soutis, Analysis of composite laminates with intra- and interlaminar damage, Prog. Aerosp. Sci. 41 (2) (2005) 152−173.

[7] A. Atas, G.F. Mohamed, C. Soutis, Progressive failure of bolted joints in composite laminates, Plast. Rubber Compos. Macromol. Eng. 41 (4−5) (2012) 209−214.

[8] T. Mitrevski, I.H. Marshall, R.S. Thomson, R. Jones, Low-velocity impacts on preloaded GFRP specimens with various impactor shapes, Compos. Struct. 76 (3) (2006) 209−217.

[9] K.L. Reifsnider, E.G. Henneke, W.W. Stinchcomb, J.C. Duke, Long-Term Fatigue Behavior of Composite Materials, vol. 813, ASTM American Society for Testing and Materials, Philadelphia ASTM STP, 1983.

[10] Talreja, R, Fatigue of composite materials − damage mechanisms and fatigue-life diagrams, Proc. R. Soc. Lond. A − Math. Phys. Eng. Sci. 378 (1775) (1981) 461−475.

[11] D. Balageas, S. Bourasseau, M. Dupont, E. Bocherens, V. Dewynter-Marty, P. Ferdinand, Comparison between non-destructive evaluation techniques and integrated fiber optic health monitoring systems for composite sandwich structures, J. Intell. Mater. Syst. Struct. 11 (6) (2000) 426−437, https://doi.org/10.1106/mfm1-c5ft-6bm4-afud.

[12] W.N. Sharpe, Springer Handbook of Experimental Solid Mechanics, Springer, 2008.

[13] Peters, K, Private Communication, 2013.

[14] G. Zhou, L.M. Sim, Damage detection and assessment in fibre-reinforced composite structures with embedded fibre optic sensors - review, Smart Mater. Struct. 11 (6) (December 2002) 925−939, https://doi.org/10.1088/0964-1726/11/6/314.

[15] L.E. Mujica, J. Vehi, W. Staszewski, K. Worden, Impact damage detection in aircraft composites using knowledge-based reasoning, Struct. Health Monit. −Int. J. 7 (3) (September 2008) 215−230, https://doi.org/10.1177/1475921708090560.

[16] T. Mizutani, Y. Okabe, N. Takeda, Quantitative evaluation of transverse cracks in carbon fiber reinforced plastic quasi-isotropic laminates with embedded small-diameter fiber Bragg grating sensors, Smart Mater. Struct. 12 (6) (December 2003) 898−903, https://doi.org/10.1088/0964-1726/12/6/006.

[17] K. Peters, Fiber-optic sensor principles, in: C. Boller, F.-K. Chang, Y. Fujino (Eds.), Encyclopedia of Structural Health Monitoring, Wiley, 2008.

[18] K. Peters, Intensity-, interferometric-, and scattering-based optical-fiber sensors, in: C. Boller, F.-K. Chang, Y. Fujino (Eds.), Encyclopedia of Structural Health Monitoring, Wiley, 2008.

[19] K. Peters, Fiber Bragg grating sensors, in: C. Boller, F.-K. Chang, Y. Fujino (Eds.), Encyclopedia of Structural Health Monitoring, Wiley, 2008.

[20] K. Peters, Novel fiber-optic sensors, in: C. Boller, F.-K. Chang, Y. Fujino (Eds.), Encyclopedia of Structural Health Monitoring, Wiley, 2008.

[21] Various-authors, Wikipedia, 2012. Available from: http://en.wikipedia.org/.

[22] M.D. Todd, G.A. Johnson, S.T. Vohra, Deployment of a fiber Bragg grating-based measurement system in a structural health monitoring application, Smart Mater. Struct. 10 (3) (June 2001) 534−539, https://doi.org/10.1088/0964-1726/10/3/316.

[23] K.S.C. Kuang, R. Kenny, M.P. Whelan, W.J. Cantwell, P.R. Chalker, Residual strain measurement and impact response of optical fibre Bragg grating sensors in fibre metal laminates, Smart Mater. Struct. 10 (2) (April 2001) 338−346, https://doi.org/10.1088/0964-1726/10/2/321.

[24] Y. Okabe, S. Yashiro, T. Kosaka, N. Takeda, Detection of transverse cracks in CFRP composites using embedded fiber Bragg grating sensors, Smart Mater. Struct. 9 (6) (December 2000) 832−838, https://doi.org/10.1088/0964-1726/9/6/313.

[25] S. Takeda, T. Yamamoto, Y. Okabe, N. Takeda, Debonding monitoring of composite repair patches using embedded small-diameter FBG sensors, Smart Mater. Struct. 16 (3) (June 2007) 763−770, https://doi.org/10.1088/0964-1726/16/3/025.

[26] G. Wang, K. Pran, G. Sagvolden, G.B. Havsgard, A.E. Jensen, G.A. Johnson, S.T. Vohra, Ship hull structure monitoring using fibre optic sensors, Smart Mater. Struct. 10 (3) (June 2001) 472−478, https://doi.org/10.1088/0964-1726/10/3/308.

[27] V. Giurgiutiu, in: Structural Health Monitoring with Piezoelectric Wafer Active Sensors, second ed., Elsevier Academic Press, 2014.

[28] F.-K. Chang, SMART layer − Built-in diagnostics for composite structures, in: 4th European Conference on Smart Structures and Materials, UK vol. 1998, 1998, pp. 777−781.

[29] M. Lin, X. Qing, A. Kumar, S.J. Beard, SMART Layer and SMART Suitcase for Structural Health Monitoring Applications, DTIC, 2005.

[30] K. Diamanti, C. Soutis, Structural health monitoring techniques for aircraft composite structures, Prog. Aerosp. Sci. 46 (8) (November 2010) 342−352, https://doi.org/10.1016/j.paerosci.2010.05.001.

[31] V. Giurgiutiu, L.Y. Yu, J.R. Kendall, C. Jenkins, In situ imaging of crack growth with piezoelectric-wafer active sensors, AIAA J. 45 (11) (November 2007) 2758−2769, https://doi.org/10.2514/1-30798.

[32] C. Bois, C. Hochard, Monitoring of laminated composites delamination based on electro-mechanical impedance measurement, J. Intell. Mater. Syst. Struct. 15 (1) (2004) 59−67, https://doi.org/10.1177/1045389x04039405.

[33] C.S. Wang, F.K. Chang, Built-in diagnostics for impact damage identification of composite structures, in: 2nd International Workshop on Structural Health Monitoring, 1999, pp. 612−621.

[34] A. Kesavan, S. John, I. Herszberg, Strain-based structural health monitoring of complex composite structures, Struct. Health Monit. −Int. J. 7 (3) (September 2008) 203−213, https://doi.org/10.1177/1475921708090559.

[35] G.M. Kamath, R. Sundaram, N. Gupta, M.S. Rao, Damage studies in composite structures for structural health monitoring using strain sensors, Struct. Health Monit. −Int. J. 9 (6) (November 2010) 497−512, https://doi.org/10.1177/1475921710365391.

[36] S. Takeda, Y. Okabe, N. Takeda, Monitoring of delamination growth in CFRP laminates using chirped FBG sensors, J. Intell. Mater. Syst. Struct. 19 (4) (April 2008) 437−444, https://doi.org/10.1177/1045389x06074085.

[37] Y. Okabe, N. Tanaka, N. Takeda, Effect of fiber coating on crack detection in carbon fiber reinforced plastic composites using fiber Bragg grating sensors, Smart Mater. Struct. 11 (6) (December 2002) 892−898, https://doi.org/10.1088/0964-1726/11/6/310.

[38] J.A. Guemes, J.M. Menendez, M. Frovel, I. Fernandez, J.M. Pintado, Experimental analysis of buckling in aircraft skin panels by fibre optic sensors, Smart Mater. Struct. 10 (3) (June 2001) 490−496, https://doi.org/10.1088/0964-1726/10/3/310.

[39] I.J. Read, P.D. Foote, Sea and flight trials of optical fibre Bragg grating strain sensing systems, Smart Mater. Struct. 10 (5) (October 2001) 1085−1094, https://doi.org/10.1088/0964-1726/10/5/325.

[40] H. Murayama, K. Kageyama, H. Naruse, A. Shimada, K. Uzawa, Application of fiber-optic distributed sensors to health monitoring for full-scale composite structures, J. Intell. Mater. Syst. Struct. 14 (1) (January 2003) 3−13, https://doi.org/10.1177/104538903032738.

[41] T. Mizutani, N. Takeda, H. Takeya, On-board strain measurement of a cryogenic composite tank mounted on a reusable rocket using FBG sensors, Struct. Health Monit. −Int. J. 5 (3) (September 2006) 205−214, https://doi.org/10.1177/1475921706058016.

[42] H.K. Kang, J.S. Park, D.H. Kang, C.U. Kim, C.S. Hong, C.G. Kim, Strain monitoring of a filament wound composite tank using fiber Bragg grating sensors, Smart Mater. Struct. 11 (6) (December 2002) 848−853, https://doi.org/10.1088/0964-1726/11/6/304.

[43] F.K. Chang, "Built-In Damage Diagnostics for Composite Structures," ICCM-10: 10th International Congress of Composite Materials, Canada, 1995, pp. 283−289.

[44] K.Y. Choi, F.K. Chang, Identification of impact force and location using distributed sensors, AIAA J. 34 (1) (January 1996) 136−142, https://doi.org/10.2514/3.13033.

[45] R. Seydel, F.K. Chang, Impact identification of stiffened composite panels: I. System development; II. Implementation Studies, Smart Mater. Struct. 10 (2) (April 2001) 354−379, https://doi.org/10.1088/0964-1726/10/2/323.

[46] J.F.C. Markmiller, F.K. Chang, Sensor network optimization for a passive sensing impact detection technique, Struct. Health Monit. −Int. J. 9 (1) (January 2010) 25−39, https://doi.org/10.1177/1475921709349673.

[47] M. Tracy, F.K. Chang, Identifying impacts in composite plates with piezoelectric strain sensors, part I: theory, J. Intell. Mater. Syst. Struct. 9 (11) (November 1998) 920−928.

[48] R. Seydel, F.K. Chang, Impact identification of stiffened composite panels: I. System development, Smart Mater. Struct. 10 (2) (April 2001) 354−369, https://doi.org/10.1088/0964-1726/10/2/323.

[49] J. Park, F.-K. Chang, System identification method for monitoring impact events, in: SPIE 2005 Smart Structures and NDE Symposium, 2005, pp. 189−200.

[50] M.A. Maseras-Gutierrez, W.J. Staszewski, M.S. Found, K. Worden, Detection of impacts in composite materials using piezoceramic sensors and neural networks, in: SPIE 1998 Smart Structures and Materials Symposium, 1998, pp. 491−497.

[51] J. Haywood, P.T. Coverley, W.J. Staszewski, K. Worden, An automatic impact monitor for a composite panel employing smart sensor technology, Smart Mater. Struct. 14 (1) (February 2005) 265−271, https://doi.org/10.1088/0964-1726/14/1/027.

[52] D.U. Sung, J.H. Oh, C.G. Kim, C.S. Hong, Impact monitoring of smart composite laminates using neural network and wavelet analysis, J. Intell. Mater. Syst. Struct. 11 (3) (March 2000) 180−190, https://doi.org/10.1106/n5e7-m37y-3mar-2kfh.

[53] D.C. Betz, G. Thursby, B. Culshaw, W.J. Staszewski, Structural damage location with fiber Bragg grating rosettes and Lamb waves, Struct. Health Monit. −Int. J. 6 (4) (December 2007) 299−308, https://doi.org/10.1177/1475921707081974.

[54] H.M. Matt, F. Lanza di Scalea, Macro-fiber composite piezoelectric rosettes for acoustic source location in complex structures, Smart Mater. Struct. 16 (4) (August 2007) 1489−1499, https://doi.org/10.1088/0964-1726/16/4/064.

[55] S. Salamone, I. Bartoli, P. Di Leo, F. Lanza Di Scala, A. Ajovalasit, L. D'Acquisto, J. Rhymer, H. Kim, High-velocity impact location on aircraft panels using macro-fiber composite piezoelectric rosettes, J. Intell. Mater. Syst. Struct. 21 (9) (2010) 887−896, https://doi.org/10.1177/1045389x10368450.

[56] P. Zhao, D. Pisani, C.S. Lynch, Piezoelectric strain sensor/actuator rosettes, Smart Mater. Struct. 20 (10) (2011) 102002, https://doi.org/10.1088/0964-1726/20/10/102002.

[57] T. Martin, J. Hudd, P. Wells, D. Tunnicliffe, D. Das-Gupta, The use of low profile piezoelectric sensors for impact and acoustic emission (AE) detection in CFRC structures, J. Intell. Mater. Syst. Struct. 12 (8) (August 2001) 537−544, https://doi.org/10.1177/10453890122145339.

[58] Y.L. Koh, W.K. Chiu, N. Rajic, S.C. Galea, Detection of disbond growth in a cyclically loaded bonded composite repair patch using surface-mounted piezoceramic elements, Struct. Health Monit. −Int. J. 2 (4) (2003) 327−339.

[59] I.C. Perez, L. Hongliang, E. Udd, Acoustic emission detection using fiber Bragg gratings, in: SPIE 2001 Smart Structures and NDE Symposium, San Diego, CA, 2001, pp. 209−215. https://www.physicalacoustics.com/by-product/aewin/.

[60] J.I. Koh, H.J. Bang, C.G. Kim, C.S. Hong, Simultaneous measurement of strain and damage signal of composite structures using a fiber Bragg grating sensor, Smart Mater. Struct. 14 (4) (August 2005) 658−663, https://doi.org/10.1088/0964-1726/14/4/024.

[61] Pysical Acoustics Corp, AEwin Acoustic Emission Software, 2012. Available from: http://www.pacndt.com/index.aspx?go=products&focus=/software/aewin.htm.

[62] C.H. Keilers, F.K. Chang, Identifying delamination in composite beams using built-in piezoelectrics — Part I: experiments and analysis; Part II: an indentification method, J. Intell. Mater. Syst. Struct. 6 (5) (September 1995) 649−672, https://doi.org/10.1177/1045389x9500600506.

[63] J.C. Duke, Acousto-Ultrasonics − Theory and Applications, Plenum Press, 1988.

[64] G.R. Kirikera, O. Balogun, S. Krishnaswamy, Adaptive fiber Bragg grating sensor network for structural health monitoring: applications to impact monitoring, Struct. Health Monit. −Int. J. 10 (1) (January 2011) 5−16, https://doi.org/10.1177/1475921710365437.

[65] J.J. Tian, Q. Zhang, M. Han, Distributed fiber-optic laser-ultrasound generation based on ghost mode of tilted fiber Bragg gratings, Opt. Express 21 (2013) 6109−6114.

[66] C.S. Wang, F.K. Chang, Diagnosis of impact damage in composite structures with built-in piezoelectrics network, in: SPIE 2000 Smart Structures and Materials Symposium, San Diego, CA, 2000, pp. 13−19.

[67] F. Yan, R.L. Royer, J.L. Rose, Ultrasonic guided wave imaging techniques in structural health monitoring, J. Intell. Mater. Syst. Struct. 21 (3) (February 2010) 377−384, https://doi.org/10.1177/1045389x09356026.

[68] E.V. Malyarenko, M.K. Hinders, Ultrasonic Lamb wave diffraction tomography, Ultrasonics 39 (4) (June 2001) 269−281, https://doi.org/10.1016/s0041-624x(01)00055-5.

[69] J.B. Ihn, F.K. Chang, Pitch-catch active sensing methods in structural health monitoring for aircraft structures, Struct. Health Monit. −Int. J. 7 (1) (March 2008) 5−19, https://doi.org/10.1177/1475921707081979.

[70] Z. Su, L. Cheng, X. Wang, L. Yu, C. Zhou, Predicting delamination of composite laminates using an imaging approach, Smart Mater. Struct. 18 (7) (2009) 074002, https://doi.org/10.1088/0964-1726/18/7/074002.

[71] V. Giurgiutiu, J. Bao, Embedded-ultrasonics structural radar for in situ structural health monitoring of thin-wall structures, Struct. Health Monit. −Int. J. 3 (2) (June 2004) 121−140, https://doi.org/10.1177/1475921704042697.

[72] L. Yu, V. Giurgiutiu, In situ 2-D piezoelectric wafer active sensors arrays for guided wave damage detection, Ultrasonics 48 (2) (April 2008) 117−134, https://doi.org/10.1016/j.ultras.2007.10.008.

[73] F. Yan, J.L. Rose, Guided wave phased array beam steering in composite plates, in: SPIE 2007 Smart Structures and NDE Symposium, San Diego, CA, 2007, p. #15.

[74] M. Collet, M. Ruzzene, K.A. Cunefare, Generation of Lamb waves through surface mounted macro-fiber composite transducers, Smart Mater. Struct. 20 (2011) 025020, https://doi.org/10.1088/0964-1726/20/2/025020.

[75] K.I. Salas, C.E.S. Cesnik, Guided wave excitation by a CLoVER transducer for structural health monitoring: theory and experiments, Smart Mater. Struct. 18 (7) (2009) 075005, https://doi.org/10.1088/0964-1726/18/7/075005.

[76] B. Xu, M. Senesi, M. Ruzzene, Frequency-steered acoustic arrays: application to structural health monitoring of composite plates, J. Eng. Mater. Technol.-Transact. ASME 133 (1) (January 2011) 011003, https://doi.org/10.1115/1.4002638.

[77] E. Baravelli, M. Senesi, M. Ruzzene, L. De Marchi, N. Speciale, Double-channel, frequency-steered acoustic transducer with 2-D imaging capabilities, IEEE Trans. Ultrason. Ferroelectr. Freq. Control 58 (8) (August 2011) 1430−1706, https://doi.org/10.1109/tuffc.2011.2000.

[78] Y. Okabe, K. Fujibayashi, M. Shimazaki, H. Soejima, T. Ogisu, Delamination detection in composite laminates using dispersion change based on mode conversion of Lamb waves, Smart Mater. Struct. 19 (11) (November 2010) 115013, https://doi.org/10.1088/0964-1726/19/11/115013.

[79] H. Sohn, D. Dutta, J.Y. Yang, M. DeSimio, S. Olson, E. Swenson, Automated detection of delamination and disbond from wavefield images obtained using a scanning laser vibrometer, Smart Mater. Struct. 20 (4) (2011) 045017, https://doi.org/10.1088/0964-1726/20/4/045017.

[80] Z. Wu, X.P. Qing, F.-K. Chang, Damage detection for composite laminate plates with A distributed hybrid PZT/FBG sensor network, J. Intell. Mater. Syst. Struct. 20 (9) (June 2009) 1069−1077, https://doi.org/10.1177/1045389x08101632.

[81] K. Worden, D.J. Inman, Modal vibration methods in structural health monitoring, in: R.S.,W. Blockley, R. Blockley, W. Shyy (Eds.), Encyclopedia of Aerospace Engineering, Wiley, 2010, pp. 1995−2004.

[82] W. Fan, P. Qiao, Vibration-based damage identification methods: a review and comparative study, Struct. Health Monit. −Int. J. 10 (1) (January 2011) 83−111, https://doi.org/10.1177/1475921710365419.

[83] A. Shahdin, J. Morlier, H. Niemann, Y. Gourinat, Correlating low energy impact damage with changes in modal parameters: diagnosis tools and FE validation, Struct. Health Monit. −Int. J. 10 (2) (2011) 199−217, https://doi.org/10.1177/1475921710373297.

[84] A.K. Pandey, M. Biswas, M.M. Samman, Damage detection from changes in curvature mode shapes, J. Sound Vib. 145 (2) (1991) 321−332.

[85] V.K. Sharma, S. Hanagud, M. Ruzzene, Damage index estimation in beams and plates using laser vibrometry, AIAA J. 44 (4) (April 2006) 919−923, https://doi.org/10.2514/1.19012.

[86] C.S. Hamey, W. Lestari, P. Qiao, G. Song, Experimental damage identification of carbon/epoxy composite beams using curvature mode shapes, Struct. Health Monit. −Int. J. 3 (4) (2004) 333−353.

[87] W. Lestari, P. Qiao, S. Hanagud, Curvature mode shape-based damage assessment of carbon/epoxy composite beams, J. Intell. Mater. Syst. Struct. 18 (3) (2007) 189−208, https://doi.org/10.1177/1045389x06064355.

[88] W.J. Staszewski, H. Sohn, Signal processing for structural health monitoring, in: R.S.,W. Blockley (Ed.), Encyclopedia of Aerospace Engineering, Wiley, 2010, pp. 2013−2025.

[89] M. Seaver, E. Aktas, S.T. Trickey, Quantitative detection of low energy impact damage in a sandwich composite wing, J. Intell. Mater. Syst. Struct. 21 (3) (February 2010) 297−308, https://doi.org/10.1177/1045389x09347020.

[90] P.F. Lichtenwalner, J.P. Dunne, R.S. Becker, E.W. Baumann, "Active Damage Interrogation Method for Structural Health Monitoring" US Patent US6006163-A, December 21, 1999.

[91] N. Hu, H. Fukunaga, M. Kameyama, Identification of delaminations in composite laminates, J. Intell. Mater. Syst. Struct. 17 (8−9) (2006) 671−683, https://doi.org/10.1177/1045389x06055816.

[92] V. Giurgiutiu, A.N. Zagrai, Embedded self-sensing piezoelectric active sensors for on-line structural identification, J. Vib. Acoust.-Transact. ASME 124 (1) (January 2002) 116−125, https://doi.org/10.1115/1.1421056.

[93] A.N. Zagrai, V. Giurgiutiu, Electro-mechanical impedance method for crack detection in thin plates, J. Intell. Mater. Syst. Struct. 12 (10) (October 2001) 709−718.

[94] A. Cuc, V. Giurgiutiu, S. Joshi, Z. Tidwell, Structural health monitoring with piezoelectric wafer active sensors for space applications, AIAA J. 45 (12) (December 2007) 2838−2850, https://doi.org/10.2514/1.26141.

[95] P. Pollock, L. Yu, S. Guo, M. Sutton, A nondestructive experimental study on damage progression in woven glass-epoxy composites, in: SPIE 2011 Smart Structures and NDE Symposium, 2011, p. 127.

[96] M. Gresil, L. Yu, V. Giurgiutiu, M. Sutton, Predictive modeling of electromechanical impedance spectroscopy for composite materials, Struct. Health Monit. −Int. J. 11 (6) (2012) 671−683.

[97] F. Lalande, Z. Chaudhry, F.P. Sun, C.A. Rogers, Debond detection using broad-band high-frequency excitation and non-contacting: laser vibrometer system, J. Intell. Mater. Syst. Struct. 7 (2) (March 1996) 176−181.

[98] W.K. Chiu, S.C. Galea, L.L. Koss, N. Rajic, Damage detection in bonded repairs using piezoceramics, Smart Mater. Struct. 9 (4) (August 2000) 466−475, https://doi.org/10.1088/0964-1726/9/4/309.

[99] V. Giurgiutiu, K. Harries, M. Petrou, J. Bost, J.B. Quattlebaum, Disbond detection with piezoelectric wafer active sensors in RC structures strengthened with FRP composite overlays, Earthq. Eng. Eng. Vib. 2 (2) (December 2003) 213−224.

[100] A.L. Gyekenyesi, R.E. Martin, G.N. Morscher, R.B. Owen, Impedance-based structural health monitoring of a ceramic matrix composite, J. Intell. Mater. Syst. Struct. 20 (7) (2009) 875−882, https://doi.org/10.1177/1045389x08099033.

[101] A. Todoroki, K. Omagari, Y. Shimamura, H. Kobayashi, Matrix crack detection of CFRP using electrical resistance change with integrated surface probes, Compos. Sci. Technol. 66 (11−12) (September 2006) 1539−1545, https://doi.org/10.1016/j.compscitech.2005.11.029.

[102] M. Kemp, Self-sensing composites for smart damage detection using electrical properties, in: 2nd European Conference on Smart Structures and Materials, Glasgow, Scotland, 1994, pp. 136−139.

[103] D.D.L. Chung, Structural health monitoring by electrical resistance measurement, Smart Mater. Struct. 10 (4) (August 2001) 624−636, https://doi.org/10.1088/0964-1726/10/4/305.

[104] A. Iwasaki, A. Todoroki, Statistical evaluation of modified electrical resistance change method for delamination monitoring of CFRP plate, Struct. Health Monit. −Int. J. 4 (2) (June 2005) 119−136, https://doi.org/10.1177/1475921705049757.

[105] Y. Hirano, A. Todoroki, Damage identification of woven graphite/epoxy composite beams using the electrical resistance change method, J. Intell. Mater. Syst. Struct. 18 (3) (March 2007) 253−263, https://doi.org/10.1177/1045389x06065467.

[106] A. Todoroki, Delamination monitoring analysis of CFRP structures using multi-probe electrical method, J. Intell. Mater. Syst. Struct. 19 (3) (March 2008) 291−298, https://doi.org/10.1177/1045389x07084154.

[107] D. Wang, D.D.L. Chung, Comparative evaluation of the electrical configurations for the two-dimensional electric potential method of damage monitoring in carbon fiber polymer-matrix composite, Smart Mater. Struct. 15 (5) (October 2006) 1332−1344, https://doi.org/10.1088/0964-1726/15/5/023.

[108] N. Angelidis, N. Khemiri, P.E. Irving, Experimental and finite element study of the electrical potential technique for damage detection in CFRP laminates, Smart Mater. Struct. 14 (1) (February 2005) 147−154, https://doi.org/10.1088/0964-1726/14/1/014.

[109] D. Wang, S. Wang, D.D.L. Chung, J.H. Chung, Comparison of the electrical resistance and potential techniques for the self-sensing of damage in carbon fiber polymer-matrix composites, J. Intell. Mater. Syst. Struct. 17 (10) (2006) 853−861, https://doi.org/10.1177/1045389x06060218.

[110] A.A. Nassr, W.W. El-Dakhakhni, Non-destructive evaluation of laminated composite plates using dielectrometry sensors, Smart Mater. Struct. 18 (5) (May 2009) 055014, https://doi.org/10.1088/0964-1726/18/5/055014.

[111] K.L. Reifsnider, P. Fazzino, P.K. Majumdar, L. Xing, Material state changes as a basis for prognosis in aeronautical structures, Aeronaut. J. 113 (1150) (December 2009) 789−798.

[112] M.B. Lemistre, D.L. Balageas, A hybrid electromagnetic acousto-ultrasonic method for SHM of carbon/epoxy structures, Struct. Health Monit. −Int. J. 2 (2) (2003) 153−160.

[113] M. Schulze, H. Heur, in: "Textural Analyses of Carbon Fiber Materials by 2D-FFT of Complex Images Obtained by High Frequency Eddy Current Imaging (HF ECI)," SPIE 2011 Smart Structures and NDE Symposium, San Diego, CA, 2012, p. #28.

[114] N.J. Goldfine, Embedded EC MWM Sensors Network, 2012. Available from: http://jenteksensors.com/embeddednetworks.php.

[115] H. Tsutsui, A. Kawamata, T. Sanda, N. Takeda, Detection of impact damage of stiffened composite panels using embedded small-diameter optical fibers, Smart Mater. Struct. 13 (6) (December 2004) 1284−1290, https://doi.org/10.1088/0964-1726/13/6/002.

[116] G. Kister, B. Ralph, G.F. Fernando, Damage detection in glass fibre-reinforced plastic composites using self-sensing E-glass fibres, Smart Mater. Struct. 13 (5) (October 2004) 1166−1175, https://doi.org/10.1088/0964-1726/13/5/021.

[117] L. Wang, G. Kister, B. Ralph, J.D.R. Talbot, G.F. Fernando, Conventional E-glass fibre light guides: self-sensing composite based on cladding, Smart Mater. Struct. 13 (1) (February 2004) 73−81, https://doi.org/10.1088/0964-1726/13/1/009.

[118] I. Sage, L. Humberstone, I. Oswald, P. Lloyd, G. Bourhill, Getting light through black composites: embedded triboluminescent structural damage sensors, Smart Mater. Struct. 10 (2) (April 2001) 332−337, https://doi.org/10.1088/0964-1726/10/2/320.

[119] E. Bocherens, S. Bourasseau, V. Dewynter-Marty, S. Py, M. Dupont, P. Ferdinand, H. Berenger, Damage detection in a radome sandwich material with embedded fiber optic sensors, Smart Mater. Struct. 9 (3) (June 2000) 310−315, https://doi.org/10.1088/0964-1726/9/3/310.

Part Three

Aerospace applications

Lightning strike direct effects

18

A. Murphy

School of Mechanical & Aerospace Engineering, Queen's University Belfast, Belfast, United Kingdom

18.1   Introduction to lightning

Lightning is a natural electrostatic discharge resulting from a build-up of a differential charge between a cloud (or mass of air) and the earth (or another remote mass of air). The lightning arc is the electrical discharge channel, which transfers and balances the remote differential charges. Different scenarios have been proposed for the formation of the unbalanced state of charge in a cloud, including the movement and collision of water or ice due to air currents and gravity. This behavior is proposed to create positive charges, which generally move upwards and negative charges, which generally move downwards. Thus, a part or series of clouds will act as a cathode, which is negatively charged and the earth or a remote weather system will act as an anode, which is positively charged. If the electric field is sufficiently intense and exceeds the dielectric strength of the air, charged electrons will flow from the cathode to the anode.

The breakdown of air will involve pilot streamers and stepped leaders, which together will propagate an initial conductive channel between the unbalanced charges. The mechanism of forming the channel involves the charged particles, free electrons, being accelerated due to the electric field. In this process, due to the speed at which the free electrons are moving, when they collide with neighboring atoms, the atoms will release an electron. The loss of an electron will ionize the atom and also start to create an ionized channel of air. Again due to the electric field, electrons progress while ions remain behind. The freed electrons subsequently collide with further atoms leading to further electron releases creating an "avalanche" of electrons, which accelerate toward the anode. During the collisions, energy will also be released, which will start to heat the channel. The avalanches of electrons propagate and extend the channel of ionized air, ultimately forming a circuit of ionized air between the cathode and anode. As electric current is inversely proportional to the impedance of a path the channel will appear to branch out irregularly and connect to any object, which will reduce the channel's resistance. An aircraft in proximity can become part of the discharge circuit resulting in an aircraft lightning strike. It has been established that the conductive properties of an object are not a major factor in the probability of a strike attachment but rather the proximity of the nearest object and the fastest, most conductive route to the ground are the influencing factors.

Once the discharge circuit is formed between the negatively charged cathode and the remote positively charged anode a massive flow of electric current occurs over a very short duration, which superheats the conducting channel, forming a highly

electrically conductive plasma channel. This highly electrically-conductive plasma channel enables the very large flow of charge in a very short period of time. This plasma channel consists of electrons, atoms, and molecules at a ground state or an excited state, positive ions, negative ions, and photons. Due to the intense currents produced during the lightning discharge, significant magnetic fields are generated, which, in turn, induce and apply electromagnetic force on the ionized air channel. The Lorentz force is the main magnetic force acting on the channel and this will modify the velocity and pressure profile within the channel and in the surrounding air. The interactions between the magnetic and velocity fields are in part controlled by Faraday's and Ampere's Laws.

18.2   Aircraft and lightning

It is commonly stated that a commercial, civil transport aircraft can be expected to be struck by lightning once per year or between 1000 and 10,000 hours of flight time. These numbers are derived from the number of reported lightning events, the number of active aircraft, and the average flight hours for aircraft. In reality, the probability for a particular aircraft to be struck by lightning is strongly influenced by the time of year, the geographic location, the local weather conditions, and the aircraft altitude. Again statistically, aircraft are also expected to experience more lightning strikes outside the cruise phase of flight (i.e., during taxi, take-off, climb, descent, hold, landing). This relates to the proximity to the ground, and thus, the weather conditions and intensity of electrostatic fields, but also the reduced ability to maneuver around adverse weather conditions. It has also been reported that of the recorded aircraft lightning strike events approximately 90% involve the aircraft inducing the phenomenon. The remaining cases are considered to have flown into an independently initiated lightning arc [1]. In both cases, the aircraft becomes part of the cathode to anode discharge circuit. Initially, the lightning attaches to an extremity point of the aircraft. The lightning path then continues from another extremity point of the aircraft in order to complete the circuit, for example to the ground, making the aircraft between the two locations part of the cathode to anode discharge circuit. The current will travel between the entrance and exit location on the aircraft by way of the shortest, most conductive path. Once the discharge circuit is completed, which now includes part of the aircraft between the attachment locations, a massive flow of electrical current takes place. The duration of the current flow is short (of the order of microseconds) during which time the current magnitude significantly varies. As the aircraft is moving forward at speed and the current flow varies significantly during a lightning event the circuit attachment points can move along the aircraft, attaching and reattaching to other locations of the aircraft.

Although lightning strikes frequently occur to the global aircraft fleet, they rarely compromise "continued safe operation" of a protected aircraft. When struck a wide range of effects are possible. The severity of effects is dependent on the energy level and duration of the strike and the attachment locations. In any case, the resulting need for inspection and associated repairs can directly impact airline operations, causing costly delays or serious service interruptions. For a metal aircraft, when a lightning

strike occurs, the lightning energy is rapidly conducted away from the attachment point, and the discharge current flow travels through the exterior aircraft aluminum structure. This is possible because of the favorable conduction properties of the airframe aluminum materials. However, where the conducting channel attaches to the aircraft, significant local mechanical damage is possible. The physical damage can be in the form of surface charring to puncture of the external skin. Such effects are labeled as direct effects and include any physical damage to the aircraft structure or systems resulting from the charge entering, transmitting through, and exiting the aircraft. The significant electric pulses and electromagnetic fields passing through the aircraft structure can also interfere with and damage electronic / electrical systems. Such effects are labeled indirect effects and require the protection of sensitive electronic devices from potentially very powerful electric pulses. Direct and indirect effects can occur together. This chapter specifically focuses on direct effects due to the significant cost and weight penalties associated with protecting composite structures, which without additional engineering, possess less favorable conduction properties when compared with traditional airframe aluminum materials.

18.3 Composite material and lightning

Aerospace manufacturers are increasingly using laminated composites to replace metal materials in primary structures with the objective of reducing aircraft weight and maintenance requirements. The use of composite material includes the extremities of the aircraft, which are the typical locations for the initial attachment of the lightning arc. Composite materials present a challenge to lightning strike protection due to the insulating nature of the polymer resin that surrounds the load-bearing fibers. The electrical resistivity is the property of a material that quantifies how strongly that material opposes the flow of electric current. Table 18.1 presents typical electrical resistivity values used by lightning strike researchers for their composite laminate materials along with properties for traditional aircraft skin aluminum alloy. Obviously, the composite resistivity properties are orthotropic, and clearly, the most conductive path is in the fiber direction (dominated by the carbon fiber properties as opposed to the resin properties). In the example given the aluminum alloy's resistance to current flow is two orders of magnitude smaller than that in the composite material fiber

Table 18.1 Room-temperature material properties used in preceding thermal-electric simulations.

Material	Resistivity (Ωm)		
	Longitudinal	Transverse	Thickness direction
IM600/133 ($V_f = 60\%$) [2]	2.78×10^{-5}	8.73×10^{-1}	5.58×10^2
Aluminum alloy (2024)	5.82×10^{-8}		

direction and six orders of magnitude smaller than that in the composite material through-thickness direction. The lower properties in the transverse and thickness direction are due primarily to the properties of the polymer constituent and the isolating nature of the reinforcing fiber lamination within the polymer (with the fibers typically possessing good electrical conductivity, as witnessed in the fiber (longitudinal) direction). Researchers have attempted to understand the relative importance of thermal and mechanical properties with respect to resisting lightning strike damage. To this end, testing with material systems with different thermal properties (glass transition temperature) and mechanical properties (mode I fracture toughness) has been completed [2]. The limited empirical results indicate a measurable benefit in a greater glass transition temperature, resulting in smaller damage area and damage depth. However, from the experimental campaign, a clear, measurable benefit was not achieved with greater fracture toughness.

It is important to point out that all such material properties are temperature dependent and strain-rate dependent. Table 18.1 presents only room temperature properties. With significant heating, the individual material constituent properties will vary and how they behave together as a conductive path, and structural unit will also change. Ultimately, with extreme heating, a composite material will char, decompose, and constituent elements ablate. This process, with the constituents converting to ash or gaseous products in different volumes at various temperature levels, will change the electrical, thermal, and mechanical properties. However, the room temperature properties are a good way to illustrate the orthotropic and relatively poor conductive properties of standard composite aerospace materials.

The immediate effect of poor conductive properties is slower and less effective charge dissipation away from any attachment point, and thus, the potential for a greater build-up of localized electrical energy. Additionally, lower thermal conductivity reduces the effective dissipation of heat generated by the lightning charge, potentially enabling the local accumulation of temperature and the possibility for serious material damage. Thus, an additional protection material is required to rapidly redistribute the intense charge and eliminate or reduce the potential for material damage. Moreover, to replicate the protective behavior of a metal airframe structure, where the discharge current flow travels around the exterior aircraft structure, the additional protective material must encompass the complete airframe forming a Faraday cage and preventing the discharge circuit from contact with passengers, crew, fuel or electronic systems. This additional protective material is required on or in the exterior structure of a composite aircraft and is called a Lightning Protection System (LPS). Without a suitable LPS, a lightning strike may significantly damage or penetrate the external structure. The contemporary method to protect composite aircraft structures is to use an outer layer of conductive material, for example, a metallic mesh, typically embedded during component manufacture. The conductive layer must be close to the surface to work effectively, and thus, directly impacts the manufacturing of components, the assembly of components, and final finishing processes, such as painting. This makes the aircraft more complex and costly to manufacture and can also be

expected to increase the structural weight. The LPS can also have an impact on aircraft operations with additional costs associated with inspection and likely repairs.

18.4 Lightning loading mechanisms

Due to the discharge, an electric current load is exerted on the aircraft at the attachment point. Also, due to the formation and existence of the superheated conducting plasma channel thermal and acoustic pressure loads are often described to occur along with the current load. However, owing to the complex and interacting physics, and the short dynamic and transient nature of the discharge and attachment, the loading mechanisms on aircraft are not well understood. Four loading mechanisms have been generally speculated, but their magnitude and influence on direct effect damage are not agreed. The loads are categorized into electrical and thermal loading, mechanical pressure/acoustic loading, and explosive and rate effect loading within the material.

Considering first electrical loading, this form of load results in Joule effect heating (or resistive heating) in the material. In this process, the passage of the electric current produces heat, which is dependent on the current load and the material resistance (Joule's first law). The current is dictated by the potential difference and again, the resistance of the material to current flow (Ohm's law). The voltage difference creates an electric field that accelerates the charge carriers in the direction of the electric field. However, when the charged particles collide with ions, particles are scattered in directions, which are not aligned with the current path. Energy is thus converted from electrical charge transfer to thermal heating.

In addition to the heat generated by the current load, a thermal conduction heat load from the conducting plasma channel is possible. Although the transfer of heat by thermal conduction is a function of the temperature difference (which would logically be expected to be significant) the duration of a lightning strike and the duration at a fixed attachment point is potentially very short. What also complicates the definition of this form of loading is the challenge of isolating the behavior, which is naturally linked with the conducting channel and as a consequence the applied electric load. Equations for this form of loading have been proposed and applied within damage analysis [3,4]. However, many researchers dismiss this form of heat loading on the assumption that its magnitude is insignificant in comparison to the scale of electric current resistive heating.

As the air acts as an insulator, the initial formation phase of the discharge circuit is via a network of crooked leader paths with numerous dead-end branches. The time taken to form the circuit depends on the length between the particular charge states (cloud and earth, for example). The return stroke, the major discharge phase of the lightning event occurs along the established circuit network. It is generally suggested, based on high-speed imaging of real lightning events, that the discharge phase along the formed circuit takes a fraction of the time taken to establish the circuit network. For example, the discharge phase has been measured to move along the establish circuit at 100,000 km/s and contain energy orders of magnitude greater that required during

the establishment of the circuit. Given the energy and speed of the return stroke, it is envisaged that it results in a physical impact on the aircraft. This occurs where the discharge circuit exits from the aircraft toward the earth (or a remote weather system) which is acting as the anode. First, an initial longitudinal pressure load is envisaged as the return stroke is formed along the discharge circuit. A radial pressure shockwave due to the rapid heating of the conducting channel is also expected (sometimes termed the acoustic load). The pressure loading is thus assumed to result from arc channel expansion and will include additional magnetohydrodynamic effects. The magnetically induced pressures, due to Ampere's law, will pull together the current streamlines in the arc channel, which intensifies the local pressure (typically termed the magnetic pinch load). In addition, the magnetic force induced by the current circulation at the attachment point also induces a mechanical pressure load in the arc column at the attachment point. There is potentially additional loading of the structure due to the current circulation at the attachment point due to the interaction between the magnetic field and the structural material (strongest with ferromagnetic materials). Furthermore, the current flowing in the specimen directly will act to create an additional internal load on the material. These final loads could be significant on a ferromagnetic based LPS embedded within a composite component. Finally, electromagnetic forces between plies of different orientation are also speculated and proposed to push ply layers apart. This mismatch would be a result of current flow in different directions in different ply layers.

It is also suggested that additional internal mechanisms are potentially responsible for further material damage. A number of mechanisms are generally suggested to cause such damage:

- The current induced heat causes vaporization of moisture, at the surface or absorbed moisture inside the material, and this, in turn, creates expanded steam (explosive vaporization), which "blows apart" the local material. Specifically for painted and composite structures with surface protection layers, a further mechanical loading mechanism has been indicated where Joule heating and vaporization of the paint or protection layer results in damage on the surface plies.
- Due to the very rapid heating, it is proposed that trapped gas from decomposing resin below the intact surface or below laminate layers, which have not completely lost their integrity, results in an outward force. The inference is that particular common forms of damage - flaying of fibers outwards and separation of surface plies (ply lift) - is a result of such an internal blast, explosion force or outgassing mechanism.
- An internal mechanical loading results from electrical load-induced thermal expansion. In this case, the surrounding structure at the ambient temperature constrains the thermal expansion of the material at the attachment point, which is rapidly heated by the application of the lightning current (via resistive heating).
- Due to dielectric breakdown and differing fiber orientations, and hence mismatch in current flow, additional electromagnetic forces may force apart ply layers and produce or exacerbate delamination.

Generally, there is still uncertainty in the mechanisms during a lightning strike, which leads to damage. This is partly due to the complex thermal, electrical, electromagnetic, and mechanical components of the event, and partly due to the limited experimental test results in the public domain.

18.5   Composite material damage due to lightning

In real lightning strike events, the damage is usually found at the lightning entrance or exit attachment points, where the energy density is at its highest. Experimental studies have identified the main damage modes occurring in composite materials struck by lightning to be fiber breakage and ablation, resin decomposition, pyrolysis, and surface erosion, ply lift (surface ply delamination) and internal delamination and matrix intralaminar cracking. However, a significant range in the volume of each type of damage is found. Foster et al. [5] attempt to characterize the typical damage from published laboratory experiments into three forms, Table 18.2.

First severe damage, which is defined by a damage zone with char residue penetrating several ply layers into the material, depending on the size of the lightning strike. This damage is mainly attributed to thermal decomposition and ablation of the fiber and resin. The damage can be generally described as an absence of resin with absent or broken and frayed fibers. Generally, there is a charred appearance, but limited residual ash and the fibers flaying outward from the surface has led to the suggestion of an internal explosion.

Second, a moderate damage zone, which is defined as a wide surface area with thermal decomposition and sharp and shiny resin. This damage is shallow, confined to the top ply layers and contains the severe damage area. In this case, the damage comprises narrow, discontinuous damage sites of exposed and broken fibers. These "scars" become larger and denser closer to the lightning attachment point. At each scar, fiber bundles have burst upwards from the surface, and fiber breakage is at the center of the uplift. Matrix cracking occurs near the root of the fiber uplift. Electron microscopy scanning determines the fibers are generally still well covered with resin, and the resin fracture surface has a relatively sharp and rugged morphology, compared with the severe damage area.

Thirdly sub-surface damage, which is defined as sub-surface intralaminar and interlaminar matrix cracking. Beneath the severe damage and moderate damage zones combined intralaminar and interlaminar damage can completely saturate the local material. A network of cracks is typically reported with potentially isolated intralaminar and interlaminar cracking remote from the severe damage zone. Delamination is generally stacking sequence-dependent and is typically the damage mode at the greatest depth.

From the above, it is clear that the failure behavior of a composite material struck by lightning is a highly complex phenomenon and involves many interactive thermal and mechanical physics. A number of authors suggest that surface damage is in the main due to thermal effects and beneath this damage is due in the main to mechanical effects resulting from the rapid nature of the event (including the thermal loading). The damage is also dependent on the intensity and form of the lightning loading, along with the specimen material constituents, material layups, and the design of the LPS. In a laboratory, the specimen fixturing and boundary conditions and specimen condition (for example moisture content) are also known to impact the damage form. In a real event on an aircraft, the surrounding structure, paint, fasteners, flight loads, etc., are all expected to further influence the damage.

Table 18.2 Damage zone definitions.

Severe damage

Characterize by an absence and/or broken fibers, with the majority of surface resin absent:

- Resin thermal decomposition due to dark appearance and char residue.
- Signs of mechanical force present: some sharp resin morphology, fractured fibers, fibers blown outwards.
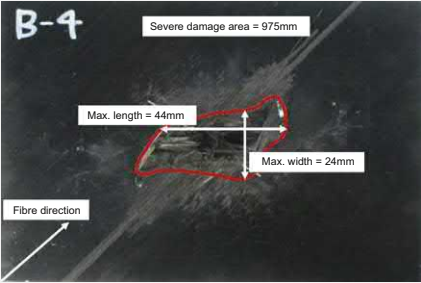
e.g.,   **Specimen B-4**   **Specimen C2-1**
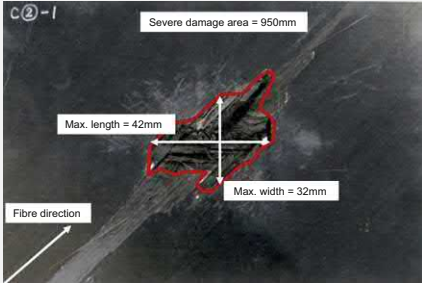
Moderate damage

Characterize by an absence of some surface resin, may also include limited fiber burst out and/or fracture:

- Some thermal decomposition
- Signs of mechanical force present: Sharp and shiny resin morphology, fractured fibers which appear to have been blown out of resin.
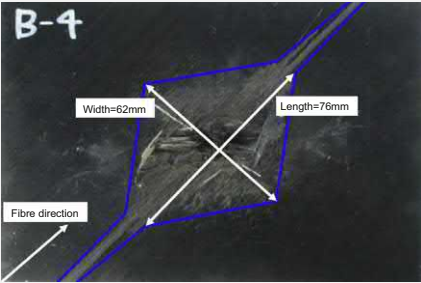
e.g.,   **Specimen B-4**   **Specimen C2-1**
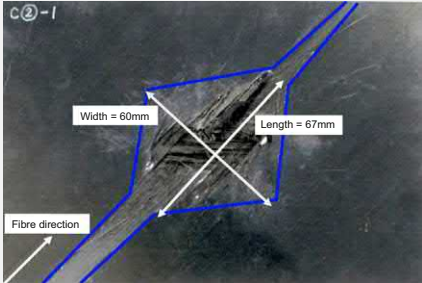
Sub-surface damage

Including intralaminar and interlaminar matrix cracking

e.g.,   **Specimen B-4**
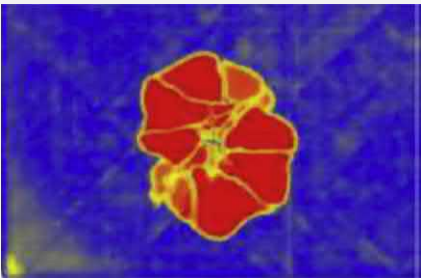
18.6 Lightning experimental testing

Test standards representing the features of real-world lightning events have been developed. The test standards are used to ensure that lightning protection systems can safely shield the underlying composite materials during the service life of an aircraft. Variants of such test procedures are also used by researchers to understand how composite material, protection systems, and lightning test parameters influence the scale and form of material damage.

18.6.1 Standard test methods and aircraft protection design

From measurements taken on test aircraft flown purposely into active lightning storms, the size of lightning impulse currents have been measured, and standardized lightning intensity and current waveforms have been established for laboratory certification testing. The standardized test waveforms and testing procedures are defined in detail in the standards [6−8]. The waveforms are defined through their maximum current (I_{MAX}), the rise time from 10% to 90% of the maximum current (T_1) and the time to reach the post-peak value of 50% of the maximum current (T_2). Tolerances are also defined on the waveform parameters as these are not directly controlled within a test. The test waveforms can also be described in terms of the total waveform electrical charge in coulombs, the integral of current over time, Eq. (18.1). The action integral is also used to describe the waveforms, representing the specific energy of the impulse current in Joules per ohm, Eq. (18.2). In both equations $I(t)$ is the transient electric current and t is time.

$$Electrical\ charge\ Q = \int_{t_0}^{t} I(t)dt \tag{18.1}$$

$$Action\ Integral\ AI = \int_{t_0}^{t} I^2(t)dt \tag{18.2}$$

A total of four current waveforms are defined in the standards. Each waveform relates to an envisaged sequence of load derived from the measured lightning events. The envisaged sequence of loading events follows on from the completion of the lightning discharge circuit. First, the return stroke begins to propagate along the formed circuit and through the aircraft; this is described by Waveform A. Once the return stroke reaches the oppositely charged state an intermediate current flow is assumed, Waveform B, followed by a continuing current, described by Waveform C. Finally, as the original cloud (mass of air) discharges another cloud is assumed active in the circuit (remembering that the aircraft is continuously moving). Thus, a second return stroke is assumed corresponding to the discharge of this new cloud or mass of air, described by Waveform D. Fig. 18.1 illustrates the four waveforms. From Fig. 18.1 it can be seen that the first
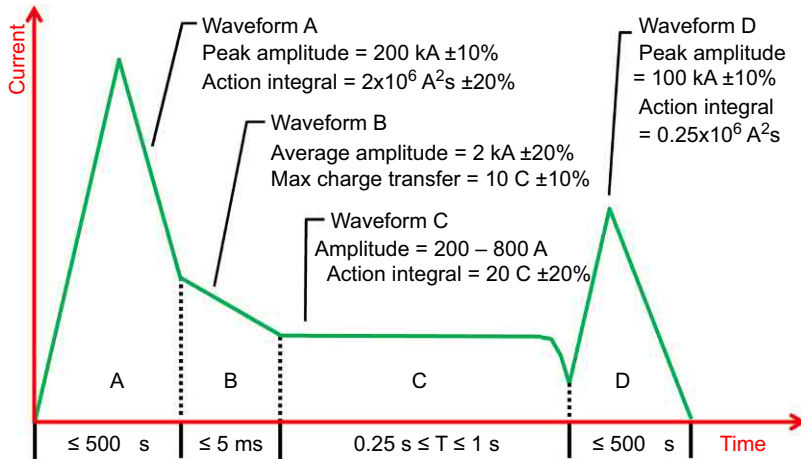
Figure 18.1 Lightning strike test waveform standards.

return stroke (Waveform A) has a high-intensity peak current (up to 200 kA) but a very short duration (up to half a millisecond). The intermediate waveform (Waveform B) is a lower intensity current and a longer duration (lasting up to 5 ms). The continuing current waveform (Waveform C) is the longest current and lasts for up to one second. The subsequent return stroke (Waveform D) is similar to Waveform A in duration (up to half a millisecond) but half the peak current.

Also derived from the original test flights flown purposely into active lightning storms, captured in-service experiences and more recently via predictive modeling is an understanding of how lightning strikes are distributed on the geometry of an aircraft - their potential frequency, intensity, and duration. Thus, zoning identifies the surfaces on an aircraft as a function of the lightning threat. The aircraft is divided into zones, and each zone is designed and tested to withstand the relevant waveforms (A to D). Together, the defined waveforms and zoning are used as the key instruments in the design and certification of an aircraft protection system. This allows the LPS to be optimized for the particular zone. For example, the extremities of the aircraft would be expected to be subject to lightning attachment and first return strokes (waveform A). Whereas other portions, for example, the main body of the fuselage could witness swept strokes or re-strikes (C and D). Other zones must safely sustain and dissipate the lightning current between the zones in which the lightning current enters and exits the aircraft. Additionally, acceptable damage and the need for repair are also coupled to the lightning strike definitions. For example, high energy strikes, above 50 kA and up to 200 kA, should not affect continued safe flight and damage will be readily detectable. For low energy strikes, less than 30 kA and above 10 kA, no repair will be needed with barely visible or no damage. Between 50 and 30 kA repairs may be needed and visible damage may occur.

For aircraft certification, the full magnitude and full range of waveforms can be applied sequentially to a single zone, and the LPS must protect and ensure flight safety. The full magnitude waveforms are generally applied to full-scale test components once

the design is matured. In the case of early screening of material systems and LPS designs, the full waveforms are too large for practical coupon level testing. Thus, reduced scale waveforms are typically used. In a laboratory, an artificial lightning strike is carried out by applying a large current through an impulse generator. The impulse generator supplies a large current over a short period of time to a specimen via a discharge probe. The test specimen is typically placed on or clamped to, an earthed test fixture to permit the current to travel to and then through the specimen to the ground in a controlled fashion. The discharge probe is positioned at a distance from the specimen, and an insulating sphere may be placed on the end of the discharge probe to avoid a direct shock wave between the probe and the surface of the specimen. Furthermore, to ensure the arc channel flows around the sphere and into the specimen, a fuse wire may be extended from the discharge probe around the sphere and positioned above the desired strike point.

18.6.2 Special test methods

In addition to the standard certification test arrangements, special test arrangements have been proposed to understand better the loading induced by lightning. For example, a number of special specimen holding fixtures and deflection measurement systems have been proposed to study pressure wave characteristics of the artificial lightning strike test waveforms [9,10]. By striking the specimen directly and striking a grounded component above the specimen and below via a central specimen hole and recording specimen deformations valuable but incomplete understanding of the pressure load has been derived. Alongside the experimental works, simulation approaches have been proposed to reverse engineer the pressure wave details from the measured specimen displacements. It is also worth noting that a number of authors have also investigated the potential to employ transverse impact test arrangements to replicate lightning strike behavior. Although both lightning strike and transverse impact tests result in many similar modes of damage, the position of damage differs considerably. The damage from a lightning strike test tends to be concentrated over the top plies only. Such a damage pattern is not typical of transverse impact loading (at high or low speed), where damage typically occurs through the thickness of the specimen. As the form and location of the damage are significantly different between the lightning strike and transverse impact damage, it has proven difficult to draw meaningful understanding directly applicable to lightning protection.

In addition, many researchers have performed and reported lightning strike experiments. Typically, these have been performed on composite material coupon scale specimens, and thus, scaled versions of the standardized test waveforms have been used. Only a small number of experimental studies have been published on composite materials, which adhere to the largest standardized certification waveform (waveform A). Table 18.3 presents a summary of many of the public domain lightning strike test results on composite materials. It is interesting to note the large variation in the applied current waveforms, varying distance between the specimen and the discharge probe, varying specimen fixturing and boundary conditions, and different material constituents and material layups. Few repeat tests are reported, and thus, given the small total

Table 18.3 Experimental setups used in the literature.

First author	Peak current (kA)/ Action integral (A^2 s)	Specimen boundary conditions	Specimen size (mm)	Specimen thickness (mm)	Material	Layup
Hirano [11]	40/22,000	Placed on surface	350 × 350	4.704	IM600/133	[45/0/−45/90]$_{4s}$
Kawakami [2,12]	40/18,500	Two edges clamped to base	140 × 140	2.2	T700/2510	[02/902]$_{2s}$
Kawakami [2,12]	80/87,000	Two edges clamped to base	356 × 254	4.1	T300 3K Tow, resin XB 3518 BD	20 layer twill weave [0/90]
Feraboli [13,14]	30/23,800	Two edges clamped to base	304.8 × 38.1	2.88	G30-500 12K fiber, HTA/7714A resin	45/02/−45/02/90]$_{s}$
Hosokawa [15]	157/-	Placed on surface	150 × 150	1	TR50S fiber Sandwich panel	Skin, [45/−45], # of plies not known
Chemartin [4]	200/-	Two edges clamped to base	100 × 100	0.2	Carbon fiber	—
Haigh [9]	100/-	Two edges clamped to base	550 × 550	—	Carbon fiber	6 layer weave
Munoz [16]	200/-	—	—	—	—	—

Gou [17]	100/-	Four edges clamped to base	406 × 406	1.778	Unidirectional carbon Fiber	[0,−45, 90, 45]$_2$
Lepetit [18]	98/,300,000	Two edges clamped to base	450 × 450	2	T700/M21	8 layer quasi-isotropic
Yamashita [19]	1.2/-	Four edges clamped to base	110 × 110	0.8−1.1	CF mat reinforced thermoplastic, Vf = 30%, Polypropylene resin	n/a

volume, the large variation in test and material parameters and the limited repetitions there is a restriction on general conclusions, which can be drawn. An additional complexity is that authors do not have a consistent definition of damage and have measured using a range of techniques with different fidelity (e.g., surface visual inspection and image analysis, cross-section observation, ultrasonic scanning, micro X-ray inspection, optical and electron microscopy).

18.6.3 Experimentally derived relationships

For each of the public domain experimental studies, the authors have typically noted probable or possible causes of the damage. Resistive heating due to the applied current is consistently identified to cause a significant amount of the measured damage, but many note that it does not completely explain all the damage witnessed. The pressure load and magnetic loads are experimentally difficult to study in isolation and are often acknowledged to exist and commonly suggested to explain variation in results or the difference between expected and measured behavior. Some correlation has been experimentally found between lightning parameters, such as action integral, electrical charge, peak current, and current rise rate with damage area, and characteristics of damage (damage depth, and surface area, and delamination area). These relationships are generally developed for a single waveform strike on a pristine specimen. Action integral is the clearest predictor of the severe damage and delamination area and damage depth. These relationships can be related back to the developed waveforms, which have specific action integral, electrical charge, and peak current values. Waveforms A and D are thus expected to generate the greatest damage depth. Waveform C is anticipated to generate significant surface damage. In addition, considering the application of more than one test waveform, the characteristics of damage (damage depth and surface area) will be dependent on the order in which the waveforms are applied. The induced damage from the preceding waveform will influence the initial thermal state of the material but also the way in which the subsequent waveform will electrically and mechanically interact with the specimen material. Damage development and current and temperature dispersion due to the preceding damage will, therefore, change from an equivalent strike on a pristine material. Thus, the damage from a single waveform will be different if applied within a combination of waveforms or in a different sequence location within a combination of waveforms.

Experimental works have also attempted to correlate between damage parameters and residual strength of the material specimens. There appears some potential correlation between peak current and residual strength, and damage area and residual strength. This suggests that residual strength of the composite could be estimated from lightning parameters or damage area, but the correlations are typically only demonstrated for individual material and layup combinations [2,11,13,14].

In summary, there is still limited understanding and quantification of the damage mechanisms through purely experimental artificial lightning strike test campaigns. Much of this lack of knowledge is due to the speed and intensity of the event, which means it is very difficult to take physical measurements near the strike point during the strike. Post-test inspection of the damage is also difficult, as there are a number of

different surfaces and internal damage modes, which are difficult to differentiate in a post-test inspection. Some caution should be taken with any regression of damage characteristics, such as depth and surface area because substantial variation is possible in the modes of damage. Moreover, a great number of variables are involved in lightning strike testing, the lightning waveform, specimen fixturing, and location relative to the discharge probe, the protection system design, and the composite materials. The specimen stacking sequence and the specimen condition (for example moisture content). Together, the expense and time required to complete tests and the volume of variables included in testing, significantly increase the difficulty of establishing a generic understanding from individual test results.

18.7   Lightning protection systems

An aircraft Lightning Protection System (LPS) relies on creating a conducting layer toward the outer surface of the aircraft, providing an equivalent form of protection to that used in an aluminum aircraft with an exterior conducting path. In this way, the LSP enables the applied lightning current to flow around the passengers, crew, fuel, and safety-critical systems. For minimizing damage, the conducting path must enable the current to remain at the exterior of the aircraft, to dissipate charge quickly, and to permit the current to flow easily from any attachment point to any other remote location, where it exits the aircraft. The LSP must also shield the aircraft systems from electromagnetic surges and interference resulting from the lightning electromagnetic effects. Again the creation of an exterior conducting path can act as a Faraday cage, and provide the necessary protection. Thus, LPS are typically in the form of a thin layer of conducting material, which is located within the external aircraft skin composite laminate. The thin layer of material is placed within the laminate toward or at the external surface during manufacture or added to the surface once the part is manufactured. The most common LPS material is a metal mesh, which offers the required conductive properties at maximum surface coverage per unit of mass. Copper and aluminum are used as LPS meshes, which can be laminated with standard aerospace materials, but special attention is required with aluminum due to the potential for galvanic corrosion.

   Meshes are available as woven fabrics constructed from specialist monolithic metal wires, which can be loom woven into drapable fabrics with wires running in both the warp and weft directions. Expanded foil meshes are also available, which can be thinner due to their manufacturing process where a monolithic metal foil is perforated and stretched to create a mesh with a specific aspect ratio diamond pattern. Both materials can be preprocessed to create preimpregnated plies for lamination during part manufacture. Or can be laminated into multilayer surface-mountable materials (surfacing films), which combine the lightning protection material with resin and or isolation layers, which improve their performance and or add supplementary functionality. Additionally, carbon and glass fabrics are available, which have small diameter metal wires woven into the toes to increase conductivity and shielding. Moreover, novel carbon and glass fibre fabrics with special conductive coatings are available.

The fabric coatings link the warp and weft toes, and thus, form the integrated conductive shielding layer. Again such fabrics may be incorporated with resins to create preimpregnated plies or may be laminated into surface-mountable materials to increase conductivity and shielding.

The current LPS are proven to protect aircraft having significant service history on a wide range of aircraft types and composite material systems. However, given the large wetted surface area of an aircraft and the nonstructural single function of the LPS materials used today, there is potential for weight saving. A common aspiration is the formulation of an appropriate conductive resin, which could perform the standard functions of load transfer and fiber protection, but which could also eliminate the need for the metal mesh. Alternatively, the manufacturing burden associated with laminating a metal mesh into each external surface component or the manual application of shielding layers on manufactured components could be lessened with more efficient and automatable ways of creating the exterior layer through coating, painting or printing. In both cases, it is also arguable that such new materials and processes could reduce the burden of operational inspection, maintenance, and repair.

Thus, numerous approaches to enhance the electrical conductivity of composite resins have been reported. In particular, with the addition of materials to form conductive structures with sufficient conductivity to act as the primary LPS. Due to their promising mechanical, electrical, and thermal properties many forms (fillers, films, etc.) of carbon fibre, carbon black, carbon nanotubes, and graphene have been investigated. However major challenges still exist for such enhancements particularly around disbursal and uniformity of additives to create the necessary conductivity, the integrity of the host polymer under high current densities (and associated thermal load), behavior at failure (with further damage induced by the failure of the added material or hosting resin) and ultimately production scale speed and cost. Again much research has been invested in approaches to create coatings, sprays, and paints with sufficient conductivity to act as an LPS. Separating the LPS from the structure could offer an advantage in simplifying manufacture, both for component production and assembly, and also improve in-service inspection and repair. Again challenges remain, relating to bond strength, integrity under high current densities, damage induced by the failure of the material, and process production scale cost and speed. In general, a major constraint of new protection solutions is the complex multiphysics, high temperatures, and short duration of strike events, which has meant that LPS design has to date been empirical and incremental. A lack of quantitative analysis and simulation methods for lightning strike events means that the current designs and new proposed designs are not being developed and optimized with a full understanding of the range of physical behaviors, which occur during a lightning strike event.

18.8   Modeling for a lightning strike on aerospace composites

A lightning strike is a highly complex phenomenon that involves many interactive physics such as electrical, magnetic, thermal, and mechanical behavior all occurring within a very short timeframe. Given the noted limitations of physical testing, the

potential of numerical simulations offers many advantages to study lightning strike events, and the resultant damage creation. A significant advantage is the potential to scrutinize, during the virtual event, the internal specimen damage behavior. Thus, computational modeling has dominated lightning strike research over recent years with authors typically modeling the electrical and mechanical loads on a test specimen based around the standard artificial lightning strike test waveforms. In modeling the test specimen behavior using the Finite Element method, for example, researchers have been able to take advantage of recent advances in numerical modeling techniques, including many associated with the simulation of composite material damage mechanics. Additionally, progress has been made in terms of modeling the thermal plasma associated with an artificial lightning strike test. Modeling of the plasma can encompass all the key physics mentioned previously, but requires a highly complex solution procedure within a multiphysics simulation, and to date, results in high computational expense.

18.8.1 Modeling specimen thermal behavior

The flow of electric current in a material is governed by the electric potential difference. In the case of an artificial lightning strike test, the potential is modeled between the arc attachment and the grounded face of the test specimen. Joule heating arises when such current flow is converted into thermal energy, and such heating can then change material properties and thereby change the current flow. In addition, the converted thermal energy may then be transferred through the material via thermal conduction or given enough energy can lead to a change of state of the material (again changing material electric properties). Thus, due to the coupled thermal-electric behavior between electrical potential and temperature fields, it is necessary to solve both fields simultaneously. This is most typically achieved using the Finite Element Method and the coupled thermal-electric equations in a two-step simulation procedure. First, a fully coupled thermal-electric analysis represents the current loading and the resistive heating, typically using a transient solution procedure. A second analysis then models the heat dissipation through the specimen using a heat transfer solution procedure.

To date, much of the modeling research has studied the influence of material property representation on the prediction of the induced specimen temperature profile [20−24]. Many of these studies attempt to replicate a single experimental work [11]. Each study represents the experimental setup and specimen with some small differences - normally driven by the computational cost of the analysis and attempts to reduce this. Together, the simulation results also permit the identification of thermal-electric behavior during a lightning strike. In general, the simulation results illustrate that when the current is initially applied to the specimen most current flows in the fiber direction, with only small magnitude current flows in the transverse and through-thickness directions. This is a result of a combination of the orthotropic material properties, Table 18.1, and the relative distances to be traveled by the current to reach the ground (at the edge and beneath the specimen). Together, with the low resistivity in the fiber direction, the long length to the ground is the route with the lowest resistance rather than the shorter, higher resistivity routes (in the transverse

and through-thickness directions). Therefore, initially, there is significant current flow in the top ply in the fiber direction, which results in top ply resistive heating along the fibers away from the current attachment. The increased top ply temperature, in turn, increases the transverse and through-thickness electrical conductivity as the resin decomposes, and the conductivity in the through-thickness direction rapidly increases. As a result, proportionally more electric current begins to flow through the thickness of the top ply than flows along the ply fibers. Similar to the behavior witnessed in the top ply, and due to the lag between current flow and temperature rise, the current in the second ply will initially flow in the fiber direction. Thus, a pattern emerges - initially, in each ply, the majority of the current flow is in the ply fiber direction before resistive heating elevates the temperature to the point when a greater proportion of current then begins to flow through the thickness of the ply. As the current flow progresses downward into the specimen, a stacking-sequence dependent temperature distribution is, thus, created.

The major modeling developments, from the noted series of studies, is the importance of material property representation. The initial studies did not represent all material properties or temperature-dependent material properties, and as a result, predicted unrealistically high temperatures. Subsequent works refined the range of temperature-dependent material properties necessary for modeling and the impact of individual properties on temperature magnitude and profile prediction. Fig. 18.2 presents some typical surface temperature profiles from these key studies. These predictions are overlaid on the moderate damage area determined from image analysis of the equivalent test specimen. In the figure, the specimen surface is binarized, such that the experimental moderate damage area is identified as the black regions, and the pristine specimen surface is identified as the white regions. The predicted temperatures, with significant zones above the glass transition temperature for common aerospace resin systems, clearly suggest that electric current resistive heating can be expected to be an important mechanism for damage. However, examining the surface temperature fields, it is clear to recognize consistent differences between the predicted temperature contours and the identified experimental damage. The temperature contours from all simulations have a similar shape, which is narrow and elongated in the surface ply fiber direction. Thus, the greatest difference between the predicted temperature and the measured damage is the width.

It is possible to use the predicted temperature fields to assess the level of material damage, either using a simple set of temperature rules or with an integrated analysis decomposition model, which can represent changing electric and thermal-electric properties with temperature during the thermal-electric analysis. A number of studies also propose and demonstrate methods to represent the ablation of specimen material. This is achieved at an element level by either removing an element, which has reached some critical temperature and reapplying the current load at the adjoining elements or modifying the properties of the element to create a near-infinite electrical conductivity and thus, the current load progresses to the adjoining elements [21,22].

However, when considering damage predictions, it is important to consider how the base material properties are identified and modeled. Given the extreme conditions being modeled for most properties, the proposed material relationships have necessarily been
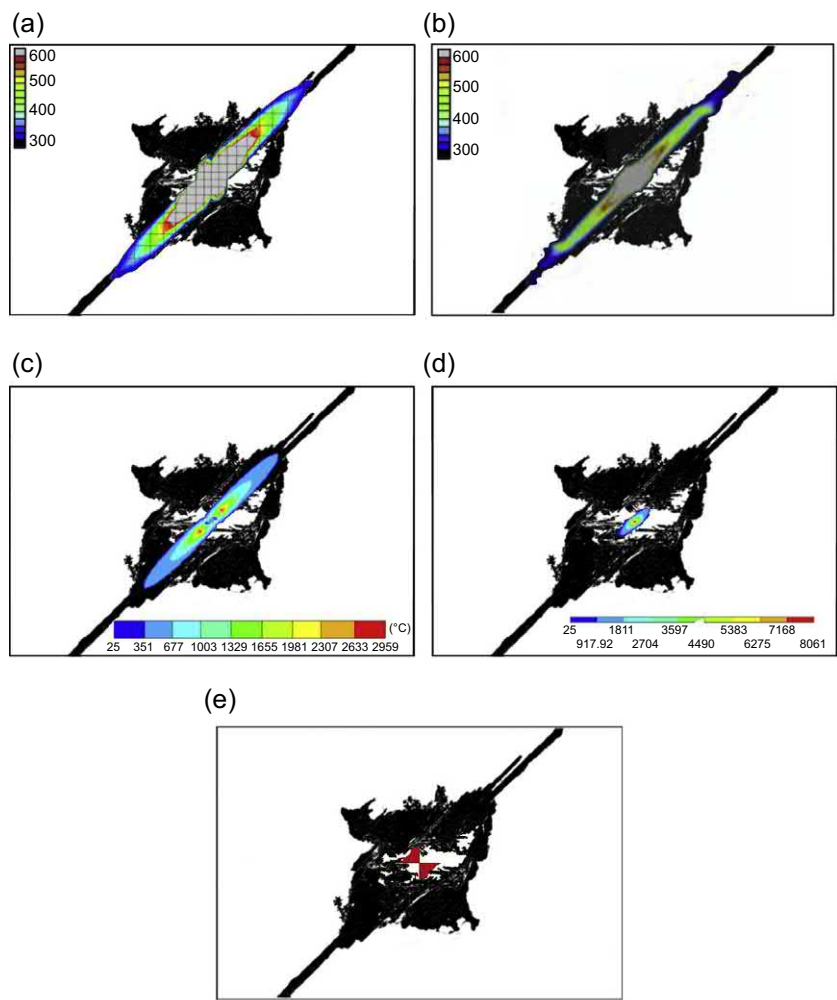
Figure 18.2 Predicted temperature fields from simulations overlaid on binarised images representing surface pristine and moderate damage areas (*white and black* respectively). (a) [20], (b) [23], (c) [22], (d) [24], (e) [21].

extrapolated from experimental data generated from lower temperature and heating rate tests. Thus, there is a significant challenge, generally associated with modeling lightning strike, with respect to material property data. The noted simulations typically predict temperatures beyond 1000°C in the specimen and with total test duration as short as half a millisecond the material state, the temperature heating rate and the temperature magnitude all have the potential to compromise the usefulness of material properties, which can be measured with standard laboratory setups. Not only is this relationship important for the prediction of the induced temperature but also for the interpretation of the predicted temperature with respect to specimen damage.

To date, Thermogravimetric Analysis (TGA) data has been widely used as a means of obtaining temperature-dependent material properties and interpreting temperature profiles from thermal-electric simulations. TGA data captures the change of mass of a material specimen in a controlled atmosphere as a function of increasing temperature. Resin decomposition occurs at a much lower temperature than that required for carbon fiber decomposition. As the resin decomposes, as a result of a series of chemical reactions, it will change its form, from a pristine solid material to combinations of ash, char, and gaseous products. Thus, material models based on TGA data typically describe a relationship between material temperature and percentage resin decomposition. The percentage resin decomposition is then further extrapolated, potentially with additional theory or test, to describe the effect of percentage resin decomposition on thermal, electrical or mechanical properties of the composite material. The temperatures required to decompose carbon fiber is beyond standard TGA hardware and is not typically represented in such models. Additionally, the temperature rates achieve within standard TGA hardware is many orders of magnitude lower than that witnessed in lightning strike thermal-electric analysis. To account for the difference between the temperature rate at which the material behavior is measurable, and the extreme conditions during a lightning strike, offsets are often proposed to represent heating rate effects. It has similarly been suggested that pressure during a lightning strike will influence decomposition and should be considered in the creation of experimental data or an additional manipulation applied to standard atmospheric test results. Thus, damage predictions based on thermal-electric analysis and TGA data requires careful interpretation and a full understanding of how the measured material properties are processed for use in the simulation. Finally, it is worth noting that TGA data typically identifies weight loss below 100°C due to moisture evaporation, this is important to note given the proposed damage mechanism of moisture explosive vaporization.

In addition to material properties, another notable uncertainty in the discussed studies, thus far, is the application of the electric current load. The load, a version of a standard waveform, is applied as a uniform electric current load through a single node or over a constant radius on the specimen surface. It is possible that the idealization of a fixed, concentrated electrical load potentially results in unrepresentative electrical energy being dissipated along a narrow band of surface fibers, as obviously seen in Fig. 18.2. Moreover, the concentration of the load would logically result in more rapid through-thickness heating, leading to accelerated through-thickness electrical conductivity and unrepresentative energy dissipation. Experimental observations suggest that a lightning channel attached to a specimen is neither constant in form, nor is it stationary.

A small number of studies have, thus modeled nonuniformity, movement, and expansion of the arc channel. In these works, assumptions have been made on how the arc attaches to the specimen based on descriptions within the experimental studies. One work [25] considers the same experimental setup [11] used as the bases for much of the material modeling developments discussed herein. This study considers four observed arc characteristics: arc channel expansion with time, asymmetric arc channel expansion, fragmented arc behavior with a fixed central portion plus an expanding portion, and finally a moving arc. Fig. 18.3 presents a typical surface temperature
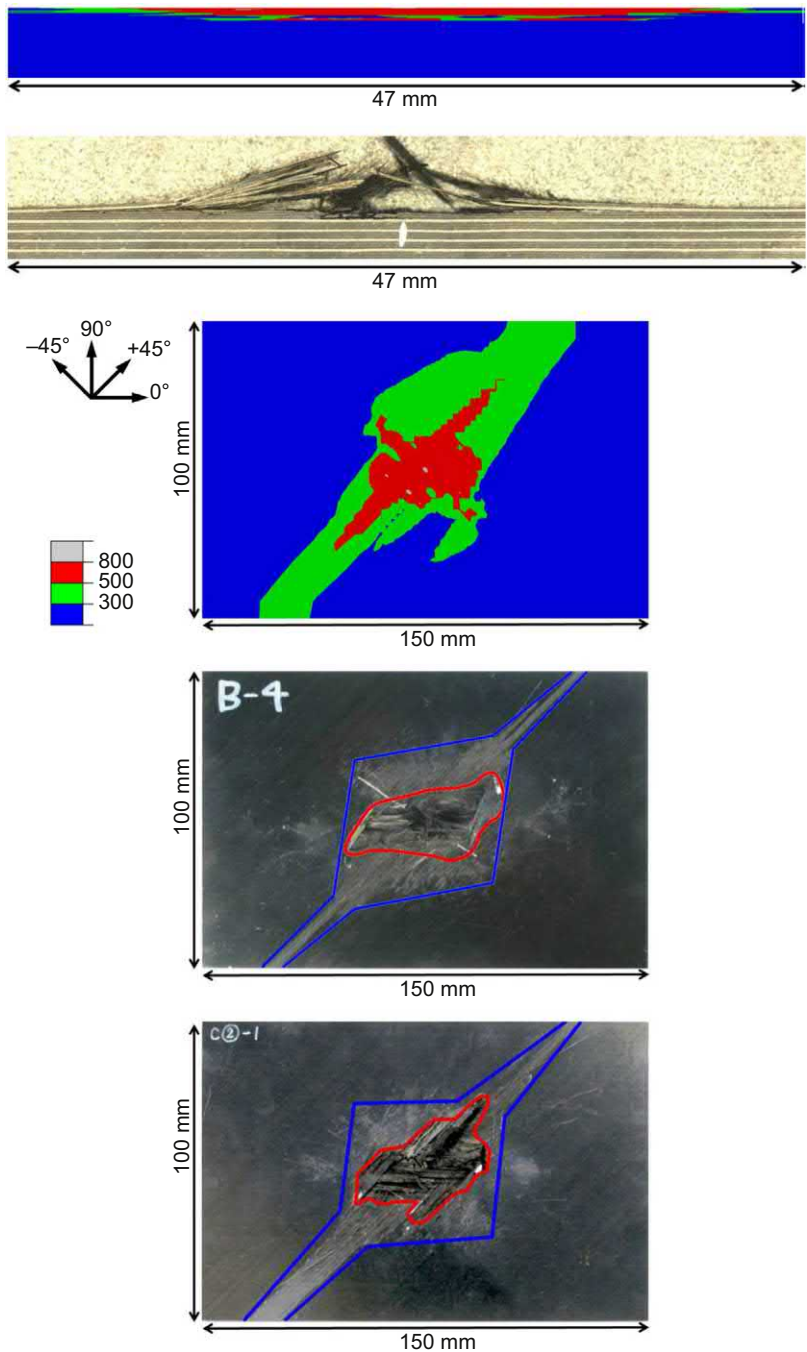
Figure 18.3 Temperature contour predictions from a thermal-electric simulation modelling combined arc expansion and arc movement along with equivalent experimental damage images [25].

prediction (with combined arc expansion and arc movement). By examining the surface temperature fields, it is possible to recognize similarities between the predicted temperature regions and the damage classifications. However, as the parameters, which describe the time-varying arc behavior are in the main assumptions the prediction results primarily indicate the importance of the arc attachment characteristics, rather than offering a measurable improvement in prediction accuracy. The authors also note that thermal behavior is only one element of the damage mechanisms and damage from mechanical effects, such as pressure loading and thermal expansion, is contained within the associated experimental results.

18.8.2   Modeling specimen pressure loading

To date, the majority of numerical studies by researchers have focused on modeling resistive heating from the electrical load. However, nonthermal loads are referenced in the experimental literature - pressure loads induced by acoustic and electromagnetic effects, explosive loads resulting from internal trapped gases, and internal specimen mechanical loading resulting from electrical load-induced thermal expansion.

Of the nonthermal loads, the shockwave or acoustic pressure load has received the greatest study. Many of the studies combine the shockwave pressure load with electromagnetic effects as in reality, the fluid pressure and electromagnetic effects are coupled. As noted earlier, researchers have used novel experimental setups to understand the magnitude and form of the pressure present during artificial lightning waveform testing. In addition, researchers have formulated approaches to calculate pressure load magnitude and distribution. In particular, Chemartin et al. [4], Gineste et al. [10] and Kawakami and Feraboli [12] describe the arc plasma physics, which results in pressure loading, and outline the use of simplifications and theoretical equations and numerical simulations to predict the load. In general, the literature suggests that the pressure load varies radically in magnitude and with time around the arc attachment point. Table 18.4 summarizes the proposed pressure loads in the literature.

With respect to the numerical analysis, again, the studies predominantly use the Finite Element Method. The time-varying nature of the pressure loads results in very rapid and local material loading, which results in pressure waves propagating through the test specimen. Damage is then a result of the propagating internal pressure. A wide range of failure criteria have been applied to predict the onset of fiber or matrix failure. Moreover, post-initiation energy-based or displacement-based damage evolution models utilizing principles of material degradation have also been employed to predict damage progression. The most recent studies have also used contact modeling methods to simulate cohesive behavior at individual ply interfaces and allow the prediction of delamination initiation and growth.

Significantly Foster et al. [25] model a large range of pressure shockwave loads specifically to cover the range proposed in the literature. The simulation results generated from explicit Finite Element simulations have been compared with measured test specimen damage. The results indicate that although the proposed pressure loads can cause damage consistent with that which is measured experimentally, the pressure load-induced damage is negligible with respect to the overall scale of damage. In

Table 18.4 Proposed lightning strike pressure load analytic expressions.

	Assumed Radius (mm)	Max magnitude for 40 kA strike(MPa)	Max magnitude for 200 kA strike (MPa)	Electromagnetic "Flux" Equation	Expansion shock wave magnitude (MPa)
Kawakami [2,12]	1, 2	25	637	—	—
Chemartin [4]	5	2	50	$\frac{\mu_0 i^2}{4\pi^2 R^2}$	—
Munoz [16]	5	2	50	$\frac{\mu_0 i^2}{4\pi^2 R^2}$	10
Haigh [9], Gineste [10]	4, 5, 6	0.5	12.7	$\frac{\mu_0 i^2}{6\pi^2 R^2}$	12.7
Reid [26]	—	—	100	—	10
Hardwick [27]	—	—	100	—	10
Foster [25]	1−5 mm	2 -	50 MPa	—	—

general, the vast majority of studies [4,9,10,12,16] demonstrate or conclude that the pressure loads are not enough to cause significant damage alone; however, they would be expected to combine with thermal effects and induce additional matrix cracking and delamination behavior.

18.8.3 Modeling specimen explosive and thermal expansion loading

Experimental authors have proposed that decomposition may result in explosive loads. A common explanation for surface ply damage is due to a trapped gas load from the decomposition of internal resin material. This form of loading relies on heating and decomposition behavior, where further decomposition within the material results in char and gas, before material in the surrounding region is decomposed to a state, which will allow the release of the generated products of the decomposition, especially gas. Chippendale [28] proposes a thermochemical decomposition model, and along with assumed decomposition ratios (90% gas, 10% char), the conservation of mass and the ideal gas law proposes an approach to evaluate the potential internal pressure load. The method also describes how Darcy's law can be used to account for leakage. Other works demonstrate the use of Finite Element Analysis to solve for such internal explosive loads [24], but such works do not to date demonstrate a clear linkage between explosion parameters and the decomposition behavior and the base material properties. Lepetit et al. [29,30] note that surface damage appears to have mainly thermal origin,

and thus, proposes a thermal model to calculate an explosive pressure from the vaporization of surface materials, for example, the protection mesh or paint on the specimen surface. The authors propose that this model could be used along with a mechanical model to evaluate material damage. These proposed explosive behaviors and loads are potentially the most complex during a lightning strike event, and as such, there has been limited progress on modeling. This is a topic that requires further research.

Finally, a small number of modeling studies have examined the potential for damage due to constrained thermal expansion. Foster et al. [31] argue that artificial lightning strike test damage typically includes evidence of mechanical damage which direct thermal loading and pressure loads are unlikely to be responsible for. A simulation study was undertaken on this basis, in which, specimen time-dependent temperature from a thermal-electric simulation was mapped into a mechanical thermal-expansion model. Due to the variation in temperature and the orthotropic thermal expansion coefficient of the composite material, the induced thermal strains are constrained and result in thermal stresses. The study identifies that no single material data set is available which represents the high heating rates, high temperatures and high strain-rates expected during a lightning strike test, and thus, the study is undertaken in three phases; first, with only temperature-dependent material properties; second, with temperature and temperature-rate dependent material properties; and third, with temperature, temperature rate and strain-rate dependent material properties. The stated logic is that individually introducing the dependencies allows an understanding of their relative importance.

The simulations predict significant ply transverse direction stresses and ply through-thickness strains. Generally, the predicted damage, in terms of surface area and depth, is comparable with measured specimen damage, which includes damage resulting from both mechanical and thermal loading. The results demonstrate the sensitivity of damage prediction to the thermal lag due to a large heating rate and the influence of strain rate. Example surface damage area predictions from Foster et al. [31] are presented in Fig. 18.4. Significantly the model simulated the same experimental setup considered in Fig. 18.3, and thus, together, these figures allow comparison between damage due to thermal-electric behavior, Fig. 18.3, and damage due to thermal expansion with and without material strain rate effect modeling, Fig. 18.4(a)
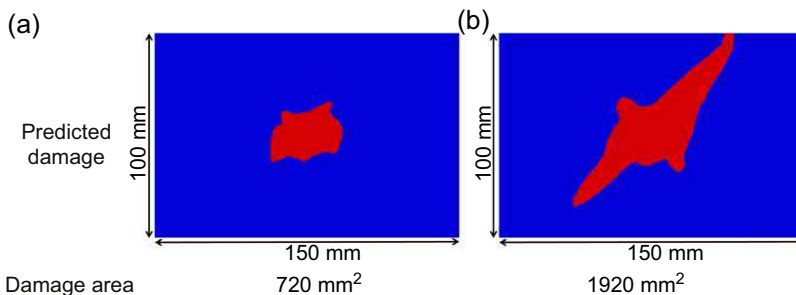
Figure 18.4 Surface damage prediction assuming; (a) no material strain-rate effect, (b) assuming a simple [31] material strain-rate effect. *Red* represents damage while *blue* represents pristine material.

and (b) respectively. The overriding conclusion, however, is that material properties are not available for the combination of extreme conditions witnessed during a lightning strike (high heating rates, high temperatures, and high strain-rates) which are necessary for such analysis. Finally, as noted with all the preceding simulations, the study is reliant on analyst assumptions on the lightning channel arc attachment to the specimen.

18.8.4 Modeling lightning plasma

While much of the simulation work to date has confirmed the importance of resistive heating in lightning strike damage and the potential role and scale of mechanical loadings, the predictions do not, in general, compare well with experimental measurements. This in part is due to the application of idealized, assumed load distributions on the specimen, for example, uniform electric current, or pressure load following a theoretically derived distribution. The key benefit of modeling the plasma is the representation of the previously discussed experimental arrangements with the real electric test conditions as simulation input parameters. As such, specimen loading conditions can be calculated and not assumed, Fig. 18.5.

Plasma simulations are typically based on Magnetohydrodynamics (MHD). MHD predicts gross plasma behavior rather than the behavior of the individual plasma components (i.e., electrons, atoms, ions, and photons, etc.). MHD represents the motion of an electrically conducting fluid in the presence of an applied magnetic field. Lightning generates magnetic fields due to the intense currents produced during
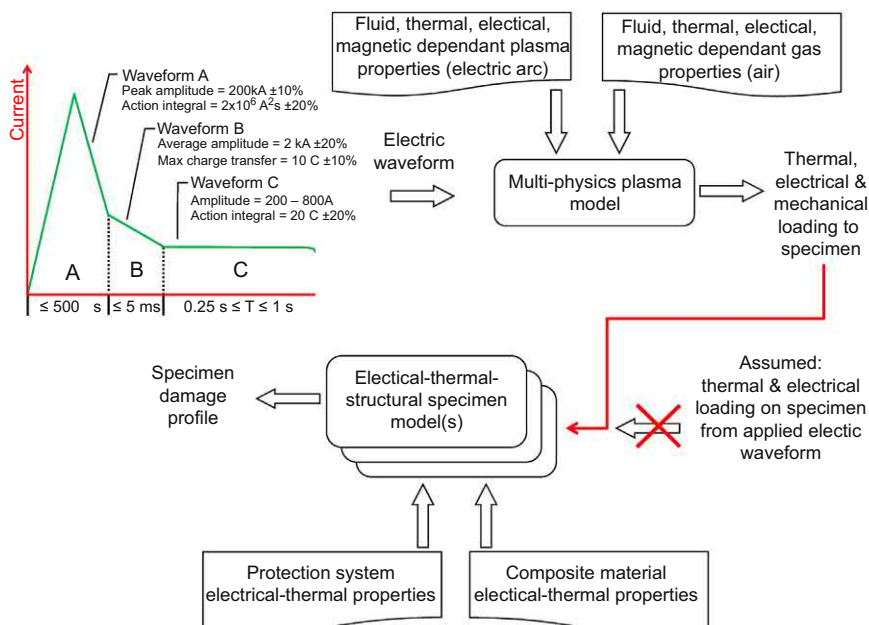
Figure 18.5 Sequential simulation framework for lightning direct effects.

discharge. The plasma produced by the ionization of air can be considered to be the fluid. Once the fluid starts conducting electricity, a magnetic field is induced and applies electromagnetic force on the flow. This magnetic force modifies the fluid flow velocity and pressure. Thus, MHD is a combination of three distinct sets of partial differential equations; Maxwell's equations of electromagnetism, Navier−Stokes equations of fluid motion, and thermal conduction equations for heat transfer. These partial differential equations can be solved numerically using the Finite Element or the finite volume method. For both methods, commercial software, which will be familiar to the engineering community is available. Accurate simulation of a thermal plasma requires calculating the plasma composition and estimation of thermodynamic and transport properties.

The modeling of lightning arc plasma has been built on models originally created to represent welding processes. In general, models are developed assuming Linear Thermal Equilibrium and Linear Chemical Equilibrium plasma. The equilibrium distribution of energy among the plasma components is determined by the temperature. Complete thermodynamic equilibrium exists when all forms of energy distribution are described by the same temperature. Thus, the coupling between mass, momentum, thermal energy, and electromagnetic conservation is at the center of the analysis calculations. MHD simulations can predict the electric current density, pressure, heat flux in and around a lightning arc channel, including at its attachment with the test specimen. Fig. 18.6 presents a typical temperature prediction from an MHD simulation for a Waveform B artificial lightning strike test. In general, modeling has been developed with the inclusion of additional physical phenomenon in order to reduce the need to define or impose simulation boundary conditions, particularly at the specimen. In general, progressive research studies have strived to reduce the need to define initial plasma boundary conditions, for example, temperatures and electrical conductivities. Additional efforts have been made to reduce the computational burden of the analysis, in particular with Finite Element based solutions, which have time-step constraints for transient heat transfer analysis.
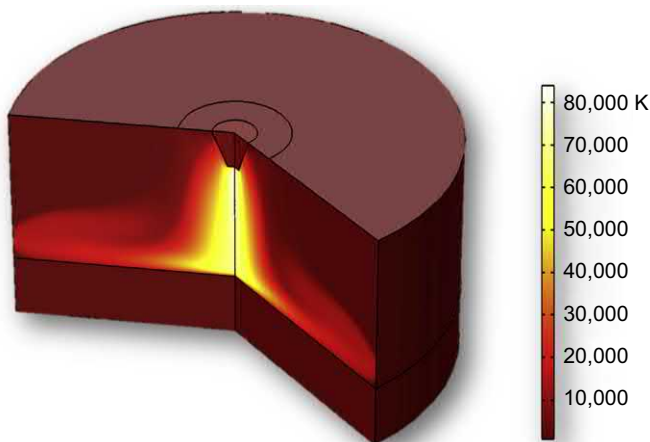
Figure 18.6 Example temperature prediction for a test Waveform B artificial lightning strike.

Important MHD simulation works include Chemartin et al. [4] who modeled the behavior of a simulated lightning strike test waveform in an effort to understand the arc attachment behavior during a Waveform C swept stroke. Abdelal and Murphy [32] followed Chemartin et al. presenting a complete description of an FE approach but modeling a 2D-axisymmetric Waveform B simulated lightning strike test condition. Abdelal and Murphy represented initial plasma formation using cold-field electron emissions and enabling the transient prediction of thermal, mechanical, and electromagnetic behavior. In order to reduce the simulation run time, they also harnessed similitude theory to increase the utility of the model as a design tool. More recently, two works have proposed CFD plasma models. Chen et al. [33] developed a coupled plasma fluid-structure simulation for test Waveform A while Wang et al. [34] completed a study on Waveform C. Both of these works created 3D simulations but included significant initial boundary condition assumptions.

Finally, research has also been conducted to integrate plasma modeling, and specimen thermal and mechanical modeling. Millen et al. and Chen et al. coupled plasma models with specimen thermal-electric models and predicted damage profiles [33,35]. Although the noted works demonstrate the potential to create a completely virtual test, there are significant constraints in their use due to limitations on available material properties, as highlighted in the previous sections.

18.9 Modeling enabled LPS design

Clearly, great potential exists to harness the power of the described modeling approaches to enhance protection system design and tailor LPS solutions to specific material systems and stacking sequences, aircraft zones, and components. The final aim of simulation development must be to enable engineers to explore the electric, chemical, thermal and mechanical processes active during a lightning strike event, specifically at the interface between the lightning current channel and the composite structure. By understanding this behavior, the great opportunity is to formulate new and elegant protection solutions, a task not possible through traditional experimental testing. In gaining such predictive simulation capability, it may be possible to harness as yet unexploited electric and chemical behaviors to enhance aircraft lightning protection. For example, to modify the plasma properties at the arc structure interface via sacrificial surface coatings, which can modify local plasma properties and increase shielding or increase arc movement, reducing local temperature build-up and consequent material damage.

Ultimately the developing modeling capability has the potential to minimize the volume of physical testing used in product development, creating direct aircraft program cost and time benefits. However, potential unknowns and variability in the physical materials and the environment in which they are manufactured suggest that computational methods cannot replace physical testing completely. Nevertheless, in other areas of structural behavior, robust, validated numerical prediction procedures have been demonstrated to reduce the number of experimental tests required to validate a new design.

As the modeling capability associated with lightning events improves and engineers become ever more reliant on simulation, the need for validation of models is evident. In aerospace, the systems engineering "V" diagram is the embedded approach to system development and validation. In this, the system is broken down to its smallest component elements for design and development. These smallest elements are tested, and are then integrated into the higher system level, tested again and so on, until the whole product is assembled and tested in its final operational state. Tests to screen candidate designs or later for performance demonstration for certification do not by design enable the best simulation validation data. Typically loading conditions, boundary conditions, discrete or focused data capture, all restrict simulation validation. Moreover, the simulations seeking to more closely represent the tested reality add detail to reproduce better test results; but getting closer to the reality of the test does not imply being closer to the reality of the aircraft in service [36]. This is particularly true for lightning tests, which are idealized representations of a natural phenomenon that exhibits great variation. Thus, as modeling capability increases, there is also a need for the physical testing associated with aircraft design and certification to evolve.

18.10   Outstanding challenges requiring further research

The design of new and novel protection solutions is constrained by the complex multiphysics, high temperatures, and short duration of strike events, which has meant LPS design has to date been empirical and incremental in nature. A lack of quantitative analysis methods has resulted in an incomplete understanding of the physics, and thus, it can be argued that the current designs are not optimized considering the full range of physical behaviors, which occur during a lightning strike event. Simulation methods show much promise to support in the development and design of improved protection systems; however, there is a requirement for better capture of experimental behavior so that simulation methods can be thoroughly critiqued and improved. Key behavior, such as arc channel expansion and movement needs to be systematically captured and studied. Moreover, for plasma model verification and validation, experimental methods must be employed to capture plasma composition and properties. Interaction between the plasma and specimen surface is also necessary if step change in the mechanism of protection is to be logically conceived. Much of this experimental data is required over a range of current waveforms - beyond the four required for certification. With regards to the prediction of damage, the most significant constraint on progress is the availability of material properties at the high heating rates, high temperatures, and high strain-rates expected during lightning strike events. Initial simulation work has identified the probable range over which data is required, but novel experimental programs are required to create the data. Modeling of explosive behavior requires much work and is again highly reliant on appropriate material data. In this case, methods need to be explored to relate conditions during the lightning strike event and material properties to explosive energy. Finally, the coupling between the plasma models and the specimen models are not fully developed with only

one-way sequential coupling demonstrated to date [35]. Part of this challenge relates to the computational cost of the plasma models, which will grow with greater coupling but also with the addition of currently missing physics and chemistry. In summary, much is still to be understood on the detailed behavior of a lightning strike event on composite material, and to translate this into engineering tools to improve the design of lightning protection systems.

Acknowledgments

References

[1] I. Metwally, A. A-Rahim, F. Heidler, W. Zischank, Computation of transient temperature profiles in objects exposed to simulated lightning currents, Int. J. Therm. Sci. 45 (7) (2006) 691−696.

[2] H. Kawakami, Lightning Strike Induced Damage Mechanisms of Carbon Fiber Composites, PhD thesis, University of Washington, 2011.

[3] A. Kaddani, C. Delalondre, O. Simonin, H. Minoo, Thermal and electrical coupling of arc electrodes, J. High Temp. Chem. Process. 3 (1994) 441−448.

[4] L. Chemartin, P. Lalande, B. Peyrou, A. Chazottes, P.Q. Elias, C. Delalondre, B.G. Cheron, F. Lago, Direct effects of lightning on aircraft structure: analysis of the thermal, electrical and mechanical constraints, J. Aerosp. Lab. 5 (1−15) (2012).

[5] P. Foster, G. Abdelal, A. Murphy, Quantifying the influence of lightning strike pressure loading on composite specimen damage, Appl. Compos. Mater. (2018) 1−23. https://doi.org/10.1007/s10443-018-9685-1.

[6] SAE ARP 5412, Aircraft Lightning Environment and Related Test Waveforms, Society of Automotive Engineers, SAE Aerospace. Aerospace Recommended Practice, 2013.

[7] SAE ARP 5414, Aircraft Lightning Zoning, SAE Aerospace, Aerospace Recommended Practice, 1999.

[8] SAE ARP 5416, Aircraft Lightning Test Methods. Society of Automotive Engineers, SAE Aerospace. Aerospace Recommended Practice, 2013.

[9] S. Haigh, Impulse Effects During Simulated Lightning Attachments to Lightweight Composite Panels. Presented at Int. Aerospace Ground Conf. on Lightning and Static Electricity, Paris, France, 2007.

[10] P. Gineste, R. Clerc, C. Castanie, H. Andreu, E. Buzaud, Assessment of Lightning Direct Effects Damages by Modelling Techniques. Presented at Int. Aerospace Ground Conf. on Lightning and Static Electricity, Pittsfield, USA, 2009.

[11] Y. Hirano, S. Katsumata, Y. Iwahori, A. Todoroki, Artificial lightning testing on graphite/epoxy composite laminate, Compos. A 41 (10) (2010) 1461−1470.

[12] H. Kawakami, P. Feraboli, Lightning strike damage resistance and tolerance of scarf-repaired mesh-protected carbon fiber composites, Compos. A 42 (2011) 1247−1262.

[13] P. Feraboli, M. Miller, Damage resistance and tolerance of carbon/epoxy composite coupons subjected to simulated lightning strike. (98195-2400), in: Presented at AIAA/ASME/ASCE/AHS/ASC Structures, Structural Dynamics and Materials Conference, Palm Springs, California, May 2009.

[14] P. Feraboli, H. Kawakami, Damage of carbon/epoxy composite plates subjected to mechanical impact and simulated lightning, J. Aircr. 47 (0021−8669/10) (2010) 999−1012.

[15] N. Hosokawa, T. Ooto, S. Kubo, M. Anzai, A. Yoshiya, A. Nakagoshi, Lightning Strike Protection for Composite Laminates by Pitch-Based Carbon Fibre Skin. Presented at the 19th International Conference on Composite Materials, Montreal, Canada, July 2013.

[16] R. Munoz, S. Delgado, C. Gonzalez, B. Lopez-Romano, D. Wang, J. Llorca, Modelling lightning impact thermo-mechanical damage on composite materials, Appl. Compos. Mater. 21 (Issue 1) (2014) 149−164.

[17] J. Gou, Y. Tang, F. Liang, Z. Zhao, Carbon nanofiber paper for lightning strike protection of composite materials, Compos. B 41 (1359−8668) (2010) 192−198.

[18] B. Lepetit, C. Escure, S. Guinard, I. Revel, G. Peres, Thermo-mechanical Effects Induced by Lightning on Carbon Fibre Composite Materials. Presented at Int. Aerospace Ground Conf. on Lightning and Static Electricity, Paris, France, 2011.

[19] S. Yamashita, I. Ohsawa, A. Morita, J. Takahashi, Fracture Behaviour of Carbon Fibre Reinforced Polypropylene under Artificial Lightning Strike. Presented at the 19th International Conference on Composite Materials, Montreal, Canada, July 2013.

[20] T. Ogasawara, Y. Hirano, A. Yoshimura, Coupled thermal-electrical analysis for carbon fiber/epoxy composites exposed to simulated lightning strike, Compos. Appl. Sci. Manuf. 41 (Issue 8) (2010) 973−981.

[21] G. Abdelal, A. Murphy, Nonlinear numerical modelling of lightning strike effect on composite panels with temperature dependent material properties, Compos. Struct. 109 (2014) 268−278.

[22] F. Wang, N. Ding, Z. Liu, Y. Ji, Z. Yue, Ablation damage characteristic and residual strength prediction of carbon fibre/epoxy composite suffered from lightning strike, Compos. Struct. 117 (2014) 222−233.

[23] Q. Dong, Y. Guo, X. Sun, Y. Jia, Coupled electrical-thermal-pyrolytic analysis of carbon fiber/epoxy composites subjected to lightning strike, Polymer 56 (2015) 385−394.

[24] Z. Liu, Z. Yue, F. Wang, Y. Ji, Combining analysis of coupled electrical-thermal and blow-off impulse effects on composite laminate induced by lightning strike, Appl. Compos. Mater. 22 (Issue 2) (2015) 189−207.

[25] P. Foster, G. Abdelal, A. Murphy, Understanding how arc attachment behaviour influences the prediction of composite specimen thermal loading during an artificial lightning strike test, Comput. Struct. Compos. Struct. 192 (2018) 671−683.

[26] G. Reid, Mechanical damage to aircraft structures from lightning strikes, Proc. Inst. Mech. Eng. G. J. Aerosp. Eng. 207 (1993) 1−14.

[27] J. Hardwick, A. Pout, C. Jones, A. Ulmann, H. Zaglauer, FULMEN Report: Investigation of the Parameters Affecting Mechanical Forces in Aluminium and CFC Plates Subject to Simulated Lightning Strikes, Transport Research and Technological Development Program, 1997.

[28] R. Chippendale, I. Golosnoy, P. Lewin, Numerical Modelling of the Damage Caused by a Lightning Strike to Carbon Fibre Composites. Presented at International Conference on Lightning and Static Electricity, Oxford, UK, September 2011.

[29] B. Lepetit, C. Escure, S. Guinard, I. Revel, G. Peres, Y. Duval, Thermo-mechanical effects induced by lightning on carbon fiber composite materials, in: Int. Aerospace and Ground Conf. on Lightning and Static Electricity, Oxford, 2011.

[30] B. Lepetit, F. Soulas, S. Guinard, I. Revel, G. Peres, Y. Duval, Analysis of Composite Panel Damages Due to a Lightning Strike: Mechanical Effects. International Conference on Lightning and Static Electricity, SEA13-25.6, Seattle, USA, 2013.

[31] P. Foster, G. Abdelal, A. Murphy, Modelling of mechanical failure due to constrained thermal expansion at the lightning arc attachment point in carbon fibre epoxy composite material, Eng. Fail. Anal. 94 (2018) 364−378.

[32] G.F. Abdelal, A. Murphy, A multiphysics simulation approach for efficient modeling of lightning strike tests on aircraft structures, IEEE Trans. Plasma Sci. 45 (4) (2017) 725−735.

[33] H. Chen, F.S. Wang, X.T. Ma, Z.F. Yue, The coupling mechanism and damage prediction of carbon fiber/epoxy composites exposed to lightning current, Compos. Struct. 203 (June 2018) 436−445.

[34] F. Wang, X. Ma, H. Chen, Y. Zhang, Evolution simulation of lightning discharge based on a magnetohydrodynamics method, Plasma Sci. Technol. 20 (No. 7) (2018).

[35] S.L.J. Millen, A. Murphy, G. Abdelal, G. Catalanotti, Sequential finite element modelling of lightning arc plasma and composite specimen thermal-electric damage, Computers & Structures 222 (2019) 48−62.

[36] M. Price, A. Murphy, Maintaining a grasp on reality − Is our validation and design effort focused in the same direction? J. Strain Analysis Eng. Design 51 (1) (2016) 72−89.

Certification and airworthiness of polymer composite aircraft

19

S. Waite

Senior Expert — Materials, Certification Directorate, EASA, Cologne, Germany

19.1 Introduction

Composite materials potentially offer many benefits to aviation which are well recognized, e.g., high strength and/or stiffness to weight ratios, potential fatigue, and maintenance benefits, etc. Consequently, the aviation industry has increasingly been using composite materials in a growing number of product applications over many decades. However, although well established in the General Aviation (GA) and the rotorcraft industries, the recently extended use of composites into significantly loaded and complex large passenger aircraft applications has required that the regulators pay particular attention to the subject, as any such potentially significant changes would do, and as has been evident in a growing number of projects, e.g., in A350 [1] and B787 [2] airframes, and other large passenger aircraft-related products, including the LEAP engine fan blade [3], A400M propeller (Ratier Figeac FH386), undercarriage structures, and composite seat frames [4]. These projects have been dominated by the use of Polymer Matrix Composites (PMCs) using an array of processes, as discussed in this chapter. However, there are also many other rapidly emerging materials and processes, for which, much of what is discussed remains relevant to some extent, but are not specifically discussed in this chapter.

The regulatory expectation is that the existing "acceptable" level of safety is to be maintained, which may be challenging when considering that the "engineering properties" of composite materials differ significantly from traditional metals, these being more directly built into the part, or repair, because they are a function of material, process, and fabrication methods, which may be sensitive to many process parameters. In particular, anisotropy can offer many potential and competing types of flaw and damage modes, some of which may be difficult to detect. Therefore, a thorough threat assessment is important for safe aircraft design, manufacture, and operation, with the assessment paying particular attention to process controls and developing a good understanding of damage tolerance.

These characteristics require a more integrated approach to initial and continued airworthiness certification, necessitating the development of new workforce knowledge and skills throughout the industry. The regulatory process can benefit significantly from sharing "lessons learned." However, this requires that any "lessons learned" be correctly defined, documented, and communicated throughout the industry. Globalization, and the evolution of a more segmented industry have added

to these challenges, noting the more integrated relationship between design, manufacture, and operational issues relative to more conventional technologies.

The regulators (certifying agencies) are required to help maintain the existing acceptable level of safety via the certification process, by which the applicants demonstrate to the regulators, via the official documents (sometimes directly supported by conformity checks, test witnessing, or interviews completed by the regulator, etc), that the appropriate level of achievement has been met, as measured relative to the aviation safety regulations (including the showing of the Means of Compliance (MoC)).

There exists a growing body of supporting guidance documentation regarding the certification and airworthiness of composite aviation structures, these typically addressing specific themes or groupings of specific themes, e.g., AMC 20−29 [5], CMH-17 [6]. However, there are still only a limited number of texts providing a broader overview of the subject from a regulatory perspective, Waite [7], Ashforth and Ilcewicz [8]. Therefore, this chapter aims to add to that limited coverage by briefly providing such an overview, linking academic understanding and process with certification as it relates to design, manufacture, and operational reality.

19.2   The regulators, regulations, and certification

The certification of composite aircraft products occurs within the bounds of many high-level regulations, which have been defined by the regulators in conjunction with industry, and which are not material, process, or fabrication method specific. However, the importance of needing to identify material, process, and fabrication methods is recognized at the legally binding product definition level. Consequently, the majority of direct regulatory engagement with composite materials typically occurs at the interpretative level, generally via guidance material and/or direct involvement with applicants and the databases supporting the products.

Noting the dependency of the "engineering properties," and a successful design, upon the integrated relationship between material, process, and fabrication methods, the regulatory confidence, and the level of regulatory involvement in any particular project, will be dependent, in part, upon the criticality of the application and/or the novelty of the material, process, fabrication methods and/or novelty of the application to the applicant. Consequently, established databases and the use of previously demonstrated successful design methodologies support efficient certification, while the certification of new materials, processes, and fabrication methods and/or applications new to applicants are likely to require further mitigating actions, e.g., the use of obviously conservative design philosophies and/or the use of fleet leader and fleet sampling strategies, whereby structure in lead time products may be subjected to additional actions (for example, additional inspections, tests, or cut-ups).

Appendix 1 provides details of the regulators, regulations, and certification by providing a brief description of the regulatory structure, including linkage to guidance documentation, within which certification of composite aircraft products occurs.

19.3 Certification of composite aircraft

Product certification is initially defined relative to requirements and guidance material which considers design, manufacture, and predicted operation based upon existing experience, expected utilization, and predicted performance, etc. This is considered to be "initial airworthiness." However, the experience may not be as expected and/ or utilization may change, resulting in unexpected and/or unacceptable performance. Therefore, the "initial airworthiness" process is to be supported by an appropriate "continued airworthiness" process defined by monitoring activities and corrective actions.

The integrated relationship between the design, manufacture and operation of composite products and composite "engineering properties" requires an appropriately integrated relationship between initial airworthiness and continued airworthiness activities. This should be defined within the certification process.

19.3.1 Initial airworthiness

A safe design is considered to be one which is adequately robust to manage all likely threats, including the explicitly defined threats in the Certification Specifications (CS). For metallic structure, Swift [9] discussed the two frame bay skin crack and cracked frame criterion, which is a relatively simple design philosophy, which can help to define a robust structure that may be capable of sustaining damages resulting from many threat sources without all threat details being explicitly and directly included within the test substantiation process (provided that it is demonstrated to be appropriate for the material and configuration selected for the design). For many established Type Certificate Holders (TCH), this approach has become common practice for metallic structures, helping to define the currently acceptable level of safety. Such an approach works, in part, for metallic structure because fatigue in metallic structures also offers the potential and realistic opportunity of finding progressive crack growth within timescales and regulatory load thresholds acceptable to the regulators and operators. However, in order to achieve "equivalence" regarding robustness in composite structure designs, the potential for more damage modes needs to be addressed, including some of which are not readily detectable, e.g., weak bonds, disbonds, delaminations. Therefore, caution should be exercised when taking such an approach to composite certification in order to ensure that all damage modes have been addressed in the substantiation test work. Furthermore, the application of seeded damage modes requires caution in order to avoid masking other competing, and potentially more critical, damage modes, e.g., a hole in a composite of similar size to a possible delamination may not represent the potential for further delamination growth, which may exist between plies but which may not exist in the physics of creating the simple hole for damage simulation purposes. Such an approach may be further challenged by the quasi-brittle performance demonstrated by some composite materials and configurations, which are not evident in the majority of metallic structures.

Composite aircraft are certified within the regulatory framework described in Appendix 1. The certifications are defined relative to a series of established product design CSs which address the majority of design and construction themes in Subparts to each CS. For example Subpart C "Structure" which includes the requirements, in part, for loads, static strength, fatigue and damage tolerance, and lightning protection (for CS25); and Subpart D "Design and Construction," which includes requirements, in part, for material properties, design values, fabrication methods, fire, and lightning protection.

Composite materials are only identified explicitly in the content of a limited number of these CS's, e.g., composite material specific specifications have been introduced into the rotorcraft CSs, i.e., 27.573, and 29.573.

Note: Until CS-23 amendment 5, CS-23 included 23.573, which also explicitly included the reference to bonded structures. However, the recent move toward performance-based requirements has moved the relatively prescriptive content to guidance documentation, ASTM F3115 [10].

The majority of regulatory references to composites occur in guidance materials. However, although little composite specific content exists in the CS specifications, many CS specifications may be significantly impacted by the use of composite materials, as captured in Appendix 1 to AMC 20−29 [5] (harmonized with FAA AC 20-107B), as referenced from key CS requirement CS-2x-603, e.g., *CS 25.603 Materials (See AMC 25.603; For Composite Materials, see AMC 20−29; For use of glass in passenger cabins, see AMC 25.603(a)).*

The suitability and durability of materials used for parts, the failure of which could adversely affect safety, must

(a) *Be established on the basis of experience or tests;*
(b) *Conform to approved specifications,* that ensure their having the strength and other properties assumed in the design data (See AMC 25.603(b); and
(c) *Take into account the effects of environmental conditions,* such as temperature and humidity, expected in service.

The table presented in AMC 20−29 Appendix 1 also identifies a broad range of specifications requiring further consideration when introducing composite materials into a design. This is presented in the form of theme groupings of key CSs, also referenced to, and discussed, in text of paras. 6−11 in the document (not repeated here), i.e.

- Para. 6: Material and Fabrication
- Para. 7: Proof of Structure— Static
- Para. 8: Proof of Structure—Fatigue and Damage Tolerance
- Para. 9 Proof of Structure—Flutter
- Para. 10: Continued Airworthiness
- Para. 11: Additional Considerations
    - Crashworthiness (including impact dynamics)
    - Fire Protection, Flammability, and Thermal issues
    - Lightning Protection
- Appendix A1.1 Applicable CSs and Relevant Guidance

- Appendix A1.2: Definitions
- Appendix A1.3: Change of Composite Materials and/or Process

The table in AMC 20−29 Appendix 1 provides useful linkage between design, production, and continued airworthiness issues in accordance with Safety Management System (SMS) principles.

19.3.2   Residual strength (RS), fatigue and damage tolerance (F&DT)

In order for a structure to function safely, and economically, throughout its lifetime, it is important that the aircraft be designed to account for all likely threats throughout manufacturing and operation. This requires that a threat assessment be completed throughout these activities, which includes the identification of the threat sources, particularly those which could impact structural performance and safety. These threats need to be characterized and included in the substantiation process. There could be a potential benefit arising from further threat assessment standardization.

Although the need for a threat assessment exists for all aspects of design, it is of particular importance to composite structure RS and F&DT certification because composites may be sensitive to process (bonding in particular) and accidental damage. A key requirement capturing this intent is CS25.571:

CS25.571: *Damage-tolerance & fatigue evaluation of structure*

*"(a) General. An evaluation of the **strength, detail design, and fabrication** must show that* ***catastrophic failure due to fatigue, manufacturing defects, environmental deterioration, or accidental damage will be avoided throughout the operational life of the aeroplane*** *… "*

*"(3) … **inspections or other procedures** must be established as necessary to **prevent catastrophic failure**, and must be included in the **Airworthiness Limitations Section (ALS)** of the **Instructions for Continued Airworthiness (ICA)** required by CS 25.1529"*

Although this text is taken from CS25, its basic intent applies more broadly to any structure of significance to maintaining safety in any product, i.e., the specification requires that all threats be considered (not only fatigue and corrosion, as metal experience has typically dictated). Structure (baseline and repairs) is to be designed to avoid catastrophic failure by ensuring that damage can be detected and repaired within substantiated inspection intervals when using substantiated inspection methods. This expectation is defined relative to regulatory reference load levels. Fig. 19.1 provides a guidance framework within which this MoC could be developed.

A structure should be capable of sustaining Ultimate Load (UL) capability throughout the operational life of the aircraft. UL is, per the CSs, typically 1.5 x Limit Load (LL). LLs are specified in the CSs and can generally be equated to the maximum loads expected throughout the operational life of the aircraft. Any period during which the structure is exposed to RS below UL capability should be minimized and damage, when detected, must be repaired to restore UL capability.
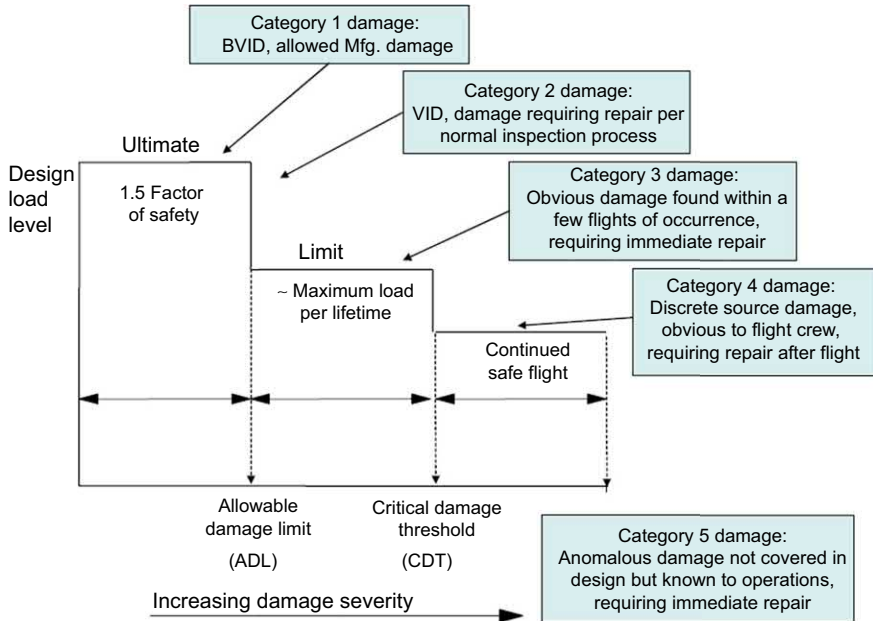
Figure 19.1 Schematic diagram showing design load levels versus categories of damage severity; Fig. 19.3 in Ref. [5].

Fig. 19.1 suggests the definition and use of "Categories" of damage terminology in order to help manage the process, as explained in AMC 20−29. However, applicants can take different approaches, provided that the underlying issues are addressed.

Category 1 damage is that which could occur in production or service and remain undetected for the life of the airframe, e.g., Barely Visible Impact Damage (BVID). The structure is to be demonstrated to sustain UL following a lifetime of operation with Category 1 damage. Typically, this capability is extended and demonstrated for slightly larger damages in order to help define Allowable Damage Limits (ADLs). This supports the design of a more commercially viable product by reducing the need for operators to repeatedly contact the TCH for disposition of many very minor damages.

Categories 2, 3, and 4 are as described in Fig. 19.1. Categories 2 requires detection within substantiated inspection frequencies using substantiated inspection methods. Category 3 should be immediately obvious within a small number of cycles of occurrence, e.g., being evident during a simple preflight walk-around inspection, requiring immediate repair accordingly. Category 4 is immediately obvious to the flight crew allowing appropriate pilot action to support Continued Safe Flight and Landing (CSF&L).

Category 5 is outside immediate certification considerations but must be reported for disposition, as discussed later in this chapter. It is important that the bounds to all damage be located and repairs completed in accordance with regulations.

Metal structure designs, being typically fatigue driven, are allowed some credit for being able to detect cracks and characterize crack growth when establishing inspection frequencies. Design typically ensures that cracking is detectable well before the structural capability is reduced to LL.

Composite structures typically require a damage "no-growth" philosophy because damage growth can be rapid, unpredictable, and may not be readily detectable. Therefore, the inspection intervals associated with likely damages require substantiation in RS and F&DT tests. Fig. 19.2 shows a schematic diagram illustrating that such damage should not remain undetected in the structure and without repair for a long time.

Ideally, a design should avoid configurations, which might result in steep RS reductions prior to reaching the detection threshold, particularly if the reduction in capability is close to regulatory load thresholds, Fig. 19.3.

19.3.3 Building-block approach

A test or analysis supported by test, building-block approach is often used to support certification, including the development of sizing criteria and analysis processes for many subjects, including static strength, RS capability, F&DT, crashworthiness; [11]. Fig. 19.4 shows an example of such an approach, as it may apply to a large passenger aircraft certification. This provides some appreciation of the extent of work necessary to generate a database, which could be considered to be adequate to support certification of a large passenger aircraft composite product. This example is supported by previous evolution in composite aircraft design concepts and technology databases. The definition of the test and analysis pyramid, and the number of test specimens necessary for certification may vary significantly from product to product, depending upon size and complexity.

When applied to F&DT certification, the base of the test pyramid is typically used to establish Environmental Knock Down Factors (EKDF) or scatter factors intended to
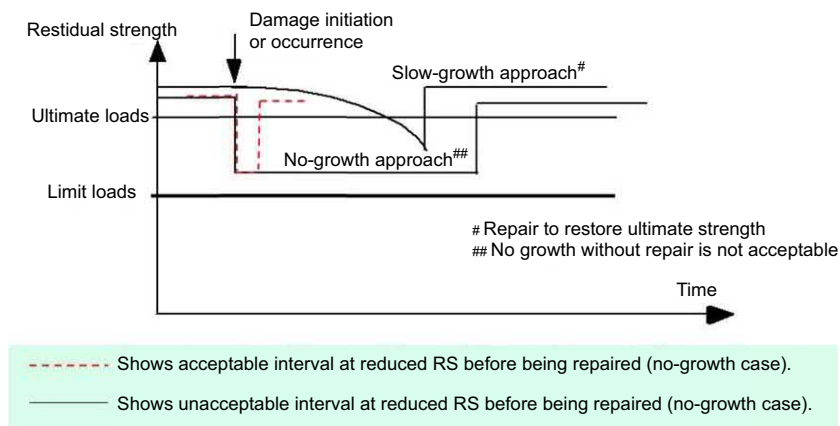
Figure 19.2 Schematic diagram of residual strength; Fig. 19.4 in Ref. [5].
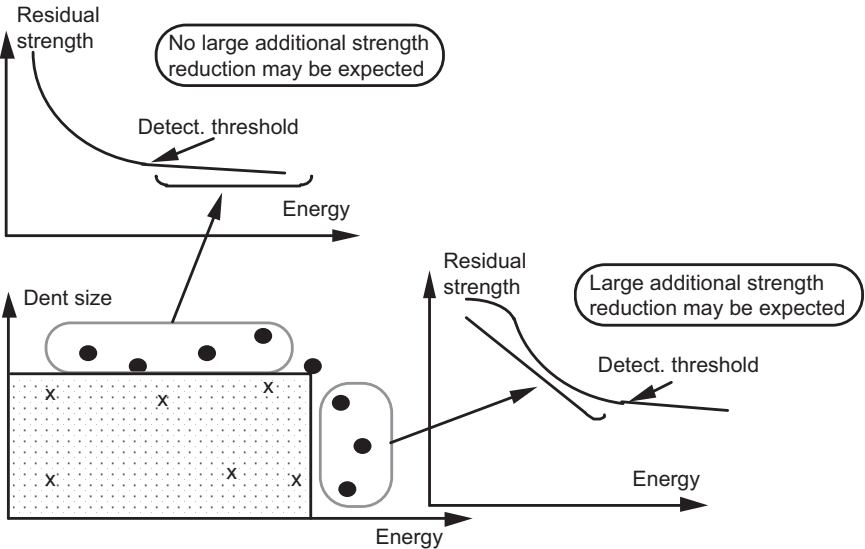
Figure 19.3 Damage detection and residual strength.
From Composite Materials Handbook − 17 (CMH-17) vol. 3 rev, 2003. https://www.cmh17.org.
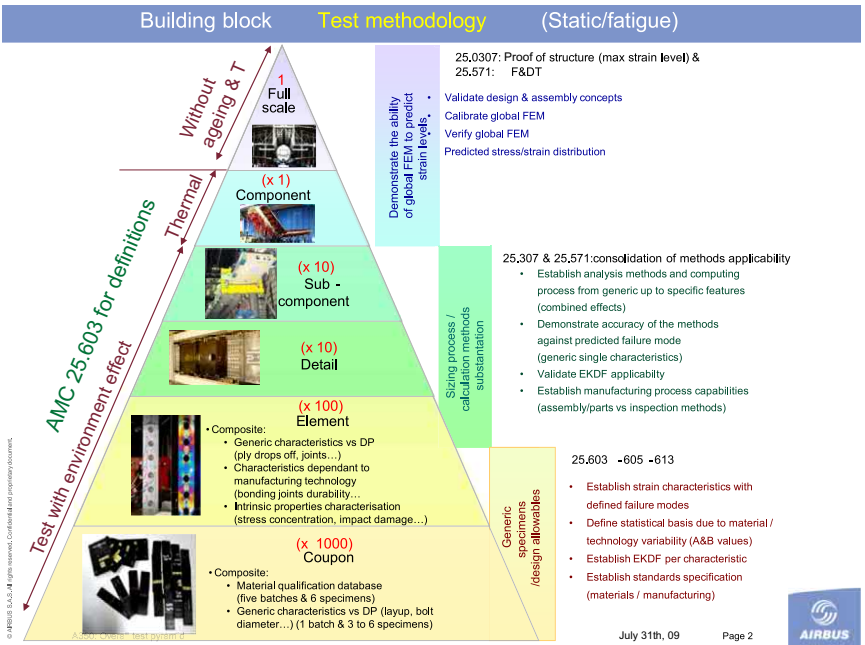
Figure 19.4 Composites─large testing program required; slide 15 in Fualdes 2016 [13].

address material and process variability, e.g., Load Enhancement Factors (LEFs). These factors are then applied to higher test pyramid tests, as appropriate, because it is usually impractical to test a large complex structure in representative environments.

The mid-pyramid can be used to investigate configured structures, including testing of some damaged structures in environmental chambers, as may be possible within the bounds of the available test facilities. The number and types of test configurations selected involve some "engineering judgment" because an industry-wide standardized method is yet to be developed. However, the selections should address the full range of configuration variables, e.g., the range of skin-stringer stiffness ratios in the design etc, and all potential damage modes. Particular care should be taken to ensure that representative Boundary Conditions (BCs) are maintained due to damage initiation and growth being sensitive to such restraints. The higher building blocks in the pyramid are generally used to validate loads and support the global Finite Element Models (FEMs). Smaller product structures, e.g., General Aviation (GA) structures, allow some variation regarding this approach, whereby a complete structure might be tested hot, including a factor for moisture.

Note: Such products tend to rely upon limited high-level testing and little mid-pyramid work. This approach may work for simple design concepts, e.g., aerobatic airframes using single spar designs, when a bending test is likely to address worst-case loading. However, if designing for multiple load paths, then a simple bend test (without a supporting mid-test pyramid) is unlikely to provide adequate grounds for certification due to the potential for unsubstantiated variation in load paths. Therefore, further high-level pyramid testing may be expected by the regulator to ensure that load paths, and the potential for competing damage modes, has been substantiated, unless addressed by other mitigating factors.

The extensive testing needs that are associated with composites, largely the result of anisotropy and data scatter, are potentially very expensive and time consuming. Furthermore, computer modeling capability is rapidly developing. Therefore, there exists considerable industry interest in using analysis to replace test. However, acceptability of such an approach is typically limited to previously validated models as used and demonstrated by the applicant, i.e., extrapolation of either design concepts and/or modeling philosophy (beyond limits of similarity, as agreed with the regulator) is discouraged. For example, and when demonstrated to be applicable, the use of more mature linear modeling techniques are more likely to be accepted as being similar than less mature nonlinear techniques. Therefore, the EASA principles of Level of Involvement (LoI), will typically be applied and test validation of new concepts and configurations are likely to be required for the foreseeable future, particularly for new and less experienced organizations. There exists scope to optimize the potential use of the test and analysis pyramids by careful selection of test configurations relative to global and local FEM capability, e.g., Figs. 19.5 and 19.6.

Much value can be gained from developing strain and failure predictions when moving up through the increasingly complex test-analysis pyramid. However, it should be noted that, for the purposes of certification, the predictions for any tests to be witnessed by the regulators should be presented to the regulators prior to the
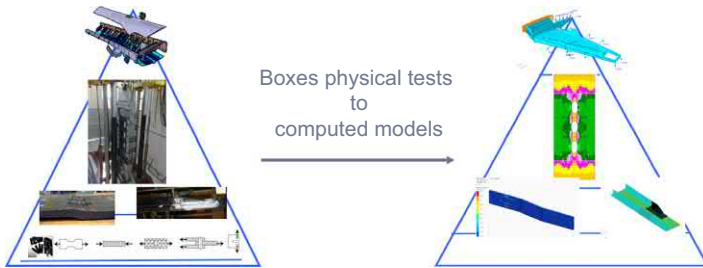
Figure 19.5 Large full-scale test numerical simulation from slide 16 in Fualdes 2016 [13].
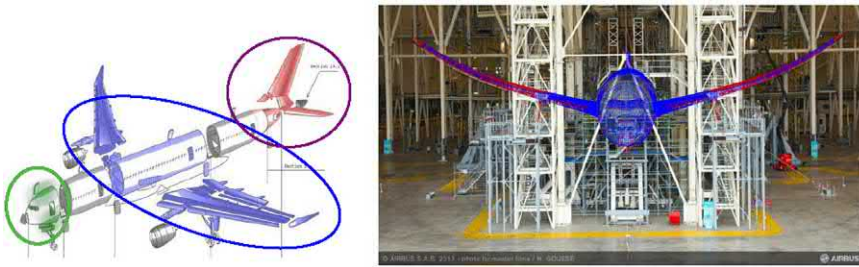
Figure 19.6 (a) and (b): A350 - Large full-scale test numerical simulation- 68 million degrees of freedom; from slide 19; Fualdes 2016 [13].

test because true prediction should not be confused with predictions tuned to directly match previous test results.

The building-block approach allows for some combined RS and F&DT certification test work to be completed together using the same test article and test sequence for composite structures. However, this requires caution because most practical structures are typically hybrid structures, i.e., a combination of conventional metals (often used at major load transfer joint locations) and composites, and the constituent materials demonstrate very different properties, e.g., data scatter, thermal coefficients, damage initiation mechanisms, etc.

High loads: Typically, fatigue testing of a metallic structure should not include load peaks, which might retard the crack tips, such that the testing becomes unrepresentative for the metals. However, composite failure is typically driven by peak loads, so load peaks should be retained in the fatigue test spectrum. The need to also apply LEFs to the composite materials, in order to address data scatter, further complicates the situation.

Low loads: Typically, metals demonstrate active crack growth throughout a significant load range, requiring that most, or all, loads be retained in the test spectrum. However, many composites are not sensitive to low loads, allowing for the potential to remove a significant, but substantiated, part from the fatigue spectrum, thus shortening the test timescale.

The significance of these challenges is a function of the material combinations selected for the design and structure complexity, requiring careful consideration during certification and resulting in several approaches as to how the test and analysis pyramid can be used for substantiation. One approach is to use separate metallic and composite test pyramids. This typically requires that the metal structure in the composite test pyramid structure be repaired and replaced (sacrificed) during the F&DT testing in order to ensure that the composite is tested with the appropriate LEFs. Alternatively, different levels in the test pyramid can be tested using different LEFs, as appropriate to the component material combinations (which may be metallic and/or composite, noting that many composite structures also comprise of different composite material and process combinations, each of which also may have different LEFs). Again, it is necessary to ensure that representative BCs are maintained. The management of LEFs in the test process is discussed in a growing body of work, e.g., Refs. [12,14].

A further challenge, arising from the use of hybrid structures (typical combinations of metal and composites), is the management of structures subjected to significant combined thermal and mechanical loads. In particular, it is impractical to combine real thermal and mechanical cycles in the testing of many large hybrid structures, e.g., hybrid wing center box structures, including fuel tanks. Industry and the regulators are working to standardize expectations better regarding this subject.

19.3.4   Structural bonding

AMC 20−29 para.6 addresses "Material and Fabrication" and highlights the importance of following a strict process in order to produce reliable and robust composite structures. Material and fabrication require significant consideration in the threat assessment, and potential flaws need to be identified and managed appropriately in the test and analysis pyramid.

For design engineers familiar with metallic structures, the para.6 text indicates that composites typically require more involvement with, and understanding of, materials and fabrication processes that may be required for many metallic structures. Para.6 highlights structural bonding as being particularly dependent upon strict process control and justifies specific attention in any threat assessment.

Historically, a reference to bonding has been assumed to refer to the structural bonding of two metal items (adherends) using adhesive. Fig. 19.7 from Ref. [15] is a reminder that the metallic aging aircraft program was initiated following several large metallic aircraft incidents, including the Aloha incident. However, the damage, in this case, resulted, in part, from an initial cold bond failure in the metallic lap joints.

The evolution of composites has resulted in an extended definition for bonded joints to include a broad array of configurations, including metals and/or composites (either in cured or uncured state, with or without additional adhesive), Fig. 19.8 from Ref. [16]. If the first item 1or 2 is initially uncured when the joint is constructed, then it is termed "co-bonded." If both, 1 and 2 are initially uncured, then it is termed "co-cured." Co-cured joints have not historically been fully addressed under the

Figure 19.7 Aloha—partially initiated by cold bonded joint failure [15].
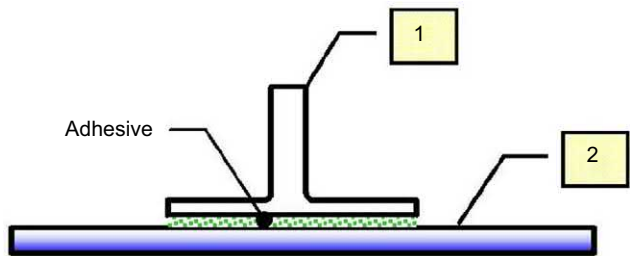
Figure 19.8 Bonded joint configurations [16].

bonded joint specification 25.573(a) (5), although such bonds have many of the attributes associated with bonded joints and should be certified accordingly. It is advisable to clarify the definition of bonding used in any discussion because some variation in terminology exists across products.

A correctly designed bonded joint is expected to fail in the adherend (cohesive failure), although failure within the adhesive may occur (also cohesive failure). Failure at the interface between the adherend and adhesive is also possible (adhesion failure). Adhesion failures are considered to be unacceptable because such failures are difficult to detect, and the RS and F&DT capabilities are difficult to characterize, Fig. 19.9; [17]. Such failures suggest poor process control. Issues requiring particular attention include cleanliness, surface preparation, surface activation (typically when using

Adhesion failure

Figure 19.9 Adhesion failure - unacceptable [17].

metallic adherends), surface protection, material compatibility, bond line thickness, all of which can result in "weak bonds" and disbonds, if not adequately controlled. Weak bonds are bonds which have not adequately completed the intended chemical reactions, leaving no obvious physical evidence of having failed to complete the process, e.g., no physical gaps. Such bonds may further degrade, yet the damage may remain undetectable.

Industry has demonstrated many years of successful bonding in many baselines, and potentially more challenging, repaired structures, e.g., there are many successful sailplanes and general aviation applications using bonded configurations, including successful extensive repairs to sailplanes, which have been completed in the maintenance environment and which required the use of bonded splices to reattach separated empennage structures to fuselage structures. However, there have also been incidents associated with bonded baseline and repaired structures.

The majority of bonding related incidents have been a limited threat to safety, largely due to the limited criticality associated with the majority of applications. However, there have been some more significant incidents, e.g., involving large passenger aircraft flight control surfaces and engine intakes. Furthermore, there have also been some incidents in which the bonded structure failure has included bonded joints which function as part of a critical single load path structure, e.g., rotorcraft blades, tail booms, etc.

Some of the more significant events include a series of incidents associated with potential environmental degradation of adhesives in both original rudder baseline metal skin−metal core sandwich structure control surfaces and repairs, followed by failure resulting from bond surface contamination in later replacement production parts. Examples of such incidents, including incidents associated with elevons of similar configuration, are addressed in a series of AAIB bulletins and reports, including [18−20], see also Fig. 19.10(a) and (b) from Ref. [18]. Further investigations of other sandwich structure control surface configurations and damage are included in the reports by Hilgers [21], Hicken [22], and related workshop discussions in recent CMH-17 meeting proceedings and EASA events. As a result of significant open sharing of "lessons learned," Airbus, in conjunction with CMH-17, has helped to develop a broader understanding of sandwich response to Ground-Air-Ground (GAG) pressure cycles in nonmetallic sandwich structure configurations. This has also resulted in a developing ASTM D30 standard associated with Mode 1 type of skin to core failure.

Some of the potentially more significant incidents involving repaired structures have included an example of radome collapse in flight, which resulted in airflow interfering with flight instrument indications. In this case, the damaged structure showing evidence of extensive disbond and possible unidentified repair, Fig. 19.11 [23]. This emphasized the importance of responsible maintenance organizations clearly identifying, and recording, having worked within TCH data limits, and the importance of demonstrating an adequate understanding of process sensitivity, from both design and production perspectives. Such understanding should be supported by extensive development work, appropriate First Article Inspections (FAI) definitions, and supporting sampling strategies in production, etc. In general, it is considered that

Right hand side of failed rudder

Figure 19.10 (a) Repaired original baseline rudder structure incident. (b) Later rudder structure incident (G-BOAE, 4/12/2002) [18].

Figure 19.11 "Repaired" bonded structure failure (not considered to be the result of a bird strike) [23].

current understanding of composite technology severely limits the scope for "reverse engineering," i.e., building a part or extensive repair referenced only to limited data, e.g., dimensions, use of mixed and selected sections of repair manuals, if not supported and approved by the TCH or STCH.

Noting the need to pay particular attention to better understanding of bonded structures, AMC 20−29, para.6 repeats the intent from CS23.573(a) (5) amdt 4, which addressed bonded structure, because elements of this specification have been used, and proved to have been relevant, for other products, including CS-P 'Propellers'. In this case, in-service experience has proved the importance of using design features intended to prevent catastrophic failure because, following a disbond event, blade

separation from a blade root has been prevented by such a feature. The CS23.573(a) (5) text is repeated below, including the addition of limitations and author comments associated with its use.

23.573(a) (5) amdt. 4 states:

*'For any bonded joint, the failure of which would result in catastrophic loss of the aeroplane, the **limit load** capacity must be substantiated by one of the following methods:*

(i) The maximum disbonds of each bonded joint consistent with the capability to withstand the loads in paragraph (a) (3) (i.e., critical limit flight loads considered ultimate) of this section must be determined by analysis, tests, or both. **Disbonds of each bonded joint greater than this must be prevented by design features;**

Limitations:

- not to be used to manage poor process - strict process control is always required for bonding (implicit in CS2x.605)
- identification **of appropriate and acceptable** "**design features**" **would benefit from standardization**

or

*(ii) Proof **testing** must be conducted on **each production article** that will apply the **critical limit design load** to each critical bonded joint;*

Limitations:

- **not practical for large airframes**
- **does not address degradation**
- **poor test load simulation can damage the airframe**

or

*(iii) **Repeatable and reliable nondestructive inspection techniques** must be established that ensure the strength of each joint.'*

Limitations:

- "**Weak bonds**" **cannot be detected visually**
- **there is no reliable industrial scale NDI means available with which to detect such defects, particularly for in-service use**

Note: The industry and regulators continue to work toward addressing these limitations. In the meantime, the regulators address the subject by expecting **strict process substantiation** and the use of conservative design concepts, as substantiated on a case by case basis (until more standardized approaches are developed). In recognition of the challenges associated with bonding, the regulators have limited bonded repair design to ensure that failure of the bonded repair will not expose the structure to less than LL capability (or higher, depending upon governing TCH criteria), in the Bonded Repair Size Limits (BRSL) Certification Memo (CM) [24].

19.3.5 Accidental impact damage

A common and potentially significant threat to composite structure arises from impact events, requiring an assessment of potential impact threat sources throughout manufacturing and in-service. Accidental impact damage may result from many sources, e.g., including in production handling, in-service tire debris, engine debris, hail, bird strike, etc., these requiring consideration relative to one or more of the categories of damage identified in Fig. 19.1. In order to properly substantiate the structure, the impact threat source is to be fully characterized, i.e., energy, geometry, stiffness, etc., in order to help determine which resulting "representative" flaws and damages require inclusion in substantiation test and analysis work. This can be a challenge because the structure responses to impact, i.e., damage initiation, damage modes, extents, locations, and growth, may be sensitive to Boundary Conditions (BCs). Furthermore, the specific impact source details, i.e., geometries and energies, are often unknown. However, the existing metallic fleet can provide a useful source of information regarding potential threat sources because metallic structure often provides witness to impact in the form of dents, gouges, and scratches. Fig. 19.12 shows the summary of such a fleet survey of complete aircraft.

The damage threats can vary from component to component, and a survey is needed to identify the most damage-prone areas and potential damage sources. For example, a fuselage is exposed to different accidental threats than an empennage or a wing, due to proximity to the ground and also servicing access. Thus, particular attention should be given in the representation of the impactor type and size.

Fig. 19.13 shows such data when processed in the context of energy levels and rate of occurrence, presented as threat zones (low, medium, and high), medium and high being applicable local to fuselage door cut-outs in this case. Noting that the threat source details are typically unknown, the missing information can be recovered by impacting structures of similar configuration in order to produce similar damages.
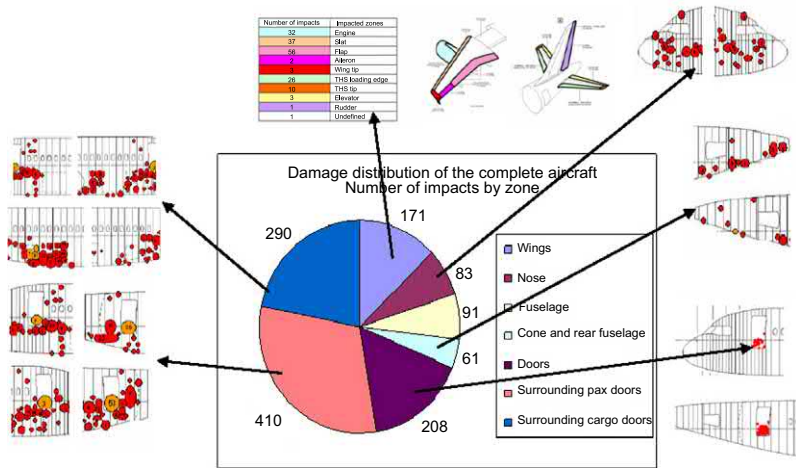
Figure 19.12 Threat characterization—fleet damage survey from slide 24; Fualdes 2016; [13].
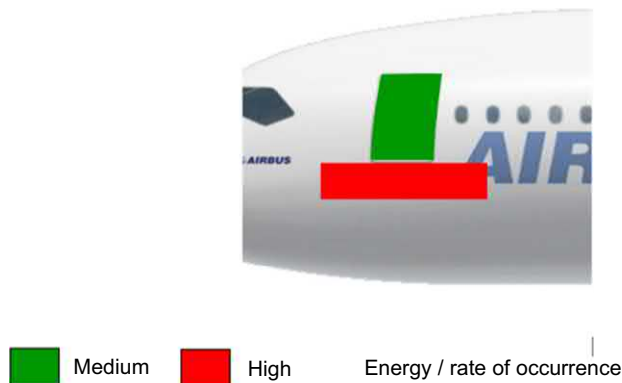
Figure 19.13 Threat characterization—Zoning; from slide16 Fualdes 2014 [1].

Once the threat has been defined, similar impacts can be applied to the composite structure, thus creating reference damage for substantiation in the composite certification process. Accidental damage may be considered to be sharp or blunt.

Sharp impacts may result in penetrations, requiring an understanding of notch behavior in order to design a robust structure. Substantiation of such data should typically be supported by using the building-block approach and involve consideration of notches ranging from fastener holes (both open and filled) in simple panels, through to large guillotine testing of configured and loaded structure (intended to represent discrete source threats, such as large engine debris impact of the pressure hull).

Blunt impacts may result in hidden damage, which may initiate at energies lower than those necessary to initiate externally detectable damage. If material screening strategies have not eliminated such materials from the selection process, and such materials are selected by the applicant, then substantiation should include thorough characterization of the material behavior throughout a range of energies, impactor geometries, and stiffnesses. An appropriate inspection method and schedule is to be then substantiated. Fig. 19.14 shows an example plot demonstrating investigation of
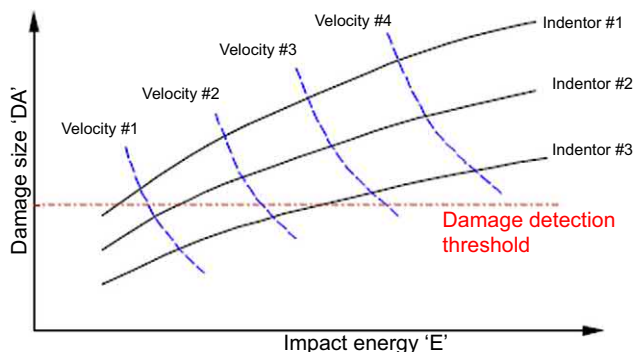
Figure 19.14 Damage characterization and detection thresholds [28].

a range of impactors at a range of velocities, as considered necessary to explore the potential for damage and its detectability following the impact of a sandwich structure, see also the "inspection and damage detection" section below.

Fig. 19.15 develops the discussion by an example of R&D work completed to show the significance of impactor geometry to dent detection following the impact of a monolithic skin and stringer panel with 25.4 and 320 mm diameter metallic impactors, respectively, at similar energy levels. When considering this structural configuration, both impactors resulted in similar small internal damages. However, the larger blunt impactor leaves no external visible indication. Although a robust design should be demonstrated to tolerate such damage through appropriate F&DT substantiation, damage resulting from multiple impacts could be more challenging, depending upon the design concept.

A further historical consideration is that threats have typically been addressed in certification by impacting conventional structures using the maximum threat stated in the specifications, e.g., a 4lb bird would be used in the bird strike test, as necessary to address CS25.631 (8lb for the empennage in accordance with FAA Part 25.631), or a maximum tire debris size would be used, as determined by the CS25.734 tire model. However, this may not be fully representative of the damage risk for composite structures due to the many competing damage modes, and the damage detection capability being a function of impactor energy, impactor geometry, impactor stiffness, BCs, etc. For example, if considering tire debris impact, the impactor is blunt and compliant (to some extent), offering the potential to deliver significant energy during a blunt impact event. Furthermore, debris, less than the maximum tire debris size, and at a lesser energy level than the maximum stated in CS25.734, might cause a disbond or
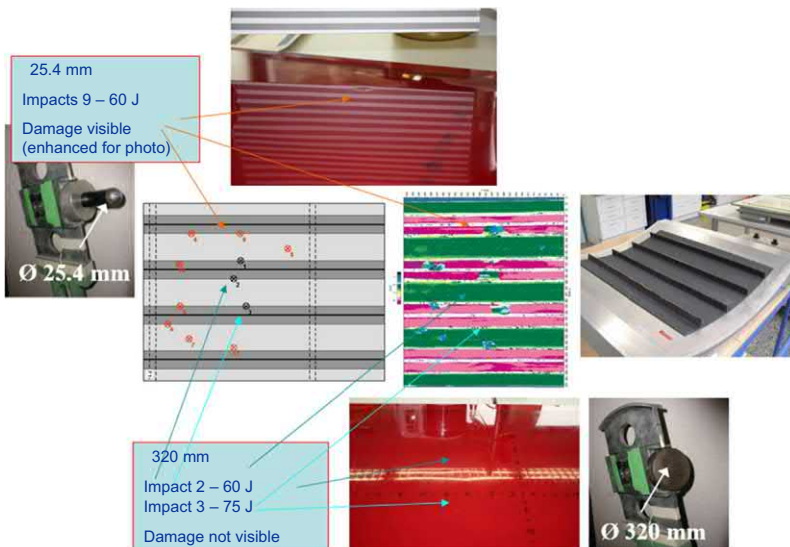
Figure 19.15 Impactor geometry and damage detection [27].

delamination in a monolithic bonded skin and stringer configured structure, or result in a crushed core in a sandwich structure such that the damage is not readily detectable. This may have both safety and commercial implications because, following a loss of tread from a tire, a decision is to be made regarding the need to NDI all structure in the debris trajectories. This requires careful consideration when satisfying CS2x.571, possibly requiring testing to address a range of impactor parameters (depending upon the design concept) in order to support the definition of maintenance instructions, as indicated in Fig. 19.14.

Similarly the hail threat may require further consideration, depending upon the aircraft configuration, because hail demonstrates a broad range of compositions Field et al., [25], providing both strengths and stiffnesses which may change the dynamics of impact, thus challenging the validity of using a steel impactor simulation for airframe test work (note frozen water-soaked cotton balls are used for windshield tests in some test standards). Recent critical sandwich structure applications have required thorough impact investigation [26], as would be expected in DOT/FAA/AR-99/49 [28]. Current accepted hail certification practice, i.e., threat source definition, integration into the design (in-flight and ground hail), and simulation are discussed in CMH-17 hail [29]. However, standardization continues to develop.

Other certification practices, established during metallic certification and which have contributed to the existing acceptable level of safety, might also need further consideration when certifying composite structures, subject to the design concept. For example, bird strike testing of metallic structures has typically been completed with unloaded structures, while real in-service structures are usually impacted under load, e.g., typically approximately 1g. Therefore, noting the engineering property differences which exist between metallic and composite structures, it cannot be assumed that the existing level of safety will be maintained by following the same certification procedures. Investigations such as UK CAA/Cranfield [30] and DLR [31] suggest that impacting composite structure subject to preload might both reduce the extent of readily detectable damage and the RS capability, depending upon the level of preload. This might be important for a design including critical flight control surfaces, which might be exposed to critical load cases when deployed on approach to landing, typically, a bird strike rich environment.

Extensive testing may be necessary to characterize all such parameters. However, demonstration of an appropriately robust large damage capability may significantly reduce the work required, provided that it can be demonstrated that the regulations can be satisfied and that the large damage capability concept has fully bounded the threat and the likely damage modes. For safety purposes, likely impacts should be managed using a comprehensive F&DT philosophy. CMH-17 [6] provides some guidance regarding deterministic and semi-probabilistic approaches. However, it should be noted that a semi-probabilistic approach requires access to a significant and credible database.

A detailed account of the current understanding of impact damage, compression strength after impact, and fatigue of impact-induced delaminations is found in Chapter 11.

19.3.6 Initial airworthiness—continued airworthiness and maintenance

In order to design for a safe and efficient structure, both commercial and safety interests can best be satisfied by designing with maintenance and modification in mind, as shown schematically in Fig. 19.16. This involves consideration of the "initial airworthiness" issues described above, e.g., robust design, allowing for useful ADLs, but also designed for easy access and inspection (minimizing the need for NDI), and ease of repair.

An efficient approach to design for a maintainable structure is for the TCH and the operators to work together, benefitting from TCH certification knowledge in conjunction with direct operator knowledge, which adds value based upon operational experience, understanding access issues, knowledge of in-service inspection capabilities, etc.

For large passenger aircraft and large rotorcraft, this dialogue typically occurs through the Maintenance Review Board (MRB) resulting in an MRB Report (MRBR). The initial maintenance requirements are provided by Maintenance Steering Group-3 (MSG-3), defining maintenance tasks and intervals, as agreed with the regulators. These are delivered in a baseline planning document, known as the Master Planning Document (MPD). The MPD forms the baseline for the development of individual aircraft Maintenance Schedules (MS), which can be adapted subject to experience (local environment, utilization, etc.), supported by appropriate evidence, and regulatory agreement.

CS2x.571 states that inspections or other procedures must be established as necessary to prevent catastrophic failure and that these must be included in the Airworthiness Limitations Section (ALS) of the Instructions for Continued Airworthiness (ICA)
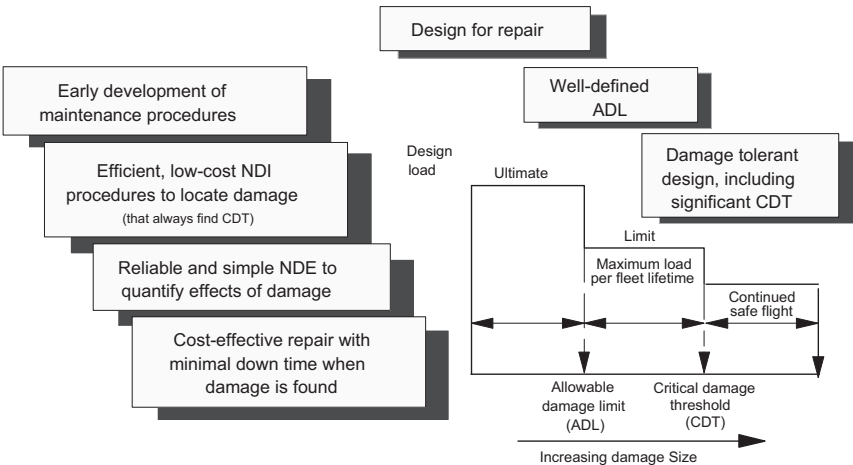
Figure 19.16 Design for maintainable structure from CMH-17, V3C14, rev g Fig. 14.10.9.1(a) [33].

required by CS 25.1529. Therefore, tasks critical to maintaining airworthiness, including inspections and life limitations, are included in the ALS. Further important documents supporting initial airworthiness include the Maintenance Manuals (MMs) and the Structural Repair Manuals (SRMs), the SRM providing ADLs and some repair instructions.

The potential benefits arising from close TCH co-operation with the operators is evident in Ref. [32], which provides practical design solutions which might improve design for ease of repair. For example, Fig. 19.17 provides an example based upon the frequent experience of damage to trailing edge structures, which are vulnerable to ground vehicle impact. Earlier designs typically bonded and fastened the trailing edges, resulting in the need to break the structure for the purposes of access and repair. This often resulted in more damage and the need for a larger and more complex repair than the original damage would have required. A potentially simple and efficient solution is to design with a gasket and removable fastener.

AC 43-214A [34] (previously AC 145-6) was written to provide guidance regarding repairs and alterations to composite and bonded aircraft structure and on facilities, equipment, and inspection processes that a Maintenance Repair Organization (MRO) must have to perform repairs and alterations. It is closely linked to AMC 20−29, yet recognizes the many different and additional practical constraints which exist in the maintenance environment relative to a large TCH using a baseline structure manufacturing facility. This document reminds the reader that repairs are intended to restore airworthiness, i.e., the Design Organization Approval (DOA) holder, usually the TCH or STCH, is to provide adequate data intended to make this possible, while the MRO is to execute the repair to the required standard.

19.3.7   Inspection and damage detection

Aircraft safety relies upon a robust F&DT philosophy, which requires the timely detection of damage, forming part of the continued airworthiness process. Chapter 16 gives a detailed account of NDT techniques in aircraft.

CS2x.571 states "… ***inspections or other procedures*** *must be established as necessary to* ***prevent catastrophic failure.***"

Furthermore, AMC 20−29 states "***The extent of initially detectable damage should be established and be consistent with inspection techniques***"
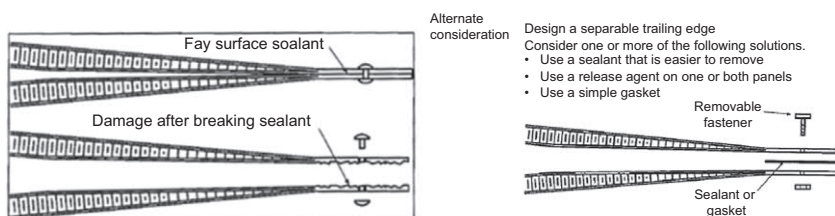
Figure 19.17 Designing for ease of repair [32].

The regulators do not certify inspection methods but accept them when substantiated as part of a certified product.

Visual inspection is the dominant inspection method, representing 80% + of inspections in service. The remainder of inspections relies upon NDI. This balance between visual inspection and NDI is unlikely to change significantly in the near future, primarily due to the cost and/or limited capability of some NDI methods. For NDI to be acceptable in-service applications, the method needs to be cheap, robust, reliable, portable, easy to operate (minimal training and qualification being required), and the data needs to be easy to interpret. Few NDI methods satisfy all of these conditions. CS2x.571 also states that "other procedures" could be used to support the DT philosophy, which could allow for the use of appropriately substantiated Structural Health Monitoring (SHM) in the future [35].

Although many NDI methods exist in R&D processes and are used to support production, surprisingly few appear as identified certification steps in the certification processes, and even fewer of these appear in-service applications. The most frequently used methods included are tap testing, Ultrasonic Testing (UT), radiography, and to some extent, thermography and shearography. Moisture meters are also used to detect free-standing and absorbed moisture.

The basics of most established NDI methods are explained in other textbooks and guidance documentation. Therefore, the following is provided only as a reminder regarding the established NDI methods, some of which are continuing to be developed. Some of these are being optimized for simplified use, e.g., the Ramp Damage Checker is a simplified Ultrasonic Testing (UT) tool intended to be used by appropriately trained inspectors who do not necessarily have specific NDI qualifications, e.g., Level 1,2, and 3; [36]. Furthermore, some methods are being developed using communication technologies to pass data directly to the TCH for processing. Fualdes 2014 [37] provides an overview of inspection and detection methods used in relation to A350 F&DT philosophy.

19.3.7.1   Visual inspection

Visual inspection is associated with a range of more specific definitions, including surveillance, normal visual, detailed visual. Each has a specific definition and will be associated with appropriate levels of access, lighting, cleanliness, distance, etc. Inspections using magnifying glasses and boroscopes may also be identified as visual inspection methods, although these should be limited to localized inspection applications due to challenges regarding an operator's ability to maintain concentration and orientation in an extensive complex structure. Furthermore, lighting difficulties and shadows may compromise damage detection.

The visual inspection definitions can be defined by the TCHs relative to substantiated Probabilities of Detection (POD) data and in the context of the TCH design philosophy. However, some more standardized definitions exist within processes, such as MSG 3.

e.g., MSG3 definition of General Visual Inspection (GVI):

"A visual examination of an interior or exterior area, installation or assembly to detect obvious damage, failure or irregularity. This level of inspection is made from within touching distance unless otherwise specified. A mirror may be necessary to enhance visual access to all exposed surfaces in the inspection area. This level of inspection is made under normally available lighting conditions such as daylight, hangar lighting, flashlight or drop-light and may require removal or opening of access panels or doors. Stands, ladders or platforms may be required to gain proximity to the area being checked. Basic cleaning may be required to ensure appropriate visibility."

Inspections are typically targeting the reliable detection of dents, cracks, scratches, gouges, and corrosion in metallic structures. However, as already discussed, many damage modes may exist in composites, some being difficult to detect, e.g., disbonds and delaminations and the correlation with dent depth data and RS capability may be of limited use; planar damage size reflecting better RS capability, Figs. 19.2–19.10 in Ref. [38]. See Chapter 12 for further data and models regarding these correlations.

When inspecting for dents, the POD should be established and shown to be conservative relative to the DT design concept used. The POD can be dependent upon many variables, e.g., surface finish, Fig. 19.18 shows the same dented panel in the same lighting. The only difference being that the dent is visible when the panel is wetted.

Color could also be significant to the successful detection of dents, Fig. 19.19 shows the bivariate plot of dent depth v width for gloss white and gloss blue panels, suggesting that increased w/d can reduce POD and that the POD for white is greater than for blue. Again, the potential for any uncertainty should be addressed by robust design philosophy.

The probability of making a valid finding (not a false alarm, or missed finding) is a function of many factors, including inspector experience, job instructions, the criticality of the component being inspected, expectations of damage, and personal biases; Psymouli et al. [39]. In order to verify the finding, the inspector might alter distance, angle, lighting, cleanliness, and complete a tactile test, e.g., tap or poke the structure. An internal inspection may be a very important part of the process. Fig. 19.20 shows a

Figure 19.18 Surface finish and damage detection [27].
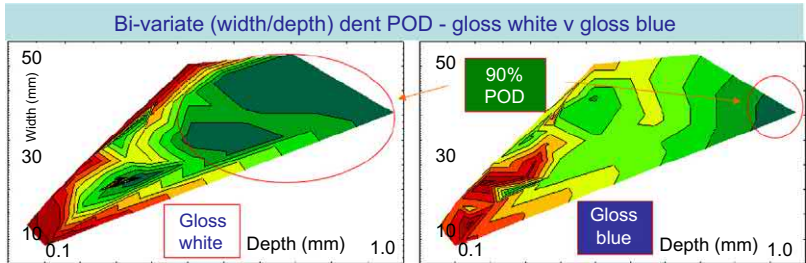
Figure 19.19 Surface finish and damage detection; Cook et al. [40].

Figure 19.20 Internal inspection following an external finding can be important [68].

large passenger aircraft horizontal stabilizer spar internal damage uncovered at a significant maintenance input sometime after external damage had been detected and a cosmetic repair applied without internal inspection having been completed. This case, highlights the importance of training and awareness regarding composite damage and inspection needs. It also highlights the importance of designing with a robust design philosophy.

Tap test: Tap testing relies upon assessing audible responses following tapping a structural surface. Damage modifies the stiffness, thereby influencing the frequency. Typically, a sharp, clear sound signifies an undamaged structure, while a dull sound signifies a damaged structure.

In its simplest form, use of a simple hand-held coin to tap a structure to detect a local damage or suspected damage site can provide useful, but very limited, supporting information in a visual damage assessment, particularly when used with thin skin structures, provided that the user has knowledge of the configuration, e.g., existing underlying structure details, etc. However, such a crude tool should not be relied upon and is of limited value for large areas of the structure. Any doubt regarding a "good" response should be followed up with the use of more reliable methods.

Tap testing exists in more automated forms, which may be more reliable and precise than the manual tapping with a coin, allowing the use of standardized frequencies, and recording of data, etc. However, such methods need thorough substantiation for specific applications and structural configurations.

Ultrasonic Testing (UT): UT functions by introducing high frequency sound into the structure and may be used to determine the existence of damage by either measuring the signal on the far side of the structure, i.e., Through Transmission (TT), or measuring the returned signal, i.e., Pulse Echo (PE). The existence of damage typically changes the signal response.

UT is available in an extensive range of equipment options, including many portable forms. Typically, the signal is coupled with the structure using a coupling agent, e.g., water jet, gel, etc., although noncoupled methods are in development. The equipment and data interpretation requires trained and qualified staff, although simplified tools are in development. UT may be useful to help establish the extent of in-plane damages, e.g., delaminations, although some of the details in multiple layers of damage may be masked by other damage signals.

Data may be developed at a point location, linearly, or in plan form, i.e., A, B, or C-scans respectively, and is typically referenced to standards, e.g., using a Flat Bottom Hole (FBH) reference panel. However, for complex parts, a "representative" reference part might be accepted as part of the reference data set, once the processes have been frozen and the FAI details established.

Radiography (X-Ray) Radiography functions by passing X-rays through the part and recording the transmitted signal, typically on film. The absorption is a function of part density, which may be changed by damage. Therefore, composites require the use of lower X-ray energies than typically denser metals. It may be necessary to use penetrants, e.g., Zinc Iodide, in order to emphasize damages, e.g., delaminations, assuming that the damage can be accessed by the penetrant. Such penetrants are very difficult to remove from the inspected parts. Radiography can be useful for indicating the extent of cracks and delamination in laminates or the existence of fluid in sandwich structures.

Fig. 19.21(a) shows a simple comparison between UT and conventional X-ray data for the same damaged specimen, while Fig. 19.21(b) shows the use of more recent technology, comparing thermographic images with visual images of a panel both before and following having been subjected to high-velocity impacts.

Radiographic equipment is typically heavy and of limited portability. It also has significant health and safety limitations. This is certainly challenging in a maintenance environment when an on-wing inspection is necessary because hangar space will be subject to access restrictions during the process.

More recent developments in UT and X-ray capability allow very detailed images of a structure to be created, including 3D images, e.g., using Computerized Tomography (CT) scans, which can be used to develop very detailed 3D images of internal structure.

19.3.8 Continued airworthiness

Initial designs may not perform as expected, potentially resulting in unsafe conditions and requiring corrective actions, e.g., repairs outside the SRM limits, etc. Furthermore, operators may wish to change the product by adding modifications, e.g., adding large antennas, or changing the utilization, e.g., change use from a passenger aircraft to a cargo aircraft or "water bomber." These may significantly impact structural performance, and safety, if not appropriately designed and manufactured. Therefore, the "initial airworthiness" process is to be supported by appropriate "continued airworthiness" processes. These are generally governed within the regulatory systems previously described.

Once in-service, unexpected issues of safety concern may be addressed by the issue of Airworthiness Directives (ADs), which may require specific inspections and/or require completion of corrective actions, e.g., delivered via Service Bulletins (SBs). ADs may also impose, or change, life limitations and can result in fleets being grounded. As is the case for "initial airworthiness," there is little specific reference to composites at the regulatory level regarding "continued airworthiness." Again, there is only limited, but increasing reference to composites at the guidance level, e.g., ACs, CMH-17 Volume 3, CMs, etc.
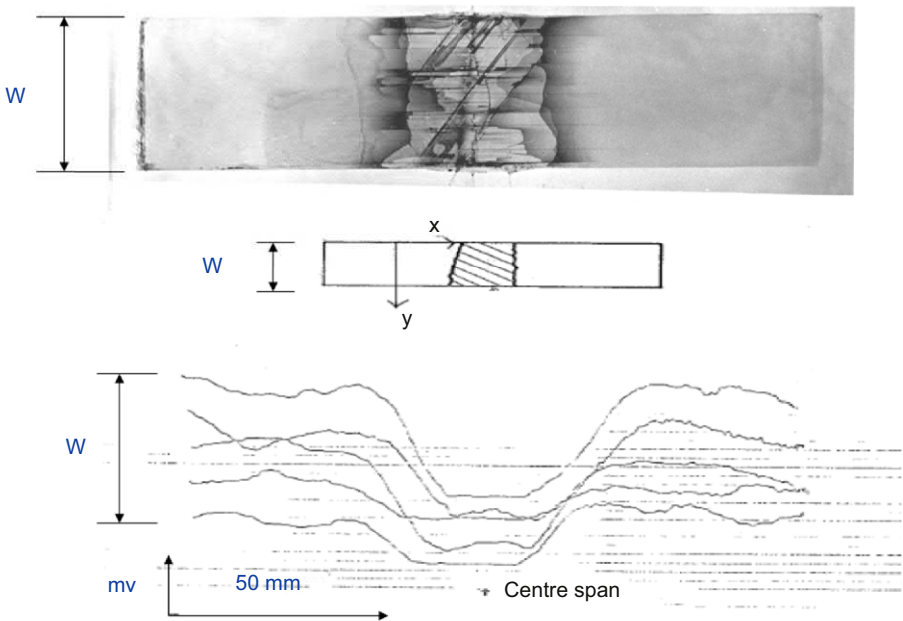
Figure 19.21 (a): Comparison between X-ray and UT (simple parallel B-scans) - indications of high strain level fatigue generated cracking and delamination in a 3-Point Bend Specimen (carbon prepreg 914C UD tape laminate); Waite [41].
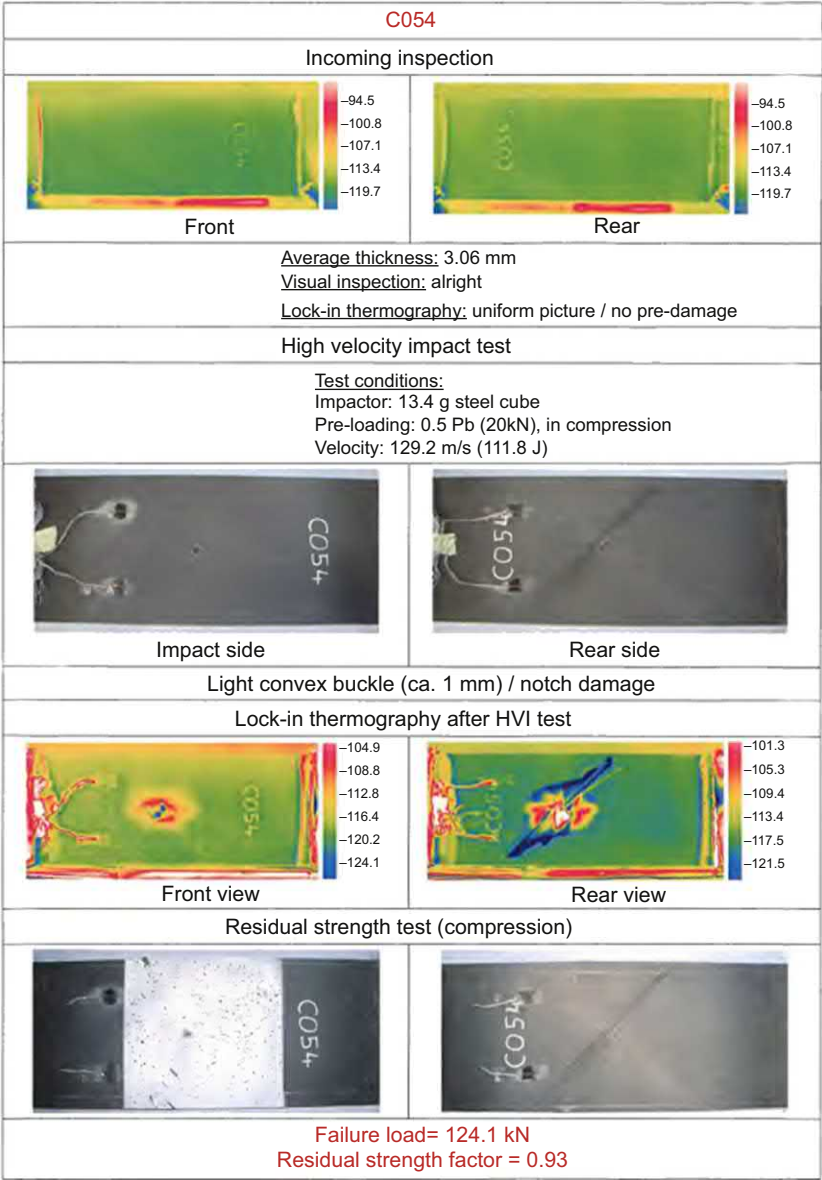
Fig. 19.21 (b) shows visual and thermographic (lock-in thermography) images of a simple carbon prepreg panel before and after the high-velocity impact [31], demonstrating the potential for thermographic methods to provide useful information in a laboratory environment.

19.3.8.1   Ground impact damage and high-energy wide-area blunt impact (HEWABI)

A threat of particular interest is ground impact, e.g., impacts with ground vehicles and equipment, etc., which account for more than 40% of aircraft damage, costing an estimated Euro 2−4 4 billion per year in repairs and lost services [42]. Fig. 19.22 shows an example. This suggests that both commercial and safety benefits might result from investing adequately in ground staff training.

Such events should be obvious, reported, and repairs completed accordingly. For this reason, such events are considered to be outside the damage threats addressed in the certification process, although the applicant is expected to provide the appropriate data necessary to ensure that all damage can be found and repaired to bring the structure back to service, should that be desired, appropriate, and economical. Such events have been identified as Category 5 in Fig. 19.1.

However, noting that composites have the potential for hidden damage, Category 5 damage has attracted some attention, particular relating to HEWABI. This has resulted in R&D work and the recognition that the workforce needs to be provided with appropriately emphasized information regarding the operation and maintenance of such products, in accordance with EASA Operational Suitability Data (OSD) principles, see Appendix A1.2, and FAA policy [43]. R&D has considered various structural configurations, including all-composite airframes, such as composite skin/stringer/ frame constructions [44], and hybrid airframes, with composite skin/stringer and metallic frame constructions [45]. These used analyses supported by test building-block approach.

Characterization of the threat source has been challenging due to the broad range of variation associated with each of the many parameters relating to the impactor (ground vehicle). For example, ground vehicles may be defined by many parameters, including mass, speed, geometry, contact point material (noting the recent move to soften vehicles by using rubber bumpers). The aircraft is also defined by many variables, including mass, geometry, contact point material, and configuration (relating to both local stiffness and aircraft level stiffness). The aircraft may be impacted over a broad range of contact angles, and it may also translate upon impact, the dynamics of the actual event being difficult to represent in either test or analysis. Consideration of these points results in challenges regarding the definition of BCs for both test and analysis.

Fig. 19.23(a) and (b), show early R&D work completed using a 5 frame hybrid test article, including an impactor with 4in diameter rubber bumper, in the test rig, and the

Figure 19.22 Ground vehicle impact [68].
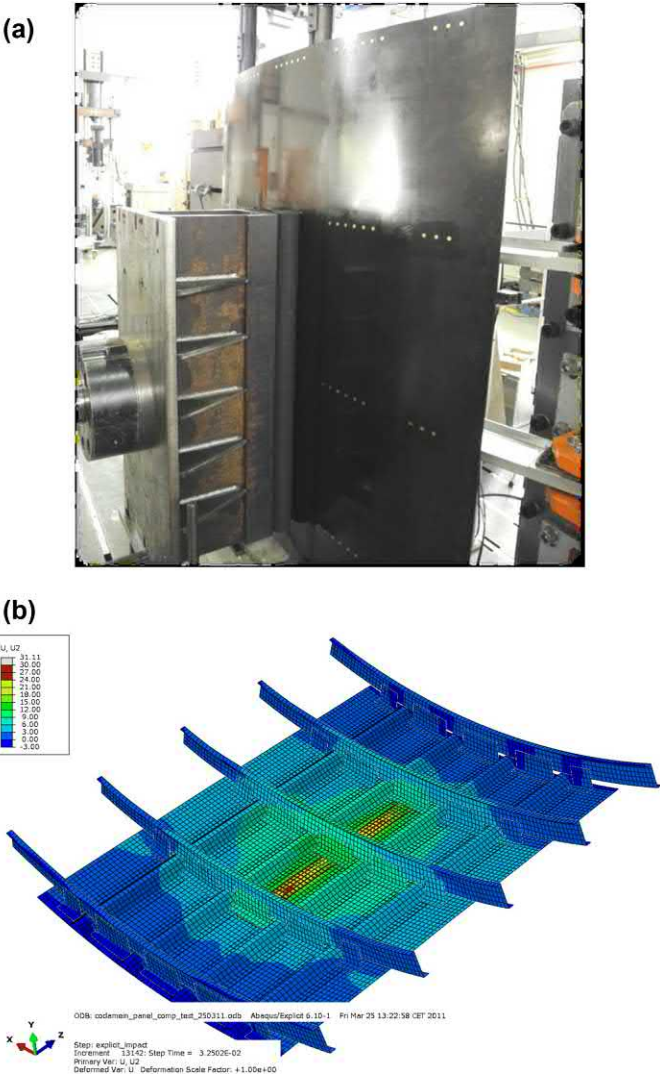
Figure 19.23 (a) Hybrid Test Article. (b) Hybrid Test Article FEM.

FEM model used to support the investigation. Fig. 19.24(a) shows that impact, equivalent to a 2500 kg vehicle at 1 m/s, produced no externally obvious damage, yet failed shear ties on the inside, Fig. 19.24(b).

Initial R&D work would suggest that it is possible to produce internal damage with little external visible damage following a significant impact outside the regulatory certification envelop, although the need to improve the representation of the BCs has been recognized. The consequences of such damage would depend very much upon the details of the design concept. For example, the failure of a number of shear
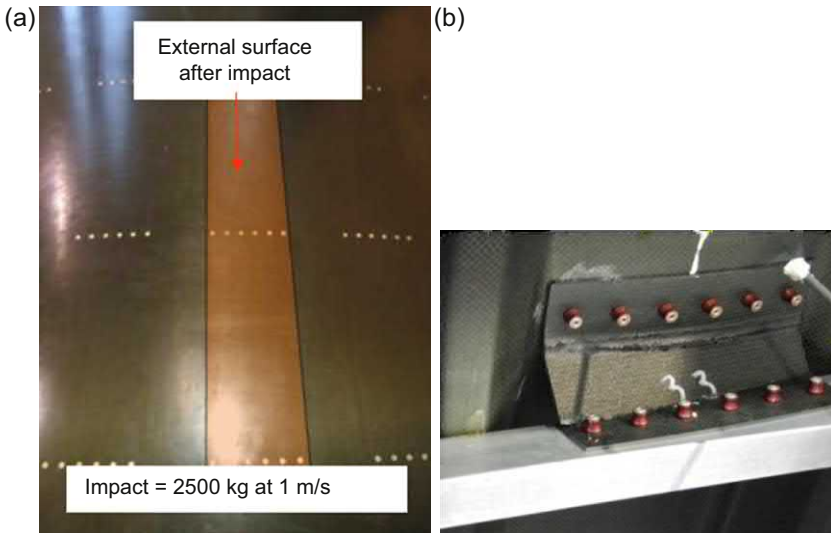
Figure 19.24 (a) Hybrid Test Article following impact—external view. (b) Hybrid Test Article following impact—internal view showing shear tie failure.

ties might be addressed by Category 2 considerations, i.e., they may be detected within the scheduled internal inspection cycle while retaining acceptable RS capability by virtue of a broader robust design strategy. Note: Robust design strategies have been demonstrated for existing product configurations, these involving significant and extensive building-block test and analysis work. Furthermore, these have been supported by significant efforts to improve workforce knowledge, as required by OSD and FAA Policy [43]; see workforce knowledge section below.

19.3.9 Product changes (repairs outside existing data limits and modifications)

The regulatory significance of product changes or repairs is normally classified as "minor" and "major"," as discussed in Appendix 1. Organizations wishing to change a structure, e.g., modifications or repairs, typically need to satisfy the original Certification Basis (CB), depending on the extent, criticality, and complexity of the change (some significant changes may require reference to later requirements, see below). Organizations wishing to develop changes typically need the appropriate organizational approvals identified in Appendix 1, although some more specific organizational approvals are also available for product changes, e.g., Ref. [46]. The DOAs may be supported by an appropriately approved Production Organization Approval (POA) holder, while "Production without Production Organization Approval" is possible under Subpart F. When addressing product changes, the changes may involve new and/or baseline structure which could be metallic or composite.

Product change can present a very significant challenge to STCHs without direct TCH support if the intended modification or repair to the composite structure is outside existing TCH published data limits, e.g., as is typically provided per the SRM or in TCH Service Bulletins (SBs), because, unlike many metallic configurations, much of the data is very material, process, and configuration specific and, typically, such data is limited by TCH willingness to share Intellectual Property (IP). Furthermore, an applicant may be significantly challenged when demonstrating equivalence to such data, if made available by the TCH. Without understanding the design allowables, damage modes, etc., it will be difficult to assess the impact upon the composite baseline structure [47]. Accordingly, applicants for such changes should understand that the regulators are unlikely to be able to approve such changes which may impact safety-critical baseline structures, e.g., Primary Structures, Principle Structural Elements (PSEs), and Critical Parts, etc., without appropriate TCH data. The developing discussion regarding composite modifications is evident in proceedings of various workshops, for example, composite modification workshops 2016, 2017 [48,49].

19.4 Other considerations

19.4.1 Crashworthiness

The existing acceptable level of safety for large passenger aircraft is provided by using various CSs such as CS25.561, 25.562, 25.721, supported by long experience of survivable accidents, the complexity of which have been beyond modeling capability and complete definition within any CS. For crashworthiness, AMC 20−29 states:

"assure that occupants have every reasonable chance of escaping serious injury under realistic and survivable crash impact conditions. A composite design should account for unique behavior and structural characteristics."

An "equivalence" approach has been adopted for recent projects, requiring that the same basic criteria be addressed: (a) retention of items of mass; (b) survivable pulse; and (c) protection of living space and (d) protection of escape routes.

A safety strategy was developed which included building and validating analytical models against previous metallic narrow-body fuselage section drop test data and applying these methods to existing "conventional" wide-body aircraft designs in order to define survivable reference criteria for final comparison with the composite wide-body airframe designs. In the absence of wide-body drop test data, the existing conventional wide-body fleet accident experience is considered to have demonstrated an acceptable level of safety over many decades when using the existing dynamic impact requirements and established design concepts. Therefore, such data was considered to provide an equivalence reference for the selected conventional comparative airframe, noting that any poor design details which might drive unacceptably low reference vertical drop speed values (Vz) would not be accepted by the regulators for application to the new composite design.

For the new designs, the design features constructed using composite materials were substantiated by test and analysis building-block work, as appropriate to the complexity and deviation of the design from conventional design practices.

Consideration was given to the potential for competing damage modes to result in changes in the governing survival criteria throughout the likely survivable Vz range, this being potentially being up to 30 ft/s (9.2 m/s) (based upon actual accident data), but depending more specifically upon reasonable survivability, reference data having been generated by the conventional configuration used for equivalence purposes, as previously discussed. This was achieved by analytical model investigations of the conventional and new designs throughout a range of drop speeds and for a range of passenger and cargo load configurations. Consideration was also given to off-axis impacts for the more complex or novel design features, i.e., for those impacts associated with realistic scenarios, including yaw, pitch, and roll, when consideration of a simple vertical impact alone might be inappropriate.

Crashworthiness certification was managed in recent projects using an EASA SC. There is a growing body of developing guidance material [50−52]. See Chapter 13 for more detail on the crashworthiness of polymer composites.

19.4.2 Thermal issues, fire protection, and flammability

The regulations have included fire protection and flammability requirements for interior structures, and structures local to the power plant, for many years. However, the increasing use of composite has required that the thermal and fire issues be more thoroughly and systematically addressed.

Thermal issues—within the design envelope: Thermal considerations require thorough exploration of the heat environment, also allowing for local equipment installations which might impact the reference structure temperatures relative to atmospheric temperatures, in order to ensure that local glass transition temperatures (Tg), will not be challenged in normal operation. Some established design practices exist regarding this point, e.g., Ref. [53]. This prescribes a commonly used minimum margin between Tg and Maximum Operating Temperature (MOT) of 50°F (28°C) for laminates, while 30°F (17°C) is expected for adhesives. For example, local electrical heat sources could contribute to an extreme atmospheric temperature, adding to the reference airframe temperature when the aircraft is on the ground and subject to heat soak at a desert airfield. Furthermore, aircraft paint color may be important for low Tg materials, as is often used in GA applications. Further safety mitigating factors are expected to address such matters, if not addressed directly within the bounds of conventional certification practices, e.g., temperature measurement devices could be used with flight restrictions and/or maneuver limitations applied for a given period following take-off (intended to allow for structure cooling), etc. It should also be noted that low temperatures may be more critical for some materials and applications. These considerations should be addressed in the material selection, qualification, and DT processes accordingly.

Fire Protection and Flammability: Beyond consideration of interiors, and structure local to power plant, there are no composite or structure specific requirements

addressing fire protection and flammability. Therefore several fire scenarios have been addressed via SCs in recent projects, i.e., in-flight fire and postcrash fire. Again, an "equivalency" strategy has been expected, and the use of the building-block approach, which is necessary because the fire behavior and structural response may be dictated by the complexity of the configuration or the fire being external or internal to the structure, etc.

The possibility of in-flight fire should be minimized, but if it occurs, it should be detected and suppressed, e.g., using extinguishing systems, etc. However, the potential for latent fires might also exist. In all cases, the damage scenarios should be managed in the context of the F&DT philosophy. Postcrash fire considerations primarily address ensuring that collapse of fuel tank structures and release of fuel does not occur following an otherwise survivable crash and fire before the passengers have evacuated the aircraft.

Compliance has largely been demonstrated by test and analysis to show that, following an otherwise survivable crash landing, there is sufficient time for passenger to egress, without fire penetration or the release of gasses and/or materials that are either toxic or reduce visibility (smoke density) or could increase the fire severity. This has included testing, which had demonstrated that the strength and stiffness of the composite structure does not reduce more than "equivalent" metallic structures when exposed to a similar pool fire. The analysis should consider various permutations of postcrash configurations, e.g., using CS25.729, including collapsed undercarriage permutations or a separated engine, in conjunction with a range of possible fuel weights and distributions.

Additional considerations include the need to inform rescue crews of any structural configurations which might change rescue procedures, including instructions regarding those new procedures, e.g., when placing ladders against composite structures previously exposed to fire, once extinguished, etc.

Safety considerations should be extended to providing guidance to recovery crews regarding the removal of the wreckage from a crash site, e.g., due to possible fiber release, etc., and the appropriate environmental measures necessary to return the site to its original use, e.g., due to soil contamination.

19.4.3   *Lightning*

AMC 20−29 para.11 addresses lightning protection. Typically, the conductive paths which are inherent to metallic structures allow the lightning energy to enter and exit the airframe with limited damage. However, composite airframes are significantly less conductive than metals, requiring a more active, lightning and static electricity management strategy. These typically involve the inclusion of embedded conductive metallic meshes, conductive surface layers or attachment of metallic strips and frames, etc., such that a complete and robust conductive network is established and maintained throughout the aircraft's operational life. The threat source remains much as identified in existing metallic zoning guidance, [54,55].

The potential for structural damage should be explored for all material combinations, particularly fastened joint combinations, considering the likely range of fastener

fit qualities and allowing for nonfunctional contact with protective meshes. Any resulting damage should be managed within the scope of the damage categories and the F&DT philosophy.

A threat requiring particular attention is that resulting in arcing, particularly in a fuel tank. The regulatory expectation is that redundancy in protection systems be demonstrated. Furthermore, such systems need special consideration in production, maintenance programs and care in repair processes. Service experience has provided examples of catastrophic failure following a lightning strike. A recent AAIB report [56] describes metal fatigue failure initiated by a small production defect in a hybrid structure rotor blade caused by arcing associated with a previous lightning strike.

Lightning considerations should extend to the protection of systems, which may result in a significant weight penalty due to the need for additional insulation. Careful investigation and characterization of the importance of paint thickness may be necessary because the composite structural response to lightning strike has been demonstrated to be very sensitive to this parameter. See Chapter 18 for a detailed account of lightning strike issues on polymer composite aircraft.

19.4.4   *Workforce knowledge, training, and teamwork*

Design, production, and maintenance organizations rely upon an appropriately qualified and experienced workforce to design, produce, and operate a safe product. Furthermore, the regulators must develop and maintain appropriate knowledge to help ensure that this is being achieved [57].

Appropriate communication between staff members, both within and between these organizations is essential. These expectations are embedded within the regulations, particularly at a high level. However, there are few detailed engineering standard practices for composites. Therefore, in order to maintain safety and minimize associated costs, good teamwork is essential. This relies upon each team member understanding their own capabilities, knowledge, and responsibilities and how these relate to the capabilities, knowledge, and responsibilities of others. Furthermore, they must know as to how and when to communicate with other team members. TCH workshop and conference presentations, e.g., Ref. [58], help to develop broader common knowledge and support improved communications. These organizations and workforces also rely upon appropriate training, including theory, "hands-on," and "On the Job Training" (OJT) to create and maintain such a workforce.

In the design environment, the large and established TCHs tend to develop technology applications and databases for future products in conjunction with in-house staff, supported by selective external training. Furthermore, they are typically resourced to interact with production and in-service activities, as would be beneficial for efficient composite design, particularly for maintenance and repair. Therefore, such organizations are well placed for knowledge transfer within their organizations, and also to develop and deliver appropriate product specific training to customers, e.g., type courses and other training courses [58].

New TCHs, or TCHs new to composites, will need to develop a substantial training strategy, which will be linked to specific configuration development. Experience has

shown that this can be a significant challenge for new GA and small rotorcraft organizations, which typically have very limited resource. Even when using established materials, problems may be encountered because previous success in established organizations has been based, in part, upon "tribal knowledge." Therefore, new organizations can potentially benefit from engaging with shared database groups [59]. Such an approach offers potential benefit to the new organization in the form of access to knowledge, experience, and data, while the new organization might initially offer other benefits to the group, e.g., document translation, etc., until it becomes a valid technical member and contributor.

Design organizations supporting the MRO community, particularly those not directly supported by TCHs, are often subject to similar resource challenges. Furthermore, they typically work within tight timescales and with limited facilities, while supporting multiple technologies from multiple TCHs using the limited published supporting manual data. Therefore, knowledge transfer, training, teamwork, and awareness become particularly important for those responsible in these environments, e.g., the EASA Certification Verification Engineers (CVEs) and supporting the design team. The significance is emphasized by the recent extensive introduction of composites into more critical large airframe structural applications because it has exposed many in the in-service environment to composites for the first time.

It is essential that the TCHs have provided to the workforce the appropriate knowledge and training regarding the product and its technologies because the arrival of new technology poses many challenges [60]. In particular, the MROs are to ensure that they develop and support appropriate maintenance workforces capable of working with these products and technologies, such that poor repair practice is avoided, Fig. 19.25, also [61,62].

(EU) No. 1321/2014 [63] addresses workforce knowledge and training, in particular, PART 66 "Certifying Staff," while workforce training organization considerations are addressed in the context of PART 147 "Training Organizations." The majority of guidance is at a high level. However, EASA is in the process of enhancing details associated with some aspects of workforce knowledge and training, e.g., licensed workforce training.

Ribbon direction???
Cell deformation???
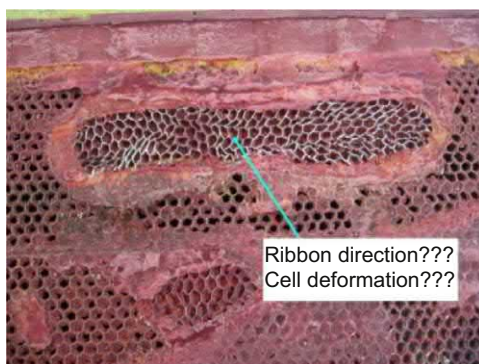
Figure 19.25 Training necessary to avoid poor repair practices; FAA case studies [62].

Furthermore, the EASA OSD strategy provides some more prescriptive links to composite knowledge expectations and training via EASA CM-MCSD-001"Maintenance Certifying Staff," which references, e.g., SAE AIR 5719 [64]. This strategy is also supported by other documents produced by SAE CACRC.

Training and awareness expectations may be particularly important to composite structures and should be extended to all levels of the operational environment, regulatory expectations including monitoring and inspection of movement areas [65] and operation of vehicles [66].

Failure to support such actions can be expensive and potentially of safety concern, e.g., Fig. 19.26 winglet and Fig. 19.27 engine examples;

In order to better standardize knowledge levels, the FAA defines three levels of knowledge:

Level I: A basic introduction to the definition of composite materials, common terminology, and basic processing.

Level II: Safety Awareness, is the level identified as required for workforce supporting composite applications.

Level III: Specialized Training is special skills needed in the industry and possibly by some regulator experts. Examples of Level 3 training include specific NDI techniques and analytical modeling methods (e.g., finite element analysis).

A series of online courses have also been developed, including a "hands-on" supplement, to support Level II knowledge for composite engineering (CSET) and manufacturing (CMT). Furthermore, a maintenance course (CMfgT) is planned for general availability. These form part of an industry and regulator composite safety strategy, and is recognized by EASA [67]. The regulatory intent is that certifying staff, e.g., Part 66 staff supporting composites, CVEs, be at Level II, as appropriate to composite design, manufacturing, or maintenance.

Figure 19.26 Pilot/ground crew wingspan awareness - two passing aircraft winglets collision (one severed) during taxiing (the previous model did not have winglets) … a potential repair challenge? [68].

Figure 19.27 Ground crew awareness—engine lowered on to steps as wing deflected during refueling [68].

19.4.5 Reporting, forensics, and database taxonomy

The regulations identify the importance of personnel engaged in aviation activities, particularly those with safety-related functions, making every effort to identify, report, and correct nonconformities and/or damage throughout production and in service. This includes individuals reporting to their respective organizations and organizations reporting to the regulators (particularly relating to incidents and accidents). Importantly, these processes also allow for anonymous reporting. It is important that organizations provide the appropriate support to the workforce regarding training and execution for these processes.

The importance of reporting systems is identified throughout the EASA regulations, including PART 21.A.3A "Failures, malfunctions and defects" [69] and in-service reporting is addressed in ADR.OR.D.030 "Safety reporting system" [70]. Although safety should always be the priority, the realities associated the time pressures, particularly in operational environments, combined with perceived threats by staff from their employers regarding continued employment following reporting an event, must be recognized, even with the availability of anonymous reporting. Therefore, every effort should be made by organizations to develop strategies to prioritize safety while minimizing the "blame culture," which might discourage reporting.

Furthermore, AMC 20-29 states:

> "Pilots, ramp maintenance and other operations personnel that service aircraft
> should be trained to immediately report anomalous ramp incidents and flight events
> that may potentially cause serious damage to composite aircraft structures."

TCHs of recent large composite products have developed training and awareness data to improve understanding of the product which should support correct actions following incidents and findings. This supports the intent of the EASA OSD strategy, and [43].

Once a finding has been made, or an incident has occurred, it is important that all available and appropriate data is correctly reported in order to ensure correct disposition. Although correct repair may be the priority for an operator, the information also has potential future safety and commercial value, but only if correctly processed and reported.

Although a correctly completed repair can resolve an immediate short term operational problem, it may not address a broader systemic matter. Furthermore, following more serious incidents and accidents, it is essential that the correct data is developed and reported in order to establish cause and appropriate corrective actions. In such cases, the availability of correct data can also help to potentially limit the scope of action required relating to the remaining fleet and may allow the effort to be directed to addressing the correct problem.

Initial Cause: Correct identification of any obvious and initial cause, if known, may support changes in process which help to avoid future reoccurrence of such events, e.g., impact events in service may be the result of particular ground vehicle driver practices. Furthermore, knowledge of the cause may help to identify likely damages throughout a structure, e.g., a high energy blunt impact, or evidence of an impact of unknown energy, would be assumed to require inspection of all load paths for remote damage resulting from load transfer, unless otherwise substantiated. It is important that all damage locations, damage modes, and defect/damage extents be identified for the purpose of completing appropriate repairs.

Forensics: If no obvious initial cause can be conclusively identified, then further forensic work may be required. It is important that all damage locations, damage modes, and defect/damage extents be investigated in order to correctly separate the cause from witness. Bonded structures can be challenging, [17,71−73]. It is important to establish whether a reported "disbond" is a correctly reported adhesion failure (a potential production/repair process error), or an incorrectly reported adherend failure (a potential design or operational error). The direction of subsequent investigation may be very different, depending upon the initial data supplied. The forensics specific to fire damaged composites is currently an initiative in the FAA Composite Plan. The loss of evidence associated with fire can be particularly challenging.

Database Taxonomy: Assuming that the correct cause has been identified and forensics have been completed, it is then important that consistent terminology [74], be used when the data is entered into the database, as otherwise the data may be lost to those searching the database. Further standardization regarding this matter is recommended for improved efficiency.

19.5 The future certification and airworthiness of polymer composite aircraft

New technologies and new applications of existing technologies are developing quickly, changing the relationship between design, production, and in-service functions. A consequence of this process is a developing approach to regulation, moving

toward "performance" based regulations, away from more "prescriptive" based regulations, e.g., as evident in the change from amendment 4 to amendment 5 of CS23. Furthermore, the EASA focus for new product certifications will be based upon criticality and novelty of design, i.a.w LoI principles.

However, the existing fleet already includes significant composite structure, some used in critical applications, potentially requiring future safety management as lessons continue to be learned. For example, recent events relating to sandwich structures in large passenger aircraft and rotorcraft products have required the review of good sandwich structure design practices [75,76] and is likely to be supported by other documentation, e.g., a Sandwich Structure Airworthiness Circular (AC) and/or guidance within CMH-17. Similarly, industry-led organizations, such as SAE CACRC, continue to work toward supporting aging composite products, e.g., Ref. [77] addresses the management and repair of metal skin - metal core sandwich structure products, many of which are out of production. Furthermore, MROs continue to research improved repair methods. Popp [78] discusses efforts to combine an array of developing technologies intended to improve bonded repair efficiency.

Lessons learned from recent large composite passenger aircraft certifications, as expressed in SCs, are being processed for potential rule and guidance changes in Aviation Rulemaking Advisory Committee (ARAC) Working Groups (WGs). For example,

1/Transport Airplane Metallic and Composite Structures Working Group—Recommendation Report to FAA (TAMCSWG). The WGs were formed to investigate:
  1. Threat Assessment
  2. Structural Damage Capability (SDC)
  3. Testing of Hybrid Structure
  4. Aging Mechanisms
  5. Inspection Thresholds
  6. Bonded or Bolted Repairs
  7. Large Modifications
  8. Inspections and the Airworthiness Limitations Section (ALS)
  9. Harmonize European Aviation Safety Agency (EASA) Aging Aircraft Rulemaking
  10. Emerging Material Technology
  11. Rotorburst Policy
  12. Cracking During Full-Scale Fatigue Test
2/Transport Aircraft Crashworthiness and Ditching Working Group Report to FAA (TACDWG). The WGs formed were:
  1. In-service Data Evaluation
  2. Crashworthiness
  3. Ditching
  4. Equipage and Protocol

The outcome of these activities is yet to be processed. However, most change recommendations are likely to be related to guidance, not rule, content. Existing guidance material continues to be revised, e.g., AC20-107B/AMC 20−29, having been issued in 2009/2010 respectively, are under consideration for revision. New guidance documentation continues to be developed in response to "lessons learned" or to

support new applications, e.g., draft SAE AIR 6337 [79] is in development to address composite seat structures.

The Industry Regulator Composite WG continues to work to identify themes of potential safety concern in large passenger airframe applications, for example, Fig. 19.28, supported by many industry standardization bodies, e.g., CMH-17, SAE CACRC, ASTM, etc. There is potential to develop similar activities for GA and the rotorcraft industries.

PMCs continue to dominate major composite airframe configurations, and processes continue to evolve, e.g., there being significant continued interest in Vacuum Assisted Resin Transfer Molding (VARTM) and developing an interest in out of autoclave prepreg technologies. However, materials and processes will also continue to evolve, continuing to require the appropriate characterization of sensitivities, dominant failure modes, etc., e.g., for CMCs, MMCs, and Additive Manufacturing (AM) methods. Furthermore, applications will continue to extend beyond airframe, engines, propellers, undercarriage, seats, etc.

Regardless of the material, process, or configuration, the regulators will be looking for the identification of key parameters and the demonstration of understanding of the sensitivity of "engineering properties" to these parameters, and how they are managed to ensure stable production such that design allowables remain valid.

There is a need for better standardization of the statistical management of the middle of the test and analysis pyramid. Furthermore, a clear understanding of damage modes will need to be demonstrated, including the use of appropriate RS and F&DT strategies. This will form an important part of the developing discussion and industry interest in the potential to increase the use of analysis in place of the test.
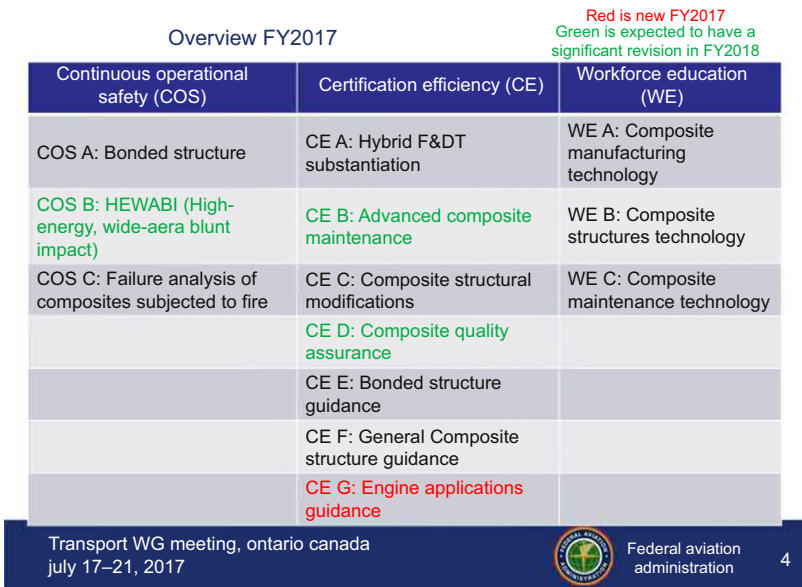
Figure 19.28 Example of FAA AVS Composite Safety Plan—2017(means of output delivery continues to evolve, subject to changing rulemaking and guidance philosophy).

Regardless of PMC airframe and passenger critical structure designs, e.g., composite seats [79], not being driven by fatigue, such structures will continue to need to show that they meet regulatory objectives throughout service lives, in accordance with the basic and legally binding regulations, Appendix 1.

The potential exists to exploit better the anisotropic properties of composites such that loaded structures can be designed to adapt to assist optimization of the aerodynamic profiles throughout the operational envelope in each phase of flight. These may be combined with Structural Health Monitoring (SHM) methods. All will require appropriate cautious management in order to establish true "airworthiness credit."

Further subjects offering the potential for improved certification efficiency, subject to R&D progress, include, hybrid structures, LEF management, inspection and damage detection (use of IT, drones, etc.), process monitoring replacing inspection, HEWABI, forensics, database management, relative static and dynamic structural performance in various damage states, etc.

Composite materials will also play a significant role relative to increasing global environmental concerns. However, the obvious potential weight benefits may be significantly offset by issues associated with production (including the materials and processes used to make them), operation challenges, and disposal of composite structures.

The Advisory Council for Aeronautical Research in Europe (ACARE) is playing a significant role in directing, i.c.w. European Industry, the aviation R&D in Europe, setting environmental targets for 2020 and beyond.

- Reduce fuel consumption and carbon dioxide (CO_2) emissions by 50% per passenger kilometer;
- Reduce nitrogen oxide (NOx) emissions by 80%;
- Reduce perceived noise by 50%; and
- Make substantial progress in reducing the environmental impact of the manufacture, maintenance as well as disposal of aircraft and related products.

The Clean Skies Program [80], currently "Clean Sky 2," forms part of this strategy. The Clean Skies program is the largest European research program developing innovative, cutting-edge technology aimed at reducing CO2, gas emissions, and noise levels produced by aircraft. Funded by the EU's Horizon 2020 program, Clean Sky contributes to strengthening European aero-industry collaboration, global leadership, and competitiveness.

Composite materials feature significantly in many of the projects in various stages of development, such projects being coordinated with EASA, as and when appropriate [81].

Above all, one the largest challenges to the industry, including the regulators, seems to be the safe management of the integrated design, production and continued airworthiness processes associated with composites in an increasingly segmented global industry. In particular, appropriate knowledge transfer and effective training will be necessary to make this possible and efficient. The industry also needs to strive to ensure composites provide a net environmental benefit relative to conventional

materials, and the industry and regulators need to move toward global harmonization and standardization, which can form a key part of an effective SMS.

Note: This chapter was written to add to the existing limited coverage of composite certification texts from a regulatory perspective. It provides a brief overview of the subject, linking academic understanding and process with certification as it relates to design, manufacture, and operational reality. Therefore, it only represents a reference to some key themes and ideas and does not represent an MoC or regulatory position for use in certification. The appropriate, and current, texts should be consulted for the purpose of any certification, and the appropriate regulators consulted for any clarifications prior to any embarking upon any project.

The content of this Chapter is partly derived from presentations given by EASA, Ente Nazionale per l'Aviazione Civil (ENAC, Italy), Airbus, Boeing, Lufthansa Technik, Adhesion Associates, Snecma, and Expliseat at the SAA-EASA Composite Materials Seminar, held at the Singapore Aviation Academy on 14−16 April 2014.

https://saa.caas.gov.sg/documents/20181/339902/SAA_Journal_2014.pdf/93eca021-cd8f-4edc-af6f-6196515bfd15.

The author wishes to thank those who supported and reviewed this chapter, particularly Chantal Fualdes (Airbus).

Appendix 1: The regulators, regulations, and certification

A1.1 The regulators and the regulations

The aviation regulators and the associated regulatory systems were established primarily to help define and maintain safety. However, the regulators were also established to help maintain a "level playing field" for the applicants (initially for local industry, but increasingly throughout global industries).

Generally, the aviation regulators, e.g., European Aviation Safety Agency (EASA), Federal Aviation Administration (FAA), Transport Canada Civil Aviation (TCCA), have been structured to address similar scopes of interest relating to all aspects of aviation safety, although the details of these organizational structures may differ.

In Europe, EASA is structured [82] to function as a centralized organization representing EU aviation regulatory interests. The EASA Certification Directorate carries responsibilities for initial airworthiness, working with the Flight Standards Directorate to support and standardize design, production, and continued airworthiness activities. EASA also relies upon the European National Airworthiness Authorities (NAAs) for the execution of many of the production and continued airworthiness processes.

The regulators typically structure the regulations to comprise of high-level legally binding "performance" based regulations supported by more "prescriptive" guidance documents. The details of these regulations may vary from regulator to regulator, although the basic intents remain similar.

The higher levels of the EASA regulations structure [83,84] are governed by the legally binding European aviation Basic Regulation EC (EU) 2018/1139, which addresses all aspects of aviation and is supported by further regulations which lay

down the Implementing Rules (IRs) relative to each of the various aspects of aviation, e.g., EC (EU) No 748/2012 PART 21 addresses a broad range of initial airworthiness aviation activities such as certification of aircraft and related products, parts and appliances, as well as the approval of design and production organizations, e.g., PART 21 Subpart J "Design Organization Approvals" and Subpart G "Production Organization Approvals," etc. Similarly, EC (EU) 1321/2014 addresses the continued airworthiness of products and the approval of organizations involved in the continued airworthiness processes, e.g., PART 145 "Maintenance Organization Approvals," PART 147 "Training Organizations," etc.

The IRs are further supported by more prescriptive nonbinding documentation, e.g., "soft law" relating to certification of aircraft and related products, parts and appliances, such as Certification Specifications 25 (CS-25) "Large Aeroplanes." The contents of many of the CSs are common to other regulators, e.g., CS-23 "Normal Category Aeroplanes," CS-25 "Large Aeroplanes," CS-27 "Small Rotorcraft," CS-29 "Large Rotorcraft", CS-E "Engines", CS-P "Propellers". EASA also supports "Sailplanes and Powered Sailplanes" in CS-22.

The CSs are further supported by other nonbinding guidance documents, e.g., Acceptable Means of Compliance (AMC), such as AMC 20−29 "Composite Aircraft Structures" (harmonized with FAA AC 20-107B), as referenced from CS25.603 (as discussed in this chapter).

EASA also produces Certification Memorandum (CMs), which support the interpretation of the existing rules and guidance. Sometimes CMs are harmonized with FAA Policy Statements (PSs), e.g., EASA CM-S-005 "Bonded Repair Size Limits" is similar to FAA PS PS-AIR-100-14-130-001.

A1.2 Certification

Product Certification is typically defined relative to requirements and guidance material as developed by the regulatory organizations in conjunction with industry consultation and support.

An aviation product is defined in PART 21.A.31 by its Type Design (TD) [85], which explicitly includes the need to identify the materials, processes, methods of manufacture, and assembly.

The regulators require that, for the issue of a product Type Certificate (TC) which supports the TD, the criteria for issue of a TC be satisfied. Issue of the TC is necessary before the Certificate of Airworthiness (C of A) can be issued for each and every product produced in order for it to be released to service.

The TC will be based upon a Certification Basis (CB), which typically comprises of reference to a particular set of specifications, e.g., EASA Certification Specifications (CSs), as appropriate to the product type and configuration at a specified amendment level at the agreed date of application.

The CB may be supplemented by additional requirements, identified as Special Conditions (SCs), when the existing requirements are not considered to adequately address the product configuration, e.g., when it introduces novel and unusual design

features, such as new materials and/or processes. SCs are often candidates for future rulemaking processes.

The increasingly rapid evolution of new technologies and pressure to apply these technologies, have moved the regulators toward "performance" based regulations, which identify high-level safety objectives, and away from the more "prescriptive" regulations, which have largely been based upon more conventional and established technology evolution.

Although this flexibility does offer potential benefits to industry, e.g., more rapid entry to the market for a particular design concept, it does also require that other mitigating actions be taken to help ensure that the existing acceptable level of safety is maintained. For example, the TCHs need to provide instructions to customers regarding the correct use of new technologies, both from a commercial and safety perspective. Therefore, EASA has developed an Operational Sutability Data (OSD) strategy [86], intended to improve the link between the product, its supporting data, and the workforce.

Furthermore, in the absence of a progressively developed and established databases, EASA is increasingly expecting product certification to be supported by a fleet leader and/or sampling strategies. Such mitigating actions are considered to be potentially important for new organizations until they can establish a credible and applicable database relating to any specific technology.

Regulators typically require that, for certification, a product be defined and supported by appropriately approved design, production, maintenance, and operational organizations at different stages in the aircraft program development. This is best achieved by appropriately integrated involvement of all parties. However, it should be noted that:

> … an appropriately approved design organization (e.g. TC or STC Holder, i.e. TCH, STCH respectively) typically holds ultimate responsibility for the product, including its initial airworthiness, and is usually directly supported by appropriately approved production organizations. Furthermore, the TCH or STCH is responsible, in part, for maintaining product continued airworthiness via delivery of continued airworthiness data, while appropriately approved maintenance organizations are also responsible for showing compliance with this data in order to ensure the continued airworthiness of the aircraft and thus its safe operation. Appropriate communication between all parties is essential for this to function safely and efficiently.

In order to further support these more integrated activities, the need to consider the regulations in a more holistic sense has been promoted by EASA via a Safety Management Systems (SMS) [87], in support of the European Plan for Aviation Safety (EPAS) [88].

SMSs provide opportunities for continuous safety enhancement. Furthermore, the regulators are working together to enhance the requirements and guidance materials with respect to the SMS concept, which is intended to support certification efficiency, e.g., the FAA's Aviation Safety Office (AVS) [8] has developed a Strategic Composite Plan in 2013, referred to as the "Composite Plan," addressing aircraft design,

manufacturing, and operation. This Composite Plan identified three focus areas: Continuous Operational Safety (COS); Certification Efficiency (CE); and Workforce Efficiency (WE), within which a number of certification-related tasks are identified, as discussed in this chapter. The themes originally identified in the Composite Plan are supported by international industry and regulators and focuses upon structural engineering issues, as well as related manufacturing procedures and maintenance practices. The plan has been reviewed annually and priority is assigned, or reassigned, to tasks based on issues that pose the greatest safety threats. Furthermore, the plan and the form of its output continue to evolve with changing regulatory strategies, although the technical themes are likely to remain relevant. These activities depend upon an industry interface and defining achievable deliverables, such as is evident in CMH-17 [6] and SAE publications by CACRC [89]. These activities are also supported by R&D activities.

EASA recognizes these international activities within its own strategy, which also identifies local themes requiring particular attention, e.g., sandwich structures, as discussed in this chapter. EASA is also working to further improve certification efficiency by developing a Level of Involvement (LoI) strategy, which prioritizes criticality and novelty in its regulatory processes [90].

Note: The regulators do not certify materials or processes directly, but accept them as part of a certified product. The applicant may gain credit for the use of the same materials and processes in future similar applications and/or by use of recognized shared database processes [59,91].

A1.3 Product change and repairs

The significance of any product changes is normally classified as "minor" and "major." A "minor change" is one that has no appreciable effect on the weight, balance, structural strength reliability, operational characteristics, or other characteristics affecting the airworthiness of the product (aircraft). All other changes are considered "major changes."

The details of the approval processes may vary among regulators. In general, for the minor changes, the regulator may grant approval without the substantiation or descriptive data. However, the data will be expected to be made available for investigation by the regulators. Approval of major changes must be substantiated by data, including descriptive data, for inclusion in the TD. An STC is issued to register the approval of change along with the TC previously issued for the product.

A repair may also be classified as major if it needs extensive static, fatigue and damage tolerance strength justification and/or testing in its own right, or if it needs methods, techniques or practices that are unusual (i.e., unusual material selection, heat treatment, material processes, jigging diagrams, etc.) [92], even if the resulting technical impact upon safety is finally determined to be of lesser significance than it initially, and potentially, could have been, based upon initial assessment.

In a situation when the certification agency finds the proposed change in design, power, thrust, or weight is so extensive that it warrants a substantially complete

investigation of compliance with the applicable regulation, then the applicant must apply for a new TC.

International harmonization efforts over many years have agreed on a rule relating to the designation of applicable regulations for product design changes. This rule is known as the "Changed Product Rule" (EU Part 21.A.101). This regulation requires that all changes to a type certificated product must show that the product complies with the airworthiness requirements applicable to the category of the product in effect on the date of the application for the change. For changes that are major, an investigation may be required on the designation of applicable regulations. As a relief, exceptions are permitted for using the earlier amendment of regulations for certain conditions. Through a joint effort with EASA and TCCA, the FAA issued "AC 21-101-1" in 2003 to support its implementation.

The aforementioned design changes are prompted by the revised purpose of the aircraft and are considered voluntary. However, a mandated design change may be required when the certifying authority finds that the design changes are either necessary to correct the unsafe condition of the aircraft or will contribute to the safety of the aircraft as presented through service experience. ADs are issued to address these mandated requirements (EU PART 21A.3B).

Note: The regulatory terms, the words of "minor" and "major" have been used to classify for both the "design changes" and "repairs" functions. While (engineering) approval may be involved for both processes, one distinct difference exists. Repair is a function intended to bring the structure to its original design strength and integrity, and therefore, the design basis remains intact. On the other hand, "design changes" may result in a revision of the original certification basis. Note: The applicant is advised to check the definitions of "major" and "minor" because there exists wording differences between the regulators, and to some extent the detailed scope of application.

Appendix 2: Glossary of terms, acronyms, and abbreviations

Abbreviations & acronyms

AAIB	Aircraft Accident Investigation Bureau (UK)
AC	Advisory Circular (FAA)
ACARE	Advisory Council of Aero Research in Europe
AD	Airworthiness Directive
ADL	Allowable Damage Limits
ALS	Airworthiness Limitations Section
AM	Additive Manufacturing
AMC	Acceptable Means of Compliance
ARAC	Aviation Rulemaking Advisory Committee
BC	Boundary Condition
BRSL	Bonded Repair Size Limits

BVID	Barely Visible Impact Damage
C of A	Certificate of Airworthiness
CACRC	Commercial Aircraft Composite Repair Committee (SAE)
CB	Certification Basis
CDT	Critical Damage Threshold
CM	Certification Memorandum
CMC	Ceramic Matrix Composite
CS	Certification Specification
CT	Computer Tomography
CSF&L	Continued Safe Flight and Landing
CVE	Certification Verification Engineer
DOA	Design Organization Approval
EASA	European Aviation Safety Agency
EPAS	European Plan for Aviation Safety
EKDF	Environmental Knock Down Factor
FAA	Federal Aviation Administration
FAI	First Article Inspection
FBH	Flat Bottom Hole
F&DT	Fatigue and Damage Tolerance
FEM	Finite Element Model
GA	General Aviation
GAG	Ground Air Ground
GVI	General Visual Inspection
HEWABI	High-Energy Wide-Area Blunt Impact
ICA	Instructions for Continued Airworthiness
IP	Intellectual Property (IP)
IR	Implementation Rule
IT	Information Technology
LEF	Load Enhancement Factor
LoI	Level of Involvement
LL	Limit Load
MoC	Means of Compliance
MM	Maintenance Manual
MMC	Metal Matrix Composite
MOT	Maximum Operating Temperature
MPD	Maintenance Planning Document
MRB	Maintenance Review Board
MRBR	Maintenance Review Board Report
MRO	Maintenance Repair Organization
MS	Maintenance Schedule
MSG	Maintenance Steering Group
NAA	National Airworthiness Authority
NDE	Nondestructive Evaluation
NDI	Nondestructive Inspection
OSD	Operational Suitability Data
PE	Pulse Echo
POA	Production Organization Approval
POD	Probability of Detection
PMC	Polymer Matrix Composite

PS	Policy Statement (FAA)
PSE	Principal Structural Element
R&D	Research and Development
RS	Residual Strength
SB	Service Bulletin
SC	Special Condition
SDC	Structural Damage Capability
SHM	Structural Health Monitoring
SMS	Safety Management System
SRM	Structural Repair Manual
STCH	Supplemental Type Certification Holder
TACDWG	Transport Aircraft Crashworthiness and Ditching Working Group
TAMCSWG	Transport Airplane Metallic and Composite Structures Working Group
TCCA	Transport Canada Civil Aviation
TC	Type Certificate
TCH	Type Certificate Holder
TD	Type Design
Tg	Glass Transition Temperature
TT	Through Transmission
UL	Ultimate Load
UT	Ultrasonic Testing
VARTM	Vacuum Assisted Resin Transfer Molding
Vz	Velocity (Z - vertical component)
WG	Working Group

Definition of terms

Critical Structure (AMC 20−29)	A load-bearing structure/element whose integrity is essential in maintaining the overall flight safety of the aircraft. This definition was adopted for this AMC because there are differences in the definitions of primary structure, secondary structure, and principle structural elements (PSE) when considering the different categories of aircraft. For example, PSE are critical structures for large aeroplanes.
Glass Transition (SAE AIR 4844)	The reversible change in an amorphous polymer or amorphous regions of a partially crystalline polymer from, or to, a viscous or rubbery condition to, or from, a hard and relatively brittle one. See Reference 2.9-ISO 472.
Glass Transition Temperature "Tg" (SAE AIR 4844)	The approximate midpoint of the temperature range over which the glass transition takes place:
Primary Structure (AC 25.1529-1A)	A structure that significantly contributes to the carrying of flight ground or pressure loads.

PSE **(AMC CS25.571** **Amdt.22 para. 2.7.2)**	An element that contributes significantly to the carrying of flight, ground, or pressurization loads, and whose integrity is essential in maintaining the overall structural integrity of the aeroplane.
Structural Bonding **(AMC 20−29)**	A structural joint created by the process of adhesive bonding, comprising of one or more previously cured composite or metal parts (referred to as adherends).
Weak Bond **(AMC 20−29)**	A bond line with mechanical properties lower than expected, but without any possibility to detect that by normal NDI procedures. Such a situation is mainly due to a poor chemical bonding.

References

[1] C. Fualdes, Revolutionising aerospace design and manufacturing, in: (Presented at the SAA-EASA Composite Materials Seminar). Singapore., April 14−16, 2014.

[2] D. Polland, Sharing on Boeing 787 experience, in: (Presented at the SAA-EASA Composite Materials Seminar). Singapore., April 14−16, 2014.

[3] B. Dambrine, Understanding composite materials, in: (Presented at the SAA-EASA Composite Materials Seminar). Singapore. 14−16 April 2014, 2014.

[4] B. Saada, Certifying a composite seat, in: (Presented at the SAA-EASA Composite Materials Seminar). Singapore., April 14−16, 2014.

[5] EASA, AMC 20-29 Composite Aircraft Structure, 2010. http://easa.europa.eu/system/files/dfu/Annex%20II%20-%20AMC%2020-29.pdf.

[6] Composite Materials Handbook − 17 (CMH-17) rev.G, 2013. https://www.cmh17.org.

[7] S. Waite, Safety management, certification and the extended use of composite materials in large passenger aircraft structures, J. Aviat. Management (2014) 68−84. https://saa.caas.gov.sg/documents/20181/339902/SAA_Journal_2014.pdf/93eca021-cd8f-4edc-af6f-6196515bfd15.

[8] C. Ashforth, L. Ilcewicz, Certification and compliance considerations for aircraft products with composite materials, in: P.W.R. Beaumont, C.H. Zweben (Eds.), Comprehensive Composite Materials II, vol. 3, Academic Press, Oxford, 2018, pp. 1−15.

[9] T. Swift, Damage tolerance capability, Fatigue 16 (1) (1994) 75.

[10] ASTM F3115, 'Specification for Structural Durability for Small Airplanes'.

[11] Composite Materials Handbook − 17 (CMH-17) vol. 3 rev.G Chapter 4 'Building Block Approach for Composite Structures', 2013. https://www.cmh17.org.

[12] Composite Materials Handbook − 17 (CMH-17) vol. 3 rev.G Chapter 12 'Damage Resistance, Durability, and Damage Tolerance', 2013. https://www.cmh17.org.

[13] C. Fualdes, in: 'Experience and Lessons Learned of a Composite Aircraft' Proceedings 30th Congress 28th September, 2016. Daejon Korea.

[14] W. Seneviratne, J. Tomblin, Deferred severity spectrum for durability and damage tolerance certification testing of hybrid structures, in: Proceedings CAMX Conference, Anaheim, CA, September 26−29, CAMX − The Composites and Advanced Materials Expo, 2016.

[15] NTSB aircraft accident report Aloha airlines, Flight 243 (1988). AAR 89/03.

[16] Airbus, in: Composite Workshop Tokyo, 2009.

[17] M.J. Davis, A. Mc Gregor, The conditions where NDI may not prevent failure in real bonded structures, in: Proceedings AINDT Inspection and Safety in Aircraft Maintenance Seminar, Brisbane, 2015.

[18] AAIB Aircraft Accident Report 5/93, Rudder Repair Example.

[19] AAIB Bulletin No 12/2000 Ref. EW/C98/5/8 (5/1998), elevon example.

[20] AAIB Bulletin No.12/2000 Ref. EW/A98/10/2 (10/1998), rudder example.

[21] R. Hilgers, Airbus rudder experience focus − sandwich disbond growth due to GAG-cycle, in: (Paper Presented at the EASA Bonded Structure Workshop). Cologne, Germany, 13−14 June 2013, 2013.

[22] H. Hicken, Airbus − new standards together, in: (Paper Presented at the EASA Bonded Structure Workshop). Cologne, Germany, 13−14 June 2013, 2013.

[23] State Commission on Aircraft Accident Investigation, Warsaw, Occurrence No. 619/10 (1/7/2011). .

[24] EASA CM-S-005 'Bonded Repair Size Limits in Accordance With CS-23, CS-25, CS-27, CS-29 and AMC 20-29'. https://www.easa.europa.eu/sites/default/files/dfu/'final' CM-S-005 Issue 01_Bonded Repair Size Limits_PUBL.pdf.

[25] P.R. Field, W. Hand, G. Cappelluti, A. McMillan, A. Foreman, D. Stubbs, M. Willows, 'Hail Threat Standardisation' EASA_REP_2007_3, 2010. https://www.easa.europa.eu/sites/default/files/dfu/EASA_REP_RESEA_2008_5.pdf.

[26] D. Wernert, in: 'Practical Robust Monocoque Sandwich Structure Design' Proceedings EASA Bonded Structure Meeting June 2013, 2013.

[27] J. Baaran, Visual Inspection of Composites EASA_REP_2007_3, 2007. https://www.easa.europa.eu/document-library/research-projects/easarepresea20073.

[28] DOT/FAA/AR-99/49 Review of Damage Tolerance of Composite Sandwich Airframe Structures. .

[29] Composite Materials Handbook − 17 (CMH-17) vol. 3 rev.G, Chapter 12, paras.12.5.2.5 and 12.5.2.6, 'Damage Tolerance − Hail'. https://www.cmh17.org.

[30] UK CAA Report CU/WA9/W30814E/62 and Cranfield University.

[31] N. Toso, A. Johnson, 'LIBCOS − Significance of Load Upon Impact Behaviour of Composite Structure' EASA.2009/3, 2009. https://www.easa.europa.eu/sites/default/files/dfu/LIBCOS_final_report_v4_1.pdf.

[32] SAE − Commercial Aircraft Composite Repair Committee (CACRC) Guidance Document AE27 'Design of Durable. Repairable, and Maintainable Aircraft Composites'.

[33] Composite Materials Handbook − 17 (CMH-17) Volume 3 rev.G fig. 14.10.9.1(a). https://www.cmh17.org.

[34] FAA AC 43-214A 'Repair and Alterations to Composites and Bonded Aircraft Structures'.

[35] SAE International, SAE ARP 6461 Guidelines for Implementation of Structural Health Monitoring in Fixed Wing Aircraft, 2013. http://standards.sae.org/arp6461/.

[36] EN 4179 'Qualification and Approval of NDT Personnel'.

[37] C. Fualdes, Detection and inspection methodologies, in: (Presented at the SAA-EASA Composite Materials Seminar). Singapore. 14−16 April 2014, 2014.

[38] DOT/FAA/AR-02/121 Guidelines for Analysis, Testing, and Non-destructive Inspection of Impact-Damaged Composite Sandwich Structures.

[39] A. Psymouli, D. Harris, P. Irving, The Inspection of Aircraft Composite Structures: A Signal Detection Theory-Based Framework, Cranfield University, for UK CAA, 2003.

[40] L. Cook, P. Irving, D. Harris, Reliability of Visual Inspection of Advanced Composite Aircraft Structures, Cranfield University, for UK CAA, 2009.

[41] S. Waite, Miscellaneous R&D Data, 1985−88.

[42] T. Pringle, Preventing Ramp and Ground Accidents, 2010. http://www.tc.gc.ca/eng/civilaviation/publications/tp185-1-07-printable-3010.htm.

[43] FAA PS-ANM-25-20 'High Energy Wide-Area Blunt Impact for Composites Structures.

[44] K. Hyonny, Impact Damage Formation on Composite Aircraft Structures, University of California, San Diego, US, 2012.

[45] P. Bishop, Composite Damage Metrics and Inspection − High Energy Blunt Impact EASA_REP_RESEA_2013_3, 2009, 2010, & 2011. https://www.easa.europa.eu/sites/default/files/dfu/EASA_REP_RESEA_2013_3.pdf.

[46] EASA Supplemental Type Certificates, Production Without Production Approval. Repairs. https://eur-lex.europa.eu/legal-content/EN/TXT/PDF/?uri=CELEX:32012R0748&from=EN.

[47] T. Walker, in: 'A Conceptual Framework for Practical Progressive Damage Analysis of Stiffened Composite Aircraft Structure with Large Notches Subjected to Combined Loading' − CMH-17, Salt Lake City Meeting, 2015.

[48] F.A.A. 'Composites, in: Mods & Alterations Workshop', Wichita 22nd July 2016, 2016.

[49] FAA, in: Workshop on Composite Modification Certification', Wichita 22−23rd August, 2017.

[50] Composite Materials Handbook − 17 (CMH-17) Vol.3 rev.G Chapter 16 'Crashworthiness and Energy Management'. https://www.cmh17.org.

[51] ASTM D30 'Committee D30 on Composite Materials'.

[52] Aerospace Structural Impact Dynamics International Conference, 4−6th June 2019, Madrid, 2019. http://asidiconference.org/.

[53] FAA PS-ACE100-2-18-1999 'Policy on Acceptability of Temperature Differential Between Wet Glass Transition Temperature (Tgwet) and Maximum Operating Temperature (MOT) for Epoxy Matrix Composite Structure'.

[54] Eurocae ED84 'Aircraft Lightning Environment and Related Test Waveforms'.

[55] Eurocae ED91 'Aircraft Lightning Zoning Standard'.

[56] AAIB, Aircraft Accident Report 1/2005, 2005.

[57] EU PART 21 GM 21.B.25(c). https://www.easa.europa.eu/sites/default/files/dfu/Annex%20I%20to%20ED%20Decision%202012-020-R.pdf.

[58] D. Polland, Composite materials Training A, in: Presented at the SAA-EASA Composite Materials Seminar). Singapore. 14−16 April, 2014.

[59] Arbeitskreis Faserverbundwerkstoffe (AFF), in: Seiteneinsteigerprogramm, Proceedings EASA GA Workshop 16−17th November, 2017. https://www.easa.europa.eu/sites/default/files/dfu/GA%20Structures%20Workshop%20Final%20Agenda.pdf.

[60] J. Popp, Impact and challenges on aircraft maintenance by the increasing use of composite materials, in: Presented at the SAA-EASA Composite Materials Seminar). Singapore. 14−16 April, 2014.

[61] M. Davis, Deficient practices in on-aircraft adhesive bonded repairs, in: Presented at the SAA-EASA Composite Materials Seminar). Singapore. 14−16 April, 2014.

[62] DOT/FAA/TC-14-20, Nonconforming Composite Repairs − Case Study Analysis, 2014. Fig.7.

[63] EASA − Part 66 'Certifying Staff', Part 147. https://eur-lex.europa.eu/legal-content/EN/TXT/PDF/?uri=OJ:L:2014:362:FULL&from=EN.

[64] SAE − Commercial Aircraft Composite Repair Committee (CACRC) AIR 5719A 'Teaching points for an awareness Class on 'Critical Issues in Composite Maintenance and Repair'.

[65] ADR.OPS.B.015 Monitoring and Inspection of Movement Area and Related Facilities. https://eur-lex.europa.eu/LexUriServ/LexUriServ.do?uri=OJ:L:2014:044:0001:0034:EN: PDF.

[66] ADR.OPS.B.025 Operation of Vehicles, https://eur-lex.europa.eu/LexUriServ/LexUriServ.do?uri=OJ:L:2014:044:0001:0034:EN:PDF.

[67] EASA, in: Materials EASA GA Workshop 16−17th November 2017, 2017. https://www.easa.europa.eu/sites/default/files/dfu/GA%20Structures%20Workshop%20Final%20Agenda.pdf.

[68] S. Waite, Miscellaneous Photos (Personal Library and/or Other Regulatory Sources).

[69] EU PART 21.A.3A 'Failures, Malfunctions and Defects'. https://eur-lex.europa.eu/legal-content/EN/TXT/PDF/?uri=CELEX:32012R0748&from=EN.

[70] ADR.OR.D.030 'Safety Reporting System'. https://eur-lex.europa.eu/LexUriServ/LexUriServ.do?uri=OJ:L:2014:044:0001:0034:EN:PDF.

[71] M.J. Davis, D.A. Bond, The importance of failure mode identification in adhesive bonded aircraft structures and repairs, in: The International Conference on Composite Materials − 12, Paris, July 1999, pp. 05−09, in: http://www.iccm-central.org/Proceedings/ICCM12-proceedings/.

[72] M.J. Davis, A. Mc Gregor, Assessing adhesive bond failures: mixed-mode bond failures explained, in: ISASI (International Society of Aviation Safety Investigators) Australian Safety Seminar, Canberra, June 2010, 2010. http://www.adhesionassociates.com/papers/56%20Assessing%20Adhesive%20Bond%20Failures%20-%20Mixed-Mode%20Bond%20Failures%20Explained.pdf.

[73] M. Davis, Crash investigation of primary structural failure in a helicopter, in: Presented at the SAA-EASA Composite Materials Seminar). Singapore, April 2014, pp. 14−16.

[74] SAE − CACRC AIR 4844 'Composite and Metal Bonding Glossary'.

[75] EASA CM-S-010 'Composite Materials − 'the Safe Design and Use of Monocoque Sandwich Structures in Principal Structural Element Applications'. https://www.easa.europa.eu/sites/default/files/dfu/CM-S-010%20Issue%2001.pdf.

[76] EASA/FAA, in: Sandwich Structures Workshop 18/9/2016, 2016. https://www.easa.europa.eu/newsroom-and-events/events/easafaa-sandwich-structure-workshop.

[77] SAE − CACRC AIR 6291 'Guidelines for Repair Process Evaluation of Aluminium Bonded Structure'.

[78] J.C.A.I.R.E. Popp, New repair technologies as first step to future bonded repairs, in: Presented at the SAA-EASA Composite Materials Seminar). Singapore, April 2014, pp. 14−16.

[79] SAE AIR 6337, 'Design, Manufacture and Performance Standard for Composite Materials Used in Aircraft Seat Structures', 2019 draft.

[80] Clean Sky 2. http://www.cleansky.eu/.

[81] EASA Signs Memorandum of Cooperation With Clean Sky. https://www.easa.europa.eu/newsroom-and-events/news/easa-signs-memorandum-cooperation-clean-sky.

[82] EASA Agency Organisation Structure. https://www.easa.europa.eu/the-agency/agency-organisation-structure.

[83] EASA Regulations Structure (High Level). https://www.easa.europa.eu/download/regulations-structure/regulations_structure.pdf.

[84] EASA Regulations. https://www.easa.europa.eu/regulations.

[85] EASA Type Certificates and Restricted Type-Certificates. https://eur-lex.europa.eu/legal-content/EN/TXT/PDF/?uri=CELEX:32012R0748&from=EN.

[86] EASA Operational Suitability Data (OSD). https://www.easa.europa.eu/easa-and-you/aircrew-and-medical/operational-suitability-data-osd.

[87] EASA − European Safety Management System (SMS). https://www.easa.europa.eu/easa-and-you/safety-management/safety-management-system/sms-europe.

[88] European Plan for Aviation Safety (EPAS). https://www.easa.europa.eu/easa-and-you/safety-management/european-plan-aviation-safety.

[89] SAE − Commercial Aircraft Composite Repair committee (CACRC). https://www.sae.org/works/committeeHome.do?comtID=TEAAMSCACRC.

[90] EASA − SMS − EASA Rules (Level of Involvement (LoI). https://www.easa.europa.eu/easa-and-you/safety-management/safety-management-system/sms-easa-rules.

[91] EASA CM-S-004 'Composite Materials − Shared Databases, Acceptance of Composite Specifications and Design Values Developed Using the NCAMP Process'. https://www.easa.europa.eu/sites/default/files/dfu/certification-docs-certification-memorandum-'final'-EASA-CM-S-004-Issue-01_Composite-Materials–Shared-Databases_PUBL.pdf.

[92] EU PART 21 GM 21.A.435 Classification of Repairs. https://www.easa.europa.eu/sites/default/files/dfu/Annex%20I%20to%20ED%20Decision%202012-020-R.pdf.

Index

Note: 'Page numbers followed by "f" indicate figures and "t" indicate tables'.

The revised edition of this book provides a detailed review of the latest research and developments in the design, manufacture, and performance of polymer composites, their use, and application in aerospace structures.

- Provides detailed discussion of the design, modelling, and analysis of conventional and advanced polymer composites used in aerospace applications.

- Provides an in-depth understanding of polymer composite properties essential to their application in aerospace structures. Factors determining properties such as tension and compression strength, stiffness and fatigue, impact and fatigue after impact are all treated.

- Features additional chapters focussed on application-specific properties that are essential in aircraft, such as lightning strike protection, damage tolerance, airworthiness, and certification issues.

Polymer composites are increasingly used in aerospace applications because of their excellent strength and durability compared to weight. Edited by two leading authorities in the field, the revised edition of this book summarizes the latest research and developments on the design, manufacture, and performance of composite components for aerospace structures. Part one includes chapters on the modeling, structure, and behavior of 2D- and 3D-woven composites; the manufacture processes used for composite materials and components; buckling and compressive strength of laminates; and manufacturing defects in composite materials. Part two discusses aspects of composite performance in aerospace structural design, including chapters on modeling stiffness and strength of structural elements; fatigue under uniaxial and multiaxial loads; fracture mechanics; and impact strength; crashworthiness; design; and failure analysis of bolted joints; response of aerospace composite to temperatures and humidity; blast response; repair, nondestructive testing of damage; structural health monitoring; airworthiness; and certification.

Polymer Composites in the Aerospace Industry is an essential reference resource for engineers, scientists, and designers working in the development of composite materials in aerospace applications.

About the Editors

Philip Irving is Emeritus Professor of Structural Integrity at the University of Cranfield, UK, and Fellow of IOM3. He has over 30 years experience in teaching and research of structural integrity of aircraft structures and has worked in collaboration with many key companies and organizations in the aerospace industry providing specialist knowledge and expertise.

Constantinos Soutis FREng is Professor of Aerospace Engineering, Director of the Aerospace Research Institute at the University of Manchester, and Fellow of the Royal Academy of Engineering. With more than 30 years of experience in working with composite structures, he has taught and performed research at some of the most highly respected universities in the world.